

ECIO 2019

European Conference on Integrated Optics

Ghent University, Belgium

Collected Manuscripts

(c) Copyright 2019 The ECIO Board. All rights reserved.

Contents

ID	Author	Title
S1.1	Ruggero Loi1, Simone Iadanza1, 2	Edge-coupling of O-band InP etched-facet lasers to polymer waveguides on SOI by micro-transfer-printing
S1.2	Yaojing Zhang, Li Tao, Dan Yi, J	Thermo-optic Nonlinearities in MoS2-on-silicon Microring Resonator
S1.3	Alicia Ruiz-Caridad1, Guillaume	Erbium-doped Yttria-stabilized Zirconia thin layers for photonic applications
S2.1	Marco Romagnoli	Graphene Photonics for Optical Communications
S2.2	Kristif Prifti1, Netsanet Tessem	8 x 40 Gb/s WDM Photonic Integrated Wavelength Switch Module for Optical Data Center Networks
S2.3	III-V On Silicon Tunable Local O	First Silicon Photonics Coherent Receiver With Heterogeneously Integrated III-V On Silicon Tunable Local Oscillator Operating At 28GBd Data Rates
S2.4	D. Benedikovic1, L. Virot2, G. A	High-speed-performing pin photodetectors with lateral silicon-germanium-silicon heterojunctions for 1.55 μm communications
S2.5	Mikko Karppinen1, Mikko Harjanne	Optical transceiver engine based on 12 μm Silicon-on-insulator waveguides and VCSELs
S3.1	Student Paper	100 GHz Multiple Colliding Pulse Generation from Cleaved Facet-free Multi-section Semiconductor Laser Diode
S3.2	Iterio Degli-Eredi and Martijn	Experimental Characterization of a Novel Energy-efficient Integrated Microwave Photonics Modulator
S3.3	Student paper	Waveguide Photonic Crystal Reflectors on InP-Membranes-on-Silicon
S3.4	Tianran Liu1, Francesco Pagliano	Low-Voltage InP MEMS Optical Switch on Silicon
S4.1	Quentin Chateiller1,2, Francesco	III-V on SOI photonic crystal devices (Invited paper)
S4.2	Imad I. Faruque 1, Gary F. Sincl	A comparison between waveguide and microresonator single-photon sources in silicon photonics
S5.1	Jos van der Tol1, Yuqing Jiao1,	InP Membrane on Silicon (IMOS) Photonics
S5.2	Mu-Chieh Lo, Robinson Guzmán, Je	Fundamental and Subharmonic Hybrid Mode Locking of Semi-assembled Semiconductor Ring Laser in InP Generic Foundry
S5.3	J.E.M. Haverkort1, A. Dijkstra1,	Direct bandgap hexagonal SiGe: A light emitter for Si-photonics?
S6.1	Peter T. Rakich1, Eric Kittlaus1	Brillouin based lasers, nonreciprocity, and cooling in silicon
S6.2	Shiyoshi Yokoyama, Guo-Wei Lu, X	110 Gbit/s On-Off-Keying Based on High Temperature Resistant Polymer Modulator
S6.3	Artur Hermans1,2, Stéphane Clemm	Growth of Organic Crystalline Thin Films with Strong Second-Order Nonlinearity for Integrated Optics
S6.4	Mamon Lamy1, Christophe Finot1,	Si and Si-rich silicon-nitride waveguides for optical transmissions and wavelength conversion around 2 μm
S7.1	Alexander L. Gaeta	Chip-Based Nonlinear Photonics
S7.2	Yi Zheng1, Minhao Pu1, Ailun Yi2	4H-SiC Microring Resonators for Nonlinear Integrated Photonics
S7.3	Andreas Boes1,2, Lin Chang2, Tha	The impact of lateral leakage on the nonlinear optical waveguide design in lithium niobate on insulator (LNOI)
S7.4	Gary F. Sinclair 1, Takafumi Ono	An Integrated Silicon Photonic Nonlinear Interferometer
S7.5	Neetesh Singh1, Ming Xin1, Nanxi	Nonlinear silicon photonics for optical frequency synthesis
S8.1	Mark G. Thompson	Integrated quantum photonic technologies for applications communications and computation

S9.1	Andreas Beling	High-Speed Photodetectors
S9.2	Zhenzhou Tang1,2,3, Jing Zhang2,	Full-Duplex Analog Radio-over-Fiber System based on an Integrated Transceiver with a Silicon Microring Modulator and a Transfer-Printed III-V Photodetector
S9.3	Junqiu Liu1, Jijun He1, Erwan Lu	Photonic Integrated Microwave Oscillator Based on Silicon Nitride Soliton Microcomb
S9.4	Kasper Van Gasse1,2, Jochem Verb	EAM-based Microwave Mixer Implemented in Silicon Photonics
S9.5	Bassem Tossoun, Géza Kurczveil,	1310 nm quantum dot waveguide avalanche photodiode heterogeneously integrated on silicon
S10.1	Amr S. Helmy1	Recent advances in Hybrid Plasmonic Circuits for Data Communications
S10.2	A. Manolis1, E. Chatzianagnostou	High-sensitivity interferometric sensors on Si3N4 platform using Surface Plasmon Polariton (SPP)-based transducers
S10.3	Guanghui Ren, Baoyue Zhang, Mark	Silicon photonics ionic sensor enabled by hybrid integrated 2D plasmonic MoO3
S11.1	Daniele Melati1, Yuri Grinberg2,	Machine-assisted design and stochastic analysis in integrated photonics
S11.2	Zunyue Zhang1, Yi Wang1, Hon Ki	Ultracompact 40-Channels Arrayed Waveguide Grating on Silicon Nitride Platform at 850nm
S11.3	B. Imran Akca1, Christopher R. D	Interleaved Silicon Nitride AWG Spectrometers
S11.4	Yeyu Tong, Wen Zhou, Xinru Wu an	Efficient Mode Multiplexer for Few-Mode Fibres Using Integrated Silicon-on-Insulator Grating Coupler
S11.5	Claudio Porzi1, Graham J. Sharp2	High-Performance Silicon Photonics Optical Filters with High-Order Distributed Feedback Resonators
S12.1	W. J. Westerveld, B. Figeys, H.	Micro-Opto-Mechanical Pressure, Sound, and Ultrasound Sensors in Silicon-Nitride Photonic Technology
S12.2	Andrea Melloni1, Faisal Ahmed Me	Boosting thermo-optic efficiency of silicon (oxy)nitride waveguides
S13.1	Shinji Matsuo	Membrane III-V phonic devices on SiO2/Si substrate
S13.2	Koen Alexander,1,4 John P. Georg	PZT-based Pockels Modulators on Silicon and Silicon Nitride Waveguides
S14.1	Jens Buus1, Ralf Meyer2	40 Years of Semiconductor Lasers, A Tribute to Markus-Christian Amann
S14.2	Rachel Won	How can you be part of Nature Photonics?
S15.1	We present platforms for monolit	Monolithic electronic-photonic integration in zero-change SOI and bulk CMOS
S16.1	Architectures against Parasitic	Evaluation of Stability of Silicon-Photonics-Based Optical Switch Network Architectures against Parasitic Errors in Switch Elements
S16.2	Nirmalendu Acharyya 1;2, Gregory	Large Q factor with small ring cavities
S16.3	for Photonic Label Router	Proposal of Integrated-Optical Circuit for Recognition of 8PSK-Coded label for Photonic Label Router
S16.4	Alessandro Aimone1, Netsanet Tes	Monolithically Integrated Wavelength-Selective Switch on InP: a Circuit Simulation-Based Design Study
S16.5	Pengli An*, Andreas Hänsel, Mart	Theoretical and Experimental Study of Distributed Bragg Reflector Lasers on SMART Photonics Platform
S16.6	Laurens Bogaert1,2,*, Jochem Ver	Germanium Photodetector with Monolithically Integrated Narrowband Matching Network on a Silicon Photonics Platform
S16.7	Laurens Breyne1, Jochem Verbist1	Flexible Integrated Silicon Photonic mm-Wave Frequency Upconversion Using GeSi EAMs
S16.8	Luis A. Bru,1 Daniel Pastor,1 an	On the characterization of integrated power splitters and waveguide losses using optical frequency domain interferometry

S16.9	Avijit Chatterjee1, Shankar Kuma	Compact Cavity Enhanced Si MSM Photodetector in SiN-on-SOI
S16.10	David A. Coucheron1, Dushan N. W	Investigation of the Background Signal from 532 nm Excitation for Waveguide-based Raman Spectroscopy and Microscopy
S16.11	Ivan B Djordjevic	Slepian-States-based DV- and CV-QKD Schemes Suitable for Implementation in Integrated Optics
S16.12	Elena Durán-Valdeiglesias1,*, We	Shaping the optical properties of carbon nanotubes via chirality-selective resonant enhancement in silicon micro-ring resonators
S16.13	Andreas Hänsel, Martijn J.R. Hec	Design and analysis of an integrated widely tunable laser
S16.14	length amplification in the C-ba	Heavily doped Er3+/Yb3+planar waveguides on silica for high gain per unit length amplification in the C-band
S16.15	Shahram Keyvaninia, Patrick Rung	Novel Concept for Polarization Splitting in InP Platforms
S16.16	Umar Khan 1;2, Yufei Xing 1;2, A	Extracting Coupling Coefficients of Directional Couplers
S16.17	Cristine C. Kores1, Nur Ismail2,	Distributed Phase Shift and Lasing Wavelength in Distributed-Feedback Resonators
S16.18	Florian Lemaitre1, Marija Trajko	Multi-Band Gap Electro-Absorption Modulator Array in a Generic Integration Platform using Selective Area Growth
S16.19	Jonas Leuermann1;2, ´I ˜nigo Mo	Intrinsic Limit of Detection for Coherent Biosensing Systems Student Paper
S16.20	Chupao Lin1,2, Roel Baets1,2, Gu	Design of slot waveguide for ultra-violet light based on atomic layer deposition
S16.21	Qiankun Liu1,*, Joan Manel Ramir	On-chip integrated resonators for long-wave infrared photonics
S16.22	Zuyang Liu 1;2, Haolan Zhao 1;2,	On the Performance of Tantalum Pentoxide and Silicon Nitride Slot Waveguides for On-Chip Raman Spectroscopy
S16.23	John McPhillimy1, Charalambos Kl	High accuracy transfer printing of III-V/SOI micro-disk resonators for non-linear application
S16.24	Viphretuo Mere,1, Hemalatha Muth	Silicon Slot Waveguide based Bulk Refractive Index Sensing of Electrolyte and Carbohydrate
S16.25	Maziyar Milanizadeh, Douglas Agu	Automatic look up table generation technique for photonic integrated circuits
S16.26	Françoıs Mondain1, Tommaso Lung	Chip-based compact squeezing experiment at a telecom wavelength
S16.27	Mohd Nuriman Nawi1, Dilla Duryha	Photonic Crystal/Photonic Wire Multiple-micro-cavity Structure
S16.28	communication	Integrated pump rejection filter for high-quality photonic quantum communication
S16.29	Jorge Parra1,*, Irene Olivares1,	Non-Volatile and Ultra-Compact Photonic Memory
S16.30	Photonic Integrated Circuit (Stu	Investigation of the Dynamical Behaviour of Mutually Coupled Lasers on a Photonic Integrated Circuit
S16.31	Mahmoud Shahin1,2, Joris Van Ker	InP-on-Si DFB Laser Diode with Distributed Reflector for Improved Power Efficiency
S16.32	Yuting Shi 1, Bernardette Kunert	Novel adiabatic tapered coupler for small III-V lasers grown on SOI wafer
S16.33	Anton Stroganov, Michael Geiselm	Silicon Nitride PICs Platform Development from a Foundry Perspective: From Concepts to Real Applications
S16.34	Waveguide Circuits	Recognition of 8QAM Coded Label by Maximum Output of Optical Waveguide Circuits
S16.35	Yufei Xing 1; 2; , Mi Wang 1; 2	Extracting Multiple Parameters from a Compact Circuit for Performance Evaluation
S16.36	Chenglin Xu1, Evan Heller1, Mary	Simulation Methodology for LiDAR on Chip
S17.1	D. Benedikovic1, C. Alonso-Ramos	L-shaped grating couplers engineered with subwavelength metamaterial for sub-decibel coupling loss

S17.2	Srivathsa Bhat, Mikko Harjanne,	Low Loss Devices fabricated on the Open Access 3 μm SOI Waveguide Platform at VTT
S17.3	Jeroen Bolk1, Huub Ambrosius1, S	Application of Optical Proximity Correction for 193 nm Deep UV enabled InP Photonic Integrated Circuits
S17.4	W. R. Bottoms1, Amr S. Helmy 2	Heterogeneous Integration Roadmap – Package Level Systems Integration: A key to maintaining the pace of progress
S17.5	L. Bsawmaii 1, E. Gamet 1, F. Ro	Large enhancement of longitudinal magneto-optical effect with an all-dielectric resonant guided-mode grating
S17.6	WenSin Chong1, SoonXin Gan1, Cho	Using the polarisation response of planar optical waveguides to determine the anisotropic complex refractive index of graphene oxide thick films
S17.7	Michael J. Connelly	Wideband Static and Dynamic Model of a Tensile-Strained Bulk Reflective SOA
S17.8	Andraž Debevc, Janez Krč and Mar	Study of Silicon Waveguides with All-dielectric Metamaterial Cladding by Numerical Simulations
S17.9	Lucas Deniel1, Mathilde Gay2, Di	O-band DAC-less PAM-4 generation with a silicon dual-drive Mach-Zehnder Modulator
S17.10	Phuong T. Do1, Carlos Alonso-Ram	Tunable optoelectronic oscillator based on silicon micro-ring resonator
S17.11	Firehun Tsige Dullo1, Øystein Iv	Development of high index contrast waveguide platform for fluorescence based optical nanoscopy
S17.12	Christof Eigner1, Laura Padberg1	Integrated single-mode frequency converter based on KTP
S17.13	Mher Ghulinyan1, Gioele Piccoli1	Ultrathin SOI strip-loaded resonators: Permanent mitigation of losses using UV light
S17.14	Bahawal Haq 1;2, Gunther Roelken	Alignment-tolerant taper design for transfer printed III-V-on-Si devices
S17.15	waveguides Student Paper	Refractive index tunability and switching with vanadium dioxide on silicon waveguides
S17.16	Erika Koussi, Hugo Bruhier, Isab	Cylindrical Integrated Optic Resonant Reflection
S17.17	Maxim Neradovskiy, Hervé Tronche	Phase-matching unsensitive to waveguide parameters variations in χ2 based nonlinear integrated optics devices
S17.18	Thach G. Nguyen, Guanghui Ren, S	New Resonance Behavior based on Bound States in the Continuum in a Silicon Photonic Waveguide Platform
S17.19	nitride rib waveguides (Student	Grating assisted contra-directional filters with high rejection ratio in silicon nitride rib waveguides
S17.20	Lars Nielsen, Martijn J. R. Hec	Reduced Timing Jitter in a Hybridly Mode-Locked Semiconductor Laser due to an Increased Modulation Curvature
S17.21	Laura Padberg 1, Matteo Santandr	Optimisation of corrugation-free Rb-exchanged waveguides in periodically poled KTiOPO4
S17.22	Olivier Parriaux, Yves Jourlin	New Resonant Diffraction Phenomenon from Silicon Grating Waveguide
S17.23	Fabio Pavanello 1;2, Grigorij Mu	Highly-efficient grating couplers based on transfer-printing technology
S17.24	Shahryar Sabouri 1, Mojtaba Sohr	Numerical Investigation of Silicon Nitride-based Frequency Comb in the Radio over Fiber System
S17.25	David Schmelz1, Martin Steglich1	Back-illuminated normal-incidence Ge-on-Si photodetectors
S17.26	N.N. Skryabin1,2,*, D.V. Khudyak	Thermal regime of femtosecond writing for a phosphate glass
S17.27	Stanisław Stopiński, Krzysztof A	Development of a Portable Optical Time Domain Reflectometer System in Photonic Integration Technology
S17.28	Takuya Toma1, Yuya Shoji1,2, Tet	Silicon Waveguide Wavelength-selective Switch Using Cascaded Microring

		Resonators and Thermo-optic Phase Shifters
S17.29	Heidi Tuorila1, Jukka Viheriälä1	GaAs-based gain waveguides with U-bend architecture enabling low loss and high yield hybrid integration on silicon photonic circuit
S17.30	Jukka Viheriälä1, Matteo Cherchi	Building blocks for mid-IR programmable light source based on GaSb-based amplified spontaneous emission sources and μm-scale Silicon-on-Insulator waveguide photonics
S17.31	Junfei Xia, Minsheng Ding, Adria	The Feasibility of Building 1024 & 4096-port Nanosecond Switching for Data Centre Networks Using Dilated Hybrid Optical Switches
S17.32	Zejie Yu,1,2 Aosong Feng,1,2 Xia	Inverse-designed low-loss and wideband polarization-insensitive waveguide crossing
S17.33	Zejie Yu, Yang Ma, and Xiankai S	Photonic welding points for arbitrary on-chip optical interconnect
S17.34	Jianhao Zhang1,2, Carlos Alonso-	road-band phase-matched multimode waveguides for application to four-wave mixing
S17.35	Julien Zichi1,, Samuel Gyger1,,	An NbTiN superconducting single photon detector implemented on a LiNbO3 single mode nano-waveguide at telecom wavelength
S18.1	David A. B. Miller	Self-configuring optical circuits
S18.2	Niels Quack1, Hamed Sattari1, Al	EMS-based Silicon Photonic Integrated Devices and Circuits
S18.3	Caterina Vigliar1, Jeremy C. Adc	Programmable Four-Photon Graph State Generator in Silicon
S18.4	Ali W. Elshaari1, *, Iman Esmaei	Reconfigurable Hybrid Quantum Photonic Circuits
S19.1	Milos Nedeljkovic1,*, Ahmed Osma	New photonic platforms for the mid-infrared
S19.2	Mario Dagenais	Nanophotonics Integration for Astrophotonics
S19.3	Ali Raza ; 1;2, St´ephane Clemm	On-chip surface enhanced Raman spectroscopy using ALD grown plasmonic nanotrenches integrated with a silicon nitride slot waveguide
S19.4	V. Mittal1, G. Devitt2, P.N. Bar	Mid-infrared absorption spectroscopy of protein aggregates using germanium on silicon waveguides
S20.1	Robert Halir1,2, Alejandro Sánch	Silicon high performance devices using subwavelength structure
S20.2	David González Andrade1, Christi	Dual-polarization Ultra-wideband Nanophotonic Beam Splitter
S20.3	Maziyar Milanizadeh1, Piero Borg	Processing free space optical beams with a silicon photonic mesh
S20.4	Manon Lamy, Marie-Maxime Mennema	Exploring titanium dioxide as a new photonic platform

Edge-coupling of O-band InP etched-facet lasers to polymer waveguides on SOI by micro-transfer-printing

Ruggero Loi[1], Simone Iadanza[1, 2], Brendan Roycroft[1], James O'Callaghan[1], Lei Liu[1], Kevin Thomas[1], Agnieszka Gocalinska[1], Emanuele Pelucchi[1], Alex Farrell[3], Steven Kelleher[3], Raja Fazan Gull[3], Antonio Jose Trindade[3], Chris Anthony Bower[3], Liam O'Faolain[1, 2] and Brian Corbett

[1]Tyndall National Institute, University College Cork, Cork, T12R5CP, Ireland.

[2]Cork Institue of Technology, Bishopstown, Cork, T12 P928, Ireland.

[3]X-Celeprint Ltd., Cork, T12R5CP, Ireland.

e-mail: ruggeroloi@gmail.com

ABSTRACT

O-band InP etched facets lasers were heterogeneously integrated by micro-transfer-printing into a 1.54 μm deep recess created in the 3 μm thick oxide layer of a 220 nm SOI wafer. A 7×1.5 μm^2 cross-section, 2 mm long multimode polymer waveguide was aligned to the ridge post-integration by e-beam lithography with <1 μm lateral misalignment and incorporates a tapered silicon waveguide. A 170 nm thick metal layer positioned at the bottom of the recess adjusts the vertical alignment of the laser and serves as a thermal via to sink the heat to the Si substrate. This strategy shows a roadmap for active polymer-waveguides-based photonic integrated circuits.

Keywords: Heterogeneous integration, III-V semiconductors laser, silicon photonics, polymer waveguides.

1. INTRODUCTION

Silicon photonic integrated circuits for application in the telecommunications wavelength domain of 1300–1600 nm use InP-based materials as these provide the most mature structures for lighting, amplification, modulation and detection [1]. InP reflective semiconductor optical amplifier chips have been edge-coupled to silicon photonics in external cavity laser configuration [2]. The edge-coupling of InP-based etched-facet lasers to SOI by heterogeneous integration inside recesses defined on the SOI has been recently demonstrated through micro-transfer-printing (μTP) [3, 4]. In this case the devices are printed directly on the Si substrate and use an n-InP cladding layer of calibrated thickness for aligning the emitting waveguide to a trident mode size converter defined on the SOI. The recesses are etched at the ends of the SOI waveguide for reduced longitudinal misalignment. A similar approach can be applied for edge-coupling an InP laser to a polymer waveguide defined on the oxide layer of an SOI. This work reports the first O-band Fabry-Perot InP laser heterogeneously integrated into a recess on the SOI by μTP and edge-coupled to an SU8 polymer waveguide. The strategy allows us to engineer the alignment of the laser along the vertical axis through an intermediate metal layer deposited at the bottom of the recess.

2. EXPERIMENTAL METHODS

Pre-released etched-facet InP O-band lasers were heterogeneously integrated by μTP to recesses fabricated on a SOI wafer [Fig 1(a)]. This technique involves shearing the coupon to the sidewall while in light contact to the bottom of the recess and then bonding the coupon when matched. A metal layer pre-deposited at the bottom of the recess allows the tuning the height of the laser waveguide along the vertical axis and sinks the heat to the Si substrate. The alignment of the emitting facet along the two remaining spatial directions is ensured by the tolerances of μTP and by matching the device to one of the sidewalls. The use of a <3 nm thin vapour coated HDMS layer improved the yield of printed devices to >90 %. A straight polymer waveguide was defined post-integration on top of the SiO_2 cladding and edge coupled to the laser with <1 μm lateral misalignment [Fig 1(b)].

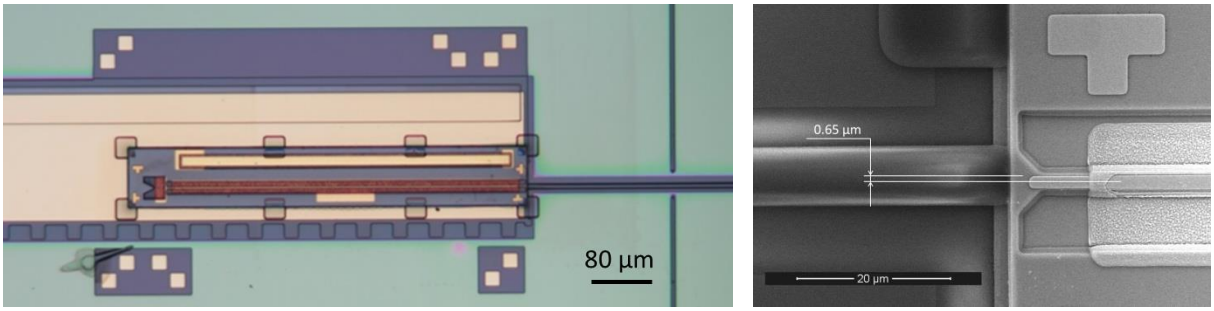


Figure 1.(a)Digital microscope image of the InP laser printed in a recess on the SOI and edge coupled to the polymer waveguide. (b) A scanning electron microscopy image of the waveguide aligned to the ridge of the laser shows <1μm lateral misalignment.

2.1 Laser devices

The lasers were pre-fabricated on the source InP wafer as dense arrays (about 1,000 devices per cm^2) of 550 µm long and 60 µm or 80 µm wide micro-transfer-printable coupons. A 500 µm long Fabry-Perot cavity was defined by two dry etched facets and passivated by an optically neutral SiO_2 layer and the back facet was then coated with a reflective metal layer. A 2 µm wide ridge etched just above the active region provides the lateral confinement of the light for single mode output. Accessible P- and N-type metal contacts were defined for testing the devices before and after transfer. The fabrication of the lasers included the steps for preparing the coupons to the undercut and the µTP as shown in previous work [5, 6]. The coupons were released from their native substrate by selectively etching a 500 nm thick InAlAs sacrificial layer arranged at the bottom of the N-InP cladding in $FeCl_3$:H_2O (1:2) kept at 1.0±0.1 °C for maximum selectivity to InP. The resulting suspended devices were then picked up and transfer-printed epitaxial-side-up to pre-fabricated recesses on the SOI.

2.2 SOI

A 220 nm SOI layer on a 3 µm thick buried oxide cladding was patterned to create 1.54 µm deep rectangular recesses suitable for edge coupling to waveguides [Fig 2]. Electron-beam (e-beam) lithography and a dry etch opened the SOI layer on the recesses area and defined some 0.6 µm wide tapered waveguides. A second etch formed the recesses on the SiO_2 without reaching the substrate. A third dry-etch opened part of the recesses, close to the printing area of the device, in order to access the Si substrate. A low rate flat evaporation of a Ti:Au (10:110) nm and a following low rate 360° angled Ti:Au (10:40) nm evaporation defined a smooth flat metal layer suitable for adhesive-less printing at the bottom of the recess. A flat and smooth metal layer is vital for achieving direct printing as imperfections and debris present on the metal surfaces require thick adhesive layers that would affect the alignment and the thermal performance [7]. High flatness and smoothness of the underlying SiO_2 surface is vital to prevent defect formation on the metal layer. The resulting surface of the metal shows flatness of <0.03 nm/µm and nominal roughness of <1 nm. The metal layer was connected to the substrate creating a thermal via for the heat sink. The metal layer thickness can be tuned with ±10 nm accuracy and allows alignment of the active region of the device to the polymer waveguide along the vertical axis. This recess design is suitable for the edge-coupling of laser coupons with different n-cladding thickness to polymer and SOI waveguides.

2.3 Polymer waveguide

A SU8 polymer layer of 1.5 µm thickness was spun on the SOI after printing the devices in the pre-fabricated recesses. The calibration of the thickness targeted a 1 µm thick layer with the difference between expected and actual thickness due to the topography present on the SOI. An etch-back of the polymer waveguide will bring the height of the waveguide back to 1 µm. An e-beam lithography defined a 7.5 µm wide and 2 mm long waveguide edge coupled to the ridge of the laser with <1 µm misalignment. The polymer waveguide incorporated a parallel SOI waveguide positioned at 4.75 µm distance far from the edge of the trench. This strategy allows etching the recesses without impacting the 140 nm wide tip of the taper. The other end of the waveguide lands in another recess which is in line to the first. Some polymer pads were defined around the coupon for locking the device in place as further processing on the sample could affect the adhesion [Fig. 1(a)].

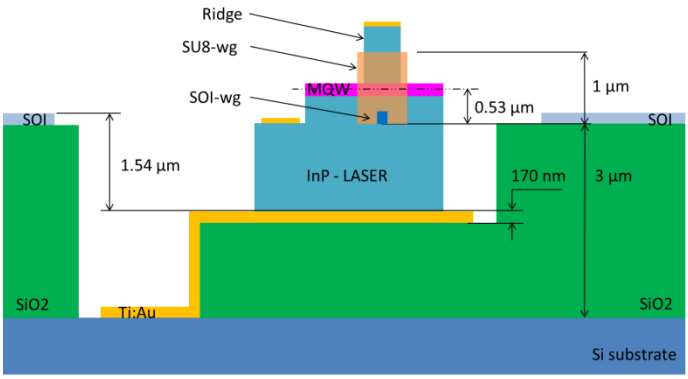


Figure 2. Diagram of the cross section of a laser printed in a 1.54 µm deep recess formed on the SOI, the 170 nm thick metal layer allows tuning the height of the active region (MQW) to 0.53 µm above the oxide layer, the 1 µm thick SU8 waveguide is aligned to the ridge.

3. EXPERIMENTAL RESULTS

The light-current characteristics of the devices show a threshold current of ~17 mA before and after µTP to the SOI that rises to ~23 mA after coupling the light to the SU8 waveguide due to reduced reflectivity on the front mirror. The laser operating at 20°C emits light at ~1340 nm wavelength. The light coupling to the polymer

waveguide was detected with an infrared (IR) camera that shows the light coming out at the end of the 2 mm long waveguide [Fig. 3b].

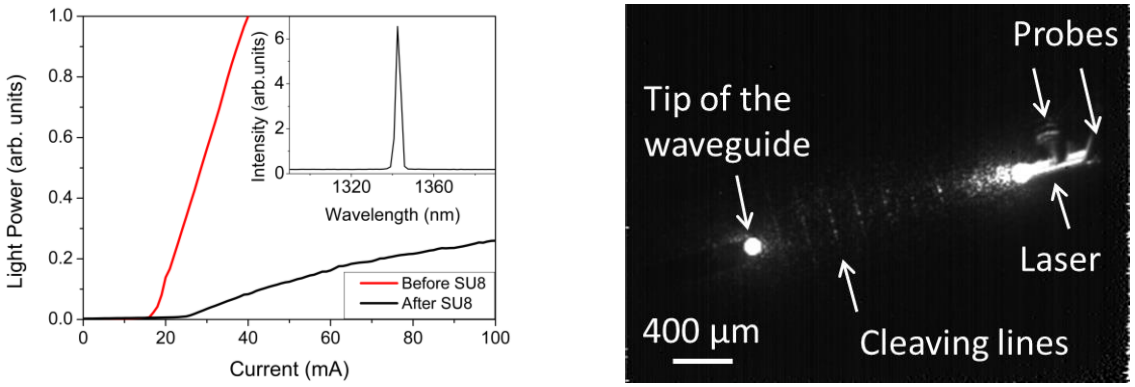


Figure 3. (a) LI characteristics for the laser printed in the recess before and after coupling the light to the SU8 waveguide. The inset shows the emission wavelength of ~1340 nm with the laser operating at 20°C before transfer. (b)IR camera imaging of the laser operating on the SOI and coupled to the 2 mm long polymer waveguide, the light comes out at the free end of the waveguide. Some transverse traces (cleaving lines) are due by recesses formed on the SOI to allow cleaving the chip.

4. CONCLUSIONS

Our approach allows the heterogeneous integration of generic thickness InP transfer printable devices in a desired location and on the desired layer of the SOI. Accurate vertical alignment of the emitting facet to the SOI is achieved through an intermediate metal layer pre-deposited at the bottom of the recess. This strategy enables use of micro-transfer-printing for the creation of PICs based on pre-fabricated devices connected by polymer waveguides or hybrid polymer-SOI waveguides. The efficiency of the light coupling can be improved by using alignment markers and pattern recognition at the transfer printer and by optimization of the polymer waveguide to make it single mode matched to the laser output. The measurement of the thermal impedance will provide a characterization of the thermal performance of the proposed laser.

ACKNOWLEDGEMENTS

Science Foundation Ireland (12/RC/2276 (IPIC) and 15/IA/2864); European Union's Horizon 2020 Research and Innovation Programme (45314 (TOP-HIT)).

REFERENCES

[1] Z. Wang, et al., "Novel light source integration approaches for silicon photonics," Laser & Photonics Reviews 11.4, 1700063 (2017).
[2] S. Iadanza, et al., “Thermally stable hybrid cavity laser based on silicon nitride gratings," Appl. Opt. 57, E218-E223 (2018).
[3] R. Loi, et al., "Micro-transfer printing for advanced scalable hybrid photonic integration," European Conference on Integrated Optics (ECIO'2018). 2018.
[4] J. Juvert, et al., "Integration of etched facet, electrically pumped, C-band Fabry-Pérot lasers on a silicon photonic integrated circuit by transfer printing." Optics express 26.17, 21443-21454 (2018).
[5] J. O’Callaghan, et al., "Comparison of InGaAs and InAlAs sacrificial layers for release of InP-based devices," Opt. Mater. Express 7, 4408-4414 (2017).
[6] R. Loi, et al., "Transfer Printing of AlGaInAs/InP Etched Facet Lasers to Si Substrates," IEEE Photonics Journal, 8, (6), 1504810 (2016).
[7] R. Loi, et al., "Thermal Analysis of InP Lasers Transfer Printed to Silicon Photonics Substrates," J. of Lightwave Technology 36.24, 5935-5941 (2018).

Thermo-optic Nonlinearities in MoS_2-on-silicon Microring Resonator

(Student Paper)

Yaojing Zhang, Li Tao, Dan Yi, Jian-Bin Xu, Hon Ki Tsang
The Chinese University of Hong Kong, Shatin, New Territories, Hong Kong
e-mail: hktsang@ee.cuhk.edu.hk

ABSTRACT

In this paper, we characterize the thermo-optic nonlinearities of a MoS_2-on-silicon microring resonator under different input powers. We experimentally observe an enhanced thermal-optic effect giving rise to about three times increase in resonance shift rate compared to that of a silicon microring resonator without MoS_2.

Keywords: thermo-optic nonlinearities, MoS_2, microring resonator.

1. INTRODUCTION

Atomically thin quasi two dimensional layers of molybdenum disulphide (MoS_2) have attracted much research interest in recent years because of their high Kerr nonlinearity, estimated to be about 10^{16} m^2/W [1], and their large bandgap which is increased by quantum confinement to about 1.9 eV for the MoS_2 monolayer. However, despite its large bandgap, MoS_2 is also known to absorb photons which have less than the bandgap energy because of the presence of defect states [3], and this has allowed MoS_2 to be used as saturable absorbers in mode-locked fiber lasers [2]. Silicon microring resonators have been used in optical delay lines [3], optical modulators [4], optical switches [5] and phase shifters for optical signal processing [6]. In this paper, we investigate whether the hybrid integration of a few layers of MoS_2 on a silicon microring resonator can enhance their Kerr nonlinearity or whether the optical characteristics of the microring is dominated by the defect state absorption in MoS_2 and thermal nonlinearity. We transfer the multi-layer MoS_2 onto the top of a silicon microring resonator. We measure the resonance shifts at different levels of continuous wave input optical powers coupled into the device. Our experimental results exhibit a large thermo-optic effect with a resonance shift rate of 0.24 nm/mW, which is about three times larger than that of a silicon microring but without the coverage of MoS_2.

2. FABRICATION

We fabricate the silicon resonator on the SOI wafer. The top silicon thickness is 250 nm and the buried oxide (BOX) is nominally 3 μm thick. The widths and heights of both bus waveguide and ring are designed as 500 nm and 250 nm, respectively. The width of gap between the bus waveguide and ring is designed to be 100 nm and the diameter of the ring resonator is about 40 μm as shown in the scanning electron microscopy (SEM) image of Figure 1(a). The light is coupled into the waveguide through uniform grating couplers. For the fabrication, we pattern both device and gratings with electron-beam lithography process. Then we deeply etch them with reactive-ion etching process. Multi-layer MoS_2 film (thickness ~5 nm) is grown on SiO_2/Si substrate by chemical vapor deposition, of which the details can be found in our previous paper [7]. Afterwards, the MoS_2 film is transferred onto the target ring resonator through a dry method assisted by viscoelastic polyvinyl alcohol film [8]. The length of the coverage is about 47 μm.

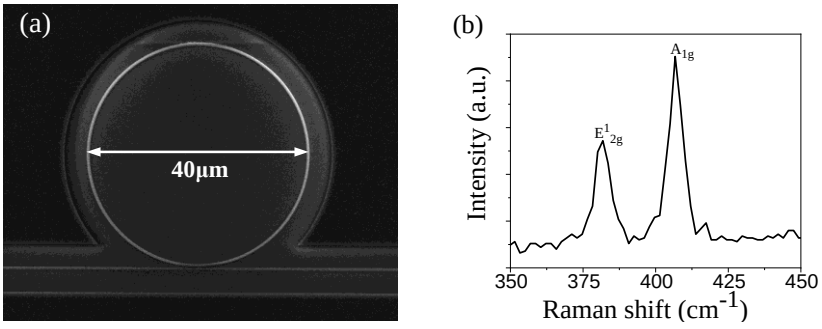


Figure 1. (a) SEM image of silicon ring resonator. (b) Raman spectrum of MoS_2 film used as the coverage of silicon ring resonator.

3. EXPERIMENTAL RESULTS AND ANALYSIS

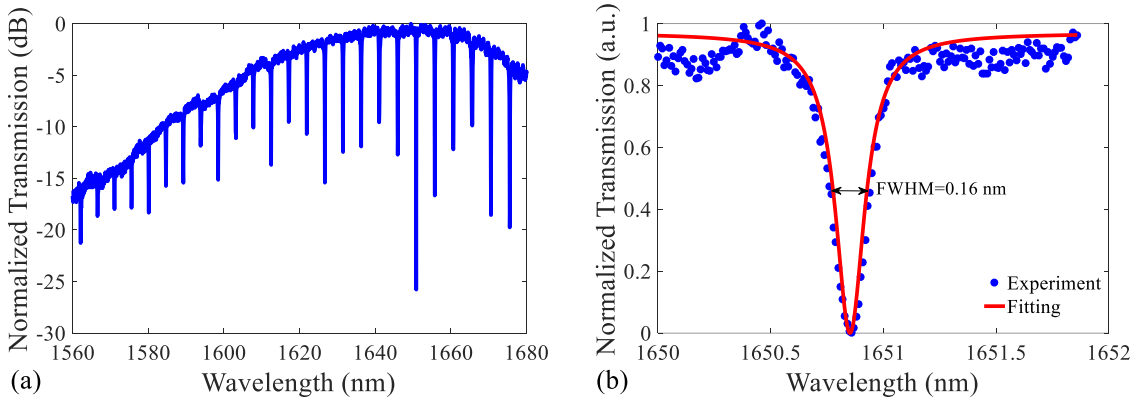


Figure 2. (a) Normalized transmission as a function of input wavelength with range from 1560 to 1680 nm. (b) Normalized transmission around 1651 nm with fitting curve from which its FWHM can be obtained as about 0.16 nm.

We first characterize the transmission of the resonator at a low coupled power. The quasi TM polarized light generated from a continuous-wave laser with power of 0.1 mW is the incident power at the waveguide grating coupler. We obtain the total fiber-chip-fiber insertion loss is about 20 dB. The free spectral range (FSR) of the microring is about 4.9 nm around 1651 nm as shown in Figure 2(a). The measured full width at half maximum (FWHM) of the resonance around 1651 nm is measured to be about 0.16 nm as shown in Figure 2(b) and the loaded quality factor derived from this measurement is $Q_L = \lambda_0/FWHM$=10300 (λ_0 is the resonant wavelength under low input power). The intrinsic quality factor $Q_i = 2Q_L/(1+\sqrt{T_0})$ (T_0 is the normalized transmission at resonant wavelength shown in Figure 2) [9] is estimated to be 19800 and the loss of ring per roundtrip is $\alpha_r = \lambda_0/(FSR \cdot Q_i \cdot R) = 8.5\ cm^{-1}$ (R is the radius of the ring) [9].

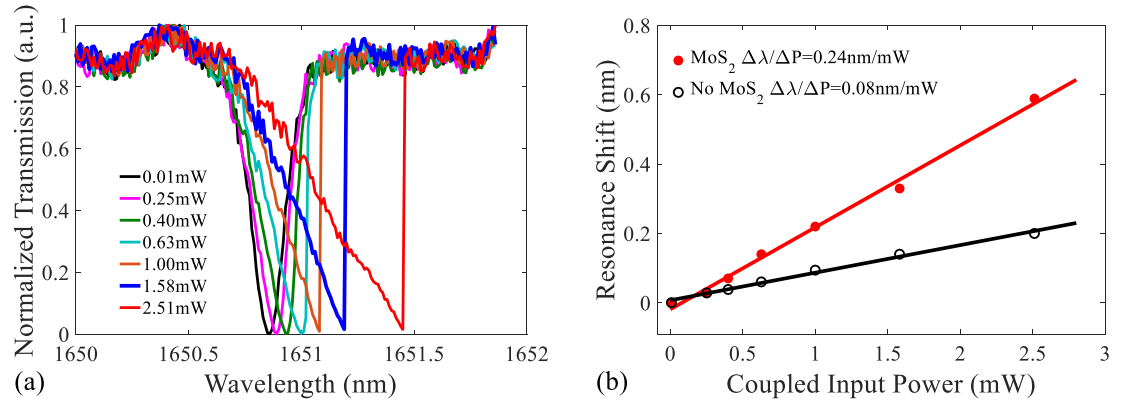


Figure 3. (a) Experimental transmission spectra at different coupled input power levels for MoS_2-on-silicon ring resonator which shows obvious thermal nonlinearities when we increase the input power. (b) Resonance shift versus coupled input power in the measurement and its corresponding fitting curve.

Next, with the same experimental setup, we increase the coupled input power into the waveguide and record the corresponding transmission around resonant wavelength of 1651 nm as shown in Figure 3(a). The coupled input power is after the loss of one grating coupler. At a low power, the resonant shape is symmetric while its shape becomes asymmetric and broader with the increase of power. The resonant wavelength is red-shifted with the increased input power. With the enhancement of the input power, thermo-optic effect leads to the redshifted resonant wavelength unlike free-carrier dispersion effect which would produce a blue shift [10]. Both phenomena stem from the changes of refractive index. In our case, the resonant wavelength is clearly redshifted with the increasing input power suggesting that the thermo-optic effect is the dominant mechanism for the nonlinear shift in resonant wavelength. Figure 3(b) illustrates the relation between the coupled input power and resonance shift and the resonance shift rate is obtained as about 0.24 nm/mW for MoS_2-on-silicon resonator while that of bare silicon resonator is 0.08 nm/mW. In the MoS_2-on-silicon resonator, the MoS_2 film absorbs the light owing to its defect states and further converts it to heat, leading to a various effective index of the waveguide due to the thermo-optic effect [11,12]. The varied effective index induces the resonance shift of the resonator.

4. CONCLUSIONS

We experimentally investigate thermal nonlinearities in MoS_2-on-silicon microring resonator. The corresponding loaded quality factor due to the additional loss from MoS_2 film is obtained as 10300. However, we observe three times increase in resonance shift rate compared to that of device without MoS_2 for the additional absorption of light from MoS_2 film due to its defect states and further converting it to heat.

ACKNOWLEDGEMENTS

This work was fully funded by Hong Kong Research Grant Council (RGC) GRF Project No. 14203318.

REFERENCES

[1] L. Liu, *et al.*: Enhanced optical Kerr nonlinearity of MoS_2 on silicon waveguides, *Photonics Res.*, vol. 3. pp. 206-209, Oct. 2015.

[2] M. Liu, *et al.*: Microfiber-based few-layer MoS_2 saturable absorber for 2.5 GHz passively harmonic mode-locked fiber laser, *Opt. Express*, vol. 22. pp. 22841-22846, Sep. 2014.

[3] J. Cardenas, *et al.*: Wide-bandwidth continuously tunable optical delay line using silicon microring resonators, *Opt. Express*, vol. 18. pp. 26525-26534, Dec. 2010.

[4] Q. Xu, *et al.*: 12.5 Gbit/s carrier-injection-based silicon micro-ring silicon modulators, *Opt. Express*, vol. 15. pp. 430-436, Jan. 2007.

[5] V. R. Almeida, *et al.*: All-optical switching on a silicon chip, *Opt. Lett.*, vol. 29. pp. 2867-2869, Dec. 2004.

[6] Q. Chang, *et al.*: A tunable broadband photonic RF phase shifter based on a silicon microring resonator, *IEEE Photonic. Tech. L.*, vol. 21. pp. 60-62, Jan. 2009.

[7] L. Tao, *et al.*: Centimeter-scale CVD growth of highly crystalline single-layer MoS_2 film with spatial homogeneity and the visualization of grain boundaries, *ACS Appl. Mater. Interfaces*, vol. 9. pp. 12073-12081, Mar. 2017.

[8] L. Tao, *et al.*: Deterministic and Etching-Free Transfer of Large-Scale 2D Layered Materials for Constructing Interlayer Coupled van der Waals Heterostructures, *Adv. Mater. Technol.*, vol. 3. pp. 1700282, May 2018.

[9] L.-W. Luo, *et al.*: High quality factor etchless silicon photonic ring resonators, *Opt. Express*, vol. 19. pp. 6284-6289, Mar. 2011.

[10] L. Zhang, *et al.*: Experimental observations of thermo-optical bistability and self-pulsation in silicon microring resonators, *JOSA B*, vol. 31. pp. 201-206, Feb. 2014.

[11] C. Horvath, *et al.*: Photothermal nonlinearity and optical bistability in a graphene-silicon waveguide resonator, *Opt. Lett.*, vol. 38. pp. 5036-5039, Dec. 2013.

[12] T. Gu, *et al.*: Molecular-absorption-induced thermal bistability in PECVD silicon nitride microring resonators, *Opt. Express*, vol. 22. pp. 18412-18420, Jul. 2014.

Erbium-doped Yttria-stabilized Zirconia thin layers for photonic applications

(Student paper)

Alicia Ruiz-Caridad[1], Guillaume Marcaud[1], Joan Manel Ramirez[2], Ludovic Largeau[1], Thomas Maroutian[1], Sylvia Matzen[1], Carlos Alonso-Ramos[1], Guillaume Agnus[1], Sylvain Guerber[1,3], Charles Baudot[3], Frederic Boeuf[3], Vladyslav Vakarin[1,4], Elena Duran-Valdeiglesias[1], Eric Cassan[1], Delphine Marris-Morini[1], Philippe Lecoeur[1], Laurent Vivien[1].

[1] Centre de Nanosciences et de Nanotechnologies, CNRS, Univ. Paris-Sud, Université Paris-Saclay, C2N - Palaiseau, 91120 Palaiseau, France

[2] III-V lab, joint lab from Nokia Bell Labs, Thales and CEA, 1 avenue Augustin Fresnel, 91767 Palaiseau Cedex

[3] TR&D STMicroelectronics SAS, Crolles, 38920, France

[4]IMEC, Kapeldreef 75,3001 Leuven, Belgium

e-mail: alicia.ruiz-caridad@c2n.upsaclay.fr

ABSTRACT

Near-infrared (near-IR) integrated photonic devices in silicon-based platforms have been studied over the last decades for applications such as on-chip optical communications and sensing. Driven by the need of more power efficient new photonic systems, the hybrid integration of functional oxides has become an attractive route to explore new physical phenomena. In this regard, Yttria-Stabilized Zirconia (YSZ) stands as an interesting material for its structural, chemical and optical properties. We recently demonstrated YSZ waveguides with propagation losses of 2 dB/cm at a wavelength of 1380 nm [1]. We have recently explored the introduction of active rare-earth dopants into YSZ waveguides to demonstrate on-chip optical amplifier. For that purpose, Er^{3+} ions are preferred due to their luminescence properties within the C-band of telecommunications. In this study, we demonstrate strong luminescence from Er-doped YSZ multilayer stacks around $\lambda = 1.54$ μm, grown by pulsed laser deposition (PLD) technique. The alternation of YSZ thin films and sub-nanometric layers of Er has enabled us to have control of the Er-Er inter-distance in the growth direction, hence being able to strongly decrease the luminescence quenching caused by upconversion processes. Moreover, the optical properties of Er-doped YSZ thin films grown on silicon nitride strip photonic waveguides under resonant pumping will be discussed in this paper.

Keywords: functional oxides, nanophotonics, rare earths, yttria-stabilized zirconia, optical gain, hybrid photonic platform.

1. INTRODUCTION

Latest advances in nanophotonics have triggered the search for low power consumption photonic devices. In this regard, engineering materials has been suggested as a powerful strategy to give birth to new functional materials willing to be implemented in silicon photonics platforms for a vast range of applications including datacom, telecom, sensing, or quantum optics [2]. In this context, functional oxides have been revealed as very interesting class of materials due to their singular characteristics comprising superconductivity, magnetism, ferroelectricity, catalytic activity, resistive switching, electro-optic effects, piezoelectricity, or optical nonlinearities, among others [3]-[6].

Despite the difficulties of hybrid integration on silicon photonics due to lattice constraints imposed by silicon, material engineering has been raised as an elegant solution to epitaxially grow high-quality crystalline functional oxide films on silicon keeping the interfaces light scattering and defect density to minima. This technique requires a buffer layer for lattice adaptation between silicon and the functional oxide and to avoid inter-diffusion between substrate and oxide materials.

An appealing material in this regard is yttria-stabilized zirconia (YSZ), extensively used as a buffer layer for functional oxides in applications as a solid electrolyte, gas sensors and fuel cells. YSZ outstanding properties include thermal and chemical stability and hardness and mechanical durability. Interestingly, YSZ also shows promising optical properties as it belongs the popular mid-index contrast material family (MiDex) [7] that is largely employed in photonics due to its low propagation loss and the absence of nonlinear phenomena, preventing two photon absorption (TPA) to dominate under high pumping conditions in the near and mid-IR; transparency from the ultraviolet to the near-infrared and a good Kerr effect puts this buffer oxide under the scope for photonic integration).

Rare-earth ions have been used as active materials for photonic devices to enhance light emission in integrated photonics to develop new light sources and optical amplifiers. One of the main challenges to confront on rare-

earth integration on a host is to keep the doping level as high as possible while avoiding quenching effects and maintaining a good crystalline quality of the host. Moreover, only low phononic materials able to avoid non-radiative effects are suitable to host rare-earth ions efficiently. Light amplification has been demonstrated in functional oxides as $LiNbO_3$ and gain for oxides as Al_2O_3 and Y_2O_3 [8]-[10], and have already demonstrated its potentiality when combined with photonic integrated circuits. Y_2O_3 thin films are good candidates as hosts for rare-earth ions in constructing active waveguides for telecommunication applications operating at 1.55 µm. Among the rare-earth ions, the erbium ion is known to have several transitions in the wavelength range within the near-infrared (near-IR) as a well as a good solubility in YSZ, making this rare-earth a perfect candidate for the development of efficient light emitting functional oxides at telecommunication wavelengths.

2. EXPERIMENTAL PROCEDURE

On a first approach, erbium-doped yttria stabilized-zirconia (Er:YSZ) thin films were deposited by pulsed laser deposition (PLD) on silicon dioxide (SiO_2) (0-100nm) encapsulated silicon nitrate (SiN_x) waveguides of 600nm on a silicon platform (Fig.1 (a)) at 800°C in an oxygen atmosphere. Laser ablation of two rotating targets of 8% mol YSZ ceramic target and metallic erbium was carried out by a KrF excimer laser (248-nm wavelength, 3-J/cm² fluence, and 5-Hz repetition rate).

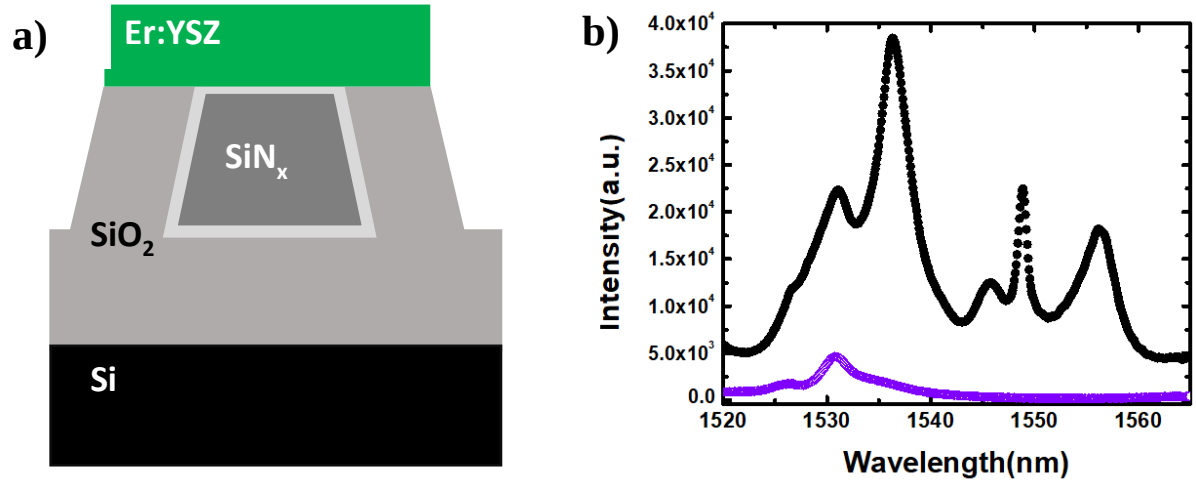


Figure 1. (a) Cross-section of a SiNx waveguide encapsulated by silicon dioxide on a silicon platform. A thin film of Er-YSZ was growth by PLD. (b) PL emission in the near-IR range of Er:YSZ thin film reveals two emissions of different intensities corresponding to the same transition: (black dotted) a locally enhanced signal showing Stark splitting for 1530, 1536 and 1548 nm and (purple dotted) an homogeneous emission with a maximum at 1530 nm.

2.1. Optical characterization

In Fig. 1(b) we observe two photoluminescence (PL) emission profiles corresponding both to erbium $^4I_{13/2} \rightarrow {}^4I_{15/2}$ transition) after exciting erbium-doped YSZ thin film at 980 nm with a continuous wave of a titanium-sapphire (Ti:Sa) laser. PL purple dots signal in Fig. 1(b) is homogeneously distributed on the sample and shows a higher intensity at 1530nm. Moreover, a local emission profile in Fig. 1(b) (black dots) proves Stark effect of the same transition with enhanced emissions at 1530, 1536 and 1548nm. Stark effect in rare-earth transitions is known to be related to the crystallinity of the sample, out of the scope of our study.

To further optically characterize our sample he have performed visible spectroscopy by pumping Er:YSZ on Si_3N_4 waveguides at a wavelength of 1480 nm. It has been evidenced strong up-conversion luminescence of erbium ions at 525, 544 and 562 (Fig. 2(a)), 656 and 679 nm (Fig. 2(b)) corresponding to $^2H_{11/2} \rightarrow {}^4I_{15/2}$, $^4S_{3/2} \rightarrow {}^4I_{15/2}$, $^2H_{9/2} \rightarrow {}^4I_{13/2}$, $^4F_{9/2} \rightarrow {}^4I_{15/2}$ and $^2H_{9/2} \rightarrow {}^4I_{11/2}$ transitions, respectively . Similar strong up-conversion has been previously observed in other material platforms displaying optical gain, hence providing an interesting scenario to further explore the gain characteristics of this new gain material for integrated photonics [11].

3. CONCLUSIONS

To sum up, high quality crystalline erbium-doped YSZ thin films were epitaxially grown on sapphire substrate and polycrystalline thin films on SiNx waveguides. Optical characterization by means of photoluminescence at 980 nm reveals erbium $^4I_{13/2} \rightarrow {}^4I_{15/2}$ transition for all the substrates and platforms and it has been noticed a local

multiple emission corresponding to Stark splitting with enhancement of luminescence. $^2H_{11/2} \rightarrow {}^4I_{15/2}$, $^4S_{3/2} \rightarrow {}^4I_{15/2}$, $^2H_{9/2} \rightarrow {}^4I_{13/2}$, $^4F_{9/2} \rightarrow {}^4I_{15/2}$ and $^2H_{9/2} \rightarrow {}^4I_{11/2}$ transitions have been measured by visible spectroscopy revealing strong erbium up-conversion when pumping at 1480nm.

Future work will focus on the study of gain in Er:YSZ on the hybrid SiN_x platform at 1.53 µm to unveilon-chip optical amplification at telecom wavelengths**.**

ACKNOWLEDGEMENTS

This work has received the funding from the European Research Council (ERC) under the European Union's Horizon 2020 Research and Innovation Program (ERC POPSTAR – grant agreement No 647342).

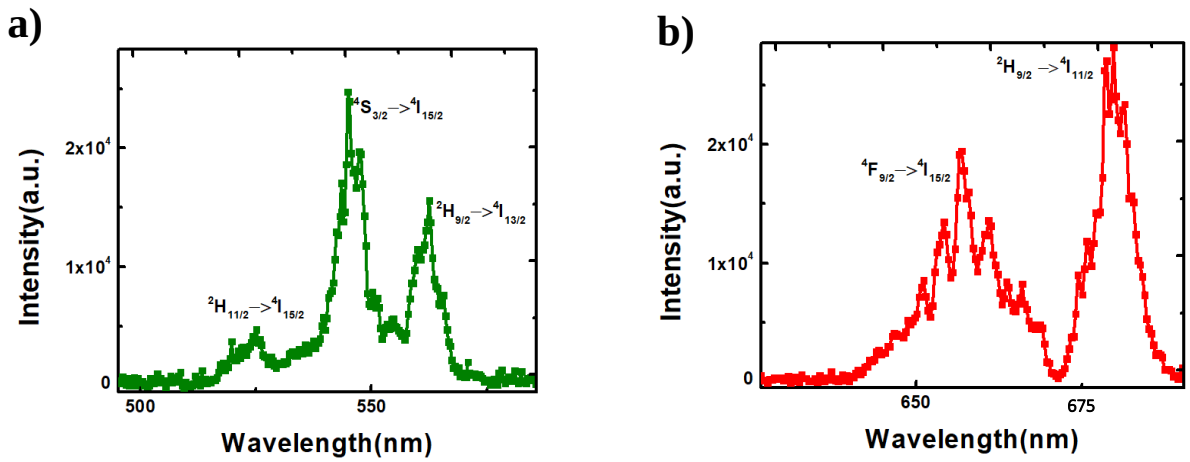


Figure 2. Spectroscopy in the visible range of wavelengths proves erbium up-conversion at different transitions corresponding to the green (a) and red (b) range of wavelengths.

REFERENCES

[1] G. Marcaud, *et al.:* High-quality crystalline yttria-stabilized-zirconia thin layer for photonic applications *Phys. Rev. Materials*, vol. 2. 035202, Nov.2018.

[2] R.J. Shiue, *et al.:* Active 2D materials for on-chip nanophotonics and quantum optics *Nanophotonics*, vol. 6, 0172, Mar. 2017.

[3] Z.R. Dai Pan, *et al.:* Novel nanostructures of functional oxides synthesized by thermal evaporation, *Adv. Functional Materials*, vol. 13. pp 9-24, Jan.2003.

[4] S. Abel, *et al.:* A strong electro-optically active lead-free ferroelectric integrated on silicon, *Nature Comm.*, vol. 4. pp. 1671, Apr. 2013.

[5] Q.Yang *et al.:* Enhancing sensitivity of a single ZnO micro-/nanowire photodetector by piezo-phototronic effect, *ACS Nano*, vol. 4. pp. 6285–6291, Oct.2010.

[6] M. Ando, *et al.:* Large third-order optical nonlinearities in transition-metal oxides, *Nature*, vol. 374, 625, Nov. 1999.

[7] Z. Zhang, *et al.:* A new material platform of Si photonics for implementing architecture of dense wavelength multiplexing on Si bulk wafer, *Science and Tech. of Adv. Mat.*, vol. 18. pp. 283-293, Apr.2017.

[8] E. Lallier, *et al.:* LiNbO3 with rare earths: lasers and amplifiers, *Proc ECO4*, 1506, 1991.

[9] J. Bradley, *et al.:*Integrated $Al_2O_3:Er^{3+}$ ring lasers on silicon with wide wavelength selectivity, *Opt. Lett.* vol. 35. pp.73-75, Aug. 2010.

[10] J. Bradley, *et al.:* Fabrication of low-loss channel waveguides in Al_2O_3 and Y_2O_3 layers by inductively coupled plasma reactive ion etching, *Appl. Phys.* vol. 89. pp. 311-318, Nov.2007.

[11] K. Suh, *et al.:* Cooperative upconversion and optical gain in ion-beam sputter-deposited $Er_xY_{2-x}SiO_5$ waveguides," *Opt. Express*, vol.18. pp. 7724-7731, Apr.2010.

Graphene Photonics for Optical Communications

(Invited paper)

Marco Romagnoli
Photonic Networks and Technologies Laboratory – CNIT, Pisa, Italy
e-mail: marco.romagnoli@cnit.it

ABSTRACT

Graphene is a gapless fermion material and this leads to a number of interesting electrooptical properties, one of them is the wavelength agnostic property, that is the possibility to operate devices at any wavelength. Waveguides topped with graphene show both electro absorption and/or refraction modulation wit excellent figure of merit. Graphene is also used in photodetection and can be implemented as bolometer or Seebeck ultrafast geometry. In the second case graphene detectors can be used in voltage mode.

Graphene is also an integrable material that results particularly compatible with silicon photonics and related materials. The wafer scale integration technology mainly require newly developed steps as graphene transfer, encapsulation and contacting. The quality of these steps determines the performance of the device.

ACKNOWLEDGEMENT

The author acknowledges funding from the European Union H2020 GrapheneCore2 Project 785219

REFERENCES

[1] M. Romagnoli *et al.*: Graphene-based integrated photonics for next-generation datacom and telecom, *Nat. Rev. Mat.*, vol. 3, pp. 392–414, Oct. 2018

8 x 40 Gb/s WDM Photonic Integrated Wavelength Switch Module for Optical Data Center Networks

Kristif Prifti[1], Netsanet Tessema[1], Xuwei Xue[1], Ripalta Stabile[1], Nicola Calabretta[1]
[1] IPI Research Institute, Eindhoven University of Technology, Eindhoven – The Netherlands
e-mail: k.prifti@tue.nl

ABSTRACT

We characterize the performance of a photonic integrated 1x8 WDM (8 channels Wavelength-Division Multiplexing) wavelength selective switch (WSS) module to realize a modular 8x8x8λ cross-connect switch. The module is based on SOA (Semiconductor Optical Amplifier) optical gates for nanoseconds wavelength and time switching operation. This technology enables the realization of low latency optical data center networks. Experimental measurements demonstrate a cross-talk lower than -35 dB, 11 dB/channel on chip gain and error-free operation at 40 Gb/s with limited penalty. The on chip gain and low cross-talk results presented in this study and the device proposed, being a scaled up version with double the channels of a previously demonstrated 4 x 4 modular architecture, validate the potentialities of this approach to scale up to an even larger channel number and hence port count.

Keywords: SOA (Semiconductor Optical Amplifier), PIC (Photonic Integrated Chip), DCN (Data Center Network), WSS (Wavelength Selective Switch).

1. INTRODUCTION

Due to emerging cloud computing, IoT, e-commerce and upcoming 5G applications more stringent requirements in terms of high bandwidth, low latency and large interconnectivity are imposed on the communication network inside the data centers [1]. In order to enable the scalable growth both of communication nodes and exchanged data traffic new architectural and technological solutions are needed. Optical switching is an attractive technology in this respect, providing data-rate and data-format transparency operation, and also avoiding the need for power hungry O/E/O conversions as well as format-dependent interfaces. Nanoseconds reconfiguration time optical cross-connect (OXC) switches have been previously considered and proposed for realizing flat optical DCNs [2-5].

The novelty of this study rests in the attempt to fulfil the scalability requirement through the performance assessment of a photonic integrated 1x8λ WDM WSS module, significantly reducing the required foot-print, hence the power consumption. Static characterization of the elements (SOAs, AWGs, etc.) and 10, 20 Gb/s NRZ-OOK single channel measurements has been performed in a recent study [6].

In this work, we experimentally assess the switching performance of a photonic integrated WDM WSS module with 40 Gb/s NRZ-OOK WDM input traffic. Results show 11 dB/channel on chip gain and error-free operation with less than 2.5 dB power penalty for WDM input operation with a cross-talk lower than -35 dB.

2. SYSTEM OPERATION

WDM OXC switches can be employed to build a novel distributed flat DCN architecture as illustrated in Fig. 1(a). The schematic of the WDM OXC switch allowing for nanoseconds wavelength, space, and time switching operation is depicted in Fig. 1(b). The non-blocking switch has N inputs each carrying M different wavelengths generated by the top-of-rack (ToR) switches. The modular structure enables the parallel processing of the N WDM inputs by the respective optical modules. Each WSS (Wavelength Selective Switch) module can select one or more wavelength channels and forward the channels to the output ports according to the switching control signals [5]. The WSS consists of two AWGs (Arrayed Waveguide Gratings) and M SOA-based optical gates. The first 1×M AWG operates as wavelength de-multiplexer. Turning on/off the M SOAs determines which wavelength channel is forwarded to the output or is blocked. The second M×1 AWG operates as wavelength multiplexer. It should be noted that the amount of SOAs is N×N×M which is only partially (< N×M) turned on simultaneously.

In this work the tested non-blocking optical switch has 1 input and 8 outputs. The input carries 8 different wavelengths generated by the ToRs. Each optical module consists of a Pre-amplifier SOA (2 mm long) at the input, a 1:2 MMI (Multimode Interferometer) power splitter that broadcasts the WDM channels to both the WSS that process the WDM inputs in parallel. The WSS consists of, two AWGs, 8 quantum well active InGaAsP/InP SOA based optical gates (950 μm), and the SOA as booster at the output (1 mm). The 1x8 AWG operates as wavelength de-multiplexer. Turning individually on or off the 8 SOA optical gates determines which wavelength channel is forwarded or blocked to the respective output. Multicast operation is also possible by turning more than one SOA. The AWGs are designed with a free spectral range (FSR) of 2 nm.

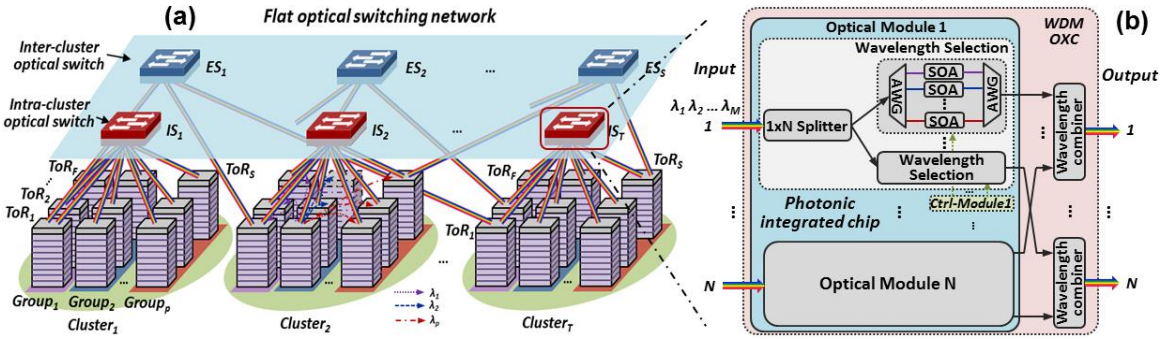


Fig. 1: (a) DCN architecture employing the distributed WDM switches. (b) Schematic of the WDM optical switch.

The broadband operation of the SOAs enables the selection of any wavelength in the C band with an On/Off response time in the order of nanoseconds. Moreover, the amplification provided by the SOAs not only compensates the losses introduced by the splitters and the two AWGs but provides on chip gain of 11 dB. The chip has been realized in a multi-project wafer (MPW) with limited space of the cell (4.6 mm x 4 mm). An image of the photonic integrated switch is shown in Fig. 2 (upper left) with colored boxes around the main components and one of the WSS module contained in the photonic chip. The light shaded electrodes are routed through on-chip metal tracks and then wire bonded to a neighbouring PCB (Printed Circuit Board) which provides a control interface for the SOA gates. Lensed fibers have been employed to couple the light in and out of the chip.

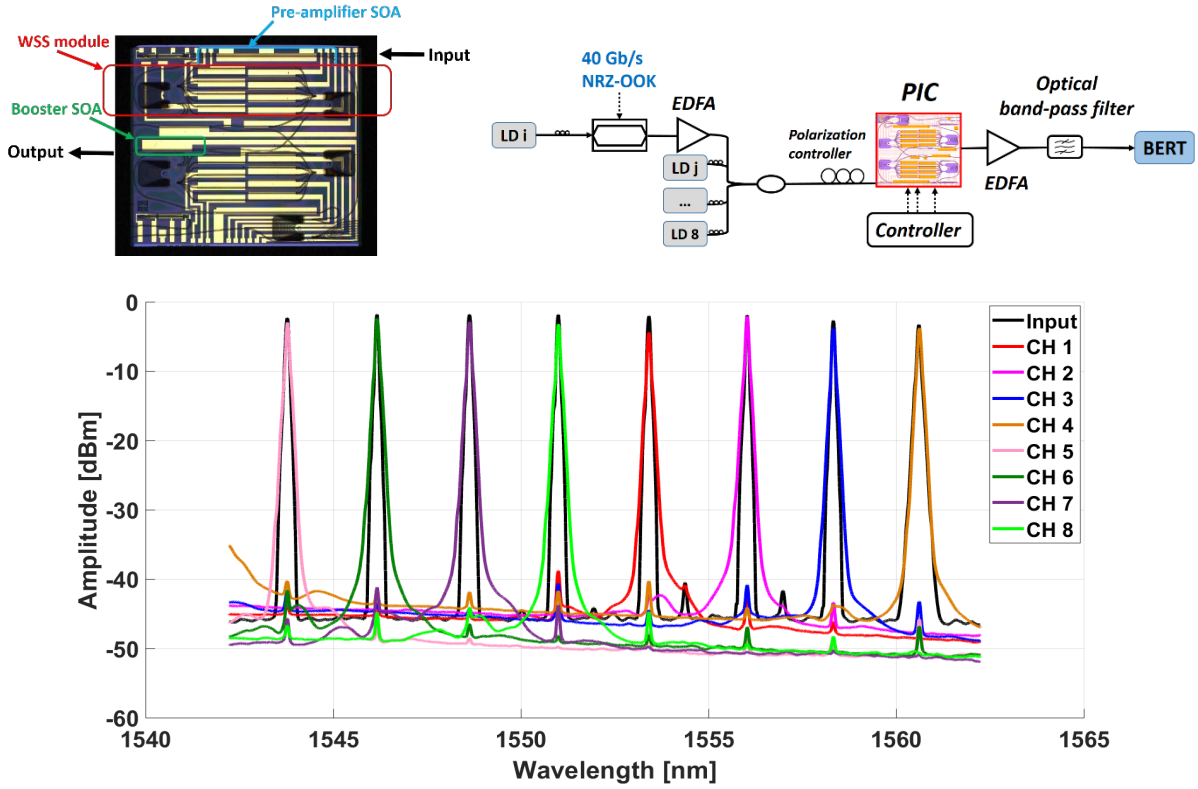


Fig. 2: Microscope image of the modular WDM photonic switch (upper left). Experimental set-up employed to assess the performance of the WDM photonic integrated optical cross-connect (upper right). The eight switched channels by the PIC (Photonic Integrated Chip), LD: Laser Diode, BERT: BER tester (bottom).

3. EXPERIMENTAL RESULTS

The experimental set-up employed to assess the 1x8λ WDM WSS photonic switch module is shown in Fig. 2 (upper right). Eight optical wavelengths spaced by 2 nm, from λ1 = 1544 nm to λ4 = 1560 nm, are generated. The WDM signal consists of only one modulated channel at a time using an NRZ OOK amplitude modulator driven by a 40 Gb/s pattern generator with 2^{15}-1 PRBS, and seven carriers. Since the availability for multiple modulators that could generate this significantly high bit rate (40 Gb/s) was limited to one instrument, this setup choice is intended to avoid the need for an additional inter-channel de-correlation stage, necessary if all channels were modulated by the same instrument, that brings more losses to the setup [6] with additional EDFA stages that deteriorate the input OSNR. The optical power of the WDM input channels was -2 dBm/channel (Fig. 2 bottom -

lossless operation). The input and output booster SOAs were biased with currents 90 mA and 60 mA, respectively. The temperature of the chip was maintained at 20°C through a water cooler. Polarization controllers were employed at the input of the chip as well as after each channel source (LD 1 to LD 8).

First, we assess the static operation of the WSS. One WDM channel at the time is statically switched at the WSS output by enabling one of the eight SOA gates at the time. The current applied at gate SOAs in On-state was 70 mA. The spectra of the switched channels are depicted in Fig.2 demonstrating on chip gain of 11 dB if considering the coupling 6 dB/facet coupling losses and a cross-talk lower than -35 dB.

To investigate the data integrity of the chip operation, BER curves, including the back-to-back as reference, are recorded and shown along with eye diagrams in Fig. 3. Clear open eye diagrams of the switched channels testify for a high quality signal. Error-free operation with a penalty less than 2.5 dB for the worst channel was measured at BER=1e-09. The main source of this penalty is considered to be the added noise by the SOAs and the limited crosstalk.

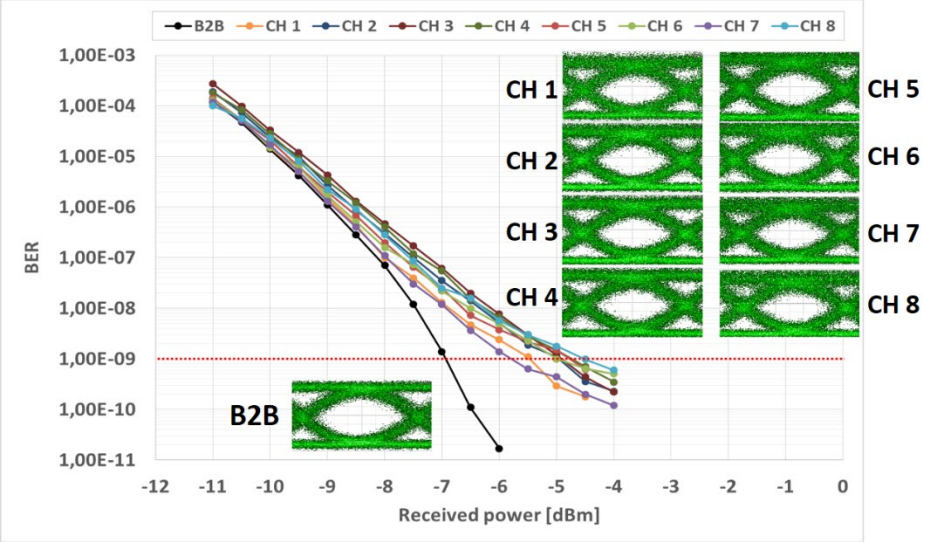


Fig. 3: BER (logarithmic scale) vs Received Optical Power curves and eye diagrams of switched channels at the output port for WDM 40 Gb/s NRZ-OOK input signal.

4. CONCLUSIONS

We have presented a modular 1x8 photonic integrated WDM optical switch including SOA based wavelength selective switches for nanoseconds wavelength and time switching operation. The system performance assessment confirmed the capability of the chip to switch a WDM signal in the wavelength domain. Experimental results show lossless and error-free operation with less than 2.5 dB penalty for data rate up to 40 Gb/s NRZ-OOK 2^{15}-1 PRBS traffic. These results together with the doubling of the channel number compared to the 1x4 switch in [7] are persuasive indications that the modular architecture could scale to a larger number of ports.

ACKNOWLEDGEMENTS

The authors of this paper would like to thank the European projects OLYMPICS and QAMeleon for supporting this work.

REFERENCES

[1] Cisco Global Cloud Index: Forecast and Methodology 2014–2019, Cisco Systems, USA. (2015).
[2] Y. Ohsita et al., “Optical Data Center Networks: Architecture, Performance, and Energy Efficiency”, Springer (2015).
[3] A. S. P. Khope, “Elastic WDM crossbar switch for data centers,” IEEE Optical Interconnects Conference, pp. 48-49 (2016).
[4] K.-I. Kitayama et al., “Torus-topology datacenter network based on optical packet/agile circuit switching with intelligent flow management,” J. Lightw. Technol., vol. 33, no. 5, pp. 1063-1071 (2015).
[5] W. Miao et al., “Towards Petabit/s All-Optical Flat Data Center Networks Based on WDM Optical Cross-Connect Switches with Flow Control,” J. Lightw. Technol., vol. 34, no. 17, pp. 4066-4075 (2016).
[6] K. Prifti et al., “Performance assessment of a nanoseconds and modular Photonic Integrated Wavelength Selective Switch for Optical Data Centre Networks,” PSC Conference (2018).
[7] N. Calabretta et al, “System Performance Assessment of a Monolithically Integrated WDM Cross-Connect Switch for Optical Data Centre Networks,” Paper W.2.F.3, ECOC 2016.

First Silicon Photonics Coherent Receiver With Heterogeneously Integrated III-V On Silicon Tunable Local Oscillator Operating At 28 GBd Data Rates

Hajar Elfaiki[1], Xavier Pommarede[1], Christophe Caillaud[1], Harry Gariah[1], Dalila Make[1], Théo Verolet[1], Karim Hassan[2], Christophe Jany[2], Stéphane Malhouitre[2], Ségolène Olivier[2], Mohand Achouche[1]

[1] *III-V Lab, joint lab of Nokia, Thales & CEA, 1 A. Fresnel, 91767 Palaiseau, France*
e-mail: hajar.elfaiki@3-5lab.fr

[2] *CEA LETI, Minatec, 17 rue des Martyrs, 38054 Grenoble, France*

ABSTRACT

We demonstrated the first coherent receiver with III-V on silicon monolithic integrated local oscillator. It shows clean QPSK constellation at 28 GBd with $1.7\,10^{-4}$ BER, and a footprint shrunk to 2 mm x 1.5 mm. The local oscillator presents a 45 nm tuning range obtained by thermally tuned Vernier filter. The compactness of the rings ensures a reduced power consumption of 200 mW sufficient to span the whole tuning range. The local oscillator shows a narrow linewidth of 150 kHz compatible with high speed coherent detection.

Keywords: Silicon Photonics, Coherent Detection, III-V on Silicon Monolithic Integration, Photonic Integrated Circuits

1 INTRODUCTION

The world data traffic is increasing exponentially since 1995, it is expected to be 100 $ZB/Month$ in 2020 [1]. Coherent transmission is a key technology to handle this huge data traffic. It enables advanced formats using both phase and amplitude modulations which ensure high spectral efficiency at high bit-rate per optical channel. To support a typical 400 Gb/s data-rate per fiber at affordable costs, silicon photonics is a very good candidate with its high integration level and low cost [2]. This platform is particularly suited for coherent receivers which require a large number of passive and active functions.
We report the first fully integrated coherent receiver (CR) achieved by monolithic integration of III-V on silicon local oscillator (LO). The silicon on insulator wafers (SOI) were fabricated using 200 mm pilot line CMOS processing tools (LETI), including the molecular bonding of III-V, while the III-V process and metallization was performed in a conventional III-V fab [3]. Integration of LO is a major advance for silicon coherent receiver. The integrated LO shows a very narrow linewidth of 150 kHz, and an output power in the Silicon waveguide around 5 dBm. That alleviates the usual coupling losses encountered with external LO. Furthermore BER measurements show no evidence of penalty related to the III-V on Silicon integration process.

2 PRELIMINARY CHARACTERIZATIONS

The schematic and layout of the chip are shown in Fig. 1 a) and b). The integrated local oscillator is a III-V on SOI tunable laser based on double-rings Vernier effect [5], with a InGaAlAs multi-quantum wells gain structure. The external input signal is coupled with a grating coupler and coherently mixed with the LO using a MMI (Multi-Mode Interferometer) 90° hybrid. 4 photodiodes (PDs) provide the beating notes enabling the quadrature demodulation principle. The PDs and LO share the same III-V epitaxy.

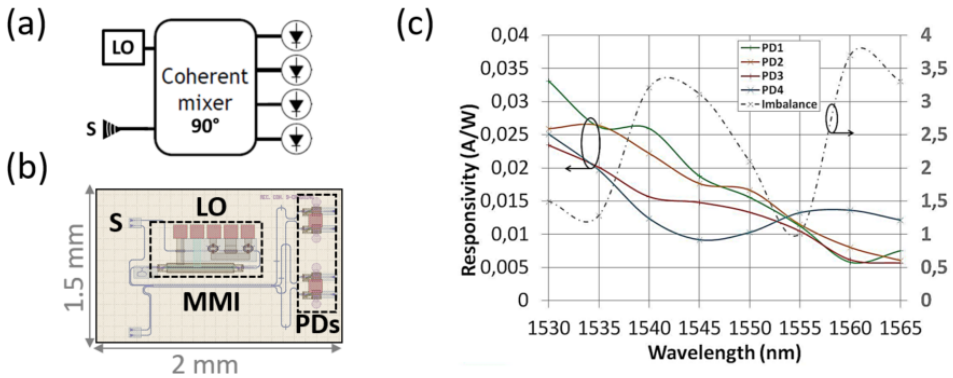


Figure 1. a) Generic schematic of coherent receiver b) Layout of the chip. c) On-chip PDs measured responsivity using external signal output while the local oscillator is turned off.

As shown in Fig. 1 c) the net responsivity of the on-chip PDs is around $0.025\,A/W$ at 1530 nm with an imbalance of 1 to 3.5 dB. The net responsivity includes fiber-to-chip coupling losses and MMI losses. MMI characterizations show a shifted transmission maximum to shorter wavelengths around 1520 nm as shown in Fig. 2 a). The MMI length must vary with the square of its width, for this CR, we had chosen a short MMI design of 1 mm which is more sensitive to manufacturing hazards [4]. That plausibly explains the shift of the MMI maximum transmission. Fig. 2 b) shows a stand-alone PD responsivity reverse biased at -1 V (maximum absorption bias). PDs are more responsive at high wavelengths in the C-band, this behavior is repeatable for all the reverse biased PDs throughout the 3 inches wafer. The PDs maximum responsivity is around $0.6\,A/W$, which is comparable to Ge-on-Si PDs [7]. Furthermore vertical coupler and gain structure are also centered at 1550 nm. Because of mismatch between MMI, gain, and PD maximum responses, we are a couple of dB below the optimal performances of the device.

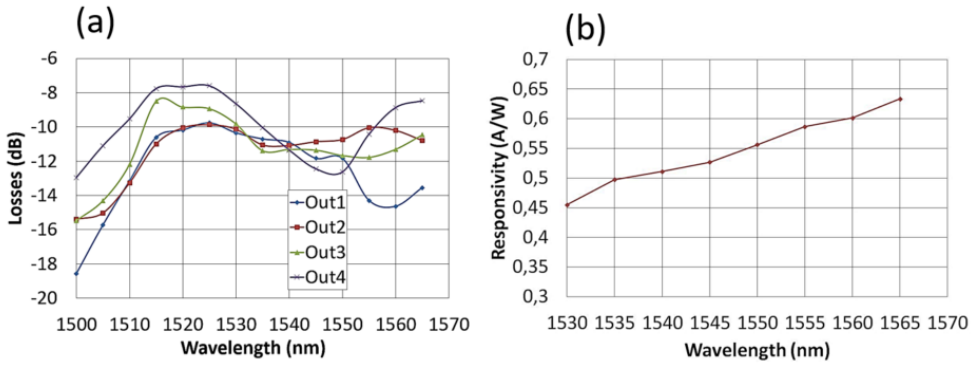


Figure 2. a) Transmission losses of the MMI. b) Stand-alone PD measured responsivity as a function of wavelength.

3 STAND-ALONE LOCAL OSCILLATOR CHARACTERIZATIONS

The laser used and shown in Fig. 3 a) comprises two Sagnac mirrors (M1 & M2), two ring resonators for the Vernier effect (R1 & R2), a phase control section, and III-V gain medium. To achieve the mode transition between the SOI and the InP bonded chip, we use tapers on the silicon waveguide which ensure a mode-index matching region between the III-V and the silicon waveguides. For the stand-alone test device, fiber grating couplers (FGC) are used to extract the light into vertical fibers. We obtain a 45 nm tuning range (see Fig. 3 c)), a 30 mA threshold current, and an fiber coupled power of 1 mW. We also performed a measurement of the power spectral density (PSD) of the LO frequency noise according to the self-heterodyne method, we obtain a 150 kHz Schawlow-Townes linewidth at 1 mW on-fiber output power, see Fig. 3 b).

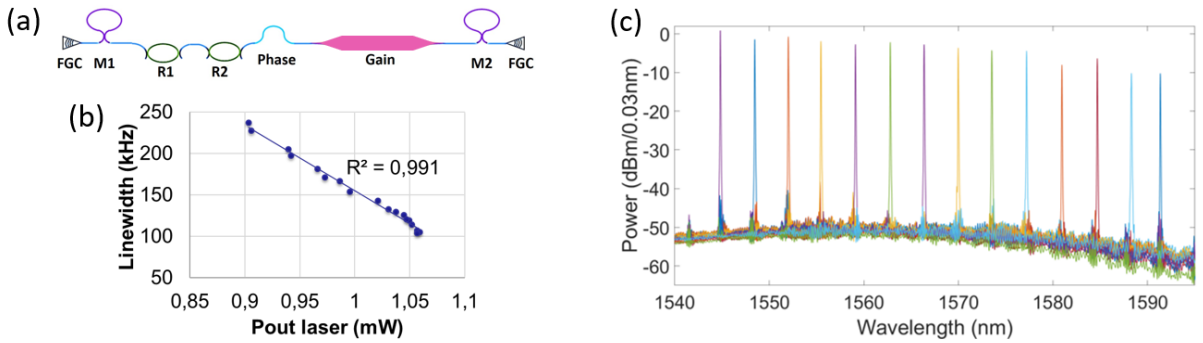


Figure 3. a) Design of the integrated tunable III-V on silicon LO. b) Laser linewidth measurement as a function of the output power. c) 45 nm measured tuning range

4 ON-CHIP CONSTELLATION MEASUREMENTS

The full chip was tested with the setup of Fig. 4 c). A tunable external laser source provides the signal. The later is modulated by an IQ-modulator (30 GHz Lithium Niobate MZ modulator) driven by a DAC and split by 50/50 coupler. One part is sent to an OSA to monitor the modulation shape, notably controlling the carrier-suppression, the other part is sent to the chip with a single mode fiber (SMF) after EDFA amplification.

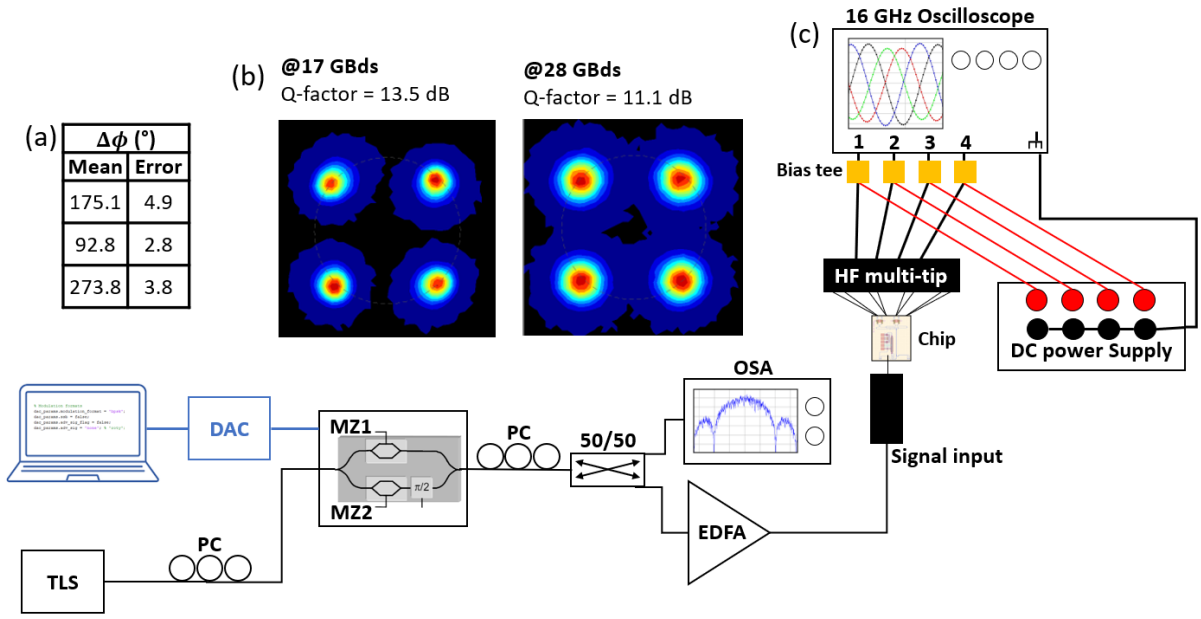


Figure 4. a) Measured dephasing errors. b) Measured constellations at 17 GBd & 28 GBd. c) Schematic of the experimental setup

The beating between the signal and the local oscillator is measured to extract the phase response. We obtain less than 5 degrees phase error for the quadrature demodulation dephasing at $180°$, $90°$, and $270°$ as shown in the table, Fig. 4 a). These results are within current system specifications for coherent receivers, and show no evidence of any impact of LO integration on SOI CR platform. To measure the constellation, the desired PRBS is generated by a Matlab script and sent to a DAC that drives the IQ-modulator in QPSK mode. After a DSP stage we obtain clean on-chip constellations, with $1.1\,10^{-6}$ BER at 17 GBd and $1.7\,10^{-4}$ BER at 28 GBd (Fig. 4 c)), it's comparable with the BER obtained in silicon photonics CR with external LO. These measurements were performed at 1545 nm wavelength, it was the shortest wavelength achievable by the integrated LO. That limits the optical received power by PDs as explained in the first paragraph. Performances are also partly limited by the experimental setup: low voltage on the oscilloscope due to on-chip experiments without TIA, and low oscilloscope bandwidth at 16 GHz.

5 CONCLUSION

We performed the first fully integrated III-V on silicon coherent receiver with LO, fabricated on 200 mm pilot line CMOS processing tools. It shows a 28 GBd QPSK constellations whose intrinsic BER does not exceed 10^{-4}. This important result shows the potential of silicon photonics for process industrialization, high level integration in compact PIC, and high speed operation. CMOS compatible process of III-V on silicon devices might be an appealing way to co-integrate the high performance Germanium photodiodes with the hybrid III-V on silicon LO for the next generation of coherent receiver [8]. This will enable to face the challenges of transmitting huge volume of data in long-haul and metro applications at low costs.

REFERENCES

[1] M. K. Weldon, *The Future X Network: A Bell Labs Perspective*. CRC Press, 2016.

[2] R. Soref, "The Past, Present, and Future of Silicon Photonics," IEEE J. Sel. Topics Quantum Electron., vol. **12**, no. 6, p. 1678-1687 (2006).

[3] G. Duan et al., "Hybrid III–V on Silicon Lasers for Photonic Integrated Circuits on Silicon," IEEE J. Sel. Topics Quantum Electron., vol. **20**, no. 4, p. 158-170, (2014).

[4] X. Pommarede,"Circuits photoniques intégrés III-V/Si pour les applications en télécommunications optiques," Ph.D. dissertation, Univ. Paris Saclay, Accessed on: April, 2017, Available: http://www.theses.fr/2017SACLC020/document

[5] H. Elfaiki et al., "Ultra Wide Hybrid III-V On Silicon Tunable Laser," Proc. ECOC, We3C1, Roma, Italy, Sept 23–27. 2018.

[6] C. Baudot et al., "Developments in 300mm silicon photonics using traditional CMOS fabrication methods and materials," IEEE International Electron Devices Meeting (IEDM) 34.3.1-34.3.4 (2017).

[7] L. Virot et al.,"High-performance waveguide-integrated germanium PIN photodiodes for optical communication applications [Invited]," Photon. Res. **1**, 140-147 (2013).

[8] B. Szelag et al., "Hybrid III-V/Si DFB laser integration on a 220 mm fully CMOS-compatible silicon photonics platform," IEEE International Electron Devices Meeting (IEDM), 24.1.1-24.1.4 (2017).

High-speed-performing pin photodetectors with lateral silicon-germanium-silicon heterojunctions for 1.55 μm communications

D. Benedikovic[1], L. Virot[2], G. Aubin[1], J.-M. Hartmann[2], F. Amar[1], B. Szelag[2], B. Karakus[2], C. Alonso-Ramos[1], X. Le Roux[1], P. Crozat[1], E. Cassan[1], D. Marris-Morini[1], C. Baudot[3], F. Boeuf[3], J.-M. Fédéli[2], C. Kopp[2], and L. Vivien[1]

[1]Centre de Nanosciences et de Nanotechnologies, CNRS, Univ. Paris-Sud, Université Paris-Saclay, 91120 Palaiseau, France

[2]University Grenoble Alpes, CEA, LETI, 38054 Grenoble, France

[3]Technology R&D, STMicroelectronics, 38920 Crolles, France

e-mail: daniel.benedikovic@c2n.upsaclay.fr

ABSTRACT

We investigate the properties of high-speed waveguide photodetectors with hetero-structured Silicon-Germanium-Silicon junctions monolithically integrated on Silicon-on-Insulator substrates. These devices take advantage of unique integration strategy that combines butt-waveguide-coupling and lateral Silicon-Germanium-Silicon pin junctions. Fabrication is robust and fully compatible with complementary metal-oxide-semiconductor technology. The resulting devices have improved responsivity and bandwidth performances. In particular, a responsivity up to 1.2 A/W and a dark-current as low as 100 nA under 1V reverse bias are experimentally demonstrated with a set of pin photodetectors. Furthermore, fast device opto-electrical responses lead to an excellent on-chip detection capability well-suited for future high-speed link traffics up to 40 Gbps. An errorless operation is achieved for established 10 Gbps and 25 Gbps data rates, providing a power sensitivities of -13.9 dBm and -11.3 dBm with a bit-error-rate of 10^{-9}.

Keywords: group-IVnanophotonics, silicon-on-insulator, germanium photodetectors, optical communications.

1. INTRODUCTION

Optical photodetectors monolithically integrated on top of mature silicon-on-insulator (SOI) waveguides are key components for on-chip applications in group-IV nanophotonics such as optical interconnects, communications, or sensing, to name a few. However, Silicon (Si), with its indirect bandgap and 1.1 μm cut-off wavelength, is not appropriate material for near-infrared light detection. Conversely, Germanium (Ge) is an ideal candidate to have efficient light detection functionality on Si chips. Despite the large lattice mismatch of Ge with Si (~4.2%), the epitaxial growth of Ge films is feasible on Si substrates. Presently, group-IV semiconductor photodetectors are considered as mature building blocks in the nanophotonic device library, with performances comparable to those typically obtained by their III-V compound counterparts [1,2].

Conventional waveguide-integrated photodetectors [3-5], i.e. micro-metric-scale single-material (homo-junction) architectures, typically call upon Ge doping and metal via-contact formation on Ge. However, such devices suffer from large absorption losses, which significantly reduce photo-responsivity. In addition, specific fabrication steps in Ge pre- and post-processing are compulsory for such structures. As an alternative, Si-contacted Ge photodetectors, in both vertical and lateral pin junction schemes, were demonstrated [6-10], with simpler fabrication process flow and enhanced performances at datacom and telecom bands.

2. PIN PHOTODETECTOR FUNDAMENTALS: DESIGN AND FABRICATION

In our work, we investigate the properties of waveguide-integrated pin photodetectors with lateral hetero-structured Silicon-Germanium-Silicon (Si-Ge-Si) junctions were designed and fabricated on SOI substrates with 220-nm Si and 2-μm buried oxide (BOX) layers, operating at 1.55 μm wavelength and transverse electrical (TE) polarization. The intrinsic Ge region, with a 260-nm-thick layer, is formed inside a ~60-nm-thick Si elongated cavity surrounded by the *p*-doped and *n*-doped lateral Si slabs (see Fig. 1(a)). The whole structure is positioned at the end of Si waveguide to enable efficient butt-coupled light injection into the photodetector. The integration approach used herein, combining butt-waveguide-coupling and lateral pin junctions, allows robust fabrication of photodetectors with production tools and processes available in Si nanophotonic foundries. This results in compact devices with judiciously controlled geometry and improved performances. From a technological point of view, it is worthwhile to note that such a fabrication scheme decreases contact access resistance, reduces fabrication steps in optical interconnect process flow and facilitates further hybrid opto-electronic integration, as surfaces are flat after fabrication. The entire device fabrication was conducted in CEA LETI's cleanroom facilities using 200 mm SOI nanophotonic platform and standard CMOS production lines [9,10].

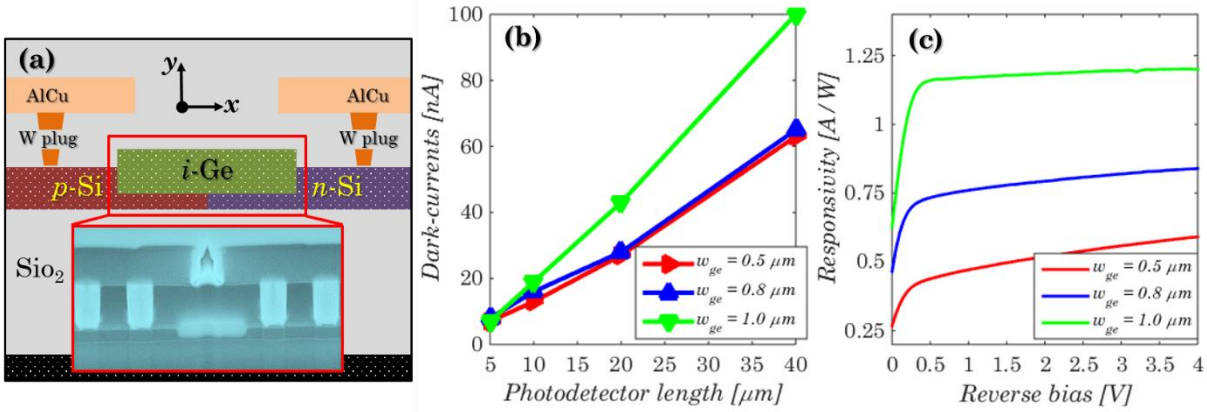


Figure 1. (a) Cross-sectional schematics of the waveguide-integrated photodetector with a lateral Si-Ge-Si junction. Inset: Scanning electron microscopy image of a device. (b) Measured dark-currents as a function of the photodetector length under 1V reverse bias. (c) Responsivity of 40-μm-long photodetectors as a function of the reverse bias for different widths of the intrinsic Ge region.

3. PIN PHOTODETECTOR EXPERIMENTS: RESULTS AND DISCUSSIONS

Devices were characterized via current-voltage, small-signal radio-frequency, and large-signal data tests [9,10].

3.1 Current-voltage characteristics and device photo-responsivity

Figure 1(b) shows the dark-current evolution versus photodetector length under 1V reverse bias for various device widths. Measured devices exhibit low dark-current values, typically well-below 10 nA for the smallest arrangements and values between 60 nA to 100 nA for the largest devices. The dark-current increases monotonously with the photodetector length, whereas the evolution with the device width is less specific. The responsivity of 40-µm-long devices versus the reverse voltage is shown in Fig. 1(c). High responsivities up to 1.2 A/W at 0.5V bias were consistently achieved for 1-µm-wide devices, with a characteristic plateau and a negligible voltage dependence. Conversely, a slight voltage dependence is observed for widths of 0.5-µm and 0.8-µm above 0.5V, for which responsivity of 0.45 and 0.74 A/W are obtained. This trend is more pronounced as the Ge width is reduced. This is likely attributed to the increased overlap between the fundamental TE mode and the lossy Si slabs, which greatly enhances absorption losses of photo-generated carriers. Si-Ge-Si photodetectors provide outstanding capability to sweep out the vast majority of electron-hole pairs within their lifetime.

3.2 Small-signal radio-frequency measurements

Figure 2 shows frequency responses for photodetectors with different widths. The normalized reference level is arbitrary for each width. Devices have been biased at 0V, 1V and 2V.

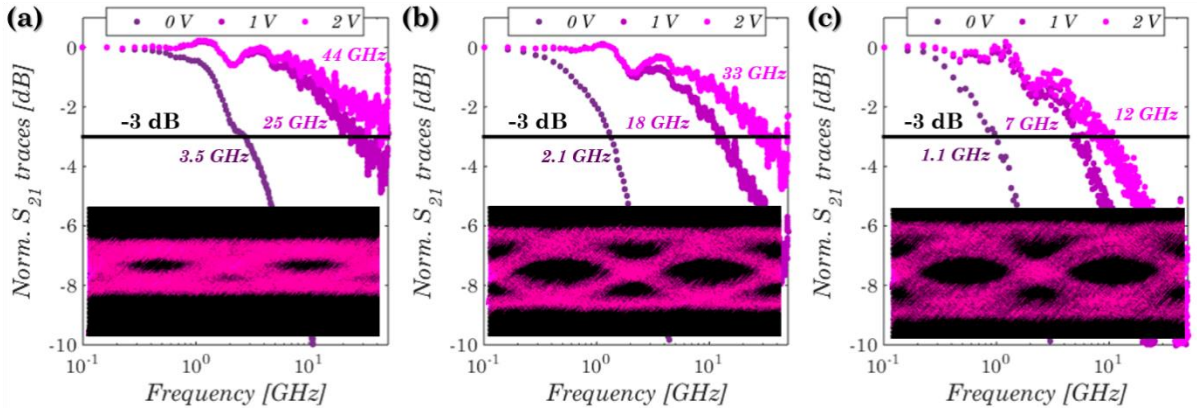


Figure 2. Normalized frequency responses of 40-µm-long hetero-structured Si-Ge-Si pin photodetectors biased at 0V, 1V, and 2V. (a) w_{ge} = 0.5µm, (b) w_{ge} = 0.8 µm, and (c) w_{ge} = 1.0 µm. Insets: Output eye diagrams at 40 Gbps link rate under 2V reverse bias.

The 3-dB cut-off frequency was measured between 1.1 and 3.5 GHz at 0V. The photodetector bandwidths are restricted in these biasing conditions due to a comparatively long transit time of carriers. Here, the built-in electric field yields an efficient collection of photo-generated carriers. As a consequence, eye diagrams remain closed under 0V bias. In a stark contrast, increasing voltage substantially enhances the device bandwidth up to 25 GHz at 1V and 44 GHz at 2V for a 0.5-µm-wide device, as shown in Fig. 2(a). The photodetector cut-off

frequency decreases inversely the width increases and is virtually independent on the length of the Ge region, indicating that the photodetector bandwidth is not limited by the RC delay. Insets in Fig. 2 shown eye diagrams of Si-Ge-Si photodetectors operating at a link rate of 40 Gbps under 2V reverse bias.

3.3 Large-signal measurements: Eye diagrams and bit-error-rate testing

Figure 3 shows bit-error-rate (BER) data as a function of the received optical power for 1-μm-wide and 40-μm-long photodetectors. More specifically, Fig. 3(a) shows BER curves for a data rate of 10 Gbps under 1V and 2V reverse bias. Optical power sensitivities, defined at 10^{-9} BER level, are equal to -10 dBm and -12.8 dBm. Fig. 3(b) depicts the BER results for conventional data rates of 10 Gbps and 25 Gbps under 3V reverse bias. BER level of 10^{-9} yields photodetector power sensitivities of -13.9 dBm and -11.3 dBm.

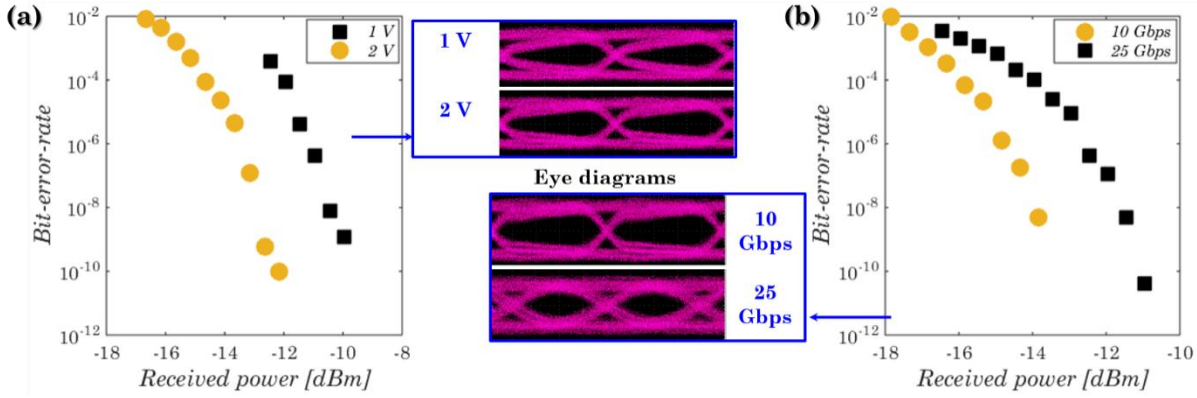


Figure 3. Bit-error-rate versus received optical power. BER assessments performed (a) at 10 Gbps data rate under 1V and 2V reverse bias and (b) at 10 Gbps and 25 Gbps data rates under 3V reverse bias. Insets: Corresponding out eye diagrams on different horizontal scales.

4. CONCLUSIONS

We experimentally demonstrated high-speed butt-coupled, lateral Si-Ge-Si pin photodetectors that operate under low-reverse-biases at telecom wavelengths. We showed responsivities up to 1.2 A/W, dark-currents as low as 100 nA, and fast device responses enabling a high-speed link trafficsignal detection up to 40 Gbps. A bit-error-free operation was achieved for conventional data rates of 10 Gbps and 25 Gbps, yielding a photodetector optical power sensitivities of -13.9 dBm and -11.3 dBm for BER at 10^{-9}. These results pave the way towards pioneering integration strategies for cost-effective on-chip photo-detection functionality on mature SOI substrates.

ACKNOWLEDGEMENTS

This work received funding from the European Research Council (ERC) under the European Union's Horizon 2020 Research and Innovation Program (ERC POPSTAR – grant agreement No 647342).

REFERENCES

[1] D. Thomson, *et al.*: Roadmap on silicon photonics, *J. Opt.*, vol. 18, pp. 073003 (2016).
[2] J. Michel, *et al.*: High-performance Ge-on-Si photodetectors, *Nat. Photonics*, vol. 4, pp. 527-534 (2010).
[3] J. Joo, et al.: High-sensitivity 10 Gbps Ge-on-Si photoreceiver operating at λ~1.55 μm, *Opt. Express*, vol. 18, pp. 16474-16479 (2010).
[4] L. Vivien, *et al*: Zero-bias 40 Gbit/s germanium waveguide photodetector on silicon, *Opt. Express*, vol. 20, pp. 1096-1101 (2012).
[5] G. Li, *et al.*: Improving CMOS-compatible Germanium photodetetcors, *Opt. Express*, vol. 20, pp. 18145-15155 (2012).
[6] Y. Zhang, et al.: A high-responsivity photodetector absent metal-germanium direct contact, Opt. Express, vol. 22, pp. 11367-11375 (2014).
[7] H. Chen, *et al.*: High-responsivity low-voltage 28-Gb/s Ge p-i-n photodetector with silicon contacts, *J. Lightwave Technol.*, vol. 33, pp. 820-824 (2015).
[8] H. Chen, *et al.*: -1 V 67 GHz bandwidth Si-contacted germanium waveguide p-i-n photodetector for optical links at 56 Gbps and beyond, *Opt. Express*, vol. 24, pp. 4622-4631 (2016).
[9] L. Virot, *et al.*: Integrated waveguide PIN photodiodes exploiting lateral Si/Ge/Si heterojunction, *Opt. Express*, vol. 16, pp. 19487-19496 (2017).
[10] D. Benedikovic, *et al.*: 25 Gbps low-voltage hetero-structured silicon-germanium waveguide pin photodetectors for monolithic on-chip nanophotonic architectures, *Photon. Res.*, (accepted) (2019).

Optical transceiver engine based on 12 µm Silicon-on-insulator waveguides and VCSELs

Mikko Karppinen[1], Mikko Harjanne[1], Tapani Vehmas[1], Christian Neumeyr[2], Aila Sitomaniemi[1], Jyrki Ollila[1], Markku Kapulainen[1], Antti Tanskanen[1], Päivi Heimala[1], Timo Aalto[1]
[1] VTT, PO Box 1000, (Vuorimiehentie 3, Espoo), FI-02044 VTT - Finland
[2] Daimlerstr. 11d, D-85748 Garching - Germany
e-mail: Mikko.Karppinen@vtt.fi

ABSTRACT

In this paper, we report the fabrication of an optical tranceiver engine that is based on a 12µm silicon on insulator (SOI) waveguide platform and directly modulated vertical cavity surface emitting lasers (VCSELs). The main motivation for using 12 µm thick SOI waveguides is low-loss coupling to standard SM fibers with relaxed alignment tolerances. We demonstrate 25.7Gb/s operation of the complete optical interconnect link channel.

Keywords: silicon photonics, silicon-on-insulator, optical interconnect, VCSEL, hybrid integration

1. INTRODUCTION

In 1–12 µm thick SOI waveguides light is almost completely confined into the waveguide core, so that the effective index is very close to the bulk refractive index of Si (~3.5) and there is very little light at the outer boundary of the Si core. This makes the waveguide components and circuits intrinsically quite insensitive to polarization, dimensional variations and surface roughness. Typical propagation loss in Thick-SOI waveguides is ~0.1 dB/cm. Large waveguide cross-section area also allows to transmit high optical powers (>1 W) without nonlinear absorption. Single-mode (SM) operation over an ultra-wide wavelength range is achieved with rib waveguides [1]. High integration density can be achieved combining SM and adiabatically coupled multi mode (MM) waveguides into the same SM circuit and by using either Euler bends or mirrors [2].

Discrete VCSELs and photodetectors (PDs) already support 28 Gb/s on-off keying (OOK), which shows a path towards 50-100 Gb/s bandwidth per wavelength by using more advanced modulation formats like PAM4. Directly modulated VCSELs enable very power-efficient optical interconnects for up to 40 km distance. There are inherent advantages in combining directly modulated, long wavelength, single mode VCSELs with thick SOI waveguides for transceiver applications. Due to direct VCSEL modulation there will be no need for high speed waveguide modulator which simplifies significantly the Si photonics chip design and fabrication. In addition, there is no need for spot-size conversion between the SOI waveguide and fiber as their mode fields match well with each other. Also, high speed PDs with sufficiently large optical aperture are available.

2. SOI WAVEGUIDE FABRICATION

The 12 µm SOI chip design is shown in Fig. 1 (left). At the bottom of the layout there is one set of four waveguides connecting to four VCSELs, and another connecting to four PDs. These waveguides are routed to another edge of the 12 µm chip for coupling into a single SM fiber array. Chip contains also an alignment loop from one SM fiber to another, which can be used in the alignment of the I/O fiber array.

In the fiber I/O interface we use 12.5 µm wide rib type SM waveguide that is followed by a rib-strip converter and 12 µm thick and 12 µm wide strip waveguides. For the VCSEL coupling, the waveguide thickness and width is reduced to 8 µm in order to better match the SOI waveguide and VCSEL mode fields. In the PD coupling, the waveguide thickness and width are both 12 µm.

SOI chip size is only 4 mm by 5 mm. We are using 90° total internal reflection (TIR) mirrors for waveguide turns. Transmitter and receiver waveguides have all also one waveguide crossing on their path. These crossings are low loss in wide waveguides as used here. The fabricated chip is shown in Fig. 1 (middle). Fabricated waveguides have good quality etched side-walls and TIR mirror facets (Fig. 1 (right)). Chip facets have been polished after dicing and an antireflection coating (ARC) has been deposited on chip level using atomic layer deposition (ALD). We have used 143 nm thick TiO_2/Al_2O_3 nanolaminate as an ARC.

3. VCSELs

Vertical Cavity Surface Emitting Lasers (VCSEL) are attractive for the optical interconnects thanks to low power dissipation and suitability for dense integration. Long-wavelength VCSELs operating at 1.3 and 1.55 µm are compatible with Si waveguides. The lasers employed in this paper consist of single-mode short-cavity 1.3µm VCSELs manufactured by Vertilas [3]. The VCSEL structure is based on Vertilas' InP Buried Tunnel Junction design and features a very short optical cavity. VCSELs exhibit a 3 dB-modulation bandwidth of up to 17 GHz (at temperature of 20°C). [1]

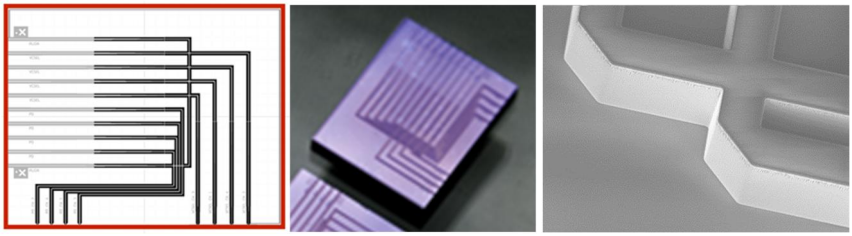


Figure 1.Left: SOI chip design with I/O ports for transmitter and receiver fibers and active alignment fibers, VCSELs and PDs. Middle: 4x5 mm chip with 12µm waveguides for routing of signals between fibers, VCSELs and PDs. Right: A scanning electron microscope image of TIR mirrors and crossings in 12 µm SOI.

4. HYBRID INTEGRATION

We have studied several integration concepts for the transceiver implementations based on hybrid integration of 12 µm SOI waveguides, VCSELs, PDs and standard SM fibers. Recently a demonstrator transceiver assembly with 4+4 channels was designed and built, including also transceiver electronics for 25 Gb/s/channel operation. The integration concept of the transceiver demo is illustrated in Fig. 2. Essentially, all the (opto)electronics was built on a printed circuit board (PCB) and then the fiber-pigtailed 12 µm SOI chip was vertically assembled on top of the PCB. This way the VCSELs and PD array were edge-coupled to the SOI waveguides at the chip facet.

The assembly process was as follows: Four discrete VCSEL dies from Vertilas were first bonded on a Si submount with ~1 µm alignment accuracy. Then this subassembly and a 4-channel PD array (4x28 Gb/s by Albis Optoelectronics) were bonded on the PCB with high precision. In addition, four-channel VCSEL driver and receiver ICs (by MACOM) were bonded right next to the VCSELs and PDs, so that very short wire-bonds could be made between them. This enabled good signal integrity for the targeted 25 Gb/s operation. Separately, the 12 µm SOI chip was aligned and adhesive bonded to a fiber-array v-groove assembly. This modular assembly approach allowed testing of the optoelectronic parts before adding the fiber-pigtailed SOI chip on top of the optoelectronic subassembly. Moreover, it allowed powering the VCSELs and the receivers while aligning the pigtailed SOI chip to them, thus enabling active alignment. All 4 VCSEL and 4 PD channels could be simultaneously aligned to their corresponding waveguide facets, thanks to the accurate positions of those active devices on the PCB. After the active alignment, the SOI chip and fiber array subassembly was fixed to its position by adhesive bonding.

The complete assembled transceiver demonstrator is shown in Fig. 3. The PCB also includes 16 pieces of high-frequency coaxial connectors for the differential electrical input and output channels of the optical transceiver.

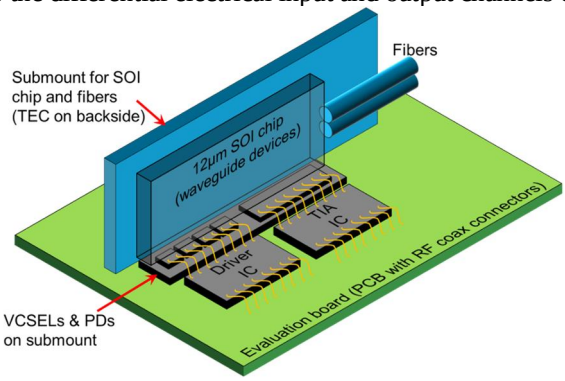


Figure 2. The integration concept of the transceiver demo. All the (opto)electronics is built on a PCB before the vertical assembly of the fiber-pigtailed 12 µm SOI chip.

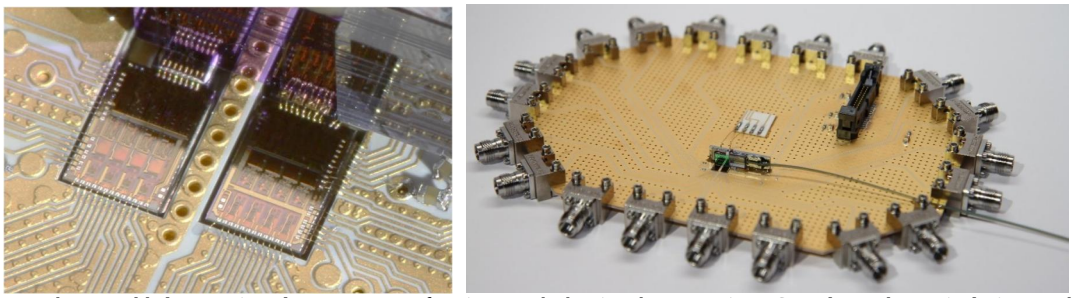


Figure 3. The assembled transceiver demonstrator. Left: Micrograph showing the transceiver ICs and optoelectronic devices on the PCB as well as the part of the SOI chip and fiber array on top of them. Right: Complete demonstrator.

5. CHARACTERIZATION

5.1 SOI chip

The channel losses for all VCSEL and PD channels were measured on chip level before the assembly. The waveguide losses were measured with SM fibers at both ends of the waveguide and with index matching oil in the fiber-chip interface. Measured losses were 1-2dB in the PD channels and 3-5dB in the VCSEL channels. In the VCSEL channels the loss is increased mainly because of the mode field mismatch between the 8µm by 8µm and SM fiber. In addition, some minor loss is expected also from waveguide tapering in the VCSEL waveguide.

Losses in the TIR mirrors are low. The loss measurement of TIR mirror test structures that were processed in the same process run, showed approximately 0.15 dB/90° loss over a wide wavelength range [2].

5.2 Optical coupling

The demonstrator assembly enabled characterisation of the various coupling losses and alignment tolerances. During the assembly process, the alignment sensitivity of the VCSEL and the SOI waveguide coupling was analysed. Approximately 1 µm transversal alignment requirements were measured for the 1 dB excess loss tolerance of the VCSEL-to-waveguide coupling [2].

The fiber-to-SOI waveguide coupling loss was measured by applying a waveguide loop circuit on the chip, which enabled routing the optical power back to another fiber channel of the fiber array (and thus active alignment during the fiber pigtailing process). This loss that includes both the fiber-to-SOI and SOI-to-fiber interfaces and the waveguide chip losses was 3-4 dB in total after the adhesive curing.

The total fiber coupling losses from the VCSELs (through the SOI waveguides) were measured ca 7-8 dB. Correspondingly, the total insertion losses from the fibers to the PDs (through the SOI waveguides) were measured ca 2-3 dB. Consequently, the overall loss of the optical data link was approximately 10 dB in the demonstrator.

5.3 Data link

The performance of the optical interconnect was characterised too. A complete optical data link was established by connecting the output fibers of transmitter channels to the input fibers of the receivers. An eye-diagram of the complete link channel operating at 25.7 Gb/s is presented in Fig 4.

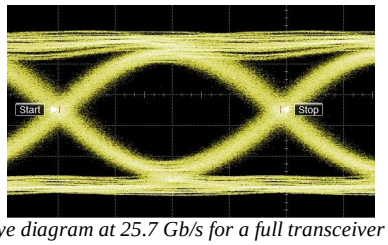


Figure 4. Measured eye diagram at 25.7 Gb/s for a full transceiver link (with CDR).

6. CONCLUSIONS

We have reported the fabrication of an optical transceiver engine that is based on a 12µm SOI waveguide platform and directly modulated VCSELs. A 25.7Gb/s operation was demonstrated for the full link channel. This transceiver concept is a simple and low cost compared to transceivers fabricated on the mainstream sub-micron SOI or even 3µm SOI platform, as there is no need for on-chip modulator or mode size converters between the waveguide chip and optical fiber. The 12µm SOI platform also enables the realization of Nx1 wavelength multiplexers/demultiplexers based on asymmetric Mach-Zehnder interferometers (AMZIs) or echelle gratings.

ACKNOWLEDGEMENTS

The SOI chip fabrication and transceiver design and packaging work was done in the OPEC project funded by Tekes – the Finnish Funding Agency for Innovation – with the grant agreement number 2814/31/2015. VCSEL development has been done in the RAPIDO project (http://www.rapido-project.eu) funded by the European Commission under the 7th Framework Programme with the grant agreement number 619806. Authors want to thank Noora Heinilehto and Antti Veijola for the packaging of the device and Mikko Kaunisto for the electronics design of the transceiver test card.

REFERENCES

[1] R. A. Soref, *et al.*; Large single-mode rib wave-guides in GeSi-Si and Si-on-SiO2, *IEEE J. Quantum Elect.* 27, 1991, pp. 1971–1974.

[2] T. Aalto, *et al.*; Optical interconnects based on VCSELs and low-loss silicon photonics, *in Proc. SPIE Proc. SPIE,* Vol. 10538, Optical Interconnects XVIII. San Francisco, USA, 29-31 Jan 2018.

[3] A. Malacarne, *et al.;* Optical Transmitter Based on a 1.3-µm VCSEL and a SiGe Driver Circuit for Short-Reach Applications and Beyond, *J. Lightwave Technol.*, Vol. 36, May, 2018, pp. 1527-1536.

100 GHz Multiple Colliding Pulse Generation from Cleaved Facet-free Multi-section Semiconductor Laser Diode

Student Paper

Jessica Cesar Cuello[1], Robinson Guzman[1], Alberto Zarzuelo[1], Mu Chieh Lo[1], Muhsin Ali[1], Guillermo Carpintero[1]

[1] University Carlos III of Madrid, UC3M, Electronics Technology Department

e-mail: rcguzman@ing.uc3m.es

ABSTRACT

A monolithically integrated semiconductor laser with a cavity laser of a 25 GHz fundamental repetition rate has been designed to generate an optical signal of four-times of the fundamental repetition rate working on the fourth harmonic colliding pulse mode locking configuration. This device was developed and fabricated within a multi-project wafer run in an InP-based active-passive generic foundry. The Fabry-Pérot laser cavity structure of the semiconductor laser is formed with two on-chip reflector building blocks rather than cleaved facets of the chip. The Fabry-Perot laser cavity length is around 1.66 mm the cavity three absorber sections symmetrically divide the cavity into four gain segments. An electrical linewidth of 350 KHz and 150 KHz with a frequency spacing of 25 GHz y 100 GHz is generated by the laser in passive regimen condition, respectively.

Keywords: semiconductor laser, electrical linewidth, multiple colliding pulse, mode locking laser.

1. INTRODUCTION

Passive mode locking (PML) based on III-V semiconductor lasers in photonic integrated circuits (PIC) generating optical frequency combs (OFC) have been increasingly attracting attention in recent years, due to its chip-scaled compactness and simplicity of DC operation. Especially, Passive mode locking laser diodes at repetition rates in millimetre-wave (mmW, 30-300 GHz) and terahertz (THz, 0.1-10 THz) ranges have been considered promising in communications, spectroscopy, and sensing [1] – [2]. However, in most cases an extremely high repetition rate (>100 GHz) of a mode-locked lasers (MLL) is corresponding to only a few hundreds of μm cavity length (<400 μm). For this reason, harmonic mode locking (HML) schemes have been investigated to produce multiple pulses per round trip in a sufficiently long cavity, thus pushing the RR beyond the low-GHz fundamental cavity round trip frequency [3]. HML is achieved by means of colliding pulse ML [4], coupled cavity ML [5], and methods based on the wavelength selectivity of distributed Bragg reflector (DBR) grating [6]. In colliding pulse ML, one saturable absorber is placed at the midpoint of cavity, where two counter propagating pulses circulate and collide, producing a train of pulses at a repetition rates that are twice the fundamental round trip frequency. Evolving from colliding pulse ML, multiple colliding pulse ML features multiple saturable absorbers concatenated with gain sections, for repetition rates multiplication >2 as has been extensively investigated [7] –[8]. Recently, a new class of on-chip broadband reflector based on the multimode interference (MMI) principle has been proposed [9], and demonstrated its wide applicability [10] – [11]. Such multimode interference reflectors (MIRs) are so simple to create in lithography with greater fabrication tolerance to replace DBRs and cleaved facets. Furthermore, they can be placed anywhere on a chip, and the transmitted light is manipulable on chip to fulfill more functionalities [12].

2. DEVICE DESCRIPTION

Fig. 1 shows a photograph of the layout of the semiconductor laser with a multi-section structure. The Perot-Perot laser cavity is formed with a pair of MIRs, in which there are four gain sections separated by three saturable absorber sections, placed at every quarter of the cavity length. The on-chip reflectors MIRs, define a cavity length (L) of around 1.66 mm, corresponding to a cavity round trip frequency of 25 GHz.

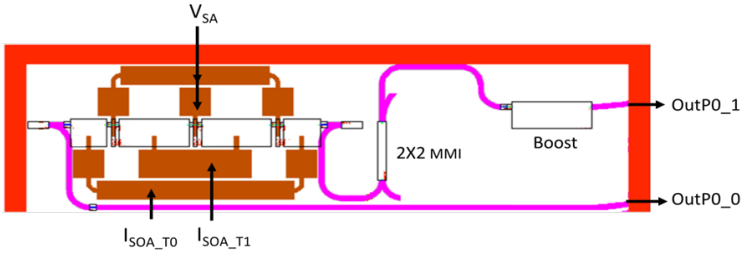


Figure 1. Photograph of the layout of the investigated semiconductor laser diode.

Every quarter (L/4) is around 0.42 mm long. In the design, all three SAs length is 20 µm. The two inner gain sections, which are much longer (~350 µm) than the two outer gain sections ~180 µm. Electrical isolation sections were inserted between every two adjacent SOAs to avoid undesirable back current flows . At each end of the cavity, one 2-port MIR terminates the straight waveguide at one port defining the overall Fabry-Pérot cavity length, but also carrying light out of the cavity through the other port. The two MIRs are ~55-µm long, having two ports with ~40% transmissivity and ~40% reflectivity, based on the multimode interference principle and internal etched reflection walls.

3. CHARACTERIZATION RESULTS

The device is glued with a thermos-conductive paste and mounted on an Alumimum Nitride (AlN) submount. This subcarrier has different DC and RF tracks for biasing of each optical component of the device. The DC pads extensions of the gain sections and the metal layer of the boost are wired bonding to the DC tracks on the submount, while the pads extensions of the saturable absorbers are wire bonding to the RF tracks. The subcarrier is placed on a cooper chuck of a probe station where is stabilized in temperature. The working temperature is set to 16ª for all the measurements. To control the integrated device, all gain sections and saturable absorbers are electrically connected to external current and voltage sources, respectively. Three DC probe needles are physically contacted on the DC tracks for the outer gain sections, inner gain sections, and boost, respectively. A RF probe head is contacted on the RF tracks for the saturable absorbers in order to inject a RF signal and to get the hybrid regimen condition. For evaluating the spectral performance on the wavelength domain and on the electrical domain, two of the optical spectrums are shown in Fig. 2, respectively. The bias conditions to get these optical spectrums are shown in Table 1. On both optical spectrums an optical frequency comb near 1577 nm is presented. For Fig 2 (a), twenty comb lines and the mode spacing between each optical mode is approximately 0.2 nm, equivalent to 25 GHz in frequency. An inset on the left side of the optical spectrum shows the modal spacing between three optical modes.

TABLE 1. Bias conditions to achieve optical frequency combs with a modal spacing of 25 and 100 GHz .

I_{SOA_T0} (mA)	I_{SOA_T1} (mA)	I_{boost} (mA)	V_{SA} (V)	Section
40	62	20	2.0	a
50	50	20	1.6	c

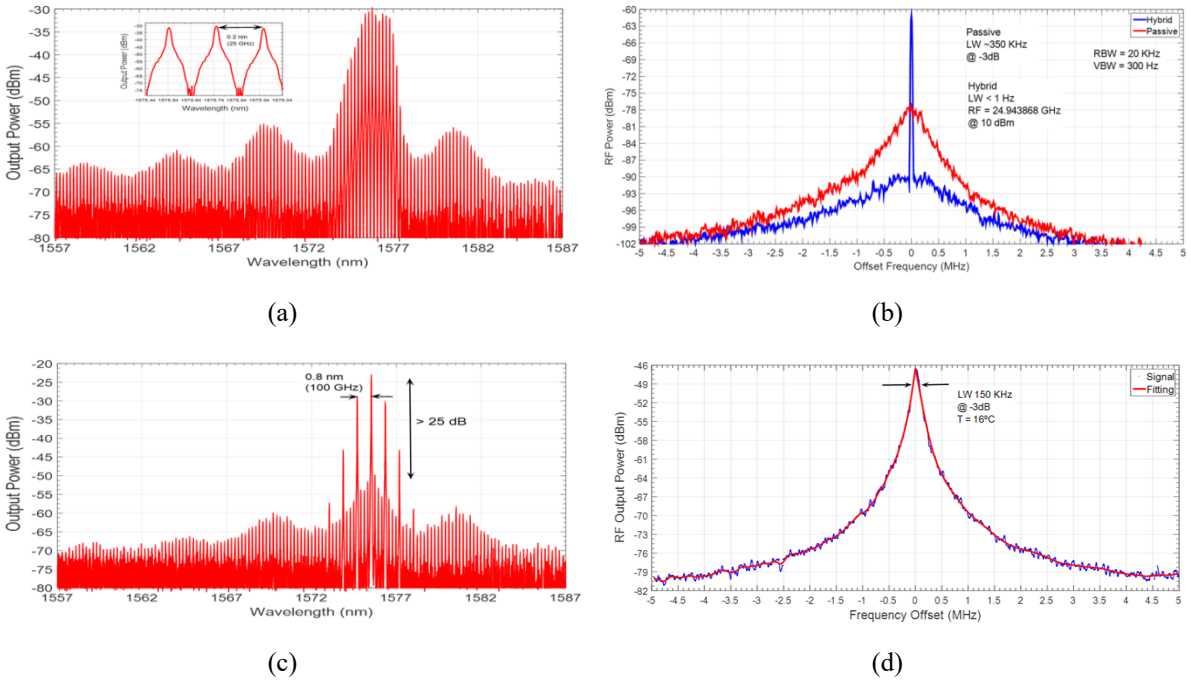


Figure 2. Optical and electrical spectrum of the multi-section semiconductor laser diode. (a) Optical frequency comb with a modal spacing of 0.2 nm (25 GHz). (b) RF electrical tone both in passive (red) and in hybrid (blue) regimen condition, thus the achieved electrical linewidth are ~350 KHz and less than 1 Hz, respectively. (c) Optical spectrum with lasing modes separated each 0.8 nm (100 GHz). (d) RF electrical tone generated at the laser output in passive regimen condition.

Regarding Fig 2(c), the optical spectrum shows seven comb lines and the modal spacing in between is around 0.8 nm, which is equivalent to 100 GHz in frequency. The seven lasing modes constitute an optical frequency comb which exhibits a suppression ratio of ~25 dB, with respect to the level of the suppressed modes that are

associated with the fundamental cavity round-trip frequency of 25 GHz. Only, three lasing modes in every four lasing modes are supressed, and thus, only one mode in every four lasing modes is excited. The electrical linewidth in passive regime condition is measured at the round-trip frequency as well as the four times the fundamental repetition rate as shown in Fig 2 (b) and (d), respectively. In Fig 2(b), the optical signal is collected at OutP0_0, getting an electrical linewidth of ~350 KHz centered around 25 GHz. In order to get hybrid regimen condition, a RF signal of 24.943868 GHz and with a power level of 10 dBm is injected into the saturable absorbers. The electrical linewidth of the generated RF signal is reduced and its value is less than 1 Hz. In Fig 2(d), the electrical linewidth of the generated electrical tone at 100 GHz ~150 KHz, and the optical signal is collected at OutP0_1, thus the electrical tone generated by the laser has an electrical level greater than the 25 GHz electrical tone.

4. CONCLUSIONS

We have successfully presented an InP mode-locked semiconductor laser for 100-GHz optical frequency comb generation. The laser cavity features multiple segments in a symmetric arrangement in which short SOAs separate the overall 1.66-mm-long resonator into four shorter divisions in equal length to achieve fourth harmonic generation. The on-chip multimode interference reflectors have shown the potential to replace the cleaved facets.

ACKNOWLEDGEMENTS

European Union's Horizon 2020 (Marie Skłodowska-Curie grant agreement No. 642355 Fi- WiN5G), Spanish Ministerio de Economia y Competitividad thourgh Programa Estatal de Investigación, Desarrollo e Inovación Orientada a los Retos de la Sociedad thougth grant iTWIT, TEC2016-76997-C3-3-R.

REFERENCES

[1] E.Avrutin, J. Marsh, and E. Portnoi, *"Monolithic and multi-gigahertz mode-locked semiconductor lasers: constructions,experiments, models and applications,"* IEEE Proceedings-Optoelectronics147, 251–278 (2000).

[2] M.-C. Lo, R. C. G. Martínez, and G. Carpintero, "*Monolithic mode locked laser-based optical frequency comb for OFDM integrated on InP generic technology platform*," in "Optical Fiber Communication Conference," (Optical Society of America, 2018), pp. Th1I–1

[3] J. H. Marsh and L. Hou, *"Mode-locked laser diodes and their monolithic integration,"* IEEE J. Sel. Top. Quantum Electron. 23, 1–11 (2017)

[4] Y. K. Chen, M. C. Wu, T. Tanbun-Ek, R. A. Logan, and M. A. Chin, *"Subpicosecond monolithic colliding-pulse mode-locked multiple quantum well lasers,"* Appl. Phys. Lett. 58, 1253–1255 (1991).

[5] E. A. Avrutin, J. H. Marsh, J. M. Arnold, T. F. Krauss, H. Pottinger, and R. M. D. la Rue, *"Analysis of harmonic (sub) THz passive mode-locking in monolithic compound cavity Fabry-Perot and ring laser diodes,"* IEE Proc. - Optoelectronics 146, 55–61 (1999

[6] S. Arahira, S. Oshiba, Y. Matsui, T. Kunii, and Y. Ogawa, *"Terahertz-rate optical pulse generation from a passively mode-locked semiconductor laser diode,"* Opt. Lett. 19, 834–836 (1994)

[7] Y. Katagiri and A. Takada, *"A harmonic colliding-pulse mode-locked semiconductor laser for stable subterahertz pulse generation,"* IEEE Photonics Technol. Lett. 9, 1442–1444 (1997).

[8] J. F. Martins-Filho, E. A. Avrutin, C. N. Ironside, and J. S. Roberts, *"Monolithic multiple colliding pulse mode-locked quantum-well lasers, experiment and theory,"* IEEE J. Sel. Top. Quantum Electron. 1, 539–551 (1995).

[9] E. Kleijn, M. K. Smit, and X. J. Leijtens, *"Multimode interference reflectors: a new class of components for photonic integrated circuits,"* J. Light. Technol. 31, 3055–3063 (2013).

[10] S. Stopinski, M. Malinowski, R. Piramidowicz, C. Kazmierski, M. K. Smit, and X. J. Leijtens, *"Photonic integrated multichannel wdm modulators for data read-out units,"* J. Light. Technol. 32, 3879–3887 (2014).

[11] P. E. Morrissey, N. Kelly, M. Dernaika, L. Caro, H. Yang, and F. H. Peters, *"Coupled cavity single-mode laser based on regrowth-free integrated MMI reflectors,"* IEEE Photonics Technol. Lett 28, 1313–1316 (2016).

[12] M.-C. Lo, R. Guzmán, C. Gordón, and G. Carpintero, *"Mode-locked laser with pulse interleavers in a monolithic photonic integrated circuit for millimeter wave and terahertz carrier generation,"* Opt. Lett. 42, 1532–1535 (2017).

Experimental Characterization of a Novel Energy-efficient Integrated Microwave Photonics Modulator

Iterio Degli-Eredi* and Martijn J. R. Heck
Aarhus Universitet - Department of Engineering, Finlandsgade 22, 8200 Aarhus, Denmark
**e-mail: ideglieredi@eng.au.dk*

ABSTRACT

We design and experimentally characterize a novel microwave (MW) photonics ring modulator based on waveguide-resonator coupling modulation. The experiments reveal that at MW frequencies corresponding to the FSR of the ring or integer multiples thereof, the resonant device generates 10 to 19 times higher MW output power than the equivalent standard Mach-Zehnder modulator, thus showing our resonant modulator paves the way for energy-efficient and low driving MW power operation. Moreover, as this resonant enhancement occurs over a bandwidth of 2 to 3 GHz, our modulator has the potential to be implemented as a key element in the upcoming microwave and millimeter wave bands of 5G networks. Finally, the device solely consists of standard building blocks provided by the multi-project wafer run of the SMART Photonics foundry, thus showing it can be fabricated in a relatively mature photonics integration process.

Keywords: Microwave Modulators, Ring Resonators, Indium Phosphide, Microwave Photonics, Integrated Microwave Photonics

1 INTRODUCTION

In order to meet the increasingly high demand of bandwidth in optical telecommunication networks, there is considerable interest in improving the speed, power consumption and footprint of MW electro-optic modulators (EOMs) through photonic integration [1], [2]. One photonic integration material platform that can be used for on-chip MW modulation, but also amplification and lasing, and where the foundry process technology has already reached a certain level of maturity in terms of scalability, reproducibility and yield, is indium phosphide (InP) [3], [4]. However, foundry based InP modulators can only efficiently operate at MW frequencies lower than 15 GHz while upcoming telecommunication networks operate at frequencies far beyond 15 GHz such as the millimeter wave bands of 5G networks [4], [5]. And when using EOMs that rely on the Pockels effect, long modulator lengths or high driving voltages (i.e. high driving MW powers) are required for efficient operation [6], [4]. To tackle these issues, one can utilize the resonant enhancement in cavities, which has already been demonstrated in silicon ring modulators [7]. In addition, waveguide-resonator coupling modulation in ring modulators has proven to be more energy efficient than modulating the refractive index in the ring cavity [8], [9]. As such, we propose a novel MW ring modulator based on waveguide-resonator coupling modulation which will be described and experimentally characterized in the next section.

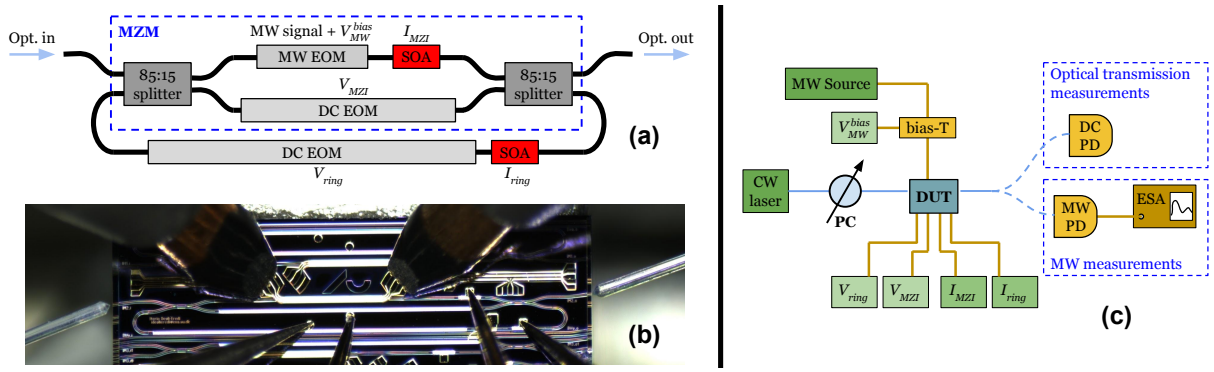


Figure 1. (a) Schematic of the ring resonator MW modulator. (b) Microscope image of the fabricated modulator with DC/MW probes and edge coupled fibers. (c) Measurement setup to obtain either the optical transmission or the MW response.

2 DESCRIPTION OF THE MODULATOR AND EXPERIMENTAL CHARACTERIZATION

2.1 Modulator principle and measurement setup

The device we consider is illustrated in Fig. 1(a): it is a ring resonator whose coupling section is a Mach-Zehnder modulator (MZM) that contains the MW EOM (length $L_{MW} = 950$ µm). The semiconductor optical

The research is supported by the Aarhus University Research Foundation AUFF, through a Lektor Starting Grant.

amplifiers (SOAs) in the MZM and ring arm are meant to compensate the insertion and ring losses respectively (the SOAs both have a length of $L_{SOA} = 200$ µm). The DC EOM in the MZM (length $L_{EOM}^{MZI} = 2.5\,\mathrm{mm}$) will be used to achieve critical coupling while the DC EOM in the ring arm (length $L_{EOM}^{ring} = 3\,\mathrm{mm}$) is meant to bias the device near resonance for a given wavelength. Finally, the splitters are 85:15 couplers (85% cross and 15% bar). The length of the connecting waveguides between the modulators and SOAs is chosen in such a way as to obtain an FSR close to 10 GHz. The device, along with some test structures, has been fabricated by the multi-project wafer (MPW) services of the SMART Photonics InP foundry and is depicted in Fig. 1(b). An external continuous-wave (CW) laser (Agilent 81600B) with polarization controller (PC) is edge coupled to the modulator, as seen in Fig. 1(c). We then either measure the transmitted optical power with an Agilent 81633A DC photodiode (PD) or, in case of MW measurements, retrieve the output MW signal from the external New Focus Model 1024 12-ps MW PD and measuring it with the R&S FSV30 electrical spectrum analyzer (ESA).

The resonant enhancement in the device can be explained as follows: during the first roundtrip, light from the CW laser with optical frequency f_c is modulated by the MW signal with frequency f_{MW} in the MZM and as a result, new frequencies $f_c + kf_{MW}$, with k integer, are generated. Via the ring waveguide, this modulated signal is fed back in the MZM, where also a 'new' unmodulated wave of the laser signal will enter of which the modulation will again generate a set of frequencies $f_c + kf_{MW}$. If these frequencies overlap in phase with the spectral content of the modulated signal from the previous roundtrip, the $f_c + kf_{MW}$ frequencies and thus the modulated signal will be resonantly enhanced - and this for all subsequent roundtrips. We expect the strongest MW response to happen when the device is tuned near resonance for a certain laser wavelength, and when the frequency f_{MW} of the MW signal is close to the FSR of the ring, thus resonantly enhancing the $f_c + kf_{MW}$ frequencies (where dispersion will ultimately put a limit on the maximally attainable k).

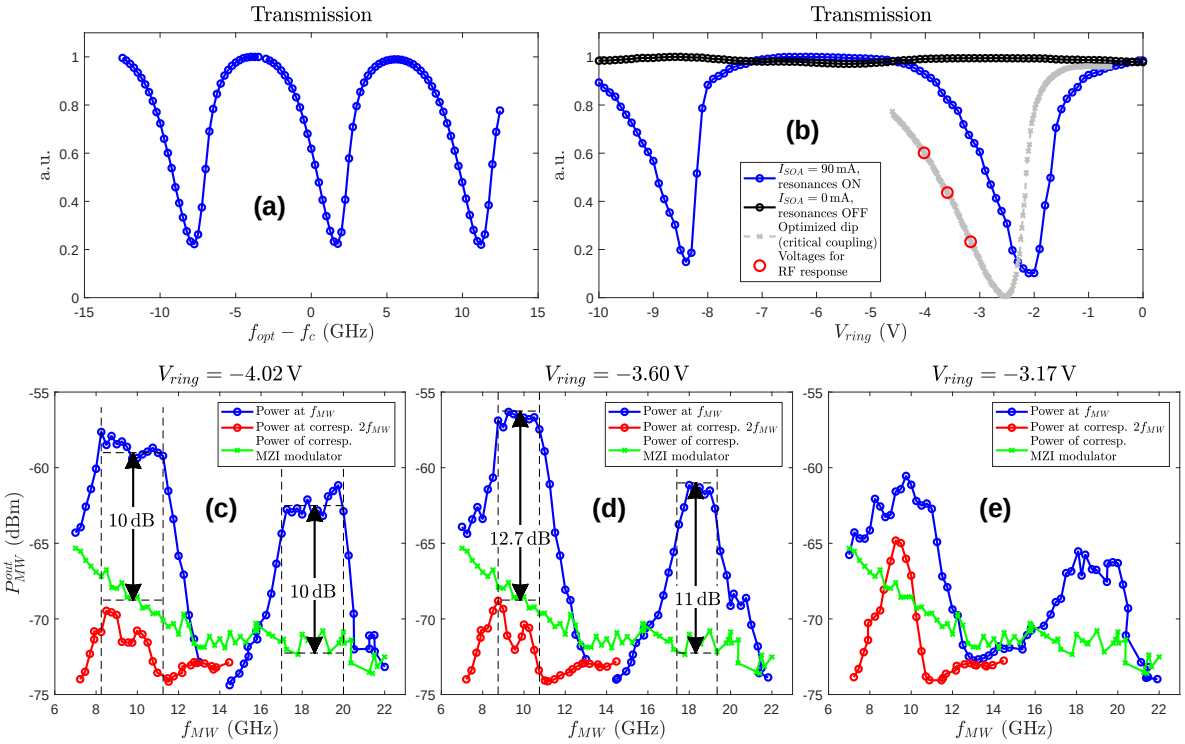


Figure 2. (a) Normalized transmission as a function of the optical frequency. (b) Normalized transmission as a function of V_{ring} (blue) together with the shape of the dip when critical coupling is achieved (grey) as well as the voltages chosen for the MW characterization (red). We also show the normalized transmission of the equivalent stand-alone MZM (black). In (c)-(e), the output MW power as a function of f_{MW} is plotted (blue) at the chosen V_{ring} values from (b) as well as the generated MW power at the corresponding $2f_{MW}$ (red). The data in (c)-(e) is compared with the generated MW power of the equivalent stand-alone MZM (green).

2.2 Measurement strategy and results

Before we experimentally characterize the MW response of the fabricated modulator, we first measure the transmission of the modulator as a function of the optical frequency of the CW laser plotted in Fig. 2(a), showing an FSR of 9.5 GHz. Then we optimize the modulator towards resonance and critical coupling. We fix the wavelength of the CW laser at $\lambda_0 = 1550\,\mathrm{nm}$ and keep the laser output power at a relatively low value of $P_0 = 5\,\mathrm{mW}$ to minimize the effect of optical nonlinearities in the ring. We set the DC voltages at $V_{MW}^{bias} = -4\,\mathrm{V}$ and $V_{MZI} = -6\,\mathrm{V}$, while the DC currents for the SOAs are set at $I_{MZI} = 5\,\mathrm{mA}$ and $I_{ring} = 90\,\mathrm{mA}$ (Fig.

1(a)), and we measure the optical output power as a function of V_{ring}, plotted in blue in Fig. 2(b) where the dips in the transmission indicate the cavity resonances. We then optimize the resonance located at $V_{ring} = -2.10\,\mathrm{V}$ towards critical coupling and find critical coupling is obtained for $V_{MZI}^{cc} = -4.17\,\mathrm{V}$ while the resonance is slightly shifted to $V_{ring}^{res} = -2.61\,\mathrm{V}$. Around the resonance, we choose a set of V_{ring} voltages where the RF response is characterized (red on Fig. 2(b)).

We now apply a MW signal of $16.5\,\mathrm{dBm}$ (from a R&S SMF100A MW signal generator) to the MW input of the MW EOM and sweep its frequency f_{MW} between $7\,\mathrm{GHz}$ and $22\,\mathrm{GHz}$ while we measure the MW output power at f_{MW} and $2f_{MW}$ on the ESA (see Fig. 1(c)). In Figs. 2(c)-(e), we show the MW response at $V_{ring} = -4.02\,\mathrm{V}$, $V_{ring} = -3.60\,\mathrm{V}$ and $V_{ring} = -3.17\,\mathrm{V}$ respectively. Figs. 2(c)-(e) clearly show resonant enhancement for MW frequencies around $f_{MW} = 9.5\,\mathrm{GHz}$ and $f_{MW} = 19\,\mathrm{GHz}$ which nicely overlaps with, respectively, one and two times the resonator's FSR of $9.5\,\mathrm{GHz}$. Another interesting observation is the fact that changing the bias voltage changes the shape of the resonant peaks: one can choose to maximize either the bandwidth of the peaks (Fig. 2(c) - at $f_{MW} = 9.5\,\mathrm{GHz}$, we obtain an MW power around $-59.0\,\mathrm{dBm}$ over a bandwidth of $3\,\mathrm{GHz}$) or the enhancement of the MW output power (Fig. 2(d) - at $f_{MW} = 9.5\,\mathrm{GHz}$, we obtain an MW power around $-56.3\,\mathrm{dBm}$ over a bandwidth of $2\,\mathrm{GHz}$). One can also opt to maximize the MW power of the generated second harmonic as Fig. 2(e) shows. Although the overall generated MW power of the second harmonic is still relatively low, the modulator under these bias conditions has the potential to be used as an electro-optic MW frequency multiplier after a further set of optimizations.

To check how well the resonant modulator performs as compared to the equivalent stand-alone MZM, we keep $I_{MZI} = 5\,\mathrm{mA}$ but turn off the SOA in the ring (i.e. $I_{ring} = 0\,\mathrm{mA}$). This ensures most of the light entering the ring waveguide is absorbed by the ring SOA and resonant enhancement is prevented. This is clear from the absence of resonance dips in its transmission spectrum plotted in black in Fig. 2(b). The MW response of this MZM, when excited with the same input MW signal with which the resonant modulator was excited, is plotted on Figs. 2(c)-(e) in green. Clearly, no resonant enhancement takes place in this device and as f_{MW} increases, the performance goes down due to the increasing MW losses in the coplanar waveguide of the MW EOM. When the resonant modulator is biased at "maximal enhancement" or where $V_{ring} = -3.60\,\mathrm{V}$ (Fig. 2(d)), the resonant modulator yields up to 19 times higher MW power for $f_{MW} = 9.5\,\mathrm{GHz}$ and $f_{MW} = 19\,\mathrm{GHz}$[1] than the stand-alone MZM. Even if we bias the resonant modulator at "wide bandwidth" or where $V_{ring} = -4.02\,\mathrm{V}$ (Fig. 2(c)), the modulator still generates a 10 times higher MW output signal.

3 CONCLUSIONS

While traditional MZMs fabricated in InP MPW runs cannot operate efficiently beyond a MW frequency of $15\,\mathrm{GHz}$ and require high driving MW powers, our novel integrated InP ring modulator has alleviated both issues by relying on both waveguide-resonator coupling modulation and resonantly enhancing the optical sidebands generated by the MW modulation and consequently the modulation depth and output MW power. We experimentally demonstrated that output MW power enhancements of 10 to 19 can be achieved at the resonances as compared to the stand-alone MZM, thus indicating the same modulation depth can be achieved at far lower driving MW powers. This not only happens for $f_{MW} = 9.5\,\mathrm{GHz}$ corresponding to the ring's FSR, but also beyond the MW EOM's bandwidth of $15\,\mathrm{GHz}$, namely twice the ring's FSR equal to $f_{MW} = 19.0\,\mathrm{GHz}$. On top of that, the enhancement around these resonances happen over a bandwidth of 2 to $3\,\mathrm{GHz}$, a feature that will be useful for the high frequency 5G bands below $40\,\mathrm{GHz}$ in Europe and elsewhere that require a bandwidth of up to 3 to $4\,\mathrm{GHz}$ [5]. Finally, the modulator only uses building blocks provided by the SMART Photonics MPW, thus showing the device can be fabricated in a relatively mature photonics integration process.

REFERENCES

[1] C. Wang et al., "Integrated lithium niobate electro-optic modulators operating at CMOS-compatible voltages," Nature, vol. 562, pp. 101–104, 2018.

[2] R. A. Griffin, S. K. Jones, N. Whitbread, S. C. Heck, and L. N. Langley, "InP Mach-Zehnder Modulator Platform for 10/40/100/200-Gb/s Operation", IEEE JSTQE, vol. 19, no. 6, pp. 158-166, November 2013.

[3] M. Smit et al., "An introduction to InP-based generic integration technology," Semicond. Sci. Technol., vol. 29, no. 8, pp. 083001, 2014.

[4] "Multiproject wafers," http://www.jeppix.eu/multiprojectwafers/, website visited in January 2019.

[5] "5G Frequency Bands," https://www.everythingrf.com/community/5g-frequency-bands, 2018, website visited in January 2019.

[6] R. Amin, J. B. Khurgin, and V. J. Sorger, "Waveguide-based electro-absorption modulator performance: comparative analysis," Opt. Express, vol. 26, no. 12, pp. 15445-15470, June 2018.

[7] J. Müller et al., "Optical Peaking Enhancement in High-Speed Ring Modulators," Sci Rep., vol. 4, pp. 6310, September 2014.

[8] W. M. J. Green, R. K. Lee, G. A. DeRose, A. Scherer, and Amnon Yariv, "Hybrid InGaAsP-InP Mach-Zehnder Racetrack Resonator for Thermooptic Switching and Coupling Control," Opt. Express, vol. 13, no. 5, pp. 1651–1659, March 2005.

[9] W. D. Sacher et al., "Coupling modulation of microrings at rates beyond the linewidth limit," Opt. Express, vol. 21, no. 8, pp. 9722–9733, April 2013.

1. For MW output powers below $-71\,\mathrm{dBm}$, the ESA measurements are highly affected by noise. We expect the actual output MW power of the stand-alone MZM around $f_{MW} = 19\,\mathrm{GHz}$ to be lower and therefore the enhancements higher than indicated on Figs. 2(d).

Waveguide Photonic Crystal Reflectors on InP-Membranes-on-Silicon

Student paper

Sander Reniers [1], Jorn van Engelen [1], Kevin Williams [1], Jos van der Tol [1], Yuqing Jiao [1]
[1] *Photonic Integration Group, Institute for Photonic Integration, Eindhoven University of Technology, PO Box 513, 5600 MB Eindhoven, The Netherlands*

e-mail: s.f.g.reniers@tue.nl

ABSTRACT

We present waveguide photonic crystal reflectors on an InP-membrane-on-silicon (IMOS). Photonic crystal holes are patterned on a waveguide using electron-beam lithography to create a broadband distributed Bragg reflector. We show simulations of these reflectors and experimental results of fabricated devices, both showing a high, free to choose reflectivity, and high quality factor Fabry-Pérot cavities. We experimentally show reflectivities >90% for the reflectors and a quality factor as high as 11,430±1,446 for a Fabry-Pérot cavity, using reflectors with a length of only 4 microns.

Keywords: photonic integrated circuits, photonic membrane, photonic crystal, waveguide reflector.

1 INTRODUCTION

The InP-membrane-on-silicon (IMOS) platform [1] consists of a 300 nm thick membrane of InP, which corresponds to the core thickness in the nanophotonic waveguides, bonded by benzocyclobutene (BCB) to a silicon carrier wafer. The thin membrane and high index contrast enable tight light confinement and small footprint devices and waveguides, the latter being 400 nm wide for the passive waveguides. Distributed Bragg reflectors (DBR) are of key importance in any (nano) photonic platform. Controllable and high reflectivity are required for creating high quality factor Fabry-Pérot cavities, e.g. for lasers. The concept of using these reflectors to create laser cavities has been previously investigated [2], with a reported simulated quality factor for the cavities of around 1,200. We experimentally demonstrate cavities with almost an order of magnitude higher quality factor. Simulation results are shown, as well as experimental results using two different measurement techniques.

2 DESIGN AND FABRICATION

The photonic crystal reflector is implemented with elliptical holes to periodically change the refractive index [3]. A taper is required for the transition between the regular waveguide (400 nm wide) to a wider waveguide section (700 nm), in which the holes are patterned. The smaller holes are included to smoothen the transition to the high index-contrast section of the reflector.

After bonding of the wafers, the substrate of the InP wafer is removed with wet etching, leaving only the 300 nm thick membrane. Typically, the core is etched to a target depth of 20 nm from the lower membrane surface. This ensures strong waveguiding while protecting the structures during subsequent processing. An image of the waveguide is shown in Fig. 1. Patterned holes in the silicon nitride mask at an intermediate step are shown in Fig. 2 for clarity. The pattern is then transferred to the semiconductor, etching the waveguide core and holes in the same etch step. In a second lithographic step, the surface grating couplers used for fiber-to-chip coupling are created. For a detailed process description, see [1].

3 SIMULATION

The photonic crystal reflectors are simulated with finite-difference time-domain software. The adiabatic taper for the transition between the normal waveguide (400 nm wide) and the reflector (700 nm wide) is not included

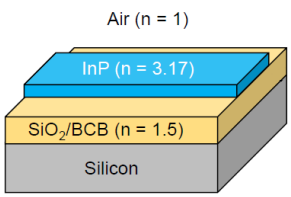


Figure 1. Example a typical IMOS waveguide.

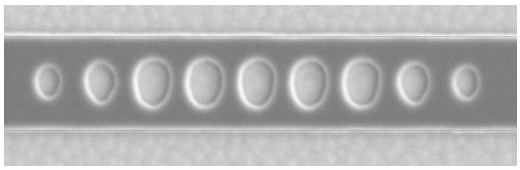


Figure 2. Scanning electron microscope (SEM) image of the photonic crystal hole reflector.

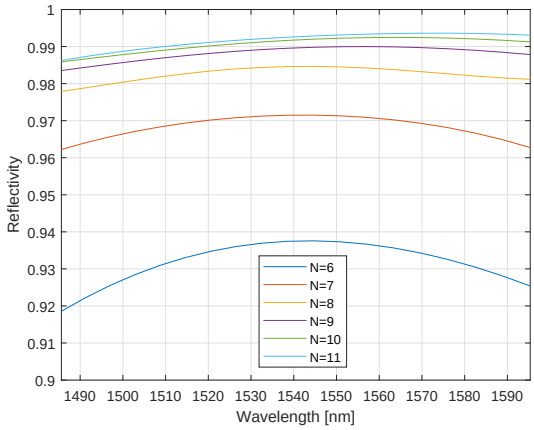


Figure 3. Simulated power reflection from a lossless photonic crystal reflector. N is the number of holes.

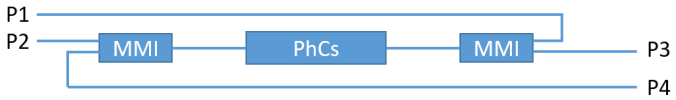


Figure 4. Schematic layout of the 4-port structure used for photonic crystal hole reflector characterization.

in the simulation model. The number of holes, which among others defines the reflectivity of the reflector, is varied for the simulation. The simulated reflection coefficients are shown in Fig. 3. From this figure, we observe that already for a low number of holes reflectivities above 90% can be expected, and even higher than 99% with an increased number of holes.

4 MEASUREMENT RESULTS AND ANALYSIS

Measurement structures for two methods of characterization are realized. The first method [4] is used to directly measure the reflectivity of a single photonic crystal reflector using a four-port measurement. For the second method, a Fabry-Pérot cavity [5] is created using two photonic crystal reflectors.

The structure that is used for the four-port measurements is schematically shown in Fig. 4. Both the power reflected by the photonic crystals holes and transmitted through the reflector can be measured in two separate measurements each. We can write the powers P_{ij} measured when the fibers are placed between port i and j as

$$P_{13} = \alpha_1\alpha_3\alpha_{\text{MMI}}^2 R P_{\text{in}}, \quad (1) \qquad P_{14} = \alpha_1\alpha_4\alpha_{\text{MMI}}^2 T P_{\text{in}}, \quad (3)$$

$$P_{23} = \alpha_2\alpha_3\alpha_{\text{MMI}}^2 T P_{\text{in}}, \quad (2) \qquad P_{24} = \alpha_2\alpha_4\alpha_{\text{MMI}}^2 R P_{\text{in}}, \quad (4)$$

where α_i is the transmission through arm i, α_{MMI} is the power transmission through the MMI ($\sim$0.5), P_{in} is the power coupled from the input fiber, R is the reflection coefficient of the reflector, and T is the transmission through the reflector. In our analysis we have assumed the reflector itself has negligible loss ($T + R = 1$), and hence we can write

$$B = \frac{P_{23}P_{14}}{P_{13}P_{24}} = \frac{(1-R)^2}{R^2}, \quad (5)$$

which gives one physical solution for the reflectivity:

$$R = \frac{1}{1+\sqrt{B}}. \quad (6)$$

In this way the measured R becomes independent of coupling and waveguide losses. By applying (5) and (6) on the measured powers P_{ij}, as given in (1)-(4), the reflection coefficient can be found for photonic crystal reflectors with various N, which is shown in Fig. 5. The shown reflection coefficients are for a lower wavelength than the targeted wavelength, which is 1550 nm. This may be understood through the wavelength-shifted transfer function for the surface grating couplers. The fringes appearing on the measurements are believed to be caused by parasitic reflections from the MMI couplers and the surface grating couplers. We observe that the reflection coefficient for a six hole reflector, over the 1490 nm to 1540 nm wavelength range, varies from 0.72 to 0.91, for an eight hole reflector it varies from 0.89 to 0.96 and for an eleven hole reflector it is above 0.96.

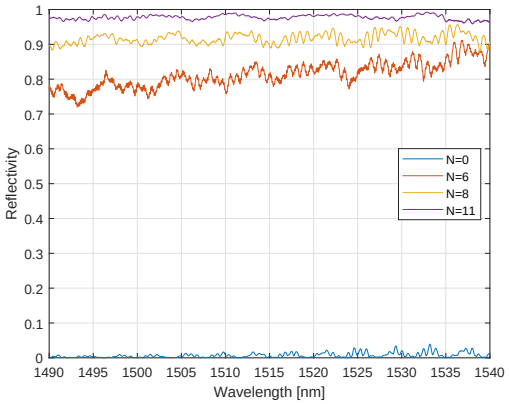


Figure 5. Reflection coefficients for photonic crystal hole reflectors with $N = 0, 6, 8, 11$, measured with the structure of Fig. 4.

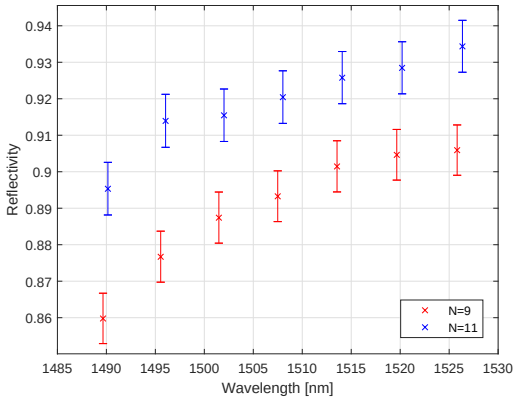


Figure 6. Reflection coefficients calculated from the Fabry-Pérot cavity measurements.



Figure 7. Schematic layout of the cavity created with two photonic crystal hole reflectors.

A Fabry-Pérot cavity is also used to measure the reflection coefficient of the photonic crystal holes, as well as the quality factor of the cavity. A schematic layout of the structure is shown in Fig. 7. The transmission spectrum for this structure is measured, and from the resonances the quality factor can be extracted by using $Q = \frac{\lambda}{\text{FWHM}}$. Furthermore, the finesse F is given by $F = \frac{\text{FSR}}{\text{FWHM}}$, and the reflection coefficient R is given by $R = \sqrt{\text{e}^{-\frac{2\pi}{F}}}$. The calculated reflection coefficients are shown in Fig. 6. The error bars on the reflectivity are due to the accuracy limits of the measurement equipment and the fringes on the measurements due to suspected parasitic reflections of the MMI couplers and the surface grating couplers. The structures with $N > 11$ could not be measured, since the transmission through the cavity was too low, probably due to the high reflectivity. The measured reflectivity is high, but somewhat lower than the values obtained from simulation, which is believed to be caused by stringent fabrication tolerances for these first prototypes.

The difference in measured reflection coefficients can be explained by the neglected losses for both measurement methods. In the four-port characterization method, the internal reflector loss is neglected, which results in a higher reflectivity. In the cavity structures, the reflector loss and the waveguide loss of the waveguide section between the two reflectors is neglected, which results in a lower derived reflectivity. The actual reflection coefficient is therefore expected to lie between these two values. An analysis on the impact of losses on the reflectivity will be presented at the conference.

5 CONCLUSION

Photonic crystal reflectors as short as 4 microns are simulated and demonstrated experimentally. Characterization of the reflectors is done using two characterization methods, both showing $> 90\%$ reflection. Therefore, the presented reflector is shown to be an important building block for our nanophotonic platform. As a result, a Fabry-Pérot cavity with a quality factor of 11,430$\pm$1,446 is experimentally demonstrated, which is very promissing for use of these cavities in lasers on IMOS.

REFERENCES

[1] J.J.G.M. van der Tol, et. al., “Indium Phosphide Integrated Photonics in Membranes,” IEEE Journal of Selected Topics in Quantum Electronics, vol. 24(1), 2018.

[2] A. Higuera Rodríguez, ”Technology Development of Nano-Scale Photonic Integrated Circuits on III-V Membranes,” PhD thesis, Eindhoven University of Technology, 2017.

[3] S.O. Kasap, ”Optoelectronics & Photonics: Principles & Practices,” Pearson, 2013.

[4] J. Pello, ”Building up a membrane photonics platform in indium phosphide,” PhD thesis, Eindhoven University of Technology, 2014.

[5] G. Hernandez, ”Fabry-Pérot Interferometers,” Cambridge University Press, 1986.

Low-Voltage InP MEMS Optical Switch on Silicon

Tianran Liu[1], Francesco Pagliano[1, 2], René van Veldhoven[1], Vadim Pogoretskii[1], Yuqing Jiao[1], Andrea Fiore[1]

[1]Department of Applied Physics and Institute for Photonic Integration,
Eindhoven University of Technology, P.O. Box 513, 5600MB Eindhoven, The Netherlands
[2]nanoPHAB, Groene Loper 19, Postbus 513, Eindhoven 5612 AP, The Netherlands
e-mail: t.liu@tue.nl

ABSTRACT

In this paper, a novel MEMS Mach-Zehnder interferometer optical switch is presented. Switching is achieved by tuning the vertical gap between two coupled waveguides through the application of a reverse bias on a p-i-n junction. The switching requires a voltage as low as 4.4V and provides an extinction ratio above 15dB within a 34 nm bandwidth in the C-band. The device also serves as a very efficient optical phase modulator, being able to modify the optical phase by more than 4π with only 6.5V voltage in a 140μm-long waveguide. Our work provides a solution to on-chip optical switching for low-voltage applications. The switch is fabricated on an indium-phosphide membrane on a silicon substrate, which enables the integration with active components (e.g. amplifiers, lasers, detectors) on a single chip.

Keywords: Optical switch, MEMS, phase modulator, Mach-Zehnder interferometer, Indium-phosphide.

1. INTRODUCTION

Switching light efficiently is essential for the development of the next-generation optical networks. However, the currently available 3D MEMS (micro-electro-mechanical-system) optical circuit switches cannot be easily integrated on a chip and present switching times in the ms range. In the past decades several integrated MEMS optical switches on different platforms have been reported [1]-[4]. Most of these switches require tens of Volts to actuate, preventing their application in low-voltage applications. In this paper, we report a MEMS optical switch based on a Mach-Zehnder interferometer, which requires a switching voltage as low as 4.4V. Though the design can be implemented on various platforms, we fabricated it on an indium-phosphide membrane bonded on a silicon substrate [5], which provides the possibility to integrate our device with active optical components on a single chip.

2. APPROACH

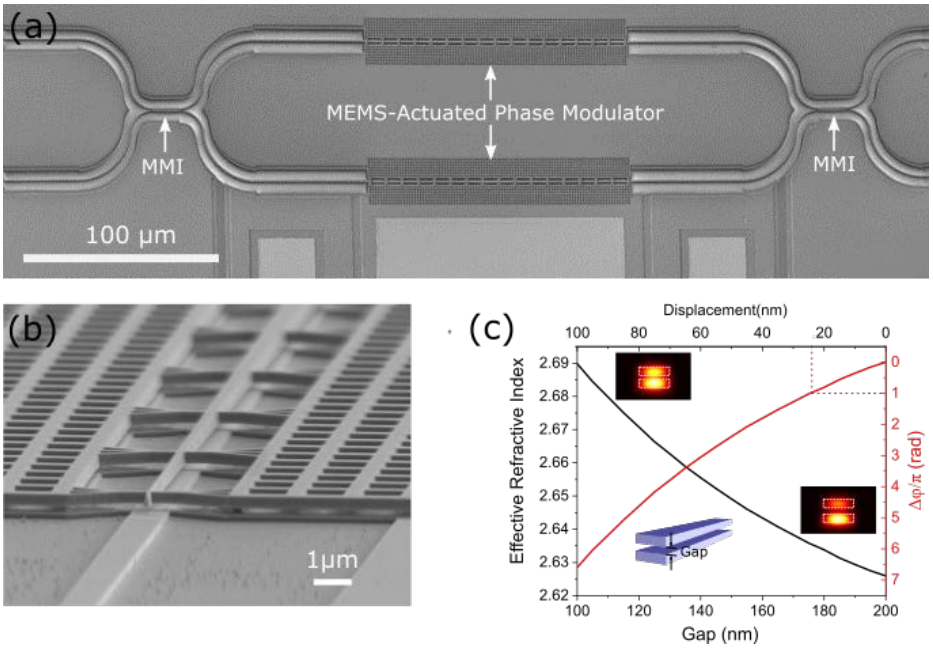


Figure 1. (a) Scanning electron microscope (SEM) image of a 2x2 switch. (b) Zoomed-in SEM image of the MEMS-actuated phase modulator. (c) Simulated ERI (effective refractive index) and phase difference (for a device length of 140 μm) as a function of vertical gap spacing and displacement of the suspended part. In the insets the sketch of the two waveguides and simulated cross-section electric field magnitude distributions in the middle of the waveguides, with gap of 100nm (left) and 200nm (right), respectively, are shown. The displacement needed for switching is marked by a dashed line.

Figure 1 (a) shows the SEM image of our optical switch. It is 2x2 switch based on Mach-Zehnder Interferometer (MZI). Two 50/50 Multi-Mode Interferometers (MMIs) split/combine light into/from two branches. MEMS-actuated modulators are implemented in both branches to ensure a symmetric optical path. Figure 1 (b) shows the details of MEMS part. A 140µm tapered InP waveguide is suspended and connected with 15µm cantilevers on both sides. The length of tapers is 60µm on both ends of the coupler to ensure adiabatic coupling. The bottom InP ridge waveguide is 1µm wide. Below the ridge waveguide the bonding layer is composed of silicon nitride, BCB and silica. The low refractive index of the bonding layer ensures a small mode volume confined in the waveguide. A layer of InGaAsP between the two InP membranes forms the intrinsic layer of the p-i-n junction, and serves as sacrificial layer to create the suspended part. At zero bias the vertical gap spacing between the suspended waveguide and ridge waveguide is 200nm, and light exits through the cross port after interference due to the symmetry of the optical path. In the actuated state, a reverse bias is applied to the junction. The electro-static force brings the coupler down and increases the ERI of the waveguide by evanescent coupling, so that the phase difference between the two branches changes. The light is switched to the through port when the phase difference reaches π.

To estimate the displacement of coupler needed for a π phase shift, we simulated the ERI change of the waveguide using a FDTD model (commercial software Lumerical FDTD Solutions). As showed in Fig. 1 (c), the ERI modulation rate is about 6.4×10^{-4}/nm. Given the length of coupler (140µm including the tapers) in this work, a displacement of 24nm is needed for a π phase shift.

3. FABRICATION

The switches are fabricated in the NanoLabNL@TU/e facility at the Eindhoven University of Technology. An InP wafer with two doped InP layers and an InGaAsP intermediate layer is grown by MOCVD. The doping level of InP is 1×10^{18} cm^{-3} for both p and n layer. The InP wafer is then flipped and bonded to a silicon wafer using benzocyclobutene (BCB). After removing the substrate of the InP wafer, a layer of silicon nitride is deposited by PECVD as hard mask. The waveguides and MEMS are defined by electron beam lithography using ZEP520 as resist. The mask is then transferred to the silicon nitride layer in RIE by CHF_3, followed by InP dry etching in ICP by CH_4/H_2. Then the same process above is repeated to define the pattern on the second InP layer. Metal contact pads (Ti 25nm/Pt 75nm/Au 200 nm) are formed by evaporation and lift-off process. Finally, the device is released by etching with $H_2O/H_2O_2/H_2SO_4$ solution and dried in a super-critical dryer.

4. EXPERIMENTAL RESULTS

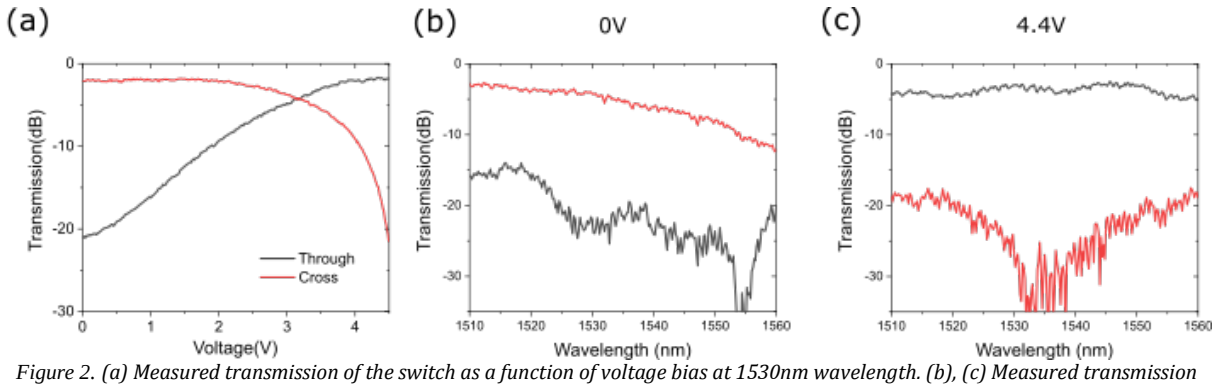


Figure 2. (a) Measured transmission of the switch as a function of voltage bias at 1530nm wavelength. (b), (c) Measured transmission spectra of the switch at 0V (b) and 4.4V (c).

Figure 2 (a) - (c) shows the transmission of the switch described above (the fiber coupling loss has been subtracted). At zero bias most of the transmission is in the cross port due to the zero phase difference between the two branches. The transmission gradually shifts to the through port with the increase of the reverse bias, until -4.4V where the extinction ratio reaches a maximum. In the actuated state the spectra of the through port is almost flat from 1510nm to 1560nm, while that for cross port at default state experiences a decline at longer wavelength side, due to the suboptimal design of MMIs. Overall, the extinction ratio remains above 15dB from 1523nm to 1557nm, which gives a bandwidth of 34nm.

To characterize the performance of our device as a phase modulator we also fabricated and measured devices with the modulator only in one of the branches. The ridge waveguide of the other branch is of the same length but a smaller width of 500nm. This causes a default path difference and therefore a small free spectral range, as showed in Fig. 3(a). However we found that the extinction ratio is similar to the devices with two modulators, indicating the insertion loss of the phase modulator is negligible. It is showed in Fig. 3(b) that the MEMS phase modulator is able to tune the phase by 4.8π rad before reaching pull-in, among the highest in literature [6]-[8] for this low actuation voltage. The corresponding ERI tuning range is as high as 0.047. Comparing with simulation it can be

estimated that the maximum displacement of the coupler is about 80 nm, i.e. 40% of the initial gap. This large travel range is presumably due to the leveraged bending of the doubly clamped actuator [9]. The simulated mechanical frequency is 550 kHz, which indicates a potential switching time around 1 μs.

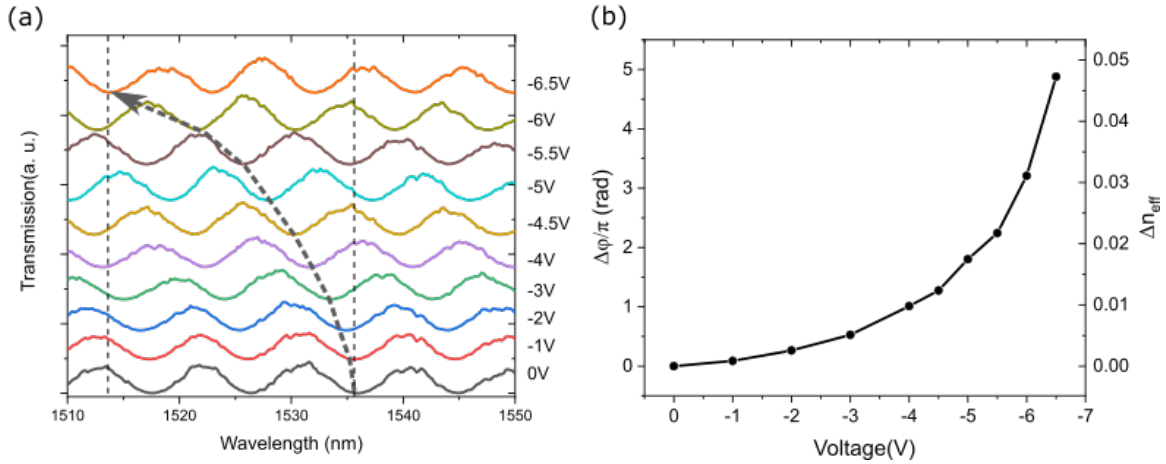


Figure 3. (a) Transmission spectra of a Mach-Zehnder interferometer with MEMS modulator in only one branch at reverse bias from 0V to -6.5V. Curves have been offset for clarity. Dashed line with an arrow tracks the wavelength shift of dip. (b) The optical phase shift and ERI change a function of voltage, extracted from (a).

5. CONCLUSIONS

We have demonstrated experimentally a 2x2 InP MEMS optical switch on silicon substrate. The footprint of the device is about 100x400 μm^2, with a small actuation voltage of 4.4V. The extinction ratio is above 15dB within a bandwidth of 34nm around C-band. The proposed device also serves as an efficient optical phase modulator, capable of tuning the phase by 4.8π rad within a coupling length of 140 μm. The device can be potentially integrated with lasers and detectors to find applications in optical communication and sensing.

ACKNOWLEDGEMENTS

We thank Dr. R. van der Heijden, Dr. N. Calabretta and Prof. K. Williams for helpful discussions.

REFERENCES

[1] T. J. Seok, *et al.*: Large-scale broadband digital silicon photonic switches with vertical adiabatic couplers. *Optica*, 3(1), 64-70, 2016.

[2] S. Han, *et al.*: Large-scale silicon photonic switches with movable directional couplers. *Optica*, 2(4), 370-375, 2015.

[3] M. W. Pruessner, *et al.*: InP-based optical waveguide MEMS switches with evanescent coupling mechanism. *Journal of Microelectromechanical Systems*, 14(5), 1070-1081, 2005.

[4] R. T. Chen, H. Nguyen, & M.C. Wu: A high-speed low-voltage stress-induced micromachined 2 x 2 optical switch. *IEEE Photonics Technology Letters*, 11(11), 1396-1398, 1999.

[5] J. J. G. M. v. d. Tol, *et al.* : Indium Phosphide Integrated Photonics in Membranes, *IEEE Journal of Selected Topics in Quantum Electronics*, vol. 24, p. 6100809, 2018.

[6] M. W. Pruessner, *et al.*: Broadband opto-electro-mechanical effective refractive index tuning on a chip. *Optics express*, 24(13), 13917-13930, 2016.

[7] M. Poot, & H. X. Tang: Broadband nanoelectromechanical phase shifting of light on a chip. *Applied Physics Letters*, 104(6), 061101, 2014.

[8] K. Van Acoleyen, *et al.*: Ultracompact phase modulator based on a cascade of NEMS-operated slot waveguides fabricated in silicon-on-insulator. *IEEE Photonics Journal*, 4(3), 779-788, 2012.

[9] E. S. Hung, & S. D. Senturia: Extending the travel range of analog-tuned electrostatic actuators. *Journal of microelectromechanical systems*, 8(4), 497-505, 1999.

III-V on SOI photonic crystal devices

(Invited paper)

Quentin Chateiller[1,2], Francesco.Manegatti[1], Gabriel Marty[1], Dimitris Fitsios[1] and Fabrice Raineri[1,2]
[1] Centre de Nanosciences et de Nanotechnologies, CNRS UMR9001, Palaiseau, France
[2] Université Paris Diderot, Sorbonne Paris Cité, Paris, France
e-mail: fabrice.raineri@c2n.upsaclay.fr

ABSTRACT

Nanophotonics will play a crucial for the convergence of microelectronics and photonics to cope with the requirements of compactness and low power consumption. During this talk I will present our recent progress on III-V on SOI photonic crystal devices such as lasers and nonlinear parametric sources.

Keywords: Nanophotonics, Photonic crystals, lasers, Nonlinear optics

A comparison between waveguide and microresonator single-photon sources in silicon photonics

Imad I. Faruque [1], Gary F. Sinclair [1], Damien Bonneau[1], John G. Rarity[1] and Mark G. Thompson[1]
[1]*Quantum Engineering Technology Labs, University of Bristol, Bristol BS8 1TL, United Kingdom*
e-mail: imad.faruque@bristol.ac.uk

ABSTRACT

For useful photonic quantum information protocols, such as quantum computing, quantum simulation, quantum machine learning, we need integrated photonic circuits to accommodate interaction of a large number of qubits [1], [2], [3], [4]. A key resource of the interaction of qubits is quantum interference. For high interference visibility, the single-photons that construct the qubits have to be indistinguishable. Measuring indistinguishability between two independent single-photon sources, we can determine the fidelity of the qubit interaction in a photonic platform. With such measurements in silicon, we have found microresonators more suitable than waveguides for such applications as it has 72% visibility without any spectral filtering. For both structures, photon number purity drastically affects the raw indistinguishability.

Keywords: Single-photon source, non-linear optics, silicon photonics, four-wave mixing, quantum computing.

1 INTRODUCTION

In general, indistinguishable single-photons correspond to the spectral purity of the single-photons: each of

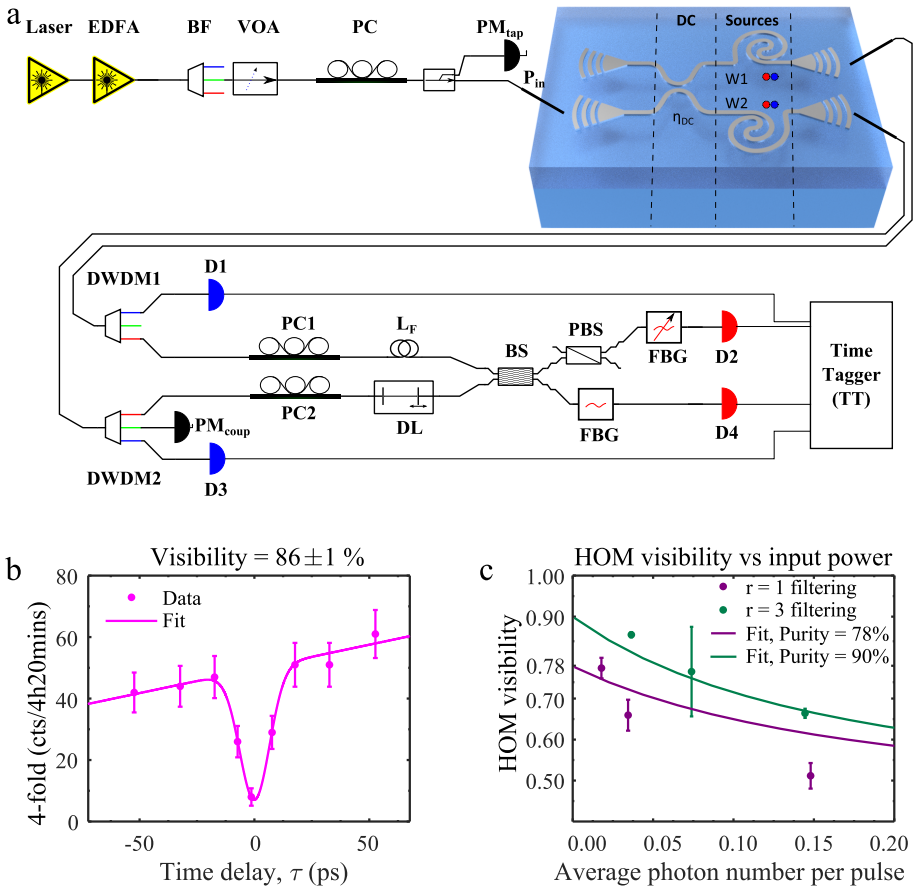


Figure 1. PIM of strip waveguide HSPSs. (a) Experimental setup for off-chip PIM. (b) HOM interferogram of heralded photons (red) from independent strip waveguides. With $r = 3$ spectral filtering and about 0.04 mean photon number 86% visibility is achieved. (c) Increase of the HOM visibility for lower mean photon number per pulse shows the detrimental effect of photon number purity. BF: Broadband Filter, VOA: Variable Optical Attenuator, DL: delay line, BS: Beam Splitter, FBG: Fibre Bragg Graiting, D: Single-photon Detector.

. I. I. F. thanks Marie Curie Actions Initial Training Network PICQUE (608062); all the authors thank Engineering and Physical Sciences Research Council (EPSRC) (EP/L024020/1, EP/K033085/1).

the photons is emitted in a single optical (spectro-temporal) mode. In heralded single-photon sources, photon-pairs are emitted through a nonlinear optical process and detecting one photon of the pair herald the presence of the other photon, thus acting as a heralded single-photon source (HSPS). In silicon, the third-order nonlinear optical process, spontaneous four-wave mixing, absorbs two pump photons (λ_p) and produce a photon-pair historically called signal-idler (λ_s, λ_i). Detecting the idler photon projects the signal photons into specific spectro-temporal modes. For the heralded signal photons to be identical (i.e. spectrally pure), the spectral shapes have to be the same, and the joint spectral density has to be separable [5].

Once all the physical qubits have near unity spectral purity, a large number of qubit interaction is feasible. In reality, spectral purity has trade-offs with photon-number purity (ratio between single-photon state and multi-photon state), heralding efficiency and the brightness (amount of photons/s). Therefore, an HSPS for scalable quantum computing/communication is characterised by a set of metrics: spectral purity (P); photon-number purity; heralding efficiency and brightness. A desired interaction among physical qubits requires these metrics to be high. All of these metrics are captured by a single experiment of photon indistinguishability measurement (PIM). In a PIM with two HSPSs, we detect the idler photons from each HSPS to herald the signal photons, which then interferes in a Hong-Ou-Mandel interferometer [6] or a Mach-Zehnder interferometer [7] as four-fold coincidences. The raw visibility of the interference indicates the indistinguishability of the heralded single-photons in the presence of the photon-number impurity and spectral impurity. The raw brightness of the four-fold coincidence indicates the heralding efficiency, loss of the device and the detection efficiency. Thus, a PIM coefficient ($\mathbb{C}_{\mathrm{PIM}}$) can be defined which efficiently captures the metrics of the HSPSs and their scalability:

$$\mathbb{C}_{\mathrm{PIM}} = \mathrm{B} \times \mathrm{V} \div \mathrm{T} \tag{1}$$

where, T is the required time for a PIM and raw brightness B captures the actual brightness, heralding efficiency and system loss. Higher the value of the $\mathbb{C}_{\mathrm{PIM}}$, better the HSPS is.

Here, we have compared the PIM of silicon waveguide and micro-resonator HSPSs. We have chosen silicon because of high component density, demonstration of electronic and photonic integration [8], low loss optical delay lines [9], high-speed electro-optic switches [10], and other necessary criteria for a linear optical quantum computing. If near ideal HSPSs are achieved in silicon, it will lead to an early demonstration of quantum advantages.

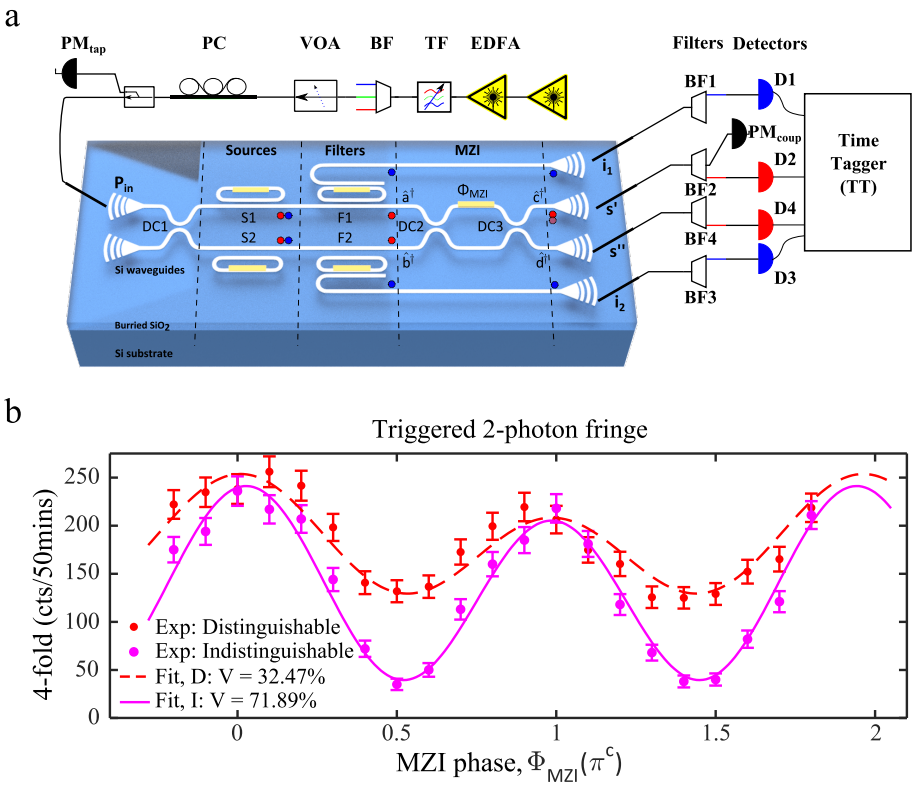


Figure 2. PIM of micro-resonator HSPSs. (a) Experimental setup for on-chip PIM. (b) Mach-Zehnder interferogram of completely distinguishable (red events) and indistinguishable (magenta events) heralded photons. Due to photon-number impurity, the raw visibility reduces to 72% from the theoretical value of 92%.

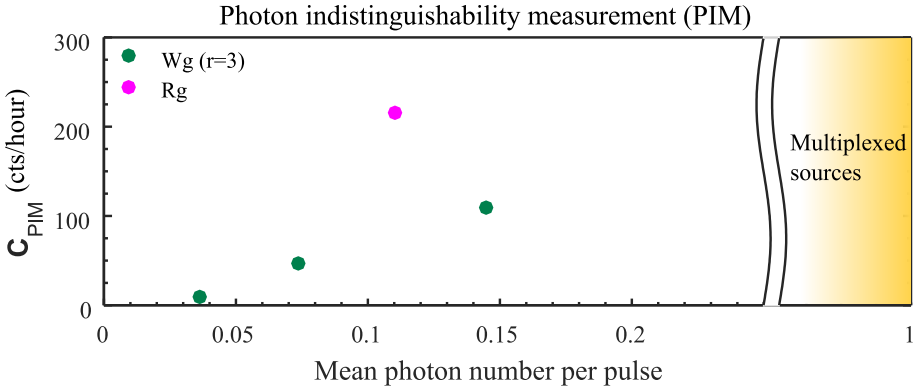


Figure 3. Comparing PIM between strip waveguide and microresonator.

2 RESULTS

We have interfered heralded single-photons, generated from strip waveguides, in an off-chip HOMI (Fig. 1) and recorded a set of interferogram for equal filtering ($r = 1$) and three times narrow filtering ($r = 3$) of the heralded photons with respect to the pump ($r = \Delta\lambda_p/\Delta\lambda_s$). We have reduced the input power in both cases (Fig. 1(c)) and observed improved raw visibility (max V $= 86\%$) due to improved photon-number purity at the expense of brightness and drastically increased integration time. Here, the y-intercept specifies the maximum achievable visibility determined by the spectral purity.

Integrating the spectral de-multiplexer and a MZI on-chip significantly reduced the complexity while improving the stability of the PIM (Fig. 2) for the microresonators. We have achieved V $= 72\%$ without any spectral filtering with high brightness due to resonant enhancements. The reduction of visibility from 92% theoretical limit is due to the photon-number impurity [11].

3 DISCUSSION AND OUTLOOK

The $\mathbb{C}_{\mathrm{PIM}}$ for waveguides and microresonators are plotted in Fig. 3 as a function of mean photon-number per pulse ($\bar{n}$). Our HSPSs are on the lower values of $\bar{n}$ emphasising their probabilistic nature. A near ideal single-photon source achieved by lossless active multiplexing (or demultiplexing) will be on the top-rightmost side of this graph. From our observation, the microresonators are more suitable candidates as HSPSs in silicon photonics. These results promises near term integration of 10+ photon experiments in SOI photonics even without multiplexed sources.

We have also observed that the integration of photonics components increases the ease of performing PIM which will be desirable for a larger photonic chip with an array of HSPSs. These PIM measurements give an understanding of the performances of HSPSs on the scalability of silicon HSPSs as it shows the basic interaction between two single-photons (i.e. two qubits). This is our first attempt to quantify the performance of HSPSs for photonic quantum information processing. It can be further improved in future by having a more complete theoretical basis from where $\mathbb{C}_{\mathrm{PIM}}$ naturally emerges.

REFERENCES

[1] E. Knill, R.Laflamme and G.J.Milburn, “A scheme for efficient quantum computation with linear optics,” Nature 409, pages 46-52 (2001).

[2] Robert Raussendorf and Hans J. Briegel, “A One-Way Quantum Computer, ”Phys.Rev. Lett. 86, 5188 (2001).

[3] Jeremy L. O’Brien, “Optical Quantum Computing,” Science 318(5856), pages 1567- 1570 (2007).

[4] Terry Rudolph, “Why I am optimistic about the silicon-photonic route to quantum computing,” APL Photonics 2, 030901 (2017).

[5] P. P. Rohde, W. Mauerer, and C. Silberhorn, “Spectral structure and decompositions of optical states, and their applications,” New Journal of Physics, 9, p. 91 (2007).

[6] C. K. Hong, Z. Y. Ou, and L. Mandel, “Measurement of subpicosecond time intervals between two photons by interference,” Phys. Rev. Lett. 59, 2044 (1987).

[7] J. G. Rarity, P. R. Tapster, E. Jakeman, T. Larchuk, R. A. Campos, M. C. Teich, and B. E. A. Saleh, “Two-photon interference in a Mach-Zehnder interferometer,” Phys. Rev. Lett. 65, 1348 (1990).

[8] Chen Sun et al., “Single-chip microprocessor that communicates directly using light,” Nature 528, pages 534-538 (2015).

[9] Guoliang Li et al., “Ultralow-loss, high-density SOI optical waveguide routing for macrochip interconnects,” Optics Express 20(11), pages 12035-12039 (2012).

[10] Stefan Abel et al., “Large Pockels effect in micro- and nanostructured barium titanate integrated on silicon,” Nature Materials, 1476-4660 (2018).

[11] I. I. Faruque, G. F. Sinclair, D. Bonneau, J. G. Rarity, M. G. Thompson. “On-chip quantum interference with heralded photons from two independent micro-ring resonator sources in silicon photonics,” Optics Express 26(16), pages 20379-20395 (2018).

InP Membrane on Silicon (IMOS) Photonics

(Invited paper)

Jos van der Tol[1], Yuqing Jiao[1], Jorn van Engelen[1], Vadim Pogoretskiy[1], Amir Kashi[1], Kevin Williams[1]
[1]Photonic Integration Group, Eindhoven University of Technology, 5600 MB Eindhoven, the Netherlands
e-mail: J.J.G.M.v.d.Tol@tue.nl

ABSTRACT
InP membranes have appeared in the last decade as a viable integrated photonics platform, suitable for adding photonic functions to silicon electronics. It combines the strengths of silicon photonics (high index contrasts and therefore small footprint devices) with those of generic InP-platforms (monolithic integration of active and passive devices). A range of functionalities has been developed on this platform, which goes by the name of IMOS (Indium phosphide Membrane on Silicon). Competitive performances have been demonstrated for lasers, fast detectors, waveguides, filters, couplers, modulators etc. The present contribution describes the recent developments in this platform regarding the technology and results. Among the latest results are record low propagation losses, improved input/output grating couplers, a variety of laser structures and improved wavelength demuliplexers These developments demonstrate that IMOS has a high potential to deliver photonic integrated circuits to a wide variety of application fields, e.g. telecom, datacom, sensing, terahertz and many others.

Keywords: Photonic integration, Indium Phosphide, Membranes, Lasers, Waveguides.

1. INTRODUCTION

Higher integration densities in silicon electronics lead to an impeding communications bottleneck [1]. Optical interconnects are therefore proposed, to be combined with electronic chips. This has given rise to SOI (Silicon-On-Insulator) photonics. However, within SOI-platforms light sources are not available, hence solutions based on heterogeneously integration with III-V semiconductor are developed [2]. However, it is possible to create a III-V photonic layer separate from the silicon, as a thin membrane on top of the CMOS-chip [3]. This technique, InP-Membrane On Silicon (IMOS), avoids the need for photonic waveguides in the silicon. It provides a full set of photonic functions and is implemented with a flexible bonding technique that provides thermal isolation. IMOS allows small footprint and low power consuming devices. The technique does not interfere with standard processing of electronic circuits. Here we will present the recent developments of IMOS.

2. IMOS CONCEPT

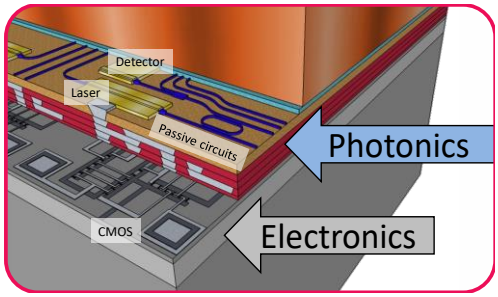


Fig. 1. Artists' impression of the InP membrane platform, with high-confinement active and passive photonic components in the InP membrane circuit, and in close connection with CMOS electronics [3].

The basic idea of the IMOS platform is depicted in Figure 1. Using post-processing techniques a thin membrane of InP is bonded with a polymer (BCB in our case) to a CMOS wafer. The membrane photonic layer contains both active (lasers, detectors, modulators) and passive (waveguides, filters, couplers, demultiplexers) devices. Only electrical contacts are needed between the electronic and photonic layers, which substantially reduces alignment requirements as compared to optical couplings. The technology developed to realize these membrane circuits is described in [4,5]. Using optimized E-beam lithography and plasma etching, processing of both sides of the membrane and careful bonding to silicon carrier wafers, high quality waveguides and a range of well-performing photonic devices are demonstrated. Here we will present mostly our latest results on active and passive devices.

3. EARLIER RESULTS

Table I reports on a number of the devices that have been realized before in the IMOS-platform. They showed several record performances for InP-based membrane photonics [3]. General characteristics are the small footprints, as a consequence of the high index contrast in the membrane, large electrical bandwidth and reproducibility in the realizations, demonstrating the high quality of the developed technology.

Table I: Realized IMOS devices [3]

Device	Dimensions	Main performance parameters	Remarks
UTC-Photodiode	10×3 μm^2	0.7 A/W responsivity >67 GHz bandwidth	3 dB bandwidth extrapolated to 110 GHz
90° bend	0.96 μm radius	0.13 dB/90°	Low loss and reflection
Arrayed Waveguide Grating	0.2 mm^2	10 dB loss	10 dB crosstalk
Planar Concave grating	400x600 μm^2	4 dB loss	25 dB crosstalk Thermal tuning over 3.7 nm
Polarization converter	5 μm long	<1 dB loss	Conversion 99%
Ring resonator	7 μm radius		Q-factor 15500
1x2 MMI coupler	2×3 μm	0.6 dB loss	

4. NEW DEVELOPMENTS

IMOS technology has improved to allow a wider range of devices, and better performance parameters. On top of that also the yield of the processing is improved, especially by introducing state-of the art techniques for BCB-bonding of the membranes. Here we will highlight some of the latest achievements.

4.1 Wafer scanner technology

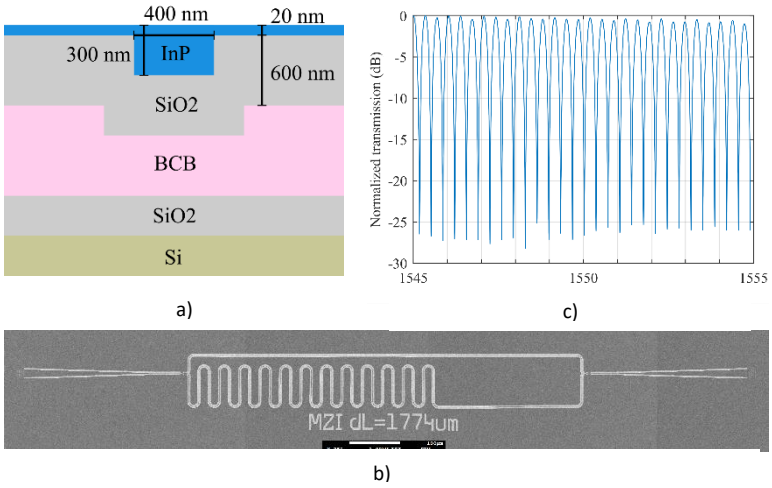


Fig. 2. Results from wafer scanner lithography. a) Cross-section of IMOS waveguide, b) MZI-structure for loss measurement, c) spectral response of the MZI.

The propagation loss of high contrast waveguide devices is critically dependent on the lithography, because of the high modal overlap with the sidewall roughness. Using special E-beam resists [4] low losses were obtained. Now we have realized devices with even better performances, using an ASML PAS5500/1100B scanner lithography tool. Figure 2a shows the cross-section of an IMOS waveguide. The propagation loss was measured with an MZ-interferometer (fig. 2b), by analyzing its spectral response (Fig. 2c). Record low values for InP-membrane waveguides of 1 dB/cm were found, suggesting a much reduced roughness.

4.2 Arrayed Waveguide Grating

Wavelength demultiplexers using the AWG-principle are challenging for membrane platforms. This is because the phase noise in the high contrast waveguides of the array can be large due to sidewall roughness. Also, a phase error can occur due to poor definition of the array arms. Using the wafer scanner lithography it is however possible to reduce the roughness and improve feature size control, resulting in better performance. Figure 3 (Left) shows a realized AWG with this technique, while figure 3 (Right) gives the measured spectral response. Losses of 3.5 dB and crosstalk levels of better than 20 dB are obtained; much improved w.r.t. the device reported in Table 1.

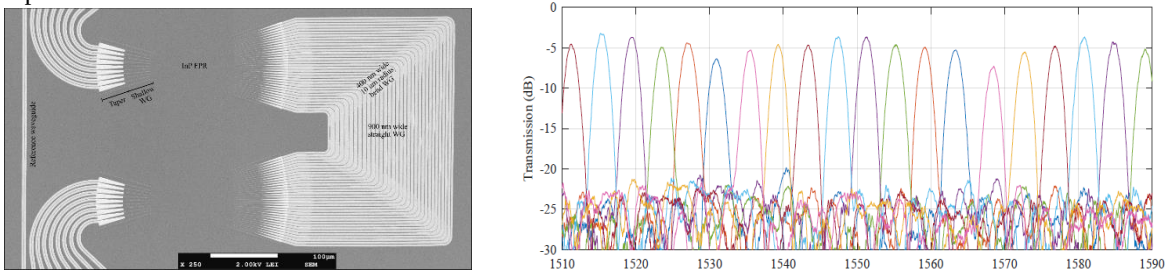


Fig. 3. Left: The AWG realized with wafer scanner. Right t: spectral response of the AWG.

4.4 Grating coupler

It is convenient to use grating couplers for optical interfacing of membrane waveguides with optical fibres. They can be flexibly placed in the circuits, allowing optimal use of space. However, there is a loss penalty associated with this. By using an apodized focusing grating coupler with metal back-reflector the transmission losses were reduced to less than 1.5 dB. Figure 4 depicts the realized grating coupler and the measured transmission spectra.

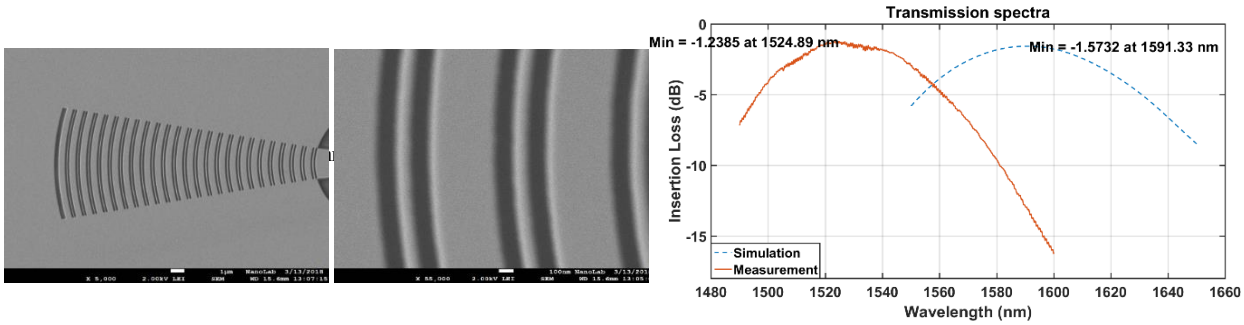


Fig. 4. Grating coupler using apodization, sub-wavelength structuring and a metal back reflector. Left: transmission spectra.

4.5 Lasers

Based on processing both sides of the membrane a SOA structure was developed, using a twin-guide approach. This SOA was used in various laser structures, which are given in Table 2.

Table.2. Recently demonstrated lasers on IMOS

	Circuit configuration	Threshold current density	Output power in waveguide	Side mode suppression ratio (SMSR)	Tunability
DBR laser	500 µm long amplifier + PhC reflectors	2 kA/cm^2	1 mW	30 dB	/
DFB laser	1 mm long cavity with quarter-λ shifted DFB grating	2.5 kA/cm^2	10 mW	60 dB	/
Tunable laser	500 µm long amplifier + micro-ring Vernier filters	2.4 kA/cm^2	0.44 mW	45 dB highest; > 30 dB over tuning range	25 nm

The DFB laser is depicted in figure 5, together with a measured spectrum, that shows a high SMSR.

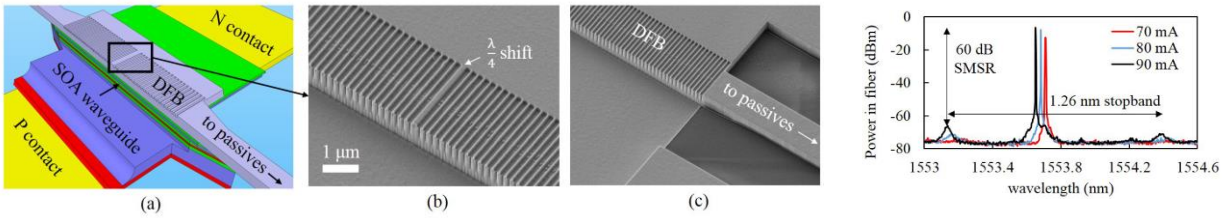


Fig. 5. DFB-laser. From left to right: schematic, DFB-grating, output connection, spectrum.

5. CONCLUSIONS

The latest developments of IMOS, a membrane based photonic integration platform are presented. Waveguide loss as low as 1 dB/cm is obtained as well as improved performance on demultiplexers and grating couplers. Furthermore the integration of SOAs into various laser cavities is shown, with good results.

8. References

[1] L.Carloni, et al, “Networks-on-chip in emerging interconnect paradigms”, Proc. 2009 NOCS, San Diego (CA), May 10 - 13, 2009.
[2] G. Roelkens et al., “III-V-on-silicon photonic devices for optical communication and sensing”, Photonics 2015, 2(3), 969-1004.
[3] J. J. G. M. v. d. Tol, et al., "Indium Phosphide Integrated Photonics in Membranes," *IEEE JSTQE*, vol. 24, p. 6100809, 2018.
[4] Y. Jiao et al., "Fullerene-assisted electron-beam lithography for pattern improvement and loss reduction in InP membrane waveguide devices," Optics Letters, vol. 39, pp. 1645-1648, 2014.
[5] Y. Jiao, et al., "Vertical and Smooth Single-Step RIE Process for InP Membrane Waveguides," J. Electroch..Soc., vol. 162, p. E90, 2015.

Fundamental and Subharmonic Hybrid Mode Locking of Semi-assembled Semiconductor Ring Laser in InP Generic Foundry

Mu-Chieh Lo*, Robinson Guzmán*, Jessica Cesar, Muhsin Ali, Alberto Zarzuelo, Guillermo Carpintero
Department of Electronic Technology, Universidad Carlos III de Madrid, 28911 Leganés, Spain
e-mail: mlo@ing.uc3m.es, guiller@ing.uc3m.es

ABSTRACT

We report on 12.5-GHz microwave generation via passive, fundamental and subharmonic hybrid mode-locking of a foundry-fabricated ring laser IC on a RF-compatible submount. The 200-kHz RF linewidth for PML is greatly reduced to Hz-level for HML, and 25-dB single-sideband phase-noise suppression for 15-dBm RF injection power is achieved. In subharmonic HML, the compromise between supermode intensity and phase noise is analyzed.

Keywords: photonic integrated circuits, mode-locked lasers, microwave photonics

Electrically driven monolithically integrated semiconductor passively mode-locked lasers (PMLL) offer a simple, compact, cost-effective and power-efficient solution to high-purity microwave generation. Phase noise and timing jitter of generated signal can further be improved by using hybrid mode-locking (HML) technique, where an electrical modulation is injected into saturable absorber of the PMLL at the resonant frequency that the PMLL is locked at. Although direct modulation at the fundamental frequency corresponding to the cavity round-trip rate is the most straightforward approach, the maximum frequency is limited to around 40 GHz due to the bandwidth of driving electronics [1,2]. However, >40-GHz bands have recently attracted attention as millimeter wave (mmW, 30 – 300 GHz) and terahertz (THz, >300 GHz) signals are promising for the next generation high-speed transmissions to deliver Gb/s data rate [3]. For this purpose, to generate stable and higher repetition-rate signal using lower frequency driving electronics is highly desirable. In this paper, we present a proof-of-concept implementation of fundamental and subharmonic HML of a foundry-fabricated semiconductor laser at 12.5 GHz. The InP photonic integrated circuit (PIC) chip is assembled with a specifically designed RF submount to support GSG (Ground-Signal-Ground) high frequency electrical feed. The signal purity and locking characteristics in terms of linewidth and single-sideband (SSB) phase noise are experimentally investigated.

The ring-geometry semiconductor laser used for fundamental and subharmonic HML is shown in Fig. 1. The ring cavity is 6.5-mm long corresponding to a repetition rate of 12.5 GHz. The cavity is composed of one 30- µm saturable absorber (SA) surrounded by two 400-µm gain sections (SOA, semiconductor optical amplifier) and 4-mm electro-optic phase modulator (EOPM) in four sections and passive waveguides/components. One 3-dB 2x2 MMI coupler guides the optical signals out of the ring cavity. The upper MLL is characterized by forward biasing the two SOA sections with a gain current (I_{SOA}) and biasing the SA with a hybrid RF-DC reverse voltage via a bias-tee (V_{SA}), as shown in Fig. 2. The signal from the waveguide output (Out) is collected with a lensed fiber and sent to electrical spectrum analyzer after a high-speed photodiode.

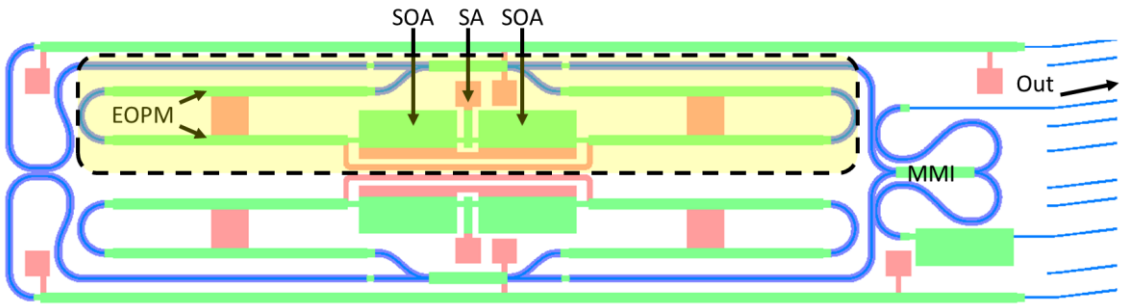


Figure 1. Schematic layout of the proposed PIC. Red: metallization layer. Green: active components (SOA and EOPM) and passive components (MMI coupler). Blue: deeply and shallowly etched waveguides.

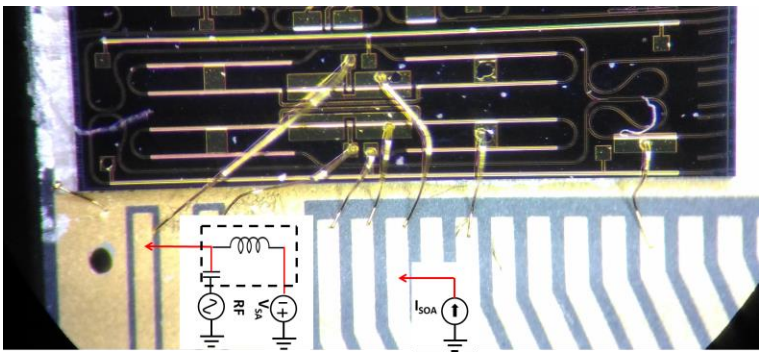


Figure 2. Microscope photograph of the semi-assembled PIC and the specifically designed RF submount. The InP chip is wire-bonded and physically placed onto the RF submount. One RF GSG probe and one DC probe are used to bias the SA and SOAs, respectively.

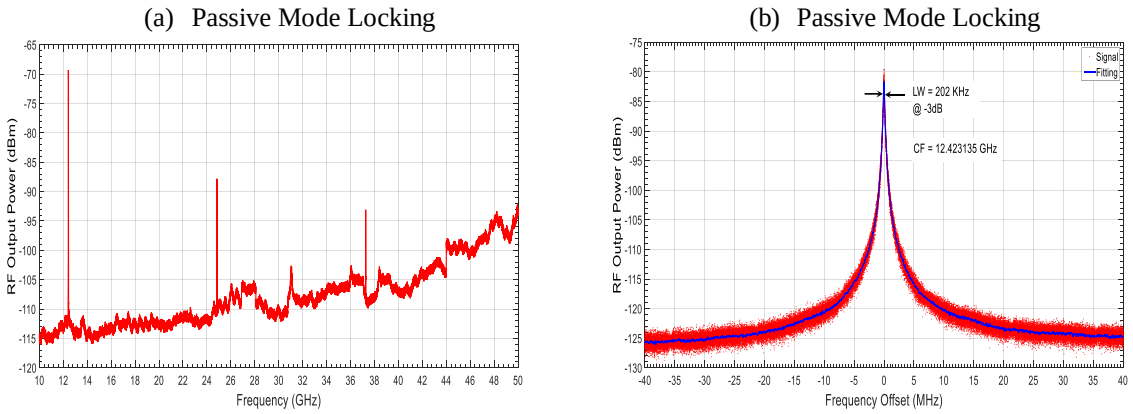


Figure 3. (a) Full-span (50 GHz), and (b) Close-up view of the RF spectrum of the MLL in PML. (I_{SOA} = 94 mA, V_{SA} = 2.35 V). Center Frequency (CF) = 12.423 GHz. 3-dB linewidth (LW) = 202 kHz.

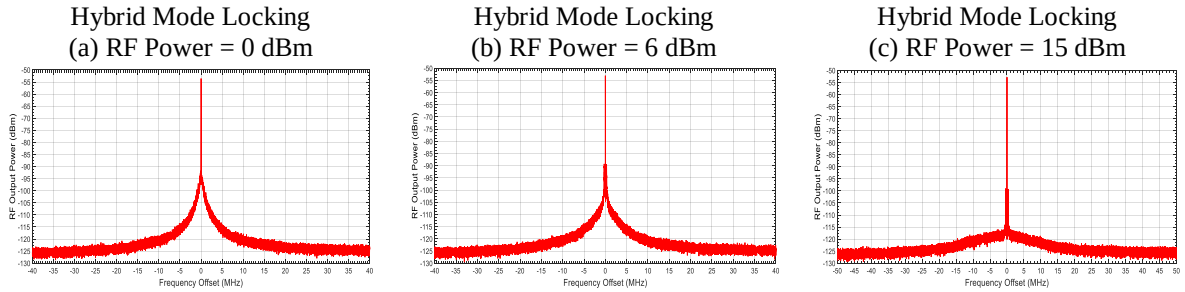


Figure 4. Close-up view of the RF spectrum of the MLL in fundamental HML. (I_{SOA} = 94 mA, V_{SA} = 2.35 V, RF Frequency = 12.423 GHz) for (a) RF Power = 0 dBm, (b) RF Power = 6 dBm, (c) RF Power = 15 dBm.

The down-converted RF spectrum of the MLL in PML for I_{SOA} = 94 mA and V_{SA} = 2.35 V is depicted in Fig. 3. In Fig. 3(a), three harmonic components are present at 12.5, 25, and 37.5 GHz. With a Lorentzian function, the 3-dB linewidth is estimated to be 202 kHz and the center frequency is found at 12.423 GHz in Fig. 3(b). The beat-note frequency is slightly tuneable by varying the bias condition and phase modulator voltage. In the close-up spectra shown in Fig. 4 the base and floor are reduced for higher RF injection power and subsequently a greater suppression ratio is achieved.

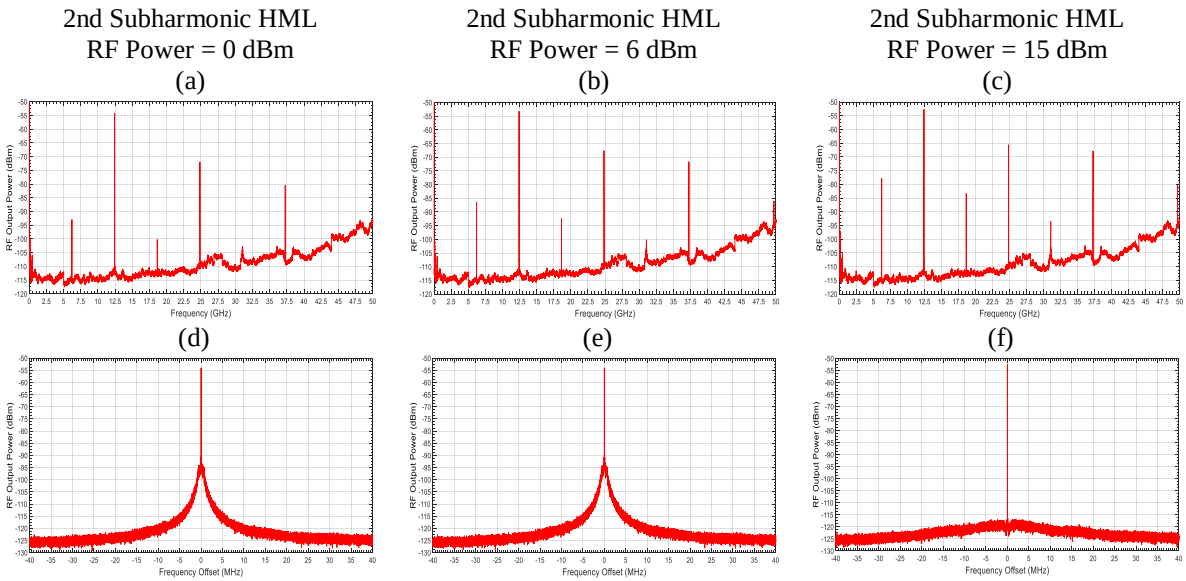


Figure 5. Full-span and Close-up view of the RF spectrum of the MLL in 2nd subharmonic HML. (I_{SOA} = 94 mA, V_{SA} = 2.35 V, RF Frequency = 6.212 GHz) for (a),(d) RF Power = 0 dBm, (b),(e) RF Power = 6 dBm, (c),(f) RF Power = 15 dBm.

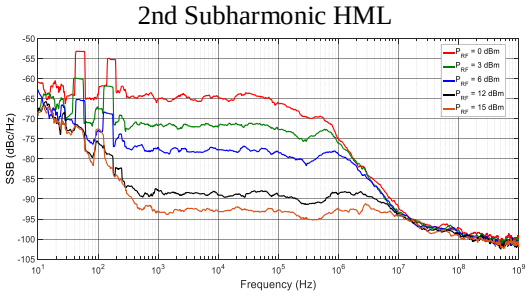


Figure 6. (a) SSB phase noise of the MLL in fundamental HML. (I_{SOA} = 94 mA, V_{SA} = 2.35 V, RF Frequency = 12.423 GHz) for RF Power = 0, 3, 6, 12, and 15 dBm. (b) SSB phase noise of the MLL in 2nd subharmonic HML. (I_{SOA} = 94 mA, V_{SA} = 2.35 V, RF Frequency = 6.212 GHz) for RF Power = 0, 3, 6, 12, and 15 dBm.

Figure 5 shows a series of full-span RF spectra and close-up RF spectra in second subharmonic HML for RF power = 0, 6, and 15 dBm, RF frequency = 6.212 GHz. The supermodes at odd multiple of the RF modulation frequency (6.212 GHz, 18.626 GHz, and 31.060 GHz) grow for higher RF injection power. The associated supermode noise resonances may negatively affect the phase noise at the sidebands of the RF resonance peak giving rise to timing jitter. Similarly, a greater signal-to-noise ratio is obtained for greater RF power. There is a trade-off between supermode intensity and RF signal-to-noise ratio. Figure 6 shows the evolution of single side-band (SSB) phase noise for a range of different RF power in fundamental HML. For RF power = 15 dBm, the SSB phase noise is significantly reduced by 25 dB within 10^3 – 10^5 Hz and not affected when the offset frequency is larger than 10^7 Hz. In conclusion, we have demonstrated the passive, fundamental and subharmonic hybrid mode locking of InP foundry-fabricated semiconductor ring laser on RF submount that supports high frequency electrical driving. The RF spectrum, beat-note linewidth, phase noise as well as supermode are analysed. The approach can be deployed for stabilized mmW generation using cost-effective photonic and affordable electronic devices.

ACKNOWLEDGEMENTS

EU H2020 Marie Skłodowska-Curie grant agreement No. 642355 FiWiN5G. Spanish Ministerio de Economia y Competitividad through Programa Estatal de Investigacin, Desarrollo e Inovacin Orientada a los Retos de la Sociedad (grant iTWIT, TEC2016-76997-C3-3-R).

REFERENCES

[1] T. Hoshida, Hai-Feng Liu, M. Tsuchiya, Y. Ogawa and T. Kamiya, "Subharmonic hybrid mode-locking of a monolithic semiconductor laser," IEEE Journal of Selected Topics in Quantum Electronics, vol. 2, no. 3, pp. 514-522, Sept. 1996.

[2] Sylwester Latkowski, Valentina Moskalenko, Saeed Tahvili, Luc Augustin, Meint Smit, Kevin Williams, and Erwin Bente, "Monolithically integrated 2.5 GHz extended cavity mode-locked ring laser with intracavity phase modulators," Opt. Lett. 40, 77-80, 2015.

[3] T. Nagatsuma et al., "Millimeter-Wave and Terahertz-Wave Applications Enabled by Photonics," IEEE Journal of Quantum Electronics, vol. 52, no. 1, pp. 1-12, Art no. 0600912, Jan. 2016.

Direct bandgap hexagonal SiGe: A light emitter for Si-photonics?

J.E.M. Haverkort[1], A. Dijkstra[1], E. Fadaly[1], Y. Ren[1], G. Reithmaier[2], D. Busse[2], J. Suckert[3], J. Furthmueller[3], M.A. Verheijen[1], S. Botti[3], J.J. Finley[2], E.P.A.M. Bakkers[1]

[1]Eindhoven University of Technology, 5600 MB, Eindhoven, The Netherlands
[2]Walter Schottky Institut, Technische Universität München, 85748 Garching, Germany
[3]Friedrich-Schiller University of Jena, 07743 Jena, Germany
e-mail: J.E.M.Haverkort@tue.nl

ABSTRACT
Hexagonal crystal phase $Si_{1-x}Ge_x$ is a direct bandgap semiconductor for x>70%. We observe tunable light emission from 1.9 up to 3.5 µm at 4K as well as amplified spontaneous emission for Hex-Ge. Applications for Si-photonics will be discussed.

Keywords: SiGe light source, direct bandgap, Silicon photonics, hexagonal crystal structure.

1. INTRODUCTION

It is a major drawback of Silicon Photonics that it is currently lacking a lightsource which can be monolithically integrated. The main problem is that group IV semiconductors like Si and Ge naturally crystallize within a cubic lattice and feature an indirect bandgap. Both Si and SiGe can however be forced to grow in the hexagonal crystal structure as has been shown by IMEC in a conventional CMOS process[1] as well as by crystal phase transfer by using a wurtzite III-V nanowire core to force the $Si_{1-x}Ge_x$ shell into the hexagonal crystal phase[2,3].

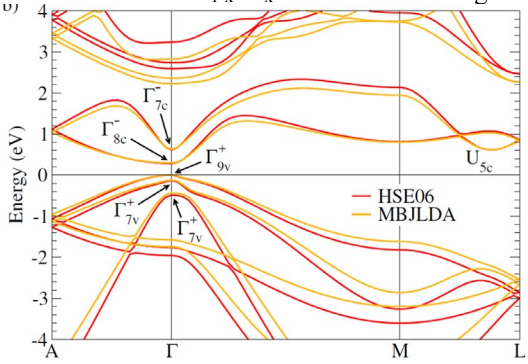


Fig. 1: Bandstructure of hexagonal Ge calculated by ab initio density-functional theory[4].

This contribution is intended to be an update of the H2020 SiLAS project which is aiming towards a hexagonal $Si_{1-x}Ge_x$ nanolaser. Within the project, evidence is currently accumulating that hexagonal $Si_{1-x}Ge_x$ is a direct bandgap semiconductor (see Fig. 1) which is capable to efficiently emit light in the wavelength region between 1.9 and 3.5µm at 4K. Slightly shorter wavelengths might be possible when we would be able to more closely approach the direct-to-indirect transition by increasing the crystal perfection.

2. WAVELENGHT TUNABILITY

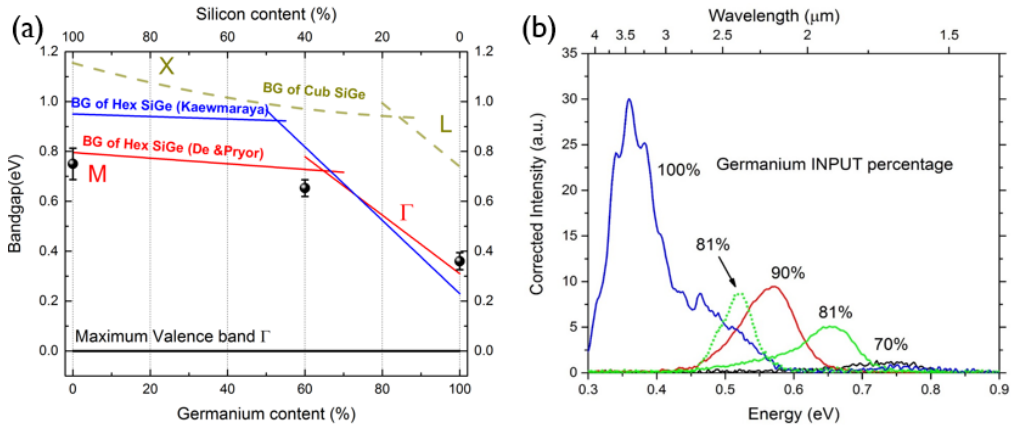


Fig. 2: (a) Linear interpolation of the band edges in Hex-SiGe based on references 7 and 8, together with our preliminary experimental data showing that Hex-SiGe becomes a direct semiconductor above 60-70% Ge. (b) Photoluminescence spectra of Hex-SiGe versus the input percentage of Ge during growth.

Both hexagonal Si and Hexagonal Ge have been predicted[4,5] to have a minimum in the conduction band at the Γ-point. However, Hex-Si is still indirect, while Hex-Ge has been predicted[4,6-8] to be a direct semiconductor (Fig. 1). By using a linear interpolation[7,8] (Fig. 2a) based on Vegard's law, which works well for SiGe alloys[6], it is suggested that Hex-SiGe becomes a direct semiconductor for Ge-compositions above 60-70%.

At the conference, we will present strongly improved data showing photoluminescence spectra which precisely coincide with *ab initio* density-functional theory as calculated by the Jena group. Preliminary photoluminescence data are presented in Fig 2b showing bandgap tunability between 1.9 and 3.5 µm. We observe that the emission intensity strongly decreases near the direct-to-indirect transition around a Ge-composition of 70% which is an experimental indication for the direct bandgap of Hex- $Si_{1-x}Ge_x$ for x>70%.

3. EVIDENCE FOR DIRECT BANDGAP EMISSION.

We present excitation power dependent photoluminescence at 4K in Fig. 3. The spectra show a single peak which is probably a consequence of high As-doping as evidenced by atom probe tomography measurements (not shown). The As-doping is due to As evaporation from the GaAs substrate as well as from the walls of the MOVPE during growth while growing hexagonal GaAs/SiGe core/shell nanowires. The spectra show a clear broadening towards higher energy at high excitation density. This phenomenon is attributed to bandfilling due to the Burnstein-Moss effect. The observation of bandfilling is a strong indication that we are observing band-to-band emission.

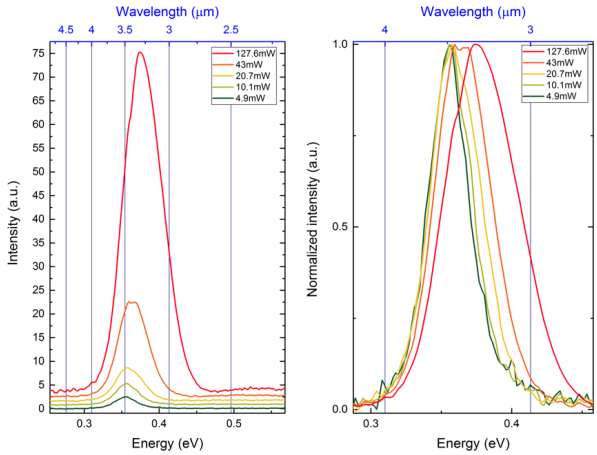


Fig. 3: Excitation dependence of the photoluminescence at 4K of hexagonal Ge shells grown around a wurtzite GaAs nanowire core showing the bandfilling behavior.

Another important observation is that we observe relatively strong room temperature emission. The ratio of the emission intensity at 4K and 300K is less than a factor 50 without apply any kind of intentional surface passivation.

4. OBSERVATION OF STIMULATED EMISSION.

Subsequently, measurements were performed at the Walter Schottky Institute on single Hex-Ge nanowire at high excitation density. The majority of the nanowires (NW0, green) show weak photoluminescence with a sub-linear power-dependence with an exponent of 0.83. Few nanowires (NW1, red) exhibit a much larger signal and show a strong super-linearity with an exponent of 8.17, which is interpreted as being light amplification via stimulated emission. A single nanowire (NW2, blue) exhibits a very strong PL signal with a slightly super-linear power dependence of 2.39 that decreases to an almost linear regime with a slope of 1.35 at ~0.1kW/cm^2. We tentatively interpret the transition to the linear regime as being due to optical feedback from the nanowire end-facets. This interpretation is further supported by Michelson interference measurements at 7K showing a 124 fs coherence time in NW2 as compared to a 27fs coherence time in NW0, indicating amplified spontaneous emission in NW2.

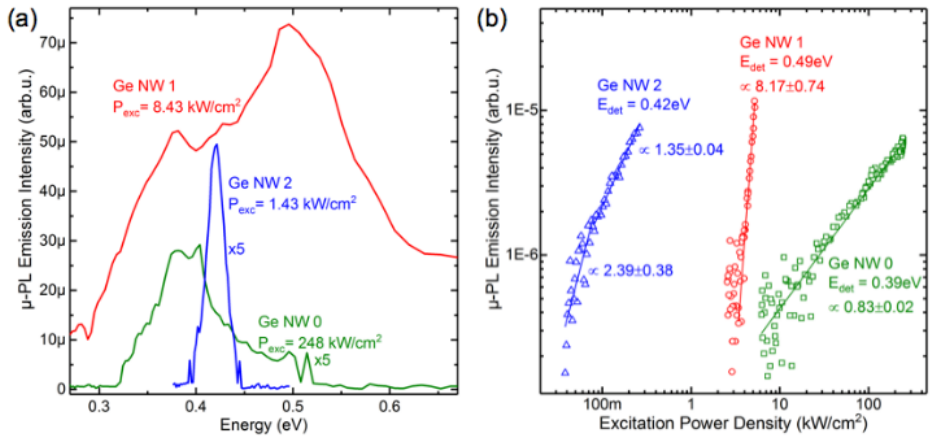


Fig. 4: : *(a) Typical micro-photoluminescence (PL) spectrum of a disordered nanowire (NW0), a wire with very few dislocation (NW1) and a wire of high crystal quality (NW2). (b) Excitation power dependence for Hex-SiGe nanowire shells with three different morphology classes.*

ACKNOWLEDGEMENTS

This work is part of the FET-OPEN SiLAS project which has received funding from the European Union's Horizon 2020 research and innovation programme under grant agreement No 735008.

REFERENCES

1. Y. Qiu, H. Bender, O. Richard, M.-S. Kim, E. Van Besien, I. Vos, M. de Potter de ten Broeck, D. Mocuta & W. Vandervorst, Epitaxial diamond-hexagonal silicon nano-ribbon growth on (001) silicon, Scientific Reports 5,12692 (2015)
2. H.I.T. Hauge, M.A. Verheijen, S. Conesa-Boj, T. Etzelstorfer, M. Watzinger, D. Kriegner, I. Zardo, C. Fasolato, F. Capitani, P. Postorino, S. Kölling, A. Li, S. Assali, J. Stangl, and E.P.A.M. Bakkers . Hexagonal Silicon Realized, Nano Lett. 15, 5855 (2015)
3. H.I.T. Hauge, S. Conesa-Boj, M.A. Verheijen, S. Koelling, and E.P. A. M. Bakkers, Single-Crystalline Hexagonal Silicon−Germanium, Nano Lett. 17, 85-90 (2017)
4. Claudia Rödl, Jürgen Furthmüller, Jens Renè Suckert, Valerio Armuzza, Friedhelm Bechstedt, Silvana Botti, Accurate electronic and optical properties of hexagonal germanium for optoelectronic applications, https://arxiv.org/abs/1812.01865v1
5. C. Rödl, T. Sander, F. Bechstedt, J. Vidal, P. Olsson, S. Laribi, and J.-F. Guillemoles, Wurtzite silicon as a potential absorber in photovoltaics: Tailoring the optical absorption by applying strain, Phys. Rev. B 92, 045207 (2015)
6. X. Cartoixa, M. Palummo, H.I.T. Hauge, E.P.A.M. Bakkers, and R. Rurali, Optical emission in hexagonal SiGe nanowires, Nano Lett. 17, 4753 (2017)
7. De and C.E. Pryor, Electronic structure and optical properties of Si, Ge and diamond in the lonsdaleite phase, J. Phys.: Condens. Matter 26 045801 (2014)
8. T. Kaewmaraya, L. Vincent and M. Amato, Accurate Estimation of Band Offsets in Group IV Polytype Junctions: A First-Principles Study, J. Phys. Chem. C 2017, 121, 5820−5828

Brillouin based lasers, nonreciprocity, and cooling in silicon

(Invited paper)

Peter T. Rakich[1], Eric Kittlaus[1], Nils Otterstrom[1], Ryan Behunin[2], Shai Gertler[1], Prashanta Kharel[1]
[1]*Department of Applied Physics, Yale University, New Haven CT, USA*
[2]*Dept. of Physics and Astronomy, Northern Arizona University, Flagstaff AZ, USA*
e-mail: peter.rakich@yale.edu

ABSTRACT

We use a new class of optomechanical waveguides–that produce enhanced light-sound coupling–to realize strong and tailorable stimulated Brillouin scattering interactions silicon photonics. Exploiting these interactions in a variety of different structures, we create high-gain Brillouin amplifiers and integrated Brillouin lasers within a silicon-on-insulator platform. Using a Brillouin active multimode waveguide to realize efficient inter-band coupling, we also demonstrate a tunable and wideband (>100GHz) nonreciprocal light propagation as the basis for multiport circulator technologies. Leveraging similar concepts in a resonant geometry, we describe a high gain unidirectional amplifier that yields ∼30dB of optical isolation. Finally, we demonstrate laser cooling of Brillouin-active phonon modes within guided-wave systems as a means of controlling noise within a broad class of Brillouin technologies.

Keywords: silicon photonics, Brillouin, waveguide, nonlinear optics

1 INTRODUCTION

Both Kerr and Raman nonlinearities are greatly enhanced by tight optical-mode confinement in nanoscale silicon waveguides[1], [2]. Counterintuitively, Brillouin nonlinearities—which arise from the coupling between photons and acoustic phonons—are exceedingly weak within these highly nonlinear silicon waveguides. This occurs because material response and poor acoustic confinement within conventional silicon on insulator (SOI) waveguides effectively stifle Brillouin nonlinearities [3]. However, new optomechanical waveguides—that control both light and sound—have recently transformed Brillouin interactions into the strongest and most tailorable nonlinearities in silicon [4], [5], [6], [7], [8].

In this paper, we explore the new device physics that enables dramatic enhancement of Brillouin nonlinearities, and we demonstrate a range of highly engineerable new stimulated Brillouin interactions in silicon waveguides by controlling both light and sound. In particular, we describe recent advancements that have yielded high performance Brillouin amplification [6], [7], [8], Brillouin laser oscillators [9], nonreciprocal light propagation [10], and phonon mode cooling techniques in silicon-based Brillouin photonics[11]. We also explore future directions and new scientific and technological opportunities offered by silicon-based Brillouin photonics.

2 MAIN TEXT

New waveguide geometries are necessary to produce efficient Brillouin interactions using in silicon photonics. It is perhaps counterintuitive that the same nanoscale silicon-on-insulator waveguides—that greatly enhance Kerr and Raman nonlinearities—effectively stifle the production of Brillouin nonlinearities. This is because the unusual acousto-optic properties of silicon cause light- and sound-fields to couple two transverse elastic wave motion, and the conditions for confinement of sound becomes increasingly stringent at sub-wavelength scales [3]. This problem is compounded by the fact that the sound velocity in silicon core exceeds that of the silica cladding, meaning that an SOI waveguide does not produce total internal reflection for sound [12]. Consequently, generated sound-fields typically radiate into the substrate of such waveguides [3]. This problem has been addressed using new suspended waveguide geometries that use either an air cladding [4], [5], [6], [7], [8] or phononic crystal cladding [13] to reduce or eliminate the leakage of sound waves into the substrate.

As a result of silicon's unusual acousto-optic properties, these Brillouin-active waveguides produce coupling between co-propagating optical waves through process termed forward stimulated Brillouin scattering (forward-SBS). Because these Brillouin-active silicon waveguides yield distinct dynamics from prior guided-wave systems–which almost exclusively couple counter-propagating optical waves via backwards stimulated Brillouin scattering (backward-SBS)[14]–conventional strategies for Brillouin based signal processing are not always directly applicable using Brillouin processes in silicon. On the other hand, the unique dynamics supported by forward-SBS open door to wideband schemes for nonreciprocal light propagation [10], new laser designs [9], and microwave-photonic signal processing schemes [13], [15] that offer an array of advantages relative to conventional backward-SBS interactions.

Forward-SBS scattering can occur through both intra-modal (intra-band) and inter-modal (inter-band) scattering processes; these two processes good are you know what happened in which have been shown to yield very different dynamics [16], [17], [18]. The first demonstrations of stimulated Brillouin scattering in silicon were made through use of inter-band forward stimulated Brillouin scattering processes within suspended waveguide structures [13]. Subsequent experimental studies improved these results to yield larger nonlinear coefficients [5] and also produce modest ($\sim$0.5dB) net amplification [6] by using different structures that more tightly confined the phonons while also reducing optical losses. However, the dimensional sensitivities within these smaller waveguide systems were shown to produce both inhomogeneous broadening [19] and excessive nonlinear absorption [20], complicating the prospect for appreciable net amplification. Robust net amplification (5dB) was subsequently demonstrated using membrane-suspended silicon waveguides having a larger mode area, low (0.15 dB/cm) propagation losses, and higher power handling[7]. Thanks to the low losses, and strong Brillouin nonlinearities provided by the system, it was able to produce net amplification for modest (5 mW) pump powers.

Building on these concepts, we present a new type of multi-mode optomechanical waveguide that produces phonon mediated coupling between optical modes with distinct spatial profiles [8]. This process, termed stimulated inter-modal (inter-band) scattering, produces unusual new nonlinear dynamics in the multimode nature of this interaction lends itself to new strategies to control Brillouin interactions [18]. For example, we use stimulated intermodal scattering to create a new type of silicon Brillouin laser described in Ref. [9]. This system first of a kind silicon Brillouin laser formed by fashioning a Brillouin active silicon waveguide into a race-track resonator that supports low loss guidance of two distinct spatial optical modes. By injecting an optical pump wave into the antisymmetric waveguide resonator mode, we are able to produce Brillouin amplification for the symmetric waveguide mode. We reach the threshold for laser oscillation at modest (11mW) pump powers. Since this system is monolithically integrated, the stability of the Brillouin laser allows us to systematically examine the internal noise characteristics of the system, which exhibits sub-kHz internal line narrowing in an unusual regime of self-oscillation.

Building on these recent works, we use this versatile form of stimulated inter-band coupling to demonstrate a variety of new interactions. Within resonant geometries, we harness this process to create new Brillouin-based optical amplifiers. Using a new 4-port optomechanical waveguide geometry, we also show that such inter-band scattering processes produce nonreciprocal light propagation that offers a promising path towards isolator and circulator technologies [10]. Finally, we use these Brillouin interactions to demonstrate laser-cooling of a continuum of phonon modes [21]. This wavevector-selective phonon cooling method opens the door to the control of dissipation and noise in Brillouin photonics.

Looking beyond these specific applications and demonstrations in silicon photonics, we explore promising new directions for Brillouin based technologies in an array of integrated waveguide systems including chalcogenide[22], [23], [24] and silica[25], [26], [27], and silicon nitride platforms[28].

ACKNOWLEDGMENT

The authors acknowledge support from the Packard Fellowship for Science and Engineering, the National Science Foundation Graduate Research Fellowship under Grant No. DGE1122492, and Yale University.

REFERENCES

[1] H. Rong, A. Liu, R. Nicolaescu, M. Paniccia, O. Cohen, and D. Hak, "Raman gain and nonlinear optical absorption measurements in a low-loss silicon waveguide," *Applied physics letters*, vol. 85, no. 12, pp. 2196–2198, 2004.

[2] M. A. Foster, A. C. Turner, J. E. Sharping, B. S. Schmidt, M. Lipson, and A. L. Gaeta, "Broad-band optical parametric gain on a silicon photonic chip," *Nature*, vol. 441, no. 7096, p. 960, 2006.

[3] P. T. Rakich, C. Reinke, R. Camacho, P. Davids, and Z. Wang, "Giant enhancement of stimulated brillouin scattering in the subwavelength limit," *Physical Review X*, vol. 2, no. 1, p. 011008, 2012.

[4] H. Shin, W. Qiu, R. Jarecki, J. A. Cox, R. H. Olsson, A. Starbuck, Z. Wang, and P. T. Rakich, "Tailorable stimulated Brillouin scattering in nanoscale silicon waveguides.," *Nature communications*, vol. 4, p. 1944, Jan. 2013.

[5] R. Van Laer, B. Kuyken, D. Van Thourhout, and R. Baets, "Interaction between light and highly confined hypersound in a silicon photonic nanowire," *Nature Photonics*, vol. 9, no. 3, p. 199, 2015.

[6] R. Van Laer, A. Bazin, B. Kuyken, R. Baets, and D. Van Thourhout, "Net on-chip brillouin gain based on suspended silicon nanowires," *New Journal of Physics*, vol. 17, no. 11, p. 115005, 2015.

[7] E. A. Kittlaus, H. Shin, and P. T. Rakich, "Large brillouin amplification in silicon," *Nature Photonics*, vol. 10, no. 7, p. 463, 2016.

[8] E. A. Kittlaus, N. T. Otterstrom, and P. T. Rakich, "On-chip inter-modal brillouin scattering," *Nature Communications*, vol. 8, p. 15819, 2017.

[9] N. T. Otterstrom, R. O. Behunin, E. A. Kittlaus, Z. Wang, and P. T. Rakich, "A silicon brillouin laser," *Science*, vol. 360, no. 6393, pp. 1113–1116, 2018.

[10] E. A. Kittlaus, N. T. Otterstrom, P. Kharel, S. Gertler, and P. T. Rakich, "Non-reciprocal interband brillouin modulation," *Nature Photonics*, vol. 12, no. 10, p. 613, 2018.

[11] N. T. Otterstrom, R. O. Behunin, E. A. Kittlaus, and P. T. Rakich, "Optomechanical cooling in a continuous system," *Physical Review X*, vol. 8, no. 041034, 2018.

[12] C. G. Poulton, R. Pant, and B. J. Eggleton, "Acoustic confinement and stimulated brillouin scattering in integrated optical waveguides," *JOSA B*, vol. 30, no. 10, pp. 2657–2664, 2013.

[13] H. Shin, J. A. Cox, R. Jarecki, A. Starbuck, Z. Wang, and P. T. Rakich, "Control of coherent information via on-chip photonic–phononic emitter–receivers," *Nature communications*, vol. 6, p. 6427, 2015.

[14] G. P. Agrawal, *Nonlinear fiber optics*. Academic press, 2007.

[15] E. A. Kittlaus, P. Kharel, N. T. Otterstrom, Z. Wang, and P. T. Rakich, "Rf-photonic filters via on-chip photonic–phononic emit–receive operations," *Journal of Lightwave Technology*, vol. 36, no. 13, pp. 2803–2809, 2018.

[16] M. Kang, A. Nazarkin, A. Brenn, and P. S. J. Russell, "Tightly trapped acoustic phonons in photonic crystal fibres as highly nonlinear artificial raman oscillators," *Nature Physics*, vol. 5, no. 4, pp. 276–280, 2009.

[17] M. Kang, A. Brenn, and P. S. J. Russell, "All-optical control of gigahertz acoustic resonances by forward stimulated interpolarization scattering in a photonic crystal fiber," *Physical review letters*, vol. 105, no. 15, p. 153901, 2010.

[18] M. Kang, A. Butsch, and P. S. J. Russell, "Reconfigurable light-driven opto-acoustic isolators in photonic crystal fibre," *Nature Photonics*, vol. 5, no. 9, pp. 549–553, 2011.

[19] C. Wolff, R. Van Laer, M. J. Steel, B. J. Eggleton, and C. G. Poulton, "Brillouin resonance broadening due to structural variations in nanoscale waveguides," *New Journal of Physics*, vol. 18, no. 2, p. 025006, 2016.

[20] C. Wolff, P. Gutsche, M. J. Steel, B. J. Eggleton, and C. G. Poulton, "Power limits and a figure of merit for stimulated brillouin scattering in the presence of third and fifth order loss," *Optics express*, vol. 23, no. 20, pp. 26628–26638, 2015.

[21] N. T. Otterstrom, R. O. Behunin, E. A. Kittlaus, and P. T. Rakich, "Optomechanical cooling in a continuous system," *Phys. Rev. X*, vol. 8, p. 041034, 2018.

[22] R. Pant, C. G. Poulton, D.-Y. Choi, H. Mcfarlane, S. Hile, E. Li, L. Thevenaz, B. Luther-Davies, S. J. Madden, and B. J. Eggleton, "On-chip stimulated brillouin scattering," *Optics express*, vol. 19, no. 9, pp. 8285–8290, 2011.

[23] D. Marpaung, B. Morrison, M. Pagani, R. Pant, D.-Y. Choi, B. Luther-Davies, S. J. Madden, and B. J. Eggleton, "Low-power, chip-based stimulated brillouin scattering microwave photonic filter with ultrahigh selectivity," *Optica*, vol. 2, no. 2, pp. 76–83, 2015.

[24] B. Morrison, A. Casas-Bedoya, G. Ren, K. Vu, Y. Liu, A. Zarifi, T. G. Nguyen, D.-Y. Choi, D. Marpaung, S. J. Madden, *et al.*, "Compact brillouin devices through hybrid integration on silicon," *Optica*, vol. 4, no. 8, pp. 847–854, 2017.

[25] J. Li, H. Lee, and K. J. Vahala, "Microwave synthesizer using an on-chip brillouin oscillator," *Nature communications*, vol. 4, p. 2097, 2013.

[26] W. Loh, A. A. Green, F. N. Baynes, D. C. Cole, F. J. Quinlan, H. Lee, K. J. Vahala, S. B. Papp, and S. A. Diddams, "Dual-microcavity narrow-linewidth brillouin laser," *Optica*, vol. 2, no. 3, pp. 225–232, 2015.

[27] J. Li, M.-G. Suh, and K. Vahala, "Microresonator brillouin gyroscope," *Optica*, vol. 4, no. 3, pp. 346–348, 2017.

[28] S. Gundavarapu, G. M. Brodnik, M. Puckett, T. Huffman, D. Bose, R. Behunin, J. Wu, T. Qiu, C. Pinho, N. Chauhan, *et al.*, "Sub-hertz fundamental linewidth photonic integrated brillouin laser," *Nature Photonics*, vol. 13, no. 1, pp. 60–+, 2019.

110 Gbit/s On-Off-Keying Based on High Temperature Resistant Polymer Modulator

(Invited paper)

Shiyoshi Yokoyama, Guo-Wei Lu, Xiaoyang Cheng, and Feng Qiu
Institute for Materials Chemistry and Engineering, Kyushu University, Japan
e-mail: s_yokoyama@cm.kyushu-u.ac.jp

Abstract

A high-temperature resistant electro-optic (EO) polymer modular is fabricated and demonstrated for generating reliable 110 Gbit/s OOK. The polymer is performed on the silicon Mach-Zehnder interferometer toward possible hybrid silicon and polymer photonic platform. We demonstrated high-bit rates signalling with low BER properties below FEC threshold. Because of the high thermal-stability of the EO polymers, negligible degradation of modulations was observed up to 90°C

Keywords: polymer modulator, silicon waveguide, on-off-keying, PAM4

1. Introduction

Recent progress of highly efficient and high-speed electro-optic (EO) modulator technology has received intensive research attentions in microwave photonics and fiber-optic networks. Among the different types of materials used in the modulator, the EO polymer offers intrinsic advantages such as a large EO coefficient (r_{33}>100 pm/V), low dielectric constant and loss, and excellent compatibility with other materials and silicon substrates. Therefore, the EO polymer modulators open up a variety of opportunities for realizing unique wideband applications. In particular, achieving higher baud rates is an important objective toward optical interconnection at short-reach applications, so that polymer modulator might be a cost-effective 100G serial solution [1]. To date, the EO polymer modulators have shown outstanding performance such as high data rate transmission, low-power consumption, and easy integration to other substrates in a form of thin film polymer modulator [2], organic-silicon hybrid [3], or traveling-wave polymer on silicon waveguide [4]. The low fabrication cost and high yield of the polymer device is another advantage as a cost-effective solution to high-volume production of assembled optical transceivers. The progress makes the polymer device as one of the few possible solutions to realize over 100 Gbaud high-speed signalization. It meets the critical demand in the emerging optical interconnects for short-reach and datacenter networks. To further highlight the superior of EO polymer modulator, as another aspect, the environmental stability is vitally important to be urgently investigated. Telcordia GR468-CORE defines the temperature condition of 85°C for 2,000 hours as a standard in industrial applications. Clearly using the EO polymer with enhanced thermo-physical resistance is a simple solution to pass such environmental tests. We have recently shown that side-chain EO polymers having the glass transmission temperature (T_g) of over 180°C are alternative to the commonly used organic EO materials [5]. The enhanced temperature stabilities of the modulators showed invariable EO coefficients and frequency response up to 40 GHz [5,6].

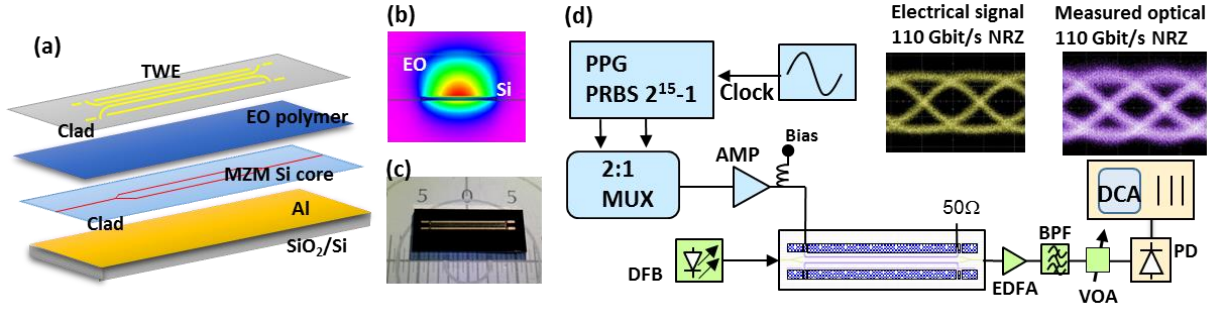


Fig. 1 The hibrid silicon and EO polymer modulator and high-speed modulation. **(a)** The layer-by-layer structure of the MZI waveguide, consisting of the bottom Al electrode, 50 nm-thick and 2 μm-wide Si core, EO polymer, SiO_2 resin claddings, and traveling-wave electrode (TWE). **(b)** The calculated modal distribution indicating a part of the optical field penetrates into the EO polymer. (**c**) A photo picture of the signal MZI modulator having a 8 mm-long TWE. **(d)** Set up for the high-speed data transmission measurement. The high-speed PPG and 2:1 MUX are used to apply the electrical signal to the MZI modulator. The laser light from the DFB at the wavelength of 1550 nm is coupled to the waveguide, and output light is conducted to the photodetecor after amplification using EDFA and passing a BPF and VOA. For high-speed modulation, 90-110 Gbit/s OOK signal is applied to the one electrode of two MZIs, and optical diagrams are measured by using a DCA. Typical electric drive signal with V_{pp}=1.5-2.5 V and the measurd optical signal are shown as the eye-diagrams.

In this paper, we expand our earlier works about the high-thermal stable EO polymer application [7] and present the high-speed on-off-keying (OOK) generation with a signalling rate of up to 110 Gbit/s. The EO polymer modulator is fabricated on a Mach-Zehnder interferometer (MZI), which consists of the hybrid silicon and polymer waveguide and RF traveling-wave electrodes. To verify the high-speed operation of the polymer modulator, the S-parameter frequency response of the fabricated polymer modulator, and the eye-diagrams and Q factors of the generated OOK signals when operating the modulator at speed up to 110 Gbit/s are measured.

2. High-speed data transmission and high-thermal stability testing

A network analyser is used to characterize the frequency response of the fabricated EO polymer MZI modulator. The measured S21 parameter indicates the 3-dB bandwidth of around 60 GHz. Though the used analyser has limited frequency bandwidth to characterize response, the 6-dB bandwidth of the polymer modulator is certainly presumed over 70 GHz, showing the capability of >100 Gbaud signalling. Figure 1d represents the experimental setup for testing the high-speed serial data modulation. The CW light from the laser with the wavelength of 1,550 nm is modulated by applying the electric driving singles. Two ~55 Gbit/s electrical pseud-random bit sequence (PRBS) streams with a length of 2^{15}-1 are firstly generated from a pulse pattern generator. Two electrical streams are then fed into an electrical multiplexer to generate a ~110 Gbit/s data signals. The signal is amplified using a linear wideband microwave amplifier and applied to the one arm of the MZI. A 50 Ω resister was connected on the output end of the traveling-wave electrode for termination. Typical fiber-to-fiber insertion loss is 10~12 dB. The modulated optical signal is amplified using an EDFA and optical noise is eliminated using a band pass filter before connecting it to a photodetector. With a peak-to-peak drive voltage of 1.5-2.5 V_{pp}, the measured optical eye-diagrams of 100 and 110 Gbit/s OOK data are recorded by using a digital communications analyzer (DCA) (Fig. 2a and 2b). It can be seen that the optical eyes are clean and open, which are relevant to the high bandwidth property of the EO polymer MZI modulator. The modulation performance is assessed using the Q-factor metric assuming the Gaussian noise limited detection of two levels noise variance of the received signal values. The metric is well suited for binary on-off signalling, thus bit error rates (BER) can be evaluated from the Q analysis. It should be noted that the obtained BER is theoretically optimized to give the minimized value. Figure 2c shows the converted curves of BERs versus the received optical power at 90, 100 and 110 Gbit/s signalizations. To correct these data, the measurements are in back-to-back and the receiver is preceded by a variable optical attenuator (VOA). For low signal power, the receiver response is fully linear allowing the receiver operation under Gaussian thermal noise. We observe that 90-110 Gbit/s OOK transmission is able to yield a BER that is below the DH-FEC threshold of 3.8×10^{-3}.

To investigate the modulator's performance dependence on the temperature, Q factors at 100 Gbit/s data rate are measured at different temperatures in Fig. 2d. A reduction of Q factor is gentle when the temperature is increased up to 90°C. Though disordering of the eye diagram is found at higher temperature, the eye diagram is completely recovered to its original activity when the device is cooled down to room temperature. Assuming that the significant degradation of the EO activity is negligible in the wide temperature range, the measured decrease of the Q factor for 100 Gbit/s at higher temperatures might be attributed to other loss factors.

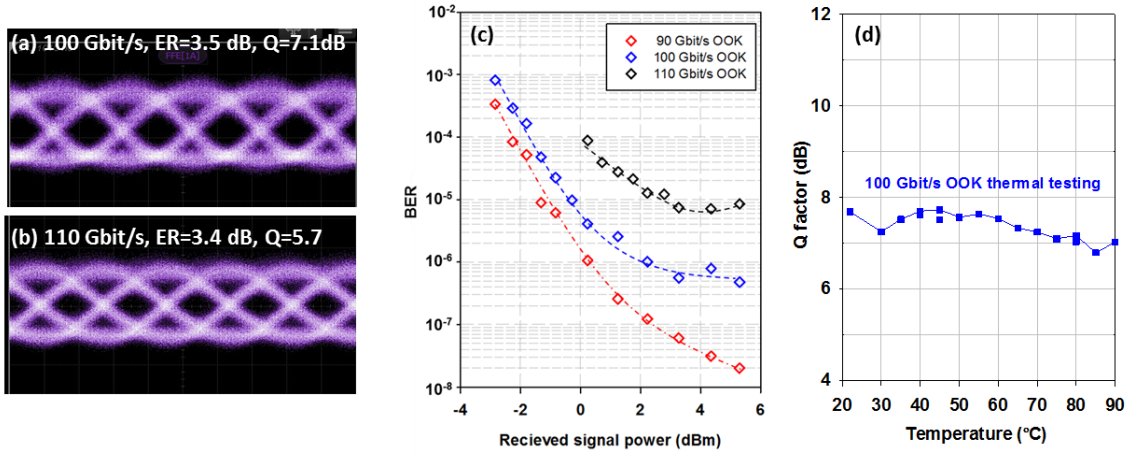


Fig. 2 (**a** and **b**) The measured optical eye-diagrams of 100 Gbit/s and 110 Gbit/s OOK transmissions. (**c**) OOK BER of the modulator for varying received signal power running at 90, 100, and 110 Gbit/s. (d) Thermal stability test of the 100 Gbit/s modulation. The temperature is ranged up to 90°C.

Conclusion

We have demonstrated >100 Gbit/s transmitters using a wideband hybrid silicon and polymer EO modulator. The hybrid modulator was optimized to perform the large bandwidth and low-driving voltage properties. With the development of high-T_g polymers, it reveals a long-term high temperature stability and thermal resistance with high bit rate operation. The measured Q factor variation of 100 Gbit/s OOK over the temperature range of 20-90°C was minimum. The device can be further improved to reveal the similar thermal resistant for faster modulations.

References

[1] H. Huang, et al., "Broadband Modulation Performance of 100-GHz EO Polymer MZMs," J. Lightwave Technol., **39**, 3647 (2012)

[2] H. Zwickel, et al., "Silicon-organic Hybrid (SOH) Modulators for Intensity-modulation / Direct-detection Links with Line Rate of up to 120 Gbit/s," Optics Express **25**, 23784 23800 (2017).

[3] H. Sato, et al., "Low Driving Voltage Mach-Zehnder Interference Modulator Constructed from an Electro-optic Polymer on Ultra-thin Silicon with a Broadband Operation," Optics Express **25**, 768-775 (2017).

[4] H. Miura, et al., "High Thermal Stability 40 GHz Electro-optic Polymer Modulators," Optics Express **25**, 28643-28649 (2017).

[5] F. Qiu, et al., "A hybrid electro-optic polymer and TiO2 double-slot waveguide modulator," *Scientific Reports* ***5***, 8561-1-6 (2015).

[6] F. Qiu, et al., "Thin TiO_2 core and electro-optic polymer cladding Waveguide modulators," *Appl. Phys. Lett.*, **102**, 233504-1-3 (2013).

[7] C. Kieninger., et al., "Demonstration of long-term thermally stable Silicon-Organic Hybrid Modulators at 85°C." Optics Express 26, 27955-27964 (2018)

[8] F. Qiu, "Ultra-thin Silicon/ Electro-optic Polymer Hybrid Waveguide Modulator," *Appl. Phys. Lett.* **107**, 123302-1-6 (2015)

Growth of Organic Crystalline Thin Films with Strong Second-Order Nonlinearity for Integrated Optics

Artur Hermans[1,2], Stéphane Clemmen[1,2,3], Roel Baets[1,2], Jan Genoe[4,5], Cédric Rolin[4]
[1] Photonics Research Group, Ghent University-imec, 9052 Ghent, Belgium
[2] Center for Nano- and Biophotonics, Ghent University, 9052 Ghent, Belgium
[3] Laboratoire d'Information Quantique, Université Libre de Bruxelles, 1050 Brussels, Belgium
[4] Large Area Electronics Department (LAE), imec, 3001 Leuven, Belgium
[5] Department of Electrical Engineering (ESAT), KU Leuven, 3001 Leuven, Belgium
e-mail: Artur.Hermans@UGent.be

ABSTRACT

We demonstrate the growth of highly nonlinear crystalline thin films of *N*-benzyl-2-methyl-4-nitroaniline (BNA) with a controllable crystal orientation. These films are obtained by crystallizing the material in a temperature gradient. Through second-harmonic generation experiments at a fundamental wavelength of 1550 nm, we found a second-order nonlinearity of (153 ± 70) pm/V. This greatly exceeds the value of 54 pm/V for $LiNbO_3$, the benchmark nonlinear crystal. Moreover, the crystalline films are grown on amorphous substrates with processing temperatures not exceeding 115°C, making them suitable for back-end photonic integration on a CMOS chip. We envisage the growth of BNA crystalline films on silicon nitride photonic integrated circuits, where a strong second-order nonlinearity is lacking.

Keywords: nonlinear materials, thin films, crystal growth, organic crystals, second-harmonic generation

1. INTRODUCTION

A whole range of optical devices relies on second-order nonlinear optical processes. Prime examples include optical parametric oscillators (OPO's) [1] and high-speed electro-optic modulators [2]. Commercial devices tend to be bulky, expensive and power-hungry. Integrating them on a photonic chip would reduce their footprint and increase their energy efficiency. Moreover, once a high-yield mass fabrication process is established, the cost per device goes down drastically.

Dedicated material platforms such as AlGaAs [3] and $LiNbO_3$ on insulator [4] are being developed. These can offer low-loss propagation and a large second-order nonlinearity (also known as second-order susceptibility $\chi^{(2)}$). But, when it comes to high-volume fabrication, silicon (Si) photonics is the technology of choice. Within Si photonics, silicon-on-insulator is the main material platform, but silicon nitride (SiN) is gaining ground as an alternative low-loss platform with a transparency window covering visible wavelengths [5]. Furthermore, SiN can be deposited at low temperatures (< 400°C) through PECVD (Plasma-Enhanced Chemical Vapor Deposition), which allows for back-end photonic integration on CMOS electronics [6]. Unfortunately, the $\chi^{(2)}$ nonlinearity of Si, amorphous SiO_2 and SiN is expected to vanish due to their centrosymmetric nature. Yet, there have been demonstrations of $\chi^{(2)}$ effects in Si [7] and SiN [8], but the exact origin remains elusive and the nonlinearities modest. Therefore, many research efforts focus on combining Si photonics with $\chi^{(2)}$ materials.

One such class of materials are the ferroelectric materials (e.g. $BaTiO_3$, $LiNbO_3$, PZT), which typically exhibit a strong Pockels effect. This makes them particularly interesting for electro-optic modulation. High-speed modulators have been demonstrated by growing epitaxial $BaTiO_3$ on Si [9] and depositing PZT (lead zirconate titanate) thin films on SiN waveguides [2].

Next to these ferroelectric materials, organic $\chi^{(2)}$ materials have received considerable attention in the context of photonic integration. Organic materials can have very large $\chi^{(2)}$ nonlinearities. Their linear and nonlinear polarizability is typically mostly electronic in origin, as opposed to inorganic ferroelectric materials, which tend to have large contributions from ionic movements [10]. Hence, the $\chi^{(2)}$ nonlinearity and permittivity of those organic materials varies little up to the near-infrared to visible frequency range. These properties make organic $\chi^{(2)}$ materials extremely interesting both for (very) high-speed modulators and nonlinear wave mixing applications. Moreover, organic $\chi^{(2)}$ materials can be processed at low temperatures, making them suitable for back-end integration on a CMOS chip. Highly efficient modulators have been realized by covering Si slot waveguides with randomly ordered organic nonlinear molecules [11]. To get a large effective $\chi^{(2)}$, the molecules need to be aligned by poling the material. Alternatively, one can make use of organic $\chi^{(2)}$ crystals which do not

The research leading to these results has received funding from the European Research Council (ERC) under the EU's Horizon 2020 research and innovation programme (grant agreement n°742299 / Video Holography). A. H. thanks FWO for funding. S. C. acknowledges the financial support of the F.R.S.-FNRS.

require poling, since the molecules are already ordered in a crystalline structure [12]. Nonetheless, growing crystalline thin films on a photonic integrated circuit (PIC) is challenging.

A well-known organic nonlinear crystal is BNA (*N*-benzyl-2-methyl-4-nitroaniline). Its nonlinearity has been determined in bulk crystals (orthorhombic crystal system, point group mm2) through second-harmonic generation (SHG) experiments at a fundamental wavelength of 1064 nm [12]. The largest nonlinear tensor element χ_{zzz} was found to be (468 ± 62) pm/V, compared to χ_{zzz} = 54 pm/V for $LiNbO_3$ [13]. Next to having a large nonlinearity, BNA is transparent in the ~500 nm to ~2 µm wavelength range and stable in water [12]. The growth of BNA crystals has already been demonstrated in silicon slot waveguides [14]-[15], where molten BNA was used to fill up slots through capillary flow before crystallizing the material. However, this approach offers little freedom in terms of device design. Ideally, one would be able to grow single crystals in thin films over large areas. In combination with photolithographic processing, this would open up numerous possibilities for the realization of highly efficient integrated $\chi^{(2)}$ devices.

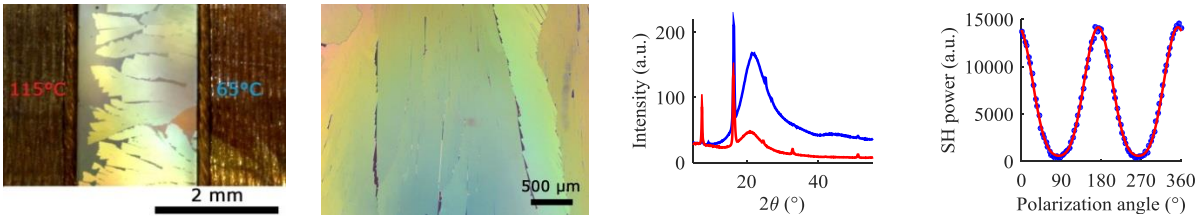
Here, we demonstrate the growth of highly nonlinear crystalline thin films of BNA with a controllable crystal orientation. The crystals are grown on amorphous substrates with processing temperatures not exceeding 115°C. This makes BNA suitable for integration on SiN PIC's and allows for back-end integration on a CMOS chip.

2. FABRICATION

We use 2 cm x 2 cm glass substrates and Si substrates with 3 µm wet oxide. After cleaning, we drop cast 100 µl of 0.4 wt% BNA in toluene solution on a glass or Si substrate. After the solvent has evaporated, we place an FDTS (perfluorodecyltrichlorosilane) treated glass cover on top. The glass cover is needed to avoid dewetting during melting. We treat the cover with FDTS to prevent sticking when we remove the cover for characterization. Next, the sample is placed on a hotplate for several minutes to melt the BNA (BNA melts at 105°C [15]) and removed again to let it crystallize at room temperature, resulting in a polycrystalline BNA film. To grow large single crystals of BNA, we move this polycrystalline film through a temperature gradient [16]. This is done with a homebuilt tool consisting of two hotplates: one set to 115°C and the other to 65°C. There is a gap of 2 mm between the hotplates. Using a stepper motor, the sample is slid from the hot to the cold stage at a speed of 0.7 µm/s. When placing the sample on our tool, we ensure that part of the sample starts out on the cold stage. This way, the polycrystalline BNA film acts as a seed. Also, for Si substrates, we place the sample on the tool with the Si facing up, to avoid creating a thermal bridge. Figure 1a shows an image of a sample on our tool, with clearly visible crystals. The glass cover is removed before characterization of the films.

3. CHARACTERIZATION

Apart from visual inspection with a microscope, the samples are characterized by x-ray diffraction (XRD) θ-2θ scans and SHG experiments. For the SHG experiments, we use a laser emitting 100 fs pulses at a wavelength of 1550 nm. The laser light is linearly polarized and the electric field direction is altered with a half-wave plate. The laser beam is perpendicularly incident onto the sample and the measurements are conducted in transmission. Before detection, the transmitted laser light is filtered out such that only the SH light remains. Also, a polarizer is present in front of the detector to select the polarization of interest. More details about the setup can be found in [17]. The SHG setup is calibrated with a BBO crystal. A transfer matrix model is used to fit the data [18].



(a) (b) (c) (d)

Figure 1. (a) Image of sample (glass substrate) on the thermal gradient tool. In the gap between the hotplates you can see growing crystals. (b) Differential interference contrast microscopy image of BNA grown on oxidized Si. The crystals grew from the top to the bottom of the image. (c) XRD θ-2θ scan (using Cu Kα radiation) of BNA grown on glass (blue) and on oxidized Si (red). (d) Power of generated second-harmonic light measured as a function of the electric field direction of the incident laser beam (for normal incidence). Blue dots are the measurement data; red line is the fitted curve. 0° corresponds to an electric field perpendicular to the optical table. The BNA crystals are oriented with their long side (direction // temperature gradient) perpendicular to the table; the transmission axis of the polarizer in front of the detector has the same orientation.

Figure 1b shows a microscopy image of BNA crystals grown on oxidized Si. The crystals grew from the top to the bottom of the image. We observe crystals that are several millimeters long and hundreds of micrometers wide. Some cracks and gaps in and in between the crystals are visible.

Figure 1c shows the XRD θ-2θ scans for BNA crystals grown on glass (blue) and oxidized Si substrates (red). Distinct peaks are visible at 8° and 16° and smaller ones at 25°, 33° and 51°. These correspond to the

higher-order diffraction peaks of BNA's (010) plane [14], though the peak at 33° also has a contribution from the Si 200 reflection. The broad peak around 21° is originating from the substrate.

Film thicknesses were measured with a surface profilometer. We observe thicknesses from 100 nm to 700 nm. Better thickness control might be achieved using alternative deposition methods like spin coating or vapor phase deposition techniques.

Knowing the out-of-plane crystal axis (from XRD), the thickness and refractive index [12], the nonlinearity can be estimated from SHG measurements. A typical measurement is shown in Fig. 1d. For BNA on glass substrates we found $\chi_{zzz} = (153 \pm 70)$ pm/V, where the large error is due to thickness uncertainty. This is close to the value of ~160 pm/V at 1550 nm reported in [19] for a bulk crystal. We also detected SHG for BNA on oxidized Si, but the roughness of the unpolished backside made $\chi^{(2)}$ quantification difficult. Our SHG measurements indicate that the crystals have a preferential in-plane orientation, with their Z- or c-axis being parallel to the temperature gradient direction (= pulling direction).

4. CONCLUSIONS

We demonstrated the growth of crystalline BNA thin films with a controllable crystal orientation on amorphous substrates utilizing a temperature gradient crystallization technique. SHG measurements indicate that the crystals grow with their Z- or c-axis along the temperature gradient direction. The nonlinear tensor element χ_{zzz} was determined to be (153 ± 70) pm/V at a fundamental wavelength of 1550 nm. Considering the crystal orientation, χ_{zzz} can be probed using waveguide TE modes and in-plane RF electric fields for modulation. Future works include the growth of BNA crystals on SiN waveguides and loss characterization.

REFERENCES

[1] J.A. Giordmaine, R.C. Miller: Tunable coherent parametric oscillation in $LiNbO_3$ at optical frequencies, *Phys. Rev. Lett.*, 14, 973, 1965.

[2] K. Alexander, *et al.*: Nanophotonic Pockels modulators on a silicon nitride platform, *Nat. Commun.*, 9, 3444, 2018.

[3] L. Ottoviano, *et al.*: Low-loss high-confinement waveguides and microring resonators in AlGaAs-on-insulator, *Opt. Lett.*, 41, 3996, 2016.

[4] C. Wang, *et al.*: Integrated lithium niobate electro-optic modulators operating at CMOS-compatible voltages, *Nature*, 562, 101, 2018.

[5] A. Rahim, *et al.*: Expanding the silicon photonics portfolio with silicon nitride photonic integrated circuits, *J. Lightwave Technol.*, 35, 639, 2017.

[6] Y.H.D. Lee, M. Lipson: Back-end deposited silicon photonics for monolithic integration on CMOS, *IEEE J. Sel. Top. Quantum Electron*., 19, 8200207, 2013.

[7] R.S. Jacobsen, *et al.*: Strained silicon as a new electro-optic material, *Nature*, 441, 199, 2006.

[8] T. Ning, *et al.*: Strong second-harmonic generation in silicon nitride films, *Appl. Phys. Lett.*, 100, 161902, 2012.

[9] C. Xiong, *et al.*: Active silicon integrated nanophotonics: ferroelectric $BaTiO_3$, *Nano Lett.*, 14, 1419, 2014.

[10] M. Jazbinsek, L. Mutter, P. Günter: Photonic applications with the organic nonlinear optical crystal DAST, *IEEE J. Sel. Top. Quantum Electron*., 14, 1298, 2008.

[11] C. Koos, *et al.*: Silicon-organic hybrid (SOH) and plasmonic-organic hybrid (POH) integration, *J. Lightwave Technol.*, 34, 256, 2016.

[12] M. Fujiwara, *et al.*: Determination of the *d*-tensor components of a single crystal of *N*-benzyl-2-methyl-4-nitroaniline, *Jpn. J. Appl. Phys.*, 46, 1528, 2007.

[13] D. A. Roberts: Simplified characterization of uniaxial and biaxial nonlinear optical crystals: a plea for standardization of nomenclature and conventions, *IEEE J. Quantum Electron.*, 28, 2057, 1992.

[14] H. Figi, *et al.*: Electro-optic modulation in horizontally slotted silicon/organic crystal hybrid devices, *J. Opt. Soc. Am. B*, 28, 2291, 2011.

[15] D. Korn, *et al.*: Electro-optic organic crystal silicon high-speed modulator, *IEEE Photon. J.*, 6, 2700109, 2014.

[16] G. Schweicher, *et al.:* Toward single crystal thin films of terthiophene by directional crystallization using a thermal gradient, *Cryst. Growth Des.*, 11, 3663, 2011.

[17] A. Hermans, *et al.*: Growth of thin film organic crystals with strong nonlinearity for on-chip second-order nonlinear optics, *Symposium IEEE Photonics Society Benelux*, Brussels, Belgium, November 2018, p. 55.

[18] D.S. Bethune: Optical harmonic generation and mixing in multilayer media: extension of optical transfer matrix approach to include anisotropic materials, *J. Opt. Soc. Am. B*, vol. 8, 367, 1991.

[19] T. Notake, *et al.*: Ultra-precise processing and Maker fringe measurements of organic N-Benzyl-2-Methyl-4-Nitroaniline crystal, *IRMMW-THz*, Nagoya, Japan, September 2018.

Si and Si-rich silicon-nitride waveguides for optical transmissions and wavelength conversion around 2 µm

Mamon Lamy[1], Christophe Finot[1], Cosimo Lacava[2], Günther Roelkens[3], Bart Kuyken[3], Periklis Petropoulos[2] and Kamal Hammani [1]

[1] *Laboratoire Interdisciplinaire Carnot de Bourgogne, UMR 6303 CNRS-Université Bourgogne-Franche-Comté, 9 av. A. Savary, 21078 Dijon cedex, France*

[2] *Optoelectronics Research Centre, University of Southampton, SO17 1BJ, Southampton, United Kingdom*

[3] *Photonics Research Group, Ghent University, imec, 9052 Ghent, Belgium*

e-mail: kamal.hammani@u-bourgogne.fr

ABSTRACT

We show that cm-long silicon or silicon-rich nitride waveguides with subwavelength transverse dimensions can efficiently sustain high-speed transmissions at 2 µm. We report the transmission of a 10 Gbit/s signal with negligible power penalty. Parametric conversion in both continuous and pulsed pump regimes is also demonstrated.

Keywords: Silicon waveguide, si-rich silicon-nitride waveguides ; 2 µm optical communications ; wavelength conversion

1. INTRODUCTION

In recent years a number of experiments have explored the potential of various materials in the 2-µm spectral region, with an emphasis on components having subwavelength transverse dimensions to ensure a high density of the photonic circuitry. For instance, efficient data transmission at 10-Gbit/s has been reported using different material platforms such as silicon germanium [1] and titanium dioxide [2]. However, no high bit-rate transmission has ever been reported at wavelengths around 2 µm in either silicon on insulator or any other CMOS-compatible platform. Here, we demonstrate for the first time, penalty-free transmission of a 10-Gbit/s on-off keying signal at 1.98 µm in cm-long Si and SRN waveguides.

In order to fulfil the need of transparent optical networks required for wavelength division multiplexing around 2 µm, frequency conversion is a critical operation that should ideally be realized all-optically. Experimental demonstrations around 2 µm have already been reported in silicon devices that exhibit a large third-order nonlinear coefficient with either picosecond pulses [3, 4] or continuous wave pumping [5, 6]. Stoichiometric Si_3N_4 is another candidate material for applications at 2 µm. However, while it benefits from the absence of two-photon absorption at these wavelengths, its nonlinearity is much lower than silicon. To overcome this limitation, SRN has been explored, since it offers the possibility to precisely engineer both the linear and nonlinear properties of waveguides at the required wavelengths and provides enhanced flexibility in designing low dispersion and highly nonlinear optical structures, operating at high optical powers [7-9]. Here, we show that the same Si or SRN waveguide structure as the one involved for transmission is also suitable for parametric wavelength conversion in the 2-µm range.

2. WAVEGUIDES UNDER STUDY AND EXPERIMENTAL SETUP

A schematic of the waveguide cross section of the Si and SRN waveguides we tested is shown in Fig. 1. Details of the fabrication can be found in [5] and [10] for the Si and SRN components respectively. The Si waveguides are 900 nm wide and 220 µm thick and samples of 7 and 2 cm length have been investigated. They are single-mode around 2 µm with an effective area as small as 0.18 μm^2 leading to a nonlinear parameter of 136 $W^{-1}m^{-1}$. An important design parameter has been the width of the waveguides, which is crucial in determining the dispersion profile of the Si waveguide. A width of 900 nm ensures that the waveguide operates in the slightly anomalous regime of dispersion at 2 µm.

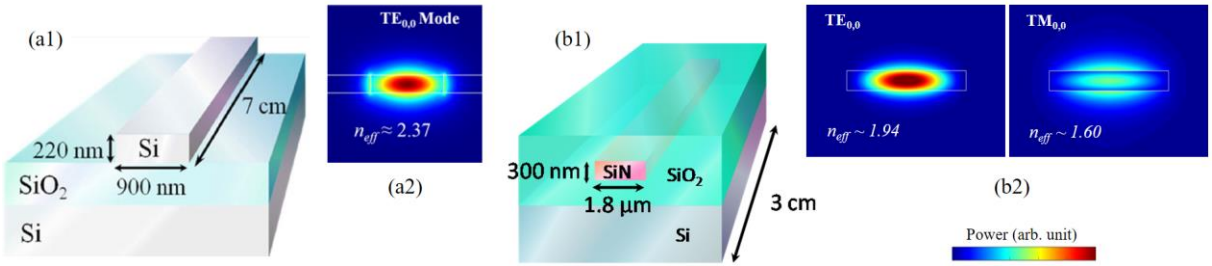


Figure 1. (a) Structure of the waveguides under investigation (panels 1) and examples of the power distribution of the fundamental quasi TE-mode and quasi-TM mode (panels 2, results from a finite difference eigenmode solver) of the Si and SRN waveguides (panels a and b, respectively).

The SRN waveguide is 3 -cm long and can sustain at least the propagation of the fundamental quasi-TE and quasi-TM modes. Its dimensions are much larger in this case (1800 nm × 300 nm), leading to a significantly lower nonlinear coefficient relative to the Si waveguides of our experiments. Owing to the rectangular shape of the waveguide, the properties of the two propagation modes differ significantly. Whereas the quasi-TE mode is highly confined within the SRN core, the quasi-TM mode is much more delocalized and a non-negligible part of the field propagates within the SiO_2 cladding. This difference in the field confinement is also reflected in the effective area that is estimated to be 0.86 μm^2 and 4.75 μm^2 for the quasi-TE and quasi-TM modes respectively. The design of this component has not been optimized for efficient dispersion management, therefore its dispersion is mainly imposed by the strong normal dispersion of the material.

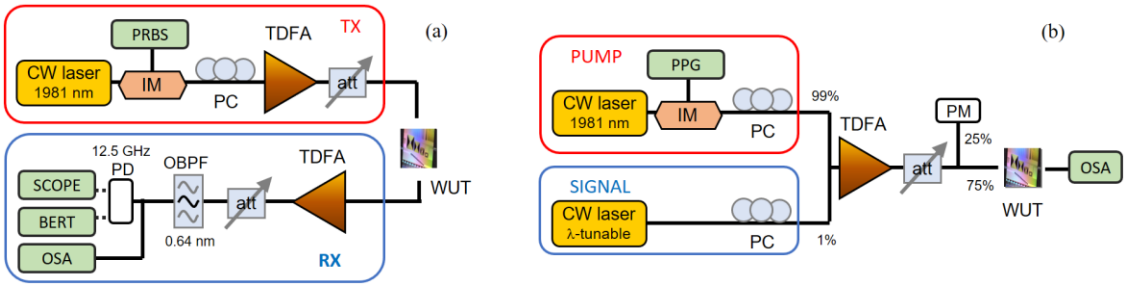


Figure 2. Experimental setups used for (a) 10-Gbit/s transmissions, (b) wavelength conversion.

In order to demonstrate the suitability of the devices for 2-µm optical communications, we have implemented the experimental setup depicted in Fig. 2(a) (more details available in [11]) and based on 2-µm commercially available devices. The transmitter (TX) was based on an intensity modulated laser diode centered at 1981 nm by means of a Niobate-Lithium modulator (IM). Then a first thulium doped fiber amplifier (TDFA) was used to boost the signal before injection into the waveguide. Light coupling in the components was achieved through butt-coupling assisted with lensed fibers. For the SRN case, due to the two-moded nature of the waveguide, the input polarization highly impacts the coupling efficiency. The receiver (RX) used a second TDFA. An optical bandpass filter (OBPF) was also inserted at the output of the system in order to limit the accumulation of amplified spontaneous emission from the TDFAs. An optical spectrum analyzer (OSA) was used to evaluate the optical signal to noise ratio (OSNR).

A second aspect of our work is to evaluate the potential of our waveguides for wavelength conversion applications (Fig. 2(b)). A CW laser tunable between 1965 and 1985 nm was used to generate a signal wave, while the pump beam was kept constant. By means of an intensity modulator driven by an electrical pulse pattern generator (PPG), we were able to study the wavelength conversion process in continuous or pulsed regimes with a typical pump duration of 100 ps. The delay between two consecutive pulses can be adjusted from 200 ps to 1.6 ns. The pump and signal waves were combined using a coupler before being simultaneously amplified by a TDFA. At the output of the system, an OSA was used to evaluate the conversion efficiency (CE) defined here as the ratio between the output powers of the signal and idler waves.

3. EXPERIMENTAL RESULTS

We have summarized the results we obtained for the 10-Gbit/s transmission at 2 µm in Fig. 3 for a 7-cm long Si waveguide and the SRN waveguide operating in the quasi-TM mode of propagation. The typical average power launched to the two waveguides was at the order of mW. Eye-diagrams are provided in panels 1 and 2 and stress that widely open eyes were obtained. The quality of the 10-Gbit/s transmitted signal was quantitatively assessed through systematic measurements of the bit-error-rate as a function of the OSNR on the receiver (panels 3). In all cases, BERs well below 10^{-9} were measured. No significant penalty was observed after transmission through the SRN waveguide whereas a 1 dB penalty, attributed to a residual Fabry-Perot effect has been recorded for the Si waveguide.

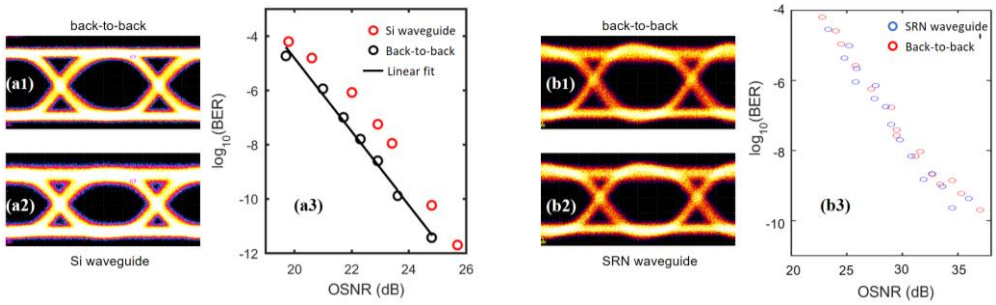


Figure 3. 10-Gbit/s eye diagram recorded in the back-to-back configuration compared to eye diagrams recorded after propagation in the WUT (panels 1 and 2 respectively). Bit-error-rate measurements (BER) as a function of OSNR (panels 3). Results for a 7-cm long Si waveguide and a 3-cm long SRN waveguide are plotted on panel (a) and (b) respectively.

Figure 4 shows the conversion efficiency as a function of the signal wavelength for the two waveguide structures with an estimated input average pump power of 12 dBm. Conversion efficiency as high as -25 dB is demonstrated with continuous pumping in the 2-cm long Si waveguide. A conversion window over 70 nm is demonstrated for the dispersion engineered Si component with an efficiency up to close -10 dB recorded with a pulsed pump. Despite the relatively large effective mode area, conversion efficiencies of ~-24 dB are measured when using a pulsed pump. The moderate bandwidth achieved for the SRN waveguide denotes that, as expected, the pump lies in the strongly normal regime of dispersion.

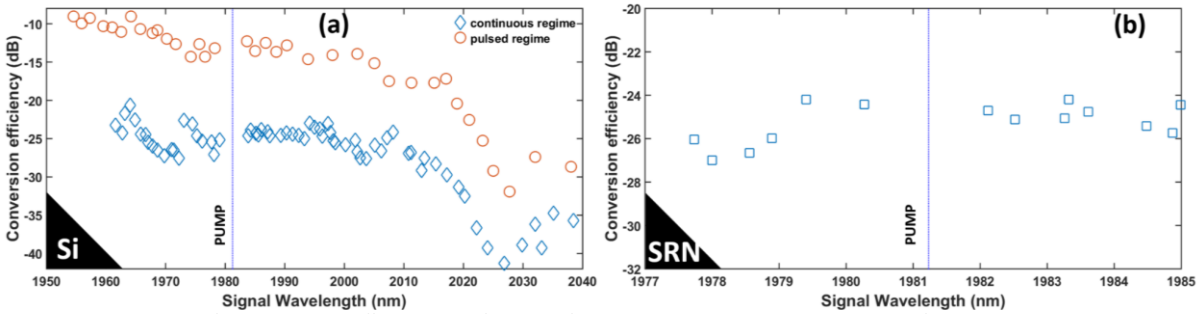


Figure 4. Evolution of the conversion efficiency as a function of the signal or idler wavelength achieved for a pump at 1981 nm. Results have been recorded (a) for the 2-cm long Si waveguide (for continuous operation and for the pulsed regime for a peak power increased by a factor 16) and (b) for the SRN waveguide (in the pulsed regime).

4. CONCLUSION

We have demonstrated that both silicon and silicon-rich silicon nitride waveguides can sustain error-free transmission of high-speed telecom signals around 2 µm in cm-long devices without any significant penalty. We have also shown that such nonlinear photonic chips are suitable for frequency conversion process. Regarding the SRN technology, this first demonstration of wavelength conversion at 2 µm is promising and significant improvement is expected with a design aiming at tailoring the waveguide dispersion. Using a thicker waveguide and taking advantage of the higher confinement of the TE-mode will be explored.

ACKNOWLEDGEMENTS

This work is financially supported by PARI PHOTCOM Région Bourgogne, by Carnot Arts Institute (PICASSO 2.0 project), by the Institut Universitaire de France, by FEDER-FSE Bourgogne 2014/2020 and by the the french “Investissements d’Avenir” program, project ISITE-BFC (contract ANR-15-IDEX-0003). The research work has benefited from the PICASSO experimental platform of the University of Burgundy.

REFERENCES

[1] M. Lamy *et al.*, "Ten gigabit per second optical transmissions at 1.98 µm in centimetre-long SiGe waveguides," *Electron. Lett.*, vol. 53, p. 1213, 2017.
[2] M. Lamy *et al.*, "10 Gbps data transmission in TiO2 waveguides at 2 um," *Appl. Sci.*, vol. 7, p. 631, 2017.
[3] S. Zlatanovic *et al.*, "Mid-infrared wavelength conversion in silicon waveguides using ultracompact telecom-band-derived pump source," *Nat. Photon.*, vol. 4, p. 561, 05/23/online 2010.
[4] B. Kuyken *et al.*, "50 dB parametric on-chip gain in silicon photonic wires," *Opt. Lett*, vol. 36, p. 4401, 2011.
[5] X. Liu , R. M. Osgood Jr, Y. A. Vlasov, and W. M. J. Green, "Mid-infrared optical parametric amplifier using silicon nanophotonic waveguides," *Nat. Photon.*, vol. 4, p. 557, 2010.
[6] R. K. W. Lau *et al.*, "Continuous-wave mid-infrared frequency conversion in silicon nanowaveguides," *Opt. Lett.*, vol. 36, p. 1263, 2011.
[7] M. R. Dizaji *et al.*, "Silicon-rich nitride waveguides for ultra-broadband nonlinear signal processing," *Opt. Express*, vol. 25, p. 12100, 2017.
[8] C. Lacava *et al.*, "All-optical Wavelength Conversion of Phase-encoded Signals in Silicon-rich Silicon Nitride Waveguides," in *Conference on Lasers and Electro-Optics*, San Jose, California, 2018, p. JTu2A.64.
[9] K. J. A. Ooi *et al.*, "Pushing the limits of CMOS optical parametric amplifiers with USRN:Si7N3 above the two-photon absorption edge," *Nat Commun*, vol. 8, p. 13878, 2017.
[10] C. Lacava *et al.*, "Si-rich Silicon Nitride for Nonlinear Signal Processing Applications," *Sci. Rep.*, vol. 7, p. 22, 2017.
[11] M. Lamy *et al.*, "Silicon Waveguides for High-Speed Optical Transmissions and Parametric Conversion around 2 µm," *IEEE Photon. Technol. Lett.*, 31 (2), p. 165-168, 2019.

Chip-Based Nonlinear Photonics

(Invited paper)

Alexander L. Gaeta
Columbia University, Applied Physics and Applied Mathematics, New York, NY, USA
e-mail: a.gaeta@columbia.edu

ABSTRACT

Over the past decade silicon nitride has emerged as an exceptional material for nonlinear optics and has led to realization of ultrahigh-performance photonic devices in fields from data communications to medicine. I will discuss nonlinear photonics using silicon-nitride chips that can be used to create chip-based optical frequency combs via supercontinuum generation and in microresonators.

Keywords: nonlinear photonics, four-wave mixing, optical frequency combs, supercontinuum generation

4H-SiC Microring Resonators for Nonlinear Integrated Photonics

Yi Zheng[1], Minhao Pu[1], Ailun Yi[2], Xin Ou[2], Haiyan Ou[1]

[1] DTU Fotonik, Technical University of Denmark, Building 343, DK-2800 Lyngby, Denmark
[2] Institute of Microsystem and Information Technology, Chinese Academy of Sciences, Shanghai, China
e-mail: haou@fotonik.dtu.dk

ABSTRACT

We demonstrate efficient four-wave mixing in high Q 4H-SiC microring resonators. We achieve a four-wave mixing conversion efficiency of -21.7 dB in a microring resonator with 79 mW pump power. Thanks to the strong light confinement in SiC waveguides with sub-micron cross-section dimensions, a high nonlinear parameter (γ) of 12.5 $W^{-1}m^{-1}$ is obtained, from which the nonlinear refractive index (n_2) of 4H-SiC is estimated to be $9.2\pm0.4\times10^{-19}$ m^2/W at telecom wavelengths.

Keywords: Nonlinear optics, integrated optics, microresonators.

1. INTRODUCTION

An abundance of nonlinear optical effects have been realized in nonlinear integrated optics, which shows great potential for a variety of applications such as high speed signal processing [1], electro-optic modulation, sensing, light amplification, etc [2]. Efficient four-wave mixing (FWM) can also lead to Kerr frequency comb generation in high quality factor (*Q*) nonlinear microresonators [3]. Therefore, tremendous effort has been made to develop nonlinear integrated material platforms and frequency combs have been achieved in different materials including silicon [4], Si_3N_4 [5], Hydex [6], Diamond [7], AlN [8], AlGaAs [9], etc.

SiC is also considered to be a suitable candidate for nonlinear integrated optics since it exhibits relatively large Kerr nonlinearity on the order of 10^{-18} m^2W^{-1}[10]. Besides, its quadratic nonlinearity is also strong (~ 30 pm/V [11]) and multi-photon absorption is absent in SiC at telecom wavelengths, e.g. ~1550 nm, due to its wide bandgap (2.4 eV-3.2 eV depending on its crystallographic type [12]). Other material properties such as CMOS compatibility, high mechanical stiffness and chemical inertness, and large thermal conductivity also make SiC an attractive platform. Moreover, point defects in SiC can be exploited for single-photon sources for quantum applications. In recent years, a few nonlinear processes have been demonstrated in SiC such as second harmonic generation [13], self-phase modulation [10] and parametric wavelength conversion [14]. In addition, Kerr nonlinearity was also reported in amorphous SiC [15]. Microresonators are key components for enhancing the efficiency of nonlinear processes due to the intra-cavity power enhancement. FWM in 3C-SiC microring resonators has been reported [16], however, the high loss of 3C-SiC microring makes it a relatively inefficient process. For nonlinear processes, high *Q* microresonators are essential since it offers large enhancement of intra-cavity optical power. In addition, as the nonlinear parameter γ expressed by $2\pi n_2/\lambda A_{eff}$ is highly dependent on the effective mode area A_{eff}, a high-*Q* microresonator with a small effective mode area is highly desired to achieve efficient nonlinear processes.

We realize efficient wavelength conversion through a FWM process in high-*Q*, 4H- SiC microring resonators with sub-micron cross-sectional dimension. –21.7 dB conversion efficiency is achieved in a 16.5-μm microring resonator with 79 mW pump power. Nonlinear parameter γ of 12.5 $W^{-1}m^{-1}$ is obtained in such high-confinement waveguides, which is over three times larger than the value achieved in 3C-SiC microresonators. Besides, we also report nonlinear refractive index of 4H-SiC at telecom wavelength range as high as $\sim9.2\pm0.4\times10^{-19}$ m^2/W.

2. FABRICATION AND CHARACTERIZAION

We applied smart-cut technique to realize SiCOI wafer [17], where ~1.1 μm SiC layer was left after the smart-cut process. A wet oxidation process was applied to thin down the SiC thickness from 1.1 μm to 600 nm while the roughness was reduced from ~5.27 nm to ~0.84 nm. The device fabrication on the SiCOI wafer started with pattern definition by electron beam lithography (EBL) in hydrogen silsesquioxane (HSQ) with a multi-pass process [18],[19]. The EBL was performed using a JEOL system (JBX-9500FS) at 100-kV. The HSQ pattern was then transferred to the SiC layer using a fluorine (SF_6)-based dry etching process in an inductively coupled plasma reactive ion etching (ICP-RIE) machine. After that, an extra wet oxidation was applied to further thin down the SiC layer thickness to 500 nm and reduce the roughness for both top and sidewall surfaces. In the end, SiO_2 was deposited as the cladding material through Low-Pressure Chemical Vapor Deposition (LPCVD) followed by Plasma-Enhanced Chemical Vapor Deposition (PECVD).

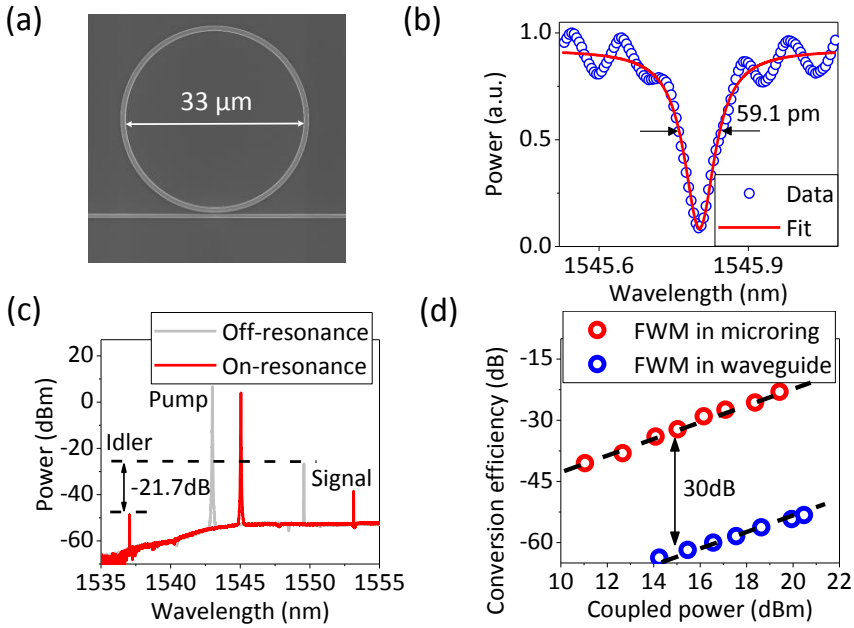


Figure 1. (a) Top-view SEM picture of a fabricated SiC microring resonator with 16.5-µm radius. (b) Measured normalized transmission spectrum of an SiCOI microresonator with fitting around 1545 nm. (c) Measured output spectra of the microresonator with the pump and signal waves off-resonance (grey curve) and on-resonance (red curve). (d) Coupled power dependent CE of a resonance in a16.5-µm radius SiC microring resonator (red) and a 3 mm long waveguide (blue).

To perform FWM experiments, we used a 16.5-µm radius microring resonator with cross-sectional dimension of 700×500 nm^2 (Fig. 1(a)), which is operated in over-coupled condition with a loaded Q of ~26,000 (the resonance linewidth is shown in Fig. 1(b)). The intrinsic Q of tested resonator was estimated to be ~70,000. In the FWM experiment, both pump and signal waves were coupled into the resonator. Figure 1(c) shows the output spectra from the resonator when the pump and signal waves are both off-resonance (grey line) and on-resonance (red line). We achieved an overall conversion efficiency (CE), defined by the ratio between the output idler power and input signal power in the bus waveguide of -21.7 dB with 79 mW of pump power. FWM conversion efficiency was also measured in a 3-mm long SiC waveguide with the same cross-sectional area as the microring resonator. As shown in Fig. 1(d), 30 dB enhancement of FWM conversion efficiency was achieved. The FWM conversion efficiency of a 104-µm-long waveguide (the physical length of tested 16.5-µm radius microring resonator) in perfect phase-matched condition (in the case of very small signal-pump detuning) can be estimated by $(P_p\gamma L_{eff})^2$, where P_p and γ are the estimated intra-cavity power and nonlinear parameter. L_{eff} is the effective interaction length of the pump and signal in the waveguide defined as $(1-e^{-\alpha L})/\alpha$, where L is the length of the device. The estimated CE was -83.5 dB. Therefore, 61.8 dB CE gain was obtained at the same pump power level in a microresonator device.

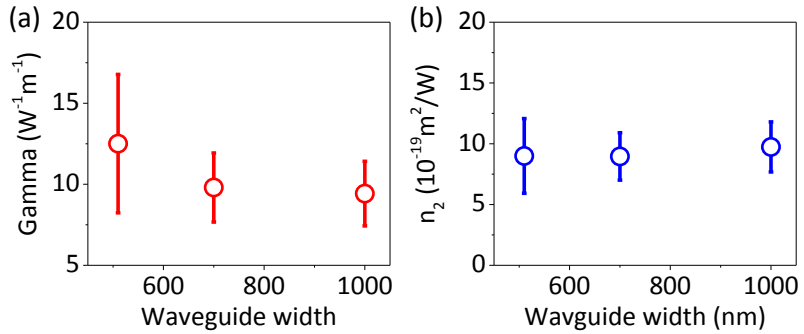


Figure 2.(a) Estimated nonlinear parameter γ and (b) nonlinear refractive index n_2 (blue) based on CE measurement on microring resonators with different cross-sectional areas.

To extract the nonlinear parameter γ, we measured the CE for 16.5-microring resonators with different waveguide widths (including 510 nm, 700 nm and 1000 nm). The red circles in Fig. 2(a) show that the estimated γ values are around 12.5, 10 and 9.4 W^{-1}m^{-1} for 500 nm thick SiC microring resonators with different waveguide widths. By calculating the effective mode areas for these waveguides, we estimated the nonlinear refractive index of 4H-SiC at telecom wavelength range is on the order of 9.2±0.4×10^{-19}m^2/W (Fig. 2(b)). The obtained γ of 12.5 W^{-1}m^{-1} is over three times larger than previous reported result in 3C-SiC waveguides [16].

3. CONCLUSIONS

In conclusion, we demonstrated efficient FWM process in 4H-SiC microring resonators. -21.7 dB conversion efficiency was achieved in a microring resonator, which is 30-dB higher than a 3-mm long waveguide at the same pump power. Highly nonlinear SiC waveguides with nonlinear parameter γ of 12.5 $W^{-1}m^{-1}$ has been realized, which is higher than previously reported value. The demonstration of this work shows potential for enabling all-optical signal processing functionalities through highly nonlinear SiC waveguides.

ACKNOWLEDGEMENTS

The authors acknowledge financial support from the Danish Research Council SPOC (DNRF123) and the National Natural Science Foundation of China (No.: 11705262, 11622545 and U1732268), Frontier Science Key Program of CAS (No.: QYZDY- SSW-JSC032), One Hundred Talent Program of CAS, International Collaboration Project of Shanghai (No.: 16520721100). We thank Assistant professor Jaime Cardenas at University of Rochester for helpful discussion on the smart-cut process in SiC. We also thank DTU Danchip for the support of the fabrication facilities and technologies.

REFERENCES

[1] M. Pu *et al.*, "Ultra-Efficient and Broadband Nonlinear AlGaAs-on-Insulator Chip for Low-Power Optical Signal Processing," *Laser Photon. Rev.*, vol. 12, no. 12, p. 1800111, Dec. 2018.

[2] J. Leuthold, C. Koos, and W. Freude, "Nonlinear silicon photonics," *Nat. Photonics*, vol. 4, no. 8, pp. 535–544, Aug. 2010.

[3] P. Del Haye, A. Schliesser, O. Arcizet, T. Wilken, R. Holzwarth, and T. J. Kippenberg, "Optical frequency comb generation from a monolithic microresonator," *Nature*, vol. 450, no. 7173, pp. 1214–1217, Dec. 2007.

[4] A. G. Griffith *et al.*, "Silicon-chip mid-infrared frequency comb generation," *Nat. Commun.*, vol. 6, no. 1, p. 6299, Dec. 2015.

[5] J. S. Levy, A. Gondarenko, M. a. Foster, A. C. Turner-Foster, A. L. Gaeta, and M. Lipson, "CMOS-compatible multiple-wavelength oscillator for on-chip optical interconnects," *Nat. Photonics*, vol. 4, no. 1, pp. 37–40, Dec. 2009.

[6] L. Razzari *et al.*, "CMOS-compatible integrated optical hyper-parametric oscillator," *Nat. Photonics*, vol. 4, no. 1, pp. 41–45, Dec. 2009.

[7] B. J. M. Hausmann, I. Bulu, V. Venkataraman, P. Deotare, and M. Lončar, "Diamond nonlinear photonics," *Nat. Photonics*, vol. 8, no. 5, pp. 369–374, Apr. 2014.

[8] H. Jung, C. Xiong, K. Y. Fong, X. Zhang, and H. X. Tang, "Optical frequency comb generation from aluminum nitride microring resonator.," *Opt. Lett.*, vol. 38, no. 15, pp. 2810–3, Aug. 2013.

[9] M. Pu, L. Ottaviano, E. Semenova, and K. Yvind, "Efficient frequency comb generation in AlGaAs-on-insulator," *Optica*, vol. 3, no. 8, p. 823, Aug. 2016.

[10] J. Cardenas *et al.*, "Optical nonlinearities in high-confinement silicon carbide waveguides," *Opt. Lett.*, vol. 40, no. 17, pp. 4138–4141, 2015.

[11] I. J. Wu and G. Y. Guo, "Second-harmonic generation and linear electro-optical coefficients of SiC polytypes and nanotubes," *Phys. Rev. B*, vol. 78, no. 3, p. 35447, Jul. 2008.

[12] V. E. Chelnokov and A. L. Syrkin, "High temperature electronics using SiC: actual situation and unsolved problems," *Mater. Sci. Eng. B*, vol. 46, no. 1–3, pp. 248–253, Apr. 1997.

[13] S. Yamada *et al.*, "Second-harmonic generation in a silicon-carbide-based photonic crystal nanocavity.," *Opt. Lett.*, vol. 39, no. 7, pp. 1768–71, Apr. 2014.

[14] J. Cardenas *et al.*, "Parametric Frequency Conversion in Silicon Carbide Waveguides," in *CLEO: 2015*, 2015, p. SF1D.7.

[15] X. Lu, J. Y. Lee, S. Rogers, and Q. Lin, "Optical Kerr nonlinearity in a high-Q silicon carbide microresonator," *Opt. Express*, vol. 22, no. 25, pp. 30826–32, Dec. 2014.

[16] F. Martini and A. Politi, "Four wave mixing in 3C SiC ring resonators," *Appl. Phys. Lett.*, vol. 112, no. 25, p. 251110, Jun. 2018.

[17] L. Di Cioccio, Y. Le Tiec, F. Letertre, C. Jaussaud, and M. Bruel, "Silicon carbide on insulator formation using the Smart Cut process," *Electron. Lett.*, vol. 32, no. 12, p. 1144, 1996.

[18] L. Ottaviano, M. Pu, E. Semenova, and K. Yvind, "Low-loss high-confinement waveguides and microring resonators in AlGaAs-on-insulator," *Opt. Lett.*, vol. 41, no. 17, p. 3996, 2016.

[19] Y. Zheng, M. Pu, H. K. Sahoo, E. Semenova, and K. Yvind, "High-Quality-Factor AlGaAs-On-Sapphire Microring Resonators," *J. Light. Technol.*, DOI: 10.1109/JLT.2018.2882305, 2018.

The impact of lateral leakage on the nonlinear optical waveguide design in lithium niobate on insulator (LNOI)

Andreas Boes[1,2], Lin Chang[2], Thach Nguyen[1], Markus Knoerzer[1], Jon D. Peters[2], John E. Bowers[2], and Arnan Mitchell[1]

[1] School of Engineering, RMIT University, Melbourne, Victoria 3001, Australia

[2] Department of Electrical and Computer Engineering, University of California Santa Barbara, CA 93106, USA

e-mail: andreas.boes@rmit.edu.au

ABSTRACT

In this contribution we show that lateral leakage at the second harmonic wavelength can cause a reduced nonlinear optical conversion efficiency in lithium niobate on insulator ridge/rib waveguides. By designing the waveguide parameters carefully, we avoided this effect, which enabled us to demonstrate a nonlinear optical conversion efficiency of ~780% $W^{-1}cm^{-2}$ in these waveguides.

Keywords: Nonlinear Optics, Lithium Niobate, Lateral Leakage, Quasi-Phase Matching.

1. INTRODUCTION

In recent years, lithium niobate on insulator (LNOI) has attracted significant interest in the integrated optics research community [1]. This interest can be attributed to the attractive material properties of lithium niobate, including strong electro optic, nonlinear optic and piezo electric effects. Furthermore, optical waveguides with strong optical field confinement can be achieved in this platform by optically loading the lithium niobate thin film with a strip of material that has a high refractive index (such as silicon nitride - SiN), or by etching the lithium niobate directly [1]. The strong optical mode confinement enables small waveguide bending radii and increased efficiency of the nonlinear optic and the electro-optic interaction. These properties enabled record breaking demonstration, such as a second-harmonic generation (SHG) efficiency of 2600% $W^{-1}cm^{-2}$ when using periodically poled waveguides [2] and a voltage length product of 2.8 Vcm when applying a voltage to co-planar electrodes [3].

The SHG efficiency of 2600% $W^{-1}cm^{-2}$ [2] was achieved by etching the lithium niobate directly, which is effective but requires dedicated fabrication approaches. Furthermore, the quasi-phase matching wavelength is strongly depended on the exact waveguide dimensions, which makes it prone to fabrication tolerances. A way to overcome these challenges is to dielectric loading the lithium niobate thin-film with a strip of SiN, as it allows one to harness the existing foundry fabrication infrastructure as only the nitride needs to be deposited and etched. However, the recently demonstrated conversion efficiency using silicon nitride loading on LNOI (160% $W^{-1}cm^{-2}$) was an order of magnitude lower compared to the theoretically predicted one (1600% $W^{-1}cm^{-2}$) [4]. The difference between the experimental and theoretical conversion efficiency has so far not been completely understood.

In this contribution, we investigate the impact of lateral leakage on SHG efficiency in strip loaded LNOI and find that the generated SH can leak into the slab modes due to TE to TM conversion [5], reducing the overall conversion efficiency of the device. We show how to design optical waveguides to avoid this effect. Applying these design considerations enabled us to demonstrate periodically poled SiN loaded LNOI waveguides with a conversion efficiency of ~780% $W^{-1}cm^{-2}$.

2. DESIGN AND SIMULATION

Lateral leakage in a photonic waveguide was first observed in silicon on insulator ridge/rib waveguides, where the TM optical waveguide mode couples to a TE slab mode, which has a higher effective refractive index [5]. The angle Θ under which the TM optical waveguide mode couples to the TE slab modes depends thereby on the phase matching ($n_{\mathrm{TE}} \sin \Theta = n_{\mathrm{TM}}$). This effect can be seen as a contribution to waveguide loss, which is unwanted in most cases.

Ridge waveguides in LNOI, such as the illustrated one in the inset of Figure 1, are prone to a similar effect. Periodically poled waveguides are usually fabricated on X-cut lithium niobate, which means that the TE polarization is used for pumping the nonlinear optical process and to employ the high nonlinear optical coefficient d_{33} along the crystallography Z-direction. However, as lithium niobate is birefringent, the effective index of the TM slab mode that surrounds the ridge waveguide, can be higher than that of the TE waveguide mode (as the ordinary refractive n_{o} index is higher than the extraordinary refractive n_{e} index in lithium niobate), resulting in coupling from TE guided mode to TM slab mode. Figure 1 shows the difference between the effective index of the TE waveguide mode and the TM slab mode ($\Delta n_{\mathrm{eff}} = n_{\mathrm{eff,TE\ waveguide}} - n_{\mathrm{eff,TM\ slab}}$) as a function of wavelength and lithium niobate thickness, using the following parameters: the silicon nitride (SiN) thickness was

400 nm, the etch depth (h_{etch}) was 350 nm and the waveguide width (w) was 2 µm. The black line in the graph indicates a refractive index difference between the modes of zero ($\Delta n_{\mathrm{eff}} = 0$), which means that waveguides that are above the black line can suffer from lateral leakage, such as the device design of Ref. [4]. One can see that the lithium niobate thin-film thickness needs to be thinner for waveguides that are designed for shorter wavelengths. For our design we chose a lithium niobate thin-film thickness of 300 nm, in order to avoid lateral leakage at the SH wavelength, when pumping the waveguide at C-band wavelengths.

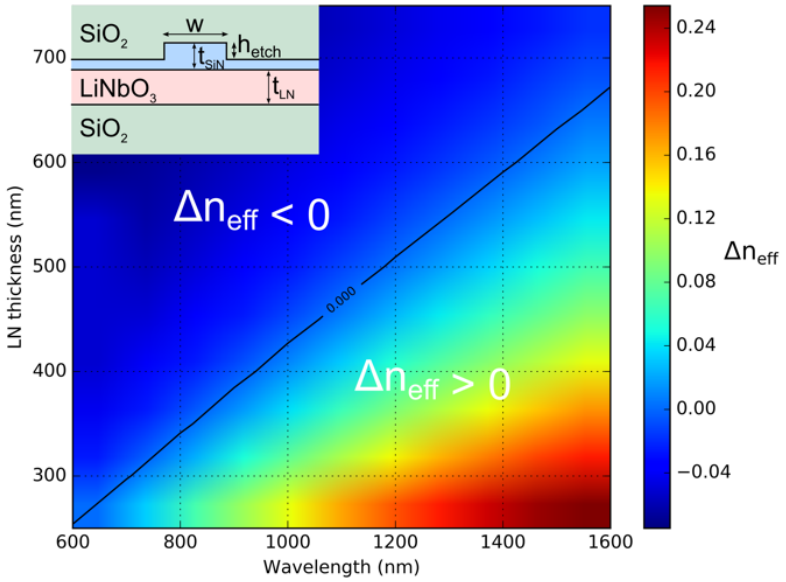


Figure 1. Effective index difference between the TE waveguide mode and the TM slab mode. Waveguide with $\Delta n_{eff} < 0$ can suffer from lateral leakage.

3. EXPERIMENTAL RESULTS

For the waveguide fabrication, we followed the fabrication steps described in Ref. [4]. First we patterned comb shaped electrodes on the surface of the lithium niobate thin-film, to which we applied three HV pulses to achieve domain inversion. The thinner lithium niobate thickness requires us to adapt the poling period of the quasi-phase matching structure to 4.98 µm. The length of the periodically poled waveguide was 4.8 mm. Afterwards, the comb electrodes for the poling process were removed by wet etching. A SiN layer with a thickness of 400 nm was deposited by reactive sputtering. The patterning of the SiN was achieved by standard lithography and a dry etching process. The waveguides were finally cladded with a SiO_2 cover layer with a thickness of 1 µm by means of PECVD.

The setup for characterizing the nonlinear waveguides is illustrated in Figure 2. Light from a tunable laser source is coupled in and out of the waveguide using lensed fibers. At the output the fundamental and SH wavelengths are separated using a wavelength division multiplexer (WDM) and detected by corresponding photodetectors.

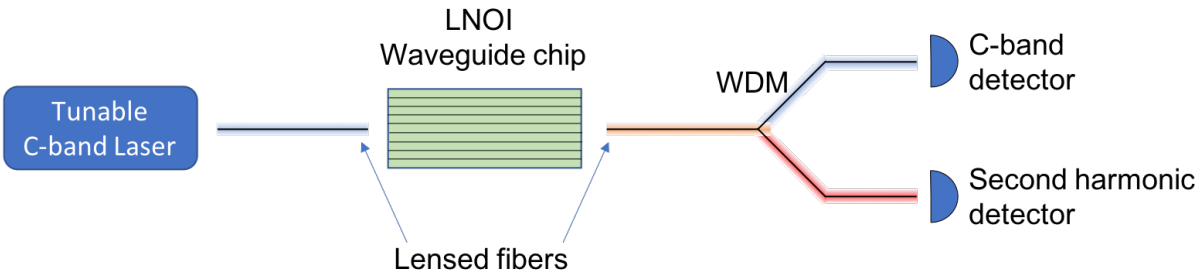


Figure 2. Illustration of the characterization setup for the SH generation in the periodically poled waveguides.

Figure 3(a) shows the fundamental and SHG power on the chip as a function of the pump wavelength. It can be seen that the SHG power is highest around a wavelength of 1.575 µm. The periodic oscillations in the fundamental and SH power can be explained by the Fabry-Perot effect from the end facets of the waveguide. Figure 3(b) shows the SHG efficiency as a function of the pump wavelength, where the green curve is a fitted sinc^2

function. It can be seen that a conversion efficiency of 780% $W^{-1}cm^{-2}$ is feasible in these waveguides, when the lateral leakage effect is avoided at the second harmonic wavelength.

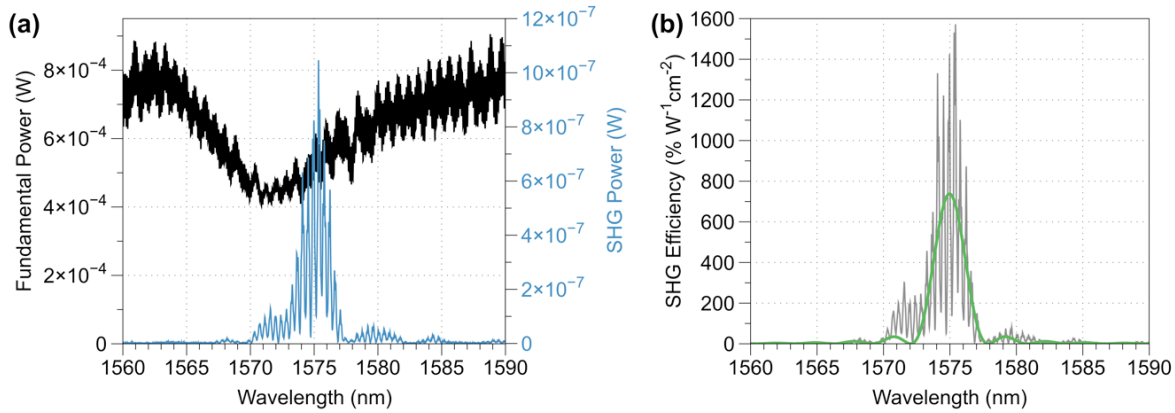


Figure 3. (a) Fundamental and SH power as a function of the pump wavelength; (b) SHG efficiency and fitted curve.

4. CONCLUSIONS

We have shown that engineering the lateral leakage of the SH in LNOI waveguides can enhance the conversion efficiency of the nonlinear optical process. This is achieved by reducing the thickness of the lithium niobate thin-film, so that the effective index of the TM slab mode is lower than the TE waveguide mode at the SH wavelength. This enabled us to demonstrate a SHG efficiency of ~780% $W^{-1}cm^{-2}$.

ACKNOWLEDGEMENTS

This research is supported by the ARC DP190102773 and DP190101576 as well as DARPA MTO DODOS contract (HR0011-15-C-055). We also would like to acknowledge Evatec AG for their support in the high quality SiN thin-film deposition.

REFERENCES

[1] A. Boes, *et al.*: "Status and Potential of Lithium Niobate on Insulator (LNOI) for Photonic Integrated Circuits," *Laser & Photon. Rev.*, vol. 24, 1700256–19, 2018.

[2] C. Wang, *et al.*: "Ultrahigh-efficiency wavelength conversion in nanophotonic periodically poled lithium niobate waveguides," *Optica*, vol. 5, 11, 1438-1441, 2018.

[3] C. Wang, *et al.*: "Integrated lithium niobate electro-optic modulators operating at CMOS-compatible voltages.," *Nature*, vol. 562, 7725, 101–104 (2018).

[4] L. Chang, *et al.*: "Thin film wavelength converters for photonic integrated circuits," *Optica*, vol. 3, 5, 531–5, 2016.

[5] M. A. Webster, *et al.*: "Width Dependence of Inherent TM-Mode Lateral Leakage Loss in Silicon-On-Insulator Ridge Waveguides," *Photon. Technol. Lett.,* vol. 19, 6, 429–431, 2007.

An Integrated Silicon Photonic Nonlinear Interferometer

Gary F. Sinclair [1], Takafumi Ono [1], Damien Bonneau [1], Mark G. Thompson [1],
Jonathan C.F. Matthews [1], John G. Rarity [1]
[1]*Quantum Engineering Technology Labs, H.H. Wills Physics Laboratory, University of Bristol, BS8 1TL, United Kingdom*
2

e-mail: gary.f.sinclair@bristol.ac.uk

ABSTRACT

We construct a nonlinear interferometer on a silicon photonic chip, where interference occurs between the production of photon pairs generated from two different spontaneous four-wave mixing waveguide sources. Nonlinear interferometers have demonstrated an improvement in measurement sensitivity beyond the shot-noise limit and offer the ability to sense and detect using light at different wavelengths. This demonstration of nonlinear interferometry on a silicon photonic chip establishes this important technology in a scalable and manufacturable chip-scale platform for the first time.

Keywords: Optical interferometry, Silicon photonics, Nonlinear optical devices

1 INTRODUCTION

Interferometric measurement of an unknown phase is of fundamental technological significance and has been the focus of much research in both the classical and quantum photonic communities. The sensitivity of a classical interferometer is fundamentally limited by the discrete photonic nature of light, leading to shot-noise limited sensitivity often called the *Standard Quantum Limit* (SQL). Several techniques have been proposed to increase the sensitivity of interferometers beyond the SQL, most noteably, by reducing the noise of the measured signal using squeezed states of light [1] and by increasing the resolution of the measurement using photon-number entangled states [2]. An alternative approach aims to increase the measured signal strength, while leaving the noise level unchanged, by replacing the beamsplitters of a conventional interferometer with parametric amplifiers [3]. This approach, referred to as a *Nonlinear Interferometer* (NLI) also finds application in the classical photonics community, due to the ability to perform phase measurement and signal detection using different wavelenghts of light [4].

Here we construct an on-chip nonlinear interferometer, composed of two spiral-waveguide photon-pair sources [6] ($1.4\,\mathrm{cm}$ long) which are pumped by a continuous-wave laser at $1544.5\,\mathrm{nm}$. The relative phase and intensity of each pump field can be controlled using the on-chip Mach-Zehnder Interferometer (MZI) and pump thermal phase-shifter. Pump 1 is demultiplexed from the photon pairs generated in source 1 by the on-chip filter (AMZI-1) and pump 2 is multiplexed into the input of source 2 by the filter AMZI-2. By adjusting the relative phase and brightness of each pump, a frustration of the photon pair generation process [5] can be demonstrated. Filtering and detection of the output photon flux is performed off-chip using two cascaded commerically available Dense Wavelength Division Multiplexers (Opneti) and superconducting nanowire single-photon detectors (Photon Spot).

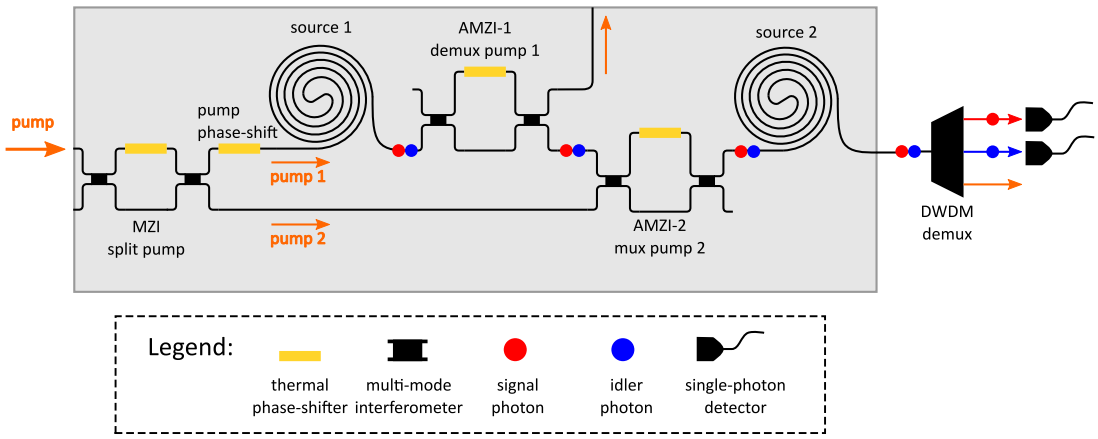


Figure 1. Layout of the on-chip nonlinear interferometer. Interference occurs between photon-pairs generated in source 1 and source 2, which are pumped by a continuous-wave laser with a controllable relative intensity and phase between each source. Single photon-detection occurs off-chip using superconducting nanowire single photon-detectors (PhotonSpot Inc).

2 RESULTS AND ANALYSIS

At the output of the NLI the state of the signal and idler modes is given by the concatenation of the two photon-pair generation processes [7], performed by source 1 and 2 with independent pumps:

$$|\psi_{\text{out}}\rangle = \left(\mathbb{1} + i\gamma P_2 e^{2i\Delta\phi_p} \int dz \int dt e^{i\Delta\beta z} \hat{A}_i^\dagger(z,t)\hat{A}_s^\dagger(z,t) + \cdots\right) \times \tag{1}$$

$$\left(\mathbb{1} + i\eta\gamma P_1 \int dz \int dt e^{i\Delta\beta z} \hat{A}_i^\dagger(z,t)\hat{A}_s^\dagger(z,t) + \cdots\right) |\text{vac}\rangle, \tag{2}$$

where γ is the waveguide nonlinearity parameter, P_n is the power of pump n, $\Delta\phi_p$ is the phase of pump 2 relative to pump 1, $\Delta\beta = 2\beta_p - \beta_s - \beta_i$ is the phase-matching term, $\hat{A}_{s|i}^\dagger$ are the creation operators acting on the signal and idler modes and η is the intermediate loss between sources 1 and 2. The spatial integrals are taken over the length of each source ($\{0, \text{L}\}$ for source 1 and $\{z_0, z_0 + L\}$ for source 2) and the temporal integrals extend over $t \in \{-\infty, \infty\}$. If we neglect events in which more than one photon-pair is generated in either source and we find the coincidence count rate between the signal and idler modes is,

$$\Gamma = \gamma^2 L^2 (\eta^2 P_1^2 + P_2^2)\,\text{sinc}^2\,(\Delta\beta_0 L/2)\left\{1 + \left(\frac{2R}{1+R^2}\right)\cos[2\Delta\phi_p - \theta_0]\right\}, \tag{3}$$

where $R^2 = (\eta P_1/P_2)^2$ is the ratio of the probability of detecting a photon pair generated in source 1 over source 2 and $\theta_0 = \Delta\beta z_0$ is a constant in our experiment. We note that the fringe visbility is given by $V = (\Gamma^{\max} - \Gamma^{\min})/(\Gamma^{\max} + \Gamma^{\min}) = 2R/(1+R^2)$. By adjust the pump powers such that the probability of detecting a photon pair from source 1 and 2 are equal ($R = 1$) we observe a maximum two-photon fringe visibility of $96.8\,\%$. We attribute the non-ideal fringe visibility to variations of the chip temperature, which result in fluctuations of the relative phase of both source pump fields.

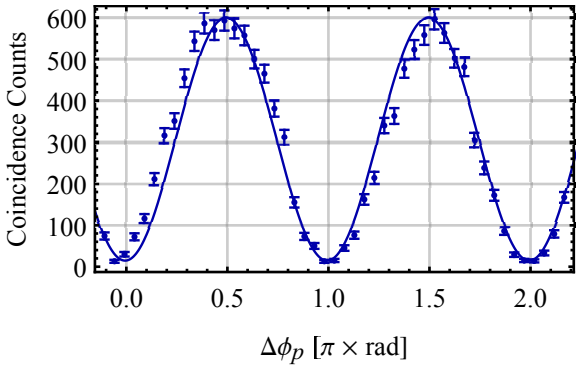


Figure 2. Coincidence counts (3 s integration time) as a function of the relative pump phase $\Delta\phi_p$.

3 CONCLUSIONS

We have constructed an nonlinear interferometer integrated on a silicon photonic chip for the first time. By adjusting the relative pump phase between each source we demonstrate frustrated photon-pair generation between both sources [5], with a maximum visibility of $96.8\,\%$, which we believe is limited by small (<2 mK) fluctuations in chip temperature. Nonlinear inteferometry has been proposed as means of increasing the sensitivity of quantum-enhanced sensors and of separating the sensing and detection wavelength of classical and quantum devices. We believe our demonstration of on-chip interferometry is an important step in bringing this highly applicable technology to the commerically and technologically promising silicon photonics platform.

REFERENCES

[1] C. M. Caves, "Quantum-mechanical noise in an interferometer,"' Phys. Rev. D, **23**, 1693–1708, (1981).

[2] M. J. Holland, and K. Burnett, "Interferometric detection of optical phase shifts at the Heisenberg limit," Phys. Rev. Lett., **71**, 1355–1358, (1993).

[3] B. Yurke, S. L. McCall, J. R. Klauder, "SU(2) and SU(1,1) interferometers," Phys. Rev. A, **33**, 4033–4054, (1986).

[4] D. A. Kalashnikov, A. V. Paterova, S. P. Kulik and L. A. Krivitsky, "Infrared spectroscopy with visible light", Nature Photonics, **10**, 98–101, (2016).

[5] T. J. Herzog, J. G. Rarity, H. Weinfurter and A. Zeilinger, "Frustrated two-photon creation via interference", Phys. Rev. Lett., **72**, 629, (1994).

[6] J. E. Sharping, K. F. Lee, M. A. Foster, A. C. Turner, B. S. Schmidt, M. Lipson, A. L. Gaeta and P. Kumar, "Generation of correlated photons in nanoscale silicon waveguides", Opt. Exp., **14**, 12388, (2006).

[7] G. F. Sinclair and M. G. Thompson, "Effect of self- and cross-phase modulation on photon pairs generated by spontaneous four-wave mixing in integrated optical waveguides", Phys. Rev. A, **94**, 063855, (2016).

Nonlinear silicon photonics for optical frequency synthesis

Neetesh Singh[1*], Ming Xin[1*], Nanxi Li[1,2], Diedrik Vermeulen[1], Alfonso Ruocco[1], Emir Salih Magden[1], Katia Shtyrkova[1], Erich Ippen[1], Franz X. Kärtner[1,3], and Michael R. Watts[1]

[1]Research Laboratory of Electronics, Massachusetts Institute of Technology, 77 Massachusetts Avenue, Cambridge, MA 02139, USA

[2]John A. Paulson School of Engineering and Applied Science, 29 Oxford Street, Harvard University, Cambridge, MA 02138, USA

[3]Centre for Free Electron Laser Science (CFEL)-DESY and University of Hamburg, Notkestrasse 85, 22607 Hamburg, Germany

Email: xinm@mit.edu, neeteshs@mit.edu

ABSTRACT

Optical frequency synthesizer, an optical counterpart of electronics frequency synthesizer is shown at chip scale using silicon photonics. We utilize the nonlinear properties of silicon, namely 3rd and electric field induced 2nd order effects for *f-2f* self-referencing. The frequency instability obtained in the telecom band is $1x10^{-12}$ at 1s level, comparable to a bench-top commercial optical frequency synthesizer system. An all on-chip silicon frequency synthesizer will have applications in the next generation optical communication, spectroscopic, detection and ranging systems making them widely available using the CMOS facility.

Keywords: Frequency synthesiser, ultrafast nonlinear optics, integrated optics, supercontinuum generation.

1. INTRODUCTION

An optical frequency synthesizer, which is phase coherently linked to the microwave frequency has various applications ranging from coherent communication, frequency metrology and optical atomic clocks [1-4].

Optical comb systems, produced through nonlinear optical processes, enable precision optical frequency synthesis in which a continuous wave (CW) laser source can be phase-locked and tuned over the wide bandwidth of a phase-locked frequency comb, to synthesize precise optical frequencies on demand. Recently a heterogeneously integrated optical frequency synthesizer was demonstrated [5]. To produce on a mass –scale, such systems need to leverage the well-established CMOS foundries. To this end, we demonstrate a silicon on insulator based optical frequency synthesizer.

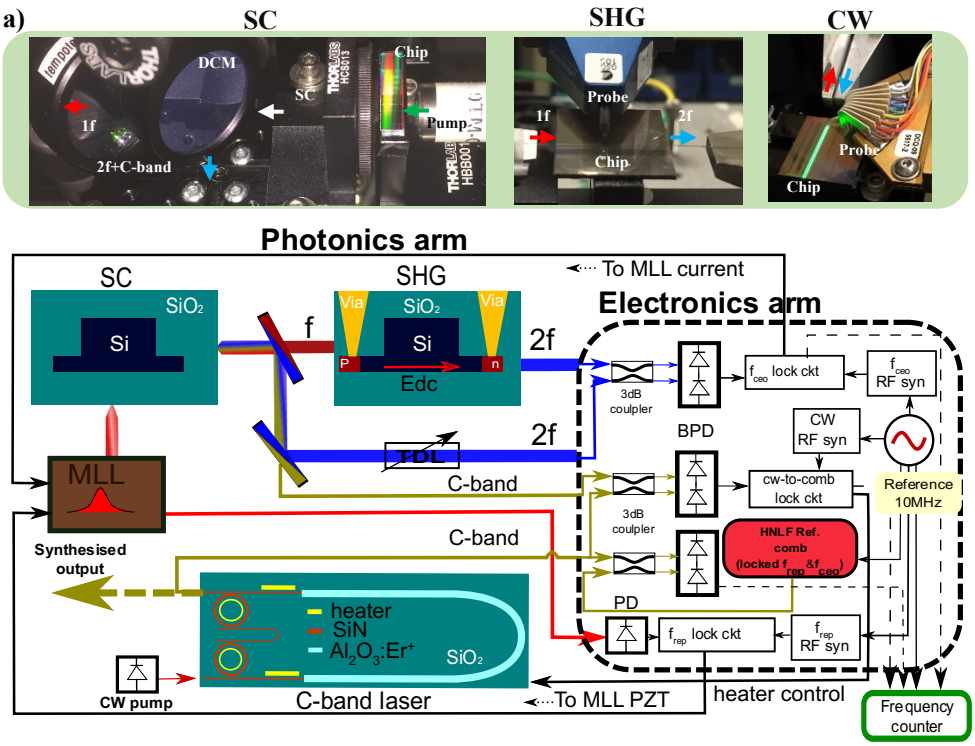


Fig.1 a) The images of the experimental setup for the supercontinuum (SC), second harmonic generation (SHG) and the tunable CW laser. b) The SPOFS circuit with its photonics and electronics arms. DCM: Dichroic mirror, TDL: Tunable delay line, BPD: Balanced photo diode, PD: Photodiode. The colored and black arrows are for optical and electronic signals. Solid and dashed lines from the RF reference (10MHz), are for locking the respective circuits and reading the values in the frequency counter, respectively. Synthesized output signal (dashed arrow from the CW laser).

The knowledge of the absolute frequency of an optical source, which is given as $f_{cw} = Nf_{rep} \pm f_{ceo} \pm f_{beat}$ in a comb system, lies at the heart of a frequency synthesizer. Here, N, f_{rep} and f_{ceo}, are the mode number, repetition frequency and the offset frequency of the mode locked laser, and the f_{beat} is the beat frequency between the CW laser and the mode locked laser (MLL) comb. We detect the f_{rep} by simply impinging a small amount of MLL signal onto a photodiode, and the f_{ceo} is detected by the silicon-based *f-2f* self-referencing scheme. Here, an MLL operating at 1.9 µm (thulium gain) producing <20 pJ pulses and <100 fs duration was used to pump a silicon waveguide to generate an octave spanning supercontinuum [6] as shown in Fig. 2(a). The *f* part around 2.3 µm was frequency doubled in an electric field induced quasi phase matched silicon waveguide [7]. The experimental and simulated SHG signal is shown in Fig. 2c. The second harmonic signal bandwidth and strength depends on the applied DC field and the group velocity mismatch between the *f* and the *2f* signal, the higher it is the lower the conversion bandwidth. The group velocity curve for the SHG waveguide is shown in Fig. 2d. The frequency doubled signal is mixed with the *2f* signal of the SC to obtain the f_{ceo} of the MLL, whose beat note is shown in Fig. 2(b). All of these frequencies are locked to a common RF reference (10 MHz), using their respective locking circuits, as shown in Fig. 1. To measure N of a low f_{rep} mode-locked laser, due to the lack of a wavemeter, a technique in which f_{rep} is slightly varied multiple times using PZT (in proportion to the CW laser linewidth) is employed [8]. We measured N with an error better than ±0.5 [9], which will improve further with an all integrated system down to <±0.02.

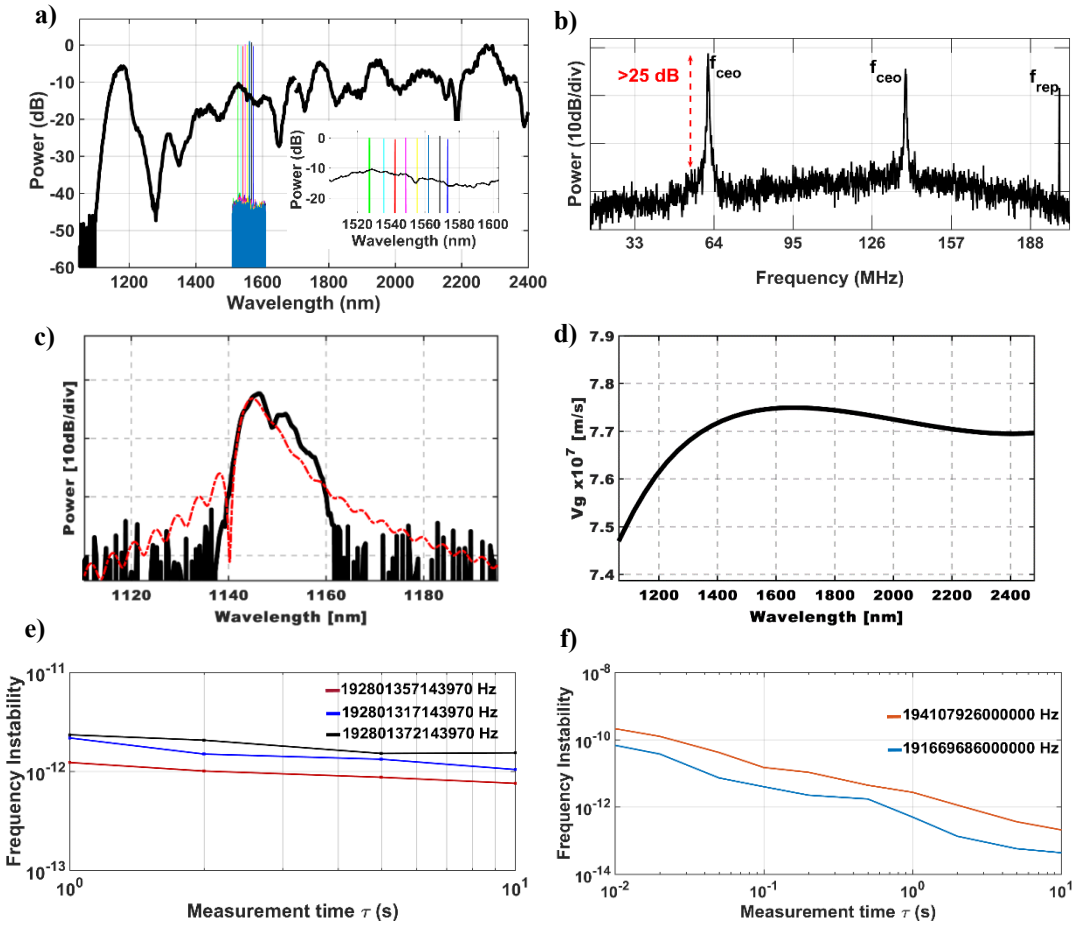


Fig.2 a) The SC spectrum with the CW laser tuning spectrum b) Measured f_{ceo} signal. c) The experimental and simulated SHG signal. d) the group velocity curve for the EFISH waveguide. e) Out-of-loop frequency instability measurement at three different frequencies f) Out-of-loop frequency instability measurement using commercial HNLF comb, showing 20 nm range tuning capability of the CW laser [6].

The absolute frequency instability of the silicon frequency synthesizer was determined using an external, out-of-loop, reference comb based on a highly nonlinear fiber (HNLF) which was also locked to the same RF reference (as shown in Fig.1). The beat between the silicon-comb stabilized CW laser and the reference comb for three different frequencies are shown in Fig 2(e), which were tuned to using the integrated heaters of the CW laser [10]. We achieved a frequency instability of 1×10^{-12} @ 1s level comparable to a commercial comb system. The tuning range was kept limited due to the combination of unavoidable high coupling losses of the SC signal at the telecom window (due to the use of free space optics), and the thermal fluctuations of the CW laser (due to the end-fire fiber coupling), which compromised the locking strength. To confirm that, we used a significantly

stronger SC signal using a commercial HNLF comb and demonstrated a tight lock, enabling a 20 nm tuning range in the C-band (Fig. 2 (f)). Thus, with an all integrated system the coupling loss and the thermal fluctuations will be entirely suppressed. The frequency instability slope can be improved to be $1/\tau$ by taking data with multiple gate times set in the frequency counter, as in Fig 2(d).

2. CONCLUSIONS

In conclusion, we have demonstrated a silicon photonics optical frequency synthesizer with frequency instability comparable to a commercial system. In future we will integrate to the frequency synthesiser an efficient rare earth doped (thulium) silicon based mode locked laser.

ACKNOWLEDGEMENTS

This work was supported under the DARPA's DODOS project; contract number HR0011-15-C-0056.

REFERENCES

1. D. J. Jones, *et. al.*: Carrier-Envelope Phase Control of Femtosecond Mode-Locked Lasers and Direct Optical Frequency Synthesis," *Science* vol. 288**,** pp. 635-639 (2000).
2. Udem, T. *et. al*: Optical frequency metrology. *Nature* 416, 233–237 (2002).
3. Nakazawa, M., Kikuchi, K. & Miyazaki, T. *Spectral density optical communication* (Springer, 2010)
4. Ataie, V. *et. al.*: Ultrahigh count coherent WDM channels transmission using optical parametric comb-based frequency synthesizer. *J. Lightwave Technol.* vol. 33, pp. 694-699 (2015).
5. D. T. Spencer, *et al.* "An optical-frequency synthesizer using integrated photonics," *Nature,* 557, 81-85 (2018)
6. N. Singh, *et. al*. "Octave-spanning coherent supercontinuum generation in silicon on insulator from 1.06μm to beyond 2.4μm," *Light Sci. Appl.* vol. 7, pp. 1-8 (2018).
7. E. Timurdogan, et. al. "Electric Field-Induced Second Order Nonlinear Optical Effects in Silicon Waveguides," *Nat. Photon*. vol. 11, pp. 200-206 (2017).
8. L. S. Ma, *et. al.* "A New Method to Determine the Absolute Mode Number of a Mode-Locked Femtosecond-Laser Comb Used for Absolute Optical Frequency Measurements," *IEEE J. Sel. Top. Quantum Electron.* vol. 9, pp. 1066-1071, 2003.
9. M. Xin, *et. al.* "An optical frequency synthesizer using a widely tunable integrated erbium tunable laser," *submitted to CLEO* (2019).
10. N. Li, et.al. "Monolithically integrated erbium-doped tunable laser on a CMOS-compatible silicon photonics platform," *Opt. Express.* vol. 26, pp. 16200-11, 2018.

Integrated quantum photonic technologies for applications communications and computation

(Invited paper)

Mark G. Thompson
Quantum Engineering Technology Labs, University of Bristol, United Kingdom
e-mail: mark.thompson@bristol.ac.uk

Abstract

Quantum photonics has emerged as a promising approach to realizing large-scale and complex quantum technologies for applications in quantum communications and quantum information processing. Here we overview recent developments presenting circuits comprising hundreds of photonic components integrated into single coherent quantum systems.

Keywords: Quantum photonics, integrated optics, quantum information processing, quantum communications.

1. Introduction

Photonics is a promising approach to realizing quantum information technologies, where entangled states of light are generated and manipulated to implement fundamentally new modes of computation, simulation and communication, as well as enhanced measurements and sensing. Historically bulk optical elements on large optical tables have been the means by which to realize proof-of-principle demonstrators in quantum physics. Integrated quantum photonics has enabled a step change in this technology by controlling and manipulating single photons within miniature waveguide circuits. This technology approach is now being used to pioneered breakthroughs in quantum communications, quantum sensing and quantum information processing. Here we present recent developments in chip-to-chip quantum communications and on-chip quantum information processing.

2. Chip-based quantum communications

Quantum Key Distribution (QKD) provides a provably secure approach to share secrete keys used to encrypt information by transmitting single photons through a quantum channel. It is one of the first commercially available quantum technologies and a leading candidate for securing communications against attacks from future quantum computers. Integrated photonics provides a stable, compact, miniaturized and robust platform to implement quantum communications systems. The inherent phase stability of integrated photonics makes it particularly suitable for manipulating quantum information encoded in different time-bins, an encoding extensively used in fiber-based QKD systems.

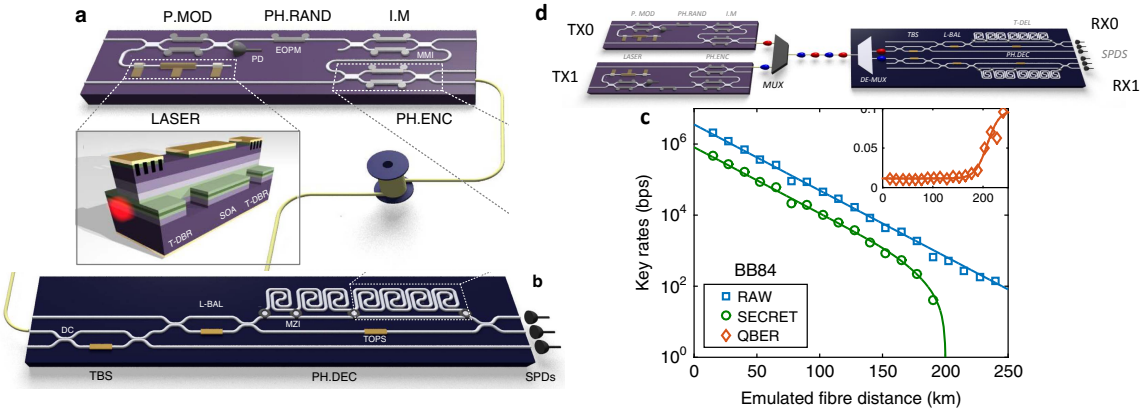


Figure 1: Chip-to-chip quantum communication system (a) InP transmitter chip (b) SiON receiver chip (c) Key rate for emulated fiber distance (d) WDM QKD link [1]

Chip-based QKD transmitters have been implemented in both the InP[1] and Silicon [2], [3] material platforms, with the first demonstration of a fully integrated chip-to-chip QKD system implemented with an InP transmitter chip and a Silicon Oxynitride receiver chip (Figure 1) [1]. These chips provide a complete chip-to-chip quantum photonic solution, and through programmable quantum circuitry can implement multiple QKD protocols, including Coherent One Way (COW) operating, Differential Phase Shift (DPS) and BB84 (see Figure 1c for an example). The data rate of these systems can be increased through wavelength division multiplexing (WDM), where multiple secrete keys are distributed within a single optical fiber on different wavelengths. Figure 1c show one such approach were a WDM-QKD system was implemented using two GHz clocked InP QKD transmitters

and a single Silicon Oxynitride receiver with integrated de-multiplexing. The InP chips are fully integrated, incorporating all the necessary components including a tunable laser source and high-speed phase modulators. Using on-chip asymmetric MZI filters for wavelength de-multiplexing, the receiver splits the two channels into independent copies of the reconfigurable decoding circuitry. The combined WDM channels increase the secrete key rate by a factor of two, to 1.11 Mbit/s over a 20 km emulated fiber. The increase in rates, and ability to scale up these circuits opens the way to new and advanced integrated quantum communication technologies and larger adoption of quantum-secured communications.

3. Chip-based quantum information processing

Quantum information processing, and particularly quantum computing, has generated much interest for its potential ability to outperform classical computing for many important tasks. Photons are considered as a promising candidate for implementing quantum information processing owing to their properties of long coherence time, ease of manipulation and light-speed transmission. The silicon-based quantum technology platform, where quantum states of light can be generated and manipulated using entirely silicon-based waveguide circuits [4], offers a range of benefits for quantum information processing, including high nonlinearities for efficient on-chip generation of quantum states of light, and high component densities for complex circuits. Using this silicon quantum photonic technology platform a wide range of quantum information processing demonstrators have been realized. Here we focus specifically on the more recent large-scale implementations.

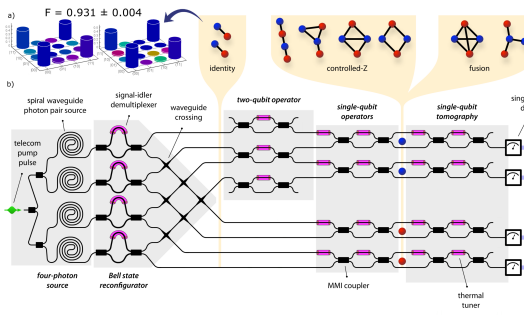


Figure 2: Graph state generator: (a) Reconstructed density matrices of on-chip Bell pairs, (b) Schematic of device [6]

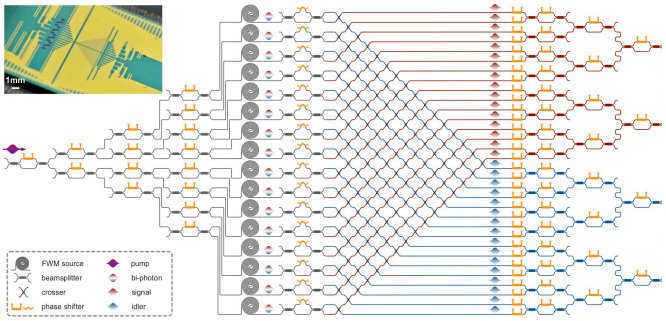


Figure 3: Highly reconfigurable quantum circuit for the generation, control and analysis of muti-dimensional quantum entanglement [5]

Programmable four-photon graph states on a silicon chip

Modern approaches to quantum information processing demands the generation of large entangled quantum states, typically graph states. To investigate such states of light, integrated quantum circuits are required that can generate and manipulate indistinguishable multi-photon states. Figure 2 show the first integrated quantum circuit capable of the on-chip generation and manipulation of four-qubit, four-photon graph states. The device generates two pairs of photons on-chip, then applies a switchable entangling gate (performing either a fusion or a controlled-*Z* operation) in order to entangle the qubit states and access all 6 of the 4-qubit graph states - creating genuine four-qubit entanglement. Whether the entangling gate is set to perform a fusion or a CZ operation determines the type of entanglement in the produced four-qubit state. The fusion operation yields Greenberger–Horne–Zeilinger type entanglement, whereas the CZ operation yields entanglement of the cluster state type. These comprise the only two classes of graph-state entanglement in four qubits, which are locally equivalent to the entire set of four-qubit graph states. The device produces Bell pairs with state-of-the-art fidelity, and the star-type graph state (inset of Figure 5) are verified by measuring that state's stabilizers.

Large-scale multi-dimensional quantum photonics

Multi-dimensional quantum systems exhibit distinct quantum properties and offer improvements in key applications such as increasing capacity in quantum communication, strengthening quantum correlations, and enriching quantum simulation and computing schemes. Photons represent a promising platform able to naturally encode and process these 'qudits' in various degrees of freedom, e.g., orbital angular momentum, temporal bin and frequency. However, these approaches present limitations in terms of controllability, precision, universality and a full integration of elements, which represent bottlenecks for further developments of multidimensional quantum photonic technologies.

By utilizing large-scale silicon quantum photonics, a chip was realized that could create, control and multidimensional entanglement up to dimensions 15 × 15 [5]. The chip (Figure 3) comprised 16 photon sources that use spontaneous four-wave mixing to generate photon pairs in a superposition across 16 optical modes; 93 thermo-optic phase shifters; 122 multimode interference beamsplitters; 256 waveguide crossers and 64 grating

couplers. Greater than 500 photonic components monolithically integrated on a single chip. This chip enables the generation of multidimensional entangled states with an arbitrary degree of entanglement and arbitrary multidimensional measurements with very high fidelity, verified by quantum state tomography and Bell violations.

4. Conclusion

Integrated quantum photonics is a versatile technology platform that is proving invaluable in the development of future quantum information technology applications, particularly in quantum communications and quantum computation. Large-scale quantum photonic circuits enable the on-chip generation and precise manipulation of complex photon states of light, whilst these stable, compact, miniaturized and robust platforms are also delivering the next generation of quantum communications devices.

5. References

[1] P. Sibson, C. Erven, M. Godfrey, S. Miki, T. Yamashita, M. Fujiwara, M. Sasaki, H. Terai, M. G. Tanner, C. M. Natarajan, R. H. Hadfield, J. L. O'Brien, and M. G. Thompson, "Chip-based quantum key distribution," *Nat Comms*, vol. 8, p. 13984, 2017.

[2] C. Ma, W. D. Sacher, Z. Tang, J. C. Mikkelsen, Y. Yang, F. Xu, T. Thiessen, H.-K. Lo, and J. K. S. Poon, "Silicon photonic transmitter for polarization-encoded quantum key distribution," *Optica*, vol. 3, no. 11, pp. 1274–1278, 2016.

[3] P. Sibson, J. E. Kennard, S. Stanisic, C. Erven, J. L. O'Brien, and M. G. Thompson, "Integrated silicon photonics for high-speed quantum key distribution," *Optica*, vol. 4, no. 2, pp. 172–177, 2017.

[4] J. W. Silverstone, D. Bonneau, M. G. Thompson, and J. L. O'Brien, "Silicon Quantum Photonics," *IEEE Journal of Selected Topics in Quantum Electronics*, vol. 22, no. 6, pp. 1–13, 2016.

[5] J. Wang, S. Paesani, Y. Ding, R. Santagati, P. Skrzypczyk, A. Salavrakos, J. Tura, R. Augusiak, L. Mančinska, D. Bacco, D. Bonneau, J. W. Silverstone, Q. Gong, A. Acín, K. Rottwitt, L. K. Oxenløwe, J. L. O'Brien, A. Laing, and M. G. Thompson, "Multidimensional quantum entanglement with large-scale integrated optics.," *Science*, p. eaar7053, 2018.

[6] J. C. Adcock, C. Vigliar, R. Santagati, J. W. Silverstone, and M. G. Thompson, "Programmable four-photon graph states on a silicon chip." arXiv:1811.03023v1, 2018.

High-Speed Photodetectors

(Invited talk)

Andreas Beling
ECE Department, University of Virginia, Charlottesville, VA 22904, USA
e-mail: andreas@virginia.edu

ABSTRACT

This talk will review advances in photodetectors for high-speed applications with focus on analog systems. Recent results from flip-chip bonded modified uni-traveling carrier photodiodes and high-power photodiode arrays on silicon will be discussed.

Keywords: photodiode, photodetector

INTRODUCTION

High-speed photodiodes continue to be critical components in a wide range of photonic systems. In analog photonics applications including radio-over-fiber, radio frequency (RF) signal generation, and antenna remoting, photodiodes (PDs) with high power handling capability and high linearity are required to maintain high RF gain and large spurious-free dynamic range [1]. To this end our team at University of Virginia has developed discrete, surface-illuminated InGaAs/InP modified uni-traveling carrier (MUTC) photodiodes that achieved -2.6 dBm RF output power at 160 GHz [2]. For integrated microwave systems on silicon, we developed arrays of Ge/Si photodiodes that provide 10 dBm RF output power at 12 GHz.

1. HIGH-SPEED MODIFIED UNI-TRAVELING CARRIER PHOTODIODES

Similar to a uni-traveling carrier (UTC) PD [3], the MUTC PD includes an un-depleted narrow-bandgap absorber and a wide-bandgap electron drift layer. In addition, and to facilitate electron transport at the heterojunction interface, an un-doped absorber with an appropriate thickness is inserted between the un-depleted absorber and the drift layer. The fact that the photocurrent is mostly based on electron transport provides higher speed since electrons typically have higher velocities than holes, especially at low electric fields. The drift layer is lightly n-type doped for charge compensation. The charge from the ionized donors pre-distorts the electric field and can counteract the space charge screening effect at a high current and thus avoids saturation [4]. A critical factor that limits the RF output power of a PD is Joule heating in the high-electric field region. We have shown that improvements in RF output power can be achieved by flip-chip bonding the PD onto an AlN or diamond substrate that has high thermal conductivity [5].

Previously, we have demonstrated back-illuminated charge-compensated MUTC PDs with 9.6 dBm RF output power at 100 GHz [6]. To enhance the 3 dB-bandwidth, these devices were designed with a high-impedance coplanar waveguide (CPW) between the PD and the RF probe pad that provided inductive peaking at 100 GHz. To increase the RF output power at higher frequencies (beyond the 3 dB bandwidth), we recently flip-chip bonded similar MUTC PDs to a low-inductance transmission line on a AlN submount. The PD's pads were attached to a CPW with a 130-µm signal-to-ground gap using thermo-compression Au-Au bonding (Fig.1 inset). A short tapered transmission line connected the stub to a 50 Ω probe pad with a 54-µm signal-to-ground gap. This optimized CPW design reduced the frequency response roll-off beyond 100 GHz and extended the usable frequency range up to 160 GHz. Figure 1 shows the measured RF output power. A 9-µm diameter PD reached a maximum RF output power of −2.6 dBm at 160 GHz and −3 V, and a saturation current of 40 mA. The dark current was 0.4 nA and the responsivity was 0.2 A/W at 1550 nm [2].

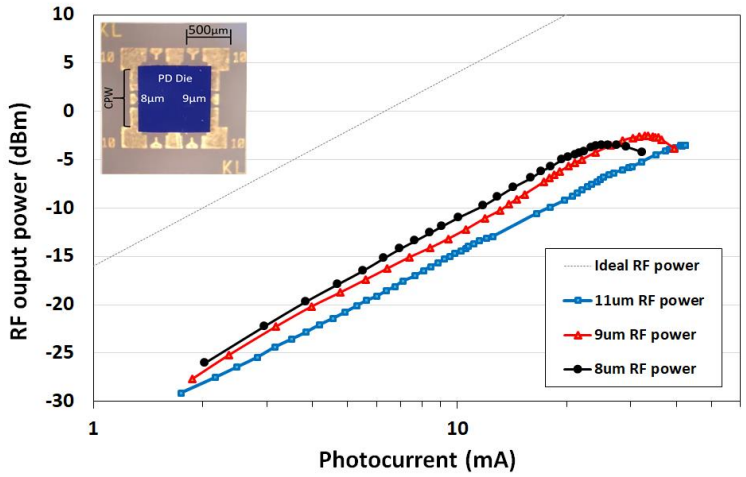


Figure 1. Radio frequency (RF) output power at 160 GHz of modified uni-traveling carrier photodiodes with 11 μm, 9 μm, and 8 μm diameters. The inset shows a PD die on the submount after flip-chip bonding.

2. HIGH-POWER GERMANIUM/SILICON PHOTODIODE ARRAYS

Recently, there has been an increasing interest in integrated microwave photonics systems, which take advantage of the silicon photonics platform to enable reliable, compact and low cost solutions [7]. These photonic integrated circuits benefit from high-power high-linearity waveguide photodiodes that can be monolithically integrated onto Si. While high-speed Ge/Si PDs with low dark current at low bias and high responsivity are well-developed for digital applications, only few high-power Ge-on-Si PDs have been reported to date [8-11].

Recently, we have demonstrated Ge/Si waveguide photodetector arrays for high-power analog applications utilizing the AIM Photonics silicon foundry [12]. Figure 2 shows a summary of the RF output power and compression measured at the 3-dB bandwidth for PD arrays and single PDs. PD arrays with 8, 4, and 2 elements have output powers of 14 dBm, 10 dBm, and -0.4 dBm at 5 GHz, 12 GHz, and 18 GHz, respectively. In comparison, single photodiodes with and without spiral inductor for inductive peaking reached -5 dBm at 34 GHz and 21 GHz, respectively.

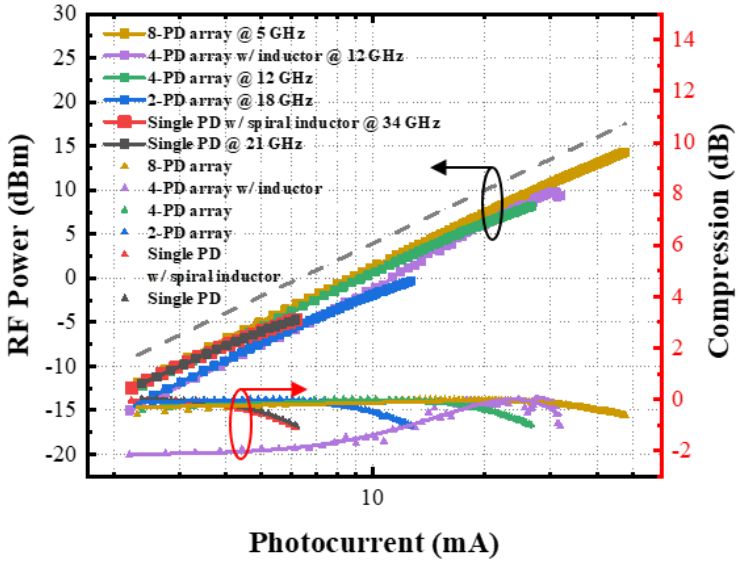


Figure 2. Summary of output RF power and compression measured at each photodetector's 3-dB bandwidth and -5 V bias.

ACKNOWLEDGEMENTS

Part of this work was supported by DARPA, the Naval Research Laboratory, and the Air Force Research Laboratory.

REFERENCES

[1] V. J. Urick, J. D. McKinney, and K. J. Williams, "Fundamentals of Microwave Photonics," Ch. 10, Wiley Series in Microwave and Optical Engineering, Kai Chang, editor, 2015.

[2] J.S. Morgan, K. Sun, Q. Li, S. Estrella, M. Woodson, K. Hay, M. Mashanovitch, A. Beling, "High-Power Flip-Chip Bonded Modified Uni-Traveling Carrier Photodiodes with −2.6 dBm RF Output Power at 160 GHz," In Proceedings of the *2018 IEEE Photonics Conference (IPC)*, Reston, VA, USA, 30 September–4 October 2018.

[3] N. Li, R. Sidhu, X. Li, F. Ma, S. Demiguel, X. Zhen, A.L. Holmes, J.C. Campbell, D.A. Tulchinsky, K.J. Williams, "High-saturation-current InGaAs/InAlAs charge-compensated uni-traveling-carrier photodiode," Phys. Stat. sol. (a) (2004), 201: 3037-3041.

[4] T. Ishibashi, N. Shimizu, S. Kodama, H. Ito, T. Nagatsuma, T. Furuta, "Uni-Traveling-Carrier Photodiodes," in Ultrafast Electronics and Optoelectronics, M. Nuss and J. Bowers, eds., Vol. 13 of OSA Trends in Optics and Photonics Series (Optical Society of America, 1997), pp. 83–87.

[5] X. Xie, Q. Zhou, Li, K.; Shen, Y.; Li, Q.; Yang, Z.; Beling, A.; Campbell, J.C. Improved power conversion efficiency in high performance photodiodes by flip chip on diamond. Optica 2014, 1, 429–435.

[6] Q. Li, K. Li, Y. Fu, X. Xie, Z. Yang, A. Beling, J.C. Campbell, "High-power flip-chip bonded photodiode with 110 GHz bandwidth," J. Lightwave Technol. 2016, 34, 2139–2144.

[7] D. Marpaung, C. Roeloffzen, R. Heideman, A. Leinse, S. Sales, and J. Capmany, "Integrated microwave photonics," Laser & Photonics Reviews, 7: 506-538. doi:10.1002/lpor.201200032, 2013

[8] M. J. Byrd, E. Timurdogan, Z. Su, C. V. Poulton, N. M. Fahrenkopf, G. Leake, D. D. Coolbaugh, and M. R. Watts, "Mode-evolution-based coupler for high saturation power Ge-on-Si photodetectors," Opt. Lett., vol. 42, no. 4, pp. 851-854 (2017).

[9] C. Chang, J. H. Sinsky, P. Dong, G. Valicourt, and Y. Chen, "High-power dual-fed traveling wave photodetector circuits in silicon photonics," Opt. Express, vol. 23, no. 7, pp. 22857-22866 (2015).

[10] A. Ramaswamy, M. Piels, N. Nunoya, T. Yin, and J. E. Bowers, "High power silicon-germanium photodiodes for microwave photonic applications," IEEE Trans. Microw. Theory Techn., vol. 58, no. 11, pp. 3336-3343 (2010).

[11] L. Bogaert, K. Van Gasse, T. Spuesens, G. Torfs, J. Bauwelinck, G. Roelkens, "Silicon photonics traveling wave photodiode with integrated star coupler for high-linearity mm-wave applications," Opt. Express **26**, 34763-34775 (2018).

[12] K. Sun, R. Costanzo, T. Tzu, Q. Yu, S. M. Bowers and A. Beling, "Ge-on-Si Waveguide Photodiode Array for High-Power Applications," *2018 IEEE Photonics Conference (IPC)*, Reston, VA, 2018, pp. 1-2.

Full-Duplex Analog Radio-over-Fiber System based on an Integrated Transceiver with a Silicon Microring Modulator and a Transfer-Printed III-V Photodetector

Student Paper

Zhenzhou Tang[1,2,3], Jing Zhang[2,3], Shilong Pan[1], Gunther Roelkens[2,3], Dries Van Thourhout[2,3]
[1] Nanjing University of Aeronautics and Astronautics, Nanjing, 210016, China
[2]Ghent University-imec, Technologiepark 126, 9052, Ghent, Belgium
[3] Center for Nano- and Biophotonics, Ghent University, Belgium
e-mail: zhenzhou.tang@ugent.be, tangzhzh@nuaa.edu.cn

ABSTRACT

A full-duplex analog radio-over-fiber (RoF) system based on an integrated transceiver is proposed. The transceiver incorporates a C-band silicon microring modulator for the electrical-to-optical (E-O) conversion of the downstream signal and an O-band III-V photodetector (PD) is transfer printed onto the same chip for the optical-to-electrical (O-E) conversion of the upstream signal. With the integrated transceiver, a proof-of-concept experiment is carried out. An error vector magnitude (EVM) less than 6 % is achieved in the X-band for a 1-Gbps 16QAM-modulated signal transmitted through 5-km single mode fiber.

Keywords: radio transceivers, microwave photonics, silicon photonics, photodetector.

1. INTRODUCTION

It is well known that next-generation wireless communication systems, 5G for example, have stringent requirements in terms of massive device connectivity, high capacity, large coverage, low latency and sustainable cost. Cloud radio access networks (CRANs) are regarded a key technical enabler, since all the remote radio heads (RRHs) are connected to a baseband unit (BBU) "pool" in the central office (CO) via optical fiber [1]. Thanks to this centralized architecture, the resources in the CO can be shared according to the traffic requirements, and it also enables co-operative radio technologies to reduce the interference between the different RRHs, allowing a further increase in their density. Obviously, to ensure a connection of a large number of cells, the cost, complexity and power consumption of the RRH is expected to be as low as possible. Analog radio-over-fiber (RoF) technology, due to its simple RRH structure, is considered one of the most convincing solutions [2]. In the analog RoF link, the signal is directly upconverted to an analog signal at the carrier frequency and transmitted to the RRH via optical fiber, so no digital-to-analog (DAC) converter and frequency conversion are needed in the RRH. In recent years, various systems based on an analog RoF architecture have been reported, focusing mainly on pushing the carrier frequency to high frequency bands (millimetre-wave [3] or even THz [4] band) or combining RoF with other techniques, such as massive MIMO [5] and coordinated multipoint (CoMP) [6], to improve the capacity and spectral efficiency.

In this paper, we propose an integrated silicon photonic transceiver for a full-duplex analog RoF system. Silicon photonics offers compatibility with the mature CMOS technology and enables low cost transceiver manufacturing in high volume, which is very attractive for the wireless communications of the future. In the proposed transceiver, a C-band silicon microring modulator is integrated to realize electrical-to-optical (E-O) conversion for the downstream link, and an O-band III-V photodetector (PD) for the upstream link is integrated onto the same chip via transfer printing technology for the optical-to-electrical (O-E) conversion. Since the transfer-printed PD is 'transparent' for the C-band downstream signal, the III-V PD is directly placed onto the grating coupler without affecting the downstream signal, which reduces the footprint of the transceiver and also enables the duplexing of C-band and O-band signals in the same optical fiber. With the integrated transceiver, a proof-of-concept experiment is carried out. An error vector magnitude (EVM) less than 6% is achieved in the X-band for a full-duplex 1-Gbps 16QAM-modulated signal transmitted through 5-km single mode fiber.

2. DEVICE AND SYSTEM

Fig. 1(a) shows the microscope image and schematic cross-section of the proposed integrated transceiver. The silicon photonic circuit, which consists of two grating couplers for the in/out coupling of light and a C-band microring modulator for the downstream modulation, is realized in imec's iSIPP25G platform. The insertion loss of each grating coupler is about 4 dB. The free spectral range (FSR) of the microring modulator is about 12.72 nm and the 3-dB RF bandwidth at −1 V bias is about 15 GHz. To realize a full-duplex communication, a PD is required for the photodetection of the upstream signal. The integration of the PD to the silicon photonic wafer is realized

by a technology called transfer printing [7]. Transfer printing, with a schematic flow shown in Fig. 1(b), is regarded as a promising solution for massively parallel integration of III-V components to another substrate, which leads to a significant improvement in material use and throughput compared to conventional wafer bonding and flip-chip-like assembly methods. In this paper, the PD to be transfer printed is designed to consist of a 1 μm thick intrinsic InGaAsP absorbing layer with a cut-off wavelength of 1.37 μm (i.e., O-band), which is 'printed' on the grating coupler to make the transceiver compact. The measured responsivity of the III-V PD in the O-band is about 0.5 A/W (4 orders of magnitude higher than that at the C-band), and the 3-dB RF bandwidth is about 11.5 GHz. The detailed information of the integrated transceiver, for example, the layer information of the PD, the process flow of the transfer printing, the S_{21} responses of the microring modulator and PD, etc., can be found in our previous publication [8].

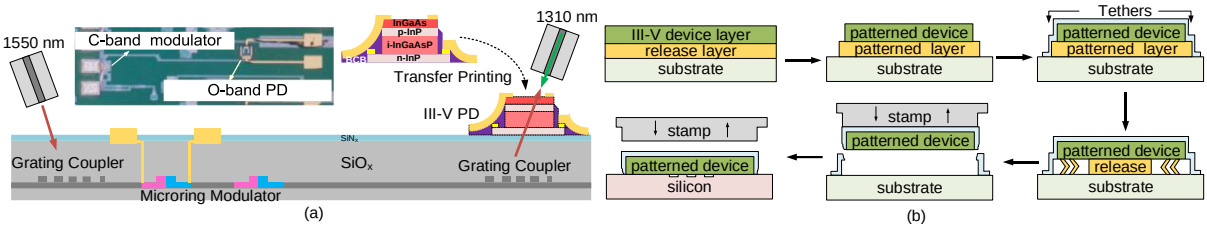


Figure 1. (a) Microscopic image and cross section of the integrated transceiver, (b) schematic flow of the transfer printing process.

Based on the proposed transceiver, a full-duplex analog RoF system can be built, as shown in Fig. 2. In the CO, a C-band optical carrier is coupled into the transceiver from a grating coupler. The optical carrier is intensity-modulated by a downstream signal in the silicon microring modulator, and coupled out of the chip by another grating coupler. The modulated signal is then transmitted to an RRH through optical fiber. In the RRH, the optical signal is demultiplexed by a wavelength division multiplexer (WDM) and sent to a PD, after being amplified by an erbium doped optical amplifier (EDFA). For the upstream link, an O-band laser source is employed in the RRH and sent to an O-band Mach-Zehnder modulator (MZM), which is driven by an upstream signal. The modulated optical signal is duplexed with the downstream signal by the WDM and transmitted back to the CO through the same optical fiber. When the light is applied to the transfer-printed III-V PD, the upstream signal is then converted to the electrical domain.

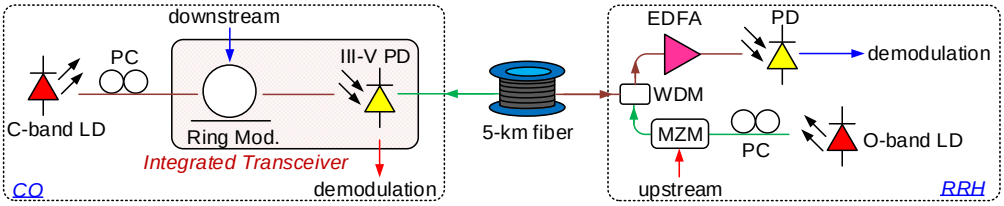


Figure 2. Schematic diagram of the full-duplex analog RoF system based on the integrated transceiver.

3. EXPERIMENT AND RESULTS

An experiment based on the scheme shown in Fig. 2 is carried out. For the downstream link, 12-dBm continuous wave (CW) light generated by a tunable laser source (Santec TSL-510) is coupled into the chip via a polarization controller (PC) in the CO. To ensure efficient E-O modulation, the wavelength of the optical carrier is set to be 1552.128 nm, aligned to the resonance of the microring modulator. Produced by an arbitrary waveform generator (Keysight M9052A), 16QAM data at a 10 GHz carrier frequency with a data rate of 1 Gb/s (250-Mbaud) is amplified by a 10-GHz RF amplifier and applied to the silicon microring modulator, coupled with a 0.7 V DC voltage through a bias tee. The modulated downstream signal is then coupled out and transmitted to a RRH through 5-km single-mode fiber. In the RRH, the downstream signal is amplified by an EDFA and sent to a commercially-available PD with a bandwidth of 20 GHz and a responsivity of ~0.7 A/W. The detected electrical signal is sent to one channel of a 63-GHz real time oscilloscope (Keysight DSA-Z 634A) to realize QAM signal demodulation.

For the upstream link, 5-dBm CW light with a wavelength of 1356 nm is generated by another tunable laser source (Santec TSL-510) and sent to an O-band modulator via another PC. The upstream signal, 250-MBaud 16QAM data with a carrier frequency of 8 GHz, is also generated by the AWG. The modulated O-band upstream optical signal is duplexed with the C-band downstream signal by the WDM and transmitted back to the CO through the same 5-km optical fiber. In the CO, the upstream signal is detected by the transfer-printed III-V PD, which is biased at -1 V, with a responsivity of 0.5 A/W. The output signal of the III-V PD is sent to another channel of the real time oscilloscope for the signal demodulation and analysis.

Fig. 3(a) shows the measured error vector magnitude (EVM) versus the received optical power for the downstream link. As can be seen, for a received optical power of -12.5 dBm, the measured EVM is about 5 %. A

clear constellation diagram is observed and shown as the inset in Fig. 3(a). We can also see that, when the 5 km optical fiber is inserted in the link, the EVM is nearly unchanged, which is due to the low fiber transmission loss in the C-band and also the low influence of fiber dispersion for the X-band RF signal transmission. Fig. 3(b) shows the EVM as a function of the received optical power for the upstream link. For a 5-km transmission link, the EVM is <6%, when the received optical power is −6 dBm. It can be seen from Fig. 3(b) that, as compared with the back-to-back (B2B) transmission, the 5-km fiber transmission link introduces a slight deterioration in the EVM, which may result from the relatively higher fiber transmission loss in the O-band. In addition, to check the crosstalk between the C-band downstream and O-band upstream in the O-band PD, a comparison between the EVM results with and without downstream signal transmission is also made. No obvious change is observed from the curves shown in Fig. 3(b).

It should be noted that, since the bandwidths of the microring modulator and the transfer-printed PD are lower than 15 and 11.5 GHz, respectively, the proposed RoF link is designed to work in the X-band. If the microring modulator would be realized in imec's newest iSIPP50G platform and a modified design is employed for the PD, the bandwidth of the transceiver can be increased, enabling millimetre wave RoF systems.

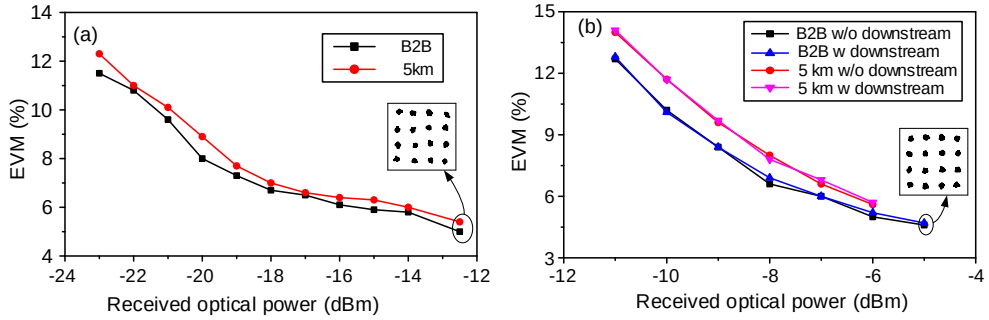


Figure 3. Measured EVM versus received optical power for (a) back-to-back and 5-km downstream link, and (b) back-to-back and 5-km upstream link with the downstream link operational or off. Inset: Constellation diagrams of the demodulated 16QAM signal.

4. CONCLUSIONS

In this paper, we present an X-band full-duplex analog RoF system based on an integrated III-V-on-silicon transceiver. The downstream link transmitter is based on a C-band silicon microring modulator with a bandwidth of 15 GHz, and the upstream link receiver is realized by the integration of an O-band III-V PD with a bandwidth of 11.5 GHz using transfer printing. Error free transmission for both the downstream and upstream links is achieved. We believe that silicon photonics together with transfer printing is an enabling technology to realize low-cost optical devices with high throughput, offering improved performance, cost-efficiency and increased functionality in future wireless communication systems.

ACKNOWLEDGEMENTS

This work was supported in part by the H2020 TOPHIT project, the National Natural Science Foundation of China (61527820) and the Fundamental Research Funds for the Central Universities. Z. Z. Tang also would like to thank the support of the China Scholarship Council.

REFERENCES

[1] China Mobile Research Institute, China, "C-RAN: the Road Towards Green RAN," White Paper (2013).
[2] Z. Tang and S. Pan, "A Q-band radio-over-fiber system for distribution of uncompressed high-definition video signals," *Photonic Netw. Commun.* , vol. 32, no. 2, pp. 179-187, Oct. 2016.
[3] J. V. Kerrebrouck, *et al.* "10 Gb/s Radio-Over-Fiber at 28 GHz Carrier Frequency Link Based on 1550 nm VCSEL Chirp Enhanced Intensity Modulation after 2 km Fiber." in *Proc. OFC2018*, pp. 1-3.
[4] X. Y. Li, *et al.* "120Gb/s Wireless Terahertz-Wave Signal Delivery by 375GHz-500GHz Multi-Carrier in a 2× 2 MIMO System." in *Proc. OFC2018*, pp. 1-3.
[5] L. Cheng, *et al*. "Experimental demonstration of sub-Nyquist sampling for bandwidth-and hardware-efficient mobile fronthaul supporting 128× 128 MIMO with 100-MHz OFDM signals," in *Proc. OFC2016*, pp. 1-3.
[6] Y. Tian, K.-L. Lee, C. Lim, and A. Nirmalathas, "Performance evaluation of CoMP for downlink 60-GHz radio-over-fiber fronthaul," in *Proc. MWP2017*, pp.1-4.
[7] B. Corbett, R. Loi, J. O'Callaghan, G. Roelkens, "Transfer printing for silicon photonics", Semiconductors and Semimetals, 99, pp.43-70 (2018)
[8] J. Zhang, *et al.*, "A Silicon Photonics Fiber-To-The-Home Transceiver Array based on Transfer-Printing-Based Integration of III-V Photodetectors, " *Opt. Express*, vol. 25, no. 13, pp.14290-14299, 2017.

Photonic Integrated Microwave Oscillator Based on Silicon Nitride Soliton Microcomb

(Student Paper)

Junqiu Liu[1], Jijun He[1], Erwan Lucas[1], Arslan S. Raja[1], Rui Ning Wang[1], Maxim Karpov[1], Hairun Guo[1], Romain Bouchand[1], and Tobias J. Kippenberg[1]

[1]*École Polytechnique Fédérale de Lausanne (EPFL), CH-1015 Lausanne, Switzerland*

e-mail: junqiu.liu@epfl.ch, tobias.kippenberg@epfl.ch

ABSTRACT

Soliton microcomb devices based on integrated waveguides are miniaturized optical frequency combs, which are ideal for portable applications for timing, spectroscopy and metrology. A particularly promising application is to build soliton-microcomb-based photonic integrated microwave oscillators. Yet, so far, soliton microcombs at microwave repetition rate have not been reported on integrated material platform, such as silicon nitride (Si_3N_4), mainly due to high optical losses in waveguides caused by the fabrication process. Here, by improving the photonic Damascene reflow process to fabricate integrated Si_3N_4 microresonators with quality factor exceeding 22×10^6, we demonstrate, not only for the first time but also with an ultralow power of 35 mW, the single soliton formation at 19.6 GHz repetition rate, in the microwave K-band. We characterize the phase noise of the soliton repetition rate, and reveal that the main issue limiting the phase noise performance is the chip input coupling. Furthermore, we demonstrate single soliton at a repetition rate as low as 9.77 GHz. Our results pave the way to low-noise, cost-effective, small-footprint, soliton-microcomb-based integrated microwave oscillator using low-loss Si_3N_4 waveguides, promising for chip-based communication, radar, high-frequency arbitrary waveform generation and spectroscopy.

Keywords: Microwave photonics, frequency comb, integrated photonics, microresonator, silicon nitride, nonlinear optics.

1 INTRODUCTION

Microresonator-based Kerr frequency combs ("microcomb") [1] enable chip-scale optical frequency combs with broad bandwidth and repetition rates in the GHz to THz domain. Operating such microcombs in the dissipative Kerr soliton (DKS) regime [2] is center to applications of timing, metrology and spectroscopy. Silicon nitride [3] is particularly promising to realize photonic integrated soliton microcombs, due to its wide transparency window from visible to mid-infrared, absence of two-photon absorption, relatively high material Kerr nonlinearity, and fabrication process is CMOS-compatible. Soliton microcombs have already been used for low-noise microwave generation, coherent communication, astronomical spectrometer calibration, and to build photonic integrated frequency synthesizers and atomic clocks.

A particularly promising application using soliton microcombs at microwave repetition rates is to build microwave oscillators based on integrated photonics, whose centre frequency is determined by the microresonator free spectral range (FSR) and thus can be freely designed by users and actively tuned using e.g. heaters [4], in contrast to conventional electronics-based microwave oscillators that have fixed center frequency and limited tunability. So far, soliton microcombs at microwave repetition rates, e.g. $f_{\text{rep}} < 20$ GHz in the microwave K-band, have been demonstrated only in silica and crystalline microresonators [5], [6]. In integrated waveguide platform such as Si_3N_4, only chaotic comb states have been observed. The crucial challenges hindering the generation of single soliton states in integrated Si_3N_4 microresonators at microwave repetition rates are related to the comparatively low quality (Q) factor, and the thermal effect in Si_3N_4 which leads to difficulty in accessing the soliton state via only laser frequency tuning.

2 RESULTS

Here, we report the single soliton formation of 19.6 GHz repetition rate in integrated Si_3N_4 microresonators, with a record-low laser power of 35 mW on the chip device (70 mW in the input fiber coupled to the chip), using an optimized photonic Damascene reflow fabrication process [7], [8], [9]. The integrated Si_3N_4 microresonator exhibits a statistical intrinsic Q factor of $Q_0 > 22 \times 10^6$ (shown in Fig. 1(a)), and a strong anomalous GVD $D_2/2\pi \sim 64.0$ kHz (shown in Fig. 1(b)), based on low-loss (linear propagation loss $\alpha < 1$ dB/m), thick (950 nm in height) Si_3N_4 waveguides. We generate the single soliton state via simple laser frequency tuning, which significantly simplifies the experimental setup. Figure 1(c) shows two single soliton spectra generated from two different samples, A and B. Sample A is undercoupled, with a loaded linewidth $\kappa/2\pi = (\kappa_0 + \kappa_{\text{ex}})/2\pi \sim 18$ MHz and coupling coefficient $\eta = \kappa_{\text{ex}}/\kappa \sim 1/3$; Sample B is overcoupled, with a loaded linewidth $\kappa/2\pi = (\kappa_0 + \kappa_{\text{ex}})/2\pi \sim 27$ MHz and coupling coefficient $\eta = \kappa_{\text{ex}}/\kappa \sim 2/3$. In sample A, a single soliton state is

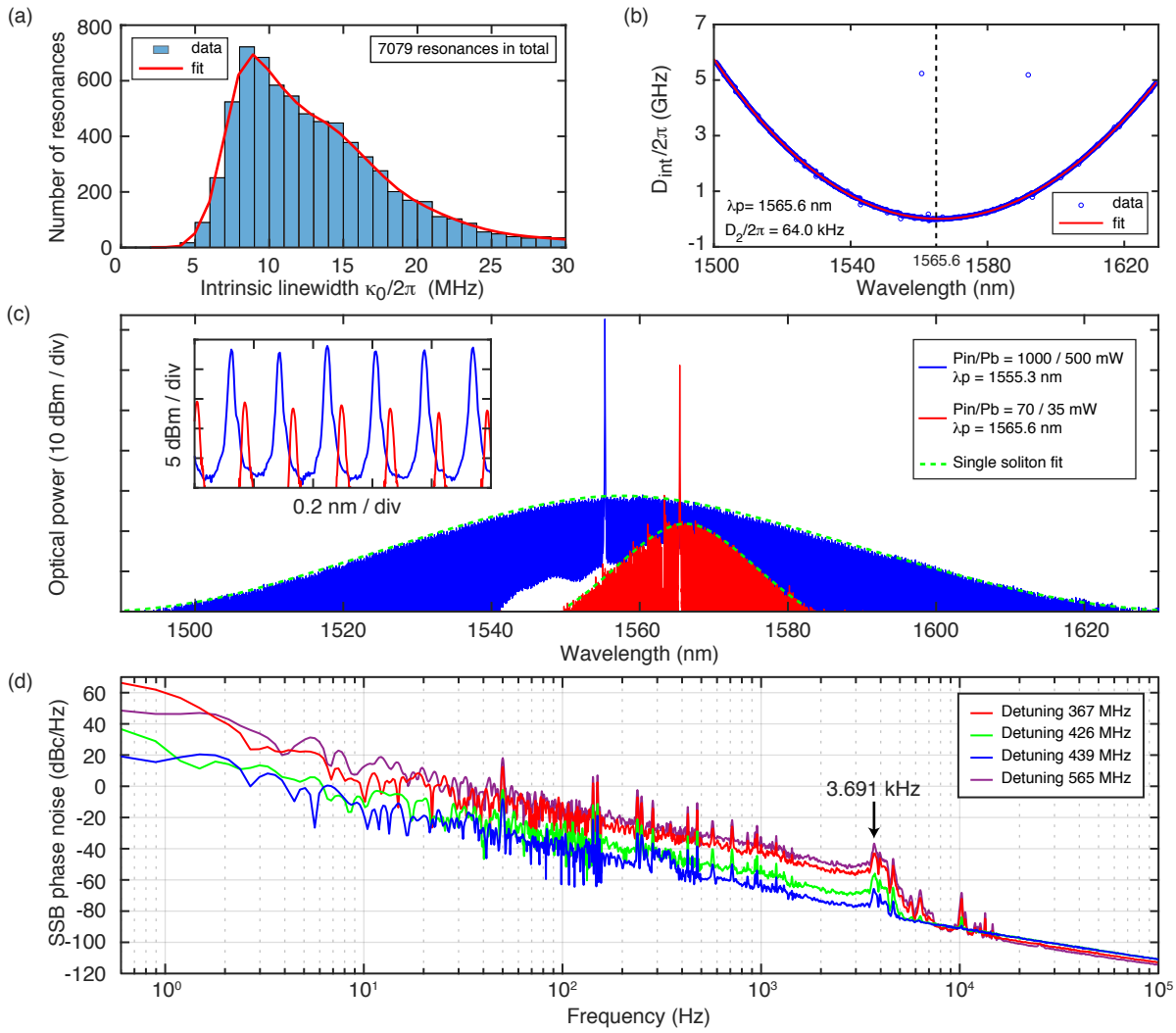


Figure 1. (a) The histogram of the intrinsic loss $\kappa_0/2\pi$ of 7079 fitted resonances, from nine characterized samples. The most probable value is $\kappa_0/2\pi = 8.5$ MHz, corresponding to statistical intrinsic $Q_0 > 22 \times 10^6$. The histogram is fitted with a non-parametric, normal Kernel distribution. (d) The fitted microresonator GVD $D_{\text{int}}/2\pi$, including $D_1/2\pi \sim 19.6$ GHz, $D_2/2\pi \sim 64.0$ kHz, and $D_3/2\pi \sim \mathcal{O}(1)$ Hz, with respect to the pump resonance $\lambda_p = 1565.6$ nm. (c) Single soliton spectra of 19.6 GHz repetition rate with 35 mW power in sample A (in red), and with 500 mW power in sample B (in blue), and their spectrum fit (in green) to extract the 3-dB-bandwidth and pulse duration. Inset: Spectrum zoom-in showing 19.6 GHz mode spacing. (d) SSB phase noise measurement at different pump-to-cavity detuning values, when the soliton repetition rate is stabilized. A quiet point is observed at the detuning of 439 MHz.

generated with 35 mW in the bus waveguide on the chip (70 mW power in the input lensed fiber), as shown in Fig. 1(c), while parametric oscillation for sideband generation is observed with 7 mW power. The single soliton spectrum fit shows 3-dB-bandwidth of 8.53 nm, corresponding to a pulse duration of 302 fs. This is not only the first Si_3N_4 single soliton at microwave K-band repetition rate, but also represents an extremely low threshold power for soliton formation, on a par with the power values in silica and crystalline microresonators [5], [6]. This power level is compatible with state-of-art silicon-based laser, thus full integration, heterogeneous or homogeneous, of on-chip lasers and Si_4N_4 nonlinear microresonators for soliton-microcomb-based microwave synthesis becomes realistic. In sample B, the input laser power is increased to 1 Watt, and a single soliton state of a bandwidth exceeding 120 nm, consisting of more than 800 comb lines, is achieved with a smooth spectral envelope. The single soliton spectrum fit shows 3-dB-bandwidth of 25.8 nm, corresponding to a pulse duration of 98.4 fs. The estimated power conversion efficiency from the continuous-wave pump to the soliton pulse is around 0.3%.

We further characterize the phase noise of repetition rate of this soliton state. The soliton repetition rate is detected on a fast InGaAs photodetector whose output electrical signal at 19.6 GHz is amplified and fed to a cross-correlator-based phase noise analyzer. We lock the driven laser's frequency and power, in order to stabilize the soliton repetition rate, and perform the single sideband (SSB) phase noise measurement using the phase noise analyzer. We perform the phase noise measurement at different detuning values as shown in Fig. 1(d). A "quiet" point [10], caused by mode crossings, is observed at the detuning of 439 MHz, which gives the

best phase noise performance compared with other detuning values. Operated at this quiet point, the absolute phase noise power spectral density of the microwave carrier exhibits levels of $\sim$ 20 dBc/Hz at 1 Hz offset Fourier frequency, $\sim$ –65 dBc/Hz at 1 kHz, and $\sim$ –120 dBc/Hz at 1 MHz. A noise floor at –120 dBc/Hz is reached above 1 MHz Fourier frequency, which is mainly caused by the low electrical signal-to-noise ratio obtained after photodetection of the soliton pulse rate due to the low soliton optical power available.

In addition, we also generate single soliton at 9.77 GHz repetition rate, in the microwave X-band, accessed via only laser frequency forward tuning and with approximately 800 mW power on the chip (spectrum not shown here).

CONCLUSION

In conclusion, we demonstrate, for the first time, the single soliton formation of 19.6 GHz repetition rate in the microwave K-band, in integrated Si_3N_4 microresonators. The high microresonator Q factor ($Q_0 > 22 \times 10^6$), enabled by the photonic Damascene reflow process, allows the single soliton formation with only 35 mW laser power on the chip device and easy access with simple laser frequency tuning. The phase noise of soliton repetition rate is characterized at different detunings, showing the approach for phase noise improvement through operation at a quiet point, and input power stabilization. The phase noise measured in our work is still 40 dBc/Hz higher than the thermo-refractive noise characterized in Si_3N_4 microresonator recently [11], revealing the considerable potential for further phase noise improvement, using better device input coupling, a pump laser with lower noise, and better fabrication process for higher Q. Nevertheless, our work represents a significant milestone on the path towards using integrated soliton microcombs for low-noise, low-power-consumption, cost-effective, customized, chip-based photonic microwave oscillators, promising for portable applications such as radar, telecommunication, spectroscopy, arbitrary waveform generation, remote sensing and wireless networks.

FUNDING INFORMATION

This work was supported by Contract HR0011-15-C-0055 (DODOS) from the Defense Advanced Research Projects Agency (DARPA), Defense Sciences Office (DSO), and by Swiss National Science Foundation under grant agreement No. 161573 (precoR).

ACKNOWLEDGMENT

The Si_3N_4 microresonator samples were fabricated in the EPFL center of MicroNanoTechnology (CMi). E.L. and M.K. acknowledge the support from the European Space Technology Centre with ESA Contract No. 4000116145/16/NL/MH/GM and 4000118777/16/NL/GM respectively. J.H. acknowledges the support provided by Prof. Hwa-yaw Tam and from the Research Student Attachment Programme of the Hong Kong Polytechnic University. H.G. acknowledges the support from the European Union's Horizon 2020 research and innovation program under Marie Sklodowska-Curie IF grant agreement No. 709249.

REFERENCES

[1] T. J. Kippenberg, R. Holzwarth, and S. A. Diddams, "Microresonator-based optical frequency combs", Science 332, 555 (2011).

[2] T. J. Kippenberg, A. L. Gaeta, M. Lipson, and M. L. Gorodetsky, "Dissipative Kerr solitons in optical microresonators", Science 361, 0036-8075 (2018)

[3] D. J. Moss, R. Morandotti, A. L. Gaeta, and M. Lipson, "New CMOS-compatible platforms based on silicon nitride and Hydex for nonlinear optics", Nature Photonics 7, 597 (2013).

[4] C. Joshi *et al*, "Thermally controlled comb generation and soliton modelocking in microresonators", Opt. Lett. 41, 2565 (2016).

[5] X. Yi, Q.-F. Yang, K. Y. Yang, M.-G. Suh, and K. Vahala, "Soliton frequency comb at microwave rates in a high-Q silica microresonator", Optica 2, 1078 (2015)

[6] W. Liang, D. Eliyahu, V. S. Ilchenko, A. A. Savchenkov, A. B. Matsko, D. Seidel, and L. Maleki, "High spectral purity Kerr frequency comb radio frequency photonic oscillator", Nature Communications 6, 7957 (2015)

[7] J. Liu *et al*, "Ultralow-power chip-based soliton microcombs for photonic integration", Optica 5, 1347 (2018)

[8] M. H. P. Pfeiffer, J. Liu, A. S. Raja, T. Morais, B. Ghadiani, and T. J. Kippenberg, "Ultra-smooth silicon nitride waveguides based on the Damascene reflow process: fabrication and loss origins", Optica 5, 885 (2018).

[9] M. H. P. Pfeiffer *et al*, "Photonic Damascene process for low-loss, high-confinement silicon nitride waveguides", IEEE Journal of Selected Topics in Quantum Electronics 24, 1 (2018).

[10] X. Yi, Q.-F. Yang, X. Zhang, K. Y. Yang, X. Li, and K. Vahala, "Single-mode dispersive waves and soliton microcomb dynamics", Nature Communications 8, 14869 (2017)

[11] G. Huang *et al*, "Thermo-refractive noise in silicon nitride based microresonators", arXiv: 1901.07112v1 (2019).

EAM-based Microwave Mixer Implemented in Silicon Photonics

(Student Paper)

Kasper Van Gasse[1,2], Jochem Verbist[1,2,3], Haolin Li[3], Guy Torfs[3], Johan Bauwelinck[3], Gunther Roelkens[1,2]
[1] Ghent University-imec, Technologiepark 15, 9052 Ghent - Belgium
[2] Center for Nano- and Biophotonics, Ghent University, Belgium
[3]IDLab, Ghent University–Imec, Technologiepark 15, 9052 Ghent - Belgium
e-mail: kasper.vangasse @ugent.be

ABSTRACT

Analogue Radio-over-Fiber (ARoF) could play an enabling role in future small-cell Radio Access Networks (RANs). The use of high-frequency carriers in 5G requires wide-band and flexible frequency converter circuits. The use of ARoF allows performing the frequency conversion in the optical domain using wide-band and flexible microwave photonic up-conversion. A lot of research has been dedicated to the development of microwave photonic mixers using $LiNbO_3$ MZMs with promising results. However, using discrete bulky components is not a scalable solution and could be difficult to use in small-cell Radio Access Networks. In this work we present a silicon photonic up-converter and transmitter circuit. The photonic integrated circuit consists of two high-bandwidth waveguide-coupled EAMs in a MZI structure. One EAM is driven by the data on an IF carrier while the other EAM is driven by a high frequency LO. We present first simulation results of the structure and compare these results to an alternative mixer topology. The fabricated EAM-MZI mixer is then fully characterized and used to up-convert 16-QAM and 64-QAM data on a 1.5-3.5 GHz IF to 26-28 GHz carrier frequencies and transmit it over 2 km of single mode fiber.

Keywords: Silicon photonics, Radio-over-fiber, Microwave photonics.

1. INTRODUCTION

In next generation mobile networks (5G) new technologies will be needed to realize Radio Access Networks (RANs) capable of serving an ever-increasing amount of connected devices. One appealing approach to realize future RANs is the use of small-cell networks in combination with Analogue Radio-over-Fiber (ARoF) for antenna remoting. Using ARoF, complex wireless signals can be transported several kilometres with very low losses. It allows to centralize signal processing, which limits the deployment and maintenance cost of the remote antenna units. ARoF links not only offer the advantage of high-frequency antenna remoting, but also allow to perform signal up-conversion in the optical domain. Microwave photonic frequency conversion has been extensively studied using $LiNbO_3$ MZMs [1,2]. Although this approach has shown very promising results, the use of discrete components does not enable the scalability needed for deployment in future RANs. Integrating the optical system on a silicon photonic chip allows to strongly reduce the footprint and production cost while allowing for high-volume manufacturing. In this work we present a silicon photonic ARoF transmitter also capable of wide-band and flexible frequency conversion. The PIC is based on two waveguide-coupled GeSi EAMs placed in a MZI structure using silicon waveguides and splitters (see Fig. 1).

2. SIMULATION RESULTS

To make a detailed analysis of the optimal performance of the circuit we first performed a simulation using VPITransmissionmaker. Two possible silicon photonic mixer topologies are considered, first a serial EAM mixer where the LO and IF EAM are optically connected in series. This system was investigated using MZMs in [1]. The second topology is the parallel EAM mixer as shown in Fig. 1. This approach has also been extensively investigated using MZMs [2]. For the simulations we used previously measured transmission characteristics of the EAM (3dB bandwidth of 65 GHz, extinction ratio of 8 dB for a voltage swing of 2 V_{pp} and a dynamic insertion loss of 8 dB). We furthermore assumed that the grating couplers have an insertion loss of 5 dB and that passive components (waveguides, splitters) are lossless. Finally, an EDFA was inserted in the link simulation with a fixed output power of 2 dBm and a noise figure of 4 dB. The result of the generated RF signals for the serial and parallel mixer are shown in Fig. 2. From these results it is clear that the parallel up-converter has a better conversion efficiency when compared to the serial structure. This is thanks to the MZI structure in the parallel system that is used to supress the optical carrier. By removing the optical carrier only the relevant signal is amplified by the EDFA. A second interesting feature is that the LO throughput is much lower in the parallel system than in the serial mixer, which requires less filtering at the output. Finally, we note a conversion efficiency of -27 dB for the parallel EAM mixer, without a TIA at the photodiode output.

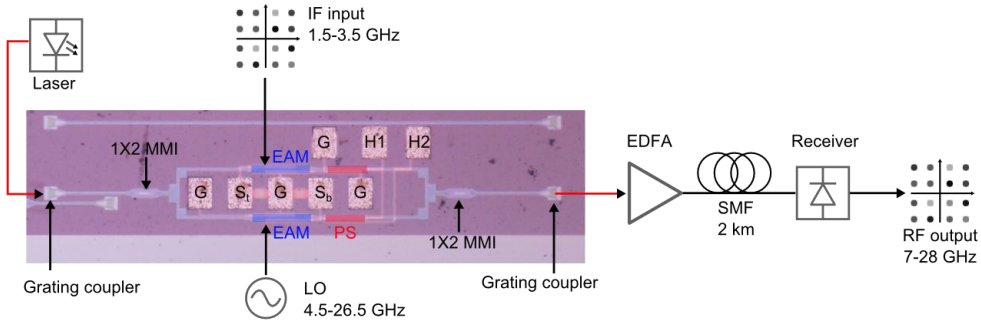


Figure 1. Overview of the parallel EAM up-conversion-transmitter link. The IF input is represented as a 16-QAM signal on a 1.5 GHz IF carrier. EAM: Electro Absorption Modulator; PS: Phase Shifter; MMI: Multi-Mode Interferometer; SMF: Single Mode Fiber.

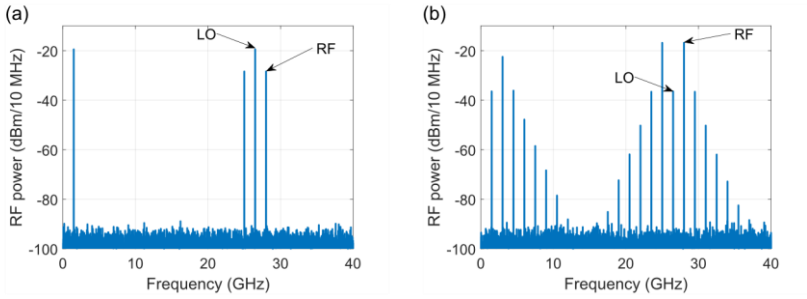


Figure 2. Simulated output from photodiode for (a) the serial EAM link and (b) the parallel link.

3. MEASUREMENT RESULTS

To characterize the up-converter/transmitter, the PIC shown in Fig. 1 was placed on a temperature-controlled stage and electrically contacted using a custom GSGSG RF probe with a 100 µm pitch. The PIC was optically interfaced with cleaved single mode fiber. A laser with an output at 1565 nm and 10 dBm output power was used as optical input.

3.1 Small-signal EAM characterization

To fully characterize the parallel EAM mixer we first measured the S21 and S11 parameters of the EAM. An on-chip parallel 70 Ohm resistor was used to have broadband matching. The result of the S21 measurement is shown in Fig. 3(a) and it shows a 3 dB modulation bandwidth exceeding 67 GHz. This very high modulation bandwidth makes the EAM an ideal candidate for the higher carrier frequencies envisioned in future mobile networks. In Fig. 3(a) the S11 of the EAM is shown, indicating a return loss better than 10 dB over the entire frequency range. Although the on-chip resistor is a straightforward and practical matching solution, the conversion efficiency could be further improved by a dedicated narrow band matching network.

3.2 System characterization

To assess the linearity of the mixer an IP3 measurement was performed as a function of the IF input power and a spurious free dynamic range of 82 $dBHz^{2/3}$ was found. This can be improved by increasing the link gain and lowering the noise floor. Using low-loss edge couplers would reduce the noise figure and a photodiode with higher saturation power would allow for a higher conversion gain. The conversion efficiency also depends on the extinction ratio of the MZI, as it determines the amount of carrier suppression achievable. Using the thermo-optic heater we can achieve a π-phase shift with 28 mW of power and an extinction ratio of 30 dB when EAMs are un-biased. This excellent extinction ratio means that the losses of the EAMs are almost identical.

3.3 Transmission experiment

Finally we performed transmission experiments where we up-convert 16-QAM and 64-QAM data on a 1.5 GHz IF to an RF carrier frequency up to 28 GHz. The carrier frequency was limited by the measurement equipment. The high 3 dB modulation bandwidth of the EAM indicates that the up-converter/transmitter could also be used for up-conversion to the 60 GHz frequency bands.

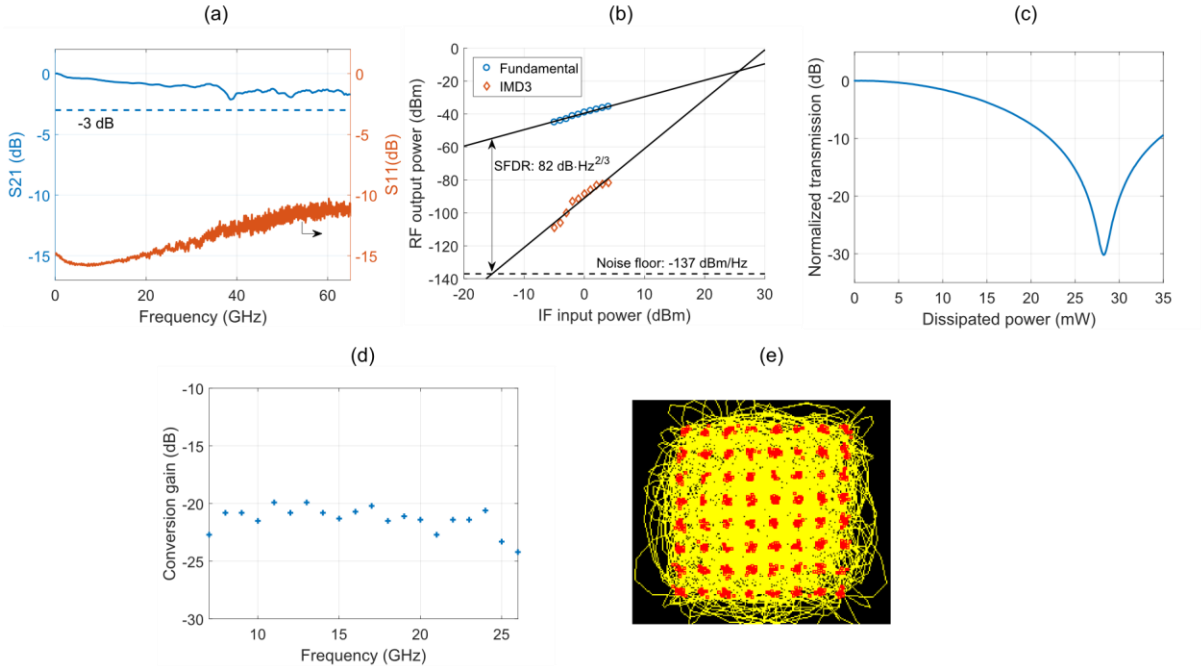


Figure 3. Measurement results of the EAM based up-converter/transmitter. (a) Small-signal measurement of a single EAM; (b) Result of a linearity (IP3) measurement. (c) Measured transmission as a function of the power dissipated in the thermo-optic phase shifter; (d) Conversion gain as function of RF output frequency for a fixed IF of 1.5 GHz. (e) Constellation diagram of 10 MBd 64-QAM data upconverted from 1.5 GHz IF to 26 GHz RF.

In a first transmission experiment we upconverted 10 MBd of 64-QAM data on a 1.5 GHz IF carrier to a 26 GHz RF carrier. The resulting (peak output power referred) rms EVM was 3.2 %, well below the 3GPP recommended maximum rms EVM for current LTE RANs of 8 % for 64-QAM signals. Both the baud rate and RF carrier frequency were limited by the bandwidth of the used equipment. Furthermore, we investigate the evolution of the EVM as a function of the LO frequency and found that the rms EVM remains between 2 and 4 % over a span of more than 20 GHz. This attest to the extremely flat response of the mixer, which is a strong advantage of this mixer. In a final transmission experiment we used an in-house programmed FPGA signal generator to create a 218 MBd 64-QAM signal on a 3.5 GHz carrier and up-converted it to a 28 GHz carrier. Given the limited bandwidth of the signal analyser, a real-time oscilloscope with native de-modulation software was used to analyse the up-converted signal. Again, the 28 GHz carrier frequency was limited by the real-time oscilloscope. For the 64-QAM signal an on-line rms EVM of 5.5 % was found, which is still well below the recommended 8 %. This degradation in signal is partially due to the bandwidth of the data, but also due to the lower quality of signal generation of the FPGA compared to the commercial signal generator.

4. CONCLUSIONS

In summary we have shown that a parallel EAM microwave photonic up-converter/transmitter is capable of transmitting 64-QAM data over 2 km of single mode fiber with rms EVM lower than 5.5 % for data rates up to 1.3 Gb/s. Given the extremely compact foot-print of the EAMs, multiple such mixers can be integrated on a single PIC and multiplexed in wavelength or space for transmission over optical fiber.

ACKNOWLEDGEMENTS

This work was supported in part by AFOSR through “Innovative Silicon and InP Integrated Photonic Devices for RF Downconversion” under Grant FA9550-18-1-0015 and in part by ERC through ATTO, new concept for ultra-high capacity wireless networks, under Grant 695495.

REFERENCES

[1] G. Gopalakrishnan, W. K. Burns, C. H. Bulmer, "Microwave-optical mixing in LiNbO3 modulators," in *IEEE Transactions on Microwave Theory and Techniques*, vol. 41, pp. 2383-2391, Dec. 1993.

[2] E. Chan, R. Minasian, "Microwave Photonic Downconverter With High Conversion Efficiency," in Journal of Lightwave Technology, vol. 30, pp. 3580-3585, Dec. 2012.

1310 nm quantum dot waveguide avalanche photodiode heterogeneously integrated on silicon

Bassem Tossoun, Géza Kurczveil, Chong Zhang, Antoine Descos, Xiaoge Zeng, Zhihong Huang, Di Liang, Raymond G. Beausoleil
Hewlett Packard Labs, Hewlett Packard Enterprise, 1501 Page Mill Road, Palo Alto, California 94304, USA
e-mail: bassem.tossoun@hpe.com

ABSTRACT

We demonstrate quantum dot (QD) waveguide avalanche photodiodes (APDs) on silicon at 1310 nm with a record high gain-bandwidth product of 240 GHz. A 3-dB bandwidth as high as 15 GHz and gain as high as ~45 were achieved. Open eye diagrams up to 12.5 Gb/s were taken and a sensitivity of -11 dB were demonstrated for the first time for any QD APD on silicon. Temperature studies were also made on these APDs, exhibiting high performance up to 60° C, and showing that these APDs can be practically used in an uncooled, WDM system on a silicon photonic platform.

Keywords: optoelectronics, avalanche photodiodes, silicon photonics, quantum dots, optical interconnects.

1. INTRODUCTION

Future high-performance computers and data centers need to be able to keep up with future high-demanding, data-driven applications such as machine learning, virtual reality, and Internet of Things (IoT). Silicon (Si) integrated photonics provides a solution for low-power, high-bandwidth interconnects that are compatible with low cost complementary metal-oxide semiconductor (CMOS) electronic processors and memory chips. We have developed all the key components for a Si photonic integrated circuit including lasers, modulators, and photodetectors. To further reduce power consumption and enhance high-temperature operation robustness, we recently successfully demonstrated quantum dot (QD)-based comb and microring lasers on our heterogeneous photonic platform. Furthermore, by using avalanche photodiodes (APDs), lasers are allowed to operate with smaller output optical power and still be detected with high sensitivity due to the APD's internal gain.

Silicon-germanium (Si-Ge) avalanche photodiodes (APDs) have shown significant potential in providing highly sensitive receivers on silicon photonic integrated circuits. However, these APDs generally require two selective area growths for Si and Ge thin films, which complicate the fabrication process and increase the cost of heterogeneous III-V-on-Si lasers that are fabricated on the same wafer [1]. One solution to this is to use the same epitaxial layers for the lasers and the photodiodes. In this paper, we report the first QD APDs heterogeneously integrated on a Si substrate, made using the same epitaxial layers and fabrication process for a recent 1310 nm hybrid QD silicon comb laser with error-free operation for 14-channels [2]. These APDs demonstrate an avalanche gain of up to ~45 and a gain-bandwidth product of 240 GHz, which are the highest for any QD APDs on Si. A maximum 3-dB bandwidth of 15 GHz and open eye diagrams up to 12.5 Gb/s were achieved, and temperature-dependent studies were conducted to exhibit high performance up to 60˚ C.

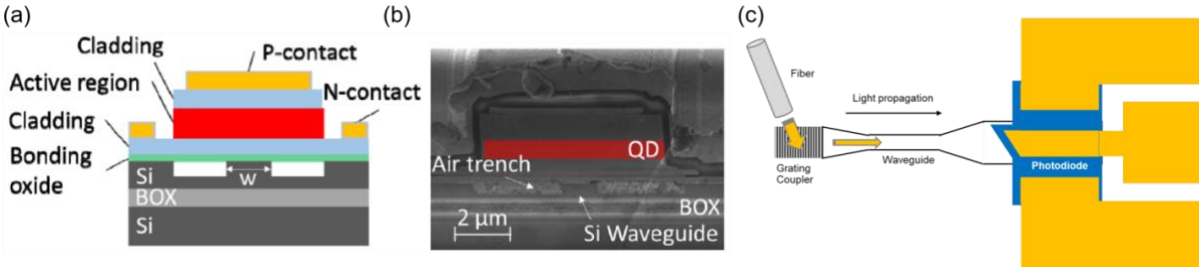


Fig. 1. (a) Cross-section schematic of the photodiode. (b) SEM cross-section of the waveguide QD on Si APD. (c) Top-down schematic of the photodiode with a fiber coupled to the input waveguide with a grating coupler.

2. DEVICE DESIGN AND FABRICATION

Fig. 1 shows a cross-section and top-down view schematic diagram as well as a SEM cross-section of the device. We couple a 1310 nm laser light from a cleaved fiber through a grating coupler, which then directs the light along a Si waveguide and finally evanescently couples light into the APD above the waveguide. First, grating couplers and passive silicon waveguides were etched onto an SOI substrate. Then, a GaAs-based p-i-n eptaxial structure with an active region of 8 layers of InAs QDs, totaling 320 nm in thickness, was bonded directly to the SOI substrate [3]. The waveguide-type lasers and photodiodes were etched, passivated, and metallized during the same

process steps. The full detailed fabrication process for these APDs, as well as QD comb and microring lasers made on the same wafer, can be found at [4].

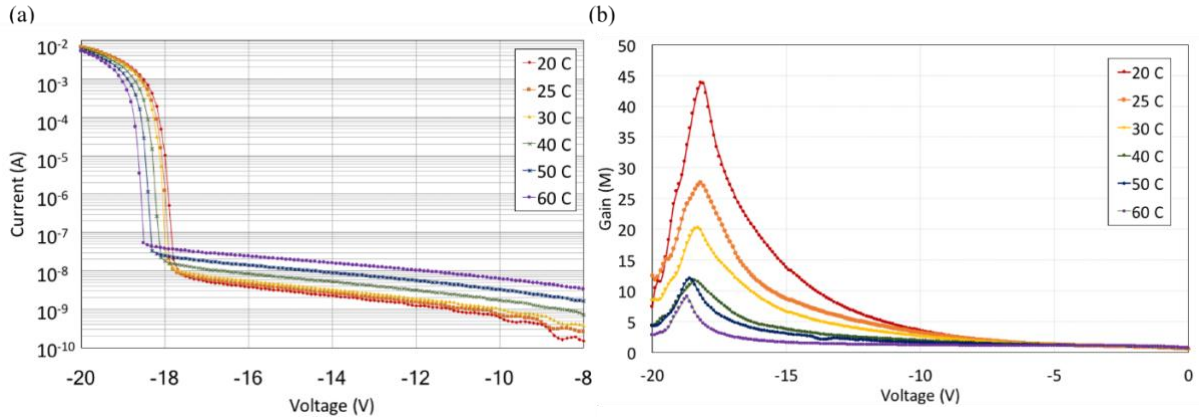


Fig. 2. (a) Dark current vs. temperature and (b) gain vs. voltage for a 11 μm × 60 μm device.

3. RESULTS

Fig. 2(a) plots the I-V curves of a 11 μm × 60 μm photodiode at different temperatures. The temperature dependence on the breakdown voltage reveals that impact ionization of free carriers is the primary physical mechanism behind the breakdown of the device. The dark current was as low was 10 pA at -1V, the lowest for any QD PD on Si to our best knowledge, and 50 μA at a bias right below breakdown voltage [5].

The gain of the device was measured and is shown in Fig. 2(b). The external responsivity at unity gain and with 8 dBm optical input power at room temperature is 0.06 A/W, and the maximum external responsivity at room temperature is 2.7 A/W. A temperature dependence on the gain, as well as a decrease in gain at high biases, have been observed and are due to the increase of dark current with temperature and bias. A maximum gain of ~45 was seen at room temperature, with avalanche gain seen up to a temperature of 60 ˚C, displaying the temperature robustness of the devices. We believe that the avalanche multiplication process occurs in the GaAs spacer layers in between the QDs and that the QDs may also be partially contributing to the multiplication gain [6].

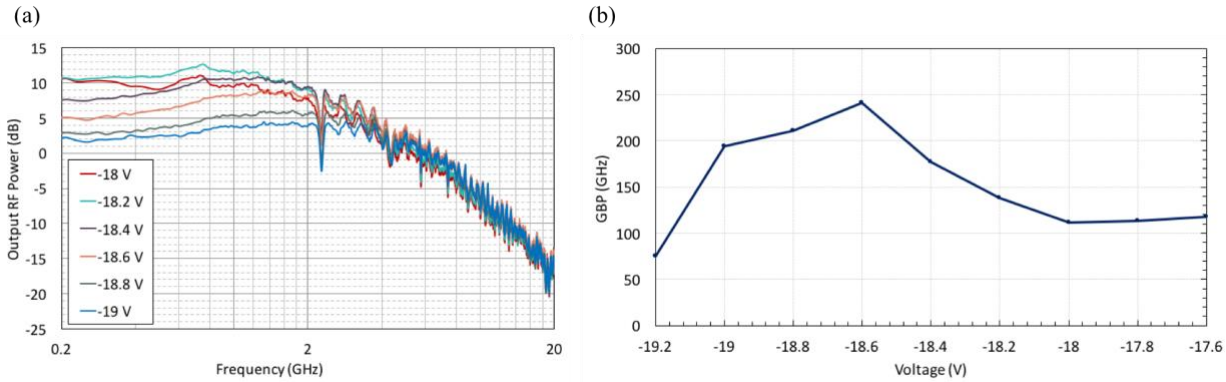


Fig. 3. (a) Frequency response of a 11 μm × 90 μm APD between -18 V and -19 V. (b) Gain bandwidth product of a 11 μm × 90 μm APD.

The S21 frequency response was measured at room temperature using an HP lightwave component analyzer (LCA). The frequency response was taken under bias voltages that provide high multiplication gain. The maximum 3-dB bandwidth measured for a 11 μm × 90 μm APD was about 8 GHz and 15 GHz for a 11 μm × 60 μm APD at -12 V bias. An inductive peaking effect was observed between -18 V and -19 V bias, which has been previously explained in other APDs to be caused by the impact ionization in the avalanche region of the device [1]. A maximum gain-bandwidth product (GBP) of 240 GHz was measured at a bias voltage of -18.6 V, as shown in Fig. 4(b). This is higher than most traditional InP-based receivers based on APDs, which is around 100-200 GHz due to their larger impact ionization coefficient *k* value [1]. This number also compares to Ge-on-Si APD counterparts which typically show higher GBP due to the low *k*-value of Si. However, they also often suffer from higher dark currents due to dislocations at lattice-mismatched Ge/Si interface.

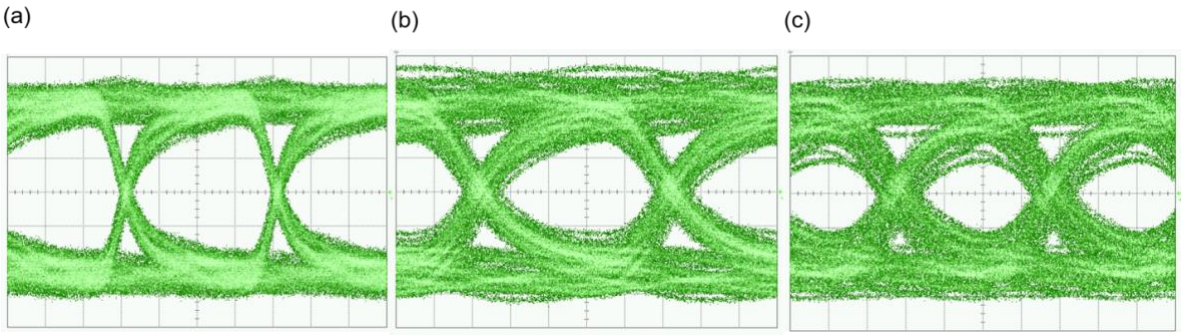


Fig. 4. Eye diagrams at (a) 5 Gb/s, (b) 10 Gb/s, and (c) 12.5 Gb/s.

These APDs provide enough multiplication gain to produce a sufficiently high signal-to-noise ratio and clear eye diagrams without the need of a transimpedance amplifier (TIA). A high-speed pseudo-random binary sequence (PRBS) signal was amplified by a 20 dB high-speed power amplifier. Then, a 1310 nm optical signal couples to an APD that is biased through a RF probe and a bias-T. The output electrical signal is monitored by a DCA86100C sampling scope in the form of an eye diagram. Figs. 4(a)-(c) show the electrical eye diagrams of a 11 μm × 60 μm APD at 5 Gbps, 10 Gbps, and 12.5 Gbps, respectively. At a gain of 40, we have obtained a signal-to-noise ratio greater than 7 dB and 5 dB at 5 Gbps and 10 Gbps, respectively. We have also obtained open eye diagrams at 12.5 Gbps, as shown in Fig. 4(c), where the data rate was limited by the pattern generator.

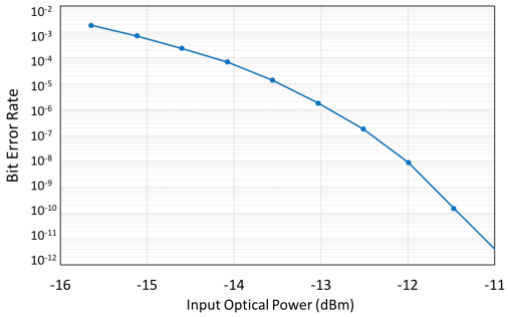


Fig. 5. Bit error rate vs. input optical power of a 11 μm × 90 μm device.

A bit error rate (BER) test was conducted using an Anritsu Bit Error Rate Tester at 10 Gb/s. At a gain of 28, the sensitivity was measured to be about -11 dBm at a BER of 1×10^{-12} and -14.6 dBm at a BER of 2.4×10^{-4}, as shown in Fig. 5. This sensitivity is a few dB higher than that of a typical Ge-on-Si p-i-n PD. Better performance is expected when a TIA is utilized. Furthermore, the epitaxial layer structure can be designed as a separate absorption and multiplication (SAM) structure in order to reduce breakdown voltage and increase multiplication gain in the device.

4. CONCLUSIONS

A QD APD heterogeneously integrated on Si was demonstrated for the first time. A maximum gain of up to 45 and a gain bandwidth product of 240 GHz were observed, which are record high results for any QD APDs on Si. These APDs achieve a low dark current and a sensitivity of -11 dBm, and have demonstrated open eye diagrams up to 12.5 Gb/s. These devices are promising candidates for on-chip monitor PDs and integrated high-speed receivers. They also leverage the same epitaxial layers and processing steps as an on-chip laser, which significantly simplifies the processing for a fully integrated transceiver on Si.

REFERENCES

[1] D. Dai et al.: Equivalent circuit model of a waveguide-type Ge/Si avalanche photodetector, *Phys. St. Solidi C 7*, No. 10, 2532–2535 (2010).
[2] G. Kurczveil et al.: On-Chip Hybrid silicon Quantum dot Comb Laser with 14 error-Free Channels, *ISLC* (Santa Fe, NM, 2018).
[3] D. Liang et al.: Highly efficient vertical outgassing channels for low-temperature InP-to-silicon direct wafer bonding on the silicon-on insulator substrate, *J. Vac. Sci. Technol. B*, Vol. 26, No. 4, p. 1560 (2008).
[4] G. Kurczveil et al.: Robust hybrid quantum dot laser for integrated silicon photonics, *Opt. Exp.*, Vol. 24, No. 14, pp. 16167-16174 (2016).
[5] B. Tossoun et al.: High-speed 1310 nm Hybrid Silicon Quantum Dot Photodiodes with Ultra-low Dark Current, *DRC* (Santa Barbara, CA, 2018).
[6] Y. Ma et al.: Enhanced Carrier Multiplication in InAs Quantum Dots for Bulk Avalanche Photodetector Applications, *Adv. O. Mat.* (2017).

Recent advances in Hybrid Plasmonic Circuits for Data Communications

(Invited paper)

Amr S. Helmy[1]

[1] The Edward S. Rogers Department of Electrical and Computer Engineering, University of Toronto, 10 King's College Road, Toronto, ON M5S 3G4, Canada

e-mail: a.helmy@utoronto.cae

ABSTRACT

I plan to discuss a novel class of nanoscale devices that address unmet performance demands for applications in data communications [1-6]. The performance of emerging generations of high-speed, integrated electronic circuits is increasingly dictated by interconnect density and latency as well as by power consumption. To alleviate these limitations, data communications using photons has been deployed, where photonic circuits and devices are integrated on platforms compatible with conventional electronic technologies. Within the dominant platform; namely Si, dielectric waveguides confine light via total internal reflection. This imposes bounds on minimizing device dimensions and density of integration. Those bounds arise due to the diffraction limit and the cross-coupling between neighbouring waveguides. Nanoscale Plasmonic waveguides provide the unique ability to confine light within a few nanometers and allow for near perfect transmission through sharp bends as well as efficient light distribution between orthogonally intersecting junctions. With these structures as a building block, new levels of optoelectronic integration and performance metrics for athermal transceivers with achievable bandwidths in excess of 500 Gbps as will be overviewed in this talk. In addition, opportunities for the role that 2D materials may pay in propelling these record performance metrics even further will be projected.

Keywords: Plasmonics, Optical transceivers, Optical interconnects, Integration, High speed optical links.

REFERENCES

[1] W. Ma and Amr S. Helmy, "Asymmetric long-range hybrid-plasmonic modes in asymmetric nanometer-scale structures," J. Opt. Soc. Am. B, Vol. 31, pp. 1723-1729 (2014).

[2] C. Lin, Amr S. Helmy. "Dynamically reconfigurable nanoscale modulators utilizing coupled hybrid plasmonics." Scientific Reports 5, 12313 (2015).

[3] Lin, R. Grassi, T. Low and Amr S. Helmy. "Multilayer black phosphorus as a versatile mid-infrared electro-optic material" ACS Nano Lett. 5, 12313 (2016).

[4] Herman M. K. Wong, and Amr S. Helmy, Performance Enhancement of Nano-Scale VO2 Modulators using Hybrid Plasmonics, IEEE J. Light. Technolo., vol. 36, pp797-808, (2018)

[5] Y. Su, P. Chen, C Lin and Amr. S. Helmy, Highly sensitive wavelength-scale amorphous hybrid plasmonic detectors, OSA Optica, Vol. 4, No. 10, 1259-1262, (2017).

[6] Y. Su, P. Chen, C Lin and Amr. S. Helmy, (2018). Submitted

High-sensitivity interferometric sensors on Si_3N_4 platform using Surface Plasmon Polariton (SPP)-based transducers

A. Manolis[1], E. Chatzianagnostou[1], G. Dabos[1], N. Pleros[1], B. Chmielak[2], A.L. Giesecke[2], C. Porschatis[2], P. J. Cegielski[2], L. Markey[3], J.C. Weeber[3], A. Dereux[3] and D. Tsiokos[1,4]

[1] Department of Informatics - Center for Interdisciplinary Research and Innovation, Aristotle University of Thessaloniki, Greece

[2] AMO GmbH, Advanced Microelectronic Center Aachen (AMICA), Otto-Blumenthal-Strasse, Aachen, Germany

[3] Laboratoire Interdisciplinaire Carnot de Bourgogne, CNRS-Université de Bourgogne, Dijon, France

[4] bialoom Ltd, 72, 28th Octovriou Avenue, Office 301, Engomi, 2414 Nicosia, Cyprus

e-mail: athanasm@csd.auth.gr

ABSTRACT

In this work, we report an interferometric plasmo-photonic sensor based on Si_3N_4 photonic waveguides and gold (Au) Surface Plasmon Polariton (SPP) stripe waveguides. The proposed approach exhibits bulk sensitivity up to 1930 nm/RIU, holding promise for compact, ultra-sensitive interferometric sensing devices. We also evince experimentally that the proposed plasmo-photonic waveguide employed at the interferometer sensing arm can be fabricated using Aluminum (Al) instead of gold, demonstrating the first step towards fully CMOS compatible plasmo-photonic interferometric sensors.

Keywords: refractive index sensor, plasmonic stripes, silicon nitride, photonic integrated circuits, CMOS metals.

1. INTRODUCTION

Plasmonic-based sensors have emerged as an attractive sensing technology for point of care applications. Compared to the evanescent wave photonic sensors, plasmonic sensors offer profound exposure of SPP modes to liquid analytes leading to enhanced sensitivity characteristics [1]. However, bulky prism-based coupling configurations [2] and high plasmonic losses [3] impede the transfer of those benefits in miniaturized and multi-functional all-plasmonic sensors. As an alternative, selective co-integration of plasmonic waveguides in low loss photonic platforms addresses those challenges while leveraging the functional benefits from both waveguide platforms [4]. In this work, we demonstrate a photonic integrated Mach-Zehnder interferometric sensor utilizing an open cladded gold stripe in one branch to serve as the sensing transducer by detecting local changes in the refractive index. The low-loss Si_3N_4 platform allows for the deployment of a MZI-based variable optical attenuator (VOA) followed by a thermo-optic phase shifter in the reference branch, in order to optimize the sensor performance. The proposed sensor was designed, fabricated and experimentally characterized, yielding bulk sensitivity values up to 1930 nm/RIU, demonstrating the functional benefits of the co-integration of plasmonic and photonic waveguides. We also evince through experimental data the dependence of bulk sensitivity from the Free Spectral Range (FSR), suggesting an effective roadmap towards compact and ultra-sensitive interferometric sensors. Following the successful demonstration of the plasmo-photonic sensor utilizing a gold stripe, we evince experimentally that the proposed plasmo-photonic waveguide employed at the interferometer sensing arm can be fabricated using Aluminum (Al) instead of gold, demonstrating the first step towards fully CMOS compatible plasmo-photonic interferometric sensors. The CMOS structures were fabricated and experimentally characterized, demonstrating Si_3N_4 to Al stripe interface loss equal to 2.86 dB and propagation losses of 0.065 dB/μm at 1550 nm, which is, to the best of our knowledge, the lowest SPP propagation losses among all single-mode Al-based plasmonic waveguides demonstrated so far at 1550 nm, reducing the propagation losses reported in our previous work [5].

2. PLASMO-PHOTONIC SENSOR

2.1 Layout and fabrication

Fig. 1(a) illustrates a schematic of the proposed plasmo-photonic sensor layout. The different cross-sections across the structure including the photonic waveguide (I), the taper end facet (II), the plasmonic waveguide (II) and the thermo-optic phase shifter (IV) are depicted in Fig. 1(b). The photonic waveguide platform relies on a 360 nm × 800 nm Si_3N_4 photonic waveguide core cladded with 600nm of Low Temperature Oxide (LTO) while relying on a 2.2 μm thick SiO_2 substrate layer (Fig.1(b)(1)). The sensing branch exploits a butt-coupling mechanism, comprised of a 100 nm × 7 μm Au SPP waveguide interfaced at its both end facets with two 7.5 μm wide linearly tapered Si_3N_4 waveguides [6]. The reference branch comprises a thermo-optic heater-based phase shifter for tuning the sensor's resonance wavelengths and a VOA for counter balancing the high plasmonic optical losses on the sensing arm, eventually maximizing field interference at the MZI output and therefore the spectral extinction ratio.

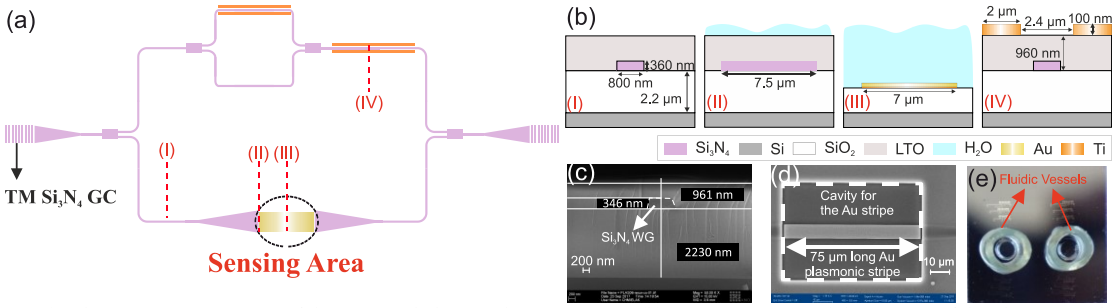


Figure 1. (a) Schematic representation of the proposed plasmo-photonic sensor. (b) Cross-sections and dimensions of the photonic and the plasmonic waveguides. (c) cross section SEM image of the photonic waveguide. (d) SEM top-view image of the gold plasmonic waveguide recessed in the cavity. (e) Photo of the fabricated sensor chip illustrating the fluidic tubes glued on top of the chip.

The phase shifter consists of two 100 nm × 2 μm titanium resistors, placed on top of the photonic waveguide, in a double-heater configuration ((Fig.1(b)(IV)). The VOA is composed of a MZI, with a thermo-optic heater-based phase shifter in one branch in order to control the attenuation of optical power with applied voltage. Moreover, two low-loss 3-dB Multi-Mode Interference (MMI) Y-junctions were utilized to allow equal power splitting ratios between the MZI branches. The fiber-to-chip coupling relied on a vertical out-of-plane coupling scheme based on Si_3N_4 Grating Couplers (GCs) for Transverse Magnetic (TM) polarization [7].

For the fabrication of the proposed plasmo-photonic sensor, a standard 6'' silicon wafer with 2.2 μm of thermally grown SiO_2 has been employed as substrate. The Si_3N_4 waveguide was deposited in low pressure chemical vapor deposition process (LPCVD). Marker layer and waveguides have been defined by optical projection lithography using an i-line stepper tool. Reactive-Ion-Etching (RIE) with CHF_3 and He chemistry has been employed for the structure transfer. Afterwards, a 600 nm thick LPCVD SiO_2 was deposited to form the LTO cladding of the photonic waveguide and annealed at 1000 °C for several hours. A Scanning Electron Microscope (SEM) image of a cross section view of the fabricated photonic waveguide is depicted in Fig. 1(c). The cavity for the plasmonic material were defined by the i-line stepper tool and etched through LTO, Si_3N_4 and SiO_2 as well by RIE with CHF_3 and He chemistry. In the final fabrication stage, the gold plasmonic stripes were deposited into the cavities by a lift-off process using e-beam lithography, thermal evaporation of gold and lift-off dissolution. The target thickness for gold was 100 nm. A very thin (3nm) titanium layer was deposited by e-gun evaporation prior to gold for an improved adhesion of gold on the sample. A SEM image of the fabricated plasmonic stripe is shown in Fig. 1(d). Silicone fluidic vessels were also glued on top of the plasmonic sensing waveguides as the means to confine the test liquid in this region alone, as shown in more detail in Fig. 1(e).

2.2 Experimental characterization

Characterization measurements were carried out to evaluate bulk sensitivity capabilities of the proposed plasmo-photonic sensor. In our measurements we tested two sensor variants with different Free Spectral Ranges (FSR) that were developed during the same process. Broadband measurements were carried out by sweeping the wavelength of a tunable laser source from 1500 nm to 1580 nm to launch light into the Si_3N_4 GCs. Moreover, voltage was applied to the titanium based heaters of the VOA in order to introduce additional losses in the reference branch as the means to maximize the extinction ratio on the output of the MZI sensor. The obtained FSR and the ER for sensor 1 were measured equal to 16 nm and 33.5 dB, respectively, while the corresponding values for sensor 2 were calculated equal to 24.8 nm and 37 dB, respectively. Sensitivity measurements were accomplished by infiltrating different buffer solutions with refractive indices ranging between 1.3327 and 1.3388 into the sensing area of each sensor. The respective spectral responses are indicatively illustrated in Fig 2(a) and 2(b), clearly revealing that the resonances are shifting to longer wavelengths with increasing refractive index of the buffer solution. Consequently, bulk sensitivity values were calculated by applying least-squares linear fitting on the resonant wavelength shift with increasing refractive index change, as shown in Fig. 2(c). Maximum bulk sensitivities were calculated 383 nm/RIU at 1527 nm and 1930 nm/RIU at 1565 nm for sensor 1 and 2, respectively. Experimental results showed that the sensor with the larger FSR exhibited also larger bulk sensitivity values, revealing the dependence of sensitivity with the FSR.

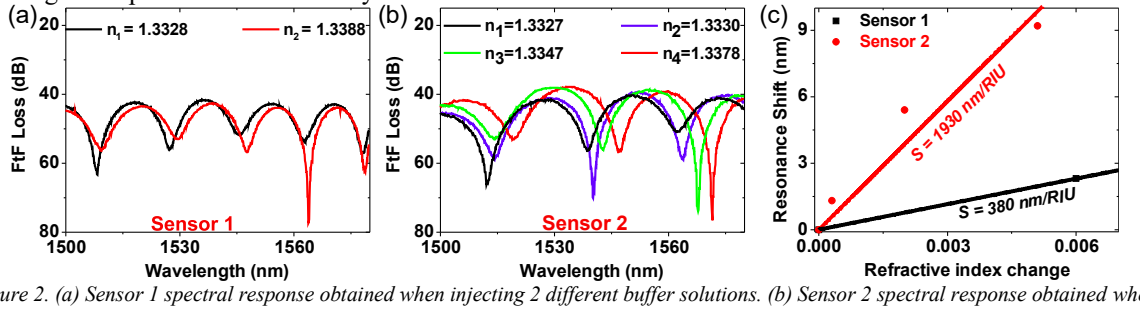


Figure 2. (a) Sensor 1 spectral response obtained when injecting 2 different buffer solutions. (b) Sensor 2 spectral response obtained when injecting 4 different buffer solutions. (c) Resonance shift versus refractive index change, illustrating linear fitting plots for each sensor.

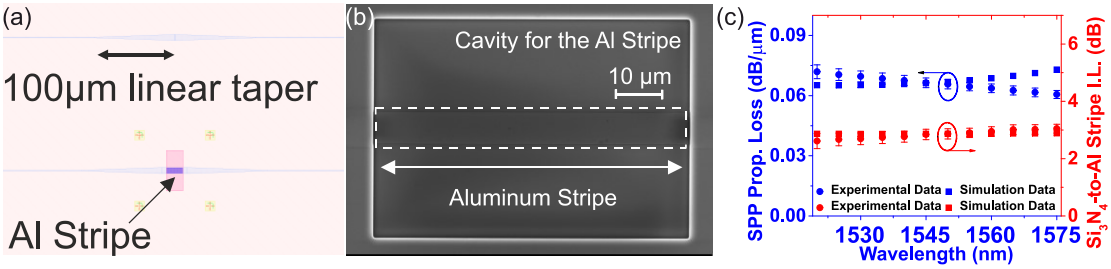


Figure 3. (a) Mask layout showing the reference waveguide and a Si_3N_4-to-Al interface test structure. (b) SEM image of the Al plasmonic stripe recessed in the cavity. (c) Broadband experimental data for the interface and propagation loss in water.

3. ALUMINUM STRIPES

The successful experimental results for the Au-based plasmo-photonic sensor motivated us to fabricate and test the proposed plasmo-photonic waveguide, employed at the interferometer sensing arm, on a separate chip, relying now on CMOS compatible plasmonic waveguides, by replacing gold with low cost Aluminum.

We evaluated the Al plasmonic waveguides in aqueous environment, by conducting broadband optical characterization based on Fiber-To-Fiber (FtF) measurements and following a standard cutback method. A highlight of the mask layout presenting the test structures that has been measured is shown in Fig. 3(a). The test structures included a reference waveguide and Si_3N_4-to-Al interface test structures with varied plasmonic stripe length (20, 50, 100, 150, 200 and 250 μm). The reference structure comprised of a 0.88 cm long straight Si_3N_4 waveguide with two 100 μm long linear tapers in the middle, interconnected to each other via 1 μm long and 7.5 μm wide waveguide. A SEM image of a 70 μm long Al stripe, recessed in the cavity between the Si_3N_4 waveguide facets, is shown in Fig. 3(b). The plasmonic propagation losses as function of wavelength have been obtained by performing a linear fitting process, based on least-squares method, to the experimental data. In order to calculate the Si_3N_4-to-Al interface loss, the losses of the reference Si_3N_4 waveguide structure were subtracted from the intercept values obtained by the fitting process and the resulting loss value was divided by a factor of two. Figure 3(c) presents the obtained characterization results for the plasmonic propagation losses and the interface loss as a function of wavelength, in comparison with the respective simulation results. Measurements dictated a plasmonic propagation loss of 0.065 dB/μm, which translates to a propagation length (Lspp) of 66.8 μm and a Si_3N_4-to-Al interface loss of 2.86 ± 0.07 dB at 1550 nm being in good agreement with the simulated values.

4. CONCLUSIONS

We demonstrate an interferometric sensor configuration, exploiting a gold based plasmo-photonic structure as the sensing element, achieving bulk sensitivity values up to 1930 nm/RIU. We also evince experimentally that the proposed plasmo-photonic waveguide employed at the interferometer sensing arm can be fabricated using Aluminum (Al) instead of gold, revealing an effective roadmap towards low-cost and CMOS-compatible integrated plasmo-photonic biosensors.

ACKNOWLEDGEMENTS

This work was supported by the European H2020 ICT PLASMOfab (no.688166) project. The authors would like to acknowledge Dr. Stefan Schrittwieser and Dr. Rudolf Heer from the Austrian Institute of Technology (AIT) for the fabrication and the adhesion of the silicone fluidic tubes on the sensor chip.

REFERENCES

[1] G. A. Lopez, M. Estevez, M. Soler, and L.M. Lechuga : Recent advances in nanoplasmonic biosensors: applications and lab-on-a-chip integration, *Nanophotonics,* vol. 6, pp. 123-136, 2017.

[2] J. Homola: Surface plasmon resonance sensors for detection of chemical and biological species, *Chem. Rev.* vol. 108, pp. 462–493, 2008.

[3] A. Khan, O. Krupin, E. Lisicka-Skrzek, and P. Berini: Mach-Zehnder refractometric sensor using long-range surface plasmon waveguides, *Appl. Phys. Lett.*, vol. 103(11), 111108, 2013

[4] X. Sun, D. Dai, L. Thylén, and L. Wosinski: High-sensitivity liquid refractive-index sensor based on a Mach-Zehnder interferometer with a double-slot hybrid plasmonic waveguide, *Opt. Express*, vol. 23, pp. 25688-25699, 2015.

[5] G. Dabos *et al.*: Aluminum plasmonic waveguides co-integrated with Si_3N_4 photonics using CMOS processes, *Scientific Reports*, vol. 8, no. 1, art. no. 13380, 2018.

[6] G. Dabos *et al.*: Plasmonic Stripes in Aqueous Environment Co-Integrated With Si3N4 Photonics, *Photonics Journal*, vol. 10, pp. 1–8, 2018.

[7] G. Dabos *et al.*: TM grating coupler on low-loss LPCVD based Si_3N_4 waveguide platform, *Opt. Commun.*, vol. 405, pp. 35–38, 2017.

Silicon photonics ionic sensor enabled by hybrid integrated 2D plasmonic MoO_3

Guanghui Ren, Baoyue Zhang, Markus Knoerzer, Arnan Mitchell, Jianzhen Ou
Electronics and Telecommunications Engineering, School of Engineering,
RMIT University P.O. Box 2462, Melbourne VIC 3001, Australia
e-mail: Guanghui.ren@rmit.edu.au

ABSTRACT

Silicon photonics has demonstrated great potential in ultra-sensitive biochemical sensing. However, it is challenging for such sensors to detect small ions which are also of great importance in many biochemical processes. Here, we introduce a silicon photonic ion sensor enabled by an ionic dopant-driven plasmonic material. The sensor consists of a micro-ring resonator (MRR) coupled with a two-dimensional (2D) re-stacked layer of near-infrared plasmonic molybdenum oxide. When the 2D plasmonic layer interacts with ions from the environment, a strong change in the refractive index results in a shift in the MRR resonance wavelength and simultaneously the alteration of plasmonic absorption leads to the modulation of MRR transmission power, hence generating dual sensing outputs which is unique to other optical ion sensors. We demonstrate proof-of-concept via a pH sensing model, showing a up to 7 orders improvement on sensitivity per unit area across the range from 1 to 13 compared to those of other optical pH sensors. Our platform offers the unique potential for ultra-sensitive and robust measurement of changes in ionic environment, generating new modalities for on-chip chemical sensors in the micro/nano-scale.

Keywords: integrated optics, silicon photonics, two-dimensional materials, doped semiconductor, ion sensor

1. INTRODUCTION

Silicon photonics has grown into a mature platform that is compatible with complementary metal-oxide–semiconductor (CMOS) technology, offering both wide bandwidth and low propagation loss overcoming the electronic bottleneck currently faced by microelectronics[1-3]. Silicon photonics has also emerged as an effective platform for biochemical sensing based on the perturbation of the evanescent field induced by the optical guided mode[4-7], through either the direct interferometric or resonant sensing of the ambient refractive index. These sensors are normally enabled by the specific interaction of two complementary molecules *via* surface functionalization. Typical examples include the functionalization with selective molecules such as DNA in the silicon photonic sensor for detecting complementary DNA/RNA strain[8, 9]. However, ionic species, which are also vital chemical components in many biochemical processes and metabolic activities of microorganisms, cannot be easily detected with current silicon photonic biosensors as the direct binding of ions onto the surface functional groups does not produce a measurable response of the ambient refractive index[9, 10].

In this regard, the realization of a sensing platform with additional measurable parameters beyond the analyte-induced ambient refractive index change should be of critical relevance for widening the application of silicon photonic based biochemical sensors. Recently, the emerging integration of two dimensional (2D) layered materials onto the silicon photonics platform provides a viable solution to obtain enhanced electronic and optical properties, mechanically flexibility, low fabrication and integration complexity, robustness, all while maintaining compatibility with CMOS technology[11-13].

In this contribution, 2D H^+ doped molybdenum oxides with NIR plasmon resonance is integrated on a silicon based micro-ring resonator to establish the label-free chemical sensing platform. The pH sensing model is used as the representative to evaluate the performance of this novel chemical sensing platform. In contrast, the unique H^+ dopants in the 2D MoO_3 host are hypothesized to be sensitive to the ambient change of ionic species concentration when the pH value is change from very acidic (pH=1) to very alkaline (pH =13) or *vice versa*. As a result, the H^+ dopant driven plasmonics is correspondingly altered and the optical absorption due to the excitation of hybrid plasmonic-optical modes in the silicon micro-ring resonator. Simultaneously, the refractive index of the 2D material also changed due to the variation of H^+ concentration, which leads to the shift of the resonant wavelength of the micro-ring resonator.

2. Design and Fabrication

To realize the 2D H^+ doped MoO_3 – silicon photonic based chemical sensing platform, a relatively high-performance micro-ring resonator (MRR) is firstly fabricated. The MRR is composed of a ring and two bus waveguides (Figure 1a). Grating couplers are used as the interface between the single mode optical fiber and the integrated Si photonic chip. As seen from the SEM image of the bare device (upper image of Figure 1b), the waveguides have width and height of 450 and 220 nm, respectively. The radius of the ring is 10 μm and the

separation distance between the ring and bus waveguide is 150 nm. After fabrication and initial characterization, 2D H^+ doped MoO_3 is deposited onto the micro-ring resonator using PTFE as a binding agent to enhance the adhesion between 2D $H_{0.3}MoO_3$ and the Si waveguide. Most of the surface area of the MRR are covered with 2D $H_{0.3}MoO_3$ nanoflakes with the relatively homogeneous thickness distribution in the region of 150 - 250 nm as evidenced by the SEM (lower image of Figure 1b) and AFM images (Figure 1c).

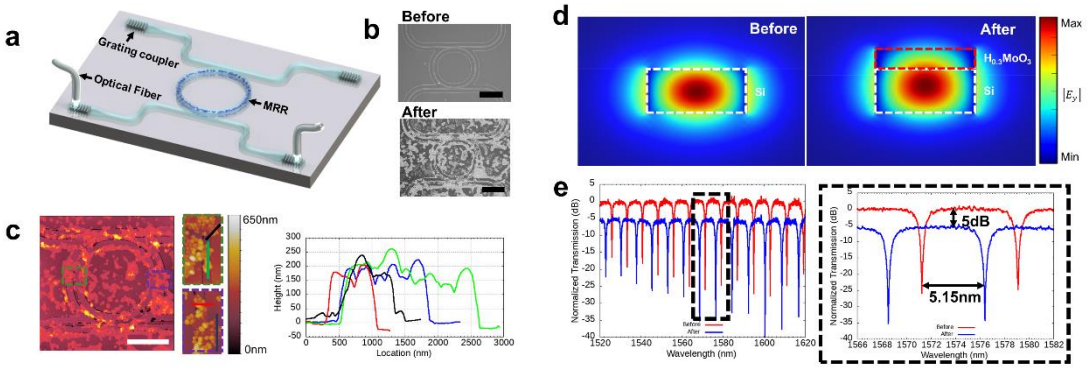


Figure1. a. Schematics of the used device; b. The scanning electronic microscope (SEM) images of the micro-ring resonator before and after $H_{0.3}MoO_3$ deposition. c. Atomic force microscope (AFM) images of the micro-ring resonator after H^+ doped MoO_3 deposition d. Numerical simulation of the optical modes in silicon waveguide before and after H^+ doped MoO_3 deposition. e. The transmission spectrum of the micro-ring resonator before and after H^+ doped MoO_3 deposition.

To explore how the 2D H^+ doped MoO_3 interacts with the silicon optical waveguide, numerical simulation was carried out. The simulation results are shown in Figure 1d. Comparing the optical modes in the waveguide before and after the H^+ doped MoO_3 deposition, the center of the optical mode is lifted, *i.e.* the mode confinement in silicon waveguide is weaker, and the evanescent field of the optical mode penetrates the whole layer of the deposited 2D H^+ doped MoO_3, which indicates the strong interaction between the optical mode in the silicon waveguide and the deposited $H_{0.3}MoO_3$. It also indicates that any change in the deposited 2D H^+ doped MoO_3 layers will affect the optical mode in the silicon waveguide.

The interaction between 2D H^+ doped MoO_3 and optical mode is also reflected on the alteration of the optical performance of the device. Figure 1e shows the measured transmission spectra before and after 2D H^+ doped MoO_3 deposition. As can be seen in the results, the resonant wavelength red shifts about 5.15 nm, and the transmission power drops about 5 dB. The resonant wavelength shift is caused by the fact that the deposited 2D H^+ doped MoO_3 material on micro-ring resonator changed the environment refractive index, which in turn caused the resonant wavelength shift.

3. RESULTS AND DISCUSSIONS

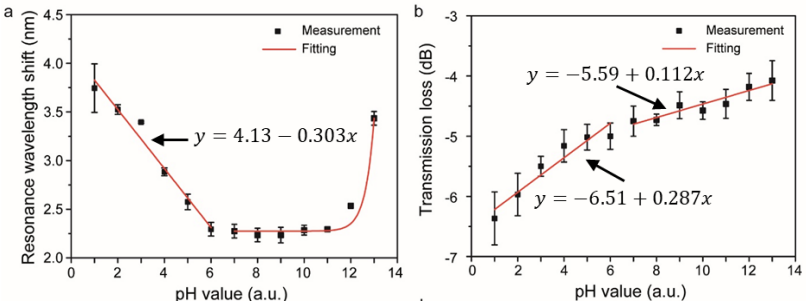


Figure2. (a). MRR resonant wavelengths of the integrated sensors as a function of pH values. (b). MRR transmission power of the integrated sensors as a function of pH values.

The ultra-sensitive ion-responsive sensor is evaluated using pH sensing as a demonstration model. Figure 2 shows the dependence of the transmission spectrum of the micro-ring resonator on the solvent pH value applied. In the measurement, two properties were analyzed, the resonant wavelength and the transmission loss of the micro-ring resonator. Figure 2b shows the transmission spectra of the MRR after 2D H^+ doped MoO_3 deposition for different pH value solvents. As can be seen, the resonant wavelength shifts for different pH values. With increasing pH value from 1 to 6, the resonant wavelength almost linearly shifts to longer wavelengths with the decreasing step of 0.32 ± 0.02 nm per pH. However, for pH values from 7 to 11, there is little change in the resonant wavelength possibly due to insufficient OH^- ions to interact with H^+ doped MoO_3. From pH 11 to 13, the resonant wavelength exponentially shifts to the longer wavelength side. Figure 2b shows the dependence of the relative

transmission loss on the solvent pH value. As can be seen, the transmission loss decreases almost linearly with the increase of the pH value, with the step of 0.2 dB for pH 1 to 6, and 0.15 dB for pH 11 to 13.

4. CONCLUSIONS

An ultra-sensitive silicon photonic based ion sensor was introduced. By integrating with dopant-driven plasmonic nanomaterials onto the silicon photonic platform, this novel ion sensor was enabled with unique ion-responsive capabilities which bare and biomolecule-functionalized silicon photonics were not able to provide. A proof of concept demonstration using a pH sensing model, has shown that the perturbation of ambient ions significantly changes the H+ dopant content and the concurrently injected free electrons in 2D plasmonic molybdenum oxides, leading to a reversible transition between semiconducting and metallic states. The dielectric properties were therefore altered, resulting in the strong influence on the resonant properties of silicon photonics due to the strong coupling of the evanescent field onto the 2D plasmonic layer. Simultaneously, the NIR plasmonic absorption of the 2D layer was affected accordingly, tailoring the light transmission property of the silicon photonic due to the matching between the plasmonic resonance and silicon operation wavelengths. As a result, the sensor could provide dual complementary outputs based on the variation of resonant wavelength shift and transmittance, leading to a wide pH detection range from 1 to 13 with a considerable response linearity. We believe that this work provides a feasible solution to realize on-chip and low-cost ion micro-sensors with high sensitivity, selectivity and repeatability for ionic changes. More importantly, the combination of this 2D plasmonic material with conventional biorecognition elements will potentially widen the applicability of silicon photonic based sensors and will have a notorious impact in the development of more advanced and sophisticated biosensors.

ACKNOWLEDGEMENTS

The authors acknowledge the generous support of the Australian Research Council (CE110001018, DP150101336 and DE160100715). Furthermore, the authors acknowledge the facilities, and the scientific and technical assistance, of the Micro Nano Research Facility (MNRF) and the Australian Microscopy & Microanalysis Research Facility at RMIT University. This work was performed in part at the Melbourne Centre for Nanofabrication (MCN) in the Victorian Node of the Australian National Fabrication Facility (ANFF).

REFERENCES

[1] R. Soref, "The Past, Present, and Future of Silicon Photonics," *IEEE Journal of Selected Topics in Quantum Electronics,* vol. 12, no. 6, pp. 1678-1687, 2006.

[2] A. Rickman, "The commercialization of silicon photonics," *Nature Photonics,* vol. 8, no. 8, pp. 579-582, 2014.

[3] A. H. Atabaki *et al.*, "Integrating photonics with silicon nanoelectronics for the next generation of systems on a chip," *Nature,* vol. 556, no. 7701, pp. 349-354, 2018/04/01 2018.

[4] M. Iqbal *et al.*, "Label-Free Biosensor Arrays Based on Silicon Ring Resonators and High-Speed Optical Scanning Instrumentation," *IEEE Journal of Selected Topics in Quantum Electronics,* vol. 16, no. 3, pp. 654-661, 2010.

[5] S. M. Lo, S. Hu, G. Gaur, Y. Kostoulas, S. M. Weiss, and P. M. Fauchet, "Photonic crystal microring resonator for label-free biosensing," *Optics Express,* vol. 25, no. 6, pp. 7046-7054, 2017/03/20 2017.

[6] A. Parkin, K. E. Dunn, M. G. Scullion, T. F. Krauss, and S. D. Johnson, "The electrophotonic silicon biosensor ´," *Nature Communications,* vol. 7, pp. 1-7, 2016.

[7] S. M. Grist *et al.*, "Silicon photonic micro-disk resonators for label-free biosensing," *Optics Express,* vol. 21, no. 7, pp. 7994-8006, 2013/04/08 2013.

[8] C. S. Huertas, S. Domínguez-Zotes, and L. M. Lechuga, "Analysis of alternative splicing events for cancer diagnosis using a multiplexing nanophotonic biosensor," *Scientific Reports,* Article vol. 7, p. 41368, 01/25/online 2017.

[9] V. Huber *et al.*, "Cancer acidity: An ultimate frontier of tumor immune escape and a novel target of immunomodulation," *Seminars in Cancer Biology,* vol. 43, pp. 74-89, 2017/04/01/ 2017.

[10] I. Kolosenko, S. Avnet, N. Baldini, J. Viklund, and A. De Milito, "Therapeutic implications of tumor interstitial acidification," *Seminars in Cancer Biology,* vol. 43, pp. 119-133, 2017/04/01/ 2017.

[11] G. Fiori *et al.*, "Electronics based on two-dimensional materials," *Nature Nanotechnology,* vol. 9, no. 10, pp. 768-779, 2014.

[12] F. Xia, H. Wang, D. Xiao, M. Dubey, and A. Ramasubramaniam, "Two-dimensional material nanophotonics," *Nature Photonics,* vol. 8, no. 12, pp. 899-907, 2014.

[13] A. K. Geim and I. V. Grigorieva, "Van der Waals heterostructures," *Nature,* Perspective vol. 499, p. 419, 07/24/online 2013.

Machine-assisted design and stochastic analysis in integrated photonics

(Invited paper)

Daniele Melati[1], Yuri Grinberg[2], Mohsen Kamandar Dezfouli[1], Abi Waqas[3], Paolo Manfredi[4], Pavel Cheben[1], Jens H. Schmid[1], Siegfried Janz[1], Alejandro Sánchez-Postigo[5], and Dan-Xia Xu[1]

[1]Advanced Electronics and Photonics Research Center, National Research Council Canada, 1200 Montreal Rd., Ottawa, ON K1A 0R6, Canada

[2]Digital Technologies Research Center, National Research Council Canada, Ottawa, ON K1A 0R6, Canada

[3]Departement of Telecommunication Engineering, Mehran University of Engineering and Technology, Jamshoro, 76062 Sindh, Pakistan

[4]Department of Electronics and Telecommunications, Politecnico di Torino, 10129 Torino, Italy

[5]Universidad de Málaga, Departamento de Ingeniería de Comunicaciones, ETSI Telecomunicación, Campus de Teatinos s/n, 29071 Málaga, Spain

e-mail: daniele.melati@nrc-cnrc.gc.ca

ABSTRACT

Integrated photonic devices are steadily making their way into many application fields including modern optical communication networks and advanced sensors. On the other hand, the design of photonic devices and circuits mostly remains a time-consuming process largely based on the designer experience. This limits the size and complexity of the parameter space that can be handled. Moreover, addressing the effect of manufacturing variability remains a fundamental challenge since small fabrication errors can have a significant impact on light propagation, especially in high-index-contrast platforms such as silicon-on-insulator. The analysis of this variability with conventional approaches (e.g. Monte Carlo) can become prohibitive due to the large number of required simulations. Recent advances in machine-assisted design methods are opening the possibility to vastly expand the number of design parameters, exploring novel functionalities and non-intuitive geometries. In this invited talk we discuss the use of machine learning methods for the design of integrated photonic devices. We show the existence of a large number of possible designs that are all equivalent with respect to a given primary design objective but with distinct properties in other performance criteria. We use pattern recognition to reveal their relationship and to reduce the dimensionality of the large design space by properly defining new design variables. Likewise, we show how efficient stochastic techniques allow a quick assessment of the performance robustness and the expected fabrication yield for each tentative device. We focus in particular on stochastic spectral methods that have been regarded as a promising alternative to the classical Monte Carlo method, achieving a considerable reduction of the simulation time. Together, the reduction in the design space dimensionality and efficient stochastic techniques allow for the integration of the fabrication tolerance considerations into the design process.

Keywords: photonic devices, silicon photonics, machine learning, stochastic processes, pattern recognition, uncertainty analysis.

1. INTRODUCTION

The design of novel photonic devices with complex and non-trivial geometries vastly increases the number of design parameters and makes manual device design impractical. Tools such as the genetic algorithm, particle swarm, gradient-based optimization, and artificial neural network are often used to search more efficiently for high-performance designs [1]. Highly compact devices employing non-intuitive geometries have been demonstrated exploiting inverse design methods. [2]. However, the ability to efficiently explore and comprehend large design spaces is still beyond reach. Moreover, the analysis of the impact of manufacturing variability remains a major challenge [3]. Classical methods for stochastic analysis such as Monte Carlo require a very large number of simulations to obtain reliable results, hampering their use in large-scale multi-parameter designs.

In this invited talk we report on the application of advanced computational approaches for the design and analysis of photonic integrated devices. We show that applications of machine learning tools can benefit the design of devices with a large number of parameters. We investigate the study case of a vertical grating coupler made in silicon-on-insulator technology [4] using a suite of machine learning tools, including global optimization, supervised learning and unsupervised machine learning pattern recognition. Starting from a small set of possible alternative designs with state-of-the-art fibre coupling efficiency we analyse the apparent

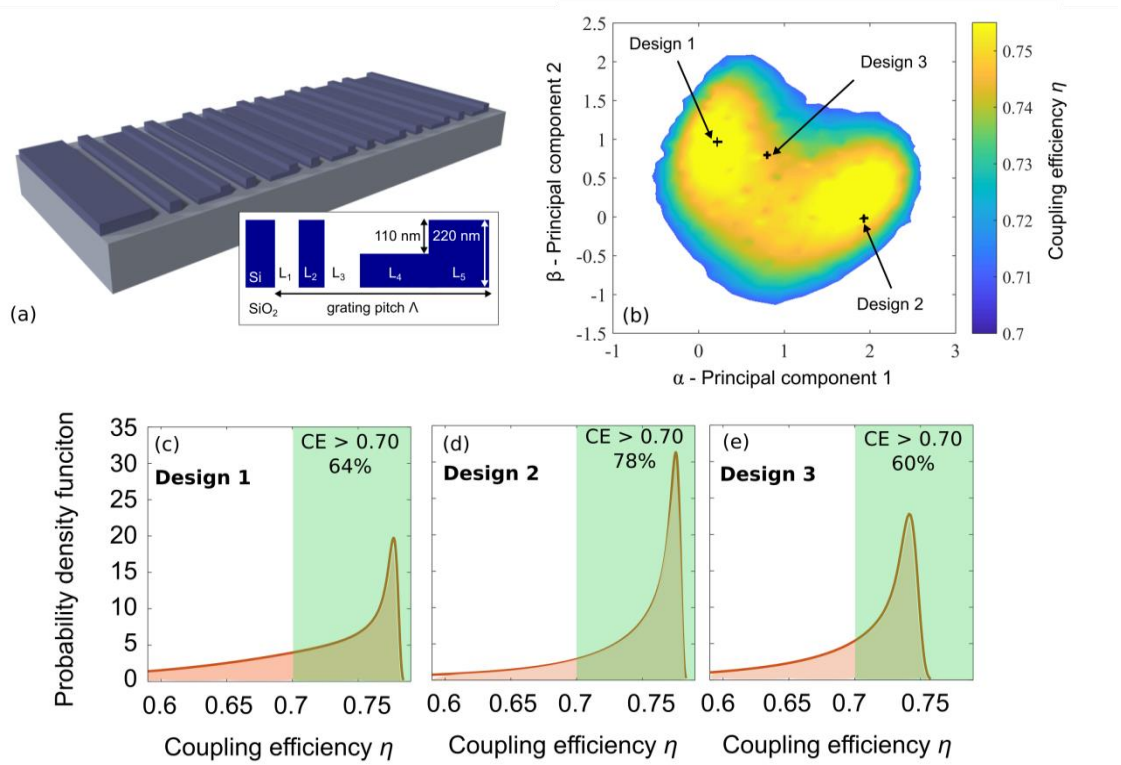


Figure 1. (a) Schematic of the vertical grating coupler. The design involves five parameters (the length of each section L_1-L_5). (b) Using a combination of machine learning techniques, including pattern recognition, the 5-D design space can be efficiently explored, identifying a 2-D sub-space (hyperplane) containing a large number of alternative grating designs all with a state-of-the-art fibre coupling efficiency larger than 0.7. (c)-(e) Probability density function of the coupling efficiency for the three designs highlighted in (b) when a standard deviation of 5 nm for the segment lengths is considered. The three designs have different fabrication yield, calculated as the probability for the device to have a coupling efficiency larger than 0.7 for the three designs (green shaded areas).

redundancy of the original five-parameter design. This analysis reveals that all good designs belong to a 2D hyperplane, a subspace within the 5D design space. Such reduction in dimensionality allows us to perform exhaustive evaluation of the subspace of good designs and identify design candidates with equivalent fibre efficiency but significant differences in other criteria such as back-reflection or robustness to fabrication variability [4].

Starting from these results, we then present the application of polynomial chaos expansion (PCE) techniques to investigate how the device performance deteriorates in the presence of dimensional variability due to fabrication uncertainty. PCE allows building a surrogate model of an unknown random function by representing its dependence on stochastic variables using an orthogonal set of polynomials. With a very limited number of initial simulations PCE provides an accurate representation of the variability, predicting its effects on the final designs and enabling the computation of stochastic quantities such as fabrication yield.

2. STOCHASTIC ANALYSIS IN HIGH-DIMENSIONAL DEVICE DESIGN

Figure 1(a) shows the vertically-emitting grating coupler considered here as a study case. The grating period consists of a pillar of 220 nm in height and an L-shaped section partially etched to 110 nm whose blazing effect ensures that light is primarily diffracted upwards. The structure dimensions L_1 - L_5 define the five-dimensional design parameter space. The design objective is the coupling efficiency CE of the diffracted TE-polarized light to a standard single mode optical fibre (SMF-28) placed vertically on top of the grating. As described in [4], a machine-learning enhanced search allows finding a collection of different good designs whose coupling efficiency is between 74% and 76%. Although coupling efficiency is the primary performance criterion for these kind of devices, there are several other important considerations to take into account, whether application specific (e.g. very low back reflections, high bandwidth) or mandated by the manufacturing process (e.g. feature size limitations). Obtaining a characterization of the subspace of good designs can significantly clarify the situation as trade-offs between various considerations become easier to calculate and visualize. For this purpose, we apply the dimensionality reduction technique within the unsupervised machine learning toolbox, specifically the principal component analysis (PCA) [5]. PCA finds a sequence of best linear approximations to the dataset

based on minimizing the least squared errors and the results explicitly show how many orthogonal linear projections are needed to represent the dataset within a certain level of accuracy. For the collection of good grating designs described above, 5 different designs are enough for PCA to reliably reveal a two-dimensional subspace that contains all possible designs with state-of-the-art coupling efficiency, and thereby excludes a large part of the design space that is no longer relevant. A reduction from five dimensions to two allows us to perform an exhaustive performance evaluation of all the designs included in the lower-dimensional subspace and generate for coupling efficiency the map shown in Fig. 1(b) using less than 1000 simulation runs. Alternatively, a similar exhaustive scan in five dimensions would require millions of simulation runs to identify the region of good designs with the same level of accuracy. The exhaustive scan of the 2D subspace identified by the PCA provides a complete map of the subspace of good designs and naturally makes it easy to choose the design to fabricate given a complete set of requirements and constraints. For example, designs 1 to 3 highlighted in Fig. 1(b) have very similar coupling efficiency of 76%, 75.5% and 74.5%, respectively, but very different back-reflections (-21dB, -40dB, and -17dB). Also the tolerance to fabrication variability is different between the three designs, as described below. Some interesting insights about a range of possible good designs can be obtained even before the exhaustive scan is performed. For example, it is straightforward to identify various minimum feature sizes that good devices can possibly have by inspecting the 2D subspace without the need to run any optical simulation. In particular, this specific grating architecture does not have good designs with a minimum feature size larger than 90 nm.

While coupling efficiency has been treated so far as a deterministic quantity, it is unavoidably subject to variability due to dimensional variations during fabrication. We can efficiently investigate this variability by computing a surrogate model for coupling efficiency exploiting a polynomial chaos expansion technique [3]. We consider coupling efficiency CE at $\lambda = 1550$. We assume for both shallow and deeply etched sections in the grating the same random width deviation δ, normally distributed with zero mean and a standard deviation of 5 nm. For the coupling efficiency, a polynomial order $P = 3$ (4 coefficients) is enough to provide a good fit. To robustly estimate the four coefficients by means of linear regression 8 values for δ are sampled according to its distribution and the corresponding designs are simulated with 2D-FDTD. The computational time required to build the surrogate model is negligible compared to optical simulation time. The entire analysis is performed with a number of simulations orders of magnitude smaller than Monte Carlo, making its application to the large number of designs shown in Fig. 1(b) possible with only a few thousands of optical simulations. Figure 1 (c)-(e) shows the probability density functions of coupling efficiency for designs 1, 2, and 3 highlighted in Fig. 1(a). The probability density functions are obtained by sampling the surrogate models 5000 times (which only takes a few seconds) and using a Gaussian kernel density estimator. During the analysis, fabrication yield is also estimated for the criterion of $CE > 0.7$. The number of devices respecting this criterion (yield) is computed integrating the corresponding part of the probability density function. Design 1 shows a longer tail towards lower values of CE compared to design 2, reducing the probability to obtain a high coupling efficiency and consequently the yield (64% instead of 78%). Design 3 has the lowest average coupling efficiency (68%) and the lowest yield (60 %).

3. CONCLUSIONS

We have shown how the introduction of machine learning tools in the design of photonic devices brings unparalleled capabilities in terms of speedup in the exploration of large design spaces and physical insight of non-intuitive geometries. Likewise, polynomial chaos expansion can be fruitfully exploited to efficiently investigate the stochastic properties of photonic devices and circuits subject to fabrication uncertainty. This makes the approach attractive for the investigation of large multi-parameter design space and machine-assisted design approaches requiring the analysis of a large number of possible alternative design solutions.

REFERENCES

[1] J. S. Jensen and O. Sigmund, “Topology optimization for nano-photonics,” Laser & Photonics Reviews, vol. 5, no. 2, pp. 308–321, Mar. 2011.

[2] A. Y. Piggott, J. Lu, K. G. Lagoudakis, J. Petykiewicz, T. M. Babinec, and J. Vučković, “Inverse design and demonstration of a compact and broadband on-chip wavelength demultiplexer,” Nature Photonics, vol. 9, no. 6, pp. 374–377, Jun. 2015.

[3] T.-W. Weng, D. Melati, A. Melloni, and L. Daniel, “Stochastic simulation and robust design optimization of integrated photonic filters,” Nanophotonics, vol. 6, no. 1, pp. 299–308, Jan. 2017.

[4] D. Melati, Y. Grinberg, S. Janz, P. Cheben, J. H. Schmid, A. Sánchez-Postigo, D.-X. Xu “Mapping the global design space of integrated photonic components using machine learning pattern recognition”, arXiv:1811.01048, November 2018.

[5] G. H. Dunteman, *Principal Component Analysis* (SAGE), 1989

Ultracompact 40-Channels Arrayed Waveguide Grating on Silicon Nitride Platform at 850nm

(Student Paper)

Zunyue Zhang[1], Yi Wang[1], Hon Ki Tsang[1]
[1] Dept. of Electronic Engineering, The Chinese University of Hong Kong, Shatin NT, Hong Kong SAR, China
e-mail: hktsang@ee.cuhk.edu.hk

ABSTRACT

We propose and demonstrate a 40-channels arrayed waveguide grating (AWG) on silicon nitride platform at 850nm. The total size of the AWG is 910× 680 μm^2. The transmission spectrum is measured. The AWG has an operating bandwidth of 60nm and has a measured insertion loss of 0.6dB. The channel crosstalk is 20dB.

Keywords: Arrayed waveguide grating, ultracompact, very near infrared, silicon nitride platform.

1. INTRODUCTION

Optical coherence tomography (OCT) is a 3D imaging technique which is widely used in ophthalmology, gastroenterology, and cardiology [1]. Time-domain OCT (TD-OCT) performs a time domain measurement of the interference signals from the mechanically scanning reference arm and the reflection from different depth of the samples. Spectral-domain OCT (SD-OCT), alternatively, fixes the reference arm and measures the optical spectrum, thus shows a faster imaging speed and higher sensitivity [2]. The key component in a SD-OCT system is the broadband spectrometer with high spectral resolution. The broad operating bandwidth make it possible to build a high-axial-resolution SD-OCT and the high spectral resolution determines the large imaging depth [3].

SD-OCT system with integrated spectrometer was recently demonstrated at 1310nm [4]. While for ophthalmology, 850nm is a better choice because tissue absorption is dominated by haemoglobin in 200-600nm and by water at the wavelength range above 1000nm [5]. Silicon nitride has a large wavelength range of transparency from about 400nm wavelength to the mid-infrared and is thus a suitable platform for integrated spectrometers operating around the 850nm wavelength range.

The basic principle for the separation of different wavelengths in an AWG was originally introduced in 1988 by M.K. Smit [6], and a large, centimetre scale, silicon oxynitride AWG spectrometer was previously reported for use in an integrated spectrometer in SD-OCT system [7]. Use of high refractive index- silicon nitride for AWG may lead to more compact designs but previous work on this platform was limited to 12 channels around the target wavelength range [8-9].

In this paper, we design and demonstrate a 40-channels AWG on silicon nitride platform at 850nm with a small footprint of only 910× 680 μm^2. The measured transmission spectrum of the AWG shows an operating bandwidth of 60nm with low insertion loss of 0.6dB and low channel crosstalk of 20dB.

2. DEVICE DESIGN

The device is design on 300nm thick silicon nitride wafer with 3.3 μm buried oxide and air cladding, waveguide width is designed to be 800nm to make sure single mode transmission at 850nm, in the meanwhile reduce the scattering loss and phase errors caused by the sidewall roughness. Fundamental TE mode is used in the AWG design. The effective index of the silicon nitride slab n_s and arrayed waveguides n_{wg} are simulated by

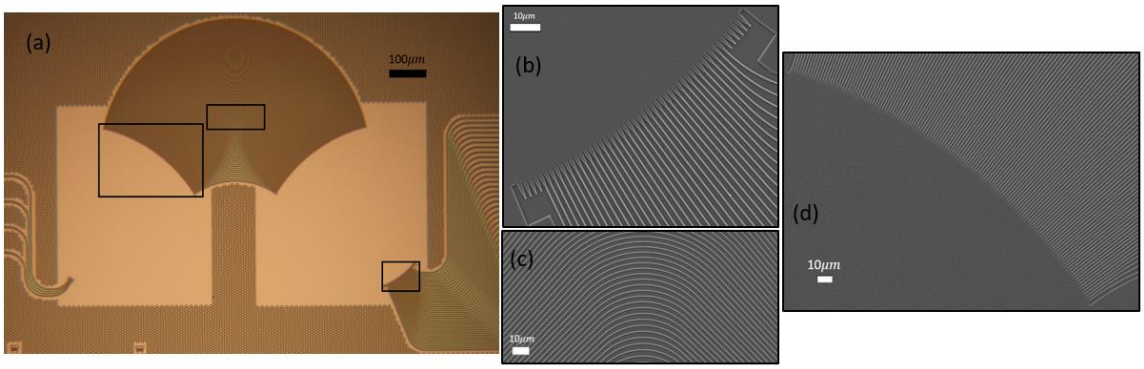


Fig. 1. (a) Microscope image of the 40-channels AWG. (b) SEM image of the output channels, parabolic tapers are used to reduce the coupling loss from FPR to waveguides. (c)SEM image of the arrayed waveguides, curve profiles are carefully designed to reduce the systematic phase errors. (d)SEM image of the interface between FPR and arrayed waveguides.

commercial Lumerical Mode Solutions and the group index of the arrayed waveguides N_g is 1.99. Due to the spectral nonuniformity [10], we start the design with a 50-channels AWG and use the central 40 channels as a spectrometer to make a more flatten transmission spectrum. 150 arrayed waveguides are used in the design. The arrayed waveguide length increment ΔL is designed to be 4.92 μm to make the free spectral range (FSR) 75 nm. The waveguide aperture of input/output waveguide and arrayed waveguides are both 2 μm. Parabolic tapers are designed and simulated to minimize the coupling loss from FPR to arrayed waveguides and input/output waveguides. The length of the free propagation region (FPR), i.e. the diameter of the Rowland circle is 386.5 μm, which determines the channel spacing of the designed AWG to be 1.5nm. We use Semi-analytical AWG model [11] to simulate the light propagation in the AWG. The simulated transmission spectrum shows the 40-channels AWG has 0.45dB insertion loss and 22dB inter-channel crosstalk. For the arrayed waveguides layout, we carefully design the radius profiles of the curves and the length of straight waveguides to minimize the systematic phase errors and the crosstalk induced, at the same time ensure the minimum total size. The overall size of the AWG is 910× 680 μm^2.

3. RESULTS AND DISCUSSION

The device is fabricated by IMEC on silicon nitride- silicon nitride multi-project wafer (MPW) platform, which shows its great potential for large-scale photonic integrated circuits and integrated spectrometers for SD-OCT system. Microscope image of the device and the enlarged SEM images are shown in Fig.1.

The AWG is tested with broadband light from a superluminescent diode (SLD) and optical spectrum analyser. Fibre-chip grating couplers designed at 850nm are used to couple light into and out of the chip. The transmission spectrum is normalized to a short straight waveguide with input and output grating couplers as shown in Fig. 2 (a). The zoom-in view of the central channel (#20) compared with the simulation spectra is shown in Fig. 2 (b).

After normalizing out the coupling losses of the grating couplers, the insertion loss of the AWG was 0.6dB. This result is only about 0.15dB higher than the simulation results. The central channels show the best inter-channel crosstalk of -20dB, which is 2dB worse than the simulation results. The difference comes from the phase errors caused by the sidewall roughness and waveguide crosstalk. The channels at short and long wavelength side show higher crosstalk which is due to the sharp drop of the SLD output power below 835nm and the grating coupling efficiency drop over 885nm, as shown in Fig.2 (c), while the lowest power can be measured is limited by the noise floor of the optical spectrum analyser of -78dBm at 850nm. The operating bandwidth of the AWG is 60nm and the channel spacing is 1.5nm, which match well with the simulation results.

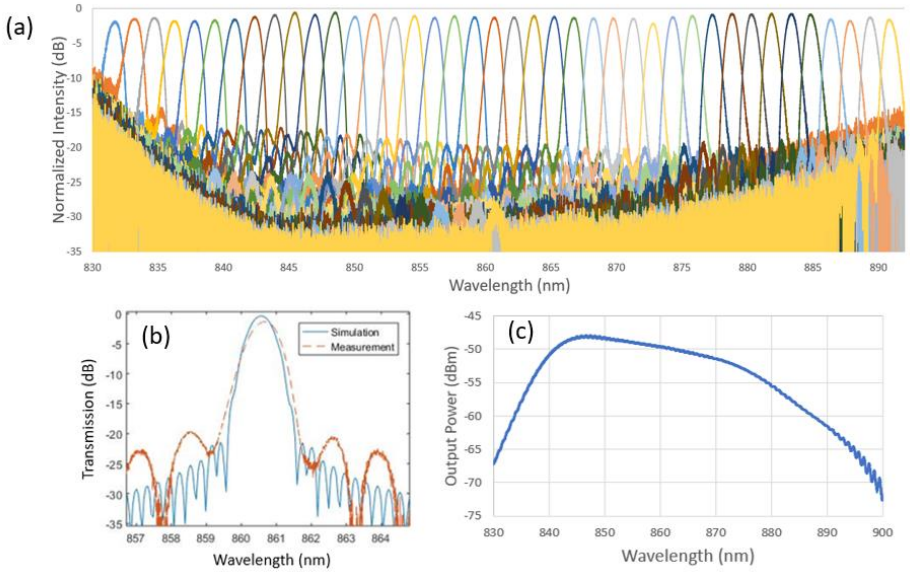


Fig. 2. (a) Measured transmission spectrum of the 40-channels AWG after normalization. (b)Zoom-in view of the central channel (#20) compared with the simulation spectrum. (c) Waveguide transmission with grating coupled in and out, used to normalize the AWG transmission spectrum, sharp power drops are shown below 835nm and over 885nm.

As a comparison, another AWG is also designed following the same design method while the waveguide width is changed to 560nm. We tested the AWG with the same experimental setup. The worst inter-channel crosstalk of the fabricated device was 13dB and the insertion loss also increases to 5dB. The degradation of the AWG performance is ascribed to the narrower width of arrayed waveguides. As the waveguide becomes narrower, the guiding mode in the waveguide has larger overlapping with the sidewall of the waveguide, thus suffering more from the sidewall roughness, which not only increases the scattering loss but also induces larger phase errors. On the other hand, the coupling between adjacent arrayed waveguides also increase for narrower waveguides because of the weaker mode confinement. For this reason, air cladding rather than SiO_2 cladding was used.

4. CONCLUSIONS

We propose and demonstrate an ultracompact 40-channels AWG on silicon nitride platform at 850nm with an overall size of $910\times 680\ \mu m^2$. The AWG, with an operating bandwidth of 60nm and channel spacing of 1.5nm, has an insertion loss of 0.6dB and inter-channel crosstalk of 20dB, which shows its great potential for large-scale photonic integrated circuits and ultracompact integrated spectrometers for SD-OCT system. A tunable laser with wider tuning range to below 830nm, and broadband fibre-chip coupling methods will be needed for further testing of the device. Higher spectral resolution and more channels can be achieved by combining this AWG with other integrated wavelength filters.

ACKNOWLEDGEMENTS

The author would like to thank IMEC for device fabrication in the BioPix program and funding from ITF grant ITS/433/17FX.

REFERENCES

[1] J. G. Fujimoto, W. Drexler: Introduction to OCT, in *Optical Coherence Tomography Technology and Applications*, W. Drexler, J. G. Fujimoto, Ed., New York: Springer-Verlag, 2008.
[2] Z. Yaqoob, J. Wu, C. Yang: Spectral domain optical coherence tomography: a better OCT imaging strategy, *Biotechniques*, vol. 39. pp. 6-13, Dec. 2005.
[3] B. I. Akca, *et al.*: Toward Spectral-Domain Optical Coherence Tomography on a Chip, *IEEE J. Sel. Top. Quantum Electron*, vol. 18. pp. 1223-1233, May/Jun. 2012.
[4] B. I. Akca, *et al.*: Miniature spectrometer and beam splitter for an optical coherence tomography on a silicon chip, *Opt. Express*, vol. 21. pp. 16648–16656, July 2013.
[5] M. E. J. van Velthoven, *et al.*: Recent developments in optical coherence tomography for imaging the retina, *Prog. Retina Eye Res.*, vol. 26. pp. 57–77, Jan. 2007.
[6] M. K. Smit: New focusing and dispersive planar component based on an optical phased-array, *Electron. Lett.*, vol. 24. pp. 385–386, Mar. 1988.
[7] V. D. Nguyen, *et al.*: Spectral domain optical coherence tomography imaging with an integrated optics spectrometer, *Opt. Lett.*, vol. 36. pp. 1293–1295, Apr. 2011.
[8] D. Martens, *et al.*: Compact silicon nitride arrayed waveguide gratings for very near-infrared wavelengths, *IEEE Photon. Technol. Lett.*, vol. 27. pp. 137–140, Jan. 2015.
[9] E. J. Stanton, *et al.*: Low-loss arrayed waveguide grating at 760 nm, *Opt. Lett.*, vol. 41. pp. 803-806, Apr. 2016.
[10] M. K. Smit, C. van Dam: PHASAR-based WDM-devices: principles, design and applications, *IEEE J. Select. Topics Quantum. Electron*, vol. 2. pp. 236–250, Jun. 1996.
[11] S. Pathak: Silicon Nano-Photonics based Arrayed Waveguide Gratings, PhD dissertation, Univ. of Ghent, 2014.

Interleaved Silicon Nitride AWG Spectrometers

B. Imran Akca[1], Christopher R. Doerr [2]
[1] VU University Amsterdam, Department of Physics and Astronomy, De Boelelaan 1081, 1081 HV Amsterdam, The Netherlands
[2] Acacia Communications, 1301 Route 36, Hazlet, NJ, USA 07730
e-mail: b.i.avci@vu.nl

ABSTRACT

Interleaved arrayed waveguide gratings (AWGs) have a great potential in providing large channel counts and narrower channel spacings for many applications, including optical communication, spectroscopy, and imaging. Here, a 75-channel silicon nitride based interleaved AWG was experimentally demonstrated. The design is comprised of a 3-channel primary AWG with 1 nm of resolution and three 25-channel secondary AWGs each with 3 nm of resolution. The final device has a spectral resolution of 1 nm over 75 nm bandwidth centered at 1550 nm. Its performance is compared with a conventional AWG spectrometer with 75 nm of bandwidth and 1 nm of resolution. The interleaved AWG demultiplexer showed lower crosstalk and better uniformity in addition to being two times smaller than the conventional design.

Keywords: AWG spectrometers, compact, interleaved, better uniformity

1. INTRODUCTION

An arrayed waveguide grating (AWG) is a planar dispersive device, which is generally used as an on-chip spectrometer in many applications [1]. Combining high resolution and large free spectral range (FSR) in a single AWG is highly desirable for numerous applications, however it is rather difficult to implement. By applying different approaches, such as cascading several AWGs, the limitations on resolution and FSR of an AWG can be overcome. Even though the cascading configuration enables us to design flexible wavelength division multiplexing devices with high channel count and channel spacing, the device size will still be an issue [2-4]. Interleaving can solve the size problem. An AWG can be interleaved using its periodic routing property [5,6]. To do so, a high resolution AWG is used as the first stage, while several coarse filters are used in the second stage. Fig. 1a illustrates the working principle. The channel spacing of the secondary AWGs, i.e. $\Delta\lambda_S$, should be equal to the free spectral range (FSR) of the primary AWG, i.e. FSR_P. In this configuration, the FSR of the secondary AWGs, i.e. FSR_S, defines the FSR of the overall configuration whereas the channel spacing of the primary AWG, i.e. $\Delta\lambda_P$, defines the overall system resolution. In this method, the requirements on resolution and passband flatness of the secondary AWGs are relatively low, as the components in their prefiltered input spectra can be easily separated with very low adjacent-channel crosstalk. Moreover, the complete device size will be much smaller compared to one that is designed with the conventional cascading method, since high-resolution AWGs are generally bigger than low-resolution AWGs, therefore a multi-stage system with one high-resolution AWG and multiple low-resolution AWGs can be smaller in overall size than one with a low-resolution AWG and multiple high-resolution AWGs.

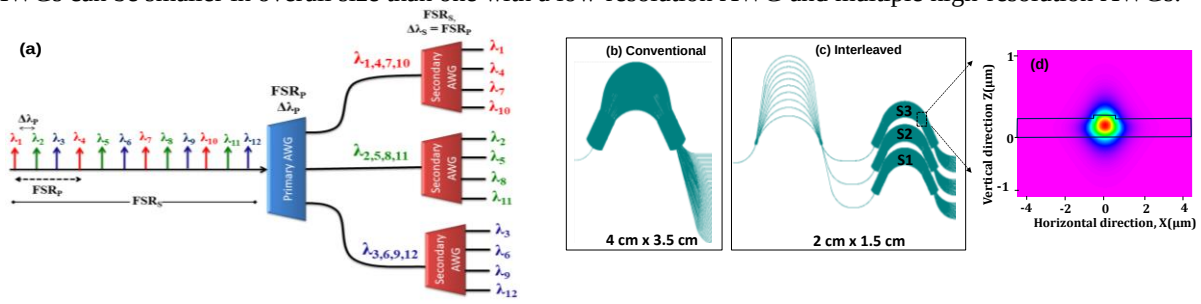


Figure 1 a. Schematic diagram of the interleaved AWG. Layout of the b. conventional and c. interleaved AWG spectrometers for the same resolution and bandwidth values. The size of the conventional design is ~ 2 times bigger than the interleaved design. d. Beam propagation method simulation of the optical mode. The blue outline shows the cross-sectional profile of the waveguide geometry.

A theoretical analysis on multi-stage WDM networks was made by Maier *et al*. including interleaved AWGs [7]. Chan *et al*. demonstrated a hybrid multiplexer by combining interleaved AWGs with free space gratings using free space configuration [8]. However, to the best of our knowledge, interleaved AWGs with large channel counts and narrow channel spacings in a CMOS compatible platform have not been experimentally demonstrated. Here, as a proof-of-principle, the performance of a two-stage interleaved AWG spectrometer with 1 nm resolution over 75 nm bandwidth centered at 1550 nm wavelength range was realized in silicon nitride (Si_3N_4) platform. A conventional AWG spectrometer with the same bandwidth and resolution values was realized in order to compare its performance with the interleaved AWG.

2. DESIGN

2.1 Waveguide geometry

The AWG spectrometers were realized using silicon nitride (Si_3N_4). The material system is a 200-nm-thick LPCVD Si_3N_4 film on an 8-μm-thick thermally-oxidized silicon wafer. A 4.0 μm thick SiO_2 layer (n = 1.47) was deposited by Plasma Enhanced CVD (PECVD) to complete the waveguiding cross-section. The refractive index of the thermal oxide and Si_3N_4 layer is 1.45 and 2.0 at 1550 nm, respectively. Single mode rib waveguides with 0.15 μm of slab height and 2.0 μm of waveguide width were designed. The effective refractive index of the fundamental transverse electric (TE) mode in the rib waveguide was calculated to be 1.55 by using beam propagation method (BPM) simulations. The optical mode profile is given in Fig. 1d. The minimum bending radius of the curved waveguides was calculated to be R = 150 μm with a bending loss of 0.1dB/cm

2.2 Demultiplexer design parameters and layout

As a proof-of-principle, an interleaved AWG spectrometer centered at λ_c = 1550 nm was designed with a channel spacing of $\Delta\lambda$ = 1 nm and a bandwidth of FSR = 75 nm. One primary and three secondary AWGs were used, which resulted in an overall device size of 2 cm x 1.5 cm. The size of a conventional AWG with the same bandwidth and resolution values is 4 cm x 3.5 cm. Size and layout comparisons of the conventional and interleaved AWG spectrometers are given in Figs. 1b and 1c. The effect of waveguide and material dispersion was included in each AWG design. The central wavelengths of the secondary AWGs were set to be the same as the output wavelength values of the primary AWG. The remaining design parameters of the devices were calculated using the standard equations for AWGs [6].

2.3 Beam propagation method (BPM) simulations

The performance of the AWGs was simulated using a 2D beam propagation method (BPM). According to BPM simulations for the conventional AWG, at the central channels, a crosstalk value of -28 dB and an excess loss of 4 dB were obtained. At the outermost channels these values are -25 dB and -16 dB, respectively. The adjacent crosstalk values for central and outer channels are 2.3 dB and 1.5 dB, respectively. The simulation results are given in Fig. 2a. The primary AWG of the interleaved design had a crosstalk value of -28 dB and excess loss value of 2.7 dB. The adjacent crosstalk value was obtained as -12 dB as shown in Fig. 2b. The simulation results of the secondary AWG centered at 1550 nm is given in Fig. 2c. Crosstalk values of -45 dB and -41 dB and excess loss values of 0.7 dB and 4.6 dB were obtained for the central and outer channels, respectively. Adjacent crosstalk value in the center is -11 dB.

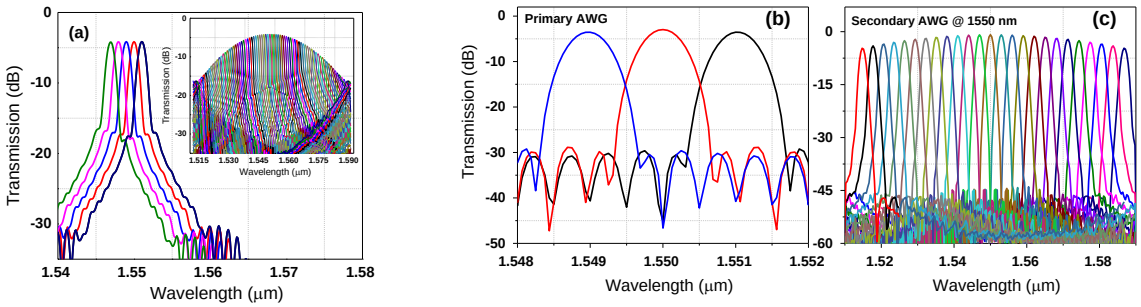


Figure 2. a. Simulation result of the central waveguides of the conventional AWG. Inset shows the complete spectrum. Simulation result of the (b) primary and (c) secondary AWG centered at 1550 nm.

3. MEASUREMENT RESULTS AND DISCUSSIONS

3.1 Measurement setup

Optical transmission measurements were performed by coupling TE-polarized light from a supercontinuum light source (NKT SuperK EXTREME, EXR4) into the input waveguide with a single-mode polarization-maintaining (PM) fiber. The output signal was sent to an optical spectrum analyzer (Yokogawa, AQ6370B) through a butt-coupled single-mode fiber. The transmission spectra measured at the output channels were normalized with respect to the transmission spectrum of a curved channel waveguide with the same radius and propagation length as the longest arrayed waveguide in the AWGs.

3.2 Conventional AWG transmission measurements

The measured transmission spectra of the central and outer waveguides of the conventional AWG are displayed in Fig. 3a. As predicted, each channel works as a band-pass wavelength filter. The measured values of resolution and FSR are consistent with the simulation results. However, a 5-dB difference between the simulated and measured crosstalk values was found which is mainly attributed to the fabrication-related phase errors. The excess loss values of 8 and 17 dB and crosstalk values of -23 and -18 dB were measured at central and outer channels, respectively.

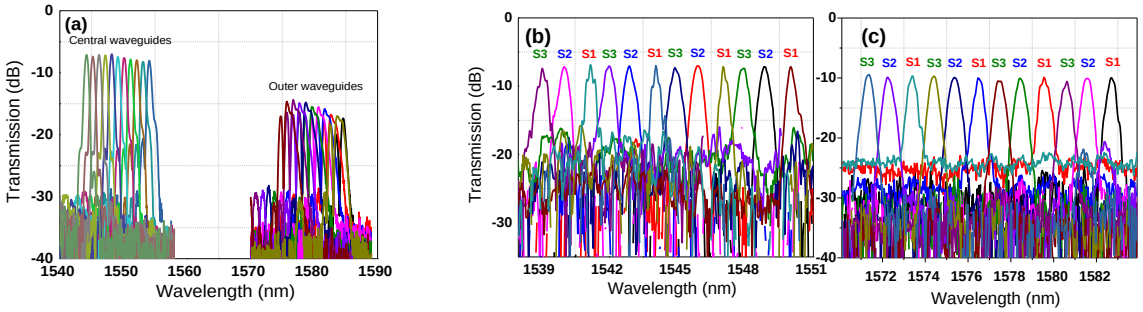


Figure 3 Measurement results of the central and outer channels of the a. conventional AWG, b. central channels of interleaved AWG, and c. outer channels of the interleaved AWG..

3.3 Interleaved AWG transmission measurements

Figures 3b and 3c display the measured transmission spectra of the central and outer output waveguides of the interleaved AWG spectrometer, respectively. S1, S2, and S3 indicates the secondary AWGs illustrated in Fig. 1c. As expected, interleaved AWG worked based on the cyclic nature and a fine resolution and large bandwidth were achieved. The overall crosstalk value of the central waveguides of the interleaved AWG is higher than predicted, because the uncoupled stray light coming from the input waveguide side contaminates the central waveguides more than the outer channels (see design of interleaved AWG in Fig. 1c). By adding a larger spatial offset between input waveguides with respect to the outer waveguides this issue can be solved easily. The adjacent crosstalk values of around -15 dB was measured for the whole range. Excess loss values of 7 dB and 10 dB were measured for the central and outer channels, respectively. A center wavelength shift of 3.3 nm was found which could be due to the insufficient etching of the rib waveguides. For this design, we did not use any on-chip heaters to tune the transmission spectrum of each sub AWG to align with the primary AWG spectrum; however, for an interleaved system with much finer resolution such heaters may be needed.

4. CONCLUSIONS

In summary, an interleaved Si_3N_4 AWG spectrometer centered at 1550 nm with 75 nm of bandwidth and 1 nm of resolution was demonstrated as a proof-of-principle. Its performance was compared with a conventional AWG having the same resolution and bandwidth specifications. Based on the measurement results, interleaved AWGs provide lower adjacent crosstalk values, and better channel uniformity especially at the outer channels in addition to its smaller device size. For a higher resolution and larger bandwidth, the size of the interleaved AWG demultiplexer becomes significantly smaller than a conventional AWG, which makes it very appealing also for many different applications including imaging, spectroscopy, astronomy, and so on.

ACKNOWLEDGEMENTS

The author thanks Assoc. Prof. Sonia M. Garcia Blanco and Meindert Dijkstra for their support in the device fabrication.

REFERENCES

[1] Tkachenko N. V., [Optical Spectroscopy], Elsevier Science, Amsterdam, (2006).
[2] K. Takada, H. Yamada, and K. Okamoto, 320-channel multiplexer consisting of a 100 GHz-spaced parent AWG and 10 GHz-spaced subsidiary AWGs, *Electron. Lett.* vol. 35, pp.824-826, 1999.
[3] K. Takada, M. Ade, T. Shibita, and K. Okamoto, A 25-GHz-spaced 1080channel tandem multi/demultiplexer covering the S-, C-, and L-bands using an arrayed-waveguide grating with Gaussian passbands as primary filter, *IEEE Photon. Technol. Lett*. vol. 14, pp. 648-650, 2002.
[4] B. I. Akca, C. R. Doerr, G. Sengo, K. Wörhoff, M. Pollnau, and R. M. de Ridder, Broad-spectral-range synchronized flat-top arrayed-waveguide grating applied in a 225-channel cascaded spectrometer, *Opt. Express* vol. 20(16), pp. 18313–18318, 2012.
[5] S. Cao et al., Interleaver technology: comparisons and applications requirements, *J. Lightwave Technol.* vol. 22, pp. 281–289, 2004.
[6] M. K. Smit and C. van Dam, PHASAR-based WDM-devices: Principles, design and applications, *IEEE J. Select. Topics Quantum Electron.* vol. 2, pp. 236-250, 1996.
[7] G. Maier, M. Martinelli, A. Pattavina, and E. Salvadori, Design and cost performance of the multistage WDM-PON access networks, *J. Lightwave Technol.*, vol. 18(2), pp. 125–143, 2000.
[8] T. K. Chan et al., 1092 Channel 2-D Array Demultiplexer for Ultralarge Data Bandwidth, *J. Lightwave. Technol.* vol. 25(3), pp. 719-725, 2007.

Efficient Mode Multiplexer for Few-Mode Fibres Using Integrated Silicon-on-Insulator Grating Coupler

Student Paper

Yeyu Tong, Wen Zhou, Xinru Wu and Hon Ki Tsang*
Centre for Advanced Research in Photonics, Department of Electronic Engineering
The Chinese University of Hong Kong, Shatin, Hong Kong
e-mail: hktsang@ee.cuhk.edu.hk

ABSTRACT

A novel high-efficiency mode multiplexer is proposed to launch four channels including two polarizations of the LP01 mode and LP11 mode into step-index few-mode fibres (FMFs). Simulations predicted the coupling efficiency to be −4.3 dB for LP01 mode and −5.0 dB for the LP11 mode. Back reflections less than −11 dB is obtained within the C band. The design was fabricated in a multi-project wafer (MPW) run for silicon photonics. Experimental coupling efficiency of −4.9 dB and −6.1 dB was obtained for LP01 and LP11, respectively. The proposed mode multiplexer is suitable for future applications with FMFs in space-division-multiplexing networks.

Keywords: Integrated optics, diffraction gratings, few-mode fibres, space-division multiplexing.

1. INTRODUCTION

Driven by the exponential growth of data traffic in recent years, use of the transmission capacity of conventional standard-single mode fibre (SSMF) has already approached the theoretical limit imposed by the Shannon's information theory and nonlinear fibre effects. Dense wavelength-division-multiplexing, polarisation multiplexing, and spectrally efficient advanced modulation formats have all been exploited to increase the optical transmission capacity in SSMFs. Introduction of the new dimension of space-division multiplexing (SDM) using few-mode fibres (FMFs) has attracted much interest to enable further growth in transmission capacity and meet continued exponential growth in data centre traffic [1]. A reliable, efficient and low-cost method to excite the different fibre modes is thus highly desired for future practical applications.

In addition to approaches employing photonic lanterns and free-space optics [1]–[3], integrated diffraction gratings implemented on silicon-on-insulator (SOI) platform is also an interesting alternative. The monolithic integration offers advantages of low cost, mass-production ability and capability of co-integration with other integrated photonic devices such as transceivers [4]. Previous demonstrations include the use of circular gratings for a special ring-core fibre [5], push-pull driven gratings[6]–[8] and a single sub-wavelength gratings [9], [10] for standard FMFs. However, due to severe mode mismatch and limited directionality, it is challenging to obtain an experimental coupling efficiency better than −20 dB with the FMFs. A coupling efficiency of −10.6 dB was demonstrated with the use of an aluminium mirror [11].

Here we report the first experimental demonstration of an efficient mode multiplexer employing a single diffraction grating for excitation of the linear polarized (LP) modes LP01 and LP11 in a standard step-index FMF (four channels including polarization diversity), with an experimental coupling efficiency of −4.9 dB and a mode-dependent loss of 1.2 dB. The proposed device has a good fabrication tolerance and was fabricated in a passive multi-project wafer (MPW) run for silicon photonics at *IMEC*, and thus is suitable for industrial large-volume manufacturing of photonic integrated circuits (PICs).

2. DESIGN AND SIMULATION

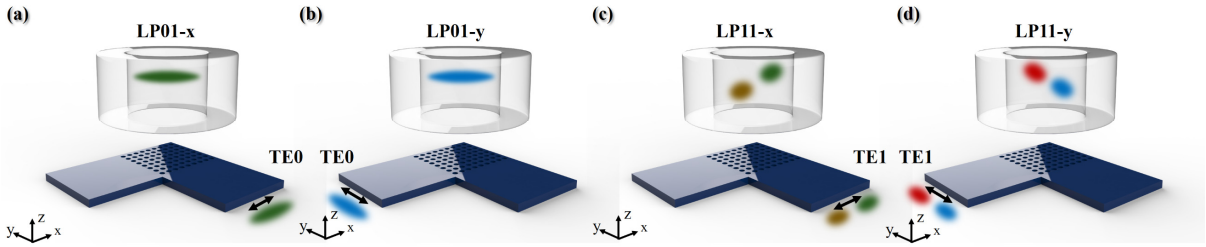


Figure 1. Schematic diagrams of mode excitation in a few-mode fibre via the waveguide grating. (a) LP01-x mode, (b) LP01-y mode, (c) LP11-x mode and (d) LP11-y mode.

The proposed grating coupler is designed for an *OFS* standard two-mode step-index FMF with a core diameter of 19.4 μm, which can support LP01 mode and LP11 mode with a mode field diameter (MFD) of 15.6 μm and 13.6 μm, respectively. The principle of mode excitation via a single diffraction grating is schematically depicted in Figs. 1(a)-(d). Transverse-electric (TE) modes, TE0 and TE1 are employed to selectively excite the LP01 mode and LP11 mode in FMF. Efficient coupling of the two TE modes is possible because the difference between their effective refractive index is very small in the wide slab waveguide and grating structure. Excitation up to four channels in FMFs is achieved by exploiting the orthogonal polarization. The silicon-on-insulator (SOI) wafer has a 220-nm-thick top silicon layer and a 2-μm-thick buried-oxide layer.

MFD of LP01 mode and LP11 mode in the step-index FMF is larger than the typical MFD of the SSMF. Reduced grating strength is thus necessary by employing the 70-nm shallow-etched subwavelength holes in the standard fabrication process provided by the fabrication foundry.

Due to the diffraction symmetry of the proposed structure, perfectly vertical coupling is required to reduce the channel-dependent coupling loss. Typical grating couplers are designed to couple the light at a small angle relative to the chip-surface normal to suppress the second-order Bragg reflection into the waveguides. We recently achieved an efficient perfect vertical coupling by using the genetic optimization with finite-difference time-domain (FDTD) simulations [12].

Schematic diagram of the proposed PICs is presented in Fig. 2 (a). Four input optical signals are coupled via the 10° off-vertical standard single-mode grating couplers to 450-nm single-mode waveguides. Asymmetric directional couplers (ADCs) with a 200-nm coupling gap are utilized for the mode multiplexer of the TE0 mode and TE1 mode [13], [14]. The 1.006-μm-wide multimode waveguide are connected to the 22-μm-wide grating by a 600-μm-long linear adiabatic taper with negligible loss for both TE0 mode and TE1 mode. 40 rows and columns of the round-shaped holes with the same diameter are utilized to cover an area of 22×22 μm^2 for the grating coupler.

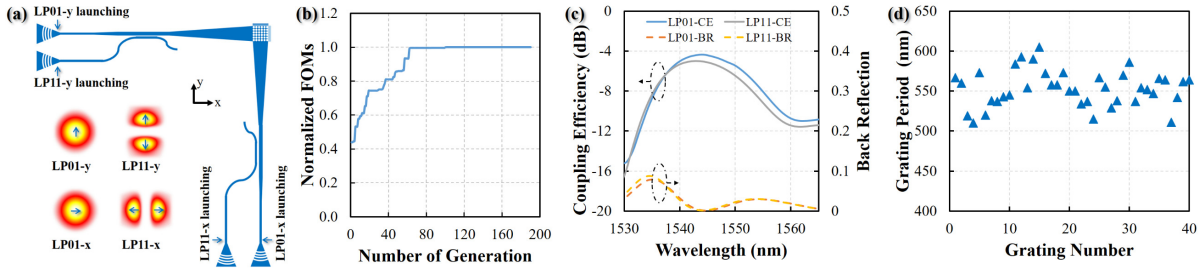


Figure 2. (a) Schematic diagram of the proposed PICs. (b) Evolutionary diagram of the normalized fitness against the number of iterations. (c) Coupling efficiency (CE) and back reflection (BR) of the final-optimized grating coupler. (d) Optimized grating periods.

Structural parameters including the grating periods, the hole diameter and the end-reflectors are optimized by the genetic optimization algorithm to suppress the back reflection and improve the coupling efficiency. The fitness F is denoted by Eq. (1), where CE is the coupling efficiency and BR corresponds to the back reflection.

$$F = \sum_{i=1}^{N} CE(\lambda_i) - BR(\lambda_i) \tag{1}$$

To save the simulation time for numerical iterations of the multiple parameters space, 2-dimentional (2-D) FDTD combined with the effective medium theory is used [15], [16] for optimization of the TE0 mode. Coupling performance of the TE1 mode is thus not considered in the optimization process, under the premise that it has a similar effective refractive index with the TE0 mode in the grating region. Coupling performance of both the TE modes was finally verified by the 3-D FDTD simulations. Due to the design symmetry of the grating structure, an equivalent performance is expected for the two orthogonal polarizations.

Evolutionary diagrams of the normalized fitness against number of iterations is shown in Fig. 2 (b). Obvious convergence progress is observed. Performances of final-optimized grating coupler are obtained by 3-D FDTD simulation as presented in Fig. 2(c). TE0 mode has a coupling efficiency of −4.3 dB (36.8%) at 1544 nm. TE1 mode has a coupling efficiency of −5.0 dB (31.8%) at 1542 nm. 3-dB bandwidth is about 20 nm for both modes. Reflection into the SOI waveguide is suppressed below −11 dB within C band. The optimized grating periods are shown in Fig. 2(d). The side length of the square-shaped holes is 286 nm, which corresponds to round-shaped holes with a diameter of 322 nm. Three rectangular slabs with a width of 190 nm and a spacing of 240 nm are used as an end reflector at the end of the grating. The minimum feature size of the proposed structure is ≥190 nm for robust fabrication using 193 nm deep-ultraviolet lithography.

3. EXPERIMENTAL RESULTS

The coupling efficiency is characterized by measuring the fibre-waveguide-fibre insertion loss with a SSMF as the input and a FMF as the output. The coupling spectrums of the LP01-x, LP01-y, LP11-x and LP11-y using a

single diffraction grating are shown in Fig. 3(a), after normalizing out the loss from the ADC, the linear taper and the single-mode grating coupler fabricated on the same chip. A coupling efficiency of −4.9 dB is obtained at 1551.0 nm for LP01-x mode and LP01-y mode. LP11-x mode and LP11-y mode have a coupling efficiency of −6.1 dB at 1549.6 nm. 3-dB bandwidth for all the four channels is about 15 nm. Output field profiles of the FMF are captured by an infrared camera with a 40× lens as shown in Figs. 3(b) and 3(c), demonstrating that the grating coupler can selectively launch LP01 and LP11 modes in the FMF. Scanning electron microscope (SEM) images of the PICs are obtained by removing the top protective resist of the same chip without oxide deposition. The fabricated ADCs, single-mode grating couplers and grating coupler for mode-selective launching are shown in Fig. 3(d) and 3(e).

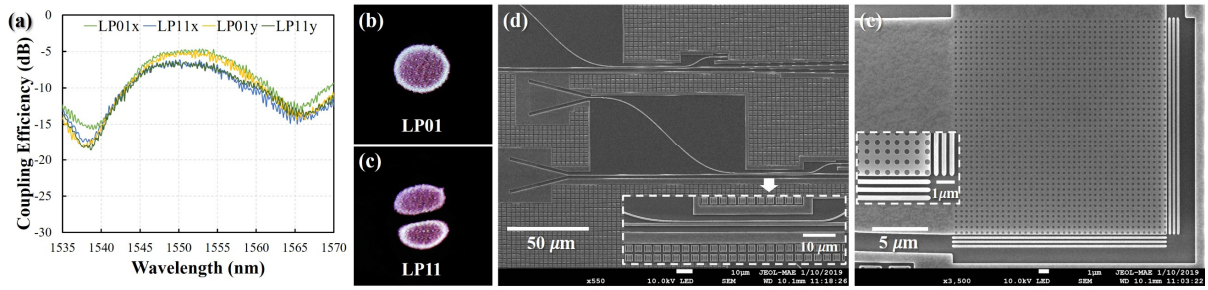


Figure 3. (a) Coupling efficiencies of the grating coupler for LP01-x, LP01-y, LP11-x and LP11-y, respectively. (b), (c) Output field profiles of the FMF when LP01 mode and LP11 mode are selectively coupled. (d) SEM image of the single-mode gratings and ADCs with a zoom-in view shown in the inset. (e) SEM image of the fabricated grating coupler with a zoom-in view shown in the inset.

4. CONCLUSIONS

We propose a novel design of the mode multiplexer employing a single diffraction grating on SOI capable of excitations of the LP01-x, LP01-y, LP11-x and LP11-y modes in a step index FMF. Coupling efficiency up to −4.3 dB is obtained in simulation with a mode-dependent loss of 0.7 dB. Experimental coupling efficiency of −4.9 dB and −6.1 dB is demonstrated respectively for two polarizations of the LP01 mode and the LP11 mode. To the best of our knowledge, this is the first experimental demonstration of such high-efficiency four-channel mode multiplexer for FMFs using integrated grating coupler on SOI. The demonstrated mode multiplexer is suitable for future applications with FMFs in space-division-multiplexing networks.

ACKNOWLEDGEMENTS

This work was funded by Hong Kong Research Grants Council/NSFC Joint Research Scheme (N_CUHK404/14). The author would like to thank *IMEC* for the device fabrication and Wen Zhou acknowledges the support from the Postdoctoral Hub - Innovation and Technology Fund (PH-ITF).

REFERENCES

[1] R. Ryf *et al.*, *Journal of Lightwave Technology*, vol. 30, no. 4, pp. 521–531, Feb. 2012.
[2] S. G. Leon-Saval *et al.*, *Optics Express*, vol. 22, no. 1, p. 1036, Jan. 2014.
[3] H. Chen, N. K. Fontaine, R. Ryf, B. Guan, S. J. B. Yoo, and T. (M. J.) Koonen, *Journal of Lightwave Technology*, vol. 33, no. 6, pp. 1147–1154, Mar. 2015.
[4] G. Roelkens *et al.*, *Journal of Nanoscience and Nanotechnology*, vol. 10, no. 3, pp. 1551–1562, Mar. 2010.
[5] C. R. Doerr, N. K. Fontaine, M. Hirano, T. Sasaki, L. L. Buhl, and P. J. Winzer, in *2011 37th European Conference and Exhibition on Optical Communication*, Sep. 2011, Th.13.A.3.
[6] A. M. J. Koonen, H. Chen, H. P. A. van den Boom, and O. Raz, *IEEE Photonics Technology Letters*, vol. 24, no. 21, pp. 1961–1964, Nov. 2012.
[7] Y. Ding, H. Ou, J. Xu, and C. Peucheret, *IEEE Photonics Technology Letters*, vol. 25, no. 7, pp. 648–651, Apr. 2013.
[8] N. K. Fontaine et al., *in OFC/NFOEC*, Mar. 2012, pp. PDP5B.1.
[9] B. Wohlfeil, G. Rademacher, C. Stamatiadis, K. Voigt, L. Zimmermann, and K. Petermann, *IEEE Photonics Technology Letters*, vol. 28, no. 11, pp. 1241–1244, Jun. 2016.
[10] Y. Ding, H. Ou, J. Xu, M. Xiong, and C. Peucheret, in *IEEE Photonics Conference*, Sep. 2012, pp. 707–708.
[11] Y. Ding and K. Yvind, in *2015 Conference on Lasers and Electro-Optics (CLEO)*, May 2015, pp. 1–2.
[12] Y. Tong, W. Zhou, and H. K. Tsang, *Optics Letters*, vol. 43, no. 23, pp. 5709–5712, Dec. 2018.
[13] X. Wu, C. Huang, K. Xu, C. Shu, and H. K. Tsang, *Journal of Lightwave Technology*, vol. 35, no. 15, pp. 3223–3228, Aug. 2017.
[14] D. Dai, J. Wang, and Y. Shi, *Optics Letters*, vol.38, no. 9, pp. 1422-1424, Apr. 2013.
[15] X. Chen and H. K. Tsang, *Optics Letters*, vol. 36, no. 6, pp. 796–798, Mar. 2011.
[16] X. Chen, C. Li, and H. K. Tsang, *Optics Communications*, vol. 283, no. 10, pp. 2146–2149, May 2010.

High-Performance Silicon Photonics Optical Filters with High-Order Distributed Feedback Resonators

Claudio Porzi[1], Graham J. Sharp[2], Marc Sorel[2], Antonella Bogoni[1]
[1] TeCIP Institute, Scuola Superiore Sant'Anna, 56124 Pisa - Italy
[2] School of Engineering, University of Glasgow, Glasgow, G12 8LP - United Kingdom
e-mail: c.porzi@santannapisa.it

ABSTRACT

Silicon photonics tunable passband optical filters with flat-top feature, large out-of-band rejection in excess of 40 dB, ultra-fast roll-off up to 1,000 dB/nm, and unprecedented passband-to-stopband ratio for high-index-contrast technology have been fabricated and characterized. The integrated filters are based on high-order distributed-feedback resonators implemented with cascaded phase-shifted Bragg gratings in silicon strip waveguides. Local micro-heaters are used for finely controlling the phases of the individual cavities of the coupled resonators and for providing additional tuning mechanism. Two different coupled-cavity resonators with passband widths of 25 GHz and 2 GHz, realized with 6th- and 5th- order filter designs, respectively, are exemplarily reported.

Keywords: Silicon photonics, integrated optical filters, waveguide Bragg gratings, Fabry-Perot filters.

1. INTRODUCTION

Integrated optical filters (OFs) boost the performances of photonic-integrated circuits (PICs), as they are required in almost any advanced operation dealing with handling and processing optical signals. In particular, the implementation of OFs through silicon-on-insulator (SOI) technological platform is highly sought after for the development and large-volume production of ultra-compact highly-functional PICs. To this scope, a huge amount of research has concentrated in the last decades on high-order coupled micro-ring resonators (MRRs), which proofed excellent performances for applications spanning from telecom/datacom to sensing and microwave photonics systems [1]-[3]. Few attention has been however devoted to integrated distributed Bragg resonators which, complimentary to the traveling-wave cavity of MRRs, implement standing-wave cavity resonators. Recently, we demonstrated high-order designs of such important class of OFs using phase-shifted Bragg gratings (PSBGs) realized in silicon strip waveguides [4]-[5]. In coupled SOI MRRs, the trade-off between ring dimensions and the ability of controlling small coupling coefficients for high-index-contrast waveguides makes challenging to realize OFs simultaneously exhibiting arbitrarily narrow passband widths and large free-spectral range (FSR) values. To date, maximum reported value of stopband-to-passband ratio in high-order silicon MRRs is about 100 [2]. On the other hand, PSBGs rely on an extremely short effective cavity of the order of the optical wavelength, which allows in principle for FSR-free operation. The range of wavelengths over which filtering operation is defined is set in this case by the grating stopband, which can be made relatively large using high-index-contrast silicon strip waveguides. To counteract the scattering of resonances among the coupled cavities in high-order filters due to unavoidable fabrication imperfections, local micro-heaters (MHs) have been successfully demonstrated for 3rd-order designs [5].

Here, we report the latest results relative to higher-order designs, enabling the realization of silicon photonics OFs with advanced features. A box-like 25 GHz-bandwidth passband transfer function with an out-of-band rejection larger than 45 dB within a 16-nm stopband region is realized in a 6th- order PSBGs, whereas a 5th- order design is exploited to realize a 2-GHz bandwidth filter with a roll-off of 1,000 dB/nm and a stopband-to-passband ratio larger than 600, confirming the unique potentials of this technique.

2. DEVICE SCHEMATIC AND FABRICATION

An integrated high-order distributed feedback resonator is obtained by cascading several symmetric waveguide Bragg Gratings (BGs) that, as in the proposed implementation schematized in Fig. 1(a), can be realized by periodically alternating two quarter-wave long waveguide sections with different width. Due to the BGs symmetry, half-wave cavities (HWCs) are formed at each interface between adjacent BG mirrors, supporting a resonant mode at the Bragg wavelength in the transmission spectrum with the typical Lorentzian shape. For M+1 BGs there are M coupled cavities, so that the overall filter transmission response can be constructed in a way much similar to coupled MRRs by controlling the Q-factor of the individual cavities through the lateral waveguide corrugation width ΔW and the number of periods N_i of the ith BGs. Local MHs are placed above the HWCs cavities for correcting the slight deviations in the optical path from their nominal half-wave values at the Bragg wavelength. Additionally, the MHs offer a convenient mean for tuning the passband window while keeping the stopband edges fixed [5], thus improving the useful wavelength range of the filtering operation. Broader although rigid tuning can

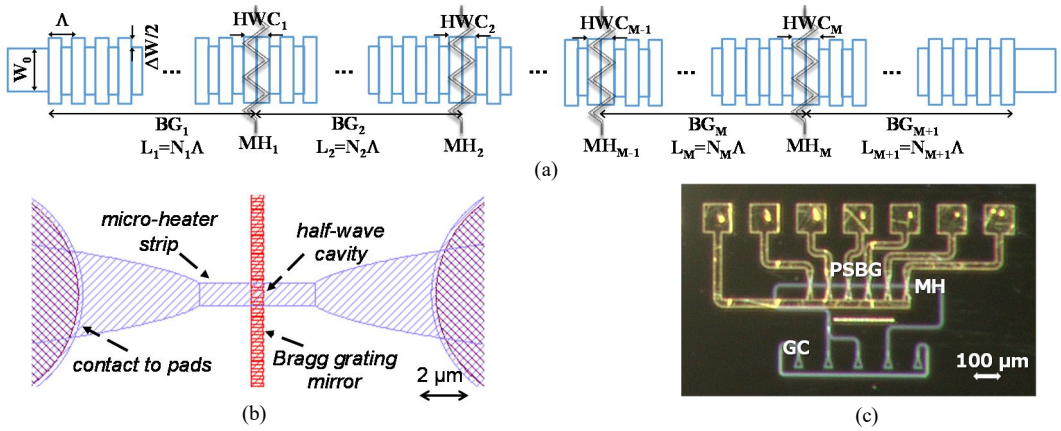


Figure 1. (a): High-order phase-shifted waveguide Bragg grating (PSBG) schematic structure; (b): Details of micro-heater (MH) mask layout; (c): Picture of a fabricated 6th-order device.

be accomplished by heating the whole grating structure [4]. The PSBGs were fabricated through electron-beam lithographic process on a silicon-on-insulator (SOI) wafer with a 3 μm-thick buried oxide layer and a 220 nm-thick core layer. The average grating waveguide width W_0 has been set to 500 nm, and the period of the corrugation Λ to 320 nm. Grating couplers (GCs) are used for vertical coupling with the input/output optical fibers. The MHs are formed by a 50 nm-thick, 1 μm-wide and 5 μm-long nichrome strip deposited on the top of a 1 μm-thick silica cladding layer. The MH mask layout is shown in Fig. 1(b). Gold metal lines and pads are used for connecting the MHs to current sources through contact probes. The typical measured contact resistance of the MHs is ~350 Ω. An image of a fabricated sample, corresponding to a 450 μm-long 6th-order PSBG design, is shown in Fig. 1(c).

3. DEVICES CHARACTERIZATION

The first considered device corresponds to a 6th-order (M=6) design with a nominal lateral waveguide corrugation ΔW of 60 nm. The measured spectral transmission, normalized to GC response, without and with cavity tuning is reported in Figure 2(a). After applying proper control signals to each MH, a sharp transmission window exhibiting an out-of-band rejection in excess of 45 dB over a 16 nm-wide stopband region is observed. The insertion loss at peak transmission is ~2.8 dB. Numerical fitting of the tuned response using the design parameters reported in the figure caption is also shown. The details of the passband window are also shown in Fig. 2(b), illustrating the flat-top box-shaped feature of the filter transfer function, with a measured maximum ripple of 0.1 dB within the 18.5 GHz-wide -1dB bandwidth. The -3dB and -40 dB bandwidth values are 24 GHz and 45.8 GHz, respectively, for a corresponding transition band roll-off of more than 400 dB/nm (3.4 dB/GHz). Finally, the passband-to-stopband ratio is ~75.

In the second considered design, targeting a narrower filter bandwidth, a higher loaded Q-factor for the HWCs is investigated. In order to mitigate the larger sensitivity to propagation loss as energy is stored for longer time within the resonator, both the filter order and grating coupling coefficient are reduced. In particular, a 5th-order (M=5) distributed feedback resonator has been constructed by cascading six waveguide BG mirrors using a nominal width variation ΔW of 48 nm. The results of device characterization are summarized in Figure 3. Also for

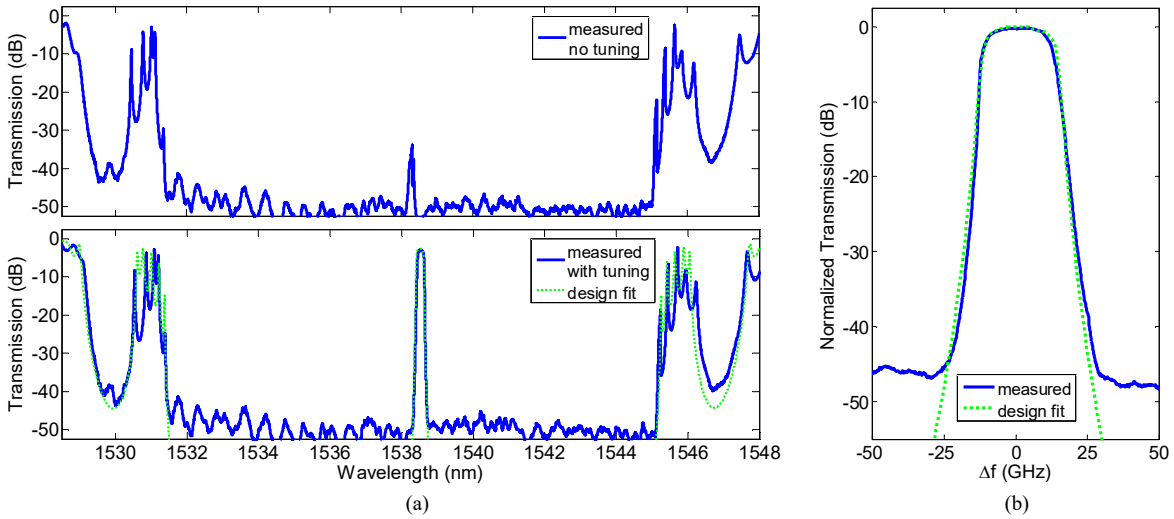


Figure 2. (a): Spectral transmission of 6th-oreder PSBG without and with control signals to MHs; Design period numbers for the Bragg grating mirrors: N_1=N_6=112; N_2=N_5=224; N_3=N_4=234; N_6=236; (b): Details of passband window.

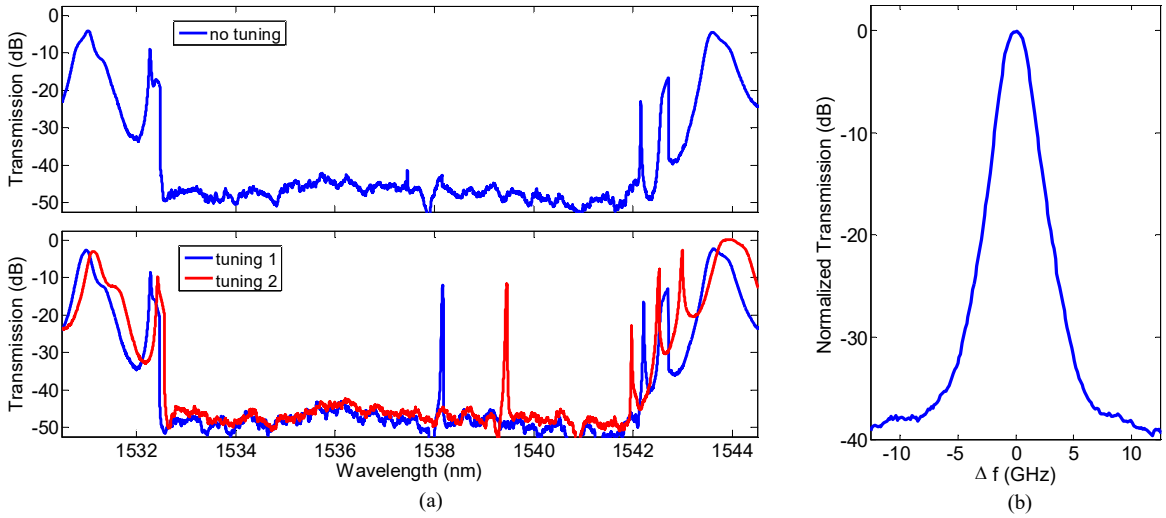


Figure 3. (a): Spectral transmission of 5th-oreder PSBG without and with control signals to MHs; (b): Details of passband window.

this case, a tuning of the resonances by individually heating each QWCs through the MHs is used to optimize the passband response to nearly 40 dB out-of-band rejection, as illustrated in Fig. 3(a). Two different levels of tuning settings are shown, from which it can be seen that heating the HWCs only slightly affect the spectral location of the stopband edges. The corresponding absorbed power excursion for the considered passband shift of ~1.3 nm is less than 2 mW for each MHs. By reducing the optical path of the HWCs from their nominal value, resonance tuning from the shorter-wavelength stopband edge side toward the longer-wavelength one can be realized. As an effect of the reduced corrugation depth for this structure, the stopband width is now ~9.5 nm. However, due to the stronger loaded Q-factor provided by proper period numbers in the BG mirrors, a very narrow and steep passband window is observed, as illustrated in Fig. 3(b). The measured -1dB and -3dB bandwidth values are 1.2 GHz and 2 GHz, respectively, for a remarkably large stopband-to-passband ratio of more than 600. As expected, the stronger sensitivity to propagation loss in this case rounds the passband window top and raises the insertion loss to ~10 dB. The effect of propagation loss in such high Q-factor structures could be reduced by using a for instance sinusoidal or triangular corrugation patterns rather than the rectangular one for the waveguide grating. Nevertheless, the sharpness of the filter transfer function is fairly preserved, with a measured -33 dB bandwidth of 9.4 GHz, for a roll-off as large as 8 dB/GHz (1,000 dB/nm) in a 3.7 GHz-wide transition bandwidth spanning over 30 dB.

4. CONCLUSIONS

We reported on the fabrication and characterization of advanced silicon photonics optical filters based on high-order phase-shifted waveguide Bragg gratings encompassing local micro-heaters for finely controlling and tuning the filter response. Design flexibility is highlighted by considering two different design concepts; a 24 GHz-bandwidth passband transfer function exhibiting box-like features with an out-of-band rejection in excess of 45 dB and 1.75 THz-wide stopband region is observed for a 6th-order cavity, whereas a high Q-factor 5th-order design provided an ultra-narrow filter bandwidth of 2 GHz, extremely fast roll-off, and stopband-to-passband ratio of 600.

ACKNOWLEDGEMENTS

The authors acknowledge the support from the technical staff at the James Watt Nanofabrication Centre (JWNC) at Glasgow University. The work was partially funded by the Engineering and Physical Sciences Research Council (EPSRC) under the CORNERSTONE project (EP/L021129/1), and by the Italian National projects PHOOD and PREVENTION.

REFERENCES

[1] M. A. Popovic, *et al.*: Tunable, fourth-order silicon microring-resonator add-drop filters, *in Proc. ECOC 2007*, Berlin, Germany, Sept. 2007, paper 1.2.3.

[2] P. Dong, et al.: GHz-bandwidth optical filters based on high-order silicon ring resonators, Opt. Express, vol. 18, pp. 23784-23789, Nov. 2010.

[3] W. Bogaerts, *et al.*: Silicon microring resonators, *Laser & Photonics Reviews*, vol. 6, pp. 47-73, Jan. 2012.

[4] C. Porzi, *et al.*: Integrated Passband Optical Filter with High-Order Phase-Shifted Bragg Grating in Silicon-on-Insulator Technology, *in Proc. ECIO 2018*, Valencia, Spain, May-June 2018, paper Fr.1.B.4.

[5] C. Porzi, *et al.*: High-Contrast, Flat-Top, Silicon-Photonics Passband Optical Filters with High-Order Phase-Shifted Bragg Gratings, *in Proc. ECOC 2018*, Roma, Italy, Sep. 2018, paper Mo3C.5.

Micro-Opto-Mechanical Pressure, Sound, and Ultrasound Sensors in Silicon-Nitride Photonic Technology

W. J. Westerveld, B. Figeys, H. Gao, C. H. Huang, F. Verhaegen, B. Troia, R. Haouari, P. Neutens, J. O'Callaghan, S. Lenci, X. Rottenberg, R. Jansen, V. Rochus
Imec, Kapeldreef 75, 3001 Leuven, Belgium
e-mail: veronique.rochus@imec.be

ABSTRACT

Micro-electro-mechanical systems (MEMS) are used in applications ranging from consumer electronics to medical diagnostics. Alternatively, optical sensors offer low-noise, remote read-out via optical fiber, and are insensitive to electromagnetic interference. We demonstrate micro-opto-mechanical sensors (MOMS) in silicon-nitride photonic technology. Experimental results and design trade-offs of pressure, sound, and ultrasound sensors are reported. Transparency for visible light offers prospective applications in life sciences, such as photo-acoustics.

Keywords: optical pressure sensor, optical microphone, ultrasound sensor, silicon photonics, silicon-nitride

1. INTRODUCTION

Micro-electro-mechanical systems (MEMS) are increasingly being used for sensing of pressure, sound, and ultrasound in applications ranging from consumer electronics to medical diagnostics. E.g. pressure sensors in wearable technology [1], microphones in laptops [2] or hearing aids [3], and micromachined ultrasound sensors (MUTs) in medical imaging [4]. Simultaneously, fiber optical sensors have demonstrated high sensitivity and offer remote readout, but for a less integrated system [5,6]. Micro-opto-mechanical sensors offer the advantages of both worlds, with prospects of high sensitivity, small footprint, and on-chip passive optical multiplexing. Imec has developed silicon-nitride visible and near-infrared integrated photonic technology in their 200 mm CMOS pilot line [7]. This technology is nowadays also offered as multi-project wafer (MPW) service via the Pix4Life photonic pilot line (www.pix4life.eu). Silicon-nitride photonics has particular advantages over silicon. The lower index contrast of SiN photonics requires a larger footprint but is more tolerant to fabrication-induced variations, which cause phase noise and hamper wavelength-division-multiplexing. For photo-acoustic imaging, SiN waveguides can be used to guide photo-acoustic excitation pulses in the visible spectrum. Alternatively, free-space pulses can pass the circuit in the out-of-plane direction [8]. The possible use of visible light allows for cost-effective silicon detectors, including imagers for massively parallel read-out. In this work, we describe the operation principles of these devices and the results of the research ongoing at Imec [9-15].

2. SENSOR PRINCIPLES AND FABRICATION

The sensors are based on a flexible membrane that deforms upon applied static, acoustic, or ultrasonic pressure (Fig 1a). A photonic Mach-Zehnder interferometer (MZI) is integrated [16], with the MZI sensing arm in the moving membrane and the reference arm on the fixed substrate (Fig 1b). Both arms are folded into a spiral to have a long sensing path. A deflection of the membrane stretches the MZI sensing arm, which causes a phase difference between the arms, which results in a change in optical intensity at the MZI output, which is measured. The change in MZI waveguide length contributes one order of magnitude stronger than the change in effective refractive index for these SiN waveguides [10]. Alternatively, ring resonators can be used as sensing element, but they are less robust to laser wavelength noise. Devices are fabricated in Imec's CMOS pilot line and use silicon-nitride photonic technology (waveguide thickness 300 nm, wavelength 852 nm) [7]. First, the SiN-on-insulator photonic circuitry is fabricated (Fig. 2a) [7]. Second, an additional 4.5 µm thick silicon-dioxide layer with low tensile stress is deposited. This layer is essential to the mechanical characteristics of the membrane, as the 2.3 µm thick SiO2 bottom cladding layer has high compressive stress causing buckling of the membrane [10,15]. Third, the membrane is formed back-side etching (DRIE) to locally remove the wafer substrate (Fig. 2b). Each application requires a specific design for the mechanical membrane characteristics and optimized photonic circuitry. These are the topics of the following sections.

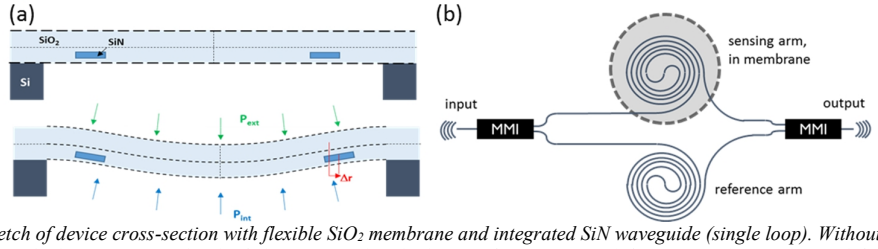


Figure 1. (a) *Sketch of device cross-section with flexible SiO_2 membrane and integrated SiN waveguide (single loop). Without (top) and with (bottom) applied pressure.* ***(b)*** *Sketch of photonic Mach-Zehnder Interferometer (MZI) for sensing the membrane deformation.*

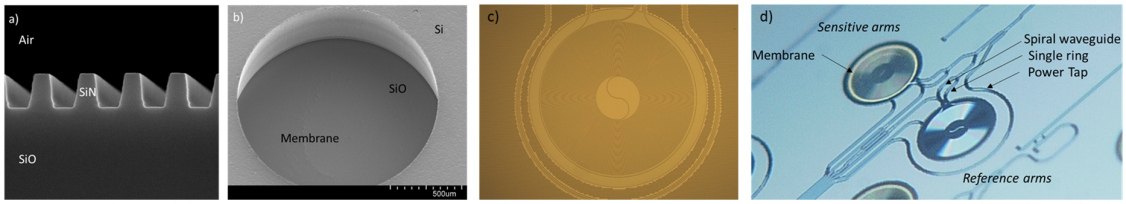


Figure 2. *Fabricated devices.* ***(a)*** *Cross-section SEM image showing an unclad grating coupler in SiN.* ***(b)*** *SEM image of membrane back-side etch.* ***(c)*** *Microscope picture of one of the arms of an MZI with a spiral loop and also with a single loop.* ***(d)*** *Microscope image of the new micro-opto-mechanical sensor. From [13].*

3. PRESSURE SENSORS

For pressure sensing it is desired to have a high precision over large pressure range. However, the optical output of the interferometer has a sinusoidal dependence on the phase difference, such that the unambiguous pressure sensing range is limited to half a period (Fig. 3b, blue curve). The sensitivity can be engineered by choosing the number of spiral loops of the interferometer arms, more loops give a higher sensitivity, however, with smaller sensing range [13]. To overcome this trade-off, our designs combine a sensitive output based on a many-loop spiral interferometer with a low-sensitive output from an additional interferometer with only a single loop over the membrane (Fig 3a). Another problem is that the interferometer is sensitive around the steep flank of the sinusoidal output, but much less sensitive at the flat tops and bottoms of the sinusoidal output. This has been overcome by using two interferometers on the same membrane in which one of the interferometers has a fixed quarter-period offset between the two arms, such that the two interferometers are sensitive in different pressure ranges within a period. For large pressures, the membrane deflection is nonlinear [10].

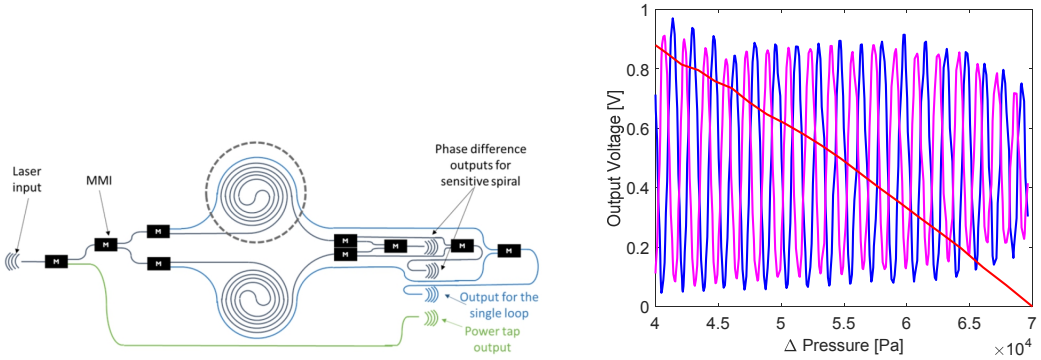


Figure 3. *New micro-opto-mechanical pressure sensor with 4 outputs. Two high-sensitive outputs with a quarter period phase shift, one low-sensitive output with large sensing range, and a power tap to compensate for laser intensity noise. High sensitive outputs share spiral MZI arms with 60 loops. Membrane diameter 1.2 mm.* ***(left sketch)*** *Schematics of photonic circuit.* ***(right plot)*** *Measured output signals. Blue curve: high-sensitive output. Magenta curve: high-sensitive phase shifted output. Red curve: low-sensitive output. From [13].*

4. MICROPHONES

Microphones require a flat frequency response for acoustical frequencies in the hearing range (20 Hz – 20 kHz). This is achieved by designing the membrane resonance frequency well above 20 kHz. Typical acoustical pressures are much lower than typical static pressures, the pain threshold is about 200 Pa. The resonance frequency of the silicon-dioxide membrane depends on its diameter, thickness, and residual initial stress (Fig. 4a). The residual stress in the fabricated membranes was measured by fitting simulations to measured resonance frequencies for different membrane diameters (Fig. 4b).

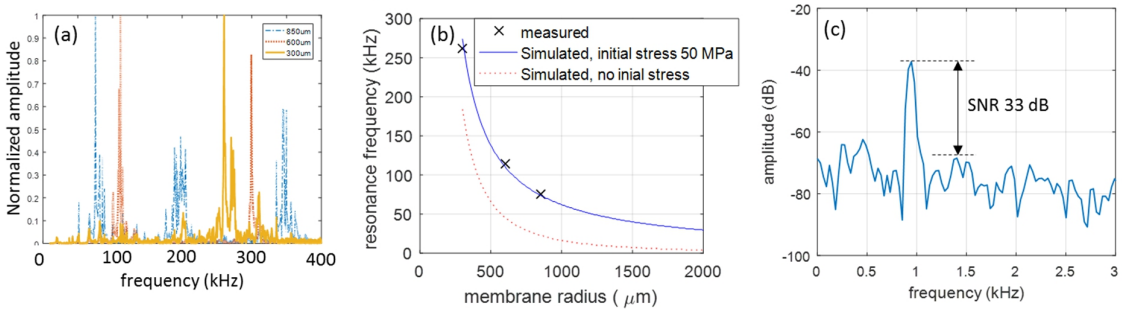


Figure 4. *Acoustical characterization.* ***(a)*** *Membrane resonance spectra measured with a laser vibrometer and shaker.* ***(b)*** *Measured and simulated membrane resonance frequencies, showing agreement for 50 MPa tensile stress.* ***(c)*** *Optical sensor response of micro-opto-mechanical microphone. A 1 kHz sound wave with pressure of 1 Pa is impinged on the membrane and optical output is recorded. From [9].*

The sensor with diameter 1.7 mm and first resonance at 80 kHz was characterized as microphone with measured SNR of 33 dB (Fig. 4c). We see large room for improvement, e.g. an optimal design would have its first resonance much closer to the hearing range (~20 kHz).

5. ULTRASOUND SENSORS

Optical micro-machined ultrasound sensors (OMUS) based on silicon photonic ring resonators showed very high sensitivity [17]. However, the device reported in [17] has high compressive initial stress and a buckled membrane [15]. We believe that reliable devices are based on neutral or slightly tensile membranes. To harvest the benefits of silicon-nitride photonics for ultrasonic and especially photo-acoustic imaging [8], current research efforts also focus on ultrasound sensing. Our theoretical and experimental studies focus on both thicker membranes as well as smaller membrane diameters (Fig 5).

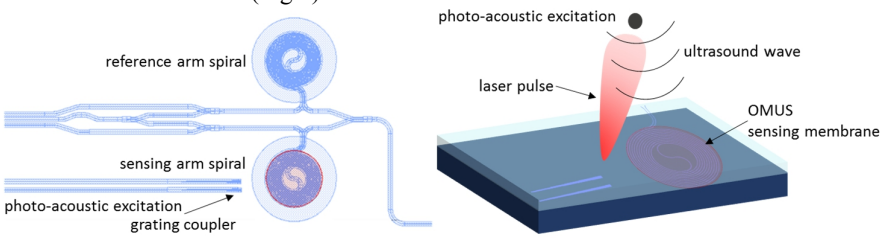


Figure 5. *OMUS for photo-acoustic imaging and spectroscopy.* ***(a)*** *Design, GDS layout.* ***(b)*** *Working principle with optical laser pulses generating acoustical waves due to photo-acoustics.*

6. CONCLUSION

We demonstrated micro-opto-mechanical pressure sensors and microphones and presented designs for ultrasound sensors, in silicon-nitride photonic technology. Important design trade-offs and solutions for these membrane-based devices were presented for the different applications. MEMS sensors are widely used and MOMS sensors have significant benefits for applications. For example, the optical technology does not suffer from electromagnetic interference which allows these devices to be used inside medical MRI systems or near heavy industrial machinery.

REFERENCES

[1] ST Microelectronics, LPS25HB High-robustness pressure sensor, flyer, Dec. 2014.
[2] ST Microelectronics, MEMS analog and digital microphones, flyer, Dec. 2014.
[3] Sonion, Data Sheet Microphone O8AC03, Mar. 2017.
[4] Szabo, T.L. Diagnostic ultrasound imaging: inside out, 2nd edn, Ch. 5, 122–160, Academic Press, 2014.
[5] Wang et al, Miniature all-silica optical fiber pressure sensor with an ultrathin uniform diaphragm, *Optics Express*, Vol. 18, pp. 9006-9014, 2010.
[6] J.A. Guggenheim et al, "Ultrasensitive plano-concave optical microresonators for ultrasound sensing", *Nature Photonics*, Vol. 11, pp. 714–719, 2017.
[7] A. Z. Subramanian et al., "Low-Loss Singlemode PECVD Silicon Nitride Photonic Wire Waveguides for 532–900 nm Wavelength Window Fabricated Within a CMOS Pilot Line," IEEE Phot. J., vol 5, 2013.
[8] Wang & Yao, "A practical guide to photoacoustic tomography in the life sciences", *Nature Methods*, 2016.
[9] H. Gao et al., "Simulation and characterization of a high-sensitive micro-opto-mechanical Microphone," *EuroSimE*, Toulouse, 2018.
[10] V. Rochus et al, "Fast analytical model of MZI micro-opto-mechanical pressure sensor", *Journal of Micromechanics and Microengineering*, vol. 28 p. 064003, 2018.
[11] B. Troia et al, Coupled multiphysics circuital modelling of micro-opto-mechanical pressure sensor systems, *Proc. SPIE 10545, MOEMS and Miniaturized Systems XVII*, 1054518, 22 February 2018.
[12] C. H. Huang et al., "Frequency response and mode shape characterization for acoustic sensor in micro-opto-mechanical technology," *IEEE International Ultrasonics Symposium (IUS),* Washington DC, 2017.
[13] V. Rochus et al., "Double MZI Micro-Opto-Mechanical Pressure Sensors for increased sensitivity and pressure range," *TRANSDUCERS*, Kaohsiung, pp. 954-957, 2017.
[14] V. Rochus et al., "Design of a MZI Micro-Opto-Mechanical Pressure Sensor for a SiN photonics platform," *EuroSimE*, Montpellier, 2016.
[15] Westerveld et al, Optical micro-machined ultrasound sensors with a silicon photonic resonator in a buckled acoustical membrane, *EuroSimE*, Hannover, March 2019, accepted.
[16] W.J. Westerveld and H.P. Urbach, *Silicon Photonics: Electromagnetic theory*, IOP Publishing, 2017.
[17] S.M. Leinders et al, "A sensitive optical micro-machined ultrasound sensor (OMUS) based on a silicon photonic ring resonator on an acoustical membrane", *Scientific Reports*, Vol. 5, Article 14328, 2015.

Boosting thermo-optic efficiency of silicon (oxy)nitride waveguides

Andrea Melloni[1], Faisal Ahmed Memon[2], Matteo Cantoni[3], Marco Asa[3] and Francesco Morichetti[1]
[1]DEIB - Politecnico di Milano, Milano, 20133 Italy
[2]Dept. Telecommunications Eng., Mehran University of Engineering & Technology Jamshoro, Pakistan
[3]Dip. Fisica - Politecnico di Milano, Milano, 20133 Italy
e-mail: andrea.melloni@polimi.it

ABSTRACT

Silicon OxyCarbide (SiOC) glass compound is introduced as a suitable material for integrated optical applications. SiOC is a low loss dielectric at telecom wavelength, has a wide refractive index tunability, can be integrated in most photonic platforms and possesses a unique high thermo-optic coefficient of 2.5×10^{-4} °C^{-1}. Here we demonstrate that the thermal tuning efficiency of silicon nitride and silicon oxynitride devices is enhanced by about four times by integrating a high-refractive index coating of SiOC with a record thermo-optic coefficient.

Keywords: *integrated photonics, thermo-optic effect, silicon oxycarbide, optical waveguides.*

1. INTRODUCTION

Silicon nitride (Si_3N_4) and Silicon OxyNitride (SiON) are well established photonic platforms, offering a good trade off between high scale of integration, low loss, low polarization sensitivity and efficient fiber–coupling. The refractive index of SiON can be tailored with the composition and both are CMOS compatible. The thermo-optic coefficient (TOC) of these dielectric materials is very low compared to semiconductors (silicon and Indium Phosphide) and is on the order of 10^{-5} °C^{-1}. If this guarantee a rather stable circuit behaviour with fluctuations of the temperature, it obliges to realize long (mm-scale) thermal actuators, requiring high electrical power (hundreds of mW for π phase shift) [1] and high working temperatures and inducing severe thermal crosstalk issues.

Recently [1, 2], we have demonstrated that Silicon OxyCarbide, or SiOC, a glass compound that has received significant attention from scientific community and has been employed in several fields of technologies [3-5], has appealing characteristics to become an enabling material for photonic integrated circuits. SiOC is a low loss dielectric at telecom wavelength, has a wide refractive index tunability, can be integrated in most photonic platforms and possesses a unique high thermo-optic coefficient of 2.5×10^{-4} °C^{-1}, one order of magnitude larger than glass-based materials and almost twice that of silicon [1, 2].

Here we show that SiOC can be used as core material to make high index contrast waveguides and that the integration of a SiOC film as upper coating of a conventional Si_3N_4 and SiON core waveguides can enhance the effective TOC up to one order of magnitude, thus enabling very efficient thermo-optic tuning.

2. Fabrication of SiOC waveguides

The SiOC films employed in this work were deposited by reactive RF magnetron sputtering from a SiC target in O_2 and Ar atmosphere, according to the process described in [1]. As shown in Fig. 1(a-c), by changing the process parameters (RF power and O_2 flow), the SiOC refractive index can be tuned from that of SiO_2 (1.45) to that of SiC (above 3) by increasing the C content. To maintain transparency in the near-IR range [see Fig. 1(b)], we selected a material composition of $Si_{0.45}O_{0.27}C_{0.27}$, as measured by X-ray photoelectron spectroscopy (XPS), resulting in a

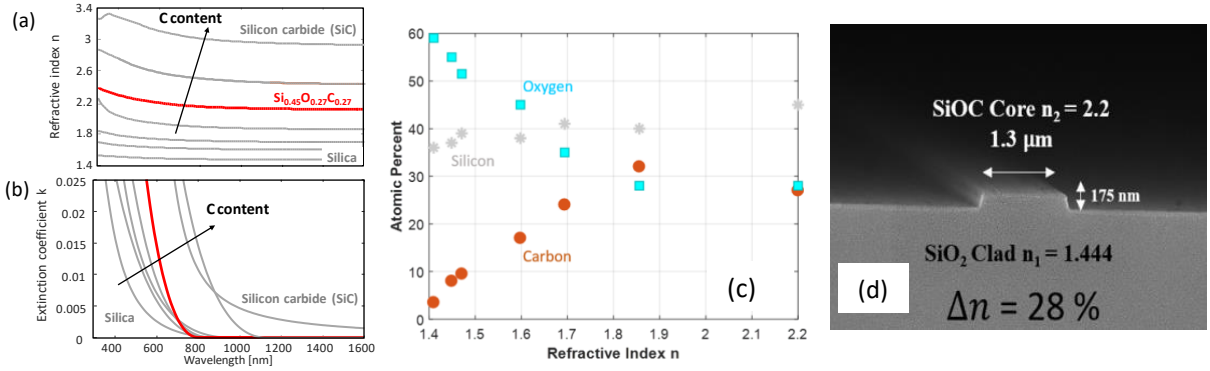


Fig. 1. Measured (a) refractive index and (b) extinction coefficient of SiOC films with increasing carbon composition (c). (d) SEM image of a SiOC strip waveguide before SiO_2 upper cladding deposition.

refractive index of 2.2 in the near-IR range. Optical waveguides were fabricated by depositing a 175-nm-thick SiOC film (core) on a silica substrate. The waveguide cross section was defined by direct-laser-writing lithography and reactive ion etching in CHF_3 (100 sccm) and O_2 (5 sccm). Figure 1(d) shows the waveguide cross section before the upper cladding deposition. After the SiOC core patterning, PECVD silica (n = 1.45) was deposited as upper cladding material. At a wavelength λ_0 =1550 nm, the strip shaped waveguide has a group index n_g = 1.93 and propagation losses of 2 dB/cm for transverse electric (TE) polarized light.

3. Thermooptic effect in SiOC

The TOC of the SiOC material has been evaluated by measuring the thermally-induced wavelength shift of a number of devices such as waveguides, Mach-Zehnder interferometers and ring resonators of both SiOC and SiOC-coated core waveguides. Details can be found in [1]. As a result, we found that the TOC of SiOC, K_{SiOC} = 2.5 $\times 10^{-4}$ °C^{-1}, is the largest ever reported for a dielectric material employed in optical waveguides.

The origin of the large TOC of SiOC is related to the increase of the dielectric polarizability near the transparency edge [6]. Figure 2 shows the TOC of various materials (black marks, data from literature [1]), which is nearly dependent on the inverse of the direct energy gap E_g and increases approaching the band gap [6]. Germanium has an even higher TOC but it is not transparent in the near-IR and not shown, while the high transparency of SiO_2 till the deep UV is associated with a very small TOC. The high TOC of SiOC (red mark), whose direct bandgap is around E_g = 3.5 eV, as derived from absorption spectra of Fig. 1(b), is well in line with this trend. This also shows that the SiOC composition employed in this work offer a good tradeoff between material transparency and high TOC.

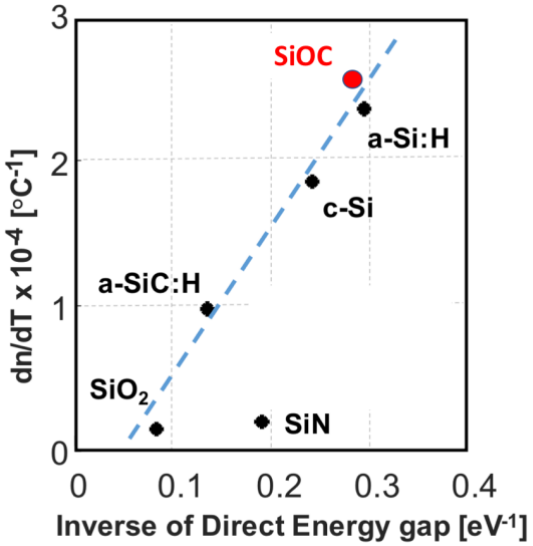


Fig.2. Dependence of the TOC of different materials on the inverse of the direct band gap energy.

4. SiOC-coated Si_3N_4 and SiON waveguides

The high TOC of SiOC can be exploited to enhance the temperature sensitivity of PICs fabricated with conventional dielectric platforms. Here, we report on the integration of a SiOC film on SiON and Si_3N_4 waveguides, according to the cross-sectional scheme shown in Fig. 3(a, c). A 60-nm-thin SiOC layer (n = 2.2) was deposited on a SiON core rib-shaped waveguide (2.5μm×1.8μm, 0.4 μm side slab), which was then buried under a SiO_2 cladding. All-pass racetrack resonators [see inset of Fig. 3(b)] were fabricated by using SiOC-coated SiON waveguides. Transmission measurements in Fig. 3(b) show a resonance shift by 250 pm when the temperature increases from 22°C to 30°C, resulting in a K_{eff} is 3.2×10^{-5} °C^{-1}. Remarkably, a thin layer of SiOC of only 60 nm increases by three times the temperature sensitivity of the native SiON waveguide (K_{SiON}=1.1×10^{-5} °C^{-1}).

SiOC has been also exploited to enhance the thermal tuning efficiency of photonic devices fabricated with conventional Si_3N_4 waveguides. As shown in the schematic of Fig. 1(c), a 350-nm-thin SiOC layer (n = 2.2) was deposited on a Si_3N_4 strip waveguide (1.2 μm × 0.3 μm), which was then buried under a SiO_2 cladding. All-pass microring resonators [see inset of Fig. 3(d)] were fabricated by using SiOC-coated Si_3N_4 waveguides. Transmission measurements in Fig. 3(d) show a resonance shift by 470 pm when the temperature increases from 25 °C to 35 °C, resulting in an effective TOC of 7×10^{-5} °C^{-1}, which is about four times higher than the TOC of

silica-buried Si_3N_4 waveguides (1.8×10^{-5} $°C^{-1}$). We expect a further increase upon the optimization of the waveguide core coated by SiOC. No additional losses have been experienced in these experiments.

These results show the potential of high-refractive-index SiOC for the realization of low-power-consumption thermally-tunable dielectric photonic platforms.

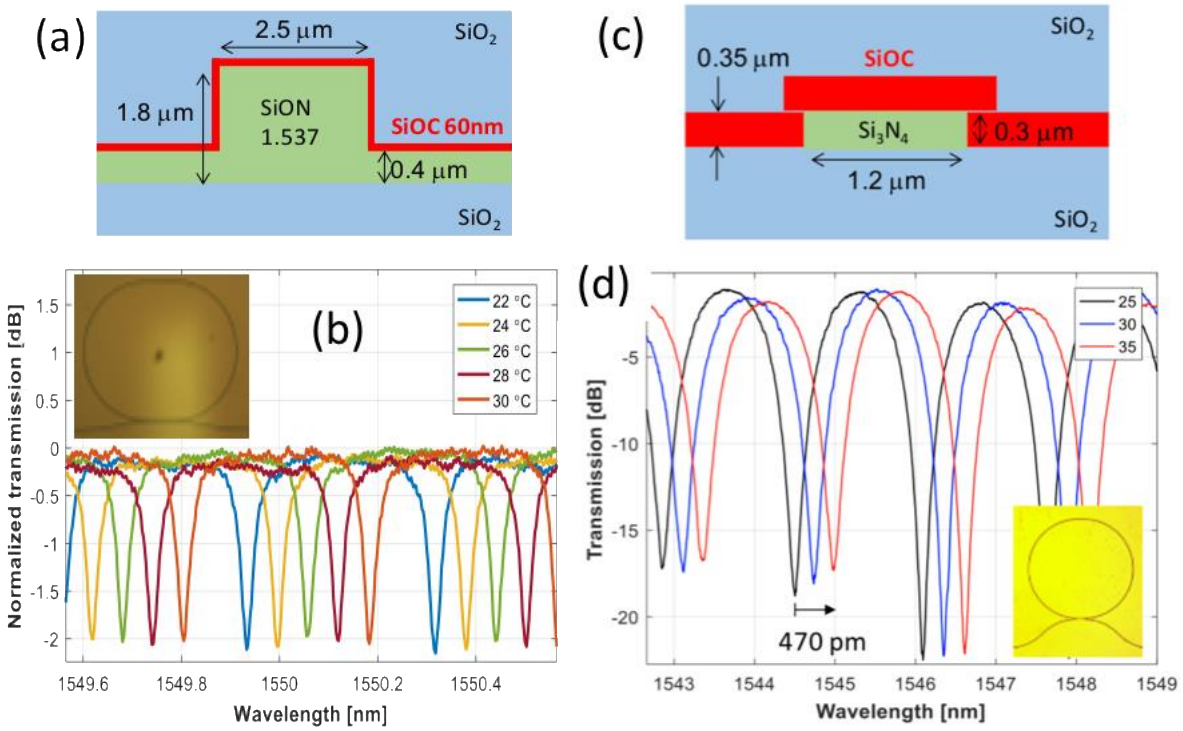


Fig.3. (a) Schematic cross-section of the realized SiOC-coated SiON rib waveguide. (b) Thermally induced wavelength shift of the transmission of a racetrack microring resonator. (c) Schematic cross-section of a SiOC-coated Si_3N_4 strip waveguide. (d) Thermally induced wavelength shift of the transmission of a microring resonator. Device pictures in the inset.

ACKNOWLEDGEMENTS

This work was partially funded by Fondazione Cariplo Project "Advanced Control Technologies for Integrated Optics (ACTIO)" Rif. 2016-0881. Fabrications have been realized in Polifab (www.polifab.polimi.it). The Authors acknowledge C. Somaschini, head of the technical staff of Polifab.

REFERENCES

[1] F. A. Memon, F. Morichetti, and A. Melloni, ACS Photonics., **5**(7), 2755 (2018).
[2] F. A. Memon, F. Morichetti, and A. Melloni, Appl. Sci., **7**(6), 561 (2017).
[3] L. David, R. Bhandavat, U. Barrera and G. Singh, "Silicon oxycarbide glass-graphene composite paper electrode for long-cycle lithium-ion batteries," Nat. Commun. **7**, 10998 (2016).
[4] V. Nikas, S. Gallis, M. Huang, A. E. Kaloyeros, A. P. D. Nguyen, A. Stesmans, and V. V. Afanas'ev, "The origin of white luminescence from silicon oxycarbide thin films," App. Phys. Letters, **104**, 061906 (2014).
[5] G. Bellocchi, F. Iacona, M. Miritello, T. Cesca and G. Franzò, "SiOC thin films: an efficient light source and an ideal host matrix for Eu^{2+} ions," Opt. Express 21(17), 20280 (2013)
[6] E. D. Palik, Handbook of thermo-optic coefficients of optical materials with applications (Academic, 1998)

Membrane III-V phonic devices on SiO_2/Si substrate

(Invited paper)

Shinji Matsuo

NTT Device and Material Labs, NTT Corp., 3-1 Morinosato-Wakamiya, Atsugi, Kanagawa 243-0198, Japan

shinji.matsuo.vm@hco.ntt.co.jp

ABSTRACT

We have developed membrane Distributed Reflector (DR) lasers and photonic crystal (PhC) lasers on SiO2/Si substrate for datacom and computercom applications. We employ direct bonding and regrowth techniques to fabricate buried heterostructure on SiO2/Si substrate. The increase of optical confinement factor is essential to achieve low operating energy.

We fabricated 8-ch DR laser array and each laser was directly modulated by 50-Gbit/s PAM-4 signal. An SiN arrayed waveguide grating (AWG) filter was used to multiplex output signals from 8-channel DR laser array. The PhC laser with 2.5-um long active region exhibited a threshold current of 22 μA and modulated a 10-Gbit/s NRZ signal with 7-fJ/bit operating energy. These results indicate that the membrane lasers on SiO2/Si substrate are highly suitable for use as a transmitter in datacom and computercom applications.

PZT-based Pockels Modulators on Silicon and Silicon Nitride Waveguides

(Invited paper)

Koen Alexander,[1,4] John P. George,[2,4] Gilles F. Feutma,[2,4] Tessa Van de Veire,[2,4] Jochem Verbist,[1,3,4] Bart Kuyken,[1,4] Jeroen Beeckman,[2,4] and Dries Van Thourhout [1,4]

[1] Photonics Research Group, INTEC, Ghent University-imec, Technologiepark 15, 9052 Ghent - Belgium
[2] Liquid Crystals and Photonics Group, ELIS, Ghent University, Technologiepark 15, 9052 Ghent - Belgium
[3] IDLab, INTEC, Ghent University, Technologiepark 15, 9052 Ghent - Belgium
[4] Center for Nano- and Biophotonics, Ghent University, Belgium
e-mail: Dries.VanThourhout@ugent.be

ABSTRACT

In this paper, we will present our recent progress on PZT-based Pockels modulators integrated on Silicon and Silicon Nitride waveguide platforms. The PZT layers are deposited using chemical solution processing methods, using a dedicated buffer layer. Large Pockels coefficients, low losses (<1dB/cm) and $V_\pi L \approx 3.2$ V.cm were measured. A bandwidth above 30GHz was obtained.

Keywords: Integrated optics, silicon photonics, optical modulators, ferroelectric materials.

40 Years of Semiconductor Lasers
A Tribute to Markus-Christian Amann

(Invited paper)

Jens Buus[1], Ralf Meyer[2]
[1] Gayton Photonics, 6 Baker Street, Gayton, Northants, NN7 3EZ, UK
[2] Walter Schottky Institute, Technical University of Munich, Am Coulombwall 4, 85748 Garching, Germany
e-mail: jbuus@btinternet.com / ralf.meyer@wsi.tum.de

ABSTRACT

For over 40 years Markus-Christian Amann (MCA) was a prominent member of the semiconductor laser community, and made numerous significant contributions to a wide range of topics. In this presentation we will review some of these contributions. We will also add some comments of a more personal character.

Keywords: Markus-Christian Amann, ridge waveguide lasers, tunable lasers, VCSELs, quantum cascade lasers.

SUMMARY

MCA started his work on AlGaAs/GaAs lasers in the late 70ies. At that time laser structures were grown by LPE, making thickness control difficult, and regrowth impossible. Simple stripe geometry structures suffered from numerous problems, making their practical use difficult. A relatively simple solution developed by MCA was the metal clad ridge waveguide (MCRW) laser. When GaInAsP/InP lasers were developed in the early 80ies the MCRW design was successfully applied to fabricate weakly index guided long wavelength lasers by a comparatively simple process.

In the early 90ies during his time as an employee of Siemens research laboratories MCA became a world leading expert on tunable lasers, inventing several different designs. The tunable twin-guide (TTG) laser is a particularly elegant design, allowing continuous electronic tuning in excess of 10 nm. Other ideas include: 1) the vertical Mach-Zehnder (VMZ) using two layers rather than two branches, 2) the amplifier-coupler-absorber (ACA) using a codirectional grating assisted coupler, and 3) the distributed forward coupled (DFC) structure. For all of these structures MCA provided both the basic idea and the detailed design. One of the results on the work on tunable lasers was the book “Tunable Laser Diodes”, published in 1998, and later updated and expanded in 2005.

Although MCA was best known as a technologist and as an inventor of laser structures, he was also an accomplished theoretician. He had a broad knowledge of mathematics, both pure and applied, and in addition he was very skilful in combining analytical and numerical methods. Some examples will be described.

Also in his second career as a university professor, MCA was driven by the motivation to turn research results into practical applications. Over the past 20 years his goal has been to develop lasers for the infrared spectral range. He and his group were able to realize lasers with emission wavelengths ranging from 1 to 250 μm on the basis of sophisticated material research and various physical concepts.

Around the turn of the millennium, he developed the concept of the buried tunnel contact, which made it possible to produce surface-emitting lasers (VCSELs) in the InP material system. With emission wavelengths of 1.3 to 2.3 μm, these devices find application in high-speed data transmission as well as in absorption spectroscopy (TDLAS) for the detection of gases. The spin-off company *VERTILAS*, which he co-founded and accompanied as a scientific adviser over the years was a result of this research.

For longer wavelengths, antimony-containing compounds are the materials of choice, but this has required the development of a completely new technology. In combination with a new design of the active region based on type-II heterostructures, electrically pumped VCSELs with emission wavelengths up to 4 μm could be fabricated.

With quantum cascade lasers, light can be generated at even longer wavelengths (roughly 6 to 12 μm). At the beginning of the 2000s, this type of laser was also realized in his working group. Due to the monolithic integration of two lasers with different wavelengths and corresponding grating structures, it was possible to produce emitters in the wavelength range from 4 to 250 μm by utilizing the Second Harmonic Generation or the Difference Frequency Generation.

Two more of his PhD students working in his research group at that time used their experience in the field of material fabrication and manufacturing of quantum cascade lasers to set up their own spin-off company, the company *BROLIS Semiconductors* in 2012.

The work of MCA has been, and is still, widely cited. In total, he has (co-)authored more than 500 publications that have been cited about 6,000 times and achieved an *h*-index of 37.

We have been privileged to have Markus-Christian Amann as a colleague and as a friend. All honour to his memory.

How can you be part of *Nature Photonics*?

(Invited paper)

Rachel Won
Nature Publishing Group, The MacMillan Campus, 4 Crinan Street, London N1 9XW, UK
e-mail: r.won@nature.com

ABSTRACT

Launched in January 2007, *Nature Photonics* is a monthly journal dedicated to optics and photonics that publishes top-quality, peer-reviewed research in all areas of light generation, manipulation and detection. This talk, although with an emphasis on *Nature Photonics*, will introduce you to all the existing and new *Nature* journals, and cover the detailed information and guidelines on scientific manuscript preparation and submission. Also presented is an overview on the editorial and peer-review processes in all *Nature* journals. You will get to know what editors seek, how to write a good cover letter and a good scientific paper, the peer review process that your paper goes through and how to make an appeal. More importantly, you will find out how you can contribute to the journals apart from publishing your research.



Monolithic electronic-photonic integration in zero-change SOI and bulk CMOS

Vladimir Stojanovic, EECS Dept. University of California, Berkeley

We present platforms for monolithic integration of silicon-photonic components into advanced SOI and bulk CMOS process nodes. These integration platforms enable large-scale electronic photonic systems with millions of transistors and thousands of photonic devices on the same die. Zero-change integration into 45nm and 32nm SOI CMOS enables powerful integrated systems with no extra cost. We also demonstrate bulk CMOS integration with several inexpensive mask layers enabling scaling beyond 32nm.

Evaluation of Stability of Silicon-Photonics-Based Optical Switch Network Architectures against Parasitic Errors in Switch Elements

Banafsheh Abasahl , Wim Bogaerts
Ghent University - Imec, Technologiepark 126, 9052 Ghent, Belgium
Center of Nano-and Biophotonics, Ghent University, Ghent, Belgium e-mail: banafsheh.abasahl@imec.be

ABSTRACT

The performance of MEMS-based optical switch networks against losses and parasitic effects in tunable elements for different architectures are simulated. A comparison between those architectures is provided considering the fact that the parasitic effects of MEMS switches are highly depend on their status.

Keywords: optical switch networks, MEMS switches, Beneš, PILOSS, cross-bar, optical circuit simulation, stochastic analysis, errors.

1 INTRODUCTION

Optical switch networks are essential platforms for all-optical communication networks. The power consumption and cost of communication networks drop dramatically if low-power and high performance silicon photonic integrated circuits with tunable components are incorporated in such networks. In order to maintain the performance of these networks in larger scales, the choice of switch architecture (i.e. the connectivity network inside the switch) is crucial. The performance of these switch networks not only depend on components losses, but also on parasitic coupling effects. These effects can give rise to distortion in the output signals, non-uniformity and crosstalk due to multi-path interference. In this work, we provide a comparison between different architectures that can be implemented in a photonic integrated circuit (PIC). Three non-blocking architectures for N×N switch networks, namely cross-bar, path-independent loss (PILOSS) [1] and Beneš [2] are implemented. A schematic representation of these networks is shown in Fig. 1. We consider a silicon photonics technology platform, but as switching elements we introduce the use of of optical MEMS [3], [4], because these switches, as opposed to optical switches based on electric heating [5], offer almost zero electric power loss at the expense of low switching speed.

2 IMPLEMENTATION OF SWITCH NETWORK ARCHITECTURES

The switch elements in this work are based on MEMS directional couplers (DC) where the spacing between the waveguides can be mechanically adjusted. For these tunable DCs, in the *bar* state, the two waveguides are

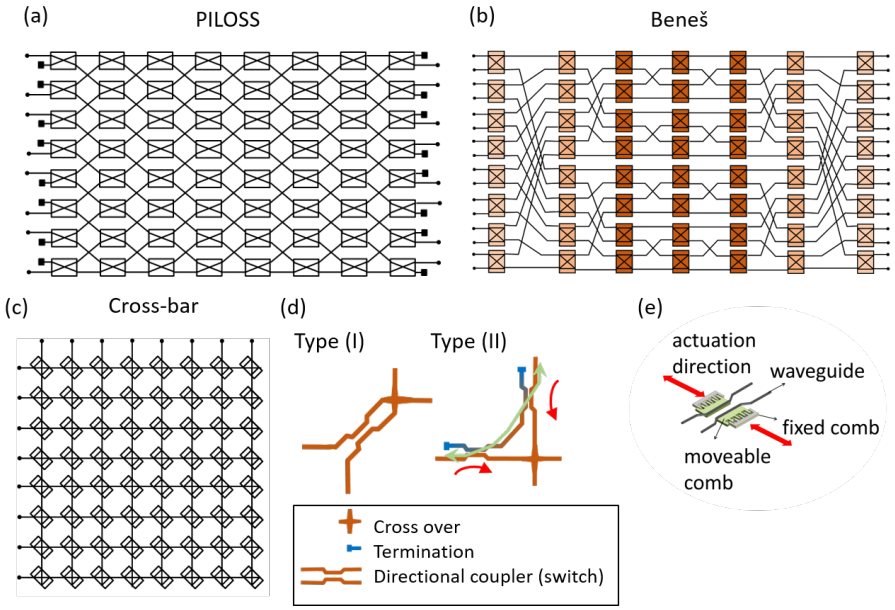


Figure 1. Switch network architectures under consideration: (a) Beneš, (b) PILOSS, and (c) Cross-bar. (d) two types of switch implementations for the cross-bar architecture, (e) a schematic representation of a MEMS directional coupler with comb actuation. Although the calculations are performed on 16×16 networks, here for the sake of clarity, 8×8 networks are presented for cross-bar and PILOSS architectures.

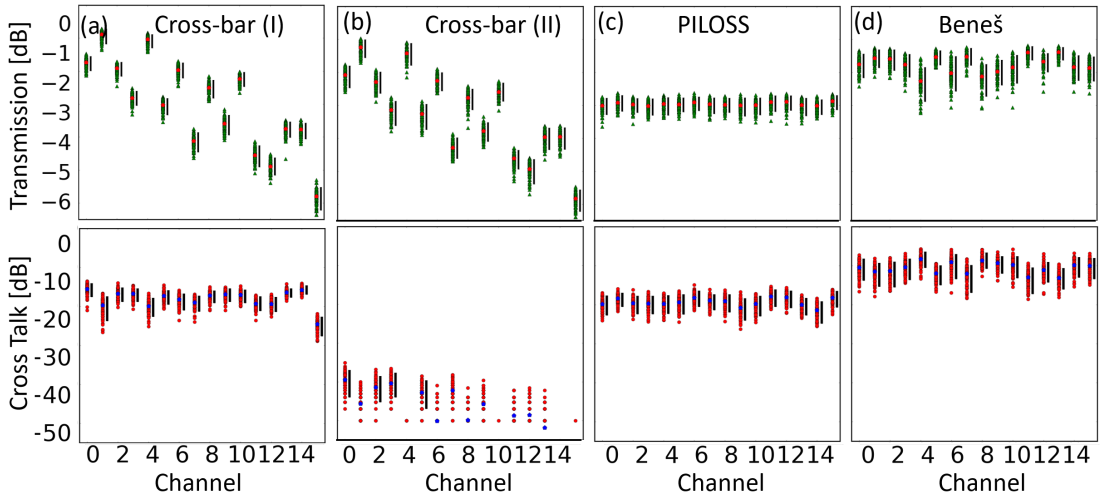


Figure 2. Distribution of the transmission (top) and cross talk (bottom) of 100-cycle Monte Carlo simulations with $\sigma_{cross} = 5\%$ for 16×16 networks with (a) cross-bar(I), (b) cross-bar (II), (c) PILOSS and (d) Beneš architectures.

sufficiently far apart that no coupling occurs. On the other hand, the two waveguides are brought close together in the *cross* state and the DC becomes more sensitive to the coupling distance and therefore it introduces higher error levels and wavelength dependence in the coupling.

The cross-bar architecture comprises of a matrix of N×N switches. The switches are always in the bar state except for the switches SE_{mn}, where the input m^{th} is to be routed to the output n^{th}. In contrast to the cross-bar architecture where the number of switches (N_{switch}) and crossovers ($N_{crossover}$) depend on the requested mapping, the PILOSS architecture offers a solution where these numbers are always constant. In each routing, only one switch is in the *bar* state, and the the rest are in *cross* states, which is not conducive for low losses and errors. In order to benefit from the performance of the DCs in the *bar* state, a combination of a DC and a cross over, like the switch shown for cross-bar type(I), is used. In this case, the 100% transmission correspond to *cross* state. For each of these two architectures N^2 switches are needed, which results in a large footprint and an accumulation of errors and losses.

A more compact solution is a routine proposed by Beneš where $N = 2^p$ inputs-outputs are routed in a layered architecture. In this case, the number of switches per routing decreases dramatically. The physical properties of the three architectures as a function of the number of input-outputs (N) are provided in Table 1. The simulations are performed for $N = 16$ using the Caphe circuit simulator by Luceda Photonics, extended with our own variability analysis routines [6]. In order to study the effect of stochastic imperfections of switches, in a 100-loop Monte-Carlo set of simulations, the coupling values assigned to each DC is randomly deviated from its ideal setting of 0 (*bar*) or 1 (*cross*), with a normal probability distribution and a standard deviation of σ_{bar} and σ_{cross}. In each case, the σ_{cross} is considered to be one order of magnitude larger than σ_{bar}. The insertion loss for the *bar* and *cross* states are considered to be 0.3 dB and 0.4 dB, respectively. For the cross-bar architecture, the performance is evaluated by incorporating two types of switch nodes, shown Fig. 1a: type (I) with a single DC and a crossover, as those considered for the other two architectures, and type (II) built of two DCs and one crossover suggested in [4]. The resulting distribution for the outputs of 16×16 networks with the these architectures are shown in Fig. 2a-d for a $\sigma_{cross} = 5\%$ and $\sigma_{bar} = 0.5\%$. The simulator evaluates the S-parameter between each input-output pair, from which the transmission and the crosstalk values are inferred. In Table 1, the outcomes of Monte-Carlo simulations, averaged over the 100 cycles and the 16 outputs, are presented.

TABLE 1. COMPARISON BETWEEN PROPERTIES OF THE THREE SWITCH NETWORK ARCHITECTURES. THE VALUES IN RED ARE FOR A 16×16 NETWORK. THE AVERAGE VALUES CALCULATED FOR $\sigma cross = 5\%$ AND $\sigma_{bar} = 0.5\%$ ARE PRESENTED IN BLUE.

	Cross bar (I)	Cross bar (II)	PILOSS	Beneš
N_{DC} ; $N_{crossover}$	N^2;N^2	$2N^2$;N^2	N^2;$N^2+(N-1)^2$	$(2\times \log_2 N-1)\times \frac{N}{2}$; $\sum_{m=0}^{\log_2 N}(\frac{N^2}{2^m}-N)$
	256; 256	512; 256	256; 225	56; 88
N_{switch} per path	1 to $2N-1$	1 to $2N-1$	N	$2\log_2 N-1$
	1 to 33	1 to 33	16	7
N_{rs}	4	4	4	-
	4	4	4	1 to 29 (Average= 10)
Transmission	-2.83 dB	-3.11 dB	-2.96 dB	-1.75 dB
Crosstalk	-17.68 dB	-45.04 dB	-19.22 dB	-10.38 dB

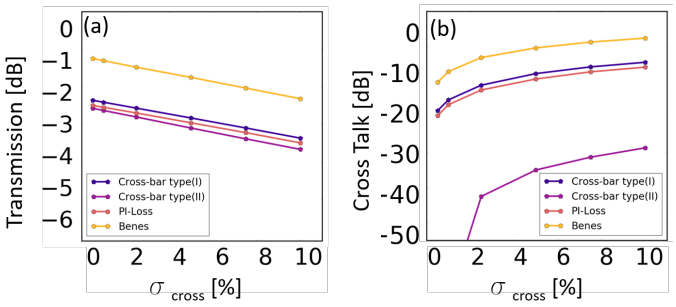


Figure 3. Average transmission (a) and cross talk (b) of the 16 channels as a function of σ_{cross}, when $\sigma_{bar} = 0.1\sigma_{cross}$ for the four architectures of Fig. 1.

3 DISCUSSION

Among the the mentioned architectures, the Beneš network with the smallest $N_{switche}$ and $N_{crossover}$ offers the minimum footprint, the lowest insertion loss and therefore the highest transmission, as can be seen in Fig. 3a. On the other hand, based on Fig. 3b, it suffers from the highest crosstalk due to the number of switches in the *cross* state being dependent on the requested map. In addition, Beneš network is indeed rearrangably non-blocking, i.e. when two sets of input-output are altered, at least one more switch must be altered. This causes a cutoff period in the other outputs which are still mapped to the same inputs. Our calculations show that for a 16×16 Beneš architecture depending on the rearrangement, N_{rs}=1 to 29 switches (with an average of 10) are needed to alter for an alteration of two input-output sets. For cross-bar and PILOSS architectures, N_{rs}=4 and the outputs experience no cutoff unless they are altered.

The number of switches and crossovers for the path between each input-output pairs is constant for Beneš and PILOSS configurations, regardless of the requested mapping. For the PILOSS configuration, as can be inferred from 2c, since there is always only one switch in the *cross* state per path, the signal and cross talk levels show the most independence to the requested mapping. On the other hand, for the cross-bar architectures, the number of elements in each path differs for each input-output combination and it can range from one switch and one crossover (when the last input is mapped to the first output) to $2N-1$ switches and crossovers (when the first input is mapped to the last output). In Fig. 2a and b, the average transmission level varies from, respectively, -0.8 dB and -1.2 dB in the second channel to, respectively, -5.7 dB and -5.8 dB in the last channel. For the Beneš network in Fig. 2d, transmission varies from -1.34 dB to -2.22 dB, while this variation reduces to 0.15 dB for the PILOSS architecture in Fig.2c. Among the studied architectures in this work, cross bar type (II) presents the lowest cross talk, due to its switch design. In fact, the errors in the DCs are bypassed to terminals and are prevented to propagate in the network. The terminals are considered to be connected to light sinks with a negligible back-reflection.

ACKNOWLEDGEMENT

This work has received funding from the European Union's Horizon 2020 research and innovation programme under grant agreement No 780283 (MORPHIC).The authors would like to thank Dr. Cristina Lerma Arce for the fruitful discussions.

REFERENCES

[1] K. Suzuki, K. Tanizawa, T. Matsukawa, G. Cong, S.-H. Kim, S. Suda, M. Ohno, T. Chiba, H. Tadokoro, M. Yanagihara, Y. Igarashi, M. Masahara, S. Namiki, and H. Kawashima, "Ultra-compact 8 8 strictly-non-blocking Si-wire PILOSS switch," Optics Express **22**, 3887–3894 (2014).

[2] H. NAKAJIMA, "Development on Guided-Wave Switch Arrays," IEICE Trans. Electronics E **82**, 297–304 (1999).

[3] U. Shah, M. Sterner, and J. Oberhammer, "High-Directivity MEMS-Tunable Directional Couplers for 10–18-GHz Broadband Applications," IEEE Transactions on Microwave Theory and Techniques **61**, 3236–3246 (2013).

[4] N. Quack, T. J. Seok, S. Han, R. S. Muller, and M. C. Wu, "Scalable Row/Column Addressing of Silicon Photonic MEMS Switches," IEEE Photonics Technology Letters **28**, 561–564 (2016).

[5] Y. Sun, Y. Cao, Y. Yi, L. Tian, Y. Zheng, J. Zheng, F. Wang, and D. Zhang, "A low-power consumption MZI thermal optical switch with a graphene-assisted heating layer and air trench," RSC Advances **7**, 39922–39927 (2017).

[6] W. Bogaerts, U. Khan, and Y. Xing, "Layout-Aware Yield Prediction of Photonic Circuits," IEEE International Conference on Group IV Photonics pp. 93–94 (2018).

Large Q factor with small ring cavities

Nirmalendu Acharyya [1,2], Gregory Kozyreff [2]
[1]*Max-Born-Institut für Nichtlineare Optik und Kurzzeitspektroskopie, D-12489 Berlin, Germany*
[2]*Optique Nonlinéaire Théorique, Université libre de Bruxelles (U.L.B.), CP 231, Campus de la Plaine, 1050 Bruxelles, Belgium*
e-mail: Nirmalendu.Acharyya@mbi-berlin.de, gkozyref@ulb.ac.be

ABSTRACT

Radiation losses are a critical problem of small-radius optical whispering gallery mode (WGM) resonators. This phenomenon is a fundamental barrier that prevents one to reduce the size of the cavity and increase the local electric field. We propose a structure around the cavity that can be built with existing technologies and that can suppress the radiation. We demonstrate this fact by a nearly exact formula that gives the enhancement of the Q factor in 2D and confirm our results by a series of numerical simulations in 3D. By decreasing mode volume while preserving photon lifetime, the performance of WGM cavities can be boosted and new limits can be reached in the many areas of research and applications where they are used, from cavity quantum electrodynamics to label-free biosensing.

Keywords: Whispering Gallery Modes, Bending losses, micro-ring resonators, small radius, Q factor.

1 INTRODUCTION

Circular dielectric cavities which support whispering gallery modes (WGM) are key elements of photonic integrated circuits [1]. Thanks to their combination of large Q factor and small volume V, photons carrying a locally large electric field can circulate for a long time without dissipation. As a result, all the forms of interaction between light and matter can be drastically enhanced: laser action [2], second- and third-harmonic generation [3], [4], scattering by particles [5], etc. In biosensing, the ratio Q/V is well known to determine the limit of detection (LOD) of the device [6].

On photonic integrated platforms, WGM cavities with Q factors as high as 10^6 can now be obtained with state-of-the art fabrication techniques [7], [8], [9]. However, in all the cases reported, such high values of Q are only reported for cavities with a large radius R compared to the optical wavelength λ, typically between 50μm and 1 mm. This necessity results from bending losses, which increase drastically as the R decreases below a threshold of about 10λ. Bending losses are the radiation of electromagnetic energy by a waveguide upon changes of direction of propagation; they represent a fundamental barrier to the reduction of microring radii as well as the radius curvature of bends in photonic circuits. Regarding bent waveguides, several attempts have already been made to reduce bending losses, notably by enclosing the waveguide by a second one [10], [11], [12]. However, the reduction of losses so obtained remains quite modest and, in the case of [10], mostly rests on an increased effective radius of curvature for the light path. In this communication, we report a way to control WGM bending losses that can lead to orders of magnitude enhancement of the Q factor. The proposed technique could allow one to maintain the large Q factors allowed by state-of-the-art material fabrication technique while diminishing the cavity radius R by several orders of magnitude. This could lead, for instance, to lower LOD in biosensing, larger efficiency in nonlinear photon generation for quantum optics sources, and micro-lasers with lower lasing threshold.

The structure proposed consists of set of concentric rings placed outside the cavity, forming a kind of 'dielectric sarcophagus' for WGM as depicted in Fig. 1. The innermost of these rings is typically located in the near field of the WGM. As we demonstrate, the Q factor can be increased by several orders of magnitudes in this way. Adding more rings to the external structure allows one to further improve the radial part of Q factor. Here, it is important to note that the external shells are too thin to guide light and that the mode energy remains concentrated in the cavity.

2 THEORY

To determine the actual bending losses of a cavity or a portion of bent waveguide is a complicated theoretical problem [13], [14]. However, it turns out that a simple and nearly exact formula can be derived for the ratio Q/Q_0 of the quality factor in the presence of the external structure (Q) to that of the bare cavity (Q_0). Consider a cylindrical geometry made of concentric dielectric shells, as in Fig. 1. The shell closest to the centre is the cavity, whose radiation we wish to suppress.

In the region of space defined by $r_{j-1} \leq r \leq r_j$ and of refractive index n_j, the electromagnetic is governed by

$$\psi(r) = \left[a_j J_\nu(n_j k r) + b_j Y_\nu(n_j k r)\right] e^{i\nu\theta - ikct}, \tag{1}$$

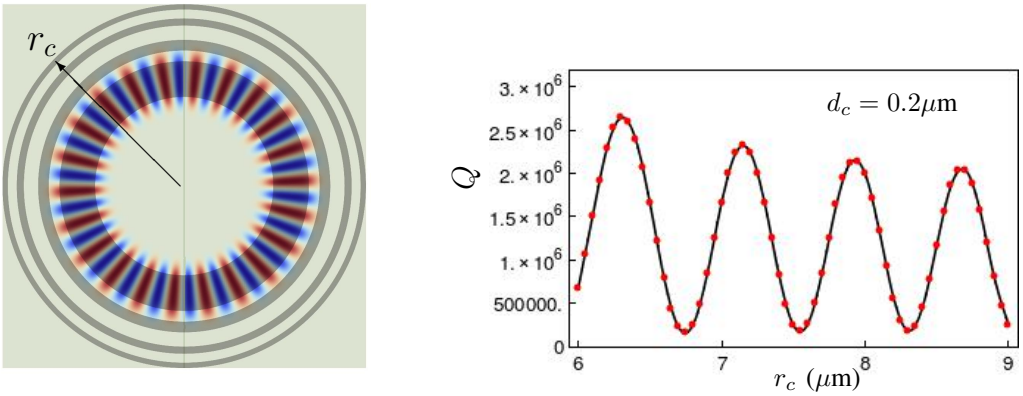


Figure 1. Left: sketch of a Al_2O_3 ring cavity with outer radius 3.2μm operating on a mode with orbital number $\nu = 22$ ($\lambda = 1.26\mu$m). Three external concentric rings are added to attenuate radiation. Without the external rings, $Q_0 \approx 15000$. Right: Q as a function of the radius of the outermost ring. The first and second rings have radii and thickness given by $(4.87, 0.23)\mu$m, and $(r_b, d_b) = (5.63, 0.21)\mu$m, respectively. The graph shows an enhancement $Q/Q_0 \approx 170$.

where $\psi = E_z$ for TE modes, $\psi = H_z$ for TM mode, r and θ are the usual cylindrical polar coordinates, c is the speed of light in vacuum and k is the complex wave number. The parameter ν is the azimuthal number; usually, for large R, $\nu \gg 1$, on the order of 1000 or more, which ensures that the radiation losses are very small. Here, we aim to achieve a large Q with small values of ν. In the central region, $(a_0, b_0) = (a_0, 0)$ in order to avoid divergence of the electromagnetic field. On the other hand, in the outermost region, Sommerfeld's radiation condition reads $(a_N, b_N) = (a_N, ia_N)$. The vectors $(a_0, 0)$ and (a_N, ia_N) can be related by a 2×2 scattering matrix S:

$$\begin{pmatrix} a_0 \\ 0 \end{pmatrix} = S \begin{pmatrix} a_N \\ ia_N \end{pmatrix}, \tag{2}$$

Above, $S = S^c S^s$, where S^c and S^s respectively describe the cavity and the dielectric shield. Their derivation follows straightforwardly from the continuity conditions between the various regions that constitute the whole system. The second of the two relations above, $S_{21}(k) + iS_{22}(k) = 0$ yields the characteristic equation for the whole system. Its solutions give the complex wave number $k = k_r - ik_i$ and the Q factor is given by $Q = k_r/(2k_i)$. By the same token, $S^c_{21}(k^c) + iS^c_{22}(k^c) = 0$ give the complex resonances of the bare cavity, associated to a quality factor $Q_0 = k^c_r/(2k^c_i)$.

To compute $k^c = k^c_r - ik^c_i$ for the bare cavity is a numerically easy task when ν is only moderately large. Conversely, a direct numerical resolution of the characteristic equation for the cavity+external rings rapidly becomes challenging as the number of rings increases. However, we have found that, with excellent numerical accuracy

$$\frac{Q}{Q_0} = \frac{k^c_i}{k_i} \approx \mathrm{Re}\left[\frac{S^s_{22}\left(k^c_r\right) - iS^s_{21}\left(k^c_r\right)}{S^s_{11}\left(k^c_r\right) + iS^s_{12}\left(k^c_r\right)}\right], \tag{3}$$

which only requires the knowledge of k^c_r associated to the bare cavity. This formula allows one to simply and rapidly evaluate the validity of a set of geometrical parameters for the outer shells. Moreover, it suggests to design the shielding structure by adding and optimising one shell at a time. Starting from a single shell, one can easily optimise its radius r_a and radial thickness thickness d_a. Next, a second shell with radius $r_b > r_a$ can be added and optimised and so on, until the entire structure is completed.

3 RESULTS

An illustration of the accuracy of formula (3) is given in Fig. 1, describing a mode with azimuthal number $\nu = 22$ in an Al_2O_3 cavity of external radius $R = 3.2\mu$m. We choose this material because it has been demonstrated to be an advantageous, CMOS compatible, host for rare-earth dopant and to hold great potential to integrate micro-lasers in photonic platforms [15], [8]. However, its index of refraction is only 1.65, a rather small value compared to other PIC materials. For the above parameters, $\lambda \approx 1.26\mu$m, which is in the emission range of Yb atoms, that can dope Al_2O_3 for lasing. In the absence of the external shielding structure, we compute that $Q_0 \approx 15000$. By optimizing a three-shell structure, one finds that the quality factor can be raised to $Q \approx 2.5 \times 10^6$ as far as radiation losses is concerned. Such value correspond to the state-of-the-art material limit of Q.

To check the validity of our design in 3D, we have carried out a series of 3D simulations. In, Fig. 2, we show the simulation of a ridge-waveguide Al_2O_3 on SiO_2. By placing a single outer ring at an optimal radius, we obtain an enhancement of quality factor $Q/Q_0 \approx 8$. Fig. 2 shows that the field stays confined in the cavity in the presence of the dielectric shield and illustrates how the intensity distribution is attenuated in the far field. Adding further rings, one can further improve Q (not shown).

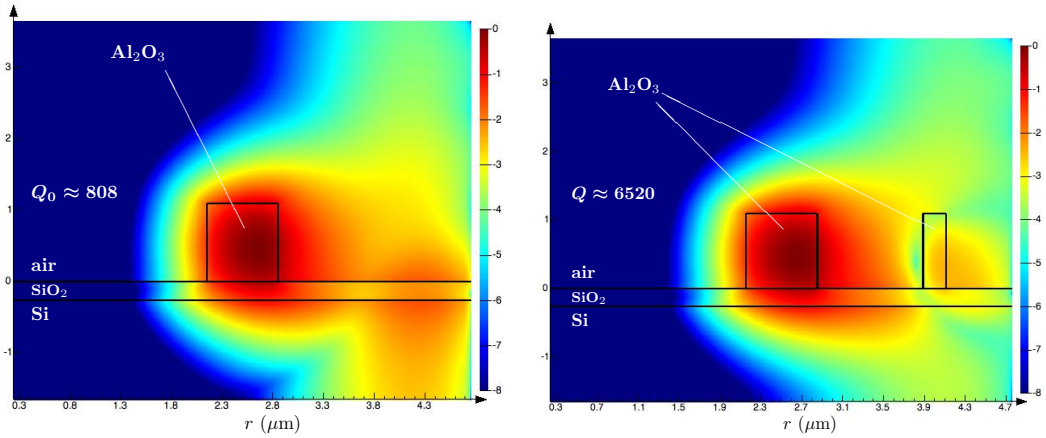


Figure 2. Mode distribution (logarithmic color scale) of a ridge Al_2O_3 ring cavity over a SiO_2 base. Bare cavity radii: inner radius $r_1 = 2.15\mu$m, $r_2 = 2.85\mu$m. Height: 1.1μm. SiO_2 thickness: 0.25μm, $\lambda = 1.26\mu$m.

4 CONCLUSION

In conclusion, we have demonstrated a way to drastically enhance the quality factor of microring cavities and bent waveguides. A simple theory has been derived that accurately predicts the gain that can be achieved by complementing the cavity with external rings. The proposed geometries have been demonstrated with Al_2O_3 but it is clear that it is not restricted to that particular material and that this structure can be made with silicon photonics or silicon nitride. Regarding the excitation of microring surrounded by other ring, one can resort to buried waveguide, as for instance in [8].

REFERENCES

[1] W. Bogaerts, P. De Heyn, T. Van Vaerenbergh, K. De Vos, S. Kumar Selvaraja, T. Claes, P. Dumon, P. Bienstman, D. Van Thourhout, and R. Baets, "Silicon microring resonators," *Laser & Photonics Reviews*, vol. 6, no. 1, pp. 47–73, 2012.

[2] K. Srinivasan, M. Borselli, O. Painter, A. Stintz, and S. Krishna, "Cavity Q, mode volume, and lasing threshold in small diameter AlGaAs microdisks with embedded quantum dots," *Opt. Express*, vol. 14, no. 3, pp. 1094–1105, Feb 2006.

[3] J. L. Dominguez-Juarez, G. Kozyreff, and J. Martorell, "Whispering gallery microresonators for second harmonic light generation from a low number of small molecules," *Nat. Commun.*, vol. 2, p. 254, 2011.

[4] T. Carmon and K. J. Vahala, "Visible continuous emission from a silica microphotonic device by third-harmonic generation," *Nature Phys.*, vol. 3, pp. 430–435, 2007.

[5] L. He, Ş. K. Özdemir, J. Zhu, W. Kim, and L. Yang, "Detecting single viruses and nanoparticles using whispering gallery microlasers," *Nat. Nanotech.*, vol. 6, no. 7, pp. 428–432, 2011.

[6] F. Vollmer, S. Arnold, and D. Keng, "Single virus detection from the reactive shift of a whispering-gallery mode," *Proc. Natl. Acad. Sci. USA*, vol. 105, p. 20701, 2008.

[7] M.-C. Tien, J. F. Bauters, M. J. R. Heck, D. T. Spencer, D. J. Blumenthal, and J. E. Bowers, "Ultra-high quality factor planar Si_3N_4 ring resonators on si substrates," *Opt. Express*, vol. 19, pp. 13 551–13 556, 2011.

[8] Z. Su, N. Li, H. C. Frankis, E. S. Magden, T. N. Adam, G. Leake, D. Coolbaugh, J. D. B. Bradley, and M. R. Watts, "High-Q-factor Al_2O_3 micro-trench cavities integrated with silicon nitride waveguides on silicon," *Opt. Express*, vol. 26, no. 9, p. 11161, apr 2018.

[9] A. E. Shitikov, I. A. Bilenko, N. M. Kondratiev, V. E. Lobanov, A. Markosyan, and M. L. Gorodetsky, "Billion Q-factor in silicon WGM resonators," *Optica*, vol. 5, no. 12, p. 1525, nov 2018.

[10] D.-P. Cai, J.-H. Lu, C.-C. Chen, C.-C. Lee, C.-E. Lin, and T.-J. Yen, "High Q-factor microring resonator wrapped by the curved waveguide," *Sci. Rep.*, vol. 5, p. 10078, 2015.

[11] P. Chamorro-Posada, "Q -enhanced racetrack microresonators," *Opt. Commun.*, vol. 387, pp. 70–78, mar 2017.

[12] ——, "Radiation in bent asymmetric coupled waveguides."

[13] K. R. Hiremath, M. Hammer, R. Stoffer, L. Prkna, and J. Čtyroký, "Analytic approach to dielectric optical bent slab waveguides," *Opt. Quantum Electron.*, vol. 37, no. 1, pp. 37–61, 2005.

[14] G. Kozyreff and N. Acharyya, "Dispersion relations and bending losses of cylindrical and spherical shells, slabs, and slot waveguides," *Opt. Express*, vol. 24, p. 28204, 2016.

[15] E. Bernhardi, M. Khan, C. Roeloffzen, H. van Wolferen, K. Wörhoff, R. De Ridder, and M. Pollnau, "Photonic generation of stable microwave signals from a dual-wavelength Al_2O_3:Yb^{3+} distributed-feedback waveguide laser," *Opt. Lett.*, vol. 37, pp. 181–183, 2012.

Proposal of Integrated-Optical Circuit for Recognition of 8PSK-Coded label for Photonic Label Router

Munkhbayar Adiya [1], Nyam-Erdene Odbayar [1], Hiroki Kishikawa [1], and Nobuo Goto [1]
[1]*Tokushima University, 2-1 Minamijosanjima-cho, Tokushima, 770-8506, Japan*
Tel: +81-88-656-9418, e-mail: kishikawa.hiroki@tokushima-u.ac.jp

ABSTRACT

This paper discusses optical label recognition which is one of the key functions for photonic label routing. Previously, we have proposed a basic waveguide-type circuit for recognition of optical label encoded in quadrature-phase-shift-keying (QPSK) format. To increase the number of labels represented with the same symbol number, we have studied 8-ary PSK (8PSK) recognition circuit based on the QPSK recognition circuit. The recognition of the proposed method is theoretically discussed and noise tolerance is also investigated.

Keywords: label recognition, optical 8PSK coded label, optical QPSK code, optical waveguide circuit, noise tolerance

1 INTRODUCTION

A conventional optical network system, electrical signal processing is applied to the routing node together with an optical-to-electrical and electrical-to-optical conversion. This conversion takes time for processing and requires power consumption which makes transmission system more complex. The optical signal processing without conversion to electrical signals is expected to be applied to routing nodes to overcome those disadvantages [1], [2], [3].

Our team has been working on several pieces of researches including waveguide-type devices for recognition of 16 quadrature-amplitude-modulation (16QAM) labels [4] and 8QAM labels [5]. These QAM modulated pulses have multiple amplitudes, which results in efficient bandwidth and high bit rate for transmission. Although the distance between codes in the signal constellation can be large compared with a single amplitude codes such as multiple PSK codes, optical recognition scheme for such M-ary PSK labels can be much simpler. Therefore, we propose an optical recognition circuit for 8PSK labels. The proposed circuit is based on the optical QPSK recognition circuit (QPRC) which consists of an asymmetric X-junction coupler, Y-branches, and a 3-dB directional coupler. The electric power consumption of the proposed circuit is considered to be low because of the passive integrated-optical devices and thresholds. The recognition is performed during optical wave propagation through the proposed passive devices and thresholds. Therefore, the processing speed is expected to be fast.

The proposed waveguide-type 8PSK recognition circuit employs two decision schemes, i.e., recognition from the maximum output port or from the minimum output port. First, the input-output relation of the recognition circuit is theoretically analyzed. Then, the bit-error-rate (BER) characteristics against optical signal-to-noise ratio (OSNR) are evaluated by numerical simulations using OptiSystem software (Optiwave Systems Inc.) in order to clarify the label recognition performance since noise tolerance is considered as one of the important factors in the telecommunication system. For the purpose of comparison, we also build a back-to-back (B2B) model which uses a digital coherent receiver to recognize 8PSK codes.

In the optical label network system, a large number of routing labels are required. Thus, we propose scaled two-symbol length 8PSK label recognition circuits for the two recognition schemes. We evaluate and compare the BER characteristics of the two recognition schemes.

2 TWO-SYMBOL LENGTH 8PSK-CODED LABEL RECOGNITION CIRCUIT

The constellation diagram of 8PSK is illustrated in Fig.1(a). The previously our proposed basic optical waveguide circuit for recognition of QPSK labels is shown in (b), which is named QPSK-phase recognition circuit (QPRC). Our proposed one-symbol 8PSK recognition circuit (8PRC) consists of two QPRCs and a "$-\pi/4$"-phase shifter as shown in (c). From the theoretical calculation, it is found that there is one maximum output port and one minimum (null) output port for each 8PSK code. The circuit structures of the maximum-output and the minimum-output detection schemes are different.

2.1 Maximum output detection scheme

Fig.2(a) shows a two-symbol RC by the maximum output detection scheme. The circuit has a two-stage connection of the 8PRCs. We use phase adjustment in order to make a complete interference between the reference signal and the second symbol signal.

Fig.2(b) shows the relative output intensities $|E_{\mathrm{out2}}^{(i)}/E_0|^2, (i = 1, \ldots, 64)$ from the theoretical calculation for the case $n = 0$.The maximum intensity is found to be 0.250 at the output port, port number of 10, 14, 12,

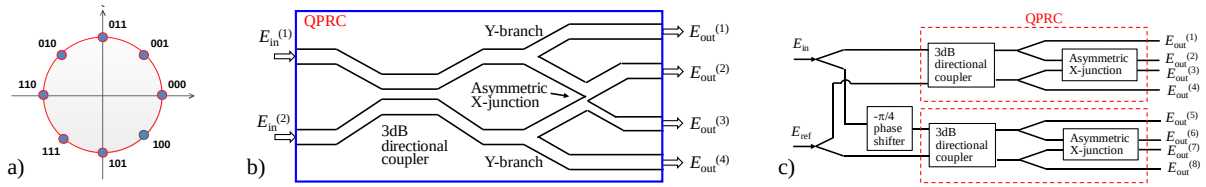


Figure 1. (a) Constellation of 8PSK coded signals, (b) a basic module for recognition of QPSK coded labels, and (c) a proposed circuit for recognition of 8PSK coded labels

16, 11, 15, 9, 13, out of 64 ports for each input of $m = 0, 1, 2, 3, 4, 5, 6, 7$, respectively. The second maximum intensity is 0.2225 (89.0 % of the maximum intensity). Similarly, for all the combination of m and n, only one maximum output is obtained at a different port. Thus, the two-symbol 8PSK labels can be recognized by the maximum-output scheme with our proposed recognition circuit using thresholding between 0.250 and 0.2225.

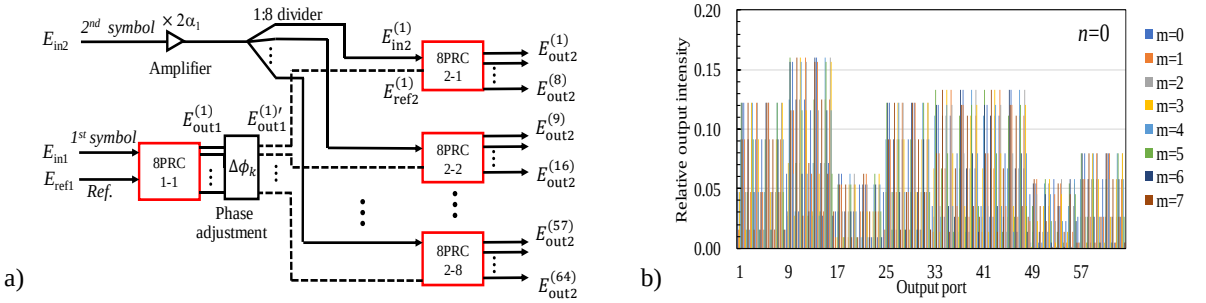


Figure 2. (a)Optical circuit for 2-symbol 8PSK label recognition by Maximum-output detection scheme and (b) Theoretical output intensities for two-symbol 8PSK codes

3 MINIMUM OUTPUT DETECTION SCHEME

Fig.3 shows a two-symbol recognition circuit by the minimum-output detection scheme. The circuit also has a two-stage connection of the 8PRCs. It is noted that the phase adjustment circuit is not employed after 8PSK 1-1 since the null output from 8PSK 1-1 is used for part of the reference signal to the second-stage 8PRCs. From the calculation, for the case n = 0, the maximum output intensity is 0.160. Null outputs are obtained at ports from 17 to 24. The second minimum outputs appear at ports from 49 to 56 and the intensity is 0.000785 (0.49 % of the maximum intensity). The two-symbol 8PSK labels can be recognized by thresholding the outputs between 0.000785 and 0.

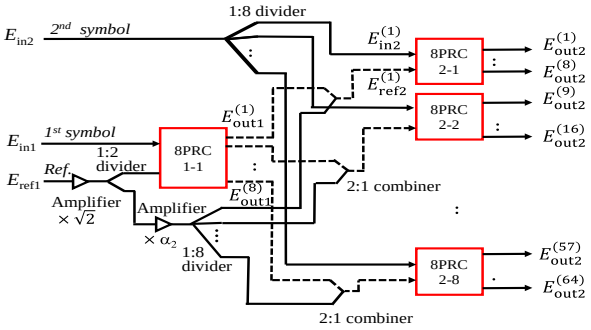


Figure 3. Optical circuit for 2-symbol 8PSK label recognition by Minimum-output detection scheme

4 EVALUTION OF NOISE TOLERANCE

To investigate the noise tolerance for the proposed two-symbol waveguide-type 8PRC, we built a simulation model using OptiSytem software (Optiwave Systems Inc.). The simulation setup for one-symbol label recognition is illustrated in Fig. 4.

A pseudo-random-bit sequence (PRBS) with the length of 214-1 is used for generating a non-return-to-zero (NRZ) sequence at half of the bit rate R0 for 8PSK signals. The sequence signal is connected to a serial-to-parallel (S/P) converter to make a sequence of 3-bit parallel signals. At the same time, a reference signal is generated by a user defined bit sequence generator with the same bit rate as that of the data signal and is connected to another S/P converter. A parallel-to-serial (P/S) converter is used to combine a data signal and a reference signal. The combined sequence is connected to a pulse-amplitude-modulator (PAM) to generate a modulation electric signal. To generate the optical 8PSK coded signal, we use a continuous wave (CW) laser at a frequency of 193.1 THz as a light source, a phase modulator (PM), and an intensity modulator (IM1) to carve the NRZ to the return-to-zero (RZ) pulse train. The component, named as Set OSNR, is used to add noise

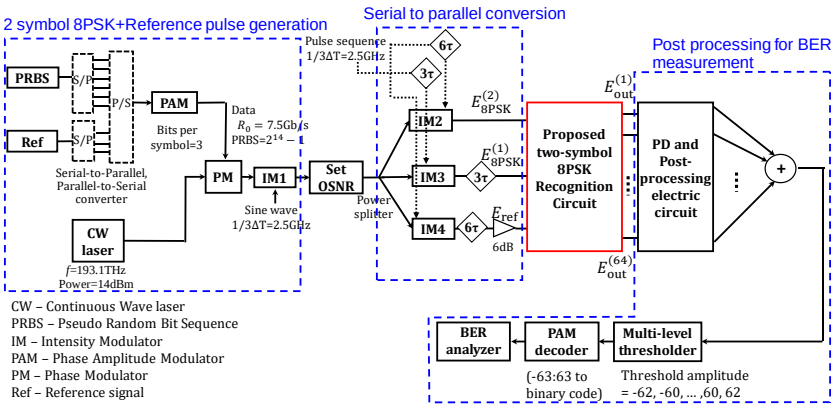


Figure 4. A simulation setup for two-symbol 8PSK recognition circuit.

to the sequential train of the 8PSK pulse and the reference pulse. The noise added signals are sent to a serial to parallel conversion circuit which consists of two intensity modulators and delays elements. The converted parallel 8PSK pulse train and the reference pulse train are incidents to the proposed label recognition circuit.

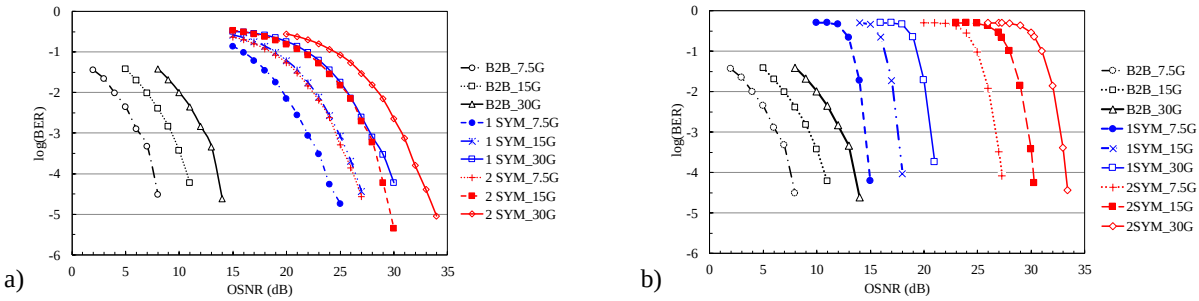


Figure 5. BER performance for one and two-symbol 8PSK labels by (a) maximum output detection scheme, (b) minimum output detection scheme.

The simulated BER performance as a function of OSNR at the receiver is shown in Fig.5. As a comparison, a BER measured by back-to-back (B2B) configuration is plotted by using a digital coherent receiver with adaptive equalization, frequency offset estimation, and carrier phase. recovery. The BER performances at the bit rate R_0 of 7.5, 15 and 30 Gb/s are plotted. For the maximum output detection scheme, the required OSNR, for example, at BER of 1.0×10^{-3} at R_0 = 7.5 Gb/s is around 22 dB and 24.5 dB for 1- symbol and 2-symbol length signals, respectively, is shown in Fig. 4(a). For the minimum output detection scheme, The required OSNR at BER of the same point is around 14.5 dB and 26.8 dB for 1-symbol and 2-symbol length signals, respectively.

5 CONCLUSIONS

We have proposed the optical waveguide-type device for recognition of optical 8PSK coded labels. The proposed device is based on the previously proposed waveguide-type circuit for recognition of QPSK coded labels. The recognition method was theoretically discussed and the noise tolerance was also investigated. The proposed circuit could recognize from either maximum or minimum output port. These two recognition schemes were compared from the viewpoint of noise tolerance. We also discussed the scalability for the proposed recognition circuits. The maximum-output detection scheme was found to be superior to the minimum-output one because the phase adjustment cannot be employed between the first-stage 8PRC and the second-stage 8PRCs for the minimum-output detection circuit.

REFERENCES

[1] I. Glesk, K. I. Kang, and P. R. Prucnal: Ultrafast photonic packet switching with optical control, Optics Express, vol. 1, no. 5, pp. 126-132, 1997.

[2] A.E. Willner, S.Khaleghi, M.R. Chitgarhi, and O. F. Yilmaz: All-Optical signal processing, J. Lightwave Technol., vol. 32. no. 4, pp. 660-680, 2013.

[3] K. Kitayama, N. Wada, and H. Sotobayashi: Architectural considerations for photonic IP router based upon opticalcode correlation, J. Lightwave Technol., vol. 18. no. 18, pp. 1834-1844, 2000.

[4] K. Inoshit, Y. Hama, H. Kishikawa, and N. Goto: "Noise tolerance in optical waveguide circuits for recognition of optical 16 quadrature amplitude modulation codes, Optical Engineering, vol. 55, no. 12, 126105, 2016.

[5] T. Surenkhorol, H. Kishikawa, N.Goto, and K. Gonchigsumlaa: Waveguide-type optical circuits for recognition of optical 8QAM-coded label, Optical Engineering, vol. 56, no. 10, 107101, 2017.

Monolithically Integrated Wavelength-Selective Switch on InP: a Circuit Simulation-Based Design Study

Alessandro Aimone[1], Netsanet Tessema[2], Kristif Prifti[2], Rui Santos[3], Nicola Calabretta[2], André Richter[1]
[1] VPIphotonics, Carnotstraße 6, 10587 Berlin, Germany
[2] Eindhoven University of Technology, De Zaale, 5600 MB Eindhoven, Netherlands
[3] SMART Photonics, High Tech Campus 29, 5656 AE, Eindhoven, Netherlands
e-mail: Alessandro.Aimone@vpiphotonics.com

ABSTRACT

Flexible optical networks have pushed the need for fast and compact switching elements. A wavelength-selective switch consisting of passive arrayed waveguide gratings (AWG)-based multiplexers and demultiplexers and active semiconductor optical amplifier (SOA)-based optical switches is presented and analyzed in detail by means of hybrid time-and-frequency-domain simulations. The performance of the component is investigated and discussed.

Keywords: Wavelength Selective Switch, AWG, SOA, Elastic Networks, Simulations, Photonics.

1. INTRODUCTION:

Next generation metro and inter-datacenter networks are required to achieve highly-efficient bandwidth utilization, enabled by the use of programmable and elastic physical optical network. Flexible and sliceable transponders, controlled by software-defined networking, promise to greatly optimize hardware resource utilization and lower costs and thus constitute the key technology for future networks [1]. All this places new and strict requirements on reconfigurable optical add/drop multiplexers (ROADMs) of which wavelength selective switches (WSS) are a the main building block. Monolithically integrated solutions are particularly attractive as they allow for faster switching, less area, and fewer optical interfaces. Recently, integrated WSS have been demonstrated for large channel spacing (500 GHz) and 4 wavelengths [2,3]. However, in practical systems employing dense wavelength division multiplexing, a WSS with larger number of channels and narrower channel is required. Scaling the number of channels with narrow channel spacing demands accurate design and performance analyses and should take into account the technology platform adopted to fabricate the circuit.

A very-high-speed 1×4 integrated WSS enabling control of 64 12.5-GHz wide frequency slices is the topic of this paper. The WSS operates over 800 GHz in the C-band and is based on the assembly of four 64-λ monolithic wavelength blockers (WBLs). The 64-λ WBL prototype here presented targets a switching time < 20 ns and is designed to be compatible with the Flex-Grid ITU standard. The proposed architecture includes Mach-Zehnder Interferometer (MZI) interleavers, arrayed waveguide gratings, and a set of active semiconductor optical amplifiers and is to be fabricated as a photonic integrated circuit (PIC) in the generic InP platform by SMART Photonics.

2. WAVELENGTH-SELECTIVE SWITCH

The fast InP 1×4 WSS will follow a broadcast-and-select architecture that allows individual control of each 12.5-GHz spectral slice to each of its outputs (Figure 1). The basic principle of operation of the 1×4 WSS involves two stages in a similar fashion as the work reported in [2,3]: in stage-1 the input signal is broadcasted via a 1×4 splitter; in stage-2 four identical WBLs, based on AWG DeMUX/MUX units and SOA switches, are used (Figure 1-a). Within a DeMUX/MUX element, a first set of AWGs is used to de-multiplex the different wavelengths. Current-driven SOAs are used to turn on and off each individual wavelength at the desired output. Finally, an additional set of AWGs and power combiners (PCs) are used to multiplex and combine the several wavelength slices, potentially amplified or filtered, back into a single channel routed to the PIC's output. The switching control is performed via externally applied electrical signals. Employing SOAs as switches has the advantage to provide on-chip amplification that compensates the losses introduced by the two AWGs, routing, and coupling: by tuning the electrical drive, the optical power of each output slice can be precisely adjusted. It also enables the independent control of each spectral slice (channel) with a switching time less than 20 ns.

The straight forward implementation of the 1x4 WSS calls for AWGs with 12.5 GHz channel spacing, which occupies a large wafer space and are practically prohibitive. To counteract this and significantly reduce the device footprint, an interleaver is employed together with AWGs with larger channel spacing: an interleaver with N output ports makes it possible to reach the target specifications by incrementing the number of DeMUX-MUX units to $4 \cdot N$ while decreasing the number of processed wavelengths per WBL to $64/N$ and increasing the required AWG channel spacing to $12.5 \cdot N$ GHz. In the proposed design, a 1:8 interleaver is used to de-interleave the dense 12.5 GHz into a sparser 100 GHz spectral grid. The total number of DeMUX-MUX elements increases to 32,

whereas the number of wavelengths within each elements decreases to 8. Finally, AWGs with a channel spacing of 100 GHz, expected to lead to a much larger yield, are used. Each of the DeMUX-MUX units within one WBL prototype is designed with a center frequency shifted of 12.5 GHz with respect to the previous one.

The 1:8 interleaver outputs' FSR are to match the channel spacing of the WBL, namely 100 GHz. The proposed design achieves this by implementing a three-stage cascaded imbalanced MZIs architecture (Figure 1-b). The first, second, and third stage are designed to have a channel spacing of 12.5 GHz, 25 GHz, and 50 GHz, respectively. In order to develop a flat top characteristic response, the first and second stages of the interleaver make use of 3 and 2 MZI units, respectively. Fine control of the power coupling ratio and the phase values are essential to maintain the functionality of the interleaver and can be obtained via the implementation of externally controlled phase shifters [4], not included in the prototype.

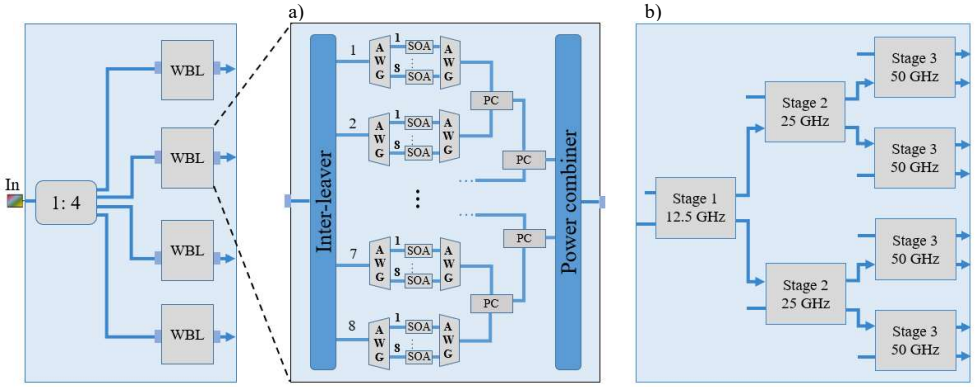


Figure 1: Architecture of the 1×4 fast WSS and detail of (a) one of the four 64-λ WBL prototypes and (b) the 1:8 interleaver

3. SIMULATION SETUP AND RESULTS

The 64-λ WBL prototype includes 11 MZIs within the interleaver and 16 AWGs plus 64 SOAs for the DeMUX-MUX stages. The large number of monolithically integrated components makes it hard to perform fast and reliable evaluation via simulation of the complete WSS. In addition, the coexistence of several passive and active photonic elements, namely the AWGs and the SOAs, poses a further challenge. Whereas the former are best described in terms of their time-invariant frequency response, the latter require the simulation to be performed sample-by-sample in time domain to properly account for their non-linear dynamics. The modeling of passive components in time domain is performed by constructing digital finite-impulse-response (FIR) filter equivalents. This constitutes a critical task: the unavoidable limited accuracy of each FIR representation quickly worsen their impact due to multiplicative effects and the large number of components in the design [5]. To overcome this issue and accurately model the device, the WBL prototype is investigated using VPIcomponentMaker Photonic Circuits using the hybrid time-and-frequency-domain approach [6].

The simulation model carefully mirrors the design architecture. Because of the large number of repeated identical sub-units, i.e. the several SOAs on a deeper level and the DeMUX/MUXes above, a hierarchical setup allows for the model to be built with just few building blocks. The DeMUX/MUX cell has a single input and output and contains a 1x8 AWG, 8 SOAs with associated quasi-DC drive, and a 8x1 AWG (Figure 2). The two AWGs are identical, but mirrored, and are assumed lossless for the early investigations. The SOAs are modeled with a sophisticated optical traveling-wave approach and include carrier dynamics and noise. The gain curves of the SMART Photonics InP SOA component are implemented: at 1550 nm net gain equal to 60 cm^{-1} is achieved for a pump current density equal to 9 kA/cm^2, whereas absorption of 230 cm^{-1} is obtained when no current is driven [7].

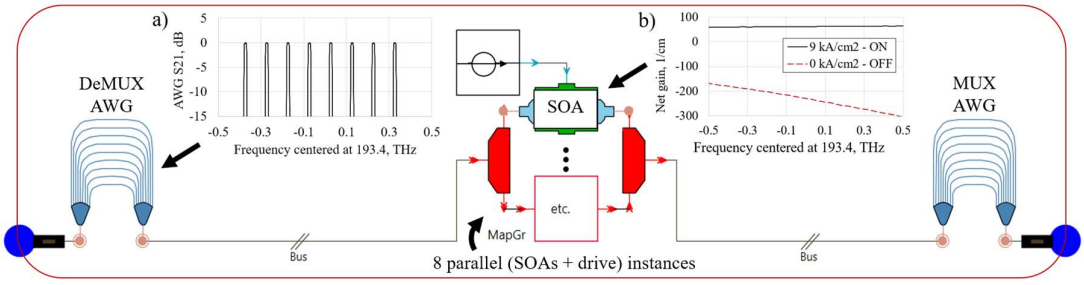


Figure 2: MUX-DEMUX unit setup including a current-driven SOA per AWG channel with detail of (a) the AWG transfer function and (b) the gain of the SOAs in the 'on' and 'off' state.

The WBL unit is simulated by instancing 8 parallel DeMUX-MUX cells, by routing each of the interleaver outputs to a different cell, and by recombining their output power into a single channel (Figure 3). The SOAs are 1.5 mm long and are driven with a pump current density of 9 kA/cm^2 for the 'on'-channels and with no current for the 'off'-channels. The steady-state frequency response of the WBL prototype is simulated for different drive configurations showing the switching capability of the unit (Figure 4). The slightly slanted transfer function is to be attributed to the SOA gain, which is increasing for higher frequencies, and can be adjusted by simply fine tuning the several pump currents. Additionally, notches are observed in the recombined output spectrum between the different slices. These are due to small misalignments between the interleaver's and DeMUX-MUX's slices and can be avoided by increasing the bandwidth of one of the two components.

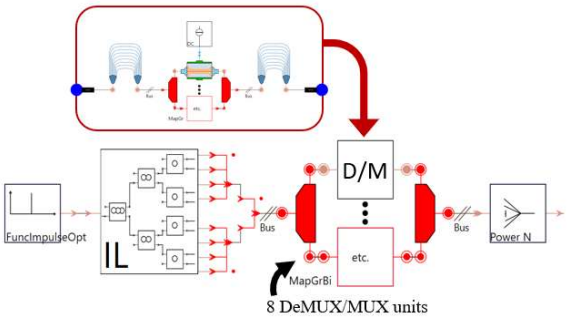


Figure 3: 64-λ WBL simulation setup including a 1:8 interleaver (IL) and 8 parallel DeMUX/MUX (D/M) units

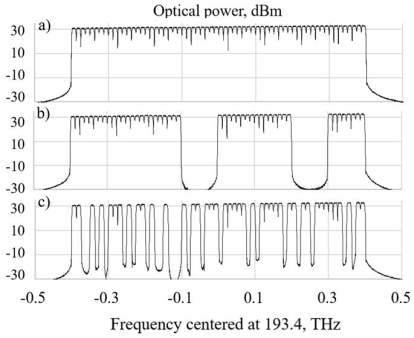


Figure 4: Steady-state transfer characteristic of the WBL (a) at max gain, (b) with 4th and 7th SOA-channels switched off, and (c) with arbitrary slicing drive.

As further test, a raised-cosine binary signal with 0.05 roll-off is fed to the interleaver input by replacing the impulse source with an optical transmitter. In order to test the WSS dynamic operation, a 10 GBd signal fitting into a single 12.5 GHz slice is launched into the structure. The immediately adjacent channels are switched on and off to investigate their impact, while all other channels are kept off. The active channels are driven with 1.5 kA/cm^2 pump current density. It is observed how the output signal spectrum is affected in the two cases and that the signal suffers only from little distortion passing through the WBL. As expected, due to the fact that the launched signal is fully contained into the single central slide, the adjacent channels show negligible impact (*Figure 5*).

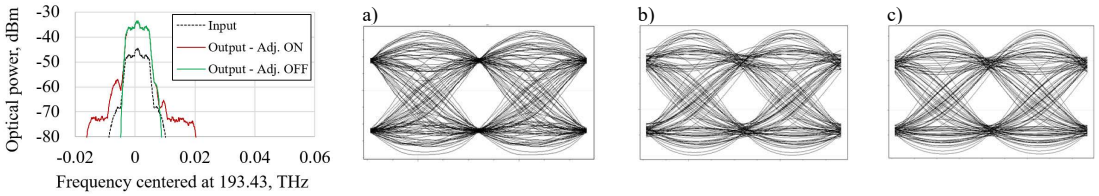


Figure 5: Signal spectra of the WBL 10 GBd input and output signals with eye diagram detail of a) the input signal, b) the output signal with adjacent slices on, and c) the output signal with adjacent slices off.

4. CONCLUSION

A monolithic WSS consisting of 4 identical WBL units has been presented. Each 64-λ WBL includes 11 MZIs, 16 AWGs, and 64 SOAs and has been investigated via hybrid time-and-frequency-domain simulations. The switching capability and impact of the selected component implementation is verified via the steady-state impulse response and large signal operation.

ACKNOWLEDGEMENTS

This work was supported through the EU-funded H2020 project ICT-QAMeleon (780354).

REFERENCES

[1] O. Rival, A. Morea, "Cost-efficiency of Mixed 10-40-100Gb/s…," *OFC and NFOEC*, Los Angeles, 2011.
[2] N. Calabretta, "Photonic integrated WDM Cross-connects for Disaggregated…," *ACP*, 2017, paper S4J.1.
[3] N. Calabretta, *et al.*, "System Performance Assessment of a Monolithically…," *ECOC*, 2016, Paper W.2.F.3.
[4] F. Horst, *et al.*, "Cascaded Mach-Zehnder wavelength…," *Opt. Express 21*, 2013, pp. 11652-11658.
[5] S. Mingaleev, *et al.*, "Towards an Automated Design Framework for Large-scale Photonic…," *SPIE*, 2015
[6] S. Mingaleev, *et al.*, "Hybrid Time-and-Frequency-Domain approach…," *NUSOD*, Rome, 2011.
[7] D. Pustakhod, *et al.*, "Method for polarization-resolved measurement of…," *IEEE PJ*, 2018.

Theoretical and Experimental Study of Distributed Bragg Reflector Lasers on SMART Photonics Platform

(Student Paper)

Pengli An*, Andreas Hänsel, Martijn J. R. Heck
Aarhus University, Department of Engineering, Finlandsgade 22, 8200 Aarhus, Denmark
*e-mail: pengli_an@eng.au.dk

ABSTRACT

Photonic integrated circuits (PICs) provide the most promising way for tunable semiconductor lasers in reducing their size, weight, power consumption and cost. In this paper, theoretical and experimental research has dedicated on three-electrode Distributed Bragg reflector (DBR) lasers on indium phosphide (InP) PICs. Theory shows that the wavelength tuning could be realized by varying current injections to both DBR grating sections and SOA section. Experiment shows that DBR laser with 750-μm cavity length can be continuously tuned over 1.4 nm with side mode suppression ratio (SMSR) above 40 dB. Moreover, the linewidth of the laser is 4 MHz with 3 mW output power. Since these DBR lasers have been realized in a mature PIC platform following the design rules, which means that they are now available as building blocks in larger-scale PICs.

Keywords: Distributed Bragg reflector lasers, tunable lasers, semiconductor laser, single-mode laser, photonic integrated circuits.

1. INTRODUCTION

Tunable semiconductor lasers attract much interest over the last few decades, due to their extensive applications from fundamental science to 'real world' applications, in which fiber optic telecommunication systems , broadband gas sensors and Terahertz emitters have a large demand for them [1]. Photonic integrated circuit (PIC) commercial fabrication platforms have a fast development over the last ten years, which provides an efficient and reliable solution to design and fabricate tunable semiconductor lasers in terms of reducing their size, weight, power consumption and cost. Among all tunable lasers, DBR lasers are single mode lasers with narrow linewidth and modest wavelength tunablity. Their characteristics make them ideal for telecommunication, gas sensor and terahertz generation use, which require a high side mode suppression ratio (SMSR) and a good stability. SMART photonics has released its DBR grating building block in last two years, which gives us the possibility to design the lasers and examine their performances in lab. Since the strongest absorption lines are at 1512, 1514, 1522, 1527, and 1531 nm for ammonia sensing, we have designed a series of DBR lasers aiming at these wavelengths. In this paper, we will focus on one DBR laser with two DBR gratings of equal length on our PICs as an example to show our simulation and experimental results.

2. DESIGN AND SIMULATION

The DBR lasers on our PICs contain three electrodes connecting with the gain section (SOA) and the two DBR grating sections separately. The two gratings work as reflective mirrors to direct back and forth the light generated in the cavity, to form a standing wave. In addition, the laser performance could be controlled by injecting currents through the three electrodes. In order to estimate the threshold current of the lasers, we need to know both the power reflection of the DBR gratings and the gain characteristic of the SOA. In this paper, we focus on the DBR laser with two DBR gratings of equal length 200 μm (Bragg wavelength at 1531 nm), and SOA of length 250 μm, while there are two electrical isolation sections to separate the gratings and SOA.

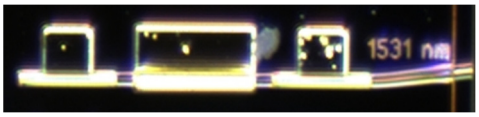


Figure 1. Microscope picture of DBR laser in this paper on PIC

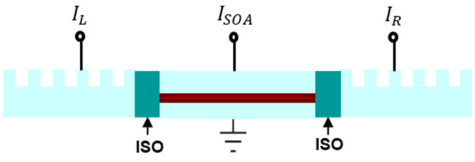


Figure 2. schematic structure of DBR laser (ISO:isolation section)

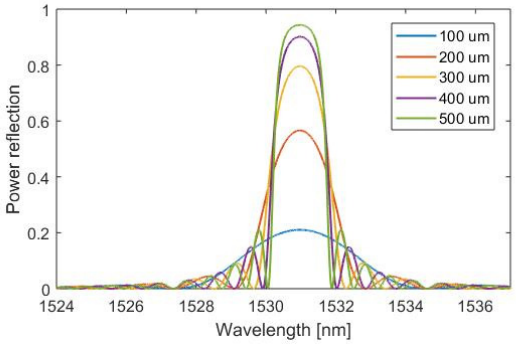


Figure 3. Simulated power reflection of gratings with different lengths

We acknowledge support from Danmarks Frie Forskningsfond through the FTP Project 2 grant "Compact Integrated Terahertz Sources", and from the Danish Innovation Fund through the ECOMETA project.

Fig. 1 demonstrates the microscope picture of the DBR laser on PIC, and Fig. 2 shows the schematic structure corresponding to this laser. The chip will be grounded from its bottom side on our lab setup.

The power reflection of the DBR gratings depends on several parameters, among which include the pitch and length of gratings that we can choose in our design. Moreover, the reflectivity of the gratings could be calculated from the equations shown in [2], and the results are shown in Fig. 3. A 200 μm long grating with Bragg wavelength at 1531 nm reflects around 57% of the light. The relevant parameters are summarized in Table 1.

The threshold current of a laser is defined as the injecting current on the SOA section, when the gain in the laser cavity equals to its cavity loss. Combining the gain curves from the design manual [3], we could estimate the threshold current for the laser in this paper is around 10 mA.

From theory, we know the refractive index of the Bragg gratings will decrease when increasing the current injection to them, due to the free-carrier plasma and band-filling effects. As a result, the wavelength tuning takes place as the Bragg reflection shifts towards shorter wavelength. According to previous research in [4], the carrier concentration in the grating section is normally within the range from $10^{18}/cm^3$ to $10^{19}/cm^3$, which corresponds to maximum around 25 mA current injection to the 200 μm long grating. The simulation result is shown in Fig. 4, which indicates the Bragg wavelength of the grating could be tuned over 10 nm if the thermal effects are not considered.

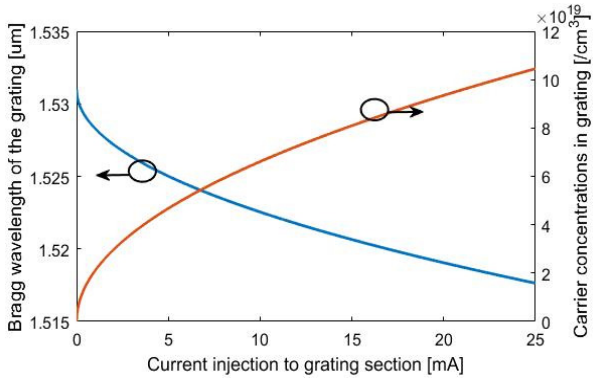


Figure 4. Wavelength tuning by current injection

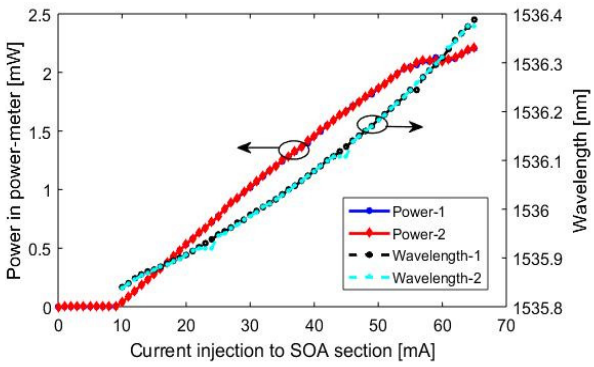


Figure 5. L-I characteristic and wavelength tuning by SOA section

TABLE 1. DESIGN AND SIMULATION PARAMETERS.

Parameter	Symbol	Value	Unit	Parameter	Symbol	Value	Unit
transverse confinement factor[a]	Γ_{xy}	4	%	length of the grating	L	200	μm
coupling coefficient[b]	$\varkappa$	50	cm^{-1}	pitch of the grating	Λ	0.2344	μm
insertion loss[b]	α	2	dB/cm	height of core layer[b]	h	500	nm
electric charge of electron	q	1.602e-19	C	Bragg wavelength	λ_B	1531	nm
current injection efficiency[a]	η_i	70-80	%	width of the grating[b]	w	2	μm
recombination in Q-material[a]	B	0.5e-10	cm^3/s	effective index[b]	n_{eff}	3.266	–

[a]Value taken from [5]
[b]Value taken from [3]

3. EXPERIMENT RESULTS

In this section, we measured the performance of three-section DBR lasers, which included threshold current value, L-I characteristic, wavelength tunability and linewidth. All the measurements performed at 15 °C. Output power and lasing wavelength were measured by Agilent power sensor module (81633A) and Yenista OSA20 respectively.

The L-I characteristic measured from the three-section DBR laser is shown in Figure 4. We obtained the threshold current of 8 mA and the maximum output power in power meter of 2.2 mW at an injection current at 65 mA. Since the output power measured by coupling the light from DBR laser on chip to a lensed fiber, and a 90/10 fiber splitter was used to give 90% output power to power-meter, the estimated coupling loss is 3-5 dB. Therefore, the maximum output power generated from the laser is around 8 mW. From this figure, we could see that the output power of the laser starts to increase slower and become unstable with higher current injection.

There is a wavelength tuning due to current injection above threshold to SOA section, measurement results have been plotted in Fig. 5. It shows that the lasing wavelength of the laser moves towards longer wavelength when increasing the injecting current above the threshold. There observes a 0.55 nm wavelength tuning with current injection in from 10 to 65 mA range. According to theory, the carrier density and the gain of SOA section will clamp at their threshold value with injecting current increasing above the threshold current. Moreover, with higher injecting current, the thermal effects start to affect the laser performance, which result in lasing wavelength

moving towards longer wavelengths. Previous research in [6] shows that the lasing wavelength of the laser will increase by 0.1 nm, with every degree temperature increase in active region of the laser.

We found that the wavelength tuning at a specific injecting current to SOA section could be realized by varying the current injections to both DBR gratings, and the tuning range is the same comparing sweeping the current injection to each DBR grating separately and giving equal current injection to both gratings. Therefore, we measured the wavelength tunability of this DBR laser by sweeping the same current injection to both gratings at different current injection to SOA section. The measurement result shows that this simple DBR laser has a good single mode performance, and it has a 1.4 nm continuous wavelength tuning range with SMSR above 40 dB. The results are plotted in Fig. 6.

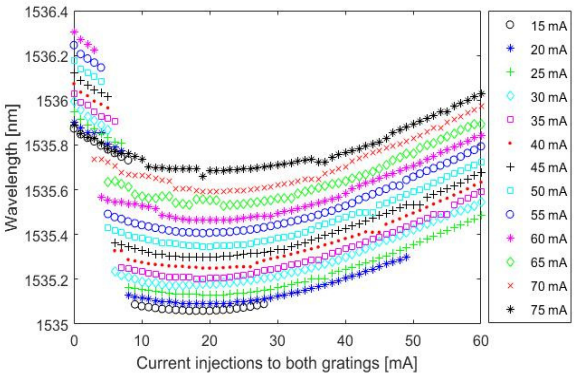


Figure 6. Wavelength tuning with SMSR above 40 dB

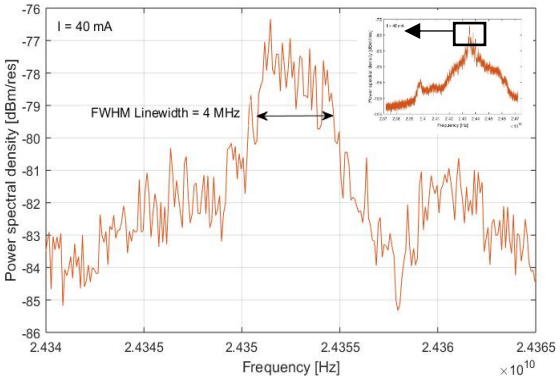


Figure 7. Linewidth measurement result

As shown in Fig. 6, at a specific current injection to SOA section (value shows in legend), the positions of the lasing peaks in the optical spectra move towards shorter wavelengths firstly when increasing the injecting current to both DBR gratings, and then move back to longer wavelengths when the current is above 20 mA to each grating. There should be several reasons resulting in this phenomenon. Firstly, the carrier density in the core layer of the waveguide is saturated when increasing the injecting current, which due to the radiative and Auger recombination. Secondly, the temperature will raise up with higher injecting current, and the thermal effects will take over to tune the wavelength back to longer wavelengths.

The linewidth measurement was done by using heterodyne technique that combining the DBR laser output optical signal with a commercial tunable laser, which has a relatively smaller linewidth of 100 kHz (Agilent 81940A). The frequency difference between these two lasers should stay within both the detecting range of external photodetector (New Focus 1024) and the electrical spectral analyzer (R&S FSV30). The measurement result is shown in Fig. 7, which illustrate that the linewidth of the DBR laser is about 4 MHz with 40 mA current injection to SOA section.

4. CONCLUSIONS

The performance of the DBR laser on SMART Photonics platform has been theoretically and experimentally investigated in this paper. The experimental results mostly meet the expected performance of the lasers. For the three-section DBR laser with 750-µm cavity length, we have observed the maximum output power of 8 mW, continuous wavelength tuning of 1.4 nm with above 40 dB SMSR, and a linewidth of 4 MHz with 3 mW output power. The measurement results show that the DBR lasers on PICs have a good single mode performance and stability, even though there is some limitation of the output power and wavelength tunability. However, the research in this paper shows that we now have building blocks to design tunable lasers for applications such as gas sensing, THz emitters, etc.

REFERENCES

[1] Coldren, Larry A., et al. Tunable semiconductor lasers: A tutorial. Journal of Lightwave Technology, 2004, 22.1: 193.

[2] Kokubun, Yasuo., et al. Encyclopedic handbook of integrated optics. CRC Press, 2005.

[3] Photonic IC design manual. SMART Photonics, 2017.

[4] Bennett, Brian R., et al. Carrier-induced change in refractive index of InP, GaAs and InGaAsP. IEEE Journal of Quantum Electronics, 1990, 26.1: 113-122.

[5] Coldren, Larry A., Scott W. Corzine, and Milan L. Mashanovitch. Diode lasers and photonic integrated circuits. Vol. 218. John Wiley & Sons, 2012.

[6] Sysak, Matthew N., et al. Hybrid silicon laser technology: A thermal perspective. IEEE Journal of Selected Topics in Quantum Electronics 17.6 (2011): 1490-1498.

Germanium Photodetector with Monolithically Integrated Narrowband Matching Network on a Silicon Photonics Platform

Laurens Bogaert[1,2,*], Jochem Verbist[1,2], Kasper Van Gasse[1], Guy Torfs[2], Johan Bauwelinck[2], and Gunther Roelkens[1]

[1] Photonics Research Group, Dept. INTEC, Ghent University–Imec, Technologiepark 126, 9052 Ghent, Belgium

[2] IDLab, Dept. INTEC, Ghent University–Imec, Technologiepark 126, 9052 Ghent, Belgium

**e-mail: Laurens.Bogaert@ugent.be*

ABSTRACT

High data rate transceivers typically consist of a system with hybrid integration of the electronics and photonics. Impedance levels provided by the opto-electronic device are often not the same as the levels desired by the electronic circuit. This mismatch introduces suboptimal operation and can even be detrimental for the overall system performance. Consequently, a matching circuit is often implemented on the electronic IC together with the main electronic functionality. Direct RF matching of the opto-electronic devices on the photonic IC has the potential to significantly reduce the overall system cost as the area cost of photonic chips is much lower. In this paper, narrowband LC-matching is shown for a germanium photodetector on the iSiPP50G silicon photonics platform to convert the output impedance to a more standard 50 Ω impedance level at 30 GHz. By tuning the photodetector reverse biasing voltage between 0 Volt and 3 Volt, a reflection coefficient lower than -20 dB is obtained over the frequency range between 24.3 and 30.4 GHz.

Keywords: Capacitors, Inductors, Narrowband matching, Photodetector, Radio-over-Fiber, Silicon photonics

1. INTRODUCTION

High data rate transceivers often make use of a complex architecture including photonics as well as electronics and typically hybrid integration is implemented where the electronic chip (EIC) and photonic chip (PIC) are manufactured separately. Opto-electronic conversion is required in the PIC to convert the data from the optical to the electrical domain and vice versa. This opto-electronic device (photodetector, electro-absorption modulator, etc.) serves as an interface to the EIC but typically has an impedance mismatch compared to the input or output impedance of the EIC. This can result in strong reflections, potential instabilities, etc. Consequently, a matching network is designed and this is typically done together with the main electronic system on the EIC. This is however suboptimal as the EIC, especially for the more advanced technology nodes, is substantially more expensive compared to the PIC [1]. The iSiPP50G silicon photonics platform includes two metal layers and consequently enables monolithic integration of RF passives on the PIC [1]-[2]. In this paper, we will focus on the narrowband matching of a Ge-on-Si photodetector but firstly the relevant active devices (Ge photodetector) and passive devices (inductors and capacitors) will be discussed.

2. GERMANIUM PHOTODETECTOR

In this paper, narrowband matching of a Ge photodetector on the iSiPP50G silicon photonics platform will be discussed. For narrowband applications, a simplified model can be used (Fig. 1, [2]). This model consists of a current source in combination with an RC filter where the junction capacitance C_j varies with the applied reverse voltage and where the series resistance R_s is nearly voltage independent. The matching network was designed using the nominal values at 2 Volt reverse biasing of the adopted Ge photodetector: $R_s \approx 35\ \Omega$ and $C_j \approx 35$ fF.

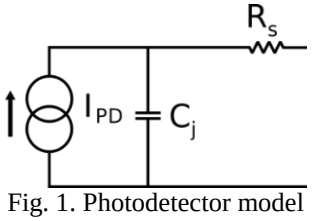


Fig. 1. Photodetector model

3. RF PASSIVES

Passive RF components are bulky and it is therefore advantageous to move them to the PIC where the cost per surface area is substantially lower. In this work, the commercial silicon photonics platform iSiPP50G from imec is being used to demonstrate a monolithically integrated matching network. The stack of this technology platform includes two metal layers and therefore allows for the introduction of RF passives on the PIC.

3.1 Capacitors

The back end of line of the iSiPP50G silicon photonics platform includes two metal layers (Cu) separated by an oxide (SiO_2). Consequently, parallel plate MIM (metal-insulator-metal) capacitors are readily available in iSiPP50G. The capacitance value [3] can be approximated by using equation (1) where ϵ_0, ϵ_r and t are fixed (respectively the permittivity of vacuum, the relative permittivity and the thickness of the oxide) and where the parallel plate overlap area A can be adjusted to size the capacitance. The second term in the approximation is a correction term to roughly include the fringe effects (with P the perimeter of the parallel plates). For the given technology platform, the formula approximates 69 aF x A [μm^2] + 34 aF x P [μm]. Measured values are approximately 10 to 15 percent lower than what is expected from this approximation. This can be attributed to an overestimation of the relative permittivity of the SiO_2 or an underestimation of the oxide thickness.

$$C = \frac{\epsilon_0 \epsilon_r A}{t} + \epsilon_0 \epsilon_r P \tag{1}$$

Secondly, the capacitors are to be used in high-speed systems. Consequently, the self-resonant frequency (SRF) should be sufficiently high. This is done by placing the parallel plate capacitor in between the bondpads to minimize the lead length and therefore maximize the SRF.

3.2 Inductors

A second important building block in lossless matching networks are spiral inductors [3]. The presence of a second metal layer allows for multi-turn spiral inductors largely extending the range of feasible inductances. The design parameters for such spiral inductors are the trace width, the spacing between turns, the radius of the inner turn and the number of turns. Minimizing the number of turns is desirable for high-speed applications to minimize the inter-winding capacitance and consequently maximize the SRF. Secondly, it is beneficial to implement the inductors on the top metal layer to minimize capacitive coupling to the substrate. The bottom metal layer is only being used to avoid crossings in multi-turn inductors. Inductors are quite predictable as they are defined by their geometry rather than the technology stack. The inductor is modelled by a series inductor-resistor combination where the losses are typically described using a Q-factor. The Q-factor represents the ratio of the imaginary and real part of the inductor impedance and is frequency dependent.

4. NARROWBAND RF MATCHING

In this section, the results of a narrowband matched germanium photodiode will be discussed. The target impedance in this design is a standard 50 Ω impedance at 30 GHz. A first order LC matching network is adopted in a low pass configuration to allow for external biasing of the photodetector.

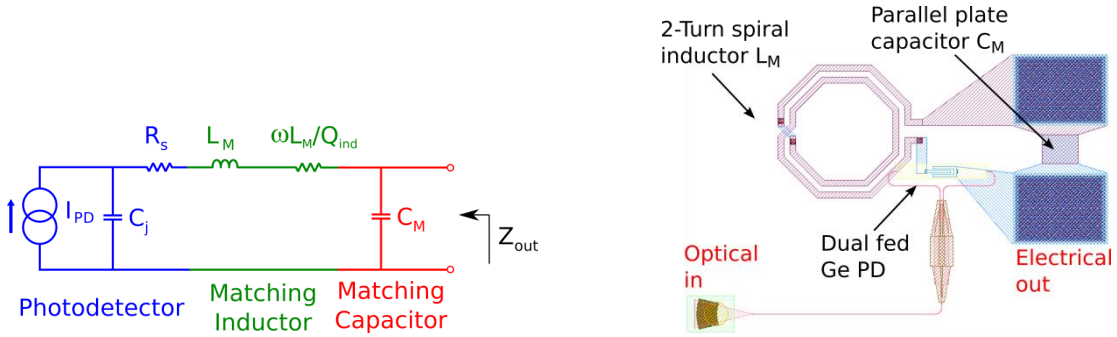


Fig. 2. LC matched photodetector; (left) equivalent network; (right) layout of the implemented design

Figure 2 depicts the implemented matching network where the finite losses of the inductor are included in the model and ω denotes the angular frequency. The impedance seen at the output of the PIC is given in equation (2). This equation is solved for a given target impedance (e.g. 50 Ω) at a certain frequency (e.g. 30 GHz) to find the desired inductance and capacitance values. Because of the a priori unknown Q-factor, this design process is iterative. The design starts from a photodetector with a junction capacitance of 35 fF and a series resistance of about 35 Ω. The designed matching network consists of a two turn spiral inductor (simulated inductance and Q-factor of respectively 730 pH and 17 at 30 GHz), lead inductances caused by the traces (around 170 pH) and a parallel plate capacitor (55 fF). Measuring the standalone variants of the implemented passives show that the

inductance value of the spiral inductor (718 pH) and the capacitance of the parallel plate capacitor (53 fF) closely match the simulated values.

$$Z_{out} = \frac{1}{j\omega C_M} \| \left[\left(j\omega L_M + \frac{\omega L_M}{Q_{ind}} \right) + R_s + \frac{1}{j\omega C_j} \right] \tag{2}$$

The performance of the matching network can be evaluated by looking at the output impedance or equivalently the output reflection coefficient S_{11} (which is shown in Fig 3). It can be seen that by changing the reverse biasing of the photodetector the frequency of optimal matching can be tuned over a wide range and that higher reverse voltages result in matching at higher frequencies due to the reduction in junction capacitance C_j of the photodetector. The junction capacitance for the measured wafer was higher than the nominal values used for the design of the matching network and therefore results in a shift of the matching frequency to somewhat lower values. This can be partially compensated for by increasing the reverse voltage. For future designs, the matching network should be designed for the capacitance value at a lower reverse voltage (e.g. 1 V) such that correction capabilities for process variations are maximized. By tuning the photodetector reverse biasing voltage between 0 and 3 Volt, a reflection coefficient lower than -20 dB is obtained over the frequency range between 24.3 and 30.4 GHz. Simulations and measurements show similar results and the discrepancies can be explained by process tolerances and the fact that a simple photodetector model was used (Fig. 1) which does not include low frequency effects.

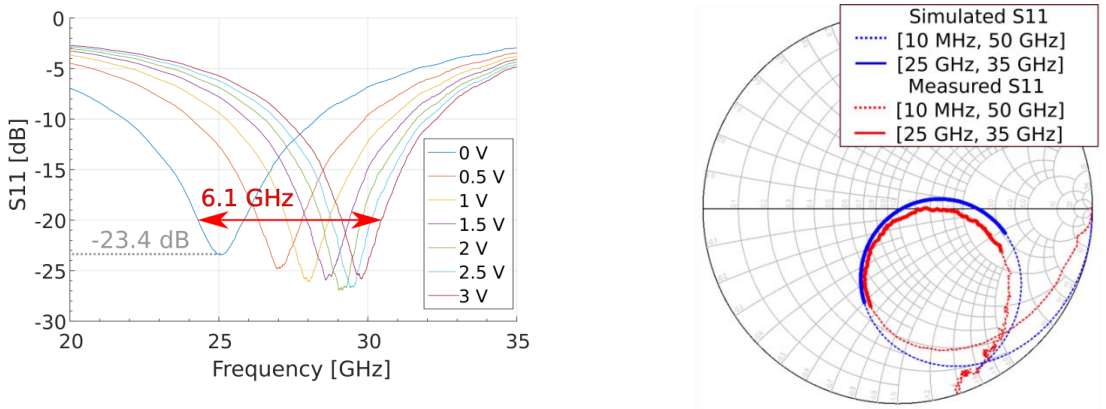


Fig. 3. (left) Reflection coefficient at the output of the LC matched Ge photodetector as a function of the reverse bias; (right) Comparison between the measured S11 at 3V and the simulated S11 using nominal values

5. CONCLUSIONS

Providing matched impedance levels at the interface between electronic and photonic ICs is typically taken care of at the electronic side. A more cost-effective way to implement this is by adding the RF passives on the silicon photonics IC. Here we demonstrate a first order low pass LC matching network monolithically co-integrated with a germanium photodetector on the iSiPP50G silicon photonics platform. Reflection coefficients lower than -20 dB are obtained between 24.3 and 30.4 GHz by tuning the biasing level of the photodetector between 0 and 3 volt. The capabilities of on-PIC RF passive circuit design are not limited to matching circuits (e.g. embedded bias tees) and can help to implement some of the basic RF functionality in a more cost-effective way.

ACKNOWLEDGEMENTS

This work was supported by the Ghent University Special Research Fund (BOF14/GOA/034), the Methusalem funding of the Flemish government, the Air Force Office of Scientific Research (AFOSR) (FA95501810015), and by the European Research Council under Grant 695495 (ATTO).

REFERENCES

[1] M.S. Nezami, *et al.*: Integrated RF Passive Low-Pass Filters in Silicon Photonics, *IEEE Photon. Technol. Lett.*, vol. 30. pp. 2052-2055, Dec. 2018.

[2] A. Novack, *et al.*: Germanium photodetector with 60 GHz bandwidth using inductive gain peaking, *Opt. Express*, vol. 21. pp. 28387-28393, 2013.

[3] T. H. Lee: The Design of CMOS Radio-Frequency Integrated Circuits, *Cambridge University Press*, 2nd Edition

Flexible Integrated Silicon Photonic mm-Wave Frequency Upconversion Using GeSi EAMs

Laurens Breyne[1], Jochem Verbist[1,2], Jing Zhang[1], Piet Demeester[1], Gunther Roelkens[1], Guy Torfs[1]
[1]Ghent University-imec, Technologiepark 126, 9052 Ghent – Belgium
[2]Now with BiFast, Belgium
e-mail: Laurens.Breyne@ugent.be

ABSTRACT

With Radio-Over-Fiber becoming an established technology for the next generation mobile communication networks, interest in integrated microwave photonic circuits is rapidly increasing. Especially photonic frequency converters receive quite some attention as they offer a very large bandwidth and high isolation. In this work, a flexible, integrated silicon photonic upconverter employing GeSi EAMs is demonstrated. The circuit performs frequency upconversion of IF as well as IQ baseband signals to an RF carrier. OSSB signals can be generated when IF upconversion is performed. We demonstrate IF upconversion from 3.5 GHz to 24-28 GHz of 87.5 Mbaud to 200 Mbaud 16QAM and 50 Mbaud 64QAM. EVMs are within the requirements of the 3GPP standard [1].

Keywords: Photonic Upconversion, Microwave Photonics, Radio-over-Fiber, Silicon Photonics

1. INTRODUCTION

It has become clear that Radio-over-Fiber (RoF) will be an enabling technology for next generation mobile communication networks, e.g. 5G. While RoF is transitioning to an established technology, interest in integrated microwave photonics is rapidly increasing. Especially the photonic frequency up- and down-conversion is receiving quite some attention. Photonic mixers offer operation over a large frequency range, high isolation and immunity to electromagnetic interference. Several well-performing mixers already exist [2,3]. Furthermore, integrated photonic mixers can offer a very small form factor by avoiding large discrete components. Integration has been shown on various platforms [2,4,5]. Of the different technology platforms, silicon photonics (Si-Ph) is very attractive, as it offers low-cost fabrication, high scalability and dense integration. Low-loss waveguides, splitters, couplers, thermo-optic and PN-junction based phase shifters are easily integrated on Si-Ph Photonic Integrated Circuits (PICs). Next to the promising heterogeneous integration with III-V materials, the Si-Ph platform used for this work offers wafer-scale fabrication of SiGe Electro-Absorption Modulators (EAMs) and photodiodes [5].

In this paper, we demonstrate frequency upconversion from a 3.5 GHz IF signal to a 24-28 GHz carrier using GeSi EAMs. Analog transmission of 87.5-200 Mbaud 16QAM signals and 50 Mbaud 64QAM is shown with EVMs below 12.5% and 8% for 16QAM and 64QAM respectively. This is line with the 3GPP requirement [1]. The proposed structure allows not only for IF upconversion, but can also upconvert in-phase and quadrature baseband signals directly to RF. With some additional modifications, phaseshifters can be added to allow using the mixer in an optical beamforming network.

2. DESIGN AND IMPLEMENTATION OF THE PHOTONIC INTEGRATED CIRCUIT

The schematic of the PIC is shown in Fig. 1 (a). As input to the circuit, two laser lines are used. These can be derived from a mode-locked laser or can be generated by an MZM biased on its minimum transmission point. As such, the relative phase noise of the two laser lines can be controlled, which is crucial for RF operation. The circuit consists of two ring resonators and a more complex EAM-based modulator. The resonance wavelength λ_{res} of Ring 1 is tuned such that it coincides with λ_{res} of Ring 2. Furthermore, λ_{res} is set to coincide with one of the incident laser lines. The result will be that in Ring 1, one laser line passes through while the other line is dropped. The dropped line will be modulated by the EAM modulator structure. In Ring 2, the unmodulated and modulated laser line are combined. The combined signal can now beat on a photodiode to perform the actual frequency upconversion.

The modulating structure itself consist of two large parts: an MZM with a phase shifter and EAM in each arm, and a cascade of a phase shifter and a single EAM. The thermo-optic phase shifters (PSes) are only used for fixed phase shifts. By using a tunable power splitter, the to-be-modulated laser line can be sent through the EAM-MZM or the single EAM. When the laser line is sent through the single EAM, only amplitude modulation is possible. An IF signal should be supplied for upconversion to the desired RF frequency. If the laser line is sent through the EAM-MZM structure, several modulation schemes are possible:

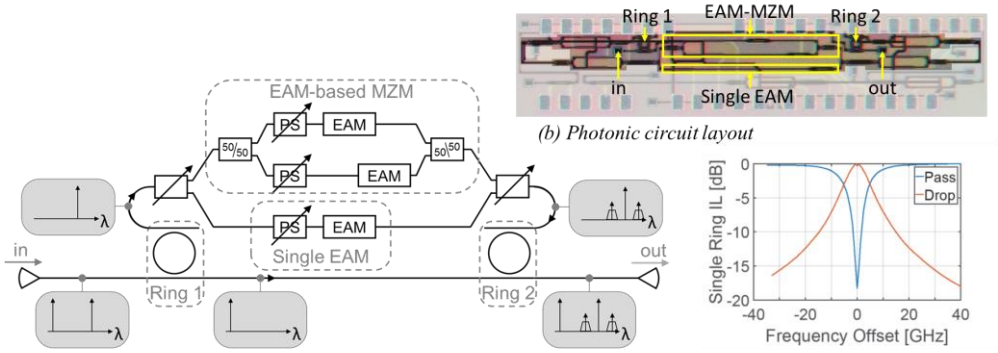
- The PSes are both set to 0°, the same signal is applied to the EAMs: this is the same as the single EAM structure.

- The top PS is set to 0° and the bottom one is set to 90°. The same IF signal is supplied to each EAM, but for the bottom EAM, a 90° phase shift (externally generated) with respect to the electrical IF carrier is added. This allows for optical single sideband (OSSB) modulation of the laser line.
- The top PS is set to 0° and the bottom one is set to 90°. Coherent modulation of the laser line is now possible. This allows to upconvert an in-phase and quadrature baseband signal directly to the desired RF-carrier by sending the in-phase and quadrature signals each to one EAM.

Other configurations are also possible, but not covered in this manuscript. For all described cases, the tunable power splitter was used in a binary mode: i.e all power was sent to the upper arm (EAM-based MZM) or lower arm (single EAM). Intermediate power splitting ratios are also possible to allow more flexibility, e.g. IQ and IF modulation or suppression of incident laser line. The annotated layout of the PIC is shown in Fig. 1 (b).

The measured transfer function of the pass and drop port of the rings is shown in Fig. 1 (c). A single ring has a free spectral range (FSR) of 4.1 nm, the full-width-half-max (FWHM) is 10.2 GHz, the extinction of the pass port and drop port is 19 dB and 29 dB respectively. The second ring limits the bandwidth of the IF or IQ-signal to its FWHM (10.2 GHz). Heaters are used to tune the resonance wavelength of the rings. If the resonance wavelengths of both rings are not perfectly aligned, the insertion loss will increase. It should be noted that there will be some leakage of the unmodulated laser line into the path for the modulated laser line. However, due to the cascade of the 2 rings, the contribution of this leakage term will be limited for sufficiently large spacings between both laser lines (e.g. > 20 dB isolation for spacings exceeding 15 GHz).

The PIC has been fabricated on imec's iSiPP50G Silicon Photonic platform. The EAMs are GeSi EAMs with a bandwidth > 50 GHz [5], the extinction ratio (ER) and insertion loss (IL) depend on the operating wavelength and biasing voltage. As the EAMs absorb some of the incident light, they can be used as monitoring photodiodes to set the resonance of Ring 1. To set the resonance of Ring 2, the photodiode used for the upconversion can be used as monitor. Low loss fiber grating couplers (FGCs) are used to interface the PIC with cleaved single mode fiber, each FGC has 4 dB loss at 1550 nm. The PIC as shown in Fig. 1 (b) measures 2.3x0.5 mm, including some additional teststructures.



(a) Photonic circuit schematic *(b) Photonic circuit layout* *(c) Ring characteristics*

Fig. 1(a): Schematic of the photonic circuit with annotated optical spectra. 50/50: 1-by-2 MMI, PS: phase shifter, EAM: electro-absorption modulator. (b) Annotated layout of the photonic circuit. The blanked out parts are bondpads and additional teststructures. (c) Transfer function of the drop and pass ports of the rings (frequency offset wrt the resonance wavelength).

3. MEASUREMENT SETUP AND RESULTS

As an experiment, a 3.5 GHz IF signal was upconverted to 24-28 GHz using the EAM-MZM, allowing single sideband communication. The full measurement setup is shown in Fig. 2.

To generate the two laser lines, a lithium niobate modulator is biased at its minimum transmission point and driven by a strong electrical signal (14 dBm). The balun is used to convert the single-ended signal from the signal generator to a differential signal to drive the dual-drive MZM in push-pull mode. In order to have an upconverted signal between 24 and 28 GHz, the frequency of the LO signal is chosen between 10.75 and 12.25 GHz (note that the IF signal is centered at 3.5 GHz and we use the upper sideband). With an optical input power of 13 dBm from the wavelength tunable laser (TLS), the resulting two laser lines each have an optical power of -5 dBm. As the MZM and the FGCs are polarization dependent, a polarization controller is placed before each of them. For simplicity, λ_{res} of Ring 1 is tuned to λ_{res} of Ring 2. In our case, this is around 1552.3 nm. The wavelength of the TLS is set such that one laser line is at λ_{res} The tunable splitter is set to send all power to the EAM-MZM. The top phase shifter is untouched, while the bottom phase shifter is set to 90°. The EAMs are biased at -1 V, the insertion loss is around 5 dB. The IF signal is brought to both arms using a 6-dB power splitter. The swing of the signal generator is chosen to minimize the EVM. A time delay (TD) is added to the electrical signal for the bottom EAM to generate a phase shift of 90° at 3.5 GHz, in order to generate the OSSB signal. The signal coming from the PIC is amplified by an EDFA and attenuated using a variable optical attenuator (VOA) to 8 dBm (the VOA allows to easily optimize the power incident on the photodiode). A 40 GHz photodiode with a responsivity of 0.6 A/W is

used as receiver. The signal from the photodiode is amplified with a low noise amplifier (LNA) with 23 dB gain. An additional bandpass filter with a passband from 23.5-32 GHz is used to suppress any out-of-band spurs, this filter has 3 dB insertion loss. Before sending the signal to a real-time oscilloscope (RTO) for demodulation, an additional 24 dB amplifier is inserted to increase the received power level sufficiently above the RTO noise floor.

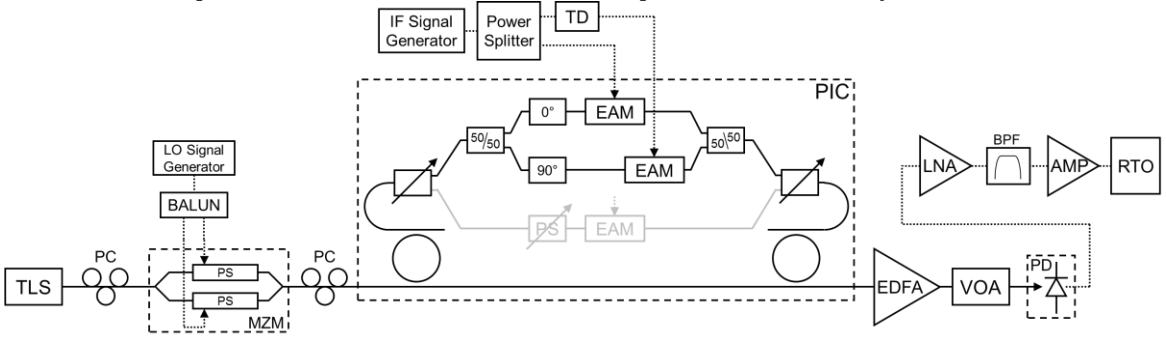
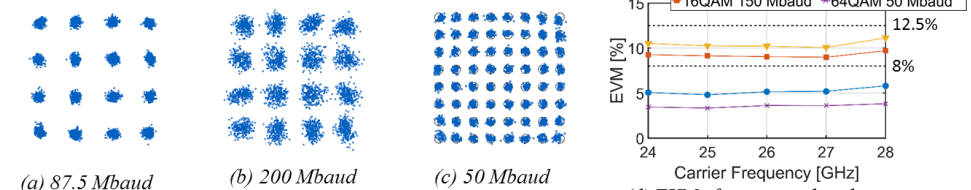


Fig. 2: Complete measurement setup. TLS: wavelength tunable laser source, PC: polarization controller, TD: electrical time delay, EAM: electro-absorption modulator, EDFA: erbium doped fiber amplifier, VOA: variable optical attenuator, LNA: low noise amplifier, BPF: bandpass filter, AMP: amplifier, RTO: real time oscilloscope

Without any signal applied to the EAMs, the power of the unmodulated and modulated laser lines before going into the EDFA is -14 dBm and -25 dBm respectively. In the described configuration (from IF Signal generator to RTO), the conversion loss measured using an IF of 3.5 GHz upconverted to 24 GHz is around 26 dB. Transmission experiments are performed where data on an IF of 3.5 GHz is upconverted to 24-28 GHz. For 87.5, 150 and 200 Mbaud 16QAM, the rolloff factor was 0.28 and the amplitude of the signals at the signal generator are 0.3, 0.46 and 0.5V respectively. The EVM was on average 5.2, 9.2 and 10.4 % respectively. For 50 Mbaud 64QAM, the EVM was on average 3.6%. The rolloff factor was 0.28, the signal amplitude was 0.32V. The 3GPP 5G NR standard requires that for the 24-28 GHz frequency band (n258), the EVM should be below 12.5% and 8% for 16 and 64QAM respectively [1]. These requirements are fulfilled over the complete band. The OSSB modulation scheme results in approximately 15 dB suppression of the lower sideband compared to the upper sideband. The phase noise was measured when upconverting a 3.5 GHz sine wave to 24 GHz using an LO of 10.25 GHz. At 100 kHz offset from the 24 GHz carrier, the phase noise is -94 dBc/Hz.



(a) 87.5 Mbaud 16QAM at 25 GHz *(b) 200 Mbaud 16QAM at 25 GHz* *(c) 50 Mbaud 64QAM at 25 GHz* *(d) EVMs for various baudrates, constellations from 24 to 28 GHz*

Fig. 3: (a)-(c): Constellation diagrams for various baudrates and constellation at an RF carrier of 25 GHz. (d): EVM at 24-28 GHz for various baudrates and constellation diagrams. The 3GPP specifications [1] requires the EVM for 16QAM and 64 QAM to be below 12.5 % and 8 % respectively.

4. CONCLUSION

We have demonstrated a flexible, integrated silicon photonic upconverter using GeSi EAMs. Altough not shown, the structure can also directly upconvert an in-phase and quadrature baseband signal to an RF carrier. Upconversion of a 3.5 GHz IF signal to an RF frequency of 24-28 GHz is shown for 87.5-200 Mbaud 16QAM and 50 Mbaud 64QAM, with EVMs within the specifications for the 3GPP NR standards [1], i.e. below 12.5% and 8% for 16QAM and 64QAM respectively.

ACKNOWLEDGEMENTS

This work was supported by the UGent Special Research Fund (BOF) and the ERC Advanced Grant 695495: "ATTO, A new concept for ultra-high capacity wireless networks".

REFERENCES

[1] 3GPP TS 38.104: "NR; Base Station (BS) radio transmission and reception," V15.4.0, 2018-03
[2] E. Chan et al, "Microwave Photonic Downconverter With High Conversion Efficiency," in *JLT 2012*
[3] T. Jiang et al, "Microwave photonic phase-tunable mixer," in *OE 2017*
[4] S. Jin et al, "RF Frequency Mixer Photonic Integrated Circuit," in *PTL 2016*
[5] K. Van Gasse et al, "Silicon Photonics Radio-Over-Fiber Transmitter Using GeSi EAMs …," in *PTL* 2019.

On the characterization of integrated power splitters and waveguide losses using optical frequency domain interferometry

(Student paper)

Luis A. Bru,[1] Daniel Pastor,[1] and Pascual Muñoz[1,2]
[1]*Universitat Politècnica de València, c/ Camino de Vera s/n - 46021 Valencia - Spain*
email: dpastor@dcom.upv.es
[2]*VLC Photonics S.L., c/ Camino de Vera s/n - 46021 Valencia - Spain*

ABSTRACT

In this paper, we propose a technique to characterize integrated power splitters and waveguide losses. Taking advantage of the time domain resolution of an optical frequency domain interferometry measurement, we present two versions of a test device comprising interferometers and the power splitters under test providing a mean to characterize the splitting power ratio of them and the losses of the employed integrated waveguides, in a single (or double) measurement wavelength-resolved scheme. We provide details on the model and examples of the numerical work supporting its validity. To conclude, we provide some discussion of the techinque, including the possible implementations for future experimental validation.

Keywords: optical frequency domain reflectometry, power splitter, multimode interferometer, integrated test structure, integrated waveguide losses.

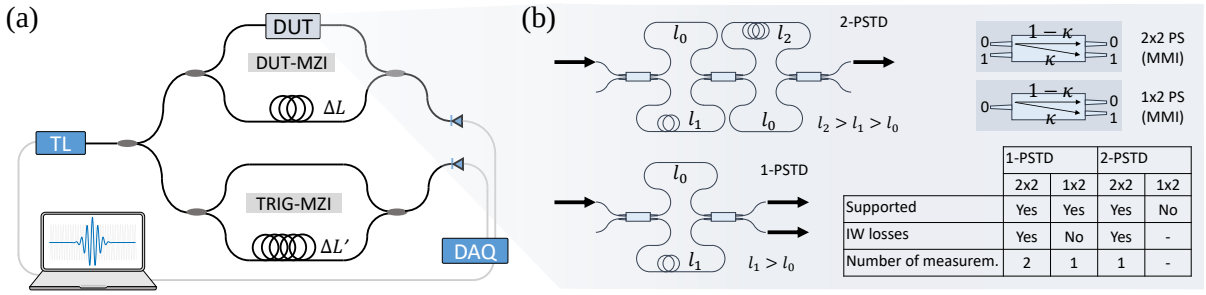
1 INTRODUCTION

Optical characterization of integrated devices conforming photonic integrated circuits (PIC) is an indispensable step in the design optimization workflow. The optical spectral amplitude response of a device under test (DUT) provided by the conventional methods becomes often insufficient to evaluate the minutiae of its performance. The availability of the optical phase response, enabled by advanced characterization methods like optical frequency domain reflectometry (more correctly denoted OFDI, standing for interferometry, when used in transmission configuration [1], [2]), permits to derive the time domain response of the DUT by Fourier analysis and turns out to be extremely useful to localize unexpected contributions and fadings explaining the performance deviations from the employed model [3].

The direct characterization of more than one input and/or output device is subject to the uncertainty of optical power coupling efficiency, which typically varies from one channel to other due to chip fabrication errors and varying measurement conditions. This is the case for 2×2 and 1×2 optical power splitters or couplers (PS), of ubiquitous use in any PIC and commonly implemented by multimode interferometers (MMI) and directional couplers (DC). A straightforward strategy to approach this issue comprises the using of a cascade of the same devices having multiple outputs to be measured and fit the outcome data to a linear function [4], implying a sequence of measurements, the more the better for an accurate mean value. Here we present a technique assisted by OFDI, which explotes the strength of the time domain response of the DUT to evaluate the power splitting ratio of PSs, as well as the integrated waveguide (IW) propagation losses, wavelength-resolved in a fast single or double measurement scheme. The technique is enabled by the use of two integrated PS test device (PSTD) versions that we present in section 2, where we also show their application range on each case and some numerical validation. Afterwards, we present our discussion and conclusions, including physical implementations on the experimental work to come in section 3.

2 THE TECHNIQUE

OFDI is a well-known technique based on homodyne detection which provides both amplitude and phase, frequency and time domain resolution [1], [2]. In Fig. 1(a) a tunable laser (TL) sweep of $\Delta\lambda$ span feeds the upper interferometer, typically Mach-Zehnder type (MZI), interrogating the DUT and generating an interferogram containing amplitude and phase spectral information of the DUT, which needs to be properly resampled by the TRIG-MZI interferogram below (fulfilling Nyquist criterion for the corresponding path length differences (PLDs) by $\Delta L' \geq 2\Delta L$) to suitably run Fourier analysis on it. The time domain response of a DUT is composed of the different events taking place on it: provided that they are spatially separated, the events can be isolated and the proportionality between their contained information (position, energy, optical phase) is conserved. This feature have been demonstrated to be extremely useful to localize and identify unexpected events in integrated devices, as well as to relate optical phase and positions to characterize performance or derive propagation parameters (e.g. [5], [6]). In this work, we explote the optical power of the temporal peaks, by intentionally proposing a test structure, to characterize PS performance and IW losses.



	1-PSTD		2-PSTD	
	2x2	1x2	2x2	1x2
Supported	Yes	Yes	Yes	No
IW losses	Yes	No	Yes	-
Number of measurem.	2	1	1	-

Figure 1. Sketch of an OFDI setup (a) and of the proposed PS test devices, including a summary table of their applicability in (b).

The main version of the PS test device (that we call 2-PSTD) is shown in Fig. 1(b) at the top, and comprises a serial combination of two MZIs and three PSs under test. The time domain transfer function of this structure is composed of 4 contributions corresponding to the 4 possible paths: the shortest one going through the shorter MZI arms (length $2l_0$), the next going through the arms below ($l_0 + l_1$), and so forth for the remaining 2 combinations, corresponding to lengths $l_0 + l_2$ and $l_1 + l_2$. In this way, each followed path hits the PS in a different combination of bar/cross states and IW lengths. The PS under test (see inset in Fig. 1(b)), a 2×2 type in this case, have bar (0-to-0 and 1-to-1 channels) and cross (1-to-0 and 0-to-1) connections, and it can be modeled by the following matrix $\hat{M}$:

$$\hat{M} = \gamma \begin{pmatrix} \sqrt{1-\kappa} & j\sqrt{\kappa} \\ j\sqrt{\kappa} & \sqrt{1-\kappa} \end{pmatrix}, \hat{P}_{a,b} = \begin{pmatrix} e^{-\alpha\frac{l_a}{2}} e^{-j\beta l_a} & 0 \\ 0 & e^{-\alpha\frac{l_b}{2}} e^{-j\beta l_b} \end{pmatrix}; \tag{1}$$

where γ stands for the insertion loss of the coupler and κ determines de PS power ratio. Matrix $\hat{P}_{a,b}$ describes the propagation regions in the MZIs for IW lengths l_a and l_b (being $a, b = 1, 2$ and 3), where the propagation is governed by β, and propagation losses given by α. The transfer function of the 2-PSTD is thus given by $\hat{M}\hat{P}_{2,0}\hat{M}\hat{P}_{0,1}\hat{M}$. By choosing the input field F_0 on the upper input, and by OFDI measurement of the upper output (span $\Delta\lambda$ and PLDs set to ΔL and $\Delta L'$), after some algebra it can be obtained the associated power coefficients Λ_i for $i = 1, 2, 3$ and 4 events as:

$$\Lambda_1 \propto \kappa^2 (1-\kappa) e^{-2\alpha l_0}, \Lambda_2 \propto \kappa^2 (1-\kappa) e^{-\alpha(l_0+l_1)}, \Lambda_3 \propto (1-\kappa)^3 e^{-\alpha(l_0+l_2)}, \Lambda_4 \propto \kappa^2 (1-\kappa) e^{-\alpha(l_1+l_2)}, \tag{2}$$

all of them under the same proportionality conditions. By trivial relations between them, we have a mean to obtain κ and α, so that 2-PSTD allows to characterize both magnitudes in a single-measurement scheme. Besides, OFDI can be applied piecewise to a sequence of sub-bands within the whole band, allowing to obtain the trend of $\kappa = \kappa(\lambda)$ and $\alpha = \alpha(\lambda)$ along $\Delta\lambda$. This is confirmed by numerical simulation of the measurament system: in Fig. 2(a) it is shown the time domain response of the 2-PSTD (with chosen lengths $l_0 = 2$ mm, $l_1 = 3$ mm and $l_2 = 4$ mm) after an OFDI measurement with wavelength sweep span $\Delta\lambda = 100$ nm centered at 1550 nm, and PLDs set to $\Delta L = 20$ cm and $\Delta L' = 80$ cm, describing a typical fiber-based OFDI system. Regarding the IWs, it is considered a second-order dispersion through $D = 1430$ ps nm^{-1}km^{-1} and varying propagation losses from 2.2 to 1.8 dB/cm along $\Delta\lambda$, as shown in black solid line in the corresponding inset. Similarly, the PS power ratio has been chosen to vary from $\kappa = 0.4$ to 0.55. The processing of the resulting interferograms has been performed piecewise to have 10 evenly distributed data along $\Delta\lambda$, where the distance between the contributions is more than enough to keep them away from each other after the corresponding time domain broadening of the peaks in the sub-bands. To account for this temporal broadening and the induced by IW dispersion, the coefficients Λ_i are obtained by integrating each peak independently. The recovered κ and α are plotted (blue points) in the corresponding insets, showing an almost perfect agreement with the starting parameters. The method has been verified to be robust against dispersion and different coupling conditions to 2-PSTD.

An alternative version to 2-PSTD is also considered, formed by a single MZI and two PSs as shown in Fig. 1(b) at the bottom (1-PSTD). The transfer function of this device is given by $\hat{M}\hat{P}_{0,1}\hat{M}$. As summarized in Fig. 1(b), the derived coefficients for each one of the outputs is not enough to get κ and α as in 2-PSTD: one of the measured outputs permits to obtain α, to be used as input data to obtain PS power ratio with the other. This structure is also used for the same purpose in [7], where the method is based on an analysis of the spectral response instead. We show numerical simulation of the technique using 1-PSTD in Fig. 2(b), using the same parameters as described above. In this case, we have 2 contributions in the time domain response for each case: the two ones corresponding to the upper output (solid line) and the ones for the other (dashed line). After processing under the same conditions as in 2-PSTD simulation, κ and α are obtained, showing again a perfect agreement with the designed parameters. Finally, just mention that 1-PSTD can be easily adapted to test 1×2 PSs power ratio.

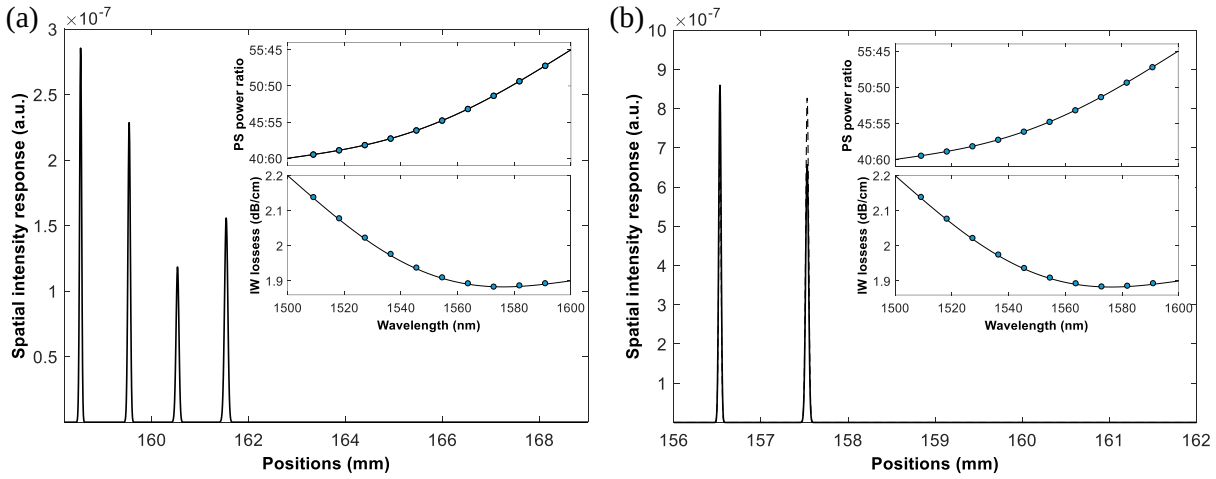


Figure 2. (a) Numerical simulation of the time domain response of the 2-PSTD. In the inset, the IW losses and PS power ratio targeted (solid line) and recoverd by the technique (dots). (b) The same plots for 1-PSTD. In the main plot, the time domain responses of both outputs are shown (solid and dashed lines).

3 DISCUSSION AND CONCLUSION

We have presented a technique to characterize PSs and IW losses by relying on OFDI. In this context, on the one hand we have proposed a more complex device (2-PSTD) allowing for single measurement, wavelength-resolved derivation of PSs power ratio and IW losses. On the other hand, a simpler version (1-PSTD) consisting of a single MZI with two PSs under test opening and closing the paths. This second device is equivalent to the used in [7] for the same purpose. However, the fact the proposed technique is based on OFDI-enabled time domain response paves the way to untangle the different contributions involved. Amongst the benefits, this allows to design a more complex structure as it is the case for 2-PSTD, enabling a single-measurement characterization, and also makes the technique robust against the presence of chromatic dispersion. Beyond, there is room to obtain other parameters such as IW dispersion [6]. Furthermore, the technique can be in principle adaptable to the integration of the OFDI structure [5], having some extra benefits as for instance, not having to depend on a bulky fiber-based setup and an intrinsic dispersion de-embedding mechanism. The proposed technique is ready to be experimentally implemented and tested in all the mentioned versions, including comparison to other existing methods to obtain IW losses and PS power ratio [4], [7], [8].

ACKNOWLEDGMENT

The authors acknowledge financial support through projects, TEC2015-69787-REDT PIC4TB, TEC2016-80385-P SINXPECT, TEC2014-54449-C3-1-R BIOSENSLOC and GVA PROMETEO 2017/103. L.A.B. also acknowledges PTA2015-11309-I.

REFERENCES

[1] U. Glombitza and E. Brinkmeyer, “Coherent frequency-domain reflectometry for characterization of single-mode integrated-optical waveguides,” J. Lightwave Technol., vol. 11 (8), pp. 1377-1384, 1993.

[2] B. J. Soller, D. K. Gifford, M. S. Wolfe and M. E. Froggatt, “High resolution optical frequency domain reflectometry for characterization of components and assemblies,” Opt. Express, vol. 13 (2), pp. 666-674, 2005.

[3] L. A. Bru et al., “OFDR applied to photonic integrated circuits,” in proceedings of ECIO 2016, pp. o-08, 2016.

[4] Z. Sheng et al., “A compact and low-loss MMI coupler fabricated with CMOS technology,” IEEE Photon. J., **4** (6), p. 2272, 2012.

[5] L. A. Bru, D. Pastor and P. Muñoz, “Integrated optical frequency domain reflectometry device for characterization of complex integrated devices,” Opt. Express, vol. 26 (23), pp. 30000-30008, 2018.

[6] L. A. Bru, Z. Ye, D. Pastor and P. Muñoz, “Multi-parameter estimation of high-Q silicon rich nitride resonators using optical frequency domain reflectometry,” Proc. SPIE Photonics West 2018 Integrated Optics: Devices, Materials, and Technologies XXII, pp. 10535-18, 2018.

[7] M. A. Tran et al., “A Robust Method for Characterization of Optical Waveguides and Couplers,” IEEE Photon. Technol. Lett., vol. 28 (14), pp. 1517-1520, 2016.

[8] F. Morichetti, “Roughness induced backscattering in optical silicon waveguides,” Phys. Rev. Lett., vol. 104 (3), pp. 033902, 2010.

Compact Cavity Enhanced Si MSM Photodetector in SiN-on-SOI

(Student paper)

Avijit Chatterjee[1], Shankar Kumar Selvaraja[1]
[1] Center for Nano Science and Engineering, Indian Institute of Science, Bangalore
e-mail: avijit@iisc.ac.in

ABSTRACT

We present compact Si metal semiconductor metal (MSM) photodetector integrated SiN ring resonator in SiN-on-SOI platform. We achieved a 10X enhancement in photocurrent with SiN resonator integrated photodetector compared to integrated waveguide configuration. A maximum responsivity of 0.08 A/W is achieved with a photodetector of just 6 µm long operated at a bias of 5 V in the 850 nm wavelength band. We present the design, fabrication and characterisation of integrated resonance photodetector. On-chip wavelength selective photodetector in 850 nm wavelength band enables next-generation scalable short-reach interconnect technology and also an opportunity for on-chip bio-sensors operating in the visible wavelength range.

Keywords: SiN-SOI, MSM photodetector, Ring resonator

1. INTRODUCTION

Silicon (Si) is an excellent photodetector in visible to near infrared wavelength (400~1100 nm) due to its relatively high responsivity. Furthermore, it is CMOS compatibility which offers excellent integration opportunity. However, the bandwidth of Si is lower than Ge or III-V photodetectors. Most of the detectors are built as bulk surface illuminated photodetectors. The responsivity of Si photodetectors could be improved by increasing the area. However, this limits the bandwidth due to enhanced depletion capacitance. Therefore, there is a trade-off between responsivity and bandwidth. Waveguide photodetectors is an alternative scheme to improve the photodetector responsivity without compromising speed. Thin Si layer in SOI substrate used in waveguide photodetector configurations overcomes the limitation of responsivity and bandwidth [1-2]. However, the maximum responsivity of Si photodetector is limited up to 0.44 A/W [3]. Recently, cavity enhanced photodetectors are explored to achieve high responsivity and large bandwidth [4-5]. By integrating with a ring resonator, wavelength selectivity can also be achieved. The wavelength selectivity offers a platform for integrated WDM photonic circuit for short reach optical interconnect operating in 850 nm wavelength band. Also, Si PDs could be used for lab-on-chip applications operating in 400-1000 nm window.

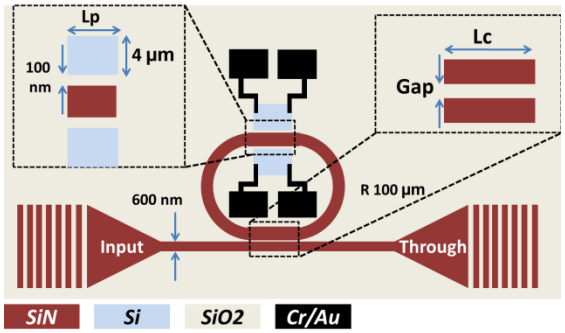


Figure 1 Schematics of the proposed structure shows the MSM photodetector integrated along the SiN ring resonator loop

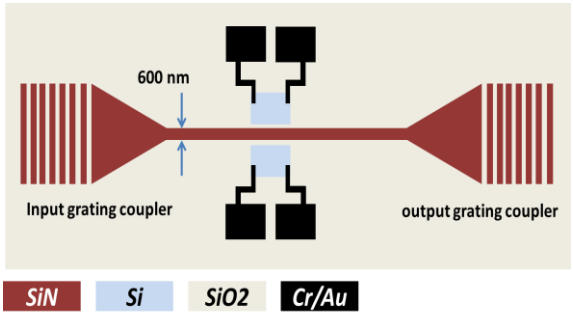


Figure 2 MSM photodetector integrated with SiN waveguide

In this paper, we propose and demonstrate a SiN ring resonator integrated Si Metal-Semiconductor-Metal (MSM) photodetector on SOI wafer. Fig. 1 shows a schematic of the proposed wavelength selective Si photodetector. A standard SOI wafer is used to fabricated the wavelength selective photodetector. SiN waveguide offers a circuit platform to realise various photonic devices while silicon is used as a photodetector. Since the top device layer in SOI wafer is crystalline, the performance of the detector is expected to be better. However, the challenge is to integrate SiN waveguides with the detector in-plane.

As a technology demonstrator, we start with an SOI wafer and use a SiN ring resonator to validate the integration process flow. Unlike vertical integration Si-on-SOI [3], in this work, we propose a compact side coupling scheme. A 220 nm thick SiN layer is used to realise a ring of 100 um radius with a coupling gap of 150 nm with the bus waveguide. A single mode waveguide of 600 nm is used to realise the circuit. SiN is used as the waveguide material because of its transparency in 850 nm window. The Si MSM photodetector is flanked on both sides of the SiN ring waveguide at an optimised gap of 100 nm. The Evanescent field from the ring

waveguide couples to both the MSM photodetector of the waveguide. To compare the ring enhancement photodetector on straight SiN waveguide with 600 nm width with a similar configuration shown in Fig. 2.

Figure 3 givens a brief overview of the fabrication process steps. The device is fabricated on an SOI substrate with 220 nm thick Si and 2 µm thick buried oxide. First, Si layer is patterned with electron-beam lithography and dry etch process to define the Si photodetector region. A thin 50 nm PECVD linear SiO_2 is deposited followed by 220 nm thick LPCVD SiN deposition on the patterned SOI. The SiN is patterned in with electron-beam lithography, and dry etch process to realise waveguide, grating coupler and ring resonator structures. Finally, metal contact pads are fabricated by with electron-beam lithography and lift-off process. Chrome/Gold metal stack is used as the metal pads to form Schottky junction on Si. Fig. 4 shows the optical image of the fabricated device.

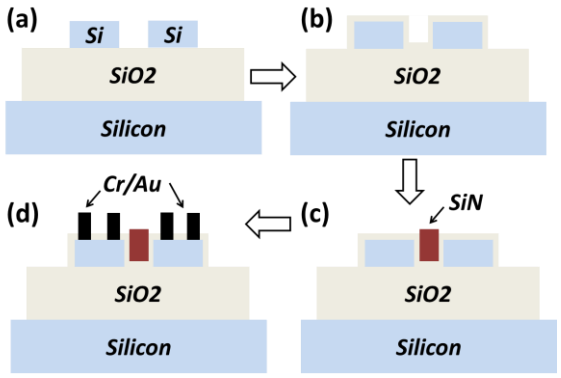


Figure 3 (a) 220 nm Si patterned in Ebeam litho and dry etch, (b) 50 nm PECVD SiO2 deposited, (c) 220 nm LPCVD SiN deposited and patterned in Ebeam litho and dry etch to define waveguide, ring, and grating coupler, (d) Lift off to define metal contacts on Si

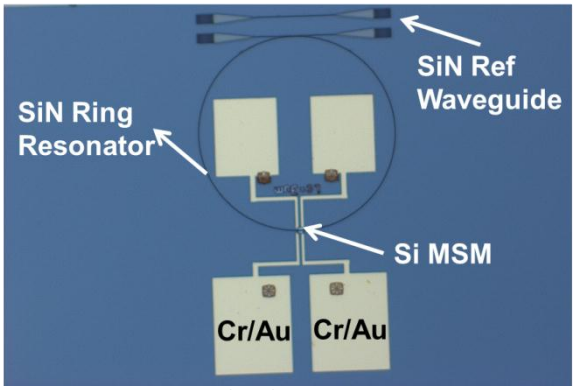


Figure 4 Optical image of the fabricated device

2. Characterisation

The spectral characteristics of the fabricated device is measured using an LED source (850-900 nm) and an optical spectrum analyser. Light is coupled in and out through grating coupler. Fig. 5 shows the normalised transmission response of SiN ring with and without Si photodetector. The transmission is normalised with a straight reference waveguide with an identical grating coupler. We observe an insertion loss of about 5 dB, which we attribute to non-optimal coupling taper between the grating and single-mode waveguide. The insertion loss could be improved with an optimised low-loss taper. The spectral response of the ring resonator shows reduced extinction and improved quality factor due to absorption in the Si MSM detector. We observed an extinction change from 14 dB to 6 dB, and quality factor enhances from 3800 to 4400 (Fig. 6 and Fig. 7).

Fig. 8 shows the IV characteristics of the MSM photodetector coupled to SiN ring and SiN waveguide. The optoelectronic characteristics of the device were measured using a narrowband laser around 870 nm. We measure a dark current as low as 10 nA at 5 V reverse bias. MSM photodetector integrated with SiN waveguide with 6 µm length gives the photocurrent of 68 nA at 5 V bias. For an MSM photodetector integrated SiN ring resonator, we measure a maximum photocurrent of 800 nA which is more than 10 times higher than the waveguide integrated MSM of same interaction length of 6 µm. Ring coupled MSM detectors having sufficient photocurrent even at very low bias voltages shows the promise for highly sensitive, and low power photodetector.

The responsivity of the MSM photodetector is estimated from the optical power coupled in the reference waveguide. Fig. 9 plots the responsivity with bias voltage for waveguide coupled and ring coupled MSM photodetector. Ring coupled MSM photodetector gives the responsivity around 0.08 A/W at 5 V compare to 0.005 A/W of waveguide integrated MSM photodetector. Fig. 10 shows the photocurrent obtained from MSM with a different coupling length of ring and bus waveguide to improve the coupling efficiency. As the coupling length increases between bus and ring (L_c), the responsivity also increases due to higher power coupling. The length of the photodetector (L_p) is kept constant while varying the power coupling. The responsivity could be further improved by increasing the photodetector length. To obtain the power enhancement inside the ring resonator, we estimated the transmission coefficient and loss coefficient of the ring resonator [6]. Based on the extinction coefficient of 6dB, FSR of 0.5 nm and FWHM of 200 pm of the MSM photodetector integrated ring resonators, we estimate a power enhancement factor of 11 inside the ring resonator at resonating wavelengths.

The estimation agrees well with the measured photocurrent enhancement of a factor of 10 compared to a waveguide integrated photodetector. MSM photodetector integrated to ring resonator also shows the similar enhancement in the photocurrent as mentioned before.

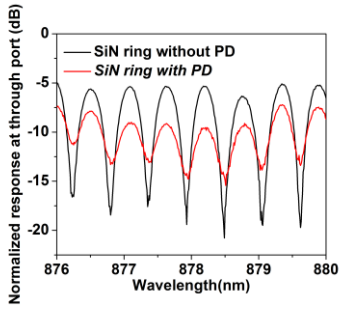


Figure 5 SiN ring response at the through port

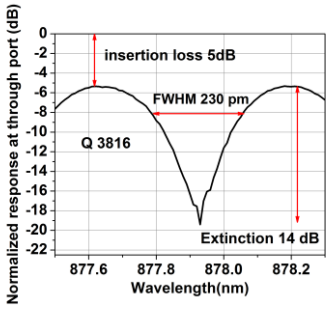


Figure 6 Resonance of a ring without MSM integrated.

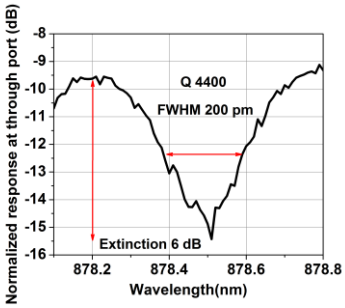


Figure 7 Resonance for ring with MSM integrated

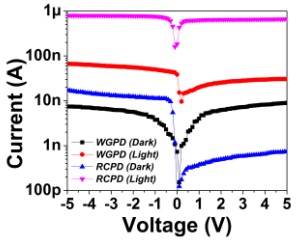


Figure 8 IV characteristics of the MSM PD integrated to SiN ring (RCPD) and SiN waveguide (WGPD)

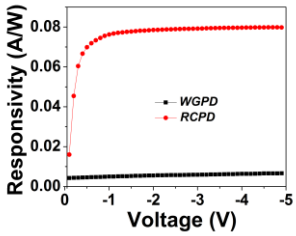


Figure 9 Responsivity Vs Bias voltage of the MSM PD integrated to SiN ring (RCPD) and SiN waveguide (WGPD)

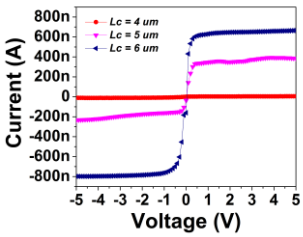


Figure 10 Ring coupled MSM photodetector IV Vs Coupling length between bus and ring (Lc)

3. CONCLUSIONS

In conclusion, we have demonstrated SiN resonator integrated silicon MSM photodetector on SOI wafer platform. By using a resonant cavity, we show 10X enhancement in photocurrent compared to a simple waveguide integrated photodetector. We achieved a responsivity of 0.08 A/W at 5 V bias around 870 nm wavelength with a Si MSM detector which is just 6 μm long. The demonstration shows a promising path towards realising an integrated Si photonic with SiN photonic circuit. The proposed combination of SiN and Si could potentially address short reach WDM requirement and sensing application as well. Furthermore, to validate the quality of photodetector, high-speed response of photodetector would confirm the suitability for data-com application.

ACKNOWLEDGEMENTS

"We thank DST-SERB for funding this research. We also acknowledge funding from MHRD, MeitY and DST Nano Mission for supporting the facilities at CeNSE".

REFERENCES

[1] Tatum, Jim A., et al.: VCSEL-based interconnects for current and future data centers, Journal *of Lightwave Technology*33.4 2015.

[2] M. Fard, Monireh Moayedi Pour, et al.: High-speed grating-assisted all-Si photodetectors for 850 nm applications, *Optics Express* 25.5 2017.

[3] Avijit Chatterjee, Saumitra, Sujit K. Sikdar, and Shankar Kumar Selvaraja: High-Speed Waveguide Integrated Si Photodetector on SiN-SOI Platform for Short Reach Optical Interconnect. *Frontiers in Optics*. Optical Society of America, 2018.

[4] Junfeng Song et al: A microring resonator photodetector for enhancement in L-band performance,Opt. Express 22, 2014.

[5] Casalino, Maurizio: Design of Resonant Cavity-Enhanced Schottky Graphene/Si Photodetectors at 1550 nm, *Journal of Lightwave Technology* 36.9 2018.

[6] McKinnon, W. R., et al.: Extracting coupling and loss coefficients from a ring resonator, *Optics express* 17.21 2009.

Investigation of the Background Signal from 532 nm Excitation for Waveguide-based Raman Spectroscopy and Microscopy

(Student paper)

David A. Coucheron[1], Dushan N. Wadduwage[2,3,4], Ganapathy S. Murugan[5], Peter T. C. So[2,3], Balpreet S. Ahluwahlia[1]

[1] Department of Physics and Technology, UiT – The Arctic University of Norway, Norway
[2] Laser Biomedical Research Center, Massachusetts Institute of Technology, Massachusetts 02139, USA
[3] Department of Biological Engineering, Massachusetts Institute of Technology, Massachusetts 02139, USA
[4] Center for Advanced Imaging, Harvard University, Cambridge MA, 02138, USA
[5] Optoelectronics Research Centre, University of Southampton, Southampton SO17 1BJ, United Kingdom
e-mail: balpreet.singh.ahluwalia@uit.no

ABSTRACT

The simple integrated waveguide has found many new applications recently, including waveguide enhanced Raman spectroscopy and chip based super-resolution microscopy. Chip based microscopy relies exclusively on visible light excitation, whereas Raman spectroscopy is done at a range of wavelengths. Here, we investigate two popular waveguide platform, Si_3N_4 and Ta_2O_5, for use at 532 nm excitation. We also present spontaneous Raman spectroscopy of methanol and iso-propanol using Ta_2O_5 strip waveguides and 532 nm excitation light.

Keywords: Waveguide, Raman spectroscopy, super-resolution imaging

1. INTRODUCTION

Integrated photonics is an important part of lab-on-a-chip technology and has already seen many applications. There are several potential advantages to using integrated photonics for e.g. biosensors, ranging from cost effectiveness and size reduction to increased sensitivity. Today, integrated photonics offers a vast number of different components, but a lot can be achieved with only the simplest component: the waveguide. Here, we focus on two recent developments in integrated photonics: waveguide based Raman spectroscopy and chip based super-resolution microscopy[1]. In both applications, the primary contribution of the waveguide is sample excitation. For fluorescence imaging applications, the excitation light will be between 405 nm and 660 nm. Raman spectroscopy, on the other hand, can be performed at both visible and near-infrared wavelengths. Lower wavelengths will increase the amount of Raman scattering and is thus favourable. Additionally, several interesting samples experience resonance Raman effects at lower wavelengths, giving a massive increase in Raman signal strength. Haemoglobin, the major component in blood, has resonance effects at around 532 nm excitation. In this paper, we discuss the challenges for both Raman spectroscopy and microscopy when moving towards visible wavelengths.

Whenever light is guided within a waveguide, a portion of the light will be guided in an evanescent field outside of the physical waveguide structure. Any sample that is in contact with the waveguide will thus interact with the evanescent field. The evanescent field intensity can be increased through careful choice of waveguide materials and design of the waveguide geometry. As the evanescent field decays over only a few hundred nanometers, it is ideal for e.g. monolayer sensing. In the field of super-resolution imaging, the high optical sectioning of the excitation is highly attractive, as it can reduce noise and yield better images by avoiding signal beyond the focal plane.

Recently, several different materials have been investigated for waveguide Raman spectroscopy. High refractive index contrast materiels (HIC) are preferred, not only due to the increased intensity of the field, but also because it offers a higher field confinement. The increased confinement allows for sharp bends and thus the waveguide can be structured in e.g. tight spiral structures. Si_3N_4 is today a well-established platform that has seen many application in the recent years, including waveguide based Raman spectroscopy. Dhakal et al. have demonstrated waveguide enhanced Raman spectroscopy using 785 nm excitation and Si_3N_4 waveguides[2]. Another material that has been investigated is TiO_2 as it has a higher refractive index[3]. A third option, is Ta2O5, has been used for Raman spectroscopy with 637 nm excitation light. Since most of the light is guided inside the waveguide structure, the excitation light will interact with the waveguide material. A Raman and auto-fluorescence signal can be generated from the waveguide material itself, which can be challenging for spectroscopic and imaging applications. We have investigated Si_3N_4 and Ta_2O_5 as possible platform going to visible wavelengths,

specifically 532 nm excitation. We also present spontaneous Raman spectroscopy of methanol and iso-propanol results using a Ta_2O_5 platform using 532 nm excitation.

2. Set-up and Background Measurements

The excitation light was coupled into the waveguides by end fire coupling through a 0.5 NA aspheric lens. All experiments were performed with a 532 nm laser (Verdi V10). Small PDMS frames were used to contain the sample to the region of interest on the waveguides and the frames were sealed off with a cover glass. Collection was done from the top through and a 60x/1.2 NA WI objective lens for the background measurements and a 40x/0.75 NA air objective lens for the hemoglobin measurements. Collection for spectroscopic measurements were performed using an Andor Holospec-F/1.8-VIS with a 532 nm edge filter (Semrock RazorEdge). For imaging, we used a Hamamatsu Orca Flash 4.0 v.2 CMOS camera. The system is sketched in Figure 1.

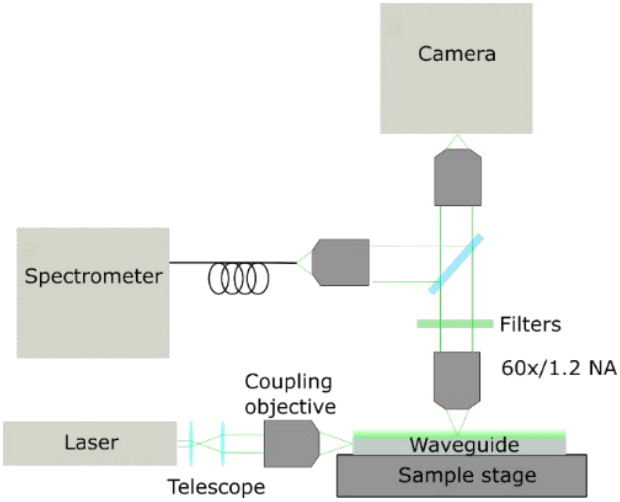


Figure 1. A 532 nm laser was coupled into the waveguide by end fire coupling through a 0.5 NA aspheric lens. A telescope was used to expand the beam prior to coupling. The waveguide was held by a vacuum chuck and placed on a three stage. The sample was placed in a PDMS chamber on the waveguide and collection performed from the top. A flip mirror was used to switch between imaging and spectroscopy.

High intensity in the evanescent field of the waveguide is desirable. Here, we employed 150 nm thick strip waveguides. The waveguides were 70 µm wide. Si_3N_4 waveguides were fabricated by first thermally growing a 2 µm SiO_2 layer in a silicon chip. Si_3N_4 was then deposited using low-pressure chemical vapour deposition at 800 °C[4]. The waveguide geometries were made by standard photolithography followed by reactive ion etching. Finally, the remaining photoresist was rinsed off. Ta_2O_5 waveguides were fabricated by first sputtering the Ta_2O_5 material, followed by conventional photolithography and finally ion beam milling was used to define the waveguides[5]. Post-fabrication annealing of Ta_2O_5 was performed at 600° C for 3 hours to further reduce the loss.

We observed a background signal from the Si_3N_4 at 532 nm wavelength, as seen in the image of the background in figure 2b. The Ta_2O_5 does not have any similar signal (figure 2a). Fluorescent beads were used to compare the background intensity with the bead intensities. Super-resolution optical microscopy through single molecule localisation requires fitting of fluorescent emitters and any background present may reduce the localisation precision. This can in turn lead to a loss in resolution. The background spectra of the two waveguides were collected to further investigate the background, without any beads present. The Ta_2O_5 background agrees very well with literature, with a main peak at approximately 680 cm^{-1} and very little background above 1000 cm^{-1}. The Si_3N_4 waveguide we used, on the other hand, has a broad and much stronger background. Based on the background results, we only used Ta_2O_5 for Raman measurements.

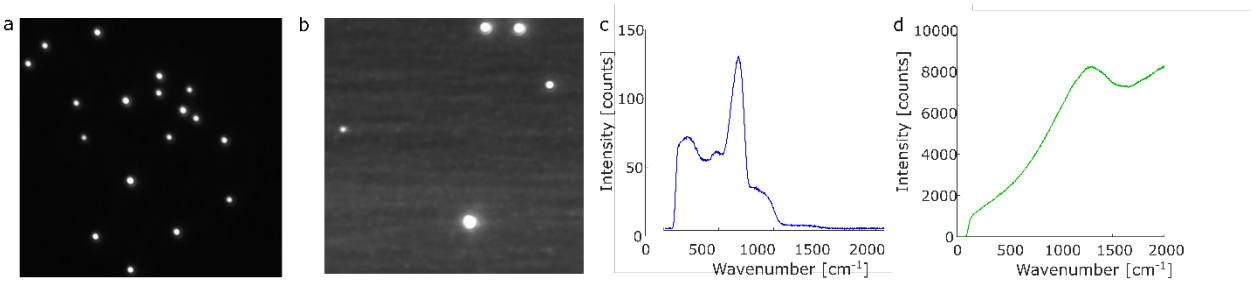


Figure 2. (a-b) Images of fluorescent beads on a 70 um wide strip waveguide of Ta_2O_5 and Si_3N_4, respectively. The contrast has been adjusted to make the bead intensities comparable. Both mages were taken through a 561 nm long pass filter. The multi-moded background pattern is clearly visible for the Si_3N_4 waveguide used. (c-d) Background spectra collected for Si_3N_4 and Si_3N_4, respectively.

3. Raman Spectroscopy

Using a Ta_2O_5 strip waveguide we measured spontaneous Raman scattering from methanol and iso-propanol samples with 532 nm excitation. 395 mW was launched through the coupling lens. The sample was filled the PDMS chamber and a cover glass was used to ceil it off. Collection was performed from the top and the resulting spectra are presented in figure 3. The two samples are easily distinguished by e.g. the peaks at 822 cm^{-1} (methanol) and 890 cm^{-1} (iso-propanol).

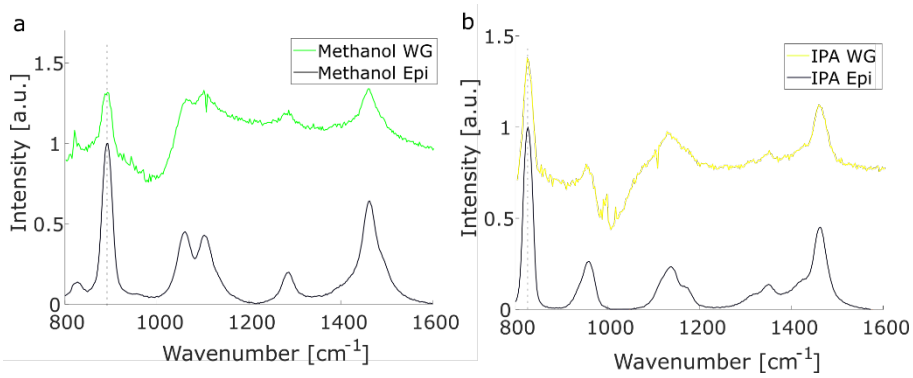


Figure 3. (a) Raman spectrum of methanol captured with waveguide excitation, compared to the spectrum collected using epi-illumination. (b) Raman spectrum of iso-propanol (IPA), with a comparison to epi-illumiation.

4. CONCLUSIONS

We have investigated Ta_2O_5 and Si_3N_4 as potential platforms for chip-based Raman spectroscopy and super-resolution imaging at visible wavelengths. Minimizing the background signal is preferential in both applications and, using the given fabrication procedures, Ta_2O_5 offers a significantly lower background signal. Using a Ta_2O_5 platform we have demonstrated spontaneous Raman using 532 nm excitation. The next step is to investigate the source of the background, as well as quantify the effect it might have on super-resolution imaging. It might be possible to reduce the background signal of Si_3N_4 waveguide platform for visible wavelengths by optimization of the fabrication process[6], which will be carried out in future work.

ACKNOWLEDGEMENTS

B.S.A acknowledges the funding from the European Research Council, (project number 336716). B.S.A and D.A.C acknowledges UiT, The Arctic University of Norway Tematiske Satsinger funding program.

REFERENCES

[1] R. Diekmann *et al.*, "Chip-based wide field-of-view nanoscopy," *Nat. Photonics*, vol. 11, no. 5, pp. 322–328, May 2017.

[2] A. Dhakal, P. C. Wuytens, F. Peyskens, K. Jans, N. Le Thomas, and R. Baets, "Nanophotonic Waveguide Enhanced Raman Spectroscopy of Biological Submonolayers," *Acs Photonics*, vol. 3, no. 11, pp. 2141–2149, Nov. 2016.

[3] C. C. Evans, C. Liu, and J. Suntivich, "TiO2 Nanophotonic Sensors for Efficient Integrated Evanescent Raman Spectroscopy," *ACS Photonics*, vol. 3, no. 9, pp. 1662–1669, Sep. 2016.

[4] J.-C. Tinguely, Ø. I. Helle, and B. S. Ahluwalia, "Silicon nitride waveguide platform for fluorescence microscopy of living cells," *Opt. Express*, vol. 25, no. 22, pp. 27678–27690, Oct. 2017.

[5] B. S. Ahluwalia, A. Z. Subramanian, O. G. Hellso, N. M. B. Perney, N. P. Sessions, and J. S. Wilkinson, "Fabrication of Submicrometer High Refractive Index Tantalum Pentoxide Waveguides for Optical Propulsion of Microparticles," *IEEE Photonics Technol. Lett.*, vol. 21, no. 19, pp. 1408–1410, Oct. 2009.

[6] A. Gorin, A. Jaouad, E. Grondin, V. Aimez, and P. Charette, "Fabrication of silicon nitride waveguides for visible-light using PECVD: a study of the effect of plasma frequency on optical properties," *Opt. Express*, vol. 16, no. 18, pp. 13509–13516, Sep. 2008.

Slepian-States-based DV- and CV-QKD Schemes Suitable for Implementation in Integrated Optics

Ivan B Djordjevic
University of Arizona, ECE Dept., 1230 E Speedway Blvd, Tucson, AZ 85721 - USA
e-mail: ivan@email.arizona.edu

ABSTRACT

To solve for low secret-key-rate (SKR) and short-distance problems of QKD in a simultaneous manner, we propose to encode information in orthogonal Slepian sequences' bases. Employment of multidimensional encoding-space enables high-spectral-efficiency-QKD so that SKR can be significantly improved. Generation, processing, and detection of Slepian-states for proposed QKD-protocols can be reliably implemented in an integrated optics platform, based on waveguide Bragg gratings.

Keywords: Quantum key distribution (QKD), Slepian-states, integrated optics, waveguide Bragg gratings.

1. INTRODUCTION

The research in QKD is getting momentum, in particular, after the first satellite-to-ground QKD demonstration. Recently, the QKD over 404 km of ultralow-loss optical fiber is demonstrated; however, with ultralow secure key rate ($3.2 \cdot 10^{-4}$ b/s). Given that quantum states cannot be amplified, the fiber attention limits the distance. On the other hand, the deadtime of the single-photon detectors (SPDs) employed in discrete variable (DV)-QKD, typically in 10-1000 ns range, limits the baud rate and therefore the secret-key rate (SKR). The continuous variable (CV)-QKD schemes, since they employ the homodyne/heterodyne detection, do not exhibit the deadtime limitation problem. Quantum repeaters would represent an ultimate solution to overcome the channel loss, but they are well beyond the reach of today's available technologies. A near-term solution would to encode quantum information into a Hilbert space with a dimension higher than the mainstream two-dimensional encoding using, e.g., polarization states of photons. A multidimensional (MD) encoding space ensures that multiple information bits can be delivered upon receiving each single photon [1], thereby optimizing the photon efficiency for high-rate QKD in the absence of quantum repeaters. Several approaches have recently been pursued to increase the dimension of the encoding space of single photons. These approaches either leverage MD parameters such as time bin, frequency qubits, position and linear momentum, orbital angular momentum (OAM), or simultaneously utilizing multiple parameters encoded in hyper-entangled states. The MD time-bin-encoded QKD can be seamlessly incorporated into standard telecom networks, as experimentally demonstrated in [2], but the time-bin encoding largely sacrifices the spectral efficiency. The second challenge lies in the scalability and cost of QKD. Like the prevailing classical communication systems, future QKD systems must provide mass productivity with low cost, reliable realignment-free operations, and small power consumptions. In this regard, photonic integrated circuits (PICs) would be a promising platform for miniaturized QKD systems, but they do not naturally accommodate the widely used qubits. Specifically, PICs are less effective in processing polarization-encoded information. In addition, the required long integrated delay line at the transmitters and the receivers for time-bin-encoded QKD schemes significantly increase the footprint of PICs for QKD and limit the scalability.

In this paper, we formulate a new framework to enable long-haul, high-rate, robust, and scalable QKD systems with MD qubits encoded in the orthogonal Slepian sequences' bases. Such an approach is highly robust against turbulence effects in free-space optical (FSO) links and dispersion effects/fiber nonlinearities in fiber-optics channels, thereby improving the QKD distance. Moreover, the MD encoding space enables high spectral efficiency QKD so that SKRs can be substantially improved. Critically, the generation, processing, and detection of Slepian states can be reliably implemented in an integrated quantum photonics platform, based on the proposed electronically controlled waveguide Bragg gratings (EC-WBGs).

2. SLEPIAN-STATES-BASED QKD PROTOCOLS SUITABLE FOR INTEGRATED OPTICS

To address the key challenges described above, we propose take a reconciled approach to develop new MD protocols and tailored efficient PICs to substantially advance scalable, high-rate, and long-haul QKD systems, as illustrated in Fig. 1, for the weak coherent states (WCS)-based scenario. By employing the proposed EC-WBGs, to be implemented in nonlinear PICs, we can develop the quantum transmitters and receivers for MD-QKD schemes and beyond. Compared to fiber Bragg gratings (FBGs) proposed in our recent publication [1], EC-WBGs can be mass fabricated in a PIC platform, in lieu of the liquid crystal platform [3], so that quantum information encoded in a large number of MUBs can be processed. As such, the scalability is significantly improved while substantially reducing the cost. Time-bin encoding is an appealing mean for implementing MD-QKD with telecom compatible components, as demonstrated in [2], where a ~ 4 Mbit/s SKR was achieved, in a back-to-back

configuration. However, as illustrated in Fig. 2(*left*), an *N*-dimensional either time-bin encoding scheme or time-frequency (t.f.) encoding requires *N* time slots with only one time bin, on average, being occupied by a photon, but the rest time slots are left vacuum. In fact, the required optical bandwidth is proportional to *N*, as illustrated in Fig. 2(*left*). To tackle the limitation of time-bin encoding we proposed recently introducing orthogonal Slepian sequence states [1], as illustrated in Fig. 2(*right*). In Slepian-encoded MD-quantum state, *every time slot* is encoded with a single-photon level signal. The temporal-spectral profile, described by a state in the Slepian sequence, represents the encoded MD quantum information. Note that different Slepian states are mutually orthogonal so that a Slepian sequence with *N* elements can be used as an encoding basis. The MD-quantum communication based on Slepian states is anticipated to enjoy high spectral efficiency and low crosstalk between multiplexed quantum channels. As illustrated in Fig. 2(*right*), the consumed optical bandwidth ($1/T$) is independent on the system dimensionality *N*. However, the bandwidth required in time-frequency QKD system is proportional to $1/\tau=N/T$.

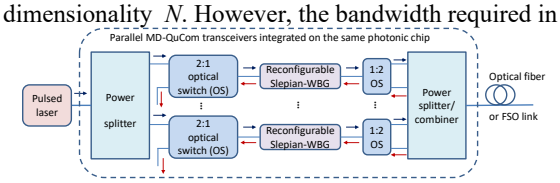


Figure 1. Illustration of parallel MD-quantum communication (QuCom) transceiver integrated on the same quantum photonic chip. Arrow →(←) denotes the transmitting (receiving) direction.

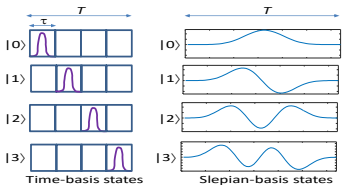


Figure 2. (Left) Time-basis in 4-D t.f. QKD (T: symbol duration, τ: bin duration, τ=T/4). (Right) Slepian- states in 4-D MD-QKD.

Given the space limitations, we only describe the *MD-DV-QKD based on Slepian-WBGs* that does not require the use of entangled states. In basic WBG-based *random base selection prepare-and-measure (PM) protocol*, illustrated in Fig. 3, we employ Slepian-WBGs with mutually orthogonal impulse responses, denoted as $\{|0\rangle, |1\rangle, \ldots, |N\text{-}1\rangle\}$ as the encoding basis for MD-QKD. Alice's encoder is composed of an adaptive, reconfigurable Slepian-WBG, to be implemented in PIC technology, and a circulator. To encode Alice randomly selects the orthogonal impulse response (IR) to be used, and a genetic algorithm (GA) is used to determine the voltages to be applied on electrodes of WBG-devise shown in Fig. 4 to reconfigure to the desired basis function $|n\rangle$. The surface-profile diffraction grating is used as one of substrates. By filling the grating groves with the dielectric, controlled by electrodes on another substrate, the waveguide is created as explained in [3]. The *m*-th electrode (m=1,2,..,M) together with grating waveguide below it serves as the *m*-th segment with refractive index $n(m)$. By properly changing the control voltages, we can tune the overall impulse response to the desired Slepian sequence. In the absence of control voltages, the default grating will represent the central Slepian sequence from the set of Slepian sequences being employed. To speed-up the reconfiguration process, the GA should be run in installation stage only to determine the set of voltages required for each basis function, with corresponding results being stored in a look-up-table (LUT). We propose to employ either aluminum nitride (AlN)- or lithium niobate (LN)-based platform to implement the proposed Slepian-sates-based MD-QKD protocols. Both AlN and LN can be integrated with silicon (Si) platforms [4] and as such are suitable for large-scale integration. To probe for Eve's presence Alice reconfigures the WBG to generate the superposition state $([0\rangle+|1\rangle+ \ldots+ |N\text{-}1\rangle)/\sqrt{N}$. On receiver side, Bob employs another reconfigurable matched-Slepian-WBG. The matched-Slepian-WBG reflects the pulse back, and the SPD at port 3 of circulator detects the presence of pulse, and Bob is able to identify the transmitted symbol, when Alice used the same basis state $|n\rangle$. When non-matched Slepian-WBG is used, Bob will not be able to detect the presence of pulse. To improve the SKR, it is possible to employ a series of matched WBGs, on Bob's side. Only the matched WBG reflects the pulse back, and corresponding SPD at circulator output port 3 will able to detect the presence of pulse and thus identify the matched IR. In sifting procedure, Alice announces the signaling intervals in which she transmitted the superposition states. These are used to check for Eve's presence/activity. If the QBER is higher than the prescribed threshold they abort protocol, otherwise, they continue with the protocol. All other signaling intervals contribute to the sifted key. After that, the classical postprocessing steps are applied.

Regarding the *MD-CV-QKD protocols*, we propose to employ Slepian-states as a new degree of freedom to implement parallel CV-QKD schemes, which is illustrated in Fig. 5, for the discrete modulation CV-QKD case. Given that optical circulators are difficult to implement in integrated optics, we propose to employ the *transmissive WBGs* instead. The transmissive FBGs have been already studied for use in picosecond optical signal processing [5], and we believe that fabrication of transmissive WBGs to generate Slepian-states will be possible too. On Alice side, the laser beam signal is split with the help of 1:*K* star coupler into *K* beams that are used as input of corresponding I/Q modulators. The RF inputs represent *K* parallel RF-assisted M-ary PSK (MPSK) signals, generated with the help of arbitrary waveform generators (AWGs) or digital-to-analog converters (DACs), which are then imposed on different transmissive WBGs with orthogonal impulse responses derived from Slepian sequences. On receiver side, Bob employs 1:*K* star coupler to split the received signal, and in each branch the projection along the matched Slepian basis function is obtained with the help with matched transmissive WBG filter. The *k*-th (k=1,2,…,K) matched WBG output signal undergoes the heterodyne detection, and in the phase noise cancellation (PNC) stage the in-phase and quadrature signals are squared and added, and after the proper

low-pass filter the output signal will be proportional to the modulated RF subcarrier, with frequency difference term being removed out. On such a way, the detected RF subcarrier signal is insensitive to the laser phase noise and frequency offset fluctuations [6]. The classical postprocessing is then applied on the whole raw key.

To illustrate high potential of proposed Slepian-sates-based QKD protocols, in Fig. 6 we provide SKR results per single Slepian-state and single wavelength for both DV- and CV-QKD protocols for different SMF distances. In simulations, we assume that recently fabricated ultra-low-loss fiber with attenuation 0.1419 dB/km at 1560 nm is used [7]. Regarding the CV-QKD protocols, we assume that heterodyne detection is used for both Gaussian modulation (GM) and RF-assisted discrete modulation (DM) with 8-states as described in [6]. The excess noise ε and the electrical noise v_{el} variances (expressed in shot noise units) are used as parameters. For distance of 200 km, when the decoy state protocol is employed, we can achieve SKR of 2.09 kb/s (per single Slepian-state and single wavelength). Now by employing 10 Slepian-states and 10 wavelengths, we can achieve total SKR of 0.209 Mb/s. On the other hand, by employing GM (for $\varepsilon=10^{-3}$ and $v_{el}=10^{-2}$) for the same distance we can achieve 3.6 Mb/s per single Slepian-state and single wavelength. Now be employing both polarization states, 10 Slepian-states, and 10 wavelength channels the total SKR of 720 Mb/s can be achieved, which would represent the record SKR for distance of 200 km. Finally, when the RF-assisted DM with 8 states is employed (for $\varepsilon=10^{-3}$ and $v_{el}=10^{-2}$), we can achieve the total SKR of 0.73 Mb/s×2×10×10=146 Mb/s.

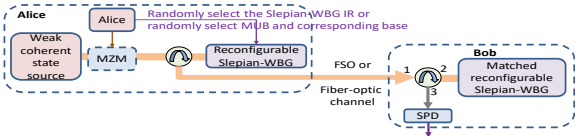


Figure 3. Reconfigurable Slepian-WBG-based WCS-QKD scheme implementing random base selection PM protocol.

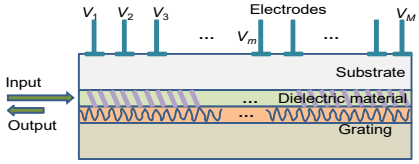


Figure 4. Implementation of Slepian-WBG (modified from [3]).

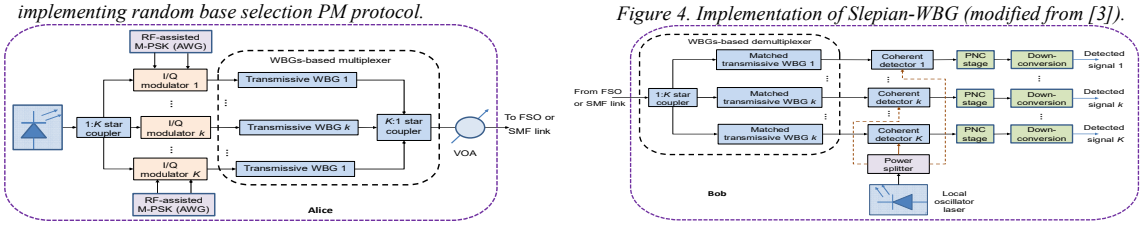


Figure 5. The proposed scheme for parallel WBGs-based RF-assisted CV-QKD protocol: (left) Alice's transmitter and (right) Bob's receiver. (Only the details for single polarization and single wavelength are shown to facilitate the explanations.)

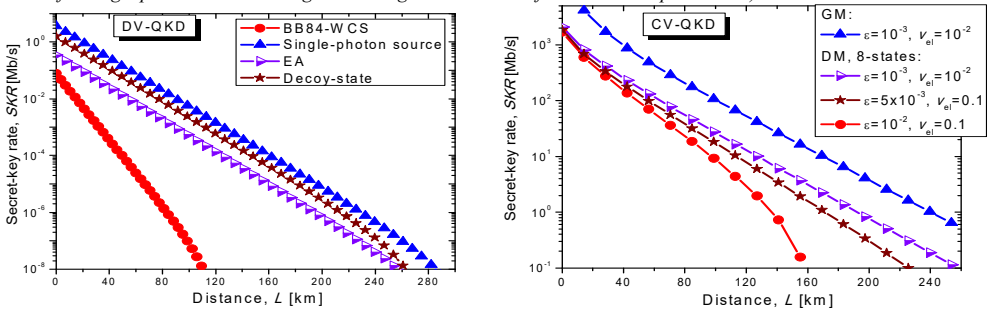


Figure 6. SKRs per single wavelength and single Slepian-sate vs. distance for: (left) DV-QKD and (right) CV-QKD protocols. For DV-QKD protocols, we assume that detector efficiency is 0.2, visibility is 0.99, dark counts' probability is 10^{-6}, the dead time of 10 ns, while the mean photon number is optimum. For CV-QKD, we assume that both detector and reconciliation efficiencies are 0.9 each. The baud rate for CV-QKD is 10 GBd, while RF subcarrier for DM is set to 10 GHz.

REFERENCES

[1] I. B. Djordjevic: FBG-based weak coherent state and entanglement assisted multidimensional QKD, *IEEE Photonics Journal*, vol. 10, no. 4, p. 7600512, 2018.

[2] N.T. Islam, *et al.*: Provably secure and high-rate quantum key distribution with time-bin qudits, *Sci. Adv.*, vol. 3, p. e1701491, 2017.

[3] C. Wu, M. G. Raymer, "Efficient picosecond pulse shaping by programmable Bragg gratings: *IEEE J. Quantum Electron.*, vol. 42, no. 9, pp. 873-884, 2006.

[4] A. Guarino, *et al.*: Electro-optically tunable microring resonators in lithium niobate, *Nature Photonics*, vol. 1, no. 7, p. 407-410, July 2007.

[5] M.R. Fernández-Ruiz, *et al.*: Picosecond optical signal processing based on transmissive fiber Bragg gratings, *Opt. Lett.*, vol. 38, pp. 1247-1249, 2013.

[6] Z. Qu, I. B. Djordjevic: Four-dimensionally multiplexed eight-state continuous-variable quantum key distribution over turbulent channels, *IEEE Photonics Journal*, vol. 9, no. 6, p. 7600408, Dec. 2017.

[7] Y. Tamura, *et al.*: The First 0.14-dB/km loss optical fiber and its impact on submarine transmission, *J. Lightw. Technol.*, vol. 36, pp. 44-49, 2018.

Shaping the optical properties of carbon nanotubes via chirality-selective resonant enhancement in silicon micro-ring resonators

Elena Durán-Valdeiglesias[1,*], Weiwei Zhang[1,†], Carlos Alonso-Ramos[1], Samuel Serna[1], Xavier Le Roux[1], Delphine Marris-Morini[1], Marta Reig[2], Niccolò Casselli[3], Francesco Biccari[3], Massimo Gurioli[3], Arianna Filoramo[2], Eric Cassan[1], and Laurent Vivien[1]

[1] Centre de Nanosciences et de Nanotechnologies, CNRS, Université Paris-Sud, Université Paris-Saclay, C2N, Orsay 91405, France

[2] CEA Saclay, IRAMIS, NIMBE (UMR 3685), LICSEN, Bât. 125, F-91191 Gif-sur-Yvette, France

[3] Department of Physics, University of Florence. European Laboratory for Non-linear Spectroscopy, 50019 Sesto Fiorentino (FI), Italy

e-mail: Elena.Duran@u-psud.fr

[†] Current address: Optoelectronics Research Centre, University of Southampton, Southampton SO17 1BJ, UK

ABSTRACT

Semiconducting single walled carbon nanotubes (s-SWNT) have an immense potential for the development of light sources in the silicon photonics platform. However, two major challenges still need to be addressed: the limited interaction between s-SWNTs and Si waveguides and the single-chirality selection. Silicon micro-ring resonators may overcome the first limitation by exploiting resonant light recirculation. Here, we demonstrate that Si ring resonators can also provide SWNT chirality-selective photoluminescence resonance enhancement, releasing a new degree of freedom to shape the optical properties of s-SWNT. Specifically, we experimentally show selective emission enhancement of either (8,6) or (8,7) SWNT chiralities present in a high-purity polymer-sorted s-SWNT solution by judicious micro-ring geometry design. In addition, we harness the large index contrast of the Si platform to experimentally demonstrate that, opposite to the common knowledge, transverse-magnetic (TM) optical modes can efficiently interact with drop-casted s-SWNTs arranged along the chip surface.

Keywords: carbon nanotubes, hybrid silicon photonics, photoluminescence.

1. INTRODUCTION

Semiconducting single walled carbon nanotubes (s-SWNTs) are direct band gap semiconductors exhibiting absorption, photo- and electro-luminescence at room temperatures from the visible to the mid-infrared wavelengths [1]-[3]. These properties make s-SWNT an appealing material for the realization of light sources and detectors for the silicon photonics technology. Driven by this application, several implementations of hybrid integration of s-SWNT with silicon have been reported, based on micro-ring resonators [4,5] and photonic crystal micro-cavities [6,7]. All these examples focus on the optimization of the interaction between s-SWNT and the transverse-electric (TE) waveguide modes. It is well known that transverse-magnetic (TM) modes in Si wires can provide strong evanescent field that can be leveraged to enhance light interaction with the waveguide surroundings. However, due to the dipole-like behaviour of the s-SWNT, interacting with the main TM electric field component (vertical orientation) would require vertically aligning the s-SWNT on the waveguide surface [8]. Although technically possible, this approach may have a limited scalability. Here we show that TM waveguide modes can have strong interaction with s-SWNT aligned parallel to the chip surface, deposited by simple and scalable drop-casting technique. On the other hand, polymer-based s-SWNT processing techniques, allow removing the vast majority of impurities in s-SWNT solutions, but have problems in achieving single SWNT chirality selection. Here we experimentally demonstrate that proper micro-resonator design enables chirality-selective resonant enhancement of the photoluminescence signal. This novel approach opens a new degree of freedom to implement single-chirality selection in hybrid Si-SWNT devices.

2. RESULTS

The first step is to study the interaction of the TE and TM waveguide polarizations with s-SWNT deposited on top. To do this we consider separately the electric field component aligned along the propagation direction, E_z, and the transversal components aligned transversally, along the chip surface, E_x, and perpendicularly, E_y. These three field orientations would maximize interaction with s-SWNTs aligned with the *z*, *x* and *y* axis, respectively (see Fig. 1). We calculate the dielectric field confinement ξ_{cladd} [9] on top of the waveguide, where the s-SWNT are, for the three electric field components as a function of the waveguide width, W_{wg}, considering waveguide modes with TE and TM polarizations. As shown in Fig. 1 the highest ξ_{cladd} is achieved for the E_y component from the TM mode. However, such configuration requires s-SWNT aligned vertically on the chip surface, rendering this

solution technologically challenging. On the other hand, we find that the E_z component in the TM mode can provide a larger dielectric field confinement than the E_x component in the TE mode, which is conventionally optimized for hybrid SWNT integration. Then, we then chose a waveguide width of W_{wg}=350 nm, yielding $\xi_{cladd} \geq 4.5\%$.

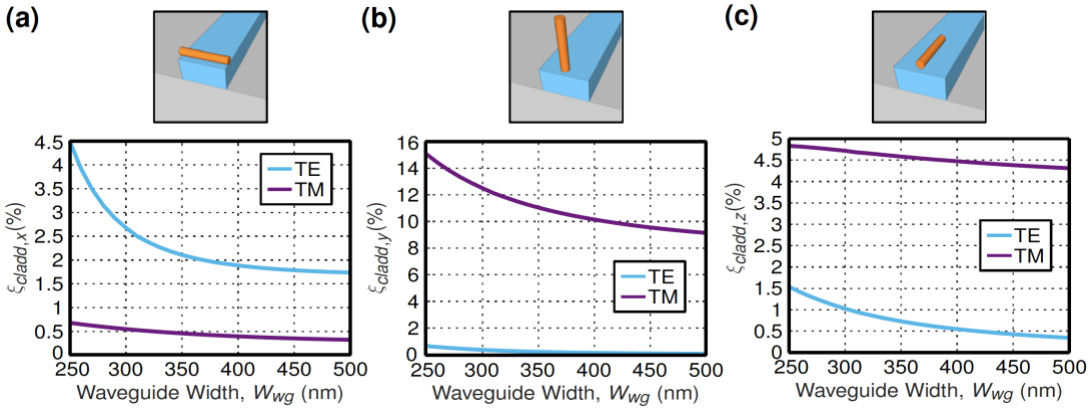


Figure 1. Dielectric field confinement on top of the waveguide, where s-SWNT are, as a function of waveguide width for (a) transversal Ex, (b) transversal Ey and (c) longitudinal Ez components of both fundamental TE and TM modes at wavelength of 1300 nm. Top panels schematically show preferred SWNTs orientation for maximized light-SWNTs interaction for each component of the electric field.

For the implementation of the micro-resonator, we implement an all-pass scheme with an asymmetric configuration where the ring and bus waveguides have a different width (see inset in Fig. 2). The goal is to yield a strong light recirculation enhancement only in a narrow wavelength range, matching the emission of a given s-SWNT chirality. This scheme allows promoting resonance enhancement of only one s-SWNT chirality, even if the solution contains different chiralities. As the bus and ring waveguides have different widths, modes propagating through them have different phase propagation constants, precluding perfect phase matching, thus resulting in a strong chromatic dispersion of the bus-to-ring coupling ratio, i.e., for a given bus-to-ring gap (G), critical coupling condition is achieved for a comparatively narrow bandwidth. Following this asymmetric coupling approach, the ring has a waveguide width of W_{wg}=350 nm (optimized for light-s-SWNT interaction) and the bus waveguide has a width of W_{bus}=270 nm. We chose a ring radius of 5 µm yielding a free-spectral range near 10 nm, easily discernible with our spectrometer.

We fabricated the silicon ring resonators by electron-beam lithography and dry etching. Then the devices were covered with a hydrogen silses-quioxane (HSQ) cladding, opening interaction windows on top of the bus-to-ring coupling region. Finally, we deposited a high-purity s-SWNT solution by drop-casting. This solution contains s-SWNTs with two chiralities, (8,6) and (8,7), with emission near 1200 nm and 1300 nm wavelength, respectively [10]. The bus-to-ring gap was varied between 80 nm and 270 nm.

To characterize the photoluminescence enhancement, we excited the s-SWNTs from the surface of the chip using a continuous wave Titane Sapphire (Ti:Sa) laser with 1.5 mW power at 735 nm wavelength (S22 excitonic transition of s-SWNT). The generated photoluminescence, coupled to the waveguide, was collected at the chip facet with a polarization maintaining lensed fiber. A polarization rotator is used at the input to set the excitation polarization and a polarization filter is used at the output to select TE or TM polarization for the photoluminescence signal. The collected spectrum was analyzed with a 320mm long spectrometer with a 950 lines/mm grating, coupled to a nitrogen-cooled InGaAs array.

In Fig. 2a we present the upper envelope of the collected photoluminescence signal in the TM polarization as a function of the wavelength for different bus-to-ring gaps. As expected from the micro-ring design, photoluminescence enhancement occurs in a narrow wavelength range, with a central wavelength increasing with the gap. This way, smaller gaps yield stronger photoluminescence signal for (8,6) s-SWNTs, while larger gaps promote emission from (8,7) chirality.

To compare the photoluminescence resonant enhancement for (8,6) and (8,7) chiralities, we define the resonance enhancement factor, as the ratio between photoluminescence intensity on resonance (I_{ON}) and off resonance (I_{OFF}), $\alpha = I_{ON}/I_{OFF}$. Then we defined the figure of merit β, as the ratio between the resonance enhancement factor for the (8,6) chirality (at 1200 nm wavelength) and the (8,7) chirality (at 1300 nm wavelength).

Figure 2b presents the figure of merit β, estimated from the measurements in Fig. 2a. It is apparent that smaller gaps favour resonance enhancement of s-SWNTs with (8,6) chirality ($\beta < 0$), while larger gaps promote the resonant enhancement of s-SWNTs with (8,7) chirality ($\beta > 0$). In addition, it can be observed that the maximum enhancement region shifts towards longer wavelengths, as the gap increases, in good agreement with the ring resonator design. These results show that by engineering the dimensions of the micro-ring resonator, it is possible

to promote resonance enhancement of the emission of a single s-SWNT chirality present in a complex mixture comprising different chiralities.

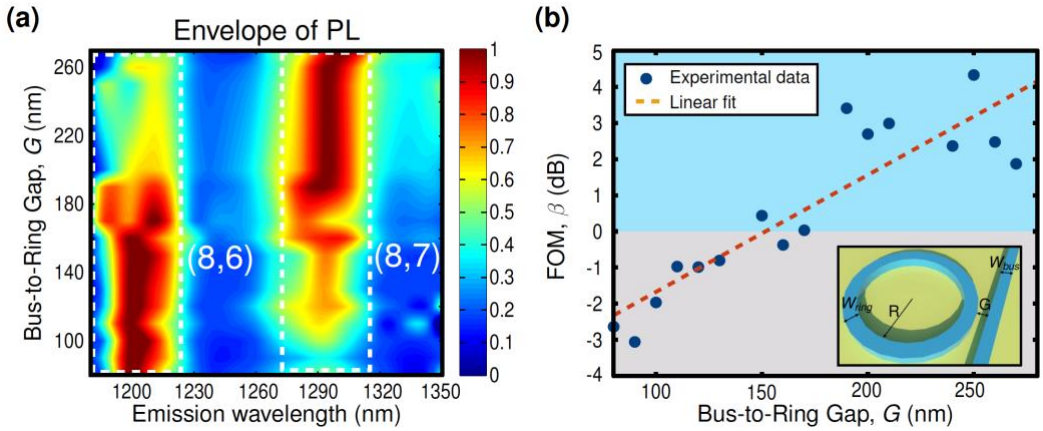


Figure 3. (a) Measured normalized photoluminescence spectrum of SWNTs deposited by drop-casting on Si micro-ring resonators with radius of R= 5 µm, and different bus-to-ring gap (d) Figure of merit estimated from measurements.

3. CONCLUSIONS

Semiconducting single walled carbon nanotubes have been recently identified as a promising solution for the implementation of light sources in silicon photonics. Despite the high purity achieved by polymer-based s-SWNT processing techniques, single SWNT chirality selection remains a challenge. In this work, we demonstrate that by integrating the s-SWNT onto Si micro-ring resonators, it is possible to realize SWNT chirality-selective resonant enhancement of the emission, opening a new SWNT chirality selection mechanism. We experimentally show selective promotion of the resonant enhancement of either (8,6) or (8,7) s-SWNT chiralities present in our solution. Unlike previously reported hybrid Si-SWNT devices [4]-[7], the ring resonators shown here harness the strong longitudinal electric field component of the TM mode to interact with the SWNT. These results open two new degrees of freedom, waveguide mode polarization and selective chirality resonance enhancement, for the implementation of s-SWNT-based devices for the silicon photonics platform.

ACKNOWLEDGEMENTS

The sample fabrication has been performed at the Plateforme de Micro-Nano-Technologie/C2N, which is partially funded by the "Conseil Général de l'Éssonne". This work was partly supported by the French RENATECH network.

REFERENCES

[1] S. Wang, *et al.*: High-performance carbon nanotube light-emitting diodes with asymmetric contacts, *Nano Lett.*, vol. 11, pp. 23–29, Nov. 2010.

[2] F. R. Wang, *et al.*: High conversion efficiency carbon nanotube-based barrier-free bipolar-diode photodetector, *ACS Nano*, vol. 10, pp. 9595–9601, Sep. 2016.

[3] M. Balestrieri, *et al.*: Polarization-sensitive single-wall carbon nanotubes all-in-one photodetecting and emitting device working at 1.55 µm, *Adv. Funct. Mater.*, vol. 27, pp. 1702341-1-1702341-9, Oct. 2017.

[4] A. Noury, et al.: Enhanced light emission from carbon nanotubes integrated in silicon micro-resonator, *Nanotechnol.*, vol. 26, pp. 345201-1-345201-8, Aug. 2015.

[5] E. Durán-Valdeiglesias, *et al.*: Integration of carbon nanotubes in silicon strip and slot waveguide micro-ring resonators, *IEEE Trans. Nanotechnol.*, vol. 15, pp. 583-589, July 2016.

[6] T. H. C. Hoang, *et al.*: Narrow-linewidth carbon nanotube emission in silicon hollow-core photonic crystal cavity, *Opt. Lett.*, vol. 42, pp. 2228–2231, June 2017.

[7] R. Miura, *et al.*: Ultralow mode-volume photonic crystal nanobeam cavities for high efficiency coupling to individual carbon nanotube emitters, *Nat. Comm.*, vol. 5, pp. 5580-2-5580-5, Nov. 2014.

[8] E. Durán-Valdiglesias, *et al.*: Tailoring carbon nanotubes optical properties through chirality-wise silicon ring resonators, *Sci. Rep.*, vol. 8, pp. 11252-1-11252-8, July 2018.

[9] R. M. Osgood, *et al.*: Engineering nonlinearities in nanoscale optical systems: physics and applications in dispersion-engineered silicon nanophotonic wires, *Adv. Opt. Photonics.*, vol. 1, pp. 162-235, Jan. 2009.

[10] N. Izard, *et al.*: Semiconductor-enriched single wall carbon nanotube networks applied to field effect transistors, *Appl. Phys. Lett.*, vol. 92, pp. 243112-1-243112-3, June 2008.

Design and analysis of an integrated widely tunable laser

Andreas Hänsel, Martijn J.R. Heck
Aarhus University - Department of Engineering, Finlandsgade 22, 8200 Aarhus, Denmark
e-mail: A.Hansel@eng.au.dk

ABSTRACT

We report our work on a widely tunable laser to be used for gas sensor applications. The laser design is inspired by earlier work using an intra-cavity filter combining three asymmetric Mach-Zehnder interferometers. In our reworked design, intra-cavity losses and footprint are drastically reduced. We compare calculated outputs with data obtained from our measurements. We achieved a tuning range of more than 10 nm with output powers in the mW range.

Keywords: indium phosphide, gas spectroscopy, photonic integrated circuits, tunable laser

1 INTRODUCTION

Photonic Integrated Circuits (PICs) have the potential to replace bulk optical equipment with cheaper and smaller devices. While for some fields PICs are already the industry standard (telecom cite), only few examples for PIC-based gas sensors have been reported, despite recent publications showing their feasibility[1], [2]. We report a widely tunable laser to be used in a gas detection setup, and discuss its performance with regards to potential ammonia (NH_3) emission monitoring. The chip has been produced as part of a multi-project wafer (MPW) run to ease the technology transfer out of the lab.

2 WIDELY TUNABLE LASER

The laser design is similar to the widely tunable laser reported by Latkowski et al. in 2015[3]. It consists of three stages of asymmetric Mach-Zehnder interferometers (AMZI). This is the state of the art system for wide tuning ranges without the use of high resolution lithography needed for sampled grating distributed Bragg reflectors (SGDBRs). The original ring laser design has been replaced with a Fabry-Perot (FP) structure, where the filter elements and the seminconductor optical amplifier (SOA) are placed between two on-chip mirrors. Both designs are shown in Figure 1. In consequence, amplifier

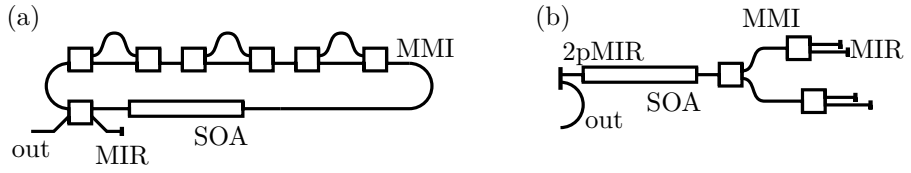


Figure 1. (a) Schematic of the ring laser in[3]. The path has been folded multiple times to make the filter section fit onto the chip. The Mach-Zehnder filter is constructed by splitting and recombining light paths with Multimode interference couplers (MMI), the gain is provided by the on-chip semiconductor optical amplifier (SOA). An MMI-reflector (MIR) is placed at the outcoupling MMI to force clockwise propagating laser light. (b) This work: Similar laser structure based on a Fabry-Perot cavity. Due to the light propagating through each active element twice per round trip, the length of the active elements can effectively be reduced by a factor two with similar performance. In addition to the elements in (a), this design uses a two-port MIR (2pMIR) to emulate a reflecting facet.

and electro-optical phase modulators (EOPMs) are passed through twice per round trip, allowing to half their footprint as compared to the ring laser design. Since SOAs and EOPMs are lossy components, this also improves the overall efficiency of the PIC. In the nested configuration, the losses due to Multimode Interference couplers (MMIs) are reduced, due to fewer light passes. This comes at the expense of a more complex tuning scheme, as the filters cannot be tuned independently and changes in one EOPM will affect multiple filters simultaneously.

2.1 Concept and tuning mechanism

In a Mach-Zehnder interferometer (MZI), light is split into two paths and subsequently recombined again, where any difference in phase leads to a difference in power transmission. In the case of AMZIs, i.e. MZIs with unequal optical path lengths in each arm, this leads to a cosine-modulated transmission

This work is funded by the Project and Innovation Fund Denmark (project number 6150-00030B).

spectrum, reducing the transmission for certain wavelengths. Combining multiple AMZI, each with different arm length differences and hence free spectral ranges (FSRs), allows for tailoring the intra-cavity transmission profile of a laser cavity to select a single longitudinal mode, effectively creating a single mode laser. With proper tuning elements, this single mode laser can be tuned, potentially across the whole supported gain wavelength range. In our design, three of such filters are embedded in a FP laser cavity, with each arm containing an EOPM that allows for 2π phase tuning (double pass). A sketch of the filter design is shown in Figure 2(c), which also highlights the nomenclature for the following calculations. Photons starting from within the cavity at mirror r_1 encounter a gain section with the length L_g and MMIs, which transmit a fraction $\alpha \lessapprox \sqrt{0.5}$ of the light field into each arm. Within these arms light in the top arm propagates through a waveguide of length L_t, before being split again. At the end of each arm, light is reflected with reflectivity r_2, backtracking their initial path. L_{FP} contains all the excess path length, e.g. due to waveguide bends.

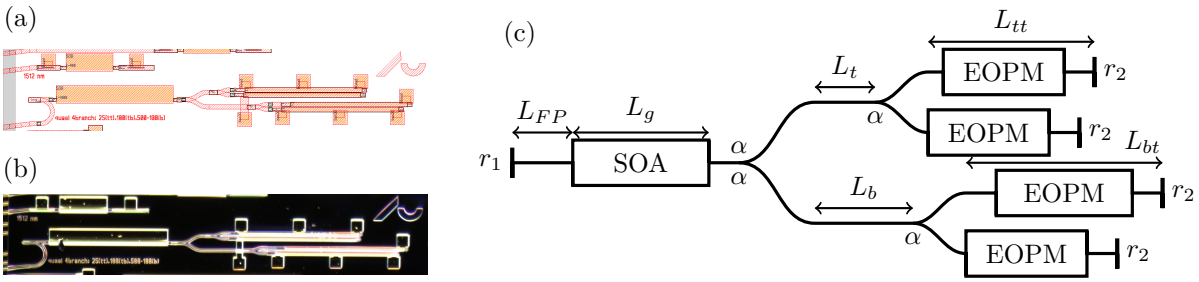


Figure 2. (a) Mask layout and (b) microscope image of the investigated circuit. (c) Sketch of the circuit along with the nomenclature of the used quantities.

During one round trip, phase and amplitude of the light with the propagation constant $\beta = n_{\text{eff}}\frac{2\pi}{\lambda_0}$ can be described by

$$q = r_1 r_2 \alpha^4 e^{2gL_g} e^{2i\beta(L_g+L_{FP})} \left[e^{2i\beta L_t}\left(e^{2i\beta L_{tt}} + e^{2i\beta L_{tb}}\right) + e^{2i\beta L_b}\left(e^{2i\beta L_{bt}} + e^{2i\beta L_{bb}}\right)\right], \quad (1)$$

with n_{eff} as the effective index and λ_0 as the wavelength of the light. Assuming a starting field of 1, the sum of the fields from all round trips can be described by $E_{\text{total}} = \frac{1}{1-q}$ for $|q| < 1$. With E_{total} and the transmittivity t_1 through the exit mirror, the output field below the lasing threshold can be calculated. Phase shifts from the EOPMs can be implemented by adding phase terms to the corresponding elements.

2.2 Mask layout and design

The chip's layout was aligned with the design rules from SMART Photonics and made use of the standard components within this platform. Figure 2 (a) and (b) show the PIC mask design and a microscope photograph of the realized PIC. SOAs and EOPMs had a length of 1 mm, with respective arm length differences of 12.5, 75, and 400 µm. The output waveguide approached the facet under an angle and was anti-reflection coated.

3 SETUP AND MEASUREMENT METHOD

Light has been coupled from the facet of the chip to a single mode lensed fiber. Five needle probes were landed on the corresponding metal contacts on the chip; the SOA was driven with a Thorlabs ITC 8022, the EOPMs were controlled with a National Instruments NI 9264. The ground contact was on the substrate side of the chip. Light in the fiber was split with a 50/50 splitter, one output leading to an Agilent 81633A power meter, the other output leading to a Yenista OSA20.

4 RESULTS

We compared the sub-threshold output of measurement and calculation, as shown in Figure 3. The slight disagreement in both curves is due to gain curve and other device parameters not being fully implemented in the calculations yet. Those parameters will be obtained from future measurements to reach a better match of theory and measurement, and to improve on future designs. Theory and experiment showed the same free spectral range (FSR) of ~ 0.1 nm. Lasing of the laser could be shown. Lasing spectrum and current dependence are shown in Figure 4. For all the measured lines, the side mode suppression ration (SMSR) exceeded 30 dB. A treshold current of 30 mA and a tuning range of more than 10 nm could be shown. The treshold current of ring laser structure was more than twice the value reported here, despite having the same SOA geometry[3]. The narrower tuning range is a

consequence of the low current density at the lasing threshold. While this is beneficial with respect to the power efficiency of the PIC, the supported gain bandwidth is not sufficient. Increasing the current through the SOA will increase the gain bandwidth, but will lead to multi-modal behaviour. A heterodyne measurement of the laser linewidth yielded a full width at half maximum (FWHM) value of $\sim 20\,\mathrm{MHz}$. Continuous tuning over $\sim 1\,\mathrm{nm}$ range has been realised by changing the operating temperature of the device (15°C to 20°C). Voltage-only tuning requires additional characterisation of the device and is work in progress. For slow applications, such as environmental gas sensing, temperature tuning is feasible.

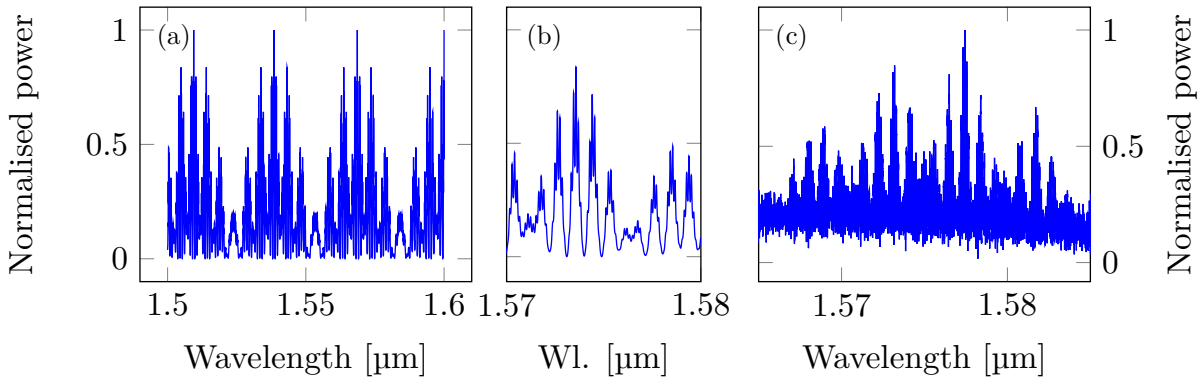


Figure 3. Normalised power spectral density. (a) Calculation, (b) zoom in on calculation, (c) measurement. In both cases, measurement and calculation, the free spectral range (FSR) was $\sim 0.1\,\mathrm{nm}$.

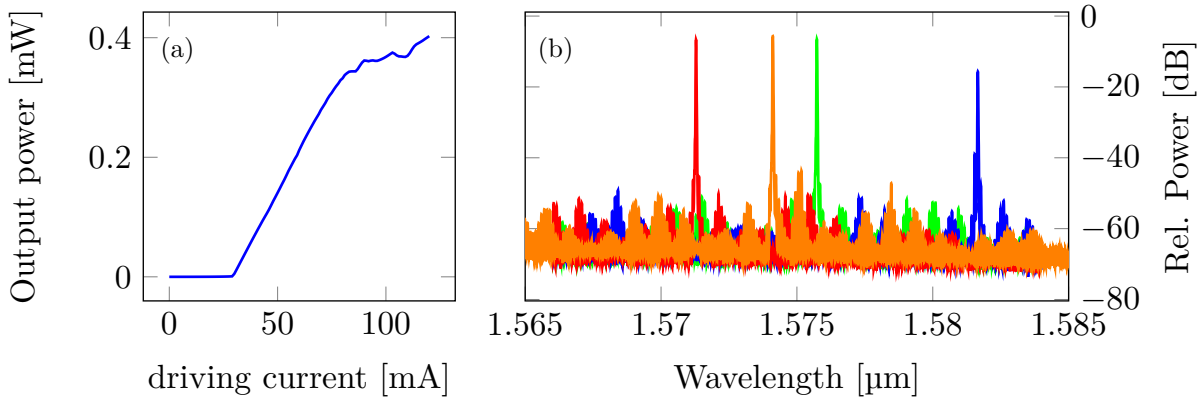


Figure 4. (a) Measured output power after fiber coupling and 50/50 splitter, (b) laser spectra for four different voltage filter settings. The side mode suppression ratio (SMSR) exceeded 30 dB.

5 CONCLUSION AND OUTLOOK

We presented our work towards a widely tunable laser to be used for gas spectroscopy. With the current configuration, more than 10 nm of tuning range could be shown, which is sufficient for multi-species gas sensing. Future work is expected to increase this tuning range and yield the device parameters required to set up continuous tuning algorithm. An increased tuning range can be achieved by increasing the threshold current density in the SOA, e.g. by reducing the SOAs length or decreasing the Q factor of the cavity. The former will further reduce the footprint, while the latter allows for additional filters in the cavity.

REFERENCES

[1] A. Hänsel and M. Heck, "Feasibility of Telecom-Wavelength Photonic Integrated Circuits for Gas Sensors," Sensors, vol. 18, 2870, 2018.

[2] L. Tombez, E. J. Zhang, J. S. Orcutt, S. Kamlapurkar, and W. M. J. Green, "Methane absorption spectroscopy on a silicon photonic chip," Optica, vol. 4, pp. 1322–1325, 2017.

[3] S. Latkowski et al., "Novel Widely Tunable Monolithically Integrated Laser Source," IEEE Photonics Journal, vol. 7, pp. 1–9, 2015.

Heavily doped Er^{3+}/Yb^{3+}planar waveguides on silica for high gain per unit length amplification in the C-band

(Student Paper)

Eduardo Henriques Dos Santos [1], Billy Richards [1], Eric Kumi Barimah [1], Paul Farrugia [2], Gin Jose [1]
[1] *School of Chemical and Process Engineering, University of Leeds, Clarendon Road, Leeds, United Kingdom*
[2] *XTERA, Bates House, Church Road, Harold Wood, Essex, United Kingdom*
e-mail: pm14ehds@leeds.ac.uk

ABSTRACT

This paper explores potential design and the likely characteristics of an Er^{3+}/Yb^{3+}co-doped waveguide amplifier based on a planar waveguide fabricated using the ultrafast laser plasma implantation method. Using this technique a layer of silica glass is modified by the implantation of tellurite glass particles in a silica glass substrate, resulting in a rare earth rich region with demonstrated concentrations of up to $1.63x10^{27}$atoms/m^3. Experimental measurements of a planar waveguide's properties are shown and the theoretical gain achievable is calculated using numerical simulations, resulting in a value of 9.5 dB/cm and a theoretical maximum of 27 dB/cm.

Keywords: Waveguide amplifiers, Erbium/Ytterbium co-doped, modelling, spectroscopy, optical communications

1 INTRODUCTION

The ubiquitous use of silica based optical fibre and Erbium Doped Fibre Amplifiers (EDFA) is due to the low loss in the Er^{3+}emission band and chemical stability. However optical fibre and indeed any other potential silica based application, suffers from low rare earth (RE) ion solubility in the host material, requiring the use of long interaction volumes (>5 metres) to achieve any meaningful degree of amplification, making it impractical for applications where size is a concern [1], [2].

Extensive research efforts have been focused on finding suitable host materials with desirable properties such as high lifetime of the Er^{3+} $^4I_{13/2}$level and capacity to incorporate high concentration of RE ions. Several promising hosts have been studied with a variety of advantages and disadvantages over silica glass [1]. A recurring theme in these efforts is that the investigated hosts are either difficult to fabricate, chemically unstable or incompatible with silica glass, impeding efforts to integrate them into the optical network.

A recently developed technique [3], [4], utilized a femtosecond laser to generate a stream of plasma and nanoparticles [5] from a rare earth (RE) rich tellurite target glass to implant it into a silica glass substrate. This created a highly doped rare earth tellurite silica (RETS) metastable region in the glass with RE ion concentrations of up to $1.63x10^{27}$ atoms/m^3 with a photoluminescence lifetime of 9.1 ms at a wavelength of $1.5\,\mu m$. In contrast the typical achievable concentration without significant clustering in silica is in the order of 10^{24} atoms/m^3 [1].

In order to guide the development of an Er^{3+}/Yb^{3+} doped waveguide amplifier (EYDWA) the emission and properties of a planar RETS waveguide were measured and this data was incorporated in an amplification model [6] in order to estimate the gain of the amplifier.

2 EXPERIMENTAL PROCEDURE

The planar waveguide was created by sequentially ablating 1% mol Er_2O_3 and 1% mol Yb_2O_3 tellurite target glasses, with a 42 fs, 1 kHz pulsed laser (KM Labs, Wyvern). This process was carried out in 12 cycles of 10 minutes Er_2O_3 glass alternated with 20 minutes of Yb_2O_3 glass, for a total of 6 hours. The composition of each target is shown in table 1.

TABLE 1. TARGET GLASS COMPOSITIONS USED FOR THE FABRICATION

mol % concentration				
TeO2	**Na2O**	**ZnO**	**Er_2O_3**	**Yb_2O_3**
79%	10%	10%	1.00%	-
79%	10%	10%	-	1.00%

The refractive index and thickness of the resulting modified layer was measured using a prism coupler (Metricon 2010) with 633 nm laser. The lifetime was measured with a time resolved fluorescence spectrometer (Edinburgh Instruments FLS970) by irradiating the sample with a 976 nm fibre-pigtailed diode laser operating at 100 mW being triggered every 100 ms for 1 ms.

3 RESULTS

The material properties are summarized in table 2

TABLE 2. PLANAR WAVEGUIDE PROPERTIES

Property	Value
Thickness	1.153 µm±0.008 µm
Refractive index	1.6150±0.0002
Lifetime	8.4 ms

Applying Marcatili's method [7] to a buried waveguide with the aforementioned properties and assuming substrate refractive index of 1.45, single mode behaviour is obtained for both 976 nm pump and wavelengths from 1500 nm to 1600 nm typically used in communications. Due to the high refractive index contrast between the core and substrate, a large portion of the energy is contained inside the waveguide as evidenced by Fig.1 the large effective refractive indices of 1.55 and 1.50 for the pump and signal respectively. This results in high overlap between the amplification media and the pump and signal fields further enhancing gain.

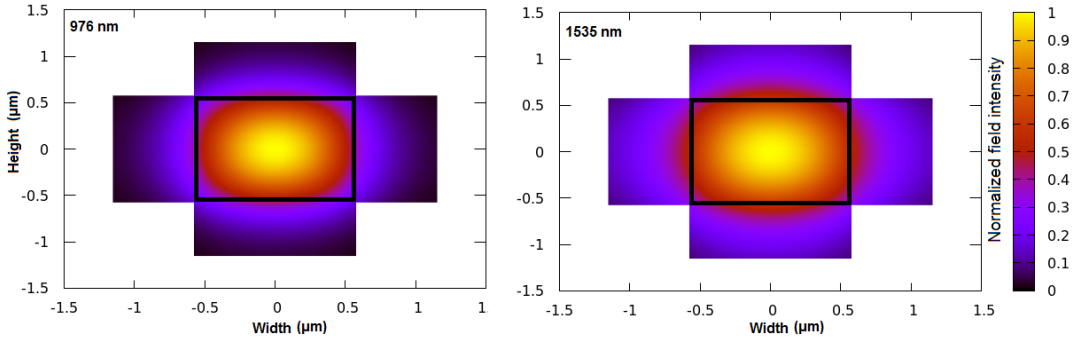


Figure 1. Normalized electric field propagation inside the waveguide

Based on previous studies [3] the expected total RE concentration is approximately 1.61x10^{21} ions/cm^{-3} for a two target process, using target glasses with 1% RE concentration. Time was partitioned in a 1:2 ratio between Er^{3+}rich and Yb^{3+}rich tellurite target glass, assuming a similar concentration partition Er^{3+} ions of 0.537x10^{21} cm^{-3} in the sample, with the remaining fraction as ytterbium ions. By using the absorption and emission cross-sections of germanium-aluminium silicate glasses found in [8], the simulated gain for a signal of 100 signals with -60 dBm power and 20 dBm of 976 nm pump power at this Er^{3+}concentration is shown in Fig.2

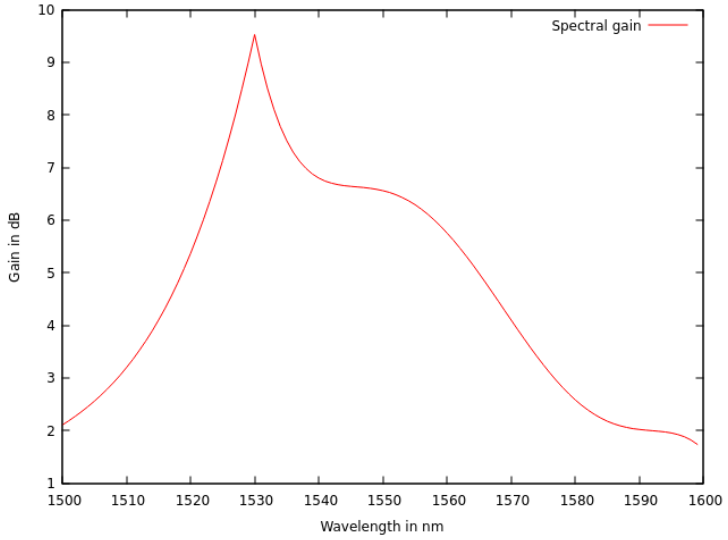


Figure 2. Theoretical gain per wavelength for low signal power

A maximum value of 9.5 dB/cm is achieved at 1530 nm and drops down to 5.2 dB/cm at 1564 nm which corresponds to the behaviour of the cross section data used for Ge-Al-Si glass amplifiers, however the RETS

layer can potentially extend the amplification window to 1600 nm as is the case with tellurite only amplifiers [9]. An upper theoretical gain limit of 27 dB/cm at 1530 nm is achievable using 1.61×10^{21} ions/cm^{-3} of pure erbium ions, however experimentally this value is unlikely due to significant Er^{3+}-Er^{3+}interactions at this concentration level as noted by Quimby et al. [10] and losses due to waveguide imperfections.

4 CONCLUSION

A 9.5 dB/cm gain is theoretically possible via femtosecond aided RETS layer formation with high refractive index contrast, enabling the fabrication of small format waveguide amplifiers with large effective index and consequently lower losses in complicated geometries (bends, splits, etc). It is likely gain values closer to the upper bound of 27 dB/cm may be achievable by judiciously co-doping with Yb^{3+} to enhance absorption of 976 nm pump light and reduce detrimental Er^{3+}-Er^{3+} interactions.

ACKNOWLEDGMENT

The author would like to thank XTERA for their financial support and technical advice throughout this PhD. This work was supported by EPSRC grant EP/M015165/1

REFERENCES

[1] W. J. Miniscalco, "Erbium-doped glasses for fiber amplifiers at 1500 nm," *Journal of Lightwave Technology*, vol. 9, no. 2, pp. 234–250, Feb 1991.

[2] G. C. Righini and A. Chiappini, "Glass optical waveguides: a review of fabrication techniques," *Optical Engineering*, vol. 53, no. 7, p. 071819, 2014. [Online]. Available: http://dx.doi.org/10.1117/1.OE.53.7.071819

[3] J. Chandrappan, M. Murray, P. Petrik, E. Agocs, Z. Zolnai, A. Tempez, S. Legendre, D. P. Steenson, A. Jha, and G. Jose, "Doping silica beyond limits with laser plasma for active photonic materials," vol. 5, no. 12, p. 2849. [Online]. Available: https://www.osapublishing.org/abstract.cfm?URI=ome-5-12-2849

[4] J. Chandrappan, M. Murray, T. Kakkar, P. Petrik, E. Agocs, Z. Zolnai, D. Steenson, A. Jha, and G. Jose, "Target dependent femtosecond laser plasma implantation dynamics in enabling silica for high density erbium doping," vol. 5, p. 14037. [Online]. Available: http://www.nature.com/articles/srep14037

[5] T. Mann, R. Mathieson, M. Murray, B. Richards, and G. Jose, "Femtosecond laser ablation properties of Er^{3+} ion doped zinc-sodium tellurite glass," *Journal of Applied Physics*, vol. 124, no. 4, p. 044903, Jul. 2018. [Online]. Available: http://aip.scitation.org/doi/10.1063/1.5040947

[6] C. Giles and E. Desurvire, "Modeling erbium-doped fiber amplifiers," *Journal of Lightwave Technology*, vol. 9, no. 2, pp. 271–283, Feb. 1991. [Online]. Available: http://ieeexplore.ieee.org/document/65886/

[7] E. A. J. Marcatili, "Dielectric rectangular waveguide and directional coupler for integrated optics," *The Bell System Technical Journal*, vol. 48, no. 7, pp. 2071–2102, Sept 1969.

[8] W. Barnes, R. Laming, E. Tarbox, and P. Morkel, "Absorption and emission cross section of Er/sup 3+/ doped silica fibers," *IEEE Journal of Quantum Electronics*, vol. 27, no. 4, pp. 1004–1010, Apr. 1991. [Online]. Available: http://ieeexplore.ieee.org/document/83335/

[9] A. Mori, Y. Ohishi, and S. Sudo, "Erbium-doped tellurite glass fibre laser and amplifier," *Electronics Letters*, vol. 33, no. 10, p. 863, 1997. [Online]. Available: http://digital-library.theiet.org/content/journals/10.1049/el_19970585

[10] R. S. Quimby, W. J. Miniscalco, and B. Thompson, "Clustering in erbium-doped silica glass fibers analyzed using 980 nm excited-state absorption," *Journal of Applied Physics*, vol. 76, no. 8, pp. 4472–4478, Oct. 1994. [Online]. Available: http://aip.scitation.org/doi/10.1063/1.357278

Novel Concept for Polarization Splitting in InP Platforms

Shahram Keyvaninia, Patrick Runge, Frederik Schröder and Martin Schell
Fraunhofer Heinrich-Hertz-Institute, Einsteinufer 37, 10587 Berlin, Germany
e-mail: shahram.keyvaninia@hhi.fraunhofer.de

ABSTRACT

A novel concept for the monolithic integration of a polarization beam splitter (PBS) on InP platforms is presented. The device is utilizing a waveguide integrated 1x2 power splitter, a variable optical attenuator (VOA) and a semiconductor optical amplifier (SOA) both based on multiple-quantum wells (MQWs). The separation of TE- and TM- polarized light is resulting from the power splitter and the different absorption and amplification coefficients in MQW-VOA and MQW-SOA. By engineering the power-splitting ratio and the MQW structure a high polarization extension ratio (PER) of above 20 dB for both polarizations over more than 40 nm optical bandwidth can be achieved.

Keywords: PBS, InP integration, VOA, SOA, polarization multiplexing, polarization diversity, photodetector

1. INTRODUCTION

Polarization control is a key element for today's polarization multiplexed optical networks and interferometric sensor systems. For the implementation of polarization demultiplexing at the receiver, a polarization beam splitter (PBS) and optionally a polarization rotator are needed. One option to implement the polarization demultiplexing stage is based on discrete polarization components, usually implemented in free-space optics [1]. The other approach is based on monolithically integrating the polarization components together with the receiver in a photonic integrated circuit (PIC) [2-3]. Monolithic InP-based PICs offer compelling solutions for large scale photonic integration, while also providing the same inherent scalability that has benefited Si-based integrated electronics. For monolithic integration, challenges are associated with active/passive integration, optical isolation and on-chip polarization handling [3]. The current designs of the PBS can be categorized into two types, mainly mode coupling and mode evolution. The mode-coupling-based PBS [4-6], utilizing the mode beating behaviour determined by device geometry and operating wavelength, is inherently fabrication sensitive and wavelength dependent, while also often an active element (e.g. thermal tuning heater) needs to overcome the fabrication mismatches. The mode-evolution-based PBS has a relatively long device length, required to achieve adiabatic transition [7]. Recently, a new concept for polarization divers detection has been proposed in [8] by making use of the properties of MQWs to detect TE and TM polarized light separately. Although a much smaller footprint proposed by this design, the speed of MQW-PD is mainly limited by the transit time in the MQW structures.
In this work, a novel design for polarization splitting is proposed. The polarization splitting with high PER can be achieved by utilizing separately absorbed/amplified signals in MQW-VOA/SOA. Since the MQW-SOA/VOA sections can be integrated together with lasers by using the same epitaxy layers, no extra regrowth step is needed for integration of the proposed PBS. This device has several interesting features for monolithic InP-integrations, offering the polarization diverse detection not only for telecommunications applications e.g. polarization diverse coherent receivers [2-4], but also for sensing and imaging applications, such as optical coherence tomography (OCT) imaging and interferometric sensing [9, 10].

2. DESIGN AND DISCUSSION

Figure 1 shows the schematic structure of the proposed device. The input signals, consisting of a mixed TE- and TM- polarized signal, are split into two arms depend on the design application by less than 50%. The splitter can be realized by using an optical element such as a directional coupler or a multi-mode interference coupler.
The signal in the upper arm passes through a monolithically integrated VOA. The TE polarized signal is absorbed by the VOA while the TM passes through the VOA and therefore will remain in the arm having low-loss. These losses are mainly due to the joints of the different epitaxial stacks. The loss for TM-polarized signal is expected to be less than 2.5 dB. By improving the butt-joint technology a total loss of less than 2 dB is achievable for the TM signal. The PER for the TM signal in this arm can be engineered by choosing an appropriate design of the MQW-VOA. A PER above 20 dB for above 40 nm optical bandwidth can be achieved. Figure 2 (left) shows the polarization dependent loss (PDL) measured for a VOA integrated with a high-speed PD while the PDL measured for the PD is <0.5 dB [11]. As shown in Fig. 1, the other part of the incoming signals (e.g. 10%) will be coupled into the lower arm. The TE-polarized signal will be amplified in the SOA while the TM signal passes through the SOA having approx. the same loss as the TM signal in the upper arm. In this arm a weaker TM signal helps to achieve a higher PER. Therefore, the higher PER for the TE signal can be enhanced by engineering the coupling ratio of the power splitter and the net gain in the SOA. Figure 2 (right) shows an example for the net gain of the MQW-SOA integrated with a high speed PD. The TE signal can be amplified for more than 20 dB, including the coupling loss in the joint section, over an optical bandwidth of 40 nm in this arm.

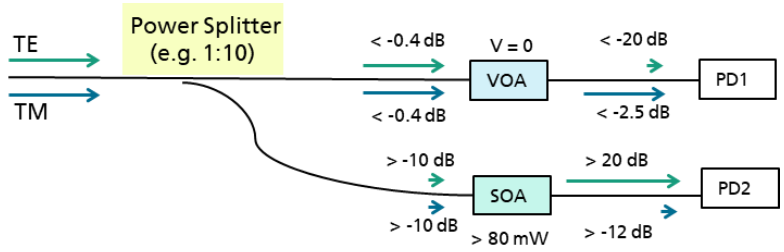


Figure 1.Proposed PBS based SOA and VOA integration with polarization independent PDs and estimated power penalties and PER in each arms for both polarization-states

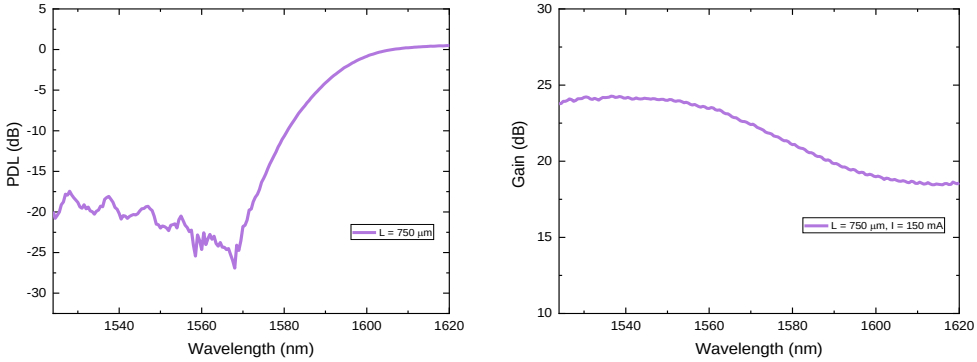


Figure 2. PDL measurement (left) of the integrated VOA, gain spectrum (right) of the integrated SOA using -15 dBm input signals; with the high-speed PD measured at room temperature.

The optimized power consumption of the MQW-SOA should be taken into account to achieve higher PER. According to Fig. 1, a weaker signal in the lower arm would be desired to achieve a higher PER for both polarizations as well as a lower insertion loss at the upper port. Therefore, the pre-amplified signal quality using SOAs integrated with high-speed PDs was investigated, especially if the detected data signal shows bit pattern effects. The results are derived from pseudorandom binary sequence (PRBS) measurements. Fig. 3 (left) shows the generated optical 56GBd NRZ signal with a pattern length of 2^{31}-1 detected by the optical input of a Keysight sampling oscilloscope. The measurement result of a photodetector chip without integrated SOA is presented in Fig.2 (right). For detecting the electrical signal of the photodetector chip, a RF probe head with a bias-T and the electrical input of the sampling oscilloscope with 70 GHz bandwidth was used. For the measurement, a SHF electrical pattern generator feeding an optical modulator with TE-polarized light at 1550 nm is used [12]. The generated optical 56 GBd NRZ signal with a pattern length of 2^{31}-1 was detected by the optical input of a Keysight sampling oscilloscope. In Fig. 2 (right) the signal quality is slightly worse for the photodetector chip even for high optical input powers, because of discrete RF components needed to connect the photodetector chip to the oscilloscope. Measurement results of a photodetector chip with a monolithically integrated SOA are presented in Fig. 4. The eye diagrams do not show any degradation due to bit pattern effects and the detected signal quality is the same as for a photodetector without SOA. Since the resonance frequency of the SOA is in the range of 1 GHz, it becomes clear that for a 56 GBd PRBS signal with a 2^{31}-1 pattern length, no bit pattern effects can be observed for the photodetector chip with monolithically integrated SOA. The measurement confirms, if the SOA is driven below its saturated regime, the patterning effects even above 56 GBds due to carrier fluctuations are expected to be small [12]. Therefore, the presented PBS scheme only shows no pattern effects for data signals with high symbol rates above the carrier lifetime frequency of the SOA gain material or below the carrier lifetime frequency.

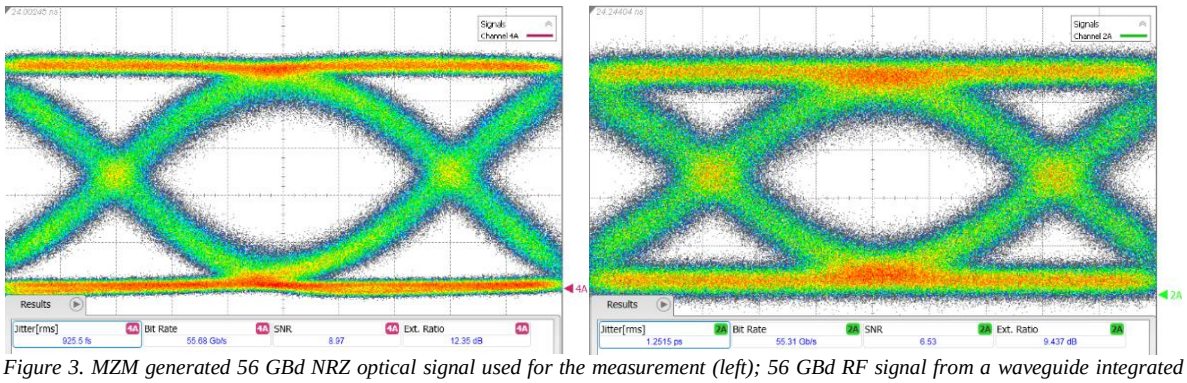


Figure 3. MZM generated 56 GBd NRZ optical signal used for the measurement (left); 56 GBd RF signal from a waveguide integrated photodetector without SOA for 0 dBm optical input power (right)

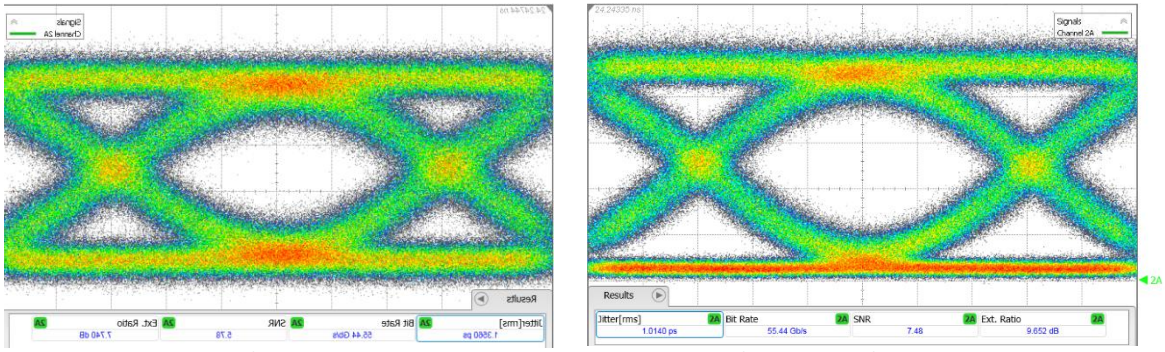


Figure 4. 56 GBd RF signal from a photodetector with monolithically integrated SOA for -15 dBm (left) and 0 dBm (right) optical input power

3. CONCLUSIONS

We presented a new PBS design based on the monolithic integration in InP technology. This device proposes a new polarization diversity network using the property of MQW-VOA and MQW-SOA. The separation of TE- and TM- polarized light is resulting from the 1x2 power splitter and the different absorption and amplification coefficients in MQW-VOA and MQW-SOA. By further improving the MQW structure and power-splitting ratio, a high PER for both polarization above 20 dB and 40 nm of optical bandwidth with an insertion loss of less than 2 dB can be achieved. The presented PBS can be integrated together with the lasers and uses the same epitaxy layer stack. Therefore, no extra regrowth step is needed. The concept offers a key component for next generation telecommunication devices and photonic sensors.

REFERENCES

[1] A. Beling et al., "Fully-integrated polarization-diversity coherent receiver module for 100G DP-QPSK," 2011 Optical Fiber Communication Conference and Exposition and the National Fiber Optic Engineers Conference, Los Angeles, CA, pp. 1-3, 2011.

[2] R. Kaiser, D. Trommer, H. Heidrich, F. Fidorra, and M. Hamacher, “Heterodyne receiver PICs as the first monolithically integrated tunable receivers for OFDM system applications,” Optical and Quantum Electronics, vol. 28, pp. 565–573, 1996.

[3] R. Nagarajan et al., "Large-scale photonic integrated circuits," in IEEE Journal of Selected Topics in Quantum Electronics, vol. 11, no. 1, pp. 50-65, Jan.-Feb. 2005.

[4] C.R. Doerr et al.,“Packaged monolithic InP dual-polarization and dual-quadrature coherent receiver,” IEEE Photonics Technology Letters, Vol. 23, N0. 11, pp. 694-969, 2011.

[5] L. M. Augustin et al., "A Single Etch-Step Fabrication-Tolerant Polarization Splitter," in Journal of Lightwave Technology, vol. 25, no. 3, pp. 740-746, March 2007.

[6] N. Abadía, X. Dai, Q. Lu, W. Guo, D. Patel, D. Plant, and J. Donegan, "Highly fabrication tolerant InP based polarization beam splitter based on p-i-n structure," Opt. Express 25, 10070-10077 (2017).

[7] W. Yuan, K. Kojima, B. Wang, T. Koike-Akino, K. Parsons, S. Nishikawa, and E. Yagyu, "Mode-evolution-based polarization rotator-splitter design via simple fabrication process," Opt. Express 20, 10163-10169 (2012).

[8] Tobias Beckerwerth, Shahram Keyvaninia, Gan Zhou and Patrick Runge “Advanced Polarization Diverse Coherent Receiver Using Waveguide Integrated MQW Photodiodes”, Advanced Photonics Congress, Zurich, 2018.

[9] A. Kersey, M. Marrone, and A. Dandridge, "Polarization diversity detection for fiber interferometers using active feedback control of output polarization-mode selection," Opt. Lett. 15, 1315-1317, 1990.

[10] Lee, H. Pahlevaninezhad, V. Yang, S. Lam, C. MacAulay, and P. Lane, "Fiber-optic polarization diversity detection for rotary probe optical coherence tomography," Opt. Lett. 39, 3638-3641, 2014.

[11] P. Runge, G. Zhou, F. Ganzer, S. Seifert, S. Mutschall and A. Seeger "Polarization Insensitive Coherent Receiver PIC for 100GBaud Communication", 2016 Optical Fiber Communication Conference (OFC), Anaheim, USA, 2016.

[12] P. Runge, et al., " Photodetector with Monolithically Integrated SOA for Pre-Amplification of High-Speed Signals with 56GBd and Above ", 2019 Optical Fiber Communication Conference (OFC), Th3B.4, San Diego, USA, 2019.

Extracting Coupling Coefficients of Directional Couplers.

Umar Khan [1,2], Yufei Xing [1,2], Antonio Ribeiro [1,2], Wim Bogaerts [1,2]
[1]*Ghent University - imec, Technologiepark 126, 9052 Ghent, Belgium*
[2]*Center for Nano- and Biophotonics, Ghent University, Belgium*
e-mail: Umar.Khan@ugent.be

ABSTRACT

We experimentally demonstrate the extraction of dispersive directional coupler parameters (coupling coefficients) using optical transmission measurements. The coupling coefficients are extracted using both direct transmission of directional couplers and through more complex *Mach-Zehnder interferometers* (MZI) and we conclude that coefficients using the MZI circuits give better accuracy.

Keywords: silicon photonics, directional couplers, parameter extraction, coupling coefficients, behavioral model, spectrum fitting.

1 INTRODUCTION

The *directional coupler* (DC) is a four-port reciprocal passive optical device frequently used for splitting and combining of optical power in ring resonators, *Mach-Zehnder Interferometers* (MZI) and optical filters. In a DC, two optical waveguides are brought so close to each other that light starts coupling evanescently. This evanescent coupling is sensitive to changes in geometrical parameters i.e. the gap between the waveguides and waveguide cross-sections. This is especially true in high-contrast silicon photonics, where the coupling parameters become quite wavelength dependent, and nanometer-level change in geometrical parameters due to fabrication variations can result into noticeably different power coupling. Such deviations will propagate and accumulate in circuits (especially filter circuits) and deteriorate the overall circuit performance[1]. Given both the importance of the component and its sensitivity, a method to accurately extract the coupling of a fabricated DC is very useful. In this research, we experimentally demonstrate the extraction of coupling coefficients of fabricated DCs using transmission measurements on two different methods, i.e. the 'naked' DC and an MZI with embedded DCs, and compare the accuracy of these two methods.

2 EXTRACTION OF COUPLING COEFFICIENTS

The coupling coefficients of DC can be extracted using different approaches [2] but in this research we focus on extraction by the fitting of the measured optical spectrum to a dispersive behavioral model. A *coupled mode theory* (CMT) based behavioural model for the DC [3] is summarized in Fig. 1a. In this model, the coupling in a DC is divided into two contributions, i.e. a length dependent field coupling $\kappa'(\lambda)$ in the straight section and the length independent 'lumped' coupling $\kappa_0(\lambda)$ in the bend sections. The wavelength dependence of these coupling coefficients is captured in a second order polynomial expansion:

$$\kappa'(\lambda) = \kappa'(\lambda_0) + (\lambda - \lambda_0)\frac{\partial \kappa'}{\partial \lambda} + (\lambda - \lambda_0)^2 \frac{\partial^2 \kappa'}{\partial \lambda^2} \tag{1}$$

$$\kappa_0(\lambda) = \kappa_0(\lambda_0) + (\lambda - \lambda_0)\frac{\partial \kappa_0}{\partial \lambda} + (\lambda - \lambda_0)^2 \frac{\partial^2 \kappa_0}{\partial \lambda^2} \tag{2}$$

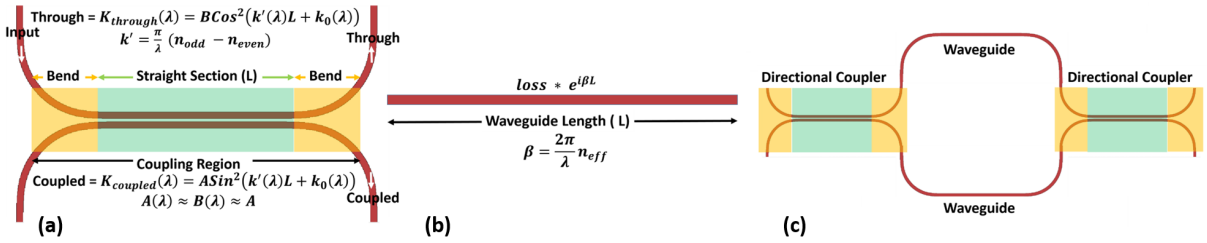


Figure 1. (a) The behavioral model for the directional coupler. Coupling length dependent power coupling in the straight section is represented as κ'. The coupling in the bend sections which is independent of the coupling length is represented as κ_0. The field coupling κ' is determined by the difference between the even and odd modes in the coupling section. (b) The behavioral model for a straight waveguide. Waveguide loss, effective index (n_{eff}) and group index (n_g) are the model parameters. (c) An MZI consisting of directional couplers and waveguides can be simulated using the behavioral models for couplers and waveguides.

We have neglected the higher order terms as they do not add much to the extraction accuracy but do complicate the fitting process. The behavioural model was implemented in the circuit simulator CAPHE from Luceda Photonics[4]. This model has six model parameters to be fitted, i.e. κ', $\frac{\partial\kappa'}{\partial\lambda}$, $\frac{\partial^2\kappa'}{\partial\lambda^2}$,$\kappa_0$, $\frac{\partial\kappa_0}{\partial\lambda}$ and $\frac{\partial^2\kappa_0}{\partial\lambda^2}$.

The MZI circuit consists of a splitter, a combiner and two waveguide arms that connect the splitter to the combiner, Fig. 1c. For the waveguide arms the model has two parameters: the effective index n_{eff} and the group n_g index at a reference wavelength λ_0, shown in Fig. 1b. This results in first-order wavelength dispersion of the effective index:

$$n_{eff}(\lambda) = n_{eff} - (\lambda - \lambda_0) \cdot \frac{n_g - n_{eff}}{\lambda_0} \tag{3}$$

So, fitting the MZI spectrum introduces two additional model parameters (n_{eff} and n_g) on top of the six DC model parameters. The extraction using both the naked DC and the MZI circuit is explained below.

2.1 Extraction using 'Naked' Directional Couplers

DCs of different coupling lengths with same waveguide cross-sections (0.45μm x 0.22μm), coupling gaps (0.25μm) and a bend radius of 5μm were designed to extract the field (κ') and lumped (κ_0) coupling coefficients. Cross-sections, coupling gaps and bending radius were kept same to keep coupling coefficients same for all the devices. The coupling lengths were varied to separate the contributions from the straight and the bend sections, as a measurement of a single coupling length cannot distinguish between the two. Designed devices were fabricated using e-beam lithography through the Australian Silicon Photonics prototyping service at RMIT Melbourne. Please note that fabricated devices were air-clad from the top.

Fabricated DCs were optically measured using a tunable laser and a photo-detector in a clean-room environment. Measured spectra of four devices with coupling lengths of 10, 20, 30 and 40 μm were fitted simultaneously to the CAPHE model shown in Fig. 1a using the *non-linear least-squares minimization and curve-fitting* (lmfit) tool for Python. The fitting was performed for same field (κ') and lumped (κ_0) coupling coefficients as bending radii, cross-sections and coupling gaps were the same for all the fitted devices. The measured and the fitted spectra are shown in Fig. 2c below. Ideally, two spectra can also be used for fitting but we have used four for increased robustness and accuracy. The accuracy can further be improved by fitting both through and cross ports simultaneously. The extracted dispersive coupling coefficients are shown in Fig. 2a and 2b. It can be noticed that the coupling coefficients increase with increasing wavelength according to our expectations.

2.2 Extraction using Mach-Zehnder Interferometers

We designed MZI circuits having the same DC as splitter and combiner to extract the coupling coefficients. Again, we used circuits with couplers of different lengths keeping waveguide cross-sections (0.45μm x 0.22μm), coupling gap (0.3μm) and bend radius (5μm) the same. The differential delay length (ΔL) between arms of the MZI was designed to be 150 μm to have multiple resonance features within the measurement range (1.5μm - 1.59μm) for increased fitting accuracy. Fabrication imperfections were taken into account while generating the layout of the designed MZI structures, Figure 3a. The couplers and waveguide arms were kept as close to each other as possible to make them less prone to fabrication variations. These MZI devices were fabricated using the imec passive silicon photonics process through the Europractice *multi-project wafer* (MPW) service. It should be mentioned here that fabricated devices have a silica (SiO_2) top cladding in contrast to air top cladding for DCs fabricated by the e-beam lithography. The gap between the waveguides was chosen to be 0.3 μm instead of 0.25μm in order to somewhat compensate the effect of this cladding difference.

The fabricated MZI devices were optically measured using the tunable laser and a photo-detector in a clean-room environment. The measured spectra for three MZI structures having DCs of coupling lengths 1.0, 7.3 and 36.1 μm were simultaneously fitted to the CAPHE circuit model using the above mentioned lmfit tool to

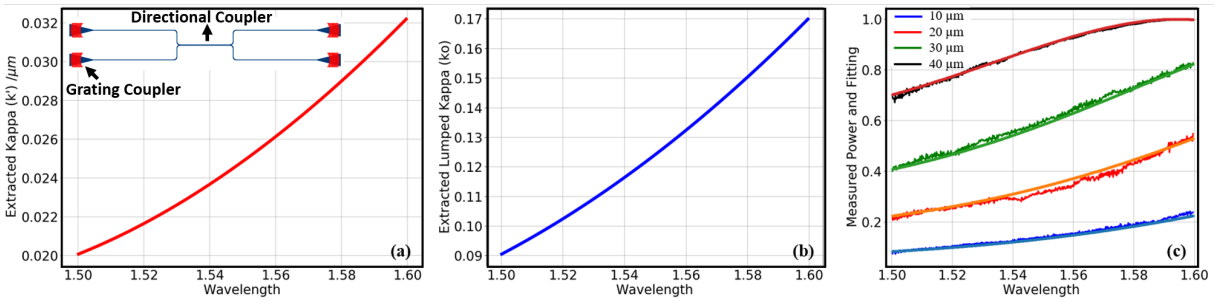


Figure 2. (a) Extracted field coupling coefficient using a 'naked' directional coupler. (b) Extracted lumped coupling coefficient. (c) Measured and the fitted spectra from the coupled port of the directional couplers with coupling lengths of 10, 20, 30 and 40 μm.

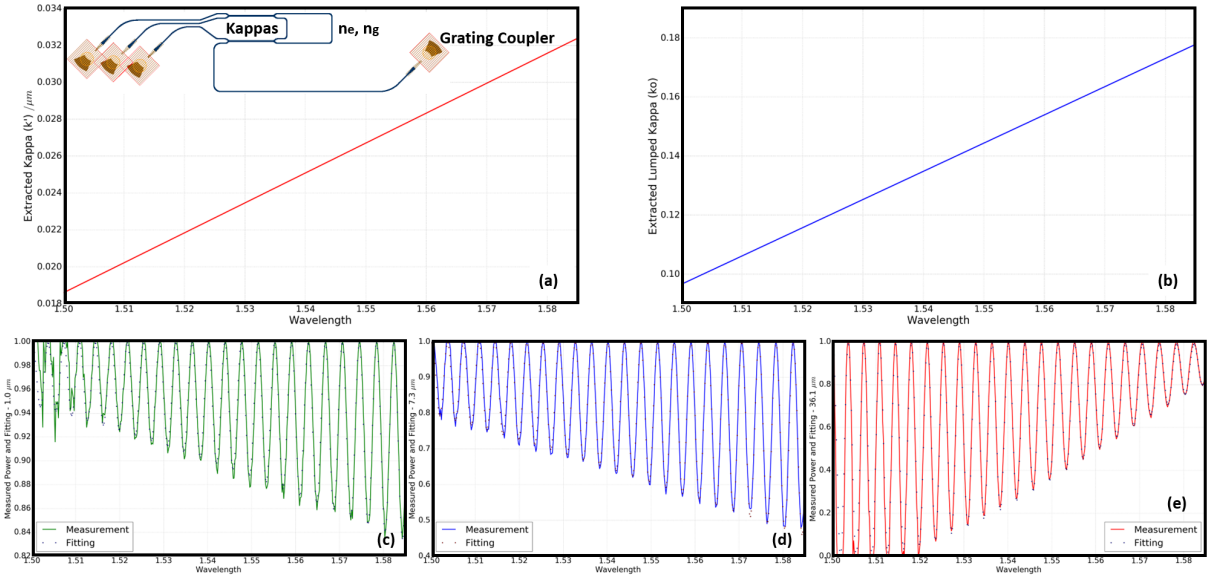


Figure 3. (a) Extracted field coupling coefficients (κ') from the MZI. (b) Extracted lumped coupling coefficient (κ_0). (c,d,e) Measured and the fitted spectra from the coupled spectra of the MZI structures with coupling lengths 7.3, 36.1 and 1.0 μm respectively.

extract six coupler related (κ', $\frac{\partial \kappa'}{\partial \lambda}$, $\frac{\partial^2 \kappa'}{\partial \lambda^2}$,$\kappa_0$, $\frac{\partial \kappa_0}{\partial \lambda}$ and $\frac{\partial^2 \kappa_0}{\partial \lambda^2}$) and two waveguide related (n_{eff} and n_g) model parameters. Effective and group indices of both MZI arms were considered to be same for these extractions neglecting the fabrication variability. The fitted and the measured spectra for the used MZI devices are shown in Fig. 3c-e. Good fitting of the spectra confirm that fabrication variability has not dramatically affected the circuit, thanks to the compact layout. The wavelength dependent field (κ') and lumped (κ_0) coupling coefficients are shown in Fig. 3a and 3b, respectively. The effective and group indices were extracted to be 2.33 and 4.23. The extracted coupling coefficient values increase with increasing wavelength and values are comparable to the values extracted for the DCs fabricated by e-beam lithography. This shows our design assumption that the effect of the cladding difference can be compensated by a larger coupling gap. The extraction errors for MZI devices were found to be smaller than the extractions from the directional couplers due to larger number of features within the measurement range.

3 CONCLUSIONS

We demonstrated experimental extraction of wavelength dependent field and lumped coupling coefficients using two different fabricated structures. The extraction was carried out by fitting of the measured spectra to the behavioral models to the transmission of a 'naked' DC and an MZI circuit. The MZI-based extraction not only provides the wavelength dependent coupling coefficients with higher accuracy and smaller errors but on top of that extracts the effective and the group indices of the waveguides. This is due to the fact that the extraction in the MZI spectra is based on the extinction ratio of the spectral features rather that the absolute power measurements which are susceptible to variations from the measurement setup (e.g. fiber alignment).

ACKNOWLEDGMENT

This work is supported by the Flemish Agency for Innovation and Entrepreneurship (VLAIO) with the MEPIC project.

REFERENCES

[1] W. Bogaerts, U. Khan, and Y. Xing, "Layout-Aware Yield Prediction of Photonic Circuits," in IEEE International Conference on Group IV Photonics, Mexico, pp. 93-94, 2018.

[2] W. Bogaerts, P. De Heyn, T. Van Vaerenbergh, K. De Vos, S. Selvaraja, T. Claes, P. Dumon, P. Bienstman, D. Van Thourhout, and R. Baets. "Silicon microring resonators," Laser Photonics Rev. 6(1), pp 47-73, 2012.

[3] Y. Xing, U. Khan, A. R. Alves Júnior, and W. Bogaerts, "behavioral model for directional coupler," in Proceedings Symposium IEEE Photonics Society Benelux, pp. 128–131, 2017.

[4] M. Fiers, T. Van Vaerenbergh, K. Caluwaerts, D. Vande Ginste,B. Schrauwen, J. Dambre, and P. Bienstman, "Time-domain and frequency-domain modeling of nonlinear optical components on circuit-level using a node-based approach," J. Opt. Soc. Am. pp. 82-900, 2012.

Distributed Phase Shift and Lasing Wavelength in Distributed-Feedback Resonators

Cristine C. Kores[1], Nur Ismail[2], Edward H. Bernhardi[3], Fredrik Laurell[1], Markus Pollnau[2,4]
[1] Department of Applied Physics, Royal Institute of Technology, Stockholm, Sweden
[2] Department of Materials and Nano Physics, Royal Institute of Technology, Kista, Sweden
[3] Visiting Scientist, Department of Materials and Nano Physics, Royal Institute of Technology, Kista, Sweden
[4] Advanced Technology Institute, University of Surrey, Guildford, United Kingdom
e-mail: m.pollnau@surrey.ac.uk

ABSTRACT

Distributed-feedback waveguide lasers based on Bragg-grating resonators generate ultranarrow-linewidth emission. The required $\pi/2$ phase shift is often introduced by a distributed change in effective refractive index, e.g. by adiabatically widening the waveguide. Despite careful design and fabrication, the experimentally observed resonance wavelength deviates, thereby placing the resonance and laser emission at a position with lower reflectivity inside the reflection band. This effect is often incorrectly attributed to fabrication errors. Here we show theoretically and experimentally that the decay of light intensity during propagation from the phase-shift center into both sides of the Bragg grating due to (i) reflection by the periodic grating and (ii) the adiabatic refractive-index change causes an incomplete accumulation of designed phase shift, thereby systematically shifting the resonance to a shorter wavelength. Calculations based on the characteristic-matrix approach and experimental studies in a distributed-feedback channel-waveguide resonator in amorphous Al_2O_3 on silicon with a distributed phase shift introduced by adiabatic widening of the waveguide according to a $\sin^2$ function show good agreement.

Keywords: Integrated Lasers, Distributed-feedback lasers, Optical resonators, Laser resonators, Bragg reflectors.

1. INTRODUCTION

Distributed-feedback (DFB) lasers [1, 2] utilize Fabry-Pérot-type resonators [3] with distributed mirror reflection and exploit the spectral selectivity of periodic Bragg gratings to generate ultranarrow-linewidth emission for various applications. An additional phase shift $\delta\phi_{design}$ of $\pi/2$ is required to design a resonance wavelength λ_{design} located at the Bragg wavelength λ_B. A common fabrication method inscribes a laser interference pattern into a photosensitive guiding region or into a cladding [2, 4], and a distributed phase shift, e.g. by widening the guiding region, increases the effective refractive index [5, 6]. Often the experimental resonance deviates from the designed wavelength because of fabrication inaccuracies or a chirp of the Bragg grating, induced thermally by optically pumping a DFB laser from one waveguide end [7]. Hillmer *et al.* [8] introduced a chirp, with a designed phase shift of $\pi/2$ distributed over different lengths, and showed that the longer this length, the more the resonance is shifted towards shorter wavelengths. Here we investigate a different effect. Our investigation [9] concerns DFB resonators, where the light intensity extends over a length comparable to the distributed-phase-shift region. Due to the distributed reflection, the intensity of light propagating from the phase-shift center in both directions into the grating decreases, depending on the grating coupling coefficient and the effective-refractive-index increase in the phase-shift region. Consequently, the oscillating light does not experience the full designed phase shift, leading to a negative wavelength shift of the resonance peak with respect to the design. We investigate this effect in a situation where it is the key effect responsible for the wavelength shift, not being overshadowed by other effects.

2. THEORETICAL INVESTIGATIONS

When the designed phase shift is $\delta\phi_{design} = \pi/2$, the resonance wavelength λ_{design} is located at the center of the reflection band. A designed phase shift $\delta\phi_{design} \neq \pi/2$ places the resonance wavelength λ_{design} at a different spectral location. Both, the reflection bandwidth and the wavelength difference

$$\delta\lambda_{\mathrm{design}} = \lambda_{\mathrm{design}} - \lambda_{\mathrm{B}} \tag{1}$$

increase with the grating coupling coefficient κ. Along the waveguide direction z, the distributed-phase-shift region is centered at position z_{ps} and extends over a length ℓ_{ps}. In this region, the waveguide is widened from its normal width w to its maximum width at z_{ps} and then narrowed back to w, with a profile $\delta w_{ps}(z)$. The effective refractive index of the waveguide mode increases with the same profile $\delta n_{ps}(z)$. The total additional phase shift accumulated by light propagating through the entire phase-shift region with constant intensity would then be given by [10]

$$\delta\phi_{\text{design}} = \frac{2\pi}{\lambda_{\text{B}}}\delta n_{\text{design}}\ell_{\text{ps}} = \frac{2\pi}{\lambda_{\text{B}}}\int_{z_{\text{ps}}-\ell_{\text{ps}}/2}^{z_{\text{ps}}+\ell_{\text{ps}}/2}\delta n_{\text{ps}}(z)dz\,, \tag{2}$$

where δn_{design} is the mean effective-refractive-index change within the phase-shift region. Our waveguide widening $\delta w_{ps}(z)$ and, hence, the effective refractive index increase $\delta n_{ps}(z)$ is designed to follow a $\sin^2$ function [5],

$$\delta n_{\text{ps}}(z) = \delta n_{\text{ps}}(z_{\text{ps}})\sin^2\left[\pi\frac{\left(z+\ell_{\text{ps}}/2-z_{\text{ps}}\right)}{\ell_{\text{ps}}}\right]. \tag{3}$$

Insertion of equation (3) into equation (2) and integration yields

$$\delta\phi_{\text{design}} = \frac{\pi}{\lambda_{\text{B}}}\delta n_{\text{ps}}(z_{\text{ps}})\ell_{\text{ps}}\,. \tag{4}$$

To obtain $\lambda_{design} = \lambda_B$, one choses $\delta n_{ps}(z_{ps})$ and ℓ_{ps} in equation (4) such that $\delta\phi_{design} = \pi/2$. However, due to a deviation $\Delta\phi_{res}$ of the actual distributed phase shift $\delta\phi_{res}$ from the designed value of $\delta\phi_{design}$,

$$\Delta\phi_{\text{res}} = \delta\phi_{\text{res}} - \delta\phi_{\text{design}}\,, \tag{5}$$

the actually obtained resonance wavelength λ_{res} is typically shorter than λ_{design} by

$$\Delta\lambda_{\text{res}} = \lambda_{\text{res}} - \lambda_{\text{design}} \quad\Rightarrow\quad \lambda_{\text{res}} - \lambda_{\text{B}} = \delta\lambda_{\text{design}} + \Delta\lambda_{\text{res}}\,, \tag{6}$$

resulting in a total wavelength shift from the Bragg wavelength of $\delta\lambda_{design} + \Delta\lambda_{res}$. This additional deviation $\Delta\lambda_{res}$ in a distributed-phase-shift DBF resonator is due to an incomplete accumulation of phase shift by the light intensity $I(z)$ that varies with position z. Consequently, $\delta\phi_{res}$ is smaller than $\delta\phi_{design}$ and amounts to

$$\delta\phi_{\text{res}} = \frac{1}{I_{\text{max}}}\frac{2\pi}{\lambda_{\text{B}}}\int_{z_{\text{ps}}-\ell_{\text{ps}}/2}^{z_{\text{ps}}+\ell_{\text{ps}}/2}\delta n_{\text{ps}}(z)I(z)dz\,. \tag{7}$$

This expression determines the accumulated phase shift and the resonance wavelength within the reflection band.

3. CALCULATIONS AND EXPERIMENTAL RESULTS

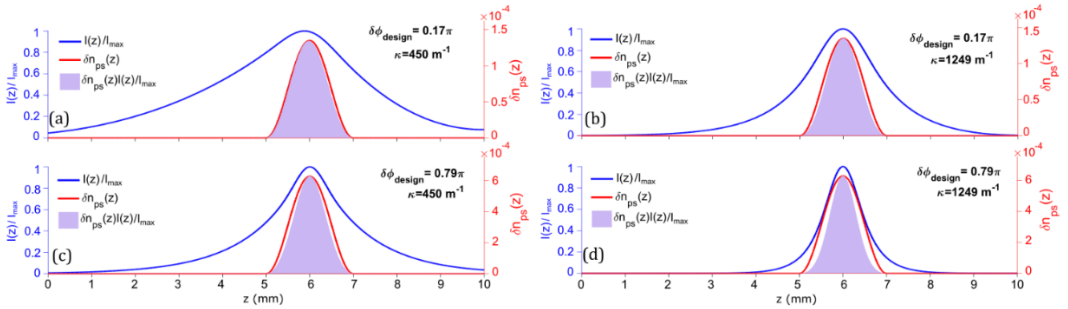


Figure 1. Refractive-index profile $\delta n_{ps}(z)$ (red curve), normalized light intensity $I(z)/I_{max}$ (blue curve) calculated at λ_{res}, and overlap product $\delta n_{ps}(z)I(z)/I_{max}$ (purple area) versus position z for grating coupling coefficients of κ = 450 m^{-1} and 1249 m^{-1} and designed phase shifts of $\delta\phi_{design}$ = 0.17 π and 0.79 π. The grating length is 10 mm and the phase-shift center is positioned at z_{ps} = 6 mm. (Figure taken from Ref. [9].)

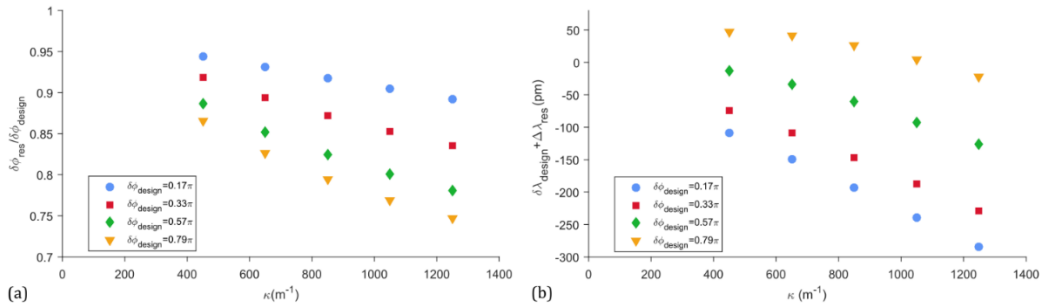


Figure 2. Simulation of (a) relative accumulated distributed phase shift $\delta\phi_{res}$ / $\delta\phi_{design}$ and (b) difference $\delta\lambda_{res} = \delta\lambda_{design} + \Delta\lambda_{res}$ between resonance wavelength λ_{res} and Bragg wavelength λ_B versus κ for designed distributed phase shifts of $\delta\phi_{design}$ = 0.17 π, 0.33 π, 0.57 π, and 0.79 π. The grating length is 10 mm and the phase-shift center is positioned at z_{ps} = 6 mm. (Figure taken from Ref. [9].)

We utilize the characteristic-matrix approach [11, 7]. The distribution of effective-refractive-index profile $\delta n_{ps}(z)$ of equation (3), the simulated normalized light intensity $I(z)/I_{max}$, and the overlap product $\delta n_{ps}(z)I(z)/I_{max}$

from equation (7) are displayed in Fig. 1. Two effects lead to an incomplete accumulation of designed phase shift. Firstly, when comparing Figs. 1(a) and 1(b) or Figs. 1(c) and 1(d), with increasing κ the light intensity is more confined to the phase-shift center, the light intensity accumulates less of the designed phase shift, hence $\delta\phi_{res}$ decreases compared to the value of $\delta\phi_{design}$ of equation (2) [Fig. 2(a)]. Consequently, in the case of a distributed phase shift, the resonance exhibits a negative wavelength shift $\Delta\lambda_{res}$ compared to the designed $\delta\lambda_{design}$ [Fig. 2(b)].

Secondly, when comparing Figs. 1(a) and 1(c) or Figs. 1(b) and 1(d), with increasing $\delta\phi_{design}$ the light intensity is more confined to the region near the phase-shift center. The slow increase in effective refractive index between the two phase-shift ends and its center leads to an additional distributed reflection and tighter light confinement. Light propagating from the phase-shift center in both directions into the grating is more reflected for larger $\delta\phi_{design}$. For increasing $\delta\phi_{design}$, obtained by increasing $\delta w_{ps}(z_{ps})$ and $\delta n_{ps}(z_{ps})$, this additional light confinement increases, hence the fraction $\delta\phi_{res}/\delta\phi_{design}$ decreases [Fig. 2(a)], resulting in larger deviations $\Delta\phi_{res}$ and $\Delta\lambda_{res}$ [Fig. 2(b)].

We investigated experimentally amorphous Al_2O_3 rib waveguides deposited by RF reactive sputtering onto a thermally oxidized silicon wafer [12] and micro-structured by reactive ion etching [13]. A corrugated homogeneous Bragg grating was inscribed into the SiO_2 top cladding [2, 4]. The effective-refractive-index increase $\delta n_{ps}(z)$ was achieved by tapering the waveguide structure according to the $\sin^2$ function of Eq. (3) over a length of ℓ_{ps} = 2 mm. The maximum increase $\delta w_{ps}(z_{ps})$ assumed the values of (a) 0.1 µm, (b) 0.2 µm, (c) 0.35 µm, and (d) 0.5 µm. The corresponding values of the effective refractive index were calculated using a mode-solver software. According to Eqs. (2)–(5), it results in a designed phase shift $\delta\phi_{design}$ of (a) 0.17 π, (b) 0.33 π, (c) 0.57 π, and (d) 0.79 π. The transmission spectra of these four waveguides were recorded. The observed resonances were systematically shifted to shorter wavelengths. Compared to the resonance wavelengths calculated from the overlap integral of Eq. (7), the experimental data show excellent agreement for the nominal κ of 650 m^{-1}, when $\delta\phi_{design}$ is small, indicating that the incomplete accumulation of designed phase shift $\delta\phi_{design}$ strongly contributes to the observed wavelength deviation. A deviation at larger $\delta\phi_{design}$ indicates that also fabrication errors play a role.

4. CONCLUSIONS

We have shown the fundamental nature of the wavelength deviation encountered in distributed-phase-shift DFB resonators. When the light intensity extends over a length comparable to the distributed-phase-shift region, the wavelength deviation is largely the result of an incomplete accumulation of the designed distributed phase shift by the light intensity that decays into the Bragg grating on both sides of the phase-shift center.

REFERENCES

[1] H. Kogelnik and C.V. Shank: Stimulated emission in a periodic structure, *Appl. Phys. Lett.*, vol. 18, pp. 152−154, 1971.

[2] E.H. Bernhardi, *et al.*, Ultra-narrow-linewidth, single-frequency distributed feedback waveguide laser in Al_2O_3:Er^{3+} on silicon, *Opt. Lett.*, vol. 35, pp. 2394−2396, 2010.

[3] N. Ismail, *et al.*, Fabry-Pérot resonator: spectral line shapes, generic and related Airy distributions, linewidths, finesses, and performance at low or frequency-dependent reflectivity, *Opt. Express*, vol. 24, pp. 16366−16389, 2016.

[4] E. H. Bernhardi, *et al.*, Monolithic distributed Bragg reflector cavities in Al_2O_3 with quality factors exceeding 10^6, *Photon. Nanostruct.*, vol. 9, pp. 225−234, 2011.

[5] K. Tada, Y. Nakano, and A. Ushirokawa, Proposal of a distributed feedback laser with nonuniform stripe width for complete single-mode oscillation, *Electron. Lett.*, vol. 20, pp. 82−84, 1984.

[6] H. Soda, *et al.*, GaInAsP/InP phase-adjusted distributed feedback lasers with a step-like nonuniform stripe width structure, *Electron. Lett.*, vol. 20, pp. 1016−1018, 1984.

[7] C.C. Kores, *et al.*, Temperature dependence of the spectral characteristics of distributed-feedback resonators, *Opt. Express*, vol. 26, pp. 4892−4905, 2018.

[8] H. Hillmer, *et al.*, Application of DFB lasers with individually chirped gratings, *Proc. SPIE*, vol. 2382, pp. 211−223, 1995.

[9] C.C. Kores, *et al.*, Accumulation of distributed phase shift in distributed-feedback resonators, *IEEE Photonics J.*, vol. 11, 1500109, 2019.

[10] H. Abe, *et al.*, Single-mode operation of a surface grating distributed feedback GaAs-AlGaAs laser with variable-width waveguide, *IEEE Photon. Technol. Lett.*, vol. 7, pp. 452−454, 1995.

[11] M. Born and E. Wolf, Principles of Optics (Pergamon, 1975), Chap. 1.

[12] K. Wörhoff, *et al.*, Reliable low-cost fabrication of low-loss Al_2O_3:Er^{3+} waveguides with 5.4-dB optical gain, *IEEE J. Quantum Electron.*, vol. 45, pp. 454−461, 2009.

[13] J.D.B. Bradley, *et al.*, Fabrication of low-loss channel waveguides in Al_2O_3 and Y_2O_3 layers by inductively coupled plasma reactive ion etching, *Appl. Phys. B*, vol. 89, pp. 311−318, 2007.

Multi-Band Gap Electro-Absorption Modulator Array in a Generic Integration Platform using Selective Area Growth

(Student paper)

Florian Lemaitre[1], Marija Trajkovic[1], Jean Decobert[2], Huub Ambrosius[1], Kevin Williams[1]
[1]*Institute for Photonic Integration, Eindhoven University of Technology, 5600 MB Eindhoven, The Netherlands*
[2]*III–V Lab, Campus de Polytechnique, 1 avenue Augustin Fresnel, F-91767 Palaiseau Cedex, France*
e-mail: f.lemaitre@tue.nl

ABSTRACT

We demonstrate the integration of 4 electro-absorption modulators (EAM) with shifted band gaps by combining selective area growth (SAG) with a generic photonic integration platform. The designed, fabricated and characterized EAMs operate in the wavelength range 1490–1550 nm, and the process allows mask layer specification of four band-gaps with 20 nm spacing. Static extinction ratio over a 2 V peak-to-peak voltage swing is beyond 10 dB for all EAMs with a variation of only 1.7 dB from device to device over the 60 nm wavelength range.

Keywords: Selective Area Growth, Generic photonic integration platform, Electro-Absorption Modulator

1 INTRODUCTION

Electro-absorption modulators (EAM) are key devices in optical communication operating at high bit-rate [1], [2] with a low drive voltage and small footprint. They have been recently introduced into the TU/e generic integration platform [3]. Using the generic integration enables the combination of active and passive devices in complex circuits, as it has been shown for a high capacity transmitter [4]. The modulation of EAM being wavelength dependent, their integration in a coarse wavelength division multiplexing (CWDM) configuration requires a control over their band gap.

Selective area growth (SAG) is a technology enabling band gap control for active devices with a single epitaxy step. With this technology, a four channels CWDM transmitter with a total of 13 different band gaps was demonstrated [5]. Previous work shows the successful combination of SAG with generic photonic integration to enable complex photonic chips with the example of a widely tunable laser source [6]. To the best of our knowledge a multi-band gap EAM array has not been integrated in a generic photonic platform.

This paper presents the integration of 4 EAMs with band gap shift by combining SAG with a generic platform fabrication process. The variation of static performance with band gap tuning is characterized and compared to EAMs from the standard generic integration platform for benchmarking.

2 EAM STRUCTURE

The active layer stack used in this work contains 6 quantum wells in order to integrate both lasers, semiconductor optical amplifiers and EAMs with a single epitaxial step. Prior to the multiple quantum wells (MQW) growth, pairs of dielectric SAG mask stripes are deposited on the wafer to locally control the MQW band gap. After the active layer stack growth, a butt-joint process is used to co-integrate active and passive devices. To characterize the variations of EAM static performance with band gap tuning, arrays of four 200 µm-long EAMs were fabricated on a 2-inch wafer. The Fig. 1 a) shows the layout of an EAM and Fig. 1 b) shows a photograph of the EAM array. The input and output waveguides are incident at the facet with an angle of 7° and the facets are anti-reflection coated. The SAG mask widths used for the EAM 1, 2, 3 and 4 are 6.4, 9.1, 12.0, and 15.3 µm respectively, providing peak photoluminescence (PL) emission wavelengths of 1503, 1524, 1545, and 1566 nm respectively. A wavelength step of 20 nm is aimed to follow the CWDM standard.

3 EXPERIMENTAL SETUP

To measure the EAM absorption as a function of bias, the chip was placed on a copper holder at room temperature without temperature stabilization. An electrical probe was used to bias the EAM and an external tunable laser was used to inject light in the EAM with 0 dBm power in fiber. A polarization maintaining fiber was used to inject the laser signal into the waveguide to excite the TE mode. The optical power transmitted through the EAM was collected at the chip output and measured with a power-meter. Lensed fibers were used to couple the light in and out of the chip, introducing a coupling loss of 3–4 dB at each facet. The absorption was recorded while sweeping the EAM bias from 0 to −8 V with a 0.1 V step.

. Research project funded by the European Commission under the Marie Curie GeTPICs project nr. 317316 (FP7-PEOPLE) and by the Dutch Ministry of Education, Culture and Science under the NWO Research School for Integrated Nanophotonics.

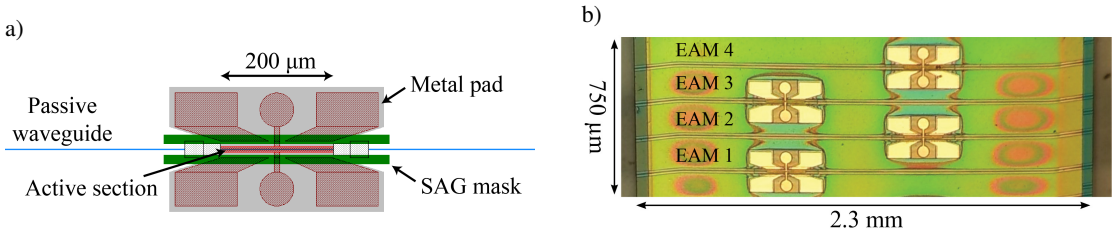


Figure 1: a) EAM layout with the SAG mask stripes. b) Picture of a fabricated EAM array.

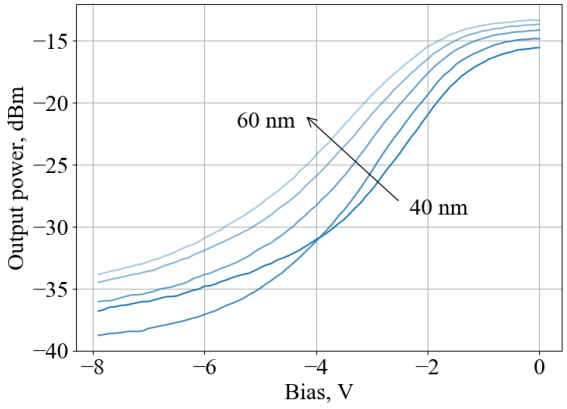


Figure 2: Transmitted optical power of the EAM 3 as a function of bias for different wavelength detuning. A laser input power of 0 dBm is used at wavelength detuning from 40 to 60 nm with a 5 nm step.

4 STATIC EXTINCTION RATIO ANALYSIS

The EAM performance analysis is performed in two steps. First, for each EAM the absorption as a function of bias is recorded for different wavelength detuning between the laser and the EAM PL peak wavelength. Then, the variation of performance with band gap tuning is measured after choosing one wavelength detuning for each EAM. To compare the EAM performance, three parameters are considered: 1- the measured transmitted optical power at 0 V EAM bias, called total insertion loss (IL), 2- the measured optical power normalized to the total IL, called static extinction ratio (ER), and 3- the bias of the inflexion point of the logarithmic ER characteristic, called optimal DC bias.

Wavelength detuning variation

In order to identify the best wavelength detuning for each EAM, we analyze the variation of EAM absorption for different laser wavelengths. The Fig. 2 shows the absorption measurement of the EAM 3 for different wavelength detuning values. The laser source was swept from 1585 to 1605 nm with a 5 nm step to provide wavelength detuning values from 40 to 60 nm. The measurements show total IL from −13.3 to −15.6 dB, maximum static ER from 20.4 to 23.9 dB and optimal DC biases from −2.2 to −3.4 V. The highest static ER is found with a wavelength detuning of 45 nm.

EAM band gap variation

The Fig. 3 shows the ER of each EAM at the wavelength detuning providing the highest static ER at −8 V. The inflexion point of the static ER in logarithmic scale are −2.5, −3.0, −2.9 and −2.8 V for the EAMs 1, 2, 3 and 4 respectively. By considering a 2 V peak-to-peak voltage swing around a bias of −2.8 V, the corresponding static ER are 10.3, 12.0, 11.2, and 11.7 dB respectively. These values are similar to the performance reported with a 200µm-long device in the standard integration platform [3].

The total IL measured for the 4 EAMs in the configuration presented in Fig. 3 ranges from 15 to 18 dB. Considering a fiber-to-chip coupling loss of 7 dB, it corresponds to an on-chip IL from 8 to 11 dB. This value is 1 to 4 dB higher than the on-chip IL reported with the standard integration platform.

5 CONCLUSION

In this paper we present for the first time the integration of electro-absorption modulators by combining selective area growth with the TU/e generic integration platform. Modulators are fabricated with photolumi-

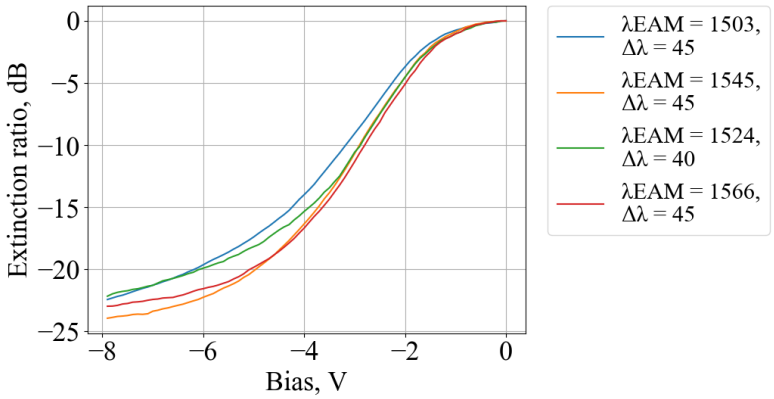


Figure 3: Extinction ratio for 4 EAMs with different band gaps in logarithmic scale from 0 to to −8 V. λEAM refers to the photoluminescence peak wavelength and Δλ refers to the wavelength detuning used for the measurement.

nescence wavelengths from 1490 to 1550 nm with a 20 nm spacing. The influence of wavelength detuning is studied for each EAM to find the conditions of operation for maximum static extinction ratio. A 2 V peak-to-peak voltage swing around a bias of −2.8 V provides a static extinction ratio beyond 10 dB for all EAMs. The success of the generic integration of EAMs with band gap choice over a 60 nm wavelength range paves the way to the integration of complex circuits for coarse wavelength division multiplexing transmitters.

REFERENCES

[1] M. Lauermann, R. Going, R. Maher, M. Lu, W. Ko, P. Studenkov, J. Ferrara, A. Hosseini, S. Corzine, J. Rahn, M. Kuntz, H. Tsai, A. Karanicolas, P. Evans, V. Lal, D. Welch, and F. Kish, "Multi-channel, widely-tunable coherent transmitter and receiver PICs operating at 88Gbaud/16-QAM," in *Optical Fiber Communications Conference and Exhibition (OFC)*, vol. 7. OSA publishing, 2017, pp. 7–9.

[2] C. Kazmierski, A. Konczykowska, F. Jorge, F. Blache, M. Riet, C. Jany, and A. Scavennec, "100 Gb/s Operation of an AlGaInAs Semi-Insulating Buried Heterojunction EML," in *Optical Fiber Communication Conference and National Fiber Optic Engineers Conference (OFC/NFOEC)*. IEEE, 2009.

[3] M. Trajkovic, F. Blache, F. Jorge, K. Mekhazni, J.-G. Provost, and H. Debregeas, "64Gb/s Electro Absorption Modulator Operation in InP-based Active-Passive Generic Integration Platform," in *44th European Conference on Optical Communication (ECOC)*. IEEE, 2018, pp. 1–3.

[4] W. Yao, M. K. Smit, and M. J. Wale, "Monolithic 300 Gb/s parallel transmitter in inp-based generic photonic integration technology," *IEEE Journal of Selected Topics in Quantum Electronics*, vol. 24, no. 1, 2018.

[5] H. Debregeas, J. Decobert, N. Lagay, R. Guillamet, D. Carrara, O. Patard, C. Kazmierski, and R. Brenot, "Selective-area-growth technology for flexible active building blocks," in *Advanced Photonics Congress*. OSA publishing, 2012, pp. 4–6.

[6] F. Lemaitre, S. Latkowski, C. Fortin, N. Lagay, R. Pajkovic, E. Smalbrugge, J. Decobert, H. Ambrosius, and K. Williams, "96 nm Extended Range Laser Source Using Selective Area Growth," in *44th European Conference on Optical Communication (ECOC)*. IEEE, 2018, pp. 3–5.

Intrinsic Limit of Detection for Coherent Biosensing Systems

Student Paper

Jonas Leuermann[1,2*], Íñigo Molina-Fernández[1,2], Alejandro Ortega-Moñux[1,2], J. Gonzalo Wangüemert-Pérez[1,2], Robert Halir[1,2]

[1] *Bionand Center for Nanomedicine and Biotechnology, Parque Tecnológico de Andalucía, 29590 Málaga, Spain*

[2] *Universidad de Málaga, Dept. de Ingeniería de Comunicaciones, ETSI Telecomunicación, Campus de Teatinos s/n, 29071 Málaga, Spain*

[*] *Corresponding author: jleuermann@bionand.es*

ABSTRACT

Optical biosensors have drawn great interest in the last years as they are able to detect trace amounts of biochemical substances without prior labeling. Interferometric structures with coherent phase read-out have recently shown to exhibit state-of-the-art limits of detections. Their fixed wavelength read-out system makes them a promising candidate for point-of-care devices for which cost is a critical factor. Over the last years the sensing community has mainly focused on the design of highly sensitive structures while little attention has been paid to the fundamental noise sources of the complete system and their influence on the optimization on the limit of detection. In this work, we analyze these noise and provide a series of guidelines to reach the fundamental limit of detection of coherent interferometric biosensors.

Keywords: photonic biosensor, Mach-Zehnder interferometer, coherent detection, fundamental limit of detection, evanescent field sensing

1 INTRODUCTION

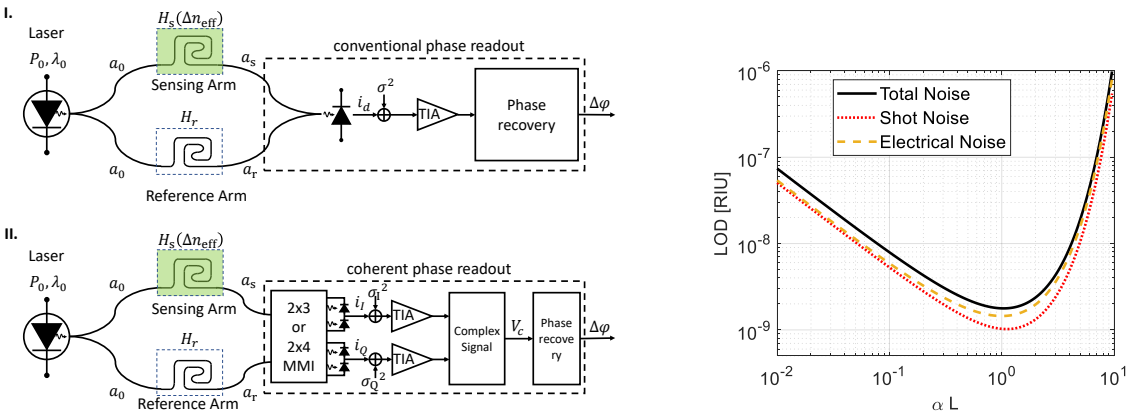
Photonic biosensors have shown to be capable of detecting trace amounts of biomolecules while keeping fabrication costs low and offering label-free detection [1]. Interferometric sensing architectures with coherent detection (using a 2x3 coupler at the interferometer output) have demonstrated *state-of-the-art* limit of detections (LOD) [2] [3], the smallest change in refractive index or concentration that can be measured with certainty. Due to the relaxed hardware requirements for the laser source compared to resonant structures which typically require wavelength sweeps, these interferometric systems are particularly suited for point-of-care devices for which cheap manufacturing is a critical factor. In the last decade there has been done a lot of research regarding the maximization of the biosensors overall sensitivity, for both resonant and interferometric architectures, using different waveguide geometries [4]–[6]. However, there is hardly any analysis about the fundamental limits of such biosensing systems. Here, we derive an analytical expression for the limit of detection of coherently detecting sensors, taking into account the noise and losses of such a system [7]. Based on this analysis, we provide clear guidelines on the optimization of sensing systems to improve the limit of detection.

2 COHERENT DETECTION

Direct and coherent detection schemes are compared in fig. 1(a). The sensing architecture consists in both cases of a Mach-Zehnder interferometer (MZI) with a sensing and a reference arm. Traditional phase read-outs typically recombine both signals in a Y-Junction or 1x2 Multi-Mode interferometer (MMI) resulting in an electrical signal

$$i_{\mathrm{d}} = \frac{RP_0}{2} \cdot \left[\frac{1 + e^{-2\alpha L}}{2} + e^{-\alpha L} \cos\left(k_0 L \cdot \Delta n_{\mathrm{eff}}\right) \right] \tag{1}$$

where R is the responsivity of the detecting photodiode (PD), P_0 the power of the laser source assuming perfect coupling, α the amplitude attenuation, L the length of the sensing arm, $k_0 = 2\pi/\lambda_0$ with λ_0 the wavelength of the propagating light, and Δn_{eff} the change in effective refractive index caused by any homogeneous refractive index change in the sensing arms surrounding buffer. Fading of the *architectural sensitivity* S_{a}, where S_{a} is defined as $|\partial i_{\mathrm{d}}/\partial \Delta n_{\mathrm{eff}}|$, and directional phase ambiguity arise directly from the sinusoidal dependency. Different approaches have been suggested to circumnavigate these effects such as slightly modulating the phase [8] of the laser or thermally modulating the phase of the reference arm [9]. Coherent detection, shown schematically in fig.1(b), a more advanced approach from the telecommunication field [10], was suggested in [3] for the first time for photonic biosensors.



(a) (b)

Figure 1. (a) Schematically comparison between the a directly (I.) and coherently (II.) detecting phase read-out. (b) Limit of detection as a function of the sensor length , including losses, with shot, electrical and superimposed noise limit.

The resulting complex current follows

$$i_{\text{c}} = i_{\text{I}} + \text{j} \cdot i_{\text{Q}} = \frac{RP_0}{2}\, e^{-\alpha L} \cdot e^{\text{j} \cdot k_0 L \cdot \Delta n_{\text{eff}}}, \tag{2}$$

with j the imaginary unit, obviously having a constant architecture sensitivity

$$S_a = \frac{RP_0}{2} k_0 \cdot L \cdot e^{-\alpha L}. \tag{3}$$

It is worth highlighting that this expression is equal to the sensitivity of a system with a conventional direct detection scheme at its point of maximum sensitivity. Therefore, to this special case the derived expressions can be extended. The complex signal readout can be accomplished by a 2x3 or 2x4 MMI with their consecutive three to four PDs for detection, both showing equal performance [10].

3 INTRINSIC LIMIT OF DETECTION

The LOD is generally defined by

$$LOD = \frac{3\sigma}{S} = \frac{3\sigma}{S_{\text{wg}} S_{\text{a}}} \tag{4}$$

where σ represents the standard deviation of the measured signal, and $S_{\text{wg}} = |\partial \Delta n_{\text{eff}} / \partial n_{\text{c}}|$ the *waveguide sensitivity* transforming any homogeneous change in refractive index to its according change in effective refractive index of the propagating sensing mode. Maximizing *waveguide sensitivity* and *architecture sensitivity* has so far been the main focus to optimize the LOD, while little attention has been paid to the linear dependency of the LOD to σ. The fundamental noise σ seen in the complex plane can be formulated as follows

$$\sigma = \sqrt{\sigma_{\text{I}}^2 + \sigma_{\text{Q}}^2} = \sqrt{\sigma_{\text{shot}}^2 + \sigma_{\text{elec}}^2} \tag{5}$$

$$= \sqrt{q \frac{RP_0}{2} \left(1 + e^{-2\alpha L}\right) B + \eta_{\text{elec}} B} \tag{6}$$

where σ_{shot}^2 and σ_{elec}^2 are the shot and electrical noise powers monitored in the in- (I) and/or quadrature-phase (Q) component of the complex signal, B the inverse of the integration time (i.e. the bandwidth of the electrical low-pass filter), and $q = 1.6 \cdot 10^{-19}\,\text{C}$ being the electron charge [7]. The resulting LOD can be formulated as

$$LOD = \frac{3}{\sqrt{2}\pi} \frac{\lambda_0}{S_{\text{wg}} L} \frac{1}{\sqrt{SNR}} \overset{L_{\text{opt}}}{\approx} \begin{cases} 1.94 \cdot \frac{\alpha\lambda_0}{S_{\text{wg}}} \cdot \sqrt{\frac{qB}{RP_0}}, & \text{if } \sigma_{\text{shot}}^2 \gg \sigma_{\text{elec}}^2 \text{ and } L_{\text{opt}} \approx \frac{1.11}{\alpha} \\ 2.6 \cdot \frac{\alpha\lambda_0}{S_{\text{wg}}} \cdot \frac{\eta_{\text{elec}}\sqrt{B}}{RP_0}, & \text{if } \sigma_{\text{elec}}^2 \gg \sigma_{\text{shot}}^2 \text{ and } L_{\text{opt}} = \frac{1}{\alpha}. \end{cases} \tag{7}$$

The signal-to-noise ratio SNR is defined as the ratio between the complex signal strength $\left(RP_0/2 \cdot e^{-\alpha L}\right)^2$ and its noise power σ^2. In figure 1(b) the LOD as a function of length L is shown for the following parameter set of $R = 1.05\,\text{A/W}$, $P_0 = 0.05\,\text{mW}$, $\lambda_0 = 1.55\,\mu\text{m}$, $S_{\text{wg}} = 0.8\,\text{RIU/RIU}$, $\alpha = 4.8\,\text{Np/cm}$, $\eta_{\text{elec}} = 3\,\text{pA}/\sqrt{\text{Hz}}$ and $B = 100\,\text{Hz}$ for a shot, electrical and superposed limited system. The minimal reachable LOD of such a

system is approximately $2 \cdot 10^{-9}\,\mathrm{RIU}$ for an impressive short length of around $2\,\mathrm{mm}$. It is worth highlighting that in case that the losses α are mainly due to the mode overlap with the buffer, i.e. $\alpha = \alpha_\mathrm{b} S_\mathrm{wg}$, the minimal reachable LOD becomes independent of the *waveguide sensitivity*. However, increasing waveguide *waveguide sensitivity* allows to reduce the optimum length. Furthermore, by moving from the near infra-red to the visible, i.e. shorter wavelengths, the LOD is improved in two different ways. First, due to the its linear dependency to λ_0 and second by the reduced absorptions losses $\alpha(\lambda_0)$ caused in the buffer media. Regardless which noise source is dominating, by choosing the bandwidth of the low-pass filter as narrow as possible the LOD can be further minimized due to $\sim \sqrt{B}$. But depending on the limiting noise source the LOD responds differently to increasing laser power P_0, scaling with $1/\sqrt{P_0}$ or $1/P_0$ for shot or electircal noise limit, respectively.

4 CONCLUSION

It has been demonstrated that the MZI based biosensors with coherent phase read-out are capable of reaching extraordinary LODs while maintaining small or moderate footprints. We have shown that reaching for the smallest LOD, the fundamental noise sources of the detection system and the absorption losses in the sensing window play a critical role in the design process. Depending on the limiting source different optimal lengths exits but $L = 1/\alpha$ results essentially in the same LOD in both cases. Furthermore, if losses increase at the same rate as the *waveguide sensitivity*, the optimization process of ultra highly *waveguide sensitivities* becomes less relevant. Using a narrow-band low pass filter for signal extraction has an improving effect on the LOD. By choosing a shorter wavelength, for example the visible regime ($\lambda_0 \approx 380 - 780\,\mathrm{nm}$), in comparison to the near infra-read ($\lambda_0 \approx 1.53 - 1.56\,\mu\mathrm{m}$) (C-Band), it has a drastic effect on the detection limit as the losses are lower by a factor of approximately 10^3. As moving to the visible light has a high impact on the photonic design process and performance the aforementioned has to be considered with caution. Nevertheless, already moving from the C to the O-Band ($1.26 - 1.36\,\mu\mathrm{m}$) will have an improving effect.

ACKNOWLEDGMENT

This project has received funding from the European Union's Horizon 2020 research and innovation programme under the Marie Skłodowska-Curie grant agreement No 713721. We would like to acknowledge the Ministerio de Economía y Competitividad, Programa Estatal de Investigación, Desarrollo e Innovación Orientada a los Retos de la Sociedad (cofinanciado FEDER), Proyecto TEC2016-80718-R, the Ministerio de Educación, Cultura y Deporte (FPU14/06121), and the Universidad de Málaga. The views presented by the authors do not necessarily state or reflect the opinions of the aforementioned institutions. The authors and executors are not responsible for any use that may be made of the information in this article.

REFERENCES

[1] X. Fan, I. M. White, S. I. Shopova, H. Zhu, J. D. Suter, and Y. Sun, "Sensitive optical biosensors for unlabeled targets: A review," *Analytica Chimica Acta*, vol. 620, no. 1-2, pp. 8–26, jul 2008.

[2] R. J. J. van Gulik, B. M. de Boer, and P. J. Harmsma, "Refractive index sensing using a three-port interferometer and comparison with ring resonators," *IEEE Journal of Selected Topics in Quantum Electronics*, vol. 23, no. 2, pp. 433–439, mar 2017.

[3] R. Halir, L. Vivien, X. L. Roux, D.-X. Xu, and P. Cheben, "Direct and sensitive phase readout for integrated waveguide sensors," *IEEE Photonics Journal*, vol. 5, no. 4, pp. 6 800 906–6 800 906, aug 2013.

[4] Q. Liu, X. Tu, K. W. Kim, J. S. Kee, Y. Shin, K. Han, Y.-J. Yoon, G.-Q. Lo, and M. K. Park, "Highly sensitive mach–zehnder interferometer biosensor based on silicon nitride slot waveguide," *Sensors and Actuators B: Chemical*, vol. 188, pp. 681–688, nov 2013.

[5] J. G. Wangüemert-Pérez, A. Hadij-ElHouati, A. Sánchez-Postigo, J. Leuermann, D.-X. Xu, P. Cheben, A. Ortega-Moñux, R. Halir, and Í. Molina-Fernández, "Subwavelength structures for silicon photonics biosensing," *Optics & Laser Technology*, vol. 109, pp. 437–448, jan 2019.

[6] D. M. Kita, J. Michon, S. G. Johnson, and J. Hu, "Are slot and sub-wavelength grating waveguides better than strip waveguides for sensing?" *Optica*, vol. 5, no. 9, p. 1046, aug 2018.

[7] Í. Molina-Fernández, J. Leuermann, R. Halir, A. Ortega-Moñux, and J. G. Wangüemert-Pérez, "Fundamental limit of detection of photonic biosensors with coherent phase readout," submitted to Optics Express.

[8] S. Dante, D. Duval, B. Sepúlveda, A. B. González-Guerrero, J. R. Sendra, and L. M. Lechuga, "All-optical phase modulation for integrated interferometric biosensors," *Optics Express*, vol. 20, no. 7, p. 7195, mar 2012.

[9] Y. E. Marin, V. Toccafondo, P. Velha, Y. Jeong, S. Scarano, A. Nottola, S. Tirelli, H. P. Jeon, M. E. Minunni, F. D. Pasquale, and C. J. Oton, "Silicon-photonic interferometric biosensor using active phase demodulation," in *Frontiers in Biological Detection: From Nanosensors to Systems X*, B. L. Miller, S. M. Weiss, and A. Danielli, Eds. SPIE, feb 2018.

[10] P. J. Reyes-Iglesias, I. Molina-Fernández, A. Moscoso-Mártir, and A. Ortega-Moñux, "High-performance monolithically integrated 120 degree downconverter with relaxed hardware constraints," *Optics Express*, vol. 20, no. 5, p. 5725, feb 2012.

Design of slot waveguide for ultra-violet light based on atomic layer deposition

Chupao Lin[1,2], Roel Baets[1,2], Gunther Roelkens[1,2] and Nicolas Le Thomas[1,2]
[1]Photonics Research Group, INTEC Department, Ghent University-imec, Technologiepark-Zwijnaarde, 9052 Ghent, Belgium
[2]Center for Nano- and Biophotonics, Ghent University, Belgium
e-mail: Nicolas.LeThomas@ugent.be

Abstract

We unveil parameter sets to achieve a low loss single mode waveguide operating at UV wavelengths. The proposed design that is compatible with atomic layer deposition technology is expected to have potential applications in integrated-photonics based UV sensing.

Keywords: Ultraviolet; Photonic integrated circuits; Guided waves

1. INTRODUCTION

Integrated photonics for sensing applications has been extensively investigated [1]. However, the ultraviolet (UV) range has not yet been explored with integrated photonics due to a lack of low loss single mode waveguides. The requirement of extreme-small waveguide dimensions at shorter wavelengths results in a high scattering loss and currently hampers its development. As many kinds of bio-materials like proteins usually have absorption bands in the UV, a new integrated platform operating in the UV can spark a myriad of applications [2]. In particular, a single mode waveguide at UV wavelengths that can enhance the light-matter interaction and increase the light collection efficiency of surrounding emitters is of paramount importance. Several methods have been reported recently but failed to implement low propagation loss and strong light-matter interaction simultaneously. The propagation loss of silicon nitride (SiN) waveguides increase dramatically below a wavelength of ~460 nm [3]. Although aluminum nitride (AlN) and aluminum oxide (Al_2O_3) waveguides have demonstrated a low loss at wavelengths near 400 nm, operation substantially below a wavelength of 370 nm still needs to be explored [3, 4]. Here, we present a slot waveguide design that can accommodate the single-mode and low-loss constraints up to 260 nm. Importantly, the waveguide design is such that it does not require any etching of the core layer and as a result minimizes the propagation losses. It can be fabricated by the atomic layer deposition (ALD) technique and therefore be promising for achieving ultra-smooth surfaces and low loss propagation at UV wavelengths.

2. STRUCTURE DESIGN AND SIMULATION RESULTS

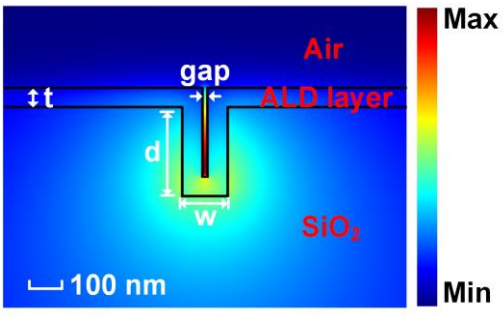


Fig. 1. Cross-section and simulated TE-mode profiles of the slot waveguide

Using COMSOL, the slot waveguide is designed and simulated for three materials used as the waveguide core, namely yttrium oxide (Y_2O_3), hafnium oxide (HfO_2) and Al_2O_3, that all exhibit low absorption at UV wavelengths [5-7]. The TE-mode profile of the slot waveguide is shown in Fig.1, with a SiO_2/Si wafer used as substrate. The waveguide-loss is generally dominated by the material absorption and scattering loss at structure surfaces. At shorter wavelengths, particularly, rough surfaces will result in a large waveguide loss in view of scattering loss proportional to $1/\lambda^4$. Therefore, improving the surface smoothness and further decreasing the scattering loss for a given material plays a crucial role for achieving a low loss waveguide operating in the UV. In this context, the slot waveguides are fabricated on pre-etched SiO_2 to avoid etching the core layer. In addition to reduce waveguide loss, the proposed structure is able to confine light tightly in the slot where the analyte of

interest is located. This property can enhance the light-matter interaction dramatically and then contribute to applications in high-sensitive bio-sensing.

Figure 2(a), (b) and (c) summarize the results of the slot waveguide structure simulated at a wavelength of 260 nm, 300 nm and 405 nm, respectively. The refractive indexes of 2.00 and 1.69 are chosen for simulation to match that of Y_2O_3/HfO_2 and Al_2O_3, respectively. The shaded areas show the range where the TE or TM mode are guided and the dotted lines represent the cutoff of the TE, TM and high-order modes. In this structure, many parameters would affect the light confinement such as the depth (d), the width (w), the slot width (gap), the thickness of the ALD layer (t), the working wavelength (λ) and the refractive index value of the ALD layer (n). Note that the cutoff of the high-order modes (orange dotted lines for n=1.69 and red ones for n=2.00) is very close to the cutoff of the fundamental slab mode. To investigate the variables of interest (gap, t, λ and n), the w and d parameters are constrained by the following relationships: aspect ratio = d/w and w=2*t + gap. In this simulation, the aspect ratio is fixed to 2, due to fabrication constraints. The TE mode emerges earlier than the TM mode with increasing the thickness of ALD layer when the gap is narrow, while the TM mode can be guided over a wider thickness range in the case of wider gaps (>10 nm). At λ=260 nm, the single mode behavior for TE and TM ranges over an ALD thickness of 14 nm for n=1.69, which plummets to a range of only ~2 nm for n=2.00. In cases of the same n value, the domain of single mode propagation become narrower at shorter wavelengths. For instance, from a wavelength of 405 nm to 260 nm for n=2.00, the width of single mode area is reduced by more than a half. This result highlights the challenge of fabricating single-mode slot waveguides for λ<300 nm and high index contrast, which can be tackled with the ALD technique.

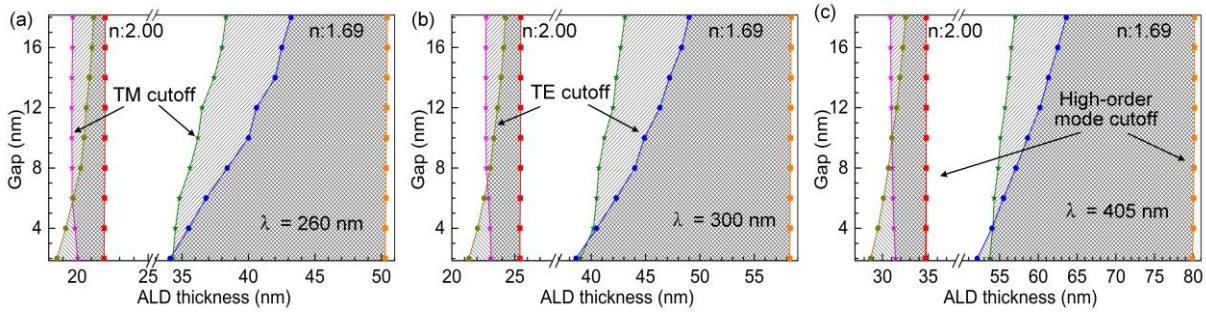


Fig. 2. Simulated mode map for the slot waveguide at a wavelength of (a) 260 nm, (b) 300 nm and (c) 405 nm, respectively. The cutoff of TE and TM modes is compared at both index values of 1.69 and 2.00.

3. **CONCLUSIONS**

We have proposed a slot waveguide design that is compatible with the ALD technique and we have quantified the typical waveguide dimensions for a single-mode operation at UV wavelength up to λ=260 nm. For a refractive index n=1.69, the thickness range of the core layer is of the order of 10 nm and drops to only 2 nm for n=2.00 and λ=260 nm. This design is promising for simultaneously achieving low-loss single mode waveguides and highly sensitive bio-sensing in the UV. We are currently processing such a waveguide.

REFERENCES

[1] Subramanian, A.Z., et al.: Silicon and silicon nitride photonic circuits for spectroscopic sensing on-a-chip [Invited], *Photonics Res.*, vol. 3, pp. B47-B58, 2015

[2] Soltani, M., et al.: AlGaN/AlN integrated photonics platform for the ultraviolet and visible spectral range, *Opt. Express*, vol. 24, pp. 25415-25423, 2016

[3] Danielli, A., et al.: Multi-layer integrated photonics from the ultraviolet to the infrared. *Proc. Frontiers in Biological Detection: From Nanosensors to Systems X*, 2018,pp. 1-10

[4] Liu, X., et al.: Ultra-high-Q UV microring resonators based on a single-crystalline AlN platform, *Optica*, vol. 5, pp. 1279-1283, 2018

[5] Aarik, J., et al.: Optical characterization of HfO2 thin films grown by atomic layer deposition, *Thin Solid Films*, vol. 466, pp. 41-47, 2004

[6] Fukabori, A., et al.: Optical and scintillation characteristics of Y2O3 transparent ceramic, *J. Appl. Phys.*, vol. 107, pp. 073501-073506, 2010

[7] Aslan, M.M., et al.: Low-Loss Optical Waveguides for the Near Ultra-Violet and Visible Spectral Regions with Al(2)O(3) Thin Films from Atomic Layer Deposition, *Thin Solid Films*, vol. 518, pp.4935-4940, 2010

On-chip integrated resonators for long-wave infrared photonics

(Student Paper)

Qiankun Liu[1,*], Joan Manel Ramirez[1,3], Vladyslav Vakarin[1], Xavier Le Roux[1], Jacopo Frigerio[2], Andrea Ballabio[2], Miguel Montesinos[1], Carlos Alonso-Ramos[1], Enrico Talamas Simola[2], Laurent Vivien[1], Giovanni Isella[1], and Delphine Marris-Morini[1]

[1] Centre de Nanosciences et de Nanotechnologies (C2N), Université Paris Sud, CNRS, Université Paris Saclay, 91120 Palaiseau, France

[2] L-NESS, Dipartimento di Fisica, Politecnico di Milano, Polo di Como, Via Anzani 42, 22100 Como, Italy

[3] Now at III-V lab, a joint lab from Nokia Bell Labs, Thales and CEA, 1 avenue Augustin Fresnel, 91767 Palaiseau Cedex

e-mail: qiankun.liu@u-psud.fr

ABSTRACT

On-chip optical resonators are extensively applied to many fields such as light sources through lasing or enhancement of material nonlinear effects, chemical and biological sensing, and optical network monitoring. Silicon-based on-chip resonators have been reported previously in near infrared (NIR) and short-wave infrared (SWIR), however integrated resonant structures remain still challenging for long-wave infrared (LWIR). In this work, we experimentally demonstrate the first on-chip integrated resonators in LWIR up to 8.4 µm. Two types of resonators, Fabry-Perot cavities and racetrack ring resonators have been both investigated. Loaded quality factors Q = 2200 and Q = 3200 have been respectively observed for Fabry-Perot cavity and racetrack ring resonator at a wavelength around 8 µm.

Keywords: Integrated optics devices, Mid-infrared, Fabry-Perot cavities, Racetrack ring resonators.

1. INTRODUCTION

Mid-infrared silicon photonics is attracting a continuously increasing number of research activities due to its wide plethora of applications, including environmental monitoring, chemical and biological sensing, disease diagnosis and free space communication[1–3]. Among them, the identification of molecules through their unique absorption lines in the fingerprint region is particularly interesting. However, the most used platform in silicon photonics, SOI shows absorption at the wavelengths beyond 3.6 µm. In this context, alternative materials have been studied, such as suspended SOI, silicon nitride, III-V semiconductors, chalcogenides, Ge-on-Si, SiGe alloys and Ge-rich graded index SiGe. Among them, Ge-rich graded index SiGe stands as a strong candidate for the demonstration of LWIR operational photonic integrated circuits, due to i) its extended transparency potentially up to 15 µm; ii) high crystalline quality; iii) high 3rd order nonlinearity; iv) high versatility of optical engineering. Moreover, recent advances on graded index SiGe platform [4–6] report the experimental confirmation of its LWIR operation and show the potential for the investigation of LWIR integrated multi-target molecule detection systems.

To accomplish this task, on-chip mid infrared integrated resonator remains still challenging. Si-based on-chip resonators have been reported previously in NIR and SWIR, however the demonstration of LWIR resonators are still in its infancy. In this paper, we report our recent advance on the LWIR integrated resonators using graded index SiGe waveguides. Fabry-Perot cavities using waveguide Bragg gratings, and racetrack ring resonators have been experimentally demonstrated [7, 8]. Bragg grating waveguides up to 8.4 µm has been experimentally demonstrated, Fabry-Perot cavities with a loaded quality factor Q of 2200 are obtained at a wavelength of 7.95 µm. In another hand, resonators display deep resonances with an extinction ratio (ER) up to 10 dB, a loaded quality factor of 3200 is measured at a wavelength around 8.05 µm. These results provide the feasibility of using graded-index SiGe waveguides for the demonstration of LWIR resonant structures, opening the path towards the further implementation of advanced LWIR photonics integrated circuits.

2. Bragg grating waveguides and Fabry-Perot cavity

The Bragg grating waveguides are implemented on graded-index SiGe platform with Ge concentration linearly increasing from the Si substrate to pure Ge, across the 6-µm-thick waveguide core. Waveguides are then designed with 4 µm etch depth and 5 µm width. Bragg gratings corrugations are defined on top of the waveguide surface with a 400 nm etch depth and a duty cycle DC of 0.5. As the low vertical index contrast, an etch depth of 400 nm is chosen since it provides in the one hand a reasonable interaction between optical mode and the top-surface waveguide corrugation, and in the other hand a good optical confinement of propagating mode in the corrugated waveguide. The interaction between optical mode and gratings can be descripted as coupling efficiency by the following equation:

$$K = \frac{\Gamma \times (n_h^2 + n_l^2) \times \sin(\pi \times DC)}{\lambda_B \times n_{eff}} \quad (1)$$

where Γ is the overlap factor between the guided optical mode and the grating region, n_h and n_l are the alternative high and low refractive index of two materials inside the grating region, DC is the duty cycle of corrugation, λ_B presents the Bragg wavelength and n_{eff} is the effective Bloch-Floquet mode at λ_B. The corrugation width is slightly narrower than the waveguide width ($W_{Corrug} < W_{WG}$), in order to improve the alignment tolerance between two-layer lithography used in the fabrication process. Optimum corrugation width of Bragg gratings has been found by performing the numerical simulation. An optimized ratio ($r = W_{Corrug} / W_{WG}$) of 70% was obtained to maximize the coupling efficiency given by equation (1), corresponding to W_{Corrug} = 3.5 µm as shown in Figure 1(a). The Bragg gratings and FP cavities were fabricated using an electron beam lithography, followed by an inductive coupled plasma (ICP) etching. Figure 1(b) presents the scanning electron microscopy (SEM) picture of the fabricated Bragg gratings.

Fabricated devices were characterized through a free-space configuration. Figure 1(c) shows the experimental results of tow FP cavities with N = 280, cavity length L_{Cav} = 70 µm and different grating period (Λ) 1.1 µm and 1.16 µm. Resonance peaks are measured at a wavelength of 7.95 µm and 8.35 µm, respectively. The -3 dB resonance bandwidths were measured to be 5.3 nm and 6.5 nm, corresponding to loaded quality factors of 1514 and 1272, respectively [4]. The estimated mirror losses are between 1.2 and 1.8%. Figure 1(d) presents the measurement result of a FP cavity with number of periods of 500, keeping the same grating period and cavity length as presented previously in figure 1(c). The cavity Q-factor is improved by increasing the grating length, the -3 dB bandwidth at a resonance wavelength of 7.95 µm is reduced down to 3.6 nm, which yields a loaded Q-factor of 2200.

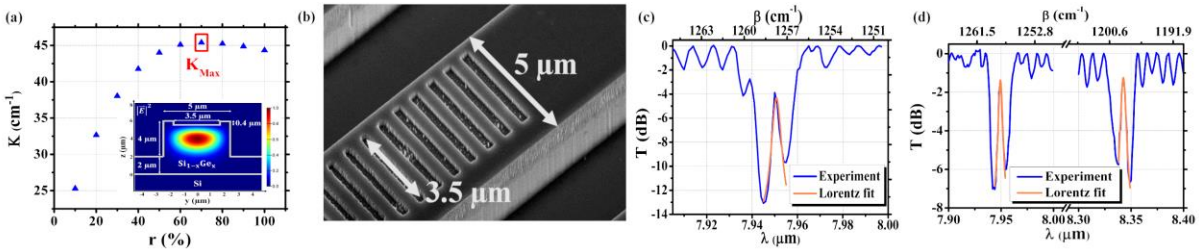


Figure 1. (a) Calculated coupling efficiency of the Bragg grating waveguide as a function of the ratio r between the shallow-etch corrugation width (W_{Corrug}) and the nominal waveguide width (W_{WG}) at a wavelength of 7.3 µm. Inset: Schematic of the waveguide cross-section with the simulated transverse magnetic (TM) mode profile in the grating region at 7.3 µm wavelength. (b) The SEM picture of a fabricated Bragg grating waveguide. (c) Measured transmittance spectrum of two different FP cavities with different design parameters: Λ = 1.1 µm (left), Λ = 1.16 µm (right), N = 280, L_{Cav} = 70 µm. Orange lines correspond to the Lorentzian fit of the central resonance. (d) Measured transmittance spectrum of a FP cavity with Λ = 1.1 µm, N = 500, L_{Cav} = 70 µm. The R-squared value of Lorentzian fit is 0.97.

3. Racetrack resonator

Another approach, racetrack resonators have been also fabricated on the graded-index SiGe platform. Unlike the FP cavity using two Bragg mirrors implemented on a same waveguide, racetrack resonator is based on a directional coupler to couple light from the bus waveguide into the resonator. The resonators were fabricated through one step of lithography and ICP etch, with a etch depth of 3 µm and 4 µm waveguide width. Comparing to the previous FP cavity waveguide design, 1 µm shallower etch depth increases the coupling coefficient of the directional coupler which leads to a shorter coupler. Moreover, 4 µm waveguide width ensures the waveguide single mode condition at interesting wavelength λ ≈ 8 µm. The gap distance (L_{Gap}) and the length of directional coupler ($L_{Coupler}$) have been chosen as L_{Gap} = 1 µm and $L_{Coupler}$ = 200 µm while considering the fabrication tolerance and the aspect ratio for the gap definition. Figure 2(a) and (b) show the SEM image of the fabricated resonators on top-view and the cross-section of a test resonator at directional coupler area, respectively.

Considering the minimum FSR value limited by the experimental setup and the waveguide propagation loss of 3 dB/cm ± 0.5 dB/cm, racetrack resonators with 5 different bending radii (R = 50 to 250 µm with a step of 50 µm) have been fabricated. Figure 2(c) shows the transmittance spectra of fabricated racetrack resonators. Clear resonances have been observed over 900 nm at a wavelength range of 8 µm, with an extinction ratio of 10 dB around the critical coupling condition. The minimum -3 dB bandwidth is measured as 2.5 nm at 8.05 µm leading to a maximum loaded quality factor of 3200. It is worth to note that the linewidth of the used QCL is specified to be below 1 cm^{-1} (i.e. below 6.5 nm at 8 µm wavelength). Furthermore, the measurement has been performed with a step of 1 nm which is the maximum resolution of the laser. This fact can limit the maximum value of the measured Q-factor. It is thus interesting to evaluate the intrinsic quality factor of the resonators which is limited only by the waveguide loss. Considering the waveguide propagation losses of 3 dB/cm, the calculated intrinsic Q-factor is at a magnitude of 10^4.

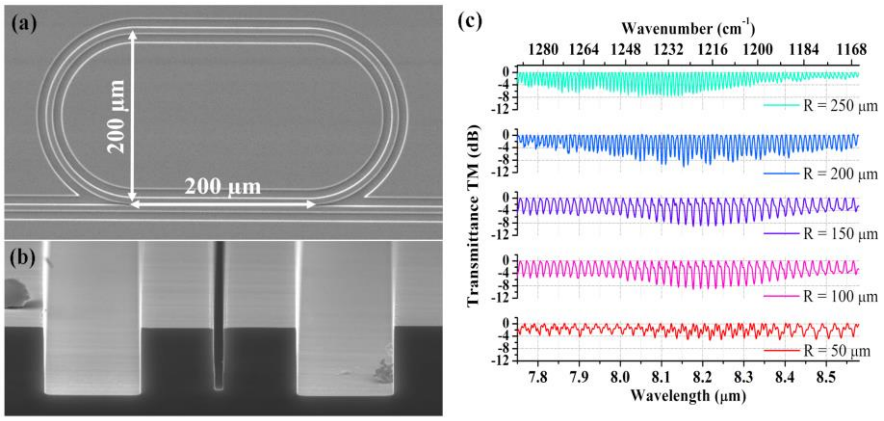


Figure 2. SEM image of the racetrack resonator (a) top view (b) cross-section of a test resonator device at the coupling area. (c) Experimental transmittance spectra of racetrack resonators with different bending radius, from bottom-up R = 50 µm (red), R = 100 µm (purple), R = 150 µm (violet), R = 200 µm (blue) and R = 250 µm (green).

4. CONCLUSIONS

In conclusion, we demonstrated Bragg-grating-based Fabry-Perot cavities and racetrack resonators operating in the long-wave MIR region at a wavelength range of 8 µm. The resonance of FP cavity is demonstrated up to 8.4 µm with a maximum loaded Q-factor of 2200 measured at 7.95 µm. Moreover, in terms of racetrack resonators, a bandwidth of over 900 nm resonances have been measured with a loaded Q-factor of 3200 at 8.05 µm. This first demonstration of resonant structure at such large wavelength in the MIR wavelength range open the path towards the further implementation of advanced LWIR photonics integrated circuits.

ACKNOWLEDGEMENTS

European Research Council (ERC) under the European Union's Horizon 2020 research and innovation program (N°639107-INsPIRE). Partial support is provided also by the TEINVEIN project funded by POR FESR 2014-2020 (ID: 242092) and by the European Union Horizon 2020 FET project microSPIRE (ID: 766955). The fabrication of the device was performed at the Plateforme de Micro-Nano-Technologie/C2N, which is partially funded by the "Conseil Général de l'Essonne". This work was partly supported by the French RENATECH network.

REFERENCES

[1] H. Lin, Z. Luo, T. Gu, L. C. Kimerling, K. Wada, and A. Agarwal, "Review article Mid-infrared integrated photonics on silicon : a perspective," **7**(2), 393–420 (2018).

[2] J. Depciuch, E. Kaznowska, I. Zawlik, R. Wojnarowska, M. Cholewa, P. Heraud, and J. Cebulski, "Application of Raman Spectroscopy and Infrared Spectroscopy in the Identification of Breast Cancer," Appl. Spectrosc. **70**(2), 251–263 (2016).

[3] Y. Zou, S. Chakravarty, C.-J. Chung, X. Xu, and R. T. Chen, "Mid-infrared silicon photonic waveguides and devices [Invited]," Photonics Res. **6**(4), 254 (2018).

[4] J. M. Ramirez, Q. Liu, V. Vakarin, J. Frigerio, A. Ballabio, X. Le Roux, D. Bouville, L. Vivien, G. Isella, and D. Marris-Morini, "Graded SiGe waveguides with broadband low-loss propagation in the mid infrared," Opt. Express **26**(2), 870 (2018).

[5] Q. Liu, J. M. Ramirez, V. Vakarin, X. Le Roux, C. Alonso-Ramos, J. Frigerio, A. Ballabio, E. Talamas Simola, D. Bouville, L. Vivien, G. Isella, and D. Marris-Morini, "Integrated broadband dual-polarization Ge-rich SiGe mid-infrared Fourier-transform spectrometer," Opt. Lett. **43**(20), 5021 (2018).

[6] D. Marris-Morini, V. Vakarin, J. Manel Ramirez, Q. Liu, A. Ballabio, J. Frigerio, M. Montesinos, C. Alonso-Ramos, X. Le Roux, S. Serna, D. Benedikovic, D. Chrastina, L. Vivien, and G. Isella, "Germanium-based integrated photonics from near-to mid-infrared applications," Nanophotonics **7**(11), 1781–1793 (2018).

[7] Q. Liu, J. M. Ramirez, V. Vakarin, X. Le Roux, J. Frigerio, A. Ballabio, E. Talamas Simola, C. Alonso-Ramos, D. Benedikovic, D. Bouville, L. Vivien, G. Isella, and D. Marris-Morini, " On-chip Bragg grating waveguides and Fabry-Perot resonators for long-wave infrared operation up to 8.4 µm," Opt. Express **26**(26), 34366-34372 (2018).

[8] J. M. Ramirez, Q. Liu, V. Vakarin, X. Le Roux, J. Frigerio, A. Ballabio, C. Alonso-Ramos, E. Talamas Simola, L. Vivien, G. Isella, and D. Marris-Morini, "Broadband integrated racetrack ring resonators for long-wave infrared photonics," Opt. Lett **44**(2), 407-410(2019).

On the Performance of Tantalum Pentoxide and Silicon Nitride Slot Waveguides for On-Chip Raman Spectroscopy

(Student paper)

Zuyang Liu [1,2], Haolan Zhao [1,2], Ali Raza [1,2], Nicolas Le Thomas [1,2], and Roel Baets [1,2]
[1]*Photonics Research Group, INTEC Department, Ghent University-imec, 9052 Ghent, Belgium*
[2]*Center for Nano- and Biophotonics, Ghent University, 9052 Ghent, Belgium*
e-mail: Zuyang.Liu@ugent.be

ABSTRACT

Waveguide-enhanced Raman spectroscopy is a promising technique for high-sensitivity molecular identification and quantification. Efficient on-chip Raman spectroscopy demands high-index-contrast waveguide platforms and a reduced photonic Raman background of the waveguide core material. Tantalum pentoxide is recently emerging as a novel CMOS compatible integrated platform. It has a moderately high refractive index of 2.11, along with a low Raman background. In this article, we investigate and identify the optimal waveguide geometry of tantalum pentoxide slot waveguides to reach the highest overall Raman collection efficiency and lowest waveguide background. Compared to the widely used silicon nitride waveguide platform, tantalum pentoxide waveguides delivers 4 times better performance concerning signal-to-noise ratio (SNR), assuming similar waveguide loss values.

Keywords: On-chip Raman spectroscopy, waveguide sensor, high-index-contrast platforms

1 INTRODUCTION

Raman spectroscopy is a label-free technique that probes the vibrational modes of molecules. These vibrational modes constitute the "fingerprints" of chemical bonds, which can be used for unambiguous molecular identification and quantification. A major challenge intrinsic to Raman spectroscopy is the extremely weak signal. One method to enhance the collection of the signal is to make use of a photonic waveguide [1]-[5]. In waveguide enhanced Raman spectroscopy, the evanescent tail of the waveguide mode overlaps with analytes, and it is employed to excite and collect the Raman signal. The tight confinement of the optical field not only enhances the light-matter interaction but also allows for an efficient collection of the generated signal. Silicon nitride waveguides have been widely explored for on-chip Raman spectroscopy of various analytes, including bulk liquids [1], monolayers [2], and low-concentration gases [4], [5]. However, PECVD silicon nitride optimized for Raman sensing has only a moderate refractive index of 1.89 and a relatively high Raman background, which induces limits in detection limit for analytes with a low concentration or a weak Raman scattering cross-section.

Tantalum pentoxide (Ta_2O_5) has recently been proposed as a novel CMOS-compatible integrated photonic platform that might substitute silicon nitride [6], [7]. Ta_2O_5 has a refractive index of 2.11 and a Raman background roughly three times lower than Si_3N_4 for vibrational modes above 1000 cm^{-1}, as shown in Figure 1(a) [8]. These advantages make Ta_2O_5 very interesting for on-chip Raman spectroscopic applications.

In this work, we compare the performance in terms of Raman collection of Ta_2O_5 and Si_3N_4 slot waveguides by taking into account the recently measured Raman background [8]. The impact of the waveguide geometry is presented systematically for both platforms.

2 METHOD OF SIMULATION

Assuming that the analyte molecules are uniformly distributed in the upper cladding with a molecular density ρ and differential Raman cross-section σ, the total power of backward-propagating Raman signal $P_s(\lambda)$ and Raman background P_{bg} normalized by the pump power are given by

$$\frac{P_s(\lambda)}{P_p} = \eta_0 \cdot \sigma(\lambda) \cdot \rho \cdot \frac{1-e^{-2\alpha L}}{2\alpha}, \qquad \frac{P_{bg}}{P_p} = \eta_{bg} \cdot \kappa \cdot \frac{1-e^{-2\alpha L}}{2\alpha}. \tag{1}$$

where α is the propagation loss, P_p is the pump power coupled into the waveguide, and L is waveguide length. κ is a phenomenological parameter that relates the strength of the Raman background to the thermodynamic fluctuations within the waveguide core [9]. It carries the same dimension as $\sigma \cdot \rho$. The specific conversion efficiencies for the signal and the background (η_0 and η_{bg}) with Stokes wavelength λ_S are defined as [1]

$$\eta_0 = \frac{n_g^2 \lambda_S^2 \iint_{\text{analyte}} |E(x,y)|^4 \mathrm{d}x\mathrm{d}y}{n_{\text{analyte}} \left(\iint_{\infty} \epsilon(x,y)|E(x,y)|^2 \mathrm{d}x\mathrm{d}y \right)^2}, \qquad \eta_{bg} = \frac{n_g^2 \lambda_S^2 \iint_{\text{waveguide core}} |E(x,y)|^4 \mathrm{d}x\mathrm{d}y}{n_{\text{core}} \left(\iint_{\infty} \epsilon(x,y)|E(x,y)|^2 \mathrm{d}x\mathrm{d}y \right)^2}. \tag{2}$$

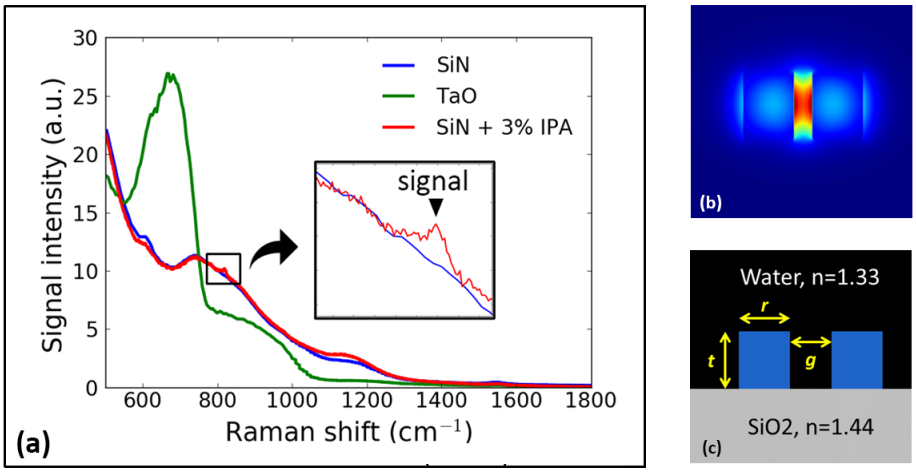


Figure 1. (a) The normalized Raman background of two platforms (reproduced from [8]) along with a typical spectrum obtained with low concentration (3%) of isopropyl alcohol (IPA) and a Si_3N_4 strip waveguide. Inset is a magnified view of the spectrum around the signal. In this situation, our ability to distinguish the signal is limited by the strength of the Raman background and the shot noise associated with it. (b) Typical electric field distribution on the slot waveguide. The field is strongly confined within the slot, inducing a much larger overlap with the analyte. (c) Waveguide cross-section with height t, gap width g and rail width r. The upper-cladding is assumed to be water, and the lower-cladding is assumed to be buried oxide. Waveguide core material are either Si_3N_4 and Ta_2O_5.

where the electric fields at pump and Stokes wavelengths are approximated to be identical. n_g is the group index of the mode, $E(x, y)$ is the electric field, and ϵ is the relative permittivity. η_0 and η_{bg} can be viewed as the product of the modal overlap factors at pump and Stokes wavelengths divided by the square of the modal area of the waveguide at these wavelengths.

For a given analyte and analyte density, we notice that the Raman signal and the background generated per unit length of a waveguide are determined uniquely by η_0 and η_{bg}. The signal-to-noise ratio (SNR) is proportional to the figure of merit (FOM) defined as

$$\mathrm{FOM} = \frac{\eta_0}{\sqrt{\eta_{bg}}}. \tag{3}$$

where we assume that the shot noise associated with Raman background is dominating the noise performance (as will be the case whenever the pump power is sufficiently high and the signal is weak relative to background).

Our analysis is limited to slot waveguides because they are known to perform better than strip or rib waveguides [10]. We compare the performance of Ta_2O_5 and Si_3N_4 slot waveguides through the numerically computed FOM. η_0 and η_{bg} are obtained from Lumerical MODE Solutions. In slot waveguides, the electric field of the TE mode is highly confined in the slot area (Figure 1(b)), resulting in stronger interaction with analytes. As illustrated in Figure 1(c), the under-cladding is assumed to be silicon dioxide (n=1.44) while the refractive index of the upper cladding is 1.33, representing water with a small analyte density. The waveguide geometry is determined uniquely by its height t, rail width r and gap g, with the gap always situated in the center of the waveguide. The FOM of both waveguide platforms with a thickness between 90 nm and 400 nm is shown in Figure 2. The rail width sweeps from 100 nm to 300 nm while the gap ranges from 20 nm to 80 nm.

3 RESULTS AND DISCUSSIONS

The performance of a series of Si_3N_4 and Ta_2O_5 slot waveguides are quantified at a pump wavelength of 785 nm using the aforementioned FOM. For each waveguide height, we analyzed the fundamental TE mode of various geometries on Si_3N_4 and Ta_2O_5 platforms separately. Results are shown in Figure 2. For Si_3N_4 slot waveguides, the optimal FOM improves with the increase of waveguide height, and its corresponding optimal geometry moves towards narrower gap and rail. The same tendency holds for Ta_2O_5 slot waveguides.

From the comparison between Si_3N_4 and Ta_2O_5 slot waveguides, we notice that almost every geometry exhibits better FOM on Ta_2O_5 platform, which agrees with our expectation. The optimal FOM of each height is indicated in Figure 2. Taking 300 nm height as an example, Ta_2O_5 can provide a FOM of 3.91, while the optimal FOM of Si_3N_4 is merely 1.60. Since the Raman background of Ta_2O_5 is roughly three times lower than Si_3N_4 for vibrational modes above 1000 cm^{-1} [8], we estimate that 300 nm Ta_2O_5 can provide 4.2 times higher SNR compared to Si_3N_4.

Apart from the shot noise generated by Raman background, the strength of the background itself also affects our ability to distinguish the signal because there is a practical limit in the accuracy of background subtraction..

Figure 1(c) displays a typical spectrum of waveguide-enhanced Raman spectroscopy with low concentration of analyte. The desired peak is almost buried by background features. In such a situation, it is convenient to consider another figure of merit namely signal-to-background ratio (SBR), which is proportional to η_0/η_{bg}. The computed SBR provided for a given geometry is always higher on the Ta_2O_5 platform. For 300 nm waveguide height, the Ta_2O_5 slot waveguide with optimal SNR generates 9.4 times higher SBR compared to the Si_3N_4 slot waveguide with optimal SNR.

It needs to be noted that the loss is not included in our simulations. If the propagation loss is not negligible, the SNR of waveguide geometries is related to the loss factor as

$$\mathrm{SNR} \propto \sqrt{\frac{1-e^{-2\alpha L}}{2\alpha}}, \tag{4}$$

resulting in a decrease of SNR with the increase of loss. Since narrower waveguides tend to have higher loss, the optimal geometry may change to a wider rail width.

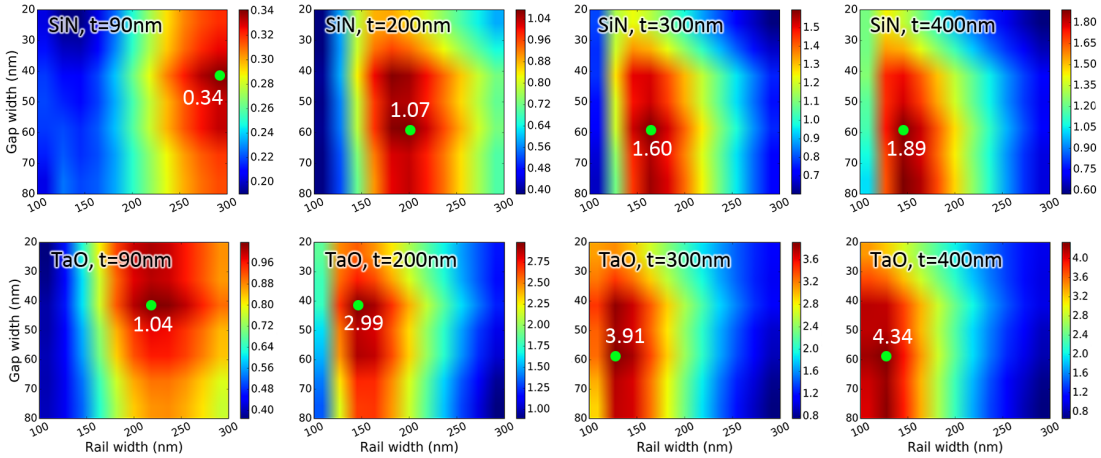


Figure 2. FOM of Si_3N_4 and Ta_2O_5 slot waveguide geometries obatined from numerical computation. The green circles indicate the optimal geometry and its corresponding FOM of each waveguide height.

4 CONCLUSIONS

We numerically computed the specific conversion efficiencies of Raman signal and background, and evaluated the performance of various slot waveguide geometries through calculation of SNR for two waveguide platforms. We conclude that Ta_2O_5 slot waveguides are considerably better than Si_3N_4 slot waveguides. When the height is 300 nm, Ta_2O_5 slot waveguides have a 4.2 times higher SNR and a 9.4 times higher SBR than Si_3N_4 waveguides.

REFERENCES

[1] A. Dhakal, A. Z. Subramanian, P. Wuytens, F. Peyskens, N. L. Thomas, and R. Baets, "Evanescent excitation and collection of spontaneous Raman spectra using silicon nitride nanophotonic waveguides," *Opt. Lett.*, vol. 39, no. 13, pp. 4025–4028, July 2014.

[2] A. Dhakal, P. C. Wuytens, F. Peyskens, K. Jans, N. L. Thomas, and R. Baets, "Nanophotonic Waveguide Enhanced Raman Spectroscopy of Biological Submonolayers," *ACS Photonics*, vol. 3, no. 11, pp. 2141–2149, Oct. 2016.

[3] C. Evans, C. Liu, and J. Suntivich, "TiO_2 Nanophotonic Sensors for Efficient Integrated Evanescent Raman Spectroscopy", *ACS Photonics*, vol. 3, no.9, pp. 1662–1669, July 2016.

[4] S. Holmstrom, T. Stievater, D. Kozak, M. Pruessner, N. Tyndall, W. Rabinovich, R. McGill, and J. Khurgin, "Trace gas Raman spectroscopy using functionalized waveguides," *Optica*, vol. 3, no. 8, pp. 891–896, Aug. 2016.

[5] N. Tyndall, T. Stievater, D. Kozak, K. Koo, R. McGill, M. Pruessner, W. Rabinovich, S. Holmstrom, "Waveguide-enhanced Raman spectroscopy of trace chemical warfare agent simulants," *Opt. Lett.*, vol. 43, no. 19, pp. 4803–4806, Oct. 2018.

[6] M. Belt, M. L. Davenport, J. E. Bowers, and D. J. Blumenthal, "Ultra-low-loss Ta_2O_5-core/SiO_2-clad planar waveguides on Si substrates," *Optica*, vol. 4, no. 5, pp. 532–536, May 2017.

[7] Z. Wang, M. N. Zervas, P. N. Bartlett, and J. S. Wilkinson, "Surface and waveguide collection of Raman emission in waveguide-enhanced Raman spectroscopy," *Opt. Lett.*, vol. 41, no. 17, pp. 4146–4149, Spet. 2016.

[8] A. Raza, S. Clemmen, M. de Goede, R. Ali, P. Hua, S. M. Garcia-Blanco, S. Honkanen, J. S. Wilkinson, and R. Baets, "High index contrast photonic platforms for on-chip Raman spectroscopy," in *Proc. ECIO 2018*, Valencia, Spain, May 2018, pp. 35–37.

[9] N. Le Thomas, A. Dhakal, A. Raza, F. Peyskens, and R. Baets, "Impact of fundamental thermodynamic fluctuations on light propagating in photonic waveguides made of amorphous materials," *Optica*, vol. 5, no.4, pp. 328–336, April 2018

[10] A. Dhakal, A. Raza, F. Peyskens, A. Z. Subramanian, S. Clemmen, N. Le Thomas, and R. Baets, "Efficiency of evanescent excitation and collection of spontaneous Raman scattering near high index contrast channel waveguides," *Opt. Express*, vol. 23, no. 21, pp. 27391–27404, Oct. 2015.

High accuracy transfer printing of III-V/SOI micro-disk resonators for non-linear applications

John McPhillimy[1], Charalambos Klitis[2], Stuart May[2], Benoit Guilhabert[1], Martin D. Dawson[1], Marc Sorel[2], and Michael J. Strain[1]

[1] Institute of Photonics, Dept. of Physics, University of Strathclyde, Glasgow G1 1RD, UK
[2] School of Engineering, University of Glasgow, Glasgow, G12 8LT, UK
e-mail: john.mcphillimy@strath.ac.uk

ABSTRACT

In this paper, we report on the heterogeneous integration of III-V-on-silicon micro-disk resonators using our high alignment accuracy transfer printing method, exhibiting loaded quality factors of $\approx 2.5\times10^4$. High absolute positional printing accuracy allows control over the devices lateral coupling gap to the silicon bus waveguide, enabling selective resonant mode excitation within the multimode micro-disk. We further report efficient non-linear conversion by four-wave mixing. A conversion efficiency of -25dB is obtained at an on-chip optical power of 2.5mW.

Keywords: Photonic Integrated Circuits, Hybrid integration, Transfer Printing, Silicon photonics, III-V semiconductors, Nonlinear optics

1. INTRODUCTION

Silicon-on-insulator (SOI) has become the standard material for the realisation of large-scale photonic integrated circuits (PICs). Its compatibility with silicon's CMOS manufacturing and high index contrast allow extremely compact device footprints, whilst its wide transparency window at the telecomm wavelengths makes it suitable for a large range of applications [1]. However, limitations such as its inefficient light generation at the telecoms wavelengths to its lack of a $\chi^{(2)}$ non-linearity inhibit the production of a full suite of photonic components necessary for highly functional PIC technology. In relation to this, the heterogeneous integration of multiple device platforms is becoming the primary method for producing integrated photonic systems which can enable future applications in areas such as telecommunications, optical sensing technologies and quantum systems [2, 3].

One area greatly benefited by integrated photonics is non-linear optics. The highly compact device geometries of on-chip integrated systems, compared to the fibre-scale architectures, enables much higher modal confinements for increased light-matter interactions over shorter distances. Many different planar material platforms are being investigated, including aluminium gallium arsenide (AlGaAs) and silicon, with the optimum platform exhibiting strong non-linear properties yet providing high-yield processing capabilities [4]. Silicon has a high $\chi^{(3)}$ material non-linearity however it suffers from two-photon absorption (TPA) when operated at the telecomm wavelengths, limiting the possible non-linear applications [5]. Alternatively, AlGaAs is another promising candidate with its large refractive index (n=3.3), large transparency window and high $\chi^{(3)}$ non-linearity [6]. Further to this, the ability to engineer its bandgap means that its TPA can be mitigated benefiting non-linear processes such as four-wave mixing (FWM) [7].

We propose the direct integration of fully fabricated AlGaAs resonators with pre-processed silicon waveguides on the SOI platform, combining both the highly non-linear properties of AlGaAs alongside the manufacturing capabilities of silicon. One potential approach to achieve this is by using transfer printing (TP). TP follows the detachment of a pre-processed device from its native substrate which is then transferred and bonded onto a receiver platform [8]. It also allows the dense integration of hybrid devices over multiple platforms all onto a single-chip making it suitable for the production of large-scale PICs. TP has already been established as a means for producing hybrid devices, with demonstrations ranging from III-V-Si on-chip lasers [9] to micro-LED arrays [10]. Using our high alignment TP technique enables the back-end micro-assembly of efficient passive platforms, where we have recently shown the vertical integration of silicon passive devices as well as the hybrid assembly of silicon and III-V resonators [11,12].

In this work, AlGaAs micro-disk resonators of varying diameters are fully fabricated on their native substrate before being transfer printed on to Si bus waveguides to produce high quality factor hybrid resonator devices. The high alignment accuracy allows selective mode excitation within the disk resonators by control over the lateral coupling gap of the disk resonator and Si waveguide. We further report the non-linear optical characterisation of the hybrid resonators by achieving efficient FWM at low optical on-chip powers. Fabrication and micro-assembly techniques will be detailed along with accompanying experimental results.

2. FABRICATION OF III-V DISK RESONATORS

III-V micro-disk resonators are fabricated from an AlGaAs epitaxially grown material stack on top of a GaAs substrate. Control over the aluminium content of the $Al_xGa_{1-x}As$ enables the production of highly selective sacrificial layers which can be used to isolate AlGaAs structures from the GaAs substrate. For this work an $Al_{0.3}Ga_{0.7}As$ layer of 270 nm thickness is grown on a high aluminium content $Al_{0.9}Ga_{0.1}As$ sacrificial layer of 0.5µm, Fig. 1(a). Micro-disk structures, of diameters ranging from 3µm to 20µm, are patterned using electron-beam lithography into a deposited HSQ resist (Fig. 1(b)) with the pattern fully etched through to the GaAs substrate using reactive ion etching, Fig. 1(c). Unlike previous transfer printing work, no support anchors are used due to the whispering gallery modes being guided in close proximity to the disk sidewalls. Following this, a buffered HF acid selectively etches the high aluminium content $Al_{0.9}Ga_{0.1}As$, which when fully removed, will release the $Al_{0.3}Ga_{0.7}As$ structures onto the GaAs substrate ready for transfer printing.

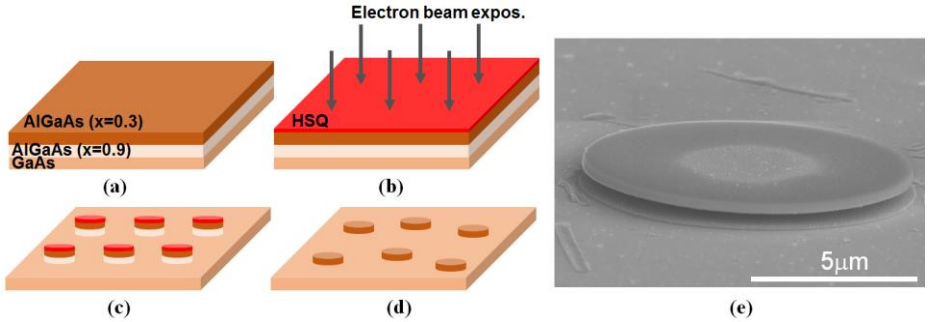


Fig 1. Schematic illustration of fabrication procedure showing (a) AlGaAs-On-GaAs substrate; (b) HSQ resist deposition and structure patterning through e-beam lithography; (c) RIE etch through to GaAs substrate leaving patterned structures of the AlGaAs stack; (d) Wet etch of sacrificial layer leaving AlGaAs disk structures distributed on the GaAs substrate, ready for transfer printing procedure; (e) SEM image of micro-disk structure on GaAs substrate with partially etched sacrificial layer.

3. TRANSFER PRINTED III-V-SOI DISK RESONATORS

The SOI receiver is comprised of a 220nm Si layer above a 2µm buried oxide. Ultra-thin Si waveguides of 220nm×500nm for single-mode TE propagation are patterned by e-beam lithography before fabricated into the Si by RIE processes, with a 100nm thick HSQ upper cladding deposited producing a planar top surface. The TP procedure detaches the disk structure from its native substrate and transfers it to the receiving substrate using a polydimethylsiloxane (PDMS) stamp, made possible by the reversible adhesion properties of the PDMS as shown in Fig. 2(a). The PDMS stamp is brought into contact with the micro-disk structure, with a quick retraction of the stamp overcoming the bond strength and releasing the micro-disk from its native substrate. Once it is moved to its pre-defined position on the receiver substrate, the device is contacted with the surface before a slow retraction of the stamp releases the device, where it is bonded to the substrate. The printing procedure uses no intermediate adhesion layers, relying on the Van der Waal bonding between the micro-disk and substrate below. For alignment, the absolute position of the disk structure is calculated using optical microscopy techniques in relation to the receiving substrate's registration markers. This produces an absolute placement accuracy of ≈100nm [12].

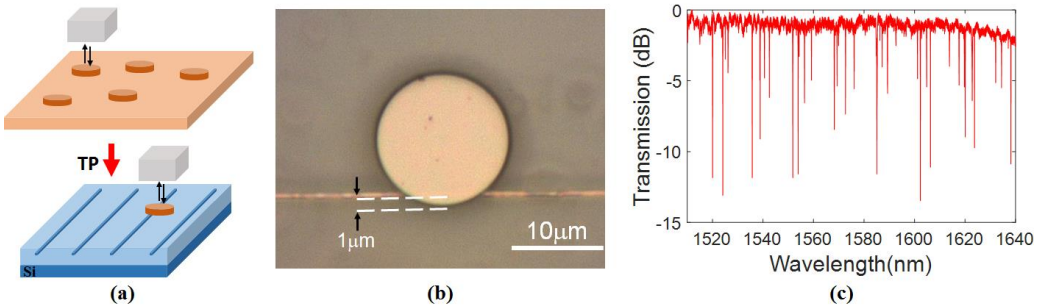


Fig 2. (a) Schematic illustration of transfer printing procedure of micro-disk structure from native substrate to SOI receiver bus waveguide using a PDMS stamp; (b) Top-view optical micrograph of the transfer printed III-V disk resonator with controlled lateral coupling gap of Δx=1µm on top of a Si bus waveguide; (c) Normalised transmission spectra of micro-assembled disk resonator over 1510-1640nm wavelength range containing high extinction multi-mode resonances.

An optical micrograph in Fig. 2(b) shows a hybrid integrated AlGaAs disk resonator evanescently coupled to a Si bus waveguide on the SOI substrate using the aforementioned micro-assembly method, with high loaded Q-factors of $\approx 2.5\times10^4$ and a FSR≈18nm. The structure has a precisely controlled lateral coupling gap of Δx=1µm to promote evanescent coupling to multiple mode families (Fig. 2(c)). The lateral gap can be manipulated during TP to selectively control the mode excitation, an effect previously requiring complex multi-fabrication steps [13].

4. FOUR-WAVE MIXING

In addition to the controllable mode coupling, we perform CW four-wave mixing (FWM) experiments using the hybrid all-pass filters micro-assembled by transfer printing. The experimental set-up (Fig. 3(a)) contains two input sources, a high-power pump beam (λ≈1560nm) and a low-power signal beam (λ≈1585nm) both TE-polarised. The output light is coupled to an optical spectrum analyser (OSA) for measurement of the FWM spectra containing the pump and signal alongside the output idler peak (λ≈1535nm), Fig. 3(b). The FWM efficiency is defined as the ratio of the output idler intensity to the input signal intensity. The first demonstrations of FWM from hybrid devices fabricated by a back-end assembly technique are detailed, with efficiencies in the range of ≈-25dB from on-chip optical power as low as Pp=2.5mW. The FWM efficiency achieved is comparable to state-of-the-art monolithic silicon devices, with identical Q-factor, at low on-chip optical powers (~33dB at 0.7mW) [14]. However, AlGaAs devices do not exhibit TPA saturation experienced by silicon when pumped at higher on-chip optical powers, as shown in Fig. 3(b).

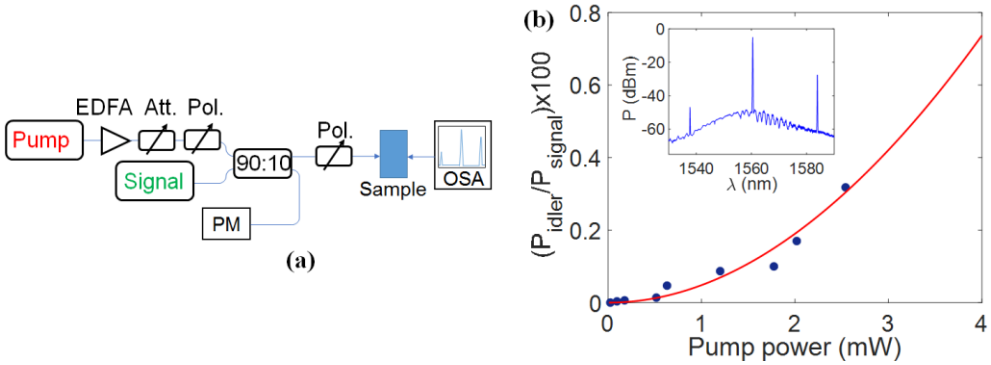


Fig 3. (a) Schematic illustration of measurement setup for FWM experiment. EDFA: Erbium doped fibre amplifier, PM: Power meter, OSA: Optical spectrum analyser; (b) FWM efficiency as a function of on-chip power, showing both experimental data and theoretical curve. (Inset: Measured FWM spectrum captured from OSA showing the idler peak (left), pump peak (centre), and signal peak (right).)

As well as the advantage of increased optical on-chip powers as a method to improve on the FWM efficiency, further optimisation of the hybrid resonator devices through techniques such as dispersion engineering and improved modal confinement can significantly increase the achievable FWM efficiency.

5. CONCLUSIONS

We present the heterogeneous integration of III-V micro-disk structures with the SOI platform using a high alignment accuracy transfer printing method. This technique enables the production of high quality hybrid resonator devices with precise control over mode resonance excitation within the disk cavity. Further to this, we present the efficient non-linear conversion of the hybrid devices by the demonstration of FWM at low optical on-chip powers.

ACKNOWLEDGEMENTS

This work was supported by the EPSRC through *Cornerstone* (EP/L021129/1) and *Parallel Heterogeneous Integration of III-V Devices on Silicon Photonic Chips* (EP/P013570/1). The authors acknowledge the staff of the James Watt Nanofabrication Centre at the University of Glasgow.

REFERENCES

[1] J. Doylend and A. Knights: *Laser & Photonics Rev., vol.* 6, pp. 504–525, 2012.
[2] M. J. R. Heck, *et al: IEEE J. Sel. Top. Quantum Electron.*, vol. 19, pp. 6100117–6100117, 2013.
[3] R. Soref: *IEEE J. Sel. Top. Quantum Electron.*, vol. 12, pp. 1678–1687, 2006.
[4] M. Pu, L. Ottaviano, E. Semenova, and K. Yvind, *Optica.*, vol. 3, pp. 811, 2016.
[5] J. Leuthold, C. Koos, W. Freude: *Nature photonics*, vol. 4, pp. 535—544, 2010.
[6] G. I. Stegeman, *et al*: *Journal of Nonlinear Optical Physics & Materials, vol.* 3, pp. 347–372, 1994.
[7] M. Pu, *et al*: *Laser & Photonic Reviews*, vol. 12, pp. 1800111, 2018.
[8] B. Corbett *et al: Prog. Quantum Electron*, vol. 52, pp. 1–17, 2017.
[9] J. Zhang *et al*: *Optics Express*, vol. 26, pp. 8821, 2018.
[10] C. Bower *et al*: *Photonics Research*, vol. 5, pp. 23—29, 2017.
[11] J. McPhillimy *et al*: *Optics Express*, vol. 26, pp. 297—300, 2018.
[12] B. Guilhabert *et al*: *Optics Letters*, vol. 43, pp. 4883—4886, 2018.
[13] M. Ghulinyan, *et al*: *IEEE Photonics Technology* Letters, vol. 23, pp. 1166-1168, 2011.
[14] M. Strain *et al*: *Optics Letters*, vol. 40, pp. 1274, 2015

Silicon Slot Waveguide based Bulk Refractive Index Sensing of Electrolyte and Carbohydrate

(Student Paper)

Viphretuo Mere[1], Hemalatha Muthuganesan[1], Pallavi Dasgupta[1], Navakanta Bhat[1] and Shankar Kumar Selvaraja[1]

[1]Centre for Nano Science and Engineering, Indian Institute of Science, Bangalore, India.

e-mail: shankarks@iisc.ac.in

ABSTRACT

In this paper, we present a slot waveguide-based on-chip bulk refractive index sensing of liquids. We experimentally demonstrate a slot-based ring resonator with a spectral sensitivity of 363 nm/RIU. We experimentally show sensing of refractive index potassium chloride various concentration and verified with Abbe refractometer. Finally, we experimentally investigated simultaneous absorption and refractive index sensing of glucose.

Keywords: slot waveguide, ring resonator, absorption sensing, photonic integrated circuit, silicon photonics.

1. INTRODUCTION

Photonic integrated circuits (PIC) as a sensor platform for sensing has drawn much attention in recent years. This is mainly because it enables the integration of several optical components on a single chip. On-chip integration of optical components has opened avenues for cost effective and scalable on-chip sensors for medical diagnostics, environmental and food quality monitoring [1-4]. Silicon PIC based sensors are typically realised on silicon-on-insulator (SOI) substrate, as silicon is transparent in the near infrared. Additionally, the compatibility of silicon with CMOS processes enables large-scale integration and volume production. Furthermore, the high index contrast allows compact photonic circuits, enabling sensor arrays for multiplex sensing on a single chip.

An important criterion for PIC sensor is the measurable change in the optical spectrum because of the compositional or density change in the environment (refractive index). In PIC, the transduction is based on the interaction of the evanescent wave of a guided mode with the environment. A perturbation in the environment is sensed by the evanescent wave, that causes a change in the waveguide parameters such as effective refractive index (n_{eff}) and group index (n_g). These waveguide parameters can be measured using interference/resonance-based devices such as ring resonators or Mach-Zehnder interferometers(MZI). Compared to MZI, ring resonator offers the advantages of higher sensitivity and smaller footprint for dense integration of sensors. Ring resonators based on wire waveguides have been demonstrated for biosensing because of their capability to achieve very low detection limit [3]. This is mainly attributed to their sharp resonance that allows accurate measurements of the spectral shift. In addtion, the strong field enhancement near the surface makes it highly attractive for surface sensing. However, wire-based ring resonators have a low spectral shift (in the orders of 100 nm/RIU) [3,4] because of their low spatial field overlap with the bulk environment. Thereby, it limits wire-based ring resonators for bulk sensing applications. Recently, slot waveguide has attracted much attention due to its inherent ability to guide light in a low index medium [1,5,6]. Unlike wire waveguides, slot waveguides have the advantage of increased spatial overlap of the evanescent and sensing environment, resulting in a higher sensitivity (nm/RIU). Hence, slot waveguides are highly attractive for bulk index sensing applications.

In this paper, we demonstrate bulk refractive index sensing using slot waveguides. The refractive index measurement is studied using different concentrations in various fluids such as potassium chloride (KCL), an electrolyte and glucose, a carbohydrate. We experimentally demonstrated both absorption and refractive index sensing of glucose by monitoring the quality factor and wavelength shift at different concentrations of glucose.

2. Principle of Operation

Figure 1 shows a schematic of a slotted ring resonator. The inset shows the cross-section of a slot waveguide and the corresponding electric field distribution in water. In a ring resonator structure, the light propagating through the straight waveguide is evanescently coupled into the ring. The wavelengths that satisfy the resonant condition ($m\lambda = 2\pi n_{eff}R$) resonate inside the ring. The wavelength sensitivity due to the variation of the cladding refractive index (Δn_{cl}) can be observed by a shift in resonant wavelength ($\Delta\lambda$). The wavelength sensitivity can be expressed as a wavelength shift per unit change in the bulk refractive index of cladding (with units of nm/RIU), given by [4],

$$S = \frac{\Delta\lambda}{\Delta n_{cl}} = \frac{\lambda_o}{n_g}\frac{\partial n_{eff-cl}}{\partial n_{cl}} \quad (1)$$

Where n_{eff} and R are the effective refractive index and the radius of the ring. In (1), $\Delta n_{eff\text{-}cl}$ is the change in the effective index because of the change in the cladding index (Δn_{cl}).

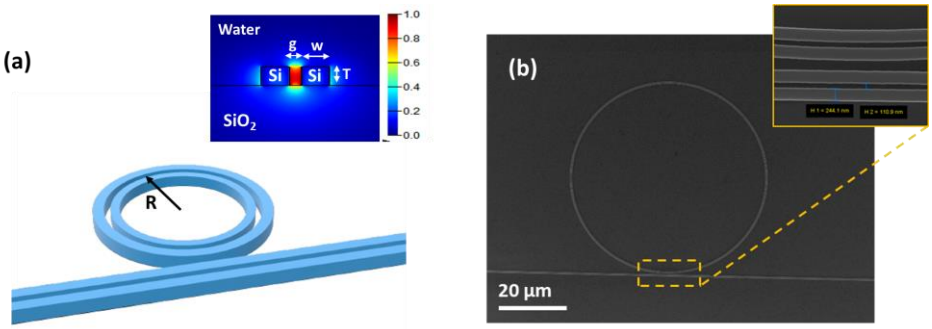


Figure 1. Schematic of slot waveguide-based ring resonator. Inset shows the simulated electric field distribution of an SOI slot waveguide in water, slot rail width (W)= 240 nm, gap (g) = 110 nm and thickness (T)= 220 nm. (b) SEM image of the fabricated slotted ring resonator, inset showing close-up view of the coupling region between the slotted ring and the bus waveguide.

3. Results and Discussion

The fabrication of slot-based ring resonator is done on SOI platform with 220 nm device layer and 2000 nm buried oxide. The fabrication involved patterning of slotted waveguides using electron beam lithography (e-beam) followed by Reactive-Ion-Etching (RIE) of 220 nm of silicon. A second e-beam lithography is performed to pattern the grating couplers followed by 70 nm etch of silicon in RIE. Figure 1(b) shows the SEM image of the fabricated device. The inset shows the coupling region of the slotted bus and ring having a radius R= 29.69 µm. A tunable laser and a photodetector are used to characterise the optical spectrum of the device. The temperature of the device is maintained at 27 ºC using a Peltier thermoelectric cooling element.

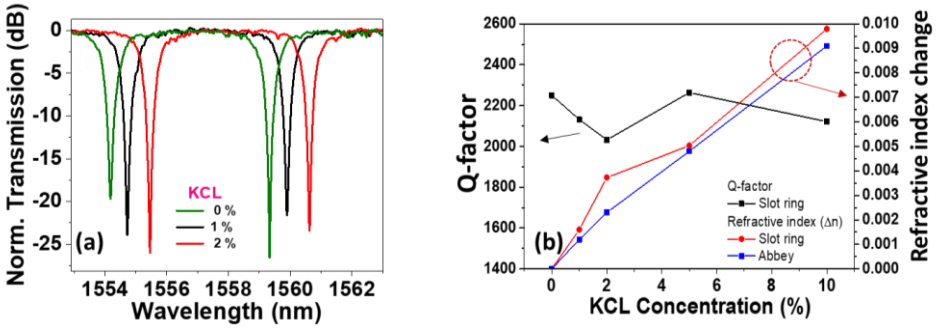


Figure 2. (a) Transmission response of the slotted ring resonator at different KCL concentrations; (b) The quality factor (Q-factor) and the refractive index change at different KCL concentrations measured using slotted ring resonator and Abbe refractometer.

Figure 2(a) shows the transmission response of the ring resonator for different consecrations of KCl. The measured free spectral range is 4.66 nm, and the corresponding group index is 2.765 at 1550 nm wavelength. Using (1), the cladding refractive index is calculated and compared with the Abbe refractometer measurement. Figure 2 shows an excellent agreement between slot-ring measurement and refractometer measurement. Based on this, we measured a sensitivity of 363 nm/RIU. The extracted quality factor (Q-factor) of the ring at different KCL concentrations indicates no sign of degradation (Fig. 2(a)) that suggest that there is negligible absorption increase at 1550 nm wavelngth band with concentration. The same experiment is performed for glucose with different concentrations as shown in Fig. 3. The ring response for different glucose concentrations is shown in Fig. 3(a,b); the Q-factor is reduced by almost half. This indicates that the presence of glucose causes attenuation of light which results in lower Q-factor of the ring resonator. The attenuation is due to broad absorption of glucose around 1550 nm band [2, 7]. Slot waveguides offer simultaneous measurement of absorption and refractive index change offers multi parameter sensing. Furthermore, resonance cavity reduced the effective device footprint as well.

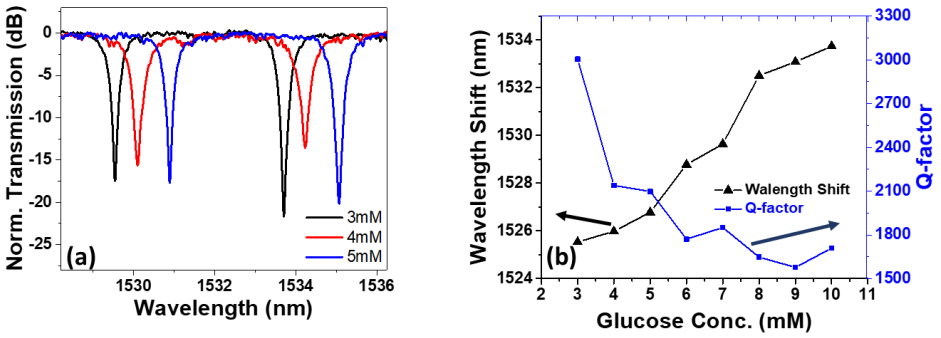


Figure 3. (a) Transmission response of the slotted ring resonator at different glucose concentrations (b) Wavelength shift and the extracted Q-factor at different glucose concentrations.

4. CONCLUSIONS

In this work, we presented a highly sensitive slot waveguide bulk index sensing platform with sensitivity of 363 nm/RIU. We experimentally demonstrated refractive index measurement of KCL and verified using Abbe refractometer. Finally, we demonstrate a simple approach for absorption and refractive index-based monitoring of glucose concentration.

ACKNOWLEDGEMENTS

"We thank SHELL India for funding this research. We also acknowledge funding support from MHRD through NIEIN project, from MeitY and DST through NNetRA"

REFERENCES

[1] J. T. Robinson, L. Chen, and M. Lipson, "On-chip gas detection in silicon optical microcavities," *Optics Express, 2008.*

[2] E. Ryckeboer, R. Bockstaele, M. Vanslembrouck, and R. Baets, "Glucose sensing by waveguide-based absorption spectroscopy on a silicon chip," *Biomed. Opt. Express*, 2014.

[3] M. Iqbal, M. A. Gleeson, B. Spaugh, F. Tybor, W. G. Gunn, M. Hochberg, T. Baehr-Jones, R. C. Bailey, and L. C. Gunn, "Label-free biosensor arrays based on silicon ring resonators and high-speed optical scanning instrumentation," *IEEE J. Sel. Top. Quantum Electron.*, 2010.

[4] P. R. Prasad, S. K. Selvaraja, and M. M. Varma, "Full-Range Detection in Cascaded Microring Sensors Using Thermooptical Tuning," *J. Light. Technol.*, 2016.

[5] T. Claes, J. G. Molera, K. De Vos, E. Schacht, R. Baets, and P. Bienstman, "Label-free biosensing with a slot-waveguide-based ring resonator in silicon on insulator," *IEEE Photonics J.*, 2009.

[6] V. Mere, R. Kallega, and S. K. Selvaraja, "Efficient and tunable strip-to-slot fundamental mode coupling," *Opt. Express*, vol. 26, no. 1, 2018.

[7] W. Zhang, R. Liu, W. Zhang, H. Jia, and K. Xu, "Discussion on the validity of NIR spectral data in non-invasive blood glucose sensing," *Biomed. Opt. Express*, 2013.

Automatic look up table generation technique for photonic integrated circuits

(Student Paper)

Maziyar Milanizadeh, Douglas Aguiar, Francesco Morichetti and Andrea Melloni
Dipartimento di Elettronica, Informazione e Bioingegneria - Politecnico di Milano,
Milano, 20133 Italy
e-mail: maziyar.milanizadeh@polimi.it

ABSTRACT

In this work we presented a technique which can be adopted to create automatically and efficiently lookup tables for arbitrary photonic integrated circuits compensating for external perturbations like thermal crosstalk. Its performance is experimentally examined in coupled microring resonators implemented in silicon photonics. These lookup tables can dynamically update themselves to new conditions of the chip upon the need.

Keywords: Automatic tuning algorithm, lookup table, thermal crosstalk

1. INTRODUCTION

Most Photonic Integrated Circuits (PICs) are kept under control and led to work in the desired condition using values for their key parameters pre-calculated or pre-determined and stored in a memory of the electronic circuit that drive and control the PIC. The generation of these values is usually very time consuming and obtained with specific measurements strongly dependent on the circuit architecture, the typical random initial state of the circuit and other uncertainties.

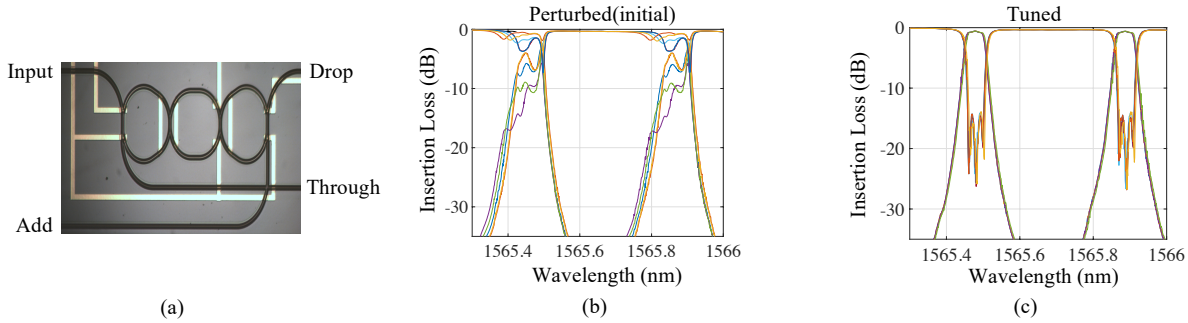
Creating a lookup table requires the tuning of the device, the extractions of the control parameters and the storage in a typically multidimensional matrix named generally lookup table. The generation of the table in a fast, efficient, precise and robust way is a challenging task that has a significant impact in the production, testing and qualification process of most PICs.

Here we propose the automatic generation of the lookup table exploiting a tuning technique robust against external perturbations and thermal crosstalk, which is one of the main reasons for slow or even failure convergence in the tuning and alignment of the circuits. Conventional tuning methods exploiting sequential tuning of individual point of the function through sweeping solutions to find the optimum status [1]. This technique can operate on filters with 5 degrees of freedom even in presence of thermal crosstalk in the time scale of a second.

2. Thermal cross-talk free tuning technique

In this section we present a novel technique, named *Thermal Eigenmode Decomposition* (TED) [2], which can be adopted in generic control algorithms to cancel out the effects of thermal crosstalk in arbitrary PICs including heat sources such as heaters, lasers or electronic drivers. In other words, the TED concept is neither circuit-specific, nor algorithm specific. This allows us to use TED in the required tuning algorithm based on the need, for example to generate lookup tables to align filters, tune lasers to the WDM grid or configure switch fabrics.

TED technique requires all the actuators to be controlled simultaneously according to appropriate weights, which are based on eigensolution of the thermally coupled system. Mathematically this implies a deterministic coordinate transformation. Here we evaluate experimentally the performance of the TED based tuning algorithm on a 3rd order coupled MRR filter. Fig. 1(a) shows a top view microphotograph of the device, which was fabricated in a



(a) (b) (c)

Figure 1: Experimental validation of automatic tuning based on TED method. (a) Top view photograph of a 3rd order coupled MRR filter fabricated in SiON technology. Measured transmission of the Through and Drop port of the filter (b) for five randomly perturbed configuration (+/- 100 pm) induced by using thermal phase shifters and (c) after automated tuning performed by using TED based method.

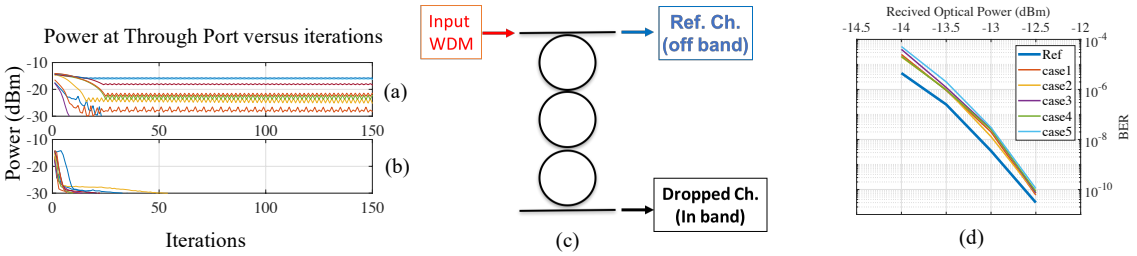


Figure 2: (a) Convergence rate of TED based tuning (with adaptive step size scheme) for 10 random cases versus (b) individually tuning of the MRRs starting from the same random perturbations. (c) schematic of the setup for bit error rate (BER) measurements. As a reference, BER was measured at Through port (in blue) while the filter was detuned from the signal then measurements were done for 5 locked filters observing the signal at drop port (in black)). (d) BER measurements comparing reference path with 5 different tuned filters. Blue curve is the reference obtained at Through port when the filter is detuned from signal. 5 other curves present BER of dropped channel showing less than half a dB power penalty in all the cases.

high-index-contrast silicon oxynitride (SiON) photonic platform (details in [3]). The round trip phase of each MRR of the filter can be individually controlled by means of metallic heater deposited on top of the waveguide uppercladding. The optical power is measured via an external photodiode and transmitted to a PC where a control algorithm determines the control signals to be applied to the heaters. Phase perturbations were intentionally introduced in every MRR of the SiON filter by applying random errors in the voltages driving the heaters around their optimum tuning point. Figure 1(b) shows the measured Through and Drop port transmission of the perturbed filter when the induced frequency spread of the MRR resonances is as large as 100 pm (12.5 GHz versus 6.5 GHz BW of the filter). A 5 Gbit/s OOK modulated signal (with carrier wavelength of 1565.470 nm) was used and the TED based tuning algorithm was targeted to minimize the output power at the Through port. Transfer function of converged filter for Through and Drop port is presented in Fig.1(c) demonstrating a fined tune frequency response obtained through this technique. To illustrate the improvement in tuning performance, TED based method was then compared to the individual tuning in terms of convergence ratio and speed. For a fair comparison, we assumed the same perturbed configurations of Fig.1(b) as the initial state of the filter and we applied both schemes with the same phase step-size for the heaters. Figure.2(a), shows that in many cases sequential tuning of individual resonators did not converge to the target filter shape and a poor Through port isolation with deep oscillations in the steady state was obtained. In contrast, the TED-based tuning did converge for all the considered initial cases in less than 40 iterations (see Fig. 2(b)). To demonstrate that these tuned frequency responses of the filters (Fig.1(c)) are optimum for the transmitted channel, using the setup in Fig.2(c) we measured the BER of dropped channel for 5 converged cases and compared it with the reference BER obtained at through port when the filter was detuned. We can see all converged cases, even if they started from different initial perturbations share the same BER performance which is less than a half dB power penalty.

3. Automatic lookup table creation

A tuning algorithm based on the TED technique is adopted in a software which can control the tuneable laser source (TLS) to automatically create a lookup table for a 3rd order coupled MRR add/drop filter based on silicon photonics. The silicon channel waveguide is 490 nm wide and is buried in a silica cladding. The filter design is optimized to have 1 THz (8 nm) FSR, 40 GHz 3dB bandwidth, and 20 dB in-band isolation. Deeply etched thermo optical actuators offers improved performance. The schematic of complete 4 port filter along the control loops is presented in Fig.3(a). A channel labeller is integrated on chip by using a thermally tuneable Mach Zehnder (MZ) modulator allowing to distinguish the operating channel at the monitor CLIPP in presence of other WDM channels. This is done by applying a shallow modulation to the channel inserted in the Add port which can be extracted from the readout signal of the CLIPP. The FPGA reads the CLIPP measurements while controlling the MZ and heaters alongside the TLS. For each row of the lookup table, it moves the TLS to the relevant wavelength and execute the tuning algorithm to find the tuned parameters of the filter for that channel. This is done till the table is completely filled up based on the performance requirements of the filter along the frequency band. Microscopic picture of the fabricated chip including the labelling MZ is presented in Fig.3(b). In the first trial, starting from natural frequency response of the filter (blue curves in Fig.3(c)), tuning algorithm is examined with a 10 Gbit/s OOK modulated channel at 1561.83 nm being launched at the Add port. This channel is labelled through the integrated MZ and the optical power is measured at the Drop port through the implemented CLIPP. Label amplitude is extracted from the CLIPP reading and minimized to find the fine-tuned filter response as presented in Fig.3(c) with green curves.

Tuning of filter in presence of DWDM channels requires the it to be optically disconnected from the bus (during the tuning process) to prevent impairing other channels. This operation is known as hitless channel tuning. In our device, this operation is achieved by switching MZ tuneable coupler connecting the filter to the bus WG between In/Out ports. This enables reaching high degrees of isolation during the tuning and realized by introduction of π

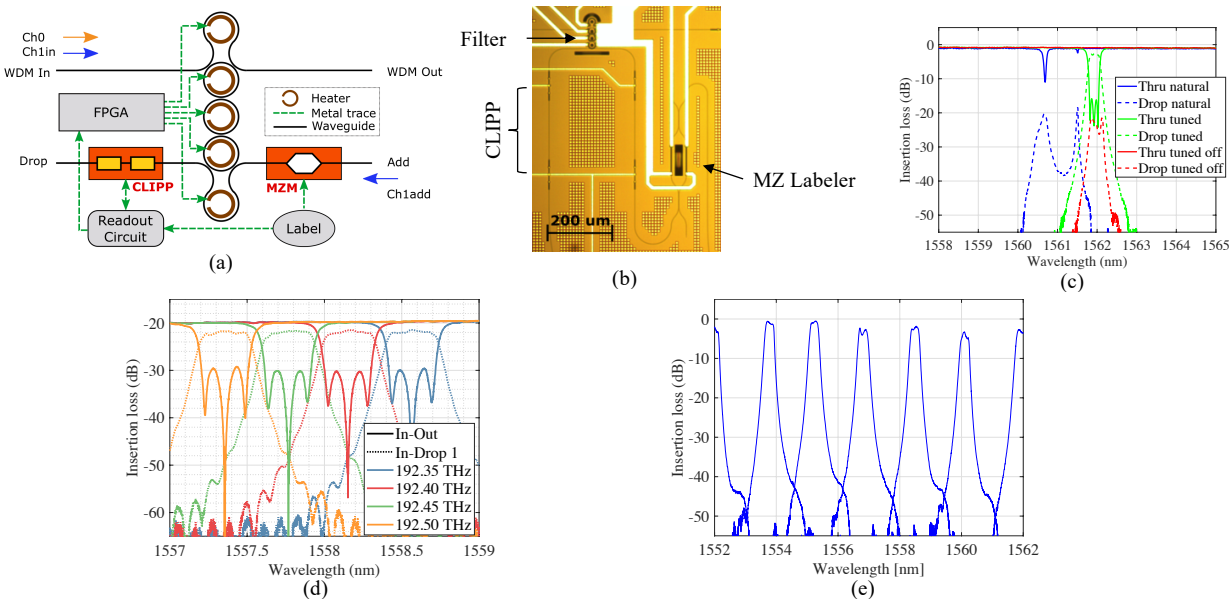


Figure 3: (a) Functional block diagram of the reconfigurable hitless filter along the relevant control elements adopted to demonstrate fine tuning and automatic look up table creation b) Filtering unit including monitoring CLIPP and on-chip labeler to mark the add signal (c) tuning of filter for one channel starting from its natural response (in blue) tuned filter response in green and tuned for disconnected case (hitless scheme) in red. (d) Through and Drop port detailed transfer function of filters for automatically created lookup table on 4 channels 50 GHz apart. (e) Drop port transfer function of filter from automatically created lookup table for 7 channels on a 10 nm span. Frequency response of filter is tailored to match the requirements of the channel without any penalty on the WDM comb.

phase shift through the implemented heater in the MZ. Unfortunately, this process introduces thermal perturbations to the filter which is needed to be considered. Brilliant point of the TED based algorithms is that, this is taken care of automatically. To demonstrate, using the fine-tuned filter (green curve in Fig.3(c)) bias of the MZ heater is modified to disconnect the filter from the bus. Since TED based algorithm was running, it automatically compensated the thermal perturbations due to this shift and maintained the filter at its channel. Red curves in Fig.3(c) presents disconnected Drop port frequency response without any wavelength drifts and centred at the channel.

Adopting this technique in a software which can shift the TLS wavelength and tune the filter for each channel, we tried to create a look up table for four different channels with 100Gbit/s DP-QPSK signal spaced at 50 GHz. Transfer functions of the filter using this automatically created lookup table for connected case is shown in Fig.3(d). Measuring the performance of these filters, we observed in all the cases required performance is satisfied. To examine this concept on a wider frequency band, using a 10 Gbit/s OOK modulated channels starting from 1552 nm, we tried to automatically create lookup table for 10 nm of channels spaced 200GHz apart. Drop port transfer function of this lookup table is presented in Fig.3(e). Frequency response of filter is automatically reshaped to match the BW of the channel without any consequence on the comb. This concept can be extended to multiple filters implemented in the same chip. Thermal perturbations from the neighbouring filters (along their tuning process) can be accounted while tuning the filters to automatically find their fined tuned conditions and create the relevant look up table. Upon the need, these lookup tables can adapt themselves to new conditions of the chip automatically. These new conditions could be large changes in working points of a neighbouring function or even failures in controlling the overall temperature of the chip through thermos optic controllers. This technique can be used to create automatically lookup tables for arbitrary photonic integrated functions with different requirements for example different routing path of a mesh, or different configuration of a tuneable bandwidth filter.

4. CONCLUSION

We presented a robust concept to automatically create lookup table for photonic integrated functions in presence of thermal cross talk in dense circuits. Through experimental trials in coupled microring resonators we demonstrate a thermal cross talk free tuning technique and its application in creating an algorithm to automatically create and update lookup tables in presence of external perturbations.

This work was supported in part by the EU H2020 Program under Grant STREAMS (no. 688172)

REFERENCES

[1] J. C. C. Mak, W. D. Sacher, T. Xue, J. C. Mikkelsen, Z. Yong and J. Poon, "Automatic Resonance Alignment of High-Order Microring Filters," Quantum Electronics, vol. 51, no. 11, pp. 1-11, 2015.

[2] M. Milanizadeh, D. Aguiar, A. Melloni, and F. Morichetti, “Cancelling thermal cross-talk effects in photonic integrated circuits,” Journal of Lightwave Technology, 2019, accepted for publication. DOI: 10.1109/JLT.2019.2892512

[3] A. Melloni, F. Morichetti, G. Cusmai, R. Costa, A. Breda, C. Canavesi, and M. Martinelli, "Progress in large integration scale circuits in SiON technology," in Transparent Optical Networks, Rome. Italy, 2007. R.G.

Chip-based compact squeezing experiment at a telecom wavelength

François Mondain[1], Tommaso Lunghi[1], Alessandro Zavatta[2,3], Élie Gouzien[1], Florent Doutre[1], Marc de Micheli[1], Sébastien Tanzilli[1], and Virginia D'Auria[1]

[1] Université Côte d'Azur, Institut de Physique de Nice (INPHYNI), CNRS UMR 7010, Nice- France

[2] Istituto Nazionale di Ottica (INO-CNR) Largo Enrico Fermi 6, 50125 Firenze, Italy;

[3]LENS and Department of Physics, Universitá di Firenze, 50019 Sesto Fiorentino, Firenze, Italy.

e-mail: virginia.dauria@univ-cotedazur.fr

ABSTRACT

We present a compact and easy-to-use set-up exploiting the association of commercial plug-and-play fibre components and integrated optics on lithium niobate for the generation and detection of squeezed light at a telecom wavelength. Light exhibits a reduced quantum noise of -2.00±0.05 dB below the shot-noise level in a single-pass configuration.

Keywords: Quantum communication; integrated optics; Squeezed states; Lithium Niobate; Homodyning.

1. INTRODUCTION

Squeezed states of light exhibit a reduce noise level with respect to the classical quantum limit represented by lasers' shot noise. In the last years, after having played a crucial role in fundamental research on light quantum properties, single- and multi-mode squeezed states have been identified as fundamental ingredients for a variety of quantum technologies ranging from quantum sensing to quantum computing and communication [1]. Nevertheless, squeezing generation and detection traditionally relies on free space systems, not scalable, requiring careful alignment and extremely sensitive to mechanical instability. Accordingly, we have been assisting in the last years to a growing interest towards the realization of compact, stable and versatile squeezing experiments compatible with practical and user-friendly realizations [2]. This effort has strongly benefitted from integrated optics on different substrates with the demonstration of on chip squeezing generation both in single pass [3] and in resonant systems [4] as well as on chip homodyne detection [5] or generation and detection [6]. These very nice results certify how the competition on the hot topic of squeezing miniaturization is increasing. At the same time, we stress that, in all these works, important building blocks of the squeezing experiment were still realized thanks to complex bulk optics systems.

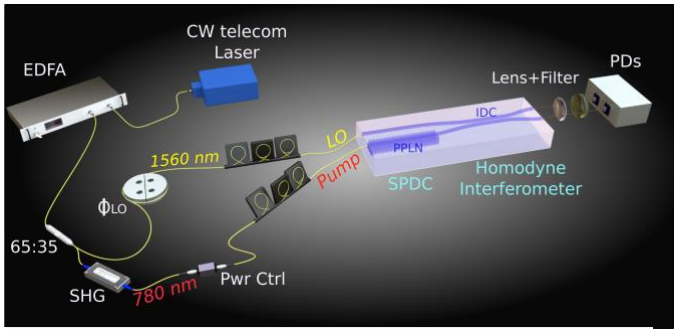


Figure 1. Experimental setup. It associates off-the-shelf fibre components with an original lithium niobate chip for the squeezing generation and detection.

In our work, we provide an original solution to the full miniaturization of continuous variable experiments by means of a hybrid approach associating integrated optics to mature classical technologies. This strategy allows gathering different tools to take advantages of compact and on-chip squeezing generation and detection as well as of the possibility of plug- and-play, versatile and stable systems based on commercial guided wave technology [7]. More in details, squeezing is generated in a single pass configuration via spontaneous parametric down conversion (SPDC) on lithium niobate and detected, directly on chip, thanks to a homodyne detector whose interferometric part relies on an integrated optical coupler. Lithium niobate is particularly suitable to develop photonic circuits, featuring high nonlinearity and the possibility of implementing quasi-phase-matching to engineer the nonlinear optical response [8]. Moreover, the high confinement of light in waveguides combined with

non-linear properties allows obtaining compact and efficient generation of squeezing even in a single pass (cavity-free) configuration [3]. On the other hand, spatial mode matching issues at homodyne interferometers are greatly simplified with single-spatial-mode splitters and combiners [2], whose splitting ratio can be controlled, whenever required**,** thanks to electro-optical effect **[**6**]**. All the other building blocks of the experiment are realized thanks to off-the-shelf components coming from telecom and non-linear optics. The wedding between integrated optics and these technologies allows realizing and extremely compact and easy-to-assemble experiment, where stability and spatial mode matching issues affecting bulk experiments are completely removed.

2. EXPERIMENTAL SETUP

Our experimental setup is sketched in Fig.1. It associates an fully fibred injection system with our home-made lithium-niobate chip.
The setup relies on a master, fibre-coupled laser generating a CW optical beam at 1560.44 nm and amplified up to 0.95 W with an erbium-doped fibre amplifier (EDFA). At the output of the EDFA, the single mode laser light is split by a high-power 65:35 fibre coupler (f-BS). The less intense output is directed to a home-made fibre stretcher allowing to scan its phase, to be subsequently used as local oscillator (LO) for the homodyne interferometer. The brighter output is frequency doubled to 780.22 nm via second-harmonic generation periodically poled lithium-niobate ridge waveguide (SHG) in a commercial and used to pump the squeezer.

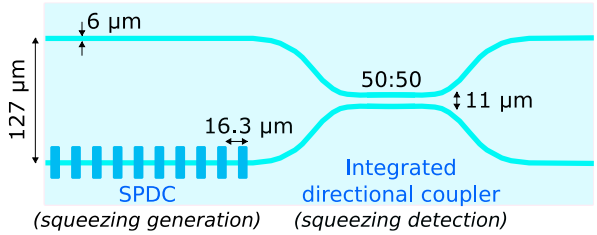


Figure 2. Photonic chip for the squeezing generation and detection.

The LO at 1560.44 nm and the pump at 780.22 nm are sent to a fibre array and coupled to the home-made photonic chip. A fibre polarisation controller (PC) on each arm is introduced to properly adjust the polarisation. The entire optical setup upstream the chip is made using by plug-and-play components guaranteeing a versatile and quick operation [2]. The chip is represented in Fig.2. Its total length is 5 cm. It includes a periodically poled waveguide for the generation of squeezing by SPDC at the telecommunication wavelength of 1540.44 nm, followed by an integrated beam-splitter, exploiting evanescent wave coupling and representing the core of the homodyne detection interferometric part. The SPDC occurs in one arm of the beam-splitter, while the other serves for the injection of the local oscillator (LO). All waveguides are obtained by soft proton exchange [8] and have a width of 6 µm. The 127 µm spacing between the input (output) waveguides is compatible with of-the-shelf fibre-arrays. The homodyne photodiodes are outside the chip and are bulk commercial components.

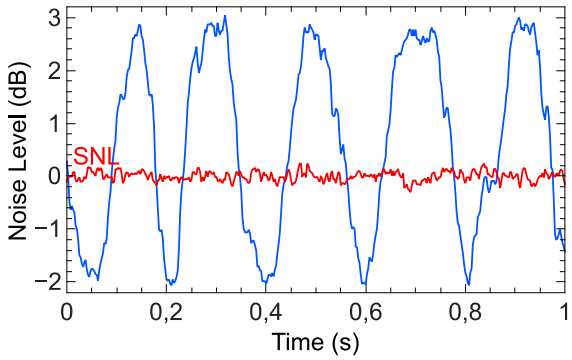


Figure 3. Normalised noise variances at 2 MHz as a function of the LO phase (proportional to the time). This measurement corresponds to the maximum coupled pump power (40 mW).

With our setup, for a CW pump power of 40 mW, we demonstrate a raw squeezing level of -2.00 ±0.05 dB, corresponding to - 3.00 ± 0.05 dB when corrected from avoidable losses (see Fig. 3) [7]. This value represents, to

our knowledge, the highest reported squeezing level in single pass configuration pumped in CW regime and it demonstrates the validity of our approach.

The demonstrated approach is extremely versatile. Moreover, our solution provides squeezed light at a telecom wavelength so as to be compatible with quantum communication in existing optical fiber networks.

Finally, we would like to stress that the perspectives with such a photonic circuit lies in the on-chip generation and characterization of Schrödinger cat states as well as CV quantum qubits, thus making our chip a flexible tool for quantum metrology and computing.

3. CONCLUSIONS

In conclusion, we have demonstrated a compact, versatile, and easy-to-handle experiment combining integrated optics on lithium niobate and off-the-shelf telecom and nonlinear components. The realised photonic circuit integrates on-chip the squeezing generation and the optical coupler of the homodyne interferometer. The squeezed light generated at telecom wavelength exhibits a noise compression of -2.00 ± 0.05 dB for a pump power of 40 mW. Outside the chip, the setup employs only plug-and-play fibrered components requiring no alignment procedures and allowing for a quick system reconfiguration. These advantages guarantee an extreme reliability and make our approach a valuable candidate for real-world applications based on continuous variable quantum systems.

ACKNOWLEDGEMENTS

This work was conducted within the framework of the project OPTIMAL granted through the European Regional Development Fund (Fond Européen de dévéloppement regional, FEDER). Authors also acknowledge financial support from the Agence Nationale de la Recherche (ANR) through the projects SPOCQ (ANR-14-CE32-0019) and Hy-Light (ANR-17-CE30-0006-01)

REFERENCES

[1] N. J. Cerf, G. Leuchs , E. S. Polzik, “Quantum Information With Continuous Variables of Atoms and Light”, Imperial College Press (2010).

[2] F. Kaiser et al., “A fully guided-wave squeezing experiment for fiber quantum networks,” Optica 3, 362–365 (2016).

[3] K. Yoshino, T. Aoki, and A. Furusawa, “Generation of continuous-wave broadband entangled beams using periodically poled lithium niobate waveguide”, Appl. Phys. Lett. 90, 041111 (2007).

[4] M. Stefszky, R. Ricken, C. Eigner, V. Quiring, H. Herrmann, C. Silberhorn, Phys. Rev. Applied 7, 044026 (2017).

[5] C. Porto, D. Rusca, S. Cialdi, A. Crespi, R. Osellame, D. Tamascelli, S. Olivares, and M. G. A. Paris, J. Opt. Soc. Am. B 35, 1596 (2018)

[6] F. Lenzini, et al. “Integrated photonic platform for quantum information with continuous variables”, arxiv: 1804.07435 (2018).

[7] F. Mondain et al., “Chip-based squeezing at a telecom wavelength,” arXiv 1811.02907 (2018).

[8] O. Alibart, et al.“Quantum photonics at telecom wavelengths based on lithium niobate waveguides”, Jour. Opt., 18, 104001 (2016).

Photonic Crystal/Photonic Wire Multiple-micro-cavity Structure

Mohd Nuriman Nawi[1], Dilla Duryha Berhanuddin[1], Ahmad Rifqi Md Zain[1,2], Richard M. De La Rue[3]
[1] Institute of Microengineering and Nanoelectronics (IMEN), Universiti Kebangsaan Malaysia (UKM), 43600, Bangi, Selangor, Malaysia
[2] John A. Paulson School of Engineering and Applied Sciences, Harvard University, Cambridge, Massachusetts, 02138, United States
[3] Optoelectronics Research Group, School of Engineering, Rankine Building, Oakfield Avenue, University of Glasgow, Glasgow G12 8LT, UK
e-mail: rifqi@ukm.edu.my

ABSTRACT

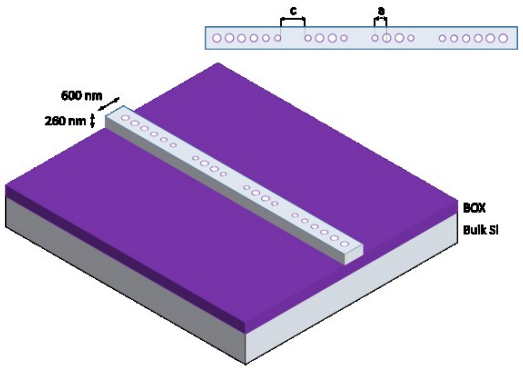
We present a study of triple-cavity 1-dimensional (1D) photonic crystal structures embedded in silicon photonic wire (PhC/PhW). Three cavity resonance wavelengths were observed. Structures with a greater number of resonance wavelengths would result from increasing the number of coupled cavities. The structure was designed to operate at fibre telecommunication wavelengths where all the resonance wavelengths fall in the C and L band regions. Factors that define the performance of the device - such as wavelength selectivity, resonance quality factor and transmission magnitude can be controlled by precise definition and simulation of the photonic crystal micro-cavity. The accuracy of the prediction of the resonance wavelengths was evaluated in both simulation and experiment, with good agreement between them. This approach is promising for exploitation in photonic integrated circuits (PICs) for wavelength division multiplexing (WDM) applications, providing a possible solution for smaller footprint devices.

Keywords: multiple-resonance, multiple-cavity, micro-cavity, 1D photonic crystal, wavelength division multiplexing, photonic integrated circuit.

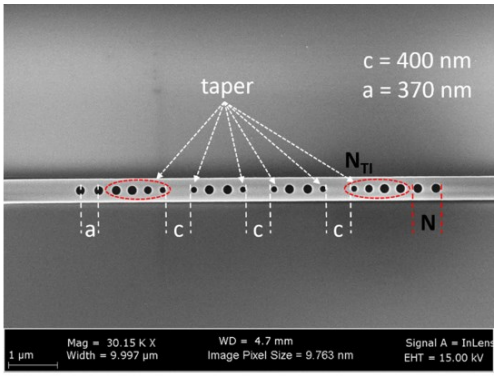
1. INTRODUCTION

The limitations of compact electronic devices form a serious bottleneck [1]. To overcome such problems, PICs have been foreseen as one of the possible solutions [2]. With current advances in fabrication technology, nanostructured devices can be realised with dimensional precision down to the nanometer scale [3]. Device structures that exploit photonic crystal principles can be used to guide and restrict the propagation of light [4]. Various device structures based on PhC principles have been investigated [5-7] . The present work focuses on 1D PhC/PhWs because of their compactness and the importance of small scale component integration. WDM technology is mature and is now widely used in the transfer of large bandwidth data between different locations. The progressively increasing demand for high data transmission rates implies continuing pressure on available space in fibre-optical networks. This issue can be addressed using PICs in which PhCs play a key role in the realisation of densely integrated photonics circuit components [1].

The 1D PhC/PhW micro-cavity concept has been well researched and can provide high quality factor resonances that are suitable for filtering in very small scale structures [8]. The wavelength selectivity can be precisely controlled by properly specifying and realising the required structure parameters [5, 8-9]. Silicon on insulator (SOI) with a silicon thickness close to 260 nm, a buried oxide thickness of 2 µm and substrate thickness of 700 µm has been chosen as the platform for the realisation of PIC due to its CMOS compatibility and ease of integration. Previous work has reported two-cavity stuctures, in which the single-cavity resonance wavelength was split into two [9]. The present work inherits the same SOI platform, with similar PhC/PhW micro-cavity structures, but uses an additional cavity, as shown schematically in Fig. 1(a).



a.



b.

Fig. 1(a). Schematic structure of 1D PhC/PhW on SOI platform with photonic wire waveguide dimensions of 600 nm width and 260 nm height. The lattice constant, a = 370 nm; cavity internal spacer distance, c = 400 nm; mirror hole radius, r = 90 nm for N number of mirror holes and hole size taper for optimization were chosen to work at telecommunication wavelength, C+L-band. Fig. 1(b). The SEM image of the fabricated device structure shows the high-quality device fabrication obtainable with currently available nanofabrication technology.

2. DEVICE STRUCTURE DESIGN AND SIMULATION RESULTS

PhC/PhW micro-cavity devices in an SOI platform with the schematic structure shown in Fig. 1(a) were designed and specified for fabrication. The photonic wire dimensions were selected to be 600 nm (width) x 260 nm (height) to guide TE-mode light. This ridge structure was supported by a silica buffer cladding with air surrounding the top and sides of the wire. As shown in Fig. 1(b), the exterior six hole mirror/taper structure had a first section that comprised two identical holes, each with a radius of 90 nm and a lattice constant, ***a*** of 370 nm, forming the Bragg mirror and a second section with four holes that form a taper in the N_{TI} region, with hole radii of 90, 92, 80 and 65 nm respectively. The distances between these taper holes were 350, 325, 315 and 300 nm respectively. The interior PhC/PhW structures comprised four holes with radii of 65, 90, 90 and 65 nm, spaced at distances of 310, 370 and 310 nm respectively. Two more PhC micro-cavities followed periodically - as mirror images of the first two structures. The interior cavity distance between each section, *c*, was designed to be 400 nm, in all cases. The inner tapers were introduced to guide the light smoothly, with reduced scattering and increased light transmission [9].

3D-FDTD analysis was used for simulation of the designed structure before fabrication. The silicon, silica and air indices were taken as 3.46, 1.45 and 1 respectively. The full multi-micro-cavity structure was designed to produce distinct resonance wavelengths in the C and L band fibre-network spectral regions, as shown in Fig. 2. The simulated resonance wavelengths were at 1534.87, 1554.63 and 1594.86 nm. The Q-factor values obtained for the three resonance wavelengths were 1136.09, 922.37 and 904.91 respectively. The wavelength spacing or free spectral range (FSR) obtained in simulation between the first resonance wavelength to the second resonance wavelength was 19.76 nm while the FSR from the second to the third resonance wavelength was 35.53 nm. The unequal FSR obtained was due to the resonance wavelengths being governed by the combination of the individual cavities in the PhC structure and the summation cavity of the overall PhC structure.

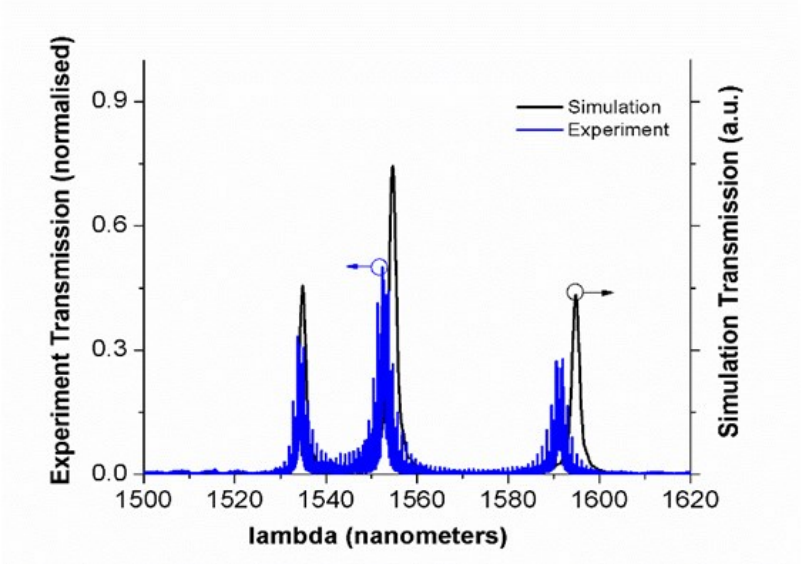


Fig. 2. Comparison between simulation and experiment results. The simulated resonance wavelengths were 1534.87, 1554.63 and 1594.86 nm while the experiment resonance wavelengths were 1534.34, 1552.77 and 1591.19 nm respectively.

3. FABRICATION AND EXPERIMENTAL RESULTS

The design was fabricated on an SOI wafer section by using electron-beam lithography (EBL) for patterning and inductively-coupled plasma reactive ion-etching (ICP-RIE) for structuring. Prior to the patterning process, hydrogen silsesquioxane (HSQ) with a thickness of 200 nm was used. The pattern was written using an Elionix ELS-F125 EBL tool. The pattern was developed with warm tetra-methylammonium hydroxide (TMAH) at 25% concentration in de-ionized water. The sample was etched using ICP-RIE with SF_6 and C_4F_8 gases, in order to remove the unwanted silicon region. Figure 1(b) shows a fabricated device.

The devices were measured using a tunable laser source range over the range 1480 nm to 1600 nm, with end-fire coupling of polarized light. The output of the device was detected using a germanium photodetector. The results obtained were normalised with respect to those of an unstructured photonic wire. The results obtained from measurements on the fabricated structure shown in Fig. 1(b) are in close agreement with the simulation results, as is shown in Fig. 2. The measured resonance wavelengths were 1534.34, 1552.77 and 1591.19 nm, respectively. Discrepancies between the simulation and measured results are probably caused by factors such as imperfect device fabrication – in particular small errors in the fabricated hole diameters [10]. The fine structure that is observable in the experimental results of Fig. 2 is primarily due to Fabry-Perot (FP) effects produced by the cleaved waveguide end-facets [9].

4. CONCLUSIONS

We have shown that properly designed multiple cavity structures result in predictable multiple resonances. This characteristic behaviour is suitable for application in WDM systems or other multiple wavelength filter applications that require photonic integration. The performance that we have demonstrated indicates that design based on available simulation tools can lead to viable fabricated devices for important applications.

ACKNOWLEDGEMENTS

This work was supported by the Ministry of Higher Education in Malaysia (MoHE) through LRGS/2015/UKM-UKM/NANOMITE/ 04/01 and LRGS (2015)/NGOD/UM/KPT.

REFERENCES

[1] B. J. Shastri *et al.*, "Neuromorphic Photonics, Principles of," in *Encyclopedia of Complexity and Systems Science*, R. A. Meyers, Ed. Berlin, Heidelberg: Springer Berlin Heidelberg, 2018, pp. 1-37.

[2] M. Smit, J. van der Tol, and M. Hill, "Moore's law in photonics," *Laser & Photonics Reviews,* vol. 6, no. 1, pp. 1-13, 2012.

[3] K. Li *et al.*, "High speed e-beam writing for large area photonic nanostructures—a choice of parameters," *Scientific reports,* vol. 6, p. 32945, 2016.

[4] J. D. Joannopoulos *et al.*, *Photonic crystals: molding the flow of light*. Princeton university press, 2011.

[5] N. Nawi *et al.*, "Enhancement and reproducibility of high quality factor, one-dimensional photonic crystal/photonic wire (1D PhC/PhW) microcavities," *Journal of the European Optical Society-Rapid Publications,* journal article vol. 14, no. 1, p. 6, February 20 2018.

[6] R. Rajasekar and S. Robinson, "Trapezoid 2D photonic crystal nanoring resonator-based channel drop filter for WDM systems," *Photonic Network Communications,* journal article vol. 36, no. 2, pp. 230-245, October 01 2018.

[7] Y.-H. Ye *et al.*, "Self-assembly of three-dimensional photonic-crystals with air-core line defects," *Journal of Materials Chemistry,* 10.1039/B207441A vol. 12, no. 12, pp. 3637-3639, 2002.

[8] A. R. Md Zain *et al.*, "Ultra high quality factor one dimensional photonic crystal/photonic wire micro-cavities in silicon-on-insulator (SOI)," *Optics Express,* vol. 16, no. 16, pp. 12084-12089, 2008/08/04 2008.

[9] A. R. Md Zain and R. M. De La Rue, "Control of coupling in 1D photonic crystal coupled-cavity nano-wire structures via hole diameter and position variation," *Journal of Optics,* vol. 17, no. 12, p. 125007, 2015/10/15 2015.

[10] R. M. De La Rue and C. Seassal, "Photonic crystal devices: some basics and selected topics," *Laser & Photonics Reviews,* vol. 6, no. 4, pp. 564-597, 2012.

Integrated pump rejection filter for high-quality photonic quantum communication

Dorian Oser [1], Florent Mazeas [2], Carlos Alonso Ramos [1], Xavier Le Roux [1],
Laurent Vivien [1], Sébastien Tanzilli [2], Éric Cassan [1], Laurent Labonté [2]
[1] *Centre de Nanosciences et de Nanotechnologies, CNRS, Universié Paris-Sud, Université Paris-Saclay, C2N, Palaiseau, France*
[2] *Université Côte d'Azur, CNRS, Institut de physique de Nice, France*
e-mail: dorian.oser@c2n.upsaclay.fr

ABSTRACT

Combining quantum and integrated photonics gives the ability of generating, manipulating, and detecting individual quantum states on single chips. Nonlinear four-wave mixing in silicon micro-ring resonators has shown an immense potential for on-chip bright photon-pair generation. However, one of the major challenges of this approach is the on-chip rejection of the pump, which severely distorts the quantum signals generated by the nonlinear process. Here, we report the integration on a single substrate of a photon-pair generator and a pump-rejection filter showing photon pair generation with a rate of 480 pairs per second for two signal/idler pairs simultaneously, with a brightness of 390 pairs/s/MHz, and a remarkably high raw visibility exceeding 95 %. All wavelengths fall within the ITU channels thus rendering this photon-pair source compatible with off-the-shelf telecom components.

Keywords: ring resonator, photonics, SFWM, multimode, Bragg filters.

1 INTRODUCTION

An integrated photon source is a fundamental building block of any quantum circuit. Bright photo-pair sources have already been demonstrated in silicon photonics, by harnessing spontaneous four-wave (SFWM) mixing in micro-ring resonators [1], [2], [3]. We have already demonstrated its promising properties in SOI for signal/idler pairs generation in where we showed high visibility and brightness for multiple pairs simultaneously [3]. However the nonlinear process used, SFWM, has the disadvantage of requiring a pump wavelength close to those of the generated photon pairs. This makes proper on-chip pump suppression a challenging task, as a large rejection must be applied ($>$100dB) on a relatively small bandwidth ($<$ 10 nm). Hence, the vast majority of reported photon-pair sources exploiting SFWM implement off-chip pump filtering. Indeed, the only demonstration of photon-pair generation with on-chip pump relayed on cascading two silicon chips chips [5]. Even if ultra-high on-chip rejection has already been demonstrated [4], [6], such filters require continuous monitoring and active tunning to achieve desired functionality, which compromise their feasibility as pump-rejection filters in complex quantum photonic circuits. Here, we present a novel approach for the implementation of ultra-high on-chip rejection without the need of any active tunning. We validate its feasibility for pump-rejection in silicon quantum photonics by experimentally demonstrating a silicon photon-pair source with a raw visibility exceeding 95 %.

2 DESIGN & FABRICATION

Waveguide Bragg gratings are widely used in silicon photonics for the implementation of advanced wavelength filtering functionalities. However, conventional Bragg filters exhibit a limited rejection capability, mainly due to phase errors arising from fabrication imperfections [7]. To overcome this limitation, we have developed a new strategy harnessing modal engineering of the waveguide gratings to minimize the sensitivity to relative phase errors, thus allowing ultra-high rejection, even in the presence of fabrication imperfections [8]. The proposed filter relies on non-coherent cascading of multi-mode gratings separated by single-mode waveguides (Fig. 1). Each grating section reflects the fundamental mode into a higher order mode, which is radiated away in the single-mode waveguide (shown in blue in Fig. 1) connecting successive Bragg filters. These properties finally allow to cascade filters by breaking the phase coherence between successive filters and thus avoiding the rejection saturation. Based on this approach we have demonstrated on chip rejection higher than 80 dB [8].

We have implemented a photon-pair source that comprises a silicon micro-ring resonator and the proposed modal-engineered Bragg filter. In this first demonstration the demultiplexing of the photon pairs (signal and idler) is done off-chip, with a filter providing 20 dB corsstalk. A multimode coupler was added before the first section of the filter to extract on a separate port the first reflection [9]. This gives easy information about the alignment of the pump laser and work as an alignment port when working at wavelength in the filter. This

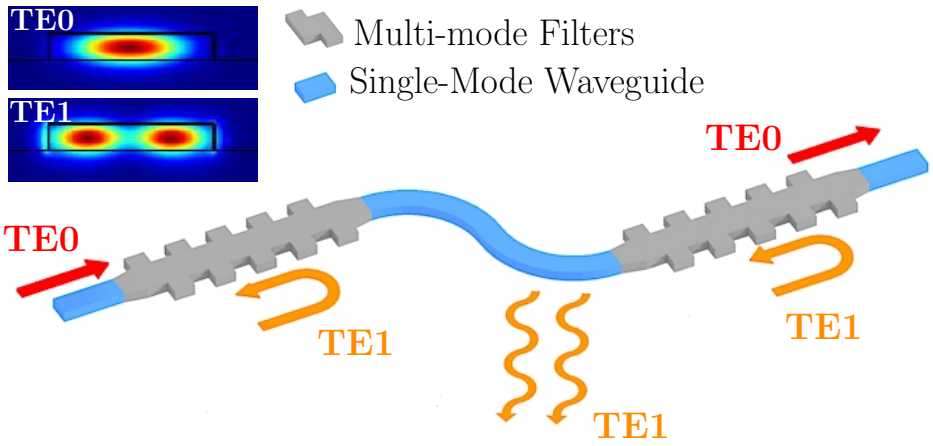


Figure 1. Schematic view of proposed cascaded filter. Fundamental mode (TE_0) is back-reflected into first order mode (TE_1). Single-mode waveguide sections separating adjacent filters radiate the back-reflected TE_1 mode away, precluding coherent interaction among different stages.

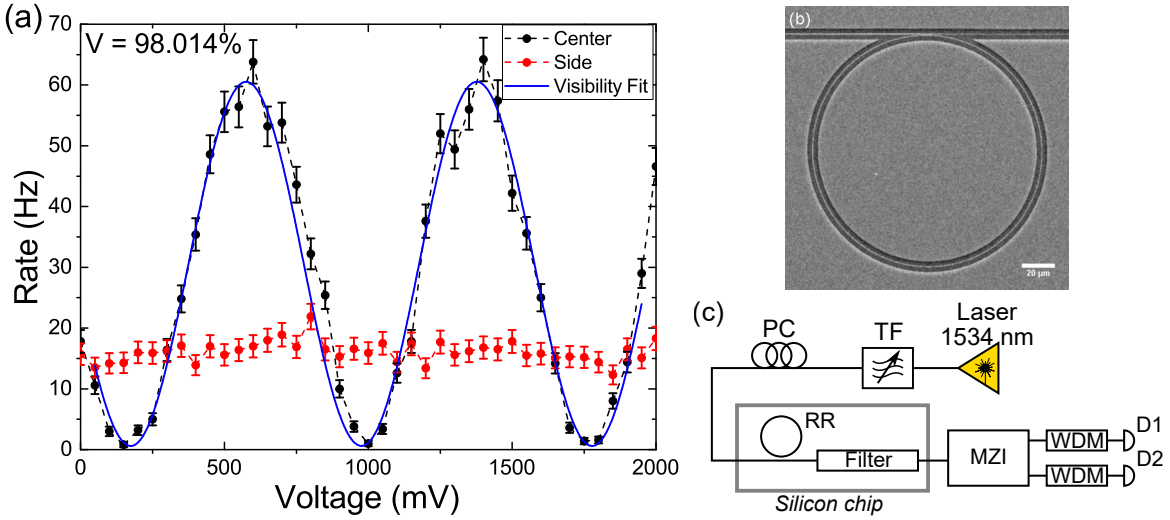


Figure 2. (a) Plots of the coincidence rate for the central (interference peak) and the average of the side peaks (coincidence peaks); each point was integrated for 5 seconds, the increment step is $50mV \sim \pi/8$, the side rate shows the stability of the measurement, the noise was not removed from the measurements. The noise is about 0.5 Hz, the error bars for all points come from Poissonian statistic of the pairs. (b) Scanning electron microscope image of the ring cavity used to make pairs of photons with SFWM. (c) Schematics of the setup used for the visibility experiments, PC is a polarization controller, TF is a tunable filter, MZI is a Mach-Zehnder interferometer, WDM is for wavelength demultiplexer, finally D1 and D2 are two photon counter detectors.

structure can generate pair of photons on all of the ring resonances and can be aligned to the telecom grid channel by carefully choosing the ring free spectral range.

Samples were fabricated on a silicon-on-insulator substrate with a silicon layer thickness of 220 nm. Electron beam lithography was used to print the patterns. The realized structure only required a single step of lithography for fabrication and no active tuning was needed. All filter sections were naturally aligned by the fabrication process.

3 RESULTS

The photon pairs produced by the source are genuinely energy-time entangled as they are produced by SFWM. Entanglement is analyzed using a folded Franson arrangement consisting of a single unbalanced fiber Michelson interferometer. In fig. 2a we plot the coincidence rate of photons coming from the interfering photon (Center), taking the same optical paths, and non-interfering photon (Side), taking different optical paths [3]. The side rate allows to see the stability of the photon generation which can be considered constant during the experiment. The interference pattern arise when changing the length of one arm of the interferometer with a piezo by applying a voltage. The visibility is measured then at destructive interferences. This shows a near perfect entanglements of the pairs generated as the visibility is close to unity. The visibility is limited by both the quality of the pairs generated but also by any residual noise. The visibility is degraded very quickly by any

noise that get to the detector as we want the coincidence rate to be the closest to zero possible. This indicates that the pump is well filtered from the integrated multimode filter.

In addition to the good visibility, this integrated filter combined with a ring yields a rate of 480 pairs per seconds for two signal/idler pairs simultaneously and a brightness of $390\,\mathrm{pairs/s/MHz}$. This was achieved by adding only a 20 dB-crosstalk de-multiplexing after the chip, on top of the integrated filter. The linear measurements of the on chip filter show a rejection of 70 dB, mainly limited by our current setup (limited sensitivity of the optical spectrum analyzer used for the analysis). However, quantum experiments suggest an even larger on-chip pump rejection.

4 CONCLUSION

We have demonstrated a new strategy using cascaded Bragg filters to reject the pump which is used for the non-linear processes. This all-passive photon-pair source, comprising on-chip pump-rejection filter, is an important step towards the full integration of an integrated heralding source. The low loss and simplicity of the proposed approach enable the implementation of photon-pair sources with a high generation rate, based on a single lithography step. The generated pairs yield a near unity visibility with no cost on the rate of the ring resonator. Only a single step of lithography is required for the fractionation This system strong promises for quantum key distribution networks as a cheap source of entangled photon pairs.

REFERENCES

[1] S. Azzini, D. Grassani, M. Davide, L.C. Andreani, M. Sorel, M.J. Strain, LG Helt, JE Sipe, M. Liscidini, D. Bajoni, "From classical four-wave mixing to parametric fluorescence in silicon microring resonators", Opt. letters **37**, 3807-3809 (2012).

[2] WC Jiang, X Lu, J Zhang, O Painter, Q Lin, "Silicon-chip source of bright photon pairs", Opt. express **23**, 20884-20904 (2015).

[3] F. Mazeas, M. Traetta, M. Bentivegna, F. Kaiser, D. Aktas, W. Zhang, C. A. Ramos, L. Ngah, T. Lunghi, E. Picholle et al., "High-quality photonic entanglement for wavelength-multiplexed quantum communication based on a silicon chip", Opt. express **24**, 28731-28738 (2016).

[4] M. Piekarek, D. Bonneau, S. Miki, T. Yamashita, M. Fujiwara, M. Sasaki, H. Terai, M. Tanner, C. Natarajan, R. Hadfield, J. O'Brien, and M. Thompson , "High-extinction ratio integrated photonic filters for silicon quantum photonics," Opt. Lett. **42**, 815-818 (2017)

[5] NC Harris, D Grassani, A Simbula, M Pant, M Galli, T Baehr-Jones, M Hochberg, D Englund, D Bajoni, C Galland, Integrated source of spectrally filtered correlated photons for large-scale quantum photonic systems, Physical Review X, **4**, 041047, 2014

[6] J. R. Ong, R. Kumar, and S. Mookherjea, Ultra-high-contrast and tunable-bandwidth filter using cascaded high-order silicon microring filters. IEEE Photonics Technology Letters, **25**, 1543-1546. (2013)

[7] D. Oser, D. Pérez-Galacho, C. Alonso-Ramos, X Le Roux, S. Tanzilli, L. Vivien, L. Labonté, E. Cassan, Subwavelength engineering and asymmetry: two efficient tools for sub-nanometer-bandwidth silicon Bragg filters, Optics letters **43**, 3208–3211 (2018).

[8] D. Oser, F. Mazeas, X Le Roux, D. Perez-Galacho, O. Alibart, S. Tanzilli, L. Labonté, D. Marris-Morini, L. Vivien, E. Cassan, C. Alonso-Ramos, Coherency-broken Bragg filters: surpassing on-chip rejection limitations, arXiv preprint arXiv:1806.08833 (2018)

[9] J. Wang, Y. Xuan, M. Qi, H. Huang, Y. Li, M. Li, X. Chen, Z. Sheng, A. Wu, and W. Li, Broadband and fabrication-tolerant on-chip scalable mode-division multiplexing based on mode-evolution counter-tapered couplers, Optics letters **40**, 1956–1959 (2015).

Non-Volatile and Ultra-Compact Photonic Memory

(Student paper)

Jorge Parra[1,*], Irene Olivares[1], Antoine Brimont[1], Juan Luis Frieiro[2], Oriol Blázquez[2], Sergi Hernández[2], Blas Garrido[2] and Pablo Sanchis[1,+]

[1] Nanophotonics Technology Center, Universitat Politècnica de València,
Camino de Vera s/n, 46022 Valencia, Spain

[2] MIND, Department of Electronics and Biomedical Engineering, Universitat de Barcelona,
Martí i Franquès 1, E-08028 Barcelona, Spain

*e-mail: *jorpargo@ntc.upv.es, [+]pabsanki@ntc.upv.es*

ABSTRACT

In this work, we propose a non-volatile and ultra-compact photonic flash memory by utilizing a transparent conducting oxide (TCO) as a floating gate. The memory acts as a non-volatile electro-absorption switch and exploits the epsilon-near-zero regime (ENZ) of the TCO floating gate for enabling the switching between two states with low and high optical losses. Our simulation shows that, by means of applying +11 V and –11 V voltage pulses, the memory is programmed or erased, respectively. Additionally, for a 5-µm-long device, the memory features negligible insertion losses and an optical extinction ratio of 35 dB with an inherent broadband wavelength operation due to its non-resonant response. This device could pave the way for developing high-density photonic memory banks on the silicon photonics platform.

Keywords: optical memory, non-volatile, epsilon-near-zero, transparent conducting oxides, silicon photonics.

1. INTRODUCTION

The current lack of memory effect in the silicon photonics platform is one of the main drawbacks in comparison with electronic circuits. Recently, all-optical memories utilizing phase-change materials have been demonstrated to tackle the von Neumann bottleneck [1–2], but optoelectronic conversion is still required in most systems. Hence, on the electro-optic side, there have been some proposals relying on the same concept as that of electronic flash memories either by exploiting the silicon plasma dispersion effect [3–6] or by integrating 2D materials such as graphene [7] to induce the optical change. However, approaches relying on weak electro-optic effects impose a trade-off between the use of resonant, narrow band and relatively compact devices or non-resonant broadband but large footprint devices. On the other hand, the integration of atomically thin materials, such as graphene, by keeping their quality is challenging which increases the difficulty for high yield and large volume manufacturing.

Conversely, transparent conducting oxides, such as indium tin oxide (ITO) or Al-doped zinc oxide (AZO), exhibit an epsilon-near-zero regime in the near-infrared spectra. This effect can be electrically tuned by carrier injection and has been exploited for ultra-fast, high-energy efficient and ultra-compact electro-optic photonic modulators [8–10].

In this work, to the best of our knowledge, we propose for the first time the use of transparent conducting oxides for non-volatile photonic memories based on a floating gate. The photonic memory is electrically programmed/erased and optically read. Furthermore, our device features an ultra-compact footprint and a non-resonant broadband optical response by exploiting the ENZ state of the TCO floating gate.

2. DESIGN

Figure 1(a) illustrates the functionality of the non-volatile photonic memory. By applying either a positive or negative voltage pulse to the control gate, the photonic mode switches between a low-loss and high-loss state induced by the ENZ regime of the TCO floating gate. The ENZ state of the TCO floating gate is achieved by accumulating electrons via the Fowler-Nordheim quantum effect on the tunneling oxide layer.

The cross-section of the structure is depicted in Fig. 1(b) and consists of a standard 500 nm × 220 nm silicon strip waveguide electrically grounded. A 6-nm-thick Al_2O_3 layer on top of the waveguide is used as the tunneling oxide which has the capacity to handle breakdown voltages reaching 30 MV/cm [11]. The floating gate is formed by a 5-nm-thick ITO layer with a low free carrier density. A high-κ material for the blocking oxide is necessary in order to lower the programming/erasing voltages and improve the retention time. Thus, we choose a 5-nm-thick TiO_2 layer ($\varepsilon_{DC} = 80$) as the blocking oxide. The control gate is also formed by a 10-nm-thick ITO layer deposited at the same conditions as the ITO floating gate. The use of a TCO instead of a metal contributes to reduce the insertion losses due to the refractive index mismatch. Finally, the structure is surrounded by a SiO_2 cladding. Atomic layer deposition (ALD) can be used to form the Al_2O_3, ITO and TiO_2 layers and plasma-enhanced chemical vapour deposition (PECVD) to clad the structure with SiO_2.

From the electrical point of view, the memory acts as two capacitors in series when applying voltage pulses and as two parallel capacitors connected to a floating voltage induced by the accumulated charge when the control gate is grounded. Further details of the electrical model used in this work can be found in [7].

Once the floating gate is electrically programmed, it forms two accumulation layers in the ITO floating gate interfaces. These accumulation layers are reported to be between 1-5 nm [12]. Since our ITO floating gate layer is 5-nm-thick, we calculate the volumetric charge density (N_e) by averaging the surface charge density to the ITO floating gate thickness. Hence, by applying the Drude model we map ITO free carrier density to its refractive index in order to compute the optical modes and obtain the corresponding propagation losses for both memory states.

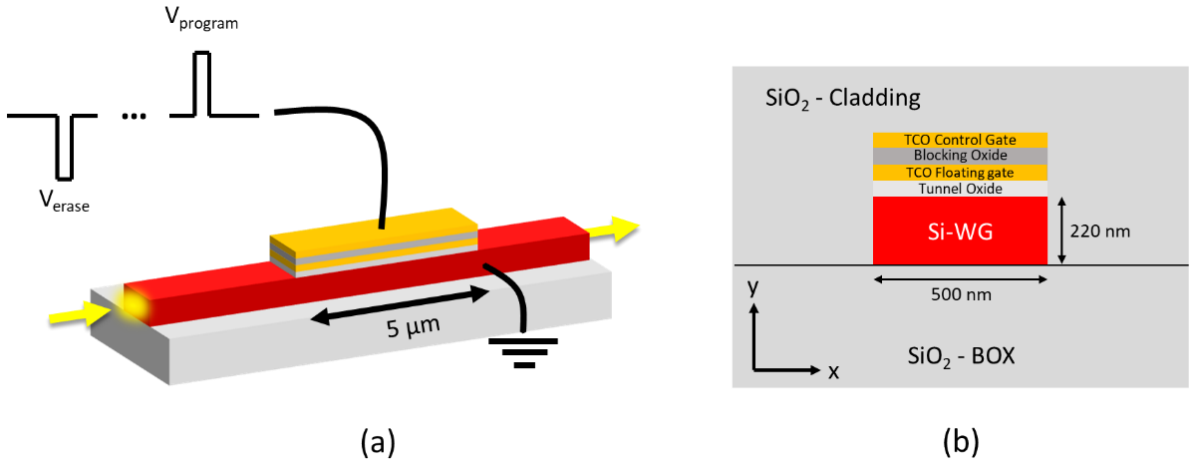


Figure 1. (a) Schematic of the ultra-compact (5µm-long) non-volatile photonic memory. The device shows a non-volatile electro-absorption switch when the memory is either programmed or erased by applying a positive or negative voltage pulse, respectively. (b) Cross-section of the memory. Tunneling and blocking oxide layers are made of Al_2O_3 and TiO_2, respectively. We choose ITO as the TCO for the floating and control gate with the following Drude parameters: $\varepsilon_\infty = 3.9$, $\Gamma = 5\times10^{13}$ rad/s, $m^* = 0.35m_e$ and $N_0 = 10^{19}$ cm^{-3}.

3. RESULTS

Figure 2(a) shows the temporal response of the memory when a pattern of programming and erasing square pulses are applied. From our simulations, the ENZ state of the ITO floating gate is attained at +11 V, hence we set this value as the programming voltage. In a similar way, the erase-pulse amplitude is found at –11 V, since for voltage amplitudes below –11 V the floating gate is fully discharged. The duration of both pulses is set at 10 µs with a 10 ns of rise and fall times.

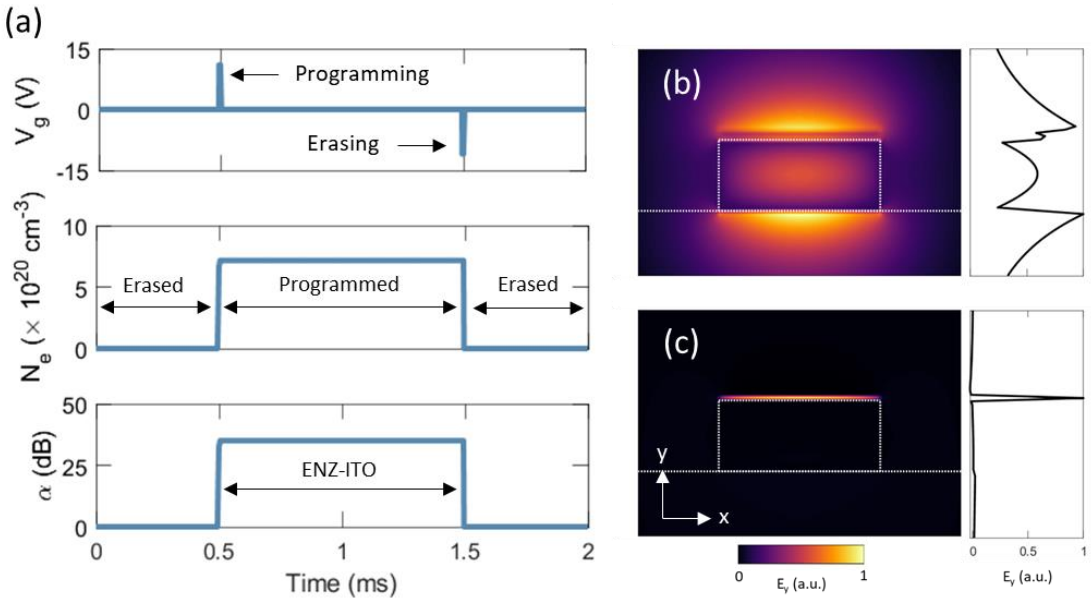


Figure 2. (a) Simulated temporal response of the device on the application of a programming (+11 V) and erasing (−11 V) voltage pulse pattern. When the program pulse is applied, the electron carrier density, N_e, of the ITO floating gate raises to ~6.5×10^{20} cm^{-3} (ENZ state) and induces 35 dB of optical losses, α, on the optical mode. (b) and (c) depict the E-field spatial distribution of the optical mode at $\lambda = 1550$ nm for the erased and programmed states, respectively.

When a programming pulse is applied to the control gate, the Fowler-Nordheim current flows through the tunnel oxide towards the ITO floating gate, which is switched to the ENZ state due to carrier accumulation. Once the programming pulse is removed, the ITO ENZ state is kept since the remaining electric field induced by the accumulated carriers is not strong enough to induce a significant leakage current. In addition, electrical simulations predict retention times of years. On the other hand, by applying the erasing pulse, the floating gate is discharged and the ITO returns to its former state. Hence, we obtain a non-volatile absorption optical switch with optical losses going from a negligible value to 35 dB for the erased and programmed memory, respectively.

The influence of the ENZ can be clearly seen on the photonic mode profiles. When the ITO floating gate has a low free carrier density [see Fig. 2(b)], it acts as a low-loss dielectric layer like the control gate and thus we obtain a typical transversal magnetic (TM) photonic mode. However, when the ITO floating gate is in the ENZ regime [see Fig. 2(c)], the optical mode is fully confined within the floating gate because the value of its absolute permittivity is almost zero. Along with this, the ITO imaginary refractive index increases turning into a highly lossy material. This combination of both strong optical confinement and optical loss variation is achieved thanks to the ENZ behaviour inherent to ITO.

4. CONCLUSIONS

In this work, a non-volatile photonic memory is proposed based on the integration of transparent conducting oxides like ITO in a silicon compatible structure. The proposed device is electrically driven and optically read. The key benefit of utilizing ITO as a floating gate is that the epsilon-near-zero regime can be exploited to achieve an ultra-compact footprint with large optical extinction ratios, negligible insertion losses and broadband response. Furthermore, the control electrical pulses have a low voltage, ultra-short duration and retention times of years have been predicted.

ACKNOWLEDGEMENTS

Funding from project TEC2016-76849 (MINECO/FEDER, UE) is acknowledged. Jorge Parra and Irene Olivares acknowledge the Generalitat Valenciana and Universitat Politècnica de València, respectively, for funding their research staff training (FPI) grants.

REFERENCES

[1] C. Rios *et al.*, "Integrated all-photonic non-volatile multi-level memory," *Nat. Photonics*, vol. 9, no. 11, pp. 725–732, 2015.

[2] X. Li *et al.*, "Fast and reliable storage using a 5-bit, non-volatile photonic memory cell," *Optica*, vol. 6, no. 1, 2018.

[3] C. A. Barrios and M. Lipson, "Silicon Photonic Read-Only Memory," *J. Light. Technol.*, vol. 24, no. 7, pp. 2898–2905, 2006.

[4] J. F. Song *et al.*, "Integrated photonics with programmable non-volatile memory," *Sci. Rep.*, vol. 6, pp. 1–7, 2016.

[5] J.-F. Song *et al.*, "Silicon photonic integrated circuits with electrically programmable non-volatile memory functions," *Opt. Express*, vol. 24, no. 19, p. 21744, 2016.

[6] M. Grajower, N. Mazurski, J. Shappir, and U. Levy, "Non-Volatile Silicon Photonics Using Nanoscale Flash Memory Technology," *Laser Photonics Rev.*, vol. 12, no. 4, pp. 1–8, 2018.

[7] Y. Li *et al.*, "Graphene-based floating-gate nonvolatile optical switch," *IEEE Photonics Technol. Lett.*, vol. 28, no. 3, pp. 284–287, 2016.

[8] V. J. Sorger, N. D. Lanzillotti-Kimura, R. M. Ma, and X. Zhang, "Ultra-compact silicon nanophotonic modulator with broadband response," *Nanophotonics*, vol. 1, no. 1, pp. 17–22, 2012.

[9] M. G. Wood *et al.*, "Gigahertz speed operation of epsilon-near-zero silicon photonic modulators," *Optica*, vol. 5, no. 3, p. 233, 2018.

[10] X. Liu *et al.*, "Epsilon-Near-Zero Si Slot-Waveguide Modulator," *ACS Photonics*, 2018.

[11] H. C. Lin, P. D. Ye, and G. D. Wilk, "Leakage current and breakdown electric-field studies on ultrathin atomic-layer-deposited Al2O3 on GaAs," *Appl. Phys. Lett.*, vol. 87, no. 18, pp. 1–3, 2005.

[12] S. Zhu, G. Q. Lo, and D. L. Kwong, "Design of an ultra-compact electro-absorption modulator comprised of a deposited TiN/HfO2/ITO/Cu stack for CMOS backend integration," *Opt. Express*, vol. 22, no. 15, p. 17930, 2014.

Investigation of the Dynamical Behaviour of Mutually Coupled Lasers on a Photonic Integrated Circuit

(Student Paper)

Alison H. Perrott [1,2], Mohamad Dernaika [1,2], Ludovic Caro [1,2], Frank H. Peters [1,2]
[1]*University College Cork, Cork, Ireland*
[2]*Tyndall National Institute, Cork, Ireland*
e-mail: alison.perrott@tyndall.ie

ABSTRACT

In this paper, we investigate the mutual injection locking properties of a photonic integrated circuit consisting of two slotted Fabry-Pérot lasers coupled together through a 1.1 mm variable optical attenuator/amplifier. The output of the lasers was observed on an electrical spectrum analyser, optical spectrum analyser and a high speed oscilloscope. Various types of dynamical behaviour were identified as a function of the coupling and the detuning between the lasers.

Keywords: Mutual injection locking, coupled lasers, photonic integration, laser dynamics.

1 INTRODUCTION

Optical injection locking of semiconductor lasers has been an area of great interest since the early 1980s [1]. The theoretical and experimental study of injection locked semiconductor lasers has resulted in many applications. For example, injection locking can be used to demultiplex an optical comb [2]. The comb lines can then be modulated individually before recombining the signal to create a coherent superchannel for coherent wavelength division multiplexing [3]. Injection locking can also be used to generate multiple phase locked coherent outputs [4], which are required for many modern day modulation formats [5].

Due to the ever increasing demand being put on optical communication networks, there is a significant move towards developing integrated devices to replace discrete optical components. Photonic integrated circuits (PICs) offer an effective solution for the advancement of system level functions at a compact scale. Integration vastly decreases the size of these systems and allows for lower power consumption and reduced cost. However, the implementation of injection locking in such a system is highly complex, due to mutual feedback between the lasers. Without feasible integrated isolators the injection locking system is no longer purely master-slave, but is now bidirectional, or mutual. In order to reliably enable applications that are based on injection locked lasers in a PIC, the limits of injection locking a system of integrated semiconductor lasers needs to be studied. In this paper we investigate the effect of the coupling and detuning between the lasers on the injection locking properties of two integrated slotted Fabry-Pérot lasers.

2 THE PHOTONIC INTEGRATED CIRCUIT

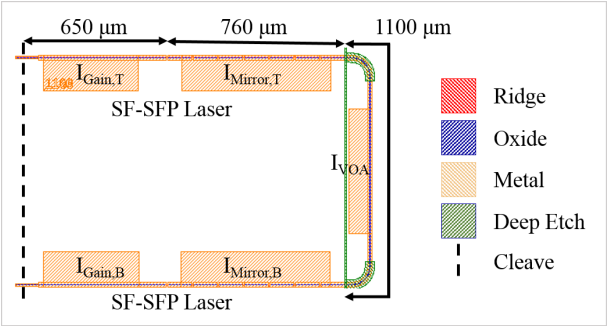


Figure 1. Schematic of the PIC with all variable parameters labelled. Two SF-SFP lasers are integrated together through a 1100 μm VOA section.

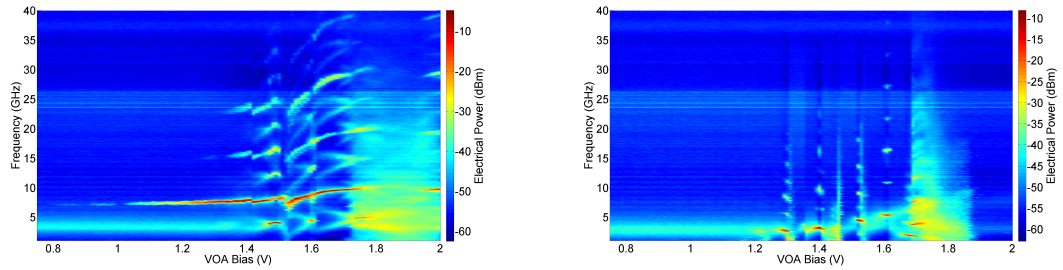
The PIC used to investigate mutual injection locking consisted of two identical single facet slotted Fabry-Pérot (SF-SFP) lasers [6] coupled together through a 1100 μm waveguide interconnect, referred to as the variable optical attenuator/amplifier section (VOA). A schematic of the full device, is shown in Fig. 1. The

. Funding: Science Foundation Ireland (SFI) (SFI 13/IA/1960).

epitaxial structure used was commercially grown 1550 nm laser material on an InP substrate, with a total active region thickness of 0.4 mm, consisting of five compressively strained AlInGaAs quantum wells. The device was fabricated using standard processing techniques, similar to [7]. The SFPs were controlled by independently biasing their respective mirror, $I_{Mirror,}$ and gain, I_{Gain}, sections. Forward or reverse biasing the VOA section controlled the amplification or attenuation of the optical signal and hence varied the power coupled between the lasers.

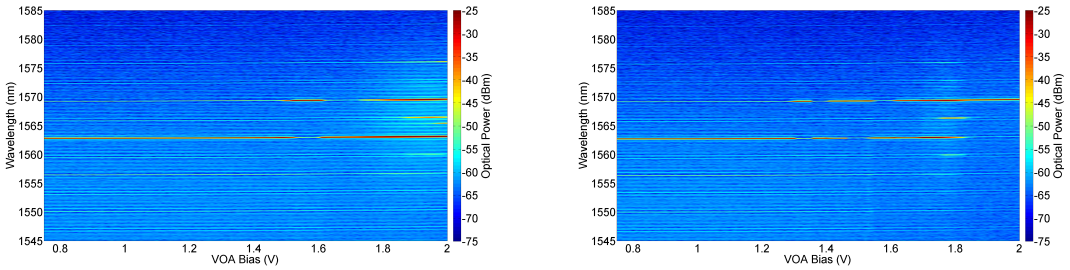
3 MUTUAL INJECTION LOCKING

Both of these lasers were tunable over a 0.5 nm range while maintaining a side mode suppression ratio greater than 27 dB, therefore the effect of the detuning, Δ, (frequency difference between the lasers, set by their mirror and gain section biases) and the coupling (percentage power emitted by one laser that couples into the other laser, proportional to the VOA bias) between the lasers on the injection locking properties of the system were investigated. For this device, the VOA section was completely absorbing below 0.75 V, therefore the VOA bias was swept from 0.75 V to 2.00 V for various detunings between -18 GHz and 10 GHz. The output of the lasers was recorded on an electronic spectrum analyser (ESA), an optical spectrum analyser (OSA) and a high speed oscilloscope (HSO). The results for -7.4 GHz and 1.3 GHz detuning are plotted in Figs. 2-4.



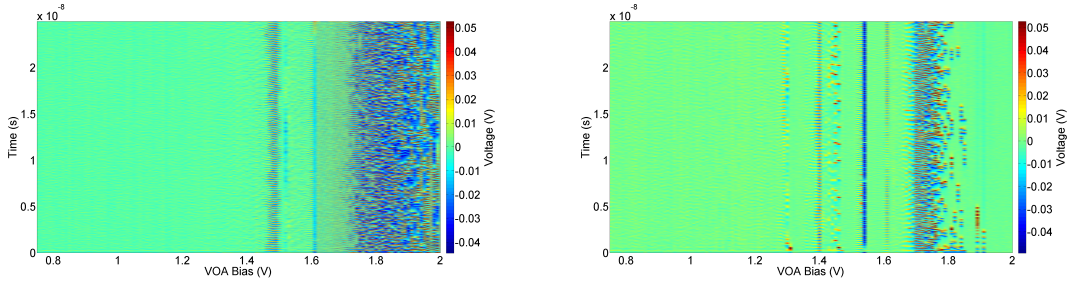
(a) (b)

Figure 2. Colour intensity plots of the ESA traces from the top SFP for (a) -7.4 GHz, (b) 1.3 GHz detuning between the lasers.



(a) (b)

Figure 3. Colour intensity plots of the OSA traces from the top SFP for (a) -7.4 GHz, (b) 1.3 GHz detuning between the lasers.



(a) (b)

Figure 4. Colour intensity plots of the HSO traces from the top SFP for (a) -7.4 GHz, (b) 1.3 GHz detuning between the lasers.

These plots are only a small example of the full data set obtained. Various patterns and regions of dynamical behaviour can be seen in the colour intensity plots. The following types of behaviour were identified;

- Uncoupled - at low VOA biases, there is very little light coupling between the lasers, hence they are almost isolated and do not interact.

- Coupled - as the VOA bias increases the VOA begins to become transparent and sufficient light couples between the lasers so that they begin to interact, causing a beat note corresponding to the detuning between the lasers to appear in the electrical spectra.
- Quiet/Locked - for small detunings (-5 GHz $< \Delta <$ 5 GHz) regions of "quiet" were observed where only the relaxation oscillations (RO's) were visible on the ESA and noise on the HSO. The natural lasing wavelength for these lasers over this bias range was approximately 1563 nm. During these quiet regions the lasers either remained at their natural lasing wavelengths, $\sim$1563 nm or jumped to a higher lasing mode at $\sim$1569 nm. Since the RO's are not suppressed, the lasers are not completely injection locked but both lasers are lasing at the same wavelength.
- Chaotic - regions of multimode behaviour, where two or more lasing modes appeared in the optical spectra and wide peaks were observed in the electrical spectra.
- Period Doubling - regions where peaks at Δ and 0.5Δ and their harmonics are seen in the electrical spectra.

The detunings and VOA biases at which these types of behaviour occurred were found and the resulting bifurcation diagram is plotted in Fig. 5.

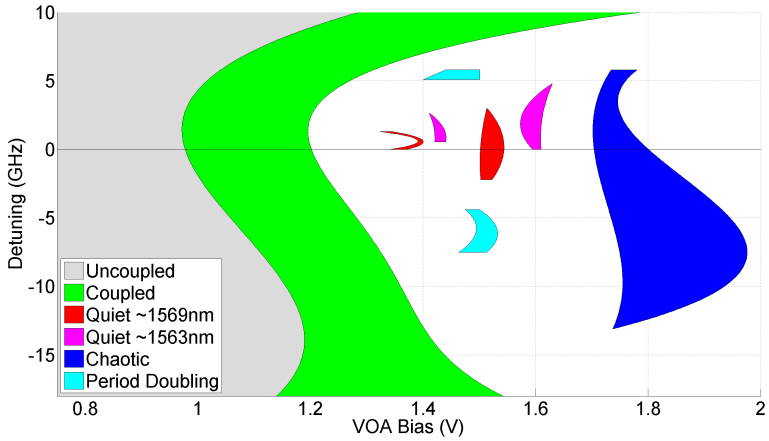


Figure 5. Bifurcation diagram showing the various types of laser dynamics as a function of the coupling and detuning between the lasers.

4 CONCLUSIONS & FUTURE WORK

We have begun to experimentally investigate the mutual injection locking properties of a PIC consisting of two integrated SFP lasers. The identification of these types of behaviour as a function of the coupling and detuning between the lasers will allow for a comparison with theoretical models. Further work will explore the repeatability of the work and also examine the dependence of the locking behaviour on the length of the delay between the lasers. It is hoped that this work will lead to a better understanding of the injection locking behaviour of lasers in next generation PICs.

REFERENCES

[1] R. Lang, "Injection locking properties of a semiconductor laser," IEEE Journal of Quantum Electronics 18, pp. 976–983, 1982.

[2] W. Cotter, et al., "Investigation of active filter using injection-locked slotted Fabry-Perot semiconductor laser," Applied optics 51, pp. 7357-61, 2012.

[3] A. Ellis and F. Gunning, "Spectral density enhancement using coherent WDM," IEEE Photonics Technology Letters 17, pp. 504–506, 2005.

[4] P. E. Morrissey, et al., "Multiple coherent outputs from single growth monolithically integrated injection locked tunable lasers," in Conference Proceedings - International Conference on Indium Phosphide and Related Materials, pp. 281–284, 2012.

[5] P. J. Winzer and R. J. Essiambre, "Advanced modulation formats for high-capacity optical transport networks," Journal of Lightwave Technology 24, pp. 4711-28, 2006.

[6] D. Byrne, et al., "A facetless laser suitable for monolithic integration," in Proceedings of the Conference on Lasers and Electro-Optics/Quantum Electronics and Laser Science Conference and Photonic Applications Systems Technologies, pp 1-2, 2008

[7] N.P. Kelly, et al., "Regrowth-free single mode laser based on dual port multimode interference reflector," IEEE Photonics Technology Letters 29, pp 279–282, 2017.

InP-on-Si DFB Laser Diode with Distributed Reflector for Improved Power Efficiency

(Student paper)

Mahmoud Shahin[1,2], Joris Van Kerrebrouck[3], Gunther Roelkens[1,2], Geert Morthier[1,2]
[1] Ghent University-imec, Technologiepark 15, Ghent, Belgium
[2] Center for Nano- and Biophotonics, Ghent University, Ghent, Belgium
[3] IDLab, Ghent University – imec, Ghent, Belgium
E-mail: Mahmoud.Shahin@ugent.be

ABSTRACT

A heterogeneously integrated InP-on-Si DFB laser diode with an active distributed reflector is demonstrated. The goal is to improve the power efficiency of the laser, by reducing the threshold current, and obtaining similar 3-dB modulation bandwidth with similar optical output power levels to previously demonstrated lasers, at lower injected current values. The device was first fabricated as a standard single-section DFB laser, then electrically isolated in two sections with unequal lengths. The shorter section is pumped and acts as an active laser section, while the other section is not pumped and acts as an absorbing distributed reflector. The threshold current was reduced from 17 mA to 9 mA, and the bias current required to achieve similar 3-dB modulation bandwidth to previously demonstrated lasers was reduced from 100 mA to 45 mA. Transmission of a 28 Gbps NRZ-OOK signal for both a back-to-back configuration and over 2 km of NZ-DS fiber is demonstrated, with bit-error-rate below the hard-decision forward-error-correction threshold.

Keywords: InP-on-Si, distributed feedback lasers, silicon photonics.

1. INTRODUCTION

Silicon photonics is given a lot of attention in recent years, due to the possibility of dense integration and its potential for large volume production at low cost. However, the main drawback that is always associated with silicon photonics is the lack of light sources, due to the indirect bandgap of silicon. One method to realize light sources on silicon is to heterogeneously integrate III-V layer stacks on Si [1]. One could use adhesive die-to-wafer bonding for this [2], in which a III-V die is bonded on top of the silicon waveguide circuit, by means of an adhesive bonding agent such as divinylsiloxane-bis-benzocyclobutene (DVS-BCB).

The distributed-feedback (DFB) laser diode is considered the preferred light source for optical data-communication applications, due to its stable single mode behaviour, accompanied with large side mode suppression ratio. In [3], a standard single-section III-V-on-Si DFB laser was demonstrated, with threshold current of 17 mA, and 3-dB modulation bandwidth of 15 GHz at 100 mA. Obviously, power efficiency is of key importance to these devices. In [4], an InP-based DFB laser with an active distributed reflector on one end (ADR-DFB), was demonstrated. It was shown that, in comparison to a standard DFB with AR-coated facets (AR-AR), an ADR-DFB could reduce the threshold current, and produce equally high optical output power levels at lower injected current values. The reported threshold current was 10 mA for the ADR-DFB, compared to 15 mA for the AR-AR laser, which is around 34% improvement.

In this paper, we report on the performance of an integrated InP-on-Si DFB laser with an active distributed reflector on one end. We aim to reduce the threshold current values, and consequently obtain similar 3-dB modulation bandwidth and data transmission with smaller injected current values. The structure of the paper is as follows. First, we discuss the design and fabrication of such a laser. Then, we report on the static characteristics, and compare the threshold current values to the case of a standard single-section DFB laser. After that, we show the dynamic characteristics, starting from small signal modulation and ending with large signal modulation experiments, and compare the bias current values to these of [3].

2. DESIGN AND FABRICATION

The 3D- and top-view of the laser structure are shown in Fig. 1 (a, b). The light is coupled from the III-V waveguide to the silicon waveguide using an adiabatic taper on both ends. The device is initially fabricated as a standard single-section DFB laser. Later, by the end of the fabrication process, an isolation etch takes place, by wet-etching the top p-InGaAs contact layer, and dry-etching 200 nm of the p-InP layer. The laser is 500 μm long (excluding the tapers) and is cut in two sections with unequal length. The lengths of the left and the right section are around 340 μm and 140 μm, respectively. To maximize the achieved relaxation oscillation frequency f_r, it is desired to design a narrow and short laser. Therefore, the short (right) laser section of 140 μm is chosen to be

pumped and modulated, compared to the 340 µm long laser in [3]. Moreover, the laser is 1.5 µm wide, as opposed to the 3.4 µm wide laser in [3]. However, as shown in Fig.1 (c), due to the V-shaped mesa structure, the width of the bottom of the p-InP is less than 1.5 µm. The tapers are electrically connected to the laser sections, each of them being 230 µm long. This suggests that the threshold current associated with the active section is less than the threshold current measured for both the active section and the taper. To measure the exact threshold current of the active section, the tapers should be electrically isolated, and only the active section should be pumped. The quantum wells are patterned 9 µm wide to avoid surface recombination. The silicon DFB grating has a period of 246 nm, with a duty cycle of 50%. The detailed fabrication process is reported in [5], and the InP layer stack parameters are the same as the ones reported in [6].

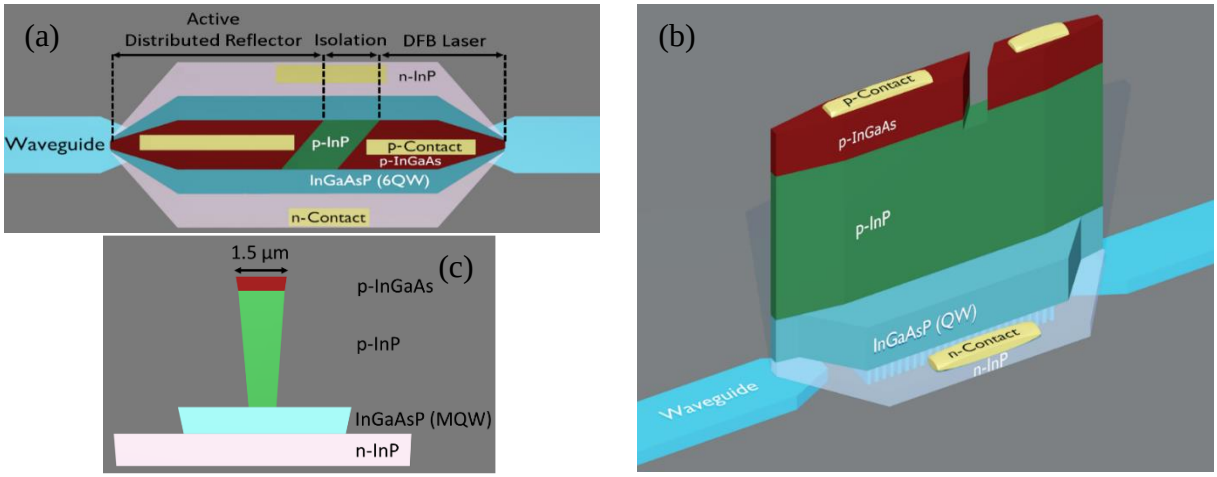


Figure 1. (a) Top- and (b) 3D-view of the fabricated laser showing two electrically isolated sections. The short (right) section is pumped and acts as a laser diode, while the long (left) section is not pumped and acts as an active distributed reflector. (c) The V-shape mesa structure

3. CHARACTERIZATION

3.1 Static characteristics

Grating couplers are used to couple the light out of the chip. The coupling efficiency of the grating couplers is -6 dB. In Fig. 2 (a), we show a comparison between the output power in the waveguide as a function of injected current. This is done in the case of: (1) injected current I_R in the right section (while I_L=0), (2) injected current while short-circuiting both sections and pumping them with a single current I_{Single} (i.e. identical to a standard single-section DFB laser). The threshold currents for each case are: (1) $I_{th,\,R}$= 9 mA and (2) $I_{th,\,Single}$ = 17 mA. As shown, $I_{th,\,R}$ is less than I_{Single} by 47%. $I_{th,\,R}$ is also 47% less than the 17 mA reported in [3]. Since the taper is also pumped, it is predicted that the actual threshold current for the right active section is around half of the measured threshold current value. The maximum output power in the waveguide was 3.55 mW for the case (1), higher than the value reported in [3] and 6 times higher than for the case (2) as shown in Fig. 2(a), measured at the same bias current. Fig. 3 (b) shows the single mode behaviour of the laser operating at 1540.5 nm with I_R = 45 mA.

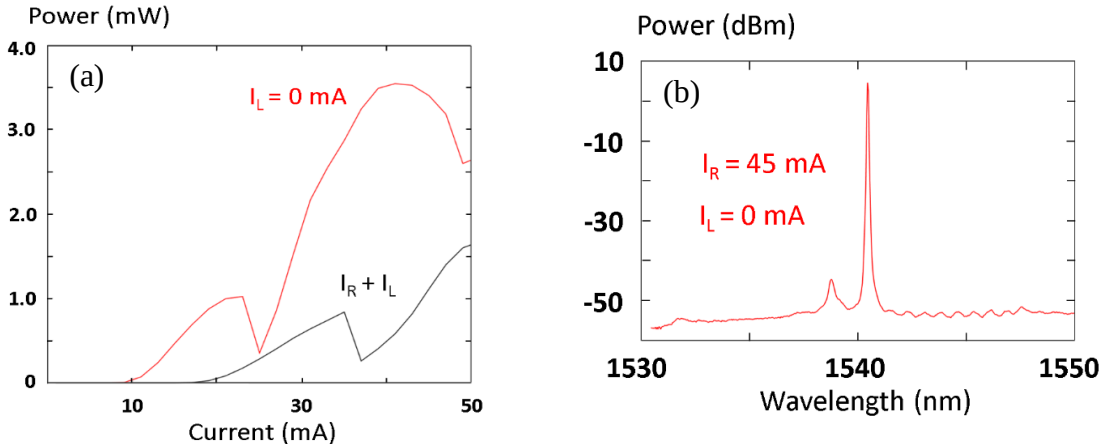


Figure 2. (a) Optical output power P_{opt} in the waveguide as a function of the current in the right section (I_R for I_L=0 mA), and as a function of the current injected in the complete laser length by short-circuiting both sections I_{Single}. (b) The spectrum of the laser showing single mode operation at 1540.5 nm for I_R = 45 mA and I_L = 0 mA

3.2 Small signal modulation

The small signal modulation response S_{21} was obtained using a vector network analyzer. The right section is modulated at two different bias currents, while the current in the left section I_L = 0 mA. The measured 3-dB modulation bandwidth is nearly 15 GHz, and is obtained at I_R = 45 mA, a 55% lower bias current than used in [3] to obtain about the same bandwidth. The drop in S_{21} at low frequencies was also observed in previous devices and is attributed to the extra modulation from the taper at low frequencies, acting as an external amplifier. The impact of this low frequency roll-off in data transmission can be minimized by reducing the word length.

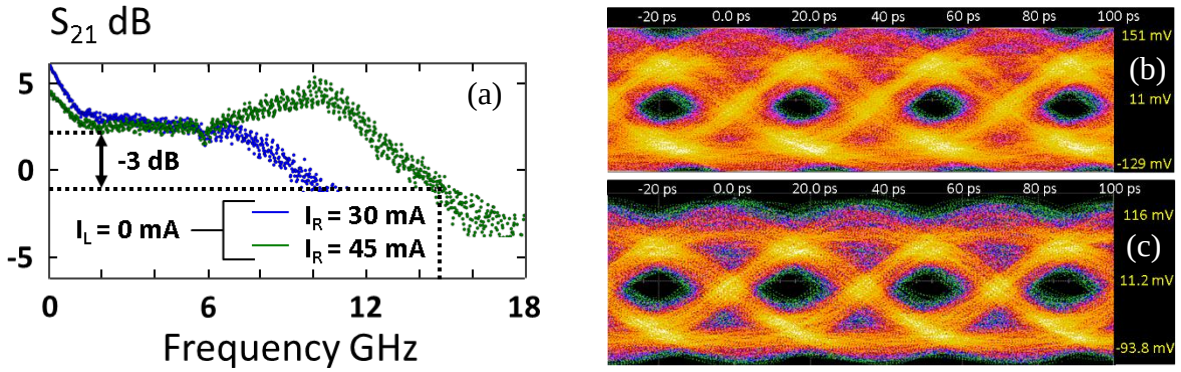


Figure 3. (a) Small signal modulation response S_{21} for two different injected currents into the right section I_R while I_L = 0 mA. The 3-dB modulation bandwidth is nearly 15 GHz for I_R = 45 mA. (b, c) Eye diagrams for transmission at 28 Gbps in the back-to-back configuration and with a 2 km NZ-DSF link for a pattern length of 2^7-1

3.3 Large signal modulation

A large signal modulation experiment was performed using an arbitrary waveform generator (AWG). After amplifying the signal using a 50 GHz RF electrical amplifier, the RF electrical signal generated by the AWG is applied to the right laser section. To boost the output optical signal, a C-band Erbium Doped Fiber Amplifier (EDFA) is used. The amplified spontaneous emission is filtered out using an optical tuneable filter. Finally, a photodetector converts the signal back to an electrical signal, which is fed to a real-time oscilloscope. Transmission of a 28 Gbps NRZ Pseudorandom-Binary-Sequence (PRBS) with a word length of 2^7-1 was verified. A voltage swing of 1.13 V_{pp} is applied to the device, at a bias current I_R = 45 mA. Fig. 3 (b, c) shows the eye diagrams for back-to-back configuration and after transmission over a 2 km long NZ-DSF link. The recorded BER with the 2 km long NZ-DSF is less than $1.0 \cdot 10^{-6}$.

4. CONCLUSIONS

An InP-on-Si DFB laser diode with active distributed reflector was demonstrated. In comparison to a standard single-section DFB laser, the threshold current is reduced by 47%, from 17 to 9 mA. The bias current required to obtain a 3-dB modulation bandwidth of 15 GHz was 45 mA, which is 55% less than the current required to obtain the same bandwidth in a single section DFB [3]. Finally, transmission of a 28 Gbps NRZ-OOK signal is shown for both a back-to-back configuration and for a 2 km long NZ-DSF link with BER below the 7% HD-FEC threshold.

ACKNOWLEDGEMENTS

The authors acknowledge the Methusalem funding of the Flemish government.

REFERENCES

[1] D. Liang et al., “Recent progress in lasers on silicon,” Nature Photonics 4, pp. 511-517, (2010).
[2] S. Keyvaninia et al., “Ultra-thin DVS-BCB adhesive bonding of III-V wafers, dies and multiple dies to a patterned silicon-on-insulator substrate,” Optical Materials Express, 3(1), pp. 35-46, (2012).
[3] A. Abbasi et al., “28 Gb/s direct modulation heterogeneously integrated C-band InP/SOI DFB laser,” Optics Express, 23(20), p.26479-26485, (2015).
[4] G. Liu et al., “Experimental demonstration of DFB lasers with active distributed reflector,” Optics Express, 26(23), pp. 29784-29795, (2018).
[5] G. Roelkens et al., “III-V-on-silicon photonic devices for optical communication and sensing,” Photonics (invited), 2(3), p.969-1004, (2015).
[6] K. Ma et al., “Demonstration of InP-on-Si Self-Pulsating DFB Laser Diodes for Optical Microwave Generation,” IEEE Photonics Journal, pp. 1504608, 9(4), (2017).

Novel adiabatic tapered coupler for small III-V lasers grown on SOI wafer

Yuting Shi [1], Bernardette Kunert [2],Marianna, Pantouvaki [2], Joris Van Campenhout [2],Dries Van Thourhout [1,2]
[1]*INTEC Department, Ghent University, Technologiepark-Zwijnaarde 126, 9052 Ghent, Belgium*
[2]*IMEC, Kapeldreef 75, 3001 Heverlee, Belgium*
e-mail: Yuting.Shi@ugent.be

ABSTRACT

While III-V lasers epitaxially grown on silicon have been demonstrated, an efficient approach for coupling them with a Silicon Photonics platform is still missing. In this paper, we present a novel design for an adiabatic coupler for interfacing nanometer scale III-V lasers grown on SOI with other silicon photonics components. The starting point is a directional coupler, which achieves 100% coupling efficiency from the III-V lasing mode to the Si waveguide TE-like ground mode. To improve the robustness and manufacturability of the coupler, a more advance tapered coupler is designed, which is less sensitive to variations in III-V waveguide dimensions and temperature variations, and still reaches a coupling efficiency close to 100%. The proposed couplers are designed for the particular case of aspect-ratio-trapping (ART) based III-V epitaxy, but it is believed that it should also be compatible with other epitaxial III-V/Si integration platforms. The presented coupler is expected to pave the way to integrating III-V lasers epitaxially grown on SOI wafers with other photonics components, one step closer towards a fully functional Silicon Photonics platform.

Keywords: Tapered coupler, III-V epitaxy, SOI wafer, small laser, Si photonics

1 INTRODUCTION

The integration of III-V semiconductors on Silicon is one of the key processes needed to build a versatile Silicon Photonics platform incorporating active and passive components. The direct epitaxy of III-V materials on Si can be considered the ultimate strategy to achieve this, but, depending on the approach, still faces challenges in reaching sufficient crystalline quality, and/or interfacing with other silicon photonics components, and/or demonstrating electrical injection. Several groups have developed novel epitaxial processes providing high quality III-V materials directly grown on silicon substrates, demonstrating optically or electrically pumped lasing. An efficient scheme for interfacing these devices with standard silicon photonics devices has not been presented however. In this paper we present a novel adiabatic coupler design to bridge epitaxial III-V devices with Si waveguides. We focus on the case of III-V nano-ridges grown on Si using the aspect ratio trapping (ART) technique [1]. The quality of this material has been investigated in detail[2] and verified by the demonstration of lasing in our previous work[3]. The proposed Si coupler can be added in the silicon layer during the standard shallow trench isolation (STI) process carried out before the III-V growth. As such the adiabatic coupler requires no additional fabrication steps and is fully compatible with the current process.

The next section presents the design of a directional coupler, which illustrates that highly efficient optical coupling is indeed feasible. The following sections then present the design of a more robust tapered coupler, which is more tolerant to process variations.

2 DIRECTIONAL COUPLER

Figure 1(a) shows a cross-section of the proposed coupler. The fabrication process starts from an SOI wafer with a 350nm thick top Si layer. The Si couplers, waveguides (WG) and trenches for subsequent epitaxy are defined in this layer through a standard STI process, leaving a 50nm thick slab layer. Next follows a Si wet etch step to open up the Si trenches for GaAs growth. After the GaAs nano-ridge epitaxy, the structure is planarized with SiO_2. This process fixes the height of the Silicon couplers and WGs to be 350nm. The GaAs ridge is set to be 350nm wide and 450nm high, in line with previous samples that showed laser operation [3]. The free variables for optimising the directional coupler are then the gap between the GaAs nanoridge and the Si WG (denoted as W_{Gap}, defined as the distance between the right edge of the GaAs trench and the left edge of the Si WG) and the width of the Si WG (denoted as W_{Si}). To have full coupling from the TE-like lasing mode of the III-V nano-ridge, shown in the inset of Figure 1(b), to the TE-like mode of the Si WG, the two modes have to be phase-matched. In practice this means the width of the Si WG has to be chosen such that the effective refractive index n_{Si} of its TE-like ground mode is equal to that of the TE-like ground mode of the III-V nano-ridge, $n_{III-V} = 2.64$, . From Figure 1(b), which shows the effective index of the first 2 eigenmodes of the Si WG as function of its width, we can derive this phase matching happens for $W_{Si} = W_{match} = 295nm$ (for a wavelength of 1310 nm). Figure 1(c), which shows a top view of the propagating field for $W_{Gap} = 240nm$, shows the periodic exchange of power between both WGs, typically for a phase matched directional coupler.

The coupling length is $45\mu m$. To get full power exchange, the phase-matched condition has to be rigorously met however and the device length has to be exactly equal to the coupling length. Therefore a directional coupler can only be optimized for a single wavelength and is highly sensitive to process variations. To illustrate this, Figure1 (d) shows how the coupling length and coupling efficiency vary when the wavelength deviates from the design wavelength (1310nm).

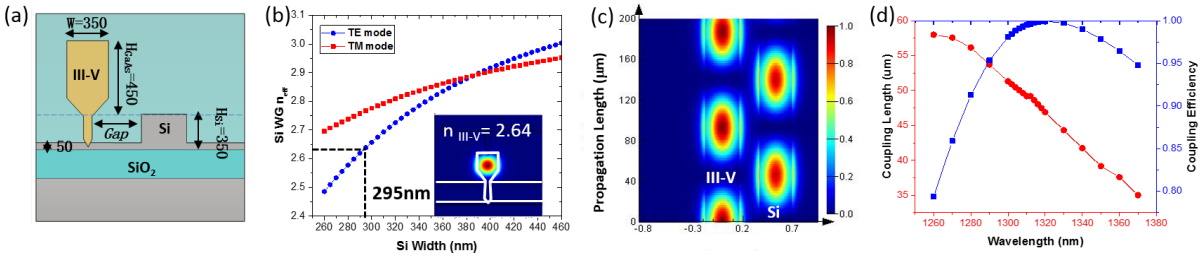


Figure 1. (a) Cross-section of the proposed directional coupler consisting of an active GaAs nano-ridge and a passive Si WG (unit: nm). (b) The calculated effective refractive index of the TE-like and TM-like ground modes of a 350nm high Si WG as a function of its width. The insert shows the lTE-like ground mode of the III-V nano-ridge WG. (c) The 2-D top view of the optical power propagating in the coupler. (d) The coupling length and coupling efficiency as a function of wavelength. The coupler was optimised for 1310nm.

3 ADIABATIC COUPLER

Given that the directional coupler is narrow-band and exhibits a low tolerance to fabrication and temperature variations, a more robust adiabatic coupler is proposed. The tapered Si WG remains in the same layer as in the directional coupler discussed above but its width is varied (Figure 2 (a)). The left edge of the coupler is kept parallel with the GaAs nano-ridge while the right edge is linearly varying along the coupler. Figure 2(b) shows the top view of the adiabatic coupler. The tapered Si WG starts with a width of W_1, ends with a width of $W_2 (> W_1)$ after a length L, and then connects to a straight WG. The respective optical modes at different cross sections of the coupler are also shown : Φ^{TE}_{III-V} is the TE-like ground mode in the standalone III-V nano-ridge; Ψ^{TE}_{+1} is the symmetric (denoted with '+') TE-like supermode at the position of W_1; Ψ^{TE}_{+2} is the symmetric TE-like supermode at the position of W_2; Φ^{TE}_{Si} is the TE-like ground mode in the standalone Si WG. For easier recognition, the symbol Φ is used to represent the standalone waveguide optical modes while Ψ is used for the supermodes in the coupling region.

The coupling from the III-V lasing mode Φ^{TE}_{III-V} to the Si WG mode Φ^{TE}_{Si} can be decomposed into three individual coupling processes. The initial optical mode Φ^{TE}_{III-V} in the active III-V nano-ridge is converted to Ψ^{TE}_{+1} at the start of the Si WG. Figure 2(b) shows that the supermode Ψ^{TE}_{+} mostly overlaps with the III-V nanoridge for a narrow width W_1 (that is Ψ^{TE}_{+1}), and with the Si WG for a wide width W_2 (that is Ψ^{TE}_{+2}). The transition from Ψ^{TE}_{+1} to Ψ^{TE}_{+2} happens in the taper region. The last step is the conversion from Ψ^{TE}_{+2} to Φ^{TE}_{Si}, after which the optical field is guided further in the standalone Si WG towards following optical components. The total coupling efficiency is the product of each individual mode coupling process.

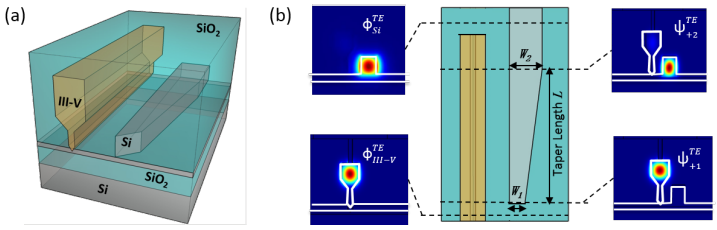


Figure 2. (a) 3-D sketch of the adiabatic coupler. (b) Top view of the coupler and the corresponding TE-like modes at different positions.

3.1 Optimisation of Coupler Widths

To get a high coupling efficiency, the widths W_1 and W_2 are first optimised. Figure 3 (a) shows the overlap of mode Ψ^{TE}_{+} with modes Φ^{TE}_{III-V} (solid line) and Φ^{TE}_{Si} (dashed line) as a function of W_{si} for $W_{Gap} = 240nm$. It is observed that W_1 should be narrower than 275nm in order to get the overlap betweenΦ^{TE}_{III-V} and Ψ^{TE}_{+1} higher than 99%, while W_2 should be wider than 315nm for overlap between Ψ^{TE}_{+2} andΦ^{TE}_{Si} higher that 99%. The intersection point is where $W_{si} = W_{match} = 295nm$. Apart from this, it has to be ensured that coupling only occurs among the four TE-like optical modes shown in Figure 2 (b), and all TM-like modes should be excluded. Figure 3 (b) shows the effective refractive index n_{eff} of the TE- and TM-like ground modes of the

separated III-V/Si WGs (solid lines) and the n_{eff} of the first four supermodes (dashed lines) of the coupler. The overlap of the dashed line with the solid line reveals whether the supermode is TE-like or TM-like, and if it is centered mostly in III-V or Si. Point A is again the phase-matched condition for Φ^{TE}_{III-V} and Φ^{TE}_{Si} where $W_{si} = W_{match} = 295nm$, while B is the phase-matched point for Φ^{TE}_{III-V} and Φ^{TM}_{Si} ($W_{si} = 235nm$), C is the phase-matched point for Φ^{TM}_{III-V} and Φ^{TM}_{Si} ($W_{si} = 325nm$), D is the phase-matched point for Φ^{TM}_{III-V} and Φ^{TE}_{Si} ($W_{si} = 355nm$). To avoid the risk of coupling to TM-like modes, the tapered coupler should include point A but exclude B and C . From this we derive the conditions $235nm < W_1 < 275nm$, $315nm < W_2 < 325nm$.

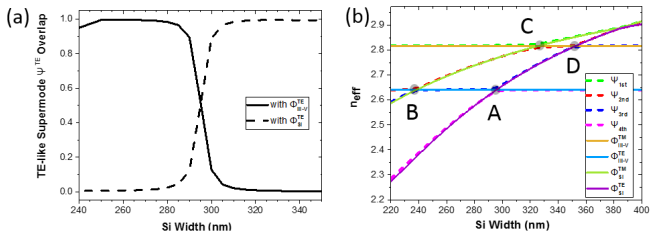


Figure 3. (a) The overlap of mode Ψ^{TE}_{+} with modes Φ^{TE}_{III-V} (solid line) and Φ^{TE}_{Si} (dashed line) as a function of W_{si} at $W_{Gap} = 240nm$. (b) The effective refractive index n_{eff} of the TE/TM-like ground modes of the separated III-V/Si WGs and of the first four supermodes.

3.2 Tapered Coupler Length

Figure 4(a) shows the coupling efficiency to the modes Φ^{TE}_{Si}, Φ^{TM}_{Si}, Φ^{TE}_{III-V} and Φ^{TM}_{III-V}, when the taper is excited by the mode Φ^{TE}_{III-V}, as function of taper length L, whereby W_2 and W_1 are chosen to be their smallest possible values of $W_1 = 275nm$ and $W_2 = 315nm$ respectively. At $W_{Gap} = 240nm$, $L = 310\mu m$, the coupling efficiency from Φ^{TE}_{III-V} to Φ^{TE}_{Si} reaches as high as 98%. Most of the remaining 2% of the power couples to the Φ^{TM}_{Si} mode in Si. Figure 4(b) shows how the optical power is exchanged between the III-V nano-ridge and the Si WG and Figure 4(c) shows a 2D image of the optical power evolution along the coupler.

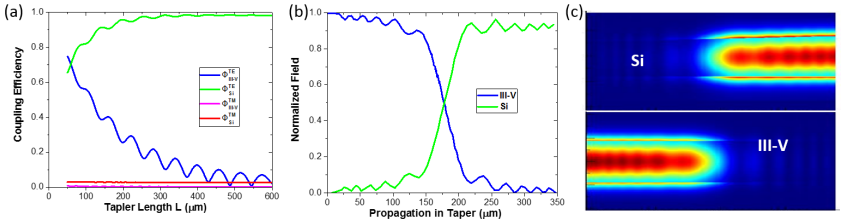


Figure 4. (a) Coupling efficiency as function of taper length L. (b) Power exchange between III-V nano-ridge and Si WG along propagation direction when $L = 310\mu m$. (c) The top-view 2-D image of optical power evolution along the coupler when $L = 310\mu m$.

4 CONCLUSION

This paper proposes a novel adiabatic coupler working in the O-band for the adiabatic mode conversion from a GaAs nano-ridge laser to a Si waveguide. The Si waveguide is compatible with our earlier presented process for the direct epitaxy of GaAs on silicon and requires no extra effort to fabricate. We show that a directional coupler design can reach a coupling efficiency of 100% but is sensitive to process and wavelength variations. To improve this, the design of a more robust tapered coupler is presented, which is more tolerant to process variations and can still achieve 98% coupling efficiency. The designed adiabatic coupler is expected to facilitate the interface between epitaxially grown active III-V devices and passive Si devices on the same substrate, opening the road towards the incorporation of III-V components in future Silicon Photonics platforms.

ACKNOWLEDGMENT

This work was supported by IMEC's industry-affiliation R&D Program on Optical I/O and by the Ghent University special research fund.

REFERENCES

[1] Kunert, Bernardette, et al. "How to control defect formation in monolithic III/V hetero-epitaxy on (100) Si? A critical review on current approaches." Semiconductor Science and Technology 33.9 (2018): 093002.

[2] Kunert, B., et al. "III/V nano ridge structures for optical applications on patterned 300 mm silicon substrate." Applied Physics Letters 109.9 (2016): 091101.

[3] Shi, Yuting, et al. "Optical pumped InGaAs/GaAs nano-ridge laser epitaxially grown on a standard 300-mm Si wafer." Optica 4.12 (2017): 1468-1473.

Silicon Nitride PICs Platform Development from a Foundry Perspective: From Concepts to Real Applications

Anton Stroganov, Michael Geiselmann
LIGENTEC SA, Lausanne, Switzerland
e-mail: michael.geiselmann@ligentec.com

ABSTRACT

Silicon Nitride based integrated photonics platforms are going through the stage of fast spread and growth due to many beneficial features such as large transparency window and low propagation losses, presence of Kerr nonlinearity and absence of Two Photon Absorption. To allow integrated photonic devices, the platform capabilities awareness in integrated photonic community and high level of technological maturity are required. At LIGENTEC, we developed the all-nitride-core platform with processes adapted for operation from visible to Mid-IR spectral range and fast fabrication turn-around. Advances and steps towards platform technological maturity from the point of view of a foundry are discussed and demonstrated.

Keywords: Integrated Photonics, Silicon Nitride, High Q Resonators, Low Loss PICs, Hybrid Integration

1. INTRODUCTION

Recent advances in photonic integrated circuits (PICs) technology made the PICs an important part in a variety of application areas from healthcare, bio-sciences and sensors, to LiDARs, high-performance computing and data-/tele- communication. Integration brings opportunities for to-date bulky, complex and expensive optical systems to be implemented in an integrated chip-scale way for increased stability and robust operation, size and power consumption reduction and cost-effective large-scale fabrication of even complex circuits.

While to-date almost any optical element can be done in an integrated way, there is no unique universal material or process to cover all the needs for their simultaneous realisation and to fit for all the application cases, so there are several different platforms employed (SOI, III-V, SiN, etc.), having their own benefits and limitations. Silicon Nitride (SiN) based platforms lately got a growing interest for having large transparency window (visible to MIR) and providing ultra-low losses compared to other PIC platforms. Combined with good thermal stability [1], it makes SiN a beneficial platform for passives. Even though no active components are directly available at the moment, they can be allowed by heterogeneous integration. Absence of Two-Photon Absorption (TPA) [2] allows high power level operations, while presence of rather large Kerr nonlinearity opens new horizons for nonlinear photonics. Silicon Nitride based platform were shown to be a prominent option for sensing devices and bioimaging; supercontinuum [3], optical combs [4] and even photon-pairs generation [5] allowed by (S)FWM in high-Q resonators, which provides a good basis for Quantum PICs and nonlinear photonics applications.

All together, Silicon Nitride based integrated photonics proved itself to be a rapidly growing sector, and manifested a need to prove its capabilities in applications, operation and fabrication.

2. LIGENTEC ADVANCES ON PLATFORM DEVELOPMENT

LIGENTEC is an open access Silicon Nitride foundry. To enforce advancement of integrated photonics and SiN in particular, we developed together with the design house VLC Photonics a Process Design Kit (PDK). The PDK is available in Luceda and Synopsys with basic elements to allow fast and efficient layout design. The company could cover the whole production cycle starting from design assistance to post-fabrication optical characterization. Moreover, Multi-Project Wafer (MPW) runs are offered to allow low-cost prototyping and proof-of-concept demonstrations. Current capabilities of foundries can be found elsewhere [6]-[7], but hereunder the focus is done more on steps being done towards industry-grade integrated devices. As a part of this, we dedicate our efforts to create and enable technical solutions to overcome current challenges and to demonstrate applicability and benificity of the integrated photonics approach.

One recent example for our visible SiN platform AN150 was a study of on-chip large Field-of-View (FOV) Total Internal Reflection Fluorescence (TIRF) microscopy, superresolution and high-throughput imaging. Similarly to sensing technologies, it utilizes the evanescent field from waveguides, and therefore precise film thickness control and high purity of materials are important. This was done as an integral part of our AN150 process optimization, adapted for visible range. Results of this study together with successful demonstration of other functional components allow us to introduce a specially adapted process for applications in a visible range.

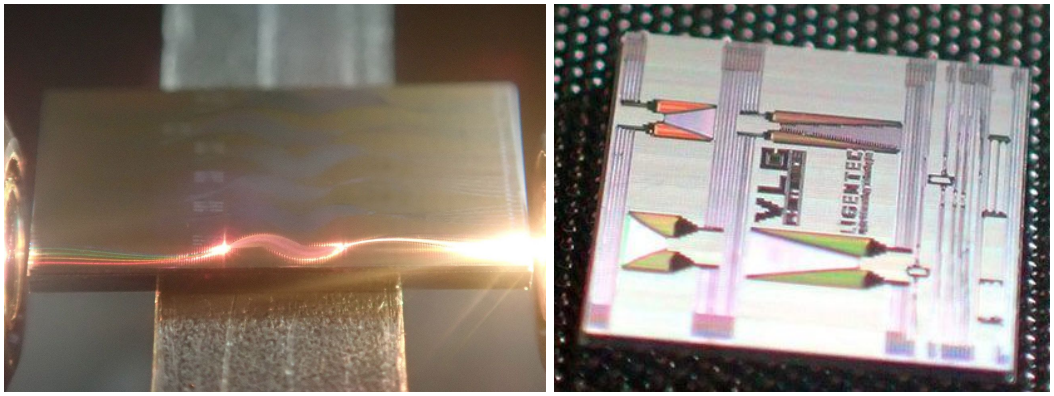


Figure 1. Compact AWGs for visible (left) and Near IR (right) spectral range operation. Chip sizes are 5x10mm (left) and 5x5mm (right). Pictures taken by VLC Photonics.

A lot of interest is gained due to the fact to use the confinement of the optical mode in out thick AN800 platform with SiN thickness of 800nm. This mode-confinement decreases chip size and provides very good propagation losses. Furthermore, AN800 SiN offers nonlinear properties for on-chip combs and supercontinuum generation, which can be utilized for stabilization and calibration purposes as well as for metrology. To enable these technology realizations, dispersion engineering needed for waveguides and high-Q microring resonators is required. Moreover, a wide tunability of devices is often desired, which can be achieved with efficient integrated heating elements. All those features are part of our AN800 process, adapted for thick nitride thickness and optimized NIR-MIR operation. Besides, for this process, efforts were put in development of efficient passives, including fiber couplers, small footprint AWGs, stable and fabrication tolerant MMIs and MZIs and long low-loss delay lines.

To open an access to integrated photonic devices, we work towards PIC packaging standards, as heterogeneous integration can allow benefits of active III-V based elements combined with ultra-low loss SiN passives,while electrical and optical interconnects with the “outside world” are inevitable for any ready-to-use device. SiN is an ideal interposer platform due to its high efficient taper couplers and adjustable spot size converters for chip to chip coupling. To mature the packaging standards and procedures, we establish collaborations with packaging partners, gradually getting closer to possibility of fast and large-scale electro-optical packaging.

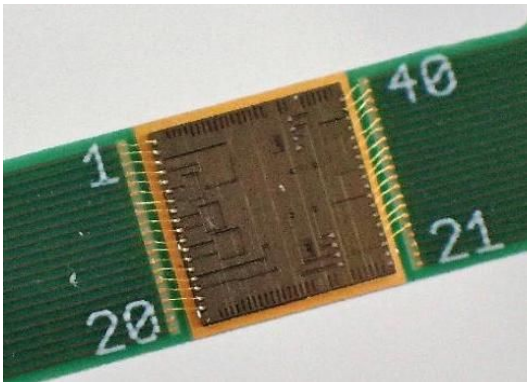


Figure 2. Image of a wire-bonded LIGENTEC photonic chip

To achieve ready-to-use level of PIC applicability, very high degree of control for many parameters is required, and all those collaborative efforts revealed the ones which appeared to be the most crucial in every case: film thicknesses and uniformity (imaging, sensing, dispersion engineering), geometrical dimensions of all the structures (dispersion engineering, reliable passives performance), flatness of bonding sites and local openings (integration and packaging, sensing), alignment precision (multi-layer structures, packaging). To enable integrated photonic devices, the process should be able to reproduce the same layout thousands of times with those parameters within the same specifications. To be able to provide high standards of fabrication, we noticeably advanced the degree of their control and reproducibility up to the level which allow us to claim our platform high technology readiness level not only for streamline planar fabrication, but also for more sophisticated PICs realisation.

To ensure the quality of end-product, evaluation of optical performance (coupling, propagation and bend losses, Q-factors, etc) is done on all the wafers. Dies with reference structures are placed in different areas on a wafer to allow alignment of optical performance with fabrication figures. Semi-automatic measurements of microring resonators with a wavelength sweep are performed routinely, which allows to extract quantitative information on coupling efficiency, achievable Q-factors and deposited materials quality. These measurements provide an additional level of process control on a post-fabrication stage, allowing to provide guarantee not only on dimensions, but on optical performance of delivered products.

3. CONCLUSION

Without any doubt, SiN is one of the PIC technology platforms that significantly evolved in the past few years, and its transparency in the visible and IR wavelength range together with its low losses makes it suitable for a variety of applications. LIGENTEC's advances on platform development and process optimization enable today high standards from low volume prototype fabrication to volume production with performance guarantees.

REFERENCES

1. A. Arbabi *et al*.: Measurements of the refractive indices and thermo-optic coefficients of Si3N4 and SiOx using microring resonances, *Optics Letters*, 38, 3878–3881 (2013)
2. D. J. Moss *et al.:* New CMOS-compatible platforms based on silicon nitride and Hydex for nonlinear optics, *Nature Photonics, 7, 597 (2013)*
3. D. Grassani *et al.:* Mid-infrared supercontinuum generation in a SiN waveguide pumped at 1.55 micron, *Frontiers in Optics (*2016)
4. V. Brasch *et al.:* Photonic chip based optical frequency comb using soliton Cherenkov radiation, *Science*, vol. 351, issue 6271, pp. 357-360 (2016)
5. S. Ramelow *et al.:* Silicon-Nitride Platform for Narrowband Entangled Photon Generation, *arXiv:1508.04358 (2015)*
6. P. Muñoz *et al.*: Silicon Nitride Photonic Integration Platforms for Visible, Near-Infrared and Mid-Infrared Applications, *Sensors*, 17, 2088 (2017)
7. M. Porcel *et al.*: Silicon nitride photonic integration for visible light applications, *Optics and Laser Technology,* 112, 299-306 (2019)

Recognition of 8QAM Coded Label by Maximum Output of Optical Waveguide Circuits

Tumendemberel Surenkhorol*, Hiroki Kishikawa, Nobuo Goto
Department of Optical Science and Technology, Tokushima University, Tokushima 770-8506, Japan
* *c501848002@tokushima-u.ac.jp*

ABSTRACT

This research work aims to implement a label recognition function of photonic router in optical domain. A waveguide type circuit has been proposed to recognize label which is considered to be an optical coded signal. The label can be identified as an unique output ports which have minimum or maximum intensity values.

In our previous work, an 8QAM (eight quadrature amplitude modulation) coded label recognition has been analyzed with the minimum output intensities of the circuit. In this paper, the 8QAM coded label recognition is investigated with the maximum output intensities. It is theoretically analyzed and noise tolerance simulation is run.

Keywords: optical 8QAM code, label recognition, optical waveguide circuit, noise tolerance

1 INTRODUCTION

The rapid development of Internet based technologies and its popularization require broadband network to have more capacities and higher transmission rate. To fulfill it, numerous kinds of research works have been investigated. Among them, transmitting information signal through network nodes in only optical form without electrical conversion is expected to accelerate processing speed of nodes [1].

Our research focuses on an optical processing of label recognition which is one of the most important functions of a photonic router. So far, number of recognition schemes have been studied for differently coded optical labels such as binary phase-shift-keying (BPSK) [2], quadrature PSK (QPSK) [3], and 16QAM [4]-[6].

We target on 8QAM coded label and for this purpose, we have been proposed passive waveguide-type label identification circuit which is expected to have low power consumption. In this work, by adjusting previously proposed minimum intensity detection circuit [7] with thresholding devices and logical post-processing circuits, 8QAM code detection is investigated by maximum output results. To review the efficiency of this method, noise tolerance simulation is run by OptiSystem software (Optiwave Systems Inc.).

2 PROPOSED RECOGNITION METHOD FOR 8QAM CODED LABEL

A constellation of our target 8QAM signal is shown in Fig. 1. It can be dealt with as two QPSK signals with different phase and amplitude values. Therefore, we propose a method based on former QPSK code recognition circuit (QPRC) [3] as shown in Fig. 2 and its input and output relations are expressed by Eq.(1).

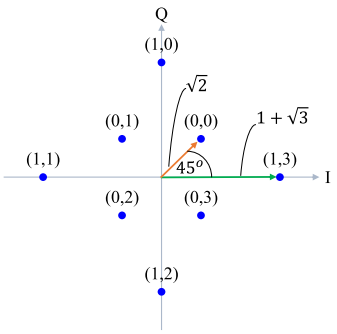


Figure 1. A constellation of 8QAM signal.

Our proposed 8QAM recognition circuit consists of two Y-couplers, an attenuator, a phase shifter, two QPRCs and threshold devices as illustrated in Fig.3(a). The thresholding values are set to be $\alpha = 1.4E_0^2$ and $\beta = 0.375E_0^2$. After the threshold devices make the output zero for inputs lower than these values, maximum intensities are discriminated by using post processing logic circuits as shown in Fig.3(b).

$$\begin{pmatrix} E_{out}^{(1)} \\ E_{out}^{(2)} \\ E_{out}^{(3)} \\ E_{out}^{(4)} \end{pmatrix} = \frac{1}{2} \begin{pmatrix} 1 & e^{j3\pi/2} \\ e^{j7\pi/4} & e^{j7\pi/4} \\ e^{j5\pi/4} & e^{j\pi/4} \\ e^{j3\pi/2} & 1 \end{pmatrix} \begin{pmatrix} E_{in}^{(1)} \\ E_{in}^{(2)} \end{pmatrix} \tag{1}$$

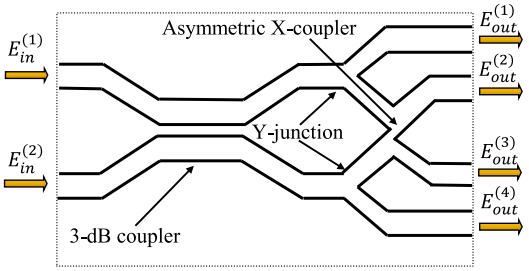


Figure 2. QPSK code recognition circuit.

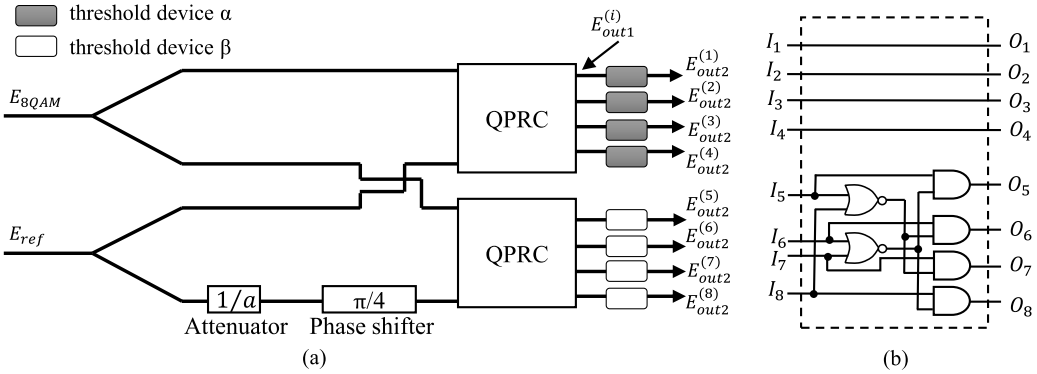


Figure 3. (a) Proposed 8QAM recognition circuit by the maximum output, (b) Post-processing logic circuit.

At the inputs of the recognition circuit, 8QAM and a reference signals are given and they can be written as $E_{8QAM} = a^m E_0 e^{j\pi/4} e^{jn\pi/2} e^{jm\pi/4}$ and $E_{ref} = aE_0$, respectively. Here, m=0, 1, n=0, 1, 2, 3, and $a = (1+\sqrt{3})/\sqrt{2}$. The reference signal is assumed to be transmitted with the 8QAM label as time-series pulses. Output intensities before thresholder and after post processing logic circuits are plotted in Fig. 4 (a) and (b), respectively. As the result shows, different outputs are found for each input code combinations.

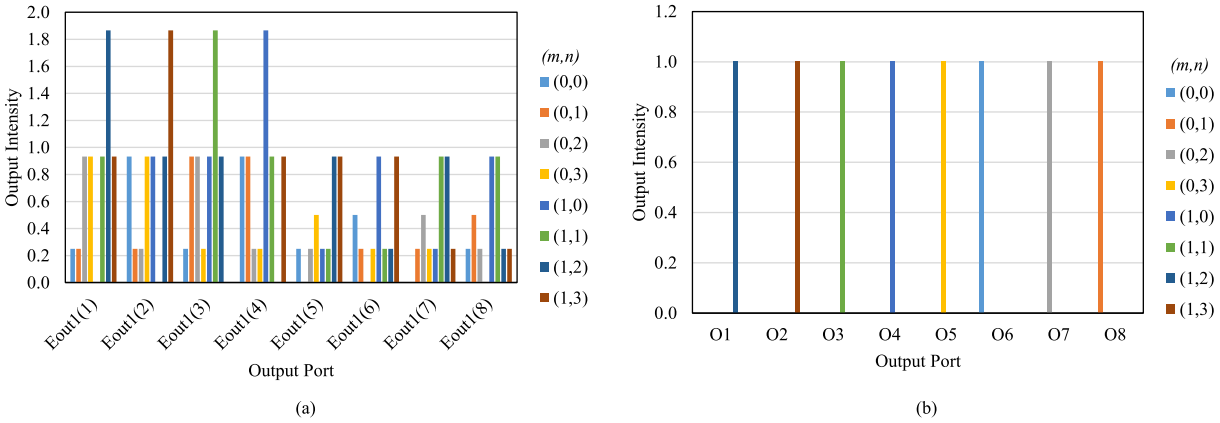


Figure 4. Output intensities (a) before thresholder and (b) after post processing logical circuit.

3 EVALUATION OF NOISE TOLERANCE

A simulation model for evaluation of noise tolerance is shown in Fig. 5. We design waveguide type recognition circuit by using discrete optical devices. The signal source is given from a continuous wave (CW) laser at wavelength of 1550 nm. The optical 8QAM pulse sequence is generated by pseudo random bit sequence (PRBS) of $2^{15}-1$. The amplified spontaneous emission (ASE) noise is considered to be added to both of the 8QAM and reference signals for evaluating noise tolerance.

Fig. 6 shows the calculated bit-error rate (BER) against optical signal-to-noise ratio (OSNR) at different bit rates of R_0= 7.5, 15.0, and 30.0 Gb/s which correspond to the symbol rates of $R_0/3$= 2.5, 5.0, and 10.0 Gbaud. The required OSNRs at log(BER)=-3 are found to be 11.5, 14.5, and 17.8 dB, respectively. At 2.5 Gbaud symbol rate, the OSNR is around 5dB higher than the back-to-back (B2B) value. In comparison, the required OSNRs at log(BER)=-3 at 2.5 Gbaud were 10 dB for 8QAM minimum-detection circuit [7] and 27 dB for 16QAM maximum-detection circuit [6].

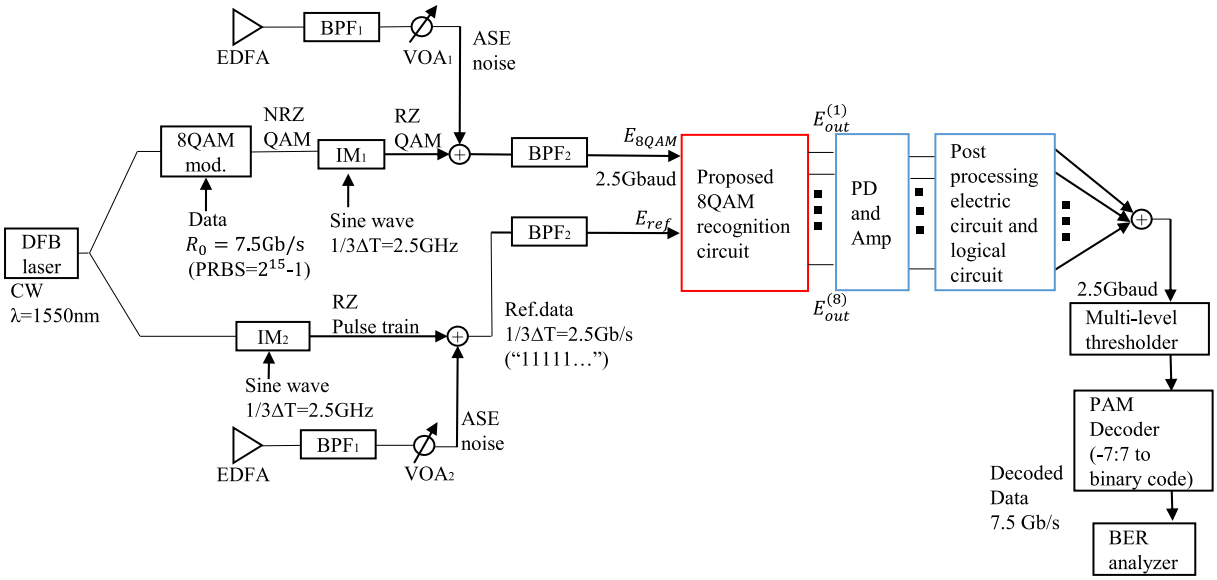


Figure 5. A simulation set-up for noise tolerance.

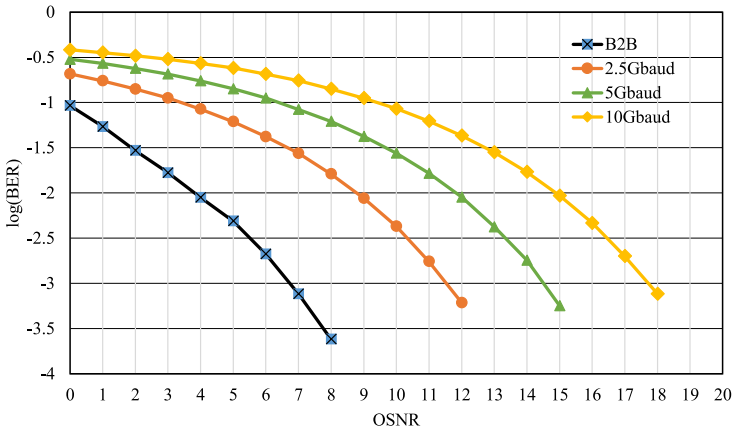


Figure 6. A simulated BER performance as a function of OSNR.

4 CONCLUSION

In this work, an operation of integrated-optic 8QAM label recognition circuit was investigated by maximum outputs. By using threshold devices and a post processing logical circuit, recognition was successfully achieved. The noise tolerance evaluation was examined as BER as a function of OSNR.

In our future work, we will work on scalability and improving noise tolerance.

REFERENCES

[1] D. J. Blumenthal, B. E. Olsson, G.Rossi, et al., "All-optical label swapping networks and technologies," J.Lightw.Technol. 18(12), 2000, pp. 2058-2075.

[2] H. Hiura, J. Narita, and N.Goto, "Optical label recognition using tree-structure self-routing circuits consisting of asymmetric X-junction," IEICE Trans.Electron., 2007, pp. 2270-2277.

[3] Y. Makimoto, H. Hiura, N. Goto, et al., "Waveguide-type optical circuit for recognition of optical QPSK coded labels in photonic router," J.Lightw.Technol., 2009, pp. 60-67.

[4] K. Inoshita, H. Kishikawa, et al., "Proposal of optical waveguide circuits for recognition of optical QAM codes," J.Lightw.Technol., 2013, pp. 2271-2278.

[5] K. Inoshita, N. Goto, et al., "Recognition of 16QAM codes by maximum output with optical waveguide circuits, thresholders, and post-processing logic circuit," IEICE Trans.Electron, 2014, pp. 448-454.

[6] K. Inoshita, Y. Hama, et al., "Noise tolerance in optical waveguide circuits for recognition of optical 16 quadrature amplitude modulation codes," Opt.Eng., 2016, 126105.

[7] T. Surenkhorol, H. Kishikawa, N.Goto, et al., "Waveguide-type optical circuits for recognition of Optical 8QAM coded label," Opt.Eng., 2017, 107101.

Extracting Multiple Parameters from a Compact Circuit for Performance Evaluation

Student Paper

Yufei Xing [1,2,*], Mi Wang [1,2], Alfonso Ruocco [1,2,3], Joris Geessels [4], Umar Khan [1,2], Wim Bogaerts [1,2]

[1]*Photonics Research Group, Ghent University-imec, Ghent, Belgium*

[2]*Center of Nano and Biophotonics (NB-Photonics), Ghent, Belgium*

[3]*currently at Cambridge Graphene Centre, Cambridge University, Cambridge, UK*

[4]*Luceda Photonics, Dendermonde, Belgium*

e-mail: yufei.xing@ugent.be

ABSTRACT

We designed a two-stage Mach-Zehnder Interferometer for process monitoring control. Using Restart-CMA-ES global optimization algorithm, we can extract multiple on-chip waveguide and directional coupler parameters simultaneously. The compact design greatly reduces the footprint and number of measurements and improves accuracy for parameter extraction, making it useful for detailed wafer-level variability analysis.

1 DESIGN OF THE MONITORING CIRCUIT

Silicon Photonics offers a high material contrast and strong light confinement, enabling large scale integration and complex circuits. However, it is also susceptible to process variation. Process variation in linewidth and thickness would affect component behavior such as effective index and group index of waveguides and coupling coefficients of directional couplers (DC). Performance variation in each component propagates and accumulates in a circuit and leads to circuit performance degradation.

To monitor the process parameters and evaluate the performance of the fabricated circuit, we designed the two-stage Mach-Zehnder Interferometer (MZI) shown in Fig. 1a. We discussed the design principle of waveguide index extraction in [1], where the low-order stage offers a reference of the effective index under the overall process variation while the high-order stage allows accurate effective index and group index extraction. The arm length differences of the two stages are 15 μm and 150 μm, and they are joined by three DCs designed at 25%, 50% and 75% cross power coupling, respectively. The gap between the waveguides in the DC is 250 nm,

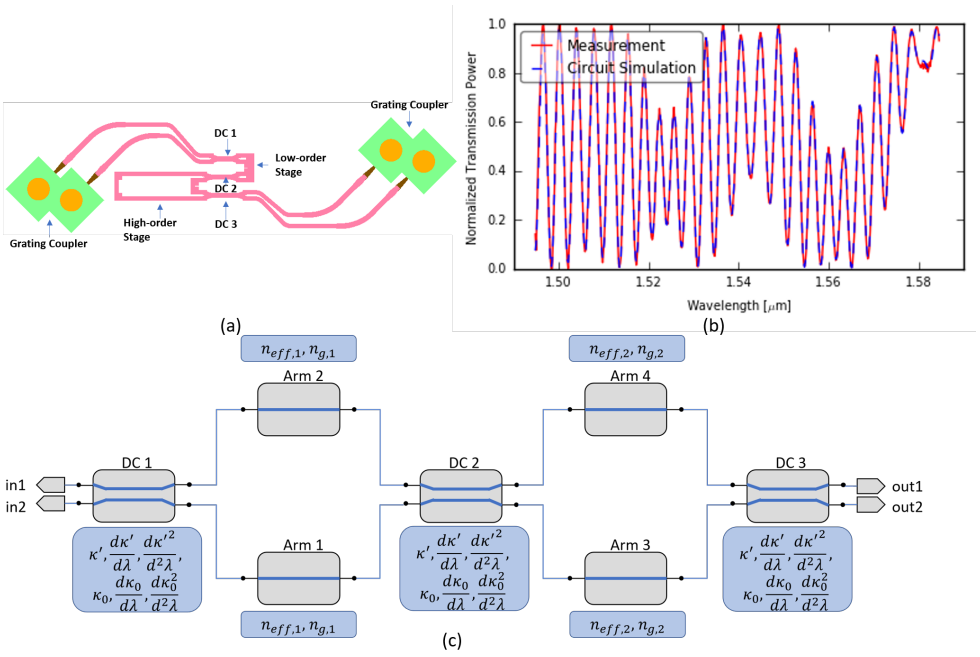


Figure 1. (a) The layout of the two-stage MZI. (b) The measured spectrum of a two-stage MZI. (c) The circuit model of the device. Two MZI stage have different n_{eff} and n_g led by the local process variation.

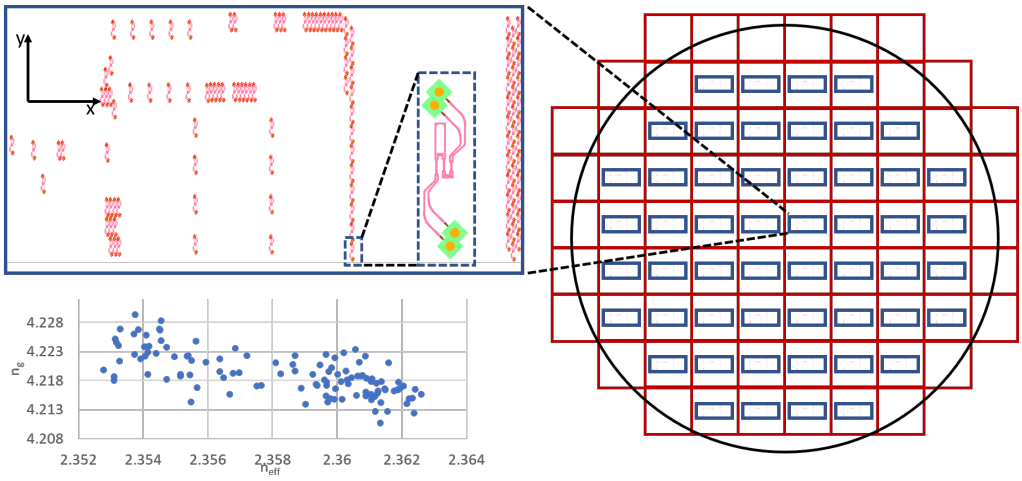


Figure 2. (a) Locations of the two-stage MZI on a die. (b) Extracted n_{eff} and corresponding n_g of die (X=0, Y=0) (in the center of the wafer). (c) Locations of dies on the wafer. Red grid indicates dies on the wafer. The black circle is the boundary of the wafer.

and the corresponding coupler lengths in three DCs are 6.65 μm, 12.91 μm, 19.17 μm. To extract the coupler parameters, we designed the three DCs with the same properties except for their coupler lengths [2]. The single circuit design greatly reduces the number of measurements required to extract the set of waveguide and DC parameters. Its compactness also reduces the local variation within the circuit which improves the extraction accuracy. To further reduce the footprint of the device, we also folded the MZI. The circuit is so compact that we can easily squeeze it in various locations on a chip to construct a granular map of the process variation on the fabricated chips as input for location-dependent variability analysis [3].

2 MULTIPLE PARAMETERS EXTRACTION BY THE RESTART-CMA-ES OPTIMIZATION

We extracted the circuit parameters by matching the optical measurement with simulated spectrum. Using the IPKISS circuit simulator we implemented the compact model of the two-stage MZI. Figure 1c shows the compact circuit model of the monitoring circuits. We assume that the effective index $n_{eff,1}$ and group index $n_{g,1}$ at $\lambda_0 = 1550\ nm$ for lower-order stage and $n_{eff,1}$ and group index $n_{g,1}$ of the high-order stage have a slight difference because of local variation. The DC model consists of length-specific coupling coefficients of the straight coupling part κ' and its first and second-order derivative $\frac{\partial \kappa'}{\partial \lambda}$ and $\frac{\partial^2 \kappa'}{\partial \lambda^2}$ of the straight coupling section parameters, and lumped power coupling of two bends κ_0 and its first and second-order derivative $\frac{\partial \kappa_0}{\partial \lambda}$ and $\frac{\partial^2 \kappa_0}{\partial \lambda^2}$. We removed the effect of grating couplers in the spectrum by measuring both the spectra from port *in1* to *out1* and *in1* to *out2* and normalized the transmission spectra to the sum of the two spectra. The solid red curve in Fig. 1b shows a normalized measured spectrum from port *in1* to port *out1*.

As in Fig. 1b, the spectrum of the circuit has a complicated shape. Standard curve fitting methods (e.g., from the scientific python package 'scipy') often only find a local minimum in the difference between the simulated and measured spectrum. The classical curve-fitting methods fail to handle the non-convex parameter landscape and will obtain a local optimum instead of the global optimum. Instead, we used the Covariance Matrix Adaptation Evolutionary Strategy (CMA-ES), which is a smart global optimization algorithm that adaptively chooses the samples to significantly reduce the number of simulations for the non-convex parameter landscape optimization [4]. The CMA-ES is especially powerful to extract multiple parameters simultaneously. However, it also does not guarantee to always find the global optimum. A variation, the Restart-CMA-ES method is a global optimization method that restarts the CMA-ES search if it only obtains a local optimum. After each restart, the population of each generation is increased to make the search more global[5] until it finds out the global optimum. While slower, it works robustly for the waveguide variation we used, i.e. (w∈[465,485] nm, t∈[205,215] nm) and DC gap ∈[100,400] nm in our experiment. As shown in Fig.1b, simulation matches measured spectrum perfectly using the algorithm. A high accuracy is usually obtained within 20,000 iterations. The behavior parameters have been extracted with good accuracy (Table 1).

3 EXTRACTION OF A DIE MAP AND A SIMPLE WAFER MAP

We measured 117 copies of the folded MZI on the die (X=0,Y=0) in the center of the wafer (Fig. 3a). Using the restart-CMA-ES method, we extracted the high-order n_{eff} and n_g as in Fig. 2b. We mapped the width and thickness of the high-order stage arm from n_{eff} and n_g using an geometry model with sub-nanometer

TABLE 1. MAPPED GEOMETRY PARAMETERS WAVEGUIDE WIDTH AND THICKNESS OF THE HIGH-ORDER STAGE ARM.

Parameter	$n_{eff,l}$	$n_{g,l}$	$n_{eff,2}$	$n_{g,2}$	κ'	$\frac{d\kappa'}{d\lambda}$	$\frac{d\kappa'^2}{d^2\lambda}$	κ_0	$\frac{d\kappa_0}{d\lambda}$	$\frac{d\kappa_0}{d\lambda}$
Extracted Value	2.356	4.228	2.356	4.220	4.173e-2	2.149e-1	1.990	2.315e-1	1.438	8.110e-1
Extracted Error	1.456e-6	1.322e-4	2.284e-7	2.105e-5	5.863e-6	9.147e-5	4.060	7.852e-5	1.266e-2	6.325e-2

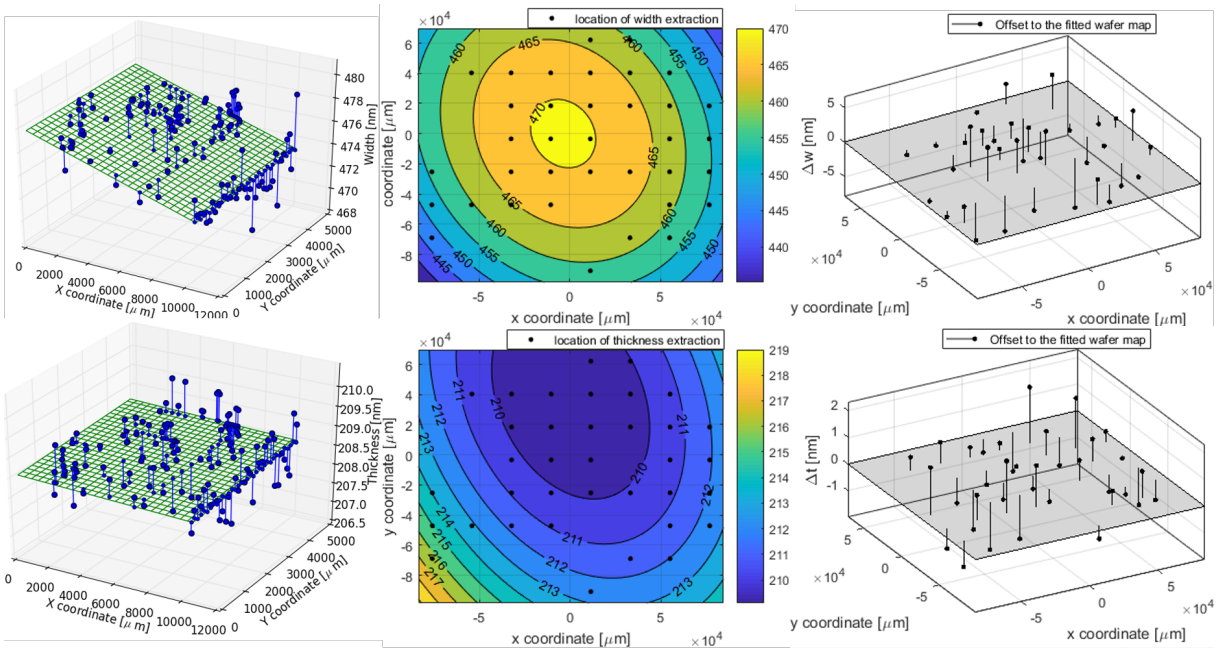


Figure 3. Top: linewidth. Bottom: thickness. (a) Extracted width map of the die. Blue solid dot: extracted value. Green grid: fitted map of extracted values using a linear function. (b) Systematic variation. (c) Random remnant. x and y coordinates give the locations of the MZIs on the die (a) or on the wafer (b,c).

accuracy[1]. The extracted linewidth on the die ranges from 468.9 nm to 479.5 nm (Fig. 3c) and thickness ranges from 207.6 nm to 209.6 nm (Fig. 3d). The standard deviations are 1.9 nm and 0.5 nm respectively.

We also measured the circuit in Fig.2a, framed by the dotted rectangle, over 35 dies over the wafer. These circuits shared the same position on every die. The extracted simple wafer map (Fig.3b) shows a clear location dependence of fabricated geometry. We fit a wafer map using a second-order bivariate polynomial. The linewidth exhibits dome-like trend which is the wafer-level systematic variation ranging from 445 to 475 nm. The residue (Fig. 3c) has a maximum of 5 nm. The wafer-level systematic variation of thickness exhibits slow-varying trend ranging from 209 to 216 nm. The residue (Fig. 3c) has a maximum of 2 nm.

4 CONCLUSION

In conclusion, we designed a folded two-stage-MZI that is very compact to extract process parameters. We applied the Restart-CMA-ES global optimization algorithm to extract multiple waveguide and DC parameters from the circuit using only two optical measurements. We mapped the fabricated linewidth and thickness of a waveguide from the extracted effective index and group index. We extracted die maps and simple wafer maps of the fabricated geometry. The compact circuit is promising for process monitoring and extracting granular wafer maps for performance evaluation and variability analysis.

REFERENCES

[1] Yufei Xing, Jiaxing Dong, Sarvagya Dwivedi, Umar Khan, and Wim Bogaerts. Accurate extraction of fabricated geometry using optical measurement. *Photonics Research*, 6(11):1008, 11 2018.

[2] Yufei Xing, Umar Khan, Antônio Ribeiro Alves Júnior, and Wim Bogaerts. Behavior model for directional coupler. In *Proceedings Symposium IEEE Photonics Society Benelux*, pages 128–131, 2017.

[3] Wim Bogaerts, Umar Khan, and Yufei Xing. Layout-aware yield prediction of photonic circuits. In *2018 IEEE 15th International Conference on Group IV Photonics (GFP)*, pages 1–2. Ieee, 2018.

[4] Nikolaus Hansen. The cma evolution strategy: A tutorial. *arXiv preprint arXiv:1604.00772*, 2016.

[5] Anne Auger and Nikolaus Hansen. A restart cma evolution strategy with increasing population size. In *Evolutionary Computation, 2005. The 2005 IEEE Congress on*, volume 2, pages 1769–1776. IEEE, 2005.

Simulation Methodology for LiDAR on Chip

Chenglin Xu[1], Evan Heller[1], Maryvonne Chalony[2]
[1]Synopsys, RSoft Design Group, 400 Executive Blvd, Ossining, NY 10562 USA
[2]Light Tech, 1128 Route de Toulon, 83400 Hyères, France
e-mail: chenglin@synopsys.com

ABSTRACT

Simulation plays a critical role in the design and optimization of LiDAR on chip, but there is no single software tool that can completely handle such a complex device. In this paper, we present a simulation methodology that decomposes the complex structure into several simpler building blocks, and applies the appropriate algorithm to each. For example, the grating coupler, which is too big for a full FDTD simulation, can be treated through a coherent combination of individual grating simulation results. This provides a feasible solution which can be run on a typical PC.

Keywords: BPM, FDTD, multi-physics, LiDAR

1. INTRODUCTION

LiDAR (Light Detection and Ranging) is a critical device for self-driving cars. Currently, the LiDAR systems being tested in cars by various companies are based on discrete components. Aside from the bulky size and moving mechanical parts, the price can be even higher than that of the car itself, making it impossible to commercialize self-driving technology. Therefore, a cheap and reliable LiDAR is the key to making the self-driving car a viable consumer product. LiDAR built on photonic integrated chips could be a potential candidate for achieving this goal, as demonstrated by teams at Ghent University[1] and MIT[2].

Due to the low efficiency of the reported prototypes, the effective detecting range is only a few meters, well below the required 200 meters for practical applications. Therefore, design optimization of the LiDAR on chip is the major task and simulation plays an essential role. However, as reported by Prof. Baets' group and shown in Fig. 1(a), LiDAR on chip is a very big and complex device. There is no single design tool can handle the whole structure. Instead, we decompose it into a few functional blocks, as shown in Fig. 1(b), and each block is simulated by the most suitable tool from the RSoft product suite [3].

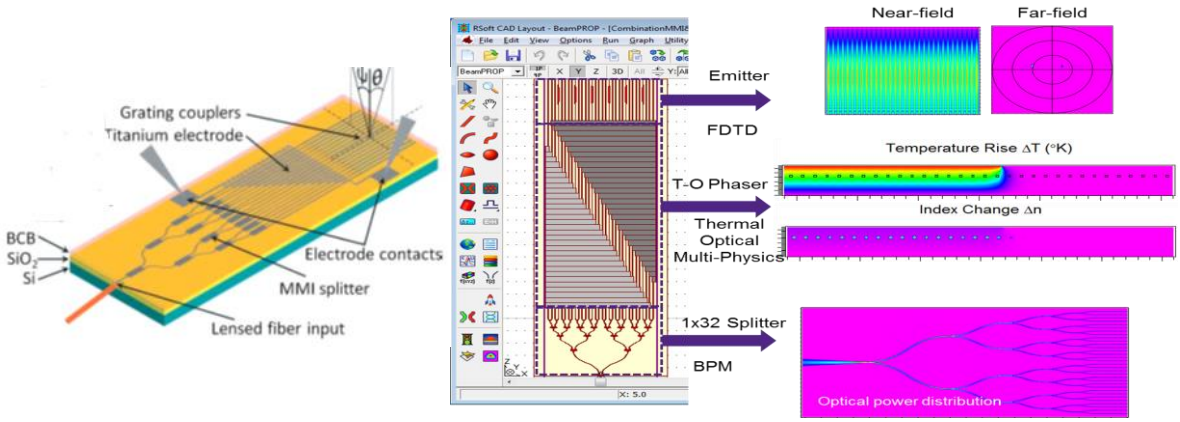


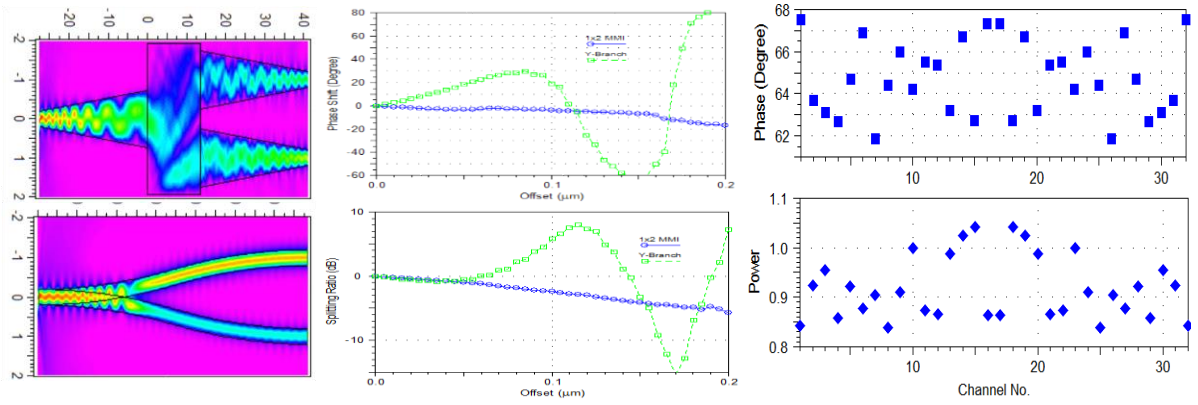
Fig. 1. (a) The example structure reported in literature [1]; (b) Decomposition of the structure and simulation strategy

Since there is little backward reflection in the power splitters, BPM (Beam Propagation Method) is the ideal algorithm for the individual 1x2 splitter and the cascaded 1x32 splitter. The following phase shifter requires a multi-physics solution to handle the combined thermal and optical problems. So, a thermal diffusion solver is used to provide the temperature dependent index perturbation of the structure, and BPM is used once again for the optical propagation. The final step is the emitter, which is typically implemented with a grating coupler. Since this involves omnidirectional light propagation, FDTD must be used. But this algorithm requires a long simulation time and significant computational resources, meaning that the emitter may be too large a problem to handle on a standard PC. To cope with this, we further decompose the problem into multiple inputs and coherently sum the output from each to obtain the final emitter response.

2. Detail Simulation Strategy

2.1 1x32 power splitter

The 1x32 power splitter used by most designers is comprised of 5 cascaded stages of 1x2 splitters. These 1x2 splitters can be either Y-branches or MMI's, each having its own pros and cons. In general, the Y-branch is simple, broadband, and polarization independent, but has a high insertion loss. The MMI is low loss but relatively complex, and is sensitive to both wavelength and polarization. These are all under the assumption of symmetric input. For the cascaded 1x32 splitter, however, the S-bends linking different stages inevitably create asymmetric input to the next stage, as shown in Fig.2(a). BPM simulation shows, in Fig. 2(b), that the MMI is more tolerant to asymmetric input and hence is a better candidate for the 1x2 splitter.



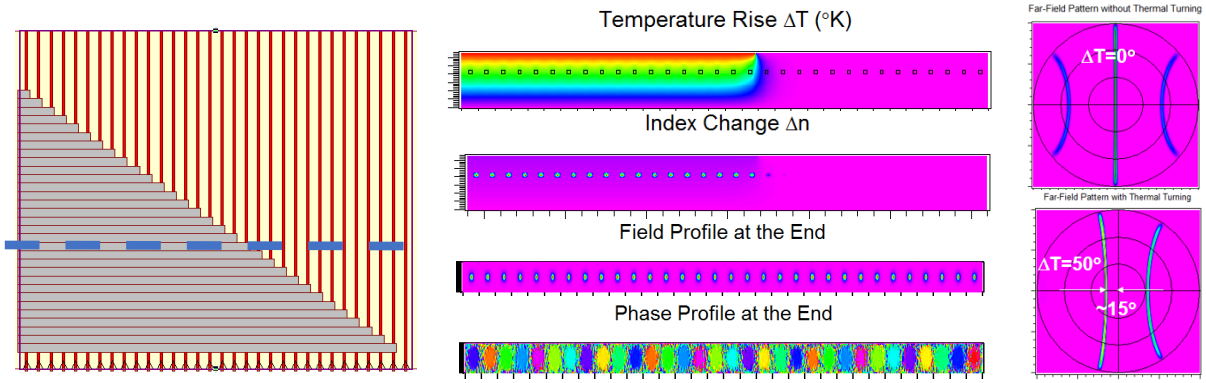
(a) *(b)* *(c)*

Fig. 2. (a) Field patterns of both MMI and Y-branch under asymmetric input; (b) Sensitivity of phase difference and splitting ratio; (c) Non-uniformity of the cascaded 1x32 splitter in both phase and power.

Although the MMI is less sensitive to asymmetric input, the effect still shows up as a non-uniformity in both power and phase of the final output, as shown in Fig. 2(c) for the 1x32 cascaded splitter with a 5° branch angle at the split. Obviously, non-uniformity can be reduced with a smaller angle at the expense of a longer device.

2.2 Thermal-optical phase shifter

Since silicon is not an electro-optic material, a thermally tuned phase shifter is used in the example, as shown in Fig. 3(a). We first solve the thermal diffusion equation to obtain the temperature distribution at each cross-section of the shifter. This profile is then converted into an index change by applying the thermo-optic coefficient. Finally, the propagating optical field is simulated with BPM to produce the complex (amplitude and phase) output field at the end of the device, as shown in Fig. 3(b). The exact phase shift can be examined from the far-field pattern, as shown in Fig. 3(c).



(a) *(b)* *(c)*

Fig. 3. (a)Topview of the thermal phase shifter; (b)calculated temperature distribution, index change, amplitude and phase of the optical field at the end; (c) far-fields from the end without and with thermal tuning.

The phase difference between adjacent waveguides is =120° for a temperature change of ΔT=50°C. The BPM predicts a steering angle of 15°, which agrees exactly with the theoretical result $\psi = sin^{-1}(2\pi\Delta\Phi/\lambda) = 15^o$.

2.3 Beam Emitter

The beam emitter is a phase matched grating coupler which couples the in-plane optical wave from the waveguide nearly vertically into free space. A waveguide width grating[2]. was used in this example, although a waveguide height grating[1] could have been used, as well. To effectively out-couple the light with minimum divergence angle, the grating must be apodized properly, so that the light is out-coupled with a uniform distribution along the grating. After an FDTD optimization, we obtained an optimal tapered width grating function, normalized to grating length. Fig. 4 shown this optimized grating and the simulated field emission.

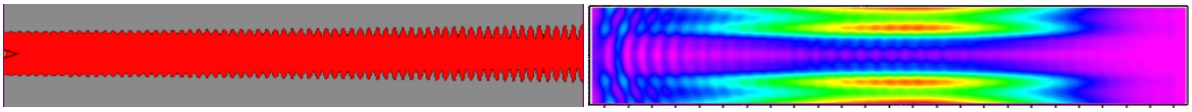


Fig. 4. optimized grating and emitted field.

Direct FDTD simulation of the 32-channel beam emitter requires about 100G RAM and a few days' computation time. So, instead of simulating the whole structure with all 32 inputs, we take an alternative approach. The input from each waveguide was simulated independently on a sufficiently large computational domain, which was determined to be about 5-waveguide widths. Each near-field above the grating, as shown in Fig. 5(a), was recorded. The total near-field, shown in Fig. 5(b), was obtained from the coherent sum of all the saved near-fields. Finally, we obtained the far-field, shown in Fig. 5(c), of the full emitter from the transform of the total near-field.

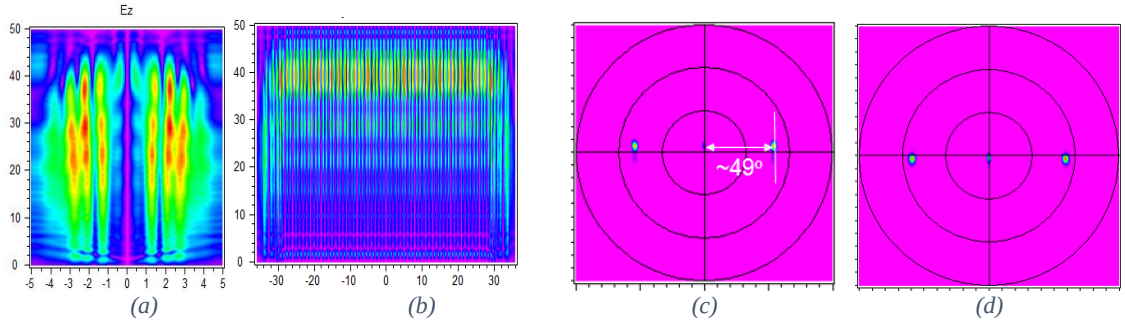


Fig. 5. (a)Emitted near-field with input from a single waveguide; (b)Coherently combined near-field with inputs from every waveguide; (c)Emitted far-field; (d)Emitted far-field at a different wavelength.

As shown in Fig. 5(c), the 1st order diffraction angle is ~49°, which is very close to the theoretical result $sin^{-1}(\lambda_0/D) = 50.8^o$. This result is obtained at ΔΦ=0° and λ=1.55μm. As we increase the phase difference ΔΦ between adjacent waveguides, the far-field pattern moves horizontally to the right. If we change the operating wavelength, the far-field pattern moves vertically as shown in Fig. 6(d). The calculated vertical angular variation is $\Delta\delta \sim 18^o$ with the tuning range λ=1.5~1.6μm, and this agrees well with the theoretical result given by $\Delta\delta = \Delta n_{eff} - \Delta\lambda/\Lambda$, where Δ is the effective index variation and Λ is the grating period.

3. CONCLUSIONS

In summary, we have demonstrated a simulation methodology for LiDAR design by decomposing the full problem into several simple blocks, each simulated with a suitable algorithm. With the proposed strategy, where each part is optimized individually, LIDAR simulation becomes tractable on a standard PC.

REFERENCES

[1] Van Acoleyen, Karel, Wim Bogaerts, Jana Jágerská, Nicolas Le Thomas, Romuald Houdré, and Roel Baets. "Off-chip beam steering with a one-dimensional optical phased array on silicon-on-insulator." *Optics letters* 34, no. 9 (2009): 1477-1479.

[2] Poulton, Christopher V., Ami Yaacobi, Zhan Su, Matthew J. Byrd, and Michael R. Watts. "Optical phased array with small spot size, high steering range and grouped cascaded phase shifters." In *Integrated Photonics Research, Silicon and Nanophotonics*, pp. IW1B-2. Optical Society of America, 2016.

[3] Synopsys RSoft products: *https://www.synopsys.com/optical-solutions/rsoft.html*

L-shaped grating couplers engineered with subwavelength metamaterial for sub-decibel coupling loss

D. Benedikovic[1], C. Alonso-Ramos[1], S. Guerber[1,2], V. Vakarin[1], G. Marcaud[1], X. Le Roux[1], P. Cheben[3], É. Cassan[1], D. Marris-Morini[1], F. Boeuf[2], C. Baudot[2], and L. Vivien[1]

[1]Centre de Nanosciences et de Nanotechnologies, CNRS, Univ. Paris-Sud, Université Paris-Saclay, C2N – Palaiseau, 91120 Palaiseau, France

[2]Technology R&D, STMicroelectronics, SAS, 850 rue Jean Monnet – 38920 Crolles, France

[3]National Research Council Canada, 1200 Montreal Road, Ottawa, Ontario, K1A0R6, Canada

e-mail: daniel.benedikovic@c2n.upsaclay.fr

ABSTRACT

Practically attractive nanophotonic technologies, mostly realized on mature silicon-on-insulator (SOI) substrates, call upon availability of efficient input/output grating-coupled optical interfaces. In this work, we demonstrate, both theoretically and experimentally, ultra-directional *L*-shaped grating couplers for low-loss light coupling between standard optical fibres and SOI chips. Experimentally, we show grating couplers without and with subwavelength (SWG) transition, seamlessly fabricated with a 193-nm deep-ultraviolet lithography. Coupling loss of -2.7 dB is measured with a low return loss as low as -20 dB. In addition, we propose an apodized *L*-shaped grating coupler layouts with coupling loss below 1 dB. Apodized fiber-chip grating couplers are designed with a sub-decibel coupling performance, together with substantially relaxed requirements in terms of minimum feature dimensions.

Keywords: fibre-chip grating couplers, deep-ultraviolet technology, subwavelength gratings, metamaterials, silicon-on-insulator platform, silicon photonics

1. INTRODUCTION

The use of surface grating couplers instead of edge couplers to couple the light between integrated circuits and optical fibres is of particular practical interest. Indeed, grating couplers enable flexible placement on the chip, wafer-scale device testing, and relaxed tolerances in fibre attachments [1,2]. More recently, several outstanding implementations of surface grating couplers were reported [3-14]. Several decisive aspects contribute to the overall coupling performance [2], however, the grating directionality is recognized as a key enabler towards development of high-efficiency surface grating couplers. More specifically, improved diffraction performance in grating couplers with additional overlayers [4], metal mirrors [5] or Bragg reflectors [6] underneath, and multi-layer [7] or multi-level device arrangements [8] have been proposed and demonstrated over years. However, such design strategies call upon additional technological steps with added fabrication complexity, which in turn, increases the overall cost. On one side, this includes precise top layer depositions or backside wafer processings. Other approaches are typically founded by custom-designed guiding layers, etching depths, and fabrications that differ considerably from those used in established photonic foundries or even mandate subsidiary frontend / backend silicon nitride layers. Alternatively, efficient surface grating couplers that advantageously exploit the unique blazing effect using only a two set of etching depths were demonstrated [9-14]. Fibre-chip grating couplers with interleaved [9-11] or *L*-shaped waveguide arrangements [12-14] were reported to demonstrate the imminent promise of such solution. Conceptual design simplicity [9,12], versatility [10,11], as well as waveguide platform portability [14] are essential ingredients for straightforward fabrication and advanced integration.

2. *L*-SHAPED GRATING COUPLERS: DESIGN, FABRICATION, AND OPTICAL TESTING

In this work, surface grating couplers were designed for a silicon-on-insulator (SOI) platform with 300-nm-thick Si waveguide and 720-nm-thick BOX, covered by silicon dioxide (SiO_2). Grating couplers were optimized for transverse electrical (TE) light injection and operation at a wavelength of 1.55 μm. As shown in the inset of Fig. 1(a), diffraction grating is formed by two-etching (full and partial) depths, with levels of 300 nm and 150 nm, respectively. The judiciously designed grating period consists of deep- and shallow-etched trenches and unetched Si slab. This geometry forms an *L*-shaped waveguide with an asymmetric radiation profile that maximizes the light diffraction towards a specific direction (here, towards an optical fibre situated above the chip). As a result, near-unity diffraction efficiency, as shown in Fig. 1(a), can be readily achieved for a wide range of geometries and wavelength span wider than 100 nm [12]. Albeit superior directionality is afforded by the *L*-shaped grating couplers, the overall performance is far beyond the desired sub-decibel coupling levels. The

performance is strongly limited by the excessively large return loss (back-reflections of 20%) and grating-fibre field profile mismatch up to 80%.

In this work, surface grating couplers were fabricated using foundry-enabled production flow in STMicroelectronics cleanroom facilities using 300 mm SOI photonic platform with 193-nm deep-ultraviolet lithography, followed by dual-level dry etching and plasma enhanced chemical vapour deposition to form a SiO_2 cladding. Devices were characterized using back-to-back measurements with cleaved standard single-mode optical fibres (SMF-28). Detailed information about grating coupler dimensions can be found in Ref. [12].

Coupling performance of two types of *L*-shaped grating couplers is shown in Figs. 1(b) and (c). In particular, a peak coupling loss of -3.4 dB at 1.56 µm was measured for a coupler without the subwavelength grating (SWG) metamaterial transition (inset of Fig. 1(b)). As compared to the nominal design, with a coupling loss of -2.2 dB, the measured device yielded a 1.2 dB loss penalty, most likely attributed to the presence of fabrication imperfections such as variations in the partial etching depth and changes in the lengths of grating trenches and tooth. The 3-dB coupling bandwidth is 46 nm. The spectral response exhibits noticeable Fabry-Perot fringes, with a magnitude up 0.85 dB, resulting in a return loss of 8%. The grating coupler with an SWG transition (inset of Fig. 1(b)) yielded a coupling loss of only -2.7 dB at 1.565 µm with a 3-dB coupling bandwidth of 62 nm and a substantially reduced magnitude of Fabry-Perot ripples down to 0.1 dB. This results in a reflectivity of around 1%. This corresponds to an eight-fold return loss reduction as compared to a grating coupler design without the use of SWG metamaterial transition.

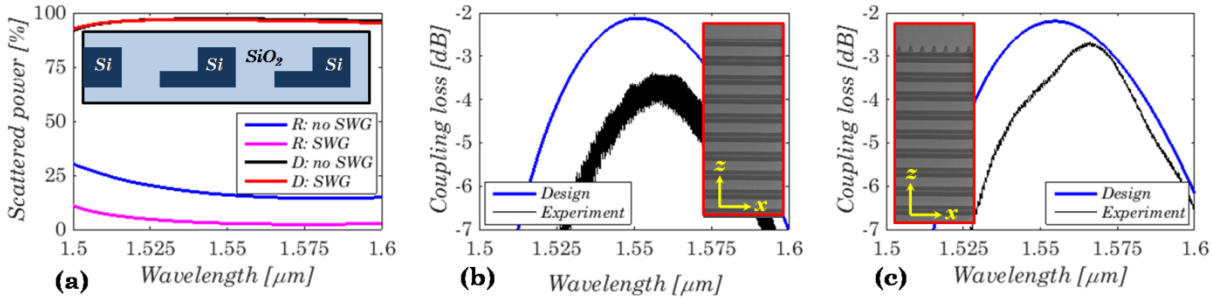


Figure 1. (a) Diffracted power from an L-shaped grating coupler as a function of wavelength. Inset: Vertical schematic of the L-shaped grating coupler. Calculated and measured coupling loss as a function of wavelength of the L-shaped grating couplers (b) without and (c) with sub-wavelength-engineered metamaterial transition. Insets of (b) and (c): Scanning electron microscopy images.

3. APODIZED *L*-SHAPED GRATING COUPLERS: TOWARDS SUB-DECIBEL COUPLING LOSS

Figure 2(a) shows a side view schematics of the proposed apodized *L*-shaped surface grating coupler. The grating coupler comprises apodized and uniform grating sections. The apodization of an *L*-shaped grating coupler was carried out by varying the effective refractive index of the SWG metamaterial in the etched grating trenches, both deep- and shallow-etch trenches, along the propagation direction to match the near-field profile of the radiated grating beam to the mode of SMF-28 optical fibre, i.e. to a Gaussian-like fibre mode profile of a 10.4 µm mode field diameter (MFD) at a wavelength of 1.55 µm. By implementing the SWG metamaterial within the etched grating trenches, the coupling strength of the grating can be properly controlled, yet without sacrificing the outstanding near-unity directionality of *L*-shaped grating couplers. This brings an additional degree of freedom to tailor the coupler performance.

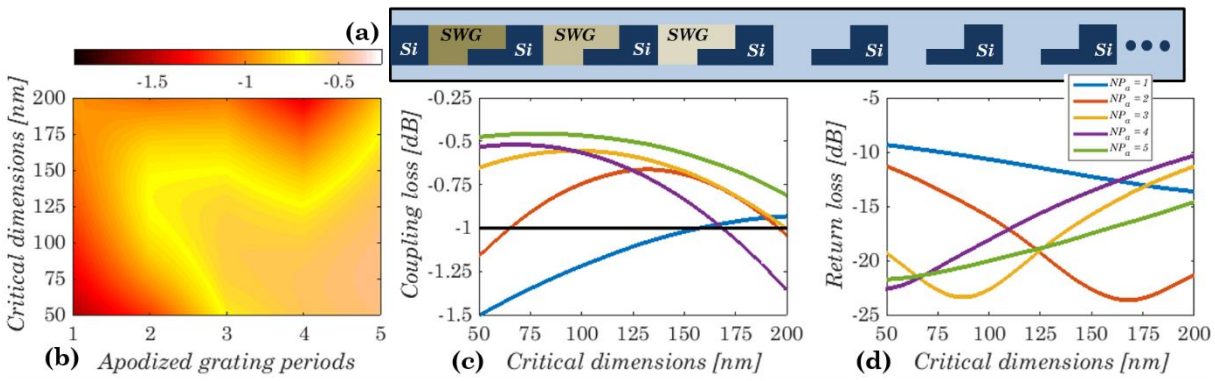


Figure 2. (a) Vertical schematics of an apodized L-shaped grating coupler with sub-wavelength-engineered trenches. (b) Colour map showing coupling loss of the L-shaped grating coupler as a function of the number of apodized periods and critical dimensions. (c) Coupling loss and (d) reflectivity of the L-shaped grating coupler as a function of critical dimensions for different numbers of apodized periods.

Figure 2(b) shows a colour map of the fiber-chip coupling losses of an apodized *L*-shaped grating coupler with an SWG metamaterial trenches as a function of the number of apodized grating periods and SWG critical dimensions. It can be observed that a wide range of device designs is suitable to provide a sub-decibel coupling losses. In particular, as shown in more detail in Fig. 2(c), grating coupler design with only 1 period engineered with SWG metamaterial yields a coupling loss of -0.95 dB for a SWG minimum feature size of 195 nm, while for 2 apodized periods of the *L*-shaped grating coupler, the coupling of -0.65 dB is predicted for a minimum dimensions of 140 nm. Furthermore, for a 5 apodized periods, the sub-decibel fiber-chip coupling performance is readily achieved for all minimum feature size criteria, with a coupling loss as small as -0.46 dB for a 100 nm feature size restrictions. The corresponding evolution of the grating coupler reflectivity as a function of the SWG critical dimensions is shown in Fig. 2(d). The reflectivity down to -23 dB is suggested by numerical simulations.

4. CONCLUSIONS

We demonstrated, both theoretically and experimentally, a set of *L*-shaped surface grating couplers engineered with sub-wavelength grating metamaterial to afford a low-loss coupling between SOI waveguides and standard single-mode fibres. Our couplers yield directionality close to the theoretical limit of 100% with a comparatively easy to fabricate geometry. Devices were fabricated with a 193-nm deep-ultraviolet lithography at STMicroelectronics. Fiber-chip coupling loss of -2.7 dB was experimentally measured with a low return loss down to -20 dB. In addition, we designed an advanced apodized low-period-count *L*-shaped grating couplers with a sub-decibel coupling performance, providing substantially relaxed requirements for minimum feature sizes up to 200 nm. These results open up a way towards deployment of low-cost and high-performance fiber-chip optical interfaces in large-volume nanophotonic applications.

ACKNOWLEDGEMENTS

This work has received the funding from the European Research Council (ERC) under the European Union's Horizon 2020 Research and Innovation Program (ERC POPSTAR – grant agreement No 647342).

REFERENCES

[1] P. Cheben, *et al.*: Subwavelength integrated photonics, *Nature*, vol.560, pp. 565 – 572 (2018).
[2] R. Halir, *et al.*: Subwavelength-Grating Metamaterial Structures for Silicon Photonic Devices, *P IEEE*, vol.106, pp. 2144 – 2157 (2018).
[3] D. Taillaert, *et al.*: Compact efficient broadband grating coupler for silicon-on-insulator waveguides, *Opt. Letters*, vol. 29, pp. 2749 – 2751 (2004).
[4] G. Roelkens, *et al.*: High efficiency silicon-on-insulator grating coupler based on a poly-silicon overlay, *Opt. Express*, vol. 14, pp. 11622–11630 (2006).
[5] D. Benedikovic, *et al.*: Subwavelength index engineered surface grating coupler with sub-decibel efficiency for 220-nm silicon-on-insulator waveguides," *Opt. Express*, vol. 23, pp. 22628–22635 (2015).
[6] C. Baudot, *et al.*: Low Cost 300 mm double-SOI substrate for low insertion loss 1D & 2D grating couplers, in IEEE Group IV Photonics, pp. 137–138 (2014).
[7] W. S. Sacher, *et al.*: Monolithically Integrated Multilayer Silicon Nitride-on-Silicon Waveguide Platforms for 3-D Photonic Circuits and Devices," *P IEEE*, vol. 106, pp. 2232 – 2245 (2018).
[8] J. Notaros, *et al.*: Ultra-Efficient CMOS Fiber-to-Chip Grating Couplers, in Optical Fiber Communication Conference, paper M2I.5 (2016).
[9] C. Alonso-Ramos, *et al.*: Fiber-chip grating coupler based on interleaved trenches with directionality exceeding 95%, *Opt. Letters*, vol. 39, pp. 5351-5354 (2014).
[10] D. Benedikovic, *et al.*: High-directionality fiber-chip grating coupler with interleaved trenches and subwavelength index-matching structure, *Opt. Letters*, vol. 40, pp. 4190-4193 (2015).
[11] Xia Chen, *et al.*: Dual-etch apodised grating couplers for efficient fibre-chip coupling near 1310 nm wavelength,*Opt. Express*,vol. 25, pp. 17864-17871 (2017).
[12] D. Benedikovic, *et al.*: L-shaped fiber-chip grating couplers with high directionality and low reflectivity fabricated with deep-UV lithography, *Opt. Letters*, vol. 42, pp. 3439-3442 (2017).
[13] T. Watanabe, *et al.*: Perpendicular Grating Coupler Based on a Blazed Antiback-Reflection Structure, *J. Lightw. Technol.*, vol. 35, pp. 4663-4669 (2017).
[14] Y. Chen, *et al.*: Experimental demonstration of an apodized-imaging chip-fiber grating coupler for Si_3N_4 waveguides," *Opt. Letters*, vol. 42, pp. 3566-3569 (2017).

Low Loss Devices fabricated on the Open Access 3 µm SOI Waveguide Platform at VTT

Srivathsa Bhat, Mikko Harjanne, Fei Sun, Matteo Cherchi, Markku Kapulainen, Ari Hokkanen, Giovanni Delrosso, Timo Aalto
VTT Technical Research Centre of Finland, 02044 Espoo - Finland
e-mail: srivathsa.bhat@vtt.fi

ABSTRACT

In this paper, the latest results on some of the building block devices and components fabricated on VTT's PIC platform, that is based on 3 µm thick Silicon-On-Insulator (SOI) waveguides [1], is presented. As part of the plans in developing the platform further, AWG and Echelle grating (EG) designs, with insertion loss in the range of 1-3 dB, and an extinction ratio reaching up to 35 dB have been designed and fabricated as part of the recent MPW run, and the measurement results are presented. Novel 45º vertical coupling TIR mirrors have also been realized (with AR coating) as a new building block on this platform, and have been integrated with the waveguides. The measured coupling losses to/from lensed fibers are below 0.5 dB, which are better in comparison to the coupling loss from the etched facets at the edges of the chip (~ 1 dB). The main advantages of this thick SOI platform are low loss, dense integration, polarization independent and broadband operation, high optical power throughput, and smooth transition from prototyping to volume production. Open access via multi-project wafer (MPW) runs, dedicated process runs, prototyping and small-to-medium volume production services are provided.

Keywords: Thick SOI Platform, AWG, Echelle Grating, Fiber-Coupling Mirrors, Low-Loss, Polarization Independent.

1. INTRODUCTION

While the VTT 3 um platform sounds ‘thick’ for any single-mode (SM) operation or for any dense integration, this is very well realized from a combination of rib-waveguide (SM operation) and strip waveguide (dense integration) geometries [2], and the ability to couple adiabatically between the two. In addition, small footprints are achieved using Euler bends [3], and the platform is low loss (0.1 dB/cm) for broadband operation from 1.2 to 4 um. In addition, the platform also supports hybrid integration of active devices, heterogenous germanium photodetectors, thermo-optic heaters, and has a better mode-matching for coupling to tapered fiber, or for coupling to fiber via interposer. Some of the building blocks that are recently developed and optimized will be discussed in the following sections.

2. BUILDING BLOCKS DEVICES AND COMPONENTS

VTT 3 µm SOI platform has its unique advantages, and various building block are being developed, and the design optimized, to support this platform. As part of a recent MPW process run, several multiplexer designs such as AWG, EG, and MZI, for varied design parameters such as channel spacing and channel count, have been included and successfully fabricated. Among these, and to demonstrate the low loss and high extinction characteristics, a 400 GHz channel spaced 1 x 11 channel AWG design, and two EG designs, with channel spacing of 800 GHz and 100 GHz, and channel count of 1 x 5 and 1 x 8 respectively have been presented. Other than that, novel vertical coupling mirrors have been successfully fabricated, measured, and the analysed results are presented below.

2.1 Multiplexing elements – AWG & EG

Multiplexers are crucial for dense integration of channel wavelengths on a chip, and for larger channel counts, the usual way to do this is with AWG and EG. While AWG has the advantage in terms of easy scaling up of the channel count for low channel spacing values, EG is more compact and better suited for larger channel spacing with a comparatively lower channel count. Both AWG and EG designs are fabricated as part of the VTT MPW process run, and the measured characteristics are presented below.

Schematic of the 1 x 11 channel AWG design for TE polarization with 400 GHz channel spacing centred at ITU 38 (1546.92) in the DWDM grid, and the measured transmission characteristic are shown in Fig.1. The insertion loss of the channels for TE is in the 1.2-2.0 dB range, and the extinction ratio is over 35 dB. Although, the bend waveguides within the AWG are not designed for TM, the insertion loss is in the 1.9-2.4 dB range, and with an extinction of about ~ 25 dB respectively.

Similarly, the microscope images of two of the EG designs, centered around 1550 nm, are shown in Fig.2. The specifications of the design are shared there-in, and the transmission plots, presented in Fig.3. Both designs have

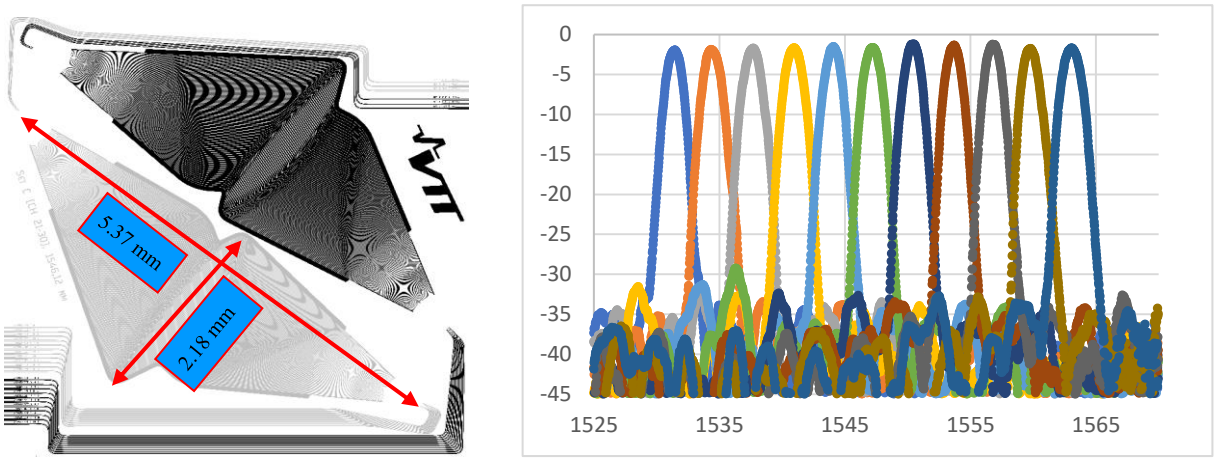


Figure 1. Schematic of an S-type 11-channel AWG design with a channel spacing of 400 GHz (left) and the measured transmission characteristics (right) showing low insertion loss and high extinction ratio for TE polarization

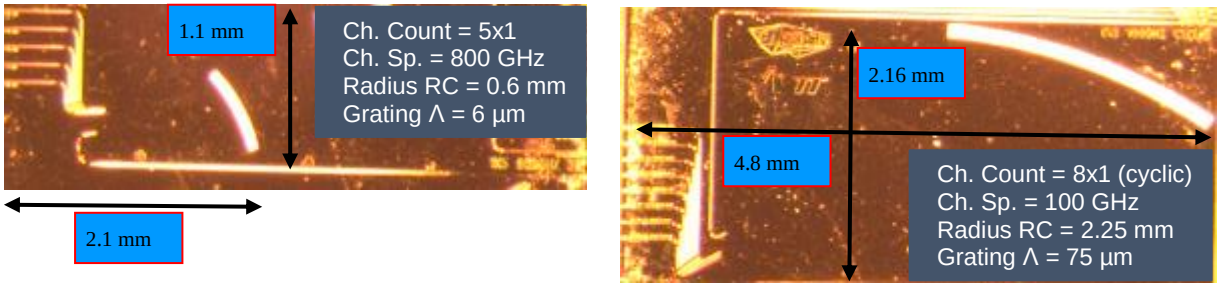


Figure 2. Microscope image of the fabricated 5x1 (800 GHz) and 8x1 (100 GHz) VTT EG design

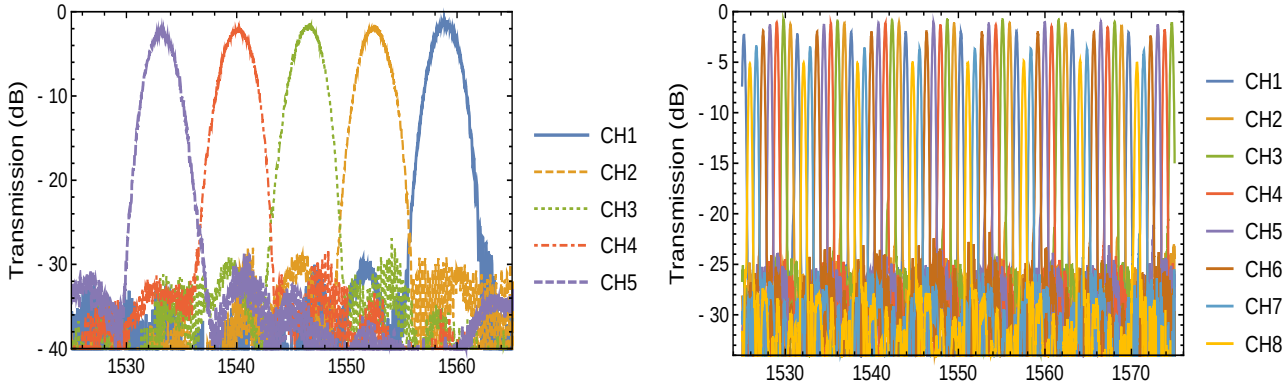


Figure 3. Measured transmission characteristic of the fabricated 5x1 (800 GHz) (left) and 8x1 (100 GHz) VTT EG designs for TE polarization

an extinction of over 25 dB. The 800 GHz channel spaced design has an insertion loss in the 1.3-2.5 dB range (TE) and 0.9-1.8 dB (TM) range, while for the 100 GHz channel spaced cyclic design, this is in the 0.9-3.5 dB (TE) and 1.0-3.8 dB (TM) respectively. Channel 8 for the latter design has a higher loss (~ 5 dB) due to a design error in positioning the output waveguide, and this can be easily corrected for in the subsequent designs.

2.2 Vertical coupling mirrors for wafer-level testing (WLT) and vertical I/O coupling

A total internal reflection (TIR) based mirror provides the highest possible reflection co-efficient at any wavelength, independent of fabrication tolerances, and will have a broadband functionality. While the standard Si etch plane produces a 54.7° tilted surface that doesn't allow for this, under special etch conditions, 45° vertical coupling TIR mirrors have been realized on the VTT 3 µm SOI platform, and the FIB cross-section image is shown in Fig (left). Further, they have been integrated with waveguides, and the coupling loss to/from lensed fibers, with the experimental setup shown in Fig (right), have been estimated over the 1520-1580 nm range. As shown in Fig. below, the total coupling loss for the reference waveguides (facet input and facet output) is in the range of 2.0-2.8 dB (so 1.0-1.4 dB per facet), while for the mirror integrated waveguides (facet input and mirror output) these are in the 1.1-1.5 dB range, for both polarizations (excluding a few outliers which could be due to damaged

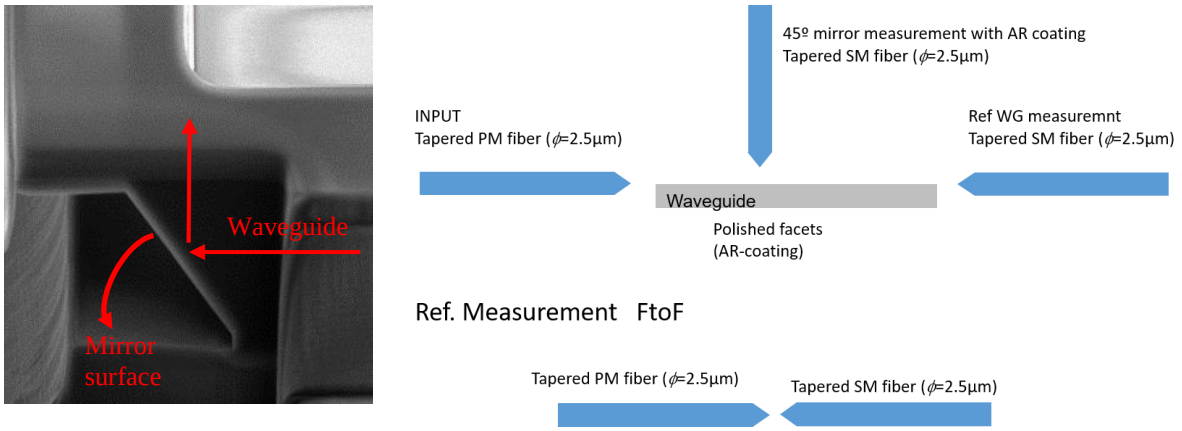


Figure 4. FIB cross-section of a 45º TIR vertical coupling mirror (left), and the characterization setup for measuring the coupling loss

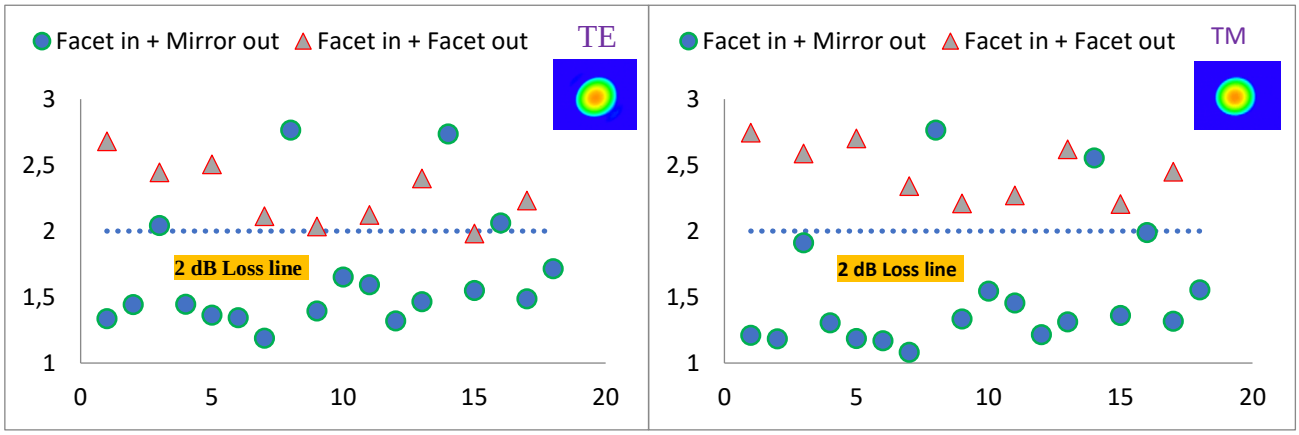


Figure 5 Plots for coupling loss analysis of the up-reflecting mirrors

waveguides). This clearly indicates that the mirror to fiber coupling loss must be below 0.5 dB over the entire C-band, and for both polarizations. Furthermore, this is ideal for vertical integration of sources and detectors on the chip, and also for accessing device performance with a wafer-level testing (WLT) setup.

3. CONCLUSIONS

As part of development and optimization of the building blocks on the VTT 3 µm PIC platform, several multiplexer designs with AWG and EG geometry have been designed and fabricated. To demonstrate the low loss, high extinction characteristics, one AWG design and two EG designs are reported. Novel 45o vertical coupling TIR mirrors with coupling loss lower than 0.5 dB have been measured. They can serve as a major break-through in terms of wafer level access to devices during and after the process run, and for hybrid integration of sources and detectors on the Si PIC chip.

ACKNOWLEDGEMENTS

This work has been partially supported by the EU PASSION Project (GA 780326).

REFERENCES

[1] T Aalto, M Cherchi, M Harjanne, F Sun, and M Kapulainen : 3-micron Silicon Photonics, *Optical Fiber Communication Conference (OFC)*, Mar. 2018.

[2] R. A. Soref, J. Schmidtchen, and K. Petermann : Large single-mode rib waveguides in GeSi-Si and Si-on-SiO2, IEEE J. Quantum Electron., vol. 27, no. 8, pp. 1971–1974, 1991

[3] M. Cherchi, S. Ylinen, M. Harjanne, M. Kapulainen, and T. Aalto : Dramatic size reduction of waveguide bends on a micron-scale silicon photonic platform, Opt. Express, vol. 21, no. 15, pp. 17814–17823, Jul. 2013.

Application of Optical Proximity Correction for 193 nm Deep UV enabled InP Photonic Integrated Circuits

(Student Paper)

Jeroen Bolk[1], Huub Ambrosius[1], Sylwester Latkowski[1], Nezih Unal[2], Daniel Ritter[2], Kevin Williams[1],
[1] Eindhoven University of Technology, Eindhoven, The Netherlands
[2] GenISys GMBH, Munich, Germany
e-mail: j.bolk@tue.nl

ABSTRACT

We present the first-time application of rule-based optical proximity correction for InP based photonic integrated circuits fabricated with 193 nm deep UV lithography. Simulations of the lithography process were used to systematically predict and preserve pattern fidelity of sidewall gratings to find optimal correction parameters. Optical proximity corrected designs were exposed in ArF resist, demonstrating high correlation with lithography simulation results and exhibiting up to 70% improved pattern fidelity.

Keywords: Optical Proximity Correction, Pattern Fidelity, Sidewall Grating, Deep UV, InP, Photonic Integrated Circuits

1. INTRODUCTION

Photonic integrated circuits (PICs) are increasing in complexity which drives a need for improved reproducibility and scalability of the manufacturing process [1], [2]. This is causing tighter tolerances on the fabrication process of such devices, and subsequently has led to the application of more advanced generations of lithography equipment for PIC fabrication [3], [4].

High resolution lithography using 193 nm light sources has been applied for years in traditional electronics semiconductor manufacturing. For InP photonics however, the application of such manufacturing capability has only recently been demonstrated for foundry scale processing [5]. The combination of non-contact lithography, reduced mask overlay errors and improved critical dimension control offer considerable advantages for reproducibility and manufacturing tolerance. The NanoLab@TU/e cleanroom in Eindhoven offers access to a lithography process that can image structures with a minimum feature sizes down to 90 nm. The need for minimum feature sizes enabled by this fabrication technology is not immediately evident from the dimensions of basic components such as a photonic waveguide. However, the absolute dimensions, roughness and overlay of these structures, have a large impact on the performance of these PICs, requiring more advanced patterning than equally dimensioned structures in traditional electronics.

In contrast to electronics where most chips have a Manhattan (orthogonal structures) type layout, PICs have less conventional shapes like curves, tapers and sub-wavelength shape modulations in various orientations as shown in Fig. 1. With some of these features reaching very small dimensions, it becomes necessary to apply Optical Proximity Correction (OPC) to realize optimal pattern fidelity in the image transfer process. Existing OPC methods have been specifically adapted for photonics to deal with the deviating shapes and orientations [6], [7]. For photonics it is not enough to look at quantifiers like width and length. It is required to look in multiple directions and quantify pattern fidelity as a figure of merit for the matching quality with the design intent.

This paper presents the simulations of the DUV projection lithography process using the GenISys LAB software, and the first-time application of rule-based OPC to optimize pattern fidelity for an InP sidewall grating demonstrator device. The simulation output was used to create an OPC enabled reticle and patterning experiments were conducted to verify the simulation outcome.

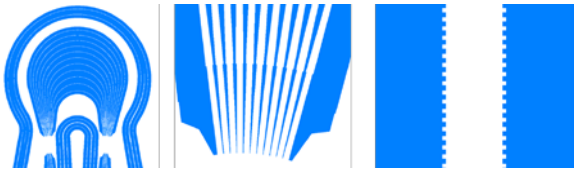


Figure 1: Examples of geometries in PICs: Bends (Left), Tapers (Middle), Subwavelength modulation features (Right).

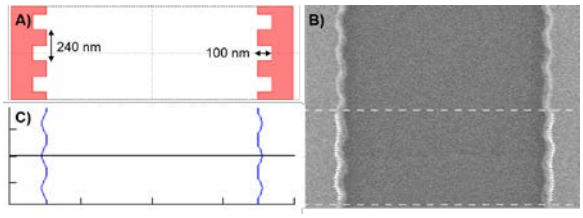


Figure 2: 1.5 µm waveguide design with sidewall grating at 240 nm pitch and width modulation of 100 nm per side (A), SEM image of fabricated resist pattern (B) and simulated resist pattern (C).

This work was performed in the NWO Applied and Engineering Sciences project: 15367.

2. OPTICAL PROXIMITY CORRECTION

An InP deep ridge waveguide with a nominal width of 1.5 µm and a sidewall grating with a period of 240 nm and width modulation of 100 nm per side was used as a demonstrator design and is illustrated in Fig. 2A. When this structure is imaged using the NanoLab@TU/e lithography process [8], the intended shape of the design is severely degraded due to diffraction and a combination of the resist and developer properties as shown in the SEM image in Fig. 2B. This can be accurately predicted using a calibrated resist and developer model and the exact illumination conditions of the exposure tool in the simulation software, as presented in Fig. 2C

The purpose of performing OPC, is to improve the resist pattern to have better match with the design-intent by pre-correcting for systematic fabrication limitations and artefacts. This is realized by introducing small dimensional changes or sub-resolution features which individually are too small to be resolved but will impact the diffraction pattern of total the exposure. When the exposed pattern is accurately predicted it becomes possible to run an entire design of experiments (DOE) of OPC variations minimizing a quantifier that describes the pattern mismatch. Fig. 3 illustrates how the pattern mismatch is quantified by performing a logical exclusive-or (XOR) operation on the intended design and simulated resist pattern from Fig. 2A and 2C respectively. The surface area of the resulting polygon can easily be extracted as a function of the applied OPC design parameters [7].

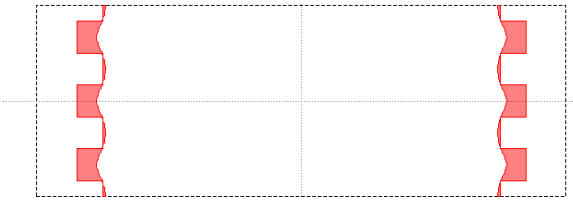


Figure 3: Resulting mismatch pattern by performing XOR logical operation on Design and Simulated resist pattern.

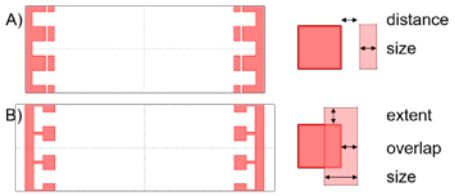


Figure 4: Scatter bar (A) and Hammerhead (B) OPC rule types applied to demonstrator design.

3. PARAMETER OPTIMIZATION

In this work we have applied two types of OPC rules. Fig. 4A shows the application of a scatter bar to the sidewall grating design which is parametrized by a size and distance. Fig. 4B shows the application of a hammerhead to the same design which is parametrized by a size, extent and overlap. Both rules were combined and applied to the initial sidewall grating design and all OPC parameters were varied at 3 levels using a 3^5 full factorial design of experiments. The resulting corrected designs were individually run through a lithography simulation followed by the resist and developer simulation. For these simulations, a calibrated ArF coating layer stack was used on top of a silicon nitride hard mask and an InP substrate. For illumination conditions annular illumination was used with a numerical aperture of 0.75 and inner and outer sigma settings at 0.55 and 0.85 respectively. Focus offset and dose were chosen based on optimal focus energy matrix settings with the standard design prior to applying OPC rules.

The resulting resist profiles were collected for each variation and the XOR surface area was derived comparing the result to the intended sidewall grating design. A model was constructed parametrizing the XOR surface area as a function of the 5 parameters and their interactions. Fig. 5 shows the predictions of the constructed XOR surface area model as a function of the simulated area for each parameter variation. This figure also shows the XOR surface area of the reference design without OPC applied, signified by the red dashed line at 0.64 µm^2. The advantage of applying OPC to the design is clearly shown in this figure. Most OPC variations are resulting in smaller XOR surface area corresponding to a better pattern fidelity. In optimal combinations, up to 70% improvement in fidelity is possible resulting in only 0.19 µm^2 XOR surface area.

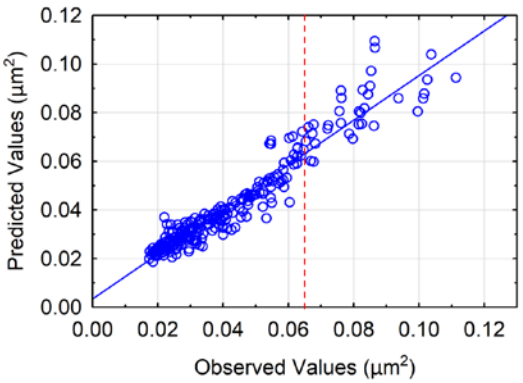


Figure 5: Model predicted surface area as a function of observed surface area of OPC parameter simulations in blue, with linear fit and reference level without OPC as red dashed line.

Feature	Scatter bar (nm)		Hammerhead (nm)		
	size	distance	size	extent	overlap
OPC-1	40	20	75	50	75
OPC-2	50	20	75	50	75
OPC-3	40	10	90	40	75
OPC-4	40	20	60	60	60
OPC-5	40	10	75	50	60
OPC-6	50	30	60	60	60

Table 1: Best simulated OPC parameter combinations of Scatter Bar and Hammerhead.

4. RETICLE AND IMAGING RESULTS

A total of six optimal OPC parameter combinations were extracted from the entire dataset and listed in Table 1. A reticle was fabricated with test structures having these different OPC rule combinations applied. The devices were exposed on an InP substrate with a silicon nitride hard mask in a focus-energy matrix. Best exposure results for each of the OPC rule combinations were collected using a Hitachi S9200 Scanning Electron Microscope (SEM). The SEM images of the resist patterns of the three best OPC enabled sidewall gratings are shown in Fig. 6, in decreasing order of simulated pattern fidelity, at optimum dose and focus. In each corner of these images, the corresponding OPC enabled design is shown as well as the simulated resist profile in the center.

These resist profiles should be compared to the exposure result of such device without OPC as was shown in Fig. 2B. All OPC designs show a significantly improved pattern fidelity. The simulated results show excellent correlation with the fabricated resist patterns. This supports our claim that the effect of OPC corrections can be simulated, making the application and optimization of OPC parameters at the software level an ideal method for generating InP structures with optimal pattern fidelity on a high-throughput exposure tool.

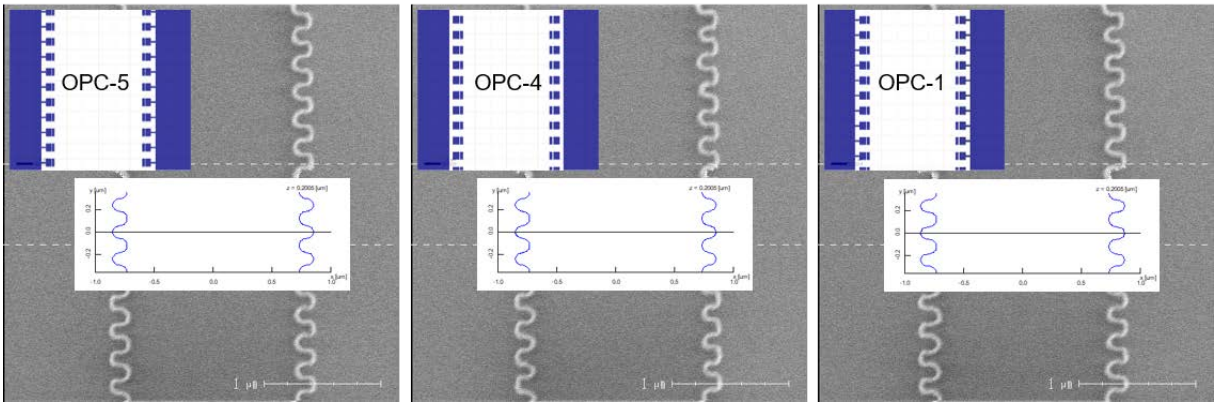


Figure 6: SEM images of sidewall gratings with best OPC rule designs in the top left corners and simulated resist pattern in the center.

5. CONCLUSIONS

Rule-based OPC was demonstrated for InP PICs using a sidewall grating device as a demonstrator. Pattern fidelity was optimized by performing an XOR operation on simulated resist profiles and the intended design and minimizing the surface area. Best OPC enabled structures show 70% improved pattern fidelity compared to a reference design without OPC applied. Well-defined OPC rules derived from simulations are the way forward to match fabricated device geometries with the design intentions.

ACKNOWLEDGEMENTS

The authors would like to thank NanoLab@TU/e for enabling the DUV experimental work as well as GenISys GMBH for providing support for and access to the simulation and OPC software.

REFERENCES

[1] JePPIX, “JePPIX Roadmap 2018,” http://www.jeppix.eu/vision/.
[2] AIM Photonics, MIT Microphotonics Center, and iNEMI, “IPSR Roadmap 2018,” https://aimphotonics.academy/roadmap/ipsr-roadmap.
[3] S. K. Selvaraja *et al.*, “193nm immersion lithography for high-performance silicon photonic circuits,” in *Proc. SPIE*, 2014, vol. 9052, p. 90520F.
[4] N. B. Feilchenfeld *et al.*, “Silicon photonics and challenges for fabrication,” in *Advanced Etch Technology for Nanopatterning VI*, 2017, vol. 10149, p. 101490D.
[5] L. M. Augustin *et al.*, “InP-Based Generic Foundry Platform for Photonic Integrated Circuits,” *IEEE Journal of Selected Topics in Quantum Electronics*, vol. 24, no. 1, pp. 1–10, Jan. 2018.
[6] C. Meagher *et al.*, “Patterning challenges for monolithic silicon photonics: AP/DFM: Advanced patterning / design for manufacturability,” in *2018 29th Annual SEMI Advanced Semiconductor Manufacturing Conference (ASMC)*, 2018, pp. 155–158.
[7] N. Zeggaoui *et al.*, “Si-photonics waveguides manufacturability using advanced RET solutions,” in *Optical Microlithography XXX*, 2017, vol. 10147, p. 1014711.
[8] J. Bolk *et al.*, “Deep UV Lithography Process in Generic InP Integration for Arrayed Waveguide Gratings,” *IEEE Photonics Technology Letters*, vol. 30, no. 13, pp. 1222–1225, Jul. 2018.

Heterogeneous Integration Roadmap - Package Level Systems Integration: A key to maintaining the pace of progress

W. R. Bottoms[1], Amr S. Helmy [2]
[1] 3MTS, California - USA
[2] *The Edward S. Rogers Department of Electrical and Computer Engineering, University of Toronto, 10 King's College Road, Toronto, ON M5S 3G4, Canada*
Both authors represent different IEEE societies within the HIR leadership; e-mail: bill_bottoms@3mts.com

ABSTRACT

In this talk we plan to provide an overview of the heterogenous road map and how it relates to photonics. Within the talk we shall also set in context the role photonics play within the package level systems integration of electronics, photonics and sensor integrated circuits with the aim of maintaining the pace of progress, as Moore's law scales.

Keywords: Heterogeneous Integration, Package Level Integration.

1. INTRODUCTION

The most efficient path for progress in electronic systems for more than 50 years has been Moore's Law scaling but the advantages of scaling CMOS are now approaching their economic end. Information technology must identify new approaches if the economic and societal benefits are to maintain their pace of progress in the post Moore's Law era. This need has accelerated innovation in new technologies to maintain the improvements in size, cost, performance and power efficiency that has driven information technology into every corner of human activity over the last 50 years. The coming changes are evident with evolutionary progress in advanced packaging, introduction of new system architectures, new device types, new materials and new processes for both design and production. The evolution includes wafer level packaging, 3D integration and heterogeneous integration of known components into a single package [1].

The revolution that is just beginning will include a complete remake of the global network, new devices for both logic and memory functions, an array of sensors of all types. The emergence of big data, the internet of things and migration of memory, logic and applications to the cloud are moving the majority of power usage from logic towards memory transport. The path toward maintaining the pace of progress for decades to come will, however, transform this evolution in the industry to an industrial revolution where new device types and other components are integrated into systems at the package level. The ultimate realization of this revolution will be full system integration of complex products in the package.

The difficult challenges that must be overcome to realize this revolution include: Cost and time required for new system design and verification; Thermal management of the increased volumetric thermal density; Stress management in both production and use cases with diverse materials and device types; Compatibility with hostile environments; Reliability issues including test access and test capability for systems with components that wear out during the useful life of the system; Security with low latency on the global network to support many of the health, safety and entertainment applications with low latency requirements

Many of the elements of this revolution are in development today and will be discussed in this presentation. These include: Artificial Intelligence as part of our design and simulation capability as well as improving speed and accuracy of decisions; Quantum computing and photonic switches will accelerate performance at dramatically lower energy levels; Quantum dots and plasmonics will decrease power and cost while reducing the need for expensive precision in thermal management; New processes and new materials to resolve thermal density and stress management issues; Orders of magnitude increase in simulation capability that can accelerate the pace of progress in development and understanding of complex systems such as the human brain; Incorporation of 2D materials into logic and memory as well as insulation, isolation and connectivity applications; Augmented reality to expand the human capability both physically and mentally

The development horizon in these areas of emerging research is 25 to 30 years. Looking back to the time before the smart phone was introduced June 29th 2007, no one imagined the impact it would have on every aspect of our lives. Today the number of smart phone users is more than 52 % of the world's adult population and that does not include cellular phones without a camera or iPads and other similar devices. It should be clear that the most important innovations in the next 25 years are things that we cannot yet imagine.

2. Relevance to Photonics

Photonics dominated long range data and telephony by the 1970s due to cost and power advantages but made slow progress during the next 30 years due to small market size and high component cost. Since the turn of the century much progress has been made due to expanding market size driven by increasing data traffic and the cost advantages of expanding volume. The global internet traffic is projected to reach 2.0 zettabytes by 2019 from .7 zettabytes in 2014, a 23% CAGR. Two thirds of this traffic will originate from non-PC devices by 2019 with growth coming from TVs, tablets, smartphones and machine to machine communication. Each one of these growth sources has some important differences that will impact their packaging requirements. Broadband speeds will more than double in the 5 year period from 2014 to 2019.

The packaging of photonic integrated circuits (PICs) will face the same challenges faced in packaging electronic ICs with the added complexity of integrating both active and passive photonic elements. Wherever possible industry must adopt and adapt the packaging technologies developed for electronics to decrease cost and time to market for packaging of individual PIC circuits and incorporating PIC circuits, photonics, plasmonic and other components into complex 3D SiP through heterogeneous integration.

There will be many specific challenges in realizing the benefits of integrating electronics and photonics into the fabric of the global network and the components attached to it. The solutions, however, cannot come from just packaging photonic components. The co-packaging of electronics, photonics and plasmonics will be required to address these substantial new challenges and meet the expanding requirements for higher performance, higher bandwidth density, higher reliability, increased security, lower latency and lower cost in the future. There will be new device types, new materials, new package production processes and new equipment required to accomplish these objectives. Some of these required innovations we know today but many specifics that must be addressed over the next 15 years are yet not known. The scope of this Roadmap Chapter is to identify electronic-photonic integration challenges with sufficient lead time so potential solutions can be identified and proven before they become roadblocks to the pace of progress for the industry. This scope covers integration of these components into emerging packaging solutions to decrease size, cost, power and latency while increasing performance and bandwidth.

3. CONCLUSIONS

In this talk we plan to provide an overview of the heterogenous integration roadmap and how it relates to photonics. We shall also discuss the many difficult challenges associated with system level of integration of photonics+ electronics. We shall also set in context the role photonics play within the package level systems integration of electronics, photonics and sensor integrated circuits with the aim of maintaining the pace of progress, as Moore's law slows down.

REFERENCES

[1] https://eps.ieee.org/technology/heterogeneous-integration-roadmap.html.

Large enhancement of longitudinal magneto-optical effect with an all-dielectric resonant guided-mode grating

Student Paper

L. Bsawmaii [1], E. Gamet [1], F. Royer [1], F. Celle [1], S. Neveu [2], D. Jamon [1]
[1]*Université de Lyon, CNRS, UMR 5516, Laboratoire Hubert Curien, Université Jean-Monnet, F-42000 Saint-Etienne, France*
[2]*Sorbonne Universités, UPMC Université Paris 06, CNRS, Laboratoire PHENIX, Case 51, 4 place Jussieu, F-75005 Paris, France*
e-mail: laure.bsawmaii@univ-st-etienne.fr

ABSTRACT

An integrated device with high magneto-optical response is currently required since there is a high demand on photonic devices employing magneto-optical effects like optical isolators and magnetic field sensors. Thus, we experimentally and numerically demonstrate a significant enhancement of the longitudinal magneto-optical response in transmission and for small angles of incidence, in a subwavelength resonant structure consisting of a dielectric grating and a magneto-optic waveguide.

Keywords: magneto-optics, Faraday effect, Kerr effects, magneto-plasmonic, resonant guided-mode grating.

1 INTRODUCTION

Most of magneto-optical (MO) effects can be described by a rotation of the plane of polarization through a magnetized MO material, which are named the Faraday effect in transmission geometry and Kerr effect in reflection geometry[1]. In recent years, these effects attract much attention due to their possible applications in optical isolators, which are important elements in laser systems. They can be used also in magnetic field sensors, MO data storage and optical modulation[1].
The enhancement of MO response can be achieved by subwavelength magneto-plasmonic structures: MO dielectric material surrounded by metallic grating. They are based on the phenomenon of an extraordinary optical transmission (EOT), where an unusual high transmission spectra can be observed[2]. Both waveguide mode and extended surface plasmon polaritons (SPPs)[3] are responsible for this exceptional behavior. Belotelov et al.[4] succeeded in increasing theoretically the Faraday and Kerr rotations in polar configuration[1] by a factor of 9 in comparison to a single Bi:YIG film, with 2D magneto-plasmonic structure. While the Faraday rotation measured by Floess et al.[5] for a 1D magneto-plasmonic structure is enhanced by a factor of 14 in comparison to a single EuS film.
Another way to exalt the MO effects is by using the all-dielectric resonant guided-mode gratings: dielectric MO waveguide surrounded by a dielectric grating. These structures are based on the phenomenon of the waveguide mode resonance[6], where a diffracted wave is coupled into the waveguide. The condition of the coupling is given by:

$$n_1 sin\theta_{inc} + m\frac{\lambda_0}{\Lambda} = n_{eff} \tag{1}$$

Where n_{eff} is the effective index of the waveguide mode, n_1 is the refractive index of the incidence medium, θ_{inc} is the incident angle, m is the diffraction order, Λ is the period of the dielectric grating and λ_0 is the vacuum wavelength for the incident light.
At resonance, a destructive interference occurs between transmitted and diffracted wave fronts[7]. Therefore, contrary to the magneto-plasmonic structure, a deep in transmittance and consequently a peak in reflectance are obtained. In these structures, a considerable MO effects can be achieved with high reflectivity which is important for applications in 3D imaging and magneto-optic data storage[1]. An enhancement of Faraday and Kerr effects has been theoretically demonstrated by Gamet el al.[8] through 1D subwavelength all-dielectric structure. An improvement by a factor of 100 and 700 in comparison to the off-resonance is obtained respectively for Faraday and Kerr effects in the polar configuration. While for the Kerr rotation in the longitudinal configuration[1], an enhancement of 10^5 was achieved.
Here, a numerical and experimental large MO response in the longitudinal configuration and in transmission, is presented for small angles of incidence (AOI) by a simple 1D all-dielectric resonant guided-mode grating.

2 FABRICATION AND CHARACTERIZATION

Our structure geometry is illustrated by Fig.1. It consists of a photoresist (PR) grating deposits on a thin layer of our MO composite sol-gel. The structure was fabricated as it follows: first a layer of MO composite with thickness t_{MO} was deposited on a glass substrate (BK7) by dip coating then treated thermally at 90°C for

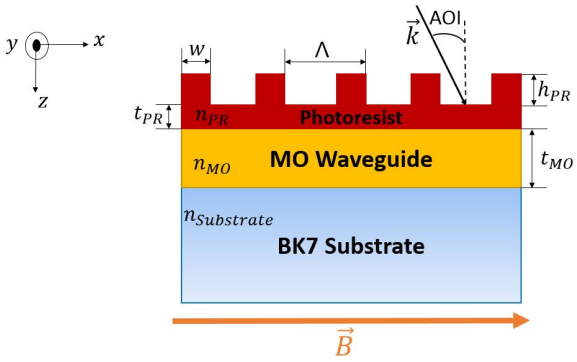


Figure 1. Schematic drawing of the sample geometry, the incidence conditions and the magnetic field orientation. The geometrical parameters of this structure are: $t_{MO} = 440nm$, $t_{PR} = 130nm$, $h_{PR} = 255nm$, $w = 400nm$ and $\Lambda = 1000nm$.

1 hour. After that the PR grating with height h_{PR}, width w and period Λ was structured on the top of the MO film using a periodic quartz-supported chromium mask. In order to have the two guided modes (TE and TM) in our structure, the grating is not clogged at the bottom and a thin layer of PR with thickness t_{PR} is kept.
Our MO composite was prepared by a liquid sol-gel preparation of Tetraethyl orthosilicate ($C_8H_{20}O_4Si$), doped by a ferrofluid containing cobalt ferrite ($CoFe_2O_4$) nanoparticles (NPs). With this sol-gel, it is possible to deposit uniform thin layers of good quality on a large scale substrate and with low thermal treatment temperature. However, it was used in the fabrication of integrated MO converters[9] and 3D magneto-photonic crystals[10].
The refractive indexes were measured by ellipsometry: $n_{PR} = 1.59$, $n_{MO} = 1.65$ and $n_{Substrate} = 1.51$ at the wavelength $\lambda = 1550nm$. The refractive index of the MO waveguide is highly dependent on the volume fraction ϕ of $CoFe_2O_4$ NPs. Here, the given value corresponds to a concentration of $\phi = 25\%$. The layer's thicknesses were also measured by ellipsometry: $t_{MO} = 440nm$ and $t_{PR} + h_{PR} = 385nm$, while the grating's parameters were measured by Atomic Force Microscopy (AFM) : $h_{PR} = 255nm$, $w = 400nm$ and $\Lambda = 1000nm$. The rotation of polarization was measured at room temperature with a homemade MO bench, where a tunable laser ($1490 - 1630nm$) is used as a source of light, a longitudinal magnetic field $\overrightarrow{B}$ (see Fig.1) is applied and a photoelastic modulator is used to increase the sensitivity of the measurements. The transmittance was measured by a near infrared spectrophotometer. The simulations have been carried out with a homemade RCWA code, taking into account the whole permittivity tensor[11].

3 RESULTS

The magnetic field $\overrightarrow{B}$ is applied in the x direction referring to Fig.1 (longitudinal configuration) and the incident angle is varied from $0°$ to $5°$. The incident light is polarized TE (in y direction) or TM (in x direction). The numerical simulations and experimental measurements of the polarization rotation in transmission $\theta(°)$ and the transmittance T, for TE-polarized incident light are plotted in Fig.2 for the different AOI. One can see that by increasing the AOI the resonance wavelength increases, this dependency is verified by (1). The presence of the large opposite rotation peaks is linked to the both transmission resonances for both polarizations (TE and TM). As seen in this figure, the measured rotations reach values of $1.1°$ and $-0.8°$ as highest values for the different AOI except the normal incidence (there is no resonant MO effects). Whereas for a simple layer of our MO material without grating ($t_{MO} = 440nm$), the MO effects are zeros for these small AOI (see inset Fig.2(b) and Fig.2(d)). Therefore, a big enhancement was achieved with our resonant dielectric structure. The advantage here is that the resonant MO effects coincides with high transmittance, greater than 60% for the different AOI. The large detected MO effect ($\theta = 1.1°$) is related to the fact that at AOI$= 0.45°$ the propagative TE mode (order $m = 1$) and the anti-propagative TM mode (order $m = -1$), resonate at the same wavelength (as seen in Fig.2(a) and Fig.2(c)). Thus, at the exit of the structure, the rotations of these two modes add up and give an important MO response. Such enhancement could be applicable in the non-destructive control or in a magnetic field sensor based on this type of structure. A good agreement can be seen between the simulations and the measurements, and the wavelength shift can be explained by the imperfection of the fabricated structure. Furthermore, for TM polarized incident light, same order of polarization rotation was achieved for the same structure (not shown here).
These values are higher than that obtained by Belotelov et al.[4] with more complex structure, made by 2D perforated gold with hole arrays deposited on a uniform Bi:YIG film. They theoretically demonstrated values of $0.78°$ and $0.63°$ for Faraday and Kerr effects respectively in the polar configuration and for TM polarized incident light. While, for the Faraday rotation, Floess et al.[5] have theoretically and experimentally demonstrated values of $14°$ and $8°$ for TE and TM polarizations respectively, with 1D magneto-plasmonic structure made by

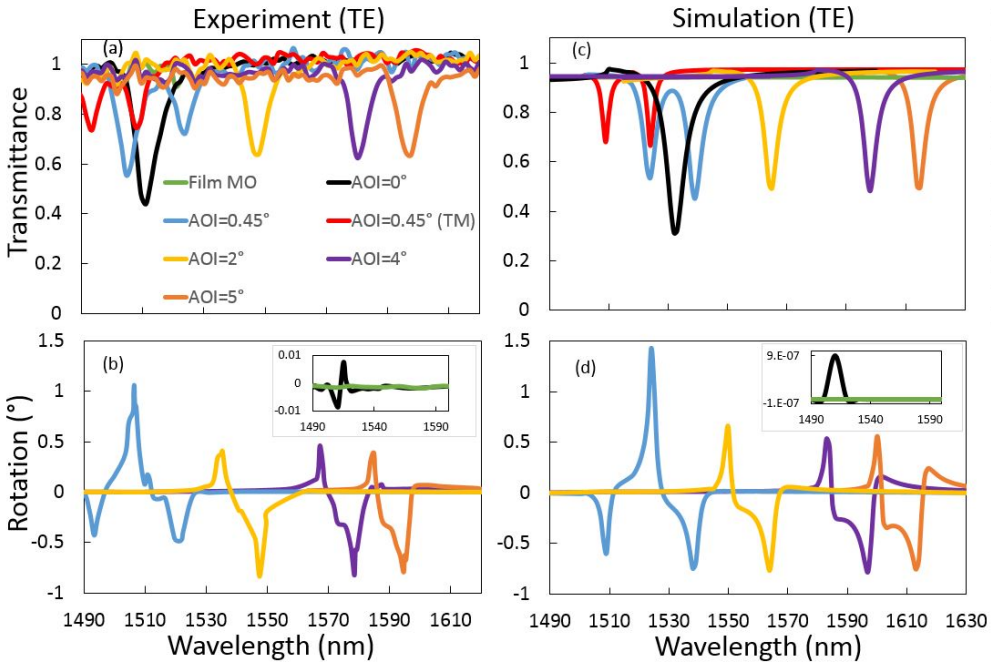


Figure 2. The left-hand column displays the measured transmittance (a) and polarization rotation (b) for TE-polarized incident light and for different angles of incident. The experimental data agree with the performed simulation shown in the right-hand column (c),(d). The inset curves in (b) and (d) represent respectively the measured and simulated polarization rotations, for our resonant structure at normal incident (AOI=0°) and for the MO film.

an embedded gold nanowires in a EuS film. But, the measurements were taken at a very low temperature of 20K since the EuS material has a maximum of MO effects at this temperature.

4 CONCLUSION

In this work, a significant enhancement of MO effect in the longitudinal configuration was experimentally and numerically demonstrated at small angles of incidence, with 1D all-dielectric resonant grating. This latter consists of a uniform MO dielectric film with a dielectric grating on the top. This structure is easily fabricated which extends its application as a magnetic field sensor or in the non-destructive testing.

ACKNOWLEDGMENT

The authors gratefully acknowledge the funding by ANR Photomagnet (ANR-16-CE09-0017).

REFERENCES

[1] A.K. Zvezdin and V.A. Kotov. *Modern magnetooptics and magnetooptical materials*. CRC Press, January 1997.

[2] T. W. Ebbesen, H. J. Lezec, H. F. Ghaemi, T. Thio, and P. A. Wolff. Extraordinary optical transmission through sub-wavelength hole arrays. *Nature*, 391(6668):667–669, February 1998.

[3] S. MAIER. *Plasmonics: fundamentals and applications*. Springer, 2007.

[4] V. I. Belotelov, L. L. Doskolovich, and A. K. Zvezdin. Extraordinary magneto-optical effects and transmission through metal-dielectric plasmonic systems. *Physical Review Letters*, 98(7):077401, February 2007.

[5] D. Floess, M. Hentschel, T. Weiss, H.U. Habermeier, J. Jiao, S.G. Tikhodeev, and H. Giessen. Plasmonic analog of electromagnetically induced absorption leads to giant thin film Faraday rotation of 14°. *Physical Review X*, 7(2):021048, June 2017.

[6] T. Sang, Z. Wang, L. Wang, Y. Wu, and L. Chen. Resonant excitation analysis of sub-wavelength dielectric grating. *Journal of Optics A: Pure and Applied Optics*, 8(1):62, 2006.

[7] D. Rosenblatt, A. Sharon, and A. A. Friesem. Resonant grating waveguide structures. *IEEE Journal of Quantum Electronics*, 33(11):2038–2059, November 1997.

[8] E. Gamet, B. Varghese, I. Verrier, and F. Royer. Enhancement of magneto-optical effects by a single 1d all dielectric resonant grating. *Journal of Physics D: Applied Physics*, 50(49):495105, 2017.

[9] H. Amata, F. Royer, F. Choueikani, D. Jamon, F. Parsy, J.E. Broquin, S. Neveu, and J.J. Rousseau. Hybrid magneto-optical mode converter made with a magnetic nanoparticles-doped SiO2/ZrO2 layer coated on an ion-exchanged glass waveguide. *Applied Physics Letters*, 99(25):251108, December 2011.

[10] E. Abou Diwan, F. Royer, D. Jamon, R. Kekesi, S. Neveu, M.F. Blanc-Mignon, and J.J. Rousseau. Large spectral modification of the Faraday effect of 3d SiO2/CoFe2o4 magneto-photonic crystals. *Journal of Nanoscience and Nanotechnology*, 16(9):10160–10165, September 2016.

[11] L. Li. Reformulation of the fourier modal method for surface-relief gratings made with anisotropic materials. *Journal of Modern Optics*, 45(7):1313–1334, July 1998.

Using the polarisation response of planar optical waveguides to determine the anisotropic complex refractive index of graphene oxide thick films

WenSin Chong[1], SoonXin Gan[1], ChoonKong Lai[1,2], WuYi Chong[1,*], Steve Madden[2], Duk Choi[2], Richard M. De La Rue[3,*], Harith Ahmad[1]

[1]Photonics Research Centre, University of Malaya, 50603 Kuala Lumpur, Malaysia.
[2]Laser Physics Centre, Research School of Physics and Engineering, The Australian National University, Canberra, ACT 260, Australia.
[3]Glasgow University Optoelectronics Research Group.
**wuyi@um.edu.my; rmdelarue@googlemail.com*

ABSTRACT

The polarisation response of graphene oxide (GO) coated planar silica optical waveguides has been studied. GO films with different thicknesses have been coated onto a planar optical waveguide with its top cladding removed via plasma etching. The solution drop-casting technique was used for GO coating. GO film thicknesses between 0.1 μm and 1.0 μm were used. GO-coated waveguides exhibit large polarisation dependent losses - and the polarisation response depends strongly on the GO coating thickness. The response was used, together with finite element analysis, to determine the complex refractive index of the GO film. The complex refractive indices of the GO film, with TE- and TM-polarised light at a wavelength of 1550 nm, were found to be 1.65+0.07*i* and 1.63+0.001*i*, respectively. The uncertainty values for the real parts of the refractive index were 0.02 and 0.01 for TM- and TE-polarised light, respectively - whereas the uncertainty values for the imaginary part of the refractive index were found to be 0.0001 and 0.01 for TM- and TE-polarised light, respectively. The estimated uncertainty values are smaller by an order of magnitude when compared with values measured using the conventional method of spectroscopic ellipsometry.

Keywords: graphene oxide, planar optical waveguide, complex refractive index, finite element analysis.

1. INTRODUCTION

Graphene oxide (GO) has been an important focus for research groups around the world because of its unique electronic and optical properties [1, 2]. Unlike graphene, which exists and retains its fundamental properties only in single- or few-layer situations, GO films are formed as stacks of graphene layers with oxygen functional groups sandwiched in between these layers, allowing GO to exist and retain its fundamental properties in a quasi-bulk form, as well as in the more widely recognised two-dimensional form. Another distinction between GO and graphene is its excellent solubility – as a result of the presence of oxygen functional groups - in water and most polar solvents - with little or no agglomeration, thereby allowing easier handling than pristine graphene. GO flakes, which have asymmetrical dimensions ranging from a few hundred nanometres to several micrometres, allow GO films to be formed in an orderly-stacked manner, using a simple drop-and-dry coating method[3].

The ready formation of GO film with orderly-stacked layers - together with the possibility of controlling its oxygen reduction level by applying heating, electrical potential, or even polarized light - forms the basis of many applications that have been demonstrated and reported in the research community. In photonics research, the orderly-layered structure of GO film allows light with orthogonal polarization states to 'see' the GO film differently – as a dielectric when the light is polarized perpendicularly to the GO layers; and as a semi-metal when the light is polarized parallel to the GO layers – thereby inducing higher propagation losses for light with the latter polarization state. This behaviour has been used to construct a waveguide polariser with a very high polarization extinction ratio that can operate over a broad wavelength range [4]. In addition, by applying an external electric field or an external light source, the optical transmittance of the GO film can be changed, thereby opening up the potential of using GO-functionalised waveguides as optical switches or modulators[5].

While the contribution of the above-mentioned work to possible applications is significant, the observed properties of GO have also led to questions about the underlying principles demonstrated, some of which have still to be verified experimentally. From the optical point of view, observations from the work mentioned above can be attributed to changes in the two fundamental parameters of the complex refractive index, i.e. the refractive index, *n*, and the extinction coefficient, *k*, of GO. The former determines the phase velocity of light traversing a GO film, while the latter determines the propagation loss for light passing through a GO film.

Much recent research effort has gone into the determination of the complex refractive index for single or few layer graphene. Although a variety of methods has been proposed, the reliability of the findings is still debatable. Both spectroscopic methods (ellipsometry and reflection spectroscopy) and non-spectroscopic

methods (picometrology, polarization-dependent attenuated total internal reflection and surface plasmon resonance) have been used to determine these values at optical frequencies, but the results reported are inconsistent – with *n* values in the range from 2.0 to 3.0 - and *k* values in the range from 0.8 to 2.03. The discrepancies observed are attributable to the different fitting approaches used in the individual methods mentioned above [6-8].

More limited work has been conducted to determine the complex refractive index of GO films [all using spectroscopic ellipsometry (SE)], with values for *n* and *k* reported to range from 1.55 to 1.90 and 0.05 to 0.48, respectively. The SE approach typically produces the large uncertainty value of ± 0.2 for *n* [9, 10].

GO-coated planar optical waveguides with large variations in polarisation response are sensitive to changes in the complex effective index of functional sections of the waveguides. By making careful experimental measurements and cross referencing with finite element analysis for the effective index of the GO-coated waveguide, the complex refractive index of graphene oxide coatings can be determined.

2. METHODS

2.1 Planar optical waveguide preparation

The optical waveguides were prepared by first depositing germanium-doped silica layers onto silicon wafers with 7 μm of thermally grown oxide as undercladding (with a refractive index of 1.444 measured at 1550 nm). The doped-silica layer thickness and refractive index were 3 μm and 1.486 respectively, measured at 1550 nm using a prism coupling technique. Straight waveguides were then fabricated using standard photolithography and plasma etching techniques. Index-matched polymer (ChemOptics ZPU-13RI) was then spin-coated on to the fabricated waveguides before being etched down to expose the top section of the waveguide, while covering most of the sidewalls. This process limits the interaction of the waveguide light with the GO coating to the top section of the optical waveguide, thereby facilitating more strongly polarisation dependent light interaction with the subsequent GO coating.

2.2 GO coating and optical measurement

GO solutions were prepared with concentrations ranging from 1.6 mg/mL to 4.0 mg/mL. GO coating was achieved by drop casting 0.5 μL of GO solution onto section of the straight waveguides. The coating region diameter was about 1 mm and the GO coating thickness was controlled between 0.1 – 1.0 μm by drop casting using different solution concentrations, as well as by multiple drop casting processes.

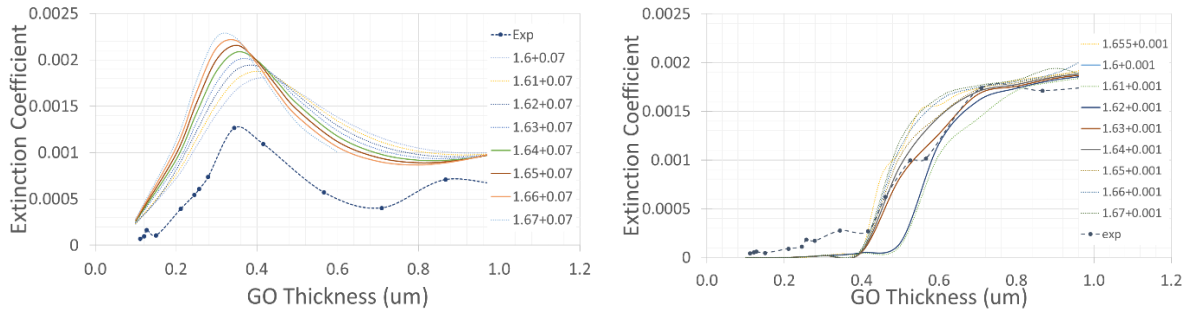
The fibre butt coupling technique was used to measure the insertion loss of the GO-coated waveguides at a wavelength of 1550 nm. The polarisation state of the laser source was controlled using a fibre polarisation controller while the polarisation states were measured using a polarimeter. The loss coefficient of the GO-coated waveguides were calculated by dividing the transmission loss caused by the GO coating with the length of the coating. The extinction coefficient was then calculated from the loss coefficient.

2.3 Finite element analysis (FEA)

FEA requires that the dimensions of the GO-coated waveguide cross-section be accurately determined. The GO coating was assumed to be a single birefringent slab. The thickness of the GO coating was varied over the range from 0.1 to 1.0 μm. Different values for the refractive index of the GO films were used in the simulation, in order to obtain the corresponding extinction coefficients of the GO-coated waveguides. The variations of the GO-coated waveguide extinction coefficient with GO coating thickness were then plotted and the results compared with the experimental results to obtain the best fit between the experimental and simulation results.

3. RESULTS AND DISCUSSION

Fig. 1(a) shows the experimentally obtained extinction coefficient of the GO-coated waveguides and corresponding simulation results for TE-polarised light propagation obtained using different values for the real part of the GO film refractive index. When the GO film refractive index was set at $1.65 + 0.07i$, the simulation matched with the experimental results. When the real part of the GO film refractive index was varied by more than ±0.02, the deviation from the experimentally obtained results becomes obvious. The same can be observed in Fig. 1(b) which compares the experimentally obtained extinction coefficients for TM-polarised light. In this case, a best fit was obtained when the complex refractive index of GO film was set at $1.63 + 0.001i$. Significant deviation from the experimentally obtained extinction coefficient curve was observed when the real part of the complex refractive index of GO film was varied by more than ±0.01.



(a) (b)

Figure 1. Extinction coefficient of (a) TE-polarized and (b) TM-polarized light propagating through GO-coated waveguides as a function of the GO-coating thickness.

4. CONCLUSIONS

We have demonstrated that the anisotropic complex refractive index of films of graphene oxide (GO) can be obtained accurately using a combination of experimental measurements and numerical simulation of light propagation in planar stripe optical waveguides that are based on doped silica and are coated with the GO. The precision of the complex refractive index measurement is about one order of magnitude better compared with the conventional spectroscopic ellipsometry technique. The approach proposed can be extended for use in determining the refractive index of many other dielectric thin films.

ACKNOWLEDGEMENTS

This work was funded in part by the Malaysia Ministry of Higher Education (MOHE) (LRGS(2015)/NGOD/UM/KPT), the Asian Office of Aerospace Research and Development (AOARD) grant (16IOA017) and the University of Malaya Research Grant (UMRG) (RP029C-15AFR).

REFERENCES

1. Borini, S., et al., *Ultrafast Graphene Oxide Humidity Sensors.* ACS Nano, 2013. **7**(12): p. 11166-11173.
2. Jiang, X.-F., et al., *Graphene Oxides as Tunable Broadband Nonlinear Optical Materials for Femtosecond Laser Pulses.* The Journal of Physical Chemistry Letters, 2012. **3**(6): p. 785-790.
3. Pengzhan, S., et al., *Suppression of the coffee-ring effect by self-assembling graphene oxide and monolayer titania.* Nanotechnology, 2013. **24**(7): p. 075601.
4. Lim, W.H., et al., *Graphene oxide-based waveguide polariser: From thin film to quasi-bulk.* Optics Express, 2014. **22**(9): p. 11090-11098.
5. Chong, W., et al., *Photo-induced reduction of graphene oxide coating on optical waveguide and consequent optical intermodulation.* Scientific reports, 2016. **6**: p. 23813.
6. Li, W., et al., *Broadband optical properties of graphene by spectroscopic ellipsometry.* Carbon, 2016. **99**: p. 348-353.
7. Cheon, S., et al., *How to Reliably Determine the Complex Refractive Index (RI) of Graphene by Using Two Independent Measurement Constraints.* Scientific Reports, 2014. **4**: p. 6364.
8. Wang, X., Y.P. Chen, and D.D. Nolte, *Strong anomalous optical dispersion of graphene: complex refractive index measured by Picometrology.* Optics Express, 2008. **16**(26): p. 22105-22112.
9. Schöche, S., et al., *Optical properties of graphene oxide and reduced graphene oxide determined by spectroscopic ellipsometry.* Applied Surface Science, 2017. **421**: p. 778-782.
10. Jung, I., et al., *Characterization of Thermally Reduced Graphene Oxide by Imaging Ellipsometry.* The Journal of Physical Chemistry C, 2008. **112**(23): p. 8499-8506.

Wideband Static and Dynamic Model of a Tensile-Strained Bulk Reflective SOA

Michael J. Connelly
Optical Communications Research Group, Dept. Electronic and Computer Engineering,
University of Limerick, Ireland.
e-mail: michael.connelly@ul.ie

ABSTRACT

Reflective SOAs (RSOAs) have promise for applications such as optical modulators in WDM PONS. Bulk polarization insensitive SOAs are realised by the use of a tensile-strained active region, which compensates for different TE and TM confinement factors. RSOA wideband models are required to predict RSOA static and dynamic behaviour. In this paper, we present a wideband static and dynamic model of a commercial tensile-strained tapered waveguide RSOA. Wavelength and carrier density dependency of the material gain and additive spontaneous emission is determined using full band structure calculations. In the static model, estimation of the amplified signal and spontaneous emission is achieved by an efficient numerical solution of travelling-wave and carrier density rate equations. Unknown model parameters are determined by least squares fitting of modelled and experimental ASE spectrums. The dynamic model extends the static model to permit SOA drive current modulation and is used to determine the RSOA response when driven by multi Gb/s NRZ data signals. There is good agreement between 1.25 Gb/s data simulated and experimental eye diagrams.

Keywords: Reflective semiconductor optical amplifier, modelling, modulator.

1. INTRODUCTION

RSOAs have promise for applications in WDM optical networks including as basic amplifiers and modulators [1]. In the latter data is superimposed on an input CW lightwave by using current modulation. Polarization insensitive rectangular cross section waveguide SOAs can be fabricated using tensile-strained bulk material [2]. There is a need for models to predict wideband RSOA static and dynamic behaviour such as static gain, noise figure, Amplified Spontaneous Emission (ASE) spectrum and current modulation response. In this paper we extend our prior work on traveling-wave SOAs [2, 3], to develop RSOA static and dynamic models. A full bandstructure model is used to determine the wavelength and carrier density *n* dependency of the material gain and additive spontaneous emission. The model includes a geometrical description of the active waveguide, including the input taper. The amplified signal and ASE are described by travelling-wave equations and numerically solved in conjunction with a carrier density rate equation. Good agreement between simulation and experiment is achieved for the static characteristics and the NRZ current modulation at multi Gb/s data rates.

2. RSOA STRUCTURE, MATERIAL GAIN, CARRIER DENSITY AND PHOTON RATE MODELS

The RSOA, shown in Fig. 1, is a commercial TO-CAN packaged device (Kamelian), having a tensile-strained InGaAsP active region sandwiched between two InGaAsP separate-confinement heterostructure layers [4]. The TE and TM confinement factors as functions of the waveguide width W (μm) are given by $\Gamma_{TE} = 0.1275W^3 - 0.5188W^2 + 0.7605W$ and $\Gamma_{TM} = 0.0704W^3 - 0.3035W^2 + 0.4648W$ [4].

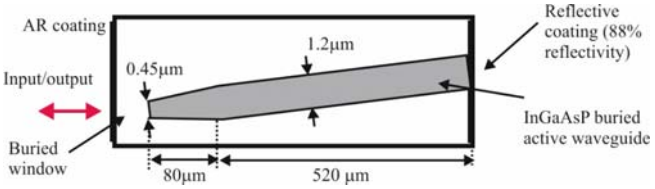


Figure. 1. Top view of the RSOA active waveguide.

The active region *n* and energy *E* dependent material and spontaneous emission gain coefficients g_m and g_{sp} and radiative recombination rates are calculated using a detailed strained-material model [2]. g_m is given by

$$g_m(E) = \frac{\hbar e^2}{2\pi\varepsilon_0 c m_0^2 n_r E} \sum_{b=LH,HH,SO} \int_0^{\infty}\int_0^{\pi} k^2 \sin\theta \left|M_b(k,\theta)\right|^2 L_z\left[E_{cv,b}(k,\theta)\right]\left[f_c(k) + f_{v,b}(k,\theta) - 1\right] d\theta\, dk \qquad (1)$$

$M_b(k,\theta)$ is the matrix element, L_z a sech intraband linebroadening function with relaxation time τ_r (a fitting parameter), $E_{cv,b}$ the conduction-valence band transition energy and Fermi functions f_c and f_v. The summation is over the light-hole, heavy-hole and split-off bands. The net gain coefficient $g_p(E,n) = \Gamma_p g_{m,p} - \alpha_p$ with polarization dependent loss $\alpha_p(n) = \alpha_0 + \Gamma_p[\alpha_1 + \alpha_2 \exp(-\alpha_e E)]n$. α_0, α_1 α_2 and α_e are the intrinsic absorption, free electron loss and two coefficients modelling intervalence band absorption [2], which are fitting parameters. Bandgap shrinkage due to the parabolic conduction band and the three non-parabolic valence bands is calculated from first principles [5]. The traveling-wave equations for the forward/backward travelling photon rates $I^{\pm}_{s,p}$ of the amplified input signal of polarization *p* (TE or TM) and for k-th ASE forward/backward photon rate spectral slice, of energy width *dE* are [2],

$$\frac{dI^{\pm}_{s,p}}{dz} = \pm g_p I^{\pm}_{s,p} \tag{2}$$

$$\frac{dN^{\pm}_{p,k}}{dz} = \pm g_p(E_k,n) N^{\pm}_{p,k} \pm \Gamma_p(z) g_{sp,p}(E_k)\, dE \tag{3}$$

, with associated boundary conditions. *n* obeys the rate equation [2],

$$\frac{dn}{dt} = \frac{\eta(n) I}{eV} - R(n) - \frac{\Gamma_{s,p}}{dW(z)} g_p (I^{+}_{s,p} + I^{-}_{s,p}) - \frac{1}{dW(z)} \sum_p \sum_k \Gamma_p(z) g_{p,k} \left[N^{+}_{p,k}(z) + N^{-}_{p,k}(z) \right] \tag{4}$$

The terms on the RHS of (4) account for electrical pumping, due to the current *I*, radiative and Auger recombination (its coefficient C_{aug} is a fitting parameter) and amplified signal and ASE carrier depletion. To determine the static signal and ASE photon rates and carrier density, the SOA is split into 64 spatial sections and the ASE into 128 spectral slices covering a range of 1250 to 1650 nm. The signal and ASE photon rates are estimated using finite difference solutions to (3, 4). The carrier density is then estimated at the centre of each section using (4), assuming $dn/dt = 0$, which in turn is used to update g_m and g_{sp}. These are then used to determine new values of $I^{\pm}_{s,p}$ and $N^{\pm}_{p,k}$. This process is continued until the photon rates converge to a steady value. The six fitting parameters $\alpha_0 = 1.94 \times 10^3\, m^{-1}$, $\alpha_1 = 8.0 \times 10^{-21} m^2$, $\alpha_2 = 8.2 \times 10^{-20} m^2$, $\alpha_e = 3.1 eV^{-1}$, $C_{aug} = 4.0 \times 10^{-41}\, m^6 s^{-1}$ and $\tau_r = 23.3\, fs$, were determined using least square fitting of the polarization resolved output ASE spectra, at different bias currents as shown in Fig. 2(a). The associated carrier density distributions, shown in Fig. 2(b), are asymmetrical, with maximum saturation occurring in the input taper. Fig. 3 shows good agreement between the experimental and simulated gain and noise figure vs. bias current characteristics.

In the dynamic model, with current modulation, (4) is solved using finite differences. At each time step the signal and ASE distributions are obtained using finite difference solutions of (2, 3), with the updated g_m and g_{sp} from (1). To verify model accuracy, the current was modulated by 2^9-1 PRBS 1.25 Gb/s NRZ data (using an 87 ps rise/fall time driver). The input CW lightwave wavelength and power was 1550 nm and -3 dBm. The bias and peak-peak modulation currents were 54 and 52 mA. Good agreement between simulated and experimental RSOA output eye diagrams was obtained as shown in Fig. 4. Pattern effects are evident because of the finite carrier recovery lifetime, but are not particularly serious. The experimental and simulated rise/fall times of 259/231 and 250/310 ps are comparable. However as the data rate increases, pattern effects become more serious as shown in the simulations of Fig. 4 for 2.5 and 5 Gb/s data and in the latter case, modulation performance is very poor.

3. CONCLUSIONS

A strained bulk RSOA wideband model was used to investigate the effects of material and geometrical parameters on performance under a wide range of operating conditions. The versatility and accuracy of the models are particularly useful for RSOA design and optimization. Future work will focus on inclusion of receiver signal-spontaneous emission beat noise in order to predict the RSOA modulator Q-factor, extinction ratio and bit-error-rate.

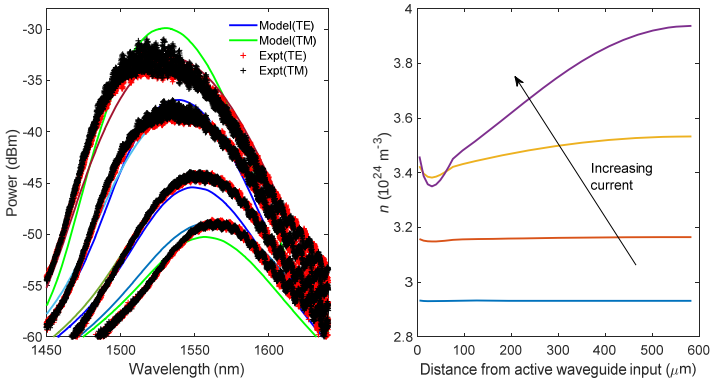


Figure. 2. (a) Simulated and experimental TE and TM ASE spectrums for bias currents of 40, 50,70,100 mA with no input signal (ripples, present on the experimental spectra are due to the non-zero reflectivity of the input facet), (b) corresponding carrier density distributions.

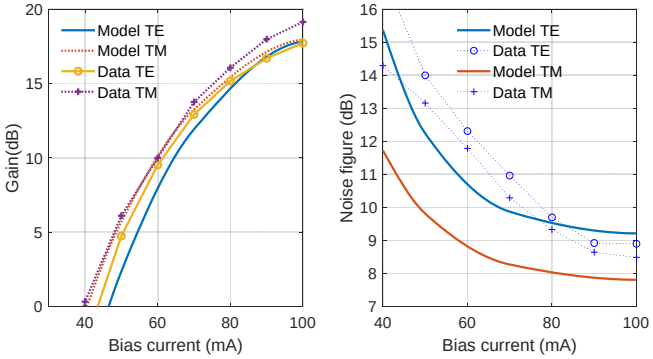


Figure. 3. (a) Small-signal gain and (b) noise figure vs. bias current at 1550 nm.

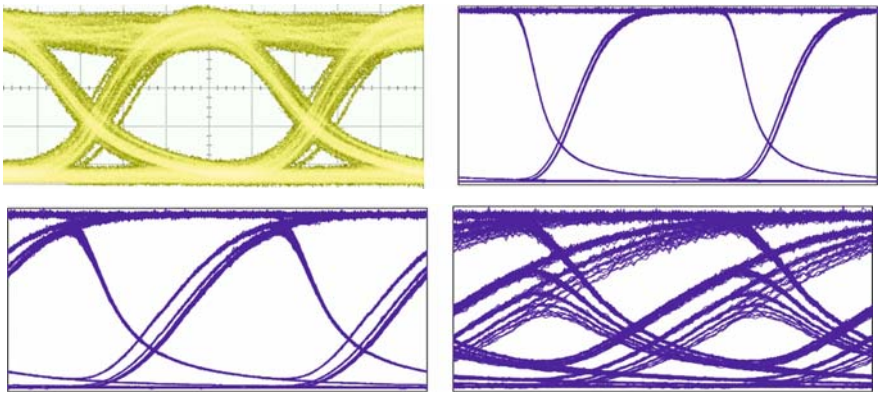


Figure. 4. Top: 1.25 Gb/s experimental and simulated eye diagrams. Bottom: 2.5 Gb/s and 5 Gb/s simulated eye diagrams.

ACKNOWLEDGEMENTS

This work was funded by Science Foundation Ireland Investigator Grant 09/IN.1/I2641.

REFERENCES

[1] E. Wong, *et al.*: Directly modulated self-seeding reflective semiconductor optical amplifiers as colorless transmitters in wavelength division multiplexed passive optical networks, *J. Lightw. Technol.*, vol. 25, pp. 67-74, Jan. 2007.

[2] M. J. Connelly: Wide-band Steady-State Numerical Model and Parameter Extraction of a Tensile-Strained Bulk Semiconductor Optical Amplifier: *IEEE J. Quantum Electron.*, vol., 43, pp. 47-56, Jan. 2007.

[3] M. J. Connelly: Wideband dynamic numerical model of a tapered buried ridge stripe semiconductor optical amplifier gate: *Proc. IEE Circuits Devices Syst.*, 2002, vol. 149, pp. 173–178, Dec. 2002.

[4] A. E. Kelly *et al.*: High performance polarisation independent reflective semiconductor optical amplifiers in the S, C, and L bands, *IEEE J. Sel. Area. Comms.*, vol. 28, pp. 943-948, Aug. 2010.

[5] M. J. Connelly: Band-gap shrinkage calculations and analytic model for strained bulk InGaAsP: *Mater. Res. Express*, vol. 2, pp. 026201, Feb. 2015.

Study of Silicon Waveguides with All-dielectric Metamaterial Cladding by Numerical Simulations

(Student paper)

Andraž Debevc, Janez Krč and Marko Topič
[1] University of Ljubljana, Faculty of Electrical Engineering, Tržaška cesta 25, 1000 Ljubljana - Slovenia
e-mail: andraz.debevc@fe.uni-lj.si

ABSTRACT

By introducing all-dielectric metamaterials into optical waveguide structures, the cross-talk between waveguides can be reduced enabling denser integration in photonic integrated circuits. In this work we present results of Finite Element Method simulations to optimize the metamaterial-based cladding of the so called e-skid waveguides in order to achieve the longest possible coupling length. We show that e-skid waveguides can have significantly longer coupling length compared to strip waveguides due to reduced skin depth. We optimize the Si based metamaterial structure in terms of number of silicon ridges, period and fill factor of silicon and show that results strongly depend on the chosen surrounding material (air or silicon dioxide).

Keywords: All-dielectric metamaterials, silicon photonics, e-skid waveguides, cross-talk, Finite Element Method

1. INTRODUCTION

One of the key goals of photonic integration is to scale down the components and connections which enables increased functionality of devices and reduced packaging costs. Silicon (Si) photonics enables dense integration of optical waveguides (WGs), with typical dimensions at telecom wavelengths of only 450 nm x 220 nm, due to large refractive index contrast of Si and SiO_2 [1]. Cross-talk between two waveguides is one of the major factors limiting further miniaturization of Si photonic integrated circuits (PIC). It limits the minimal separation between two WGs, as well as prevents further reduction of WG width.

One way to overcome these issues is to use all-dielectric metamaterials as the WG cladding. By periodically exchanging two dielectric materials with different refractive indexes we can fabricate a composite material which can be approximated with a homogenous anisotropic material, if the period is shorter than the wavelength of light. Recently a phenomenon of relaxed total internal reflection at the interface of isotropic and anisotropic material has been demonstrated [2]. By increasing the permittivity of one material in the direction parallel to the interface, the skin depth of electric field can be significantly reduced. This phenomenon is used to design extreme skin-depth (so-called e-skid) WGs, which have the potential to reduce cross-talk and further miniaturize WGs subsequently increasing integration density. Recently the first E-skid WG has been experimentally demonstrated on silicon integration platform consisting of a Si core and a Si/Air (or SiO_2) metamaterial cladding [3]. It has been shown that the coupling length of TE-like mode (length at which all the power from one WG is transferred to the other WG) can be significantly reduced by designing the side cladding from periodical subwavelength silicon ridges.

The performance of E-skid WGs relies heavily on the parameters of the metamaterial cladding such as period (*P*), fill factor of Si *(ff)* and number of ridges. In this contribution we show the results of a numerical study to optimize the E-skid WG so that cross-talk can be reduced as much as possible for the case of air and SiO_2 surrounding.

2. METHODS

We applied Finite Element Method (FEM) simulations of E-skid WGs and systems of two WGs using COMSOL Multiphysics program package. A 2-D mode analysis was performed to find the propagating modes and electric fields in the cross-section of the WG. The coupling lengths were calculated with the eigenmode expansion method (EME) [4] from effective indexes of the symmetric and antisymmetric super-modes of the system of two WGs.

3. RESULTS

All simulated WGs have a constant silicon thickness (WG height) of 220 nm. The core width was chosen to be 350nm. The wavelength at which we performed simulations was set to 1550 nm. The substrate is assumed to be buried oxide from SiO_2 and top material is either air or SiO_2. We assumed a minimal lateral feature size of fabrication process to be 50 nm. Figure 1 shows normalized *x*-component of electric field of the first TE-like mode of a strip WG (a) and E-skid WG (b) with 4 Si ridges on each side and air as the surrounding material. The period (*P*) is set to 100 nm in this simulation. It can be observed that the evanescent electric field outside of the core of the E-skid WG is confined in the wells between Si ridges. In comparison to the strip WG, the evanescent field of

the E-skid WG is observed to be confined closer to the WG core. This can better be seen from Fig. 2a where x-components of electric field in the centre cross-section of the WG are plotted. The plotted fields are scaled to the constant mode power of 1mW. We can see that electric fields of E-skid WGs are lower outside of WG core compared to that of the strip WG. If we only chose two Si ridges, the electric field outside of WG core is stronger than if we choose 4, however, it is still significantly smaller than electric field of the strip WG. In case of a SiO_2 surrounding material (Fig. 2b) similar effects can be observed, although they are less pronounced due to higher refractive index of SiO_2.

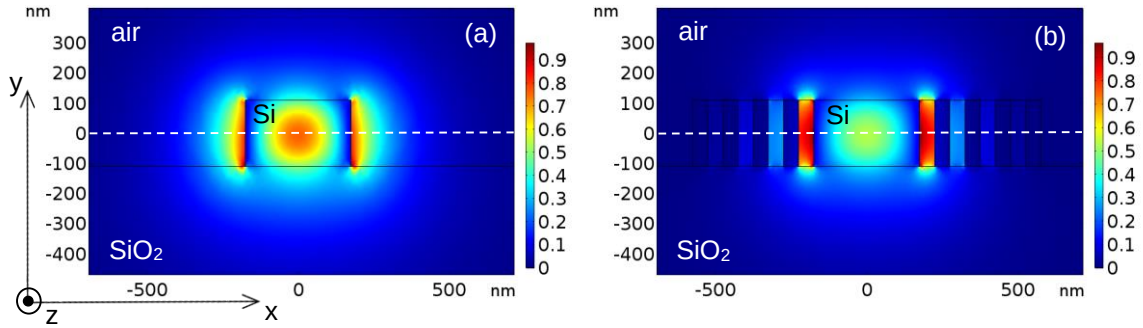


Figure 1. Normalized x-component of electric field of the first TE-like mode of a strip WG (a) and e-skid WG (b). Top material is air in both cases. Period of metamaterial cladding of E-skid WG is 100 nm and number of Si ridges is 4.

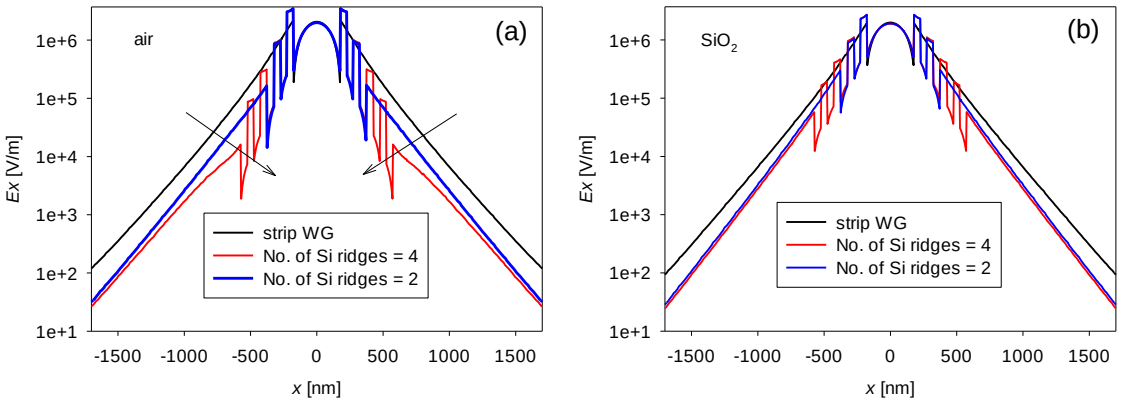


Figure 2. X-components of electric field of the strip and e-skid WGs with air (a) and SiO_2 (b) as the surrounding material in the middle cross section of the WG (as marked with white dashed line in Fig.1). All fields are scaled to the constant mode power of 1 mW.

Further we simulate the system of two adjacent E-skid WGs and check the effects of the geometrical parameters of the metamaterial structure on the WG coupling length L_x. The L_x presents the required length of the WG for signal to transfer to adjacent WG. In our case it presents a figure of merit of integration density of WGs on a photonic chip. Larger the value of L_x is, lower is the signal cross-talk and higher integration density is possible. We chose the geometry with centre to centre separation of WGs to be 1.2 µm.

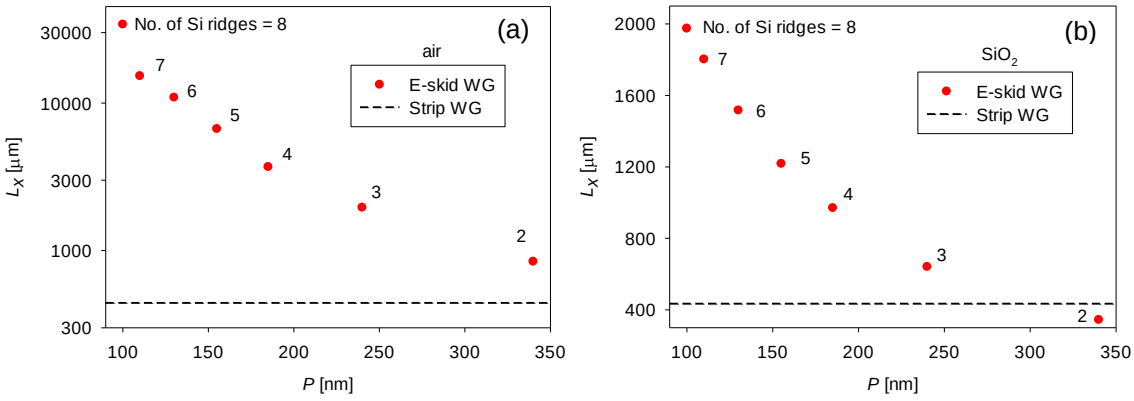


Figure 3. Coupling length of e-skid WGs with air top material in logarithmic scale (a) and SiO_2 top material in linear scale (b) at different periods of metamaterial. Numbers of Si ridges between WGs are also indicated on the graphs.

Figure 3 shows L_x of E-skid WGs when P is varied. Coupling lengths were calculated only at discrete periods at which the gap between WG cores was fully and symmetrically filled with the metamaterial. Number of ridges

had to be decreased accordingly as specified by numbers given inside the graph (indicating the total number of ridges between WG cores). L_x of WGs with air as the surrounding material was calculated to be 442 µm and 34 mm for strip and E-skid WG with P = 100 nm respectively. L_x of E-skid WGs with P = 100 nm was increased by a factor of 77 in case of air as the surrounding material and by a factor of 4.5 in case of SiO_2 as the surrounding material compared to strip WGs. As expected from simulations of single WG system, L_x is decreasing with longer P and reduced number of Si ridges. In case of SiO_2 as the surrounding material, the performance of E-skid WG with only one ridge of metamaterial is worse than the performance of the strip WG.

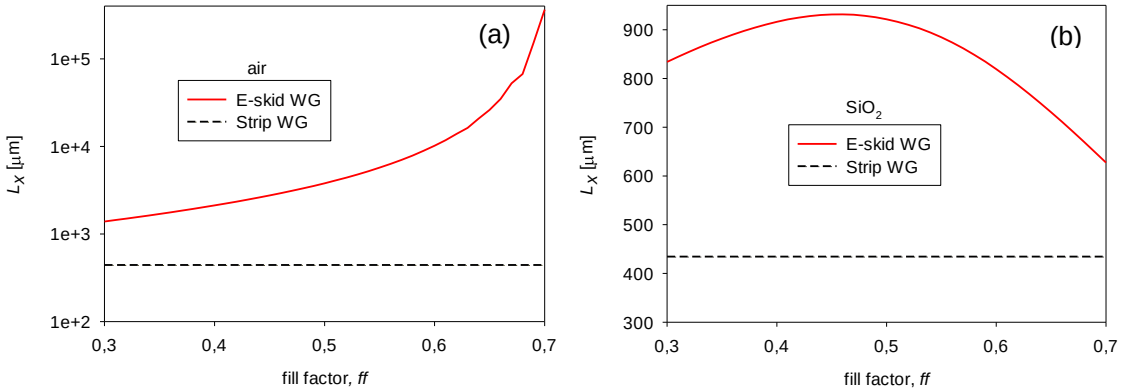


Figure 4. Coupling length of e-skid WGs with air top material in logarithmic scale (a) and SiO_2 top material in linear scale (b) in dependence of fill factor (fraction of Si) of metamaterial. P=185 nm and number of periods is 2.

We also studied how fill factor (*ff*) of metamaterial (fraction or duty cycle of Si material) influences the coupling length. We present the case with the P of 185 nm (2 ridges of Si on each side) which enables us to vary the *ff* from 0.3 to 0.7 without violating the chosen minimal feature size. Fig. 4 shows L_x in dependence of *ff* for the two surrounding materials. In case of air as the surrounding material (Fig. 4a), the L_x increases drastically when *ff* is increased. In case of 2 ridges of Si (P = 185 nm) and *ff* of 0.7, the coupling length is 36 cm. By increasing the fill factor, the permittivity in the z-direction increases, which further reduces the skin depth. This indicates that we can in some cases improve performance of E-skid WGs, by increasing the period and reducing number of Si ridges in order to increase the fill factor. The same effect cannot be observed in case of a SiO_2 top material (Fig.4b). Here the L_x is decreasing, if we increase the *ff* above 0.5. By increasing the fill factor, the evanescent field decays faster, however close to the WG core it is locally larger than in case of *ff* of around 0.5, which is the origin of the unexpected behaviour.

4. CONCLUSIONS

We performed FEM simulations of silicon waveguides with metamaterial cladding - E-skid WGs - and evaluated the cross-talk between two WGs. We studied how changing number of Si ridges, period and fill factor of silicon of the metamaterial cladding influences the coupling length for the case of air and SiO_2 surrounding. It was determined that in some cases (air as the surrounding material) reducing number of Si ridges and increasing the period of the metamaterial to enable larger fill factor of silicon, can result in a significantly longer coupling length. This is not the case when top material is SiO_2 with higher refractive index, where the effect of duty cycle is reversed. Therefore when designing E-skid WGs, care needs to be taken to optimize the metamaterial cladding in order to achieve the lowest possible cross-talk.

ACKNOWLEDGEMENTS

A. Debevc acknowledges Slovenian Research Agency (ARRS) for funding his PhD studies, all authors for funding the Research Programme P2-0197.

REFERENCES

[1] W. Bogaerts *et al.*, “Nanophotonic waveguides in silicon-on-insulator fabricated with CMOS technology,” *J. Light. Technol.*, vol. 23, no. 1, pp. 401–412, Jan. 2005.

[2] S. Jahani and Z. Jacob, “Transparent subdiffraction optics: nanoscale light confinement without metal,” *Optica*, vol. 1, no. 2, pp. 96-100, Aug. 2014.

[3] S. Jahani *et al.*, “Controlling evanescent waves using silicon photonic all-dielectric metamaterials for dense integration,” *Nat. Commun.*, (2018) 9:1893 May 2018. DOI: 10.1038/s41467-018-04276-8.

[4] L. Chrostowski and M. Hochberg, *Silicon photonics design: from devices to systems*, 2015. Cambridge, UK: Cambridge University Press.

O-band DAC-less PAM-4 generation with a silicon dual-drive Mach-Zehnder Modulator

(Student Paper)

Lucas Deniel[1], Mathilde Gay[2], Diego Pérez-Galacho[1,3], Charles Baudot[4], Laurent Bramerie[2], Oskars Ozolins[5], Fréderic Boeuf[4], Laurent Viven[1], Christophe Peucheret[2], Delphine Marris-Morini[1]

[1] Centre de Nanosciences et de Nanotechnologies, CNRS, Univ. Paris-Sud, Université Paris-Saclay, 91120 Palaiseau, France

[2] Univ Rennes, CNRS, FOTON – UMR 6082, F-22305 Lannion, France

[3] now at : ITEAM research institute, Universitat Politècnica de València, Camino de Vera s/n, 46022, Valencia, Spain

[4] ST Microelectronics, 850 rue Jean Monnet, 38920 Crolles, France

[5] Networking and transmission Laboratory, RISE AB, Kista, Sweden

e-mail: lucas.deniel@u-psud.fr

ABSTRACT

4-level pulse amplitude modulation (PAM-4) is the chosen modulation format for next generation optical short-reach data communications such as intra-datacenter communications. On-chip generation of PAM-4 signals is possible using a single dual-drive Mach-Zehnder modulator (MZM). By driving the modulator with two voltage-unbalanced binary signals it is possible to avoid any power hungry electrical digital-to-analog converter (DAC). PAM-4 signal generation at 20 Gbit/s is demonstrated using a silicon dual-drive MZM in the O-band. A bit error rate (BER) of 3.8×10^{-3} is measured at -6 dBm input power.

Keywords: Silicon, Mach-Zehnder modulator, PAM-4, O-band, DAC-less.

1. INTRODUCTION

For the next generation of intra-datacenter and short-reach data communications, 4-level pulse amplitude modulation (PAM-4) has been chosen as a convenient format to fulfill the increasing spectral efficiency requirements. Silicon photonics is a promising technology for these applications as it provides economical, flexible, and low-power solutions, in addition to its mature complementary metal-oxide semiconductor (CMOS) fabrication process and the possibility of co-integration with electronics [1, 2].

Usually, PAM-4 signal generation is done in the electrical domain, and this signal is used to drive the electro-optical modulator. In this case, power hungry digital-to-analog converters (DAC) are needed to convert 2-level non-return-to-zero (NRZ) data-streams into 4-level ones. For this reason, the generation of PAM-4 signals in the optical domain was proposed and successfully demonstrated using various structures of silicon modulators on which two different NRZ binary sequences were directly applied. These structures are sometimes referred to as optical DACs, and most of these demonstrations were done in the C-band [3-5]. Interestingly, the well-known dual-drive Mach-Zehnder modulator (MZM) structure is used for classical OOK modulation, but it was demonstrated that it could also be used for quadrature phase shift keying (QPSK) and PAM-4 generation, making it an interesting choice for the evolving transmission standards. [6, 7]

We demonstrate optical PAM-4 generation at 20 Gbit/s using an O-band silicon dual-drive MZM. In the first part, we introduce the MZM design and the phase shifter characteristics. A numerical model is then used to find out the peak-to-peak voltages to apply on the MZM arms to obtain 4 equally spaced intensity levels while benefiting from the transmission full dynamic range. Experimental results are then reported, including bit error rate measurements.

2. MODULATOR DESIGN AND PHASE SHIFTER CHARACTERISTICS

The device fabrication was carried out by ST-Microelectronics on a 300-mm silicon-on-insulator (SOI) technological platform [8]. The optical access of the chip are ensured by grating couplers. The combiner and splitter of the MZM structure are 3-dB 1×2 multimode interference (MMI) based couplers. Each arm contains a phase shifter which consists in a 1-mm-long lateral PN junction embedded in a rib waveguide, operating in depletion regime. The waveguide height is 300 nm and its width is 400 nm, allowing propagation of the fundamental TE mode, while the slab part is 50-nm thick. The targeted doping concentrations are 5×10^{17} cm^{-3} for the P region and 4.5×10^{17} cm^{-3} for the N region. Higher doping concentrations of about 10^{19} cm^{-3} are used near the electrical contacts to reduce the access resistance, thus enhancing the modulator bandwidth. Traveling wave coplanar electrodes on the surface of the chip are used for radio-frequency (RF) waves propagation and metallic

strips are used as resistors (heaters) close to each arm to thermally tune the static operating point of the MZM, by applying a DC voltage.

Static characterizations of the phase shifter efficiency were made experimentally by tracking the resonance wavelengths of a ring resonator, as it allows a precise measurement of the phase variation within the waveguide as a function of the applied voltage. The measured phase shifter efficiency varies from 1.1 V cm at -0.5 V to 1.4 V cm at -7 V. A 17-GHz electro-optical bandwidth was measured on the MZM using an Agilent 86030A 50 GHz Lightwave Component Analyzer.

The phase shifter insertion loss was estimated as a function of the voltage through a numerical model. First, carrier concentrations within the PN junction as a function of the applied voltage are obtained using an electrical simulation. Soref model is then used to calculate the corresponding local absorption coefficients, and a mode solver is finally used to estimate the total effective attenuation factor of the waveguide. Loss estimation varies from 1.8 dB mm^{-1} at 0V to 1.1 dB mm^{-1} at -7V.

3. PAM-4 MZM MODEL AND COMPARISON WITH EXPERIMENTAL RESULTS

As the effective index change is not linear with the applied voltage, and as the insertion loss depends on the applied voltage, finding the dynamic voltage amplitudes to apply on each arm to obtain 4 equally-spaced intensity levels while maximizing the extinction ratio in the optical domain is not straightforward. For this reason, the following equations are numerically implemented to model the MZM:

$$E_n = \frac{E_{\mathrm{IN}}}{\sqrt{2}} \exp\left(-\left(\alpha_{eff} + \Delta\alpha_{eff}(V_n)\right)L\right) \exp\left(\mathrm{j}\frac{2\pi}{\lambda}\left(n_{eff} + \Delta n_{eff}(V_n)\right)L\right) \quad (1)$$

$$E_{\mathrm{OUT}} = \frac{E_1 e^{j\frac{\theta_H}{2}} + E_2 e^{-j\frac{\theta H}{2}}}{\sqrt{2}} \quad (2)$$

where E_{IN} is the input electric field, E_n is the electric field at the output of arm labelled n, E_{OUT} is the output electric field, L is the phase shifter length, λ is the wavelength, θ_H is the static phase shift introduced by thermal heaters, α_{eff} and n_{eff} are the effective attenuation factor and refractive index of the optical mode, respectively, $\Delta\alpha_{eff}(V_n)$ and $\Delta n_{eff}(V_n)$ are the effective attenuation factor change and refractive index change of the optical mode, respectively, under the application of the voltage V_n on the phase shifter labelled n. $\alpha_{eff} + \Delta\alpha_{eff}(V_n)$ is estimated and $\Delta n_{eff}(V_n)$ is calculated as described in the previous section.

Fig. 1(a) shows the PAM-4 levels obtained with the MZM numerical model by applying peak-to-peak voltages of 4 V on one arm of the MZM and 7 V on the other. Fig. 1(b) shows an eye diagram obtained experimentally by applying the same voltages to the real silicon MZM, biased at the quadrature point. The matching of level spacings between the two figures demonstrates the numerical model accuracy.

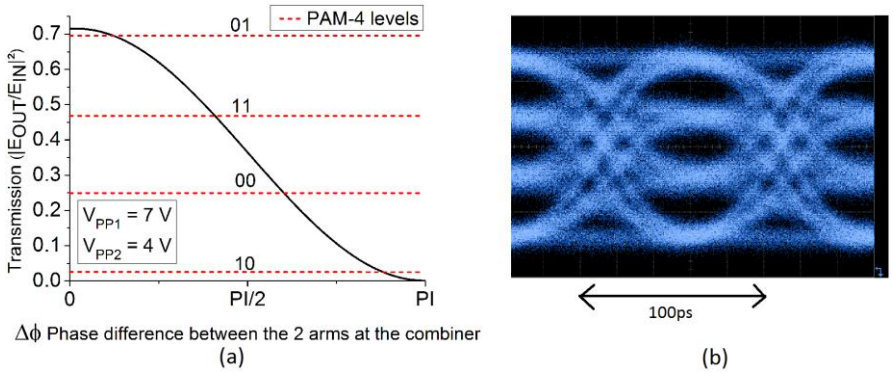


Figure 1. (a) Obtained PAM-4 levels by applying a 4-V peak-to-peak voltage on one arm and 7-V peak-to-peak voltage on the second arm on the silicon MZM numerical model. (b) Experimental eye diagram obtained after applying the same peak-to-peak voltages on the silicon MZM.

4. BER MEASUREMENTS

A BER measurement is conducted to evaluate the MZM PAM-4 performance under this dual-driving method. For this experiment, light is produced by an external cavity laser at 1310 nm and input to the device after being amplified with a semiconductor optical amplifier (SOA). At the output of the chip, the modulated beam is amplified with a praseodymium doped fiber O-band amplifier and split in two paths with a fibered directional coupler. One half of the power is sent to a 25-GHz oscilloscope displaying the eye-diagram in real time. The other half is sent to a 40-GHz photodiode and the converted electrical signal goes through a 35-GHz amplifier before being received

by the error counter of a BER tester. Two complementary pseudo random binary sequences (PRBSs) are generated electrically at a 10-Gbit/s rate. One of them is delayed by 200 ps with an RF tunable delay line, and both signals are amplified with tunable gain RF amplifiers. A -4-V DC voltage is added on both lines with DC bias tees to bias the PN junction in reverse. The two driving signals are then injected into the RF electrodes of the MZM via RF probes before being absorbed by 50 Ω terminations loaded after DC blocks on the electrical output. The peak-to-peak voltages are set to 4 V on one arm and 7 V on the other one by tuning the RF amplifier gains. The optical power received on the photodiode is swept from -8.5 to 0.5 dBm for the BER measurement. Fig. 2 shows the obtained BER values as a function of the received power.

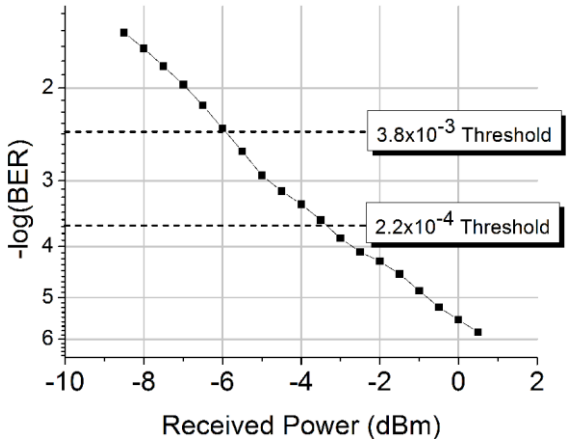


Figure 2. Measured O-band PAM-4 BER with the silicon MZM driven by a 7-V_{PP} and a 4-V_{PP} PRBS as a function of the received optical power.

It can be seen that the BER is under the 3.8×10^{-3} hard-decision forward-error-correction (HD-FEC) threshold for a received power of -6 dBm and under the 2.2×10^{-4} KP4 threshold for a received power of -3.4dBm.

5. CONCLUSIONS

A 20-Gbit/s PAM-4 signal was generated at 1310 nm using a silicon dual drive MZM driven by two different NRZ binary signals. After an introduction of this modulator design and characteristics, a numerical model was presented and used to find out the optimum voltages to apply to each arm of the MZM for PAM-4 generation. Finally, a BER under the HD-FEC threshold of 3.8×10^{-3} was measured for a received power of -6 dBm using the silicon MZM as an optical PAM-4 generator.

ACKNOWLEDGEMENTS

This work was supported by the European project Cosmicc (H2020-ICT-27-2015-688516).

REFERENCES

[1] IEEE P802.3bs 400 GbE Task Force, http://www.ieee802.org/3/bs/index.html.
[2] W. Shi *et al.*: Silicon photonic modulators for PAM transmissions, *J. Opt.*, vol. 20. 083002, July 2018.
[3] A. Roshan-Zamir *et al.*: A 40Gb/s PAM4 optical DAC silicon microring resonator modulator transmitter, *in Proc. MWSCAS 2017*, Boston, MA, 2017, pp. 1089-1092.
[4] D. Patel *et al.*: Silicon photonic segmented modulator-based electro-optic DAC for 100Gb/s PAM-4 Generation, *IEEE Photon. Technol. Lett.*, vol. 27. pp. 2433-2436, Dec. 2015.
[5] R. Li *et al.*: Silicon photonic ring-assisted MZI for 50Gb/s DAC-less and DSP-free PAM-4 transmission, *IEEE Photon. Technol. Lett.*, vol. 29. pp. 1046-1049, June 2017.
[6] L. Zheng *et al.*: Silicon PAM-4 optical modulator driven by two binary electrical signals with different peak-to-peak voltages, *Opt. Lett.*, vol. 42. pp. 2213-2216, June 2017.
[7] D. Pérez-Galacho *et al.*: QPSK modulation in the O-band using a single dual-drive Mach-Zehnder silicon modulator, *J. Lightw. Technol.*, vol. 36. pp. 3935-3940, Sept. 2018.
[8] C. Baudot *et al.*: Daphne silicon photonics technological platform for research and development on WDM applications, *in Proc. SPIE 9891*, 2016, 98911D.

Tunable optoelectronic oscillator based on silicon micro-ring resonator

(Student paper)

Phuong T. Do[1], Carlos Alonso-Ramos[2], Xavier Le Roux[2], Laurent Vivien[2], Isabelle Ledoux[1], Eric Cassan[2] and Bernard Journet[1]

[1] LPQM (CNRS UMR-8537) École normale supérieure Paris-Saclay, Centrale Supelec, Université Paris-Saclay, 61 avenue du Président Wilson, 94235 Cachan Cedex, France

[2] C2N (CNRS UMR-9001), Univ. Paris-Sud, Université Paris-Saclay,10 Boulevard Thomas Gobert, 91120 Palaiseau, France

e-mail: thi-phuong.do@ens-paris-saclay.fr

ABSTRACT

A new silicon optoelectronic oscillator (OEO) system is proposed and experimentally demonstrated. The proposed OEO, generates the microwave signal by beating the un-modulated and amplitude-modulated versions of the same laser source. The drop port of a silicon micro-resonator is used to select one of the side band lobes generated by the amplitude modulation, thus serving as frequency selective element in the OEO. In this scheme, the microwave frequency generated is determined by the wavelength separation between the laser and the ring resonance. Thus, seamless microwave frequency tuning can be achieved just by sweeping the wavelength of the laser source. A proof-of-concept demonstration is implemented, experimentally showing microwave frequency generation in the range from 5.9 GHz to 18.2 GHz.

Keywords: Silicon photonic, function integration, silicon microring resonator, optoelectronic oscillator.

1. INTRODUCTION

The generation of broadband and low noise microwave and millimetre wave signals is of paramount importance for a plethora of applications, including among other, radar, wireless communications, optical signal processing, warfare systems, etc [1]. Among various types of microwave and millimetre wave generation approaches, the optoelectronic oscillator (OEO) is a particularly interesting solution due to its capability to provide spectrally pure and wideband tunable signals [1]. However, the tunability of the conventional OEO is limited by the tunability of the microwave filter inside the loop, especially for high operation frequency. Microwave photonic filters (MPF) are a promising alternative to overcome this limitation, allowing reconfigurable microwave signal generation in OEO with a wide tuning range [2,3]. Moreover, the progress of integrated microwave photonics (IMWP) [4] provides now a solid framework for the possible full integration of OEOs. Several efforts in this direction have been demonstrated recently [5-7]. M. Merklein et al. in [5] demonstrated an ultrawide frequency tunable signals up to 40 GHz by using OEO based on Stimulated Brillouin Scattering (SBS). However, this system is complicated as it requires the use of two lasers. In [6], integrated optoelectronic oscillator based on InP has been investigated, but the frequency tunable range is limited at around 20 MHz. Silicon on insulator (SOI) is also being investigated. Driven by its immense potential for mass deployment and relying on several available existing building blocks (e.g. all-Si modulators, Ge on Si detectors, etc) [8-10], SOI is considered as a promising solution to implement ultra-compact OEO that could be fabricated in leveraging large volume fabrication processes, high complexity and low cost. In this context, a tunable OEO based on silicon micro-disk resonator with a frequency tuning range from 3 to 6.8 GHz was proposed and demonstrated [7]. This OEO relies on a phase-modulator and a notch filtering provided by the micro-disk in an all-pass configuration.

Here, we propose a new approach for the implementation of Si OEO that allows for wideband tunability in the microwave signal generation. The oscillation signal is created by the beating between the optical source and one of the sideband lobes generated by intensity modulation. This sideband lobe is selected by a silicon add-drop ring resonator (RR) working as an optical bandpass filter. We experimentally show that by tuning the wavelength of the source, the microwave frequency generated by the OEO can be tuned within the range from 5.9 to 18.2 GHz, which is limited by the elements available in the experimental setup.

2. PRINCIPLE OF OPERATION

The basic schematic and principle of operation of the proposed OEO are depicted in Fig. 1. In the proposed tunable OEO, the optical signal coming from laser source is separated in two branches, one is sent directly to photo-detector (PD) while the other is sent to an intensity modulator (IM). Initially, the modulator signal gets just seeded by white noise existing inside the loop. This signal is then passing through an add-drop RR before being

sent to the PD. At the initial stage, before closing the loop, point (1) in Fig. 1b, the signal entering the PD comprises the laser source and resonances of the RR. If the laser wavelength and one of the resonances of RR have the same phase and the distance between them is in close proximity in working range of the loop, then a beating of frequency will be generated. This beating signal is converted as an RF frequency (f_1) through PD (point (2)). The generated RF signal is sent back to modulator in order to close the loop. The output signal of the modulator now can be seen as in point (3), in which one of the side band of the modulation signal is matched with the resonance peak of the RR. The RR now can be viewed as an optical filter, select only one sideband lobe of the modulated signal. The signal goes to the PD at the 2nd round trip, as denoted in point (4), then again create an RF signal with frequency f_1 at the output of the PD. Since this point, the loop is oscillating with a frequency f_1.

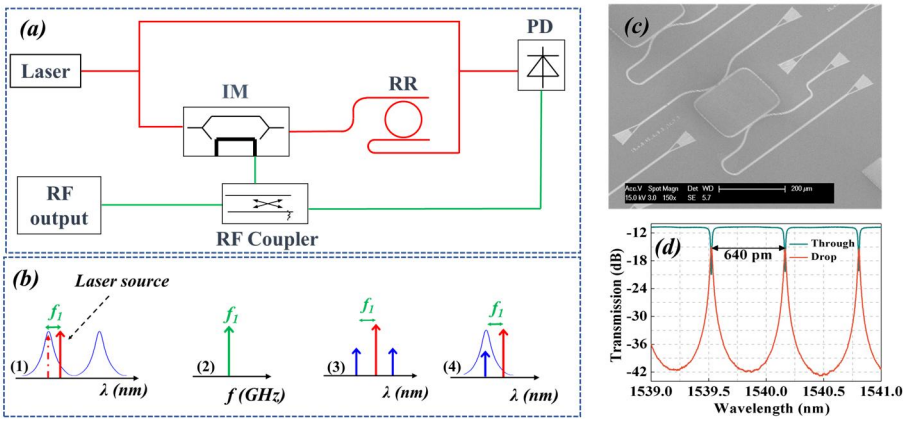


Figure 1. Basic schematic (a) and principle of operation (b) of the proposed tunable OEO, SEM of the fabricated ring resonator (c) and the optical transmission of the device (d) (coupling gap: 300nm, coupling length: 4.5 μm). IM: Intensity modulator, RR: Ring resonator, PD: Photo-detector.

The main idea behind this approach is to control the frequency of the microwave signal by the wavelength spacing between the laser source and the resonance of resonator. Since this spacing can be changed either by sweeping the wavelength of the laser or by shifting the resonance peak of the RR, this approach yields simple tunability mechanism.

3. EXPERIMENTAL RESULTS.

For the proof-of-concept demonstration of the proposed OEO, we integrate only the micro-ring resonator in the silicon chip. The RR is an add-drop silicon ring resonator, implemented with 450-nm-wide strip waveguide, fabricated from SOI wafer with 220 nm thick Si thin film on top of a 3 μm buried oxide layer. The fabrication result shows in Fig.1c. Fig.1d illustrates for optical transmission of the device. We obtained optical transmission with free spectral range FSR at FSR_λ = 640 pm, corresponding with $FSR_{fre} \approx 77$ GHz. Optical quality factor Q_{opt} of the RR has been investigated by fitting the resonance peak through the Lorentzian function, by doing so, the Q_{opt} at 8.1×10^4 has been obtained.

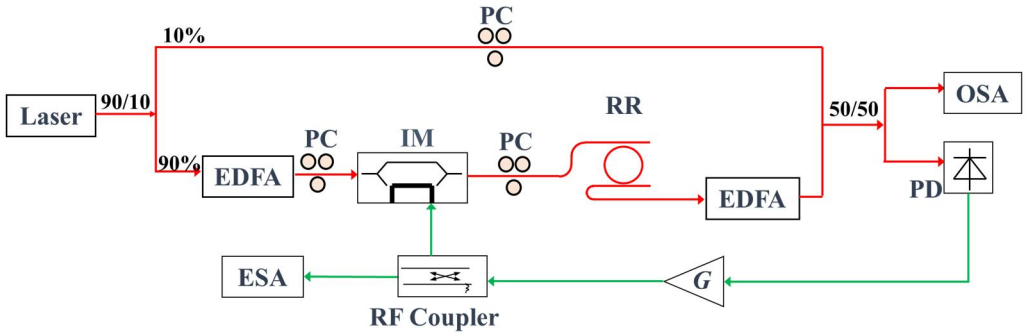


Figure 2. Experiment setup for tunable OEO. EDFA: Erbium doped amplifier, PC: Polarization controller, OSA: Optical spectrum analyser, G: RF amplifier and ESA: Electric spectrum analyser.

Figure 2 shows the experimental setup used to characterize the OEO. A 90/10 optical splitter is used to separate the light source from tuneable laser. 90 % of the optical power is sent to the Erbium doped amplifier (EDFA) followed by the IM, RR and a second EDFA. Signal at the output of second EDFA is combined with the other 10 % of the optical source (see Fig. 2) using 50/50 optical combiner. In the experiment setup, the polarization controller (PC) has been used in order to proper control the polarization matching between the laser source and the signal at the output of the second EDFA. At the output of the optical combiner, one arm is connected with the

optical spectrum analyser (OSA) in order to read the laser or resonance wavelength while the other is connected with the PD. The final setup includes RF amplifier, RF coupler and electrical spectrum analyser (ESA).

The oscillation signal then is generated by placing the wavelength of the laser close to one of the resonances of the ring. Fig.3a illustrates the electrical spectrum of the generated microwave signal at 5.9 GHz with resolution bandwidth of 2.2 kHz and span of 6 MHz.

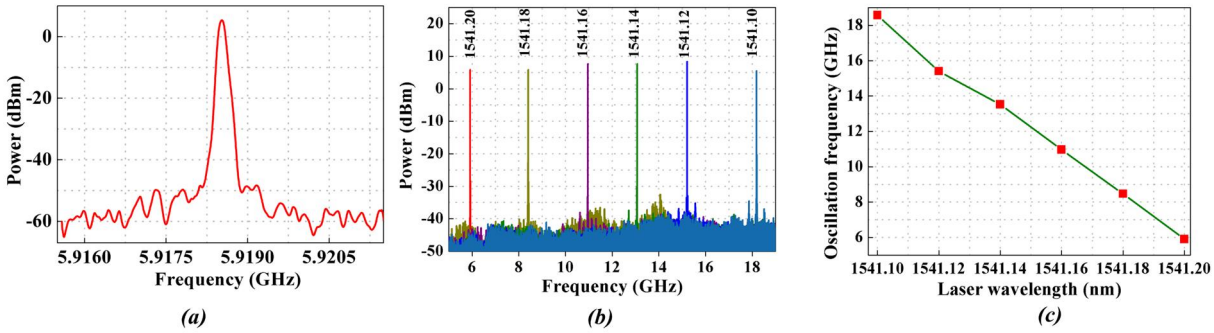


Figure 3. Oscillation spectrum of generated signal (a) and oscillation signal change with different laser wavelength (b) and plot of the oscillation frequency depend on laser wavelength.

In order to quantify the tunability capability of the OEO, we sweep the wavelength of the laser and collect the microwave signal in the ESA. Fig.3b shows the measured oscillation spectrum with different laser wavelengths, with a tuning range of 12.3 GHz, between 5.9 GHz and 18.2 GHz. Fig.3c illustrates the linear variation of the oscillation signal as a function of the laser wavelength. In this case, the RR resonance is placed in the right side of the laser, therefore, the wavelength spacing between laser and resonance peak is decreased when the laser wavelength is increased, thus resulting in the decrease of the frequency of the microwave signal.

4. CONCLUSION.

As a conclusion, a novel OEO, based on add-drop Si micro-ring resonator, providing wideband tunability in the frequency of the microwave signal generated. The oscillation signal is created via the beating between a laser source and a sideband lobe produced by the intensity modulation of the same laser. We show experimentally that by changing the wavelength spacing between the optical source and the resonance wavelength, a microwave signal is generated with a tuneable frequency range from 5.9 GHz to 18.2 GHz. These results are an important step towards the implementation of tuneable OEO based on silicon photonics.

ACKNOWLEDGEMENTS

This work is included in the MORSE project supported by the LaSIPS (Paris-Saclay University). The sample fabrication has been performed at the Plateforme de Micro-Nano-Technologie/C2N, which is partially funded by the "Conseil Général de l'Essonne". This work was also partly supported by the French RENATECH network.

REFERENCES

[1] W. Li *et al.,* An Optically Tunable Optoelectronic Oscillator, *J. Light. Technol.*, vol. 28, no. 18, pp. 2640–2645, 2010.

[2] J. Capmany *et al.,* Microwave photonics combines two worlds, *Nat. Photonics*, vol. 1, no. 6, pp. 319–330, 2007.

[3] J. Zhang *et al.,* Tunable Optoelectronic Oscillator Incorporating a Single Passband Microwave Photonic Filter, *IEEE Photonics Technol. Lett.*, vol. 26, no. 4, pp. 326–329, 2014.

[4] D. Perez *et al.,* Integrated microwave photonics, *Laser & Photonics Rev.*, pp. 1–30, 2012.

[5] M. Merklein *et al.,* Widely tunable, low phase noise microwave source based on a photonic chip, *Opt. Lett.*, vol. 41, no. 20, p. 4633, 2016.

[6] J. Tang *et al.,* Integrated optoelectronic oscillator, *Opt. Express*, vol. 26, no. 9, pp. 554–557, 2018.

[7] Z. Weifeng *et al.,* Silicon Photonic Integrated Optoelectronic Oscillator for Frequency-Tunable Microwave Generation, *J. Light. Technol.*, vol. 36, no. 19, pp. 4655–4663, 2018.

[8] N. Li *et al.,* Monolithically integrated erbium-doped tunable laser on a CMOS-compatible silicon photonics platform, *Opt. Express*, vol. 26, no. 13, pp. 16200-16211, 2018.

[9] C. Xiong *et al.,* A monolithic 56 Gb / s silicon photonic pulse-amplitude modulation transmitter, *Optica*, vol. 3, pp. 1060–1065, 2016.

[10] S. Lischke *et al.,* −1 V bias 67 GHz bandwidth Si-contacted germanium waveguide p-i-n photodetector for optical links at 56 Gbps and beyond, *Opt. Express*, vol. 24, no. 5, pp. 4622–4631, 2016.

Development of high index contrast waveguide platform for fluorescence based optical nanoscopy

Firehun Tsige Dullo[1], Øystein Ivar Helle[1], David Andre Coucheron[1], Marcel Lahrberg[1], Jean-Claude Tinguely[1] and Balpreet Singh Ahluwalia[1]*

[1] Department of Physics and Technology, UiT, The Arctic University of Norway, Klokkargådsbakken N-9019, Tromsø, Norway

e-mail: balpreet.singh.ahluwalia@uit.no

ABSTRACT

High-index contrast (HIC) based photonics integrated circuit platforms have played a vital role in integrating complex optical components in a small footprint. Here, we report chip-based nanoscopy (CbN) by using HIC waveguide platforms. In CbN, the waveguide chips generate, deliver and steer the laser illumination pattern. By using a nanoscopy technique of single molecule localization, we demonstrate CbN with a resolution of 50 nm. Furthermore, we show that chip-based structured illumination microscopy can overcome the 2× resolution enhancement set by the objective launch in conventional linear SIM.

Keywords: High index contrast, Silicon nitride, optical nanoscopy, super-resolution microscopy.

1. INTRODUCTION

Photonics integrated circuit (PIC) platforms have played a central role in miniaturizing and integrating complex optical components in a small footprint [1]-[5]. Among previously reported works on PIC platforms, those that are based on high index contrast (HIC) have gained the most attention. HIC waveguides have strong confinement of the light inside the waveguide because of the high refractive index contrast between the waveguide and the cladding material. HIC material also allows fabricating of optical functions in much smaller footprint, due to tight bend radii. Tight confinement of light inside HIC waveguide also enables fabrication of thin (e.g. 100 -100 nm thickness) optical waveguide enhancing the intensity of the evanescent field at the surface of the waveguide. Silicon on insulator (SOI) photonics waveguide platform, which is HIC waveguide platform, is a well-established technology. However, this technology is limited since silicon is only transparent above 1.1µm. Silicon nitride (Si_3N_4) which is transparent between 0.4 and 5 µm is widely used instead of silicon for a visible and near infrared wavelength range. This is particularly relevant for Raman spectroscopy, fluorescence spectroscopy and chip based super resolution microscopy.

Fluorescence microscopy has had a major impact on biomedical research, however, is bounded with the diffraction limit barrier inherent in optical microscopy [6]-[9]. Recent innovations have led to the development of super resolution microscopy also known as optical nanoscopy that allows for observation of fluorescent samples at resolutions below the diffraction limit. The methods of optical nanoscopy include techniques such as; the patterned light illumination techniques such as Stimulated Emission Depletion (STED) and *Structured Illumination Microscopy* (SIM) and localization-based techniques, which includes (direct) Stochastic Optical Reconstruction Microscopy ((d)STORM) and Photo-activation Localization Microscopy (PALM).

The conventional optical nanoscopy rely on using the same objective lens for both illumination and collection which results in a system complexity, small field of view, high-cost and slow imaging speed [1]. In this work, we report chip based nanoscopy (CbN) that can overcome these limitations.

2. Working Principle of Single molecule localization microscopy and structured illumination microscopy

Single molecule localization microscopy (SMLM): SMLM is a super-resolution imaging technique that utilises time-resolved localisation of switchable fluorophores, i.e. fluorophores that can be switched between a fluorescent “on”- and a dark “off”-state. Only a small and resolvable subset of all fluorophores attached to the sample is activated to the fluorescent “on”-state. As the signal originates from a single molecule, it is possible to find the position of each fluorophore with sub-resolution precision e.g. 20-50 nm by fitting 2-D Gaussian fit. After image acquisition the fluorophores are switched to the “off”-state (either using laser excitation or stochastical) and another subset is activated and imaged as mentioned before. Iteration of this process over several thousand images allows a multitude of fluorophores to be localised, whereupon the precise knowledge of their positions is used for the reconstruction of a super-resolved image. For performing SMLM in direct stochastic optical resonctruction microscopy (*d*STORM) mode, high intensity in the evanescent field is required, in the orders og 1-10KW/cm^2.

Structured illumination microscopy (SIM) works by using a patterned illumination to excite the sample. The overlap between the high frequency of the sub-diffraction details within the sample and the high frequency of the illumination pattern creates Moiré patterns, a pattern of lower frequency which is well collected by the objective. These Moiré patterns contain high frequency spatial information that would not be interpretable through diffraction-limited imaging. The pattern position and orientation is changed; to untangle the high frequency and isotropic resolution, respectively, and the emitted fluorescence signal for each position is recorded. Here, we report that creating the patterned illumination on a photonics chip enhances the resolution set by the objective launch in conventional linear SIM (λ/4N.A.) because photonic waveguide can create finer illumination pattern than the one set by the state-of-the-art objective lens since photonics waveguide gives better N.A. Furthermore, using photonics waveguide miniaturizing and integrating complex optical components.

3. Experimental Set-up and Results

In CbN, the photonics chip is used both for holding the sample under investigation (replacing the conventional glass-slide/coverslip), and for generating the required illumination needed to acquire super-resolved images [3]-[4], such as in SMLM and SIM. An experimental set-up for chip based nanoscopy is shown in a Fig. 1 a. A laser light is coupled into a waveguide chip by using objective lens or optical fiber. The samples are illuminated using the evanescent field present on top of the waveguide surface. The emitted fluorescence signal is collected using an upright microscope, fitted with an objective lens. Silicon nitride (Si_3N_4) based photonics waveguide platform for fluorescence nanoscopy is thoroughly investigated and opted [4]. The use of high-refractive index material allows to generate high intensity in the evanescent field, enabling the blinking (switch on and off) of the fluorophores: a key prerequisite for localization microscopy. The waveguide was made of 1-1000 µm wide and of thickness of 150 nm. The use of wide waveguides are essential to illuminate large group of cells (See Fig. 1c), while thin waveguides enable to enhance the surface intensity of the evanescent field.

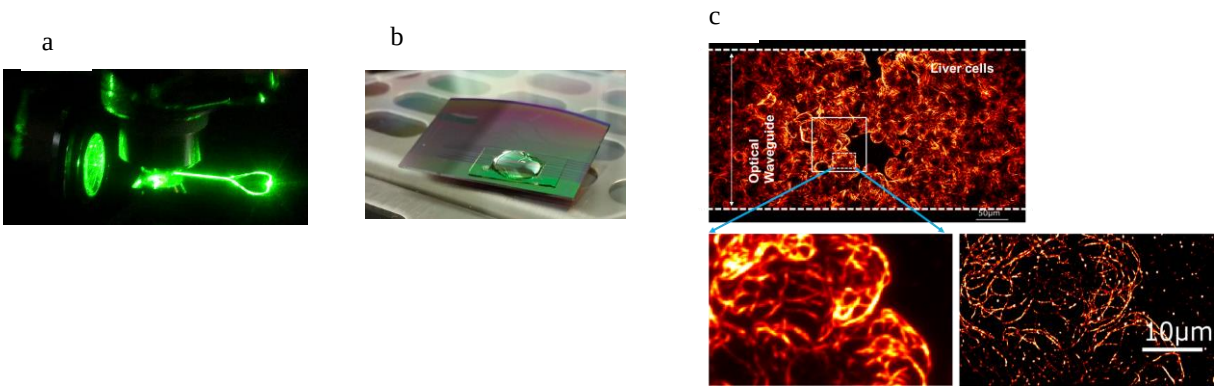


Fig.1a) Schematic diagram of chip-based nanoscopy, b) optical waveguide with a PDMS chamber;c) Chip-based TIRF and (d) chip-based dSTORM of liver sinusoidal endothelial cells (LSECs).

4. CONCLUSIONS

High-index contrast (HIC) based photonics integrated circuit platforms have played a vital role in integrating complex optical components in a small footprint. It has been shown that high surface intensity on top of HIC wavegudie platform can be exploited to perform super-resolution optical microscopy. In CbSIM, photonics chips are used to generate the illumination pattern needed for different optical nanoscopy methods. Furthermore, use of photonics waveguide miniaturizes complex optical microscopy which is presently based on free-space bulk optical components.

ACKNOWLEDGEMENTS

B.S.A acknowledges the funding from the European Research Council, (project number 336716).

REFERENCES

[1] Subramanian et al., “Silicon and silicon nitride photonic circuits for spectroscopic sensing on-a-chip”, Photonics Research 3 (5), B47-B59 (2015)

[2] Yurtsever . et al., “Photonic integrated Mach-Zehnder interferometer with an on-chip reference arm for optical coherence tomography”, Biomedical Optics Express 5 (4), 1050-1061 (2014)
[3] Estevez . et al., “Integrated optical devices for lab-on-a-chip biosensing applications”, Laser photonics 6 (4), 463-487 (2012)
[4] J-C Tinguely et al., “Silicon nitride waveguide platform for fluorescent microscopy of living cells”, Optics Express 25 (22), 27678-27690 (2017)
[5] R. Diekmann et al., “Chip-based wide field-of-view nanoscopy”, Nature Photonics 11, 322 (2017)
[6] Lothar S. et.al., “A guide to super-resolution fluorescence microscopy”, J. Cell Biol, 190, 165, 2010
[7] Betzig, E. et al., “Imaging intracellular fluorescent proteins at nanometer resolution”, Science 313 (5793), 1642-1645 (2006)
[8] Gustafsson et al., “Surpassing the lateral resolution limit by a factor of two using structured illumination microscopy”. J Microscopy 198 (2), 82–87 (2000)
[9] Hell, S. W et al., “Breaking the diffraction resolution limit by stimulated emission: stimulated-emission depletion fluorescence microscopy”, Opt Lett 19, 780-782 (1994)

Integrated single-mode frequency converter based on KTP

Christof Eigner[1], Laura Padberg[1], Matteo Santandrea[1], Harald Herrmann[1],
Benjamin Brecht[1], Christine Silberhorn[1]
[1]*Paderborn University, Department of Physics - Integrated Quantum Optics - 33098 Paderborn - Germany*
Tel: +495251 60 5896, Fax: +495251 60 5886, e-mail: christof.eigner@uni-paderborn.de

ABSTRACT

Waveguide circuits play a key role in modern integrated optics and provide an appealing approach to scalability in quantum optics. We report on periodically poled waveguides in z-cut potassium titanyl phosphate ($KTiOPO_4$ or KTP), a material that has recently received growing interest due to its unique dispersion properties. We fabricated channel waveguides guiding in a single-mode regime around 800 nm. In combination with a periodic poling the devices allow for type-II second harmonic generation / sum frequency generation from 801 nm to 400.5 nm with high efficiency of 2.3%/W·cm^2. Low attenuation values of 1.2 dB/cm (1.7 dB/cm) we determined at a wavelength of 800 nm for TE (TM) polarization. Temperature dependence of the second harmonic process we found to be 35 pm/K. The low temperature dependence and high nonlinear conversion efficiency make our waveguides ideally suited for future operations in classical nonlinear integrated optics and integrated quantum networking applications.

Keywords: integrated optics, quantum optics, waveguides, frequency conversion, material processing

1 INTRODUCTION

Potassium titanyl phosphate ($KTiOPO_4$ or KTP) is a well known and established material in bulk optics. KTP offers the advantage of a wide transparency range (365-4300 nm), which, in combination with the large nonlinear coefficients of the material, allows for applications with high power densities in the visible wavelength range. The high mechanical and chemical resistance and the low refractive index change with temperature make KTP devices impervious to temperature fluctuations and changes in humidity [1]. Furthermore, unique dispersion properties make KTP the material of choice for a variety of quantum optical systems [2]. Another key property of KTP is its high resistance to photorefraction; this obviates the need for high temperature operation when using high pump powers, hence facilitating room-temperature operation. The possibility to periodically pole the crystal allows the exploitation of the full transparency range for nonlinear conversion processes.
To exploit the benefits of tightly confined fields in integrated nonlinear optical devices, reliable fabrication techniques for waveguide structures are required [4], [5], [6]. In this work we demonstrate the fabrication of high-performance periodically poled rubidium-exchanged waveguides in KTP. We characterized our devices with respect to transmission losses and spatial mode properties; our waveguides are single mode at 800 nm. Finally, we realized an efficient second harmonic generation (SHG) with an efficiency of 2.3 %/W·cm^2.

2 SAMPLE FABRICATION

We fabricated spatially single-mode waveguides in commercially available flux-grown KTP substrates with dimensions of 10x6x1 mm^3 along the crystallographic a, b and c axes. In the first step, the samples were periodically poled with 8.56 μm period, allowing type-II conversion from 800 nm to 400 nm (Fig. 1a)). Due to the larger domain nucleation on -c face, a periodic resist structure was defined on this face in a lithographic process. Both sides of the sample (+c and -c) were coated with a metallic layer to improve the electrical contact. To invert the spontaneous polarization, we applied several high voltage pulses above the coercive field strength of 2.1 kV/mm to our sample. For controlling the poling progress, in-situ monitoring (as developed by Karlsson et al. [3]) was used which is based on electro-optically induced polarization switching. After successful poling, we removed the metal electrodes and photo resist in an ammonia solution, which simultaneously acts as a selective etchant that visualizes the domain structure, see Fig. 1c).
In the periodically poled substrates, we fabricated waveguides along the crystallographic a-axis in a rubidium (Rb) potassium (K) ion exchange process (compare to Fig. 1b)). The masked exchange process defines waveguides, and they realize the mode confinement. The ion exchange takes places in a Rb nitrate ($RbNO_3$) bath at 330 °C for 5 minutes. The exchange depth of 6-8 μm has been determined (with an accuracy up to $\pm$0.4 μm) by energy-dispersive x-ray spectroscopy (EDX) measurements of the Rb concentration with a scanning electron microscope. After the exchange, we polished the end facets to facilitate incoupling of light into the waveguides. To determine the transmission losses of the waveguides, we used the non-destructive Fabry-Perot method. We measured attenuation of 1.2 dB/cm (1.7 dB/cm) for TE (TM) polarization at 800 nm, respectively.

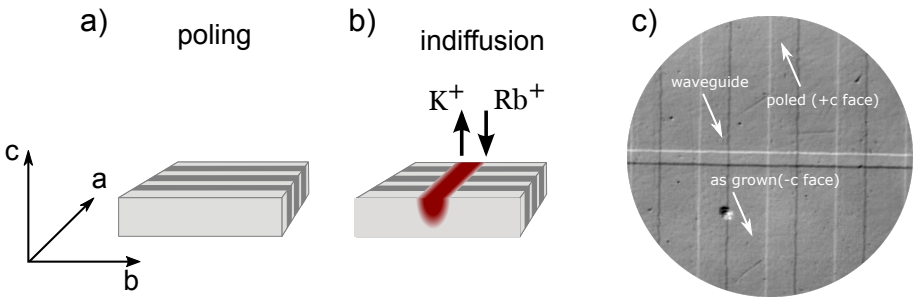


Figure 1. a) Periodically poled KTP substrate. b) Waveguides are formed in KTP by a masked Rb-exchange c) Selectively etched surface of a periodically poled substrate. In the horizontal direction, a waveguide is shown.

3 SECOND HARMONIC GENERATION

The waveguides used for second harmonic generation, have widths of 1.5-4.5 μm and guide only the fundamental mode at 800 nm. First of all we measured the near field of the fundamental modes at 800 nm (see Fig. 2b). A surface refractive index increase of Δn=0.011 for both polarizations was estimated comparing the measured modes with FEM simulations of the systems.

Next, we measured the nonlinear behavior by second harmonic generation. The setup is shown in Fig. 2a). Linearly polarized light at 45° with respect to the c-axis from a continuous wave Ti-sapphire laser is coupled to the waveguide via lens coupling. The computer-controlled laser generates pump light between 700 nm and 1000 nm. Power and polarization are controlled with a polarizing beam splitter and a half-wave plate. In the waveguide, horizontally polarized light is generated in a type II process at 400 nm. After the waveguide, we use a short pass filter and a colored glass filter to suppress the pump light. The generated light is detected on a power meter. The measured phase matching curve is shown in Fig. 2c). The measurement shows a pronounced peak, but due to various resonances in the experimental set-up, Fabry-Perot type oscillations are superimposed onto this phase-matching curve. The SHG efficiency is calculated as:

$$\eta_{exp} = \frac{P_{SHG}}{P_{pump}^2 \cdot l^2} \cdot 100\%. \tag{1}$$

where P_{SHG} is the second harmonic (SH) power, P_{pump} is the pump power behind the waveguide and l is the length of the poled fraction of the crystal. The efficiency is corrected for end-face reflection losses and the transmission losses of the short pass filter and the colored glass filter.

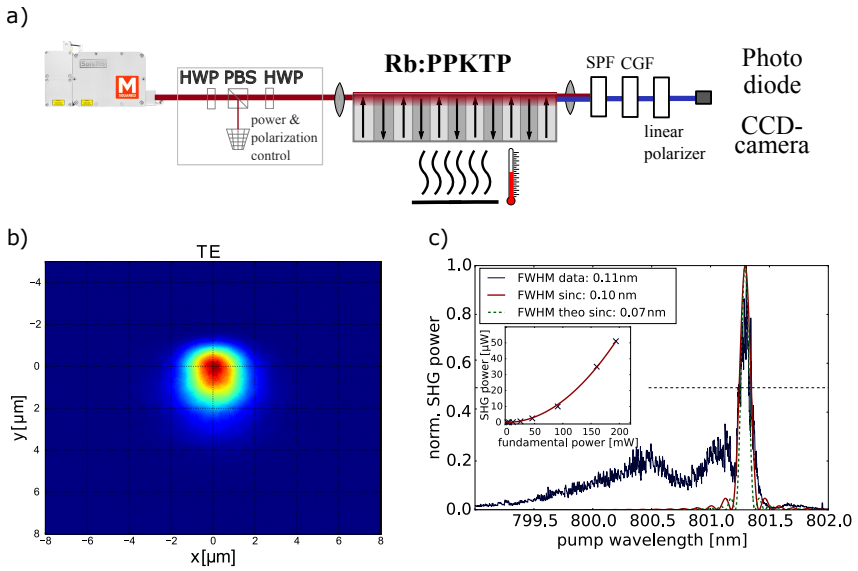


Figure 2. a) Setup to investigate the second harmonic generation. The computer-controlled cw Ti-sapphire laser generates pump light between 700 and 1000 nm. Power and polarization are controlled with a polarizing beam splitter (PBS) and half-wave plates (HWP). The light is coupled into the waveguide with a 45° polarization with respect to the crystal c-axis. The generated light is collimated with a lens that features an antireflective coating for the SH wavelength. The pump light is filtered out with a short pass filter (SPF) and an additional colored glass filter (CGF). The light is detected on a power meter. b) Measured near field of the fundamental mode. c) Measured second harmonic power as a function of pump wavelength.

The highest conversion efficiency of η_{exp} = 2.3 %/W·cm^2 was found for a 3 μm wide waveguide. Furthermore, we measured the temperature dependence of the phase matching and determined a variation of 35 pm/K.

4 CONCLUSION

We have fabricated periodically poled Rb-exchanged channel waveguides in z-cut KTP, which are single-mode at 800 nm. Furthermore, we successfully demonstrated type-II second harmonic generation in a periodically poled (8.56 μm poling period) waveguide with an efficiency of η_{exp} = 2.3 %/W·cm^2. Our waveguides are promising candidates for highly efficient frequency converters, which can readily be integrated into existing optical networks.

REFERENCES

[1] J. D. Bierlein, H. Vanherzeele, "Potassium titanyl phosphate: properties and new applications," J. Opt. Soc. Am. B 6, 622, 1989.

[2] V. Ansari, E. Roccia, M. Santandrea, M. Doostdar, C. Eigner, L. Padberg, I. Gianani, M. Sbroscia, J. M. Donohue, L. Mancino, M. Barbieri, and C. Silberhorn, "Heralded generation of high-purity ultrashort single photons in programmable temporal shapes," Opt. Express **26**(3), 2764-2774 (2018).

[3] H. Karlsson, F. Laurell, and L.K. Cheng "Periodic poling of $RbTiOPO_4$ for quasi-phasematched blue light generation," Appl. Phys. Lett. 74(11), 1519–1521 (1999)

[4] C. Eigner, M. Santandrea, L. Padberg, M. F. Volk, C. E. Rüter, H. Herrmann, D. Kip, and C. Silberhorn "Periodically poled ridge waveguides in KTP for second harmonic generation in the UV regime," Opt. Express Vol. **26**(22), 28827-28833 (2018)

[5] M. F. Volk, C. E. Rüter, M. Santandrea, C. Eigner, L. Padberg, H. Herrmann, C. Silberhorn, and D. Kip, "Fabrication of low-loss Rb-exchanged ridge waveguides in z-cut KTiOPO 4 ," Opt. Mater. Express 8(1), 82–87 (2018)

[6] S. Müller, T. Calmano, P. W. Metz, C. Kränkel, C. Canalias, C. Liljestrand, F. Laurell, and G. Huber, "Highly efficient continuous wave blue second-harmonic generation in fs-laser written periodically poled Rb:KTiOPO 4 waveguides," Opt. Lett. 39(5), 1274–1277 (2014)

Ultrathin SOI strip-loaded resonators: Permanent mitigation of losses using UV light

Mher Ghulinyan[1], Gioele Piccoli[1,2], Martino Bernard[1,3] and Georg Pucker[1]
[1] Centre for Materials and Microsystems, Fondazione Bruno Kessler, I-38123 Trento, Italy
[2] University of Trento, I-38123 Trento, Italy
[3] Department of Information Engineering, University of Brescia, I-25123 Brescia, Italy
e-mail: ghulinyan@fbk.eu

ABSTRACT

The performance of integrated micro-photonic devices relays majorly on the mitigation of optical losses. Here, we report on the design, fabrication and characterization of Silicon Nitride strip-loaded guiding optical components realized on a sub-30 nm ultra-thin SOI platform [1]. Omitting physically etched boundaries within the guiding core is known to suppress significantly the scattering loss, as shown by us previously for Si3N4 devices. Here, contrary to expectations, the freshly fabricated SOI devices suffer large losses of 5 dB/cm. We first relate this to the absorption by free carriers, which accumulated under the positively charged Si3N4 loading layer, and successively, demonstrate that exposures to UV light neutralize progressively and permanently Si3N4's bulk charge, associated with diamagnetic K^+ defects. As a result, a net decrease of electron concentration in the SOI layer reduces the propagation losses down to 0.9 dB/cm. We performed accurate cavity linewidth measurements showing how the intrinsic cavity Q's boost from 70,0000 up to 500,000 after UV illumination. Our results may open routes towards engineering of new functionalities in photonic devices, unveil the origin of induced optical nonlinearities in Si3N4/Si micro-photonic systems, as well as envisage possible integration of these with standard as well as ultrathin SOI electronics.

Keywords: Silicon-on-insulator, silicon nitride, waveguides, optical loss, ultraviolet light.

1. INTRODUCTION

Circular microresonators, in which the electromagnetic radiation is confined via resonant circulation, are essential building blocks for planar integrated photonics [2]. The spectral width of resonances in these devices is inversely proportional to the amount of optical power which is lost per round trip. Generally, the power is lost due to material absorption, α_m, scattering on boundary imperfections, α_{sc}, and out-radiation, α_{rad}, due to the curved geometry. A reducing the intrinsic loss enables a number of applications from passive filtering in optical communication networks to quantum optics, space and sensing. Thus, in order to push the device characteristics to an ultimate limit, the challenge is to limit the intrinsic losses to only that of the material [3]. Towards this goal, approaches, such as strong modal confinement and realization of smooth device boundaries are necessary to achieve minute contributions from radiative and scattering loss.

Here we report on the design, fabrication and characterization of high-Q micro-optical components on a sub-30nm thick SOI platform [1]. In these devices, the light is guided in the Si slab layer underneath a patterned layer of loading stoichiometric Si3N4. The absence of physically etched device boundaries in the SOI layer is expected to provide with ultimately low losses, limiting them to that of the intrinsic absorption of the lightly doped p-type Si layer. We have used successfully this approach in past to achieve resonance quality factors $Q \sim 4 \times 10^6$ on an 80 nm thick Si3N4 platform with SiO2 loading strips [4]. Here, surprisingly, we measured up to 5 dB/cm propagation losses in the freshly fabricated silicon devices. We related these losses to the absorption of free (mirror) carriers within the Si layer, which are accumulated due to the presence of a large fixed positive charge in the Si3N4 material. Successively, we neutralized permanently the charge in Si3N4 by exposing our devices to 254nm wavelength UV light. As a result, the propagation losses improved permanently summing to 0.9 dB/cm. The corresponding Q's of ring resonators thus boosted from an initial 70,000 up to 500,000.

2. RESULTS AND DISCUSSION

We realized the samples starting from 6" SOI wafers with a 3 μm-thick buried oxide (BOX) and a 250 nm (100)-Si device layer of a nominal resistivity of 15 Ω.cm (Soitec). The Si layer thickness was reduced down to 27nm via thermal oxidation and removal of the grown oxide in a buffered HF solution. A 145 nm thick LPCVD Si3N4 film was deposited at 780°C. The wafer was patterned lithographically using a Nikon stepper and transferred to Si3N4 using a combination of ICP dry etch, finalized with e wet etch for the last 10 nm with a wet

This work has been partially funded by Italian Ministry of Education, Universities and Research (MIUR) within the project NEMO (2015KEZNYM)

etching step to guarantee a smooth top surface of the Si device layer (Fig. 1). The fabricated chips were diced and characterized in optical transmission experiments.

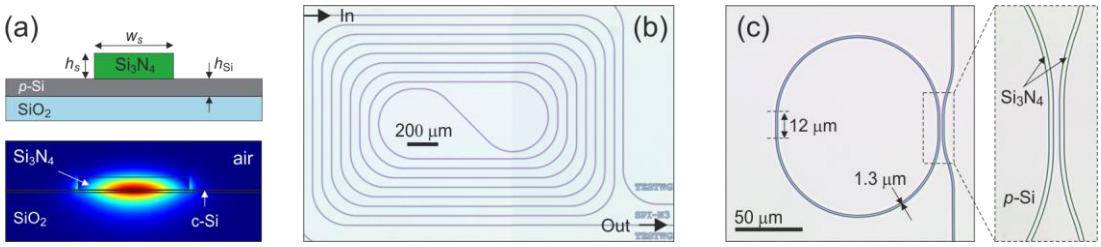


Figure 1. (a) The cross-sectional view of the waveguide and the distribution of the simulated electric field intensity of a transverse electric (TE)-polarized mode. Optical micrographs of a typical (b) spiral waveguide and (c) a ring resonator.

We report in Fig. 2(a) the results of waveguide transmission experiments. The freshly fabricated waveguides. show a propagation loss of about 3.83(0.26) dB⁄cm according to the Beer–Lambert law (red squares), which, if attributed to sidewall scattering, are unexpectedly high for the adopted processing technology [4].

In order to proof the hypothesis of charge-related losses, we performed systematic electrical capacitance measurements using a Hg probe, first, on test samples with the same Si3N4 layer deposited on Si substrates of 15 15 Ω.cm resistivity. Detailed measurements and analysis of C-V curves allowed us to both extract the Nitride's fixed charge as well as permitted to study the effect of UV exposure on its electrical characteristics. In particular, we found that the as-deposited Si3N4 layer contains a large amount of net positive electrical charge related to diamagnetic charge centers K^+ [5]. The C-V curves for these freshly deposited samples has a characteristic flat-band voltage value of $V_{fb} \approx -7.8$ V. The areal density of the corresponding to this situation net positive charge amounts to $\sigma \approx 1.7 \times 10^{12}$ cm^{-2}, in agreement with previous estimations reported for SiNx films deposited using other techniques [6].

Successively, we exposed the film to UV light (254 nm), which is known to neutralize the positively charged K^+ centers into diamagnetic K^0 ones [5]. We carefully characterized the behaviour of the flat band voltage and corresponding charge density attenuation as a function the UV exposure duration. In particular, we succeeded to reduce by more than three orders of magnitude the charge density in Si3N4, bringing it down to 3.1×10^9 cm^{-2}. This value is comparable to the density of charge traps of very-high-quality oxide/Si interfaces, which is also close to the density of dopant ions per centimetre square for a silicon layer of 15 Ω.cm resistivity. Thus, we concluded that the UV exposure could have a large impact on the attenuation of losses in integrated devices.

Therefore, we exposed to UV light the same spiral devices for 21h and measured again the propagation losses. In fact, the waveguides showed significantly improved characteristics (blue diamonds), where the propagation loss has decreased down to 1.55(0.28) dB⁄cm. Note, that the insertion loss of the waveguides has remained unchanged, since the UV exposure does not affect the quality of facets and the fibre-chip butt coupling. Still, the small number of available spirals provides with few experimental data, which explains the large error bars of experimental points in Fig. 2(a). This limitation was surpassed by measuring many ring resonators and analysing dozens of resonances per ring, therefore, avoiding also errors due to fluctuations of the waveguide facet quality.

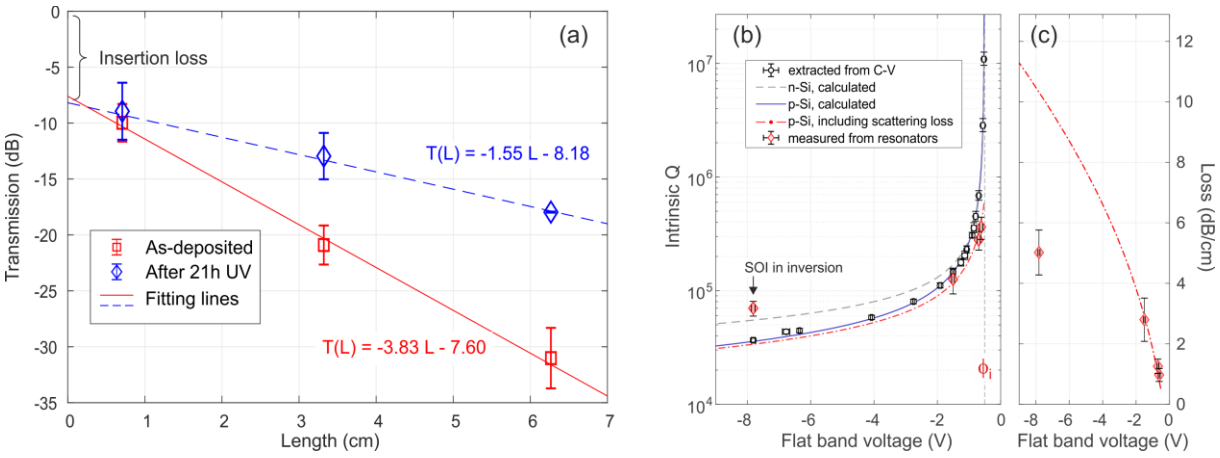


Figure 2. (a) Attenuation of the propagating optical power measured for waveguides of different length before (squares) and after exposure to UV light for 21h (diamonds). (b) Experimental and expected trends of the intrinsic Q of ring resonators as a function of the UV-modified flat-band voltage for p-type Si (blue continuous line). (c) The intrinsic loss α_i, corresponding to that Q's extracted from the ring resonators' spectra (diamonds), plotted against the calculated one (dashed-dotted line).

Figure 2(b) summarizes the measurements of ring resonators – from freshly prepared devices to UV exposures of different duration. The Q-factors estimated from optical measurements on ring resonators are shown as red diamonds, where each point is the result of the analysis of at least ten different resonances per ring. The first point of this dataset, corresponding to the UV-untreated devices, shows an average intrinsic Q of about 70,000, in accordance with the corresponding MOS capacitance experiment. Finally, the rest of the data from the ring resonators, corresponding to long exposures to UV light, can be fit to good approximation by including an additional residual loss with an associated $Q_{ad} \approx 6 \times 10^5$ (red dashed-dotted curve). The corresponding loss values, based on the results from the ring resonators, and the calculated curve for p-type Si in the situation of residual loss are shown in Fig. 2(c). Thus, we revealed a net improvement of losses down to 0.9 dB/cm at the longest exposures, improving the rings' intrinsic Q-factors from 70,000 to 500,000. Finally, we can relate the carrier-induced optical losses to the MOS capacitance measurements of the flat-band voltage (not shown here).

3. CONCLUSIONS

Our results may open the door to the implementation of UV-induced charge modification for the design and study of new photonic devices in which the space-charge-related static electric fields can be engineered to modulate the linear and nonlinear refractive indices of materials. In addition, our findings are general and may be implemented also in other geometries of guiding devices and material systems where silicon nitride is present, such as widely used standard SOI waveguides. We also envisage the possibility of compact integration of micro-photonic components with ultra-thin SOI electronics in the future.

ACKNOWLEDGEMENTS

The authors thank Prof. L. Pavesi for providing access to optical measurement facility of Nano-Science Laboratory at the University of Trento. The authors also acknowledge fabrication facility support by the Micro-Nano Fabrication Laboratory of FBK.

REFERENCES

[1] G. Piccoli, M. Bernard, and M. Ghulinyan: Permanent mitigation of loss in ultrathin silicon-on-insulator high-Q resonators using ultraviolet light. *Optica* 5, 1271 (2018).
[2] D. G. Rabus: Integrated Ring Resonators (Springer, 2007).
[3] H. Lee *et al.*: Chemically etched ultrahigh-Q wedge-resonator on a silicon chip. *Nat. Photon.* 6, 369 (2012).
[4] L. Stefan *et al.*: Ultra-high-Q thin-silicon nitride strip-loaded ring resonators. *Opt. Lett.* 40, 3316 (2015).
[5] C. Schriever *et al.*: Second-order optical nonlinearity in silicon waveguides: inhomogeneous stress and interfaces. *Adv. Opt. Mater*. 3, 129 (2015).
[6] D. Krick, P. Lenahan, and J. Kanicki: Electrically active point defects in amorphous silicon nitride: an illumination and charge injection study. *J. Appl. Phys.* 64, 3558 (1988)

Alignment-tolerant taper design for transfer printed III-V-on-Si devices

(Student paper)

Bahawal Haq [1,2], Gunther Roelkens [1,2]
[1]*Photonics Research Group, Department of Information Technology, Ghent University - imec iGent, Technologiepark-Zwijnaarde 15 - 9052 Ghent - Belgium*
[2]*Center for Nano- and Biophotonics (NB-Photonics), Ghent University - Ghent - Belgium*
e-mail: bahawal.haq@ugent.be

ABSTRACT

In this paper, we present the design of a 1.0 μm misalignment-tolerant taper for the evanescent coupling of light in a III-V-on-silicon opto-electronic device realized on an SOI waveguide platform with 400 nm thick Si device layer. The designed taper is also fabrication tolerant and is suitable for the transfer-printing-based integration of pre-processed III-V devices on Si photonics waveguide circuits. The design procedure is flexible and can take into account the limitations in critical dimensions imposed by the fabrication process.

Keywords: III-V/Si integration, Transfer Printing, Adiabatic taper

1 INTRODUCTION

Micro-Transfer printing is an emerging technique for the integration of III-V epitaxial layers and pre-processed devices on Si photonic circuits [4][2]. This technique is highly modular in terms of the integration of different III-V epitaxial layer structures / devices. Moreover, it allows for efficient III-V usage and massively parallel integration [1]. A key building block that needs to be realized by III-V semiconductors on a silicon waveguide circuit is a semiconductor optical amplifier. By locally removing the back-end stack of the silicon photonic integrated circuit, SOAs - pre-processed on the native substrate - can be transfer printed on top of the silicon device layer and evanescently-coupled to the underlying silicon waveguide circuit. The process of transfer printing and the resulting photonic integrated circuit is shown in Fig. 1 (a) and (b) respectively.

The idea is to process the epitaxial layer structure grown on its III-V native substrate, while incorporating a sacrificial layer between the device layer stack and the substrate. By encapsulating the devices and etching the sacrificial layer, the devices are released from the III-V substrate and can be picked up from the source wafer and printed on the silicon photonic target wafer using a PDMS stamp. Like in any other hybrid integration technique, integrating preprocessed devices using transfer printing requires high alignment accuracy. State-of-the-art transfer printing tools have an alignment accuracy of 1 to 1.5 μm 3σ, depending on the size of the array of devices that are being transferred [1]. Therefore, the adiabatic taper that is commonly used to couple light between the silicon waveguide and the III-V-on-silicon device must have a high alignment tolerance. In this paper, we present the design of such an adiabatic taper structure.

2 DESIGN AND SIMULATION

Designing of an optimal III-V-on-silicon taper structure can be realized using the formalism described in [3], where a two-mode coupled-waveguide system is assumed. In this formalism the shape of the shortest adiabatic taper structure can be found by solving (1),

$$\gamma = tan[sin^{-1}(2\epsilon^{\frac{1}{2}} \int_{z_0}^{z} \kappa(z`)dz`)] \tag{1}$$

where $\gamma \equiv \frac{(\beta_2-\beta_1)}{2\kappa}$, $\frac{\beta_2-\beta_1}{2}$ is the mismatch of the propagation constants between the individual uncoupled waveguide modes, ϵ is the fraction of power in the unwanted mode, κ is the coupling strength between the two

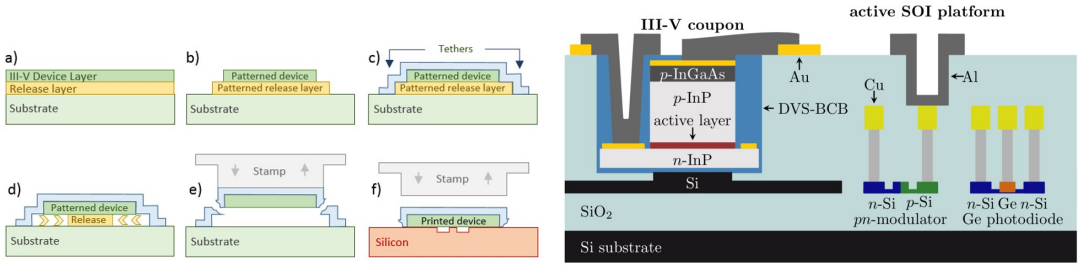


Figure 1. (a) Transfer printing process flow, (b) Transfer printed III-V coupon on SOI

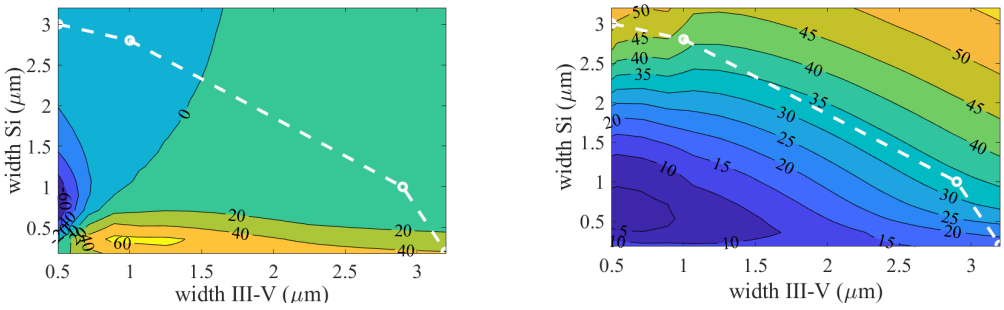


Figure 2. (Left) Calculated values of γ for several waveguide width combinations of III-V and Si, (Right) Calculated values of κ in mm^{-1}

waveguide modes ($\kappa_{mp} = \frac{k_0^2}{2\beta} \int \int_{-\inf}^{+\inf} (n'^2 - n_p^2) F_m * F_p dxdy$, where F_m and F_p are the normalized eigen modes of the each uncoupled waveguide and must be normalized such that $\int \int_{-\inf}^{+\inf} |F_m(x,y)|^2 dxdy = 1$, where n' is the refractive index profile of the coupled waveguide system, n_p is the refractive index profile of the uncoupled waveguide and β is the propagation constant of the coupled mode). Equation 1 gives us the optimal γ distribution along the length of the III-V and silicon taper structure, assumed to be along the z-axis. Subsequently, it can rewritten by assuming κ to be linearly varying between two consecutive points along z as

$$z_N = \frac{sin(tan^{-1}\gamma_N)}{\epsilon^{\frac{1}{2}}(\kappa_{N-1} + \kappa_N)} - \frac{2}{\kappa_{N-1} + \kappa_N}[\sum_{i=0}^{N-1} A_i] + z_{N-1}] \tag{2}$$

where $z = z_N$ is a point N along the length of the taper that begins at $z = z_0$, $A_i = \frac{1}{2}(\kappa_{i-1} + \kappa_i)(z_i - z_{i-1})$ and γ_N is the value of γ at $z = z_N$. In order to design the taper structure κ and γ were calculated for all possible width combinations of III-V and silicon waveguide, assuming a lateral misalignment of 1μm as the worst case. A standard III-V epitaxial stack used for evanescently-coupled optical amplifiers and lasers was used [4]. The device cross-section printed on SOI spin coated with BCB is shown in Fig. 1(b). The DVS-BCB adhesive bonding layer thickness is assumed to be 60 nm for all calculations. The map of γ and κ is shown in Fig. 2. When γ is greater than 10, the III-V waveguide is wide and the Si waveguide is narrow, and light is mostly confined in the III-V waveguide and when γ is less than -10, the light is predominately confined in the Si waveguide. The zero contour line is the phase matching line and corresponds to III-V and Si widths at which the optical modes are phase matched. Now, we have the freedom to choose any set of III-V and Si width pairs from the contour map such that γ values goes from negative to positive crossing the zero line to realize a transition from the silicon waveguide to the III-V waveguide. Each chosen trajectory will correspond to a new taper structure. If, however, we choose the widths pairs that correspond to higher κ values, the taper coupling length can be shortened. After the selection, the values of γ and κ are inserted in (2) and their location along the propagation direction z is calculated, thereby defining the taper geometry .

However, there is one more criterion that the adiabatic Si and III-V taper should follow in order to avoid power coupling into higher order modes. The local half angle of the Si and III-V taper must follow $\theta < \frac{\lambda_0}{2Wn_{eff}}$. This means that the tapering should be slower than the diffraction of the fundamental mode of each waveguide. After taking into account both the aformentioned adiabacity criteria and choosing a set of III-V and taper width pairs, shown by the dashed white line in Fig. 2, the taper shape calculated from (2) was exported into a 3D EME solver and the power coupling between Si and III-V was simulated. The taper shape and the simulated coupling with respect to lateral misalignment is shown in Fig. 3. The III-V waveguide width varies from 0.51 μm to 3.2 μm whereas the silicon tapers from 3 μm to 0.2 μm. The taper is 225 μm long. The coupling efficiency drops to -3 dB at 1.2 μm lateral misalignment.

During the processing, the width of the taper structure can vary, therefore, the design should have, besides good alignment tolerance, also a good fabrication tolerance. In particular, the isotropic etching of the QWs can lead to a width of the QWs narrower than designed. The effect of the variation of the III-V layer stack width including QWs and QWs width alone, while the tapers are 1 μm misaligned, is shown in Fig. 4(a) and Fig. 4(c). The coupling efficiency doesn't changes rapidly in case of widening of the taper and QWs as compared to narrowing. Moreover, the coupling efficiency decreases less than 1 dB for a reduction of the width by 250 nm from the design width. The coupling efficiency changes much more rapidly if the thickness of n-InP and BCB is reduced shown in Fig. 4(c) and Fig. 4(d), respectively. This is due to the change in κ between the III-V and Si waveguide. The impact of a layer thickness increase is less than in case of a decrease.

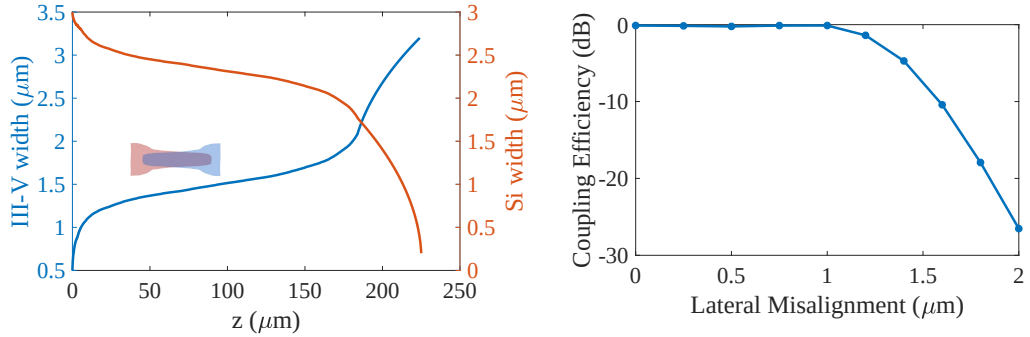


Figure 3. (Left) III-V and Si taper structure geometry, (Right) Simulated coupling efficiency plotted against lateral misalignment for the designed taper

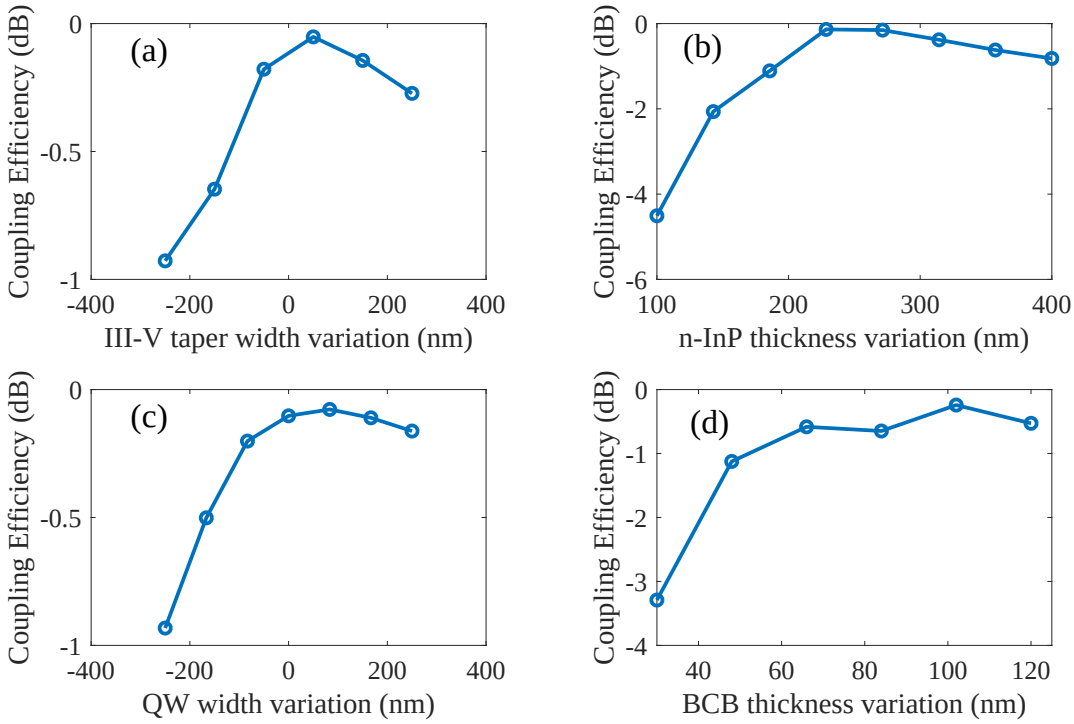


Figure 4. Effect on coupling efficiency with 1 μm misaligned III-V and Si taper of (a) III-V taper width variation, (b) n-InP thickness variation, (c) QW width variation, and (d) BCB thickness variation

CONCLUSION

In this paper, we present an alignment tolerant adiabatic taper structure for transfer printing preprocessed III-V SOAs evanescently coupled to Si photonic integrated circuit. The adiabatic taper structure has an alignment tolerance of 1 μm and is compact (225 μm).

REFERENCES

[1] A. D. Groote, P. Cardile, A. Z. Subramanian, A. M. Fecioru, C. Bower, D. Delbeke, R. Baets, and G. Roelkens. Transfer-printing-based integration of single-mode waveguide-coupled iii-v-on-silicon broadband light emitters. *Opt. Express*, 24(13):13754–13762, Jun 2016.

[2] J. Juvert, T. Cassese, S. Uvin, A. de Groote, B. Snyder, L. Bogaerts, G. Jamieson, J. V. Campenhout, G. Roelkens, and D. V. Thourhout. Integration of etched facet, electrically pumped, c-band fabry-perot lasers on a silicon photonic integrated circuit by transfer printing. *Opt. Express*, 26(17):21443–21454, Aug 2018.

[3] X. Sun, H.-C. Liu, and A. Yariv. Adiabaticity criterion and the shortest adiabatic mode transformer in a coupled-waveguide system. *Opt. Lett.*, 34(3):280–282, Feb 2009.

[4] J. Zhang, B. Haq, J. O'Callaghan, A. Gocalinska, E. Pelucchi, A. J. Trindade, B. Corbett, G. Morthier, and G. Roelkens. Transfer-printing-based integration of a iii-v-on-silicon distributed feedback laser. *Opt. Express*, 26(7):8821–8830, Apr 2018.

Refractive index tunability and switching with vanadium dioxide on silicon waveguides

Student Paper

Vadivukkarasi Jeyaselvan [1], Anand Pal [2], P. S. Anil Kumar [2], Shankar Kumar Selvaraja [1]
[1]*Centre for Nano Science and Engineering, Indian Institute of Science, Bangalore, India*
[2]*Department of Physics, Indian Institute of Science, Bangalore, India*
e-mail: vadivu@iisc.ac.in

ABSTRACT

In this paper, we demonstrate a vanadium dioxide (VO_2) based absorption modulator on silicon-on-insulator platform. The optical modulation is achieved by thermally tuning (local) the refractive index (phase) of VO_2. We use a micro-ring resonator for optical modulation in our experiment. The device shows a low insertion loss of 1.48 dB and high extinction ratio change of 16 dB. The transition spectrum analysis yields an approximately 1.2 change in refractive index across the transition. Mach-Zehnder configuration is used to analyze the switching performance of the device.

Keywords: optical modulator, vanadium dioxide, phase change material, ring resonator, Mach-Zehnder interferometer

1 INTRODUCTION

Recently, phase-change materials (PCMs) have shown great promise for applications in integrated optics platform [1] due to their broad band operation and CMOS compatibility. Of all the PCMs, VO_2 has gained particular attention because of its transition from insulating, optically transmissive monoclinic phase to metallic and optically opaque tetragonal rutile phase at very near to the room temperature (68 °C). The insulator-metal transition (IMT) in VO_2 can be achieved by applying thermal [2], optical [3] or electrical stimuli [4]. These two phases has a high contrast in the electrical resistivity ($>$ 3 order) and optical constants (Δn $>$ 1 and an order change in Δk) in the telecommunication wavelength region. The higher contrast in refractive index offers a possibility of compact and energy efficient devices, and finds application in optical modulators [1] and photonic memories [5]. The incorporation of VO_2 in these devices depends on the phase purity of the sample as the film quality determines the switching property. Due to the multiple oxidation states of vanadium, optimization of the deposition and fabrication condition of VO_2 modulator are very critical.

In this work, we demonstrate an absorption type optical modulator on silicon-on-insulator (SOI) platform by tuning the refractive index of VO_2 using thermal energy. VO_2 is deposited using pulsed-laser deposition (PLD) technique [6]. The IMT is achieved by locally heating the material in proximity to the silicon waveguides. As the temperature increases from room temperature to 100 °C, the refractive index of the VO_2 changes from $3.21 + i0.17$ to $2.15 + i2.79$, respectively [7]. The change in refractive index (Δn) is exploited to realize an optical modulation. We present material, device fabrication and characterization of pulsed laser deposited VO_2. We use Si ring resonator to measure the change in refractive index of VO_2. We also analyse the switching performance of the device and optimized the operation condition for the VO_2 based modulators.

2 FABRICATION OVERVIEW

The device is fabricated on a SOI substrate with 220 nm thick device silicon layer and 2 μm buried oxide. The GDS design of passive device i.e., Ring resonator (RR) and Mach-Zehnder Interferometer (MZI) is done using IPKISS package and is fabricated through Europractice [8]. Fig. 1(a-d) shows the schematic cross-section of a planarized Si passive device from Europractice MPW run. A shallow etched single mode rib waveguide is used to realize RR and MZI. To fesilitate light coupling, grating coupler is used. On top of the planarized waveguide a 40 nm thick SiO_2 liner is deposited using plasma enhanced deposition technique. A 40 nm thick VO_2 film is deposited on patterned substrate by Pulsed Laser deposition (PLD) using V_2O_5 as a target material at 580 °C under 10 mTorr oxygen pressure [6]. The sample is then spin coated with photoresist and patterned using direct laser writer. Finally, the excess VO_2 is etched using reactive ion etching process by a mixture of Ar and Cl gas followed by wet etching to soft land on 40 nm SiO_2 (Fig. 1(c)). Ti/Pt (10/90 nm) is used as the contact material for VO_2. Fig. 1(e) shows the microscope image of the fabricated device with the VO_2 deposited on the ring resonator.

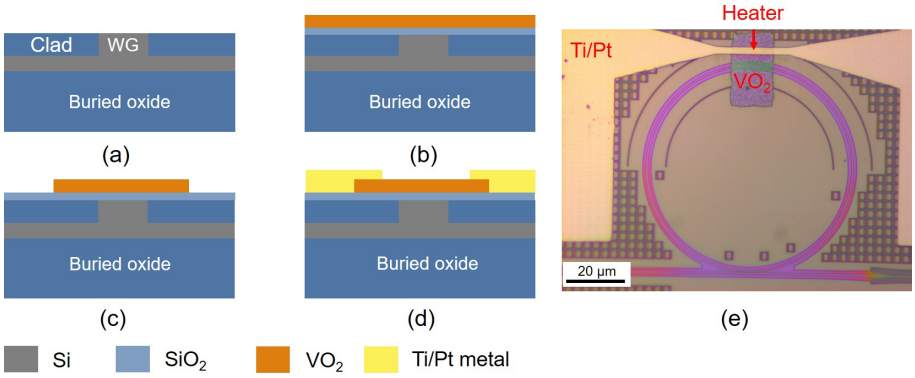


Figure 1. (a)-(d) Fabrication process flow of VO_2 modulator and (e) Microscope image of the VO_2 deposited on the ring resonator.

3 RESULTS AND DISCUSSION

3.1 Material Characterization

The phase purity and IMT of the fabricated VO_2 device are characterized using XRay Diffractometer (XRD), Raman spectrometer and temperature dependent electrical resistivity measurement. Fig. 2(a) and (b) shows the x-ray diffraction pattern and the raman spectrum of the monoclinic VO_2 at room temperature. The temperature dependent electrical resistance of the device during heating and cooling are shown in Fig. 2(c). As clearly seen from Fig. 2(c), the film shows a three order of change in electrical resistance across the transition.

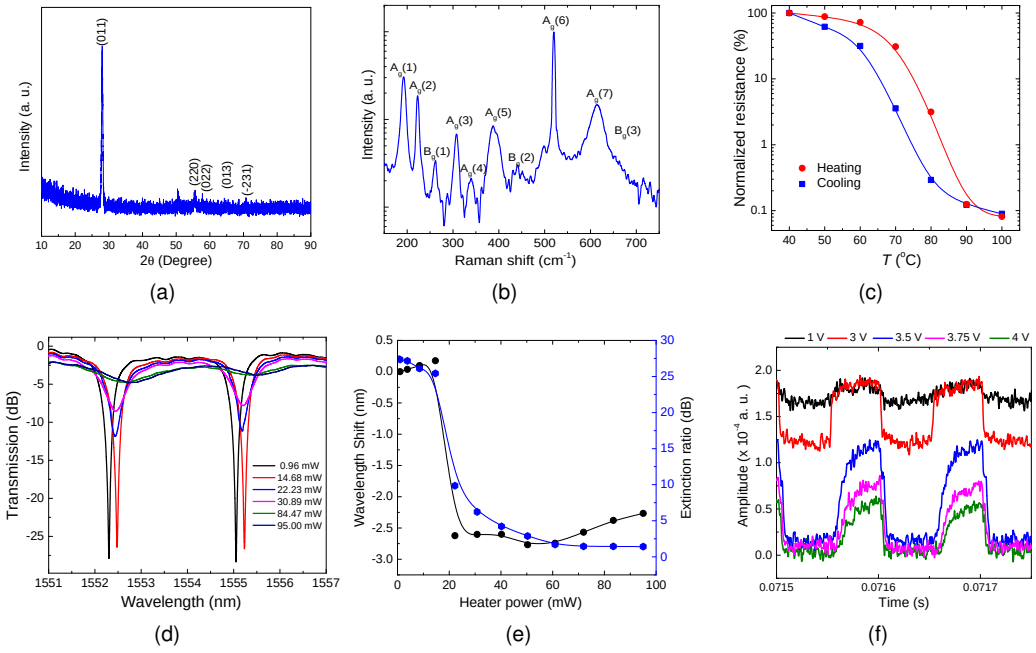


Figure 2. (a) XRD pattern, (b) Raman spectrum (For better visualization, the Y axis is plotted with logarithmic scales), (c) Temperature dependent electrical resistance measurement during heating and cooling cycle across the transition of the studied device, (d) Transmission spectrum of VO_2 modulator with lateral heaters, (e) Wavelength shift and Extinction ratio extracted from the spectrum, and (f) Switching of the device by fixing the bias voltage and changing the peak-peak voltage (V_{pp}). The solid line through the points in (c) and (e) are to guide the eyes.

3.2 Device Characterization

Fig. 2(d) shows the transmission spectrum of the partially VO_2 covered micro-ring resonator with different heater power. Since the VO_2 is deposited on 40 nm oxide, the insertion loss of the device is comparatively less (1.48 dB) due to reduced interaction of the waveguide mode with the VO_2. The IMT is achieved by locally heating the VO_2 using lateral micro heaters. As the temperature increases, the change in refractive index of the material results in a spectral change in the ring response across the phase transition ($\sim$20 mW). The extinction

ratio, wavelength shift (seen in Fig. 2(e)) and FWHM are extracted from the transmission spectrum. The spectral shift is calculated using equation (1) [9]. From the spectral shift, we can obtain the Δn_{VO_2} since the equivalent thermo-optic coefficient (TOC) of a waveguide system (dn_{eff}/dT) is a superposition of the TOC of the individual materials, which is given by equation (2) [10],

$$\frac{dn_{eff}}{dT} = \frac{2\pi R \Delta\lambda}{\lambda_0 L} \tag{1}$$

$$\frac{dn_{eff}}{dT} = \sum_i \frac{d(\Gamma_i n_i)}{dT} = \Gamma_{Si}\frac{dn_{Si}}{dT} + \Gamma_{SiO_2}\frac{dn_{SiO_2}}{dT} + \Gamma_{VO_2}\frac{dn_{VO_2}}{dT} \tag{2}$$

where n_{eff} is the effective index of the waveguide, R is the radius of the ring (35 μm), $\Delta\lambda$ is the measured wavelength shift from the spectrum, λ_0 is the centre wavelength of the ring without VO_2, L is the length of the VO_2 (19 μm), Γ_i is the confinement factor in i^{th} material and dn_i/dT is the TOC of the material. The TOC of Si is 1.8 $\times$ $10^{-4}/°$C. The TOC of SiO_2 ($10^{-7}/°$C) is small (not included in the calculation). The confinement factor in the silicon and VO_2 can be obtained using modal simulation (finite difference method). In the dielectric phase, the confinement factor in Si and VO_2 is 71.3 % and 3.4 %, respectively. In this phase, the mode is pulled in to the VO_2 layer because of large n_{VO_2}. After the phase transition, since n_{VO_2} reduces, the mode is pulled down towards the waveguide, thereby the confinement factor inside the silicon increases (74.18 %) and while confinement decreases in VO_2 (1.6 %). From this, Δn_{VO_2} is calculated to be ≈1.2 which matches well with the reported value in the literature [7]. The loss induced by VO_2 is calculated using equation (3) [7]. The loss increases from 0.1 dB/cm to 0.38 dB/cm and also there is a 70 % decrease in transmission during IMT.

$$Loss(dB/cm) = 4.343 \times \frac{2\pi n_g L}{\lambda_0 Q_{ring}} \tag{3}$$

where n_g is the group index and Q_{ring} is the quality of the ring resonator. The switching performance have been analyzed with similar device using Mach-Zehnder interferometer. To obtain the ON and OFF time of the switch, the device is biased near the dielectric phase, the frequency is fixed to 1 MHz and amplitude of the signal is varied from 1 V_{pp} to 4 V_{pp}. Fig. 2(f) shows the switching performance of the device. The raising edge represents MIT (metal-insulator transiiton) and falling edge indicates IMT. When the amplitude is greater than 3 V_{pp} the insertion loss of the device increases. And also the rise time and fall time increases from 2.15 μs to 13.2 μs and 1.39 μs to 7.49 μs, respectively. It can also be seen that IMT is faster than MIT transition. The switching speed can be further improved by providing optical or electric field trigger.

4 CONCLUSION

We have demonstrated a VO_2 based absorption modulator by local heating technique and measured the Δn_{VO_2} across the transition. We have presented a PLD deposited VO_2, studied electrical and optical phase transition of the film on SOI wafer. We demonstrated intensity modulator using MZI configuration.

ACKNOWLEDGMENT

We acknowledge funding support from MHRD through NIEIN project, from MeitY and DST through NNetRA project. V.J. acknowledges Ministry of Electronics and Information Technology (MeitY), Govt. of India for the student fellowship and S.K.S acknowledges MeitY for the faculty fellowship.

REFERENCES

[1] K. J. Miller, *et al*., "Optical phase change materials in integrated silicon photonic devices," Optical Materials Express, vol. 8, no. 8, pp. 2415-2429, 2018.

[2] J. D. Ryckman, *et al*., "Photothermal optical modulation of ultra-compact hybrid Si-VO_2 ring resonators," Optics express, vol. 20, no. 12, pp. 13215-13225, 2012.

[3] J. D. Ryckman, *et al*., "Ultra-compact silicon photonic devices reconfigured by an optically induced semiconductor-to-metal transition," Optics express, vol. 21, no.9, pp. 10753-10763, 2013.

[4] A. Joushaghani, *et al*., "Wavelength-size hybrid Si-VO_2waveguide electroabsorption optical switches and photodetectors," Optics express, vol. 23, no.3, pp. 3657-3668, 2015.

[5] C. Rios, *et al*., "Integrated all-photonic non-volatile multi-level memory," Nature Photonics, vol. 9, no. 11, pp. 725, 2015.

[6] S. N. Gupta, *et al*., "Metallic monoclinic phase in VO_2 induced by electrochemical gating: In situ Raman study," EPL (Europhysics Letters), vol. 115, no. 1, pp. 17001, 2016.

[7] R. M.Briggs, *et al*., "Compact silicon photonic waveguide modulator based on the vanadium dioxide metal-insulator phase transition," Optics express, vol. 18, no. 11, pp. 11192-11201, 2010.

[8] $http://www.europractice-ic.com/SiPhotonics_technology_imec_passives.php$.

[9] W. Bogaerts, *et al*., "Silicon microring resonators," Laser Photonics Rev. vol. 6, no. 1, pp. 47–73, 2012.

[10] S. Feng, *et al*., "Athermal silicon ring resonators clad with titanium dioxide for 1.3 μm wavelength operation," Optics express, vol. 23, no. 20, pp. 25653-25660, 2015.

Cylindrical Integrated Optic Resonant Reflection

(Student Paper)

Erika Koussi, Hugo Bruhier, Isabelle Verrier, Nicolas Crespo-Monteiro, Olivier Parriaux, Yves Jourlin
Lyon University at Saint-Etienne, CNRS, Institut d'Optique Graduate School,
Laboratoire Hubert Curien UMR 5516, 42023 Saint-Etienne, France
e-mail: yves.jourlin@univ-st-etienne.fr

ABSTRACT

A sol-gel TiO_2/photoresist two-layer is coated at the inner wall of a fused silica tubular cylinder by controlled pulling. The photosensitive layer is exposed to the interferogram generated by a radial phase-mask centred on the cylinder axis illuminated by an axial UV beam. This results in a photoresist grating having an integer number of lines parallel to the axis. A metal cone of 90° apex is introduced in the tube; it reflects a collimated IR axial beam which it transforms into a cylindrical wave incident perpendicularly onto the TiO_2/resist waveguide grating. The spectral component satisfying the mode coupling synchronism condition experiences a holistic resonant reflection over 2π which the cone redirects to a detection unit. The presentation describes the design of the cylindrical functional structure and demonstrates the occurrence of TE and TM resonant reflection experimentally.

Keywords: Grating waveguide, mode coupling, resonant reflection, cylindrical wave.

1. INTRODUCTION

The phenomenon of resonant reflection of a plane wave from a planar grating waveguide was identified and analysed in the mid-eighties [1]. Since then it has been demonstrated experimentally regarding how close to 100% it can be, what governs its spectral width, its polarization and angular dependence. It has been used mainly in biosensing [2] and laser emission control [3] as well as in a wide diversity of functional devices and subsystems. The fabrication of the waveguide and grating is increasingly benefiting from the background of planar microelectronic technologies; this may be one reason why waveguide and diffraction concepts have not been concretely translated in a circularly cylindrical geometry despite the interesting features that a grating waveguide at the wall of a cylinder can exhibit for sensing, polarization transformation, or laser feedback. A cylindrical diffractive integrated device or subsystem is not just a planar device rolled up: there is a major spatial coherence problem in that a grating for instance must have an integer number of periods over 2π; if this can be achieved, one immediately sees an essential difference between planar and cylindrical geometries, e.g., a very narrow resonance in a planar geometry requires an infinitely long and very low efficiency grating addressed by a plane wave of infinite extent, whereas the same spectral width can be achieved with a waveguide at the wall of a centimetre size cylinder coupled by a stitchingless grating addressed by a cylindrical wave, the coupled guided mode having a multiturn propagation length. Printing a stitchingless grating at the wall of a cylinder with an integer number of periods can actually be achieved by benefiting again from planar technologies: a planar radial grating defined by electron beam, then reactive ion etching, comprising an integer number of azimuthal periods, illuminated by a collimated UV beam generates a 3D interferogram whose high contrast projection at the cylinder wall defines the desired stitchingless grating with a number of periods twice that of the radial phase-mask [4]. This optical coordinate transform is the enabling key for exploring, and possibly applying new functions, and implementing the same functions as in planar integrated optics, but in a different configuration. One of the functions, resonant reflection from a grating waveguide, is here designed, and experimentally demonstrated. We want to point out that the structures considered here are not of the mirco-nanoresonator type such as planar ring resonators or whispering gallery mode microspheres: the structure dimensions are of the order of 10^2 to 10^3 wavelengths with the consequence that use can be made of the geometrical and physical quantities of planar integrated optics.

2. WAVEGUIDE GRATING DESIGN AND FABRICATION

Pulling from a liquid phase is the easiest way of obtaining constant thickness sol-gel TiO_2 and photoresist layers at the inner wall of a tubular cylinder. Considering the difficulty of making any measurement inside the tube, a planar sample undergoes the same processes and serves as an experimental reference. Figure 1a) shows the cross-section of the planar reference with the measured layer thicknesses, grating period and duty cycle, assuming a binary profile. Waveguide grating modelling gives the resonant reflection wavelength of the TE_0 and TM_0 modes under normal incidence in the near infrared with the 960 nm period that will be fabricated at the wall of a cylinder of 4 mm inner radius (Fig. 1b)). As expected, the TM resonance spectral width is notably smaller than the TE one

as the waveguide grating radiation coefficient of a TM mode in a direction normal to the surface is significantly smaller than the TE's.

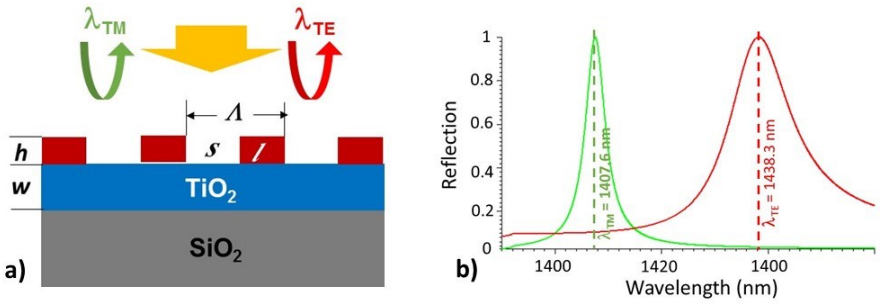


Fig. 1 Planar waveguide grating modelling of TE and TM polarization resonant reflections (red and green lines, resp.) under normal incidence. w = 340 nm, h = 376 nm, Λ = 960 nm, s = 526 nm. SiO_2, TiO_2, resist index: 1.45, 1.7, 1.67.

Figure 2 shows the SEM scans of a few periods of the radial phase-mask. Note that the period in nanometers varies with the radius whereas the angular period is uniquely defined. The phase-mask is illuminated by a collimated axial beam at 355 nm wavelength. The + and – 1st transmitted diffraction orders form an angle with the cylinder axis and interfere at the wall with high contrast since the 0th order propagates along the axis without contributing to the wall interferogram.

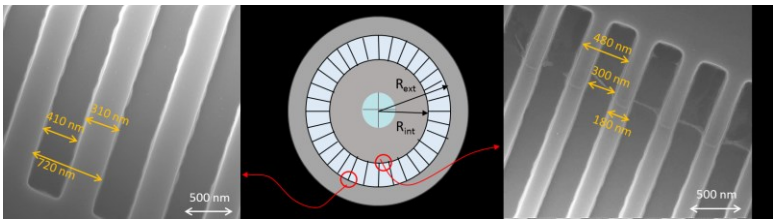


Fig. 2 SEM scans of the radial phase-mask grating at the smaller and larger radii.

The only characterization that can be made of the cylindrical grating at this stage is a diffraction picture under white light shown in Fig. 3.

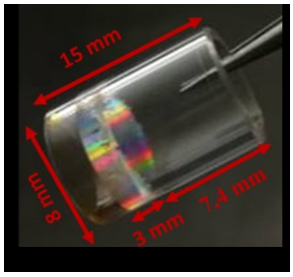


Fig. 3 Diffractogram of the waveguide grating at the inner wall of the cylinder under white light illumination

3. THE MEASUREMENT SETUP

The occurrence of resonant reflection from a cylindrical grating waveguide is given in the spectral domain. The collimated, linearly polarized beam of a fiber white light Supercontinuoum source (WLSC in Fig. 4) propagates through a beam splitter and impinges onto a circular metal cone of 90° apex introduced into the silica tube. It reflects the axial incident beam and transforms it to a cylindrical wave that impinges normally all over 2π onto the grating waveguide at the cylinder inner wall. The expected TE and TM reflected spectral components are redirected by the cone in the form of superposed collimated axial beams, which the beam splitter directs to a spectrometer of 6 nm resolution.

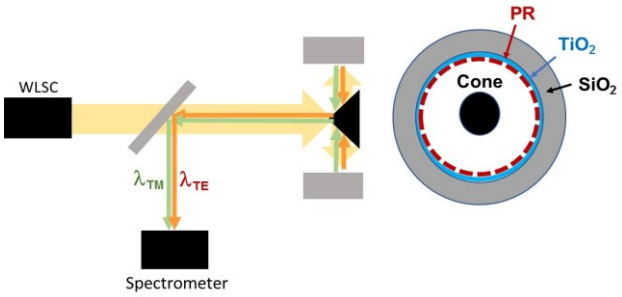


Fig. 4 Measurement setup with WLSC white light supercontinuum, beam splitter, metal cone and micro structured cylinder

4. EXPERIMENTAL EVIDENCE OF RESONANT REFLECTION

Figure 5 gives the spectra delivered by the spectrometer. Two peaks in arbitrary units are clearly present at 1410 and 1437 nm wavelength; the two calculated 100% peaks of Fig. 1 are reminded to ease the polarization identification. No conclusion can be drawn at this preliminary experimental stage as to the amplitude of the peaks since the polarization distribution in the incident cylindrical wave is not controlled; it is a mixture of TE and TM polarizations as the incoming collimated beam is linearly polarized. Pure TE (or TM) polarization at the wall would require a radially (azimuthally) polarized incident beam.

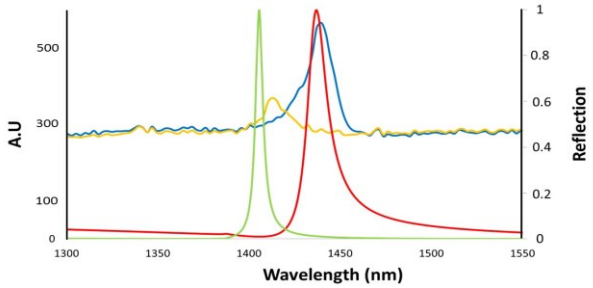


Fig. 5 Simulated (TE red, TM green) and experimental resonant reflection spectra (TE blue, TM yellow)

No conclusion can be drawn as to the reflection line width either, for the spectrometer resolution is not sufficient to finely resolve the peaks. Quite unexpected and remarkable technologically: the resonance wavelengths in the modelling, and in the cylindrical structure are very close which suggests that the layer pulling technique is reliable and little dependent of the geometry of the coated surface.

5. CONCLUSION, PERSPECTIVES

The reported experiment gives access to a new space for waveguide optics. Applications can be envisaged in evanescent wave sensing, laser feedback and rotation sensing [5]. In order to benefit from the possibility of very high spectral resolution in a mm/cm-size resonant diffractive element a big effort is to be made in a low-loss waveguide technology; work is in progress on a germanium-doped silica waveguide at a cylinder wall.

ACKNOWLEDGEMENTS

This work was supported by the LABEX MANUTECH-SISE (ANR-10-LABX-0075) of Université de Lyon, within the program "Investissements d'Avenir" (ANR-11-IDEX-0007) operated by the French National Research Agency (ANR), within the project R2EX (Axis 3).

REFERENCES

[1] G. A. Golubenko, *et al*.: Diffraction characteristics of planar corrugated waveguides, *Opt Quant. Electron.* vol. 18. pp 123-128**,** March 1986

[2] Ye Fang : Label-free cell-based assays with optical biosensors in drug discovery, *ASSAY & Drug Dev. Tech*., vol. 4, Nov. 2006

[3] N. Destouches, et al.: Narrow band resonant grating of 100% reflection under normal incidence, *Opt. Express*, vol. 14, pp. 12613-12622, Dec. 2006.

[4] S. Tonchev, et al.: Subwavelength cylindrical grating by holistic phase-mask coordinate transform, *Opt. Express*, vol. 12, pp. 7946-7953, March 2012.

[5] O. Parriaux, et al.: Cylindrical grating rotation sensor, US Patent 20100245841

Phase-matching unsensitive to waveguide parameters variations in χ^2 based nonlinear integrated optics devices

Maxim Neradovskiy, Hervé Tronche, Elizaveta Neradovskaia, Martin Richter, Ulrich Kuhl, Pierre Aschiéri, Florent Doutre, Tommaso Lunghi, Pascal Baldi, and Marc P. De Micheli
Université Côte d'Azur, CNRS, Institut de Physique de Nice, 06100 Nice, France
e-mail: marc.de-micheli@inphyni.cnrs.fr

ABSTRACT

Using Soft Proton Exchanged (SPE) waveguides in lithium niobate for nonlinear interactions combining quasi-phase-matching and modal phase-matching allowed us to precisely determine the index profile of SPE waveguides and show that they can present phase-matching configurations unsensitive to waveguide parameters variations. Numerically we have shown that this property is due to the particular index profile of the SPE waveguides and that it can be extended to other material combinations as soon as they present similar index profiles.

Keywords: nonlinear optics, unsensitive phase-matching, waveguide index profile, overlap.

INTRODUCTION

At the beginning of nonlinear integrated optics, the idea of using modal dispersion to compensate for material dispersion was envisioned and tested several times [1,2] and some authors noticed that it was a way to obtain noncritical phase-matching conditions [3,4]. Nevertheless, as soon as the Quasi-Phase-Matching techniques have been available, the community focussed on the optimization of devices using the first order mode for both interacting wavelengths. This choice was motivated by the fact that in this case it is easier to optimize the overlap between the interacting modes and to couple the light in and out of the nonlinear waveguide. Nevertheless, in this configuration, the phase-matching in optical waveguides is so critical that any inhomogeneity becomes problematic [5] and that the fabrication tolerances limit the application possibilities [6].

In this paper we show that using Soft Proton Exchanged (SPE) waveguides in PPLN and combining quasi-phase-matching (QPM) and modal-phase-matching (MPM) allows obtaining phase matching conditions, associating a TM_{00} mode for the fundamental and a TM_{10} mode for the harmonic, unsensitive to the waveguide width. Furthermore, we show that it is possible to exploit the many Second Harmonic Generation (SHG) processes in the same waveguide, to reconstruct precisely the index profile of these SPE waveguides.

Further numerical studies allowed us to show that the unsensitivity of the TM_{00}-TM_{10} combination in SPE waveguides is linked to the particular index profile of these waveguides and that this unsensitivity can be extended to other material combinations with completely different waveguide dimensions as long as the shape of the index profile is maintained.

1. Experimental observation of the unsensitivity and determination of the index profile.

We measured the second harmonic generation spectra of SPE waveguides fabricated in a PPLN crystal through a mask presenting openings of width 5, 6, 7 and 8 µm. At the output of the waveguide, the collected beams at λ and $\lambda/2$ were separated and sent either on a joule meter or a camera to measure either the energy of the pulses or the energy transverse spatial distribution of the mode. In figure 1, we present one of these spectra, in which we observed mainly three phase-matching configurations: (1) TM_{00} at λ and TM_{00} at $\lambda/2$, (2) TM_{00} at λ and TM_{02} at $\lambda/2$, and (3) TM_{00} at λ and TM_{10} at $\lambda/2$. For the two first configurations, the phase matching is sensitive to the waveguide width, but for the third one, the sensitivity is extremely small. To understand this phenomenon, we first determined the index profile and the dispersion of the waveguides that allow obtaining all these SHG processes. Based on previous studies, we looked for an index profile given by the following equation :

$$n(x,y,\lambda) = n_{LN}(\lambda) + \delta n_0(\lambda) * f(x) * g(y) \qquad (1)$$

For the substrate dispersion $n_{LN}(\lambda)$ we used a classical Sellmeier equation :

$$n_{LN}(\lambda)^2 - 1 = \frac{2.9804\,\lambda^2}{\lambda^2 - 0.02047} + \frac{2.5981\,\lambda^2}{\lambda^2 - 0.0666} + \frac{8.9543\,\lambda^2}{\lambda^2 - 416.08} \qquad (2)$$

For the waveguides, the dependences on width (x) and depth (y) were taken of the type :

$$f(x) = \frac{1}{1 + e^{\left(\frac{x}{w} - \left(\frac{MaskWidth}{2} + L\right)\right)}} \quad \text{and} \quad g(y) = e^{-\left(\frac{y}{b}\right)^{\alpha}} \qquad (3)$$

while the dispersion of the index increase due to the SPE process is supposed to have the following shape [7] :

$$\delta n_0(\lambda) = \delta n_0 + \delta * e^{-a\,\lambda} \qquad (4)$$

The waveguides index profile and dispersion are therefore represented by 7 unknown parameters, w, L, b, α, δn_0, δ and a which can be precisely determined using 7 or more equations each observed SHG signal giving a different equation. We obtained the best fit with :

w = 0.7289, L = 2.2244, b = 0.572, α = 0,672, δn_0 = 0.0458, δ = 0.241, and a = -6.0543.

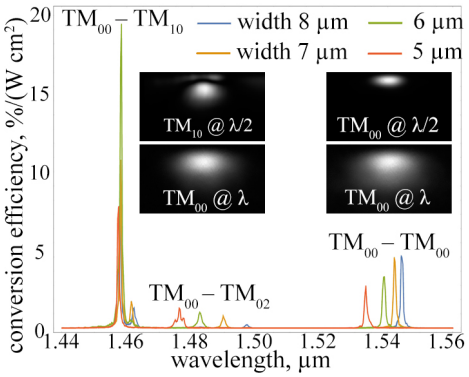


Fig. 1. Phase matching spectra of SPE WG realized on PPLN using different modal configurations for Λ=16.4 µm.

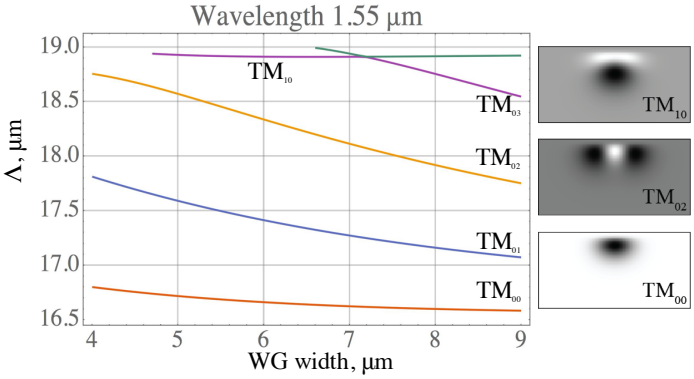


Fig.2. Numerically calculated phase-matching period compensating for the phase mismatch Δβ between TM_{00} mode at λ and TM_{ij} modes at λ/2 as a function of the waveguide width. In this figure, the colors represent the sequence number of the modes by decreasing effective indices. Pictures represent the energy profile of the harmonic modes that have been observed experimentally.

2. Numerical Studies

2.1 Phase mismatch in SPE waveguides

Using these parameters, in Fig. 2, we plot the poling period Λ necessary to compensate for the phase mismatch $\Delta\beta$ between the TM_{00} mode at λ and any of the TM_{ij} modes (i and j being the number of zeros of the field along the depth and width axes respectively) supported by these waveguides at λ/2 as a function of the waveguide width. This phase mismatch is represented by the quantity: $\Delta\beta = \frac{4\pi}{\lambda}\left[n_{ij}\left(\frac{\lambda}{2}\right) - n_{00}(\lambda)\right]$, where $n_{ij}(\lambda/2)$ is the effective index of the TM_{ij} mode at the harmonic wavelength λ/2, and $n_{00}(\lambda)$ is the effective index of the TM_{00} mode at the fundamental wavelength λ.

In Fig. 2, we can see that $\Delta\beta$ varies more or less with the width of the waveguide whatever mode is chosen for the harmonic frequency, except when the harmonic is carried by the TM_{10} mode. In this case and in this range of width, the waveguide index profile is such that the TM_{00} mode at λ and the TM_{10} mode at λ/2 have the same variation with the waveguide width and therefore the quantity $\Delta\beta$ remains unchanged. It can be compensated by a periodic inversion of the sign of the nonlinear coefficient with a period $\Lambda = 2\pi/\Delta\beta$. This corresponds to an unsensitive phase matching configuration which is quite remarkable as the phase matching is preserved whatever the waveguide width, chosen in a range that extend from 4 to 8 µm at least. Note that numerically we can calculate the phase mismatch between the TM_{00} mode at λ and the TM_{01} or the TM_{03} mode at λ/2, but no SHG is observed experimentally corresponding to these combinations because the overlap between the interacting mode is very poor in these cases. Numerically, we can plot similar curves presenting $\Delta\beta$ as a function of the waveguide depth or of the index increase (Fig. 3 and 4), and we observe the following result: for the TM_{00} mode at λ and the TM_{10} mode at λ/2, the phase-mismatch in SPE waveguides do not vary significantly with any of the waveguide parameters.

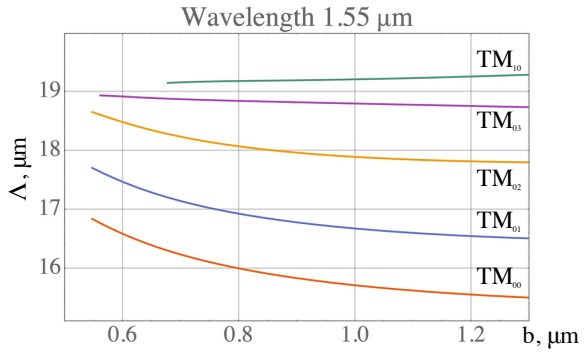


Fig.3. Numerically calculated phase-matching period compensating for the phase mismatch Δβ between TM_{00} mode at λ and TM_{ij} modes at λ/2 as a function of the waveguide depth parameter b.

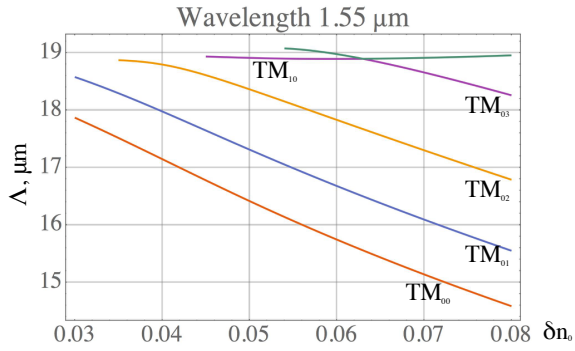


Fig.4. Numerically calculated phase-matching period compensating for the phase mismatch Δβ between TM_{00} mode at λ and TM_{ij} modes at λ/2 as a function of waveguide index increase δn_0.

2.2 Influence of the shape of the index profile on the phase mismatch in SHG processes

To see whether this unsensitive phase matching configuration can be extended to other type of waveguides, we introduced in our calculations values typical of waveguides that can be obtained by varying (by steps or continuously) the Al content in a stack of AlGaN layers. In this case and for λ=1.5µm, the δn_0 can be as high as 0.226 and the width and the depth have to be reduced accordingly to keep the waveguide single mode at the fundamental frequency. In this case, the modal dispersion is strong enough to compensate for the material dispersion and the interaction between the TM_{00} mode at λ and the TM_{10} mode at λ/2 is again unsensitive to the variation of the waveguide parameters as soon as the dependence on depth (y) of the index profile is a function of the type $g(y) = e^{-\left(\frac{y}{b}\right)^{\alpha}}$, with 0.3 < α < 0.7 depending on the waveguide width, which is the same shape as the one of the SPE waveguides.

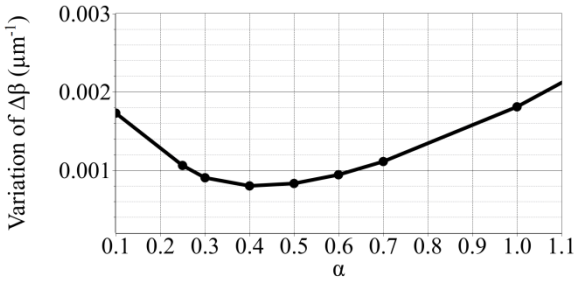


Fig. 5. Amplitude of the variation of Δβ as a function of the parameter α of the shape of the index profile along the depth. The amplitude of variation is equal to Δβmax(x) – Δβmin(x) when the waveguide width x varies between 0.5 and 1 µm.

This is shown in Fig. 5, where we plotted the amplitude of the variation of Δβ when the width of the waveguide varies between 0.5 and 1µm as a function of the parameter α of the shape of the index profile along the depth.

3. CONCLUSIONS

Exploring numerically and experimentally the influence of the shape of the waveguide index profile on the sensitivity of the SHG process to the waveguide fluctuations, we have discovered that as soon as the dependence on depth of the index profile is of the shape $g(y) = e^{-\left(\frac{y}{b}\right)^{\alpha}}$, with 0.3 < α < 0.7, the interaction between the TM_{00} mode at the fundamental frequency and the TM_{10} mode at the harmonic frequency is very unsensitive to all the waveguide parameters variations. We have also shown experimentally, that the efficiency in this configuration can be higher in this unsensitive configuration than for the interaction between TM_{00} modes at both frequencies. We now have to study in more details the overlap issues in order to determine the potential of this unsensitive configuration and see whether they allow designing devices less sensitive to waveguides tolerances.

ACKNOWLEDGEMENTS

This work has been conducted within the framework of the project OPTIMAL granted by the European Union by means of the Fond Européen de développement régional (FEDER). The authors also acknowledge financial support from the Agence Nationale de la Recherche through the project ANR-14-CE26-0036-01 and the support of Université Côte d'Azur.

REFERENCES

[1] W. Sohler and H. Suche, Second-harmonic generation in Ti-diffused $LiNbO_3$ optical waveguides with 25% conversion efficiency, *Appl. Phys. Letters*, **33**(6), 518 (1978).

[2] A. Azema, *et al.*, Efficient SHG with clad Ti:$LiNbO_3$, *J. of Quantum Electronics*, **17**, 2486-2488 (1981).

[3] W.K. Burns and R.A. Andrews, Noncritical phase matching in optical waveguides, *Appl. Phys. Lett.* **22**, 143 (1973) 1994

[4] M. L. Bortz *et al.*, Noncritical Quasi-Phase-Matched Second Harmonic Generation in an Annealed Proton-Exchanged $LiNbO_3$ Waveguide, *Transactions on Quantum Electronics*, **30** (12), 2953-2960 (1994)

[5] M. M. Fejer et al. , Inhomogeneities in waveguides dimension is a serious problem for guided wave frequency conversion devices, Appl. Phys. Lett. 57, 2294 (1990).

[6] M. Santandrea et al., Fabrication limits of waveguides in nonlinear crystals and their impact on quantum optics applications, https://arxiv.org/pdf/1809.08802.pdf

[7] K. El Hadi *et al.,* Spectral measurement of the film–substrate index difference in proton-exchanged $LiNbO_3$ waveguides, *Applied Optics* **37**(27) 6463-6467, (1998)

New Resonance Behavior based on Bound States in the Continuum in a Silicon Photonic Waveguide Platform

Thach G. Nguyen, Guanghui Ren, Steffen Schoenhardt, Markus Knoerzer, Andreas Boes, and Arnan Mitchell
School of Engineering, RMIT University, Melbourne,VIC3001, Australia
e-mail: thach.nguyen@rmit.edu.au

ABSTRACT

A new type of resonance in silicon photonics is demonstrated, which is achieved by coupling between a continuum of TE slab modes to a discrete TM mode of a silicon ridge to create a single sharp resonance. Theoretical description of the phenomenon and experimental results are presented.

Keywords: photonic integrated circuits, silicon photonics, resonator, bound states in the continuum

1. INTRODUCTION

One of the most important building blocks of integrated photonics are optical resonators. These are crucial for many applications including wavelength filtering and routing, modulation, laser cavities, nonlinear optics as well as sensing. In silicon photonics, resonators are often based on rings, micro-disks or Fabry-Perot resonators. Recently, the alternative approach to realize resonators based on so-called bound states in the continuum (BICs) photonic structures has been explored [1]. These structures can exhibit a single resonance of infinite narrow linewidth over a broad wavelength range. In photonics, it has been shown that BIC can be formed by symmetry-protected bound states, radiation cancellation from two or more coupled resonators or radiation cancellation from a single resonance such as in photonic crystal slabs, a low-index waveguide on a high-index membrane [2].

In this work, we present the first demonstration of a new resonance behavior, which is based on bound states in the continuum, in silicon photonics. This resonance is achieved by coupling a continuum of un-bound TE modes in a single mode silicon slab into a single propagating TM mode of a ridge waveguide on the slab.

2. THEORY

Figure 1(a) illustrates the cross section of a thin-shallowly etched silicon photonic waveguide. It has been demonstrated in a such waveguide, that a TM guided mode will leak equally into TE slab mode propagating on both sides of the waveguide [as illustrated in Fig. 1(b)] due to TM/TE polarization coupling at the ridge walls [3]. The leakage TE slab mode propagates at a particular angle to the ridge. This angle is given by:

$$\theta = \cos^{-1}\left(\frac{n_{tm}}{n_{te}}\right) \quad (1)$$

where $n_{tm}$and $n_{te}$are the effective index of the TM guided mode and TE slab mode in the claddings, respectively. This phenomenon is called 'lateral leakage'. The leakage loss rate depends on the geometry of the ridge and ridge width. At some 'magic' widths, the leakage can be resonantly cancelled due to destructive interference of the leakage from the two side walls, resulting in low loss TM mode [3, 4]. This leakage cancellation behavior can be considered as bound sate and the continuum [5].

When one considers the reserve process, where a broad TE beam is incident toward the ridge as illustrated in Fig. 1(c), it is expected that the TE beam will undergo some reflection due to the difference in refractive index between the slab and ridge regions. The calculated reflection as a function of the incident angle due to Fresnel reflection resulting from the refractive index difference is shown in Fig. 1(d), labelled 'Background'. However, in this calculation, the TE/TM coupling at the ridge walls is ignored. To account for the TE/TM coupling, we used a full vectorial simulation based on mode-matching method to simulate the reflection and transmission when a TE slab mode was incident on the ridge. In Fig. 1(d), the curve labelled 'Rigorous' shows the reflection as a function of the incident angle from the rigorous simulation. When taking the TE/TM coupling into account, 100% reflection occurs at a certain angle at which the incident TE wave is phase-matched to the TM guided mode in the ridge. Far away from this phase-matching angle, the rigorously calculated reflection approaches the background Fresnel reflection.

A similar behavior can be expected when the incident angle is fixed and one looks at the spectral response of the system. Figs. 1 (e) and (f) show the simulated transmission and reflection as functions of wavelength for different ridge widths, respectively. This behavior can be explained by the fact that the guided TM mode in the ridge and the incident TE slab mode can only be phase-matched at a particular wavelength since they have different dispersion characteristics. At this phase-matching wavelength, the TE slab mode couples strongly to TM mode in the ridge, resulting in 100% reflection. The reflection drops when moving away from this phase-matching wavelength.

It is clear from the simulated spectral responses that the ridge behaves like a resonator to the TE beam with the spectral bandwidth depending on the ridge width. When the ridge approaches the 'magic' width, the bandwidth of the resonance decreases to zero. This behavior can also be considered as BIC [6].

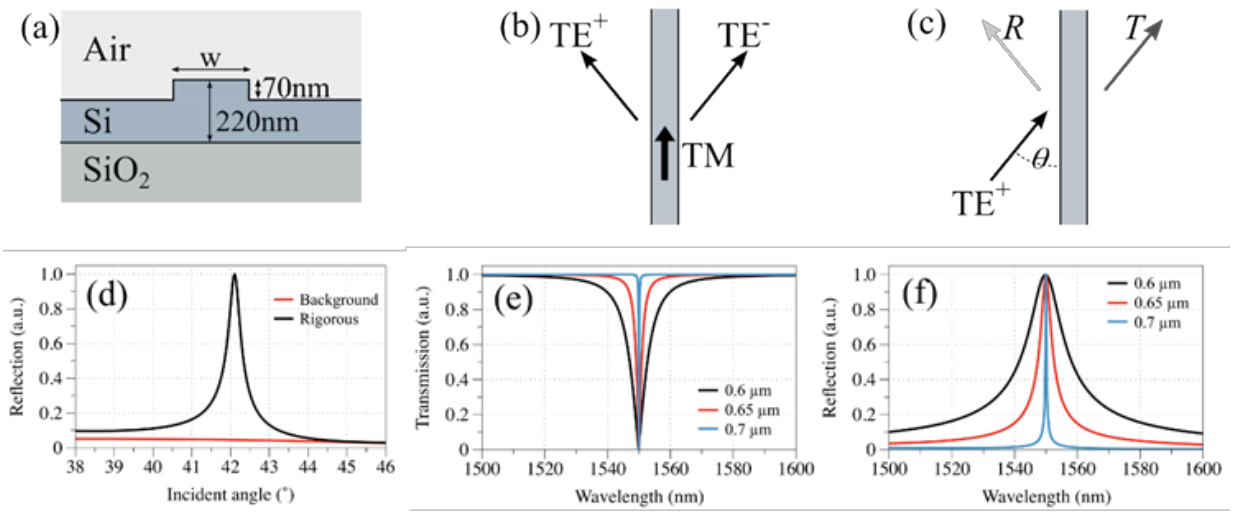


Figure 1. (a) Schematic of the ridge cross-section; (b) Illustration TM mode of a ridge leaking to TE slab modes on either side; (c) Illustration of the reverse process, where the ridge is illuminated with a TE slab mode from one side; (d) Reflection as a function of the incident angle for w = 0.6 μm; (e) and (f) Transmission and reflection as a function of wavelength for different ridge widths.

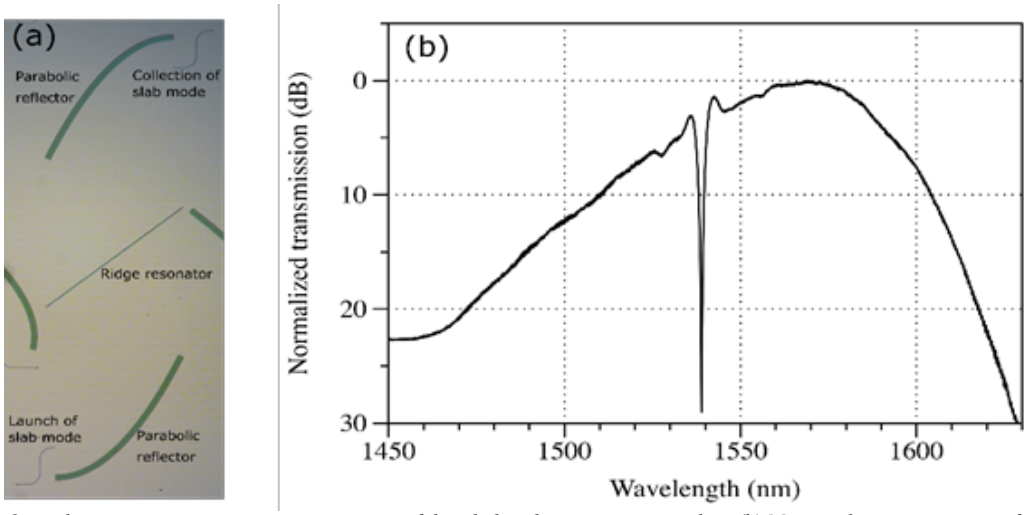


Figure 2. Optical microscope image giving an overview of the whole ridge resonator test chip; (b) Measured transmission as a function of the wavelength.

The full transfer function of an excitation beam on the ridge can be considered to be composed of the superposition of a background component (due to Fresnel reflections) and a resonance describing the gradual coupling of the TE beam into the TM bound mode and the reciprocal leakage of this energy back into the TE continuum. Using the temporal coupled mode theory approach, it is possible to derive a closed form expression enabling accurate prediction of the resonant spectral response of a beam reflection from a ridge based on propagation behavior of TM mode and the Fresnel coefficients of the ridge walls. The reflection coefficient of a TE beam on a ridge can be expressed as:

$$R = \frac{j[(n_{te}\cos\theta - n_{tm})r - n'_{tm}t]}{j(n_{te}\cos\theta - n_{tm}) + n'_{tm}} \tag{2}$$

where r and t are the background Fresnel reflection and transmission coefficient of the non-resonant process, $n_{tm} + jn'_{tm}$ is the complex effective index of the leakage TM mode.

3. EXPERIMENT RESULTS

As a proof of concept demonstration, we fabricated a system to launch a Gaussian beam at a ridge. The device was fabricated on a diced piece of SOI wafer with a 220-nm-thick Si guiding layer and a 3-μm-thick SiO_2 buried oxide layer using electron beam lithography (EBL) and reactive ion etching (RIE). A 650 nm wide ridge was formed by partially etching 70 nm of the silicon layer. Parabolic reflectors were used to generate and collect broad TE beams. The device was interfaced to input/output optical fibers using grating couplers. Fig. 2(a) shows the optical microscope image of the fabricated device.

To characterize the wavelength response of the resonator, a tunable C-band laser (Agilent 81600B) and an in-built optical power detector (Agilent 81635A) were used to measure the transmitted power as a function of the wavelength. Fig. 2(b) shows the measured transmission as a function of wavelength. The transmission spectrum exhibits a broad envelope that is defined by the spectral efficiency of the grating couplers. When the ridge resonator is present, the device exhibits a single, sharp resonance over a broad wavelength range. The resonance has an extinction ratio of approximately 25 dB and a full width at half maximum of 2.95 nm, which corresponds to a Q-factor of around 520, matching very well with the theoretical prediction.

4. CONCLUSIONS

In summary, we have demonstrated, to the best of our knowledge, the first demonstration of a new type of resonator on silicon photonics. The resonator is based on bound states in the continuum. It is formed by the coupling of the unbound TE mode in a slab to the guided TM mode in the ridge and coupling back into TE slab mode. The experimental results confirm the predicted behavior.

REFERENCES

[1] [1] D. C. Marinica, A. G. Borisov, and S. V. Shabanov, "Bound States in the Continuum in Photonics," *Phys. Rev. Lett.* 100, 183902 (2008).

[2] [2] C. W. Hsu, B. Zhen, A. D. Stone, J. D. Joannopoulos, and M. Soljačić, "Bound states in the continuum," *Nat. Rev. Mater.* 1, 16048 (2016).

[3] [3] M. A. Webster, R. M. Pafchek, A. Mitchell, and T. L. Koch, "Width Dependence of Inherent TM-Mode Lateral Leakage Loss in Silicon-On-Insulator Ridge Waveguides*," IEEE Photon. Technol. Lett.* 19, 429 (2007).

[4] [4] T. G. Nguyen, R. S. Tummidi, T. L. Koch, and A. Mitchell, "Rigorous Modeling of Lateral Leakage Loss in SOI Thin-Ridge Waveguides and Couplers," *IEEE Photon. Technol. Lett.* 21, 486 (2009).

[5] [5] C. Zou, J. Cui , F. Sun, X. Xiong, X. Zou , Z. Han, and G. Guo, "Guiding light through optical bound states in the continuum for ultrahigh-Q microresonators," *Laser & Photonics Review* 9, 114 (2015).

[6] [6] E. A. Bezus, D. A. Bykov, and L. L. Doskolovich, "Bound states in the continuum and high-Q resonances supported by a dielectric ridge on a slab waveguide," *Photon. Res.* 6, 1084-1093 (2018).

Grating assisted contra-directional filters with high rejection ratio in silicon nitride rib waveguides

(Student Paper)

Xiaomin Nie [1,2], Nina Turk [1,2], Zuyang Liu [1,2], Roel Baets [1,2]
[1]*Ghent University - imec, Photonics Research Group, Technologiepark 126, B-9052 Ghent, Belgium*
[2]*Center for Nano- and Biophotonics, Ghent University, Belgium*
e-mail: Xiaomin.Nie@ugent.be

ABSTRACT

In this work, we report an on-chip filter that has a high rejection ratio and an unlimited free spectral range (FSR) on the red side of the stop/pass band. This filter is based on a grating assisted contra-directional coupler and is fabricated with one step electron-beam lithography on a silicon nitride rib waveguide platform. This type of filter is able to couple the light into a bus waveguide contradirectionally, instead of reflecting the light back to the input as in the case of a Bragg reflector. We experimentally demonstrate a filter with a stop band centered at 789 nm with an average rejection ratio of 43 dB and bandwidth around 1.7 nm.

Keywords: on-chip filter, silicon nitride, grating assisted contra-directional coupler, e-beam lithography.

1 INTRODUCTION

On-chip filters are essential components for a wide range of applications including lasers, optical sensors [1] and wavelength-division multiplexers (WDM) [2]. Various types of filters such as Bragg gratings, Mach-Zehnder cascades [3] and ring resonators [4] have been studied and developed on a diversity of waveguide platforms. As one of the most popular on-chip filters, ring-resonator add-drop filters have received a lot of attention. Nevertheless, they are not suitable for applications that require a very large or unlimited free spectral range (FSR). For example, in an on-chip Raman spectroscopic system [5], one wants to reject the pump light while leaving the wide spectral range where Raman signals are generated unaffected. In such situations, a Bragg reflector provides a suitable solution. However, the fact that the Bragg reflector directly reflects light back to the input could be problematic to the laser source. Usage of Bragg reflectors in such situations would require the integration of an on-chip circulator, which is difficult and might bring extra complexity and cost. Filters based on the grating assisted contra-directional coupler (GACDC) can be a good candidate in such cases. They inherit the merit of large FSR from the Bragg reflectors, while have no, or very weak, reflection at the operating wavelength. As a compact 4-port device, GACDCs are attractive as wavelength-selective add-drop filters and pump rejection filters. GACDCs were first implemented in planar optical waveguides based on silica and III-V materials [6]. After that, researchers have developed GACDCs on silicon-on-insulator (SOI) platform at the telecommunication wavelengths [7]. However, little effort has been spent to implement GACDCs operating at shorter wavelength on the silicon nitride platform where optical bio-sensing applications such as on-chip Raman spectroscopy are growing and developing. In this paper, we demonstrate a GACDC filter implemented for TE-like modes on the silicon nitride rib waveguide platform. To allow device operation in the near infrared region (such as at the often used wavelength of 785 nm), the gratings need to have a period smaller than what can be achieved by conventional deep-UV lithography. Therefore, e-beam lithography is used to realize the current prototype device. In the future however the proposed device can be realized by deep-UV immersion lithography in a CMOS fab.

2 WORKING PRINCIPLE

The proposed GACDC consists of two silicon nitride rib waveguides with different width and a first order grating in between, as shown in Fig. 1(a). When light containing different wavelength components is injected into the waveguide a, different types of coupling can occur when the corresponding phase-matching condition fulfilled. At wavelength λ_D, the forward-propagating mode in waveguide a can be coupled to the backward-propagating mode in waveguide b when the following phase-matching condition is fulfilled with the assistance of the grating.

$$k_a(\lambda_D) - \frac{2\pi}{\Lambda} = -k_b(\lambda_D) \tag{1}$$

where $k_{a,b}(\lambda_D) = 2\pi n_{a,b}/\lambda_D$, with $n_{a,b}$ the effective refractive index of modes in waveguide a and b. This is the inter-waveguide contra-directional coupling. Solving (1), we get the expression $\lambda_D = (n_a + n_b)\Lambda$.

What can also happen is the coupling between the forward and backward mode in waveguide a at wavelength λ_a determined by:

$$k_a(\lambda_a) - \frac{2\pi}{\Lambda} = -k_a(\lambda_a) \tag{2}$$

where $k_a(\lambda_a) = 2\pi n_a/\lambda_a$. This is the intra-waveguide back reflection. Again, we can calculate that $\lambda_a = 2n_a\Lambda$. In some applications, to make sure that the filter has a flat spectral response in the long wavelength region. it is preferable to have $n_a < n_b$, which means the signal should be injected into the narrow waveguide.

The coupling strength can be estimated by calculating the coupling coefficient κ_D and κ_a according to the coupled mode theory [8]:

$$\begin{aligned} \kappa_a &= \frac{\pi}{\lambda n_a} \iint e_a^*(x,y)\Delta\epsilon_1(x,y)e_a(x,y)dxdy \\ \kappa_D &= \frac{\pi}{\lambda n_a} \iint e_a^*(x,y)\Delta\epsilon_1(x,y)e_b(x,y)dxdy \end{aligned} \tag{3}$$

where $\Delta\epsilon_1(x,y)$ stands for the first order Fourier expansion coefficient of the perturbation introduced by the grating and $e_{a,b}(x,y)$ is the normalized electric field distribution of the fundamental TE-like mode in waveguide a or b. With the coupling coefficient, we can calculate the theoretical transmission at the through port when perfect phase matching is fulfilled:

$$T = 1 - \tanh^2\left(|\kappa|^2 L\right) \tag{4}$$

where L is the total length of the grating.

3 SIMULATION AND DESIGN

To design the filter, we use a commercial mode solver FIMMWAVE. The intensity distribution is shown in the cross section in Fig. 1(b). Solving the modes for different wavelengths will generate dispersion curves, which can be used to calculate the phase matching condition and determine the corresponding grating period for a desired filtering wavelength.

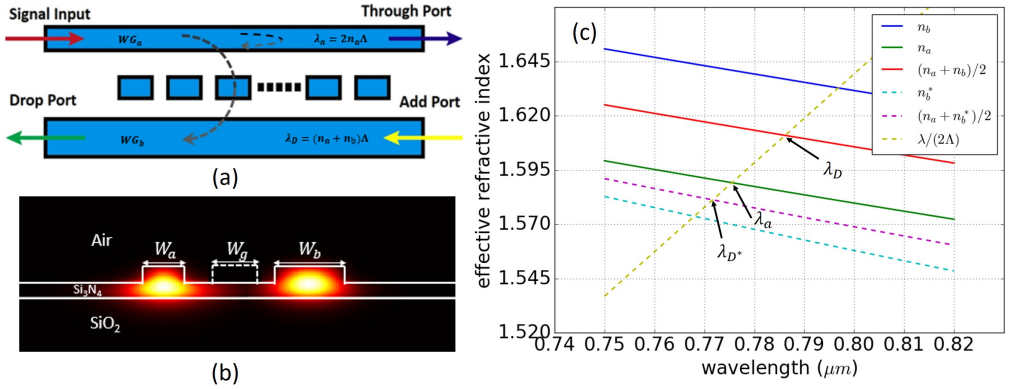


Figure 1. (a) Schematic top view of the proposed GACDC. (b) Cross-sectional with the simulated intensity distribution of the fundamental TE-like modes in the rib waveguides. (c) Dispersion curves of the modes. Phase matching wavelengths are indicated with arrows.

We consider a device that contains two rib waveguides with width W_a=340 nm and W_b=580 nm. The two waveguides are placed 780 nm away from each other with a grating in between with width W_g=320 nm, period Λ=244 nm and grating duty cycle η=0.5.

In Fig. 1(c), we plot the effective refractive index curve for the fundamental TE-like modes in the rib waveguides a and b as well as their average. These dispersion curves intersect with the curve $y = \lambda/(2\Lambda)$ at the wavelength λ_a=776 nm for the intra-waveguide back reflection and λ_D=787 nm for the inter-waveguide contra-directional coupling. The contra-directional coupling coefficient is calculated from the simulated electric field distribution: κ_D=9.06$\times 10^{-3}$ μm^{-1}.

According to (4), theoretically, the extinction ratio at the contra-directional coupling wavelength can go infinitely high as one keeps increasing the total length of the grating. Realistically however, there should be a limitation. To explore what extinction ratio we can achieve in practice by increasing the grating length, a variety of lengths up to L=4.9 mm is considered in the design.

The devices were fabricated on a silicon nitride wafer with one step of e-beam lithography and reactive-ion etching (RIE). The full thickness of the silicon nitride layer is 300 nm and the desired etch depth is 150 nm.

4 MEASUREMENT RESULTS AND DISCUSSION

The fabricated devices are measured on a setup which contains two fibers that are positioned near-vertically (10 degree away from normal) to the chip. The light is coupled into and out of the chip through on-chip grating couplers. The devices are first measured with a broadband supercontinuum source to characterize the spectral response in a relatively wide wavelength range. An optical spectrum analyzer (OSA) is used to analyze the

spectral response of the GACDC filters. The through-port spectrum of a device with L=4.9 mm is shown in Fig. 2(a) together with a transmission spectrum of a reference waveguide. We can immediately notice three dips in the transmission spectrum. The two dips at 789 and 777 nm are in agreement with the two intersections λ_D and λ_a shown in Fig. 1(c). The small discrepancy could be explained by the fabrication uncertainties. Variations in the waveguide widths, etch depth as well as the wafer thickness can change the effective indices of the waveguide modes and shift the exact wavelengths at which phase matching happens. A third dip at around 775 nm can be explained as the contra-directional coupling between the forward propagating mode in waveguide a and a high order TM-like backward propagating mode in waveguide b. After we add the dispersion curves of this high order mode labeled with n_b^* and the average labeled with $(n_a + n_b^*)/2$ in Fig. 1(c), the third intersection at wavelength λ_D^* emerges, in agreement with the measurement result. In the spectrum, we can also observe the drop of transmission in the wavelength range shorter than 770 nm. This is due to the fact that in this wavelength range, the grating starts to couple light into the radiation modes in the oxide cladding.

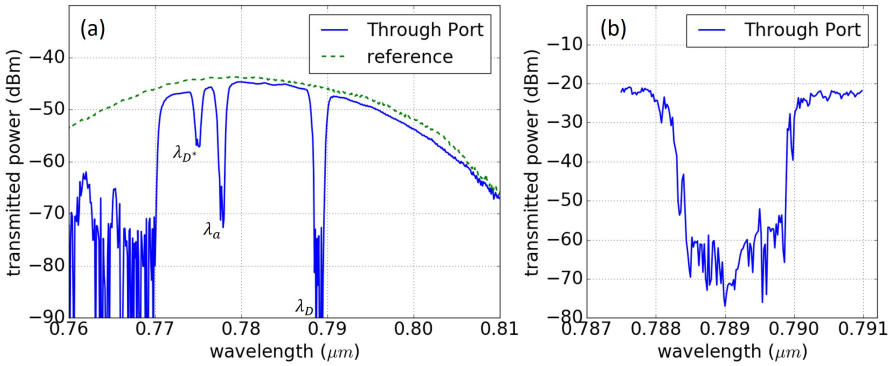


Figure 2. Measured through-port transmission spectra of a fabricated GACDC device: (a) measured with a supercontinuum source in a wide wavelength range, (b) a high resolution zoom-in measurement with a Ti:Sapphire tunable CW laser.

To take a closer look at the contra-directional dip at λ_D, we use a Ti:Sapphire tunable CW laser together with an optical power meter to scan the spectrum in the wavelength region centered around λ_D with a step size of 20 pm. The measured transmission spectrum is shown in Fig. 2(b), where we can see a stop band with bandwidth around 1.7 nm and rejection ratio on average 43 dB.

The reasons why we could not get even higher rejection ratio could be multifold. On the one hand, fabrication uncertainties and non-uniformities introduce stitching errors and geometrical variations that could reduce the extinction ratio and broaden the bandwidth of the stop band. On the other hand, light having leaked into the 150 nm thick Si_3N_4 slab could travel around in the chip and set a lower boundary to the signal strength that one can measure on the chip. Future work will focus on the investigation of these effects.

5 CONCLUSION

We designed and characterized an on-chip GACDC filter that operates in the near infrared range (< 800 nm) on a silicon nitride rib waveguide platform. The working principle was explained, followed by the simulation results that allowed us to design the filter. Experimentally, we demonstrated a device that has a stop band centered at the inter-waveguide contra-directional coupling wavelength λ_D=789 nm. The extinction ratio measures in average 43 dB, while the bandwidth is around 1.7 nm. On the red side of the stop band, the filter offers a flat spectrum response with an unlimited FSR. All these features make it suitable and promising as a pump rejection filter for applications such as on-chip Raman spectroscopy.

REFERENCES

[1] K. De Vos, I. Bartolozzi, E. Schacht, P. Bienstman, and R. Baets,"Silicon-on-insulator microring resonator for sensitive and label-free biosensing," Opt. Exp., vol. 15, no. 12, pp. 7610–7615, 2007.

[2] X. Wang, W. Shi, R. Vafaei, N. A. F. Jaeger, and L. Chrostowski, "Uniform and sampled Bragg gratings in SOI strip waveguides with sidewall corrugations," IEEE Photon. Technol. Lett. 23, 290–292, 2011.

[3] F. Horst, W.M. Green, S. Assefa, S.M. Shank, Y.A. Vlasov and B.J. Offrein, "Cascaded Mach-Zehnder wavelength filters in silicon photonics for low loss and flat pass-band WDM (de-)multiplexing" Optics express, 21(10), pp.11652-11658, 2013.

[4] F. Xia, M. Rooks, L. Sekaric, and Y. Vlasov, "Ultra-compact high order ring resonator filters using submicron silicon photonic wires for on-chip optical interconnects," Optics express, 15(19), pp.11934-11941, 2007.

[5] A. Dhakal, A. Subramanian, P.C. Wuytens, F. Peyskens, N. Le Thomas, R. Baets, "Evanescent excitation and collection of spontaneous Raman spectra using silicon nitride nanophotonic waveguides," Optics Letters, 39(13), p.4025-4028, 2014.

[6] M. Qiu, M. Mulot, M. Swillo, S. Anand, B. Jaskorzynska, A. Karlsson, and A. Forchel, "Photonic crystal optical filter based on contra-directional waveguide coupling," Applied Physics Letters, 83(25), 5121-5123, 2003.

[7] W. Shi, X. Wang, W. Zhang, L. Chrostowski, and N. A. F. Jaeger. "Contradirectional couplers in silicon-on-insulator rib waveguides," Optics letters, 36(20), 3999-4001, 2011.

[8] P. Yeh and H.F. Taylor, "Contradirectional frequency-selective couplers for guided-wave optics," Applied optics, 19(16), pp.2848-2855, 1980.

Reduced Timing Jitter in a Hybridly Mode-Locked Semiconductor Laser due to an Increased Modulation Curvature

(Student Paper)

Lars Nielsen*, Martijn J. R. Heck
Aarhus University - Department of Engineering, Finlandsgade 22, 8200 Aarhus N, Denmark
**e-mail: ln@eng.au.dk*

ABSTRACT

Low-noise microwave oscillators are essential to several applications, and mode-locked lasers are good candidates for the realization of these. The total timing jitter of an actively mode-locked laser has previously been shown to be inversely proportional to the modulation curvature of the driving signal. This paper presents the first numerical study on the timing jitter in a semiconductor hybridly mode-locked laser, when the reverse bias voltage of the saturable absorber is driven with different modulation curvatures. It is confirmed that also for these lasers, the total timing jitter scales reciprocally with the modulation curvature. Thus, according to the numerical model, the performance of a mode-locked laser based oscillator will improve by increasing the bandwidth of the signal driving the saturable absorber. Coupled opto-electronic oscillators, as well as clock extraction from pulse trains in optical time division multiplexing systems, can improve from this.

Keywords: Mode-locked lasers, hybrid mode-locking, timing jitter, photonic integrated circuits, laser modelling, microwave photonics.

1 INTRODUCTION

Generation of low-noise microwave signals is essential for several applications, including Doppler radars [1], and optical communication [2]. Mode-locked lasers (MLL) are promising candidates for such oscillators, especially when incorporated in a coupled opto-electronic oscillator (COEO) [3]. In this, an opto-electronic feedback loop feeds the output of the MLL back to an intra-cavity modular loss element, such as a saturable absorber (SA). Thus, a COEO might be viewed as a hybridly MLL in which the driving signal is a delayed copy of the output from the MLL itself. Thus, it is reasonable to argue that by optimizing the low-noise performance of a hybridly MLL, one also improves the performance of a stand-alone COEO that incorporates this MLL. Also, clock extraction in optical time division multiplexing (OTDM) systems [4] can improve from this.

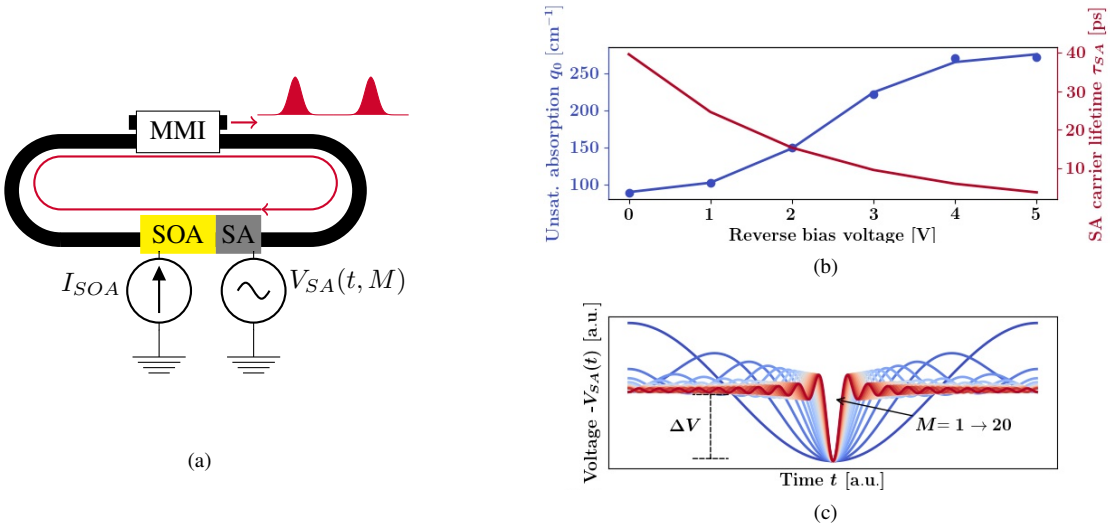
It has previously been shown, analytically, that the total timing jitter of an actively MLL is reduced when the modulation curvature of the driving signal is increased [5]. For a pure sinusoid this can be done either by increasing the amplitude or the frequency. The analytical expression is short and efficient, but it is based on numerous assumptions, such as small round-trip loss, no saturable absorption, and a Gaussian pulse shape. The aim of this work is to validate the expression for a semiconductor hybridly MLL, in which these assumptions do not hold. The study is based on a numerical model for a semiconductor MLL in which the driving signal is applied to the reverse bias voltage of the SA. In order to keep the validity of the model as high as possible, the parameter values used for the simulation are tailored towards InP based semiconductor lasers, by extracting values from measurements presented throughout literature.

2 METHODS

This work is based on the computationally efficient MLL model developed by Vladimirov and Turaev [6], which consists of three coupled equations. Two differential equations determine the evolution of the saturable gain and absorption, and a third equation governs the evolution of the optical field. The model assumes unidirectional lasing as depicted in Fig. 1(a), which in general is not true for a ring MLL. However, quasi-unidirectional operation can be achieved from an asymmetric cavity configuration [7]. Also, the focus of this study is on hybrid mode-locking (ML), which relates to pulse shaping dynamics and not directly to bidirectional versus unidirectional operation.

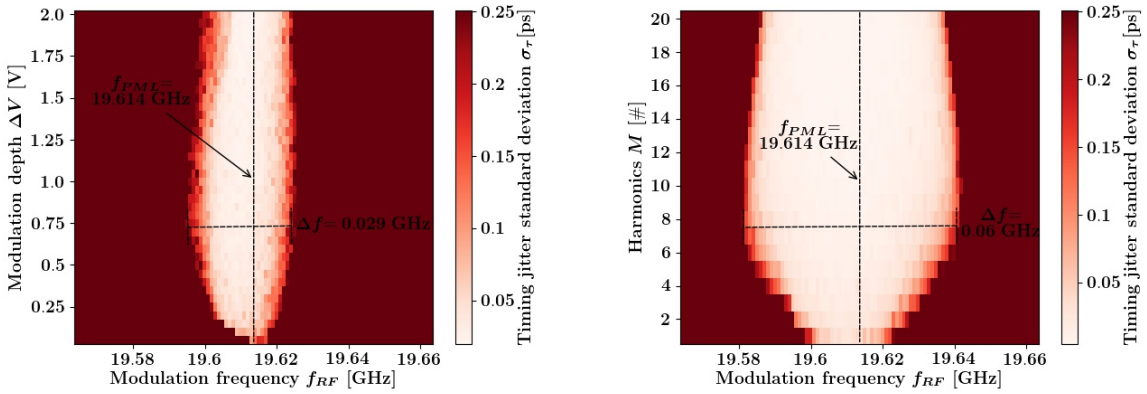
A ring MLL configuration with a total cavity length of $4200\ \mu\mathrm{m}$, corresponding to a pulse repetition rate around $20\ \mathrm{GHz}$, is studied. It incorporates a $750\ \mu\mathrm{m}$ long semiconductor optical amplifier (SOA), and a $60\ \mu\mathrm{m}$ long reverse biased SOA, namely a SA. The values for the parameters in this model have been tailored towards the generic InP foundry platform available at SMART Photonics [8], by mostly extracting, either directly or indirectly, values from work related to this platform. Especially important to hybrid ML is the voltage dependency of the SA unsaturated absorption q_0 and carrier lifetime τ_{SA}, presented in Fig. 1(b). Other parameters are listed in the caption of Fig. 1(a). The reverse bias voltage modulation signal is on the form $V_{SA}(t, M) = \Delta V \sum_{m=1}^{M} \frac{1}{M} \cos(m \cdot 2\pi \cdot f_{RF} \cdot t) - V_{bias}$, as depicted in Fig. 1(c). The operating point of the MLL was chosen to $I_{SOA} = 90\ \mathrm{mA}$ and $V_{bias} = 2\ \mathrm{V}$, and passive ML was identified at $f_{PML} = 19.614\ \mathrm{GHz}$.

The research is supported by the Aarhus University Research Foundation AUFF, through a Lektor Starting Grant.



(a) (b) (c)

Figure 1. (a) Schematic of the simulated laser. The following parameter values are used for the simulation: bimolecular recombination coefficient $B = 10^{-16}$ m^3/s [9], SOA transparency carrier density $N_{tr,SOA} = 1.08 \cdot 10^{24}$ m^{-3}, SOA differential gain $a_{N,SOA} = 1.25 \cdot 10^{-20}$ m^2, amplified spontaneous emission (ASE) power spectral density $N_0 = -186$ dBW/Hz, SOA carrier lifetime $\tau_{SOA} = 1.58$ ns, center wavelength $\lambda_0 = 1560$ nm, total gain bandwidth $\omega_L = 12 \cdot 10^{12}$ rad/s [10], stability factor $s = 20$ [11], group velocity $v_g = 8.2429 \cdot 10^7$ m/s, group velocity dispersion (GVD) $k'' = 4 \cdot 10^{-24}$ s^2/m [12], waveguide active area $\sigma_{xy} = 0.0624$ μm^2, confinement factor $\Gamma = 0.074$ [9], SOA linewidth enhancement factor $\alpha_{SOA} = 3$ [13]. The same linewidth enhancement factor is used for the SA $\alpha_{SA} = 3$. The round-trip attenuation factor $\kappa = 0.0884$ is found from the sum of losses due to output coupling in the multi-mode interferometer (MMI), and linear losses in the passive and active waveguides. (b) Plot of SA unsaturated absorption [14] and carrier lifetime [15] vs. reverse bias voltage. (c) Plot of different modulation curvatures of the SA reverse bias voltage.



(a) (b)

Figure 2. Locking range map based on timing jitter standard deviation in a 750 ns interval, for (a) increasing modulation depth and (b) increasing number of harmonics. Values above the free running timing jitter standard deviation 0.25 ps have been rounded to this value.

3 RESULTS

In Fig. 2(a) the locking range is mapped for different modulation depths ΔV when the number of harmonics is fixed to $M = 1$. The locking range is defined as the region for which the timing jitter is below that of the free running MLL. The locking range is asymmetric and the maximum locking range is 0.029 GHz for a modulation depth of 0.75 V. The locking map for an increasing M, and a fixed $\Delta V = 0.5$ V, is shown in Fig. 2(b). The locking range widens for a small M and becomes 0.060 GHz around $M = 7$, after which it narrows.

The phase noise was computed from the output of a 50-μs long simulation, for both free running passive ML, and hybrid ML with $M = 1 \rightarrow 4$. The modulation frequency was fixed to $f_{RF} = 19.610$ GHz, and the modulation depth to $\Delta V = 0.5$ V. The plots are shown in Fig. 3(a), each being an average of 100 simulations. It is seen, from the flattening at lower frequencies, that the random walk is eliminated by locking the MLL to an external ideal clock. Also, it is seen that the flattening level is lowered by increasing the number of harmonics. In accordance with [5] the phase noise is of the form $\mathcal{L}(f) = k_0/(f^2 + f_c^2)$, and fits are shown as dashed black lines. The total phase noise power is found by integrating over all frequencies, leading to the finite value $\pi k_0/f_c$. Taking the root of this and dividing by the oscillation frequency gives the data points for the total timing jitter in Fig. 3(b). According to [5] the total timing jitter variance should be inversely proportional to the modulation curvature, which is given by the second derivative at the minimum of the driving signal, depicted

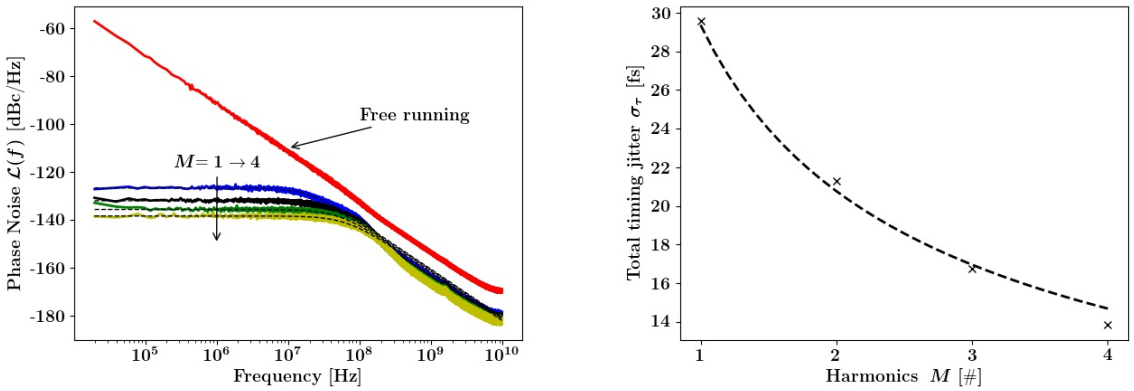


Figure 3. (a) Phase noise of free running and hybridly MLL. (b) Total timing jitter computed from fitted curves in (a).

in Fig. 1(c). Since the signal is assembled from M cosines, the dominating part in the second derivative is the term with the highest frequency, i.e. $(2\pi f_{RF} M)^2 \cdot (\Delta V/M) = (2\pi f_{RF})^2 M \Delta V$. Note that the $1/M$ scaling of the driving signal leads to a linear, and not squared, dependency between the modulation curvature and M. Thus the data points in Fig. 3(b) are fitted to $\sigma_\tau(M) = k_1/\sqrt{M}$, which is shown as a black dashed line.

4 CONCLUSION

It has been shown that the timing jitter of a semiconductor hybridly MLL is reduced just by increasing the number of frequency components, i.e. the bandwidth, of the driving signal. The trend is close to that predicted by the analytical expression in [5]. Thus, this expression is confirmed as a design tool for reduction of timing jitter in a semiconductor hybridly MLL. This result benefits the design of oscillators which incorporate a semiconductor MLL, such as the COEO. The results indicate that the timing stability of this configuration should improve by increasing the bandwidth in the opto-electronic feedback loop. Also, the MLL locks to a wider frequency range when the bandwidth of the driving signal is increased, which makes it more tolerant towards deviations in the oscillation frequency of the external high quality-factor feedback element.

REFERENCES

[1] D. B. Leeson and G. F. Johnson, “Short-term stability for a Doppler radar: requirements, measurements, and techniques,” Proceedings of the IEEE, vol. 54, no. 2, pp. 244–248, February, 1966.

[2] R. Corvaja and S. Pupolin, ”Phase noise effects in QAM systems,” in Proc. 8th Int. Symp. Personal, Indoor and Mobile Radio Communications (PIMRC ’97), vol. 2, Helsinki, Finland, pp. 452–456, September, 1997.

[3] X. S. Yao, L. Davis, and L. Maleki, “Coupled optoelectronic oscillators for generating both RF signal and optical pulses,” Journal of Lightwave Technology, vol. 18, no. 1, pp. 73–78, January, 2000.

[4] S. Arahira, S. Sasaki, K. Tachibana, and Y. Ogawa, ”All-optical 160-Gb/s clock extraction with a mode-locked laser diode module” IEEE Photonics Technology Letters, vol. 16, no. 6, pp. 1558-1560, June 2004.

[5] L.A. Jiang, ”Ultralow-Noise Modelocked Lasers,” Doctoral dissertation (retrieved from MIT Libraries), pp. 41–44, May, 2002.

[6] A. G. Vladimirov and D. Turaev, “Model for passive mode locking in semiconductor lasers,” Physical Review A, vol. 72, no. 3, p. 033808, September 2005.

[7] L. Nielsen, E. A. J. M. Bente, E. den Haan, and M. J. R. Heck, ”Theoretical and experimental investigation of unidirectionality in an integrated semiconductor ring mode-locked Laser with two saturable absorbers,” IEEE Journal of Quantum Electronics, vol. 54, no. 5, pp. 1–10, October ,2018.

[8] L. M. Augustin, et al., “InP-based generic foundry platform for photonic integrated circuits,“ IEEE Journal of Selected Topics in Quantum Electronics, vol. 24, no. 1, pp. 1–10, January, 2018.

[9] U. Bandelow, M. Radziunas, A. Vladimirov, B. Hüttl, and R. Kaiser, ”40 GHz mode-locked semiconductor lasers: theory, simulations and experiment,” Optical and Quantum Electronics, vol. 38, no. 4-6, pp. 495–512, March, 2006.

[10] D. Pustsakhod, K. Williams, and X. Leijtens, “Fast and robust method for measuring semiconductor optical amplifier gain,“ IEEE Journal of Selected Topics in Quantum Electronics, vol. 24, no. 1, p. 3100309, January, 2018.

[11] G. Fiol, et al., “Hybrid mode-locking in a 40 GHz monolithic quantum dot laser,“ Applied Physics Letters, vol. 96, no. 1, p. 011104, January, 2010.

[12] D. Zhao, D. Pustakhod, K. Williams, and X. Leijtens, “High resolution optical frequency domain reflectometry for analyzing intra-chip reflections,” IEEE Photonics Technology Letters, vol. 29, no. 16, pp. 1379–1382, August, 2017.

[13] G. Liu, and X. Jin, and S. Chuang, ”Measurement of linewidth enhancement factor of semiconductor lasers using an injection-locking technique,” IEEE Photonics Technology Letters, vol. 13, no. 5, pp. 430–432, May, 2001.

[14] D. Pustakhod, K. Williams, and X. Leijtens, “Method for polarization-resolved measurement of electroabsorption,” IEEE Photonics Journal, vol. 10, no. 2, pp. 1–11, February, 2018.

[15] J. R. Karin, et al., “Ultrafast dynamics in field-enhanced saturable absorbers,” Applied Physics Letters, vol. 64, no. 6, pp. 676–678, February, 1994.

Optimisation of corrugation-free Rb-exchanged waveguides in periodically poled KTiOPO4

(Student paper)

Laura Padberg [1], Matteo Santandrea [1], Raimund Ricken [1], Christof Eigner [1], Christine Silberhorn [1]
[1]*Department of Physics - Integrated Quantum Optics, Paderborn University, 33098 Paderborn, Germany*
e-mail: laura.padberg@uni-paderborn.de

ABSTRACT

Waveguide circuits are a key component for modern integrated optics and scalable quantum optics applications. In this paper we present our studies on rubidium-exchanged waveguides fabricated in periodically poled bulk potassium titanyl phosphate (KTiOPO4 or KTP). We show that face polarity affects the diffusion mechanism of the rubidium, thus leading to different waveguide depths depending on the exposed face polarity. Simulations show that this effect could significantly reduce the efficiency of a process. Employing energy dispersive X-ray spectroscopy (EDX), we analysed a set of waveguides fabricated with different production parameters. Based on this result,

we optimised the fabrication process and were able to produce waveguides with reduced corrugations.
Keywords: nonlinear optics, integrated optics, quantum optics, material processing, waveguide fabrication

1 INTRODUCTION

Highly efficient integrated frequency converters provide a compact solution to the problem of interfacing components of a quantum network operating at different wavelengths [1]. For an efficient conversion, potassium titanyl phosphate (KTP) offers large nonlinear optical and electro-optic coefficients [2]. A wide transparency range from the infrared to the ultraviolet [3] as well as a large anisotropy of the domain growth [4], which aids in the periodic poling of the material. An inversion of the spontaneous polarisation enables quasi phase matching (QPM) [5] and opens the possibility to adress any wavelength combination in the transparancy range. Furthermore, KTP offers large advantages in the visible wavelength regime due to a very high optical damage resistance [6] and a low photorefraction [7]. Since it is possible to produce waveguides in KTP [8], this platform is a perfect candidate for an integrated device [9]. For these reasons, the development of periodically poled waveguides in potassium titanyl phosphate is of great interest.

2 DIFFUSION PROPERTIES OF WAVEGUIDES IN KTP

It is possible to fabricate waveguides in KTP by a rubidium-potassium exchange, which results in a local exchange of rubidium in the KTP bulk material. The higher refractive index of the rubidium exchanged KTP allows waveguiding [10]. The rubidium-potassium exchange takes place in a rubidium nitrate melt, which can be modelled as an infinite bath. For the diffusion process in an infinite bath with an concentration-independent diffusion coefficient D, we expect a complementary error function [11]

$$c(x,t) = c_0 \cdot \mathrm{erfc}\left(\frac{x}{2\cdot[D(T)\cdot t]^{1/2}}\right), \tag{1}$$

where c is the concentration of rubidium ions inside the crystal, c_0 is the surface concentration of rubidium and t is the exchange time. The point $x = 0$ describes the surface of the crystal, while $x > 0$ describes the concentration inside the crystal. A complete knowledge of the parameters in (1) is critical for the reliable fabrication of rubidium exchanged waveguides. The biggest unknown parameter is the diffusion coefficient D, that depends on the melt composition and exchange temperature. One simple empirical law to describe the evolution of the diffusion coefficient with the temperature T is the Arrhenius law [12]

$$D = D_0 \cdot \exp\left(-\frac{E_A}{k_B\cdot T}\right), \tag{2}$$

where k_B is the Boltzmann constant. The diffusion constant D_0 and the activation energy E_A are empirical values and we have to estimate them separately for each melt composition.
The best way to compare different melts is through their diffusion coefficient D. Anyway, a more practical parameter is the waveguide penetration depth d, that can be defined as $c(x,t)/c_0 = \mathrm{erfc}(1)$, that is [12]

$$d = 2\cdot[D(T)\cdot t]^{1/2}. \tag{3}$$

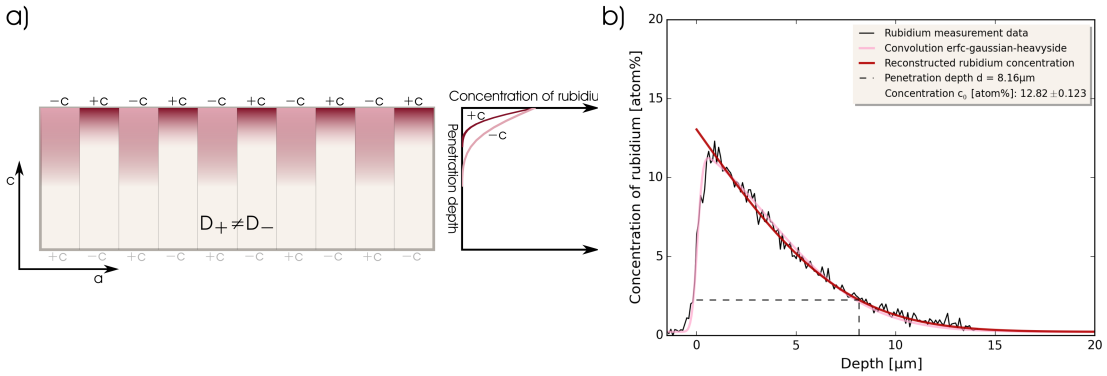


Figure 1. a) Schematic illustration of a channel waveguide in a periodically poled bulk KTP sample with different diffusion coefficients $D_+ \neq D_-$. The shaded areas in red and rose show the rubidium concentrations. b) Measured rubidium concentrations in black and fit of the convolution of the complementary error, gaussian and heaviside function in rose. The red line shows the reconstructed concentration profile. From the concentration profile we calculated the depth.

2.1 Corrugated waveguides

Preliminary investigations on planar waveguides have shown that the diffusion coefficients depends not only on the melt but also on the crystallographic orientation and they are unequal $D_+ \neq D_-$ for our fabrication parameters. We can then assume that waveguides fabricated in periodically poled crystals might have different diffusion coefficients for the poled and unpoled regions. These alternating diffusion coefficients lead to alternating depths, see (3), and therefore to a corrugated waveguide in a periodically poled crystal, see Fig. 1a). Simulations have shown that corrugated waveguides could significantly reduce the efficiency of a process.

To characterise the concentration profiles of rubidium inside the waveguide we employed an energy dispersive X-ray spectroscopy (EDX) method. From these measurements we are able to calculate the diffusion coefficients of each waveguide, see Fig. 1b). By varying the melt composition, exchange temperature and time we optimised the process to fabricate waveguides with less, down to no, corrugations.

3 ANALYSIS OF PERIODICALLY POLED CHANNEL WAVEGUIDES

For the analysis and optimisation of the corrugation effect we periodically poled bulk KTP samples. Followed by a photolithographic patterning of a titanium mask on the KTP perpendicular to the c-axis. This defines an exchange mask with waveguide widths varying from 1.5 μm to 4.5 μm. The Rb-K exchange is performed by immersing the sample for 60 min in a exchange melt at 330°C. In our case, the standard melt is a rubidium nitrate melt ($RbNO_3$) with potassium nitrate (KNO_3) and barium nitrate ($Ba(NO_3)_2$). After the fabrication, the waveguides are characterised by measuring with EDX the concentrations of rubidium and therefore the penetration depths of the waveguides for both face polarities. The average penetration depths for all measurements are plotted over the waveguide width in Fig. 2a) for the $-$c (unpoled) and +c (poled) face. A difference between the diffusion on the +c and -c face is evident from the plotted data. This is consistent with the evidence reported for planar waveguides. This confirms our hypothesis that the fabrication of waveguides in periodically poled bulk material results in corrugated waveguides. Also, a second interesting behaviour showed up. The waveguide depth increases as its width decreases. This is not expected in a simple 1D diffusion model and thus might indicate that a more complex diffusion dynamics has to be considered for small waveguides.
To avoid the corrugation effect we optimised our exchange melt and exchange parameters. With an optimised rubidium nitrate melt with higher potassium content and an exchange temperature of 366.5 °C we were able to reduce the corrugation effect [13], see Fig. 2b). Comparing the previously fabricated waveguides in the standard melt with our optimised melt, we could reduce the impact of different penetration depths depending on the poled and unpoled regions from roughly 2.2 μm to 0.9 μm. We expect that further optimisations can be made to improve the waveguides. Beside the strong reduction of the corrugation, these waveguides are also single mode for 1550 nm.

4 CONCLUSION

In conclusion, we could show that the fabrication of waveguides is affected by the polarity of the face on which they are produced in periodically poled bulk KTP. With an optimised melt and fabrication parameters we could reduce the difference between the penetration depth from roughly 2.2 μm for our standard process to 0.9 μm for our optimised process. So we are able to produce less corrugated waveguides in periodically poled KTP material.

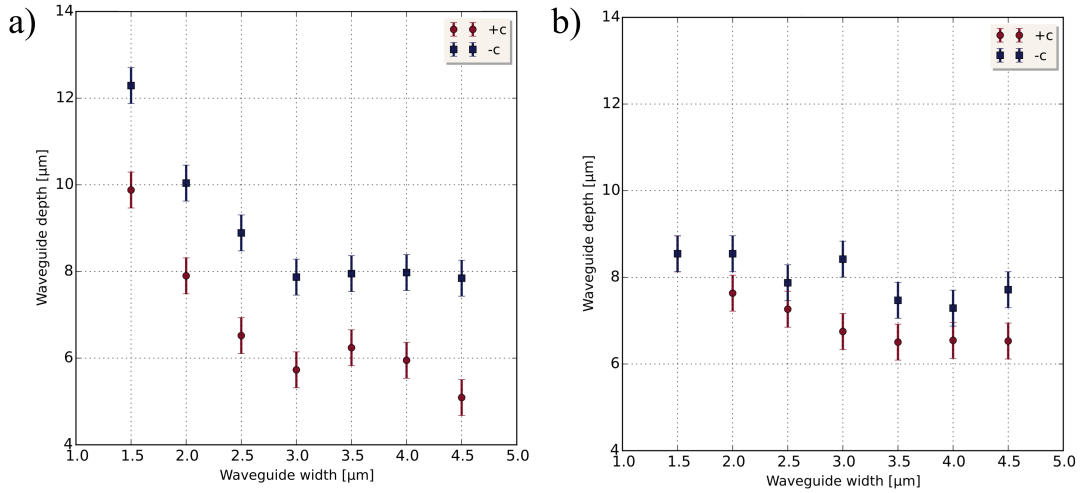


Figure 2. Waveguide depth depending on the waveguide width and poled, unpoled regions of a sample produced in the previous melt a) and optimised melt b). The error of the waveguide depth is ± 0.4 μm.

ACKNOWLEDGMENT

Funded by the Deutsche Forschungsgemeinschaft (DFG, German Research Foundation) – Projektnummer 231447078 – TRR 142

REFERENCES

[1] N. Maring, P. Farrera, K. Kutluer, M. Mazzera, G. Heinze, and H. de Riedmatten, "Photonic quantum state transfer between a cold atomic gas and a crystal," Nature, vol. 551, pp. 485–488,2017

[2] J. Bierlein, and H. Vanherzeelen, "Potassium titanyl phosphate: properties and new applications," Journal of Optical Society of America B, vol. 6, p. 622, 1989

[3] G. Hansson, H. Karlsson, S. Wang, and F. Laurell, "Transmission Measurements in KTP and Isomorphic Compounds," Applied Optics, vol. 39, pp. 5058-5069, 2000

[4] C. Canalias, J. Hirohashi, V. Pasiskevicius, and F. Laurell, "Polarisation-switching characteristics of flux-grown $KTiOPO_4$ and $RbTiOPO_4$ at room temperature," Journal of Applied Physics, vol. 97, pp. 124105-9, 2005

[5] D. S. Hum, and M. M. Fejer, "Quasi-phasematching," Académie des sciences, vol. 8, 2007

[6] N. Stus, S. Dubb S, D. Stratiychuk, and V. Lisnyak, "The mechanical properties of $KTiOPO_4$ single crystals," Journal of Alloys and Compounds, vol. 366, pp. L13-L15, 2004

[7] D. K. T. Chu, H. Hsiung, L. K. Cheng, and J. D. Bierlein, "Curie Temperature and Dielectric Properties of Doped and Undoped $KTiOPO_4$ and Isomorphs," IEEE Transactions on Ultrasonics. Ferroelectrics and Frequency Control, vol. 40, 1993

[8] V. Ansari, E. Roccia, M. Santandrea, M. Doostdar, C. Eigner, L. Padberg, I. Gianani, M. Sbroscia, J. M. Donohue, L. Mancino, M. Barbieri, and C. Silberhorn, "Heralded generation of high-purity ultrashort single photons in programmable temporal shapes," Opt. Express, vol. 26, pp. 2764-2774, 2018

[9] C. Eigner, M. Santandrea, L. Padberg, M. F. Volk, C. E. Rüter, H. Herrmann, D. Kip, and C. Silberhorn, "Periodically poled ridge waveguides in KTP for second harmonic generation in the UV regime," Opt. Express, vol. 26, pp. 28827-28833, 2018

[10] J. Bierlien, A. Ferretti, L. H. Brixner, and W. Hsu, "Fabrication and characterization of optical waveguides in $KTiOPO_4$," Applied Physics Letters, vol. 18, pp. 1216-1218, 1987

[11] J. Crank, "A Theoretical Investigation of the Influence of Molecular Relaxation and Internal Stress on Diffusion in Polymers," Journal of Polymer Science, vol. 11, pp. 151-168, 1984

[12] Yu. N. Korkishko, and V. Fedorov, "Ion exchange in single crystals for integrated optics and optoelectronics," Gordon and Breach Science Pub., Cambridge International Science Publishing, 1999

[13] L.Padberg, C.Eigner, M. Santandrea, and C. Silberhorn, Az. 10 2018 108 636.9. (2018).

New Resonant Diffraction Phenomenon from Silicon Grating Waveguide

Olivier Parriaux, Yves Jourlin

Lyon University at Saint-Etienne, CNRS, Institut d'Optique Graduate School,
Laboratoire Hubert Curien UMR 5516, 42023 Saint-Etienne, France
e-mail: parriaux@univ-st-etienne.fr

ABSTRACT

The excitation of a grating waveguide mode from a high-index incidence medium by means of the $+1^{st}$ and -2nd diffraction orders of the grating in the neighbourhood of the -1st order Littrow condition causes a lossless 100% isolation switching between the propagative 0th and -1st reflected orders upon a wavelength or angular scan under the condition that all orders in the low-index transmission medium are evanescent. This purely reflective diffractive effect only occurs if the excited mode effective index is larger than 3. Considering that the waveguide is corrugated, silicon and related microstructuring technologies is thus the adequate implementation material. This new resonant diffraction effect can be used for wavelength and angular control, and biochemical sensing.

Keywords: Grating waveguides, resonant diffraction, mode coupling, silicon photonics

1. INTRODUCTION

Since the mid-eighties a number of resonant diffraction effects have been found, theoretically analysed, experimentally demonstrated, and used in industrial application. "Resonant diffraction" is a process whereby an incident free-space wave impinges onto a waveguide associated with a periodic corrugation or index modulation, gets synchronously coupled and partially trapped into a mode of the waveguide by a diffraction order of the grating, then re-radiated into the adjacent sub- and superstrates where a possibly high contrast interference occurs with the uncoupled 0th diffraction orders. This process is often referred to as a Fano resonance. The best known and most used effect is that of resonant 0th order reflection [1] implemented in a number of biochemical sensors [2]. More recently, ultra-narrow 100% resonant reflection under normal incidence from a high contrast binary grating was disclosed [3] and analysed [4]; it still requires an intelligible phenomenological analysis. The coupled mode needs not be a truly guided mode: high, possibly 100% -1st order diffraction efficiency can be obtained by the grazing excitation of a leaky mode, and the interferential cancellation of the 0th reflected order [5].

It is paradoxically as an outcome of the study of a plasmonic effect that the insight came for the lossless, purely dielectric reflective switching effect presented here. A switching effect between the 0th and -1st reflected orders was observed from the periodically undulated surface of a metal surface [6]; this high contrast effect occurred for the TM polarization in both angular and wavelength spectra in the neighbourhood of the -1st order Littrow condition. At either side of the Littrow angle θ_L where the -1st order efficiency is maximum, its efficiency suddenly drops to 0 where the 0th order reaches a high maximum. This occurs if the wavelength/period ratio λ/Λ is such that the $+1^{st}$ grating order couples the incident wave to the forward-propagating plasmon, and its -2nd order to the backward-propagating plasmon.

This switching effect between 0th and -1st reflected orders exhibits high contrast under the condition that the sole 0th and -1st orders have a propagative character in the incident medium and that the transmitted orders are forbidden. The last condition is inherently satisfied if the surface wave is a surface plasmon at a metal surface. It can also be satisfied as shown in Ref [7] if the surface wave is the TE or TM mode of a mirror-based dielectric slab grating waveguide. The purpose of the present contribution to the field of high-contrast resonant diffractive phenomena is to disclose yet another, strictly lossless version of the same switching principle that forbids the propagation of transmitted orders without mirror, and which lends itself to a particularly simple monolithic implementation: all possible transmitted orders are evanescent, i.e., they all experience total internal reflection.

2. THE COUPLING MECHANISM

The above condition imposes the refractive index n_i of the incident medium to be larger than that of the transmission medium, n_t, the incidence angle θ_i to be larger than the critical angle $\theta_c = \arctan(n_i/n_t)$, and the grating vector $K_g = 2\pi/\Lambda$ to point outside the half-circle of radius $k_0 n_t$ ($k_0 = 2\pi/\lambda$) in the Ewald circle representation of Fig. 1. The dielectric grating waveguide of refractive index n_g, thickness w, and period Λ is placed monolithically at the basis of the incident medium as suggested by the inset of Fig. 1 that shows the cross-section of the coupling structure. Analogously to the plasmonic functional structure of Ref. [6], the central angular operation point is set to be the -1st order Littrow angle θ_L given by $\sin\theta_L = \lambda/(2n_i\Lambda)$. Figure 1 summarizes in the spatial frequency domain the coupling mechanisms involved in the switching effect between the reflected 0th and -1st grating orders

at constant wavelength in the case $3K_g > 2k_0n_e$ where n_e is the effective index of the waveguide mode excited by the grating +1st and -2nd diffraction orders in the forward and backward directions resp. (propagation constant k_0n_e).

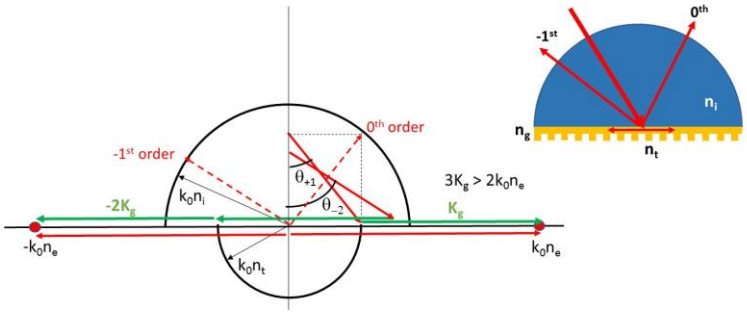


Figure 1 Ewald circles in the spatial frequency domain illustrating the conditions on the incidence angle in the medium of high index n_i for the total reflection of all diffraction orders while the +1st and -2nd grating orders excite the forward and backward propagating waveguide mode. The inset is an example of a monolithic device in the direct space.

To forbid the 0th (resp. -1st) transmitted order to have a propagative character without mirror, the incidence angle θ_{+1} (θ_{-2}) ensuring the excitation of the forward (backward) propagating mode via the +1st (-2nd) grating order must satisfy the condition $n_i sin\theta_{+1} \geq n_t$ (resp. $n_i sin\theta_{-2} \leq \lambda/\Lambda - n_t$). Setting θ_{+1} and θ_{-2} at their above limit, their relationship with the Littrow angle θ_L is :

$$sin\theta_{+1} + sin\theta_{-2} = 2\, sin\theta_L \tag{1}$$

For any incidence angle θ_i within the above limits in the high index incident media, the angle θ_{-1} of the propagative reflected -1st order is:

$$sin\theta_{-1} = \lambda/(n_i\Lambda) - sin\theta_i = 2\, sin\theta_L - sin\theta_i \tag{2}$$

with the condition $sin\theta_{-1} \geq n_t/n_i$ to ensure the evanescent character of the transmitted -1st order. Expressions (1) and (2) imply that $\theta_{-1} = \theta_{+1}$ when $\theta_i = \theta_{-2}$ and θ_{-2} when $\theta_i = \theta_{+1}$.

The expected switching effect between the reflected 0th and -1st orders as sketched in the angular domain in Fig. 2c) was analysed by a coupled wave formalism. This was accomplished in Ref. [8] where the coupled surface wave is the TM plasmon mode at a periodically undulated metal-dielectric interface. This theoretical model revealed that the switching in the angular domain between a -1st order maximum at the Littrow angle and its cancellation and 0th order maximum at two neighbouring angles at either side of the latter is a result of destructive and constructive interferences between +1st and -2nd order coupled forward and backward propagating plasmon modes re-radiating back into the incidence medium, the 3rd order of the rather deep grating coupling the two plasmon modes to each other. The same mechanism operates here. There is a limitation, however: looking back at Fig. 1, k_0n_e is about as large as $3k_g/2$. Yet K_g must be at least as large as k_0n_t to forbid all transmitted orders to have a propagative character. Consequently, k_0n_e must be at least as large as $3k_0n_t$, thus n_e at least as large as $3n_t$. n_t is no less than 1 with air (1.33 in the case of a biosensor with a water solution). Therefore, n_e must be at least as large as 3 (4 with a water analyte) which implies that high refractive index semiconductors only are appropriate as the grating waveguide material; silicon above its gap is the ideal choice for manufacturing reasons whereas germanium or amorphous silicon can be considered with a water analyte.

3. LOSSLESS MIRRORLESS SWITCHING DEVICE

The definition of the operation point of a lossless, mirrorless diffractive switch between 0th and -1st reflected orders is here made on an experimental model (ref. inset of Fig. 1) at 1500 nm wavelength composed of a 1.45 index silica incidence medium, a silicon slab waveguide of 3.5 index and thickness w_g topped with a binary silicon grating of 0.5 duty cycle, period Λ, and depth h. The transmission medium where all transmitted orders are evanescent is air, $n_t = 1$. The polarization is TE, but can well be TM too. In a first step the desired Littrow angle and angular range are chosen which sets the period. Next step is a 2D optimization of the 0th and -1st order efficiency to find the grating depth and waveguide thickness. Figure 2 shows the outcome of the search process: a) and b) sketch the diffraction efficiency in false colours in the (Λ,θ) plane of the 0th and -1st reflected orders; c) is its cross-section at $\Lambda = 688$ nm illustrating the switching effect in the angular domain. The field at the 0th order maxima has the symmetry of the TE_0 mode; that at the Littrow angle is a hybrid mode.

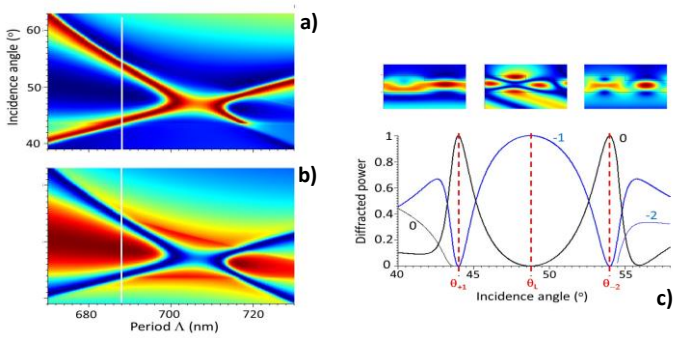


Figure 2 General (Λ,θ) chart of a device with n_i = 1.45, n_g = 3.5, n_t = 1 at λ = 1500 nm and $w_g(\lambda)$ = 330.26 , $h(\lambda)$ = 143.49 nm. a) 0th order, b) -1st order. c) Angular scan at period Λ = 688 nm (Littrow angle θ_L = 48.75°) of 0th and -1st orders (thin lines: transmitted propagating -2nd and 0th orders). The field mappings represent the resonant transverse electric field modulus at angles θ_{+1}, θ_L and θ_{-2}.

4. WAVELENGTH (DE)MULTIPLEXER APPLICATION

The presentation will describe the implementation of the resonant effect in different functional devices. We will limit ourselves here to a nearly 100% efficiency two-wavelength demultiplexing scheme. Figure 3 is the angular scan of the 0th order of a smaller wavelength λ_m, and of the -1st order of a larger wavelength λ_n in the same structure. The inset of Fig. 3 shows that both wavelength channels impinge from the silica incident medium under the same angle θ_{mn}, the λ_m channel is totally reflected whereas the λ_n channel is close to 100% diffracted in direction θ_{n-1} slightly off the Littrow angle. Conversely, two angularly separated incident channels under angles θ_{mn} and θ_{n-1} are efficiently superposed in direction θ_{mn}.

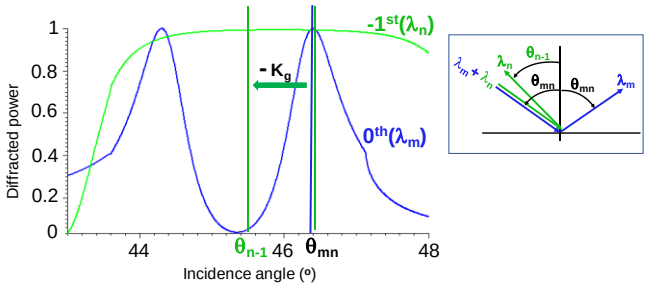


Figure 3 Angular spectra at λ_m = 1510 nm and λ_n = 1525 nm with Λ = 732 nm, w_g = 275.264 nm, h = 279.3 nm. The λ_m channel is reflected forward. The λ_n channel is diffracted back by the -1st order grating constant -K_g under the angle θ_{n-1}.

5. CONCLUSION

The new, non-Fano, lossless resonant diffraction phenomenon disclosed relies upon above-gap semiconductor grating waveguide mode coupling and high-contrast constructive/destructive interference in the incidence medium.

REFERENCES

[1] G. A. Golubenko, *et al.*: Diffraction characteristics of planar corrugated waveguides, *Opt Quant. Electron.* vol. 18. pp 123-128**,** March 1986

[2] N.M. Lyndin, et al.: Analytical methods and apparatus employing an optical sensor device with refractive index modulation, *US Patent 6218194*, April 2001.

[3] E. Bonnet, et al.: High resonant reflection of a confined free space beam by a high contrast segmented waveguide, *Opt Quant. Electron.* vol. 35. pp 1025–1036, Sept. 2003.

[4] V. Karagodsky, C.J. Chang-Hasnain: Physics of near-wavelength high contrast gratings, Opt. Express vol. 20. pp. 10888-895, 2012.

[5] A.V. Tishchenko, V.A. Sychugov: High grating efficiency by energy accumulation in a leaky mode, *Opt. Quant. Electron.*, vol. 32. pp. 1027-1031, Aug. 2000.

[6] J. Sauvage-Vincent, et al.: Low-loss plasmon-triggered switching between reflected free-space diffraction orders, Opt. Express vol.22. pp13314-13321, May 2014.

[7] O. Parriaux: Guided-mode triggered switching between TE orders of a metal-based grating-waveguide, JEOS:RP, vol. 10. id.15040, Aug. 2015.

[8] A.V. Tishchenko, O. Parriaux: Coupled-mode analysis of the low-loss plasmon-triggered switching between the 0thand -1st orders of a metal grating, IEEE Photonics J. vol.7, Aug. 2015.

Highly-efficient grating couplers based on transfer-printing technology

Fabio Pavanello [1,2], Grigorij Muliuk [1,2], Gunther Roelkens [1,2]
[1]*Ghent University - imec, Technologiepark 15, 9052 Ghent, Belgium*
[2]*Center for Nano- and Biophotonics, Ghent University, Belgium*
e-mail: fabio.pavanello@ugent.be

ABSTRACT

We propose a new approach that allows highly efficient fiber-to-chip coupling using transfer-printing technology. The novelty of the approach relies on the integration of a mirror between a top (source) grating coupler circuit and a bottom (target) photonic integrated circuit (PIC) and on a wide directional coupler to transfer the light between the two waveguide layers before tapering the waveguide to single mode widths. We propose an apodized, partially etched, grating coupler integrated with a directional coupler implemented in amorphous Si, while a crystalline 220nm Silicon-on-Insulator (SOI) platform is used for the target PIC. We achieve a simulated 2D coupling efficiency of 96.2% (-0.17 dB) with a 1 dB bandwidth of 45 nm. The bandwidth takes into account the broadband directional coupler, which is very compact. The alignment tolerance along the direction orthogonal to the light propagation is better than +/- 2 μm to achieve an insertion loss penalty lower than 1 dB, which is well within reach with transfer printing.

Keywords: Silicon photonics, grating couplers, transfer-printing technology.

1 INTRODUCTION

Transfer-printing is an emerging technology which allows to heterogeneously integrate photonic integrated circuits and devices (PICs) that are fabricated separately e.g. on a Silicon-on-Insulator (SOI) platform and on a III-V platform. The technique allows for high throughput assembly because of the parallel nature of the printing process (large arrays of devices can be assembled in a single printing cycle, compared to flip-chip integration where a single device is assembled at a time). Also the device size can be extremely small, down to a few micron a side. [1]. This integration technique provides a clear path towards resolving some of the major problems of current silicon photonic platforms, which do not offer suitable materials as gain medium and where III-V modulators and photodetectors may achieve higher performance compared to their silicon counterparts for particular applications. Another key challenge for photonic integrated circuits is the high efficiency and robust fiber-to-chip light coupling. In particular, grating couplers allow to achieve vertical coupling on a compact footprint, contrary to approaches based e.g. on spot-size converters [2]. Here, we propose a novel fiber-to-chip grating coupler approach based on transfer-printing technology, which consists of depositing an Au patch acting as a mirror onto the target PIC before printing the source grating coupler + directional coupler. By achieving the transfer of light from the top grating coupler to the target PIC using a very wide directional coupler prior to the tapering of the waveguide to single mode widths, it is possible to print grating structures with very compact footprint and with very high alignment tolerance, thus providing a concrete path towards high-throughput, robust and high-efficiency I/O ports patterned on a single source wafer and transferred in a single printing operation.

2 DESIGN AND PERFORMANCE

2.1 Target and source PIC specifications

The target PIC is based on a 220 nm SOI platform with a 70 nm partial etching step (see Fig. 1(a)). A 100/50 nm thick SiO_2/BCB bi-layer is present to promote the adhesion with the printed grating coupler structure. The reason of having a dielectric bi-layer is to reduce the thickness variations associated with the BCB layer (used as a bonding agent) during processing, while at the same time providing planarization and encapsulation for the rib waveguides. The cross-section of the grating structure on the source wafer is based on a custom SOI platform with a 265 nm thick a-Si layer deposited on a 150 nm thick SiO_2 layer. The latter is deposited on a bulk Si substrate which will be underetched in the transfer printing process flow, when the a-Si device coupons are released from their substrate. The thicknesses of the a-Si layer and of the bottom SiO_2 layer on the source wafer are determined by design as explained below. Another 150 nm thick SiO_2 layer is then deposited above the a-Si layer to have a symmetrical structure to balance the stress which will prevent the released structure from buckling. After the printing a 850 nm thick polymer with the same refractive index as SiO_2 is deposited for planarization. A 70 nm thick Au mirror is deposited after partially etching a recess in the target PIC (see Fig. 1(b)). This section defines where the grating coupler will be printed.

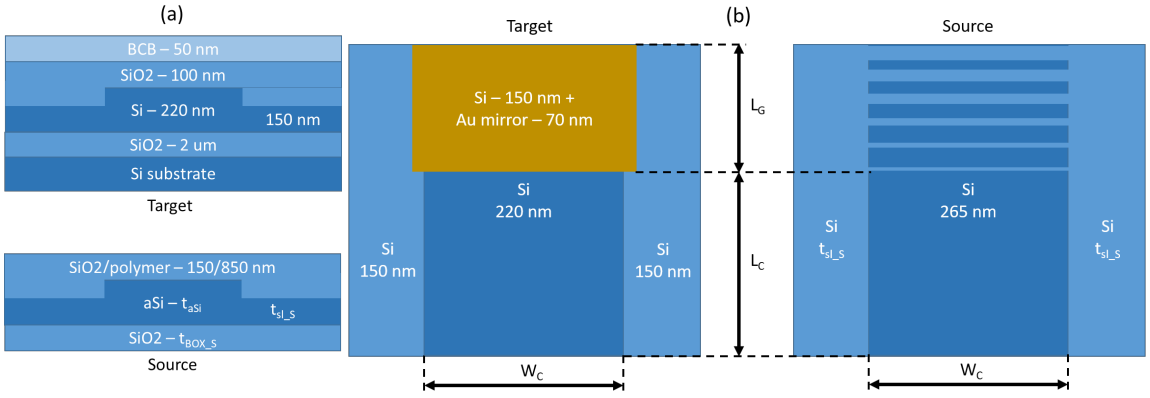


Figure 1. Target and source waveguide cross-sections and top views. (a) Cross-sections of the target and source structures. Parameters t_{aSi}, t_{sl_S} and t_{BOX_S} are determined by design. (b) Top view of the target and source structures. The PICs will be vertically stacked through transfer printing achieving an abrupt interface at the end of the coupler on the grating coupler structure, while the target PIC waveguide will continue with a taper to single mode waveguide.

2.2 Grating coupler and directional coupler designs

The thickness t_{aSi} of the a-Si layer (n = 3.35 at 1550 nm from measurements) is determined by simulating the supermodes' effective index dispersion as a function of the thickness (t_{aSi}) and by selecting the thickness t_{aSi} = 265 nm at which anti-crossing appears (initial separation between waveguides of 400 nm). This results in phase matching between the a-Si and c-Si waveguide. Afterwards, the vertical separation of the two waveguides is determined by aiming at approximately 20 µm coupling length L_C for compactness. This leads to a total separation of 300 nm and a SiO_2 BOX thickness for the source structure t_{BOX_S} of 150 nm. This value is used as initial input in the grating simulation. The coupling width $W_C = 13.5$ µm is kept equal to the grating width to achieve optimal mode matching with the 10.4 µm mode field diameter of the gaussian beam of the fiber without introducing any tapering on the source structure. The 2D grating simulation is performed in Lumerical FDTD launching the mode into the waveguide 10 µm away from the first tooth and recording the scattered field at the top surface of the source PIC (1 µm above the top a-Si waveguide) as done in [2] assuming angled cleaved fibers and a SiO_2 index matched environment. The electric field recorded is multiplied by the analytically computed magnetic field of the fiber mode and integrated along the direction of propagation to extract the coupling efficiency after power normalization [2]. The grating apodization for mode matching of the scattered field with the fiber mode field is based on the methodology introduced in [3] where a linear coefficient FF_{lin} is applied for the fill factor, which is tailored along the propagation direction taking into account local corrections of the grating period according to the grating formula $k_0 \sin(\theta) = k_0 n_{eff}^G - K$ where k_0 is the vacuum wavevector, θ the fiber angle, K is the reciprocal lattice vector and $n_{eff}^G = FF n_{eff}^{thick} + (1-FF) n_{eff}^{thin}$ is the grating effective index with n_{eff}^{thick} and n_{eff}^{thin} the effective indices for full and partial thickness waveguides, respectively. A 20

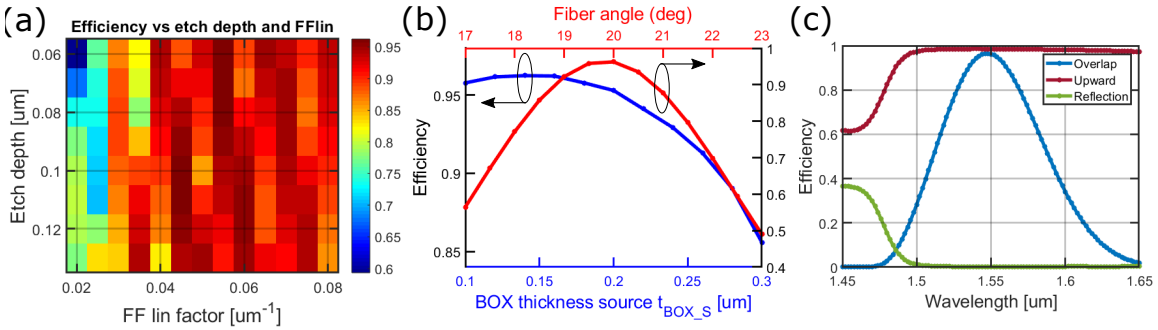


Figure 2. Performance of the grating coupler. (a) Sweep of the linear fill factor FF_{lin} and of the etch depth. (b) Sweep of the BOX thickness t_{BOX_S} on the grating coupler source wafer using the optimal values found in (a). The angle is swept to find the optimum by using the optimal value of t_{BOX_S}. (c) The grating response versus wavelength. Only a small mismatch of approximately 2.5% is present compared to the upward radiation at 1550 nm.

deg angle has been chosen because it provided the highest scattered power (without Gaussian overlap) for the choice of thickness t_{BOX_S} of 150 nm using an initial guess for the linear fill factor (0.05 µm^{-1}) and the etch depth (100 nm) in order to sweep multiple designs at their respective angles. The grating is composed of 25 periods. The design flow consists first of sweeping the linear fill factor coefficient and the etch depth of the grating (see Fig. 2(a)). This allows to find the optimum linear fill factor $FF_{lin} = 0.045$ µm^{-1} and the optimal

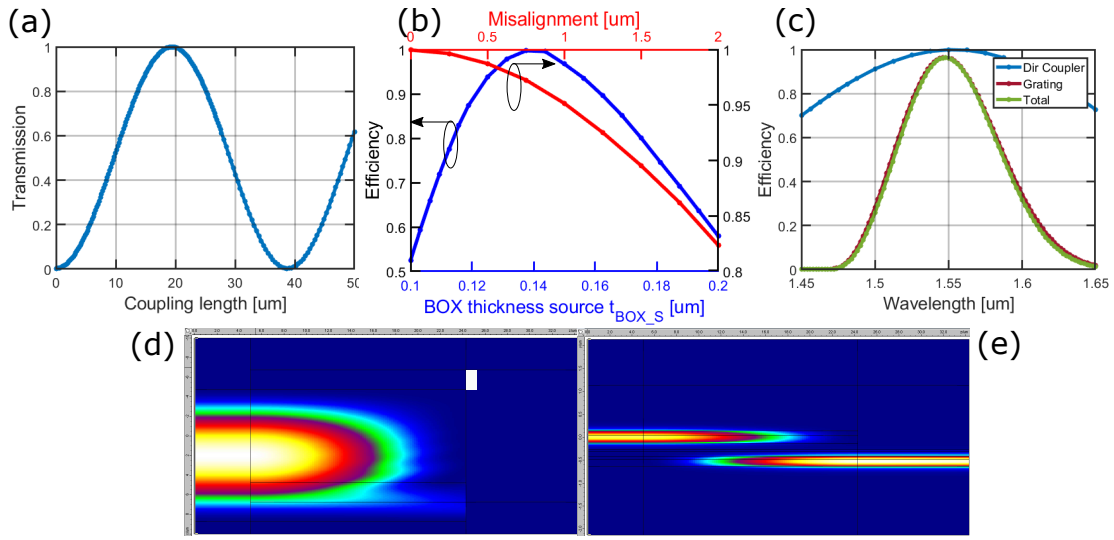


Figure 3. Performance of the directional coupler. (a) Transmission versus coupling length. (b) Efficiency as a function of the misalignment and variation of BOX thickness. (c) The directional coupler response versus wavelength. The grating coupler response has been added as well in order to compute the total bandwidth of the device which is dominated by the grating coupler. (d) shows a top-view of the simulation with 2 µm of misalignment, indicated by the white bar. (e) shows a cross-section of the same simulation.

etch depth, t_{sl_S} = 165 nm. A fine sweep of the BOX thickness t_{BOX_S} allows to optimize the interference upward leading to a value of 140 nm as in Fig. 2(b). The last sweep is on the fiber angle, where we keep the optimal design fixed varying the angle. This leads to an optimal angle of 20 deg as in design and to a simulated efficiency of 96.2% (-0.17 dB) shown in Fig. 2(c). The total power radiated upward is close to 99%. The difference is due to the imperfect overlap with the gaussian mode. The reflection reaches -27 dB around the central wavelength thanks to the apodization and the small etch step. The total length of the grating section is 18.4 µm.

The optimal value for the BOX thickness t_{BOX_S} of the source PIC and the optimal etch depth are used in the final simulation of the directional coupler to simulate the correct coupling length. The simulation carried out using fimmwave is based on 3 sections: the input section based on the cross-section of the waveguide structure on the source wafer Fig. 1(a), the coupling section that corresponds to the stack of source and target structures and the output section based on the target PIC. A nearly lossless power transfer (see Fig. 3(a)) can be achieved with a length of 19.3 µm where the reflection is negligible because of the large separation between the waveguides. Fig. 3(b) shows the response of the directional coupler to tolerances such as lateral misalignment (source PIC and target PIC are misaligned orthogonal to the propagation direction) and variation of BOX thickness t_{BOX_S} (or of BCB thickness because of their similar refractive indices). It is possible to achieve better than 1 dB of insertion loss with a misalignment as large as +/- 2 µm thanks to the wide waveguides. The broadband behavior allows to achieve a directional coupler 1dB bandwidth of 144 nm, while the overall 1dB bandwidth of the grating coupler + directional coupler is 45 nm, dominated by the grating coupler response as shown in Fig. 3(c). Figs. 3(d)-(e) show the top view and the cross-section of a simulation with misalignment of 2 µm where it is possible to observe the effect of the presence of a misalignment on the optical mode distortion.

3 CONCLUSIONS

The proposed approach paves the way for efficient, compact and robust fiber-to-chip coupling using transfer-printing technology allowing to easily integrate multiple I/O ports onto a PIC. The compactness of the coupler allows also to reduce the costs of the source structure, which may be fabricated using e.g. e-beam, immersion lithography or extreme UV lithography for the best performance.

REFERENCES

[1] A. De Groote, P. Cardile, A. Z. Subramanian, A. M. Fecioru, C. Bower, D. Delbeke, et al., "Transfer-printing-based integration of single-mode waveguide-coupled III-V-on-silicon broadband light emitters," Opt. Exp., vol. 24, pp. 13754–13762, 2016.

[2] D. Taillaert, P. Bientsman and R. Baets, "Compact efficient broadband grating coupler for silicon-on-insulator waveguides," Opt. Lett. vol. 29, pp. 2749–2751, 2004.

[3] R. Marchetti, C. Lacava, A. Khokhar, X. Chen, I. Cristiani, D. J. Richardson, et al. , "High-efficiency grating-couplers: Demonstration of a new design strategy," Scientific Reports, vol. 7, pp. 1–8, 2017.

Numerical Investigation of Silicon Nitride-based Frequency Comb in the Radio over Fiber System

(Student Paper)

Shahryar Sabouri [1], Mojtaba Sohrabi [2], Mircea Catuneanu [1], Dirk Plettemeier [2], Kambiz Jamshidi [1]
[1] Integrated Photonic Devices Group, [2] Chair of Radio Frequency and Photonics Engineering,
Technische Universität Dresden Dresden, Germany
e-mail: shahryar.sabouri@tu-dresden.de

ABSTRACT

To generate carriers with high frequencies in the central office, an integrated frequency comb using optical solitons is studied. Both single and double solitons in a silicon nitride microring cavity are investigated numerically for this purpose. The parameters required for the single solitons with the frequency spacing equal to the resonator free spectral range (FSR) and power suppress ratio of -2dB and double solitons with the frequency spacing of multiple (1-3) resonator FSR and power suppress ratio of -1dB is obtained.

Keywords: Solitons, Silicon nitride, Radio over Fiber, Photonic integrated circuits.

1. INTRODUCTION

Radio-over-Fiber (RoF) technique is a promising solution to distribute data for base stations [1,2]. The main advantage is the possibility to transmit the modulated RF signal over optical fibers with link lengths of several kilometers from Central Office (CO) to the Base Station (BS) (Fig. 1a). Moreover, to generate high-frequency signals (60 GHz and beyond), it has been believed that photonic devices can be better candidates than the conventional electrical techniques because of lower cost and impairments like phase noise [3]. In the central office (CO) of a RoF system, generating a high-frequency carrier signal (60 GHz and beyond) by optical means requires a modulator and RF signal source (see Fig. 1c). In terms of bandwidth, however, a dual-electrode Mach Zehnder modulator has some limitations and signal/carrier generation in a spacing of 60 GHz is not easily achievable [4]. In order to increase the frequency of the carrier signal even further, several methods can be used, including frequency combs. In this paper, we study the formation of stable Kerr comb solitons based on a silicon nitride microring cavity (Fig. 1b). The optical spectrum of such stable solitons provides a train of frequency lines with a spacing more than 60 GHz suitable for BS working in this frequency such as [5]. As it is shown in Fig.1c (bottom), by filtering the intended line through the train of lines in the generated comb, the carrier will be generated in the desired frequency.

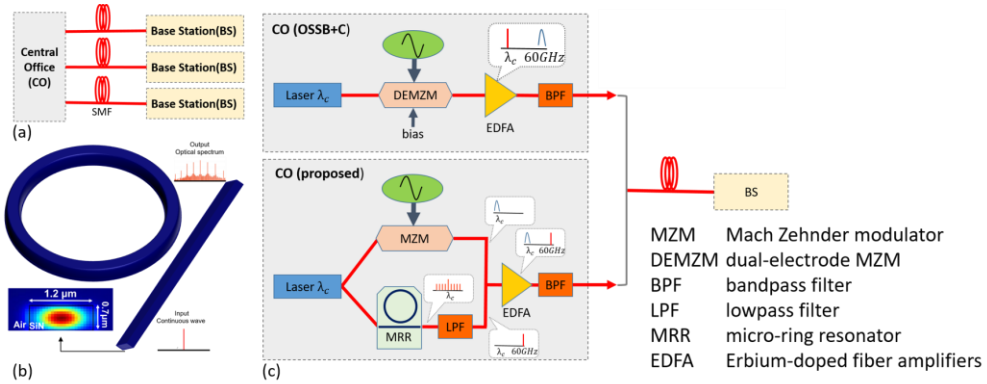


Figure 1. a) Schematic view of a RoF system. b) The studied silicon nitride microring cavity to generate comb frequency lines. C) The Central Office (CO) of a RoF system represented by [2] (top) and proposed in this paper (bottom).

2. SOLITON-BASED KERR COMB MODEL

In order to generate a frequency comb in an integrated photonic circuit, a microring resonator is needed. The input signal, which is a continuous wave generated by a tunable laser, is coupled from the bus waveguide into the microring. The radius of the ring cavity defines the free spectral range (FSR) of the optical spectrum. The intended line spacing in the output-spectrum could be a multiple of the engineered FSR [6, 7]. Single FSR spacing can be

achieved when a single soliton forms in the ring cavity. Soliton refers to an optical field that travels without distortion during propagation due to the balance between nonlinear and dispersive effects in the medium [8]. Once the soliton is formed, it keeps its stability, shape, and power.

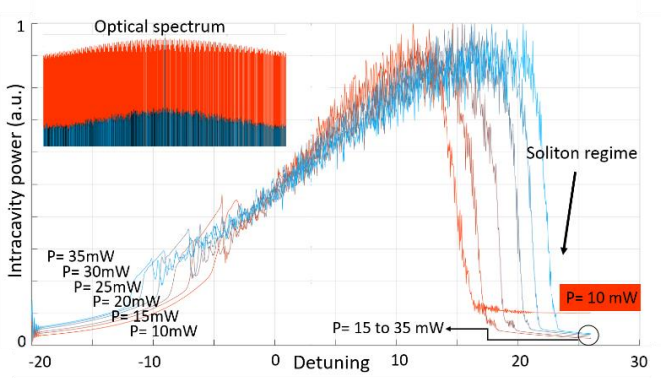


Figure 2. The detuning vs intracavity power for different laser input power. The optical spectrum after detuning is presented.

In this paper, the aim is to get stable soliton where we can have a train of frequency lines spacing more than 60 GHz. To satisfy this, the intracavity field must be studied. Lugiato Lefever equation (LLE) models the intracavity field which is influenced simultaneously by nonlinearity, dispersion, and loss:

$$\frac{\partial \psi}{\partial \tau} = -(1 + i\alpha) + i|\psi|^2\psi - i\frac{\beta}{2}\frac{\partial^2 \psi}{\partial \theta^2} + F \quad (1)$$

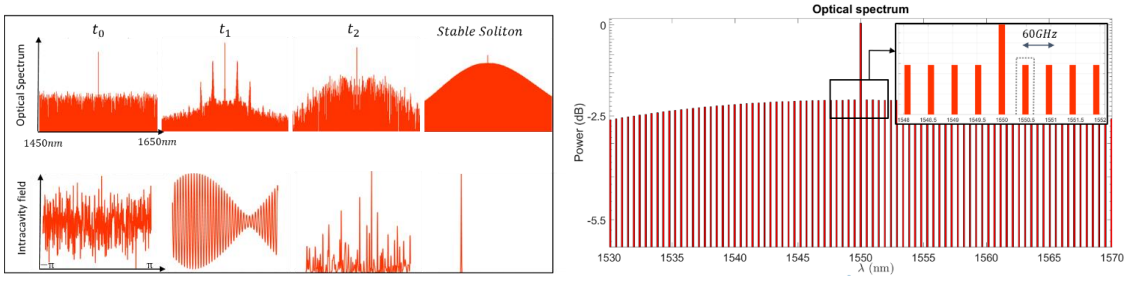
where ψ is the intra-cavity field, α describes the normalized wavelength detuning, β refers to dispersion, F is the normalized pump field intensity, θ is the angular vector of the cavity, and τ is the dimensionless time[6]. We have numerically investigated the formation of the desired soliton in LLE by considering the input power and detuning of the laser.

3. RESULTS

First, the required parameters to obtain solitons in a cavity have to be found. The detuning must be stopped in the soliton regime (upper branch of the bistability curve [9]). However, one can be in the soliton regime but no soliton is formed in the output. That's because of the second parameter to be considered: input power. As it is shown in Fig. 2, all detuning stop in the soliton regime, but only for the power of around 10 mW, the soliton is formed in the cavity.

3.1 Single Soliton

To get a single stable soliton, an input power of 9.7 mW is needed. Figure 3a shows the transient formation of the single soliton into the cavity for a large spectrum. At the beginning (t_0), only the input pump power is observed. At t_1, secondary and higher orders of the comb line are generated through the nonlinearity interactions into the ring: self-phase modulation (SPM), cross phase modulation (XPM), four-wave mixing (FWM), and modulation instability. Finally, all the mentioned nonlinearity mechanisms and dispersion compensate each other and reach an equilibrium, where the single stable soliton is formed. As the FSR of the microring is around 60 GHz, the optical spectrum is scaled in Fig. 3b, where the lines are located in the equidistant spacing of 1×FSR (60 GHz or 0.48 nm). The very first lines have approximately similar power (about 2dB less than the pump power). By filtering each of these lines (based on the required bandwidth), the stable carrier can be obtained.

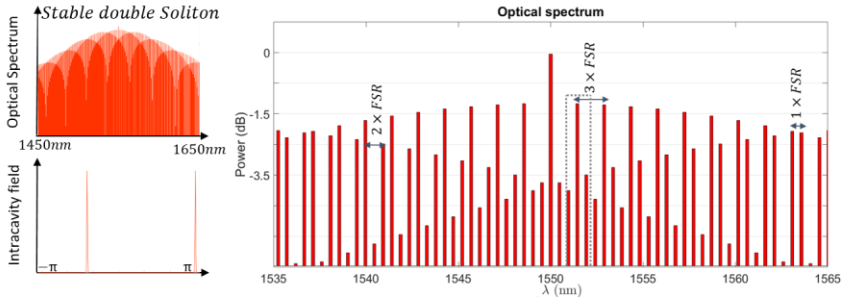


(a) (b)

Figure 3. a) The transient formation of a single soliton (Intra field cavity and its spectrum). b) The optical spectrum of the ring cavity in the range of 40nm. The spacing of the comb lines is 60GHz or 0.48 nm.

3.2 Double Soliton

In a microring cavity, under proper conditions, more than one soliton can exist. In the above-mentioned structure, for instance, only by decreasing the power to 8.5 mW, the second soliton can be formed. Both solitons remain stable and keep their waveform within the microring cavity (Fig. 4a-bottom). The advantage of this multi-soliton field is that in the frequency domain, their optical spectra overlap and provide an alternative form of frequency comb (Fig. 4a-top). Figure 4b shows the possibility of filtering carriers at different distances: 1-3×FSR (60-180 GHz). Comparing the single soliton spectrum, however, the power of the first line close to the central frequency is much less. On the other hand, to generate carriers with higher frequency, a double soliton is a better option where the power of a line in a distance of 3×FSR is only 1 dB less than the pump power (see Fig. 4b).



(a) (b)

Figure 4. a) Intra field cavity and its spectrum. b) The optical spectrum of the ring cavity in the range of 40nm. The spacing of the comb lines is 60GHz or 0.48 nm.

4. CONCLUSIONS

In order to generate carriers with high bandwidth (>60 GHz) to be used in the central office in a Radio over Fiber system, a frequency comb based on integrated photonic devices has been employed. A silicon nitride microring cavity has been designed to provide an FSR of about 60 GHz. We have numerically modelled and studied the intracavity field under nonlinear Kerr effect, to investigate the formation of stable solitons. The laser detuning and power have been studied to obtain a stable single-soliton and a double-soliton. In terms of single-soliton, the frequency spacing with 1×FSR and power suppress ratio of -2 dB and for double-soliton, the frequency spacing of multiple FSR and power suppress ratio of -1 dB is obtained.

ACKNOWLEDGEMENTS

This work is supported in part by the German Research Foundation (DFG) in the context of the “Silicon-on-insulator based integrated optical frequency combs for microwave, THz and optical applications” project.

REFERENCES

[1] A. Nirmalathas, *et al.*: Digitized radio-over-fiber technologies for converged optical wireless access network., *J. of Lightwave Technol.*, 28(16), pp.2366-2375, Aug. 2010.

[2] D. Novak, et al.: Radio-over-fiber technologies for emerging wireless systems. *IEEE J. of Quantum Electronics*, 52(1), pp.1-11, Jan. 2016

[3] V. Sharma, *et al.*: Challenges to radio over fiber (RoF) technology and its mitigation schemes–a review. *Optik-International J. for Light and Electron Optics*, 123(4), pp.338-342, Feb. 2012.

[4] R. Hosseini, L. Mirzoyan, K. Jamshidi: Energy Consumption Enhancement of Reverse-Biased Silicon-Based Mach–Zehnder Modulators Using Corrugated Slow Light Waveguides. *IEEE Photonics Journal*, 10(1), pp.1-7, Feb. 2018.

[5] M. Sohrabi, *et al.*: 60 GHz MIMO transceiver design for base station of radio over fiber, *5th international conference on millimiter wave and terahertz technologies Tehran*, Dec. 2018.

[6] C. Godey, *et al.*: Stability analysis of the spatiotemporal Lugiato-Lefever model for Kerr optical frequency combs in the anomalous and normal dispersion regimes. *Physical Review A*, 89(6), p.063814, Jun. 2014.

[7] S. Sabouri, *et al.*: Stable Turing patterns using silicon nitride ring cavity. *Latin America Optics and Photonics Conference*, pp. Th2E-5, Nov. 2018.

[8] R. Hamerly, *et al.*: Conditions for Parametric and Free-Carrier Oscillation in Silicon Ring Cavities. *J. of Lightwave Technology*, 36(19), pp.4671-4677, Oct. 2018.

[9] T. Herr, 2013. Solitons and dynamics of frequency comb formation in optical microresonators *No. THESIS_LIB. EPFL*, 2013.

Back-illuminated normal-incidence Ge-on-Si photodetectors

David Schmelz[1], Martin Steglich[1], Kay Dietrich[1], Thomas Käsebier[1], Uwe D. Zeitner[1]
[1] Institute of Applied Physics, Friedrich-Schiller-Universität, Albert-Einstein-Straße 15, 07745 Jena - Germany
e-mail: David.Schmelz@uni-jena.de

ABSTRACT

Backside illumination enables an increase in photoactive area and numerical aperture of Ge-on-Si photodetectors for SWIR applications. The transparency of silicon in the infrared range ($\lambda > 1.1$ µm) allows a nearly lossless propagation of incoming light through the Si substrate and also an application of optical microstructures on the rear side of the Si substrate. Moreover, an aluminium front contact covering the whole top area serves as a mirror which extends the optical propagation of the detectable SWIR light through the absorbing layers and hence increases the quantum efficiency. We developed back-illuminated Ge-on-Si photodiodes to verify these concepts. Especially the usage of light trapping structures shows great potential. Among the different microstructures we chose black silicon (b-Si) as a promising light trapping candidate. After the fabrication, photodiodes with different configurations were evaluated. The obtained results show a strong increase of the quantum efficiency due to both, the existence of an Al mirror and the application of b-Si.

Keywords: Ge-on-Si, pin-photodiode, Backside illumination, SWIR, Microstructures, Black silicon

1. INTRODUCTION

According to many investigations in the field of thin-film technology, by now it is possible to implement almost every common infrared photodetection material on silicon substrates [1]-[6]. Front-illuminated sensors usually suffer from area limitations due to the presence of electronic circuits. Moreover, incoming light has to pass through multiple layers of metal and dielectrica which causes reflection, deflection and absorption losses. Hence, the substantial advantage of backside illumination is an increase in photo-active area and numerical aperture. Yet, VIS back-illuminated photodetector chips need to be back-thinned to a thickness of only a few microns to reduce absorption losses within the substrate. This drawback is no longer existent for short wavelength infrared (SWIR) photodetectors thanks to the transparency of the silicon substrate in the SWIR range. Incoming light propagates without extinction towards the front side where the detection material is located. The silicon substrate even serves as an optical longpass filter due to its transparency only for wavelengths greater than 1.1 µm.

Furthermore, this enables the application of micro- and nanostructures on the backside, such as polarizers, diffraction gratings, computer generated holograms (CGHs), antireflection structures or plasmonic structures which can improve the performance of the photodetector or, alternatively, may be used for sophisticated metrology applications.

2. FABRICATION OF GE-ON-SI PHOTODIODES

In order to investigate the feasibility of back-illuminated, Si-based SWIR photodetectors, we established a process chain to manufacture vertical Ge-on-Si photodiodes, starting from an epitaxial layer stack (Fig. 1a) grown by molecular beam epitaxy (MBE). This process chain has been extensively tested and first Ge-on-Si photodiodes have eventually been produced (Fig. 1b). Ge-on-Si photodiodes can efficiently detect light up to a wavelength of 1550 nm which corresponds to the direct bandgap of germanium [1],[2]. Further detection materials, such as GeSn alloys [3], InGaAs [4], 2D materials [5] or HgCdTe [6] on Si wafers are also conceivable.

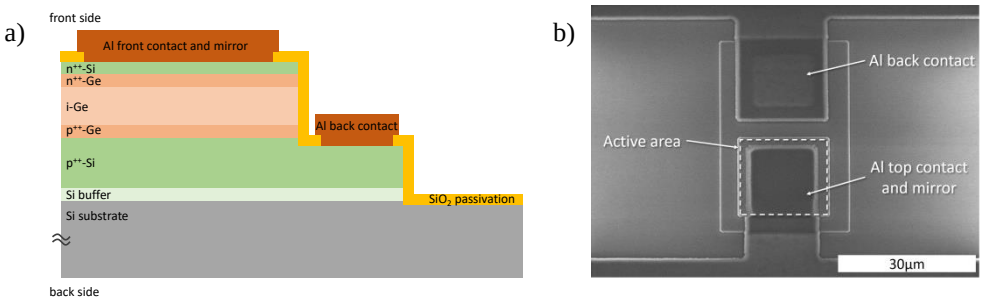


Figure 1. (a) Design of a vertical Ge-on-Si photodiode. (b) SEM picture of a manufactured Ge-on-Si photodiode (top view).

Fig. 1a shows the design of the photodiodes consisting of a double mesa structure with a vertical p-i-n doping profile. The p- and n-layers, with a thickness of 100 nm each, are relatively highly B- respectively Sb-doped of about 10^{20}cm^{-3}. This enables a strong built-in electrical field and a depletion region that spans the entire intrinsic

layer. The latter implies that these devices are able to generate an inherently high photocurrent even in zero bias operation (photovoltaic mode). While the whole germanium region is light absorbing, only the absorbed photons within the intrinsic layer account for the photocurrent. Photocarriers generated within the doped areas are not collected due to high Auger recombination in conjunction with slow carrier diffusion. For an intrinsic layer of 300 nm and a total Ge layer thickness of 500 nm, this results in an internal collection efficiency of about 60%.

For a front side illuminated photodiode, the top contact can only cover the peripheral area due to the need of an illumination window. On the contrary, in backside illumination configuration, the 500 nm thick Al top contact metallization covers the whole photoactive area. Upon illumination from the rear, the aluminium acts as a mirror with a reflectivity of more than 91%, thus extending the optical path length through the Ge diode and almost doubling the absorption and respectively the quantum efficiency, within one passage through the photodiode. The buried layer contact is connected via the lower mesa level. It consists of a 400 nm thick B-doped Si.

We produced photodiodes with active areas from 20 µm to 500 µm width and a differing Al top contact covering in one case the whole area and in the other only the peripheral area leaving an open illumination window for front side illumination. The 250 nm thick SiO2 passivation layer is a λ/4-coating for a wavelength of 1500 nm and hence serves as an antireflection layer. The photodiodes were characterized over a wavelength range from 1440 nm to 1640 nm using a tunable, fiber-coupled laser AQ2200-136 by Yokogawa and a source measure unit (SMU) 2601 by Keithley. The laser is collimated and subsequently focused through the backside of the substrate on the front side located photodiodes. A numerical aperture of 0.13 results in relatively small propagation angles around 2° within the Si substrate. For the Al mirror configuration, this leads to several transits of the propagating light through the photodiode due to reflections on the Al mirror and the rear side surface. Calculating these reflections, with reflectivities of 91% between Si and Al and 31% between Si and Air, results in an absorption enhancement factor of approximately 2.5 compared to the configuration without Al mirror. The measurements displayed in Fig. 2 validate this enhancement factor. The dashed line indicates the measurements of the configuration without Al mirror multiplied by 2.5. A photodiode with a relatively large active area of 200 µm width was surveyed. For smaller areas and higher numerical apertures, this consideration may not be valid albeit.

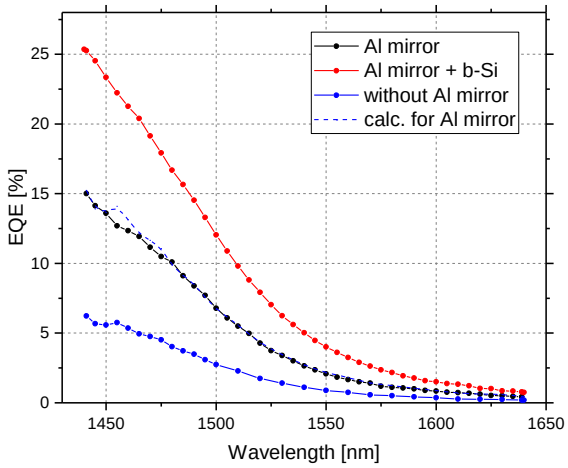


Figure 2. Measured external quantum efficiency (EQE) spectra of Ge-on-Si photodiodes with a lateral active area of 200 x 200µm² each. Configurations with and without an aluminium mirror are compared. Additionally, measurements of a chip with Al mirror configuration and black silicon (b-Si) microstructures are displayed.

Already at 1440nm, the spectrum shows a quickly descending external quantum efficiency (EQE) towards higher wavelengths while the band gap of germanium would be expected at 1550 nm. This can be explained by compressive strain within the epitaxial layers. The thermal expansion coefficient of germanium is larger compared to silicon. After the epitaxial growth at high temperatures; the layers cool down and thus a compressive strain is induced. Compressive strain modifies the band structure and shifts the band gap towards smaller wavelengths [1],[7]. Applying an additional relaxation step during the epitaxial growth process can turn this effect from compressive to tensile strain and extend the absorption spectrum to higher wavelengths instead [1],[2],[7]. However, this fact is not essential for the presentation of our principle results.

3. MICROSTRUCTURING THE BACKSIDE

After front side processing, we can also fabricate a designated microstructure on the silicon rear side of the photodetector. For example, scattering microstructures can be used to ‘trap’ the light inside the detector and thus increase the light absorption [8] and quantum efficiency [2],[9], respectively.

One approach comprises the application of stochastic needle-like structures, called black silicon (b-Si) shown in Fig. 3a. Besides its antireflection effect, it induces a transmissive scattering with a broad angular spectrum when coupling the incoming light through the b-Si structure. A great amount of light is scattered into angles above the

angle of total reflection (~17°) which hinders the light from leaving the chip again. Thus, the absorption can be increased significantly by a factor of 3 to 5 depending on the present layer thickness and wavelength [2],[9].

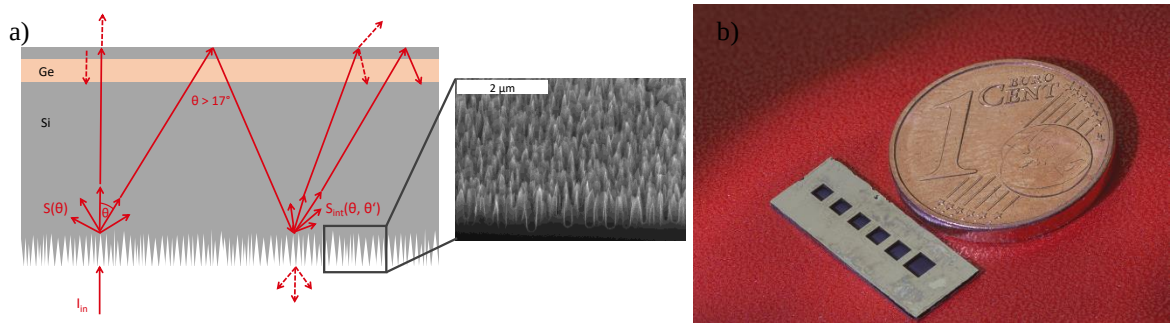


Figure 3. (a) Scheme of light trapping with b-Si. (b) Locally back-thinned and b-Si-structured rear side of Ge-on-Si photodiodes.

The advantage of b-Si over other microstructures is its simple and cost-efficient stochastic formation which does not require any lithographic technology. However, other microstructures could be more precisely adapted to the exact specifications of the particular device. Possible light trapping structures comprise plasmonic structures, diffraction gratings or CGHs [10].

The application of such structures makes further considerations necessary. The principle of light trapping is based on scattering or diffraction of incoming light into higher angles. While this increases the overall optical absorption for large area photodiodes, smaller photodiodes are easily missed by the scattered rays, thus causing signal reduction or optical crosstalk and blurring (in the case of sensor arrays). To ensure the propagation of light into the desired photodiodes two options are conceivable: either a local backside etch or an optical separation of the individual sensor pixels by deep narrow trenches. A local backside etch appears to be the rather viable option. For now, the etching was done by ICP-RIE (inductively coupled plasma – reactive ion etching) dry etching. The chips were back-thinned to a residual thickness of 50 µm which is sufficiently thin for devices with lateral dimensions > 100 µm. Subsequently a b-Si structure was fabricated within the etched indentation (see Fig. 3b). The measurements of these devices showed a significant improvement of the EQE presented in Fig. 2.

4. CONCLUSIONS

In conclusion, the presented investigations prove the feasibility of the concept of a back-illuminated Ge-on-Si photodiode. Backside illumination in combination with metallic front reflectors can significantly enhance the quantum efficiency of Ge-on-Si photodiodes. In addition, it gives the opportunity for the application of sophisticated microstructures such as diffraction gratings, wire grid polarizers or light-trapping structures. As example, we demonstrated a further increase in quantum efficiency by applying a b-Si light-trapping structure to back-thinned Ge-on-Si photodiodes. Generally, backside illumination opens a pathway towards efficiency enhancements and sophisticated, integrated sensor solutions.

REFERENCES

[1] J. Michel, J. Liu, and L.C. Kimerling: High-Performance Ge-on-Si photodetectors, *Nature Photonics*, vol. 4, pp. 527-534, July 2010.

[2] M. Steglich, *et al.*: Ge-on-Si photodiode with black silicon boosted responsivity, *Applied Physics Letters*, vol. 107, 051103, Aug 2015.

[3] M. Oehme, *et al.*: GeSn p-i-n detectors integrated on Si with up to 4% Sn, *Applied Physics Letters*, vol. 101, 141110, Oct 2012.

[4] A. R. Hawkins, *et al.*: High gain-bandwidth-product silicon heterointerface photodetector, *Applied Physics Letters*, vol. 70, pp. 303-305, Jan 1997.

[5] S. Goossens, *et al.*: Broadband image sensor array based on graphene-CMOS integration, *Nature Photonics*, vol. 11, pp. 366-371, May 2017.

[6] J. M. Peterson, *et al.*: High-Quality Large-Area MBE HgCdTe/Si, *J Electron Mater*, vol. 35, pp. 1283-1286, Jan 2006.

[7] Y. Ishikawa, *et al.*: Strain-induced band gap shrinkage in Ge grown on Si substrate, *Applied Physics Letters*, vol. 82, pp. 2044-2046, Mar 2003.

[8] E. Yablonovitch and G.D. Cody: Intensity Enhancement in Textured Optical Sheets for Solar Cells, *IEEE Trans. Electron Devices*, vol. 29(2), pp. 300-305, Febr 1982.

[9] M. Steglich, *et al.*: Improvement of Ge-on-Si photodiodes by black silicon light trapping, *Applied Physics Letters*, vol. 102, 111110, Mar 2013.

[10] S. Mokkapati, and K. R. Catchpole: Nanophotonic light trapping in solar cells, *Journal of Applied Physics*, vol. 112, 101101, Nov 2012.

Thermal regime of femtosecond writing for a phosphate glass

(Student Paper)

N.N. Skryabin[1,2,*], D.V. Khudyakov[3], S.K. Vartapetov[3], and I.V. Mel'nikov[1]

[1] Moscow Institute of Physics and Technology, Dolgoprudny, 141700 Moscow Region, Russian Federation

[2] Quantum Technologies Centre, M. V. Lomonosov Moscow State University, Moscow, Russian Federation

[3] Physics Instrumentation Center of the GPI RAS, Troitsk, Moscow Region, Russian Federation

E-mail: nikolay.skryabin@phystech.edu

ABSTRACT

We report on peculiarities of femtosecond writing in phosphate glass at a thermal regime in the sense of two different types of written tracks demonstrated. The operation diagram is shown for a wide range of laser repetition rates (< 2 MHz) and pulse energies (< 400 nJ). In addition, we explain the mechanism of formation of periodic bubble-like structures and present some discussions for a thermal regime in other materials.

Keywords: Femtosecond-laser writing, refractive index, thermal regime, phosphate glass.

INTRODUCTION

Femtosecond (fs) writing is a technology where a refractive index is modified inside optical materials by fs laser pulses that enables technologists to create different kinds of both passive and active photonic devices based on waveguides or grating [1]. There are two regimes of writing [2] - a non-thermal regime, where the material cools down after each pulse and that occurs at low (< 200 kHz) repetition rates (RR), and a thermal regime (TR), where local heat accumulation occurs each pulse at high RR (> 200 kHz), correspondingly. The TR has several advantages [3], which are: (i) transverse section of tracks becomes more circular and larger, (ii) structure of tracks becomes smooth and so provides written waveguides with low losses, and (iii) lower pulse energy (PE) and higher scan speeds can be exploited at TR.

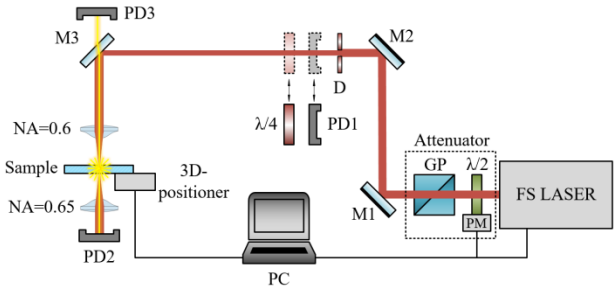


Figure 1. The experimental setup for femtosecond writing and measurement of transmitted laser and plasma glow radiation power

The TR is found experimentally for many materials, including silicate [4, 5], borosilicate [4, 6, and 7], phosphate [4, 8] and chalcogenide [9] glasses, and lithium niobate crystal [10, 11]. The research is limited to the specific RRs and PEs of available lasers. Besides, it is not clear a prior at what value RR it should be aimed. The TR is believed to happen at the RR about 1 MHz [7, 8, 9]. Sometimes it has been achieved it by making use of high-RR (25 MHz) lasers [4, 9] and ultrahigh-RR (80 MHz) oscillators [6]. However, void- or bubbles-like structures have been observed in some materials with increasing the RR instead of usual growth of the transverse section of tracks [4]. The reason for this phenomenon as well as overall picture of the TR is still not fully understood.

In this report, we demonstrate two different types of fs written tracks at TR in phosphate glass for first time to the best of our knowledge. We manage to distinguish tracks without and with internal structure as tracks type A and type B, respectively. The fundamental difference in physical processes is described in terms of operation diagram of the types A and B for a wide range of laser RR (< 2 MHz) and PE (< 400 nJ). A mechanism for the formation of bubble-like structures is proposed as a cyclic transition between the types. Finally, we provide recommendations for an experiment where the RR pertinent to the TR should be found in borosilicate glass, $LiNbO_3$ and Yb:KGW crystals.

1. EXPERIMENTAL DESIGN AND METHODS

The experimental setup for a fs writing is shown in Fig. 1. Yb-fiber laser (Avesta) provided 350-fs pulses at 1040-nm wavelength with a M^2 < 1.2 beam quality. The fundamental RR of the oscillator (2.11 MHz) was divided by a multiple built-up output acousto-optic modulator to lower the RR. The power of laser radiation was attenuated by a system of a half-wave plate on piezo-motor, Glan prism and photodiode PD1. Laser pulses were focused inside a phosphate glass sample (30x15x2 mm) by an aspherical lens (Thorlabs C610TME-C) with a numerical aperture (NA) of 0.6 and compensation of spherical aberrations at a depth of 850 μm. The sample was placed on a three-dimensional automated stage and moved relatively to the focus of the optical system with speed 50 μm/s. The laser polarization was parallel to the scanning direction. The transmitted laser beam was collected by a lens with NA = 0.65 and a photodiode PD2 measured continuously its power. During the

experiment, the photodiode PD3 also measured the power of the plasma glow discharge through the lens with NA = 0.6 and dichroic mirror M3.

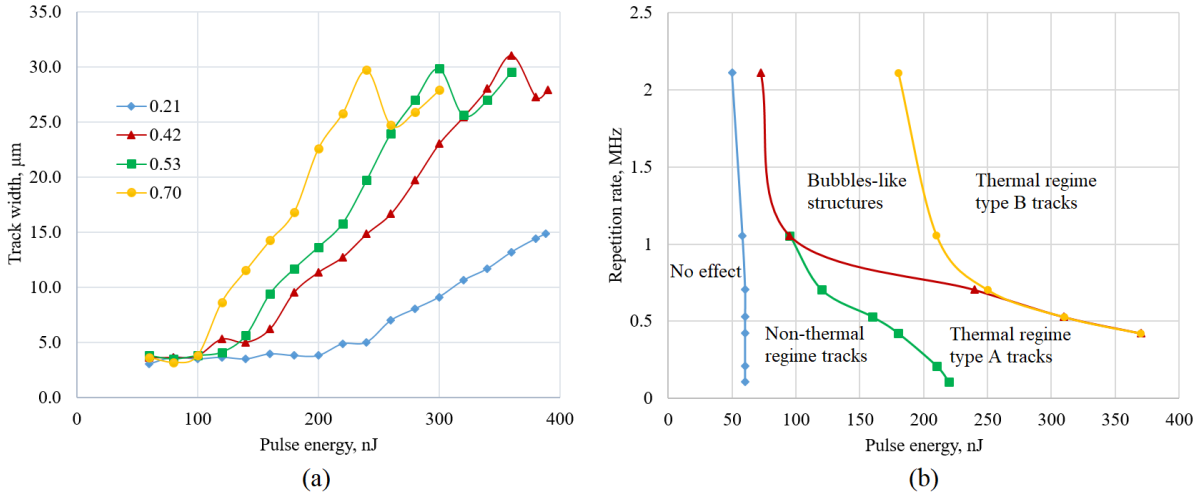


Figure 2. (a) The PE dependence of the track width measured from microscopy images at 0.21, 0.42, 0.53 and 0.70 MHz laser RR; (b) The characteristic diagram of the transition to the TR.

2. RESULTS AND DISCUSSION

For a wide range of the RR (0.11 – 2.11 MHz), series of tracks are produced with the PE ranging from 60 nJ to a maximum of 400 nJ. At a relatively low RR 0.21 - 0.70 MHz, a fracture of monotonic broadening of the track size with a grow in PE is observed. The dependence of the track width on the PE and RR is shown in the plot (Fig. 2a). The fracture can be associated with formation of the secondary structure (not shown here) inside the track, i.e. at a certain frequency, starting with a specific PE, the internal structure of the track changes, and the track size decreases. We distinguish tracks without and with internal structure as tracks type A and type B respectively. There also is a second inner layer observed as the type B. At higher RR 1.06 - 2.11 MHz, the situation looks different. Starting with some energy, void- or bubbles-like structures appear and then change to tracks of the type B. The characteristic diagram of the transition to the TR is shown in Fig. 2b.

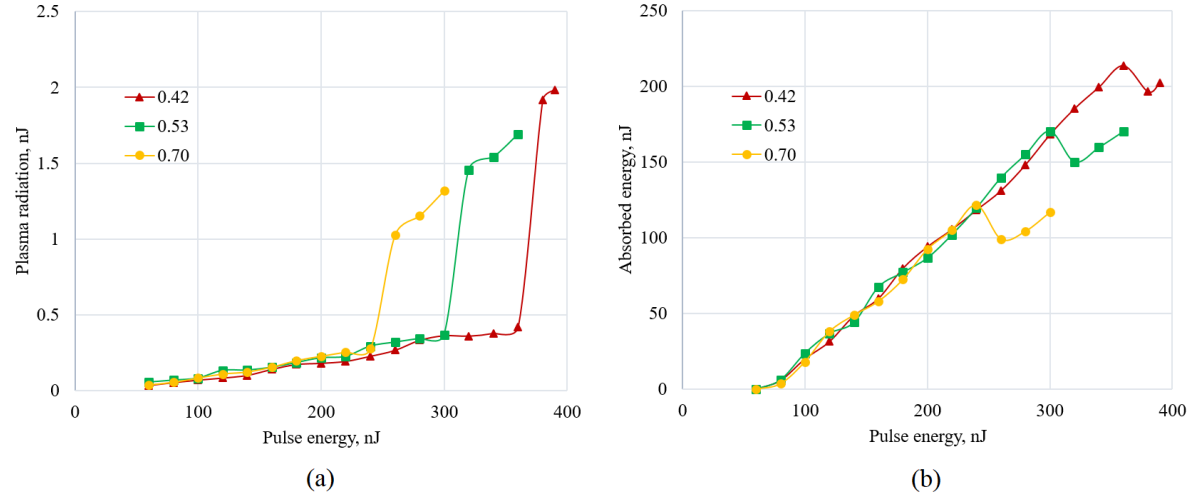


Figure 3. (a) The PE dependence of plasma glow radiation energy (b) and incident PE dependence of absorbed energy at 0.42, 0.53, 0.70 MHz laser frequencies

In order to study and distinguish different types of tracks, we determine the absorbed laser radiation by measuring the transmitted laser radiation during the writing. Since there is also a plasma glow in the focus, we also its radiation power is also measured. It turned out that during the writing tracks of type B, the plasma radiation is sharply increased by about 4 times (Fig. 3a). Totally, this radiation does not exceed 1% of the absorbed energy. The experimental dependence of absorbed energy on initial PE are shown in Fig. 3b, where there are clearly visible signatures in the transition from the type A to type B, i.e. the energy absorption drops drastically when the track type B is being written. That is, it is tempting to suggest from the data observed that the formation of the bubble-like structure is caused by a local temperature grow. It is also tempting to declare

that there are three different mechanisms of material heating: (a) simple heating without melting, (b) melting after each laser pulse followed by rapid solidification, (c) a molten state in the focal region, so the energy of the pulse is absorbed in the liquid phase of the material.

The reasons for the absorption energy signature are not fully understood, but we assume it relates to the transition to the TR with a molten state in the focus where the liquid phase absorbs fewer laser power. It may be the case of a plasma defocusing or a change in the width of the band gap. However, the fact that the absorption has a signature, gives a qualitative explanation for the formation of the bubble-like structure. We believe that there is a periodic variation near the phase transition, and the track is obtained between types A and B. Therefore, the material absorbs the laser radiation and heats up, and when the magnitude of the lower temperature curve starts to exceed the melting temperature, the absorption in the liquid phase goes down; the material turns into the solid and starts absorbing more energy, etc. Besides, it is known that the thermal conductivity of the material also increases as the temperature rises up, which leads to faster cooling at higher temperatures.

As we show, there is no stable TR at any randomly chosen frequency. Each material has a convenient RR and PE band for it. For phosphate glass, we determined type A the convenient RR to be 0.4-0.7 MHz. In a similar way, we found for borosilicate glass a band of convenient RR to be 0.5-1.0 MHz. Type A tracks should be sought at the frequency "under" the bubbles-like structures formation RR. For example, in Yb:KGW at a RR of 2 MHz, bubbles start appearing at energy of 150-200 nJ, while at RR of 1 MHz there are no bubbles at the energies up to 400 nJ. Therefore, the TR should be searched around at frequencies around 1.5 MHz. For lithium niobate the broadening of tracks begins at 2 MHz, so the search of the TR should be in the range of RR 3-5 MHz. We noted that there is a correlation between the coefficient of thermal conductivity and RR [12].

The TR writing is extremely important for some applications. It is necessary to clearly define the boundaries of ranges A and B tracks types in order to operate at particular one. Type A tracks show itself as a low loss single- or multimode waveguides [4]. Type B tracks, despite of its inner structure, are useful for the fast writing of high NA depressed cladding waveguides with large mode area, which are used as hybrid laser amplifiers [13].

ACKNOWLEDGEMENTS

We gratefully acknowledge M. Bukharin and F. Popov for their valuable contributions to this research. It is also supported by the RFBR grant № 18-42-130005\18.

REFERENCES

[1] R. Osellame, G. Cerullo, and R. Ramponi, Eds., "Femtosecond-laser micromachining: Photonic and Microfluidic Devices in Transparent Materials," Springer Berlin, (2012).
[2] R. R. Gattass, L. R. Cerami, and E. Mazur, "Micromachining of bulk glass with bursts of femtosecond laser pulses at variable repetition rates," Opt. Express 14, 5279-5284 (2006).
[3] S. M. Eaton *et a*l., "Transition from thermal diffusion to heat accumulation in high repetition rate femtosecond laser writing of buried optical waveguides," Opt. Express 16, 9443-9458 (2008).
[4] R. Osellame *et al*., "Optical properties of waveguides written by a 26 MHz stretched cavity Ti:sapphire femtosecond oscillator," Opt. Express 13, 612-620 (2005).
[5] K. Minoshima *et al*., "Photonic device fabrication in glass by use of nonlinear materials processing with a femtosecond laser oscillator," Opt. Lett. 26, 1516-1518 (2001).
[6] M. Will *et al*., "High-speed fabrication of optical waveguides inside glasses using a high repetition-rate fiber CPA system," Proc. SPIE 5339, Photon Processing in Microelectronics and Photonics III (2004).
[7] S. M. Eaton *et al*., "Heat accumulation effects in femtosecond laser-written waveguides with variable repetition rate," Opt. Express 13, 4708-4716 (2005).
[8] R. Osellame *et al*., "Waveguide lasers in the C-band fabricated by laser inscription with a compact femtosecond oscillator," IEEE J. Sel. Top. Quantum Electron. V. 12, № 2. P. 277–285 (2006).
[9] A. Zoubir *et al*., "Direct femtosecond laser writing of waveguides in As2S3 thin films," Opt. Lett. 29, 748-750 (2004).
[10] A. H. Nejadmalayeri and P. R. Herman, "Rapid thermal annealing in high repetition rate ultrafast laser waveguide writing in lithium niobate," Opt. Express 15, 10842-10854 (2007).
[11] M. Dubov, S. Boscolo, and D. J. Webb, "Microstructured waveguides in z-cut LiNbO3 by high-repetition rate direct femtosecond laser inscription," Opt. Mater. Express 4, 1708-1716 (2014).
[12] M. A. Bukharin, D. V. Khudyakov, and S. K Vartapetov, "Heat accumulation regime of femtosecond laser writing in fused silica and Nd:phosphate glass," Appl. Phys. A 119: 397 (2015).
[13] M. A. Bukharin, A .D. Lyashedko, N. N. Skryabin, D. V. Khudyakov, S. K. Vartapetov, "Improved optical efficiency of bulk laser amplifiers with femtosecond written waveguides," Proc. of SPIE. T. 98930G. C. 98930G-7 (2016).

Development of a Portable Optical Time Domain Reflectometer System in Photonic Integration Technology

Stanisław Stopiński, Krzysztof Anders, Sławomir Szostak and Ryszard Piramidowicz
Warsaw University of Technology, Institute of Microelectronics and Optoelectronics,
Koszykowa 75, 00-662 Warsaw, Poland
e-mail: stanislaw.stopinski@pw.edu.pl

ABSTRACT

In this work we present and discuss a concept of an integrated optical time domain reflectometer realized in indium phosphide generic integration technology. The proof-of-the-concept chip has been designed, manufactured and tested with respect of applicability in real measuring systems. In general, the correctness of the proposed approach has been confirmed, simultaneously indicating necessary modifications of the design. As a result, the optimized variants of the photonic integrated circuit have been proposed.

Keywords: optical time domain reflectometer, application specific photonic integrated circuit, generic integration technology, indium phosphide

1. INTRODUCTION

Optical time domain reflectometry (OTDR) is a measurement technique commonly used for characterization of optical fibers and fiber-optic communication systems [1]. It utilizes the phenomena of the Rayleigh backscattering and Fresnel reflections – a series of laser pulses is launched to an optical fiber and the power of the returning signal is monitored in the time domain. Careful analysis and processing of the recorded time traces enables extraction of the most important parameters of optical links such as attenuation of fibers, losses at splices and connectors, length of the links and location of the events with respect to the distance to the reflectometer. It also allows localizing breaks, damages or deformations present in a fiber-optic link. A substantial advantage of the reflectometry techniques is the ability to perform measurements while having access to the single end of an optical fiber only, which is essential for application in already deployed telecom networks.

Optical time domain reflectometer systems, which are currently available on the market, can be divided into two major groups depending on the application targeted. Highly advanced equipment of excellent performance in terms of dynamic range, maximal measurement distance and accuracy is mostly used by optical fiber manufacturers and in specialized laboratories. For such equipment, the compact size and energy consumption level are obviously not of primary concern – state-of-the-art devices are rather bulky and power hungry. Furthermore, interpretation of the results requires professionally trained and highly skilled personnel, which limits common use of this type of devices by technicians in the field.

On the contrary, portable OTDRs are typically used for diagnostics of the network in central offices or in the field. The main requirements for the portable devices are quite obvious – small size and weight, low energy consumption, compatibility with battery supply and low cost of manufacturing. These are complemented by the demand of the prompt, automated interpretation of the results. The continuous evolution of telecommunication and sensing networks into all fiber-optic systems leads to the conclusion that the market for portable OTDR devices will dynamically increase. In this work we propose a novel optical time domain reflectometer system, which is realized in a form of a monolithic application specific photonic integrated circuit. The devices have been designed and manufactured in the generic integration technology on indium phosphide technology platforms. Two generations of optical chips are demonstrated and discussed with respect of applicability in real measuring systems.

2. PHOTONIC INTEGRATED CIRCUIT – 1st GENERATION

The scheme of the first generation of integrated OTDR modules is presented in Figure 1. It comprises a directly modulated DFB laser, operating around 1550 nm, as the source of the optical pulses. The laser is connected to a 2×2 MMI coupler, the outputs of which are routed to a spot-size-converter, which enables edge-coupling of the signal to an analyzed optical fiber, and to an integrated PIN photodiode, which provides time-domain monitoring of the outgoing pulses. The remaining input of the coupler is connected to another PIN photodiode, responsible for detection of the backscattered and reflected light. Figure 1 presents also the mask layout of the circuit of dimensions 6 mm × 1 mm, which was placed in a standard cell of the Heinrich Hertz Institute process [2], and a microscope picture of the chip fabricated in the generic process provided by HHI on a multi-project wafer.

The fabricated chips were mounted on a copper block and thermally stabilized during the measurements. Optical coupling was provided through a cleaved SMF fiber due to the presence of spot-size-converters at the chip outputs. The interface of the DFB laser is compatible with the G-S-G high-speed electrical probes, which were

used for driving both with a DC bias and pulsed signals. Static measurements have proven the basic performance of the laser – the maximum fiber-coupled power is around 0.75 mW while driven at 150 mA, the laser operates on a single mode (λ = 1546.5 nm) with side mode suppression ratio around 45 dB.

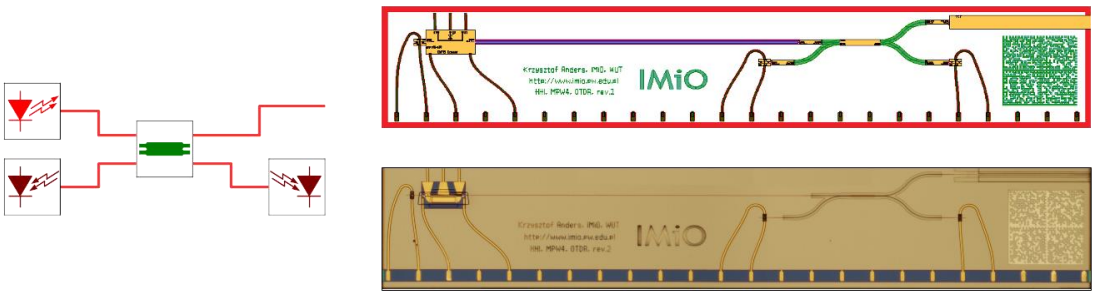


Fig. 1. Circuit scheme, mask layout and a microscope picture of the first generation of integrated optical time domain reflectometer.

Dynamic measurements were performed with the use of a pulsed signal of a different time duration (between 20 ns and 20 µs) and constant repetition rate (f = 1 kHz) driving the DFB laser. The output of the chip was connected to a spool of single mode fibers of different length (5-20 km). The photocurrent from the photodiode (reverse bias of 2.0 V) was amplified using a transimpedance amplifier and visualized on the oscilloscope. Additionally, a discrete photodetector was connected as a reference to the end of the analyzed fiber link.

Figure 2 presents the recorded time traces for different conditions and configurations of the characterization setup. It should be noted that without averaging the signal, the trace suffers from significant noise, which is clearly visible in Figure 2a. This phenomenon is quite typical for reflectometric measurements, the signal-to-noise ratio increases with the number of recorded samples (square-root dependence). The improvement of the signal quality is visible in Figure 2b, for which 8192 samples were taken. Three pulses can be distinguished in the graph. The first, strong blue pulse, is a result of reflection at the chip facet and defines the reference of the OTDR trace (zero time point). The second (red pulse) is detected by the external photodetector and corresponds to a single pass of the pulse – from the source to the end of the fiber link. The third (weak blue) pulse is a result of a double pass – from the source to the end and after reflection at the end back to the source. The time difference of approximately 24 µs between consecutive pulses corresponds well to the length of the analyzed link of 5 km.

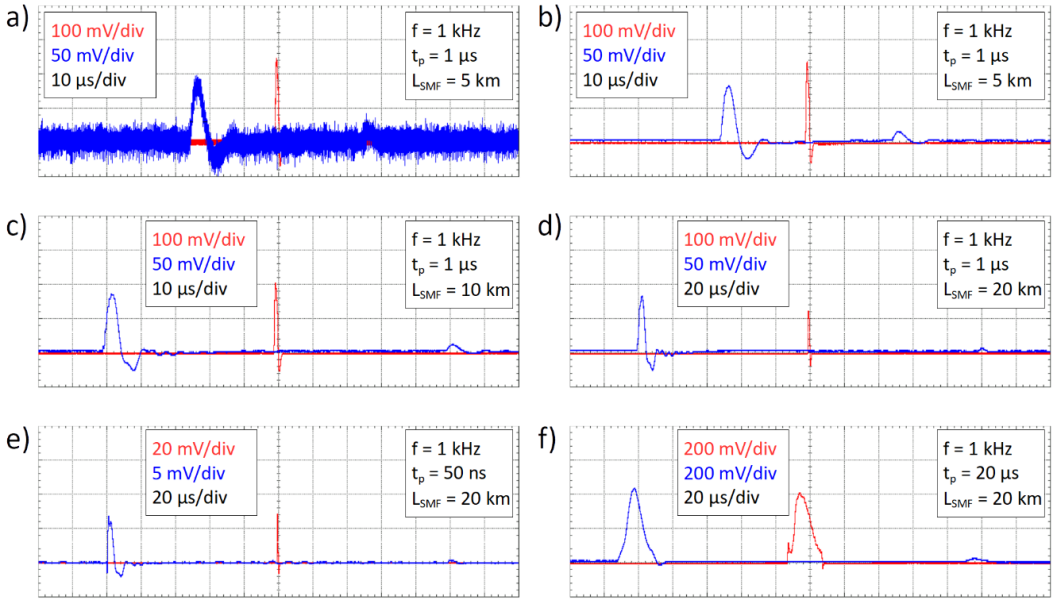


Fig. 2. Recorded time traces for OTDR experiments.

The performance of the OTDR system was tested for different conditions and the obtained results are visualized in Figures 2c-2f. For the length of the link up to 20 km, a detectable reflection at the end of the fiber was observed for pulse duration in the range between 50 ns and 20 µs. For the pulses shorter than 50 ns the signal was too low to be detected.

3. PHOTONIC INTEGRATED CIRCUIT – 2nd GENERATION

The second generation of the integrated OTDR unit comprises a number of test circuits, designed for determining a solution of the best performance. The circuits were realized using the SMART Photonics technology

platform. As light sources either Fabry-Perot or DBR lasers are used. External modulation is provided either by an electro-absorption section or a Mach-Zehnder interferometer with electro-optic phase shifters. Every laser-modulator combination is designed in two variants – with and without a booster semiconductor optical amplifier, positioned prior to the output 2×2 MMI coupler. Each circuit uses a PIN photodiode with a ground-signal-ground electrical interface for monitoring of the backscattered and reflected signal. The main difference in comparison to the first generation circuits is the presence of the booster amplifier (the Rayleigh signal for the first generation circuit was too weak to be detected) and a photodiode with a high-speed electrical interface (the electro-optical bandwidth is 18 GHz) in order to avoid the ringing effect. Furthermore, the chip outputs are angled, so that the influence of the parasitic reflection at the facet is minimized.

Figure 3a presents the circuit scheme for the variant with the Mach-Zehnder modulator (MZM), with both types of lasers at its inputs. The outputs of the MZM are then connected either directly or through an SOA to the output coupler. Such a circuit provides a possibility of testing two types of lasers with and without a booster, which is an equivalent to four distinct circuits. On the contrary, as the electro-absorption modulator has only a single input and output, for independent circuits have been designed – Figure 3b presents two variants, which are realized with both types of lasers. Mask layout of the designed cell is presented in Figure 3c. The chips are currently being fabricated in the SMART Photonics laboratories.

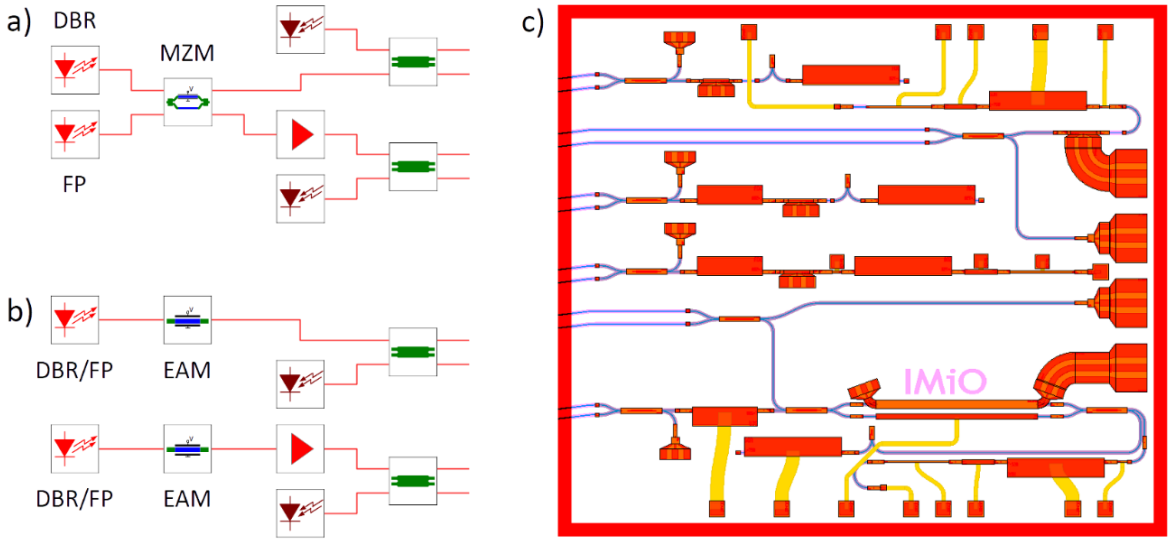


Fig. 3. Circuit scheme and mask layout of the second generation of integrated optical time domain reflectometers.

Simultaneously we have initiated R&D works on the development of the electronic circuitry for precise controlling the key parameters of the laser and detector as well as processing all gathered data. After solving all problems with powering, stabilizing, steering and data processing the "classical" electronic circuits are planned to be replaced by a dedicated electronic integrated circuit (EIC) it the final version of the device.

SUMMARY

Two generations of integrated units for portable optical time domain reflectometers have been demonstrated. The proof-of-the-concept device has been designed, manufactured and tested with respect of applicability in real measuring systems. In general, the correctness of the proposed approach has been confirmed, simultaneously indicating necessary modifications of the design, mostly with respect to the level of the output optical power, parasitic reflections and photodetectors bandwidth. An optimized design of the photonic circuit has been proposed.

ACKNOWLEDGEMENTS

This work has received support from the EU Horizon 2020 research and innovation programme under grant agreement No. 687777 (PICs4All). Stanisław Stopiński would like to thank for the support granted by the dean of the Faculty of Electronics and Information Technology of Warsaw University of Technology.

REFERENCES

[1] M. K. Barnoski and S. M. Jensen, "Fiber waveguides: A novel technique for investigating attenuation characteristics", Applied Optics, vol. 15, no. 9, pp. 2112-2115, 1976.

[2] M. Smit et. al., "An introduction to InP-based generic integration technology InP general", Semiconductor Science and Technology 2014, Volume 29, Number 8, p. 083001

Silicon Waveguide Wavelength-selective Switch Using Cascaded Microring Resonators and Thermo-optic Phase Shifters

Takuya Toma[1], Yuya Shoji[1,2], Tetsuya Mizumoto[1]
[1] Department of Electrical and Electronic Engineering, Tokyo Institute of Technology,
2-12-1 Ookayama, Meguro-ku, Tokyo, 152-8550 - Japan
[2] Laboratory for Future Interdisciplinary Research of Science and Technology,Tokyo Institute of Technology,
2-12-1 Ookayama, Meguro-ku, Tokyo, 152-8550 - Japan
e-mail: tmizumot@pe.titech.ac.jp

ABSTRACT

A wavelength selective switch is fabricated for routing wavelength channels in a wavelength division multiplexing network. The device uses a Mach-Zehnder interferometer configuration incorporating wavelength selective phase shifters, which are composed of cascaded microring resonators and waveguide thermo-optic phase sifters. The fabricated device works as a hitless wavelength selective switch with on/off switching ratios of 23 and 20 dB in two wavelength channels of 1532.5 and 1536.7 nm, respectively.

Keywords: silicon photonics, wavelength selective switch, Mach-Zehnder interferometer, microring resonator

1. INTRODUCTION

A wavelength-selective switch (WSS) is a key component to construct a wavelength division multiplexing network. It works as a routing switch for designated wavelength channels. Microring resonator (MRR) based switches are investigated to select a designated wavelength channel for switching to and from a bus line [1]-[3]. These switches have the advantages of a small footprint and adequate scalability of the wavelength channel. However, they have the disadvantages of being unavailable for hitless operation. As other configurations, arrayed waveguide gratings (AWGs) or caved gratings are used for demultiplexing wavelengths and are combined with a Mach-Zehnder interferometer (MZI) based routing switch [4]. The switch tends to have a large footprint due to AWG and/or a poor (de)multiplexer design flexibility. A micro electro-mechanical systems (MEMS) based approach [5] has an issue of integration complexity.

Previously, we proposed a novel WSS composed of wavelength selective phase shifters embedded in an MZI [6]. In this article, we fabricate the WSS based on wavelength selective phase shifters to demonstrate the hitless operation in a two wavelength channel WSS.

2. DEVICE CONFIGURATION

The configuration of the WSS investigated in this article is shown in Fig. 1. The designated wavelength signals that are resonant in cascaded MRRs are coupled from outer arms to inner arms through MRRs, whereas other wavelength signals are radiated away from the device. Hence, this configuration works as an MZI for the designated wavelength signals. Phase shifters (PSs) are placed in outer arms. Each set of PSs and MRRs work as a wavelength-selective phase shifter for the designated wavelength channel at which the cascaded MRRs are in resonance.

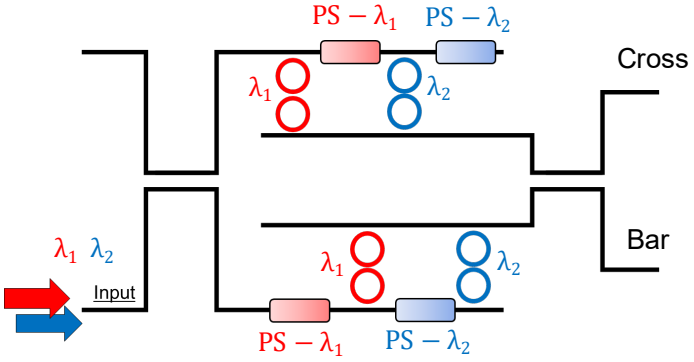


Figure 1. Configuration of wavelength selective switch based on phase shift.

Let us consider the signal of designated wavelength λ_1 that is resonant in the first (left) cascaded MRRs. A signal launched into the lower arm goes through PS-λ_1, while the signal launched into the upper arm goes through no PS. The phase difference ϕ_1 between the two signals is controlled by PS-λ_1. The output port of the designated

wavelength λ_1 is switched between the cross and bar ports of the MZI depending on the phase difference ϕ_1=0 and π, respectively, for that channel. On the other hand, signals that are non-resonant in the first cascaded MRRs propagate in the lower and upper arms. They go through PS-λ_1 evenly. Consequently, the phase change given by a pair of PS-λ_1 does not affect the signals that are non-resonant in the first MRRs. For the designated wavelength λ_2 that is resonant in the second (right) cascaded MRRs, the phase difference ϕ_2 between two arms is controlled by PS-λ_2 located in the lower arm. The output port of the designated wavelength λ_2 is switched between the cross and bar ports depending on the phase difference ϕ_2=0 and π, respectively.

3. FABRICATION and CHARACTERIZATION

The device was fabricated in a 220-nm-thick silicon layer on an SOI wafer. The waveguide pattern was drawn by using an electron beam lithography, and was transferred to a SiO_2 mask layer. The waveguide was formed by using a reactive ion etching with SF_6 gas. After fabricating silicon waveguides, a 2-μm-thick SiO_2 over cladding layer was deposited by PCVD. 10-μm-wide, 230-μm-long and 50-nm-thick Cr heaters were formed by a lift-off technique to provide PS through a thermo-optic effect. An electric current was fed to the heaters through a 200-nm-thick Au electrode. A pair of PS-λ_i's (i=1 or 2) were connected in series so that an equal phase shift was provided in two PS-λ_i's with a single power supply.

3-dB couplers were composed of 480-nm-wide waveguides with a coupling length of 14 μm for 575-nm spacing between two parallel waveguides, which were designed to be fabrication-tolerant. The cascaded MRRs were designed so as to provide a FWHM pass band width of 1.7 nm and a free spectral range (FSR) of 11 nm. The details of the cascaded MRRs and the measured transmittance spectra are shown in Fig. 2.

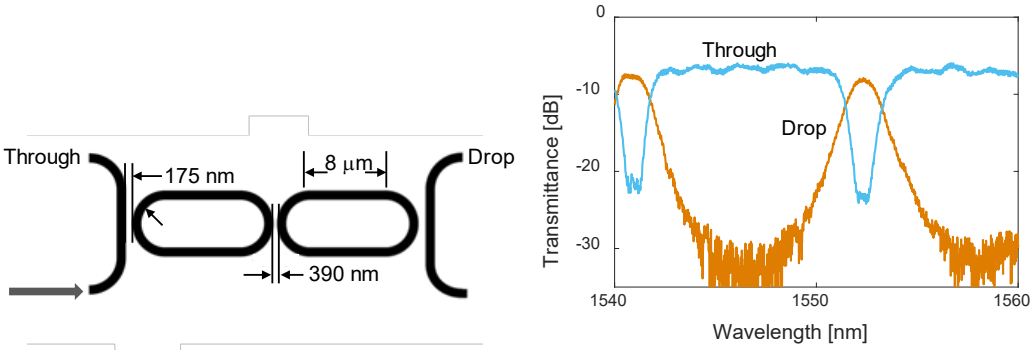


Figure 2. Structure and measured transmittance spectra of cascaded MRRs.

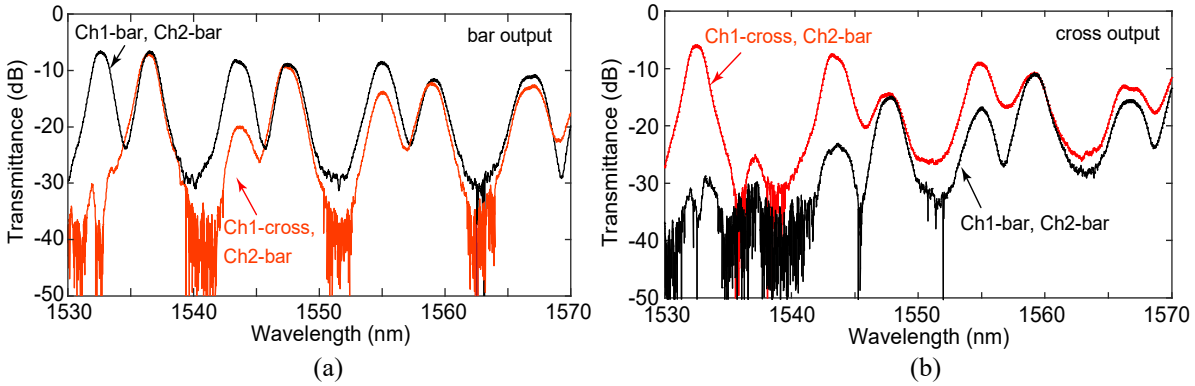


Figure 3. Transmission spectra measured at the (a) bar and (b) cross ports of fabricated WSS.

A broadband light source was used to measure the transmission characteristics of fabricated WSS. The TM mode lightwave was launched into an input port through a lens-tipped optical fiber. The output of WSS was coupled to another lens-tipped optical fiber to measure an output power at the bar and cross ports. The measured transmission spectra are shown in Fig. 3. Figures 3(a) and (b) show the transmittance measured at bar and cross ports, respectively. In the figures, the black lines denote the transmittance when the WSS is set so that the signals of both channel-1 (a center wavelength of 1532.5 nm) and channel-2 (a center wavelength of 1536.7 nm) are transmitted to the bar port. On the other hand, the red lines correspond to the case where only the channel-1 signal is switched to the cross port. It is clearly observed that the transmittance of channel-2 signal is not affected by switching the output port for the channel-1. Similar responses are observed at longer wavelengths with a periodicity of ~11 nm, which corresponds to the FSR of cascaded MRRs. They, however, exhibit poor on/off switching ratios

at longer wavelengths. This is attributable to that the splitting ratio of 3-dB couplers used in an MZI deviates from 50:50 at the wavelengths except λ=1530-1540 nm.

Focusing on a wavelength range of 1530-1540 nm, the transmission spectra measured at the bar port are shown in Fig. 4 for four switch states; ch-1 on/ ch-2 on (black line), ch-1 off/ ch-2 on (red line), ch-1 on/ ch-2 off (blue line) and ch-1 off/ ch-2 off (green line). The on/off switching ratios measured at the bar port are 23 and 20 dB for channels 1 and 2, respectively. Clearly shown is that the fabricated WSS works as a hitless switch.

Figure 5 shows the transmission change measured at λ=1536.7 nm as a function of a drive power supplied to a phase shifter PS-λ_2. A drive power of 40 mW is needed to obtain π phase shift. Complimentary output is observed at the bar and cross ports.

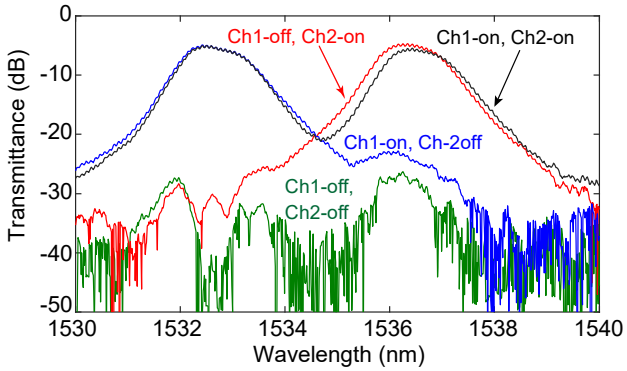


Figure 4. Transmission spectra measured at the bar port for four switch states.

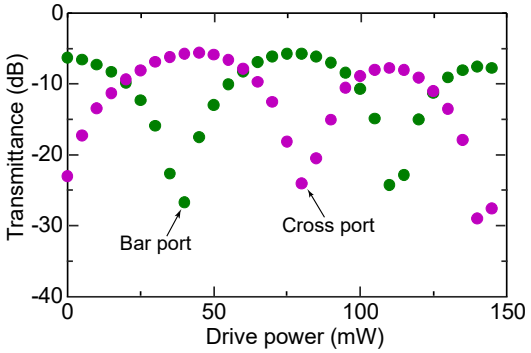


Figure 5. Transmittance vs drive power supplied to a phase shifter of channel 2.

4. CONCLUSIONS

We have fabricated the WSS based on wavelength selective phase shifters. The fabricated device works as a hitless WSS with on/off switching ratios of 23 and 20 dB in two wavelength channels of 1532.5 and 1536.7 nm, respectively. Although the present devices works as a two wavelength channel WSS, it is possible to increase the number of wavelength channel in a single MZI by properly designing cascaded MRRs and 3-dB couplers.

ACKNOWLEDGEMENTS

This work was supported by MIC/SCOPE #162103103; JST CREST #JPMJCR15N6 and #JPMJCR18T4; JSPS KAKENHI #16K06295.

REFERENCES

[1] Y. Goebuchi, M. Hisada, T. Kato, and Y. Kokubun: Optical cross-connect circuit using hitless wavelength selective switch, *Opt. Express*, vol. 16, pp. 535-548, Jan. 2008.

[2] T. Hu, H. Qiu, P. Yu, C. Qiu, W. Wang, X. Jiang, M. Yang, and J. Yang: Wavelength-selective 4×4 nonblocking silicon optical router for networks-on-chip, *Opt. Lett.*, vol. 36, pp. 4710-4712, Dec. 2011.

[3] D. Geuzebroek, E. Klein, H. Kelderman, N. Baker, and A. Driessen: Compact wavelength-selective switch for gigabit filtering in access networks, *IEEE Photonics Technol. Lett.*, vol. 17, pp. 336-338, Feb. 2005.

[4] S. Nakamura, S. Takahashi, M. Sakauchi, T. Hino, M. Yu, and G. Lo: Wavelength selective switching with one-chip silicon photonic circuit including 8×8 matrix switch, *in Technical Digest OFC/NFOEC 2011*, Los Angeles, USA, March 2011, paper OTuM2.

[5] G. N. Nielson, D. Seneviratne, F. Lopez-Royo, P. T. Rakich, Y. Avrahami, M. R. Watts, H. A. Haus, H. L. Tuller, and G. Barbastathis: Integrated wavelength-selective optical MEMS switching using ring resonator filters, *IEEE Photonics Technol. Lett.*, vol. 17, pp. 1190-1192, June 2005.

[6] K. Miura, Y. Shoji, and T. Mizumoto: Mach–Zehnder wavelength selective switch embedded with microring resonators, *Jpn. J. Applied Phys.*, vol. 56, 22201, Jan. 2017.

GaAs-based gain waveguides with U-bend architecture enabling low loss and high yield hybrid integration on silicon photonic circuits

(Student Paper)

Heidi Tuorila[1], Jukka Viheriälä[1], Nouman Zia[1], Matteo Cherchi[2], Timo Aalto[2], Mircea Guina[1]
[1] Optoelectronics Research Centre, Physics Unit, Tampere University, 33101 Tampere, Finland
[2] VTT Technical Research Centre of Finland, Espoo 02044, Finland
e-mail: heidi.tuorila@tuni.fi

ABSTRACT

We present a U-bend design for traveling wave III-V gain devices, such as semiconductor optical amplifiers and laser diodes. The design greatly simplifies the butt-coupling between the III-V chip and silicon-on-insulator photonic circuit by bringing the I/O ports on one facet. This removes the need for precise dimension control otherwise required for 2-side coupling, therefore increasing the yield of mounted devices towards 100%. The design, fabrication and characterization of the U-bend device based on Euler bend geometry is presented. The losses for a bend with a minimum bending radius of 83 µm are 1.1 dB. In addition, we present an analysis comparing the yield and coupling losses of the traditionally cleaved devices with the results that the Euler bend approach enable, with the final conclusion that the yield is improved by several times while the losses are decreased by several dB.

Keywords: hybrid integration, III-V, semiconductor optical amplifiers, silicon-on-insulator, coupling losses

1. INTRODUCTION

Silicon photonics and photonic integrated circuits (PICs) provide an attractive platform enabling efficient and flexible signal transfer and processing, which is instrumental for several fields of application, such as telecom, datacom, and sensing. Photonic circuits based on silicon offer low loss waveguides and can be manufactured using existing CMOS facilities. However, their main limitation is the inability to offer optical gain. To overcome this major limitation, heterogeneous, monolithic, and hybrid integration [1] of III-V semiconductors on the silicon platform haves been intensively addressed during the last decade. While heterogeneous and monolithic integration have the advantage of innate alignment of the waveguides between the two material systems, they lack the flexibility of hybrid integration [2], which allows for separate manufacturing of the waveguide platform and the gain chip thus being able to take advantage of the CMOS lines. This is especially advantageous for smaller production volumes and specialized custom devices.

The hybrid integration requires high alignment precision between the Si and III-V waveguides within sub-micron precision. The positioning of the chip can be achieved with the current alignment systems. However, the chip dimension control when using standard methods of scribing and cleaving can result in chip length variation of several microns. Because the pit on the photonics chip reserved for the gain chip is pre-fabricated, the lack of control of the III-V chip dimensions leads to chips too long or short for the designed slot. For devices such as travelling-wave semiconductor optical amplifiers (TW-SOA) with I/O ports at the opposing sides of the chip and with tilted waveguides this can result in significant coupling losses and poor yield.Our solution to this problem is to use a U-bend design for the waveguide of the III-V device where the I/O ports are brought on one side of the chip, as shown in Fig. 1. This design removes the need for precise cleaving and dimension control because only

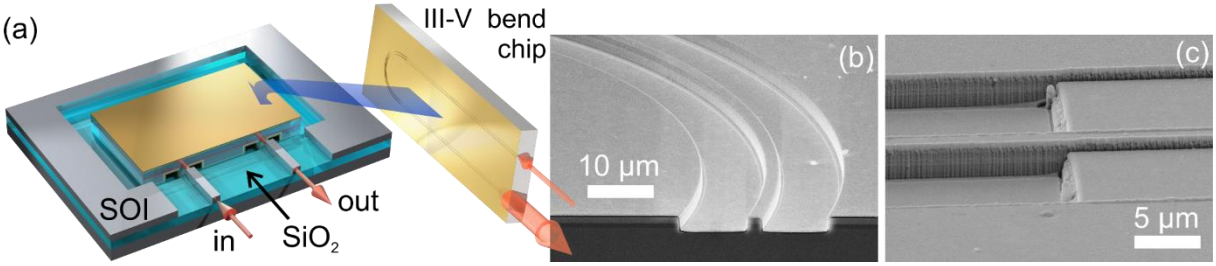


Figure 1. (a) Integration of III-V semiconductor chip with U-bend geometry on silicon-on-insulator (SOI) chip. The I/O ports are on the same side of the chip thus alleviating the requirement for precise dimension control of the chip. (b) Scanning electron microscope (SEM) image of the bend. (c) SEM image of the step between the bent and straight RWG.

one facet needs to be accurately positioned. The U-bend shape is based on Euler spiral design to ensure compact bends with minimized losses [3], [4]. The key features of the design, fabrication and characterization of the U-bend waveguide gain devices and the effect the design has on the yield of the usable devices are discussed.

2. DEVICE DESIGN AND FABRICATION

The Euler bend design has been previously used for Si waveguides to reduce bend losses and has been refined here for use with GaAs-based gain material system. The U-bend consists of two mirror symmetric arcs with a radius of curvature that decreases with increasing arc length with the effective bend radius 1.38 times the minimum bending radius [3]. The minimum bending radius was chosen based on a simulation of the mode propagation through the bend. The simulation used a full-vectorial mode-expansion and tilted overlap integrals resulting in a very efficient three dimensional model [4] and was applied for radii between 1 µm and 200 µm with ridge waveguide (RWG) width varying between 1.0 µm and 2.5 µm. Based on this we chose for testing a 2.5 µm wide ridge with minimum bending radii of 83 µm, 103 µm and 133 µm. The bend area was etched deep through the quantum well structure to ensure lateral mode confinement while the straight sections were etched only until the surface of the topmost cladding layer.

The design was implemented for gain devices operating at 1300 nm wavelength on GaAs with a double quantum well InGaAsN structure, which was placed within 320 nm GaAs waveguide layers itself surrounded by 1 µm $Al_{0.6}Ga_{0.4}As$ cladding layers [5]. The waveguide was defined using two photolithography and dry etch steps, and SiN_x to provide high index difference for improved mode confinement. After this, on the p-side the contact metal layer was deposited followed by a thinning of the wafer to a thickness of 110 µm. Finally, a contact metal layer was deposited on the n-side followed by annealing and cleaving into chips. Although these devices are designed to be used as SOA, for the characterization of the material properties and bend losses the facets of the devices were left uncoated, exhibiting approximately 28% back-reflection to allow laser operation. Typically, our TW-SOA is designed for as small as possible feedback from the facet using proper facet coating and a tilt between WG and facet with approx. 7° angle.

3. CHARACTERIZATION

For the characterization, we used a set of U-bend chips and for a reference a set of RWG chips. The U-bend chips had varying lengths of straight segment of 700 µm, 1700 µm and 3040 µm with varying bend lengths of 519 µm, 645 µm and 843 µm for each straight segment variant. The straight RWG chips had cavity lengths of 800 µm, 1000 µm, 2000 µm and 3000 µm. The devices were operated as laser diodes (LD) at 20°C, in continuous wave mode with bias of 0-200 mA.

The bend loss analysis is based on the derivation of the treatment of Fabry-Perot LDs described by Coldren [6] and is discussed more in depth in [7]. In addition to the standard loss terms: mirror losses α_m and internal losses α_i, we include into the treatment coupling losses α_c from the mode transition from straight RWG into the bend section and the bend losses α_b. As the condition for the device to operate as a LD the losses must equal the threshold modal gain $\Gamma g_{th} = \alpha_i + \alpha_m + \alpha_b + \alpha_c$. By substituting this into the original derivation, we reach an equation

$$\alpha_b = (k_b - k_s)\eta_i ln\left(\frac{1}{R}\right) - \alpha_c \quad (1)$$

where η_i is internal quantum efficiency, R reflectivity and k_b and k_s are the slopes presented in Fig. 2 (a) for bend and straight RWG devices respectively. This derivation assumes the gain equal through the entire bend device. In Fig. 2 (a), the inverse of the differential quantum efficiency η_i is plotted as a function of the cavity length for all measured devices. Here we assume the loss to be the same for all the tested bends as there is no difference between

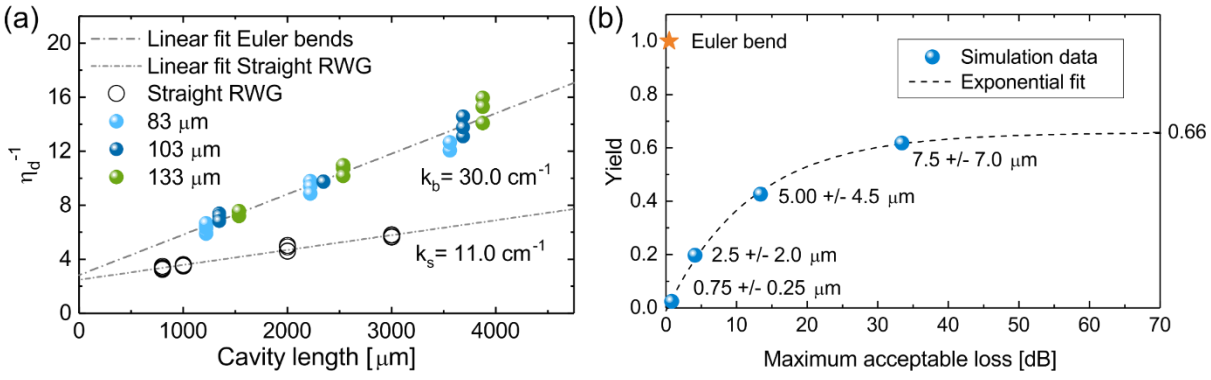


Figure 2. (a) Inverse of the differential quantum efficiency plotted as a function of cavity length for U-bend and straight waveguide devices. (b) The yield of the traditional straight waveguides tilted 7° as a function of the simulated coupling loss.

the slopes between different bends. This assumedly means that the bend radius can still be further decreased without additional losses.

The coupling loss α_c was estimated by using simulation with Eigen Mode Expansion (EME) for the reflectance and transmittance at the step interface. The reflectance was estimated to be 3×10^{-4} and coupling efficiency 89.9% leading to a loss of 0.46 dB. From Fig. 2 (a) we get the values k_b=30.0 cm^{-1} and k_s=11.0 cm^{-1}. With equation (1) we can calculate the total bend loss for the devices to be 9.2 cm^{-1}. For a bend device with 83 µm minimum bending radius and bend length 519 µm the single-pass bend loss is 1.1 dB.

To estimate the impact of the Euler bend design on the integration losses and the yield the coupling loss between 7° tilted SOA chip and 7.257° tilted, 3 µm thick and 4 µm wide SOI waveguides was simulated using Finite-Difference Time-Domain (FDTD) method. As a result, for a coupling with air gap of 0.5 µm reserved for alignment error with the Euler bend chip, the loss was estimated to be 0.3 dB. Simulations were also made for cases with air gaps with certain uncertainties allowed for traditional chips: 0.75 ± 0.25 µm, 2.50 ± 2.00 µm, 5.00 ± 4.50 µm and 7.50 ± 7.00 µm. Resulting maximum losses for each case were respectively: 0.8 dB, 4.1 dB, 13.4 dB and 33.4 dB.

Experiments have shown that the traditional scribe and cleave method provides devices with device length standard deviation of 8.0 µm. We calculated the probability of obtaining devices within the afore mentioned limits by assuming normal distribution and standard deviation of 8.0 µm. These probabilities were then plotted as a function of the calculated maximum losses. The plots presented in Fig. 2 (b) can be fitted with an exponential curve from which we can estimate that maximum achievable yield to be 66%.The yield of the Euler bend devices suitable for integration in regards to their dimensions should essentially reach 100%. This does not take into account any other failure mechanisms, but merely commenting on the need for dimension control of the chips.

4. CONCLUSIONS

We have presented a U-bend design using Euler-bend shape to bring I/O ports of gain waveguides on one facet and reduce coupling losses between III/V gain chips and SOI waveguides when utilizing hybrid integration. The discussion introduced the design, manufacturing and bend loss analysis. Simulation of the coupling losses and an analysis on the improvement in yield when compared to traditional gain chips is discussed.

As an example, we can see that if the maximum acceptable loss is 5 dB, the resulting yield is 22%. In comparison, if we use the Euler bend design, by default the yield approaches 100% with the expected loss of 0.3 dB. Taking into account the penalty of 1.1 dB from the bend losses for 83 µm minimum bending radius the total reduction in losses would be 3.6 dB with a yield 4.5 times larger when using the Euler bend design instead of the traditionally cleaved straight waveguide chips.

ACKNOWLEDGEMENTS

We wish to thank Dr Heikki Virtanen for his help for providing the design for the rib waveguide section. Funding for the RAPIDO project, received under EU FP7-ICT-2013-11, grant agreement no.619806, is gratefully acknowledged.

REFERENCES

[1] Z. Zhou, B. Yin, and J. Michel: “On-chip light sources for silicon photonics,” *Light Sci. Appl.*, vol. 4, no. 11, p. e358, Nov. 2015.

[2] T. Aalto, *et al.*: “GaAs-SOI integration as a path to low-cost optical interconnects,” 2011, vol. 7941, p. 79410S.

[3] M. Cherchi, *et al.*: “Dramatic size reduction of waveguide bends on a micron-scale silicon photonic platform,” *Opt. Express*, vol. 21, no. 15, p. 17814, Jul. 2013.

[4] M. Cherchi, *et al.*: “The Euler bend: paving the way for high-density integration on micron-scale semiconductor platforms,” *SPIE Photonics West 2014-OPTO Optoelectron. Devices Mater.*, vol. 8990, 2014.

[5] D. Fitsios, *et al.*: “High-gain 1.3 µm GaInNAs semiconductor optical amplifier with enhanced temperature stability for all-optical signal processing at 10 Gb/s,” *Appl. Opt.*, vol. 54, no. 1, pp. 46–52, 2015.

[6] L. A. Coldren, S. W. Corzine, and M. Mashanovitch: *Diode lasers and photonic integrated circuits*. Wiley, 2012.

[7] H. Tuorila, *et al.*: “Low loss GaInNAs/GaAs gain waveguides with U-bend geometry for single-facet coupling in hybrid photonic integration,” *Appl. Phys. Lett.*, vol. 113, no. 4, p. 041104, Jul. 2018.

Building blocks for mid-IR programmable light source based on GaSb-based amplified spontaneous emission sources and µm-scale Silicon-on-Insulator waveguide photonics

Jukka Viheriälä[1], Matteo Cherchi[2], Heidi Tuorila[3], Nouman Zia[3], Eero Koivusalo[3], Samu-Pekka Ojanen[3], Pentti Karioja[2] and Mircea Guina[3]

[1] Faculty of Natural Sciences and Engineering, Tampere University, 33720 Tampere, Finland

[2] VTT Technical Research Centre of Finland Ltd, Finland

[3] Optoelectronics Research Center, Physics Unit, Tampere University, 33720 Tampere, Finland

e-mail:jukka.viheriala@tuni.fi

ABSTRACT

Industrial and environmental sensing applications require compact, robust and cost effective mid-IR light sources for multiline spectroscopy. An essential feature of such source is the ability to generate multiple-emission lines on demand, i.e. in a programmable fashion. Building blocks for an integrated programmable light sources operating 2 to 3 µm wavelength band are presented. Our approach is based on µm-scale Silicon-on-Insulator technology and GaSb-based quantum well broadband emitter demonstrates. In particular, we focus on presenting state-of-the-art developments of amplified spontaneous emission sources emitting within 2 µm to 2.65 µm quantum-wells and present their application as semiconductor optical amplifiers. Progress towards emission at 3 µm using GaInAsSb/AlGa(In)AsSb quantum wells in single-transvers-mode superluminescent LEDs is also discussed. Moreover, performance merits for various circuit elements prepared using micron-scale Silicon-on-insulator technology are described; these include waveguides with low propagation and bend losses and echelle gratings for wavelength selection.

Keywords: Silicon Photonics, mid-IR, superluminescent diodes, semiconductor optical amplifiers, GaSb-laser, spectroscopy

1. INTRODUCTION

The wavelength region 2–3 µm is well known for its use in the spectroscopic sensing due to the strong molecular absorption of some important gases, such as CO [1] , CO_2 [2], NH_3 [3], N_2O [4], and it is also relevant for detection of complex molecules from liquids [5]. More and more spectroscopic applications are realized with multi-line methods combined with artificial intelligence to allow better discrimination between complex mixtures of species [5]; this calls for development of light source with capability to switch its emission to match different emission lines. From application perspective, increasing environmental awareness, and new applications for example related to food safety, creates a demand for affordable and compact spectroscopic measurements systems with increased functionality, making mid-IR (laser) market one of the fastest growing sectors in photonics [6].

Here we present a toolkit to build miniaturized light sources based on hybrid integration of III-V light sources on silicon photonic circuits, exploiting their complementarity. The silicon photonics platform is based on micron-scale Silicon-on-Insulator (SOI) technology utilizing large core 3 µm thick waveguides with low propagation and bending loss ensuring also very good mode matching between SOI-waveguides and III-V waveguides. Light sources and amplifiers are produced using molecular beam epitaxy (MBE) for fabrication of GaInAsSb/AlGa(In)AsSb – quantum wells, ensuring emission in the 2–3 µm band**.** In particular, we present state-of-the-art mid-IR superluminescent diodes (SLEDs) and low loss waveguide technology. These building blocks are discussed in a context of programmable light source, where silicon photonic filters select specific lines from the wide emission spectrum provided by SLEDs. Nevertheless, similar building blocks could as well be used to build smart laser sources through suitable feedback configurations.

2. High power superluminescent diodes for 1.9 µm to 2.65 µm wavelength band

The SLED-architecture is based on single mode ridge waveguide technology utilizing tailored gain provided by GaInAsSb QWs placed within AlGa(In)AsSb waveguide and barrier layers. Further details of fabrication are given in references [7], [8]. This material system can be used to provide broad range of wavelength by tailoring compositions of QWs and barriers to obtain favourable QW confinement and strain profile. For longer wavelengths both Auger recombination and carrier leakage from QW increase limiting achievable output power of the source. These mechanisms can, to some extent, be countered by chip design utilizing double pass gain scheme or by driving conditions [8] of SLED allowing to achieve milliwatt-level amplified spontaneous emission sources up to

2.7–2.8 μm wavelength. Table 1 summarizes the features we have demonstrated for SLEDs, demonstrating state-of-the-art power and spectral density. In particular, we would like to point out the recent double pass SLED chip design which enabled to double the output power to beyond 100 mW level, and is as well applicable to be used as reflective semiconductor amplifier, for example to build integrated mid-IR tuneable lasers using micron-scale SOI-waveguide technology.

TABLE 1. OVERVIEW OF SELECTED SLED DESIGNS TESTED AT ROOM TEMPERATURE.

Wavelength	**Average power**	**Spectral width**	**Double pass gain**	**Notes**
1950 nm	*60 mW / CW*	60 nm	No	Details [7]
2000 nm	*120 mW /CW*	40 nm	Yes	Not published.
2550 nm	3.3 mW / QCW	120 nm	No	QCW driving optimized see details in [8]
2600 nm	*7.5 mW / QCW*	33 nm	Yes	Not published.
2650 nm	*1.5 mW / QCW*	200 nm	No	Not published.
3000 nm	*N.A.*	500 nm	No	Multimode waveguide

3. Building blocks for mid-IR silicon photonics with μm-scale Silicon-on-Insulator technology

In this part we focus on presenting the features of some basic building blocks of the SOI platform: waveguide propagation losses, bend losses, and performance of echelle grating used to filter desired wavelengths. For the measurements, we have used two different light sources: 1) a commercial supercontinuum source (from LEUKOS, France) operating in the 1100–3600 nm range, and combined with a band pass filter and a polarizer to select TE-polarization only; 2) a distributed feedback (DFB) laser, with nominal operation at 2646 nm wavelength and output power of 6.7 mW. With both sources the light was coupled into polarization maintaining fibre (PMF) that was then butt-coupled to the silicon chip. The signal was gathered from the opposite side of the chip with a single-mode fiber (SMF).

The propagation losses were measured using the DFB laser and waveguides of different lengths. The waveguides had a 1.875 μm wide spiral strip geometry as depicted in Figure 1 (a). The lengths of the waveguides were 1.7 cm, 8.3 cm, 14.9 cm, and 21.5 cm with spirals with identical number of bends. The measurements resulted in propagation losses of 0.54 dB/cm at 2.65 μm wavelength range, in agreement with previously reported results at 3.4 μm wavelength [9].

The bend losses were analysed with cascades of several different bend types: 1) 3 rib waveguide S-bends, with 5 mm radius arc sections 2) 34 Euler S-bends of a 1.875 μm wide strip waveguide 3) 172 L-bends of a 1.5 μm wide strip waveguide with 12.5 μm minimum bending radius 4)120 L-bends of a 1.875 μm wide strip waveguide with 18 μm minimum bending radius 5) 72 L-bends of a 1.875 μm wide strip waveguide with 29 μm minimum bending radius 6) 52 L-bends of a 1.875 μm wide strip waveguide with 41.5 μm minimum bending radius. The waveguides are depicted in Figure 1 (b). The bend losses were compared to a straight rib reference waveguide and the resulting values for different waveguide geometries are: 1) 0.24 dB/bend, 2) 0.019 dB/bend, 3) 0.042 dB/bend, 4) 0.015 dB/bend, 5) 0.016 dB/bend, and 6) 0.021 dB/bend.

The filter based on echelle grating diffracting light into four different channels was characterized using the supercontinuum source with TE-polarization. Figure 1 (c) displays part of the grating and the separate channels. The spectrum from each channel was measured using a monochromator and the output wavelengths for each channel were: 1) 2645.0 nm, 2) 2647.8 nm, 3) 2680.2 nm, and 4) 2697.4 nm. Due to limited resolution the monochromator offers the linewidth for the channel 1 was estimated using the DFB laser. The laser wavelength was tuned with input current from 2644.6 nm to 2646.5 nm and the output power through the filter channel 1 was measured as a function of the wavelength. From this we could estimate the linewidth to 1.1 nm.

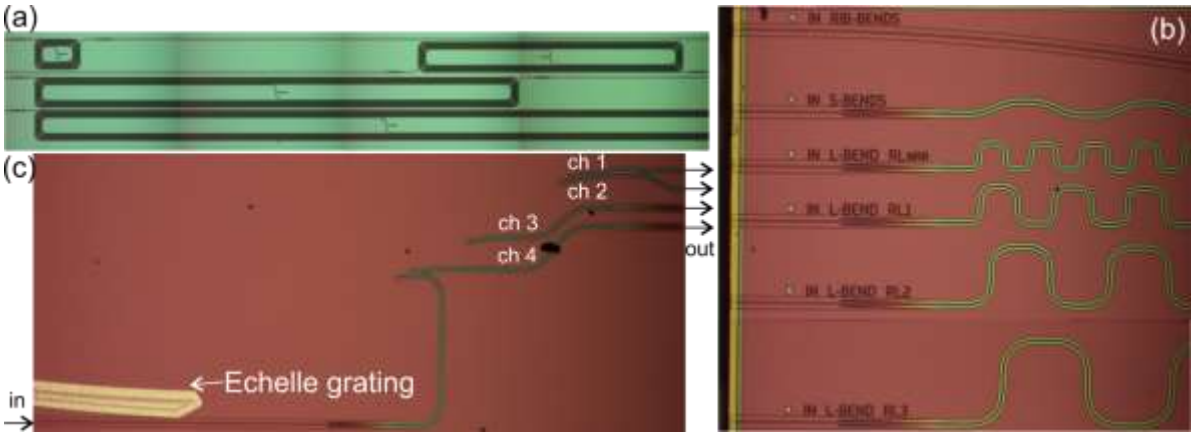


Figure 1. (a) Spiral waveguides with different lengths for propagation loss analysis with cut-back method. (b) Bend waveguides with different bend geometries. (c) Echelle grating filter with four different output wavelengths.

4. CONCLUSIONS

State-of-the-art developments of the key blocks forming a platform for programmable broadband silicon photonics integrated mid-IR light sources are presented. The specific features we demonstrate are:

- Lowest loss silicon photonics waveguides beyond 2 µm, i.e. propagation loss as low as 0.54 dB/cm and very low loss and compact bends;
- Capability to filter, multiplex and de-multiplex light with an echelle grating;
- Gain chips allowing amplified spontaneous emission generation at state-of-the-art spectral density or to be used as reflective semiconductor optical amplifiers;
- Highest power GaSb-based SLEDs, delivering 120 mW at 2 µm.

ACKNOWLEDGEMENTS

We acknowledge financial support provided by as part of EU H2020 MIREGAS project and Business Finland project RAPSI (decision no. 1613/31/2018).

REFERENCES

[1] X. Chao, J. B. Jeffries, and R. K. Hanson, "Absorption sensor for CO in combustion gases using 2.3 µm tunable diode lasers," *Meas. Sci. Technol.*, vol. 20, no. 11, p. 115201, 2009.

[2] P. Werle, F. Slemr, K. Maurer, R. Kormann, R. Mücke, and B. Jänker, "Near- and mid-infrared laser-optical sensors for gas analysis," *Opt. Lasers Eng.*, vol. 37, no. 2, pp. 101–114, Feb. 2002.

[3] M. Webber, R. Claps, F. V. Englich, F. Tittel, J. B. Jeffries, and R. K. Hanson, "Measurements of NH 3 and CO 2 with Distributed-Feedback Diode Lasers Near 2.0 m in Bioreactor Vent Gases," *Appl. Opt. - APPL OPT*, vol. 40, pp. 4395–4403, Aug. 2001.

[4] H. Herbin, N. Picqué, G. Guelachvili, E. Sorokin, and I. T. Sorokina, "N2O weak lines observed between 3900 and 4050 cm−1 from long path absorption spectra," *J. Mol. Spectrosc.*, vol. 238, no. 2, pp. 256–259, Aug. 2006.

[5] R. M. Balabin and S. V. Smirnov, "Melamine detection by mid- and near-infrared (MIR/NIR) spectroscopy: A quick and sensitive method for dairy products analysis including liquid milk, infant formula, and milk powder," *Talanta*, vol. 85, no. 1, pp. 562–568, Jul. 2011.

[6] "Mid-ir lasers growing four times faster than total laser market, according to Strategies Unlimited." [Online]. Available: https://www.strategies-u.com/articles/press-releases/mid-ir-lasers-growing-four-times-faster-than-total-laser-market-according-to-strategies-unlimited.html. [Accessed: 15-Jan-2019].

[7] N. Zia, J. Viheriälä, R. Koskinen, A. Aho, S. Suomalainen, and M. Guina, "High power (60 mW) GaSb-based 1.9 µm superluminescent diode with cavity suppression element," *Appl. Phys. Lett.*, vol. 109, no. 23, p. 231102, Dec. 2016.

[8] N. Zia *et al.*, "GaSb superluminescent diodes with broadband emission at 2.55 µm," *Appl. Phys. Lett.*, vol. 112, no. 5, p. 051106, Jan. 2018.

[9] G. Z. Mashanovich *et al.*, "Low loss silicon waveguides for the mid-infrared," *Opt. Express*, vol. 19, no. 8, pp. 7112–7119, Apr. 2011.

The Feasibility of Building 1024 & 4096-port Nanosecond Switching for Data Centre Networks Using Dilated Hybrid Optical Switches

Junfei Xia, Minsheng Ding, Adrian Wonfor, Richard V. Penty, Ian H. White
Centre for Photonic Systems, Electrical Engineering Division, Department of Engineering,
University of Cambridge, 9 JJ Thomson Avenue, Cambridge CB3 0FA, UK.
e-mail: jx248@cam.ac.uk

ABSTRACT

We propose a new 16x16 butterfly dilated hybrid switch. Recursive dilated Beneš and Clos-4-Beneš architectures based on this achieve a 4dB power penalty floor reduction in a 1024-port switch over existing hybrid schemes. A 4096 port switch is proposed with a 12dB input power dynamic range of a penalty less than 3dB.

Keywords: Integrated optical devices; optical switching; data centre.

1. INTRODUCTION

Modern data centres are pivotal enablers for data storage/data interaction, data processing and cloud computing applications. These services critically require both highly scalable and low latency intra-data centre communications [1]. Every 12-15 months, the data traffic in data centres is doubling [2] and hence conventional electronic top-of-rack (ToR) packet switches face a challenge in terms of the requirement of increasing port count. Data centres currently deploy a folded-Clos "Fat-Tree" network topology which requires increasing numbers of tiers, hence more O-E-O stages, and higher cost, as the number of interconnections is scaled up. A high-port-count optical switch therefore becomes an attractive candidate to address this challenge since it can flatten the switching network topology [3].

For future data centre applications, optical switches should have the following features: large port scalability, short reconfiguration time, low power consumption, low crosstalk and low loss. Recently, optical switches based on microelectromechanical systems (MEMs) have been reported to achieve a high-radix (1000+ ports) and less than 4dB optical loss [4]. Silica-based thermo-optic Mach-Zehnder Interferometers (MZIs) switches have been manufactured with 32x32 port counts [5]. However, these switches have a reconfiguration time in the range of milliseconds to microseconds. Although Si photonic switches have been demonstrated with nanosecond switching timescales [6], their inherent optical loss does not allow scaling to large port counts as no gain mechanism is available for loss compensation. Alternatively Indium Phosphide based active optical components such as electro-optic MZIs and Semiconductor Optical Amplifiers (SOAs) can reconfigure signals on nanosecond timescales and can compensate for the loss from the passive elements. A 2x2 port dilated hybrid MZI-SOA switch element has been previously designed and experimentally demonstrated. This is lossless, has low crosstalk [7] and can function as a key building block for large radix switches. In addition, a cascaded 16x16 hybrid switch has been emulated with -35dB crosstalk and 15dB Input power dynamic range (IPDR) at a power penalty less than 1dB [8].

In this paper, we review the design of a 2x2 dilated hybrid switching element. We propose a 16x16 monolithic hierarchical integrated hybrid building block to enable scaling of port count. The switching performance is assessed by simulation and compared with previous 16x16 hybrid switch designs in terms of both energy consumption and power penalty. Based on this switching block, two different 1024 cascaded switch fabric designs based on existing hybrid switching blocks are described and the switching performance is reported. Finally, quantitative assessment shows that this design can achieve up to 4096 port counts with 2.3dB power penalty without the need for forward error correction (FEC).

2. CHARACTERISATION OF A 16x16 4-ARY 4-FLY BUTTERFLY DILATED HYBRID SWITCH

Previously, we have demonstrated a 4x4 dilated Beneš switch composed of four 2x2 dilated Beneš switches which exhibit crosstalk of -47dB and an IPDR of 13dB for a penalty less than 0.05dB.[8,9] In this work, a 4-ary 4-fly dilated butterfly is proposed to improve the dynamic switching performance compared with the cascaded 16x16 dilated Beneš. As shown in Fig 1a, a fundamental 2x2 dilated block is built with four MZI elements and eight SOAs. The combination of MZI and SOA avoids the split loss inherent in the SOA-based broadcast-and-select switches and mitigates the unwanted crosstalk of MZI-based switches. A dilated Beneš architecture is also implemented to reduce the crosstalk further. Fig 1b shows the conventional multistage switch formed by cascading 2x2 dilated hybrid switches. 2.55dB average loss is introduced from the waveguide crossings and thus 7.65dB of total shuffle network loss needs to be compensated to achieve a lossless switching operation.

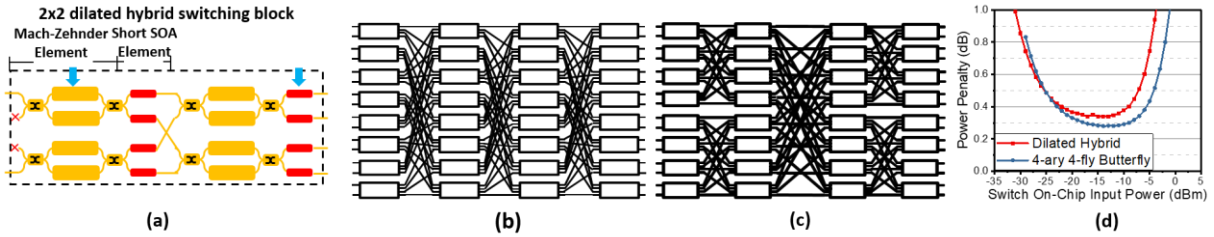


Figure 1. (a) Layout of a 2x2 dilated Beneš hybrid switch (b)Schematic of 16x16 dilated Beneš hybrid building block (c)Schematic of 16x16 4-ary 4-fly dilated Butterfly hybrid build block (d) Power penalty at a BER of 10^{-9} as a function of switch on-chip input power

Fig 1c shows a 16x16 butterfly switching block consisting of four 8x8 dilated hybrid building blocks. For a single route from an input to an output, the loss of the butterfly topology is 2.5dB lower than that of the dilated Beneš. The performance of two 16x16 monolithic hybrid switches has been simulatedand compared using the commercial VPI simulator with parameters fitted from previous data. An optical signal at 1553.6nm is modulated with a 10Gb/s NRZ 2^{31}-1 PRBS. Fig 1d depicts the power penalties at a bit error rate (BER) of 10^{-9} versus switch input power between two hybrid switches. 18dB IPDR with a penalty less than 0.5dB is realised for the dilated hybrid switch while 21dB IDPR is achieved by the 16x16 4-ary 4-fly butterfly topology. The dilated butterfly structure also exhibits a 0.3dB power penalty floor.

3. IMPROVED 1024 PORTS HYBRID SWITCHING ARCHITECTURE ASSESSMENT

High port count hybrid switches have been reported with a Clos-Beneš architecture using fibres to connect sub-switches. [10] However, only if hard-decision FEC at BER of 10^{-5} or soft-decision FEC at BER of 10^{-3} is allowed, can 1024 ports be achieved with a penalty floor of 1.75dB or 1dB, respectively [11].

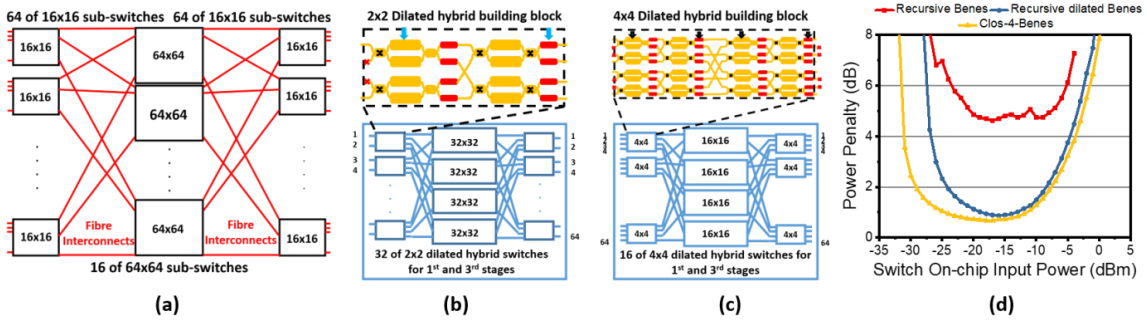


Figure 2. (a)Schematic of 1024-port Clos-16-Beneš hybrid switch (b) Schematic of 64-port recursive dilated Beneš hybrid sub-switch (c) Schematic of 64-port Clos-4-Beneš hybrid sub-switch (d)Power penalty at 10^{-9} BER versus switch on-chip input power for 1024-port hybrid switches using 3 types of 64-port sub-switches

This proposed design reduces the shuffle network loss but increases the MZI-induced crosstalk, and therefore the crosstalk from every MZI on the path accumulates, degrading the expected signal. In this work, we retain the Clos-fibre- Beneš architecture but use a dilated sub-fabric for the switches used in all Clos-based three stages to suppress the crosstalk. As shown in Fig 2a, a 1024-port hybrid switch contains sixty-four 16x16 sub-switches used for the first and last stages, sixteen 64x64 sub-switches deployed for the middle stage. Fig 2b indicates the schematic of 64x64 sub-switch based on the recursive dilated Beneš architecture. By implementing the existing 2x2 dilated hybrid building block, a recursive dilated Beneš architecture can decrease the crosstalk induced by a single MZI from -20dB to -35dB [12,13]. Fig 2c shows the other 64x64 hybrid building block based on a Clos-4-Beneš architecture. This design is based on cascaded 4x4 integrated dilated hybrid building blocks and a 16x16 4-ary 4-fly butterfly architecture. Power penalties of 3 different 1024-port switching fabrics are depicted in Fig 2d at a BER of 10^{-9}. A 5dB penalty floor is achieved in the 1024-port hybrid switch using 64 Beneš sub-switches in the middle stage. The proposed 1024-port switches using the recursive dilated Beneš structure and Clos-4-Beneš architecture exhibit 15dB IPDR and 21dB IPDR with a penalty less than 2dB. The penalty floor of the 1024-port switch using recursive dilated fabric for the middle stage is 0.9dB, and the switch based on Clos-4-Beneš 64-port sub-switches has a penalty as low as 0.7dB.

4. 16x16 HYBRID SWITCHING ELEMENT FOR FURTHER SCALABILITY FEASIBILITY

The 16x16 4-ary 4-fly Butterfly dilated hybrid switch proposed in this paper has been optimised and investigated according to the experimentally derived parameters of components integrated on a typical chip. Larger scale optical switches can be realised by connecting 16x16 dilated building blocks as switching elements using a recursive Clos architecture. For example, a 256-port hybrid switch based on a Clos architecture can be achieved

as shown Fig 3a, where 16x16 integrated hybrid switches are utilised as switching elements in our proposed structure.

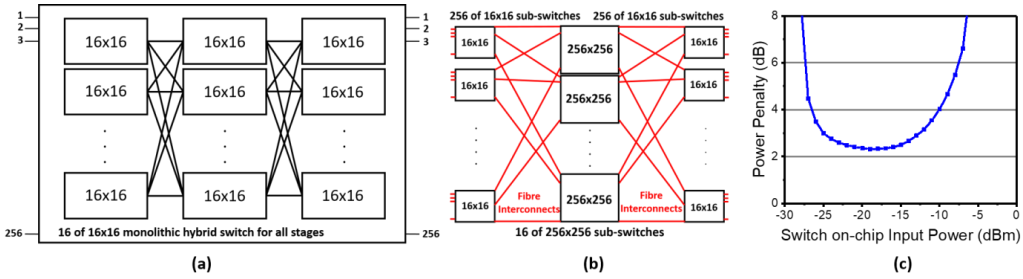


Figure 3. (a) Schematic of 256-port Clos hybrid switch (b) Schematic of 4096-port hybrid switch (c) Power penalty at 10^{-9} BER as a function of switch on-chip input power for 4096-port recursive Clos hybrid switch

Using this approach a 4096-port hybrid switch can be constructed by using a similar 3-stage Clos topology with 16x16, 256x256 and 16x16 sub-switches (Fig.4b). Without the need for FEC, as shown in Fig 3c, a 2.3dB penalty (at 10^{-9} BER) is achieved for the 4096-port with sub-switches using 16x16 and recursive 256x256 ports. A 12dB IPDR with a penalty less than 3dB can be achieved.

5. CONCLUSION

This paper describes recent research on hybrid MZI-SOA switch architectures. A 4-ary 4-fly dilated butterfly switching architecture is proposed and compared with a dilated Beneš fabric, and exhibits a 2.5dB lower shuffle loss and a 3dB wider IDPR. Based on existing 2x2, 4x4 and proposed 16x16 switches, two 1024-port switches using two alternative 64x64 sub-switches can be achieved with 15dB and 21dB IPDR of 2dB penalty respectively. 4dB lower penalty is achieved in 1024-port switches compared with switch using recursive Beneš architecture. Additionally, this paper for the first time assesses the feasibility of 4096-port hybrid switches using 16x16, 256x256, 16x16 sub-switches. The estimated 12dB IPDR for a penalty less than 3dB demonstrates that the hybrid switch can be scaled up to very high port count and therefore has great potential for future data centre networks.

ACKNOWLEDGEMENTS

The author would like to acknowledge funding from Cambridge Trust Scholarship and Eric Lowe for fruitful discussion.

REFERENCES

[1] Funnell, *et al.*: Hybrid Wavelength Switched-TDMA High Port Count All-Optical Data Centre Switch, *J. Lightwave Technol.*, vol.35.pp 4438-4444, 2017

[2] Singh, Arjun, *et al.*: Jupiter rising: A decade of Clos topologies and centralized control in Google's Data-center network, *ACM SIGCOMM Computer Communication Review.* Vol. 45. No. 4. ACM, 2015.

[3] Mellette, et al.: A scalable, partially configurable optical switch for data center networks, *J. Lightwave Technol.*, vol.35.pp 136-144, 2017

[4] Kim, J., *et al.*: 1100 x 1100 port MEMS-based optical crossconnect with 4-dB maximum loss, *IEEE Photonics Technology Letters.*, vol.15.pp 1537-1539, 2003

[5] Tanizawa, Ken, *et al.*: Ultra-compact 32× 32 strictly-non-blocking Si-wire optical switch with fan-out LGA interposer, *Optics express.*, vol.23.pp 17599-17606, 2015

[6] Dupuis, Nicolas, *et al.*: Design and Fabrication of Low-Insertion-Loss and Low-Crosstalk Broadband 2x2 Mach–Zehnder Silicon Photonic Switches, *J. Lightwave Technol.*, vol.33.pp 3597-3606, 2015

[7] Cheng, Qixiang, *et al.*: Scalable, low-energy hybrid photonic space switch, *J. Lightwave Technol*, vol.31.pp 3077-3084, 2013

[8] Ding, Minsheng, *et al.*: Hybrid MZI-SOA InGaAs/InP photonic integrated switches." *IEEE Journal of Selected Topics in Quantum Electronics* vol.24.pp 1-8, 2018

[9] Cheng, Qixiang, *et al.*: Low-energy, scalable hybrid crosspoint switch design, *CLEO: Science and Innovations. OSA*, 2013.

[10] White, Ian, *et al.*: High Port Court Switch Architectures for Data Center Applications, *Photonic Networks and Devices. OSA*, 2017.

[11] Ding, M., *et al.:* Scalable, low-power-penalty nanosecond reconfigurable hybrid optical switches for data centre networks, *CLEO: Applications and Technology. OSA*, 2017.

[12] Dorren, B. H. P., *et al.*: A chopped quantum-well polarization-independent interferometric switch at 1.53µm, *IEEE journal of quantum electronics* vol.36.pp 317-324, 2000

[13] Maat, D. H. P., *et al.*: Polarization-independent dilated InP-based space switch with low crosstalk, *IEEE Photonics Technology Letters* vol.12.pp 284-286, 2000

Inverse-designed low-loss and wideband polarization-insensitive waveguide crossing

Student Paper

Zejie Yu,[1,2] Aosong Feng,[1,2] Xiang Xi,[1] and Xiankai Sun[1,*]

[1]Department of Electronic Engineering, The Chinese University of Hong Kong, Shatin, New Territories, Hong Kong

[2]These authors contributed equally to this work

[*]*e-mail: xksun@cuhk.edu.hk*

ABSTRACT

Polarization-insensitive waveguide crossings are desired because photonic networks usually involve light with different polarizations. Here, we propose a polarization-insensitive waveguide crossing on a 250-nm silicon-on-insulator platform by using an inverse-design method. In simulation, the designed waveguide crossing can maintain insertion loss below 0.18 (0.25) dB in the wavelength range of 1440–1640 nm for the TE_0 (TM_0) mode and achieve the minimal insertion loss as small as 0.08 (0.07) dB at the wavelength of 1550 nm. The crosstalk maintains below −32 dB and −35 dB for the TE_0 and TM_0 modes, respectively. Experimentally, the fabricated waveguide crossing achieves measured insertion loss less than 0.20 (0.25) dB for the TE_0 (TM_0) mode with the minimal insertion loss as small as 0.1 dB. The measured crosstalk is below −28 dB and −31 dB for the TE0 and TM0 modes, respectively. Therefore, our proposed waveguide crossing can be widely applied in photonic integrated circuits to construct photonic systems with the capabilities of polarization control and mode (de)multiplexing.

Keywords: optical devices, integrated photonics, silicon photonics.

1. INTRODUCTION

Photonic systems are becoming more and more complicated and the number of devices integrated on a single chip is also increasing exponentially. In a planar photonic circuit, waveguide crossings with negligible influence on the propagating light are indispensable. Many waveguide crossings have already been demonstrated and some of them have shown negligible insertion loss and crosstalk for light with TE polarization [1, 2]. A complex photonic system usually needs to control and process light with different polarizations, so waveguide crossings which can transport light perfectly for different polarizations are highly desired. However, a polarization-insensitive waveguide crossing connecting wire waveguides with compact sizes and negligible insertion loss and crosstalk is yet to be realized. Photonic inverse design is a generic and robust design method which explores the full parameter space of device structures. Devices with complicated functions can be designed by using this method. Numerous devices have been proposed and demonstrated including polarization rotator [3], reflector [4], waveguide bend [5-7], etc.

Here, we propose a low-loss and wideband polarization-insensitive waveguide crossing by using an inverse-design method. The simulated insertion loss and crosstalk maintain less than 0.18 (0.25) dB and −32 (−35) dB in the wavelength range of 1440–1640 nm with the minimal values reaching 0.08 (0.07) dB and –37 (–38) dB, respectively, at the wavelength of 1550 nm for the TE_0 (TM_0) mode. Experimentally, the fabricated waveguide crossing maintains low insertion loss less than 0.20 dB (TE_0 mode) and 0.25 dB (TM_0 mode), and the crosstalk maintains less than −28 dB (TE_0 mode) and −31 dB (TM_0 mode) in the wavelength range of 1440–1640 nm. At the wavelength of 1550 nm, the insertion loss and crosstalk can reach as small as 0.10 (0.10) dB and −35 (−32) dB for the TE_0 (TM_0) mode. Therefore, the inverse-designed and experimentally demonstrated waveguide crossings have great potential as a standard module in the silicon photonic integrated circuitry for constructing high-density photonic integrated networks.

2. DEVICE DESIGN METHOD

The devices were designed on a silicon-on-insulator (SOI) wafer with a 250-nm-thick silicon layer embedded inside silicon oxide. Figure 1(a) shows the conventional waveguide crossing, where the purple and gray regions denote silicon and silicon oxide, respectively. Figure 1(b) is a conceptual illustration of our proposed waveguide crossing. We take the waveguide crossing structure shown in Fig. 1(c) as an example to illustrate the design process. The design optimization region is restricted within a circle of 3 μm radius denoted by the blue line. Four continuous lines are used to delineate the borders of the waveguide crossing, and these lines are fitted from the discrete green dots by the triple spline interpolation. The position of each discrete dot is described by the radial and angular coordinates (r_i and θ_i). Due to the rotational symmetry, we only need to optimize 1/8 of the entire structure as shown in Fig. 1(c). During the optimization, the black dots which are used for connecting the waveguides were fixed. The angular coordinates θ_i of the discrete dots were also fixed. The greedy optimization method was

adopted to determine the radial coordinates r_i of the discrete dots. We first generated a random value for each dot, then optimized them in series. During the serial optimization, we varied the individual r_i and restricted the dot within the blue circle, while fixing all the other dots. The best r_i's were obtained after comparing the structural transmission of all attempted values. After several rounds of r_i optimization from the first dot to the last, the process was stopped when the insertion loss of both the TE_0 and TM_0 modes at 1550 nm could not be reduced in additional optimization runs. Based on the structure obtained from the greedy optimization method, we subsequently adopted a random-walk method to further improve the performance of the waveguide crossing. The radii r_i's of all dots were given a slight random variation. If the resulting insertion loss reduced, the change was accepted; otherwise, the change was discarded. This process was stopped when the insertion loss was below 0.1 dB. After ~48 hours of optimization by using a normal 16-core desktop computer, we obtained the final design of polarization-insensitive waveguide crossing as shown in Fig. 1(c). Figures 1(d) and 1(e) plot the normalized transmission spectra of the optimized and conventional waveguide crossings. The insertion loss of the TE_0 (TM_0) mode can maintain less than 0.18 (0.25) dB in the wavelength range of 1440–1640 nm and reach as small as 0.08 (0.07) dB at the wavelength of 1550 nm. The crosstalk of the optimized waveguide crossing maintains below −32 (−35) dB for the TE_0 (TM_0) mode. By contrast, the minimal insertion loss of the conventional waveguide crossing is higher than 1.35 (0.84) dB, and the crosstalk is higher than −16 (−19) dB for the TE_0 (TM_0) mode in the same wavelength range.

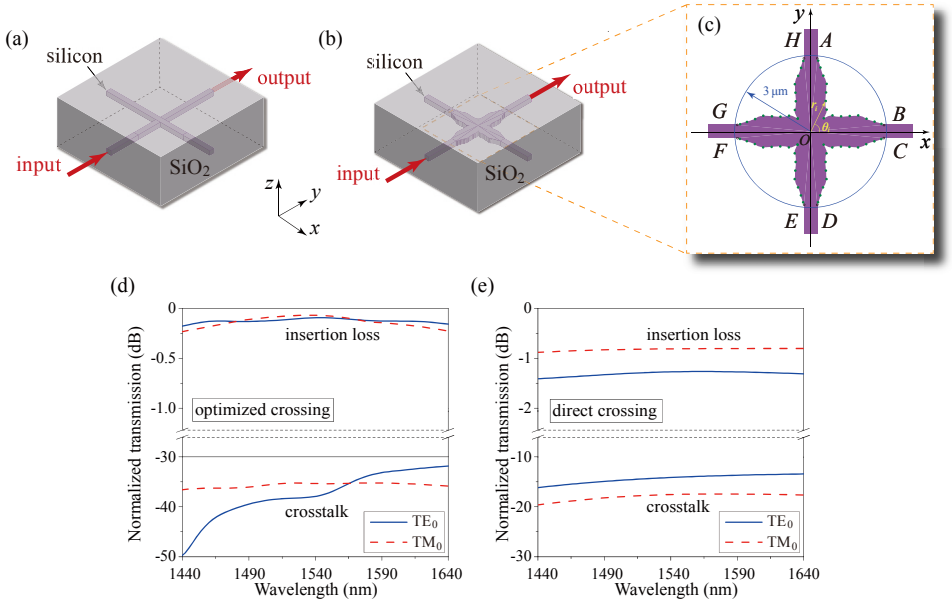


Figure 1. (a) Schematic of the conventional waveguide crossing. The purple and gray regions represent Si and SiO_2, respectively. (b) Schematic of the inverse-designed waveguide crossing. (c) Top view of the inverse-designed waveguide crossing, the borders of which are defined by four continuous lines AB, CD, EF, and GH going through the green dots. (d),(e) Normalized insertion loss and crosstalk spectra of the optimized (d) and conventional (e) waveguide crossing for the TE_0 (blue solid lines) and TM_0 (red dashed lines) modes.

3. EXPERIMENTAL RESULTS

The waveguide crossing devices were fabricated on a SOI wafer with 250-nm Si device layer on 3-μm buried oxide. The device patterns were defined along with the input and output waveguides and grating couplers in a single step of electron-beam lithography with ZEP520A resist. Then, the patterns were transferred to the top silicon layer by inductively coupled plasma reactive-ion etching with SF_6/C_4F_8 gas chemistry. Last, a 2.5-μm-thick silicon oxide layer was deposited on the top as an upper cladding by plasmon-enhanced chemical vapor deposition. Figures 2(a) and 2(e) are the optical microscope images of the fabricated devices for characterizing the insertion loss and crosstalk of the optimized and conventional waveguide crossings, respectively. We adopted on-chip grating couplers to couple light from an optical fiber into and out of the devices, because grating couplers can work not only as power couplers but also as mode selectors to couple light with the desired polarization into and out of the devices. Devices composed of a pair of grating couplers connected by a straight waveguide were used to extract the insertion loss and crosstalk without waveguide crossings. We cascaded multiple optimized waveguide crossings in a single device in order to measure the small insertion loss. Figures 2(b) and 2(f) are the scanning electron microscope (SEM) images which are zoomed in at the optimized and conventional waveguide crossings, respectively.

We characterized the fabricated devices by spectroscopic measurement of their optical transmission. A tunable semiconductor laser was used to measure the wavelength dependence of the waveguide crossings in the wavelength range of 1440–1640 nm. The light was sent over a single-mode fiber with its polarization state adjusted by a fiber polarization controller and then coupled into the device under test via the input grating coupler. A photodetector was used to collect the light coupled out of the output grating coupler. For the TE_0 mode, the normalized transmission spectra measured from the through and cross ports of the optimized and conventional waveguide crossings are plotted in Figs. 2(c) and 2(g), respectively. The measured insertion loss and crosstalk of the optimized waveguide crossing maintain below 0.20 dB and −28 dB in the wavelength range

of 1440–1640 nm. As a comparison, the insertion loss and crosstalk of the conventional waveguide crossing are higher than 1.00 dB and −16 dB in the same wavelength range. For the TM_0 mode, the normalized transmission spectra measured from the through and cross ports of the optimized and conventional waveguide crossings are plotted in Figs. 2(d) and 2(h), respectively. The measured insertion loss and crosstalk of the optimized waveguide crossing maintain below 0.25 dB and −31 dB in the wavelength range of 1440–1640 nm. As a comparison, the insertion loss and crosstalk of the conventional waveguide crossing are higher than 0.65 dB and −25 dB in the same wavelength range. It should be noted that previous demonstrated waveguide crossings were designed for only one polarization and could not achieve low insertion loss for both the TE_0 and TM_0 modes simultaneously [8, 9]. Although some optimized crossings considered both the TE_0 and TM_0 modes, they suffer from larger insertion loss and narrower operating bandwidths [10, 11].

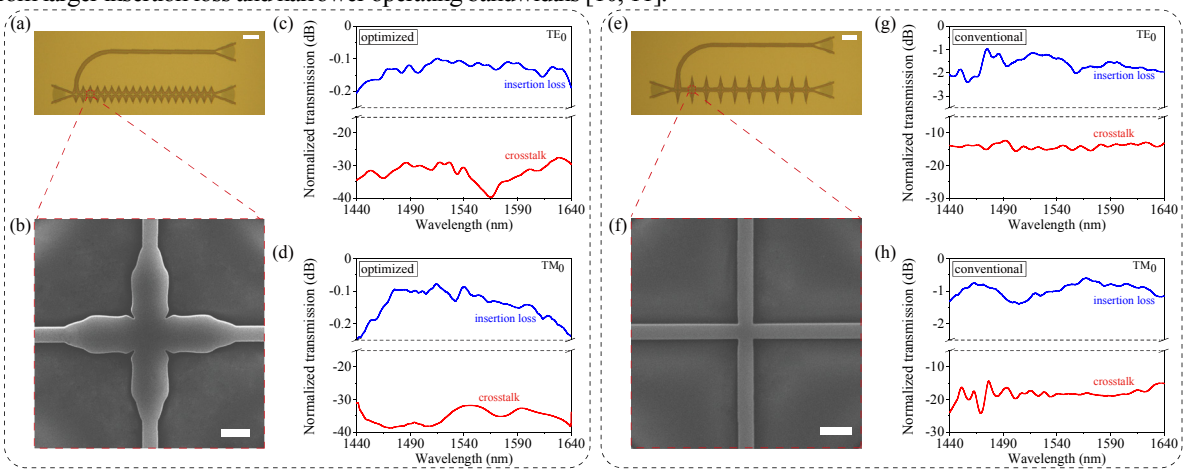


Figure 2. (a),(e) Optical microscope images of the fabricated optimized (a) and conventional (e) waveguide crossing. (b),(f) Scanning electron microscope (SEM) images of the fabricated optimized (b) and conventional (f) waveguide crossing. (c),(g) Experimental insertion loss (blue lines) and crosstalk (red lines) spectra of the optimized (c) and conventional (g) waveguide crossing for the TE_0 mode. (d),(h) Experimental insertion loss (blue lines) and crosstalk (red lines) spectra of the optimized (d) and conventional (h) waveguide crossing for the TM_0 mode. The scale bars represent 20 μm in (a) and (e), and 1 μm in (b) and (f).

ACKNOWLEDGEMENTS

This work was supported by the Early Career Scheme (Project No. 24208915) and the General Research Fund (Project No. 14208717) sponsored by the Research Grants Council of Hong Kong, and by the NSFC/RGC Joint Research Scheme (Project No. N_CUHK415/15) sponsored by the Research Grants Council of Hong Kong and the National Natural Science Foundation of China.

REFERENCES

[1] W. Bogaerts, *et al.*: Low-loss, low-cross-talk crossings for silicon-on-insulator nanophotonic waveguides, *Opt. Lett.*, vol. 32. pp. 2801–2803, Oct. 2007.

[2] Y. Liu, *et al.*: Ultra-low-loss CMOS-compatible waveguide crossing arrays based on multimode Bloch waves and imaginary coupling, *Opt. Lett.*, vol. 39. pp. 335–338, Jan. 2014.

[3] Z. Yu, *et al.*: Genetic-algorithm-optimized wideband on-chip polarization rotator with an ultrasmall footprint, *Opt. Lett.*, vol. 42. pp. 3093–3096, Aug. 2017.

[4] Z. Yu, *et al.*: Genetically optimized on-chip wideband ultracompact reflectors and Fabry-Perot cavities, *Photon. Res.*, vol. 5. pp. B15–B19, Dec. 2017.

[5] B. Shen, *et al.*: Metamaterial-waveguide bends with effective bend radius $<\lambda_0/2$, *Opt. Lett.*, vol. 40. pp. 5750–5753, Dec. 2015.

[6] J. S. Jensen, O. Sigmund: Systematic design of photonic crystal structures using topology optimization: Low-loss waveguide bends, *Appl. Phys. Lett.*, vol. 84. pp. 2022–2024, Mar. 2004.

[7] Z. Yu, *et al.*: Photonic welding points for arbitrary on-chip optical interconnects, *Nanophotonics*, vol. 7. pp. 1679–1686, Sept. 2018.

[8] Y. Ma, *et al.*: Ultralow loss single layer submicron silicon waveguide crossing for SOI optical interconnect, *Opt. Express*, vol. 21. pp. 29374–29382, Nov. 2013.

[9] Y. Liu, *et al.*: Ultra-low-loss CMOS-compatible waveguide crossing arrays based on multimode Bloch waves and imaginary coupling, *Opt. Lett.*, vol. 39. pp. 335–338, Jan. 2014.

[10] P. J. Bock, *et al.*: Subwavelength grating crossings for silicon wire waveguides, *Opt. Express*, vol. 18. pp. 16146–16155, June 2010.

[11] S.-H. Kim, *et al.*: Tilted MMI crossings based on silicon wire waveguide, *Opt. Express*, vol. 22, pp. 2545–2552. Jan. 2014.

Photonic welding points for arbitrary on-chip optical interconnects

Student Paper

Zejie Yu, Yang Ma, and Xiankai Sun*
Department of Electronic Engineering, The Chinese University of Hong Kong, Shatin, New Territories, Hong Kong
e-mail: xksun@cuhk.edu.hk

ABSTRACT

Achieving low-loss waveguide routing with arbitrary configuration is crucial for both classical and quantum photonic applications. To manipulate light flows on a chip, the conventional wisdom relies on waveguide bends of large bending radii and adiabatic mode converters to avoid insertion losses from radiation leakage and modal mismatch, respectively. However, those structures usually occupy large footprints and thus reduce the integration density. To overcome this difficulty, this work presents a fundamentally new approach to turn light flows arbitrarily within an ultracompact footprint. A type of "photonic welding points" joining two waveguides of an arbitrary intersecting angle has been proposed and experimentally demonstrated. These devices with a footprint <4 μm^2 can operate in the telecommunication band over a bandwidth of at least 140 nm with an insertion loss <0.5 dB. Their fabrication is compatible with photonics foundry processes and does not introduce additional steps beyond those needed for the waveguides. Therefore, they are suitable for mass production of PICs and will enhance the integration density to the next level.

Keywords: optical devices, integrated photonics, silicon photonics.

1. INTRODUCTION

Along with the great progress of information technologies, photonic integrated circuits (PICs) are playing crucial roles in computation and communication tasks, and will replace their electronic counterparts at some occasions. However, a major issue in the development of PICs is the limited integration density because the sizes of most photonic devices are tens of micrometers. Inverse design has been proven to be an effective method to reduce the feature size of photonic integrated devices. Previously demonstrated devices include polarization rotator [1], polarization beam splitter [2], wavelength demultiplexer [3], reflectors [4], and cloaking [5], all of which have a footprint only at the micrometer scale. To date, the efforts have been made on reducing the sizes of individual devices. Reduction of the footprint of PIC interconnection, which is of equal importance, is yet to be demonstrated.

Here, we adopt an inverse-design method to design a new type of structures, namely the "photonic welding points," for connecting two waveguides with an arbitrary bending angle on a chip. The feature sizes of these photonic welding points are all within 4 μm^2, which are about two orders of magnitude smaller than conventional waveguide bends. The insertion loss from both simulation and measurement results maintains below 0.5 dB in the wavelength range of 1440–1580 nm. Such photonic welding points have many distinct advantages. First, unlike the electrical welding points which may introduce an additional insertion loss due to impedance mismatch for high-frequency signals, such photonic welding points are free from this problem, and thus can be safely employed in PICs for high-frequency applications. Second, the structures are optimized only through engineering the shape of the borders, which can be described by a continuous and differentiable function. Such structures with gradually varying borders can be fabricated with high fidelity and also introduce minimal scattering loss to the transmitting light. Third, the fabrication process of the photonic welding points is CMOS compatible and requires only one step of lithography and etching. Therefore, the demonstrated photonic welding points can be employed as a standard module in photonic integrated circuitry for boosting the density of photonic integration to the next level.

2. DEVICE DESIGN METHOD

In the conventional wisdom, two waveguides can be joined by a waveguide bend to change the propagation direction of light as shown in Fig. 1(a), where the gray part denotes SiO_2 and the purple part denotes silicon. The photonic welding point realized within a small area as shown in Fig. 1(b) is expected to connect waveguides with negligible insertion loss and crosstalk. We take the photonic welding point shown in Fig. 1(c) as an example to explain the design process. The devices are designed on a silicon-on-insulator (SOI) platform with 220-nm Si layer on 3-μm buried oxide. We draw a small rectangle with orange dashed line as shown in Fig. 1(c) to indicate the design optimization region of the photonic welding point. Two continuous lines *AB* and *CD*, which are determined by the green discrete dots, delineate the borders of the photonic welding point structure, where the purple region denotes silicon unetched and the white region denotes silicon fully etched. The position of each discrete dot is

described by the radial and angular coordinates (r_i and θ_i). The final r_i and θ_i are determined after several rounds of greedy optimization [6].

Without loss of generality, we designed the photonic welding points for connecting two 0.5-μm-wide waveguides with the bending angle of 30°, 60°, 90°, 120°, and 150°. Figure 1(d) shows the structures connected by the optimized photonic welding points in the green regions. Figure 1(e) shows the simulated electric field |**E**| profiles of the fundamental transverse-electric (TE_0) mode at 1.55 μm transmitting through the photonic welding points, which clearly indicate that light is confined tightly in the photonic welding points, thus avoiding the bending loss caused by small bend radii. The uniform intensity patterns in the output waveguide also prove no crosstalk introduced by the photonic welding points. Figure 1(f) shows the structures of conventional waveguide bends connecting the two waveguides, with the inner radius of the waveguide bend 0.15 μm to maintain the same footprint of the corresponding photonic welding points. For light in the communication band around $\lambda = 1.55$ μm, the waveguide bend with inner radius $\sim\lambda/10$ will inevitably introduce a large insertion loss due to the modal mismatch and sharp bending. Figure 1(g) shows the simulated electric field |**E**| profiles of the TE_0 mode at 1.55 μm transmitting through the waveguide bend, which clearly indicate the leakage of light from the waveguide bend. The intensity oscillation of light as seen in the output waveguide indicates that the light is not pure TE_0 mode anymore. Figure 1(h) shows the normalized spectra of transmission through the photonic welding points and waveguide bends, where the blue solid lines represent transmission from the photonic welding points and the red dashed lines represent transmission from the waveguide bends. A comparison between the blue solid and red dashed lines concludes that the waveguide bends will introduce significantly higher insertion loss, which is proportional to the bending angle, but the photonic welding points can avoid this loss and transport light from one waveguide to the other with any bending angle.

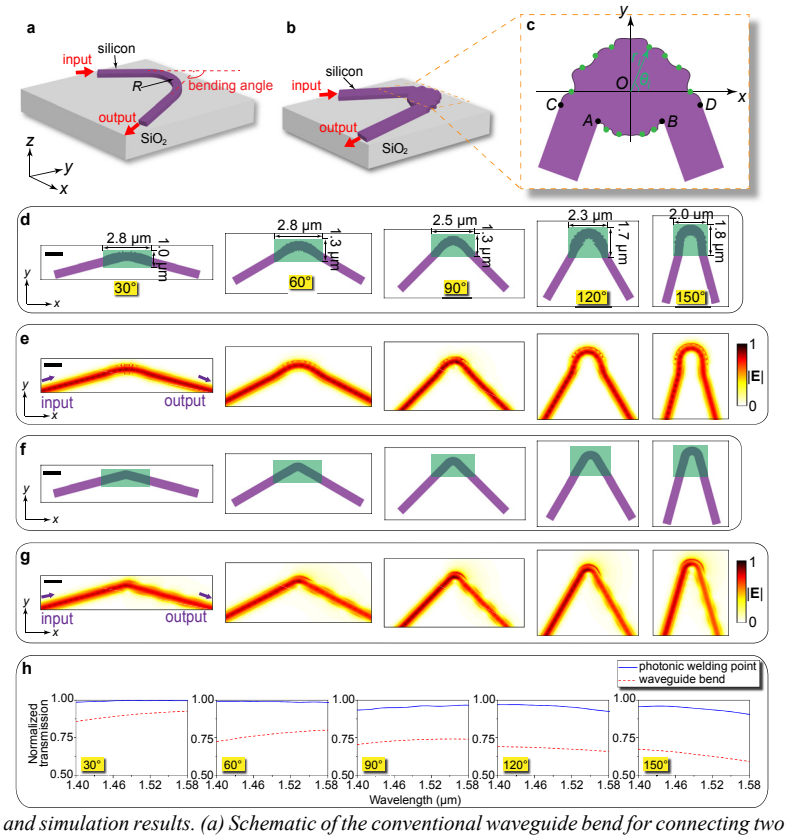


Figure 1. Design process and simulation results. (a) Schematic of the conventional waveguide bend for connecting two nonparallel waveguides. R is the inner radius of the waveguide bend. (b) Schematic of the photonic welding point for connecting two nonparallel waveguides. (c) Top view of the photonic welding point. (d) Optimized structures of photonic welding points connecting two waveguides with the bending angle of 30°, 60°, 90°, 120°, and 150°. (e) Simulated electric field profiles of the TE_0 mode at 1.55 μm transmitting through the photonic welding points. (f) Schematic of waveguide bends connecting two waveguides with the bending angle of 30°, 60°, 90°, 120°, and 150°. The inner radius of all waveguide bends is 0.15 μm. (g) Simulated electric field profiles of the TE_0 mode at 1.55 μm transmitting through the waveguide bends. The purple arrows indicate the light input and output directions. (h) Normalized transmission spectra of photonic welding points (blue solid lines) and waveguide bends (red dashed lines) connecting two waveguides with the bending angle of 30°, 60°, 90°, 120°, and 150°. The scale bars in all figures in (d)–(g) represent 1 μm.

3. EXPERIMENTAL RESULTS

The devices of photonic welding points and waveguide bends were fabricated on a SOI wafer with 220-nm Si device layer on 3-μm buried oxide. The upper panel of Fig. 2(a) contains optical microscope images of devices for

characterizing the insertion loss of photonic welding points connecting waveguides with the bending angle of 30°, 60°, 90°, 120°, and 150°, and the lower panel contains the corresponding scanning electron microscope (SEM) images zoomed in at the joint, all of which have a footprint less than 4 μm^2. The upper panel of Fig. 2(b) contains optical microscope images of devices for characterizing the insertion loss of waveguide bends connecting two waveguides with the bending angle of 30°, 60°, 90°, 120°, and 150°, and the lower panel contains the SEM images zoomed in at the joint. Figure 2(c) plots the normalized transmission spectra of a single photonic welding point and a single waveguide bend. It is clear that the two types of spectra (measured and simulated) agree with each other. The insertion loss of the photonic welding points all maintains <0.5 dB in the entire wavelength range of 1440–1580 nm, while that of the waveguide bends increases with the bending angle and can reach up to 3.0 dB.

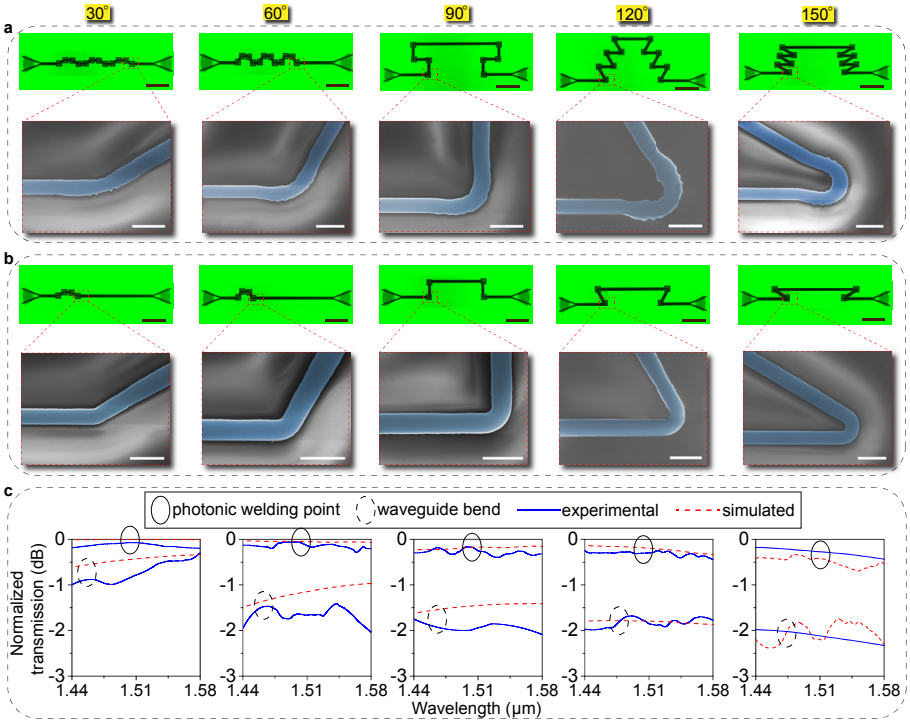


Figure 2. Device images and measurement results. (a) Optical microscope and SEM images of the fabricated devices for measuring the transmission loss of photonic welding points connecting two waveguides with different bending angles. (b) Optical microscope and SEM images of the fabricated devices for measuring the transmission loss of waveguide bends connecting two waveguides with different bending angles. The scale bars represent 40 μm in all optical microscope images and 1 μm in all SEM images. (c) Experimental and simulated normalized transmission spectra of single photonic welding point and waveguide bend for connecting two waveguides with different bending angles. Blue solid lines represent the experimentally measured results, and red dashed lines represent the simulated results.

ACKNOWLEDGEMENTS

This work was supported by the Early Career Scheme (Project No. 24208915) and the General Research Fund (Project No. 14208717) sponsored by the Research Grants Council of Hong Kong, and by the NSFC/RGC Joint Research Scheme (Project No. N_CUHK415/15) sponsored by the Research Grants Council of Hong Kong and the National Natural Science Foundation of China.

REFERENCES

[1] L. Lu, *et al.*: Inverse-designed ultra-compact star-crossings based on PhC-like subwavelength structures for optical intercross connect, *Opt. Express*, vol. 25. pp. 18355–18364, July 2017.

[2] B. Shen, *et al.*: An integrated-nanophotonics polarization beamsplitter with 2.4 × 2.4 μm^2 footprint, *Nat. Photonics*, vol. 9. pp. 378–382, May 2015.

[3] A. Y. Piggott, *et al.*: Inverse design and demonstration of a compact and broadband on-chip wavelength demultiplexer, *Nat. Photonics*, vol. 9. pp. 374–377, May 2015.

[4] Z. Yu, *et al.*: Genetically optimized on-chip wideband ultracompact reflectors and Fabry-Perot cavities, *Photonics Res.*, vol. 5. pp. B15–B19, Dec. 2017.

[5] B. Shen, *et al.*: Increasing the density of passive photonic-integrated circuits via nanophotonic cloaking, *Nat. Commun.*, vol. 7. pp. 13126, Nov. 2016.

[6] Z. Yu, *et al.*: Photonic welding points for arbitrary on-chip optical interconnects, *Nanophotonics*, vol. **7**. pp. 1679–1686, Sept. 2018.

Broad-band phase-matched multimode waveguides for application to four-wave mixing

(Student Paper)

Jianhao Zhang[1,2], Carlos Alonso-Ramos[1], Laurent Vivien[1], Sailing He[2], Eric Cassan[1]
[1] Centre for Nanoscience and Nanotechnology (C2N), CNRS, University Paris-Sud, University Paris-Saclay, 91120 Palaiseau, France
[2] Centre for Optical and Electromagnetic Research, Zhejiang University, Hangzhou 310058, China
e-mail: jianhao.zhang@u-psud.fr

ABSTRACT

We present a general method to equalize the frequency spacings for application to inter-modal degenerate four-wave mixing in a multimode waveguide. By applying the proposed method, the dispersion of the modes can be controlled allowing flexible phase to frequency and wave vector phase matching (PM) between several propagative modes. Taking advantage of the proposed method, PM can be satisfied over a wide wavelength range, e.g. bridging from telecom wavelength to almost 2 μm. In addition, the reported approach releases new degrees of freedom to tune group velocity dispersion to achieve four-wave mixing in single-mode waveguides for on different material platforms and waveguide thicknesses. We believe that this method has an immense potential for a plethora of all-optical signal processing applications in the telecom range, mid-infrared light generation and Brillouin scattering with selectable phonon energy.

Keywords: Phase-matching, nonlinear processes, dispersion, multi-mode operation, broadband conversion, self-adaptive boundary.

1. INTRODUCTION

Nonlinear processes are of paramount relevance for on-chip signal processing and spectroscopy in the near- and mid-infrared [1]. Functions like optical parametric amplification based on the Kerr effect, have been demonstrated [2] on the mainstream silicon (silicon, silicon nitride, silicon/germanium compound) platform. Among these works, compensating the intrinsically material dispersion and the nonlinearity-induced dispersion, plays a key role [3], especially when considering the four-wave mixing processes (FWM). To tackle this phase matching (PM) problem, different waveguides with optimized dimensions have been proposed, still showing a limited control of the dispersion profile. Figure 1(a) shows phase and energy matching conditions as well as typical dispersion profile in conventional FWM based on single-mode operation.

In this context, we focus on multimode waveguides for the realization of phase matching with a wavelength span up to few hundreds of nanometers. We consider 3 waveguide modes. We present a novel method for facilitating FWM in multimode graded-profile waveguides. By introducing a "self-adaptive boundary" approach, we simultaneously satisfy energy conservation and wavevector matching multimode waveguides for nonlinear purposes, see Fig, 1(b). This approach obviates the requirement for an exact dispersion by ensuring an equal frequency spacing between modes in a remarkably wide propagation wavevector range.

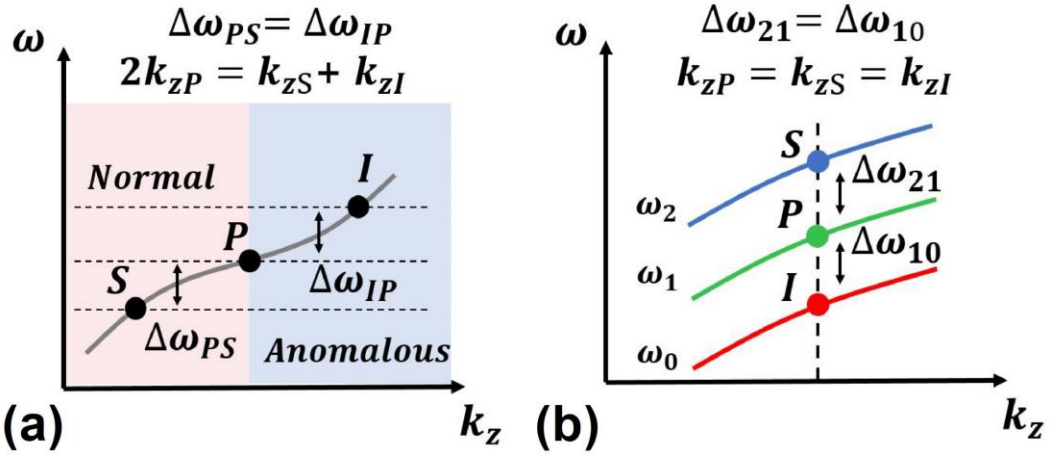


Figure 1. Schematic of (a) degenerate four wave mixing operating in a single-mode waveguide with anomalous dispersion and (b) operating within an inter-modal scheme regardless the absolute dispersion provided that all dispersion curves are obtained by translating the same curve with a constant frequency step (e.g. $\Delta\omega_{21}=\Delta\omega_{10}$ here).

2. COMPARISONS AND RESULTS

As it is well known, in a two-dimension step-index slab waveguide (infinite depth along the x axis), the eigen equation for modes propagating along the z axis with an electric field polarized along y axis reduces to [4]:

$$ha = \frac{m\pi}{2} + arctan(\frac{\gamma n_w^2}{h n_c^2}) \quad (1)$$

in which n_w and n_c is the material index of waveguide core and cladding while $h = \sqrt{(k_0^2 n_w^2 - k_z^2)}$ and $\gamma = \sqrt{(k_z^2 - k_0^2 n_c^2)}$ are the wavevector along the y axis, inside and outside the waveguide core, respectively. The dispersion curves from solution equation (1) for the first four order modes (with corresponding mode order m=0, 1, 2, 3), are shown in the inset of Fig. 2(a) with the index profile and the mode profiles of the first three order mode depicted at the bottom-right corner. Silicon and silicon dioxide are chosen here as the materials (material dispersion was considered) while the waveguide width $2a$ was set at 700 nm. Clearly for a fixed wavevector k_z (tracked at $k_z = 1.08 \times 10^7 \text{m}^{-1}$ here), the frequency spacing between mode m and m+1 increases sharply with m, hampering the degenerate FWM process. By conducting the derivative of equation (1) to n_{eff}, we can obtain an analytical frequency spacing as:

$$\frac{d\omega}{dm} = \frac{d}{dn_{eff}}\left(\frac{k_z c}{n_{eff}}\right) / \frac{dm}{dn_{eff}} \approx \frac{c\pi\sqrt{n_w^2 - n_{eff}^2}}{2an_w^2} \quad (2)$$

Using this equation (2), we represent the analytically continuous frequency spacing $\frac{d\omega}{dm}$ for a waveguide with a=350 nm, n_w=3.48, n_c=1.445, as in Fig. 2(b). The effective index n_{eff} of the first 4 modes are marked by the circles in the figure, $\frac{d\omega}{dm}$ at which are well coincident with the discrete calculation results coming from the dispersion curves shown in Fig. 2(a). This confirms that the analytical frequency spacing $\frac{d\omega}{dm}$ can be considered as an effective figure of merit to investigate how the frequency spacing evolves with the waveguide dimension and the index profile. From Fig. 2(b), we notice that the frequency spacing is almost proportional to $\sqrt{n_w^2 - n_{eff}^2}$, in the usual range of n_{eff} (1.6 to 3.3, for silicon waveguide cladded by silica). This comes from the reciprocal relationship between ω and n_{eff} for an unchanged k_z, on the left part of equation (1), compared to the almost linear phase increasement with m on the right.

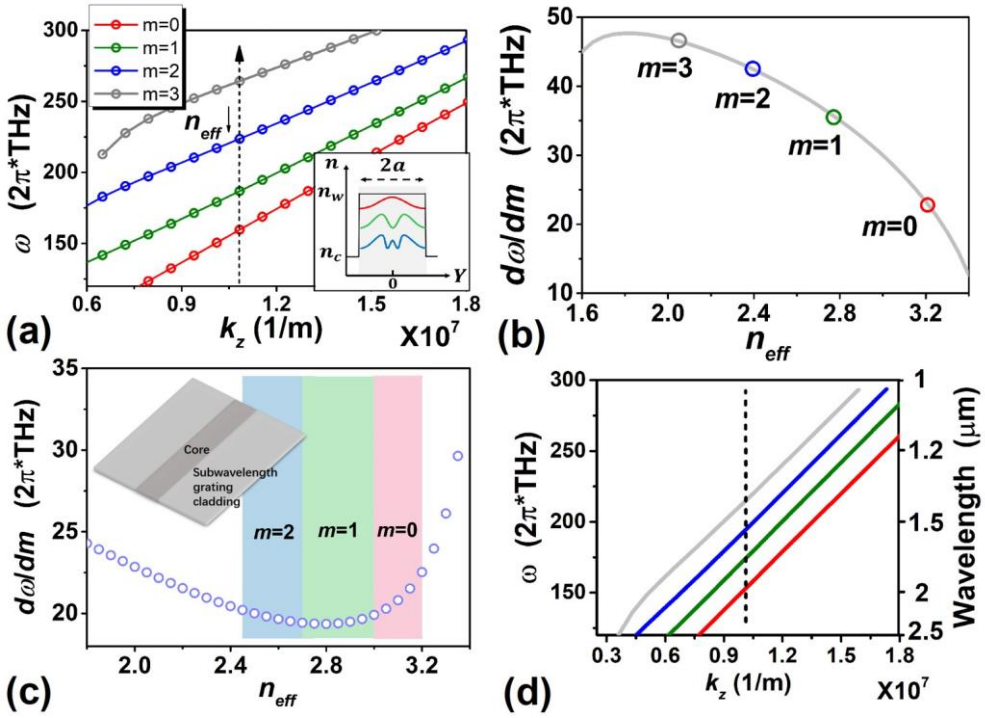


Figure 2. (a)Dispersion curves of first 4 modes of a two-dimension silicon waveguide with silica cladding, propagating along z axis. The width is $2a$ = 700nm. The index profile of the waveguide and mode distribution is plotted in the inset. (b) Analytical frequency spacings as a function of effective index n_{eff} of the waveguide in (a). (c) Analytical Frequency spacings as a function of effective index n_{eff}, of a waveguide using self-adaptive boundary. The n_{eff} points, corresponding to the first 3 modes, are labelled by the color regions. (d) Dispersion curves of first 4 modes with self-adaptive boundary, calculated using 3D FDTD.

To overcome this limitation, we propose to implement a subwavelength engineered waveguide lateral cladding (see top-left of Fig. 2(c)) that enables the implementation of a tailorable index profile. By introducing a scenario inherited from potential wells and adopting a well-designed index profile, we are able to create an effective photon well along the transverse direction (perpendicular to the wave-propagation direction) for fine tuning the waveguide dispersion.

The optimized waveguide has a=800 nm, n_w=3.48, n_c=1.45 and a well-designed index profile. Frequency spacings as a function of n_{eff} using equation (3) are plotted in Fig. 2(c). The frequency spacings change no longer monotonously, instead, a new tendency is created with a local minimum ($n_{eff} \approx$2.8). The index region of the first 3 modes are labelled by colour regions which is right around the turning point of the curve and indicating the possibility of identical frequency spacing.

To validate these theoretical predictions, we conducted 3D FDTD calculation based on the parameters used in Fig. 2(c) and displayed the corresponding dispersion curves of the first 4 order modes in Fig. 2(d). Clearly, all the curves are almost parallel and separated by a very a close frequency spacing of around 20.5 THz, which is perfectly coincident to the prediction indicated by the analytical calculation.

3. CONCLUSION

We propose a new approach for designing multimode graded waveguides capable of reshuffling the needed conditions (simultaneous satisfaction of the energy conservation and wavevector phase matching) for the exploitation of degenerate FWM, offering a flexible strategy for versatile material platforms regardless the thickness and intrinsic dispersion of the considered optical waveguide modes. We provide a thorough analytical explanation and numerical confirmation of the theoretical predictions. The proposed approach can be scaled up (e.g. 5 modes or 7 modes), with the possibility of achieving phase-matching for wavelength ranges over a few hundreds of nanometers, which we believe will benefit nonlinear applications, e.g. light generation in mid-infrared wavelength and applications in which dispersion manipulation is of first priority.

ACKNOWLEDGEMENTS

The French ANR agency is acknowledged for the its support through the SITQOM project and MIRSPEC project (ANR-17-CE09-0041)

REFERENCES

[1] J. Leuthold, *et al.*: Nonlinear silicon photonics, *Nat. Photon.*, vol. 4. pp. 535-544, Aug. 2010.
[2] M. A. Foster, *et al.*: Broad-band optical parametric gain on a silicon photonic chip, *Nat.*, vol. 441. pp. 960-963, Jun. 2006.
[3] M. A. Foster, *et al.*: Broad-band continuous-wave parametric wavelength conversion in silicon nanowaveguides, *Opt. Exp.*, vol. 15. pp. 12949-12958, Octo. 2007.
[4] K. Okamoto: Fundamentals of Optical Waveguides, London: Elsevier, 2006.

An NbTiN superconducting single photon detector implemented on a $LiNbO_3$ single mode nano-waveguide at telecom wavelength

(Student paper)

Julien Zichi[1,*], Samuel Gyger[1,*], Mohammad Amin Baghban[1,*], Ali W. Elshaari[1], Katia Gallo[1], Val Zwiller[1]

[1] Department of Applied Physics, Royal Institute of Technology, Albanova University Centre, Roslagstullsbacken 21, 106 91 Stockholm, Sweden

[*] The authors contributed equally.

e-mail: gyger@kth.se

ABSTRACT

Fiber-coupled superconducting nanowire single photon detectors are a ubiquitous tool for quantum optics experiments as they offer near unity detection efficiency over a broad wavelength range, low dark count rate, excellent time resolution and high saturation rate. Nevertheless, advancing quantum optics experiments and applications beyond the few-photon limit requires large scale integrated systems of quantum sources and detectors. In recent years there has been a tremendous progress with integrating single photon detectors with a variety of photonic platforms. This includes attempts on ion-diffused waveguides in $LiNbO_3$, a non-linear and electro-optic material with widespread use for signal processing, frequency conversion, and quantum optics devices. However the realization of superconducting detectors on single mode waveguides remains elusive. Here we present an NbTiN superconducting single photon detector integrated directly on a $LiNbO_3$ single mode nanophotonic waveguide at telecom wavelength, with a high critical current density and a dark count rate of 3 mHz at 99% of its critical current.

Keywords: SNSPD, lithium niobate integrated optics, integrated detector, NbTiN, lithium niobate-on-insulator.

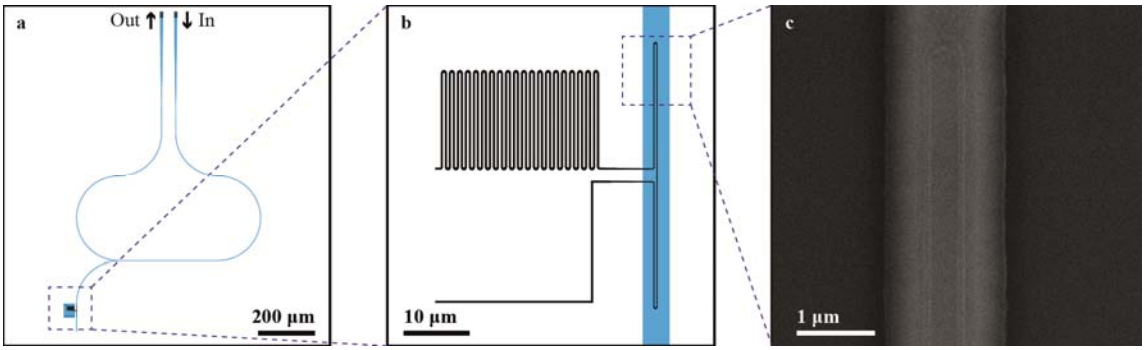


Figure 1: a) Schematic of the circuit. b) Schematic of the SNSPD above the waveguide. c) SEM micrograph of the SNSPD.

1. INTRODUCTION

Superconducting nanowire single photon detectors (SNSPDs) revolutionized quantum optics experiments, they offer unique properties combining near unity single photon detection efficiency [1], [2], mHz dark count rate [3], few picoseconds time resolution [4], [5] and tens of MHz detection rate [2]. SNSPDs have made a number of fundamental physics studies possible, and have become the detector of choice for many applications such as in LiDAR [6], quantum key distribution [7], biomedical imaging [8] and CMOS testing [9]. Making use of the evanescent coupling of the light field propagating in waveguides, it has been demonstrated that SNSPDs are the perfect candidates for on-chip detector integration [10]. Such integration has been demonstrated with several platforms, such as silicon-on-insulator, silicon nitride-on-insulator, diamond, and GaAs/AlGaAs [11]. Lithium niobate ($LiNbO_3$) is a particularly attractive photonic material as it possesses a wide transparency window from 0.4 to 5 µm, nonlinear- and electro-optical properties [12] and it is widely used for classical but also quantum integrated optics [12]. The relatively large geometries of traditional LN waveguides [13] does not allow an efficient coupling to SNSPDs as afforded by nanophotonic circuits on other platforms. Integrating SNSPDs on $LiNbO_3$ nanophotonic waveguides is thus of paramount importance. Here we integrate a niobium titanium nitride (NbTiN) SNSPD on a single-mode $LiNbO_3$-on-insulator (LNOI) photonic wire. NbTiN superconducting detectors have been shown to offer high time resolution and high count rates, while they can be operated at a temperature as high

as 3 K due to the high critical temperature of the material. Furthermore, the etched, slab geometry of our waveguides allows for short bending radii and therefore space-efficient circuits.

2. FABRICATION AND CHARACTERIZATION

We first fabricated the LNOI waveguide circuit, starting from a commercial thin film LNOI wafer, which offers an index contrast between the waveguide core and the bottom cladding of 0.7. The patterning of the LNOI layer followed the process described in [14], involving electron-beam lithography and dry etching of the LiNbO3 using Ar-milling. This enables the simultaneous fabrication of sub-micron waveguides, grating couplers and tapers for coupling in and out of chip as well as markers and pedestals for the SNSPD. The LNOI photonic circuit consists of a 50:50 Y-splitter, with the input port terminated by a grating coupler, one output port terminated by an SNSPD, and the second output port terminated by another grating coupler (Figure 1.a). We subsequently deposited a 9 nm thick NbTiN film on the LNOI circuit using magnetron co-sputtering in an Ar and N_2 gas mixture from two ultra-pure targets of Nb and Ti at room temperature. The detector was patterned on top of the LNOI waveguide into an 78 µm long and 85 nm wide hairpin nanowire by electron-beam lithography. After development, the pattern was transferred to the NbTiN by dry etching with CF_4 and O_2 chemistry (Figure 1.b and c). Additionally, we fabricated test structures and measured LNOI waveguide losses of 19 dB/cm with a dedicated room-temperature setup. The device was mounted on a PCB and placed on an XYZ nano-positioner in a cryostat operated below 100 mK. The detector was DC biased with a commercial SNSPD driver from the company Single Quantum, featuring a bias tee, 2-stage room-temperature amplification and an internal counter. Laser light was coupled through the input grating coupler using a 40x objective mounted next to the sample, and through four optical windows.

3. RESULTS

We measured the IV characteristics of the device and our structure exhibits a critical current of 48.5 µA, which corresponds to a high current density of 63.3×10^9 A/m^2. Figure 2.a shows a typical pulse of the detector at a bias of 48 µA, with a 1/e dead time of 4.5 ns extracted from the exponential decay fit. Using an attenuated pulsed laser at 1546 nm, we recorded the coincidence histogram between the synchronization signal of the laser and the SNSPD pulses, revealing a FWHM timing jitter of 60 ps, as reproduced in Figure 2.b. Moreover, we measured a dark count rate of 3 mHz over a period of 27 minutes when the detector was biased at 99% of its critical current, as shown in Figure 2.c. The predicted detection efficiency of the waveguide-integrated device is 97% from simulations. We are currently working on extracting the efficiency value from the measurements and the loss calibration.

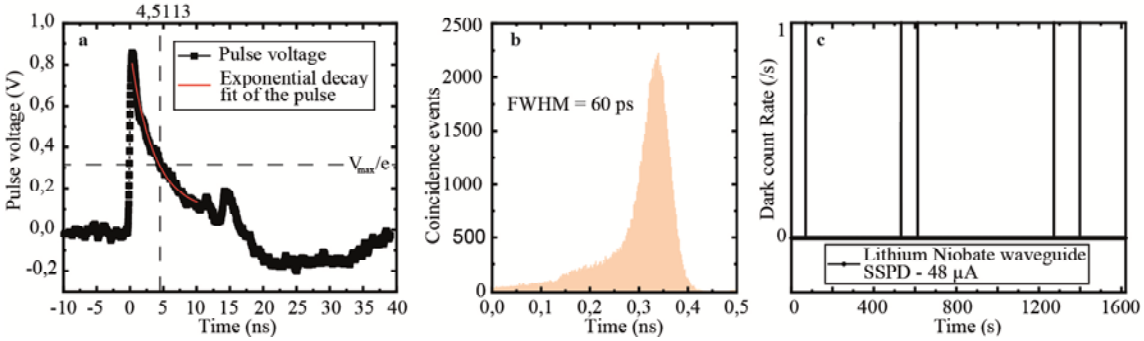


Figure 2: a) Pulse of the SNSPD and exponential fit of the pulse decay. The ripples originate from the readout configuration. b) Timing jitter measurement of the device, measured with a pulsed laser. c) Measurement of a dark count rate of 3 mHz of the device biased at 99% of its critical current.

4. CONCLUSION

We demonstrated the first NbTiN SNSPD implemented on a LNOI circuit. LNOI nanophotonic waveguides provide an excellent confinement of the light field and allow for low footprint devices. The hybrid LNOI-SNSPD device was successfully operated at telecom wavelengths and cryogenic temperatures, exhibiting a high critical current and a low dark count rate. The results represent a step towards the implementation of on-chip, low timing jitter and high-bandwidth single photon detection capabilities of SNSPDs on LNOI, a promising new platform for integrated quantum photonics.

ACKNOWLEDGEMENTS

S.G. acknowledges funding by the Swedish Research Council (VR) under the grant Optik Kvantavläsning (875994). V.Z. acknowledge the support of the ERC grant (ERC-2012-StG) and VR grant for international recruitment of leading researchers (ref: 2013-7152). M.A.B and K.G. gratefully acknowledge support from the Optical Quantum Sensing Research Environment (grant no. 2016-06122) and the Swedish Research Council (grant no. 2018-04487). A.W.E acknowledges support from the Swedish Research Council (Vetenskapsrådet) Starting Grant (ref: 2016-03905) and MARIE SKŁODOWSKA-CURIE Individual Fellowship under REA grant agreement no. 749971 (HyQuIP).

REFERENCES

[1] F. Marsili, *et al.*, "Detecting single infrared photons with 93% system efficiency," Nat. Photonics, vol. 7, no. 3, pp. 210–214, Mar. 2013.
[2] I. Esmaeil Zadeh, *et al.*, "Single-photon detectors combining high efficiency, high detection rates, and ultra-high timing resolution," APL Photonics, vol. 2, no. 11, p. 111301, Nov. 2017.
[3] C. Schuck, W. H. P. Pernice, and H. X. Tang, "Waveguide integrated low noise NbTiN nanowire single-photon detectors with milli-Hz dark count rate," Sci. Rep., vol. 3, no. 1, p. 1893, Dec. 2013.
[4] B. A. Korzh, *et al.*, "Demonstrating sub-3 ps temporal resolution in a superconducting nanowire single-photon detector," arXiv, pp. 1–26, Apr. 2018.
[5] I. E. Zadeh, *et al.*, "A single-photon detector with high efficiency and sub-10ps time resolution," pp. 1–6, Jan. 2018.
[6] A. McCarthy, *et al.*, "Kilometer-range, high resolution depth imaging via 1560 nm wavelength single-photon detection," Opt. Express, vol. 21, no. 7, p. 8904, Apr. 2013.
[7] K. Takemoto, *et al.*, "Quantum key distribution over 120 km using ultrahigh purity single-photon source and superconducting single-photon detectors," Sci. Rep., vol. 5, no. 1, p. 14383, Nov. 2015.
[8] N. R. Gemmell, *et al.*, "A compact fiber-optic probe-based singlet oxygen luminescence detection system," J. Biophotonics, vol. 10, no. 2, pp. 320–326, Feb. 2017.
[9] J. Zhang, *et al.*, "Noninvasive CMOS circuit testing with NbN superconducting single-photon detectors," Electron. Lett., vol. 39, no. 14, p. 1086, 2003.
[10] W. H. P. Pernice, *et al.*, "High-speed and high-efficiency travelling wave single-photon detectors embedded in nanophotonic circuits," Nat. Commun., vol. 3, no. 1, p. 1325, Jan. 2012.
[11] S. Ferrari, C. Schuck, and W. Pernice, "Waveguide-integrated superconducting nanowire single-photon detectors," Nanophotonics, vol. 7, no. 11, pp. 1725–1758, Oct. 2018.
[12] R. S. Weis and T. K. Gaylord, "Lithium Niobate: Summary of Physical Properties and Crystal Structure," Appl. Phys. A, vol. 37, pp. 191–203, Dec. 1985.
[13] M. G. Tanner, *et al.*, "A superconducting nanowire single photon detector on lithium niobate," Nanotechnology, vol. 23, no. 50, p. 505201, Dec. 2012.
[14] M. A. Baghban, *et al.*, "Bragg gratings in thin-film LiNbO_3 waveguides," Opt. Express, vol. 25, no. 26, p. 32323, 2017.

Self-configuring optical circuits

(Invited paper)

David A. B. Miller
Ginzton Laboratory, Stanford University, 348 Via Pueblo Mall, Stanford CA 94305, USA
e-mail: dabm@stanford.edu

ABSTRACT

Integrated technologies like silicon photonics offer the ability to fabricate complex systems, with large numbers of elements. This raises two questions: can we exploit that complexity for new functions, and could we manufacture, control and stabilize the systems, especially since they may be complex interferometric networks whose paths must be set to small fractions of a wavelength? Recently, we have understood new mathematical and architectural ways of thinking about optics, including for novel functions, such as arbitrary linear processing; for example, any linear optical process at a given wavelength can be implemented with a mesh of two-beam interferometers. This understanding itself has fundamental implications, such as proving new laws for thermal radiation. Just as important, however, is that we now also understand ways in which such complex interferometric systems could be configured and stabilized. Indeed, simple, progressive algorithms can set up these meshes automatically, including designing themselves to solve problems. There are even approaches that allow the system to compensate automatically for imperfections in fabrication of network elements. These advances are promising for a growing set of potential applications in sensing, optical communications, microwave photonics, and general linear processing for classical and quantum applications.

Keywords: integrated photonics; silicon photonics; Mach-Zehnder interferometers; linear processing

The optics of lenses, mirrors, and masks enabled a class of analog linear optical processing such as Fourier transforms and correlations. With devices such as spatial light modulators (SLMs), diffractive optical elements, and their modern successors in metamaterials, specific kinds of linear optical transforms have remained interesting, especially for imaging applications. But, even with the programmability of SLMs, simple optical architectures do not allow arbitrary linear operations to be performed [1], and designing and programming such systems can be complicated and time-consuming.

Recently, however, another class of optical systems has been emerging, enabled by silicon photonics technology and some fundamental realizations about optical systems. These systems are based on meshes of two-beam (usually Mach-Zehnder) interferometers [2-13], which can be fabricated in silicon photonics. Indeed, one such realization is that any linear optical component can be emulated by an appropriate set of such two-beam interferences [3].

A second realization is that all linear optical devices are mode converters [4] – that is, any such device can be completely described as transforming an orthogonal set of input functions one by one to a corresponding orthogonal set of output functions; equivalently, we can usefully describe any linear optical system by the singular value decomposition (SVD) of its scattering operator, and also we can state that, for any linear scatterer, there is always set of orthogonal communications channels through it [4,5].

In a particularly practical twist, the Mach-Zehnder mesh architectures can directly represent such an SVD [3], and this in turn gives us a simple constructive proof that any linear optical element is possible in principle. One surprising consequence is that we can rewrite Kirchhoff's laws of thermal radiation [5], now incorporating diffraction and even non-reciprocal systems (neither of which was possible before), and establishing a total of 4 new laws. Another fundamental consequence is that we can conclude that any linear optical element can be emulated at a given wavelength by a collection of two-beam interferometers [3].

A further key realization is that there are simple and completely progressive algorithms that allow us to set up these meshes of interferometers [2,3,6-12]. By a sequence of simple single-parameter feedback loops based on minimizing or maximizing power on photodetetectors, the entire mesh can set itself up without any calculations by training it with the singular value functions. This kind of approach allows a wide range of self-designing, self-configuring, self-perfecting [8,9] and self-stabilizing optical systems, including self-aligning beam couplers [2], automatic laser beam power combiners [2], arbitrary linear transforms [3], systems that can losslessly separate overlapping light beams [5,7,11], including automatically undoing scattering between beams [5,11], automatic target tracking [6], and automatically establishing the best orthogonal channels through any linear optical system [6].

Potential applications of such meshes include mode multiplexing and demultiplexing in fiber or free-space communications [11], linear optical processors [3,13] for classical processing (e.g., for optical neural networks) or quantum processing (since these systems are nominally loss-less), and many possibilities in sensing systems. In extensions of such networks to include some forward and backward paths, a wide range of microwave photonics

circuits can also be emulated (see, e.g., [14]). These various basic realizations and practical possibilities offer many intriguing new directions in optics.

ACKNOWLEDGEMENTS

This work is supported by a MURI grant from the U. S. Air Force Office of Scientific Research (Grant No. FA9550-17-1-0002).

REFERENCES

[1] D. A. B. Miller, "How complicated must an optical component be?" J. Opt. Soc. Am. A 30, 238-251 (2013) http://www.opticsinfobase.org/josaa/abstract.cfm?URI=josaa-30-2-238

[2] D. A. B. Miller, "Self-aligning universal beam coupler," Opt. Express 21, 6360-6370 (2013) http://www.opticsinfobase.org/oe/abstract.cfm?URI=oe-21-5-6360

[3] D. A. B. Miller, "Self-configuring universal linear optical component," Photon. Res. 1, 1-15 (2013). http://www.opticsinfobase.org/prj/abstract.cfm?URI=prj-1-1-1

[4] D. A. B. Miller, "All linear optical devices are mode converters," Opt. Express 20, 23985-23993 (2012) http://www.opticsinfobase.org/oe/abstract.cfm?URI=oe-20-21-23985

[5] D. A. B. Miller, L. Zhu, and S. Fan, "Universal modal radiation laws for all thermal emitters," PNAS 114, no. 17, 4336-4341 (2017) doi:10.1073/pnas.1701606114

[6] D. A. B. Miller, "Establishing optimal wave communication channels automatically," J. Lightwave Technol. 31, 3987 – 3994 (2013) DOI: 10.1109/JLT.2013.2278809 http://ieeexplore.ieee.org/xpl/articleDetails.jsp?arnumber=6581883

[7] D. A. B. Miller, "Reconfigurable add-drop multiplexer for spatial modes," Opt. Express 21, 20220-20229 (2013) http://www.opticsinfobase.org/oe/abstract.cfm?URI=oe-21-17-20220

[8] D. A. B. Miller, "Perfect optics with imperfect components," Optica 2, 747-750 (2015). doi: 10.1364/OPTICA.2.000747 https://www.osapublishing.org/optica/abstract.cfm?uri=optica-2-8-747

[9] C. M. Wilkes, X. Qiang, J. Wang, R. Santagati, S. Paesani, X. Zhou, D. A. B. Miller, G. D. Marshall, M. G. Thompson, and J. L. O'Brien, "60 dB high-extinction auto-configured Mach–Zehnder interferometer," Opt. Lett. 41, 5318-5321 (2016) http://dx.doi.org/10.1364/OL.41.005318

[10] A. Ribeiro, A. Ruocco, L. Vanacker, and W. Bogaerts, "Demonstration of a 4 × 4-port universal linear circuit," Optica 3, 1348-1357 (2016) https://doi.org/10.1364/OPTICA.3.001348

[11] A. Annoni, E. Guglielmi, M. Carminati, G. Ferrari, M. Sampietro, D. A. B. Miller, A. Melloni, and F. Morichetti, "Unscrambling light – automatically undoing strong mixing between modes," Light Science & Applications 6, e17110 (2017) doi: 10.1038/lsa.2017.110

[12] D. A. B. Miller, "Setting up meshes of interferometers – reversed local light interference method," Opt. Express 25, 29233-29248 (2017) https://doi.org/10.1364/OE.25.029233

[13] Y. Shen, N. C. Harris, S. Skirlo, M. Prabhu, T. Baehr-Jones, M. Hochberg, X. Sun, S. Zhao, H. Larochelle, D. Englund, and M. Soljacic, "Deep Learning with Coherent Nanophotonic Circuits," Nature Photonics 11, 441-446 (2017) doi:10.1038/nphoton.2017.93

[14] D. Pérez, I. Gasulla, and J. Capmany, "Field-programmable photonic arrays," Opt. Express 26, 27265-27278 (2018) https://doi.org/10.1364/OE.26.027265

MEMS-based Silicon Photonic Integrated Devices and Circuits

(Invited Paper)

Niels Quack[1], Hamed Sattari[1], Alain Y. Takabayashi[1], Yu Zhang[1], Pierre Edinger[2], Carlos Errando-Herranz[2], Kristinn B. Gylfason[2]

[1] École Polytechnique Fédérale de Lausanne, EPFL, CH-1015 Lausanne, Switzerland
[2] KTH Royal Institute of Technology, Malvinas väg 10, SE-100 44 Stockholm, Sweden

e-mail: niels.quack@epfl.ch

ABSTRACT

Photonic integrated circuits have seen a dramatic increase in complexity over the past decades, a development which has been accelerated by recent applications in datacenter communications and enabled by the availability of standardized mature technology offerings. Among the approaches currently being pursued to further enhance functionality and to reduce power consumption in photonic integrated circuits, mechanical movement of wave-guiding structures at the micro- and nanoscale provides unique opportunities, by virtue of access to a strong modulation of the effective index and the possibility to include mechanical latching and thus non-volatile states. In particular, movable wave-guiding structures can be exploited to perform basic operations in photonic integrated circuits on-chip, such as phase shifting, attenuation or photonic switching. Due to their small footprint and low insertion loss, such MEMS-based components can be integrated to form large arrays containing several thousand unit cells with outstanding system performance, paving the way for efficient implementation of large-scale reconfigurable photonic integrated circuits.

Keywords: MEMS, NEMS, Silicon Photonics, Programmable, Reconfigurable, Photonic Integrated Circuits.

1. INTRODUCTION

The field of Silicon Photonics has been evolving rapidly over the past decades, and today's advanced standardized technology platforms include a wealth of library components. Passives include low loss waveguides, grating and edge couplers, splitters and combiners, etc., and heaters, high-speed modulators, and detectors, are representative of the high-performance active device selection (e.g. IMEC's iSiPP50G [1]). Experimental demonstrations of an inspiring novel concept of programmable photonic circuits [2, 3] have recently been implemented [4] using such standard components, whereby a single physical photonic network on-chip can be dynamically re-configured to address multiple functions. However, scaling to large networks poses significant challenges, due to the associated increase in power consumption, footprint and insertion loss, as current implementations of programmable photonics make use of inefficient solutions such as the thermo-optic effect or free carrier dispersion. MEMS-enabled photonic devices provide a promising avenue to address these challenges with compact, low-loss and low-power consumption actuation mechanisms and the possibility to implement non-volatile states by including mechanical latching.

2. MEMS IN SILICON PHOTONICS

Enabling MEMS movable structures in Silicon Photonics requires integration of actuation mechanisms and capability to manufacture freestanding structures, to allow for mechanical degrees of freedom. Among the well-studied MEMS actuation mechanisms, electrostatic actuation has been shown to be compatible with Silicon Photonics technology with the minimal required modification: mechanically movable structures have been fabricated by dedicated surface micromachining technology [5] or by augmenting Silicon Photonics wave-guiding structures with adequate sacrificial layer removal processes [6, 7, 8] (Fig. 1a). The former gives access to additional degrees of freedom in three dimensions: such an approach offers advantages in photonic design optimization and the potential to include complex three-dimensional routing patterns. The latter however is fully compatible with standard Silicon Photonics platform technologies [9]. This compatibility is of particular interest, as it maintains access to the most advanced and optimized silicon photonic foundry components, including passive and active components, such as grating couplers, modulators, photodetectors, etc. on full 200 mm wafer processes (Fig. 1b).

3. SILICON PHOTONIC MEMS DEVICES AND CIRCUITS

The basic building blocks for reconfigurable photonic circuits include phase shifters, variable couplers (or switches) and attenuators. Surface micromachined technology allows implementation of such devices using vertical mechanical movement (Fig. 1a) [5]. This approach also permits the use of buckling-beam based bistability [10] to achieve non-volatile states. Combining individual building blocks has been demonstrated for

large arrays of up to 240 × 240 switching matrices [11], and is facilitated by the 3D architecture that allows for using a minimum of coupling elements, and efficient electrical interfacing by row-column addressing [12].

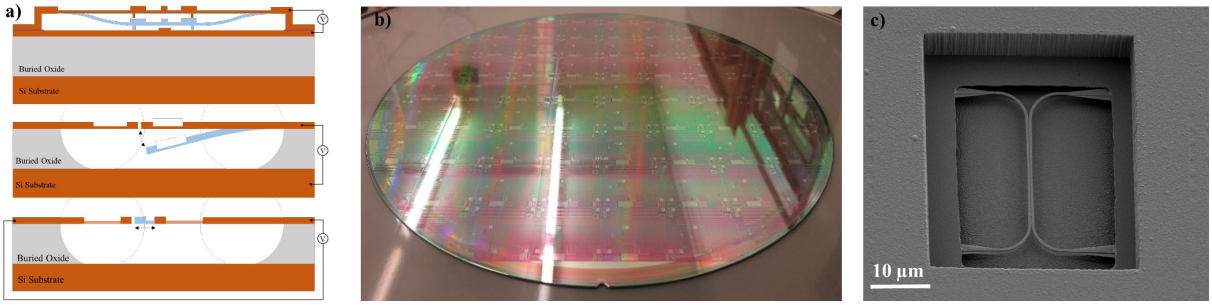


Figure 1: a) Cross section schematic of Silicon Photonics platforms, visualizing actuation concepts for MEMS in Silicon Photonics by vertically moving Surface Micromachined multi-layer waveguide structures (top), out-of-plane (middle) or in-plane (bottom) displacements in single-layer photonic platforms. b) MEMS can be included on full 200mm silicon photonic wafers, by selective window opening and sacrificial layer etch to form c) freestanding waveguides.

In single-layer silicon photonic structures (Fig 1a), on the other hand, mechanical movement can be realized both in-plane [13] and out-of-plane [8]. The advantage of this approach is its compatibility with standard silicon photonic platforms. The European H2020 Project 'MORPHIC' [14] is currently implementing such an approach that uses post-processing on IMEC's iSiPP50G platform. A selective access window opening is created, and a sacrificial layer etch of the buried oxide layer provides access to freestanding wave-guiding structures, as shown in the scanning electrode microscope recording of a freestanding directional coupler in Fig. 1c.

4. CONCLUSIONS

MEMS movable structures in photonic integrated circuits allow for the implementation of low-power and non-volatile photonic building blocks such as phase shifters, couplers and switches, and attenuators. Introducing MEMS in a standard Silicon Photonics platform provides a promising path to enable highly efficient large-scale programmable photonic integrated circuits.

ACKNOWLEDGEMENTS

This project has received funding from the European Union's Horizon 2020 research and innovation programme under grant agreement No 780283 (MORPHIC – www.h2020morphic.eu). N. Quack acknowledges funding from the Swiss National Science Foundation (SNSF) under grant No. 157566, and H. Sattari from the Hasler Foundation under grant No. 17008.

REFERENCES

[1] P. P. Absil, P. Verheyen, P. De Heyn, M. Pantouvaki, G. Lepage, J. De Coster, and J. Van Campenhout, "Silicon photonics integrated circuits: a manufacturing platform for high density, low power optical I/O's," Optics Express, 23, 7, 9369-9378, 2015.
[2] D. Perez, I. Gasulla, and J. Capmany, "Towards programmable microwave photonic processors," Journal of Lightwave Technology, vol. 36, no. 2, pp. 519–532, 2018.
[3] J. Carolan, et al., "Universal linear optics," Science, 349, 6249, 711–716, 2015.
[4] A. Ribeiro, A. Ruocco, L. Vanacker, and W. Bogaerts, "Demonstration of a 4 × 4-port universal linear circuit," Optica 3, 1348-1357 (2016)
[5] N. Quack, T. J. Seok, S. Han, H. Sattari, T. Graziosi, M. Kiss, R. S. Muller, and M. C. Wu, "Surface Micromachined Silicon Photonic MEMS: A Scalable Technology Platform for Photonic Network Components," in Advanced Photonics 2018, OSA 2018, NeM4F.1.
[6] S. Abe and K. Hane, "Variable-Gap Silicon Photonic Waveguide Coupler Switch With a Nanolatch Mechanism," IEEE Photonics Technology Letters, 25, 7, 675–677, 2013.
[7] C. Errando-Herranz, N. Le Thomas, and K. B. Gylfason, "Low-power optical beam steering by microelectromechanical waveguide gratings," Opt. Lett. 44, 855-858 (2019).
[8] S. Han, T.J. Seok, N. Quack, B.-W. Yoo, and M.C. Wu, "Large-scale silicon photonic switches with movable directional couplers," Optica, 2, 4, 2015.
[9] J. Jacobs, T. Graziosi, M. Kiss, S. Han, T. J. Seok, M. C. Wu, N. Quack, "Die Level Release of Silicon Photonic MEMS," in International Conference on Optical MEMS and Nanophotonics (IEEE OMN), 2016.
[10] H. Sattari, A. Toros, T. Graziosi, N. Quack, "Bistable Silicon Photonic MEMS Switches", SPIE OPTO, 10931-13, 2019.
[11] T. J. Seok, K. Kwon, J. Henriksson, J. Luo, M. C. Wu, "240x240 Wafer-scale Silicon Photonic Switches," OFC 2019, Th1E.5.
[12] N. Quack, T. J. Seok, S. Han, R. S. Muller, M. C. Wu, "Scalable Row/Column Addressing of Silicon Photonic MEMS Switches", IEEE Photonics Technology Letters, vol. 28, num. 5, p. 561-564, 2016.
[13] P. Edinger, C. Errando-Herranz, and K.B. Gylfason, "Low-Loss MEMS Phase Shifter for Large Scale Reconfigurable Silicon Photonics," accepted for publication in International Conference on Micro Electro Mechanical Systems (IEEE MEMS), 2019.
[14] MORPHIC project website https://h2020morphic.eu/

Programmable Four-Photon Graph State Generator in Silicon

(Student Paper)

Caterina Vigliar[1], Jeremy C. Adcock[1], Raffaele Santagati[1], Joshua W. Silverstone*[1], Mark G. Thompson[1]
[1]*Quantum Engineering Technology (QET) Labs, H. H. Wills Physics Laboratory & School of Computer, Electronic Engineering & Engineering Mathematics, University of Bristol, Merchant Venturers Building, Woodland Road, Bristol BS8 1UB, UK*
**e-mail: josh.silverstone@bristol.ac.uk*

ABSTRACT

The realisation of functional architectures on a mass-manufacturable technology able to provide high-density and high-quality hardware will be necessary for quantum computing. Graph states represent the state-of-the-art architectures for optical quantum computing [1], while silicon photonics has demonstrated to be the perfect candidate for the realisation of integrated optical components [2]. Here we report the first experimental demonstration of a silicon chip able to generate and manipulate all the existing graph states of four qubits. We demonstrate the generation of the two main classes of graphs by measuring both the 'star' and 'line' graph states and implement multipartite Mermin inequalities to show their entanglement properties. Furthermore, we develop an error model of the device and bound the dominant sources of error using Bayesian inference. So far, the scaling up of silicon quantum photonics has only seen boosts in the complexity of the circuits, increasing the number of waveguides as a route to larger Hilbert spaces [3] while keeping the number of scattered photons to one or two. Here, for the first time, we encode quantum information on four on-chip generated photons and perform non-trivial measurements on them.

Keywords: Integrated, Quantum, Photonics, Silicon, Graph-States, Computing.

1. INTRODUCTION

Graph states are key entangled resources for quantum information processing. They are quantum states which can be drawn as graphs, with vertices representing qubits and edges representing entanglement. They are crucial ingredients for measurement-based quantum computing, where single-qubit measurements on a specific graph state drive the required task. Moreover, they play central roles in topological quantum error correction [4], simulation of complex processes and dynamics [5], quantum secret sharing [6], entanglement enhanced spectroscopy and quantum metrology, open destination teleportation and cryptographic protocols.

Graph states have seen numerous realisations, in both optics [7] and other platforms [8], but a fast-reconfigurable generation of arbitrary graphs on chip has never been achieved in integrated optics. Here we present a device able to combine the generation of four photons with their manipulation, allowing to prepare both classes of four-qubit graph state entanglement, i.e. classes closed under local unitary transformations. We refer to these classes by their best-known members: 'star' S_4, and 'line' L_4.

2. DEVICE OPERATION AND CHARACTERIZATION

Our device operates in four stages, as pictured in Fig. 1. (1) Bright 1550 nm pump pulses coherently excite four spiral photon pair sources, where pairs of non-degenerate signal and idler photons are generated by spontaneous four-wave mixing. We aim to generate a superposition of four photons (two pairs) between all of the sources. (2) Four asymmetric Mach-Zehnder interferometers allow to spatially separate the signal (red) and idler (blue) photons. The crossings configuration enables the realisation of two disentangled Bell pairs between sources 1-3 and 2-4. (3) A reconfigurable two-qubit postselected entangling gate (R-PEG) allows us to perform the missing correlation between the two Bell pairs: it can be configured to be a fusion gate or a controlled-Z gate depending on the class of graphs needed (the 'star' class or the 'line' class). (4) Then a series of two Mach-Zehnder interferometers on each qubit perform local unitaries and tomography rotations. The detection of a four-fold coincidence postselects on the success of the entangling gate, selecting the correct part of the overall final state. The electronic reconfigurability is provided by thermo-optical phase shifters; on- and off-chip coupling is realised by focussing vertical grating couplers; pump rejection is obtained with off chip filters before detection with superconducting nanowire single-photon detectors.

Before measuring the overall four-photon graph states, an estimate of the photons' indistinguishability is needed since high-quality two-photon interference between photons generated by different sources is crucial to the device's operation. We measure a heralded Hong-Ou-Mandel (HOM) interference fringe, between the signal

photons of sources 2 and 3, on an R-PEG MZI, heralded by the idler photons. We find a visibility of $V = (N_{max} - N_{min})/(N_{max} + N_{min}) = 0.82 \pm 0.02$, where N_{max} and N_{min} are the maximum and minimum values of the fitted sinusoid. Shown in Fig. 2d, this is the highest such visibility measured on a chip to date.

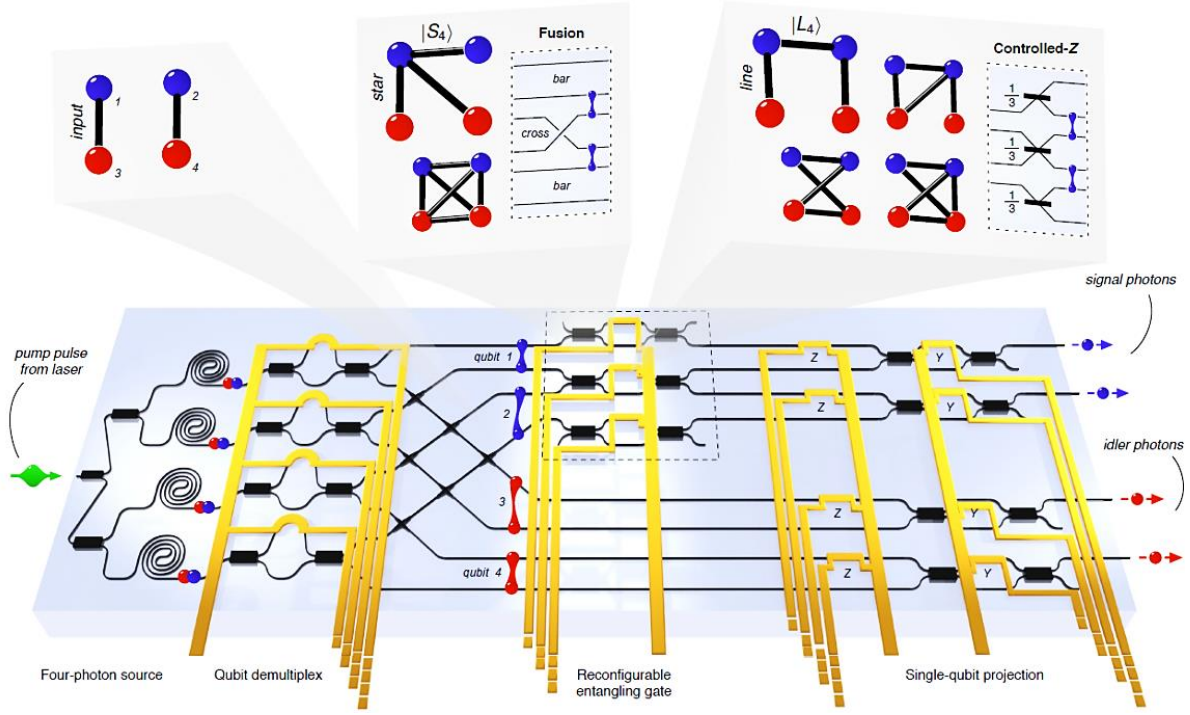


Figure 1. Chip schematic: four photon pair sources, producing four photons in superposition; a qubit demultiplexer, which configures that superposition into a product of two Bell pairs; a reconfigurable postselected entangling gate (R-PEG); and four single-qubit projection and analysis stages, formed of Mach-Zehnder interferometers implementing Z and Y rotations. Corresponding graph states are indicated above each stage: 'star' or 'line' graph states, can be obtained for fusion or controlled-Z R-PEG configurations, respectively.

3. GRAPH STATES GENERATION

The four-photon 'star' and 'line' graph states can be verified by measuring their 16 stabilisers [9]. Their expectation values are plotted in Fig. 2a-b, for S_4 and L_4 respectively. From these observables, we can compute fidelities, shown in Table 1: both states satisfy the $F \geq 1/2$, thus witnessing genuine multipartite entanglement.

In order to support the observation of four-partite entanglement, we investigate the nonlocal properties of the generated graph states by measuring Mermin-type inequalities [9], since they are specifically crafted for graph states and require only stabilizer observables. For each graph state, we measure two types of Mermin operators, M_{II}^G and M_{III}^G, that require two and three measurement settings each party respectively. Results are listed in Table 1 and plotted in Fig. 2c. S_4 exceeds both $M_{II}^G < 2$ and $M_{III}^G < 12$ classical bounds. L_4 exceeds the classical bound for M_{II}^G, but not for M_{III}^G which is more strict. The higher postselection penalty of the controlled-Z, required to generate L_4, results in a decreased fidelity, of which M_{III}^G is a simple rescaling.

4. ERROR MODELLING

In light of the values obtained for the state fidelities, an analysis of the sources of error is needed. The most realistic error factors are the effect of partial distinguishability of the sources, high squeezing inducing multi-photon pair generation and normally distributed phase errors. To quantify their contribution, we want to estimate the distinguishability parameter (σ), the pairs-per-pulse parameter (p) and average phase error (δ) that matches the observed outputs.

A useful method to address this kind of problem can be found using Bayesian Parameter Estimation protocols, having built for each of these error models, an independent simulator that outputs four-fold simulated rates for each of the stabiliser measurement configurations and for each generated state. The probability distributions for the three parameters are reported in Fig.2e-g. The values obtained, for the 'star' and the 'line' respectively, from fitting the probability distributions with a Gaussian distribution are $\sigma_{S,L} = \{0.82 \pm 0.01, 0.82 \pm 0.01\}$, $p_{S,L} = \{0.036 \pm 0.009, 0.037 \pm 0.012\}$ and $\delta_{S,L} = \{0.185 \pm 0.007\ \text{rad}, 0.182 \pm 0.009\ \text{rad}\}$. They are compatible with the parameters measured with direct techniques like HOM dips, coincidence to accidental measurements and crosstalk measures. This approach can reveal additional device performance information from existing data as no new measurements are required.

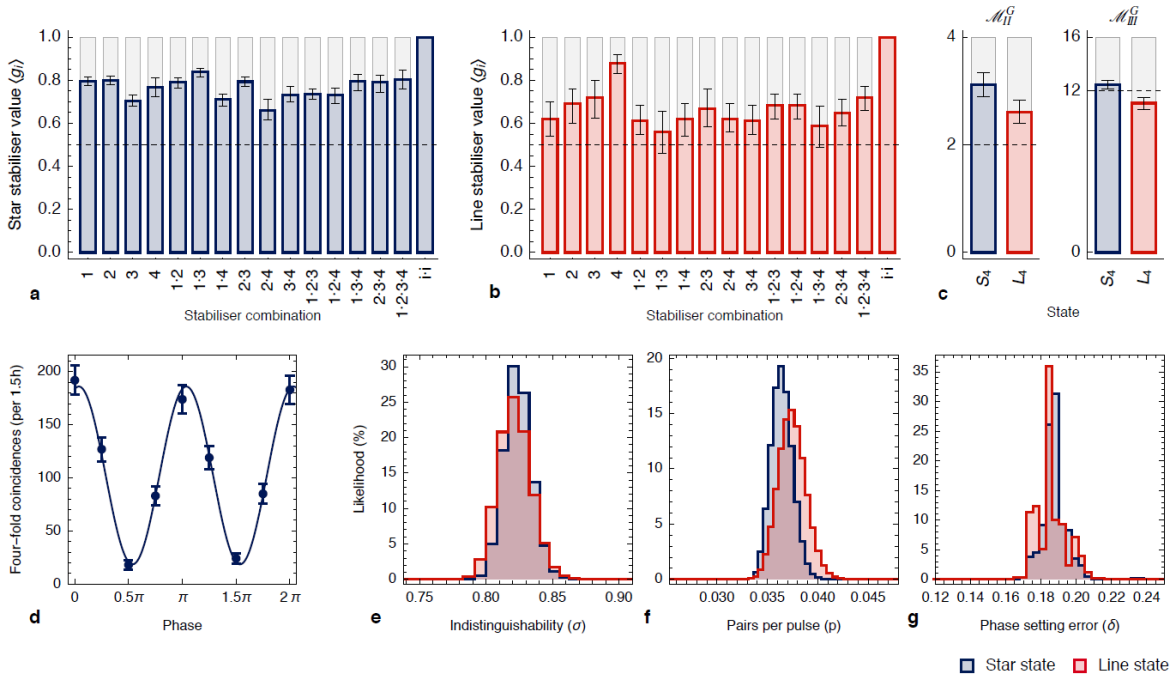


Figure 2. Summary of experimental data. ***a, b.*** *Stabiliser observables of the star and line graph states.* ***c.*** *Mermin parameters (M_{II}^G and M_{III}^G). Local hidden variable bounds are indicated with a dashed line. Values are reported in Table 1.* ***d.*** *On-chip Hong-Ou-Mandel interference, with HOM fringe visibility of V= 0.82 ± 0.02. Probability distributions for the (**e**) indistinguishability, (**f**) source brightness and (**g**) phase error, derived via a Bayesian parameter estimation method.*

TABLE 1. MEASURED PARAMETERS.

State	Fidelity	$M_{II}^G(2,4)$*	M_{III}^G	Count Rate
S_4	0.78±0.01	3.17±0.07	12.45±0.12 (12,16) *	5.7 mHz
L_4	0.68±0.02	2.61±0.14	10.93±0.29 (12,16) *	1.1 mHz
$\phi^+_{(1,3)}$	0.97±0.01	2.79±0.01**	3.90±0.03 (2,4) *	1.8 kHz
$\phi^+_{(2,4)}$	0.97±0.01	2.71±0.01**	3.88±0.03 (2,4) *	1.9 kHz

*Classical and quantum bounds are listed in parentheses, where they apply.

**Indicates a Bell-CHSH test for the initial Bell pairs.

5. CONCLUSIONS

We have shown to be able to reprogram a silicon chip containing four integrated single photon sources and tens of passive and reconfigurable components to generate all classes of four-qubit graph states. Extending chip-scale quantum optics into the multi-pair regime is a crucial step, together with the increase of circuit complexity, towards large-scale quantum computing with photons. Future developments in on-chip photon number now depend solely on reducing loss and increasing rates. The reconfigurable generation of arbitrary graphs on chip, never achieved before in integrated optics, will speed up the development of many graph-based applications.

REFERENCES

[1] T. Rudolph: Why I am optimistic about the silicon-photonic route to quantum computing, *APL Photonics 2*, 030901 (2017).

[2] S. Chung, et al.: A monolithically integrated large-scale optical phased array in silicon-on-insulator cmos, *IEEE Journal of Solid-State Circuits*, vol. 53, pp. 275–296 (2018).

[3] J. Wang, et al.: Multidimensional quantum entanglement with large-scale integrated optics. *Science*, vol. 360, Issue 6386, pp. 285-291, (2018).

[4] R. Raussendorf, et al.: Topological fault-tolerance in cluster state quantum computation, *New Journal of Physics*, vol. 9, 199 (2007).

[5] I. M. Georgescu, et al.: Quantum simulation, *Rev. Mod. Phys.*, vol. 86, pp. 153–185 (2014).

[6] D. Markham, et al.: Graph states for quantum secret sharing, *Physical Review A*, vol. 78, 042309 (2008).

[7] P. Walther, et al.: Experimental one-way quantum computing, *Nature*, vol. 434, 169 (2005).

[8] B. Bell, et al.: Experimental demonstration of a graph state quantum error-correction code, *Nature communications*, vol. 5, 3658 (2014).

[9] O. Gühne & G. Toth, Entanglement detection, *Physics Reports*, vol. 474, pp. 1–75 (2009).

Reconfigurable Hybrid Quantum Photonic Circuits

Ali W. Elshaari[1, *], Iman Esmaeil Zadeh[2], Ronan Gourgues[3], Efe Büyüközer[4], Thomas Lettner[1], Peng Zhao[5], Eva Schöll[1], Samuel Gyger[1], Michael E. Reimer[6], Gabriele Bulgarini[3], Johannes W. N. Los[3], Julien Zichi[1], Sander N. Dorenbos[3], Dan Dalacu[7], Philip J. Poole[7], Klaus D. Jöns[1], Val Zwiller[1]

[1] Quantum Nano Photonics Group, Department of Applied Physics, Royal Institute of Technology (KTH), Stockholm 106 91, Sweden
[2] Optics Research Group, ImPhys Department, Faculty of Applied Sciences, Delft University of Technology, Lorentzweg 1, 2628 CJ Delft, The Netherlands.
[3]Single Quantum B.V., 2628 CH Delft, The Netherlands
[4]Department of Mechanical and Process Engineering, ETH Zurich, CH - 8092 Zurich, Switzerland
[5]Department of Electronic Engineering, Tsinghua National Laboratory for Information Science and Technology, Tsinghua University, Beijing, China
[6]Institute for Quantum Computing and Department of Electrical & Computer Engineering, University of Waterloo, Waterloo, Ontario N2L 3G1, Canada
[7]National Research Council of Canada, Ottawa, ON K1A 0R6, Canada.
[*]*e-mail: elshaari@kth.se*

ABSTRACT

In this paper, we realize hybrid quantum photonic circuits, combining III-V quantum sources, silicon nitride photonics, piezo-electric crystals, and superconducting materials. We developed a pick and place technique to deterministically integrate on-demand single photon sources with silicon nitride waveguides. We also show that we are able to configure the photonic circuit and control the emission properties of the quantum sources using strain-tuning. Finally, we build a full quantum transceiver consisting of a nanowire quantum dot source, a single stage ring resonator filter, and a waveguide-coupled superconducting single photon detector, all on a single chip.

Keywords: Quantum dots, waveguides, piezoelectric, SNSPD, ring resonators, silicon nitride

1. INTRODUCTION

Photons are ideals carriers for quantum information, they travel at the speed of light with possibility of several degrees of freedom for encoding such as polarization [1], time-domain [2, 3], frequency-domain [4], and even combinations of more than one coding schemes [5, 6]. In order to take advantage of the potential computation and communication applications photons offer, large scale integrated systems with on-demand single photon sources need to be realized. There are generally two schemes to generate single photons on-chip, either through non-linear interactions [7-9], or using bright optical transitions in atoms-like structures [10-13]. Each approach has its own advantages and disadvantages in terms of the photonic circuit quality, on-demand emission of photons, and control of the quantum source properties. Here we combine IIIV quantum sources with silicon nitride photonics[14-16], piezo-electric crystals[17], and superconducting nanowire single photon detectors[18] to realize different hybrid systems that surpass the limitations imposed by each material platform enabling new functionalities and applications.

2. Strain-reconfigurable hybrid photonic circuits

Strain is a particularly attractive tuning mechanism for quantum emitters and circuits, as it provides negligible thermal budget which is compatible with integration of superconducting single photon detectors. Our goal is to build hybrid quantum photonic circuits directly on a piezoelectric substrate[17]. We start with a commercially available PMNPT crystal and perform a polishing routine to smooth the surface for photonic circuit integration (RMS roughness 22.5nm). We metallize top and bottom surfaces forming contacts to apply electric field across the substrate [17]. We form the photonic layer by depositing bottom cladding of silicon oxide and a waveguide core layer of silicon nitride. Next, we employ electron beam lithography and reactive ion etching to form different photonic elements like waveguides and resonators in the silicon nitride layer. In order to combine the circuits with IIIV quantum sources, we developed a pick and place technique to transfer single InP/InAsP nanowire quantum dots and deterministically couple them to the waveguides on the piezoelectric substrate. To increase the strain transfer between the piezoelectric substrate and the quantum emitter, we deposite a thin layer of silicon nitride and silicon oxide to anchor the nanowire to the substrate[17]. Figure 1a shows an artistic representation of the device, while Figures 1b and 1c show SEM images of the nanowire quantum dot and the ring resonator filter[17].

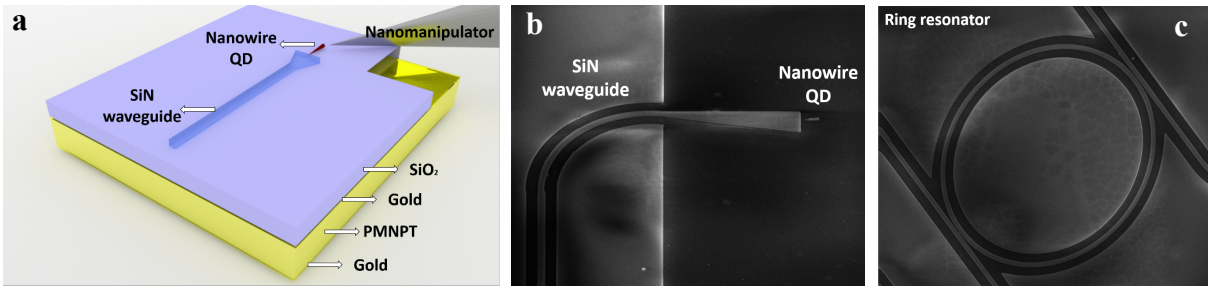


Figure 1. (a) Artistic representation of a silicon nitride photonic waveguide coupled to nanowire quantum dot, all fabricated on piezoelectric substrate. (b)SEM image of nanowire QD coupled to SiN waveguide. (c) Ring resonator filter fabricated on piezoelectric substrate.

Applying electric field across the piezoelectric crystal exerts biaxial strain which is transffered to the top photonic layer hosting the quantum emitters. In Figure 2a, we show second order correlation function of the nanowire quantum dot with multiphoton emission probability $g^{(2)}(0)=0.1\pm0.04$, well below the classical limit. Figures 2b and 2c show tuning of the quantum emitter and a ring resonator filter, respectively, for different voltages applied to the piezoelectric crystal[17].

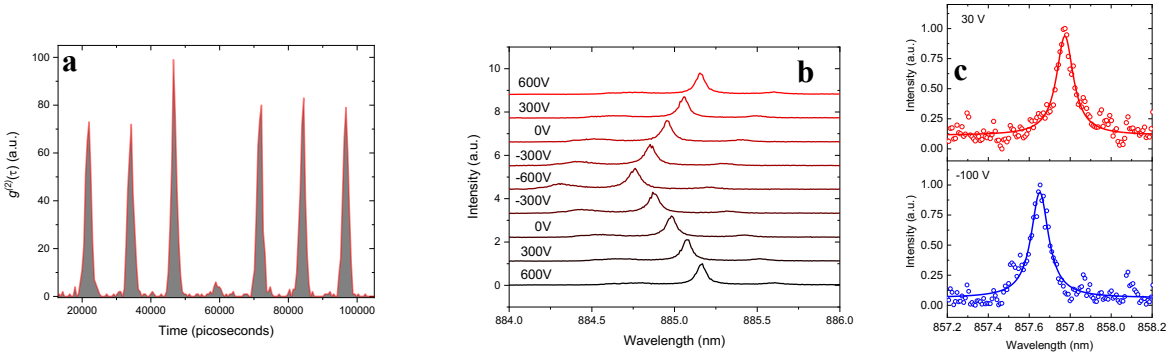


Figure 2. (a) Second order correlation function waveguide integrated nanowire quantum dot, $g^{(2)}(0)=0.1\pm0.04$. (b) Tuning of waveguide-coupled nanowire QD emission as a function of the voltage applied to the piezoelectric crystal. (c) Tuning drop port transmission of a ring resonator filter with voltage applied to the piezo.

3. On-chip quantum transceiver

Our ultimate goal is to generate, manipulate, and detect quantum states of light on-chip. Superconducting nanowire detectors are very attractive for detecting quantum states of light on-chip, they can be evanescently coupled to photonic waveguides, and they offer low dark counts with high time resolution. High performance single-photon detectors require sputtering high-quality superconducting films and precise control over the nanowire dimensions during lithography and etching steps. Any imperfections in the nanowire width will affect the performance of the detector by limiting the device switching current well below its theoretical critical current. Here, we developed a deterministic approach to couple only the best detectors to our photonic circuits and quantum sources. In this proof of concept, we realized the circuits on a silicon substrate. We start by sputtering NbTiN films on an oxide bottom cladding grown on a silicon wafer. Next, we perform electron beam lithography and dry etching to realize an array of detectors. After testing all of the detectors and identifying the best performing ones, we deposit silicon nitride as photonic guiding layer. Next, we pattern the photonic circuit to couple waveguides only to the best performing detectors. Finally, we transfer nanowire quantum dot to the photonic circuit chip. The process is deterministic, we test all the detectors and quantum sources independently, then build any arbitrary circuit configuration with the desired emission and detection characteristics[18].

Figure 3a shows SEM image of the selected superconducting detector, it shows detection saturation at 80% of its critical current with flood illumination, high critical current of 11.6 μA, and timing-jitter of ~23 picoseconds as shown in Figure 3b. We excite the nanowire QD using 515 nm pulsed laser. The wavelength is chosen within the absorption window of silicon nitride, so that the waveguide core acts as a natural filter to supress the pump and pass only the single photons emitted from the QD at ~880 nm. We filter the emission of the QD using a ring resonator filter, terminated with superconducting detector at the drop port to detect the QD emission. Using a time-resolved start-stop correlation measurement with the laser signal, we measure the QD signal decay time of 0.62 ± 0.02 ns.

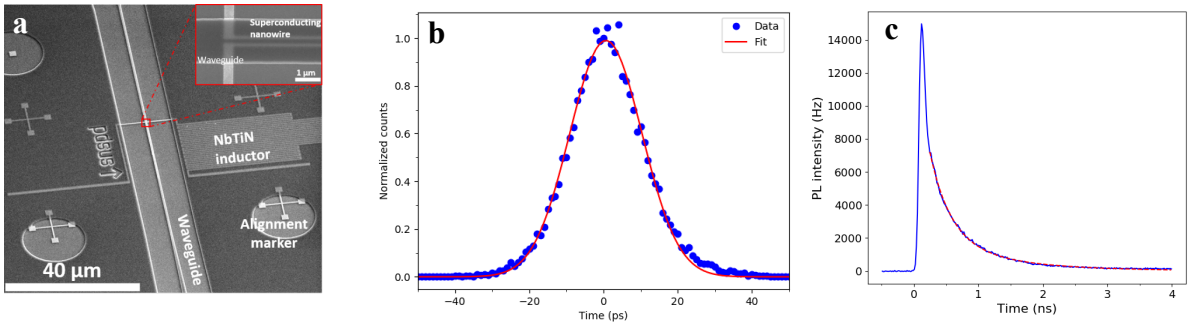


Figure 2. (a) Suerconducting single photon detector fabricated under silicon nitride waveguide. (b) Selected detector with ~23ps time resolution and detection saturation (c) lifetime measurement of the quantum emitter using the on-chip detector through the waveguide and the ring resonator.

4. CONCLUSIONS

We presented our approach for realizing reconfigurable quantum photonic circuits. We showed that strain can be used to tune waveguide-integrated quantum sources and reconfigure integrated optical elements on-chip. Additionally, we realized a full quantum transceiver on-chip from generation to detection, with high control over the detector characteristics, and the quantum source properties in terms of emission wavelength and brightness. We measured the emission lifetime of a nanowire quantum dot with waveguide-coupled detector with 23 picoseconds timing-resolution. We believe that the presented results are very important for the advancement quantum integrated photonics, with applications for quantum communication, computing, and sensing.

ACKNOWLEDGEMENTS

A.W.E acknowledges support from the Swedish Research Council (Vetenskapsrådet) Starting Grant (ref: 2016-03905) and MARIE SKŁODOWSKA-CURIE Individual Fellowship under REA grant agreement no. 749971 (HyQuIP). V.Z. acknowledge the support of the ERC grant (ERC-2012-StG) and VR grant for international recruitment of leading researchers (ref: 2013-7152). I.E.Z. acknowledges the support of NWO LIFT-HTSM for Physics 2016-2017, project nr 680-91-202 and support from Single Quantum B.V. (SQ). K.D.J. acknowledges funding from the MARIE SKŁODOWSKA- CURIE Individual Fellowship under REA grant agreement no. 661416 (SiPhoN) and funding from European Union's Horizon 2020 research and innovation programme under grant agreement No. 820423 (S2QUIP). R.G acknowledges support by the European Commission 9 via the Marie-Sklodowska Curie action Phonsi (H2020-MSCA-ITN-642656).

REFERENCES

[1] N. Akopian, N. H. Lindner, E. Poem, Y. Berlatzky, J. Avron, D. Gershoni, *et al.*, "Entangled Photon Pairs from Semiconductor Quantum Dots," *Physical Review Letters,* vol. 96, p. 130501, 04/06/ 2006.

[2] R. Wakabayashi, M. Fujiwara, K.-i. Yoshino, Y. Nambu, M. Sasaki, and T. Aoki, "Time-bin entangled photon pair generation from Si micro-ring resonator," *Optics Express,* vol. 23, pp. 1103-1103, 2015.

[3] H. Jayakumar, A. Predojević, T. Kauten, T. Huber, G. S. Solomon, and G. Weihs, "Time-bin entangled photons from a quantum dot," *Nature communications,* vol. 5, p. 4251, 2014.

[4] T. Kobayashi, R. Ikuta, S. Yasui, S. Miki, T. Yamashita, H. Terai, *et al.*, "Frequency-domain Hong–Ou–Mandel interference," *Nature Photonics,* vol. 10, pp. 441-444, 2016.

[5] J. T. Barreiro, N. K. Langford, N. A. Peters, and P. G. Kwiat, "Generation of Hyperentangled Photon Pairs," *Physical Review Letters,* vol. 95, p. 260501, 12/19/ 2005.

[6] M. Prilmüller, T. Huber, M. Müller, P. Michler, G. Weihs, and A. Predojević, "Hyperentanglement of Photons Emitted by a Quantum Dot," *Physical Review Letters,* vol. 121, p. 110503, 09/12/ 2018.

[7] P. J. Shadbolt, M. R. Verde, PeruzzoA, PolitiA, LaingA, LobinoM, *et al.*, "Generating, manipulating and measuring entanglement and mixture with a reconfigurable photonic circuit," *Nat Photon,* vol. 6, pp. 45-49, 01//print 2012.

[8] J. W. Silverstone, BonneauD, OhiraK, SuzukiN, YoshidaH, IizukaN, *et al.*, "On-chip quantum interference between silicon photon-pair sources," *Nat Photon,* vol. 8, pp. 104-108, 02//print 2014.

[9] X. Qiang, X. Zhou, J. Wang, C. M. Wilkes, T. Loke, S. O'Gara, *et al.*, "Large-scale silicon quantum photonics implementing arbitrary two-qubit processing," *Nature Photonics,* vol. 12, pp. 534-539, 2018/09/01 2018.

[10] N. Somaschi, V. Giesz, L. De Santis, J. C. Loredo, M. P. Almeida, G. Hornecker, *et al.*, "Near-optimal single-photon sources in the solid state," *Nature Photonics,* vol. 10, p. 340, 03/07/online 2016.

[11] L. Schweickert, K. D. Jöns, K. D. Zeuner, S. F. Covre da Silva, H. Huang, T. Lettner*, et al.*, "On-demand generation of background-free single photons from a solid-state source," *Applied Physics Letters,* vol. 112, p. 093106, 2018.

[12] P. Senellart, G. Solomon, and A. White, "High-performance semiconductor quantum-dot single-photon sources," *Nature Nanotechnology,* vol. 12, p. 1026, 11/07/online 2017.

[13] X. Ding, Y. He, Z. C. Duan, N. Gregersen, M. C. Chen, S. Unsleber*, et al.*, "On-Demand Single Photons with High Extraction Efficiency and Near-Unity Indistinguishability from a Resonantly Driven Quantum Dot in a Micropillar," *Physical Review Letters,* vol. 116, p. 020401, 01/14/ 2016.

[14] I. E. Zadeh, A. W. Elshaari, K. D. Jöns, A. Fognini, D. Dalacu, P. J. Poole*, et al.*, "Deterministic Integration of Single Photon Sources in Silicon Based Photonic Circuits," *Nano Letters,* vol. 16, pp. 2289-2294, 2016/04/13 2016.

[15] A. W. Elshaari, I. E. Zadeh, A. Fognini, M. E. Reimer, D. Dalacu, P. J. Poole*, et al.*, "On-chip single photon filtering and multiplexing in hybrid quantum photonic circuits," *Nature Communications,* vol. 8, 2017.

[16] A. W. Elshaari, I. E. Zadeh, K. D. Jöns, and V. Zwiller, "Thermo-Optic Characterization of Silicon Nitride Resonators for Cryogenic Photonic Circuits," *IEEE Photonics Journal,* vol. 8, pp. 1-9, 2016.

[17] A. W. Elshaari, E. Büyüközer, I. E. Zadeh, T. Lettner, P. Zhao, E. Schöll*, et al.*, "Strain-Tunable Quantum Integrated Photonics," *Nano Letters,* vol. 18, pp. 7969-7976, 2018/12/12 2018.

[18] R. Gourgues, I. Esmaeil Zadeh, A. W. Elshaari, G. Bulgarini, J. W. N. Los, J. Zichi*, et al.* (2018, October 01, 2018). Controlled integration of selected detectors and emitters in photonic integrated circuits. *ArXiv e-prints*. Available: https://ui.adsabs.harvard.edu/#abs/2018arXiv181103979G

New photonic platforms for the mid-infrared

(Invited paper)

Milos Nedeljkovic[1,*], Ahmed Osman[1], Jordi Soler Penadés[1], Tiantian Li[2], Callum G. Littlejohns[1,4], Zhibo Qu[1], Yangbo Wu[1], Wei Cao,[1] Alejandro Sanchez Postigo[3], Alejandro Ortega-Moñux[3], Gonzalo Wangüemert-Pérez[3], Robert Halir[3], Íñigo Molina-Fernández[3], Hong Wang[4], Zhiping Zhou[2], Graham T. Reed[1], and Goran Z. Mashanovich[1]

[1] *Optoelectronics Research Centre, University of Southampton, Southampton, SO17 1BJ United Kingdom*
[2] *State Key Laboratory of Advanced Optical Communication Systems and Networks, School of Electronics Engineering and Computer Science, Peking University, Beijing, 100871 China*
[3] *Universidad de Málaga, Departamento de Ingeniería de Comunicaciones, ETSI Telecomunicación, Spain*
[4] *Silicon Technologies Centre of Excellence, Nanyang Technological University, 639798 Singapore*
**e-mail: m.nedeljkovic@soton.ac.uk*

ABSTRACT

Mid-infrared (MIR) group-IV photonics has seen rapid development in recent years amidst interest in developing integrated photonic systems that could be used for applications in sensing and free-space communications. In particular there is a focus on mid-infrared absorption spectroscopy, since many gases, chemicals, and biological molecules exhibit strong and unique absorption features in this part of the electromagnetic spectrum (approximately 3-16 μm). To achieve this low loss waveguide platforms must be developed that span the MIR. To this end we have investigated suspended silicon, germanium-on-silicon, and suspended germanium waveguides, which are expected to be transparent throughout the MIR range. Optical absorption and phase modulators may also be useful in a variety of integrated MIR systems, but modulation in Si and Ge in the MIR is not yet well understood. We have therefore fabricated and tested silicon-on-insulator free carrier injection modulators for 3.8 μm, and germanium-on-silicon carrier injection modulators for 3.8 μm and 8 μm.

Keywords: silicon photonics, mid-infrared, waveguides

1. GROUP-IV MATERIAL PLATFORMS FOR PHOTONICS

Silicon-on-insulator (SOI) is the most popular platform for Silicon Photonic in the near-infrared, but SiO_2 has high absorption above 4 μm, therefore alternative group-IV waveguide platforms are required to access longer wavelengths. We have demonstrated low loss suspended Si waveguides, in which the SiO_2 below the Si core in SOI waveguides is removed by wet etching with hydrofluoric acid, at wavelengths up to 7.7 μm [1]. Unfortunately, this is near the end of the transparency region of Si, so to reach even longer wavelengths the Si waveguide core can be replaced with germanium, which is transparent up to 16 μm. We have demonstrated germanium-on-silicon (GOS) waveguides at up to 8.5 μm [2], and suspended Ge waveguides at 7.7 μm [3]. Both of these platforms are expected to provide access to almost the whole transparency range of Ge. The GOS waveguides benefit from a simpler fabrication process, but due to their more symmetrical refractive index profile suspended Ge waveguides can be engineered for a stronger evanescent field, which would benefit sensing applications in which a high mode overlap with an external analyte would be desirable.

2. MID-INFRARED MODULATORS FOR GROUP-IV PLATFORMS

Looking beyond waveguides and other passive devices, in the longer term active devices, namely light sources, modulators, switches, and detectors, will also be required to make integrated sensing systems.

Until recently there has been little exploration of modulation in the mid-infrared in group-IV materials. Nevertheless, intensity modulation or phase shifting may be important in MIR sensing circuits for on-chip signal processing and switching, or in phased arrays for beam steering, or in a MIR free-space communication system for modulating a light beam. We have previously published equations that predict the strength of the free-carrier plasma dispersion effect in both Si and Ge in the MIR. We have used those equations to design SOI free carrier injection modulators for 3.8 μm [4], and GOS modulators for 3.8 μm and 8 μm, and fabricated and tested each device. SOI electroabsorption modulators exhibited modulation depths of up to 34 dB, while electrorefraction modulators achieved a modulation efficiency $V_\pi L_\pi$ of 0.052 V.mm with a modulation depth of 22 dB and data rate of 125 Mbit/s. GOS electroabsorption modulators achieved a modulation depth greater than 35 dB at 3.8 μm, and it was found that the free carrier absorption is approximately 4.9 times stronger at 8 μm.

ACKNOWLEDGEMENTS

This work is supported by the Royal Academy of Engineering (RF201617/16/33), Engineering and Physical Sciences Research Council (EP/N00762X/1, EP/N013247/1, EP/R004951/1), and by the National Research Foundation of Singapore (NRF-CRP12-2013-04).

REFERENCES

[1] J. S. Penadés *et al.*, "Suspended silicon waveguides for long-wave infrared wavelengths," *Opt. Lett.*, vol. 43, no. 4, pp. 795–798, 2018.

[2] M. Nedeljkovic *et al.*, "Germanium-on-silicon waveguides operating at mid-infrared wavelengths up to 8.5 μm," *Opt. Express*, vol. 25, no. 22, pp. 27431–27441, 2017.

[3] A. Osman *et al.*, "Suspended low-loss germanium waveguides for the longwave infrared," *Opt. Lett.*, vol. 43, no. 24, pp. 5997–6000, 2018.

[4] M. Nedeljkovic *et al.*, "Silicon-on-insulator free-carrier injection modulators for the mid-infrared," *Opt. Lett.*, vol. (in press), 2018.

Nanophotonics Integration for Astrophotonics

(Invited paper)

Mario Dagenais
Department of Electrical and Computer Engineering, University of Maryland, College Park, MD 20742
e-mail: dage@ece.umd.edu

ABSTRACT

Astrophotonics is used to reject sharp emission lines in the earth atmosphere and allows for the observation of the spectrum of faint celestial objects using earth telescopes. An integrated filter is demonstrated that can reject 47 telluric narrow OH lines and that can reach high throughput. A new type of integrated optical filter is also demonstrated that would facilitate the detection of life in the atmosphere of exoplanets with much smaller telescopes.

Keywords: integration, photonics, Bragg gratings, exoplanets, OH lines

TECHNICAL DESCRIPTION

Astrophotonics is the technology at the crossroads between astronomy and integrated nanophotonics that is used to realize more compact optical instruments.[1], [2] This technology can be used to reverse a trend of spiralling costs of instruments for larger telescopes in astronomy. It can also realize high-resolution spectrometers small enough for space telescopes. Current approaches use large lenses, mirrors and gratings. Our approach is to couple the telescope beam directly to a miniature optical-fiber-fed integrated photonic device [1]. In order to do this, one needs to use adaptive optics techniques to make the beam from the telescope to be as close as possible to being diffraction limited. Then the light goes through a photonic lantern. Multimode fibers are required to collect light that has been smeared by atmospheric turbulences. The light is then tapered down to several single mode fibers. Efficient coupling is achieved in both direction if the number m of (unpolarised) excited modes in the MMF is equal to the number of SMFs in the bundle on exit from the taper. At 1.55 µm, the number of supported modes is typically 7, so the lanterns are 1 x 7. High coupling efficiency fiber-to-waveguide couplers developed in our group are used to bring the light from the SMFs of the photonic lantern into waveguides to extract the emission lines (the telluric OH lines) that appear in ground based telescope observations. In our group, we have developed an algorithm (the layer peeling, layer adding algorithm) for making optical filters that reject 96% of the dominant near infrared lines [3]. There are several 100's of OH lines in the spectral region of interest. These lines are narrow (.1 nm) and they appear between 0.8 and 2.3 µm. For our studies, we are mostly interested in wavelengths between 1.0 and 1.7 µm. The filters that we make are based on complex waveguide Bragg gratings (CWBW) to reject narrow lines of 0.1 nm bandwidth, with a rejection ratio above 15-20 dB, while maintaining good throughput between the lines so that the spectrum can be analysed. These CWBGs suppress the OH lines before entering the spectrograph. These lines completely dominates most astronomical targets, in particular faint celestial objects of interest to us whose

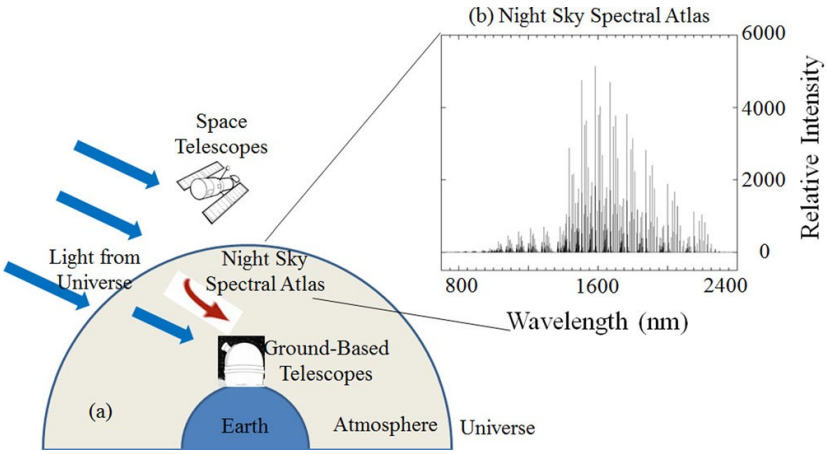


Fig. 1 Ground space telescope operation is hindered by the night sky OH emission lines in the earth atmosphere

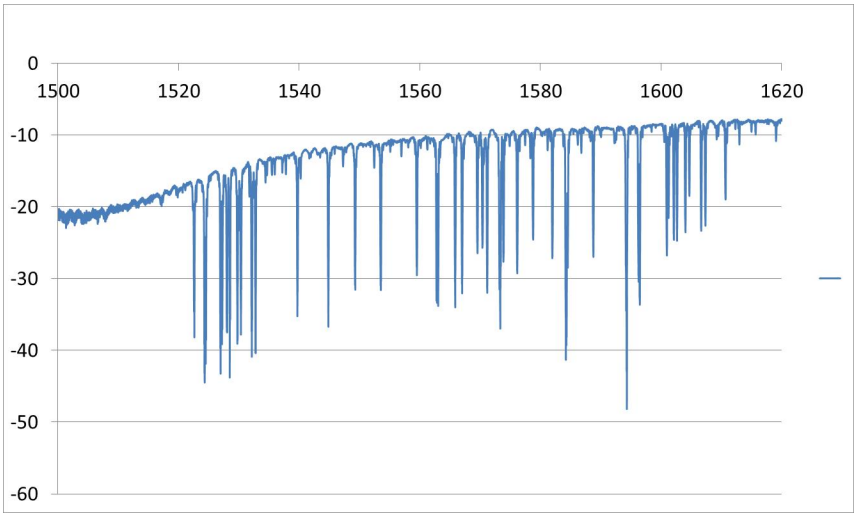


Fig. 2 A complex Bragg grating is used to reject 47 sharp spectral lines with an accuracy better than 0.1 nm over the 1522 – 1610 nm spectral range.

emission is shifted into the near-infrared spectral region due to the universe expansion following the Big Bang. After filtering the OH lines, the light is directed to an arrayed waveguide grating (AWG). The output from the AWG is dispersed vertically using micro prisms to separate the different orders and the light is finally butt-coupled to a cooled 2-dim array of detectors.

Another application of astrophotonics is directed toward searching for biosignatures in the atmosphere of exoplanets. The detection of life on another planet would be one of the greatest discoveries of all time. We would like to come up with an instrument to measure the spectroscopic signature of life in the atmosphere of exoplanets. Recently, an integrated device has been realized that allows the measurement of both the transmitted and the reflected light [4]. Such a device can be used to measure light going through the atmosphere, or reflected by the atmosphere, of a planet. By adjusting the bandwidth and location of the optical filters, it is possible to look at some spectral signature of life in the atmosphere of planets. Fig. 3 shows the calculated transmission and reflection spectrum from an earth-like planet orbiting a M dwarf star [5], [6]. By creating an optical bandpass filter to detect light in the spectral emission range of a life indicator molecule and comparing this light level with the background emission, it is possible to detect the possibility of life on a planet using a much smaller telescope.

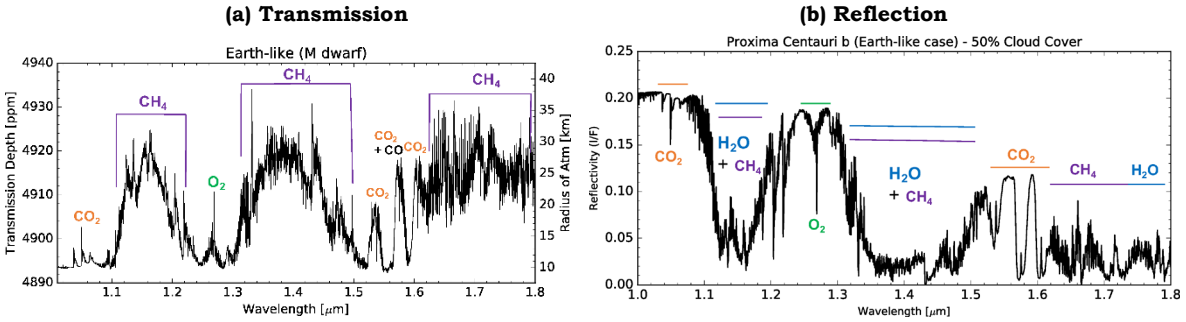


Fig. 3 (a) Transmission spectrum in parts per million (ppm) of the atmosphere of an Earth-like planet orbiting a M dwarf star. (b) Reflectance spectrum of an "Earth analog" orbiting a late M dwarf star similar to Proxima Centauri. (based on Meadows and E. Schwieterman, 2018)

We have implemented such a filter using 2 complex Bragg gratings and two multimode interference splitters. This is shown in Fig. 4.

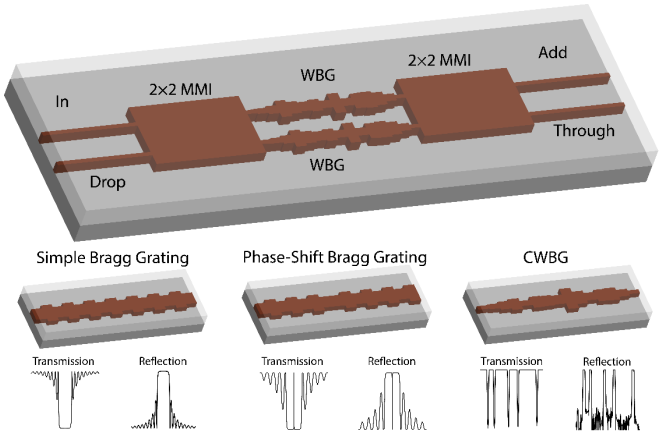


Fig. 4 Implementation of a filter with different transmission/reflection bands that can be used for exoplanet life detection.

CONCLUSION

Two applications of nanophotonic integration are presented. One application facilitates the observation of weak celestial object by rejecting the OH emission lines in the earth atmosphere. In the second application, we have proposed an integrated filter for helping the detection of life signature in earth-like planet orbiting a star.

ACKNOWLEDGEMENTS

The author acknowledges financial support from the Keck Foundation, NSF (awards # ATI 1711377 and EFMA 1741651) and NASA (award # 16-APRA16-0064)

REFERENCES

[1] J. Bland-Hawthorn *et al.*, "PIMMS: photonic integrated multimode microspectrograph," presented at the SPIE Astronomical Telescopes + Instrumentation, San Diego, California, USA, 2010, p. 77350N.

[2] P. Gatkine, S. Veilleux, and M. Dagenais, "Astrophotonic Spectrographs," *Appl. Sci.*, vol. 9, no. 2, p. 290, Jan. 2019.

[3] T. Zhu, Y. Hu, P. Gatkine, S. Veilleux, J. Bland-Hawthorn, and M. Dagenais, "Arbitrary on-chip optical filter using complex waveguide Bragg gratings," *Appl. Phys. Lett.*, vol. 108, no. 10, p. 101104, Mar. 2016.

[4] S. Xie et al., "Add-drop filter with complex waveguide Bragg grating and multimode interferometer operating on arbitrarily spaced channels.," *Optics Lett.*, p. (submitted for publication).

[5] V. S. Meadows *et al.*, "The Habitability of Proxima Centauri b: Environmental States and Observational Discriminants," *Astrobiology*, vol. 18, no. 2, pp. 133–189, 2018.

[6] E. W. Schwieterman *et al.*, "Exoplanet Biosignatures: A Review of Remotely Detectable Signs of Life," *Astrobiology*, vol. 18, no. 6, pp. 663–708, Jun. 2018.

On-chip surface enhanced Raman spectroscopy using ALD grown plasmonic nanotrenches integrated with a silicon nitride slot waveguide

('Student Paper')

Ali Raza [*,1,2], Stéphane Clemmen [1,2,3], Michiel Van Daele [4], Jolien Dendooven [4], Matthew B. E. Griffiths [5], Seán T. Barry [5], Andre Skirtach[2,6], Christophe Detavernier [4], Roel Baets [1,2]

[1]*Ghent University - imec, Technologiepark 126, 9052 Ghent, Belgium*
[2]*Center for Nano- and Biophotonics, Ghent University, Belgium*
[3]*Laboratoire d'information quantique, Université Libre de Bruxelles, 1050 Bruxelles, Belgium*
[4]*Department of Solid State Sciences, COCOON Research Group, Krijgslaan 281, 9000 Ghent, Belgium*
[5]*Department of Chemistry, Carleton University, 1125 Ottawa, Canada*
[6]*Department of Biotechnology, Ghent University, 9000 Ghent, Belgium*
***e-mail: ali.raza@ugent.be**

ABSTRACT

We present an enhanced Raman spectroscopy using sub 10 nm plasmonic nanotrenches directly grown on a silicon nitride slot waveguide using atomic layer deposition (ALD). A novel ALD process for gold deposition at 100° C is used, the precursor and reactant used for this process are Me_3AuPMe_3 and H_2 plasma, respectively. The fabricated Raman sensor exhibits $\sim 1.5 \times 10^{-8}$ pump to Stokes conversion efficiency for a monolayer of 4-Nitrophenol. This is at least an order of magnitude higher than the state of art nanoplasmonic waveguide based Raman sensors.

Keywords: Nanoplasmonics, Integrated Optics, Surface enhanced Raman spectroscopy, Waveguide enhanced Raman spectroscopy, Monolayer sensing, Atomic layer deposition.

1 INTRODUCTION

Surface-enhanced Raman spectroscopy (SERS) is a sensing technique that uses a nanoplasmonic structure to enhance the light in a nanometer-sized gap hence producing high electric field hot spots [2]. The analyte molecules present in these hot spots are then excited and the scattered Raman signal is collected either by a high NA microscope objective or a higher index contrast waveguide. The former technique is called free space SERS and the latter is known as waveguide based SERS [5]. Various nanoplasmonics structures i.e. nanobowties [5], [6] and nanotriangles [10] etc. have been integrated on a photonic platform to demonstrate waveguide based SERS. The fabrication of these plasmonics structures demands high resolution and alignment dependent patterning techniques. Recently, enhanced Raman spectroscopy using a hybrid nanoplasmonic waveguide [1], [7] has been demonstrated whereby mass scalable UV-photolithography is used. Despite all these design and technological advancements, the detection of an ultra-small concentration of weak Raman scatterers, demands further sensitivity improvement. One of the key applications in this regard is the single molecule spectroscopy [12] on a photonic chip.

In this work, we present an on-chip Raman sensor that uses plasmonic nanotrenches directly defined on a single mode silicon nitride Si_3N_4 slot waveguide using atomic layer deposition. Highly conformal ALD of Al_2O_3 and Au allows defining the nanotrenches in a more controlled and uniform fashion all along the waveguide width and length. Furthermore, the gold layer is deposited by a novel gold ALD process. The SERS performance of the resulting sensor is characterized using a monolayer of 4-Nitrophenol.

2 METHODS

2.1 Fabrication

The sensor is fabricated in three steps. In the first step, Si_3N_4 slot waveguides are fabricated using 193 nm optical lithography and subsequently etched by fluorine based inductive coupled plasma-reactive ion-etch process [8] to get the final structure as depicted in Fig. 1. Then a 40 nm layer of Al_2O_3 is deposited using ALD. Finally, a 100 μm window is defined using DUV lithography followed by an ALD deposition of a 24 nm thick gold layer composed of 7.9 nm wide nanotrenches. A home built ALD reactor with a base pressure of 2×10^{-6} mbar is used to deposit the Al_2O_3 and Au layers [3]. Both layers are deposited at a substrate temperature of 100°C. The Al_2O_3 layer is deposited using TMA and H_2O as the precursor and reactant, respectively. The used pressure for both gases is $6\text{x}10^{-3}$ mbar. Au is deposited with a new ALD process, using Me_3AuPMe_3 and H_2 plasma (20% H_2 in Ar) as the precursor and reactant. A pressure of 1 mbar is used for the Au reactant and

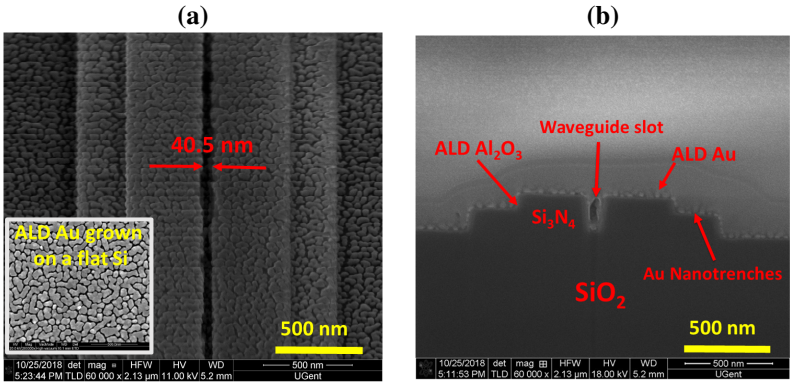


Figure 1. The SEM images of the fabricated on-chip SERS device. a) Top view. Inset shows the Au island directly grown on a flat Si substrate. b) The SEM cross section of the waveguide showing the stack of the material layers.

6x10^{-3} mbar for the hydrogen gas. In order to characterize the free space SERS strength of the ALD gold islands, a nanostructured gold layer is also grown on a flat silicon substrate as shown in Fig. 1.a (inset).

After the patterning, the chip was thoroughly cleaned with Acetone/IPA/DI water and dried with N_2 gun. For the monolayer coating, the chip was immersed in 1mM solution of 4-Nitrophenol (pNTP) in Ethanol. pNTP selectively binds to the gold using a thiol−gold bond.

2.2 Experiment

A confocal Raman microscope (WITEC Alpha 300R+) equipped with 100x/0.9 objective is used to characterize the Raman sensor. We acquire Raman spectra in a back-reflection geometry. A 785 nm laser and -70°C cooled Andor IDUS 401 CCD camera is used. All spectra are recorded using 1 mW pump power and a 1 sec integration time. For on-chip Raman measurements, the light is edge coupled to the waveguide and the polarization is aligned to the TE-mode of the waveguide. Also, same experimental conditions are used for free space SERS substrates. Further details about the experiment are reported in [7].

3 RESULTS AND DISCUSSION

In the first set of experiments, free space SERS performance of ALD gold layers is characterized. In order to optimize the gold thickness, four different thicknesses of ALD gold are deposited on a flat Si substrate using 100, 200, 400 and 800 ALD cycles. The measured Raman spectra are shown in Fig. 2.a (inset). Each spectrum is recorded by optimizing the CCD counts for the 1339 cm^{-1} ($\nu_s(NO_2)$) [4] Raman mode of pNTP . Very weak pNTP peaks were measured with the gold substrate where 100 ALD cycles are used. On the other hand, the stronger pNTP Raman modes appear in a Raman spectrum measured from substrate with 800 ALD gold cycles. This is attributed to the formation of nanotrenches $\simeq$ 7.9 nm size that lead to a huge field enhancement. Based on the 1339 cm^{-1} Raman mode, the pump to Stokes conversion efficiency (P_s/P_p) is measured using the method reported in [6]. The measured values of P_s/P_p are shown in Fig. 2.a. A highest value of P_s/P_p = $(8.7 \pm 0.4) \times 10^{-9}$ is recorded for the 800 ALD cycles SERS substrate. This is almost one order of magnitude weaker than state of art free space SERS substrates such as a nanodome substrate [11] with $P_s/P_p \sim 7 \times 10^{-8}$. However, it is worth mentioning that in the present case, a nanoplasmonic gap of 7.9 nm is achieved without any patterning technique and with further optimization of ALD gold process, P_s/P_p can be greatly enhanced.

After the free space SERS characterization, the Raman spectrum is measured using an on-chip SERS sensor. The spectrum is shown in Fig. 2. b. In order to reduce the silicon nitride background [9], the length of the access waveguide is limited to 1 μm. The measured spectrum contains all the pNTP Raman modes. The measured P_s/P_p measured for the 1339 cm^{-1}mode is $\sim 1.5 \times 10^{-8}$. Note that a coupling loss of 4.2 dB/facet has been taken into account for the on-chip P_s/P_p value. This is $\sim$ 2 times stronger than its free space counterpart. This is attributed to the long interaction length (few microns), leading to an efficient excitation and collection of Raman signal. Also, this is an order of magnitude stronger than the previously reported nanoplasmonic waveguide based on-chip Raman sensor where P_s/P_p = $(1.0 \pm 0.057) \times 10^{-9}$ [7]. This substantial improvement is ascribed to the formation of 7.9 nm wide nanotrenches inside Si_3N_4 slot waveguide. This leads to an efficient modal overlap between a photonic and a plasmonic mode hence producing a huge Raman enhancement $|E|^4$.

CONCLUSION

We have reported a SERS sensor for an on-chip Raman spectroscopy using a novel ALD process of gold. Me_3AuPMe_3 and H_2 plasma are used as the precursor and reactant, respectively. The formation of 7.9 nm wide nanotrenches along the width and length of the Si_3N_4 slot waveguide leads to a large pump to Stokes

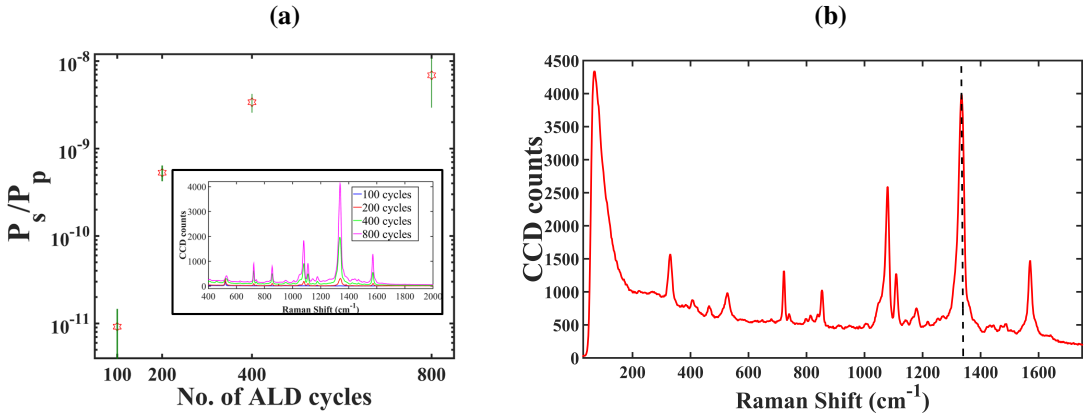


Figure 2. a) The pump to Stokes (P_s/P_p) conversion efficiency of ALD grown Gold on a flat Si substrate. The inset shows the Raman spectra of NTP measured from SERS substrates grown with four different number ALD cycles. b) The NTP Raman spectrum measured from an on-chip Raman sensor. The dotted line at 1339 cm^{-1} represents the strongest mode of pNTP ($\nu_s(NO_2)$).

conversion efficiency of 1.5 $\times$ 10^{-8}. This is the highest on-chip pump to Stokes conversion efficiency known to the date.

ACKNOWLEDGMENT

The authors acknowledge Liesbet Van Landschoot (UGent) for taking the SEM images. This research was funded by the FWO Belgium. Stéphane Clemmen thanks the F.R.S-FNRS for financial support. We also acknowledge the support of BOF (UGent, Belgium).

REFERENCES

[1] Q. Cao, J. Feng, H. Lu, H. Zhang, F. Zhang, and H. Zeng. Surface-enhanced Raman scattering using nanoporous gold on suspended silicon nitride waveguides. *Opt. Express*, 26(19):24614–24620, Sep 2018.

[2] E. Le Ru and P. Etchegoin. *Principles of Surface-Enhanced Raman Spectroscopy: and related plasmonic effects*. Elsevier, 2008.

[3] E. Levrau, K. Van de Kerckhove, K. Devloo-Casier, S. Pulinthanathu Sree, J. A. Martens, C. Detavernier, and J. Dendooven. In situ ir spectroscopic investigation of alumina ald on porous silica films: Thermal versus plasma-enhanced ald. *The Journal of Physical Chemistry C*, 118(51):29854–29859, 2014.

[4] M. A. Mahmoud. Surface-enhanced Raman spectroscopy of double-shell hollow nanoparticles: Electromagnetic and chemical enhancements. *Langmuir*, 29(21):6253–6261, 2013. PMID: 23647422.

[5] F. Peyskens, A. Dhakal, P. Van Dorpe, N. Le Thomas, and R. Baets. Surface enhanced Raman spectroscopy using a single mode nanophotonic-plasmonic platform. *ACS Photonics*, 3(1):102–108, 2016.

[6] F. Peyskens, P. Wuytens, A. Raza, P. Van Dorpe, and R. Baets. Waveguide excitation and collection of surface-enhanced Raman scattering from a single plasmonic antenna. *Nanophotonics*, 2018.

[7] A. Raza, S. Clemmen, P. Wuytens, M. Muneeb, M. Van Daele, J. Dendooven, C. Detavernier, A. Skirtach, and R. Baets. ALD assisted nanoplasmonic slot waveguide for on-chip enhanced Raman spectroscopy. *APL Photonics*, 3(11):116105, 2018.

[8] A. Z. Subramanian, P. Neutens, A. Dhakal, R. Jansen, T. Claes, X. Rottenberg, F. Peyskens, S. Selvaraja, P. Helin, B. D. Bois, K. Leyssens, S. Severi, P. Deshpande, R. Baets, and P. V. Dorpe. Low-loss singlemode pecvd silicon nitride photonic wire waveguides for 532 x2013;900 nm wavelength window fabricated within a cmos pilot line. *IEEE Photonics Journal*, 5(6):2202809–2202809, Dec 2013.

[9] N. L. Thomas, A. Dhakal, A. Raza, F. Peyskens, and R. Baets. Impact of fundamental thermodynamic fluctuations on light propagating in photonic waveguides made of amorphous materials. *Optica*, 5(4):328–336, Apr 2018.

[10] P. C. Wuytens, A. G. Skirtach, and R. Baets. On-chip surface-enhanced Raman spectroscopy using nanosphere-lithography patterned antennas on silicon nitride waveguides. *Opt. Express*, 25(11):12926–12934, May 2017.

[11] P. C. Wuytens, A. Z. Subramanian, W. H. De Vos, A. G. Skirtach, and R. Baets. Gold nanodome-patterned microchips for intracellular surface-enhanced Raman spectroscopy. *Analyst*, 140(24):8080–8087, 2015.

[12] R. Zhang, Y. Zhang, Z. Dong, S. Jiang, C. Zhang, L. Chen, L. Zhang, Y. Liao, J. Aizpurua, Y. e. Luo, et al. Chemical mapping of a single molecule by plasmon-enhanced Raman scattering. *Nature*, 498(7452):82, 2013.

Mid-infrared absorption spectroscopy of protein aggregates using germanium on silicon waveguides

V. Mittal[1], G. Devitt[2], P.N. Bartlett[3], H. M. H. Chong[4], G. Z. Mashanovich[1], S. Mahajan[2] and J. S. Wilkinson[1]

[1] Optoelectronics Research Centre, University of Southampton, Southampton, SO17 1BJ United Kingdom
[2] Institute for Life Sciences, University of Southampton, Southampton, SO17 1BJ United Kingdom
[3] School of Chemistry, University of Southampton, Southampton, SO17 1BJ United Kingdom
[4] School of Electronics and Computer Science, University of Southampton, Southampton, SO17 1BJ United Kingdom
e-mail: v.mittal@soton.ac.uk

ABSTRACT

Proteins in human samples can be used to detect the onset of a group of neurodegenerative diseases such as Alzheimer's and Parkinson's by studying their conformational (shape and structure) changes that can cause cognitive impairment. Proteins form aggregates from normal state (monomers) to disease state (amyloid deposition and fibril formation in central nervous system) that is associated with disease progression. These changes can be diagnosed and monitored using mid-infrared (MIR) absorption spectroscopy by studying line shapes and relative absorbance of amide bands. We have demonstrated MIR spectroscopy of proteins in three stages of aggregation: monomers, oligomers and fibrils of Bovine Serum Albumin (BSA) protein on a germanium on silicon (GOS) waveguide in the MIR wavelength region of 5.2 – 10 μm (1900 – 1000 cm^{-1}). The protein samples were also characterised by atomic force microscopy to confirm their structure.

Keywords: mid-infrared, spectroscopy, protein, waveguide, integrated optics, biosensing

1. INTRODUCTION

The MIR region corresponding to the spectral range from 2-25 μm of the electromagnetic spectrum coincides with the molecular vibrational energies. When MIR light is passed through a sample, intermolecular bonds are excited to the higher vibrational states by absorbing the same energy as the difference between its ground and excited states [1]. This enables sensing of unknown analytes using their fingerprint absorption spectra in this region to detect specific bonds. Fourier transform infrared (FTIR) spectroscopy is routinely used for the analysis of bio-chemical species to determine analytical information. However, due to the strong water absorption in the MIR, cuvette length longer than 10-20 μm cannot normally be used and narrow cuvettes tend to clog with real samples. Attenuated total reflection (ATR) spectroscopy combined with FTIR has been used to overcome this problem. However, the number of discrete reflections in a conventional ATR element is severely limited while using an optical waveguide, which is essentially a thinner ATR element, greatly increases the effective number of reflections per unit length to the extent that in a monomode waveguide a continuous evanescent wave is achieved along the waveguide surface, significantly improving the sensitivity of the device for a given length and have sample volume. MIR evanescent field absorption spectroscopy offers high selectivity over a wide range of compounds and requires less sample volume than the other conventional techniques. Current microfabrication technologies render optical chip mass-producible and hence low-cost as well as allowing integration of various optoelectronics and microfluidics components on the same chip.

Proteins are key functional biomolecules in life and their aggregation is a pathological hallmark for determining neurodegenerative diseases. Conformational changes in aggregation results in the deposition of β-sheet rich toxic amyloids or fibril formation which are both associated with disease progression [2]. The MIR absorption in proteins predominantly occurs due to vibrations of the polypeptide backbones also referred to as amide bands. The amide I, II and III bands lie at wavelengths between 5-10 μm and are used as marker of secondary protein structure. The amide peaks can be analysed by spectral deconvolution to study the structure of proteins and their aggregates.

2. EXPERIMENTAL WORK

2.1 Waveguide fabrication and characterisation

A 3 μm thick GOS 6 inch wafer from IQE Silicon Compounds Ltd was used to fabricate the waveguides. Multimode waveguides of 20 μm wide were patterned lithographically and etched using fluorine chemistry in an inductively coupled plasma (ICP). The end facets were prepared using ductile dicing. Waveguide measurements were carried out using the apparatus shown in Fig.1 a). A quantum cascade laser (QCL) (Block Engineering Inc.) tunable from 1900-800 cm-1 (wavelength of 5.3 – 12.9 μm) was used as the light source and two zinc selenide

(ZnSe) objective lenses were used for input and output coupling. Prior to taking transmission spectra the QCL was set to 12.9 µm and the waveguide output was imaged on an infrared camera (Xenics-Gobi 640) following alignment, and the output intensity profile in TM polarisation is shown in Fig. 1 b).). Simulation of modal intensity distributions (COMSOL) in TM polarisation show a FWHM of 10.1 µm and 2.3 µm, along the x and y axis respectively. A thermoelectrically-cooled mercury cadmium telluride (MCT) detector (VIGO System) was used to record the signal from the collection objective lens. The signal from the MCT detector was recorded on a computer which also tuned the QCL, and a software package (LaserTune), was used to process the spectra. As a simple paper-based fluidic structure, a strip of filter paper is used to introduce aqueous analyte onto the surface of the waveguide and to define the evanescent absorption pathlength. A parafilm cover was used on top of the filter paper to avoid sample evaporation. It has been established that the presence of filter paper on the surface of waveguide does not itself significantly alter the optical transmission [3].

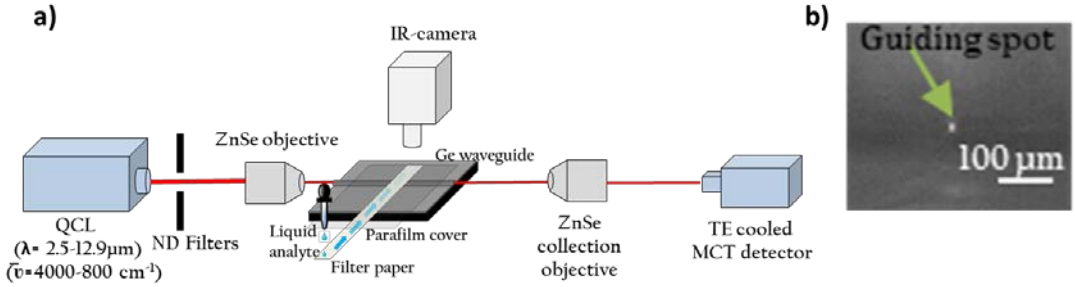


Figure. 1. a) Experimental apparatus and b) Infrared camera image of the GOS waveguide output at a wavelength of 12.9 µm.

2.2 Protein sample preparation

A 900 µM BSA (Sigma Aldrich) solution of the monomeric protein was prepared by mixing it in double distilled water (pH = 3). The monomer solution was kept in an Eppendorf tube in a water bath maintained at 65ºC for 10 min to form agglomerates called Oligomers. To make fibrils, the monomer solution in an Eppendorf tube was kept for 24 hours in the water bath maintained at 65 ºC. For AFM measurement, the fresh protein samples were diluted 1/1000 and then allowed to bind to a mica substrate for two minutes, which was then washed 4 times in double distilled water and allowed to dry. For MIR absorption spectroscopy, the proteins samples stored in Eppendorf tube were introduced on the waveguide surface by using a pipette.

.

3. RESULTS AND DISCUSSION

AFM was performed to confirm protein aggregation before taking the MIR measurements. Fig. 2 (a), (b) and (c) shows the 1µm x 1µm AFM images of the monomers, oligomers and fibrils of BSA protein respectively. It is clearly observed from the images that the monomers aggregate together to form bigger assemblies known as oligomers as seen in Fig. 2 (b) and to form ribbon-like structures known as fibrils as observed in Fig. 2 (c).

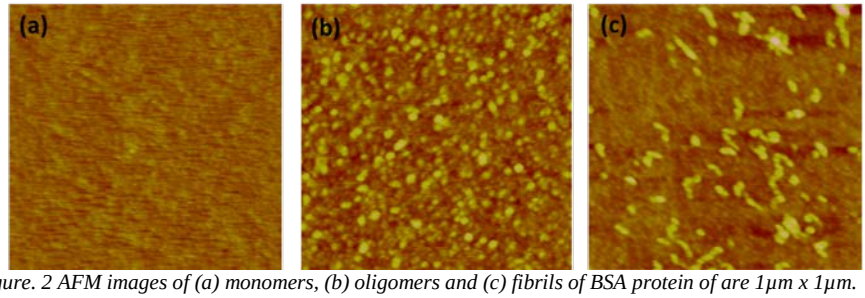


Figure. 2 AFM images of (a) monomers, (b) oligomers and (c) fibrils of BSA protein of are 1µm x 1µm.

The BSA absorption spectra aqueous buffer and the monomers, oligomers and fibrils at the surface of the waveguide were measured using a 2 mm wide, 4 cm long filter paper strip placed on the surface of the waveguide as shown in Fig. 1.The aqueous buffer (water) from the Eppendorf tube was pipetted onto the tail of the filter paper to allow it to travel to the waveguide and a transmission spectrum with buffer alone was first recorded as a reference spectrum. Then the waveguide surface was cleaned and a monomer solution was pipetted on a fresh filter paper of a similar width. The transmission spectrum for the monomer sample was then recorded. The transmitted power

spectrum from the monomer sample was divided by the transmitted power spectrum from the buffer reference spectrum, and the resultant monomer absorption spectrum was obtained. 10 sample scans were taken and averaged and the data were smoothed using 10-point adjacent averaging. Oligomer and fibril samples were measured in the same way and their absorption spectra are shown in Fig. 3(a). The amide I, II and III peaks at 1650 cm^{-1}, 1540 cm^{-1} and between 1200-1350 cm^{-1}, respectively, are clearly observed. Fig. 3 (b) shows the amide I and II region of the absorption spectra taken from Fig. 3 (a) to clarify that the absorption peaks shift towards higher frequencies with aggregation. For the amide I peak, the absorption frequency for monomers and oligomers are both at 1650 cm^{-1}, whereas for fibrils it has shifted to 1660 cm^{-1}. For the amide II peak, the absorption frequency for monomers is at 1540 cm^{-1}, that of oligomers is at 1545 cm^{-1} and that of fibrils are at 1550 cm^{-1}.

Shifts in peak absorption frequencies and an increase in both amide I and II has been observed from monomer to fibril formation and indicates in β-sheet secondary structure. The increase in absorbance may be due to an increased amount of sample in the focal volume because fibrils are far larger than monomers. Fibrils are also insoluble in water so they may deposit onto the surface of the waveguide as a solid film hence increasing the absorbance.

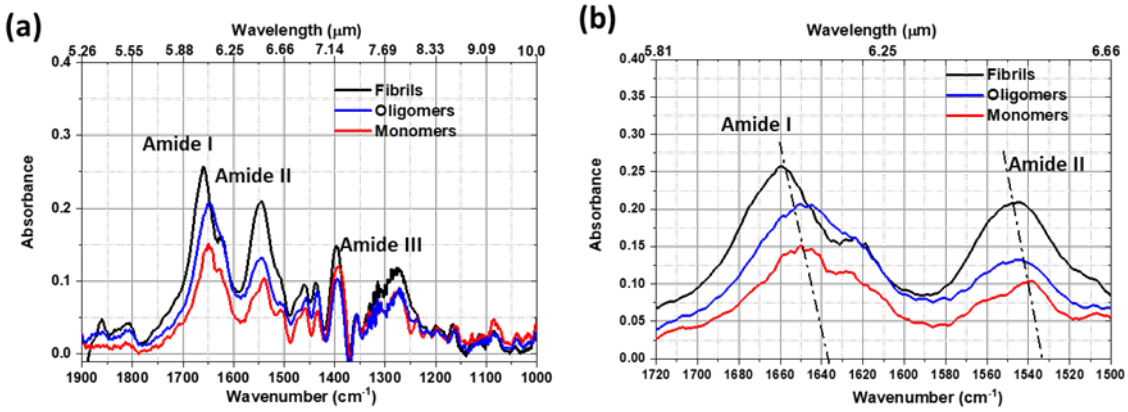


Figure. 3 (a) Waveguide absorption spectra of BSA for monomers, oligomers and fibrils of BSA and (b) zoomed in spectra from (a) to show the peak shifts for the amide I and II peaks.

4. CONCLUSIONS

Germanium on silicon waveguides were fabricated and evanescent field absorption spectroscopy was demonstrated using aqueous solutions of bovine serum albumin. The spectroscopy of monomers and both oligomers and fibrils clearly demonstrated their Amide I, II and III absorption peaks in the MIR region between 1900 cm^{-1} and 1000 cm^{-1}. Changes in the absorption frequencies, absorption strength and lineshapes of the Amide I and II peaks is observed which can potentially be used to distinguish between the three stages of agglomerate formation and can help in early diagnosis of clinically relevant neurodegenerative diseases. In future, deconvolution of line shapes for different secondary structures (α-helix, β-sheets and random coils and turns) of amide bands will be studied in detail using multivariate analysis.

ACKNOWLEDGEMENTS

The authors would like to acknowledge the EPSRC Electronic-Photonic Convergence Platform grant (EP/N013247/1), a Royal Society Wolfson Research Merit Award**,** European Research Council (IDEAS-ERC) (FP7/2007-2013, No. 291216) and ERC grant (NanoChemBiovision 638258).

REFERENCES

[1] A. I. López-Lorente, *et al.:* Mid-infrared thin-film diamond waveguides combined with tunable quantum cascade lasers for analyzing the secondary structure of proteins. *Phys. Status Solidi A,* vol. 213 pp. 2117-2123, 2016.

[2] G. Devitt, *et al.:* Raman spectroscopy: An emerging tool in neurodegenerative disease research and diagnosis, *ACS Chem. Neurosci.*, vol. 9. pp. 404-420, 2018.

[3] V. Mittal *et al.:* Chalcogenide glass waveguides with paper-based fluidics for mid-infrared absorption spectroscopy, *Opt. Lett.* vol. 43, pp. 2913-2916, 2018.

Silicon high performance devices using subwavelength structures

(Invited paper)

Robert Halir[1,2], Alejandro Sánchez-Postigo[1], Jose M. Luque-González[1], Alaine Herrero-Bermello[3], Jonas Leuermann[2], Alejandro Ortega-Moñux[1], Gonzalo Wangüemert-Pérez[1,2], Aitor V. Velasco[3], Jose de-Oliva-Rubio[1], Jens H. Schmid[4], Pavel Cheben[4], Jordi Soler Penadés[5], Milos Nedeljkovic[5], Goran Z. Mashanovich[5], and Íñigo Molina-Fernández[1,2]

[1] Universidad de Málaga, Departamento de Ingeniería de Comunicaciones, ETSI Telecomunicación, Spain
[2] Bionand Center for Nanomedicine and Biotechnology, Málaga, Spain
[3] Instituto de Óptica, Consejo Superior de Investigaciones Científicas, Madrid, Spain
[4] National Research Council Canada, Ottawa, Ontario, Canada
[5] Optoelectronics Research Centre, University of Southampton, Southampton, UK
e-mail: rhalir@uma.es

ABSTRACT

Silicon photonics is poised to solve challenges in areas such as datacom, environmental monitoring and diagnostics, by leveraging the economies of scale afforded by CMOS manufacturing. This requires a wide variety of integrated silicon devices, including fiber-to-chip couplers, polarization splitters and waveguide couplers, operating both in the near-infrared and the mid-infrared wavelength range. However, the reduced set of materials available in this platform can often limit the performance of these devices. Subwavelength structures enable the synthesis of optical metamaterials, with properties than can be tuned to enhance device performance, by using fully etched silicon structures with a periodicity smaller than the wavelength of light. Here we review the basic operating principles of these structures, discuss how to efficiently model them, and report on the latest advances in this rapidly growing field.

Keywords: silicon photonics, subwavelength structures, dielectric metamaterials, high performance devices

SILICON SUBWAVELENGTH STRUCTURES

More than 130 years ago, Hertz used wires spaced at a subwavelength pitch to synthesize artificial materials which he used to study the polarization of electromagnetic waves [1]. The same principle of subwavelength engineering is currently used in silicon photonics: by segmenting silicon waveguides with a pitch below the wavelength of the propagating mode an equivalent medium is created, which exhibits both controllable refractive index and dispersion [2]. This has enabled polarization independent fiber-to-chip couplers with insertion losses below 1dB, waveguide couplers with bandwidths exceeding 300nm, as well as mid-infrared waveguides that can be fabricated in a single etch step and exhibit losses below 1dB/cm, to name a few examples [3]. Such devices are key enablers for systems such as ultra-broadband coherent receivers or integrated midinfrared sensors for environmental monitoring. Subwavelength structures typically exhibit feature sizes of the order of 100nm and larger, so that they can be fabricated using CMOS lines, paving the way for widespread adoption in silicon photonics. Recently reported strategies to furthermore gain control over the anisotropy of the metamaterial open exciting new possibilities for the subwavelength structures [4].

ACKNOWLEDGEMENTS

This work was supported by the Ministerio de Economía y Competitividad, Programa Estatal de Investigación, Desarrollo e Innovación Orientada a los Retos de la Sociedad (cofinanciado FEDER), Proyecto TEC2016-80718-R, and the Universidad de Málaga.

REFERENCES

[1] H. Hertz.: Ueber Strahlen elektrischer Kraft, *Wiedemanns Ann.*, vol. 36, p. 769, 1888.
[2] P. Cheben, *et al.*: Subwavelength integrated photonics, *Nature*, vol. 560, pp. 565–572, 2018
[3] R. Halir, *et al.*: Subwavelength-Grating metamaterial structures for silicon photonic devices, *Proc. IEEE*, vol. 106, pp. 2144–2157, 2018
[4] J. M. Luque-González, *et al.*: Tilted subwavelength gratings: controlling anisotropy in metamaterial nanophotonic waveguides, *Opt. Lett.*, vol. 43, pp. 4691–4694, 2018

Dual-polarization Ultra-wideband Nanophotonic Beam Splitter

David González Andrade[1], Christian Lafforgue[2,3], Elena Durán-Valdeiglesias[2], Xavier Le Roux[2], Mathias Berciano[2], Eric Cassan[2], Delphine Marris-Morini[2], Aitor V. Velasco[1], Pavel Cheben[4], Laurent Vivien[2], Carlos Alonso-Ramos[2,*]

[1] Instituto de Óptica Daza de Valdés, Consejo Superior de Investigaciones Científicas (CSIC), Madrid 28006, Spain

[2] Centre de Nanosciences et de Nanotechnologies, CNRS, Université Paris-Sud, Université Paris-Saclay, C2N, Orsay 91405, France

[3] École Normale Supérieure Paris-Saclay, Université Paris-Saclay, Cachan 94230, France

[4] National Research Council Canada, 1200 Montreal Road, Ottawa, Ontario K1A0R5, Canada

e-mail: Carlos.Ramos@u-psud.fr

ABSTRACT

High-performance optical beam splitters are of fundamental importance for the development of advanced silicon photonics integrated circuits. However, the performance of state-of-the-art silicon nanophotonic splitters is limited in terms of bandwidth and polarization dependence. Here, we present a new beam splitter approach that exploits modal engineering in slotted waveguides to overcome these limitations, enabling ultra-broadband polarization-insensitive optical power splitting. The proposed splitter relies on a single-mode slot waveguide that is gradually transformed into two strip waveguides by a symmetric taper, yielding equal power splitting. Based on this concept, we experimentally demonstrate insertion loss and power imbalance lower than 1 dB for both, transverse-electric (TE) and transverse-magnetic (TM) polarizations in an unprecedented bandwidth of 390 nm (1260 - 1650 nm).

Keywords: beam splitter, silicon-on-insulator, ultra-wideband, dual-polarization.

1. INTRODUCTION

The high index contrast in Si wire waveguides enables the implementation of ultra-compact photonic circuits. However, this tight modal confinement also poses important challenges for the realization of polarization-independent circuits with a large bandwidth. Hence, silicon-on-insulator (SOI) circuits typically operate in a single polarization state, within a limited wavelength range. More specifically, the performance of conventional silicon beam splitters is particularly limited by the strong wavelength and polarization sensitivity of the SOI platform.

Several beam splitters with different advantages and limitations have been proposed over the past few years. Directional couplers (DCs) are typically narrowband and exhibit a strong polarization dependence [1],[2]. Silicon-bent [3] and subwavelength-grating-assisted DCs [4] have recently been demonstrated to exhibit polarization-independent or ultra-broadband behaviour separately. Y-junctions suffer from strong insertion loss due to the abrupt discontinuity at the branch intersection. Different Y-branch variations have been recently reported, alleviating this limitation with relatively broad bandwidths [5],[6]. Multimode interference couplers (MMIs) achieve low losses but provide only limited bandwidth- and polarization-dependent behaviour. Sub-wavelength engineering has been applied to increase the operational bandwidths of MMIs [7], but only in single-polarization operation.

In this work, we present a novel beam splitter concept harnessing modal engineering in slotted waveguides to provide ultra-broadband and polarization-independent operation. We experimentally show insertion loss and power imbalance below 1 dB in an unprecedented bandwidth of 390 nm for both the transverse-electric (TE) and transverse-magnetic (TM) polarizations.

2. DESIGN

The proposed beam splitter is schematically shown in Fig. 1. A single-mode slot waveguide is used to equally split the injected power into two output strip waveguides in a wavelength- and polarization-agnostic fashion. The proposed device comprises three sections: a strip-to-slot mode converter, a slot waveguide and a slot-to-strip splitting transition. The single-mode operation of the slot waveguide is of fundamental importance to our device as it precludes any wavelength-dependent mode beating, which is the main bandwidth limitation in DCs and MMIs. The adiabatic strip-to-slot mode converter circumvents any abrupt index discontinuity, which is the major source of loss in conventional Y-junctions. In addition, the symmetric slot-to-strip transition yields equal power splitting between the two output waveguides, independent of the polarization and wavelength.

For the design of the splitter, we considered 220-nm-thick Si with a buried silicon dioxide layer (BOX) and polymethyl methacrylate (PMMA) upper cladding. Input and output waveguides have a width of and W_I = 450 nm. In the optimized splitter, the central slot waveguide has a rail width of W_R = 150 nm and a slot width of G_S = 100 nm, that ensure single-mode behaviour in the wavelength range between 1200 nm and 1700 nm. The lengths of the different sections of the coupler are optimized to minimize insertion loss by 3D EME simulations [8].

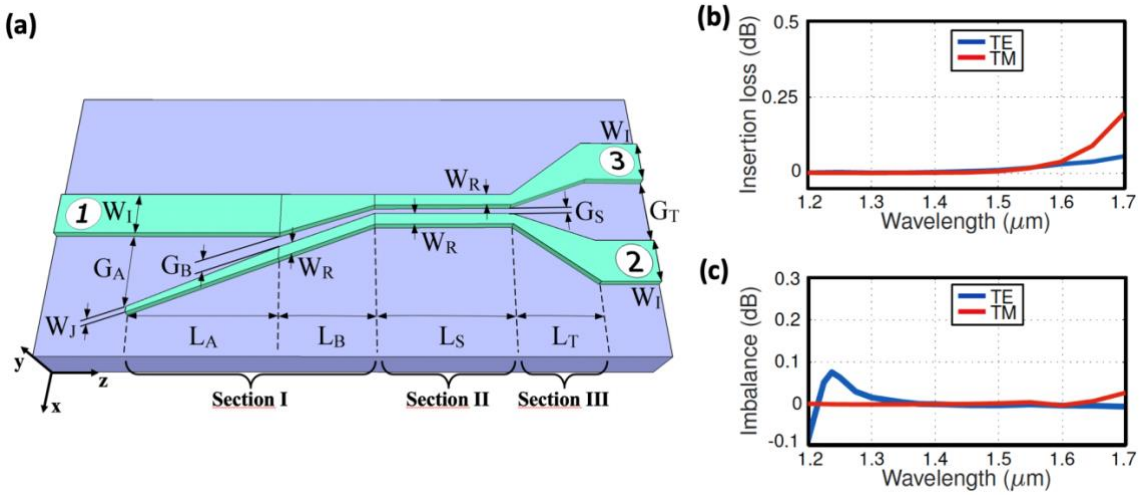


Figure 1. (a) Schematic of the proposed nanophotonic beam splitter based on single-mode slot waveguide. Calculated insertion loss (b) and power imbalance (c) for the optimized splitter considering both, TE and TM polarizations.

To assess the performance of the splitter, we considered the insertion loss (IL), defined as the amount of power relative to the input power that is not transferred to any output, and the imbalance (IB), defined as the power difference between the two output ports. As shown in Figs. 1(b) and (c), the proposed splitter yields calculated IL lower than 0.5 dB and imbalance better than 0.3 dB for both, TE and TM polarizations in the wavelength range between 1200 nm and 1700 nm.

3. EXPERIMENTAL RESULTS

The silicon beam splitter was fabricated using electron beam lithography (Nanobeam NB-4 system, 80 kV) and dry etch process. Then, the circuits were covered with a 1-μm-thick PMMA layer. Figure 2 shows the scanning electron microscope (SEM) images of the fabricated device.

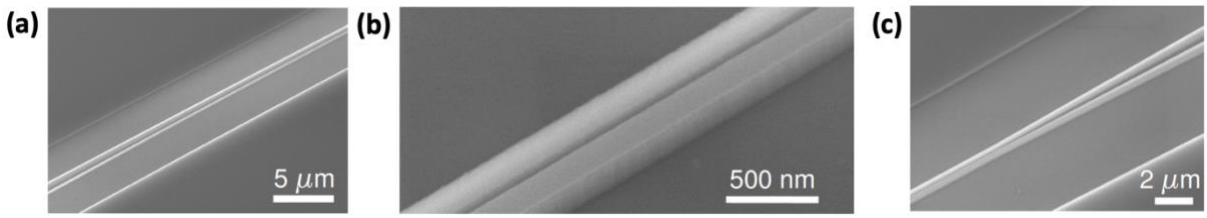


Figure 2. Scanning electron microscope (SEM) images of the fabricated device, showing (a) strip-to-slot transition at the input of the splitter, (b) central slot region, and (c) slot-to-strip transition at the output of the splitter.

To experimentally characterize the splitter, we used two configurations: a Mach-Zehnder interferometer (MZI) and cascaded splitters. The MZI configuration allows precise estimation of the imbalance, while the configuration comprising cascaded splitters allows accurate characterization of the insertion loss.

In the MZI configuration, two identical splitters are connected in a back-to-back configuration with an arm length difference of 40 μm. We estimated the power imbalance from the measured extinction ratio. As shown in Fig. 3(a), our splitter ensures an imbalance below 1 dB in the full wavelength range for both polarizations.

To characterize insertion loss, we cascaded five beam splitter stages. Insertion loss is extracted from the linear regression fitting of the transmission in the five splitters. Figure 3(b) shows that the proposed splitter provides insertion loss lower than 1 dB in a 390 nm bandwidth, between 1260 nm and 1650 nm wavelength, for both TE and TM polarizations.

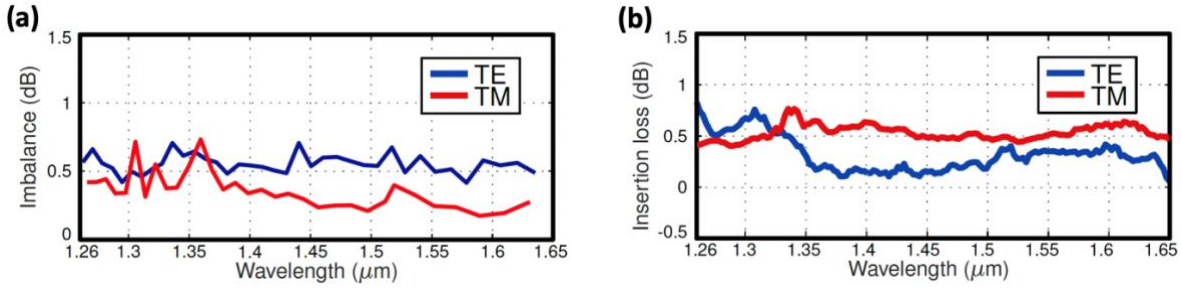


Figure 3. (a) Experimental power imbalance extracted from the measured extinction ratio in a MZI comprising two identical slot-based power splitters. (b) Measured insertion loss of a single splitter extracted from measurement of 5 cascaded splitters.

4. CONCLUSIONS

In conclusion, we report the experimental demonstration of an ultra-broadband and polarization-independent optical beam splitter. The proposed device relies on a single-mode slot waveguide with a symmetric slot-to-strip transition. The single-mode operation of the slotted section prevents wavelength-dependent mode beating, which is the major bandwidth limitation in conventional DCs and MMIs. On the other hand, the symmetric geometry ensures equal power splitting for both the TE and TM, independent of the wavelength. Based on this concept, we experimentally show near-ideal power splitting with insertion loss and power imbalance below 1 dB for both TE and TM polarizations, covering the O, E, S, C and L telecommunication bands. The proposed optical beam splitter opens new venues for the implementation of dual-polarization and ultra-broadband silicon photonics circuits.

ACKNOWLEDGEMENTS

This work has been funded in part by the Spanish Ministry of Science, Innovation and Universities under grants TEC2015-71127-C2-1-R (FPI scholarship BES-2016-077798) and IJCI-2016-30484; and the Community of Madrid (P2018/NMT-4326). This project has received funding from the Horizon 2020 research and innovation program under the Marie Sklodowska-Curie grant No. 734331. This work has been partially funded by the Agence National pour la Recherche, Project MIRSPEC (ANR-17-CE09-0041) and the H2020 European Research Council (ERC) (ERC POPSTAR 647342).

The sample fabrication has been performed at the Plateforme de Micro-Nano-Technologie/C2N, which is partially funded by the "Conseil Général de l'Éssonne". This work was partly supported by the French RENATECH network.

REFERENCES

[1] Y. Wang, *et al.*: Compact broadband directional couplers using subwavelength gratings, *IEEE Photonics J.*, vol. 8, pp. 1–8, May 2016.
[2] R. Halir, *et al.*: Colorless directional coupler with dispersion engineered sub-wavelength structure, *Opt. Express*, vol. 20, pp. 13470–13477, May 2012.
[3] X. Chen, *et al.*: Polarization-insensitive broadband 2x2 3 dB power splitter based on silicon-bent directional couplers, *Opt. Lett.*, vol. 42, pp. 3738–3740, Oct. 2017.
[4] H. Yun, *et al.*: Ultra-broadband 2x2 adiabatic 3 dB coupler using subwavelength-grating-assisted silicon-on-insulator strip waveguides, *Opt. Lett.*, vol. 43. pp. 1935–1938, Apr. 2018.
[5] Y. Zhang, *et al.*: A compact and low loss Y-junction for submicron silicon waveguide, *Opt. Express*, vol. 21, pp. 1310–1316, Jan. 2013.
[6] Y. Wang, *et al.*: Ultra-broadband and low-loss 3 dB optical power splitter based on adiabatic tapered silicon waveguides, *Opt. Lett.*, vol. 41, pp. 2053–2056, May 2016.
[7] R. Halir, *et al.*: Ultra-broadband nanophotonic beamsplitter using an anisotropic sub-wavelength metamaterial, *Laser Photonics Rev.*, vol. 10, pp. 1039–1046, Nov. 2016.
[8] MODE Solutions, Lumerical Solutions Inc. http://www.lumerical.com/.

Processing free space optical beams with a silicon photonic mesh

(Student Paper)

Maziyar Milanizadeh[1], Piero Borga[1], Francesco Morichetti[1], D.A.B. Miller[2], Andrea Melloni[1]
[1]Dipartimento di Elettronica, Informazione e Bioingegneria - Politecnico di Milano, Milano, 20133 Italy.
[2]Ginzton Laboratory, Stanford University, Spilker Building, Stanford, CA 94305, USA
mail: maziyar.milanizadeh@polimi.it

ABSTRACT

Photonic integrated meshes made of tuneable interferometers enable us to implement functions programmable on demand and are being envisioned as the optical counterpart of electronic field programmable gate arrays. Several examples of photonics processors capable of performing arbitrary linear operations have been recently proposed, and are expected to find applications in different areas, from the on-chip processing of telecom signals to microwave photonics, and from quantum optics to neural networks. In this work, we use a reconfigurable mesh of silicon photonic Mach-Zehnder Interferometers (MZIs) to manipulate free-space optical beams. Among the variety of functionalities that can be implemented, we demonstrate beam steering, beam coupling from a free space optical source to a single mode waveguide and automatic identification of the direction of arrival of a beam from a free space source.

Keywords: silicon photonics, reconfigurable photonic integrated circuits, free space optics

1. INTRODUCTION

Photonic integrated circuits (PICs) consisting of generic programmable architectures that can be reconfigured during operation are emerging as a promising approach for advanced processing of optical signals. Examples of programmable PICs and optical processors have been recently proposed in different application fields, including microwave photonics [1], mode manipulation in telecommunications [2], quantum [3] and neural networks [4].

Silicon photonics (SiP) is a promising photonic platform for the realization of large scale integration of photonic processors, not only because of the high degree of device miniaturization, but also because of the possibility to integrate fast and power-efficient tuning elements and on-chip monitor photodetectors, which are necessary for robust reconfiguration and control of the photonic architecture. Recently, we demonstrated that a SiP mesh of Mach-Zehnder Interferometers (MZIs) can self-configure to perform automatic reconstruction and unscrambling of guided modes which have been strongly mixed during the transmission through a multimode waveguide. In this work, we demonstrate that the same architecture can be effectively used to manipulate free-space optical beams. A number of optical functions are implemented, including beam steering, beaming back to the source, and identification and coupling of a free space beam coming from an arbitrary direction.

2. SILICON PHOTONIC MESH

The photonic integrated circuit (PIC) consists of a triangular mesh of Mach-Zehnder Interferometers (MZIs) arranged as in the scheme of Fig. 1a, which was fabricated on a standard 220 nm SiP platform by using 500 nm wide channel waveguides (see Fig. 2a). The four ports labelled as RPi consist of an array of radiating elements (grating couplers) with a mutual spacing of 127 μm to either couple a free-space optical beam into the photonic chip or to radiate a guided-wave signal out to the free space. All the balanced MZIs integrate 3 dB directional couplers with a gap of 300 nm and a length of 40 μm. Two phase shifters are integrated in each MZI by using TiN metal strips (1 μm x 100 μm) to implement amplitude- and phase-tuneable couplers. At the output port of each MZI, on-chip photodetectors (here realized through CLIPP transparent detectors by using the same TiN used for thermal tuners) are used to locally monitor the switching state of each MZI and implement automatic tuning and stabilization procedures.

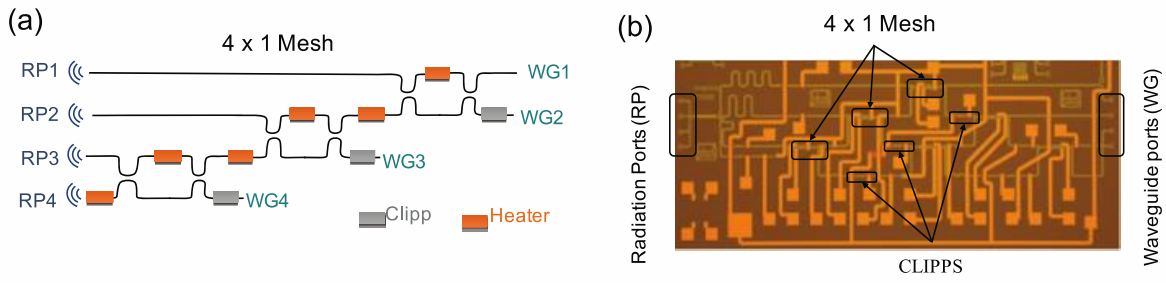


Figure 1: (a) Schematic representation of a 4 x 1 triangular mesh and (b) its implementation on a conventional silicon photonic platform. The overall footprint of the circuit is 3.7 mm by 1.5mm.

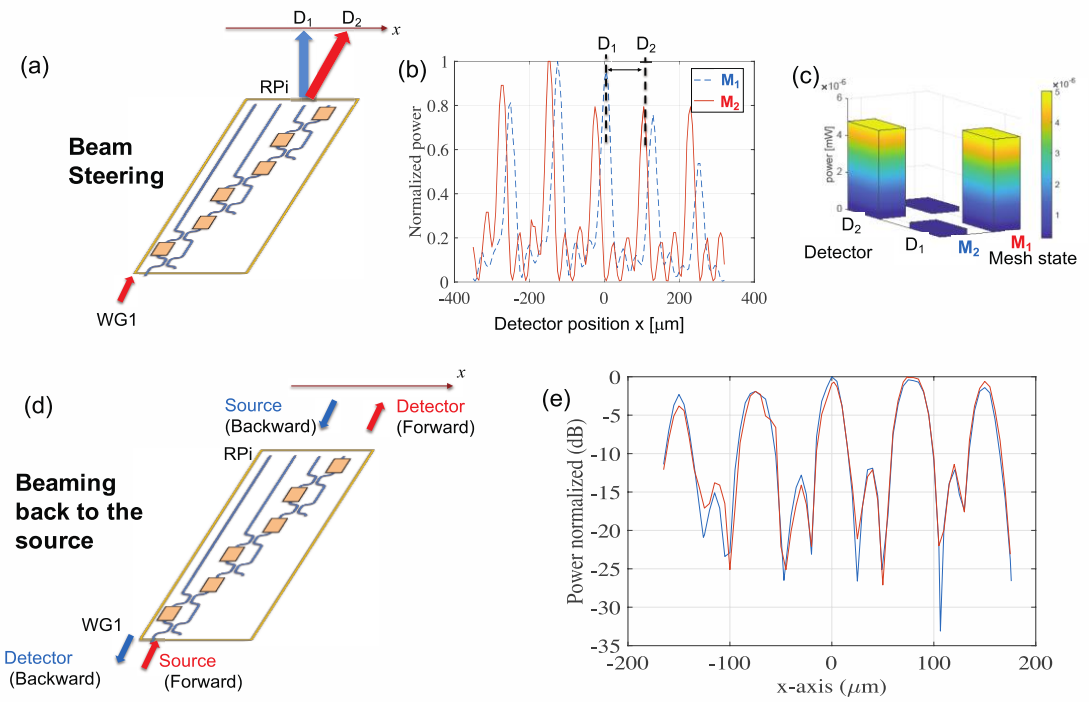


Figure 2: (a) Schematic representation of the beam steering experiment. (b) Free-space radiation pattern measured at the distance of 11 mm from the grating array RPi when the light is coupled to input port WG1 and the mesh is tuned in two different states M_1 and M_2. (c) Optical power measured by a detector (collimator) placed at positions D_1 and D_2 when the mesh is configured in states M_1 and M_2; (d) schematic representation of the "beaming back" experiment: the source and the detector are swapped to observe the behavior of the mesh when the direction of the optical propagation is reversed. (e) Comparison between the field pattern measured by a free-space detector moving along the *x*-axis when the source is coupled to port WG1 (red line) and the optical power measured by a detector coupled to port WG1 when a free space source moves along the x- axis (blue line).

The silicon photonic chip was mounted on an electronic printed circuit board hosting the drivers of the thermal tuners and the electronics for the read-out of the on-chip detectors. More details on the circuit design, fabrication technology and electronic circuit for the automatic control of the mesh can be found in [1]. All the experiments reported in this work were carried out at a wavelength of 1530 nm.

3. STEERING, COUPLING AND IDENTIFICATION OF A FREE SPACE OPTICAL BEAM

The SiP mesh was employed to manipulate free space optical beams, and, in detail, the following functionalities were demonstrated:

(a) Beam steering. As a first application we used the mesh to demonstrate the steering of a free space optical beam. To this end, we injected into the mesh an optical signal from port WG1 (see Fig. 2a) and we measured the radiation pattern generated by the grating array (RPi) for different tuning states of the mesh. The radiation pattern was measured by sampling the optical field along the transverse x-axis with a probe fiber with a resolution dx = 5 μm. Figure 2(b) shows the radiated field at a distance of (11 mm) from the output ports when the mesh is tuned in order to maximize the power received by a first detector D_1 (placed in x = 0, mesh state M_1) and by a second detector D_2 (x = 100 μm, mesh state M_2). The spacing between the maxima of the field pattern (about 150 μm, corresponding to an angular spacing of about 1°) is related to the large physical distance (127 μm) between radiating elements. Figure 2(c) shows the optical power collected by a detector (1 mm fiber collimator spaced 51.5 cm away from the chip) placed at the same angular direction of D1 and D2, when the mesh is tuned in states M_1 and M_2. Though the steering angle is rather limited, this demonstrate high resolution in the control of the radiation direction.

(b) Beaming back to the source. We also investigated the behaviour of the mesh when the direction of the optical propagation is reversed, that is when the source and the receiver are swapped. A free space beam coming from a collimator (beam waist 1 mm) at a distance of 6.5 mm from the mesh was used to shine the light on the grating array RPi while a photodiode was coupled to port WG1 (blue arrows in Fig. 2d). The blue curve in Fig. 2(e) shows the optical power at the photodiode (WG1) when the position of the collimator (free space beam) is shifted along the *x*-axis. The red curve is the power collected by the sliding collimator (receiver) when a light source is coupled to port WG1 and the grating array is used as a radiating antenna (red arrows in Fig. 2e). The good matching between the forward and backward behaviour demonstrate the capability of the mesh to beam the

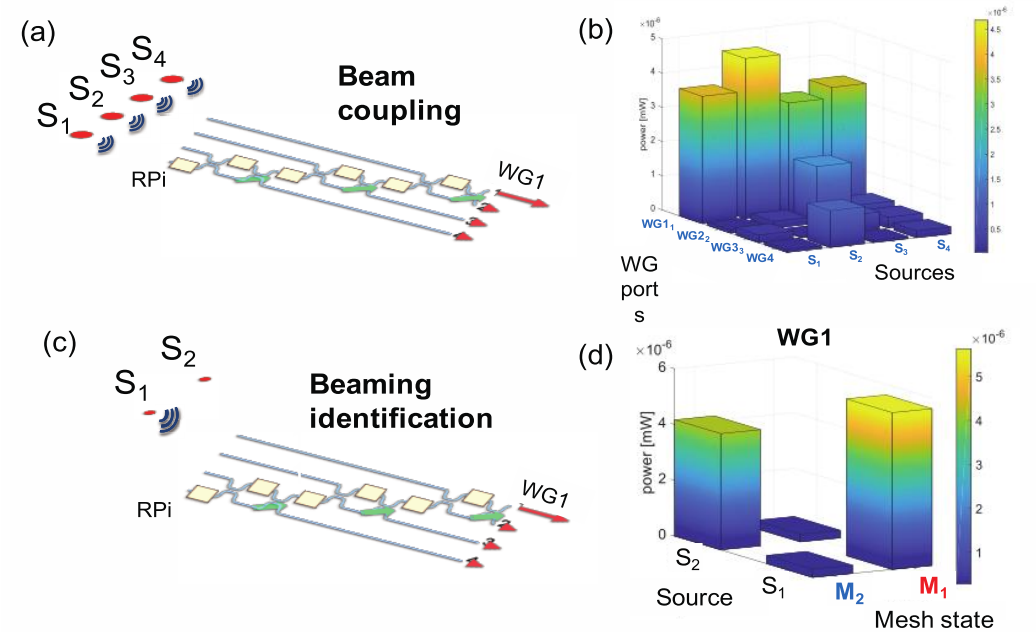


Figure 3: (a) Schematic representation of the beam coupling experiment. (b) Optical power coupled at the waveguide ports (WG_1-WG_4) when the mesh is configured to couple the light from an arbitrary free space source (S_1-S_4) to port WG1. (c) Schematic representation of the beam identification experiment. (d) Optical power coupled at port WG1 when the mesh automatically self-configures to maximize the power coming from an unknown source (S_1 or S_2).

field back toward a free-space source along an arbitrary direction, this operation not being achievable with a conventional mirror.

(c) Beam coupling and source identification. The high angular resolution of the mesh can be exploited to couple into a single-mode optical waveguide a free-space beam coming from an arbitrary direction of arrival, while minimizing the coupling from other directions. To demonstrate this concept, four free space optical beams (S_1-S_4) were simultaneously shone on the grating array RPi by using an array of 4 fibers spaced by d = 127 μm at a distance of 5.5 mm from the mesh (see Fig. 3a). When a beam for a given fiber impinges on the grating array, the mesh automatically self-configures by following a progressive tuning scheme [2] in order to maximize the transmission to port WG1. Figure 3(b) show the power coupled to the waveguide ports WGi when the mesh is configured to couple the light from S_1- S_4 to WG1. This feature implies that the mesh can automatically identify the direction from which a beam is arriving. In Fig. 3(c)-(d) a beam is coming from a source whose position is not known (it can either be S_1 or S_2). The mesh automatically self-configures to maximize the coupling to WG1 and once convergence is achieved, the phase shifts (voltages) are applied to the thermal tuners of the MZIs of the mesh identify the position of the source.

4. CONCLUSION

We demonstrate manipulation of free-space optical beams by using a 4x1 self-configuring SiP mesh. The performance of the mesh in steering, coupling and identifying free-space beams can be improved by optimizing the design of the radiating elements, whose number can be scaled up without impairing the progressive self-configuration procedure employed for the tuning of the mesh. Applications are envisioned to more advanced free-space optical processing, including phase front reconstruction, beaming through scattering media and chip-to-chip free space communications.

This work was partially supported by the European Commission through the H2020 project STREAMS (grant 688172) and by Fondazione Cariplo through the project ACTIO (grant 2016-0881).

REFERENCES

[1] D. Pérez, et al., "Toward Programmable Microwave Photonics Processors," J. Lightwave Technol. 36, 519-532 (2018)

[2] Annoni, A. et al. Unscrambling light—automatically undoing strong mixing between modes. Light: Science & Applications 6, e17110 (2017).

[3] X. Qiang, et al., "Large-scale silicon quantum photonics implementing arbitrary two-qubit processing," Nat. Photonic, vol. 12, pp. 534–539 (2018)

[4] Y. Shen er al., "Deep learning with coherent nanophotonic circuits," Nat. Photonics, vol. 11, pp, 441–446 (2017)

Exploring titanium dioxide as a new photonic platform

Manon Lamy, Marie-Maxime Mennemanteuil, Jean-Claude Weeber, Christophe Finot, Kamal Hammani
Laboratoire Interdisciplinaire Carnot de Bourgogne (ICB), UMR 6303 CNRS - Université Bourgogne Franche-Comté, 9 avenue Alain Savary, BP 47870, 21078 Dijon Cedex, France
e-mail: Kamal.Hammani@u-bourgogne.fr

ABSTRACT

We report the development of titanium dioxide-based waveguides for applications in the near- and mid-infrared. Thanks to embedded metal grating couplers, we demonstrate error free 10 Gbit/s optical transmissions at 1.55 and 2 µm. We also demonstrate octave-spanning supercontinuum in cm-long waveguides. We explore the way to improve such waveguides through optimized fabrication process.

Keywords: Titanium Dioxide waveguides, Integrated optical materials, Optical Communications, Supercontinuum generation, Nonlinear integrated optics

1. INTRODUCTION

Since the 1980s, it becomes clear that the speed of electronics would limit the information capacity. Therefore, integrated photonic devices were strongly desirable to avoid electronic circuits and to allow low footprint and low power consumption. Naturally, main efforts have focused on the silicon-on-insulator technology. The choice of SOI has been driven by the high nonlinearity of silicon and its compatibility with low-cost large-scale production using CMOS infrastructure. However, its strong two photon absorption (TPA) at telecommunication wavelength is still an issue. Therefore, to avoid this limitation, one could find another nonlinear platform.

Various materials have been investigated: other Silicon-based platform such as Silicon Germanium [1] or silicon nitride [2], III-V material or chalcogenides [3]. Each material provides specific advantages but also strong potential limitations. The perfect material is still to be discovered but it is true that in recent years silicon nitride has emerged as a very promising and versatile candidate.

Here, we plan to explore another platform: the titanium dioxide (TiO_2). This material, well known for its photocatalytic properties or its performance for solar cells, remains largely unexplored in the field of nonlinear photonics. Compared to silicon nitride, the titanium dioxide exhibits similar nonlinear index ($\sim 0.2 \times 10^{-18}$ m²/W) as well as higher linear refractive index (typically 2.4 versus 2.0 for Si_3N_4). This is critical because it leads to stronger confinement and therefore to higher effective nonlinearities. It has also an easier deposition process. Here, we show that this platform can be used for optical telecommunication and confirm the strong nonlinear potential.

2. TITANIUM DIOXIDE STRUCTURES FOR OPTICAL COMMUNICATIONS

In this first part, we present titanium dioxide waveguides operating at 1.55 µm and 1.98 µm wavelengths. After having described the design of the TiO_2 devices we detail experimental set-ups and validation of the components for error-free transmission of a 10 Gb/s on-off keying signal at the two different spectral regions.

2.1 Design and fabrication of the couplers and the waveguides

Whatever the platform used, a crucial step is always to efficiently inject the light into the device. Basically, there are two main ways to couple light from an optical fiber to a photonic waveguide: the end-fire coupling (also known as butt-coupling) or grating coupling. Thanks to the ease of TiO_2 deposition, we have been able to consider embedded metal grating couplers (Fig. 1(a)) allowing etching free process. Recently, such metal grating couplers have been used to demonstrate high coupling efficiencies [4]. Unlike previous studies, we considered a metal (Au) grating buried between two TiO_2 layers on a glass substrate. This provides an additional degree of freedom and better coupling efficiency [5].

We optimized the geometric parameters with 2D numerical simulations using a commercial finite element-based software, namely COMSOL Multiphysics, to target the best performance, around 1.55 µm wavelength on one side and around 2.0 µm on the other side, with an incident angle of 30° fixed by the experimental set-up constraints. The simulated source has a TM polarization for the considered embedded gratings. For the two considered spectral bands, the best set of parameters is obviously different.

Then the devices have been fabricated combining widely-spread techniques such as reactive DC magnetron sputtering to deposit titanium dioxide layers, electron beam lithography, thermal evaporation and reactive-ion etching. The fabricated devices have the following measured parameters, respectively at 1.55 µm and at 2 µm: a top layer thickness h_{top} of 189 nm and 235 nm, a grating period Λ of 1375 nm and 1900 nm and a grating line

width w_1 of about 610 nm and 630 nm. For the whole devices, the bottom layer thickness h_{bottom} is 69 nm and the gold thickness h_{Au} is 56 nm.

2.2 Test of the devices coupling efficiency

Before transmitting an optical signal in the titanium dioxide waveguides, we have measured their total losses. The structures under test should ideally present a good total coupling efficiency to enable high speed optical transmissions at 1.55 µm and 1.98 µm. Their losses are measured with a set-up composed of two optical focusers based on lensed fibers. IR and visible cameras allow us to adjust the focusers onto the grating couplers to optimize the injection and collection of the light. A powermeter and optical spectrum analyzer allow us to optimize the focusers adjustment and record the output light.

At 1550 nm, we have measured losses as low as - 8dB per facet with a -3dB transmission bandwidth covering the whole C-band with a fair agreement with numerical simulations as shown in Fig. 1(b). At 2000 nm, the coupling losses per facet reach - 10 dB. The difference between the numerical simulations and the efficiency measured experimentally can be in a large extend assigned to discrepancies between the targeted values and the values reached at the end of the various fabrication processes. Future improvements may involve metal mirror under the gratings [9] or parabolic gratings [10]. However, the coupling efficiencies are already sufficient for the transmission of a coded signal.

2.3 Transmission at 1.55 µm and at 1.98 µm

For both wavelengths, a 10 Gb/s signal coded through a 2^{31} pseudo random bit sequence (PRBS) generator is transmitted through the waveguides and a bit error tester or a high speed sampling oscilloscope to image eye diagrams are used as diagnostic tools of the transmission quality (show in insets of Fig. 1(b) and (c)) .

At 1.55 µm, the figure 1(b) shows wide-opened eye diagrams meaning a transmission without any degradation confirmed by an error free BER measurement (not shown here). At 2 µm, the results on BER between the back-to-back configuration and with the presence of the waveguides are very similar [6].

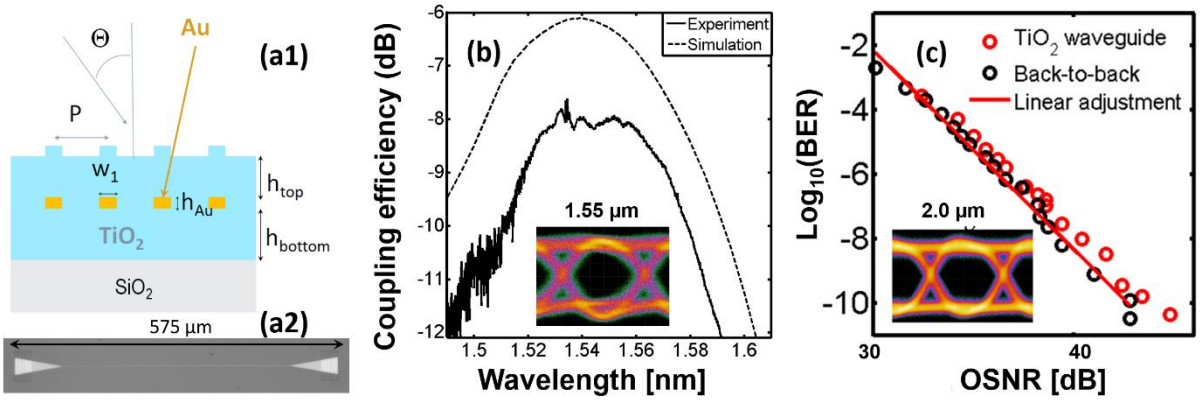


Figure 1. (a1) sketch of the embedded metal grating in titanium dioxide layer (side view). (a2) Top view of 1.5 µm-wide waveguide with visible camera. (b) Coupling efficiency per facet of embedded grating coupler as a function of the injected wavelength. The experimental results are compared with numerical simulations. The inset shows eye diagram of 10Gb/s signal transmitted into the waveguide. (c) BER measurement as a function of the OSNR. The inset shows the typical eye diagram after the waveguide at 2 µm.

3. TITANIUM DIOXIDE WAVEGUIDES FOR SUPERCONTINUUM GENERATION

To become an interesting photonic platform for nonlinear functionalities, a material has to exhibit a strong Kerr coefficient. A way to stress the nonlinear potential of TiO_2 waveguides is to evaluate its potential in the context of supercontinuum generation [7].

Contrary to previous waveguides, here we consider thicker TiO_2 layers of 450 nm that are deposited on a 2" silicon wafer, covered with 2 µm of silica, still by reactive direct current magnetron sputtering of a 99.9% pure titanium target under argon and oxygen-controlled atmosphere. Then, 2.2 cm-long ridge waveguide having about 1.5 µm is patterned thanks to an UV lithography. After the reactive ion etching, the residual mask is stripped from the waveguides. Details of the structure used in the following experiments are presented in Fig. 2(a) as well as the dispersion profile of the fundamental TE mode (Fig. 2(b)).

The input pulses are provided by a femtosecond laser source centered at 1560 nm with a peak power up to a few tens of kW. Due to the length of standard anomalous fiber between the fs-laser output and the TiO_2 waveguide, the central wavelength of the pulse is shifted toward 1640 nm. In order to optimize the light injection through butt-

coupling, two 1-mm long tapers have been included in the TiO_2 device. The broadest spectrum we obtained is plotted in Fig. 2(c1) along with the input pump spectrum. An octave-spanning supercontinuum is generated from 1050 nm up to 1910 nm, which represents an improvement by much more than one order of magnitude compared to [8]. The third harmonic is also generated into the waveguide so that visible light is also clearly observed by the naked eye as can be seen from the picture taken from the top of the waveguide (Fig. 2(c2)).

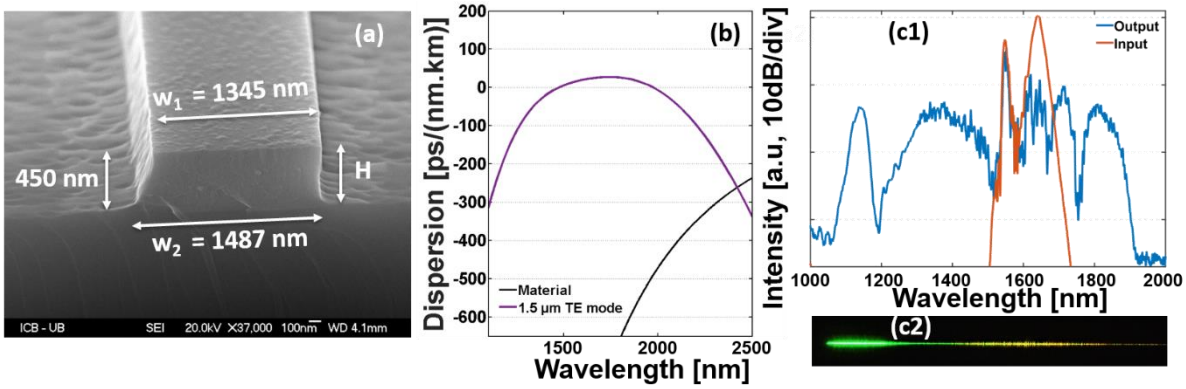


Figure 2. (a) Scanning Electron Microscope image of the cleaved strip waveguide (b) Dispersion properties for the fundamental $TE_{0,0}$ mode. (c1) Optical supercontinuum obtained at the output of the waveguide (solid blue line) compared to the input pulse spectrum (red solid line). (c2) Image of the emitted visible light from the waveguide (total length ~ 6.5 mm).

4. CONCLUSIONS

We have demonstrated error-free transmission of high bit rate signals through titanium dioxide waveguides. A new design of embedded metal grating has been tested for coupling / decoupling the signal in the C-band as well as around 2 µm. Such embedded configuration was made possible thanks to the ease of fabrication of this material. In order to confirm the nonlinear potential of the TiO2, we have demonstrated the generation of an octave spanning supercontinuum.

These studies clearly demonstrate that titanium dioxide can be an alternative platform for integrated photonic. However, to date, the main drawback remains the propagation losses. We are currently working on different ways to improve the fabrication mainly regarding the etching that has been identify as the main origin of losses since it causes strong roughness of sidewall [9].

ACKNOWLEDGEMENTS

This work was supported by the European Union within the framework of the operational Program FEDER-FSE Bourgogne 2014/2020, by the Région Bourgogne (Pari Photcom) and by the French "Investissements d'Avenir" program, project ISITE-BFC (contract ANR-15-IDEX-0003).

REFERENCES

[1] Hammani, K., *et al.*, Optical properties of silicon germanium waveguides at telecommunication wavelengths. *Opt. Express*, **21**(14). pp. 16690-16701, 2013.

[2] Porcel, M.A.G., *et al.*, Two-octave spanning supercontinuum generation in stoichiometric silicon nitride waveguides pumped at telecom wavelengths. *Optics Express*, **25**(2). pp. 1542-1554, 2017.

[3] Lamont, M.R.E., *et al.*, Supercontinuum generation in dispersion engineered highly nonlinear (γ = 10 /W/m) As2S3 chalcogenide planar waveguide. *Optics Express*, **16**(19). pp. 14938-14944, 2008.

[4] Scheerlinck, S., *et al.*, Efficient, broadband and compact metal grating couplers for silicon-on-insulator waveguides. *Opt. Express*, **15**(15). pp. 9625-9630, 2007.

[5] Lamy, M., *et al.*, Broadband metal grating couplers embedded in Titanium dioxide waveguides *Opt. Lett.*, **42**(14). pp. 2778-2781, 2017.

[6] Lamy, M., *et al.*, Demonstration of High-Speed Optical Transmission at 2 µm in Titanium Dioxide Waveguides. *Applied Sciences*, **7**(6). pp. 631, 2017.

[7] Hammani, K., *et al.*, Octave Spanning Supercontinuum in Titanium Dioxide Waveguides. *Applied Sciences*, **8**(4). pp. 543, 2018.

[8] Evans, C.C., *et al.*, Spectral broadening in anatase titanium dioxide waveguides at telecommunication and near-visible wavelengths. *Opt. Express*, **21**(15). pp. 18582-18591, 2013.

[9] Evans, C.C., C. Liu, and J. Suntivich, Low-loss titanium dioxide waveguides and resonators using a dielectric lift-off fabrication process. *Opt. Express*, **23**(9). pp. 11160-11169, 2015.